

# BAINITE IN STEELS

THEORY AND PRACTICE

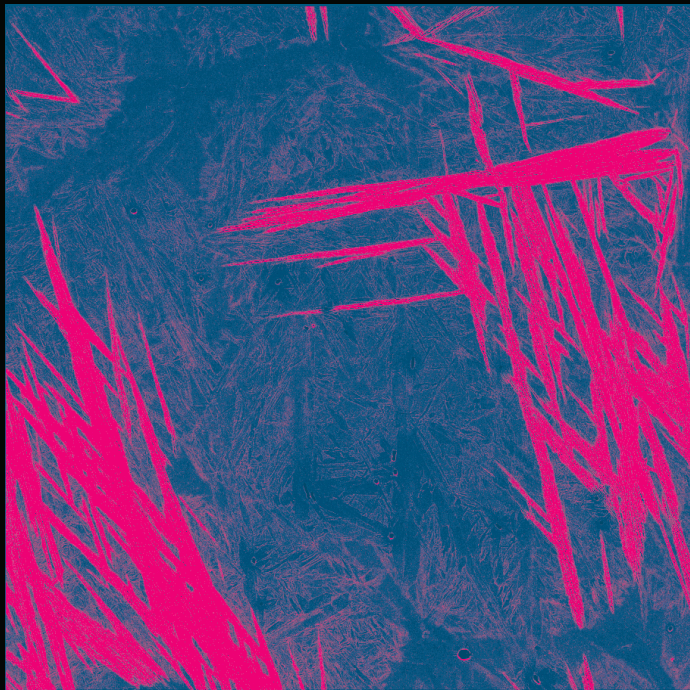
---

THIRD EDITION

---

H. K. D. H. BHADESHIA

---



# **BAINITE IN STEELS**



---

# **BAINITE IN STEELS**

## **Theory and Practice**

**Third edition**

---

**H. K. D. H. Bhadeshia**  
University of Cambridge and POSTECH



Copyright ©2015, H. K. D. H. Bhadeshia.

The author has asserted his moral right.  
First edition published 1992; second edition published 2001.

Published by Maney Publishing on behalf of the Institute of Materials, Minerals & Mining

Maney Publishing is the trading name of W. S. Maney & Son Ltd  
Maney Publishing, Suite 1C, Joseph's Well, Hanover Walk, Leeds LS3 1AB, UK  
[www.maneypublishing.com](http://www.maneypublishing.com)

No part of this publication may be reproduced, stored in a retrieval system, or transmitted in any form or by any means, electronic, mechanical, photocopying, recording, scanning, or otherwise, without either the prior written permission of the Publisher, or appropriate authorization.

Limit of Liability/Disclaimer of Warranty: While the publisher and author have used their best efforts in preparing this book, they make no representations or warranties with respect to the accuracy or completeness of the contents of this book and specifically disclaim any implied warranties of merchantability or fitness for a particular purpose. No warranty may be created or extended by sales representatives or written sales materials. The advice and strategies contained herein may not be suitable for your situation. You should consult with a professional where appropriate. Neither the publisher nor author shall be liable for any loss of profit or any other commercial damages, including but not limited to special, incidental, consequential, or other damages.

Trademark notice: Product or corporate names may be trademarks or registered trademarks, and are used only for identification and explanation, without intent to infringe.

Maney Publishing ISBN: 978-1-909662-74-2  
Maney Publishing stock code: B0819  
Printed and bound by Charlesworth Press, Wakefield, UK

# CONTENTS

---

Preface	xv
Acknowledgments	xvii
Acronyms	xix
<b>Nomenclature</b>	<b>xx</b>
<b>1 Introduction</b>	<b>1</b>
1.1 The Discovery of Bainite	2
1.2 The Early Research	4
1.2.1 Crystallography	5
1.2.2 The Incomplete Reaction Phenomenon	5
1.2.3 Carbon Redistribution	6
1.2.4 Thermodynamics	9
1.2.5 Paraequilibrium	10
1.2.6 Kinetics	12
1.3 Bainitic Steels: Industrial Practice	14
1.4 Summary of the Early Research	15
<b>2 Bainitic Ferrite</b>	<b>17</b>
2.1 Sheaves of Bainite	17
2.1.1 Morphology	17
	<b>v</b>

2.1.2	Thickness of bainite plates	21
2.1.3	Stereology	23
2.2	Dislocation Density	24
2.2.1	Quantitative Estimation of Dislocation Density	26
2.3	Chemical Composition	27
2.3.1	Substitutional Alloying Elements	27
2.3.2	Interstitial Alloying Elements	31
2.4	Crystallography	33
2.4.1	Crystallography: Block Size, Austenite Grain Boundary	39
2.4.2	Autocatalytic Nucleation	40
2.5	Crystallographic Theory	42
2.5.1	Application to Bainite	43
2.5.2	High-Resolution Studies of the Shape Change	46
2.5.3	The Shape Change: Further Considerations	48
2.5.4	Shape Change and the Superledge Mechanism	52
2.5.5	The Structure of the Interface	52
2.5.6	The Crystallography of a Lath of Bainite	54
2.6	Unit Cell Symmetry	55
2.6.1	Symmetry of Interstices	55
2.6.2	Tetragonality of Bainitic Ferrite	56
2.7	Microstructure of Bainite: The Midrib	58
2.8	Summary	59

### **3 Carbide Precipitation 61**

3.1	Upper Bainite	61
3.2	Lower Bainite	64
3.2.1	Precipitation within Lower Bainitic Ferrite	64
3.2.2	Precipitation between Lower Bainitic Ferrite Platelets	67
3.3	Kinetics of Carbide Precipitation	68
3.3.1	Partitioning and Distribution of Carbon	68
3.3.2	Kinetics of Precipitation from Residual Austenite	70
3.3.3	Kinetics of Precipitation within Bainitic Ferrite	72
3.4	Crystallography of Carbide Precipitation in Bainite	75
3.4.1	Cementite: Orientation Relationships	75
3.4.2	The Habit Plane of Cementite	76
3.4.3	Three-Phase Crystallography	76
3.4.4	Interphase Precipitation	77
3.4.5	Relief of Strain Energy	79
3.4.6	Epsilon-Carbide	79
3.4.7	Eta- and Chi-Carbides	81
3.5	Chemical Composition of Bainitic Carbides	83
3.6	Summary	85

<b>4</b>	<b>Tempering of Bainite</b>	<b>87</b>
4.1	Introduction	87
4.2	Tempering Kinetics	90
4.3	Tempering of Steels Containing Austenite	90
4.3.1	Redistribution of Substitutional Solutes	92
4.3.2	Decomposition of Austenite	93
4.3.3	Tempering of Nanostructured Bainite	95
4.4	Coarsening of Cementite	98
4.5	Secondary Hardening and the Precipitation of Alloy Carbides	99
4.6	Changes in the Composition of Cementite	100
4.6.1	Remanent Life Prediction	102
4.6.2	Theory for Carbide Enrichment	103
4.6.3	Effect of Carbon on Carbide Enrichment	105
4.7	Low-Temperature Tempering of Mixed Microstructures	106
4.8	Sequence of Alloy Carbide Precipitation	106
4.8.1	Effect of Starting Microstructure on Tempering Reactions	111
4.9	Changes in the Composition of Alloy Carbides	111
4.10	Precipitate-free Zones	112
4.11	Precipitation Hardening with Copper	113
4.12	Summary	115
<b>5</b>	<b>Thermodynamics</b>	<b>117</b>
5.1	Deviations from Equilibrium	117
5.2	Chemical Potential	118
5.3	Stored Energy due to Transformation	120
5.4	Thermodynamics of Growth	122
5.4.1	Substitutional Solutes during Growth	122
5.4.2	Interstitial Solutes during Growth	122
5.4.3	Approach to Equilibrium	127
5.5	Quench and Partitioning	128
5.6	Summary	129
<b>6</b>	<b>Kinetics</b>	<b>131</b>
6.1	Thermodynamics of Nucleation	131
6.1.1	Transformation-Start Temperature	132
6.1.2	Evolution of the Nucleus	135
6.2	Possible Mechanisms of Nucleation	138
6.3	Bainite Nucleation	141
6.4	Empirical Methods for the Bainite-Start Temperature	142
6.5	The Nucleation Rate	143
6.5.1	Grain Boundary Nucleation	144

6.6	Growth Rate	144
6.6.1	Theory for the Lengthening of Plates	144
6.6.2	Growth Rate of Sheaves of Bainite	148
6.6.3	Growth Rate of Sub-Units of Bainite	148
6.6.4	Solute Drag	150
6.7	Partitioning of Carbon from Supersaturated Bainitic Ferrite	153
6.8	Growth with Partial Supersaturation	154
6.8.1	Stability	155
6.8.2	The Interface Response Functions	157
6.8.3	Data on Transformation with Partial Supersaturation	160
6.8.4	Summary	161
6.9	Cooperative Growth of Ferrite and Cementite	161
6.10	Overall Transformation Kinetics	162
6.10.1	Isothermal Transformation	162
6.10.2	Incorrect formulation of incubation time	164
6.10.3	Mechanistic Formulation of the Avrami Equation	165
6.10.4	Austenite Grain Size Effects	167
6.10.5	Anisothermal Transformation Kinetics	167
6.11	Simultaneous Transformations	169
6.11.1	Special Cases	169
6.11.2	Precipitation in Secondary Hardening Steels	170
6.11.3	Time-Temperature-Transformation Diagrams	171
6.11.4	Continuous Cooling Transformation Diagrams	173
6.11.5	Boron, Sulphur and the Rare Earth Elements	176
6.11.6	Niobium and hardenability	179
6.12	Superhardenability	181
6.13	Effect of Chemical Segregation	183
6.14	Martensitic Transformation in Partially Bainitic Steels	185
6.14.1	Autocatalysis	187
6.15	Phase Field Models	190
6.15.1	Introduction to Phase Fields	190
6.15.2	Phase Field Simulation of Bainite	192
6.16	Summary	194
<b>7</b>	<b>Upper and Lower Bainite</b>	<b>195</b>
7.1	Matas and Hehemann Model	195
7.2	Quantitative Model	197
7.2.1	Time to Decarburise Supersaturated Ferrite	197
7.2.2	Kinetics of Cementite Precipitation	197
7.2.3	Quantitative Estimation of the Transition Temperature	199
7.2.4	Comparison of Theory and Experimental Data	200
7.3	Mixed Microstructures by Isothermal Transformation	203

7.4	Other Consequences of the Transition	204
7.5	Comparison with Tempering of Martensite	204
7.6	Summary	205
<b>8</b>	<b>Stress and Strain Effects</b>	<b>207</b>
8.1	Mechanical Driving Force	208
8.2	The $B_d$ Temperature	211
8.3	General Observations	212
	8.3.1 Externally Applied Stress	212
	8.3.2 Internally Generated Stress	213
8.4	Effect on Microstructure	214
	8.4.1 Extent of Variant Selection	215
8.5	Effect of Hydrostatic Pressure	217
8.6	Mechanical Stability of Retained Austenite	218
8.7	Transformation under Constraint: Residual Stresses	220
8.8	Anisotropic Strain due to Transformation Plasticity	223
	8.8.1 Interactions between Variants	225
8.9	Influence of Plastic Strain	225
8.10	Stress-Affected Carbide Precipitation	226
8.11	Plastic Deformation and Mechanical Stabilisation	228
	8.11.1 Theoretical Basis	228
	8.11.2 Experimental Evidence	230
	8.11.3 Transformation from Recovered Austenite	235
	8.11.4 Technological Implications of Mechanical Stabilisation	235
8.12	Summary	236
<b>9</b>	<b>From Bainite to Austenite</b>	<b>239</b>
9.1	Heating a Mixture of Austenite and Upper Bainitic Ferrite	240
	9.1.1 One-Dimensional Growth from a Mixture of Austenite and Bainitic Ferrite	244
	9.1.2 Estimation of the Parabolic Thickening Rate Constant	245
9.2	Anisothermal Transformation	247
9.3	Heating a Mixture of Cementite and Bainitic Ferrite	247
9.4	Irradiation-Induced Rapid Heating	249
9.5	Summary	249
<b>10</b>	<b>Acicular Ferrite</b>	<b>251</b>
10.1	General Characteristics and Morphology	251
10.2	Mechanism of Growth	254
10.3	Mechanism of Nucleation	257
10.4	Nucleation and The Role of Inclusions	258
	10.4.1 Aluminium and Titanium Oxides	262

10.4.2	Sulphur	263
10.4.3	Phosphorus	266
10.4.4	Nitrogen, Titanium and Boron	266
10.4.5	Boron and Hydrogen	269
10.4.6	Stereological Effects	271
10.5	Effect of Inclusions on the Austenite Grain Size in Welds	272
10.6	Influence of Other Transformation Products	272
10.6.1	Some Specific Effects of Allotriomorphic Ferrite	273
10.7	Lower Acicular Ferrite	277
10.8	Stress-Affected Acicular Ferrite	278
10.9	Effect of Strain on the Acicular Ferrite Transformation	280
10.10	Inoculated Acicular Ferrite Steels	280
10.10.1	Structural Steel	280
10.10.2	Acicular Ferrite Forging Steels	282
10.10.3	Steelmaking Technology for Inoculated Alloys	283
10.11	Summary	285
<b>11</b>	<b>Other Morphologies of Bainite</b>	<b>287</b>
11.1	Granular Bainite	287
11.2	Inverse Bainite	289
11.3	Columnar Bainite	290
11.4	Alloy Pearlite	291
11.5	Grain Boundary Lower Bainite	292
11.6	Coalesced Bainite	293
11.6.1	Mechanism	295
11.6.2	Coalesced Bainite in Weld Metals	297
11.7	Spiky Pearlite	299
11.8	Summary	302
<b>12</b>	<b>Mechanical Properties</b>	<b>303</b>
12.1	General Introduction	303
12.2	The Strength of Bainite	304
12.2.1	Hardness	304
12.2.2	Tensile Strength	307
12.2.3	Effect of Austenite Grain Size	308
12.2.4	Effect of Tempering on Strength	308
12.2.5	The Strength Differential Effect	309
12.2.6	Temperature Dependence of Strength	310
12.3	Ratio of Proof Stress to Ultimate Tensile Strength	310
12.4	Ductility	313
12.4.1	Ductility: The Role of Retained Austenite	314
12.5	Impact Toughness	315

12.5.1	Fully Bainitic Structures	317
12.6	Fracture Mechanics Approach to Toughness	318
12.6.1	Microstructural Interpretation of fracture toughness	319
12.6.2	Cleavage Path and Crystallography	323
12.6.3	Cleavage Crack Initiation	324
12.7	Temper Embrittlement	324
12.7.1	650°C Reversible Temper Embrittlement	324
12.7.2	300→350 °C Temper Embrittlement	325
12.7.3	300→350 °C Tempered-Martensite Embrittlement	326
12.8	Fatigue Resistance of Bainitic Steels	327
12.8.1	Fatigue of Smooth Samples	328
12.8.2	Fatigue Crack Growth Rate	330
12.8.3	Two-Parameter Approach to Growth Rate	334
12.8.4	Arresting Fatigue Cracks	334
12.8.5	Fatigue in Laser Hardened Samples	335
12.8.6	Fatigue and Retained Austenite	336
12.8.7	Fatigue and Cementite	336
12.8.8	Corrosion Fatigue	336
12.8.9	Gigacycle Fatigue Tests	338
12.8.10	Rolling Contact Fatigue	339
12.9	Stress Corrosion Resistance and Hydrogen	341
12.10	Delayed Fracture	344
12.11	The Creep Resistance of Bainitic Steels	345
12.11.1	Heat Treatment	348
12.11.2	$2\frac{1}{4}$ Cr1Mo Type Steels	349
12.11.3	1CrMoV Type Steels	349
12.11.4	$\frac{1}{4}$ CrMoV Type Steels	351
12.11.5	Enhanced Cr-Mo Bainitic Steels	351
12.11.6	Tungsten Strengthened Steels	352
12.11.7	Regenerative Heat Treatments	354
12.11.8	Comparison with Martensitic Creep-Resistant Steels	355
12.11.9	Transition Metal Joints	357
12.12	Reduced-Activation Steels	358
12.13	Steels with Mixed Microstructures	361
12.14	Summary	364
<b>13</b>	<b>Modern Bainitic Steels</b>	<b>367</b>
13.1	Alternatives to the Ferrite-Pearlite Microstructure	368
13.2	Strength	370
13.3	Bainitic Steels	371
13.4	Controlled-Rolling of Bainitic Steels	373
13.4.1	Crystallographic Texture	375

13.5	Rapidly Cooled Control-Rolled Steels	378
13.5.1	Pipeline and Plate Steels	378
13.5.2	Process Parameters	379
13.5.3	Chemical Segregation	382
13.5.4	High-temperature processed pipe steel	382
13.6	Steels with High Formability	387
13.6.1	TRIP-Assisted Steels	389
13.6.2	$\delta$ -TRIP Steels	412
13.6.3	Weldability of TRIP-assisted steels	414
13.6.4	Dieless-Drawn Bainitic Steels	416
13.7	Ultra-Low-Carbon Bainitic Steels	418
13.8	Bainitic Forging Steels	421
13.9	High Strength Bainitic Steels without Carbides	423
13.10	Thermomechanically Processed High-Strength Steels	429
13.10.1	Ausformed Bainitic Steels	429
13.10.2	Strain Tempered Bainitic Steels	430
13.10.3	Creep Tempering of Bainite	430
13.11	Flash Processing	432
13.12	Bainite in Rail Steels	433
13.12.1	Track Materials	433
13.12.2	Silicon-rich Carbide-free Bainitic Rail Steels	436
13.12.3	Wheels	437
13.12.4	Bearing Alloys	438
13.13	Bainitic Cast Irons	442
13.13.1	Austempered Ductile Cast Irons	443
13.13.2	Abrasive Wear of Bainitic Cast Irons	448
13.13.3	Erosion of Austempered Ductile Cast Iron	450
13.13.4	Wear of Mixed Microstructures	451
13.14	Bainitic Cast Steels	451
<b>14</b>	<b>Nanostructured Bainite</b>	<b>455</b>
14.1	Introduction	455
14.2	Nanostructure	456
14.3	Alloy Design	458
14.4	Crystallography and Surface Relief	461
14.5	Distribution of Solutes	462
14.6	Origin of Elementary Mechanical Properties	465
14.6.1	Evolution of Hardness	467
14.6.2	Compression Tests	467
14.6.3	Charpy Impact Energy	468
14.7	Impulse Loading	469
14.8	Fatigue	471

14.9	Acceleration of Transformation	473
14.9.1	Compromise Between Strength and Speed	475
14.9.2	Cyclic Heat Treatment	475
14.10	Case-Hardening and Cladding	477
14.11	Powder Metallurgical Nanostructured Bainite	479
14.12	Spheroidisation of Nanostructured Bainite	479
14.13	Wear of Nanostructured Bainite	482
14.13.1	Dry Sliding-Friction	482
14.13.2	Three body Abrasion	485
14.14	Aspects of Corrosion	487
14.15	Hydrogen Migration Through Nanostructure	487
14.16	Low-Carbon Nanostructured Bainite	488
14.17	Welding	490
14.18	Summary	491
<b>15</b>	<b>Other Aspects</b>	<b>495</b>
15.1	Bainite in Iron and its Substitutional Alloys	495
15.2	The Weldability of Bainitic Steels	496
15.3	Electrical Resistance	497
15.4	Internal Friction	498
15.5	Internal Stress	499
15.6	Sound Velocity	500
15.7	Bainite in Iron-Nitrogen Alloys	501
15.8	Effect of Hydrogen on Bainite Formation	502
15.9	Magnetically-Induced Bainite	503
15.10	Characterisation of Bainite	503
15.10.1	Optical Microscopy and Hardness	503
15.10.2	Dilatometry	505
15.10.3	Atomic Force Microscopy	506
15.10.4	X-ray Diffraction and Retained Austenite	506
15.10.5	Electron Backscattered Diffraction	507
15.10.6	Kernel Average Misorientation	507
<b>16</b>	<b>The Transformations in Steel</b>	<b>509</b>
16.1	Key Characteristics of Transformations in Steels	512
16.2	Notes Related to Table 16.1	514
	<b>Bibliography</b>	<b>515</b>
	Author index	571
	Subject index	586



## PREFACE

---

The choreography of atoms when one crystal structure changes into another is seminal in determining all aspects of the shape, composition, state, time dependence and properties of the product. The appeal of bainite is in the elegance of the coordinated dance that the atoms perform, one that is visibly moving to watch, as massive upheavals develop on the surfaces of transforming specimens. In the absence of scale, these could be mistaken for the formation of a mighty range of mountains. It is these displacements that shatter illusions about randomness. And the upheavals are accompanied by rumbles, the acoustic signals that indicate a relaxation time of just  $10^{-5}$  s. More than anything else, these are the features of the bainite transformation that keep steels ahead of any other structural material and serve to inspire young and old scientists to dig ever deeper into the mysteries of reactions in the solid-state.

We can now see more atoms than ever before, both small and large. It is simple then to conclude that the interface between bainitic ferrite and austenite is clean, and therefore, that the influence of solutes on the transformation is merely to alter the relative thermodynamic stability and strength of the parent and product phases. Making the atoms visible has revealed a remarkable, possibly monumental, discovery that the ferrite retains a large excess of interstitial atoms in solid solution. Not just at defects, but in solid solution. The symmetry of the lattice then changes and certain properties become anisotropic whereas in the cubic form they are not.

Steels are often processed to encourage a non-random distribution of crystal orientations in order to enhance particular shaping technologies that exploit the anisotropic properties of textured materials. On the other hand, the variation in mechanical properties with the orientation of the test specimen remains a sore in the application of bainitic steels for transmission pipelines.

Bainite has been probed with instruments that cost billions to install and which produce vast quantities of data. This has shown that the austenite remains calm at every point prior to the beginning of transformation, after which it loses all semblance of uniformity. The description of the remaining austenite then depends on the size and shape of the region explored. Such graded structures could in principle be engineered to optimise properties.

A new mechanism of coarsening has emerged, one that does not place emphasis on interfacial energy and does not require diffusion. Plates that are similarly oriented in space touch and merge, leaving behind faint vestiges of their original boundaries. This is a coalescence process and its boundary conditions have been established.

All-in-all, the subject can no longer be regarded as hazy. In the light of the totality of evidence available, it would be lazy to call bainite “controversial”. The theory of the transformation as described in this book is sufficiently well-established to be applied routinely in the design and manufacture of alloys with previously unheard of combinations of properties. Who would have thought that it were possible to create a material that contains 100 million square metres of hard interfaces within a metre cube, without the intervention of deformation or rapid processing? And that such a structure would have the intricacy necessary to resist the infusion of hydrogen?

This preface gives no more than an inkling of what is to follow in the pages ahead. There is much more to say about bainite – this 3rd edition is about 40% larger to cope with the developments over the last fifteen years or so, not just in the theory of transformations but also in the exploration of more complex properties and combination of properties. To quote Miracle (2015), “there is much work between measuring a single attractive property in a single alloy to demonstrating credibility for a particular application”. A number of entirely new steel classes are covered in the modern steels bit, some of which admittedly fall into the category of concept cars, i.e. they fire the imagination but may or may not become folklore. With one exception, I have kept the arrangement of chapters to be the same as in previous editions.

The book is intended for those who have a deep interest in steels, alloy design and transformations in the solid state. For the committed scholar, the first and second editions remain available.

H. K. D. H. BHADSHIA

*Cambridge, U.K. and Pohang, Republic of Korea, 2015*

## ACKNOWLEDGMENTS

---

I remain grateful to many who helped me enormously when I first started this adventure: this includes the late Professors J. W. Christian, M. Cohen, Sir Robert Honeycombe, C. M. Wayman. These were amongst the giants of metallurgy and yet spared their time in nurturing others. My colleagues did a lot to shape my ideas and continue to do so: Dr S. A. David, Professor D. V. Edmonds, Dr H. Harada, Professor D. Hull, Professor C. J. Humphreys, Professor J. F. Knott and Professor G. B. Olson.

I have over the years enjoyed the privilege of working with many younger scientists who have contributed to my understanding of bainite. I will list the names below, but this in itself does not do justice to their contributions, which appear in the main body of this book with appropriate acknowledgment.

In approximate chronological order, they are Jer Ren Yang, Martin Strangwood, Alistair Sugden, Ashraf Ali, Shaid Amin Khan, Shafiq Mujahid, Manabu Takahashi, Gethin Rees, Suresh Babu, Marty Gregg, Sally Parker, Naomi Chester, Shiv Brat Singh, Steven Jones, Mike Lord, Elizabeth Swallow, Philip Shipway, Pascal Jacques, Francisca G. Caballero, Thomas Sourmail, Harsha Sree Lalam, Miguel Angel Yescas-Gonzalez, Catherine Pitt, Kazutoshi Ichikawa, Joseph Robson, Liou Chun Chang, Nobuhiro Fujita, Mathew Peet, Philippe Opendaker, Carlos Garcia-Mateo, Mohamed Sherif, Sourabh Chatterjee, Sourabh Kundu, Guo Lei, Jun Hak Pak, Hong Seok Yang, Jae Hoon Jang, Minsung Joo, Jiawen Chen, Rongshan Qin, Dong Woo Suh, Hala Salman Hasan, Hongliang Yi, Seung-Woo Seo, Dae Woo Kim, Aseel Al-Hamdany, Arijit Saha Podder, Yan Pei, Ashwin Pandit, Eunju Song, Sourav Das, Jae Yong Chae, David Bombac, Danyi Luo, Lucy Fielding, Hector Pous-Romero, Wilberth Solano-Alvarez (who also provided the cover picture), Christopher Hulme-Smith and Edward Pickering deserve a special mention in this respect.

I should also like to express my gratitude to John Garnham for being so generous with his knowledge on bainitic rail steels, to David Gooch for discussions on creep resistant bainitic steels, to Lars-Erik Svensson for introducing me to the acicular ferrite, and to Greg Olson for so many inspiring discussions on bainite. I thank H.-O. Andren, S. S. Babu, G. Barritte, P. Clayton, D. V. Edmonds, M. Farooque, G. Fournalis, I. Gutierrez, P. Jacques, B. Josefsson, T. Maki, Y. Ohmori, H. Ohtsuka, M. Oka, J. Race, G. Rees, J. M. Rodriguez-Ibabe, M. Takahashi, H. Tamehiro, R. Thomson, B. J. P. Sandvik, M. Umemoto and the late Javier J. Urcola for providing micrographs, as acknowledged in the text. I have appreciated the ability to call on publishers to allow me to use figures without charge, as appropriately acknowledged in the text.

A particular debt of gratitude to Christopher Hulme-Smith and Mark Hull for proof reading the entire draft; this work they did in their 'spare' time!

I dedicate this book to Narmada, my late father Dharamshi, Pravin, Dina, Sunita, Maya and Anika. I look forward to reading excerpts from the book to my grandson and grandnieces.

H. K. D. H. B.

## ACRONYMS

---

BCC	Body-centred cubic	HV	Vickers hardness
BCT	Body-centred tetragonal	KS	Kurdjumov-Sachs
CE	Carbon equivalent	LEFM	Linear-elastic fracture mechanics
FCC	Face-centred cubic	NW	Nishiyama-Wasserman
P-LE	Partitioning local equilibrium	p.p.m.	Parts per million by weight
NP-LE	Negligible partitioning local equilibrium	RE	Rare earth additions
ILS	Invariant-line strain	SCR	Stress corrosion cracking resistance
IPS	Invariant-plane strain	SSAW	Self-shielded arc weld
FATT	Fracture assessed transition temperature	TRIP	Transformation-induced plasticity
HAZ	Heat-affected zone of welded joints	TTT	Time-temperature-transformation
HREM	High-resolution electron microscopy	CCT	Continuous cooling transformation
HSLA	High-strength low-alloy steels	ULCB	Ultra-low carbon bainitic steel
HTP	High-temperature processed	UTS	Ultimate tensile strength
		WOL	Wedge opening loading

## Nomenclature

---

$\alpha$	Allotriomorphic or idiomorphic ferrite forming by reconstructive transformation
$\alpha'$	Martensite
$\alpha_1$	One-dimensional parabolic thickening rate constant
$\alpha_b$	Bainite
$\alpha_s$	Secondary ferrite
$\alpha_{lb}$	Lower bainite
$\alpha_{ub}$	Upper bainite
$\beta$	Constant in inclusion theory; alternatively, an autocatalytic factor
$\gamma$	Austenite
$\gamma'$	Carbon-enriched austenite
$\Gamma$	Capillarity constant
$\delta_b$	Boundary thickness
$\Delta$	Uniform dilatation accompanying transformation; alternatively, the average distance between neighbouring particles in tempered martensite
$\epsilon$	Plastic strain
$\epsilon_1$	Average transverse thickness of dislocation cell structure in martensite
$\epsilon_r$	Resolution
$\zeta$	Uniaxial dilatation normal to the habit plane
$\theta$	Cementite
$\kappa$	Mean % planar misfit between inclusion and ferrite
$\kappa$	Percent planar matching during epitaxial nucleation
$\lambda$	Interledge spacing; alternatively an intersite jump distance during diffusion
$\mu$	Shear modulus

**xx**

$\mu_i$	Chemical potential of element $i$
$\nu$	Poisson's ratio
$\rho$	Density
$\rho_A$	Spacing of close-packed planes
$\rho_d$	Dislocation density
$\sigma$	Applied stress
$\sigma_0$	Intrinsic strength of martensite, not including microstructural strengthening
$\sigma_a$	Cyclic stress amplitude in a fatigue test
$\sigma_C$	Critical stress in fracture mechanics, related to $K_{IC}$ ; alternatively, solid solution strengthening due to carbon
$\sigma_c$	Volume of a molecule of $\text{Fe}_3\text{C}$ less $3 \Omega_{\text{Fe}}$
$\sigma_F$	Stress necessary for the propagation of cleavage fracture
$\sigma_g$	Strengthening due to grain boundaries
$\sigma_N$	Normal stress on the habit plane
$\sigma_p$	Work of fracture, per unit area of crack surface
$\sigma_r$	Stress as a function of the distance $r$ ahead of the crack tip
$\sigma_s$	Saturation value of $\sigma_{iy}$ in a fatigue test
$\sigma_y$	Yield stress or proof stress in monotonic loading tests
$\sigma_{\text{Fe}}$	Strength of pure annealed iron
$\sigma_{\theta\alpha}$	Interfacial free energy per unit area
$\sigma_{iy}$	Instantaneous flow stress at any particular stage of a test
$\sigma_{SS}$	Solid solution strengthening due to substitutional solutes
$\sigma_{UTS}$	Ultimate tensile strength
$\tau$	Incubation time before the growth of an individual particle begins during isothermal transformation, or before a detectable degree of overall transformation. Alternatively, the shear stress resolved along the shear direction
$\tau_\mu$	Athermal resistance to dislocation motion
$\tau_o$	Resistance to dislocation motion
$\tau_T$	Shear stress driving the motion of a transformation interface
$\psi$	Constant in weld metal inclusion formation theory
$\psi$	Volume fraction, or volume fraction divided by the equilibrium or some other limiting volume fraction
$\psi_a$	A specific value of $\psi$
$\Omega$	Volume per atom
$\Omega_{\text{Fe}}$	Volume of an atom of Fe in $\alpha$
$\Delta a_m$	Minimum detectable increase in austenite layer thickness
$a$	Length of an edge crack, or lattice parameter
$A_f$	Temperature at which the transformation to austenite is complete
$A_i$	Atomic weight of element $i$
$A_s$	Mean free slip area in statistical theory for plasticity
$A_s$	Temperature at which the transformation to austenite begins
$Ac_3$	Temperature at which a sample becomes fully austenitic during heating
$Ae_1$	Temperature separating the $\alpha + \gamma$ and $\alpha$ phase fields for a specific alloy
$Ae_3$	Temperature separating the $\alpha + \gamma$ and $\gamma$ phase fields for a specific alloy
$Ar_3$	Temperature at which austenite begins to transform to ferrite during cooling
$\bar{A}$	Mean areal intercept in stereology
$b$	Magnitude of Burgers vector of dislocation

$B_\sigma$	A temperature below which bainitic transformation is considered to be stress-assisted and above which it is considered to be strain-induced, during transformation under the influence of an externally applied stress
$B_d$	Highest temperature at which bainite forms under the influence of an externally applied stress
$B_S$	Bainite-start temperature
<b>B</b>	Matrix representing the Bain deformation
$c$	Length of an edge crack, or length of a microcrack nucleus
$c_d$	Diameter of a penny-shaped crack in a spheroidal particle
$c_i^{\alpha\theta}$	Concentration of element $i$ in phase $\alpha$ in equilibrium with phase $\theta$
$c_o$	Carbide thickness
$C_i$	Constants, with $i = 1, 2, 3 \dots$
$d$	Interatomic spacing along a specific crystallographic direction
$D$ or $D_\gamma$	Diffusivity of carbon in austenite
$D_i^\alpha$	Diffusivity of element $i$ phase $\alpha$
$D_\alpha$	Diffusivity of carbon in ferrite
$D_{eff}$	Effective diffusion coefficient
$D_T, D$	Topological and fractal dimension, respectively
<b>d</b>	Vector describing the shear component of an IPS
$\overline{D}$	Weighted average diffusivity of carbon in austenite
$E$	Young's modulus
$f^*$	Attempt frequency for atomic jumps across an interface
$f_1$	Normalised supersaturation
$f_C$	Activity coefficient for carbon in austenite
$f_N$	Empirical function in nucleation theory
$\Delta G$	General term representing driving force
$\Delta G^{\gamma \rightarrow \alpha}$	Free energy change for transformation without composition change
$\Delta G_{chem}$	Chemical driving force
$\Delta G_{mech}$	Mechanical driving force
$\Delta G_{strain}$	Coherency strain energy during nucleation
$\Delta G^\circ$	Standard free energy of formation
$\Delta G_m$	Molar Gibbs free energy change on transformation; alternatively, the maximum molar Gibbs free energy change accompanying nucleation
$\Delta G_m$	Molar Gibbs free energy
$G$	Growth rate
$G^*$	Activation free energy for nucleation, or for interfacial motion
$G_1^*$	Activation free energy for the growth of an embryo into a nucleus
$G_2^*$	Activation free energy for the transfer of atoms across the nucleus/matrix interface
$G_O^*$	Activation free energy to overcome the resistance to dislocation motion without the aid of a chemical driving force
$G_i^0$	Molar Gibbs free energy of pure $i$
$G^\alpha$	Free energy of phase identified by superscript
$G_F$	Free energy per unit area of fault plane
$G_N^\alpha$	Function specifying the critical value of $\Delta G^{\gamma \rightarrow \alpha}$ at the $M_S$ temperature
$G_N$	Function specifying the free energy change needed in order to obtain a detectable rate of nucleation for Widmanstätten ferrite and bainite
$G_s$	Strain energy per mole
$G_{dd}$	Free energy dissipated in the process of solute diffusion ahead of an interface

$G_{id}$	Free energy dissipated in the transfer of atoms across an interface
$G'_{id}$	Free energy term describing the maximum glide resistance of dislocations
$G_{SB}$	Stored energy of Widmanstätten ferrite
$G_{SW}$	Stored energy of bainite
$h_{\alpha}$	Ledge height at the interface between $\alpha$ and the parent phase
$\Delta H^{\gamma\alpha}$	Enthalpy change during the $\gamma \rightarrow \alpha$ transformation
$H$	Hardness of martensite
$H_0$	Hardness of virgin martensite
$H_1$	A function in the theory of diffusion-controlled growth
$H_F$	Hardness of tempered martensite when all excess carbon has precipitated
${}^v I$	Nucleation rate per unit volume
$J$	Diffusion flux
$k$	Boltzmann constant
$k_{\epsilon}$	Coefficient in an equation for the strength of tempered martensite
$k_{\gamma}$	Parameter describing the stability of retained austenite
$k_A$	Constant in the Avrami equation
$k_e$	Equilibrium solute partitioning coefficient
$k_g$	Constant relating lath size to strength
$k_i$	Partitioning coefficient for alloying element $i$
$k_p$	Coefficient representing the strengthening effect of cementite particles; alternatively, a solute partitioning coefficient
$\Delta K$	Stress intensity range during fatigue testing
$\Delta K_O$	Threshold value of stress intensity range during fatigue crack growth
$K_I$	Stress intensification factor in fracture mechanics
$K_{IC}$	Critical value of $K_I$ , a measure of the toughness of a material
$K_{IE}$	Threshold stress intensity for environment-induced delayed cracking
$K_{ISCC}$	Threshold value of stress intensity below which stress corrosion cracks do not grow at a perceptible rate
$K_{max}$	Maximum value of stress intensification factor in fatigue cycle
$K_{min}$	Minimum value of stress intensification factor in fatigue cycle
$\overline{\Delta l}_m$	Maximum relative length contraction due to isothermal reaustenitisation
$\overline{L}$	Mean intercept length in stereology, grain size
$\overline{L}_{\gamma}$	Austenite grain size
$L$	Average distance moved by dislocations during plastic deformation
$l$	Spacing between dislocations
$L_S$	Lower bainite start temperature
$m$	Paris constant in fracture mechanics
$m_i$	Mass fraction of element $i$
$M$	Mobility of an interface
$M_{\sigma}$	Temperature below which martensite can be induced by stress
$M_d$	Highest temperature at which martensite forms under the influence of an externally applied stress
$M_F$	Temperature at which 95% martensite is obtained
$M_S$	Martensite-start temperature
$M_S^{\infty}$	Martensite-start temperature for infinitely large austenite grain size
$n$	Time exponent in the Avrami equation
$n_A$	Number of atoms in an embryo involved in nucleation
$n_p$	Number of close-packed planes involved in the faulting process during dislocative nucleation

$n_{\text{Fe}}$	Number of iron atoms per unit volume of $\alpha$
$N$	Number of cycles in fatigue loading
$N_V$	Number of particles per unit volume
$N_C$	Absolute number of carbon atoms
$p$	Péclet number (a dimensionless velocity) or autocatalytic factor
$P$	Pressure
<b>P</b>	Matrix representing a homogeneous invariant-plane strain deformation
$q$	Half the increase in the thickness of austenite during one-dimensional growth
$Q$	Activation energy
<b>Q</b>	Matrix representing an inhomogeneous lattice-invariant deformation
$\bar{r}$	Mean particle radius at time $t$
$\bar{r}_0$	Mean particle radius at time zero
$r$	Radius of a disc; alternatively, the distance ahead of a crack tip; alternatively the tip radius of a growing plate, particle radius
$r_1$	Proof stress to ultimate tensile stress ratio
$r_2$	Ratio of $\sigma_a$ to $\sigma_s$
$r_C$	Critical distance in fracture mechanics, related to $K_{IC}$ ; alternatively, critical tip radius at which the growth of a plate ceases
$r_e$	Value of $r_2$ at the endurance limit in fatigue
$R$	Universal gas constant; alternatively, the semi-axis of an oblate ellipsoid; alternatively, the ratio of $K_{min}$ to $K_{max}$ in fatigue
$R^\gamma$	Electrical resistivity of phase identified by superscript
$R_d$	Rate at which growing austenite dilutes
<b>R</b>	Matrix for rigid body rotation
$s$	Shear component of the IPS shape deformation
$s_A$	Apparent shear strain
$S_1, S_2$	Functions in the Trivedi model for the growth of parabolic cylinders
$S_V$	Interfacial area per unit volume
<b>S</b>	Deformation matrix in the crystallographic theory of martensite
$\Delta t$	Time interval between the nucleation of successive sub-unit during sheaf lengthening
$t$	Time; alternatively, the thickness of a disc
$t_1$	Time for isothermal transformation to bainite during austempering of cast iron
$t_2$	Time to the beginning of carbide precipitation from austenite during austempering
$t_\theta$	Time for the precipitation of cementite from ferrite
$t_a$	Time required to reach a given fraction $\xi$ of isothermal transformation
$t_c$	Time required for a sub-unit to reach a limiting size
$t_d$	Time required to decarburise a plate of bainite
$t_i$	Time interval for step $i$ in a series of isothermal heat treatments
$t_p$	True thickness of a plate
<b>t</b>	Traction defining the state of stress on a plane
$T$	Temperature
$T^{\gamma\alpha}$	Austenite to ferrite transformation temperature
$T_0$	Temperature at which $\gamma$ and $\alpha$ of the same composition have the same free energy
$T'_0$	As $T_0$ , but accounting for the stored energy of ferrite
$T_\gamma$	Isothermal austenitisation temperature
$T_\theta$	Temperature at which the $T_0$ curve and $\gamma/\gamma + \theta$ phase boundary intersect

$T_a$	Ambient temperature
$T_c$	Critical Zener ordering temperature for carbon atoms in ferrite; alternatively, the temperature below which cementite can in principle precipitate in association with upper bainitic ferrite
$T_F$	Temperature at which accelerated cooling is stopped
$T_h$	The temperature below which the nucleation of displacive transformations first becomes possible at a detectable rate
$T_i$	Isothermal transformation temperature
$T_M$	Melting temperature
$T_R$	Temperature at which rolling deformation is stopped
$T_r$	Temperature below which a midrib is found in lower bainite plates
$T_t$	Transition temperature for impact toughness
$T_{nr}$	Temperature below which austenite does not recrystallise during hot deformation
$T_{om}$	As $T_0$ , but forcing the Zener ordering of carbon atoms in the ferrite
$v^*$	Activation volume
$\Delta V_V$	Minimum detectable change in volume fraction
$\Delta V_m$	Change in molar volume on transformation
$V$	Volume of a sample
$V^\alpha$	Volume of phase $\alpha$
$V_e^\alpha$	Extended volume of phase $\alpha$
$V_m^\theta$	Molar volume of phase $\theta$
$V_\alpha^s$	Velocity of steps in the $\alpha$ /parent phase interface
$V_\tau$	Volume per particle
$V_d$	Diffusion field velocity
$V_i$	Velocity of an interface calculated on the basis of its mobility
$V_k$	Velocity of an interface calculated using a solute trapping function
$V_l$	Plate lengthening rate
$V_S$	Sheaf lengthening rate
$V_u$	Volume of sub-unit
$V_V$	Volume fraction
$V_V^\gamma$	Volume fraction of austenite
$V_V^I$	Volume fraction of inclusions
$V_V^{\max}$	Maximum volume fraction
$V_{\max}^S$	Maximum volume of a sheaf
$w$	Thickness of a bainite sub-unit
$w_i$	Weight percent of element $i$
$w_i^{sol}$	Weight percent of element $i$ , in solution
$W$	Width of a fracture toughness specimen for a $K_{IC}$ test
$\bar{x}$	Average mole fraction of carbon in an alloy
$\bar{x}_X$	Average concentration of $X$ in cementite
$x^\theta$	Thickness of cementite particle
$x^{\alpha\gamma}$	Mole fraction of carbon in ferrite which is in equilibrium or paraequilibrium with austenite
$x^{\gamma\alpha}$	Mole fraction of carbon in austenite which is in equilibrium or paraequilibrium with ferrite
$x_\alpha$	Carbon in $\alpha$ at interface
$x_\alpha^\alpha$	Mole fraction of phase $\alpha$
$x_\gamma$	Carbon concentration in austenite

**xxvi**

$x_{\gamma}^I$	Carbon concentration in austenite before the start of austenite growth
$x_m$	Maximum carbon supersaturation permitted in ferrite, on thermodynamic grounds
$x_X$	Concentration of $X$ in cementite
$x_X^{\alpha\theta}$	Concentration of $X$ in ferrite which is in equilibrium with cementite
$x_{Ae_3}$	Carbon concentration given by the $Ae_3$ curve
$x_{T'_0}$	Carbon concentration given by the $T'_0$ curve
$y$	Semi-axis of an oblate ellipsoid
$Y$	Compliance function in fracture mechanics; alternatively, a constant in the theory of thermally activated dislocation motion
$z$	Coordinate normal to the interface plane; alternatively, a constant in the theory of thermally activated dislocation motion
$z_d$	Effective diffusion distance
$Z$	Position of the interface along coordinate $z$ .

# CHAPTER 1

---

## INTRODUCTION

---

We begin with a historical survey of the exciting early days of metallurgical research during which bainite was discovered, covering the period up to about 1960, with occasional excursions into more modern literature. The early research was usually well conceived and was carried out with enthusiasm. Many of the original concepts survive to this day and others have been confirmed using the advanced experimental techniques now available. The thirty years or so prior to the discovery of bainite were in many respects formative as far as the whole subject of metallurgy is concerned. The details of that period are documented in the several textbooks and articles covering the history of metallurgy,<sup>1</sup> but a few facts deserve special mention, if only as an indication of the state-of-the-art for the period between 1920-1930.

The idea that martensite was an intermediate stage in the formation of pearlite was no longer accepted, although it continued to be taught until well after 1920. The  $\beta$ -iron controversy, in which the property changes caused by the paramagnetic to ferromagnetic transition in ferrite were attributed to the existence of another allotropic modification ( $\beta$ )

<sup>1</sup>Notable historical works include: “The Sorby Centennial Symposium on the History of Metallurgy”, published by the A.I.M.E. in 1965 (includes an article by Bain himself), the commentary by H. W. Paxton (Davenport et al., 1970), and by H. W. Paxton and J. B. Austin (Paxton and Austin, 1972). Paxton’s 1970 article is published along with a reproduction of the classic 1930 paper on the discovery of bainite by Davenport and Bain, and is based on first hand historical knowledge obtained directly from Davenport and Bain. An additional commentary was published recently (Bhadeshia, 2010a).

of iron, was also in its dying days.<sup>2</sup> The first evidence that a solid solution is an intimate mixture of solvent and solute atoms in a single phase was beginning to emerge (Bain, 1921b,a) and it soon became clear that martensite consists of carbon dispersed atomically as an interstitial solid solution in a tetragonal ferrite crystal. Austenite was established to have a face-centred cubic crystal structure, which could sometimes be retained to ambient temperature by quenching. Bain had already proposed the homogeneous deformation which could relate the face-centred cubic and body-centred cubic or body-centred tetragonal lattices during martensitic transformation. It had been established using X-ray crystallography that the tempering of martensite led to the precipitation of cementite, or to alloy carbides if the tempering temperature was high enough. Although the surface relief associated with martensitic transformation had been observed, its importance to the mechanism of transformation was not fully appreciated. Widmanstätten ferrite had been identified and was believed to precipitate on the octahedral planes of the parent austenite; some notions of the orientation relationship between the ferrite and austenite were also being discussed.

It was an era of major discoveries and great enterprise in the metallurgy of steels. The time was therefore ripe for the discovery of bainite. The term “discovery” implies something new. In fact, microstructures containing bainite must have been encountered prior to the now acknowledged discovery date, but the phase was never clearly identified because of the confused microstructures that followed from the continuous cooling heat treatment procedures common in those days. A number of coincidental circumstances inspired Bain and others to attempt isothermal transformation experiments. That austenite could be retained to ambient temperature was clear from studies of Hadfield’s steel which had been used by Bain to show that austenite has a face-centred cubic structure. It was accepted that increasing the cooling rate could lead to a greater amount of austenite being retained. Indeed, it had been demonstrated using magnetic techniques that austenite in low-alloy steels could exist at low temperatures for minutes prior to completing transformation. The concept of isothermal transformation was already exploited in industry for the manufacture of patented steel wire, and Bain was aware of this through his contacts at the American Steel and Wire Company. He began to wonder “whether exceedingly small heated specimens rendered wholly austenitic might successfully be brought unchanged to any intermediate temperature at which, then their transformation could be followed” and he “enticed” E. C. Davenport to join him in putting this idea into action.

### 1.1 The Discovery of Bainite

During the late 1920s, in the course of these pioneering studies on the *isothermal* transformation of austenite at temperatures above that at which martensite first forms, but below that at which fine pearlite is found, Davenport and Bain (1930) discovered a new microstructure consisting of an “acicular, dark etching aggregate” which was quite unlike the pearlite or martensite observed in the same steel (Fig. 1.1). They originally called this microstructure “martensite-troostite” since they believed that it “forms much in the man-

<sup>2</sup>It is generally assumed today that the ferrite lattice is body-centred cubic both above and below the Curie transition. However, the ordering of spins in the ferromagnetic state makes it incompatible with cubic symmetry (White, 2007). If the spins are aligned along the  $z$  axis, then rotations about the  $x$  or  $y$  axes must be combined with time reversal to preserve the directions of the spins, the magnetic point group becomes tetragonal. It follows that the ferrite structure below the Curie temperature is tetragonal, but the extent of tetragonality is very small and neglected in most experiments on complex microstructures in steels.

ner of martensite but is subsequently more or less tempered and succeeds in precipitating carbon”.

The structure was found to etch more rapidly than martensite but less so than troostite (fine pearlite). The appearance of “low-range” martensite-troostite (formed at temperatures just above the martensite-start temperature  $M_S$ ) was found to be somewhat different from the “high-range” martensite-troostite formed at higher temperatures. The microstructure exhibited unusual and promising properties; it was found to be “tougher for the same hardness than tempered martensite” (Bain, 1939), and was the cause of much excitement at the newly established United States Steel Corporation Laboratory in New Jersey. It is relevant to note here the contributions of Lewis (1929) and Robertson (1929), who were the first to publish the results of isothermal transformation experiments on eutectoid steel wires, probably because of their relevance to patented steel. But the Davenport and Bain experiments were unique in showing the progressive nature of the isothermal transformation of austenite, using both metallography and dilatometry, and in providing a clear interpretation of the structures. Others may have published micrographs of structures that could be identified now as bainite, generated by isothermal transformation, for example Robertson, but the associated discussion is not stimulating. This conclusion remains contentious (Bhadeshia, 2013b; Hillert, 2011).<sup>3</sup> The present author is convinced about the clarity of the Davenport and Bain experiments, which were particularly successful because they utilised very thin samples. Their method of representing the kinetic data in the form of time-temperature-transformation curves turned out to be so simple and elegant, that it would be inconceivable to find any contemporary materials scientist who has not been trained in the use or construction of “TTT” diagrams.

In 1934, the research staff of the laboratory named the microstructure “Bainite” in honour of their colleague E. C. Bain who had inspired the studies, and presented him with the first ever photomicrograph of bainite, taken at a magnification of  $\times 1000$  (Smith and Bowles, 1960; Bain, 1963).

The name “bainite” did not immediately catch on. It was used rather modestly even by Bain and his co-workers. In a paper on the nomenclature of transformation products in steels, Vilella et al. (1936) mentioned an “unnamed, dark etching, acicular aggregate somewhat similar to martensite” when referring to bainite. Hoyt, in his discussion to this paper appealed to the authors to name the structure, since it had first been produced and observed in their laboratory. Davenport (1939) ambiguously referred to the structure, sometimes calling it “a rapid etching acicular structure”, at other times calling it bainite. In 1940, Greninger and Troiano used the term “Austempering Structures” instead of bainite. The 1942 edition of the book *The Structure of Steel* (and its reprinted version of 1947) by Gregory and Simmons contains no mention of bainite.

The high-range and low-range variants of bainite were later called “upper bainite” and “lower bainite” respectively (Mehl, 1939) and this terminology remains useful to this day. Smith and Mehl (1942) coined the term “feathery bainite” for upper bainite which forms largely, if not exclusively, at the austenite grain boundaries in the form of bundles of plates, and only at high reaction temperatures, but this description has not found frequent use. Both upper and lower bainite were found to consist of aggregates of parallel plates, aggregates which were later designated sheaves of bainite (Aaronson and Wells, 1956).

<sup>3</sup>It has been said that Hultgren (1920) published micrographs of “bainite” in tungsten-containing steels, but the interpretation was necessarily weak given the time period in which the work was done. There are phrases such as “partly dark areas”, “formation of streaks”, and statements that the “ferrite formation is caused by an increase in the crystallisation power of ferrite . . .” that are difficult to accept as identifying the discovery of bainite.

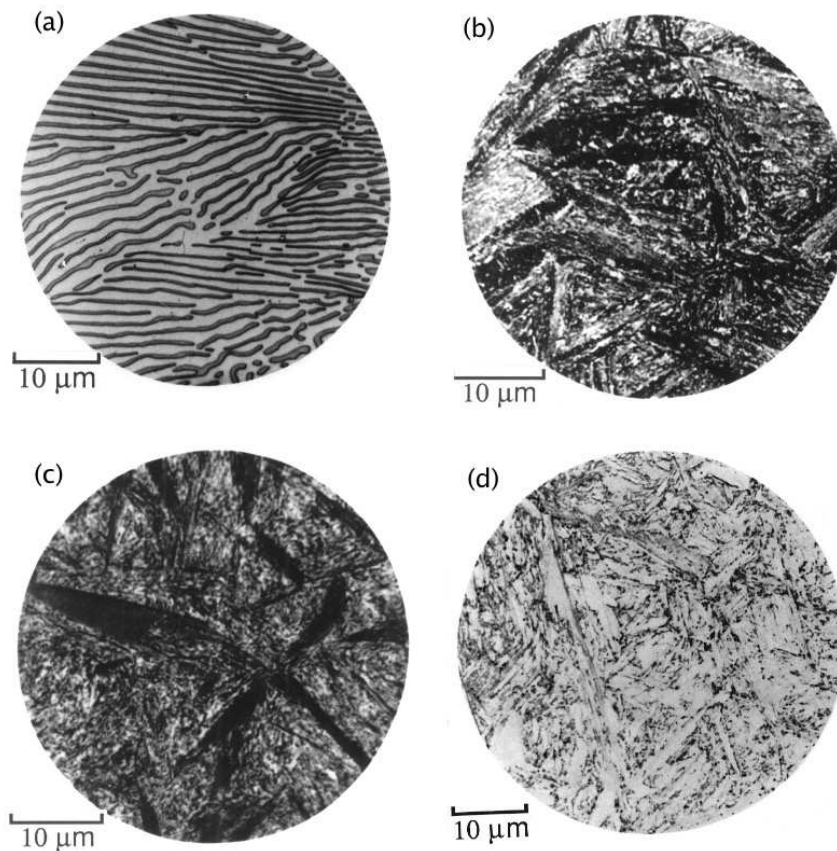


**Figure 1.1** Microstructures in a eutectoid steel. (a) Pearlite formed at 720 °C; (b) bainite obtained by isothermal transformation at 290 °C; (c) bainite obtained by isothermal transformation at 180 °C; (d) martensite. The micrographs were taken by Vilella and were published in the book “The Alloying Elements in Steel” (Bain, 1939). Notice how the bainite etches much darker than martensite, because its microstructure contains many fine carbides.

## 1.2 The Early Research

Early work into the nature of bainite continued to emphasise its similarity with martensite. Bainite was believed to form with a supersaturation of carbon (Wever and Lange, 1932; Wever and Jellinghaus, 1932; Portevin and Chevenard, 1937; Portevin and Jolivet, 1938). It had been postulated that the transformation involves the abrupt formation of flat plates of supersaturated ferrite along certain crystallographic planes of the austenite grain (Vilella et al., 1936). The ferrite was then supposed to decarburise by rejecting carbon at a rate depending on temperature, leading to the formation of carbide particles which were quite unlike the lamellar cementite phase associated with pearlite. The transformation was believed to be in essence martensitic, “even though the temperature be such as to limit the actual life of the quasi-martensite to millionths of a second”. Bain (1939) reiterated this view in his book “The Alloying Elements in Steel”. Isothermal transformation studies were by then becoming very popular and led to a steady accumulation of data on the bai-

nite reaction, still variously referred to as the “intermediate transformation”, “dark etching acicular constituent”, “acicular ferrite”, etc.

In many respects, isothermal transformation experiments led to the clarification of microstructures, since individual phases could be studied in isolation. There was, however, room for difficulties even after the technique became well established. For alloys of appropriate composition, the upper ranges of bainite formation were found to overlap with those of pearlite, preceded in some cases by the growth of proeutectoid ferrite. The nomenclature thus became confused since the ferrite which formed first was variously described as massive ferrite, grain boundary ferrite, acicular ferrite, Widmanstätten ferrite, etc. On a later view, some of these microconstituents are formed by a “displacive” or “military” transfer of the iron and substitutional solute atoms from austenite to ferrite, and are thus similar to carbon-free bainitic ferrite, whereas others form by a “reconstructive” or “civilian” transformation which is a quite different kinetic process (Buerger, 1951; Christian, 1965a).

### 1.2.1 Crystallography

By measuring the crystallographic orientation of austenite using twin vestiges and light microscopy, Greninger and Troiano (1940) were able to show that the habit plane of martensite in steels is irrational. These results were consistent with earlier work on non-ferrous martensites and put paid to the contemporary view that martensite in steels forms on the octahedral planes of austenite. They also found that with one exception, the habit plane of bainite is irrational, and different from that of martensite in the same steel (Fig. 1.2). The habit plane indices varied with the transformation temperature and the average carbon concentration of the steel. The results implied a fundamental difference between bainite and martensite. Because the habit plane of bainite approached that of Widmanstätten ferrite at high temperatures, but the proeutectoid cementite habit at low temperatures, and because it always differed from that of martensite, Greninger and Troiano proposed that bainite from the very beginning grows as an aggregate of ferrite and cementite. A competition between the ferrite and cementite was supposed to cause the changes in the bainite habit, the ferrite controlling at high temperatures and the cementite at low temperatures. The competition between the ferrite and cementite was thus proposed to explain the observed variation of bainite habit plane. The crystallographic results were later confirmed using an indirect and less accurate method (Smith and Mehl, 1942). These authors also showed that the orientation relationship between bainitic ferrite and austenite does not change very rapidly with transformation temperature and carbon content and is within a few degrees of the orientations found for martensite and Widmanstätten ferrite, but differs considerably from that of pearlitic ferrite/austenite. Since the orientation relationship of bainite with austenite was not found to change, Smith and Mehl considered Greninger and Troiano’s explanation for habit plane variation to be inadequate, implying that the habit plane cannot vary independently of the orientation relationship. The fact that the habit plane, orientation relationship and shape deformation cannot be varied independently was proven later with the crystallographic theory of martensite (Bowles and Mackenzie, 1954; Wechsler et al., 1953).

### 1.2.2 The Incomplete Reaction Phenomenon

It was known as long ago as 1939 that in certain alloy steels “in which the pearlite change is very slow”, the extent of transformation to bainite decreases, ultimately to zero, as the

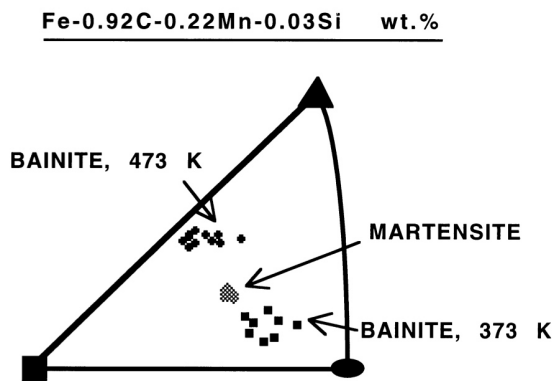


**Figure 1.2** An example of the results obtained by Greninger and Troiano (1940), showing the irrational habit of bainite, which changed as a function of the transformation temperature. Notice also that the habit plane of bainite is different from that of martensite in the same steel.

transformation temperature is increased (Allen et al., 1939). For example, the bainite transformation in a Fe-2.98Cr-0.2Mn-0.38C wt% alloy was found to begin rapidly but cease shortly afterwards, with the maximum volume fraction of bainite obtained increasing with decreasing transformation temperature (Klier and Lyman, 1944). At no temperature investigated did the complete transformation of austenite occur solely by decomposition to bainite. The residual austenite remaining untransformed after the cessation of the bainite reaction, reacted by another mechanism (pearlite) only after a further long delay. Cottrell (1945), in his experiments on a low-alloy steel, found that the amount of bainite that formed at 525 °C ( $\ll A_{e_3}$ ) was negligible, and although the degree of transformation increased as the isothermal reaction temperature was decreased, the formation of bainite appeared to stop before reaching completion. Other experiments on chromium-containing steels revealed that the dilatometric expansion due to bainite became larger as the transformation temperature was reduced, Fig. 1.3 (Lyman and Troiano, 1946). Oddly enough, the bainite transformation did not seem to reach completion on isothermal heat treatment, even though all of the austenite could readily transform to pearlite at a *higher* transformation temperature (Klier and Lyman, 1944). Often, the transformation of austenite at lower temperatures occurred in two stages, beginning with the bainite reaction which stopped prematurely, to be followed by the formation of pearlite at a slower rate. It is significant that the two reactions may only be separated by a long delay in well-alloyed steels; in plain carbon steels “the second reaction sets in within a few seconds after the beginning of the bainite reaction” (Klier and Lyman, 1944).

### 1.2.3 Carbon Redistribution

X-ray and other experiments indicated that the formation of bainite enriches the residual austenite in carbon. Klier and Lyman (1944) took this to mean that the austenite, prior to its transformation to bainite, becomes compositionally unstable and separates into carbon-rich and carbon-depleted volumes; in modern terminology, this would require uphill diffusion. The low carbon regions were then supposed to transform into supersaturated bainite of the same composition, by a “martensite-like” lattice rearrangement, to be followed soon after by the precipitation of iron carbides. A similar suggestion had been made earlier by Kurdjumov (1933) in the context of Widmanstätten ferrite: “regions of low carbon concentration in the  $\gamma$  crystal result from diffusion within the  $\gamma$  phase, and these regions can at this time transform into the  $\alpha$  phase . . .”. Entin (1962) seemed to rediscover this idea, leading

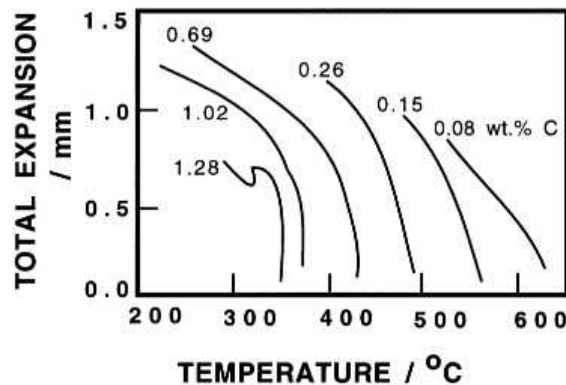


**Figure 1.3** Temperature dependence of the total dilatometric expansion due to the formation of bainite (Lyman and Troiano, 1946). Transformation to bainite does not begin until a critical temperature  $B_S$ , which is well below the equilibrium  $A_{e3}$  temperature. The amount of bainite that can form at any temperature increases with the undercooling below  $B_S$ .

Aaronson et al. (1966a) to prove using thermodynamics that an austenitic Fe-C solid solution cannot spontaneously undergo separation into carbon-rich and carbon-poor regions. There is no tendency for the austenitic solid solution to undergo spinodal decomposition. The concept nonetheless seems to crop up with notorious regularity even in modern literature (Prado, 1986; Prado et al., 1990; Kang et al., 2005). High-intensity X-ray *in-situ* experiments using synchrotron facilities seemed at one stage to indicate that the austenite unit cell splits into two identical lattices but with different lattice parameters prior to the onset of the bainite transformation (Babu et al., 2005, 2007). Amongst the interpretations presented was the spinodal decomposition of the austenite, recognising that Aaronson et al. (1966a) had demonstrated this to be impossible, but arguing that the available thermodynamic data may not be appropriate for the low temperature (300 °C) at which the experiments were done. Subsequent higher-resolution experiments established that these reports were based on an incorrect analysis of limited X-ray data, and that the austenite remains homogeneous with a unique lattice parameter prior to transformation into bainite, Fig. 1.4 (Stone et al., 2008). Neutron diffraction experiments confirm this conclusion (Koo et al., 2009).

The proof by Aaronson et al. does not of course rule out random fluctuations of composition, of the type associated with any solid solution in dynamic equilibrium. It has therefore been argued that the nucleation of bainite is favoured in regions of austenite where the carbon concentration is relatively low as a consequence of fluctuations (Yu et al., 1989). Indeed, carbon-free regions of several thousand iron atoms can exist at all temperatures in austenite of eutectoid composition (Russell, 1971). The difficulty arises when it is claimed that these carbon-depleted regions lead to an enhancement of the nucleation rate. For every such region there must also exist a carbon-enriched region where the probability of ferrite nucleation is presumably reduced, thereby balancing the effects of the depleted regions. Consequently, there may be no advantage in adopting this microscopic approach. The usual macroscopic thermodynamic model in which the driving forces are calculated for uniform composition should suffice.

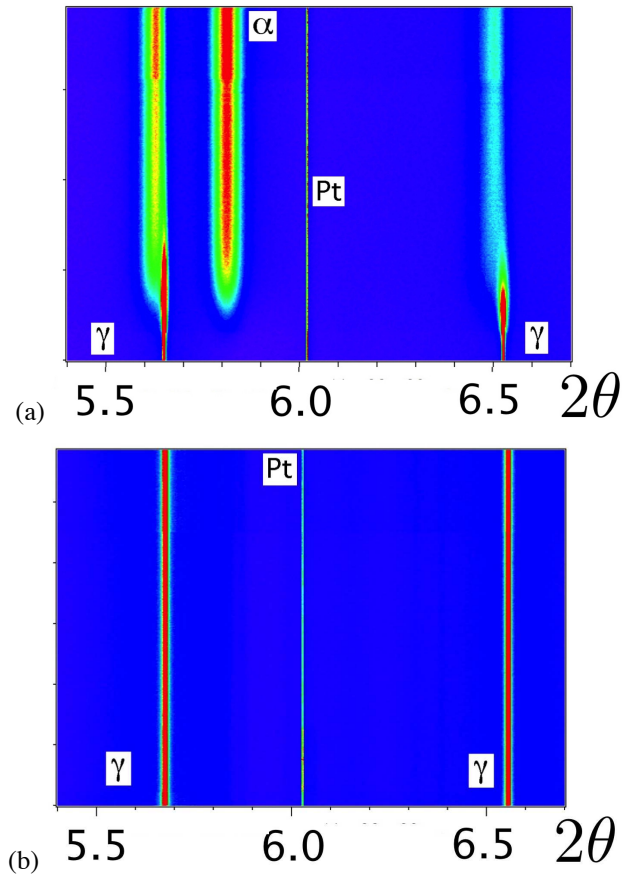


**Figure 1.4** X-ray diffraction during isothermal holding. The vertical scale represents the progress of time, a blue and red represent low and high intensities respectively. (a) Transformation at 300 °C, showing that the austenite has a unique lattice parameter prior to the formation of carbide-free bainite. (b) Holding at 200 °C for ten hours prior to the onset of bainite, showing the absence of any peak splitting. After Stone et al. (2008).

It has also been suggested that the segregation of carbon to dislocations will create a depleted region in the austenite which stimulates the nucleation of bainite (Zhao et al., 2007). The analysis is, however, flawed because it fails to account for the rapid diffusivity of carbon in austenite over the dimensions typical during nucleation.

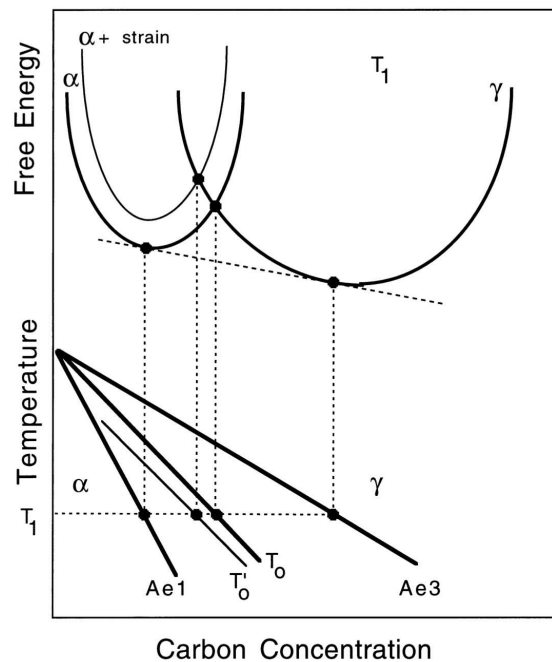


**Figure 1.5** Schematic illustration of the origin of the  $T_0$  curve on the phase diagram. The  $T'_0$  curve incorporates a strain energy term for the ferrite, illustrated on the diagram by raising the free energy curve for ferrite by an appropriate quantity.

#### 1.2.4 Thermodynamics

In a far reaching paper, Zener (1946) attempted to give a rational thermodynamic description of the phase transformations that occur in steels. He assumed that bainite growth is diffusionless, any carbon supersaturation in bainitic ferrite being relieved subsequent to growth, by partitioning into the residual austenite. The atomic mechanism of bainite growth was not discussed in detail, but he believed that unlike martensite, there is no strain energy associated with the growth of bainite. Thus bainite should form at a temperature just below  $T_0$ , where the austenite and ferrite of the same composition have identical free energies (Fig. 1.5).

However,  $T_0$  is frequently used in martensite theory for the temperature at which austenite and martensite (i.e. supersaturated tetragonal "ferrite") have the same free energy; for clarity, we follow Christian and Edmonds (1984) and call this temperature  $T_{om}$ . The Bain strain applied to a random interstitial solution of carbon in austenite automatically produces the ordered tetragonal form of ferrite if the carbon atoms are trapped in their original sites, but Zener also supposed that the tetragonal form may be regarded as a result of an ordering

of the interstitial atoms into one set of sites of the cubic structure. He derived an equation for the critical temperature  $T_c$  at which the cubic and tetragonal forms of ferrite have the same free energy.  $T_c$  rises with interstitial solute content, and thus intersects the  $M_S$  temperature and also has a joint intersection with the  $T_0$  and  $T_{om}$  temperatures. Clearly  $T_{om}$  lies below  $T_0$  at low carbon contents and above  $T_0$  at high carbon contents. According to one interpretation (Owen et al., 1964), martensite formed above room temperature is cubic at carbon contents below the intersection of  $M_S$  and  $T_c$  (above 2.5 at% carbon in plain iron-carbon alloys) and tetragonal above it. As Zener pointed out, martensite cannot form until the driving force obtained by supercooling below the  $T_0$  or  $T_{om}$  temperature is large enough to provide the necessary strain energy.

It is usually assumed that bainite forming first as fully supersaturated ferrite nevertheless has a cubic structure, but it would seem more logical to assume a tetragonal structure even if the temperature of formation is above  $T_c$ . This is because the Bain deformation leaves the initial state as tetragonal and any disordering would follow subsequently (Christian, 1992).

The Zener model failed to provide an explanation of why the strain energy should exist for martensite and not for bainite. On the other hand, it explained the data showing that the degree of transformation to bainite increases with supercooling from zero at an upper limit, which is generally known as the bainite-start or  $B_S$  temperature. The carbon that partitions into the austenite *after* the formation of bainite changes its composition, until it eventually becomes thermodynamically impossible for the austenite to transform and the reaction stops. For a given alloy, a larger undercooling below  $T_0$  would allow more bainite to form before diffusionless growth becomes impossible. Consistent with experimental data, the model also requires the bainite 'C' curve of the TTT diagram to tend asymptotically to infinite time (Fig. 1.6) at a temperature corresponding to the  $T_0$  or  $T_{om}$  temperature whichever is higher, since the transformation of austenite without a composition change cannot occur above this limit.

The initial plates of bainite, unlike those of many martensites, often grow to a limited size less than that of the parent austenite grain. Zener suggested that a layer of cementite around the plate stifles its subsequent growth.

### 1.2.5 Paraequilibrium

By 1947, it was evident that the cementite associated with bainite is different from that found in pearlite. The latter was always found to have a different substitutional solute concentration when compared with the average value, whereas the cementite in bainite had about the same substitutional content as the matrix from which it grew. Hultgren (1947) has cited several references that report magnetic, chemical and X-ray data on extracted carbides that confirm this difference between the two kinds of cementite.

Hultgren was at the time proposing a model for the role of substitutional alloying elements in steels; at high temperatures where diffusion rates are reasonable, these elements can redistribute during transformation in a way consistent with equilibrium. The transformation was then said to occur under "ortho-equilibrium" conditions. This contrasts with "paraequilibrium" in which the substitutional alloying elements are unable to partition, although carbon, which is a fast diffusing interstitial element, redistributes between the phases until its chemical potential is uniform throughout.

The mechanism of pearlite growth was not clear in those days, but the transformation was believed to be initiated by the nucleation of cementite. This led to the contrasting suggestion that bainite is initiated by the nucleation of ferrite (Mehl, 1939; Smith and Mehl,

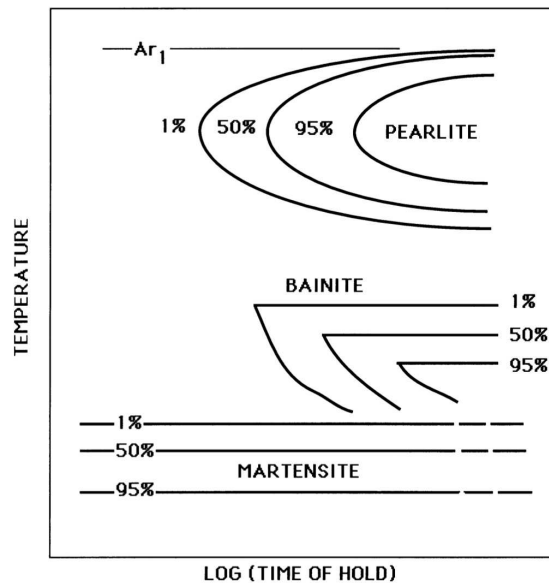


**Figure 1.6** Schematic TTT diagram illustrating the flat tops on the bainite C-curves (Zener, 1946).

1942; Mehl, 1948). Hultgren put these ideas together and proposed that upper bainite begins with the nucleation and growth of ferrite with a paraequilibrium carbon concentration, causing the residual austenite to become enriched in carbon. This bainitic ferrite, unlike the ferrite associated with pearlite, was believed to have a rational Kurdjumov-Sachs or Nishiyama-Wasserman orientation relationship with the parent austenite in which it grows. This was considered to explain the observed difference in ferrite morphologies in bainite and pearlite. Bainitic ferrite was always found to consist of individual plates or sheaves whereas the ferrite in pearlite apparently formed alternating plates of a regularly spaced two-phase lamellar aggregate. The enrichment of austenite with carbon should eventually cause the paraequilibrium precipitation of cementite from austenite in a region adjacent to the bainitic ferrite. At the time, pearlitic cementite was thought to bear a rational orientation relation to the austenite grain into which the pearlite colony grows, and Hultgren proposed, without any evidence, that bainitic cementite should be randomly orientated to the austenite in which it precipitated. This process of ferrite and subsequent cementite precipitation then repeated, giving rise to the sheaf of bainite. Hultgren therefore considered upper bainite to be similar to pearlite but growing under paraequilibrium conditions and different in the orientation relations with austenite.

No explanation was offered for the occurrence of paraequilibrium with bainite, nor for the existence of the various orientation relationships. He admitted the possibility that bainite formed at lower temperatures (later known as *lower* bainite) “forms directly”, implying that the bainitic ferrite formed with a supersaturation of carbon, although the mechanism was not discussed.

The model of pearlite formation involving the repeated formation of ferrite and cementite was abandoned when Hillert (1962) demonstrated that a pearlite colony really consists of two interwoven crystals, one of ferrite and the other of cementite. Hillert (1957, 1962)

also pointed out an important distinction between pearlite and upper bainite; in the former case, the ferrite and cementite phases grow cooperatively, whereas in the latter case, the plates of bainitic ferrite form first with the precipitation of cementite being a subsequent reaction.

### 1.2.6 Kinetics

Experiments indicated that martensite can grow very rapidly in steels, a plate taking a few microseconds to grow right across an austenite grain (Wiestner, 1932; Hannemann et al., 1932; Forster and Scheil, 1936, 1937). Bunshah and Mehl (1953) later measured the growth rate to be as high as  $1 \text{ km s}^{-1}$ , i.e. about one-third of the velocity of sound in iron. This gave rise to the incorrect impression that martensitic transformation does not involve a “nucleation and growth process”. Thus, Smith and Mehl (1942), wondered whether bainitic structures form by a process of nucleation and growth or whether the plates spring full-formed from the matrix lattice “as they do in the transformation to martensite”. A nucleation and growth model was favoured since the sizes of the reacted regions apparently increased with time at the reaction temperature. This was consistent with the work of Wever and his co-workers (Wever and Lange, 1932), who found that in the bainite transformation range, the austenite decomposes relatively slowly. Furthermore, the progress of the bainite transformation could be represented by means of a C-shaped curve on a TTT diagram (Davenport and Bain, 1930), with a well defined incubation period before the beginning of isothermal transformation. Martensitic transformation, on the other hand could not be suppressed by the fastest available quench rates (Troiano and Greninger, 1946); it seemed to form athermally and was represented on the TTT diagram by a family of lines parallel to the time axis (Cohen, 1946). The bainite reaction was found to follow C-curve kinetics even below the  $M_S$  temperature (Howard and Cohen, 1948).

It is in this context that Ko and Cottrell (1952) attempted to investigate whether bainite is “a nucleation and growth reaction, or like martensite, forms in a fraction of a second”. They also wanted to establish whether the transformation leads to surface relief effects similar to those associated with martensitic transformations. Ko and Cottrell were able to demonstrate, through hot-stage light microscopy, that bainite grows relatively slowly and that its formation causes the shape of the transformed region to change, the shape change being characterised qualitatively as an invariant-plane strain (Fig. 1.7). They also noted that unlike pearlite which is not hindered by austenite grain boundaries (Mehl, 1948), bainite growth terminated at austenite twin or grain boundaries. The transformation was therefore similar to martensite, and Ko and Cottrell attempted to identify any clear differences that may exist between martensite and bainite.

It was known already that martensite first forms at a large undercooling below the  $T_0$  temperature, at which ferrite and austenite of identical composition have equal free energy (Zener, 1946; Cohen et al., 1950). Since diffusionless transformation is *thermodynamically* feasible below  $T_0$ , the extra undercooling was believed necessary to account for the strain and to a lesser extent, the interface energy associated with the formation of the martensite plate. Bainite, which forms at higher temperatures, must have a different mechanism consistent with the smaller driving force available at elevated temperatures. Ko and Cottrell argued that a “coherent nucleus” can develop either into martensite or into bainite depending on the driving force available for transformation, the nucleus developing into martensite below  $M_S$ . At the higher temperatures where bainite occurs, “coherent growth” can only “take place when the strain due to the density change is relieved”. This could happen if the amount of carbon dissolved in bainite is reduced, either by diffusion from

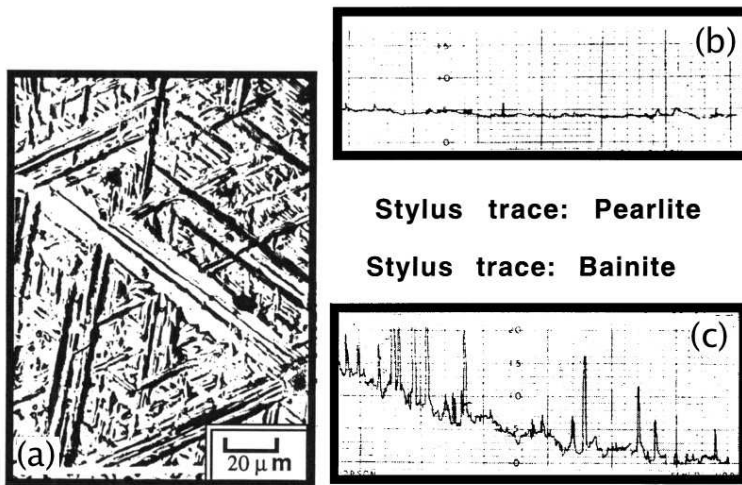


**Figure 1.7** Surface effects observed during the transformation of pre-polished samples of austenite (Ko and Cottrell, 1952). (a) Surface relief due to the formation of bainite. (b) Line traces obtained by traversing a stylus across the surface of a pearlitic and a bainitic sample. Notice the severe upheavals caused by bainite, which contrast with the negligible relief due to pearlite.

bainite or by precipitation within bainite, or by a combination of these processes, depending on the transformation temperature. It is not clear from their description whether they envisaged initially diffusionless growth, followed by carbon diffusion to provide the driving force for further growth, or whether the diffusion and interface migration are coupled so that precipitation within the ferrite (for lower bainite) or carbon rejection to the austenite (for upper bainite) takes place at the moving interface. The former mechanism is illogical since the extra driving force is only available after a stage of initial growth to martensite which should not be possible (according to their growth condition) above  $M_S$ . Provided there is some way of circumventing the difficulty of forming the initial coherent nucleus (of whatever composition), the second type of growth model would allow bainite to form above  $M_S$ , and indeed above  $T_0$ . In some later work, Ko (1953) distinguished between incoherent ferrite and “acicular ferrite” which he proposed should be regarded as carbon-free bainitic ferrite.

Kriesement and Wever (1956) pointed out that the appearance of bainite changes continuously between upper and lower bainite, and postulated that the microstructure evolves by the repeated and alternating nucleation and growth of lamellae of cementite and ferrite, from austenite. Unlike pearlite, the growth direction of the macroscopic plate of bainite was supposed to be normal to the plane of the lamellae. Although this particular mechanism has since been shown to be incorrect, they identified clearly the condition necessary for cementite precipitation to occur from residual austenite during the bainite transformation. Cementite precipitates from austenite if the carbon concentration of the latter exceeds that given by the extrapolated  $\gamma/\gamma + \theta$  phase boundary.

Although many of the characteristics of bainite, especially the morphology and the shape deformation, had been found to be similar to those of martensite, a different microstructural approach was developed by Aaronson (1962). He used the Dubé morphological classification (Dubé et al., 1958; Heckel and Paxton, 1961) for all non-pearlitic forms

of ferrite and attributed the morphological variations to the dependence on the growth kinetics of an interface and to the nature of the site from which a precipitate crystal develops. In particular, plate morphologies were regarded as the result of the formation of immobile, partly coherent, planar interfaces which can grow normal to themselves only by the lateral migration of “ledges”. In a later discussion of bainite, Aaronson (1969) developed the “microstructural” definition in which bainite is regarded simply as a non-lamellar two-phase aggregate of ferrite and carbides in which the phases form consecutively, as distinct from pearlite where they form cooperatively. Aaronson stated that according to this definition, the upper limiting temperature of bainite formation should be that of the eutectoid reaction ( $Ae_1$ ), and he denied that the kinetic  $B_S$  temperature has any fundamental significance. In those alloy systems where there seems clear evidence for a separate C-curve for bainite, the bainitic “bay” and the apparent upper limit of bainite formation ( $B_S$ ) were attributed to a special effect of certain alloying elements on the growth kinetics. Aaronson equally dismissed the observation of surface relief as a basis for classifying the various forms of ferrite.

### 1.3 Bainitic Steels: Industrial Practice

In spite of the early optimism about the potential of bainitic steels, commercial exploitation took many years to become established. The steels were not better than quenched and tempered martensitic steels, partly because of the coarse cementite particles associated with bainite and because the continuous cooling heat treatments which were popular in industry, could not in practice produce fully bainitic steels. The use of lean alloys gave mixed microstructures whereas intense alloying led to intolerable quantities of martensite. It was not until low-alloy, low-carbon steels containing boron and molybdenum were introduced by Irvine and Pickering (1958) that fully bainitic steels could be produced in commercial quantities using continuous cooling heat treatments. Nonetheless, martensitic steels dominated the high-strength steel market, with their better overall mechanical properties and well understood physical metallurgy principles.

Even lower carbon concentrations than conceived by Irvine and Pickering could have led to better bainitic steels, with strength and toughness due to the sub-micrometre size grain structure of bainite. However, technology was not in those days sufficiently advanced to cope with the necessarily higher cooling rates required to produce bainite in very low-carbon steels, as the steel left the hot-rolling mill. The first system designed to accelerate cooling of hot sheet steel as it leaves the mill, was at the United Steel Company (UK), probably as a means to reduce the length of the run-out table which allows the strip to cool to a specified temperature before coiling. The faster cooling was achieved using a laminar water jet system (Adcock, 1962). The first papers discussing the metallurgical benefits of accelerated cooling were presented in 1965 (Morgan et al., 1965). The technology of accelerated cooling designed to produce partially or wholly bainitic microstructures in very low-carbon, microalloyed steels has been now perfected with the new class of steels well established (DeArdo, 1988).

An area of major success for bainite was in creep resistant steels, where the so-called  $2\frac{1}{4}\text{Cr-1Mo}$  steel was known to be one of the best alloys for creep strength and microstructural stability in large components (Miller et al., 1940). The microstructural aspects of the steel may not have been appreciated in those days, but on continuous cooling it transforms into carbide-free upper bainite. In most applications, the microstructure is then heavily tempered at  $700^\circ\text{C}$  for several hours in order to relieve any residual stress. The temper-

ing treatment and service at elevated temperatures causes the precipitation of a series of metastable alloy carbides, which together with solid solution strengthening by molybdenum, greatly enhance the creep strength. This particular alloy even now sustains the energy generation industry (Lundin et al., 1982).

#### 1.4 Summary of the Early Research

By the beginning of the sixties, bainite was regarded as a transformation product differing significantly from various forms of proeutectoid ferrite as well as from pearlite and martensite. The results of the early research can be summarised as follows (Fig. 1.8).

Bainite can be obtained by isothermal transformation at all temperatures where the formation of pearlite and proeutectoid ferrite is sluggish, and also at temperatures below the martensite-start temperature. Upper bainite, which forms at high temperatures, was found to consist of sheaves of ferrite plates with cementite particles located between the plates. By contrast, lower bainite was characterised by fine cementite particles within the bainitic ferrite plates in addition to those between the plates.

Observations using light microscopy indicated that bainite sheaves lengthen at a rate much slower than martensite plates. Bainite sheaves were found to have irrational habit planes, the indices of which differed from those of martensite in the same alloy. The orientation relationship between bainitic ferrite and austenite was on the other hand similar to that between martensite and austenite. Bainite plates were never found to cross austenite grain boundaries and the formation of bainite was, like martensite, observed to cause the shape of the parent crystal to change. This shape deformation is in present day terminology better described as an invariant-plane strain.

In steels where transformation to bainite could be carried out without interference from other reactions, experiments demonstrated that the degree of transformation to bainite decreases (ultimately to zero) and that the time taken to initiate the reaction increases rapidly with increasing isothermal transformation temperature. This led to the definition of a bainite-start temperature above which there is no reaction. This temperature was always found to lie well within the (metastable)  $\alpha + \gamma$  phase field. Other reactions could follow bainite, but in all cases, the rapid growth of bainite stopped prematurely before the austenite was fully transformed.

The prevailing, albeit rather ill-defined concept of the bainitic reaction as involving a martensitic type interface combined with carbon diffusion-controlled growth had already led to the suggestion of bainitic reactions in non-ferrous alloys. In particular, the observation of surface relief effects apparently combined with compositional changes in the decomposition of some  $\beta$ -phase copper-zinc alloys had been used in a pioneering paper by Garwood (1954-1955) to identify this decomposition as bainitic, and the difficulties in accounting for such a reaction in purely substitutional alloys had been emphasised by Christian (1962). This remains an interesting aspect of transformation theory (Christian, 1997).

The early emphasis on the similarities between bainitic and martensitic transformations still dominated the literature in the 1960s. The contrasting views of Aaronson and co-workers were only beginning to emerge. This led to controversy but also stimulated research. There is now a clear picture of the mechanism of transformation, the quantitative aspects of which have contributed significantly to the design of some remarkable steels.

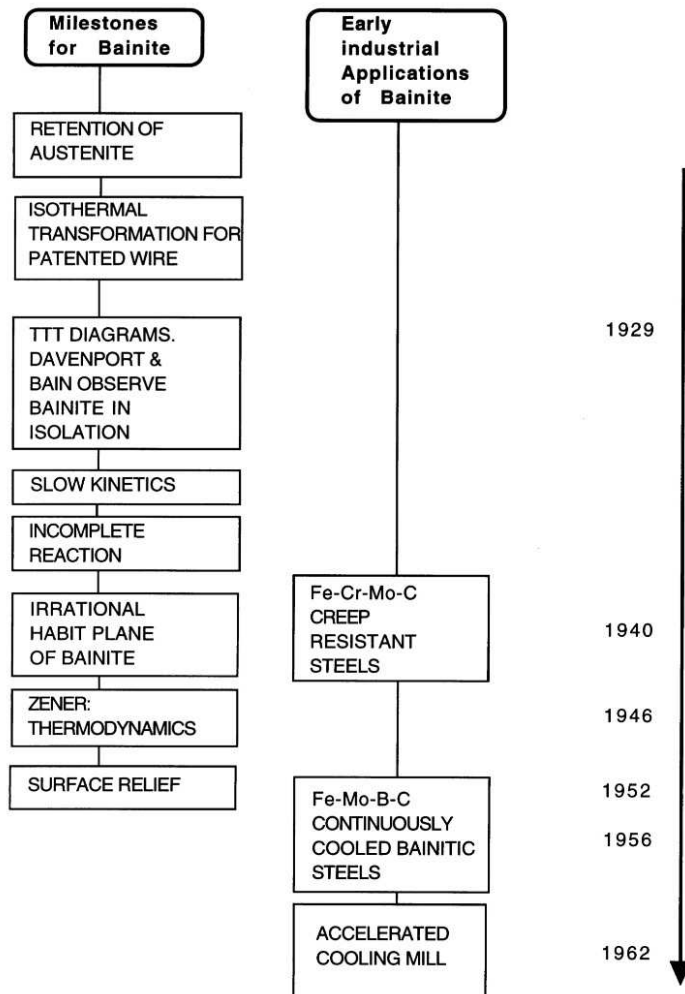


**Figure 1.8** Flow chart illustrating some of the important milestones in the history of bainite.

## CHAPTER 2

---

### BAINITIC FERRITE

---

The growth of pearlite occurs at a common transformation front with the austenite. The growth of the ferrite and cementite phases is coupled and their compositions are complementary since the carbon which cannot be accommodated by the ferrite is incorporated into the cementite. This contrasts with bainite which occurs in separable stages, first the growth of ferrite, followed by the precipitation of carbides. This chapter deals with the ferritic component of bainite, focusing on its morphology, crystallography, constitution and kinetics.

#### 2.1 Sheaves of Bainite

##### 2.1.1 Morphology

Both upper and lower bainite consist of aggregates of plates of ferrite, separated by untransformed austenite, martensite or cementite (Fig. 2.1). The aggregates of plates are called *sheaves* (Aaronson and Wells, 1956) and the plates within each sheaf are the *sub-units*. The sub-units are not isolated from each other but are connected in three dimensions. It follows that they share a common crystallographic orientation.

Many observations, including two-surface analysis experiments, show that the shape of a sheaf is that of a wedge-shaped plate (Oblak et al., 1964; Srinivasan and Wayman, 1968c). The thicker end of the wedge begins at the nucleation site which is usually an austenite grain surface. The sub-units which make up the sheaf have a lenticular plate

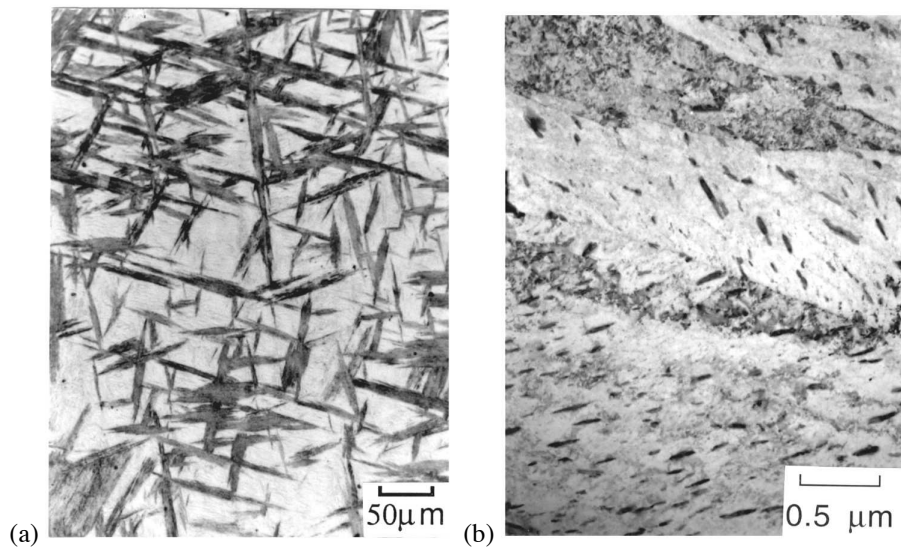


**Figure 2.1** (a) Light micrograph illustrating sheaves of lower bainite in a partially transformed (395 °C) Fe-0.3C-4Cr wt% alloy. The light etching matrix phase is martensite. (b) Corresponding transmission electron micrograph illustrating sub-units of lower bainite.

or lath morphology, whose form is most prominent near the edge or tip of a sheaf where impingement effects are minimal (Fig. 2.2).

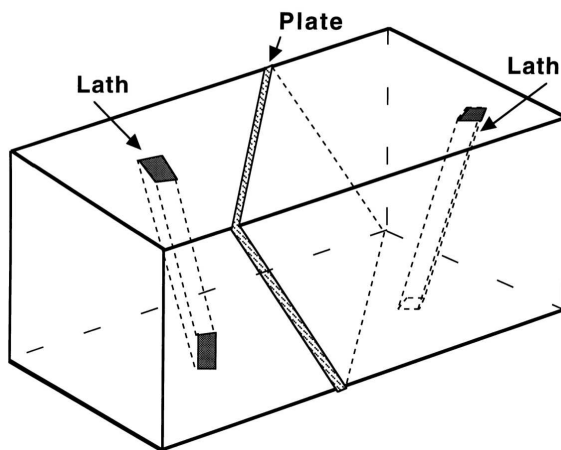


**Figure 2.2** The three-dimensional shape of a plate and of a lath.

The shape is best observed in partly transformed specimens. The dimensions of a sub-unit are uniform within a sheaf because each sub-unit grows to a limiting size. New sub-units are most frequently nucleated near the tips of existing sub-units rather than on their sides. The overall morphology of a sheaf is illustrated in Fig. 2.3.

When the sub-units are in the form of laths, they are longest along the close-packed direction of the ferrite which is most parallel to a corresponding close-packed direction of the austenite (Davenport, 1974). As with martensite, plates tend to form at low tempera-

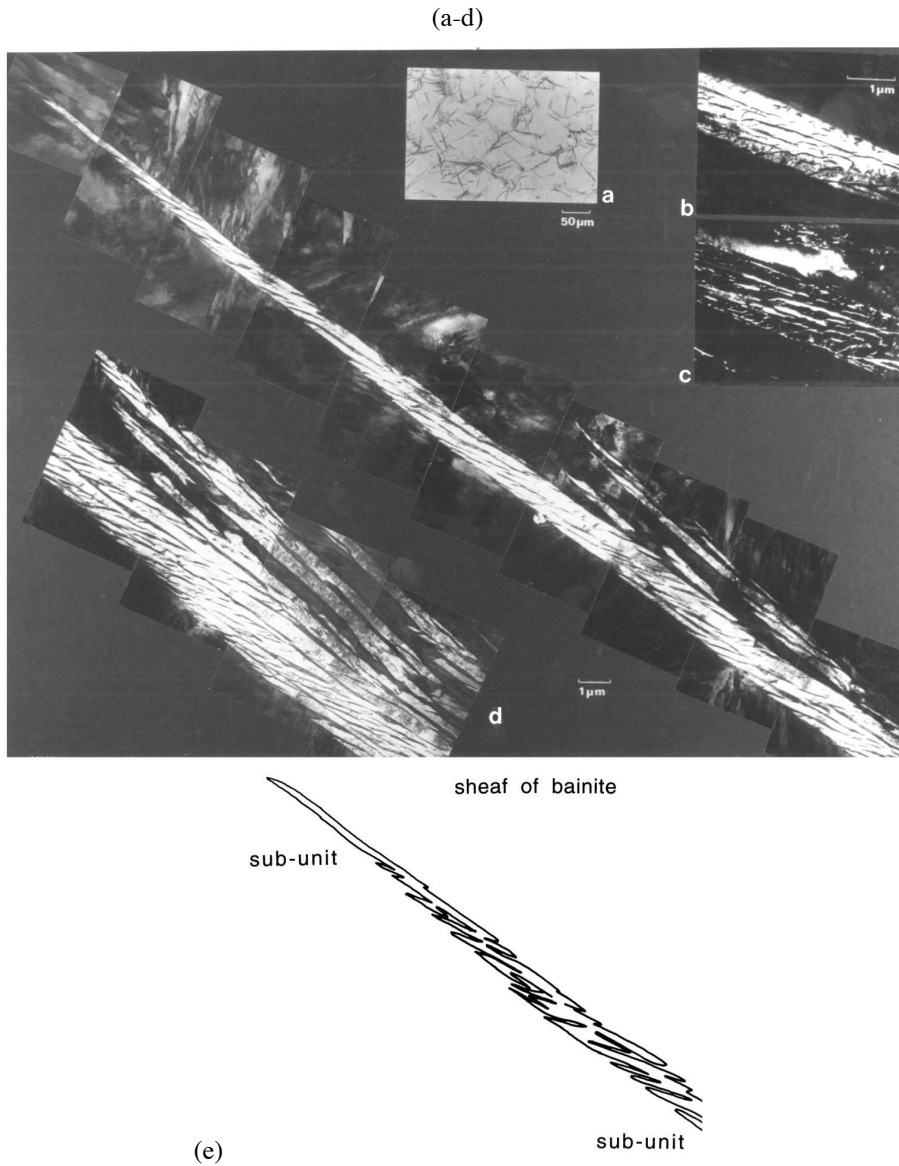


**Figure 2.3** (a) Transmission electron micrograph of a sheaf of upper bainite in a partially transformed Fe-0.43C-2Si-3Mn wt% alloy. (a) Light micrograph. (b,c) Bright field and corresponding dark-field image of retained austenite between the sub-units. (d) Montage showing the structure of the sheaf. (e) Corresponding outline of the sub-units near the sheaf tip region.

tures, large carbon concentrations or in strong austenite, Fig. 2.4 (Kelly and Nutting, 1960; Davies and Magee, 1970b,a, 1971; Haezebrouck, 1987). Thus, a plate morphology can be induced by increasing the strength of the austenite even if the transformation temperature is increased at the same time (Laverroux and Pineau, 1974). Similarly, the lath to plate transition can be induced using a magnetic field to change the driving force for transformation, without altering the transformation temperature (Korenko, 1973).<sup>1</sup>

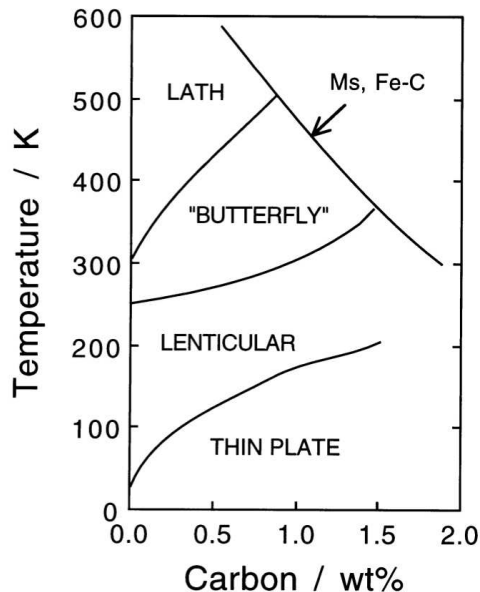


**Figure 2.4** The shape of martensite crystals as a function of the transformation temperature and carbon concentration of Fe-Ni-C alloys (Maki and Tamura, 1986).

The physical basis for these correlations is not clear because the variables described are not independent. The strength of the austenite must play a role because it determines the extent to which the shape change is plastically accommodated. Lath martensite is associated with this plastic accommodation which ultimately stifles the growth of the lath.

This hypothesis has been developed in detail by Haezebrouck (1987) who proposed that a plate shape is promoted by rapid radial growth and a high yield stress in the parent phase. Both of these factors favour elastic growth, where irreversible defects are not created during transformation. A high growth rate is equivalent to a high strain rate, which makes yielding more difficult. The radial growth must be elastic for small particles but whether this can be sustained as the particle grows depends on the flow behaviour of the austenite. The effect of plasticity is to cause the radial growth to arrest. If plasticity sets in at an early stage of growth, it is assumed that lath martensite is obtained. The model is consistent with experimental data, including the Korenko experiment and the growth arrest. It does not, however, address the *shape* transition. A plate to lath transition depends on a change from isotropic to anisotropic radial growth.

<sup>1</sup>A three-dimensional reconstruction of a series of optical micrographs led Wu and Enomoto (2002) to conclude that the bainite sub-units have rod-like cross-sections. However, the resolution of the method is compromised, both by the use of optical microscopy and by the image analysis software. Their own transmission microscopy images show only plate sections. A rod shape is also inconsistent with the observed shape deformation.

The observed variations in microstructure as a function of temperature are summarised in Fig. 2.5.

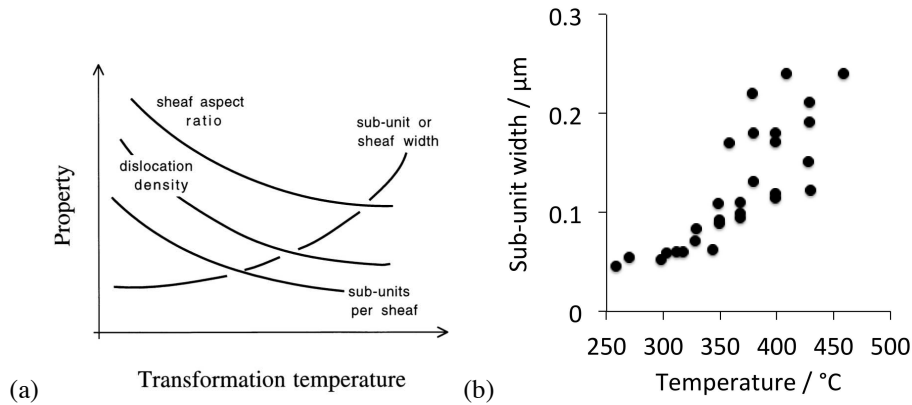


**Figure 2.5** (a) Qualitative trends in microstructure as a function of the transformation temperature. (b) Measurements of the bainite sub-unit thickness as a function of the transformation temperature for a variety of steels (Chang and Bhadeshia, 1995a; Singh and Bhadeshia, 1998a).

Such changes in microstructure are illustrated vividly in Fig. 2.6, where the microstructure represents the effects of an abrupt change in the transformation temperature from 420 $^{\circ}\text{C}$  to 290 $^{\circ}\text{C}$ . This has resulted in a bimodal scale with a dramatic reduction in the plate size on lowering the temperature. An additional benefit of such a two-step heat treatment is the refinement of the islands of residual austenite (Wang et al., 2014b), which if too coarse, can compromise the toughness of the steel.

### 2.1.2 Thickness of bainite plates

If the shape deformation is elastically accommodated then the plates can in principle maintain an elastic equilibrium with the matrix. They may continue to thicken isothermally until the strain energy balances the available free energy. It follows that if the plates are allowed to grow freely, they should be thicker at lower temperatures where the driving force is the greatest. This contradicts the experimental data because bainite is never elastically accommodated. Direct observations have shown that there is considerable plastic relaxation in the austenite adjacent to the bainite plates (Swallow and Bhadeshia, 1996), that also causes a broadening of austenite X-ray diffraction peaks during the course of transformation, as the austenite accumulates defects (Dutta et al., 2013). The dislocation debris generated in this process resists the advance of the bainite/austenite interface, the resistance being greatest for strong austenite. The yield strength of the austenite must then feature in any assessment of plate size. In this scenario, the plates are expected to become thicker at high temperatures because the yield strength of the austenite will then be lower. Dynamic recovery at high temperatures may further weaken the austenite and lead to coarser plates. Indeed, high-temperature bainite often contains sub-grains which are finer for lower transformation temperatures (Pickering, 1958). These boundaries form by the recovery of the dislocation structure during transformation.

The thickness must also be influenced by impingement between adjacent plates; as in all transformations, a large nucleation rate corresponds to a finer microstructure.

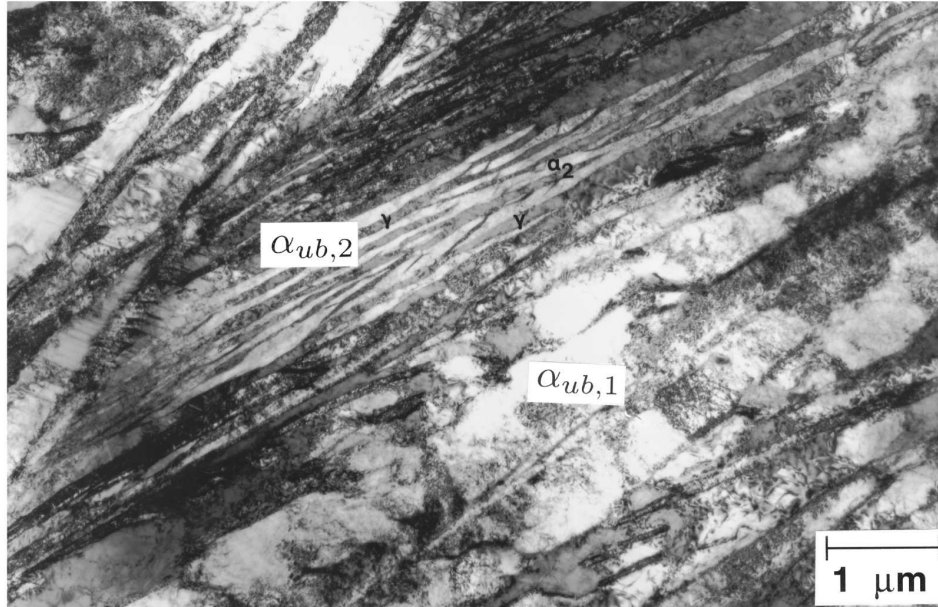


**Figure 2.6** A bimodal distribution of bainite plate thickness ( $\alpha_{ub,1}$  and  $\alpha_{ub,2}$ ), obtained by changing the isothermal transformation temperature from 420°C to 290°C (Papadimitriou and Fourlaris, 1997).

The perceived effect of temperature could be indirect since both strength and the nucleation rate are strongly dependent on temperature. A quantitative analysis indicates that temperature has only a small independent effect on the thickness of bainite plates (Fig. 2.7). The main conclusion is that strong austenite and high driving forces lead to a finer microstructure. These outcomes have been confirmed by Caballero et al. (2004).

The relationship between plate thickness ( $t$ ,  $\mu\text{m}$ ), driving force ( $\Delta G^{\gamma\alpha}$ ,  $\text{J mol}^{-1}$ ), absolute temperature and the strength of austenite ( $\sigma_y^\gamma$ , MPa) is highly non-linear which is why the original analysis was carried out using a neural network (Singh and Bhadeshia, 1998a). However, as a rough guide, Azuma et al. (2005) have derived the following polynomials based on the same data:<sup>2</sup>

$$t \simeq 0.478 + 1.2 \times 10^{-4}T + 1.25 \times 10^{-4}|\Delta G^{\gamma\alpha}| - 2.2 \times 10^{-3}\sigma_y^\gamma \quad (2.1)$$

with  $\sigma_y^\gamma \simeq [1 - 0.26 \times 10^{-2}T_r + 0.47 \times 10^{-5}T_r^2 - 0.326 \times 10^{-8}T_r^3]$   
 $\times 15.4(4.4 + 23w_C + 1.3w_{Si} + 0.24w_{Cr} + 0.94w_{Mo} + 32w_N)$  MPa

where  $w_i$  represents the concentration in wt% of the element identified by the subscript, and  $T_r = T - 25$  and  $T$  is the temperature in °C. The equation is based on original data where the thickness ranged from 0.053-0.330  $\mu\text{m}$ .

<sup>2</sup>The equation for strength was stated incorrectly when reproduced in (Azuma et al., 2005) from (Singh and Bhadeshia, 1998a).

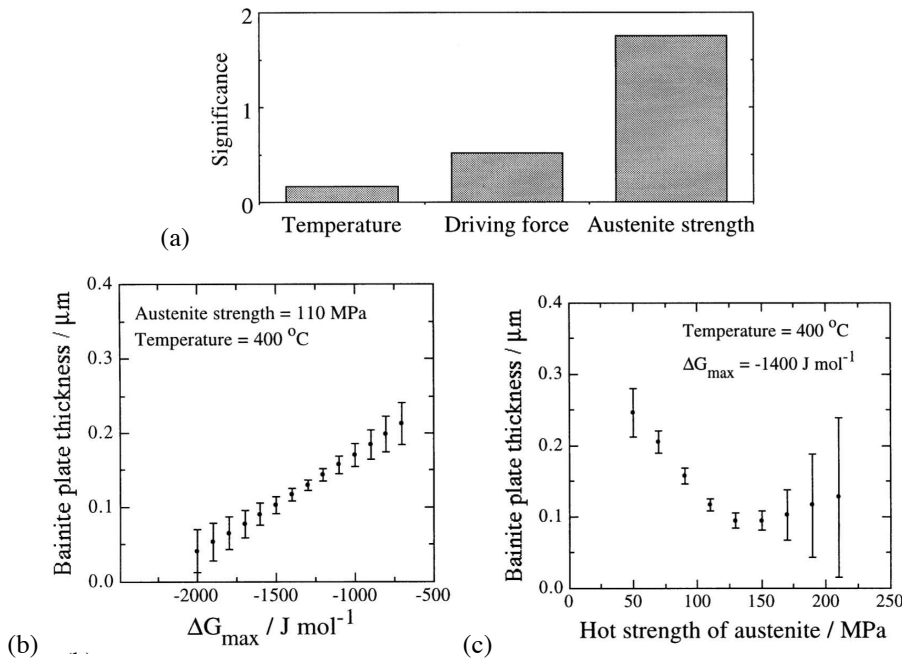


**Figure 2.7** (a) The neural network perceived significance of each of the variables plotted on the horizontal axis, in influencing the thickness of bainite plates. The vertical scale represents the ability of the variable to explain variations in plate thickness. (b) Variation in thickness with the chemical driving force. (c) Variation in thickness with the strength of the austenite. After Singh and Bhadeshia (1998a).

### 2.1.3 Stereology

Crystals of bainite are anisotropic in shape. Their size is characterised by measuring the thickness on a random section in a direction normal to the long edges of the plates. The average value of many such measurements gives an apparent thickness which can be useful in correlations with mechanical properties. The true thickness requires stereological effects to be taken into account. If a plate is represented as a disc of radius  $r$  and thickness  $t$  with  $r \gg t$ , then the mean intercept length is given by  $\bar{L}_3 = 2t$ , and the mean intercept area is given by  $\bar{A} = 2rt$  (Fullman, 1953). These intercepts must be taken at random.

The appropriate measure of the grain size is dependent on the application. For example, the strength will be a function of the dimensions of the slip planes within individual plates (Naylor, 1979; Daigne et al., 1982). Assuming that there is a random distribution of slip plane orientations, the grain boundary strengthening term is of the form  $\sigma_g = k_g M^{-1}$ , where  $k_g$  is a constant and  $M$  is the mean value of the larger diameter of a slip plane. This differs from the Hall-Petch relation where it is the inverse square root of grain size which matters (Chapter 12).

The stereology of a sheaf is rather more complicated than implied by a mean lineal intercept. This is because from a topological point of view, it is a *rough* object; the amount of  $\alpha_b/\gamma$  interface per unit volume,  $S_V$ , depends on the resolution  $\epsilon_r$  with which measurements are made:

$$S_V = S_V^0 \epsilon_r^{D_T - D} \quad (2.2)$$

where  $S_V^\circ$  is the surface to volume ratio of a smooth object,  $D_T$  the topological dimension and  $D$  the fractal dimension.<sup>3</sup> The fractal dimension can be derived by measuring  $S_V$  as a function of resolution; such experiments have been done (Kang and Bhadeshia, 2006), with  $D = 3.59$  so that:

$$\ln \{S_V/\text{m}^{-1}\} = 0.59 \ln \epsilon_r^{-1} + 5.4 \quad (2.3)$$

where the units of  $\epsilon_r$  are in metres. The fractal dimension is less than 4 because the sheaf does not possess a true fractal character, due to the limited number of generations of sub-units. From a physical point of view, it is expected and observed that there are only two generations leading to a bimodal distribution of sub-unit sizes (Olson et al., 1990). The largest generation represents platelets that have formed to the point where mechanical stabilisation stifles their growth, and the smaller ones are the sub-operational embryos that have yet to develop into the rapid growth stage (section 6.3). Therefore, the increase in  $S_V$  as a function of resolution is less rapid when compared with  $D = 4$ , as illustrated in Fig. 2.8. A relationship such as that in equation 2.3 can be used in structure-property correlations. For example, when considering toughness, it may be appropriate to account for  $S_V$  with  $\epsilon_r > 10^{-5}$  m given the size of a typical plastic zone, whereas to consider the segregation of hydrogen to interfaces, a much greater  $S_V$  is appropriate with  $\epsilon_r < 10^{-7}$  m.

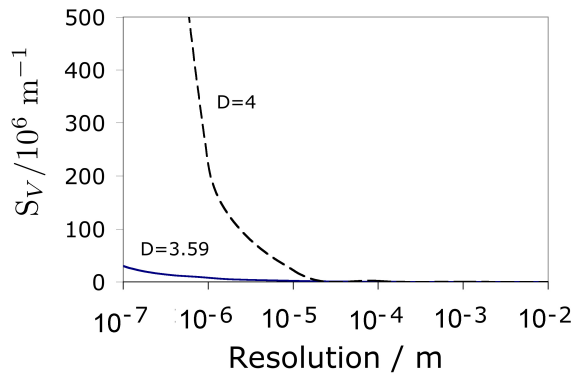


**Figure 2.8** Comparison of measured variation in  $S_V$  versus that calculated for an ideal fractal where families of sub-units grow in many generations of self-similar formations, each on a finer scale.

## 2.2 Dislocation Density

Popular opinion is that bainite has a high dislocation density but there are few quantitative data to support this notion. Transmission electron microscopy has revealed a dislocation density  $\rho_d$  of about  $4 \times 10^{14} \text{m}^{-2}$  for an alloy with  $B_S \simeq 650^\circ\text{C}$ . To put this in context, the same dislocation density can be obtained by elongating an iron sample by 7% (Takaki, 2003). It is also useful to compare against allotriomorphic ferrite obtained at  $800^\circ\text{C}$  in the same steel with  $\rho_d \simeq 0.5 \times 10^{14} \text{m}^{-2}$  (Smith, 1984). These data are similar to measurements on continuously cooled steel in which  $\rho_d\{\text{bainite}\} \simeq 1.7 \times 10^{14} \text{m}^{-2}$  and  $\rho_d\{\text{allotriomorphic ferrite}\} \simeq 0.37 \times 10^{14} \text{m}^{-2}$  (Graf et al., 1985). It is significant

<sup>3</sup>A perfect sphere is smooth, with  $S_V$  equal exactly to  $4\pi r^2/(4/3)\pi r^3$  and  $D_T = 3$ . Measures of perimeter and surface area are not well-defined for objects that are rough, because they depend on the resolution of the measurement technique.

that bainite contains more dislocations than allotriomorphic ferrite even when they form at similar temperatures.

The defect structure of bainite is often attributed to the shear transformation mechanism. However, such a mechanism need not leave dislocations in the ferrite if the shape deformation is elastically accommodated. Thermoelasticity in martensites and shape memory alloys depends on the elastic accommodation of the shape deformation and the movement of any interfaces must occur without the creation of defects. It is only if the shape deformation is accompanied by plastic relaxation (Fig. 2.9) that the dislocations associated with this plastic strain are inherited by the product phase. Indeed, even the local misorientations associated with dislocation debris in the austenite are inherited by the bainite (Godet et al., 2004).

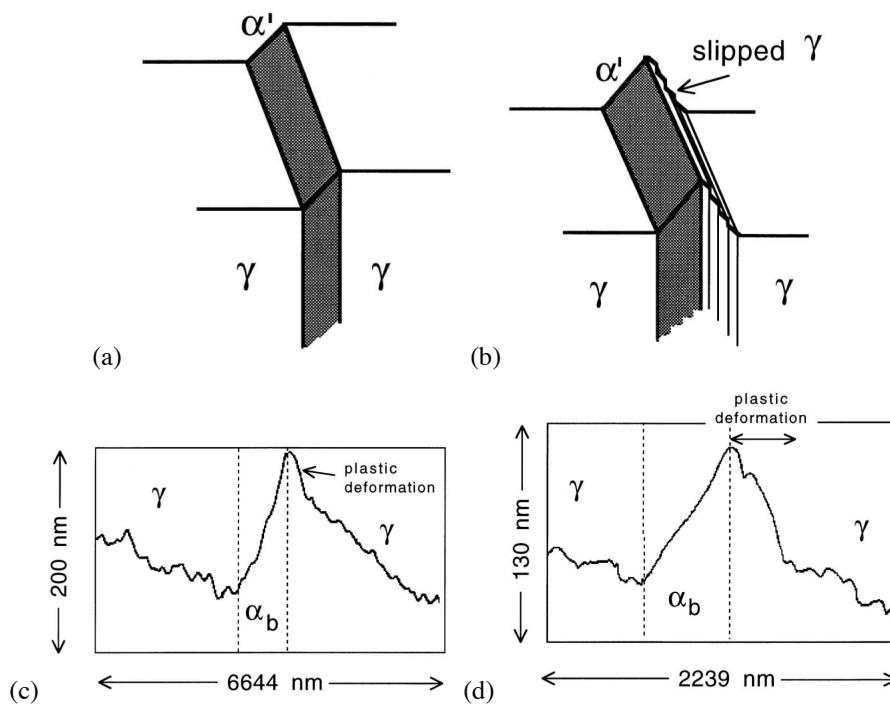


**Figure 2.9** (a) A perfect invariant-plane strain surface relief effect. (b) One where plastic relaxation of the shape change occurs in the adjacent matrix. (c,d) An actual atomic force microscope scan across the surface relief due to a bainite sub-unit (Swallow and Bhadeshia, 1996).

It is conceivable that the ferrite plate itself might relax. After all, the strength of both ferrite and austenite decreases at high temperatures. However, theory predicts that for a plate shape, the strains are mostly accommodated in the austenite (Christian, 1965b, 1975). Hence, atomic-force microscope scans show that the displacements within the bainitic ferrite are much more regular than in the adjacent austenite (Fig. 2.9c). The plastic accommodation is more evident in Fig. 2.9d, where the strain is seen to extend into the austenite to a distance about equal to the width of the bainite.

Plastic relaxation has featured in many early observations. When polished samples of austenite are transformed to bainite, the adjacent austenite surface does not remain planar, but instead exhibits curvature that is characteristic of slip deformation (Srinivasan and

Wayman, 1968c). Hot-stage transmission electron microscopy has shown that growth is accompanied by the formation of dislocations in and around the bainite (Nemoto, 1974). Direct observations of the austenite/bainite interface show accommodation in both phases, Fig. 2.10. The austenite adjacent to the bainite can accommodate the shape deformation by mechanical twinning or faulting, with the density of defects increasing as the transformation temperature decreases (Bhadeshia and Edmonds, 1979a; Sandvik and Nevalainen, 1981; Sandvik, 1982a). These accommodation defects are common in martensitic transformations (Jana and Wayman, 1970).

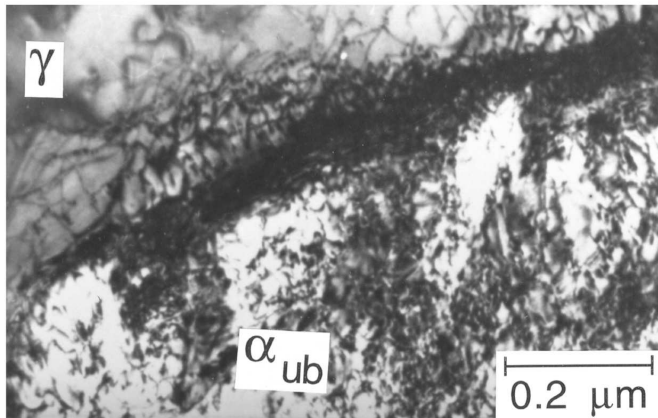


**Figure 2.10** Intense dislocation debris both at, and in the vicinity of the bainite/austenite transformation front (Bhadeshia and Edmonds, 1979a).

The dislocation density of bainitic ferrite increases as the transformation temperature is reduced (Pickering, 1967a). X-ray line profile measurements show an increase in the lattice strain due to dislocations as the transformation temperature is reduced. This can be used to estimate the dislocation density; isothermal transformation to bainite at 300, 360 and 400 °C gave dislocation densities of  $6.3 \times 10^{15}$ ,  $4.7 \times 10^{15}$  and  $4.1 \times 10^{15} \text{ m}^{-2}$  respectively (Fondekar et al., 1970).

### 2.2.1 Quantitative Estimation of Dislocation Density

It might be assumed that for low-alloy steels the dislocation density depends mainly on transformation temperature via the influence of the latter on the strength of the parent and product phases. It should then be possible to treat all of the displacive transformations, martensite, bainite and Widmanstätten ferrite, together. This leads to an empirical relationship for the upper bound of dislocation density, valid for transformation temperatures in the range 473-942 K (Fig. 2.11) derived originally by Takahashi and Bhadeshia (1990) but modified to include modern data on the dislocation density of nanostructured bainite obtained by isothermal transformation at 200 °C (Li and Jin, 2010; Mateo and Caballero, 2005) as:

$$\log_{10} \rho_d = 10.292 + \frac{5770}{T} - \frac{10^6}{T^2} \quad (2.4)$$

where  $\rho_d$  is the dislocation density in  $\text{m}^{-2}$ , and  $T$  is the reaction temperature in kelvin. For martensite the transformation temperature is taken to be the  $M_S$  temperature. Although

the dislocation densities of martensite measured by Norström (1976) are also plotted in the Fig. 2.11, those data were not used in deriving the expression because of uncertainties in the method used to assess the thickness of the thin foil samples used.

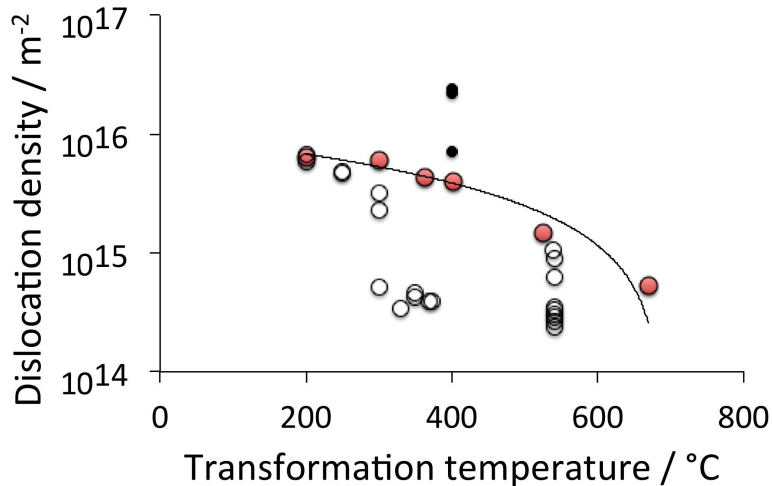


**Figure 2.11** Dislocation density of martensite, bainite, acicular ferrite and Widmanstätten ferrite as a function of the transformation temperature. The line is used as the basis for equation 2.4, derived from the red filled-points only. The three black filled-points are from (Sahu, 2005) on what is assumed to be bainite formed in stainless steel during isothermal transformation; these points are not included in the derivation of equation 2.4.

A single point from Cornide et al. (2011) on bainite transformed at 300 °C is also included in the plot; the data are claimed to be from nanostructured bainite but in fact the higher than conventional heat-treatment temperature leads to a coarser microstructure. However, the interesting result from this study is that the retained austenite contains a similar dislocation density, as expected from plastic accommodation effects. The dislocation density was found to be non-uniform, with the largest density at the  $\alpha_b/\gamma$  interfaces, as can be seen in Fig. 2.10.

## 2.3 Chemical Composition

### 2.3.1 Substitutional Alloying Elements

There is no long-range redistribution of substitutional solutes during the growth of bainitic ferrite (Aaronson and Domian, 1966, e.g.). High resolution experiments confirm this on the finest conceivable scale (Bhadeshia and Waugh, 1982b,a; Stark et al., 1988, 1990; Josefsson and André, 1988, 1989; Caballero et al., 2007; Pereloma et al., 2007; Caballero et al., 2008b, 2010c; Timokhina et al., 2011b). The ratio of the iron to substitutional solute atoms remains constant everywhere during the formation of bainite. This is not surprising given the displacive character of the transformation and the low diffusivity of substitutional atoms at the temperatures where bainite forms. By contrast, all atoms, including iron, must diffuse during a reconstructive transformation. Thus, it is possible to distinguish between a displacive and reconstructive mechanism even in pure iron.

A reconstructive transformation can be imagined to occur in two steps (Fig. 2.12): the change in crystal structure is achieved as in a displacive transformation; matter is then transferred in such a way that the shape deformation and strain energy associated with the first step is minimised. The matter must be transported over a distance about equal to the dimensions of the particle unless the interface is incoherent. This mass flow has been described as “reconstructive diffusion” (Bhadeshia, 1982b, 1985b).

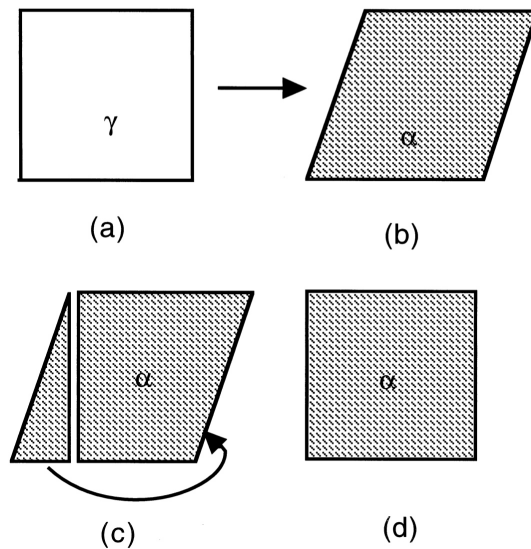


**Figure 2.12** Schematic illustration of the mass transport necessary to achieve reconstructive transformation, in both pure metals and alloys. Step (a) to (b) represents displacive transformation, whereas (a) to (d) represent reconstructive transformation. The mass transport illustrated in (c) eliminates the shape change due to the shear.

The diffusion necessary for the lattice change provides an opportunity for the solvent and solute atoms to partition during transformation. In an alloy steel, the carbon atoms, which are in interstitial solution, can migrate at rates many orders of magnitude greater than the iron or substitutional solute atoms (Fig. 2.13). For diffusion-controlled growth the compositions at the transformation front are in local equilibrium, given by a tie-line of the phase diagram. However, the tie-line has to be chosen in such a way that both the carbon and the substitutional solute ( $X$ ) can keep pace with the moving interface in spite of their vastly different diffusion coefficients. This can happen in two ways (Hillert, 1953; Kirkaldy, 1958; Purdy et al., 1964; Coates, 1972, 1973b,a). First, the tie-line controlling the interface compositions is such that the gradient of carbon in the austenite is minimised (Fig. 2.14a). This is known as *partitioning, local equilibrium* or P-LE mode because there is long-range partitioning of  $X$ . The P-LE mode of growth applies when the undercooling below the equilibrium transformation temperature is small.

The second possibility is that a tie-line is selected so that the concentration gradient of  $X$  is large, thereby compensating for its small diffusivity (Fig. 2.14b). This is the *negligible partitioning local equilibrium* mode of transformation in which the ferrite has nearly the same  $X$  concentration as the austenite. This NP-LE mode occurs at large undercoolings below the equilibrium transformation temperature.

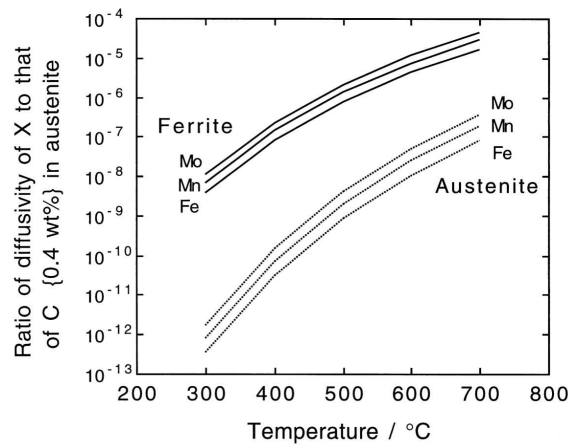


**Figure 2.13** A comparison of the diffusivities of iron and substitutional solutes relative to that of carbon (in austenite at a concentration of 0.4 wt%), in FCC and BCC iron, over the bainite transformation temperature range [data from Fridberg et al. (1969)].

In the NP-LE mode, the concentration of  $X$  is uniform except for a small “spike” in the parent phase adjacent to the interface. As the ratio of interstitial/substitutional diffusion rates increases, the width of this spike decreases, and when it becomes of the order of atomic dimensions, the concept of local equilibrium at the interface is invalid and has to be replaced, assuming the growth is nevertheless diffusion-controlled, by that of paraequilibrium (Hultgren, 1951; Rudberg, 1952; Aaronson et al., 1966a,b). In conditions of paraequilibrium, there is no redistribution of Fe +  $X$  atoms between the phases, the Fe/ $X$  ratio remaining uniform right up to the interface. One interpretation of the paraequilibrium limit is that reconstructive transformation occurs with all displacements of the Fe+ $X$  atoms taking place in the incoherent interface; another interpretation might be that only displacive transformation can occur. In either case, to quote from Coates, “the slow diffuser and the solvent participate only in the change of crystal structure”. Paraequilibrium implies that a constant Fe- $X$  ratio is maintained everywhere.

In conclusion, the experimental evidence that bainitic ferrite maintains the same iron to substitutional atom ratio as its parent austenite, is consistent precisely with the displacive mechanism and approximately so with reconstructive transformation. However, in the latter case when local equilibrium (or indeed any state between local and paraequilibrium) exists at the interface, there will be a significant perturbation to the substitutional solute content in the proximity of the interface. Experiments which have a chemical and spatial resolution on an atomic scale have all failed to show any evidence for the redistribution of alloying elements (Cr, Mn, Mo, Ni, Si) at the interface between bainitic ferrite and austenite, Fig. 2.15 (Bhadeshia and Waugh, 1982b,a; Stark et al., 1988, 1990; Josefsson and Andrén, 1988, 1989). These experiments were all based on steels where other reactions, such as the precipitation of carbides, do not interfere with the formation of bainitic ferrite. Measurements of the growth rates of grain boundary allotriomorphs of ferrite from austenite in alloy steels under conditions where bulk segregation is not observed (Kinsman and Aaronson, 1973; Bradley et al., 1977) indicate calculated thicknesses of the spike of much less than 0.1 nm, and although these results are complicated by the effect of grain

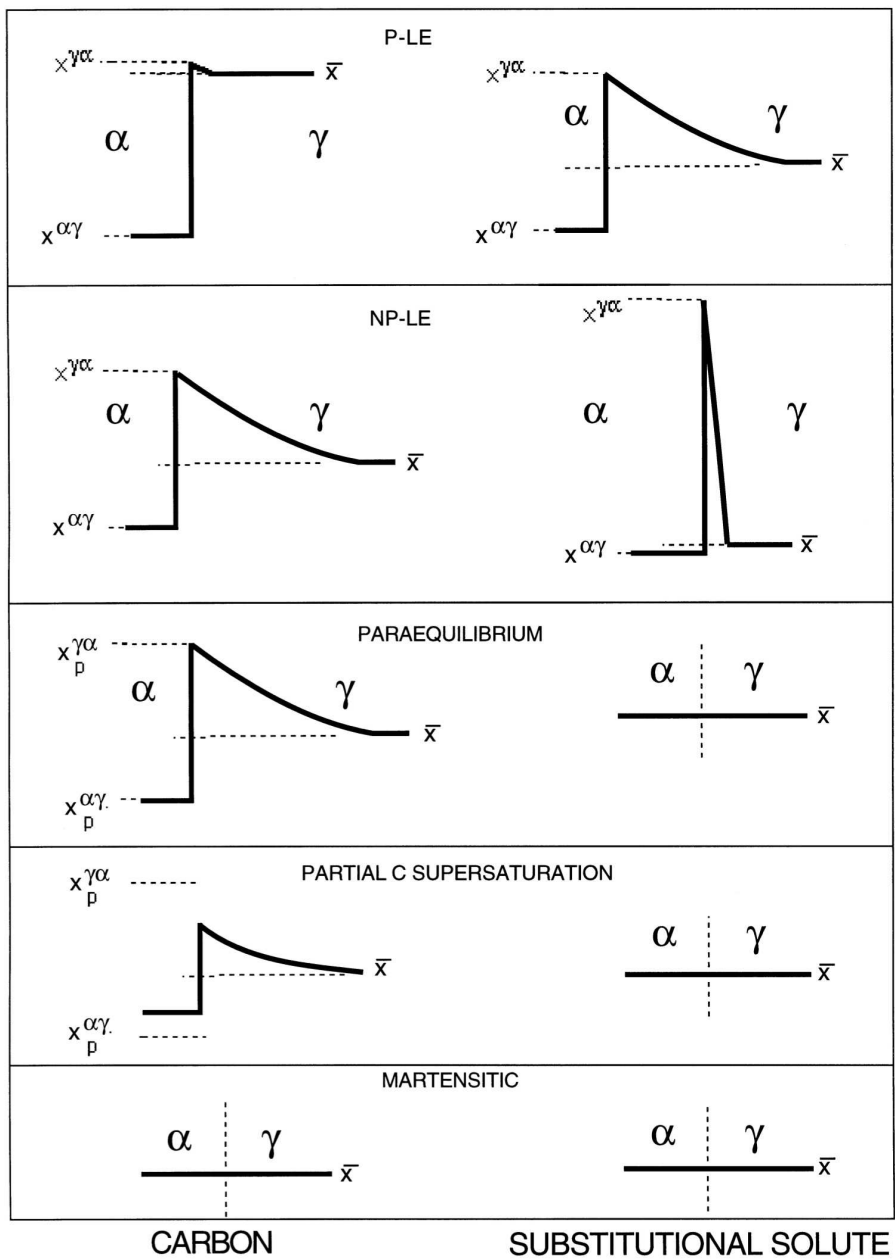


**Figure 2.14** The composition variations expected in the vicinity of the transformation interface, for a variety of growth mechanisms.

boundary diffusion, they are in general agreement with the concept that the lattice diffusion rate is inadequate to sustain local equilibrium at the growing interface. Only at temperatures above 600 °C, has the segregation of some (though by no means all) substitutional elements been obtained in grain boundary allotriomorphs (Aronson and Domian, 1966b).

Allotriomorphs are agreed to form by reconstructive mechanisms, but the absence of bulk segregation at moderately high transformation temperatures reinforces the belief, derived from the observed shape change, that bainitic ferrite forms at lower temperatures by a displacive rather than a reconstructive mechanism.

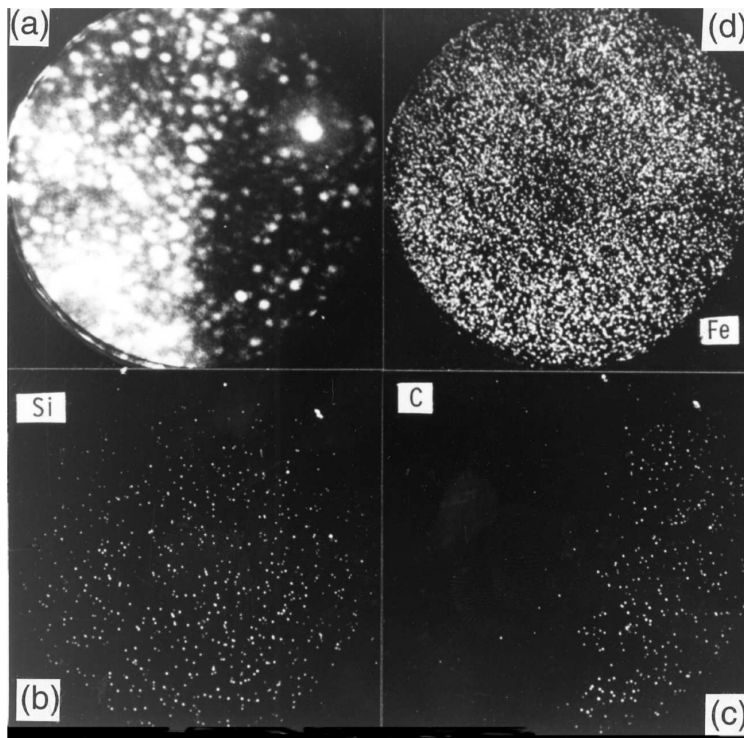


**Figure 2.15** Imaging atom-probe micrographs, taken across an austenite-bainitic ferrite interface in a Fe-C-Si-Mn alloy. The images confirm quantitative data (Bhadeshia and Waugh, 1982a) showing the absence of any substitutional atom diffusion during transformation. (a) Field-ion image with the darker region corresponding to austenite; (b) corresponding silicon map; (c) corresponding carbon map; (d) corresponding iron map.

### 2.3.2 Interstitial Alloying Elements

A particular experimental difficulty with the bainite transformation is that in the case of upper bainite at least, it is almost impossible to say anything about the initial carbon content of the ferrite. This is because the time taken for any carbon to diffuse from the supersaturated ferrite into the austenite can be small. For the moment we refer to the interstitial content of bainitic ferrite *after* transformation. As will be seen later, the concentration *during* transformation is likely to be different.

Internal friction experiments indicate that the amount of carbon which associates with dislocations in bainitic ferrite increases as the transformation temperature decreases, but is independent of the average carbon concentration in the steel, at least in the range 0.1–0.4 wt% C (Pickering, 1967b). This is consistent with the observation that the dislocation

density of bainitic ferrite increases as the transformation temperature is reduced. The insensitivity to the carbon concentration is because most of the carbon ends up in the residual austenite. The results also show that at some stage during the evolution of bainitic ferrite, it must have contained a higher than equilibrium concentration of carbon.

These observations have been confirmed directly by using microanalysis on an imaging atom-probe, which has demonstrated quantitatively (Fig. 2.16) that the *post-transformation* carbon content of bainitic ferrite tends to be much greater than equilibrium (Bhadeshia and Waugh, 1982b; Stark et al., 1988, 1990; Josefsson and Andrén, 1988, 1989; Caballero et al., 2007; Pereloma et al., 2007; Caballero et al., 2008b, 2009b, 2010c; Hu and Wu, 2011). Precise electron diffraction experiments using convergent beam Kikuchi lines to measure the lattice parameter of the bainitic ferrite also show that it contains a much larger concentration of carbon than expected from equilibrium (Zhang and Kelly, 1998). X-ray experiments on bainite in very high carbon austenite show similar results (Kutsov et al., 1999; Garcia-Mateo et al., 2003c).

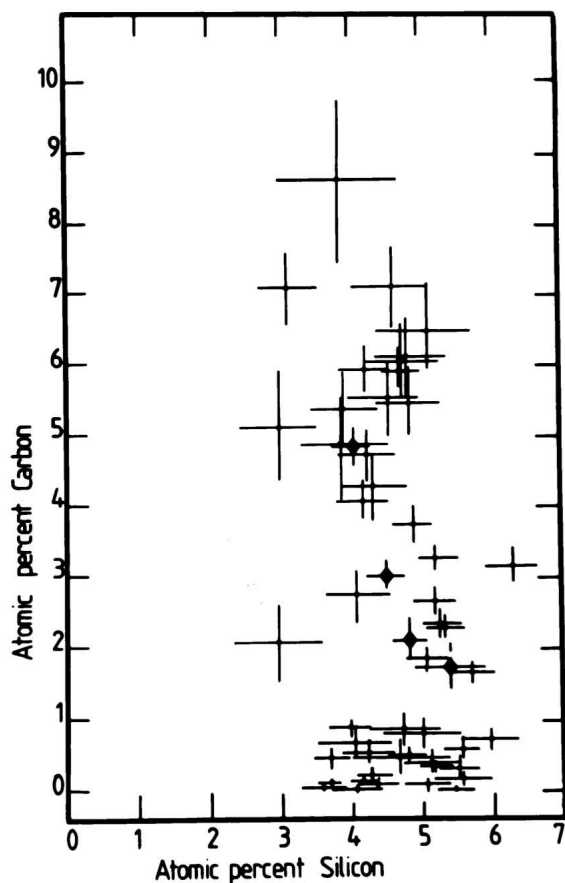


**Figure 2.16** Atom-probe determinations of the carbon and silicon concentrations of bainitic ferrite in an Fe-C-Mn-Si alloy transformed to upper bainite (Bhadeshia and Waugh, 1982b). The average carbon concentration in the alloy is 1.93 at.%, so all concentrations below that level are measurements from bainitic ferrite.

## 2.4 Crystallography

The properties of bainitic steels are believed to depend on the crystallographic texture that develops as a consequence of transformation from austenite. As an example, the ease with which slip deformation is transmitted across the adjacent plates of bainitic ferrite must be related to their relative orientation in space. Bainite grows in the form of clusters of plates called sheaves, with little misorientation between the plates within any given sheaf. Where they touch, adjacent plates are separated by low-misorientation grain boundaries.

The relative orientations of the bainitic ferrite and its parent austenite are always close to the classic KS (Kurdjumov and Sachs, 1930) and NW (Nishiyama, 1934; Wassermann, 1933) relationships (Fig. 2.17), although as will become evident later, they can never be exactly KS or NW. These two rational relations differ only by a relative rotation of  $5.26^\circ$  about the normal to the parallel close-packed planes of the two structures. The exact relative orientation is found in martensite to be intermediate and irrational, as is predicted by the crystallographic theory. High accuracy is required to compare theory with experiment since the predicted orientation relation is insensitive to input parameters such as lattice spacings or lattice invariant deformation. In the case of bainite, as in that of lath martensite, such precision is difficult to achieve partly because of the experimental difficulties in retaining austenite and partly because of the high dislocation densities. Nevertheless, modern techniques allow precise measurements, and data both on  $\gamma/\alpha$  bicrystals and on hundreds of thousands of bicrystals confirm that the exact orientations do not occur in practice (Nolze, 2004; Godet et al., 2004). Such observations can be taken to support the conclusion that the transformation is consistent with the phenomenological theory of martensitic transformations.

In spite of these difficulties, it is significant that the experimental data always lie well within the *Bain region* which encompasses the KS and NW relationships. The Bain strain is the pure part of the lattice deformation which for displacive transformations in steels converts austenite into ferrite or martensite, Fig. 2.18 (Bain, 1924). During the Bain strain, no plane or direction is rotated by more than  $11^\circ$  so that any pair of corresponding planes or directions may be made parallel by utilising a lattice deformation in which the Bain strain is combined with a rotation of not more than  $11^\circ$  (Crosky et al., 1980). This defines the Bain region. The experimentally observed orientation relations are expected to lie within this region for displacive but not necessarily for reconstructive transformations. Thus, allotriomorphic ferrite is known to grow into austenite grains with which it has an orientation which is random or outside of the Bain region (King and Bell, 1975). It is therefore significant that bainitic ferrite always exhibits an orientation which is close to KS or NW and well within the Bain region.

There is an interesting consequence of the requirement that bainite must be within the Bain region of orientations. It is accepted that allotriomorphic ferrite, when it nucleates at an austenite grain surface, must also grow with an orientation relationship which is close to KS or NW in order to minimise the activation energy for nucleation. But allotriomorphic ferrite *grows* most rapidly along austenite grain boundaries with which it has a random orientation. Once nucleated, it therefore grows selectively, away from its original nucleation site. A grain of ferrite then has a large fraction of its interface with the austenite with which it has a random orientation. Bainite can only nucleate from allotriomorphic ferrite at the small fraction of interfaces where the orientation is in the Bain region (Fig. 2.19).

Pickering (1967b) has suggested that the crystallography of bainite can be explained if the individual plates or laths adopt different variants of the NW or KS orientations, such that the ferrite orientations within a sheaf can be generated simply by rotation about the

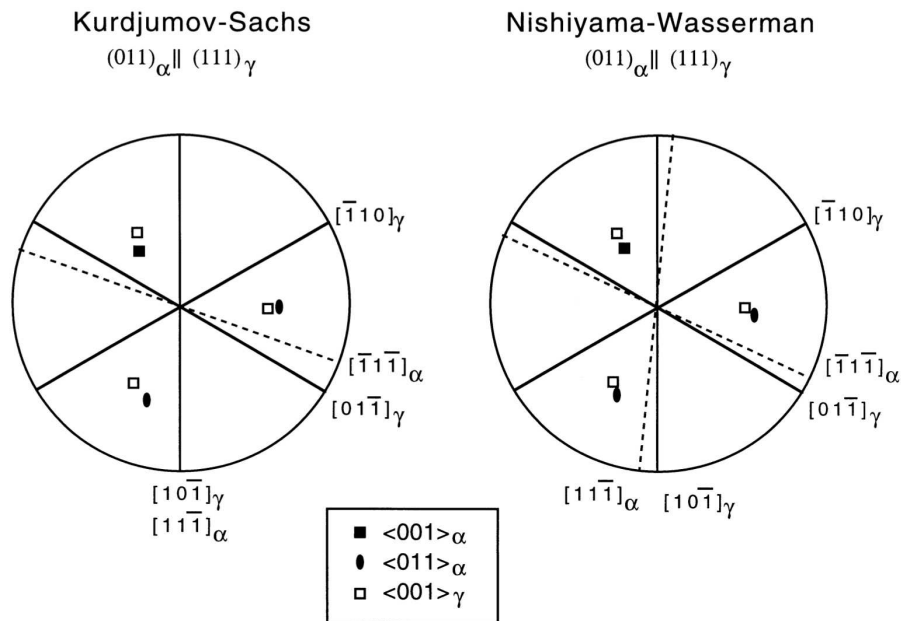


**Figure 2.17** Stereographic representation of the (a) Kurdjumov-Sachs and, (b) Nishiyama-Wasserman orientation relationships. Note that NW can be generated from KS by a rotation of  $5.26^\circ$  about  $[0\ 1\ 1]_\alpha$ .

normal to a specific close-packed plane of the austenite. In this way, the bainite laths may nucleate side by side in rapid succession, the transformation strains determining the variant and hence the exact sequence. This early work was based on measurements of only ferrite-ferrite orientation relations, since the specimens may have contained only thin films of austenite which are observable only with high resolution microscopy. However, it must be admitted that results from more recent work in which measurements of the direct austenite-ferrite relations have been made are still contradictory. There is general agreement that adjacent plates or laths in bainite all have a  $\{1\ 1\ 0\}_\alpha$  plane almost parallel to the same close-packed  $\{1\ 1\ 1\}_\gamma$  and that the macroscopic habit plane is near to  $\{1\ 1\ 1\}_\gamma$  in upper bainite but is irrational in lower bainite. Most investigators (Bhadeshia and Edmonds, 1980b; Sandvik, 1982a) find all the plates within a sheaf have a common orientation, but Sarikaya et al. (1986) claim that whilst some groups of adjacent laths have a common orientation, others have either different variants of the orientation relationship, or in lower bainite are twin-related. Similar discrepancies exist in crystallographic measurements on lath martensite where three types of orientation relation between adjacent laths of a packet are reported by some workers (Eterashvili et al., 1981; Sarikaya et al., 1986) and only one common orientation by others (Wakasa and Wayman, 1981; Sandvik and Wayman, 1983).

When there is a common orientation, the plates within a sheaf have small misorientations; there is also an appreciable spread of orientation within a single plate because of its high dislocation density. Direct crystallographic analysis indicates that all plates within a sheaf have an irrational orientation relation with the austenite which is closer to NW than

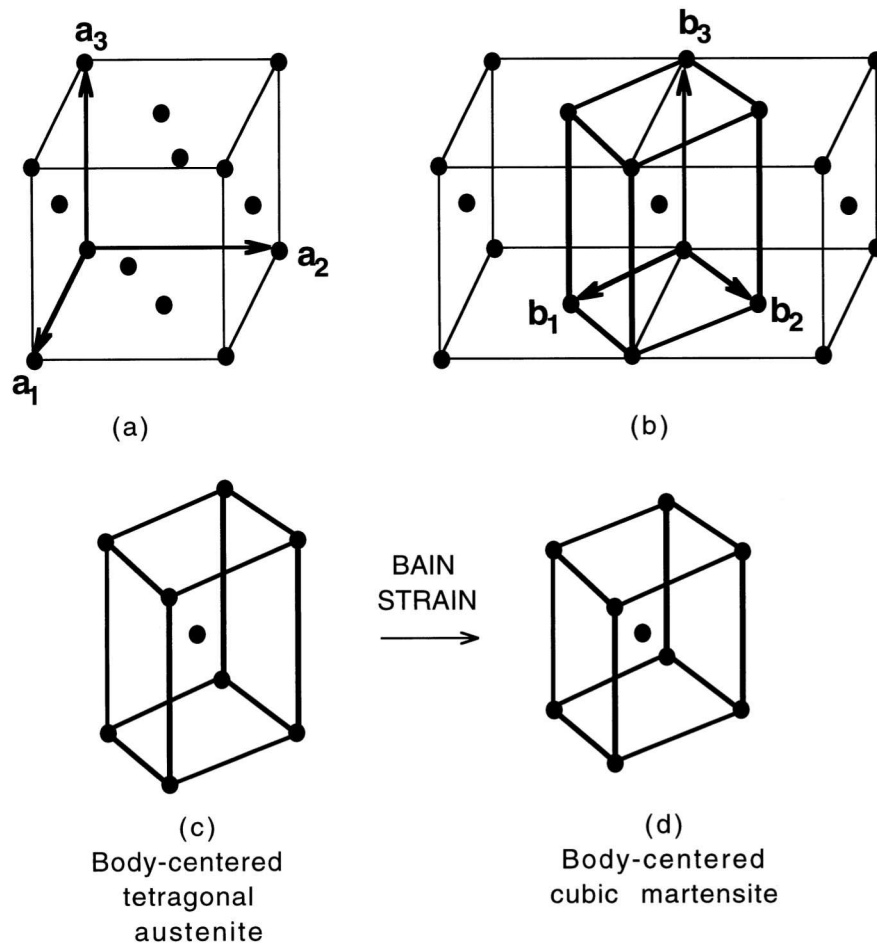


**Figure 2.18** (a) Conventional FCC unit cell of austenite, with basis vectors  $a_1, a_2, a_3$ . (b) Relation between the FCC and body-centered tetragonal cell ( $b_1, b_2, b_3$ ) of austenite. (c,d) Bain strain deforming the austenite lattice into a BCC martensite lattice.

to KS (Sandvik, 1982a). Moreover, the shape deformations of all the plates are identical, Fig. 2.20, in agreement with earlier work (Srinivasan and Wayman, 1968c; Bhadeshia and Edmonds, 1980b). One further crystallographic observation made by Sandvik is of considerable interest. He found that twins formed in the austenite adjacent to the ferrite, and that the ferrite laths were able to grow through the twins, producing a reorientation of the lattice and also displacing the direction of the twin boundaries in the manner expected for a displacive (shear) transformation.

Similar results for the relative orientations of adjacent plates were obtained in a careful examination of lath martensite by Sandvik and Wayman, using an iron-nickel-manganese alloy which contained appreciable retained austenite (Sandvik and Wayman, 1983). They found that although the laths had slight relative misorientations of up to  $2^\circ$ , they all exhibited the same variant of the parent-matrix orientation relation, and thick layers of austenite between adjacent laths indicated that the laths did not form as a result of self accommo-

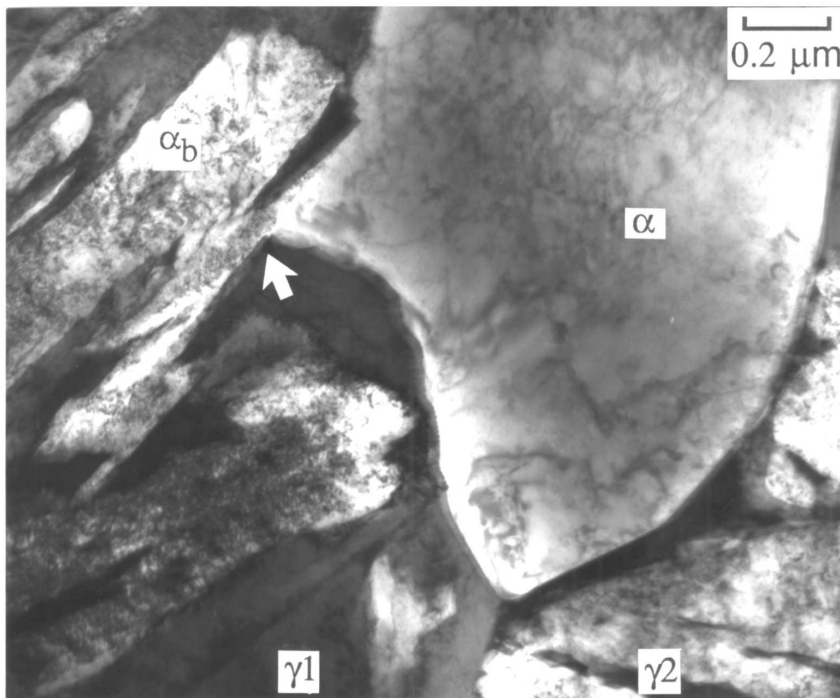


**Figure 2.19** Transmission electron micrograph showing an allotriomorph of ferrite at an austenite grain boundary. The allotriomorph is related to  $\gamma_1$  by an orientation relationship which is close to KS, but is randomly orientated with respect to the lower grain. Consequently, a bainite plate has been able to nucleate from the allotriomorph only on the side where the orientation is suitable (Babu and Bhadeshia, 1991)

dation of their shape strains. This form of lath martensite thus seems to be similar, in substructure at least, to the bainite investigated by Sandvik.

One possible reason for a common orientation might be that the individual plates of a sheaf are not separate crystals but are continuously connected portions of the growth front of one original nucleus. At the relatively high temperatures at which bainite (and lath martensite) form, the shape change may cause plastic deformation of the structure leading to copious generation of dislocations which stop the forward growth of a plate after it has attained a certain size. "Nucleation" of a new plate would then simply be resumed growth caused by breakaway of a part of the original interface in a region near but not at the tip. In bainite, the growth would resume only after some carbon had been rejected from the ferrite into the austenite and would be most likely where pinning by dislocation debris is minimal and where the driving force is highest due to rapid dispersion of the carbon rejected to the austenite.

An alternative model is that the individual plates are completely separated from each other by thin layers of austenite, so that each is separately nucleated, but always in the same orientation. In general, the stress field at the tip will favour the same variant, whereas that at the side of the plate encourages an accommodating variant (Fig. 2.21).

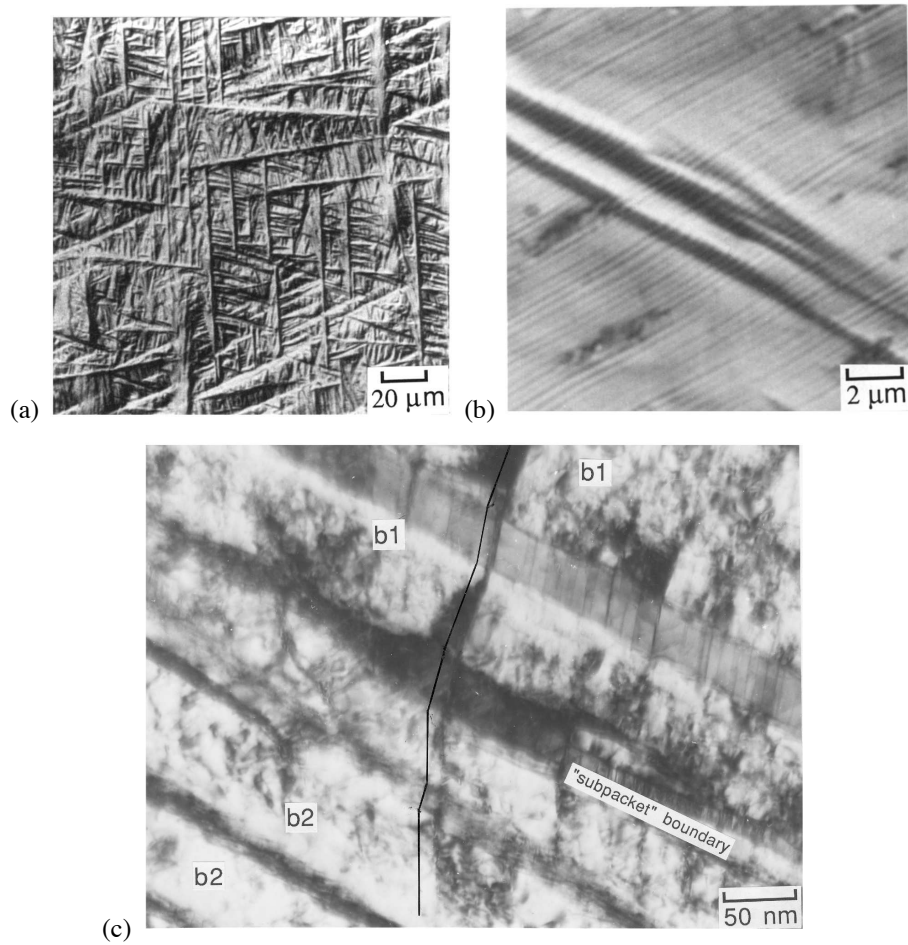


**Figure 2.20** (a) Nomarski differential interference contrast micrograph showing the general surface displacements due to upper bainite. (b) Higher magnification Nomarski image showing identical surface relief for all the sub-units within a given sheaf. (c) Sandvik's experiment showing the displacement of twin boundaries (parallel to the black line) caused by individual sub-units of bainite. The ferrite variants b1 and b2 belong to separate sheaves. (Sandvik, 1982a; Bhadeshia, 1978).

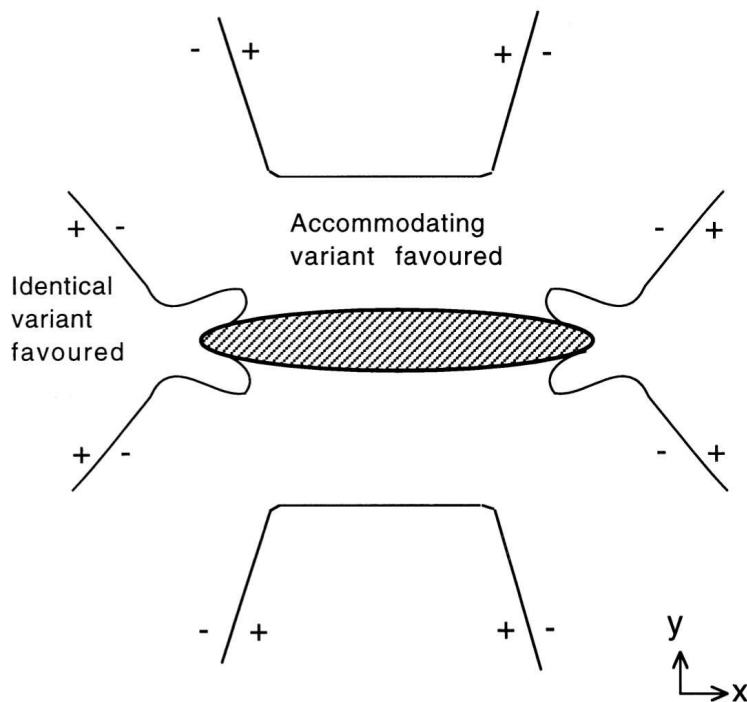


**Figure 2.21** Stress field contours of a martensitic particle lying in the  $xz$  plane with the transformation shear in the  $x$  direction. The positive signs represent regions where plates with the same shear direction are favoured, whereas the regions with the negative signs favour the formation of accommodating variants (Olson and Owen, 1976).

Mutual accommodation of the shape deformation can occur between sheaves rather than between plates in each sheaf. Sandvik (1982a) measured the misorientations between neighbouring sheaves and found that these correspond to different variants of his irrational orientation relation in which the same austenite  $\{1\ 1\ 1\}$  plane is parallel to a ferrite  $\{1\ 1\ 0\}$  plane. The six variants which satisfy this condition lead to four different relative orientations, one of which is only  $3^\circ$  from the original orientation and the others are respectively  $8^\circ$ ,  $11^\circ$  and  $14^\circ$  away from a twin orientation. Sandvik comments that the first misorientation is difficult to detect, and that it is difficult to distinguish the remaining three from each other. He also comments that only the variant with orientation relation  $14^\circ$  from a twin relationship gives efficient self accommodation, and this was observed fairly infrequently. Adjacent sheaves are thus attributed to random association, although it is not clear why they should then all have the same pair of parallel close-packed planes. Sandvik and Nevalainen (1981) have also suggested that adjacent sheaves of bainitic ferrite are approximately twin related, and correspond to variants of a near NW orientation. Transmission electron microscopy by Josefsson and Andrén (1989) has confirmed these observations in a Fe-Cr-Mo-C steel.

### 2.4.1 Crystallography: Block Size, Austenite Grain Boundary

The arrangement of individual bainite orientations within an austenite grain can have a profound effect on the mechanical properties because this determines the length scale over which cleavage cracks or other deformation phenomena are not impeded (Gourgues et al., 2000; Lambert-Perlade et al., 2004b; Bhattacharjee et al., 2004; Kim et al., 2007; Yan et al., 2010). Martensite laths in low-alloy steels tend to cluster together and organise hierarchically into blocks and packets within a given austenite grain (Maki, 1990). A block consists of laths which are in similar orientation in space, whereas a packet is the cluster of blocks which share the same  $(111)_\gamma$  to which the corresponding  $(011)_{\alpha'}$  is almost parallel. It is the size of the block that has an influence on toughness.

A similar description of blocks and packets applies to bainite. The initial orientation of a bainite plate is determined by the nucleation site. There are 24 such orientations present within a given austenite grain, but the variant which permits the lath to maintain a similar orientation with the adjacent austenite grain is favoured (Furuhara et al., 2008). The size of a block of such favoured laths will therefore scale with the austenite grain size, since the laths nucleated at a particular  $\gamma$ -grain face will tend to adopt the same orientation. The crystallographic texture of the parent austenite will influence the possibility that the ferrite will adopt a favourable orientation to all the austenite grains with which it is in contact. A small enough austenite grain transforms into a single block, leading to a direct relationship between  $\bar{L}_\gamma$  and the packet size (Rancel et al., 2011; Jacques, 2003b). However, this direct relationship ceases when  $\bar{L}_\gamma \gtrsim 30 \mu\text{m}$  because each grain is then transformed into several differently oriented blocks (Fig. 2.22).

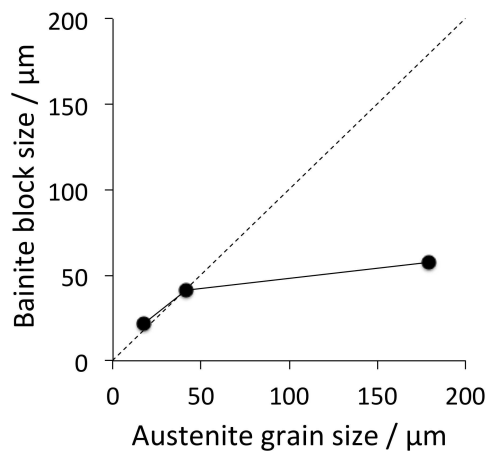


**Figure 2.22** Relationship between the bainite packet size and  $\bar{L}_\gamma$ . Data from Rancel et al. (2011).

However, the role of the austenite grain boundary diminishes as transformation progresses because crystallographic variant selection then becomes dominated by plastic accommodation effects which favour the formation of identically oriented adjacent laths, leading to a coarsening of the bainite block size (Furuhara et al., 2008). This is particularly so when the undercooling for transformation is small, since variant selection effects become less important at large driving forces (Kundu, 2007; Bhadeshia et al., 2014).

An increase in the carbon concentration while maintaining the same transformation temperature will coarsen the block size because of the reduction in the driving force (Furuhara et al., 2006). The same should therefore apply when the concentration of other solutes that

reduce the driving force, and if the transformation temperature is increased, as illustrated in Fig. 2.23.

A corollary is that anything that favours particular crystallographic variants will also lead to block coarsening; transformation under the influence of an external stress is known to make the bainitic microstructure much less random, i.e. increase the block size (Fig. 8.6). Plastic deformation of the austenite prior to transformation has a similar effect (Fig. 8.19). The number of variants per austenite grain decreases when the latter is in a deformed state (Cabus et al., 2007). However, an increase in driving force reduces the influence of such deformation, so martensite block size is much less affected than that of bainite (Kawata et al., 2006). To summarise, a small block size conducive to better toughness can be obtained by:

- (i) reducing the austenite grain size;
- (ii) ensuring a random crystallographic texture in the austenite;
- (iii) transforming at a large undercooling below  $B_S$ ;
- (iv) transforming from unstressed and undeformed austenite.

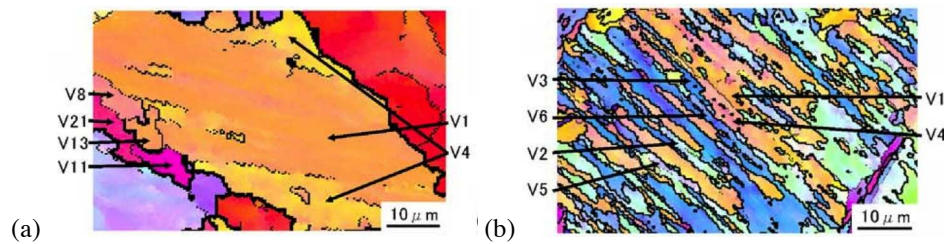


**Figure 2.23** Orientation maps showing how the block size of bainite decreases on reducing the transformation temperature, in Fe-0.3C-9.02Ni wt%. (a) Transformed at 450 °C. (b) Transformed at 350 °C. V1 etc. refer to crystallographic variant numbers. Reproduced with permission from Elsevier, from Furuhashi et al. (2006).

### 2.4.2 Autocatalytic Nucleation

Autocatalytic nucleation is a term commonly associated with martensitic transformations (Raghavan and Entwisle, 1965; Magee, 1970). The nucleation of martensite in steels is believed to begin at structural imperfections in the parent phase, such as arrays of dislocations. These are the preexisting defects which, on cooling below the  $M_S$  temperature, dissociate into suitable partial dislocations in a way which leads to the nucleation of martensite (Olson and Cohen, 1976). The defects are not all identical (they vary in potency) and are stimulated to grow into plates of martensite at different degrees of undercooling below the  $M_S$  temperature. This is the cause of the classical behaviour observed for athermal martensitic reactions, in which the volume fraction of martensite varies only with the undercooling below  $M_S$ .

The initial number density of preexisting defects typically found in austenite is not large enough to explain the kinetics of martensitic transformation. The extra defects necessary to account for the faster than expected transformation rates are attributed to autocatalysis:

when plates of martensite form, they induce new embryos which are then available for further transformation. Three mechanisms have been proposed for autocatalysis (Olson and Cohen, 1981b). In stress-assisted nucleation, the activation of less potent defects at a given temperature is induced by the internally generated elastic stresses arising as a consequence of the shape change due to transformation. In strain-induced autocatalysis, the creation of new and more potent nucleating defects is induced by some plastic accommodation in the parent phase. Finally, *interfacial autocatalysis* refers to the nucleation of new martensitic units from the existing martensite/austenite interfaces. Autocatalysis is responsible for the *bursts* of transformation (Fig. 2.24) that occur in certain martensitic steels, whence the initial formation of a plate stimulates a disproportionately large degree of further transformation, sometimes causing the emission of audible clicks.



**Figure 2.24** A burst of autocatalytic martensitic transformation in a Fe-30Ni-0.31C wt% alloy. Such bursts are not observed during bainitic transformation.

All of these effects arise as a consequence of the severe elastic and plastic disturbance of the austenite in the immediate vicinity of a plate of martensite. It is the shape change due to the martensitic transformation that is the cause of the disturbance. On this basis, autocatalysis should also feature prominently in bainitic transformations which are accompanied by similar shape deformations. There is, however, a significant difference in that bainite grows at relatively small driving forces, where defects induced by transformation do not seem to play as crucial a role in stimulating further nucleation. The initial nucleation event is almost always confined to the austenite grain surfaces, which presumably contain the most potent defects for nucleation. Intragranular nucleation of bainite can essentially be ignored except when nonmetallic particles may act as nucleation surfaces. The initial formation of a plate of bainite (or of a lath of martensite) must lead to appreciable elastic and plastic strains, but this does not seem to cause the nucleation of other plates in different orientations, as happens with plate martensite, and bursts of transformation are not observed. In the case of bainite, this may be because the driving force is only adequate for the formation of a carbon-free nucleus, may be impossible to form in the carbon enriched region around an existing plate. Whatever the reason, it seems that strain-induced autocatalysis does not play an important role in bainite formation. As already discussed, there is some evidence for stress-assisted autocatalysis if it is indeed true that adjacent sheaves form in such a way as to help accommodate each other's shape deformation.

## 2.5 Crystallographic Theory

The deformation which converts the face-centred cubic structure of austenite to the body-centred cubic or body-centred tetragonal structure is known as the Bain strain (Fig. 2.18). Its principal deformation consists of a compression along the vertical axis  $\mathbf{a}_3$  and a uniform expansion along  $\mathbf{a}_1$  and  $\mathbf{a}_2$ . However, this deformation does not produce the experimentally observed orientation relationship; nor is it consistent with the observed invariant-plane strain shape deformation. An invariant-plane strain, on the other hand, cannot convert austenite into ferrite. Crystallographic theory is able to resolve all of these difficulties which will now be summarised (Wechsler et al., 1953; Bowles and Mackenzie, 1954; Mackenzie and Bowles, 1954a,b).

The Bain strain is a *pure* deformation because it leaves three mutually perpendicular directions unrotated, though distorted. The distortions  $\eta_i$  along these unrotated axes are defined as the ratios of the final to the initial lengths and are called the *principal distortions*. The Bain strain defines completely the lattice change so no further deformation is needed to complete the change in crystal structure.

Suppose that the austenite is represented by a sphere with its unit cell edges denoted by the vectors  $\mathbf{a}_i$  with  $i = 1, 2, 3$ , as illustrated in Fig. 2.25a,b. The Bain strain changes the sphere into an ellipsoid of revolution about  $\mathbf{a}_1$ . There are no lines in the  $(0\ 0\ 1)_\gamma$  plane which are undistorted. However, it is possible to find lines such as  $wx$  and  $yz$  which are undistorted by the deformation, but are rotated into the new positions  $w'x'$  and  $y'z'$ . Since they are rotated by the Bain deformation they are not invariant-lines. In fact, the Bain strain does not produce an invariant-line strain (ILS). An invariant-line is necessary in the interface between the austenite and martensite in order to ensure a glissile interface.

The Bain strain can be converted into an invariant-line strain by adding a rigid body rotation as illustrated in Fig. 2.25c. The rotation reorients the  $\alpha'$  lattice but has no effect on its crystal structure. The effect of the rotation is to make one of the original undistorted lines (in this case  $yz$ ) invariant so that the total effect  $\mathbf{RB}$  of the Bain strain  $\mathbf{B}$  and the rotation  $\mathbf{R}$  is indeed an invariant-line strain. This is the reason why the observed irrational orientation relationship (KS/NW type) differs from that implied by the Bain strain. The rotation required to convert  $\mathbf{B}$  into an ILS precisely predicts the observed orientation from the Bain orientation.

It is apparent from Fig. 2.25c that there is no possible rotation which would convert  $\mathbf{B}$  into an invariant-plane strain because there is no rotation capable of making two of the non-parallel undistorted lines into invariant-lines. Thus, it is impossible to convert austenite into  $\alpha'$  martensite by a strain which is an invariant-plane strain. A corollary to this statement is that the two crystals cannot ever be joined at an interface which is fully coherent and stress-free.

It remains to resolve the inconsistency that  $\mathbf{BR}$  is an ILS whereas the observed shape deformation is an IPS. The operations needed to explain this are illustrated in Fig. 2.26. When combined with an appropriate rigid body rotation, the net homogeneous lattice deformation  $\mathbf{RB}$  is an invariant-line strain (step *a* to *c*), the invariant-line being normal to the plane of the diagram and passing through the point  $x$ . Inconsistent with this, the observed shape deformation is an invariant-plane strain  $\mathbf{P}_1$  (step *a* to *b*) but this gives the wrong crystal structure. The invariant-plane of the shape deformation is defined by  $xw$ . If, however, a second homogeneous shear  $\mathbf{P}_2$  is combined with  $\mathbf{P}_1$  (step *b* to *c*), then the correct structure is obtained but the wrong shape since

$$\mathbf{P}_1\mathbf{P}_2 = \mathbf{RB}. \quad (2.5)$$

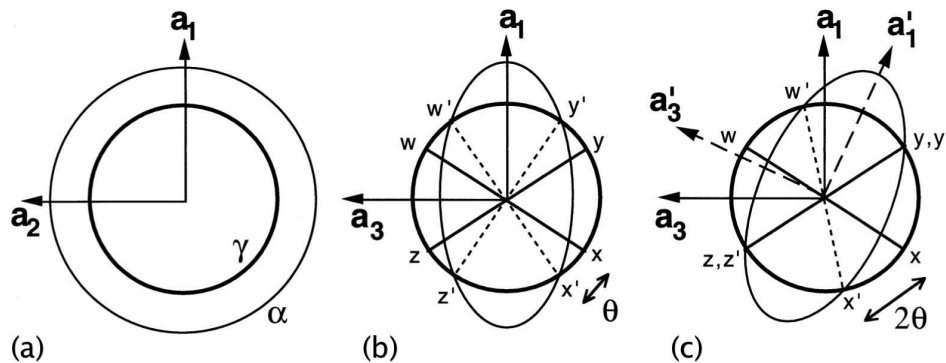


**Figure 2.25** (a) and (b) show the effect of the Bain strain on austenite, which when undeformed is represented as a sphere of diameter  $wx = yz$  in three-dimensions. The strain transforms it to an ellipsoid of revolution. (c) shows the invariant-line strain obtained by combining the Bain strain with a rigid body rotation.

Notice that a combination of two non-coplanar invariant-plane strains gives an invariant-line strain, the invariant-line lying at the intersection of the two invariant-planes. The discrepancies are all resolved if the shape changing effect of  $P_2$  is cancelled macroscopically by an inhomogeneous lattice-invariant deformation, which may be slip or twinning as illustrated in Fig. 2.26. Notice that the habit plane in Fig. 2.26 e,f is given by a fragmentation of the original plane  $xw$ , due to the inhomogeneous lattice-invariant shear. This is why the habit plane of martensite has peculiar indices. In the absence of a lattice-invariant deformation as in the  $\gamma \rightarrow \epsilon$  transformation, the sequence stops at step *b* and therefore the habit plane has rational indices  $\{1\ 1\ 1\}_\gamma$ .

The theory neatly explains all the observed features of martensite crystallography. It is easy to predict the orientation relationship, by combining the Bain strain with a rigid body rotation which makes the net lattice deformation an invariant-line strain. The habit plane does not have rational indices because the amount of lattice-invariant deformation needed to recover the correct the macroscopic shape is not usually rational. A substructure is predicted, consisting either of twins or slip steps, and this is observed experimentally. The transformation goes to all the trouble of ensuring that the shape deformation is macroscopically an invariant-plane strain because this reduces the strain energy when compared with the case where the shape deformation might be an invariant-line strain.

Finally, we note that the invariant-line lies at the intersection of the habit plane and the plane on which the lattice-invariant shear occurs. This is obvious since only the line common to the two invariant-planes can be invariant to their combined effect.

### 2.5.1 Application to Bainite

We have seen that the bainite transformation exhibits crystallographic features and surface relief effects identical to those associated with martensitic reactions. It is then natural to assume that the phenomenological theory of martensite crystallography should be applicable to bainite. The theory predicts a unique relationship between the habit plane, shape deformation, orientation relationship, lattice types and lattice-invariant deformation. It can

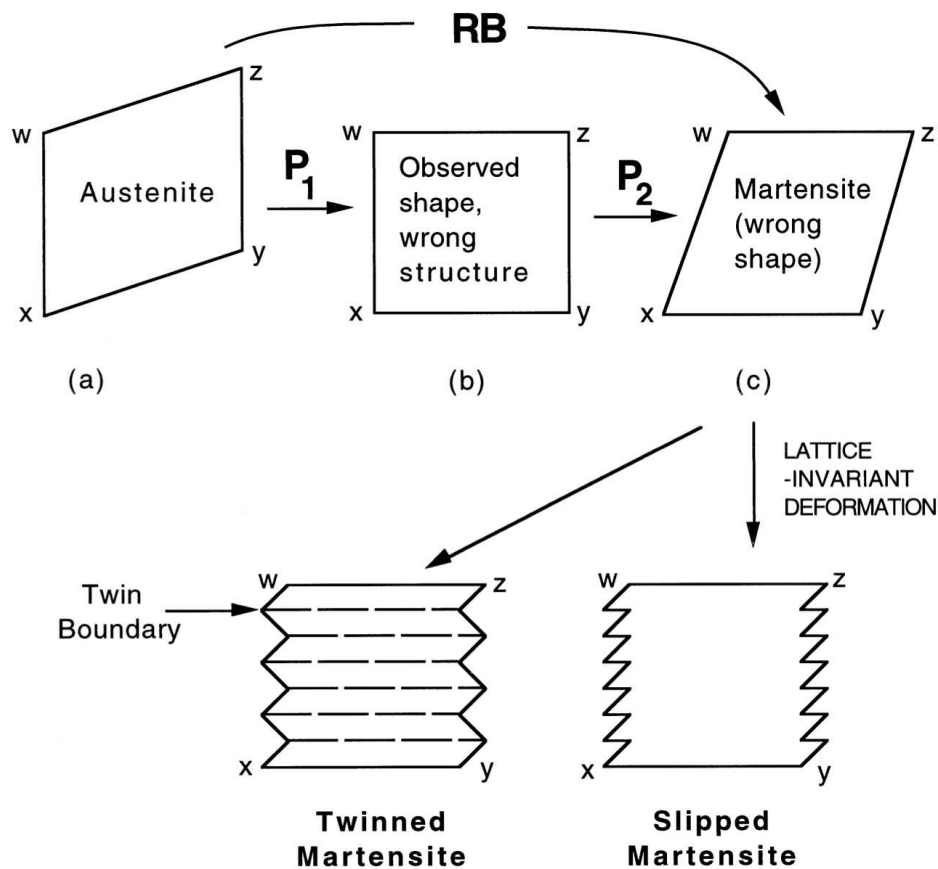


**Figure 2.26** The essential features of the phenomenological theory of martensite crystallography. (a) represents the austenite crystal and (c), (d) and (e) all have a body-centred cubic structure. (b) has an intermediate structure between FCC and BCC (or BCT). Although (c) has the BCC structure, its shape is inconsistent with the observed invariant-plane strain. The effect of the inhomogeneously applied lattice-invariant deformations is to correct the shape change to an IPS, without altering the structure.

be tested satisfactorily when all these variables are determined as a set. Many of the early data [reviewed by Bowles and Kennon (1960)] are incomplete in this sense, although consistent with the theory. The early measurements of habit planes must now be interpreted to refer to the habit planes of bainite sheaves, rather than of the individual plates.

A considerable difficulty in applying the theory to bainite is the lack of accurate structural information which is needed as input data. Thus if bainite grows with a full supersaturation but the carbon escapes in a short time, the measured lattice parameters of upper bainitic ferrite will not relate to the initially formed structure, which may even have been tetragonal. A problem exists for lower bainite if appreciable carbide precipitation has taken place before any measurements are possible.

Srinivasan and Wayman (1968c,a) reported the first detailed results on the crystallography of sheaves of lower bainite in a Fe-1.11C-7.9Cr wt% alloy ( $B_S \simeq 300^\circ\text{C}$ ,  $M_S \simeq -34^\circ\text{C}$ ) in which large quantities of austenite remained untransformed at ambient temperature. Each sheaf was found to have just one planar face when examined using light microscopy, and this was taken to be the habit plane. The irrational habit plane indices were found to exhibit a degree of scatter beyond experimental error, the mean indices being close to  $(2\ 5\ 4)_\gamma$  relative to the orientation variant in which  $(1\ 1\ 1)_\gamma$  is almost parallel to  $(0\ 1\ 1)_\alpha$  and  $[\bar{1}\ 0\ 1]_\gamma$  is at a small angle to  $[\bar{1}\ \bar{1}\ 1]_\alpha$ ; this is henceforth called the *standard variant*. The martensite habit plane in the same alloy is close to  $(4\ 9\ 4)_\gamma$  and the difference in the two habits and in the exact orientation relations led Srinivasan and Wayman to the conclusion that the mode of displacive transformation is different in bainite and martensite. Their measured habit plane is only about  $6^\circ$  from that found for a different alloy by Sandvik (1982a), who pointed out that his result applied to an individual plate whereas that of Srinivasan and Wayman was for the average habit of a sheaf.

The shear component of the shape deformation, as averaged over the entire sheaf, was measured to be  $\simeq 0.128$ , the magnitude of the total shape strain being  $\simeq 0.129$  (Table 2.1). This is consistent with the earlier data of Tsuya (1956) and Speich (1962). The actual shape strain for an individual sub-unit must of course be larger, and was estimated using crystallographic theory as being  $\simeq 0.23$ ; as will be seen later, this compares well with other published data. These values are in good agreement with a measurement of the shear component of the shape strain (0.22) of an individual sub-unit (Sandvik, 1982a) and with a value of 0.26 measured using atomic force microscopy (Swallow and Bhadeshia, 1996).

**Table 2.1** Magnitude of the shape strain component parallel to the habit plane in sheaves of lower bainite in Fe-1.11C-7.9Cr wt% alloy. The value of the shear is derived by measuring the tilts for each sheaf on two separate surfaces. After Srinivasan and Wayman (1968a).

Sheaf number	Tilt on surface	Tilt on surface 2	Angle of shape shear	Shear
1	$5^\circ 48'$	$3^\circ 56'$	$7^\circ 9'$	0.1254
2	$5^\circ 24'$	$6^\circ 24'$	$8^\circ 27'$	0.1486
3	$5^\circ 17'$	$4^\circ 20'$	$7^\circ 0'$	0.1228
4	$6^\circ 45'$	$4^\circ 15'$	$7^\circ 55'$	0.1393
5	$6^\circ 9'$	$4^\circ 21'$	$8^\circ 20'$	0.1466
6	$3^\circ 43'$	$3^\circ 3'$	$5^\circ 13'$	0.0916
7	$4^\circ 15'$	$3^\circ 42'$	$8^\circ 24'$	0.1474
8	$4^\circ 0'$	$4^\circ 30'$	$6^\circ$	0.1035

Srinivasan and Wayman showed that their data on lower bainite are indeed consistent with solutions based on the phenomenological theory of martensite. The crystallography was, as expected, inconsistent with the lattice-invariant deformation being twinning since

transformation twinning is not observed in bainitic ferrite.<sup>4</sup> It was found that the sheaf habit plane and orientation relationship could be predicted for an undistorted habit plane if it is assumed that the lattice invariant shear is irrational in both plane and direction. On the other hand, if the habit plane is permitted to undergo a small isotropic contraction, then the lattice-invariant shear (for the standard variant) consists of a double shear on the planes  $(1 \bar{1} 1)_\gamma$  and  $(1 0 1)_\gamma$  in the common direction  $[\bar{1} 0 1]_\gamma$  (these correspond to  $(1 0 1)_\alpha$ ,  $(1 1 2)_\alpha$  and  $[\bar{1} \bar{1} 1]_\alpha$  respectively). This double system is equivalent to a single shear on an irrational plane, and is not associated with any of the difficulties encountered in theories which postulate more general combinations of lattice-invariant shears. The component planes on which the interface dislocations would glide are those most usually considered as candidates for single lattice-invariant shears in the martensite theory. However, at the time of the Srinivasan and Wayman work, it was not fully appreciated that the so-called habit plane of a sheaf which they measured, may differ from that of a plate within a sheaf which Sandvik measured, and it is not yet clear whether the phenomenological theory of martensite should be applied to the sheaf or the plate. It may be more important to minimise long-range distortions over the whole sheaf, in which case the invariant plane condition would apply to the apparent habit plane of the sheaf, but in cases where there are reasonably thick layers of austenite between the plates, it seems more logical to apply the theory to the individual plate.

### 2.5.2 High-Resolution Studies of the Shape Change

Of the transformation products listed in Table 2.2, both Widmanstätten ferrite and martensite can be obtained in the form of plates that are readily resolved using optical microscopy. Their shape deformations have been known for many decades, the measurements being made from the deflection of scratches or optical interference fringes on a surface polished flat prior to transformation.

However, the microstructure of bainite consists of fine plates of ferrite, each of which is only some 0.2  $\mu\text{m}$  thick, which is below the limit of resolution in light microscopy. This has made it difficult to establish the surface relief introduced as bainite grows. Sandvik (1982a) first measured the shear strain of a single bainite plate using transmission electron microscopy to reveal the transformation-induced deflection of twins in austenite. He determined the shear strain  $s$  to be close to 0.22.

New methods have recently become available for the quantitative, high-resolution measurement of surface topography using scanning tunnelling or atomic force microscopy. The techniques have confirmed Sandvik's observations which revealed that the shear strain associated with an individual plate of bainite is about  $0.26 \pm 0.02$ , consistent with the magnitude expected from the phenomenological theory of martensite crystallography (Swallow and Bhadeshia, 1996). An example of an image of the surface displacements is presented in Fig. 2.27; a complete summary is available in Bhadeshia (2014a).<sup>5</sup>

<sup>4</sup>A twinned interface is never thermodynamically favoured because of the creation of internal twin boundaries. But it can move more rapidly than when slip is the lattice-invariant deformation mode. Consequently, martensite which grows at high velocities will tend to contain transformation twins (Olson and Cohen, 1981a).

<sup>5</sup>There are similar studies using atomic force microscopy, which show the large shear displacements associated with the formation of bainite (Yang et al., 2001b). However, they are interpreted irrationally to indicate diffusional transformation.

**Table 2.2** Shape deformations for a variety of transformation products, where  $s$  is the shear strain parallel to the habit plane and  $\zeta$  is the dilatation normal to the habit plane.

Transformation	$s$	$\zeta$	Morphology	Reference
Widmanstätten ferrite	0.36	0.03	Thin plates	Watson and McDougall (1973)
Bainite	0.22	0.03	Thin plates	Sandvik (1982a)
	0.26		Thin plates	Swallow and Bhadeshia (1996)
	$\geq 0.24$		Thin plates	Yan and Bhadeshia (2013)
Nanostructured bainite	$\geq 0.45$		Fine plates	Peet and Bhadeshia (2011)
Martensite	0.24	0.03	Thin plates	Dunne and Wayman (1971)
Allotriomorphic $\alpha$	0	0.03	Irregular	
Idiomorphic $\alpha$	0	0.03	Equiaxed	

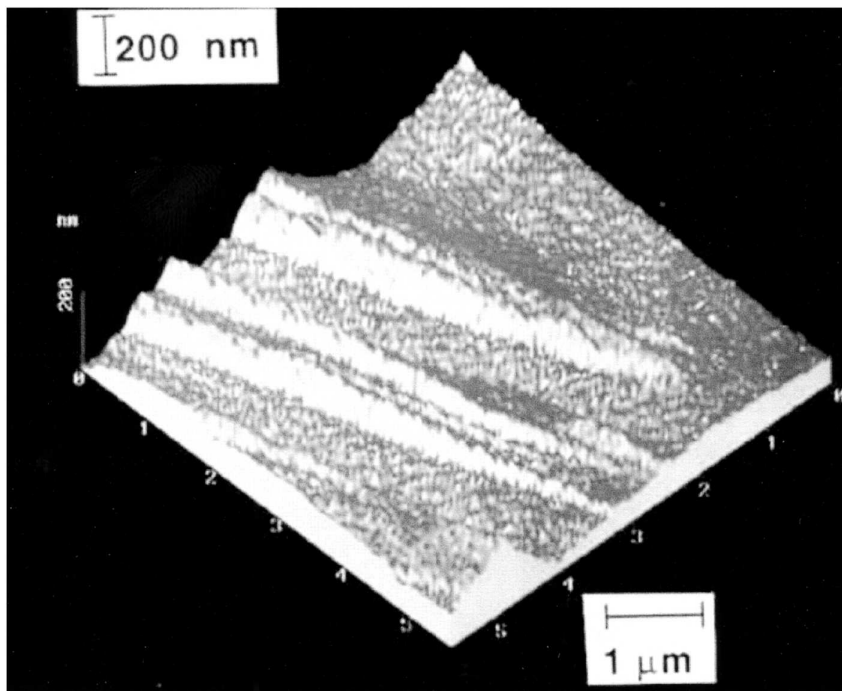


**Figure 2.27** High-resolution atomic-force microscope plot of the displacements caused by the formation of a single sub-unit of bainite. The surface was flat before transformation. Note the plastic deformation caused in the adjacent austenite (Swallow and Bhadeshia, 1996).

The atomic force microscopy has demonstrated that the smaller values of  $s$  measured in early work using light microscopy arise because the low resolution causes an averaging of the shape strain over the sheaf.

The plastic relaxation is of course, ultimately responsible for the arrest in the growth of the bainite plates, giving the sub-unit and sheaf hierarchies in the microstructure of bainite; as discussed in section 2.1, it also leads to an increase in the dislocation density of the bainite. It is not clear how the plastic accommodation might influence the development of the crystallography of bainite.

Although the displacive mechanism itself is established, significant detail remains to be resolved with respect to the displacive nature of the bainite reaction (Bhadeshia, 2014a). The theoretical background to the crystallography of displacive reactions has been summarised by equation 2.5 with the product  $\mathbf{RB}$  being a total deformation that leaves a line invariant. The existence of such a line is a necessary condition for martensitic transformation (Christian, 2003b; Bhadeshia, 2001c). The  $\mathbf{RB}$  at the same time predicts the observed orientation relationship.  $\mathbf{P}_1$  is the shape deformation matrix representing the invariant-plane strain and  $\mathbf{P}_2$  is a lattice-invariant deformation that could be slip or twinning. The plane on which  $\mathbf{P}_1$  occurs is of course the habit plane of the bainite in the present context. The point that emerges from this equation is that the shape deformation, orientation relationship and the crystallographic indices of the habit plane are all connected mathematically. All three of these quantities have been measured independently or as incomplete sets, but there never has been an experiment where they have been simultaneously determined for an individual bainite sub-unit. The reason of course is that this would be a difficult experiment given the fine scale of the sub-unit, but modern techniques including combination of atomic force microscopy, focused-ion beam machining and transmission electron microscopy could resolve the problem and bring closure to the subject.

### 2.5.3 The Shape Change: Further Considerations

In talking about the application of the phenomenological theory of martensite to bainite, the classical view (Hull, 1954; Bilby and Christian, 1956; Christian, 1962) that the experimentally observed invariant-plane strain shape deformation implies a coordinated movement of at least the iron and substitutional atoms was implicitly accepted. Given that there has been some confusion in the literature about the interpretation of this shape change, it is worth presenting an assessment of the significance of the shape change (Christian and Edmonds, 1984; Christian, 1990). The problem is important since the strain energy associated with the shape deformation when transformation occurs under constraint cannot be ignored in the thermodynamic and kinetic descriptions of bainitic reactions, irrespective of the mechanism by which the shape change is proposed to arise.

The intersection of a plate of bainitic ferrite with a free surface causes that surface to tilt about the lines of intersection. This is the description of an invariant-plane strain, which is due to the combined effects of the lattice deformation and a lattice-invariant deformation. The tilting produced is homogeneous on a macroscopic scale, indicating that the net atomic displacements include common non-random components which accumulate during growth. This is an obvious conclusion, but the term *net atomic displacements* needs to be deconvoluted in order to assess the degree of diffusion which can be tolerated before the transformation must be regarded as a reconstructive reaction.

Focusing attention on equivalent lattice points which define unit cells (not necessarily primitive) of the two structures containing the same number of atoms, a change in shape will accompany transformation if the new set of lattice points can be related to the original set by a homogeneous deformation. It is then possible to specify (in a localised region at least) how particular vectors, planes and unit cells of one structure are derived from *corresponding* vectors, planes and unit cells of the other structure. This is termed a lattice

correspondence and it defines the pure lattice deformation which carries the original lattice points, or some fraction of those points into points of the new lattice.

When interstitial atoms are present, they may move over large distances without affecting the correspondence; this is sometimes expressed by stating that there is an atomic correspondence for the solvent and substitutional solute atoms but not for the interstitials. A further relaxation of the condition is to allow the solvent and substitutional solute atoms to be displaced during transformation among the sites specified by the lattice correspondence, but not to create new sites or destroy any specified sites; in this way the lattice correspondence is preserved but there is no longer an atomic correspondence. Thus, a systematic shape change implies a lattice correspondence even if accompanied by some diffusion of atomic species. As will become evident later, the existence of this correspondence and the shape change requires an interface which is at least semi-coherent.

The detailed implications of the shape change on the mechanism of growth can be illustrated using the virtual operations illustrated in Fig. 2.28. A region of the matrix is first removed (leaving behind an equivalent hole) and then allowed to undergo unconstrained transformation with the help of a homogeneous lattice deformation which is not in general an invariant-plane strain (Fig. 2.28a,b). The particle is then allowed to have any required composition by transferring suitable numbers of solute atoms between interstitial sites in the particle and the matrix, and/or by interchanging atoms of substitutional species in the particle with atoms in the matrix (operation  $c$ , Fig. 2.28).

A number of further operations are now possible before the particle is reinserted into the hole in the matrix, in order to reduce the strain energy:

- (i) The volume and shape of the particle may be made equal to that of the hole, by transferring atoms over long distances from the particle to sinks within the matrix or at its surface (operation  $d_1$ , Fig. 2.28). The strain energy then vanishes.
- (ii) The total number of atoms in the particle may be conserved but its shape may nevertheless be adjusted by the creation and removal of atom sites. The strain energy is effectively that of a hole in the matrix filled with a compressible fluid of different natural volume. For a plate shaped particle, the minimum in strain energy for this case corresponds to an IPS with a zero shear component, with the expansion or contraction being normal to the habit plane (operation  $d_2$ , Fig. 2.28). A plate shaped particle will give the lowest strain energy if the volume change is appreciable, but there will only be a *preferred* habit plane if there is appreciable anisotropy of either the elastic properties or the interfacial energy.
- (iii) The shape of the particle may be changed by conservative plastic deformation. The lowest strain energy for a plate-shaped particle then occurs if the plastic deformation converts the lattice deformation into a shape deformation which is an IPS on the habit plane, as in the theory of martensite crystallography (operation  $d_3$ , Fig. 2.28).
- (iv) The shape of an epitaxially coherent particle (which has interfacial dislocations with Burgers vectors that have an edge character and which lie in the interface plane) may be changed by the removal or addition of particular planes of atoms, e.g. by dislocation climb from one surface to another, again giving lowest strain energy for an IPS on the habit plane of a plate precipitate. If there is no reconstruction of the atom sites, the shape change may retain an appreciable shear component (operation  $d_4$ , Fig. 2.28).

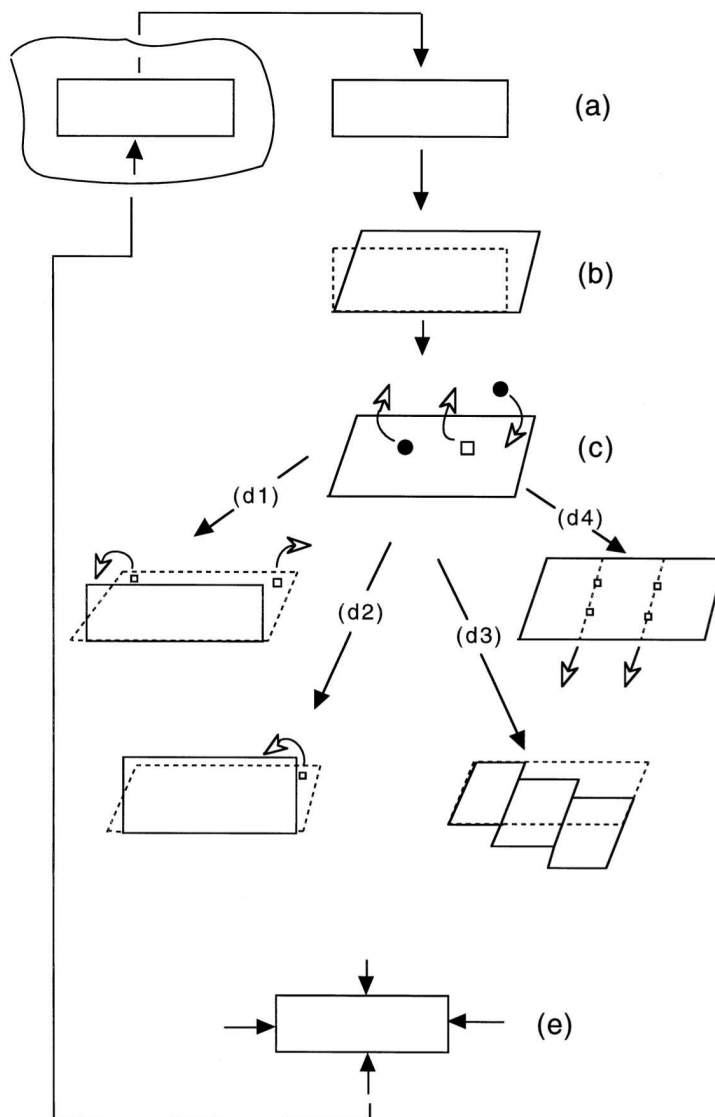


**Figure 2.28** Schematic diagram illustrating the virtual operations required to form a particle in a constraining matrix, after Christian and Edmonds (1984).

Particles of type  $d_1$  and  $d_2$  both require long range diffusion or mass transport, and there is no obvious reason why large scale redistributions of solute atoms cannot at the same time occur between the product and parent phases, if demanded by thermodynamic equilibrium. In  $d_1$  there is no shape change, whereas  $d_2$  will lead to surface rumpling due to the volume change accompanying transformation; both of these kinds of transformation are therefore reconstructive. Shear stresses and strains are not transferred across the interface, which behaves in some respects as a liquid-like layer. Since there is no continuity of planes or

vectors, the interface can be displaced only as a result of individual atomic migration and its velocity will depend on atomic mobility.

It could also be argued that in case (iv), the need to have sufficient atomic mobility for interfacial dislocations to climb means that in reality, other diffusion processes might also occur which remove the shear component of the shape deformation (Christian, 1962).

This leaves only the martensitic type change (iii) as a likely candidate for an IPS shape change, but step *c* (Fig. 2.28) ensures that the shape change cannot be taken to imply diffusionless transformation. It is easy to see how interstitial atoms can partition between the phases during growth without affecting the IPS shape change. There may also be an interchange of substitutional atoms (of the type necessary to induce ordering in equiatomic random alloys), but it is likely that the migration of these atoms can only occur over a few interatomic distances – otherwise, any longer range diffusion would destroy the shape change and its associated strain energy at the same time. It is therefore to be concluded that one implication of the observation of an invariant-plane strain shape change with a significant shear component is that any diffusion of solvent or substitutional atoms during transformation must be absent or minimal.

Suppose that there is an IPS deformation with a large shear and at the same time there is a composition change implying diffusion in the substitutional lattice. Such a transformation has been called diffusional-displacive transformation (Christian, 1994, 1997). This does not negate the consequences of the shape deformation, for example the strain energy, the plate shape, the requirement for a glissile interface etc. The existence of the shape deformation means that the diffusion flux is not adequate to eliminate the displacive character of the transformation, and furthermore, the fact that most of the atoms must move in a co-ordinated manner to produce the displacements in the first place. It is a mistake to imagine that the association of diffusion with a phase transformation means that it can be treated as a reconstructive reaction which is close to equilibrium. The IPS shape deformation with its shear therefore remains evidence for the displacive character of the transformation mechanism when the atomic mobility is clearly inadequate to permit the elimination of the shape deformation.<sup>6</sup>

Further implications of the shape change become clear when its relationship with the interfacial structure is considered. The interface in cases (iii) and (iv) is semicoherent because for coherency  $\mathbf{R}\mathbf{B} = \mathbf{P}$ , an equation which is rarely satisfied in general, and not satisfied for the FCC to BCC or BCT transformation in steels. For the epitaxial semicoherency illustrated in (iv), coherent patches on the invariant-plane are separated by interface dislocations whose motion with the interface requires climb and hence diffusion of atoms in substitutional sites. The semicoherent interface may alternatively be glissile; the interface dislocations then glide conservatively as the interface moves and growth does not require diffusion and hence has a high mobility even at low temperatures (case iii). For ferrous bainite the mobility of the solvent and substitutional atoms is negligible, and the experimental observation of a shape deformation with a significant shear component gives strong evidence that the bainitic-ferrite/austenite interface is semicoherent and glissile.

<sup>6</sup>It has long been known that atomic ordering can develop during martensitic transformation (Bowles and Wayman, 1979). In recent work, weak superlattice reflections have been observed in iron-nickel steels transformed to bainite (Wilson et al., 2001) and in martensite (Ohmori et al., 2001).

### 2.5.4 Shape Change and the Superledge Mechanism

The lattice correspondence that is implied by the IPS shape deformation is a relationship between the lattices of the parent and product phases, independent of the orientation of the actual interface between the enclosed particle and the matrix. It follows that all the interfaces surrounding an enclosed particle of bainitic ferrite must be semicoherent (Christian, 1990). It is not tenable to consider some interface orientations to be incoherent (“disordered”) while semi-coherency is maintained on other interface orientations, as is sometimes implied in the superledge mechanism of bainitic growth (Aaronson et al., 1970). This mechanism considers that the growth of bainitic ferrite plates occurs by the propagation of macroscopic ledges on the habit plane. The model requires at least two differently oriented macroscopic interfaces around an enclosed bainitic ferrite particle, the invariant-plane and the superledge. Macroscopic interfaces like these can only exist if the distortion due to the coherency between the parent and product lattices is within an elastically tolerable range, i.e. if the shape deformation across the interface is a close approximation to an IPS. Thus, the presence of two different orientations of macroscopic interface means that there are two invariant-planes between the parent and product crystals, a situation only possible if the net shape deformation is zero, in contradiction with experimental evidence.

All interface orientations other than the invariant-plane of the observed IPS shape deformation (which is also the habit plane of the bainitic ferrite) must be small coherent steps in the semi-coherent habit plane interface. The small steps are in forced *coherency* with the matrix, and have the characteristics of transformation dislocations which can glide and climb conservatively, also called coherency dislocations, (Olson and Cohen, 1979). Coherency implies that all the corresponding planes and lines are continuous across the step; thus, these transformation dislocations are not lattice discontinuities. There is therefore no difficulty in these transformation dislocations climbing and gliding conservatively even when the Burgers vector is not parallel to the line vector.<sup>7</sup> The strain energy associated with the small steps is tolerable only because of their small size. It is therefore considered that large steps (or “superledges”) are most improbable because of their high strain energy (Christian, 1990).

### 2.5.5 The Structure of the Interface

It has already been pointed out that any atomic height steps in the bainitic/austenite interface are transformation dislocations, with strain fields whose character can be specified by assigning a Burgers vector to each such dislocation. The motion of these steps (or coherency dislocations), which are in forced coherency, leads to phase change: there is continuity of planes and vectors across the steps so that regions of the parent lattice are homogeneously deformed into that of the product as the steps are displaced. Since the energy of the step varies with the square of the magnitude of its Burgers vector, the step is restricted to atomic height, which is another way of stating that superledges are impossible on a bainitic/austenite interface. The anticoherency or interface dislocations cause the lattice-invariant deformation as the interface is displaced.

There are no decisive observations of the structure of the bainitic-ferrite/austenite interface, but general conclusions can nevertheless be deduced using other experimental data

<sup>7</sup>The terms transformation dislocation and coherency dislocation are identical. They are distinct from the adjectives “interface”, “intrinsic”, “misfit” and “anticoherency”, all of which are used to describe dislocations which form an intrinsic part of the boundary structure (Olson and Cohen, 1979; Christian, 1990).

and theoretical considerations. The observation of an invariant-plane strain shape change accompanying the growth of bainitic ferrite, when combined with the negligible mobility of the solvent and substitutional solute atoms, provides strong evidence that the structure of the transformation interface must be glissile. The number of iron and substitutional solute atoms is conserved during growth. Since they are not required to diffuse during transformation, the interfacial mobility is expected to be high even at low temperatures.

A semicoherent interface containing a single array of anticomherency dislocations is considered to be glissile when the dislocations are able to move conservatively as the interface migrates. The dislocations must therefore all be pure screw dislocations, or have Burgers vectors which do not lie in the interface plane. The interface plane is the irrational invariant-plane or habit plane of the bainite plate. A glissile interface also requires that the glide planes (of the anticomherency dislocations) associated with the ferrite lattice must meet the corresponding glide planes in the austenite lattice edge to edge in the interface along the dislocation lines (Christian and Crocker, 1980).

If more than one set of anticomherency dislocations exist, then these should either have the same line vector in the interface, or their respective Burgers vectors must be parallel (Christian and Crocker, 1980). This condition ensures that the interface can move as an integral unit. It also implies that the deformation caused by the anticomherency dislocations when the interface moves can always be described as a simple shear (caused by a resultant anticomherency dislocation which is a combination of all the anticomherency dislocations) on some plane which makes a finite angle with the interface plane, and intersects the latter along the line vector of the resultant anticomherency dislocation.

Obviously, if the anticomherency dislocation structure consists of just a single set of parallel dislocations, or of a set of different dislocations which can be summed to give a single glissile anticomherency dislocation, then it follows that there must exist in the interface, a line which is parallel to the resultant anticomherency dislocation line vector, along which there is zero distortion. Because this line exists in the interface, it is also unrotated. It is an *invariant-line* in the interface between the parent and product lattices. When full coherency is not possible between the two structures (as is the case for the FCC to BCC transformation), then for the interface to be glissile, the transformation strain relating the two lattices must be an invariant-line strain, with the invariant-line lying in the interface plane.

An interesting consequence of the restriction that the transformation strain must be an invariant-line strain is that models of the ferrite-austenite interface as a single array of anticomherency dislocations are not possible for any orientation between Nishiyama-Wasserman and Kurdjumov-Sachs if the most densely-packed planes of the two structures are regarded as exactly parallel (Knowles et al., 1982; Christian, 1990). This is because for realistic values of the lattice parameters, it is not possible to obtain a transformation strain which is an invariant-line strain if the planes are exactly parallel. If it is assumed that the interface contains just one set of anticomherency dislocations then the predicted orientation relation always has the most densely-packed planes of the two structures at a small angle (about  $0.5^\circ$ ) to each other - such a small deviation is unfortunately difficult to detect experimentally.

There have been a few high resolution studies of the interface between bainite and austenite (Kajiwara et al., 1999; Kajiwara, 2003; Furuhashi et al., 2003; Ogawa and Kajiwara, 2006). Atomic steps have been observed, which probably correspond to the coherency dislocations whose motion accomplishes transformation, although the details of the strain fields have not been interpreted. Transmission electron microscopy has shown that the dislocations that would accomplish the lattice-invariant deformation, i.e. the anti-

coherency dislocations, are screws, with Burgers vector  $\frac{a_\gamma}{2}\langle 0\bar{1}1\rangle_\gamma \equiv \frac{a_\alpha}{2}\langle 1\bar{1}1\rangle_\alpha$  (Moritani et al., 2002). In the same study, the anticoherency dislocations in the interface of martensite were found to be identical to those observed in the  $\alpha_b/\gamma$  interface. Furuhashi et al. (2003) found that lath martensite and bainite have similar interfaces with austenite. A factor to bear in mind is that prolonged isothermal transformation can conceivably lead to relaxations in the interfacial structure, once the  $\alpha_b/\gamma$  boundary has ceased to move (Ohmori, 2002; Moritani et al., 2002). The essential conclusion though, is that the  $\alpha_b/\gamma$  interface is glissile.

### 2.5.6 The Crystallography of a Lath of Bainite

The sub-units of a bainite sheaf may adopt the morphology of a plate or of a lath, where the latter is idealised as a parallelepiped of dimensions  $a$ ,  $b$ , and  $c$ , with  $a > b > c$ . The lath shape is adopted when the transformation occurs at high temperatures. The crystallography of such laths has been characterised in detail and to a high level of accuracy, by Davenport (1974), as follows:

Growth direction	$[\bar{1}01]_\gamma \parallel [\bar{1}\bar{1}1]_\alpha$
Habit plane (area = $ab$ )	$(232)_\gamma \simeq \parallel (\bar{1}54)_\alpha$
Face of area = $ac$	$(101)_\gamma$
Orientation relationship (KS)	$[\bar{1}01]_\gamma \parallel [\bar{1}\bar{1}1]_\alpha$ $(111)_\gamma \parallel (011)_\alpha$

where the crystallography is, for consistency, stated in the standard variant described earlier. Hence, the major growth direction of each lath corresponds to the parallel close-packed directions from the  $\alpha$  and  $\gamma$  lattices. This is consistent with less direct trace analysis results which indicated that the major growth direction of the laths lies along  $\langle \bar{1}\bar{1}1 \rangle_\alpha$  (Goodenow et al., 1965; Oblak and Hehemann, 1967; Ohmori and Honeycombe, 1971). The habit plane indices are significantly different from earlier data which indicated a  $\{111\}_\gamma$  habit (Greninger and Troiano, 1940; Oblak and Hehemann, 1967; Ohmori and Honeycombe, 1971) but those analyses were either of insufficient precision or were concerned with the apparent habit planes of sheaves (Davenport, 1974). Davenport also demonstrated that sets of two groups of laths with a common growth direction, but with virtually orthogonal habit planes, tended to form in close proximity. There is as yet, no detailed analysis available which can predict these results.

Sandvik (1982a) has measured, using single surface trace analysis, the habit planes of individual sub-units. The mean habit plane is close to  $(0.373\ 0.663\ 0.649)_\gamma$  for an orientation relationship in which  $(111)_\gamma \parallel (011)_\alpha$  and  $[\bar{1}01]_\gamma$  is approximately  $4^\circ$  from  $[\bar{1}\bar{1}1]_\alpha$  (such an orientation is close to the Nishiyama-Wasserman orientation relationship). The habit plane was not found to vary significantly with transformation temperature. Using data from high-resolution observations of the displacements of austenite twins by the shape deformation due to transformation, he was able to show that the shear component of the shape strain of a sub-unit is about 0.22. Sandvik also showed that the observed shape strain direction and magnitude are close to the corresponding parameters for the classic  $\{225\}_\gamma$  and  $\{31015\}_\gamma$  martensites in steels.

## 2.6 Unit Cell Symmetry

It has been generally assumed that the unit cell of bainitic ferrite is cubic; however, there is growing evidence that this is not the case when the crystallography is characterised at an early stage of transformation. To understand this, it is necessary first to introduce the crystallography of interstitial carbon.

### 2.6.1 Symmetry of Interstices

Fig. 2.29 shows the hard-sphere models of the octahedral and tetrahedral interstices in ferrite and austenite. The interstices in ferrite are not regular; one of the axes of the octahedral hole has a length  $a_\alpha$ , the lattice parameter of ferrite, whereas the other two are along the  $\langle 110 \rangle$  directions with length  $\sqrt{2}a_\alpha$ . The shortest axis has four-fold symmetry so a vacant octahedral site in ferrite has tetragonal symmetry  $\frac{4}{m} \frac{2}{m} \frac{2}{m}$ . As a result, placing a carbon atom in the octahedral site causes essentially a uniaxial distortion which leads to a *reduction* in the tetragonality of the interstitial site, though an increase in the tetragonality of the original cubic lattice if carbon atoms act in concert and align parallel to one of the cube edges.

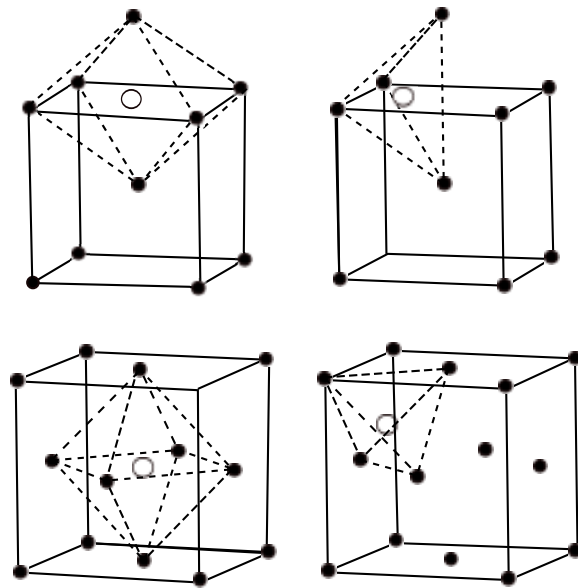


**Figure 2.29** Schematic representation of the octahedral and tetrahedral interstices (open circles) in ferrite and austenite.

The tetrahedral interstice in ferrite is also irregular with two edges parallel to  $\langle 100 \rangle$  directions, and the remaining four being along  $\langle 111 \rangle$  directions, with lengths  $a_\alpha$  and  $a_\alpha\sqrt{3}/2$  respectively. The lines joining the corners of the tetrahedron to its centre are of the form  $\langle 210 \rangle$ .

The largest atom that can fit without distortion in an octahedral site is  $(\frac{1}{2} - \frac{\sqrt{3}}{4})a_\alpha = 0.067a_\alpha$ , in contrast to  $(\frac{\sqrt{5}}{4} - \frac{\sqrt{3}}{4})a_\alpha = 0.126a_\alpha$  for the tetrahedral hole. And yet, carbon atoms predominantly occupy the octahedral sites, because distortion of the tetrahedral in-

terstice is more uniform with all four “bonds” stretched, whereas it is primarily the cube edge which accommodates the distortion in the octahedral case. The strain energies for the two cases when Poisson’s effects are neglected are proportional to (Beshers, 1965):

$$U_O \propto 2(r_i - r_o)^2 E_{100}$$

where  $r_i$  is the interstitial-atom radius,  $r_o$  is the radius of the undistorted hole and  $E$  is the Young’s modulus along the crystallographic direction identified in the subscript. For the tetrahedral site,

$$U_{Te} \propto 4(r_i - r_o)^2 E_{210}$$

so for  $r = 0.08$  nm,  $U_{Te}/U_O = 1.38$ . More recent calculations suggest that there is a substantial difference in the chemical energy of solution between the octahedral and tetragonal sites, which makes the former interstice the favoured site for carbon atoms (Fors and Wahnström, 2008).

In contrast to ferrite, the octahedral interstices in austenite are regular (Fig. 2.29) so carbon causes an isotropic expansion that has a much weaker interaction with dislocations, thus the hardening of austenite by carbon is relatively small. But more significantly, there is only one octahedral interstice per iron atom in austenite, but three in the case of ferrite or martensite. The Bain strain (Fig. 2.30) compresses the austenite cell along the  $z$  axis with uniform expansion along the  $x$  and  $y$  axes. Suppose that three carbon atoms are located in the octahedral interstices marked ‘o’ in the austenite, then as a consequence of the Bain strain, they would all end up in just one of the three sub-lattices of octahedral interstices in the resultant body-centred cell, making it tetragonal. It is this ordering which leads to the tetragonality of martensite in steels.

### 2.6.2 Tetragonality of Bainitic Ferrite

Like any ordering phenomenon, the carbon atoms will tend to randomise if the temperature is above that for Zener ordering (Fisher et al., 1949), in which case, the martensite will not be tetragonal, but cubic. However, this is an after-effect, in which carbon atoms initially ordered by the Bain strain would tend to disorder assuming sufficient mobility.

It is important to note that the diffusionless transformation of austenite containing carbon in the first instance necessarily leads to a body-centred tetragonal lattice (Honda and Nishiyama, 1932; Christian, 1992).

However, for this tetragonality to be preserved, carbon must remain ordered, and it is only recently that it has been possible to retain the tetragonality by isothermal transformation at a low temperature ( $\approx 200$  °C). Under these circumstances, the carbon forced into bainitic ferrite due to diffusionless transformation, can remain there for prolonged periods, permitting the tetragonality to be preserved. The early conclusion that the excess carbon in bainitic ferrite is largely located at defects (Bhadeshia and Waugh, 1982b,a) is not correct; modern atom-probe techniques have revealed substantial quantities to be present in solid solution (Caballero et al., 2013b, 2012; Pereloma et al., 2012). The fact that carbon remains in solid solution in spite of prolonged isothermal heat treatment at

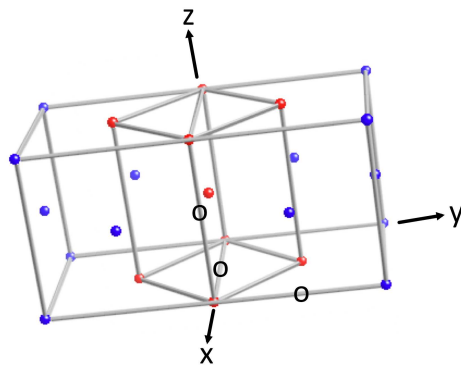


**Figure 2.30** The blue atoms represent two adjacent unit cells of face-centred cubic austenite. The red represent a body-centred tetragonal (bct) cell of austenite, which can be deformed into a body-centred cubic cell, by compression along the vertical axis and uniform expansion along the horizontal axes. The locations marked 'o' represent octahedral interstices on the cube edges of the austenite, where carbon may reside.

temperatures where it can easily partition into the residual austenite, or following tempering heat-treatments (Garcia-Mateo et al., 2004; Caballero et al., 2010b), indicated that there may exist a different equilibrium between tetragonal ferrite and austenite, and first principles calculations (Jang et al., 2012) confirmed that the solubility of carbon should in these circumstances increase, explaining its reluctance to partition. Synchrotron X-ray experiments in which a transformed sample was heated at  $300\text{ }^{\circ}\text{C h}^{-1}$  revealed that the bainitic ferrite unit cell lacked cubic symmetry, but as the sample became tempered, the tetragonality decreased as illustrated in Fig. 2.31 (Hulme-Smith et al., 2013a). This represents the first experimental evidence for the tetragonal symmetry of bainitic ferrite, but it is likely that the existence of non-cubic symmetry has in the past been ignored since the assumption that it should be cubic was all pervasive. Further work has confirmed these results (Caballero et al., 2014; Hulme-Smith et al., 2015). Furthermore, measurements have shown that the thermal expansion coefficient of bainitic ferrite is not isotropic, as would be expected from a non-cubic lattice (Dutta et al., 2014).

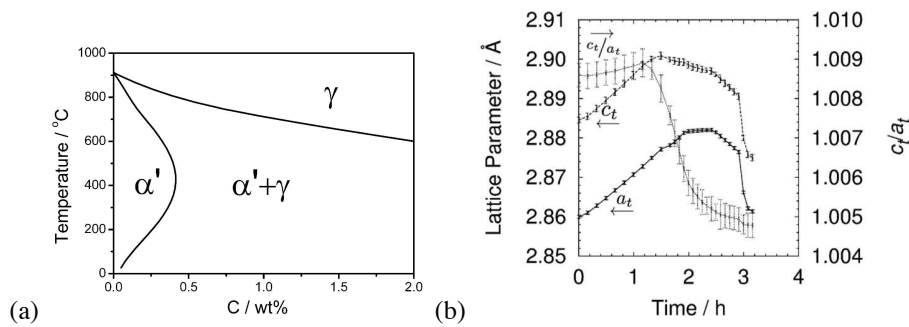


**Figure 2.31** (a) Binary phase diagram of the Fe-C system allowing equilibrium between body-centred cubic ferrite and austenite. After Jang et al. (2012). (b) Lattice parameters of bainitic ferrite, as a function of time during heating at  $300\text{ }^{\circ}\text{C h}^{-1}$ . The austenite began to decompose after about 2 h where the temperature reached about  $600\text{ }^{\circ}\text{C}$ . After Hulme-Smith et al. (2013a).

## 2.7 Microstructure of Bainite: The Midrib

High-carbon steels can sometimes transform to plates of lower bainite which do not have a homogeneous microstructure (Okamoto and Oka, 1986). When observed using light microscopy, a macroscopic plate of lower bainite is seen to have a black line running centrally along its axis (Fig. 2.32). Transmission electron microscopy reveals that this line corresponds to a centrally located, coplanar thin plate of martensite which is sandwiched between regions of lower bainite. The lower bainite containing the midrib is actually found to evolve in two stages, from thin-plate martensite which forms first by the isothermal transformation of austenite, and which then stimulates the growth of the adjacent bainite regions.

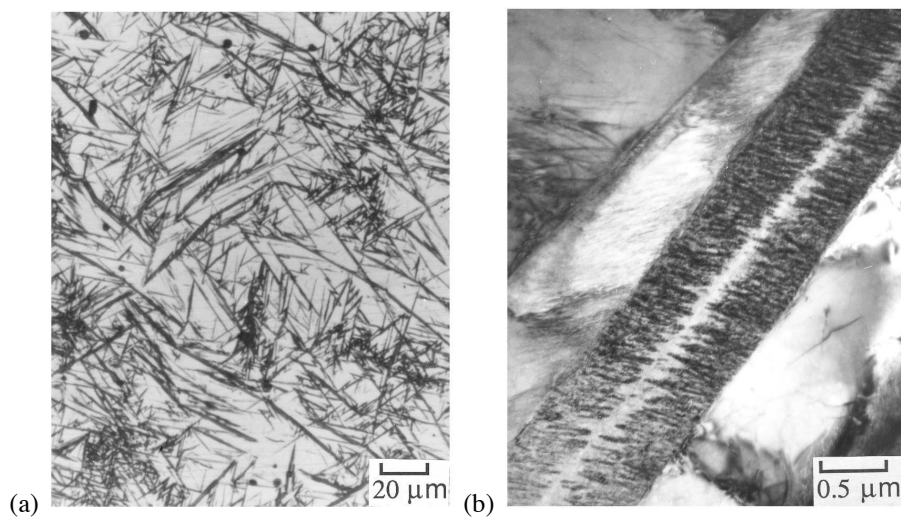


**Figure 2.32** Optical and transmission electron micrographs of the midrib associated with lower bainite in a plain carbon steel. After Okamoto and Oka (1986).

Okamoto and Oka deduced that at relatively high transformation temperatures, the steels react to give lower bainite without a midrib, but as the transformation temperature is reduced to below a certain temperature  $T_r$ , this is replaced by the lower bainite with a thin-plate martensite midrib, which then gives way to just the thin-plate martensite; at a sufficiently low temperature (below the conventional  $M_S$  temperature), ordinary martensite with a lenticular plate morphology forms by the athermal transformation of austenite.

It was noted above that both the lower bainite containing the midrib, and thin-plate martensite isothermally form in the temperature range  $T_r \rightarrow M_S$ . Okamoto and Oka demonstrated that the difference between these two temperatures diminishes as the carbon concentration of the steel decreases, until at about 1 wt% C, it becomes zero. Consequently, neither of these phases have been reported to occur in lower carbon steels.

The terminology *thin-plate martensite* has its origins in work done on nickel-rich Fe-Ni-C alloys, where the martensite transformation temperatures are well below  $-100^\circ\text{C}$  (Maki et al., 1973, 1975). The martensite then tends to form as extremely thin, parallel-sided plates in preference to much thicker lenticular plates, especially as the carbon concentration is increased. Because of their large aspect ratios, the thin plates are elastically accommodated in the austenite matrix; their interfaces remain glissile. The plates can therefore thicken as the temperature is reduced, or indeed become thinner as the temperature is raised.

## 2.8 Summary

Bainite grows in the form of clusters of thin lenticular plates or laths, known as sheaves. The plates within a sheaf are known as sub-units. The growth of each sub-unit is accompanied by an invariant-plane strain shape change with a large shear component. The sub-units are to some extent separated from each other by films of residual phases such as austenite or cementite, so that the shape strain of the sheaf as a whole tends to be much smaller than that of an isolated sub-unit. The plates within any given sheaf tend to adopt almost the same crystallographic orientation and have identical shape deformations. Because of the relatively high temperatures at which bainite grows (where the yield stresses of ferrite and austenite are reduced), the shape strain causes plastic deformation which in turn leads to a relatively large dislocation density in both the parent and product phases; other kinds of defects, such as twinning and faulting are also found in the residual austenite. This plastic accommodation of the shape change explains why each sub-unit grows to a limited size which may be far less than the austenite grain size. The dislocation debris stifles the motion of the otherwise glissile interface. Consequently, the sheaf as a whole grows by the repeated "nucleation" of new sub-units, mostly near the tips of those already existing.

The bainitic ferrite/austenite orientation relationship is always found to lie well within the Bain region; this and other features of the transformation are broadly consistent with the phenomenological theory of martensite crystallography. The growth of bainitic ferrite undoubtedly occurs without any redistribution of iron or substitutional solute atoms, even on the finest conceivable scale at the transformation interface. Therefore, theories that rely on interfacial segregation or solute drag are necessarily ill-conceived.

There have been remarkable developments in understanding the role of carbon during the growth of bainite. There is no doubt that bainitic ferrite contains a much larger concentration of carbon than expected from an equilibrium between ferrite and austenite. In the past, these observations have been attributed to the carbon depositing at dislocations. However, it is now firmly established that exceptionally large concentrations of carbon re-

main in solid solution within the bainitic ferrite. This excess carbon causes the unit cell of the ferrite to become non-cubic.

Some of the carbon is, during the course of transformation, either partitioned into the residual austenite, or in the case of lower bainite, also precipitated as carbides within the ferrite. We shall see that even this redistribution occurs after the diffusionless growth of bainitic ferrite, as discussed in in Chapters 5 and 6.

All of the observed characteristics of bainitic ferrite prove that it grows by a displacive transformation mechanism, which provides a theoretical framework for the design of bainitic steels.

## CHAPTER 3

---

# CARBIDE PRECIPITATION

---

Carbides are largely responsible for the commercial failure of many of the early bainitic steels. The alloys could not compete against the quenched and tempered martensitic steels with their finer dispersions of carbide particles. Mechanical properties are discussed in Chapter 12; the purpose here is to deal with the nature and extent of carbide precipitation reactions in the context of the mechanism of the bainite transformation.

### 3.1 Upper Bainite

In upper bainite the carbides precipitate from austenite which is enriched in carbon; upper bainitic ferrite itself is free from precipitates (Fig. 3.1a). The most common carbide is cementite but there are notable exceptions, particularly in steels containing large concentrations of silicon. For example, the orthorhombic carbides reported by Schissler et al. (1975) and the *c*-carbide discovered by Sandvik (1982b), Table 3.1. Transition carbides, such as  $\kappa$  and the various orthorhombic forms listed in Table 3.1, only form because they are easier to nucleate, so they eventually transform into cementite.

Carbon is partitioned into the residual austenite during the bainite reaction. Cementite precipitation becomes possible when its carbon concentration  $x_\gamma$  exceeds the solubility limit given by the extrapolated  $\gamma/(\gamma + \theta)$  phase boundary (Kriesement and Wever, 1956). This is illustrated in Fig. 3.1b, where the shaded area represents austenite which is unstable to the precipitation of cementite. It follows that if there are no kinetic hindrances, carbide

**Table 3.1** Carbides in bainite or in tempered bainite. Fe,M/C is the ratio of metal to carbon atoms. Actual lattice parameters are alloy dependent. See also a review by Yakel (1985).

Carbide	Crystal System	Lattice parameters / Å	Fe,M/C	Reference
$\kappa$	Hexagonal	$a = 6.9$ $c = 4.8$	1.37	(Deliry, 1965; Pomey, 1966)
$\epsilon$	Hexagonal	$a = 2.735$ $c = 4.339$	2.4-3	(Hofer et al., 1949; Jack, 1950, 1951)
$\chi$	Monoclinic	$a = 11.563$ $b = 4.573$ $c = 5.058$ $\beta = 97.44^\circ$	2.2 or 2.5	(Hägg, 1934)
$\eta$	Orthorhombic	$a = 4.704$ $b = 4.318$ $c = 2.830$	2	(Hirotsu and Nagakura, 1972)
$\text{Fe}_3\text{C}$	Orthorhombic	$a = 4.525$ $b = 5.087$ $c = 6.743$	3.0	
$\text{M}_7\text{C}_3$	Orthorhombic	$a = 4.526$ $b = 7.010$ $c = 12.142$	7/3	(Morniroli et al., 1983)
$(\text{Fe, Si})\text{C}_x$	Orthorhombic	$a = 8.8$ $b = 9.0$ $c = 14.4$		(Konoval et al., 1959)
$(\text{Fe, Si})\text{C}_x$	Orthorhombic	$a = 6.5$ $b = 7.7$ $c = 10.4$		(Schissler et al., 1975)
$(\text{Fe, Si, Mn})\text{C}_x$	Orthorhombic	$a = 14.8$ $b = 11.4$ $c = 8.5$		(Schissler et al., 1975)
$\text{M}_{23}\text{C}_6$	Cubic F	$a = 10.621$	23/6	
$\text{M}_6\text{C}$	Cubic F	$a = 11.082$	6	
$c$	Triclinic	$a = 6.38$ $b = 5.05$ $c = 4.59$ $\alpha = 90.0^\circ$ $\beta = 70.1^\circ$ $\gamma = 84.7^\circ$		(Sandvik, 1982b)

precipitation will accompany the growth of upper bainite if the transformation temperature is below  $T_C$  (Fig. 3.1b).

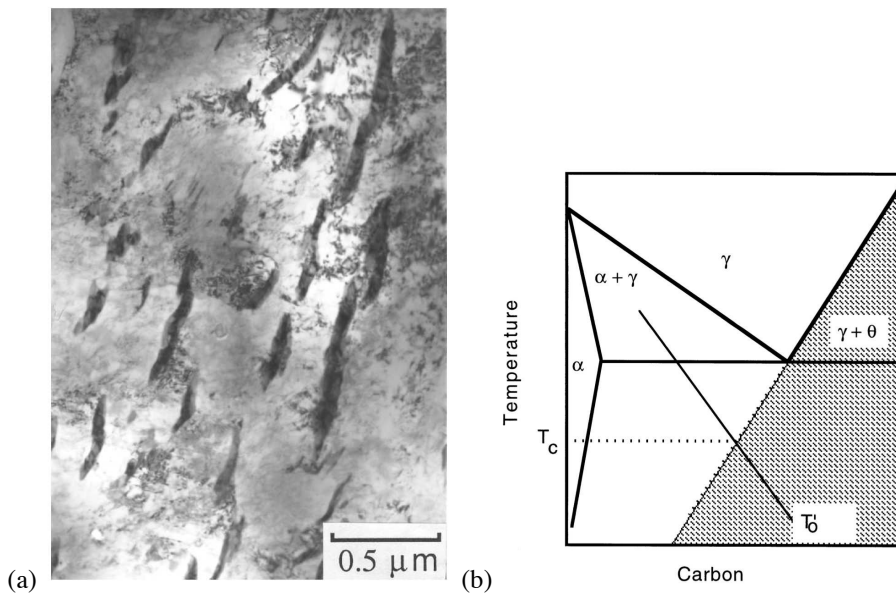


**Figure 3.1** (a) Distribution of cementite particles between the ferrite platelets in upper bainite (AISI 4340 steel). (b) Thermodynamic condition which must be satisfied before cementite can precipitate from austenite (shaded area).

The precipitation of carbides is peripheral to the formation of bainitic ferrite. On the other hand, their precipitation reduces the carbon concentration in the residual austenite, thus stimulating the formation of a further quantity of ferrite (designated  $\alpha$ ). Given the

very small diffusion coefficients of iron and substitutional atoms at the temperatures involved (Fig. 3.2), and the absence of an incoherent interface or grain boundary to start the process, it is unlikely that this secondary ferrite forms by reconstructive transformation. Sandvik (1982b) has proposed that the decomposition of the residual austenite involves the displacive formation of a triclinic carbide, close to cementite in structure, and the subsequent formation of a small amount of *bainitic* ferrite. Nakamura and Nagakura (1986), in a study of the second stage of martensite tempering, suggested that cementite and ferrite form directly from austenite, the cementite nucleating on the ferrite/austenite boundaries and growing by rapid diffusion along this boundary. They also proposed that the secondary ferrite, which they called bainite, grows martensitically, from the carbon depleted austenite. Regions of secondary ferrite were observed to be twinned – this was taken to indicate the formation of self-accommodating crystallographic variants of bainitic ferrite.

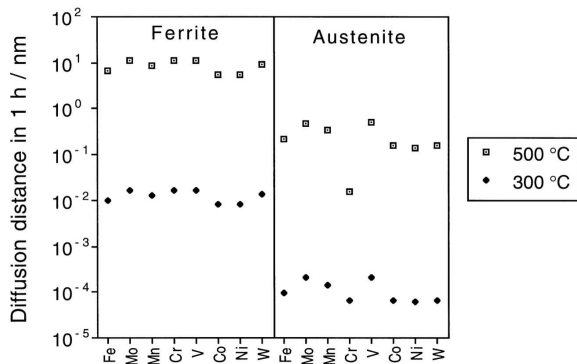
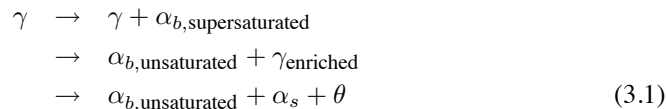


**Figure 3.2**  $2(Dt)^{1/2}$  estimate of the diffusion distances for metal atoms in iron during one hour at temperature.

The sequence of reactions can be summarised as follows ( $\alpha_s$  = secondary ferrite):



This contrasts with the cooperative growth of cementite and ferrite during the formation of pearlite in plain carbon steels:



When pearlite grows in substitutionally alloyed steels, the austenite, ferrite and cementite may coexist in equilibrium over a range of temperatures, with the equilibrium compositions of all the phases changing with the temperature:



The composition of the residual austenite ( $\gamma'$ ) is then expected to differ from that at the beginning of transformation. The reaction therefore stops before all the austenite is consumed.

In planar sections, the cementite particles in upper bainite are parallel to the habit planes of the bainitic ferrite plates. Using transmission electron microscopy, Fisher (1958) showed that these particles are in the form of irregular ribbons in three dimensions, particularly when bainite forms at high temperatures. Carbide precipitation also occurs at the austenite grain boundaries and this may influence mechanical properties, especially toughness in

high strength steels (Pickering, 1958). The austenite grain boundaries are favoured heterogeneous nucleation sites so the carbides there can be expected to be coarse. When high carbon steels ( $> 0.45\text{C wt\%}$ ) are transformed in the bainite temperature range, there is a tendency for cementite to precipitate as thin films on the austenite grain surfaces (Stickels, 1974). These thin films are detrimental to toughness and their growth can be retarded by lowering the transformation temperature.

### 3.2 Lower Bainite

Lower bainite also consists of a non-lamellar aggregate of ferrite and two kinds of carbides. As in upper bainite, there is some precipitation from the enriched austenite. A finer dispersion of plate-like carbides is also found inside the ferrite plates. A common observation is that these latter carbides precipitate in a single crystallographic variant within a given ferrite plate, whereas the tempering of martensite leads to the precipitation of many variants of cementite (Fig. 3.3).

#### 3.2.1 Precipitation within Lower Bainitic Ferrite

There are many observations that reveal the precipitation of carbides from supersaturated lower bainite in a process identical to the tempering of martensite. Hot-stage transmission electron microscopy has shown that the lower bainitic ferrite remains supersaturated with carbon some time after the completion of the ferrite growth (Kang et al., 1990).

Unlike the microstructure of tempered martensite, the carbides tend to adopt a single crystallographic variant in a given plate of lower bainite. They have their longest axes inclined at about  $60^\circ$  to the "growth direction" of the ferrite platelets (Anonymous, 1955; Irvine and Pickering, 1958; Speich, 1962; Shimizu et al., 1964). The angle quoted must of course vary as a function of the plane of section; for lower bainitic ferrite with a habit plane  $(0.761\ 0.169\ 0.626)_\gamma$ , the cementite precipitates on  $(1\ \bar{1}\ 2)_\alpha$  giving an angle of  $57^\circ$  between the  $\alpha_{lb}$  and cementite habit plane normals (Bhadeshia and Edmonds, 1980b). Similar results have been obtained by Ohmori (1971). In some cases, the carbides have been found to form on several different variants of the  $\{1\ 1\ 2\}_{\alpha_{lb}}$  plane, although a particular variant still tends to dominate (Srinivasan and Wayman, 1968c; Lai, 1975; Bhadeshia and Edmonds, 1979a). In fact, a re-examination of published micrographs sometimes reveals the presence of several variants which were not noticed in the original publication [see for example, Fig. 5, Yu et al. (1989)].

Early experiments using Curie point measurements and dilatometry gave hints that the carbides are not always cementite (Wever and Lange, 1932; Wever and Jellinghaus, 1932; Allen et al., 1939; Antia et al., 1944). The orthorhombic transition carbide discovered in high-silicon transformer steels by Konoval et al. (1959) has been reported to precipitate from lower bainitic ferrite in Fe-1.15C-3.9Si wt% alloy (Schissler et al., 1975). Nevertheless, the most common transition carbide in lower bainite is  $\varepsilon$ -carbide, first identified by Austin and Schwartz (1952) and subsequently confirmed by many others.

Matas and Hehemann (1961) interpreted these results to suggest that the initial carbide in hypoeutectoid bainitic-steels is  $\varepsilon$ , which is then replaced by cementite on holding at the isothermal transformation temperature. The rate at which the  $\varepsilon$ -carbide converts to cementite increases with temperature, but also depends on the steel composition. A high silicon concentration retards the reaction, as is commonly observed in the tempering of martensite (Owen, 1954; Gordine and Codd, 1969; Hobbs et al., 1972).

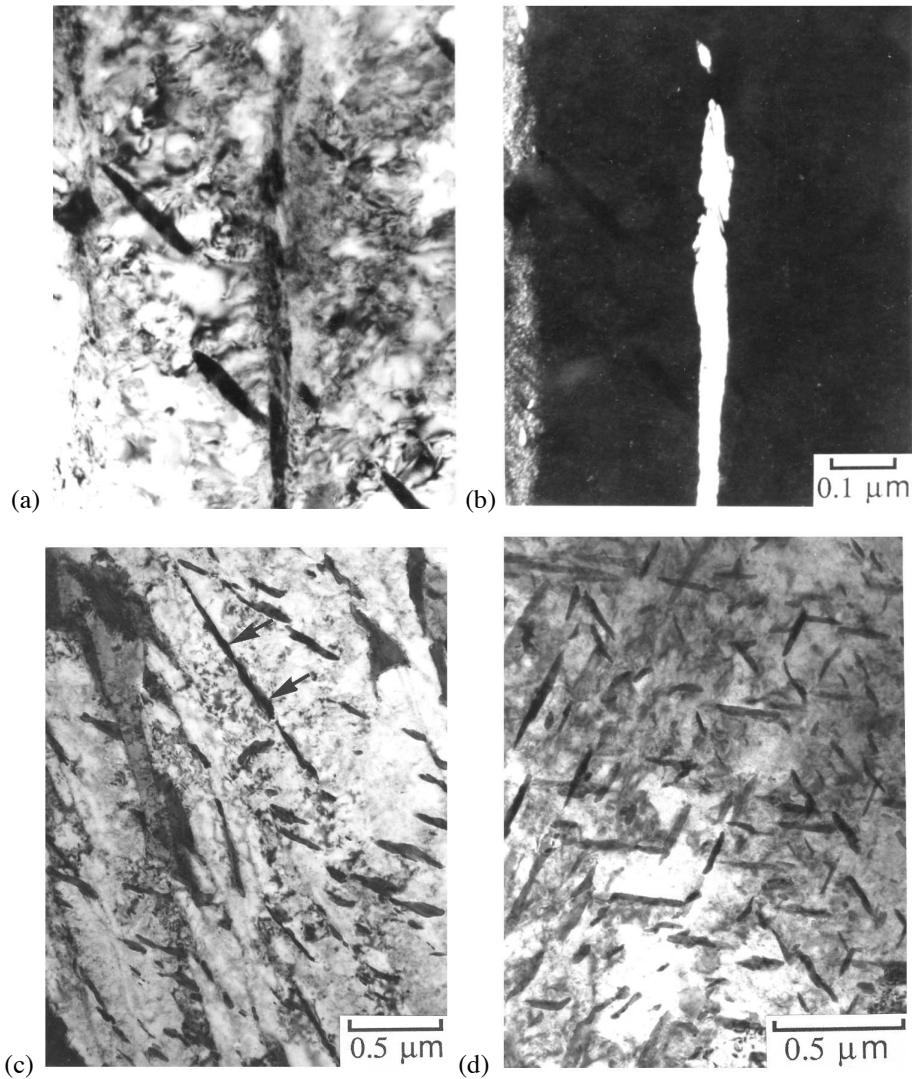


**Figure 3.3** (a-c) Fe-0.3C-4.08Cr wt%. (a) Lower bainite obtained by isothermal transformation for a short time period (435°C, 10 min). Shows particles of cementite within the platelets but not between the platelets. (b) Corresponding dark field image showing the films of austenite between the bainitic ferrite platelets. (c) The same sample after prolonged heat treatment (435 °C, 30 min) at the isothermal transformation temperature, causing the precipitation of carbides between the ferrite platelets. (d) Typical multi-variant carbide precipitation in tempered martensite (415 °C, 50 min, AISI 4340 steel). After Bhadeshia and Edmonds (1980b).

The detection of  $\varepsilon$ -carbide in lower bainite is important because it implies a large excess ( $\geq 0.25$  wt%) of carbon trapped in bainitic ferrite when it first forms (Roberts et al., 1957). However,  $\varepsilon$ -carbide is not always found as a precursor to the precipitation of cementite in lower bainite. Bhadeshia and Edmonds (1979a) failed to detect  $\varepsilon$ -carbide in a high-silicon medium-carbon steel (Fe-3.0Mn-2.02Si-0.43C wt%) even during the early stages of the lower bainite transformation. The steels in which  $\varepsilon$ -carbide has been observed during the formation of lower bainite are listed in Table 3.2.<sup>1</sup>

**Table 3.2** Compositions of steels (wt%) in which  $\varepsilon$ -carbide has been found in lower bainite. The carbon concentration quoted for the alloy studied by Dubensky and Rundman (1985) represents an estimate of the concentration in the austenitic matrix of an austempered ductile cast iron.

C	Si	Mn	Ni	Cr	Mo	V	Reference
0.87	-	-	-	-	-	-	Austin and Schwartz (1952, 1955)
0.95	0.22	0.60	3.27	1.23	0.13	-	Matas and Hehemann (1961)
0.60	2.00	0.86	-	0.31	-	-	Matas and Hehemann (1961)
1.00	0.36	-	0.20	1.41	-	-	Matas and Hehemann (1961)
0.58	0.35	0.78	-	3.90	0.45	0.90	Matas and Hehemann (1961)
1.00	2.15	0.36	-	-	-	-	Deliry (1965)
0.60	2.00	0.86	-	0.31	-	-	Oblak and Hehemann (1967)
0.60	2.00	-	-	-	-	-	Hehemann (1970)
0.41	1.59	0.79	1.85	0.75	0.43	0.08	Lai (1975)
0.54	1.87	0.79	-	0.30	-	-	Huang and Thomas (1977)
0.85	2.55	0.3	-	-	-	-	Dorazil and Svejcar (1979)
0.74	2.40	0.51	-	0.52	-	-	Sandvik (1982a)
1.3	3.09	0.17	-	-	-	-	Dubensky and Rundman (1985)
0.40	2.01	-	4.15	-	-	-	Miihkinen and Edmonds (1987b)
0.71	1.83	0.52	0.02	0.5	0.19	-	Jung et al. (1997)
0.57	1.39	0.74			0.44		Liu and Luo (2006)
0.77	0.30	0.23	0.07	1.38	0.02		Song et al. (2013)

These observations can be rationalised in terms of a theory of tempering due to Kalish and Cohen (1970), who showed that it is energetically favourable for carbon atoms to remain segregated at dislocations when compared with their presence in the  $\varepsilon$ -carbide lattice (Bhadeshia and Edmonds, 1980b), and a similar argument has been used to explain the absence of this transition carbide in nanostructured bainite (Caballero et al., 2007). Carbon becomes trapped at dislocations and if the density of dislocations is sufficiently large, then the carbon is not available for the formation of  $\varepsilon$ -carbide. In such cases, precipitation of the more stable cementite occurs directly from supersaturated ferrite. Kalish and Cohen estimated that a dislocation density of  $2 \times 10^{12} \text{ cm}^{-2}$  should prevent  $\varepsilon$ -carbide precipitation in steels containing up to 0.20 wt% carbon. This can be extrapolated to bainite bearing in mind that there are two competing reactions which help relieve the excess carbon in the

<sup>1</sup>  $\varepsilon$ -carbide has been reported in bainite produced by continuous cooling transformation, in a Fe-0.15C-0.94Mo-2.12Cr wt% steel (Baker and Nutting, 1959) and in a Fe-0.34C-1.25Mn-1.39Ni-0.34Mo wt% alloy isothermally transformed to bainite (Fondekar et al., 1970). In both cases, the evidence quoted is uncertain. A study by Yu (1989) on similar steels has not revealed  $\varepsilon$ -carbide.

ferrite: partitioning of carbon into the residual austenite and the precipitation of carbides in the bainitic ferrite. The reactions interact since partitioning reduces the amount of carbon available for precipitation, and vice versa. Judging from available data (Table 3.2), the average carbon content of the steel must exceed about 0.55 wt% to permit the precipitation of  $\varepsilon$ -carbide. Otherwise, the partitioning of carbon into the austenite depletes the bainitic ferrite too rapidly to permit  $\varepsilon$ -carbide.

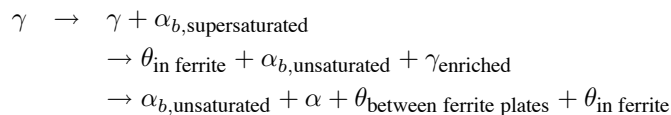
Nickel enhances the precipitation of  $\varepsilon$ -carbide which can therefore be obtained in bainite at lower carbon concentrations,  $\approx 0.4$  wt% (Miihkinen and Edmonds, 1987b). Rao and Thomas (1980) have demonstrated a similar effect of nickel in martensitic steels; they found  $\varepsilon$ -carbides and cementite to be the dominant carbides during the tempering of martensite in Fe-0.27C-4Cr-5Ni and Fe-0.24C-2Mn-4Cr wt% steels respectively. Other substitutional solutes may also affect  $\varepsilon$ -carbide precipitation, but there are no systematic studies. As with martensite, when lower bainite is tempered, the metastable  $\varepsilon$ -carbide transforms to cementite and the reaction is accompanied by a volume contraction, which can be monitored accurately using dilatometry (Hehemann, 1970).

It is interesting that  $\eta$ -carbide ( $\text{Fe}_2\text{C}$ ) has also been observed in lower bainitic ferrite obtained by transforming the austenitic matrix of a high-silicon cast iron (Franetovic et al., 1987a,b). This carbide has previously only been reported in tempered martensite (Hirotsu and Nagakura, 1972; Nagakura et al., 1983) and so reinforces the conclusion that the carbides precipitate from carbon-supersaturated lower bainitic ferrite. Like  $\varepsilon$ -carbide, the carbon concentration has to exceed some critical value before the  $\eta$ -carbide can be detected in lower bainite (Franetovic et al., 1987a,b).

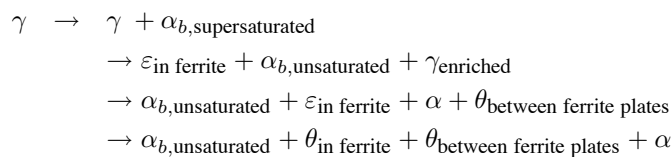
### 3.2.2 Precipitation between Lower Bainitic Ferrite Platelets

There is no essential difference between upper and lower bainite when considering the precipitation of carbides from the carbon-enriched austenite. However, in lower bainite some of the excess carbon precipitates in the ferrite, thus reducing the quantity partitioned into the austenite (Hehemann, 1970). This in turn leads to a smaller fraction of inter-plate cementite when the austenite eventually decomposes. An important consequence is that lower bainite often has a higher toughness than upper bainite, even though it usually is stronger. The precipitation reactions for lower bainite can be summarised as follows:

*Case 1: High dislocation density*



*Case 2: Low dislocation density*



$\kappa$ -carbide was discovered in high-carbon steels transformed to lower bainite (Deliry, 1965; Pomey, 1966). It occurs as a transition carbide, precipitating at a late stage of the transformation, from the carbon-enriched residual austenite. The carbide has a high solubility for silicon and on continued holding at the isothermal transformation temperature, transforms to  $\chi$  which in turn eventually gives way to the more stable cementite.

### 3.3 Kinetics of Carbide Precipitation

#### 3.3.1 Partitioning and Distribution of Carbon

The carbon concentration of bainitic ferrite during transformation is of major importance in determining the kinetics of carbide precipitation. The transformation, however, occurs at high temperatures so some of the excess carbon in the ferrite can be removed by precipitation or by partitioning into austenite. These two processes occur simultaneously, although one or the other may dominate depending on temperature. They can both be rapid because of the high mobility of carbon in iron.

The partitioning of excess carbon from ferrite into austenite has been simulated experimentally (Matas and Hehemann, 1960, 1961) by tempering mixtures of martensite and retained austenite. Single crystals of austenite were cooled below the  $M_S$  temperature (350 K) to obtain two microstructures, one containing 50% martensite and the other 90% martensite in a matrix of austenite. The crystals were then tempered at 405 K to allow the carbon to diffuse from martensite into austenite. The tempering induced the rapid precipitation of  $\varepsilon$ -carbide, thereby lowering the carbon concentration of the martensite to 0.22 wt%, a value consistent with that quoted by Roberts et al. (1957) for the equilibrium between martensite and  $\varepsilon$ -carbide. Continued tempering led to further reductions in the carbon concentration of the martensite as the carbon partitioned into the austenite. This partitioning occurred more rapidly for the sample containing less martensite, presumably because the larger amount of residual austenite provided a bigger sink for carbon. The idea of enriching the austenite with carbon partitioned from martensite during the tempering of the two-phase mixture has taken on a new momentum since the development of the associated theory by Speer et al. (2003). An elegant summary of the current state-of-the-art is available in Speer et al. (2015).

The distribution of carbon in the residual austenite is not homogeneous after isothermal transformation to bainite (Fig. 3.5). The enrichment is greater in the immediate vicinity of bainite platelets or in the regions trapped between the platelets (Schrader and Wever, 1952; Matas and Hehemann, 1961; Bhadeshia and Waugh, 1982b; Bhadeshia, 1983b; Scott and Drillet, 2007; Caballero et al., 2011b; Garcia-Mateo et al., 2012a).<sup>2</sup> Some of the measurements referred to here used the atom-probe technique and a comparison has been published using X-ray analysis of the lattice parameters of the austenite (Garcia-Mateo et al., 2012a). However, there are likely to be difficulties in making such comparisons because of the huge differences in sampling volumes between the two techniques, combined with the fact that the scale of the heterogeneous distribution is much greater than that of the sample size in the atom-probe (Bhadeshia, 2015).

<sup>2</sup>In dual-phase steels, the non-uniform distribution of carbon in the austenite manifests differently. Here, allotriomorphic ferrite is the dominant phase, the residual austenite decomposes into martensite in the vicinity of the  $\alpha/\gamma$  interface, but into bainite at the core of the austenite where the carbon concentration is smaller (Waterschoot et al., 2002). In TRIP-assisted steels, it is the lower carbon austenite that transforms first (Streicher-Clarke et al., 2005).

Carbon causes an expansion of the austenite so in some cases, two lattice parameters have been observed for the retained austenite, corresponding to different levels of carbon in the heterogeneous austenite within a single specimen (Matas and Hehemann, 1961; Taran et al., 1997; Kutsov et al., 1999). In many cases, the austenite which is relatively poor in carbon decomposes to martensite on cooling to ambient temperature. Indeed, two different martensite-start temperatures have been reported, the one for blocky austenite being greater than that for the film austenite (Lawrynowicz, 2002). Fig. 3.4 shows the evolution of the lattice parameters of austenite during the course of the bainite reaction, illustrating the development of the non-uniform distribution of carbon, together with dilatometric data illustrating distinct separation of the martensite-start temperatures.

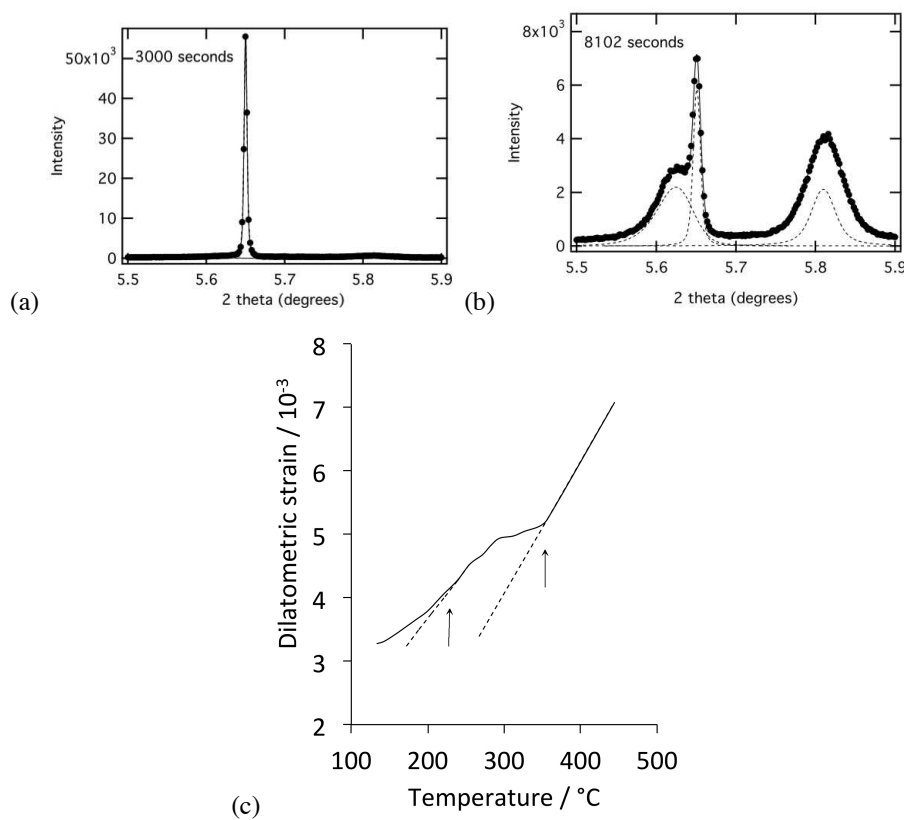


**Figure 3.4** Austenite  $\{111\}$  and ferrite  $\{110\}$  reflections during isothermal transformation. Solid lines represent the fit achieved; the individual peak profiles less the background are the dotted lines. (a) Pattern during the fully austenitic state, (b) following some formation of bainite; the  $\{111\}_\gamma$  data reflect the distribution of carbon. Details of this *in situ* synchrotron X-ray experiment on nanostructured bainite are available in Stone et al. (2008). (c) Detection of two distinct stages of martensitic transformation (identified by the arrows) in austenite that has a non-uniform distribution of carbon, after Lawrynowicz (2002).

If those regions of austenite that are poorer in carbon then transform into martensite, the measurement of the carbon concentration of austenite ( $x_\gamma$ ) using an X-ray method should overestimate  $x_\gamma$  if it is assumed that there is a homogeneous distribution of carbon in the residual austenite that existed at the isothermal transformation temperature. For example,

for upper bainite in a high-silicon steel, X-ray measurements gave  $x_\gamma = 1.7$  wt%, whereas volume fraction data gave an average concentration of 1.35 wt% (Le-Houillier et al., 1971).

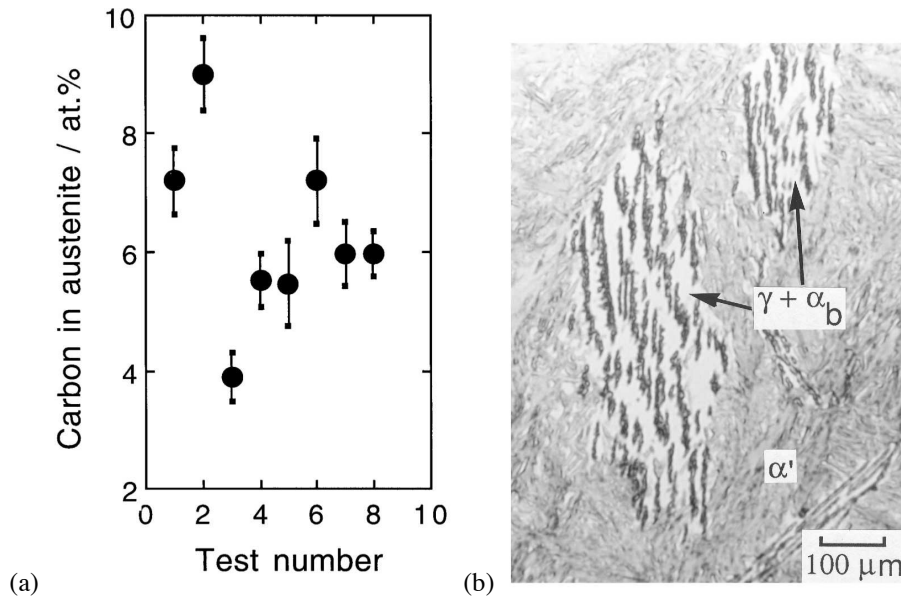


**Figure 3.5** The nonuniform distribution of carbon in the residual austenite associated with bainitic ferrite. (a) Direct measurements of the carbon concentration using an atom-probe; Fe-0.39C-2.05Si-4.08Ni wt%, isothermally transformed at 340 °C for 10 h (Bhadeshia and Waugh, 1982a). (b) Rim of austenite retained around a sheaf of bainite in Fe-0.81C-1.98Si-3Mn wt% steel, where the carbon concentration is expected to be largest.

### 3.3.2 Kinetics of Precipitation from Residual Austenite

Carbide formation lags behind that of bainitic ferrite, to an extent which depends both on the transformation temperature and on the alloy composition. In steels which transform rapidly, the delay may not be detectable. Using a chemical technique which separates precipitated carbon from that in solid solution, together with dilatometry, it has been shown that for high transformation temperatures, the amount of carbide formed is proportional to that of bainitic ferrite at any stage of the reaction (Vasudevan et al., 1958). At lower temperatures, carbide precipitation follows significantly after the formation of bainitic ferrite.

With lower bainite, it is necessary to distinguish between the carbides within the bainitic ferrite which precipitate rapidly, and those which form by the slower decomposition of the carbon-enriched residual austenite (Fig. 3.3a,c). The slow rate of precipitation from austenite is due to the difference in the diffusion rates of carbon in ferrite and austenite, and because the supersaturation is larger for ferrite.

Striking evidence that the formation of carbides lags behind that of bainitic ferrite is found in silicon-rich steels. Thus, carbides do not form in upper bainite in Fe-0.31Cr-0.86Mn-2.00Si-0.60C wt% even after holding at the isothermal transformation temperature for several hours (Matas and Hehemann, 1961). Similar results have been reported by Le-Houillier et al. (1971), Sandvik (1982b) and by many other researchers.

Silicon is usually present in steels as an aftermath of the deoxidation reactions involved in the steelmaking process. At large concentrations it retards the formation of cementite from austenite, making it possible to obtain a carbide-free microstructure of just bainitic ferrite and austenite. For the same reason, silicon favours the formation of grey cast iron with graphite instead of the cementite found in low-silicon white cast irons. It is well known that the precipitation of cementite during the tempering of martensite is significantly retarded by the presence of silicon (Bain, 1939; Allten and Payson, 1953; Owen, 1954; Keh, 1963; Gordine and Codd, 1969; Hobbs et al., 1972). This has been exploited in the design of one of the most successful ultrahigh-strength steels with the commercial designation 300M, reviewed by Pickering (1979).

Silicon has an incredibly low solubility in cementite that is in equilibrium with austenite (Jang et al., 2009, 2010) and ferrite (Miyamoto et al., 2007). Fig. 3.6 shows that in contrast to manganese, all the tie-lines connecting cementite to austenite radiate from a small region near the Fe-C axis in the case of the Fe-C-Si ternary, whereas the cementite is able to readily accommodate manganese until  $\text{Mn}_3\text{C}$  is obtained. If it is forced, by the paraequilibrium transformation mechanism, to inherit the silicon as it grows then the driving force for precipitation is greatly reduced, thus retarding precipitation (Bhadeshia, 2003), Section 3.5. Fig. 3.7 shows a dramatic comparison between the equilibrium and paraequilibrium phase diagrams in the iron-rich corner, for temperatures at which bainite commonly forms. A marked increase in the size of the austenite phase field occurs on constraining the system to paraequilibrium transformation conditions. Thus, the addition of silicon can change the alloy from being in the  $\gamma + \theta$  phase field under equilibrium conditions, to a single phase austenite field when the cementite grows without the partitioning of silicon. A comprehensive set of calculations like these has been published more recently, for both cementite and  $\text{Fe}_2\text{C}$  (Shaposhnikov and Mogutnov, 2008).

The large influence of silicon on the kinetics of precipitation from austenite, as illustrated in Fig. 3.8a (Kozeschnik and Bhadeshia, 2008). Bearing in mind that “300M” steel is essentially a silicon-enriched version of “4340” steel, the corresponding effect of silicon on cementite precipitation during the tempering of martensite is extremely small except when the carbon concentration in solution is also small. This is surprising at first sight because it contradicts experience, but consistent with earlier work (Ghosh and Olson, 2002); the anomaly can be understood once it is realised that the driving force for precipitation from supersaturated ferrite is very large. However, if the carbon is trapped at dislocations in the martensite (Kehoe and Kelly, 1970), then the amount available for precipitation decreases so the observed effect of silicon would be larger as shown in Fig. 3.8b for the lower carbon concentrations.

It was at one time thought that the retardation occurs because silicon stabilises transition carbides at the expense of cementite (Reisdorf, 1963; Gordine and Codd, 1969) but experiments have shown that the transition carbides are not particularly enriched in silicon (Barnard et al., 1981a).

Aluminium in solid solution also retards tempering reactions (Allten, 1954; Langer, 1968; Bhat, 1977). The effect is believed to be identical to that of silicon although detailed solubility data are not available. New alloys developed for the automobile industry sometimes exploit phosphorus in solution to prevent cementite precipitation, although the mechanism by which this happens is not clear (Mahieu et al., 2002b).

Carbide-free bainitic microstructures can be obtained in steels containing little or no silicon or aluminium, for example in Fe-Cr-C alloys (Bhadeshia, 1980; Qiao et al., 2009), in low-carbon steels (Yang and Bhadeshia, 1987a), in copper-containing steels (Thompson et al., 1988) and in Fe-Mn-V-C steel (Lawrynowicz, 2012). The classic “ $2\frac{1}{4}\text{Cr1Mo}$ ” steel

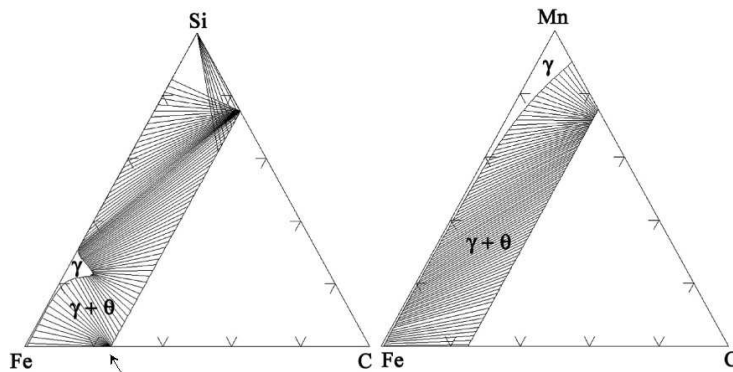


**Figure 3.6** Calculated sections of the Fe-Si-C and Fe-Mn-C phase diagrams for 500 °C using thermodynamic data for cementite generated from first principles calculations, which are then implemented in a phase diagram calculation package that already had data for austenite (Jang et al., 2010).

which is used in vast quantities in the electricity generation industry has a carbide-free bainitic microstructure. It is not yet possible to predict the effects of alloying elements on carbide precipitation reactions during the bainite transformation.

It is worth noting that when martensite in a secondary hardening steel is tempered, a large silicon concentration retards cementite precipitation and hence promotes the early precipitation of alloy carbides. This is because carbon becomes more available in high-silicon steels (Delagnes et al., 2005).

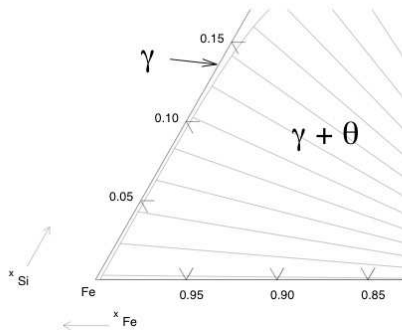
### 3.3.3 Kinetics of Precipitation within Bainitic Ferrite

It is particularly interesting that the precipitation of cementite from martensite or lower bainite can occur at temperatures below 400 K, in time periods too short to allow any substantial diffusion of iron atoms. The long-range diffusion of carbon atoms is of course necessary, but because carbon resides in interstitial solution, it can be very mobile at temperatures as low as 210 K (Winchell and Cohen, 1962).

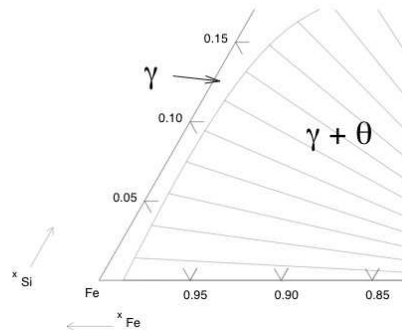
The formation of cementite or other transition carbides of iron, in these circumstances of incredibly low atomic mobility, must differ from diffusional decomposition reactions. It has been believed for some time that the cementite lattice is generated by the homogeneous deformation of ferrite, combined with the necessary diffusion of carbon into the appropriate sites - in effect a displacive mechanism with paraequilibrium.<sup>3</sup> The nature of the necessary displacements for generating cementite or  $\epsilon$ -carbide structures have been considered phenomenologically by Andrews (1963) and the subject has been reviewed by Yakel (1985). The models are not sufficiently developed to predict transformation kinetics except that they do not involve the diffusion of substitutional atoms and hence are consistent with rapid kinetics even at low temperatures.

<sup>3</sup>Displacements consistent with large shear deformations have been measured for proeutectoid cementite plates, where the tilt angle varied from 20-50° because of stereological effects (Yan et al., 2013). Such displacements are entirely consistent with the paraequilibrium, displacive formation of cementite.

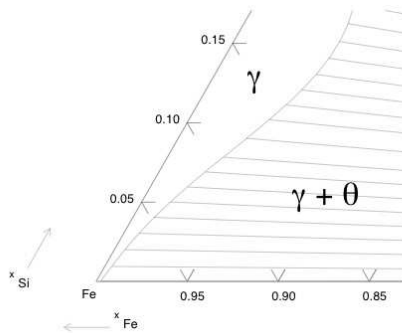
a) Equilibrium 573K



b) Equilibrium 773K



c) Paraequilibrium 573K



d) Paraequilibrium 773K

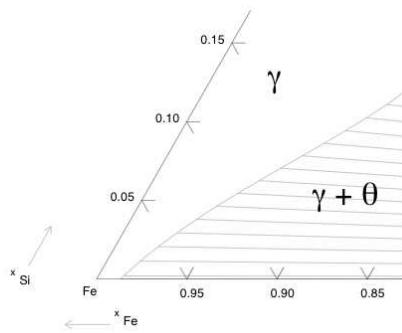


**Figure 3.7** The Fe rich corner of the equilibrium (a,b) and paraequilibrium (c,d) Fe-Si-C phase diagram at 573 K and 773 K. After Lord (1998).

The lack of atomic mobility over the temperature range where bainite grows has consequences also on the alloy carbides (such as  $\text{Mo}_2\text{C}$ ) which require diffusion to grow. The size of such carbides is restricted by the distance through which the substitutional atoms can diffuse during the time scale of the experiment. This is illustrated by experiments in which the transformation of a Fe-Mo-C alloy was studied over a wide range of temperatures with the carbide type, size and composition being characterised at the highest spatial and chemical resolution possible (Stark and Smith, 1987). Fig. 3.9 shows that the measured particle sizes correlate well with the random walk distance  $2(D_{\text{Mot}}t)^{0.5}$ , which is a measure of atomic mobility. In niobium steels, Nb(C,N) particles only grow to a size of 10 nm and when bainite forms at temperatures in excess of 580 °C (Park and Lee, 2007).

A second consequence is related to the mechanism by which the ferrite itself grows. The crystallographic change from  $\gamma \rightarrow \alpha$  may occur without any diffusion. However, if the mechanism is reconstructive, then mass transport is essential during growth even when there is no change in composition (Bhadeshia, 1985b). The transformation can then only proceed at a rate consistent with this diffusion, in which case substitutional solutes like molybdenum have an opportunity to precipitate. It is noteworthy that Stark and Smith

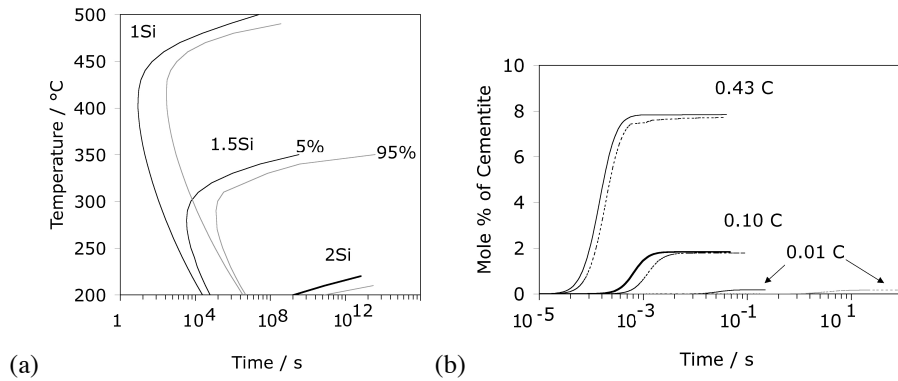


**Figure 3.8** (a) Calculated time-temperature-precipitation diagram for paraequilibrium cementite from austenite of composition Fe-1.2C-1.5Mn-1.5Si wt%. (b) Kinetics of paraequilibrium precipitation at 315°C, from martensite in 4340 (continuous curve, 0.43C wt%) and 300M (dashed curve) steels. After Kozeschnik and Bhadeshia (2008).

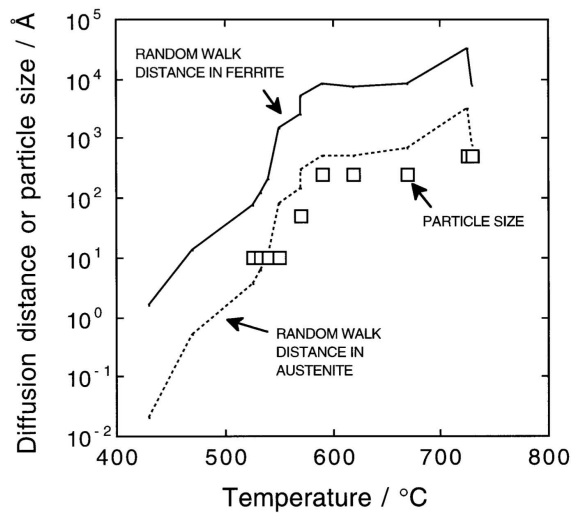


**Figure 3.9** Correlation of random walk distance for molybdenum atoms with the measured molybdenum carbide particle size (data due to Stark and Smith, 1987). The curves are the calculated  $2(D_{Mo}t)^{0.5}$  values for specific heat-treatments. Molybdenum carbide was never found with bainite, only with ferrite which grew by reconstructive transformation.

(1987) only found molybdenum carbides in ferrite which grew by a reconstructive transformation mechanism, and never in association with bainitic ferrite.

### 3.4 Crystallography of Carbide Precipitation in Bainite

During isothermal heat-treatments of the type used to generate bainite, the steel is not held at temperature for periods long enough to permit the long-range diffusion of substitutional atoms. Only iron carbides, such as  $\varepsilon$ ,  $\kappa$ ,  $\eta$  or cementite therefore precipitate. Other carbides which require the partitioning of substitutional solutes cannot form.

#### 3.4.1 Cementite: Orientation Relationships

Shackleton and Kelly (1965) studied the orientation relationships between ferrite and cementite in bainite. The relationships were found to be identical to those known for cementite in tempered martensite. They most frequently observed the tempering or Bagaryatskii (1950) orientation relationship:

$$\begin{aligned} \{001\}_\theta &\parallel \{211\}_\alpha \\ \langle 100 \rangle_\theta &\parallel \langle 0\bar{1}1 \rangle_\alpha \end{aligned}$$

The next prominent  $\alpha/\theta$  orientation relationship, also found in tempered martensite, was:

$$\begin{aligned} \{001\}_\theta &\parallel \{\bar{2}\bar{1}5\}_\alpha \\ \langle 100 \rangle_\theta &\text{ within } 2.6^\circ \text{ of } \langle 3\bar{1}1 \rangle_\alpha \\ \langle 010 \rangle_\theta &\text{ within } 2.6^\circ \text{ of } \langle 131 \rangle_\alpha \end{aligned}$$

In upper bainite, the large number of observed  $\alpha_b/\theta$  orientation relationships could all be derived assuming that the cementite precipitates from austenite with the Pitsch (1962)  $\gamma/\theta$  relationship:

$$\begin{aligned} \{001\}_\theta &\parallel \{\bar{2}25\}_\gamma \\ \langle 100 \rangle_\theta &\text{ within } 2.6^\circ \text{ of } \langle \bar{5}5\bar{4} \rangle_\gamma \\ \langle 010 \rangle_\theta &\text{ within } 2.6^\circ \text{ of } \langle \bar{1}\bar{1}0 \rangle_\gamma \end{aligned}$$

The  $\alpha_b/\theta$  relationships can be generated from the  $\gamma/\theta$  relationship by allowing the ferrite to be a variant of the Kurdjumov and Sachs  $\alpha/\gamma$  orientation relationship.

These results have been confirmed and are important in understanding the mechanism of the bainite transformation. They suggest that in lower bainite the carbides precipitate from ferrite which contains an excess of carbon. After all, precisely the same  $\theta/\alpha$  orientations are found during the tempering of martensite.

The  $\theta/\alpha$  orientation relationship found by Isaichev (1947) also occurs in lower bainite (Ohmori, 1971; Huang and Thomas, 1977). Using rational indices, the Isaichev relationship can be expressed as follows:

$$\begin{aligned} \langle 010 \rangle_\theta &\parallel \langle 1\bar{1}\bar{1} \rangle_\alpha \\ \{103\}_\theta &\parallel \{101\}_\alpha \end{aligned} \quad (3.4)$$

The Isaichev orientation relationship is close to that of Bagaryatskii making them difficult to distinguish using conventional electron diffraction. Accurate measurements on tempered martensite have repeatedly identified the Isaichev orientation relationship and this has led to the suggestion that the Bagaryatskii orientation does not exist (Zhang and Kelly, 1998).

### 3.4.2 The Habit Plane of Cementite

Using single surface trace analysis, Shackleton and Kelly showed that for the tempering orientation relationship, the habit plane of cementite in lower bainitic ferrite is in the vicinity of the zone containing  $\{1\bar{1}2\}_\alpha$  and  $\{0\bar{1}1\}_\alpha$ , corresponding to  $\{101\}_\theta$  and  $\{100\}_\theta$  respectively. The results are vague because of the irregular shape of the cementite particles and inaccuracies in the technique used. The long dimension of the cementite laths was found to be approximately  $\langle 1\bar{1}\bar{1}\rangle_\alpha$ , corresponding to  $\langle 010\rangle_\theta$ . Note that for these data, the crystallographic indices have justifiably been quoted with respect to both the  $\alpha$  and  $\theta$  lattices since some of the trace analyses were carried out using diffraction information obtained simultaneously from both lattices. The results are consistent with the habit plane of cementite containing the direction of maximum coherency between the ferrite and cementite lattices, i.e.  $\langle 010\rangle_\theta \parallel \langle 1\bar{1}\bar{1}\rangle_\alpha$  (Andrews, 1963).

For some alloys, the observation of streaks in electron diffraction patterns has been interpreted to indicate a cementite habit of  $\{001\}_\theta \parallel \{211\}_\alpha$  (Srinivasan and Wayman, 1968a). However, similar streaking has been observed for a cementite habit plane close to  $\{201\}_\theta$ . It is likely that the streaking is due to faulting on the  $\{001\}_\theta$  planes (Ohmori et al., 1971).

In upper bainite, the carbides precipitate from austenite and hence do not exhibit a consistent set of habit plane indices relative to ferrite. Relative to cementite the habit is close to  $\{101\}_\theta$  with a long direction near  $\langle 010\rangle_\theta$  (Shackleton and Kelly, 1965).

### 3.4.3 Three-Phase Crystallography

Crystallographic information can be interpreted in depth if the data are obtained *simultaneously* from austenite, ferrite and cementite. The first such experiments were reported by Srinivasan and Wayman (1968c,a) and subsequent contradictory data were given by Bhadeshia (1980). The two sets of data using *rational* indices as approximations to the measurements are as follows:

(Srinivasan and Wayman, 1968c,a)

$$\begin{aligned} [111]_\gamma &\parallel [011]_\alpha \parallel [100]_\theta \\ [\bar{1}01]_\gamma &\parallel [\bar{1}\bar{1}1]_\alpha \parallel [010]_\theta \\ [1\bar{2}1]_\gamma &\parallel [2\bar{1}1]_\alpha \parallel [001]_\theta \end{aligned}$$

(Bhadeshia, 1980)

$$\begin{aligned} [111]_\gamma &\parallel [011]_\alpha \\ [0\bar{1}1]_\gamma &\parallel [\bar{1}\bar{1}1]_\alpha \\ [0\bar{1}1]_\alpha &\parallel [100]_\theta \\ [1\bar{1}\bar{1}]_\alpha &\parallel [010]_\theta \\ [211]_\alpha &\parallel [001]_\theta \end{aligned}$$

For the first set of data, the habit plane of the cementite within the lower bainitic ferrite is found to be  $(1\ 1\ 2)_\alpha$ , corresponding to  $(1\ 0\ 1)_\gamma$ . Srinivasan and Wayman noted that this coincides with the presumed lattice-invariant deformation of lower bainite, implying that this somehow explains the single crystallographic variant of cementite in lower bainite, as compared with the many found when martensite is tempered. When the lattice-invariant deformation is slip, as is the case for bainite, it is incredibly difficult to establish any microstructural evidence in its support, although Ohmori (1989) has claimed that the cementite traces in lower bainite can often be seen to be parallel to the traces of transformation twins in adjacent and approximately parallel plates of martensite. Srinivasan and Wayman interpreted the presence of the carbide on the appropriate planes to lend support to the proposed mode of lattice invariant deformation in bainite. It was pointed out that the results may not be generally applicable, because they found that for a Fe-3.32Cr-0.66C wt% alloy the cementite habit plane seemed to be  $\{0\ 0\ 1\}_\theta$  unlike the case for the richly alloyed sample.

Unfortunately, the second set of data above (Bhadeshia, 1980) is not in agreement with the Srinivasan and Wayman hypothesis, and they noted themselves that the cementite habit plane in another Fe-Cr-C alloy containing less chromium and carbon was  $(0\ 0\ 1)_\theta$  rather than  $(0\ 1\ 0)_\theta$ . Thus, although the lattice-invariant deformation may be linked to the nucleation of cementite under some circumstances, it does not provide a consistent explanation in others. It also does not explain why multiple variants of carbides are observed in martensites.

#### 3.4.4 Interphase Precipitation

An alternative view is that the cementite of lower bainite nucleates and grows at the austenite-ferrite interface, a process which is well established in the high temperature precipitation of carbides and is described as *interphase precipitation* (Honeycombe and Pickering, 1972). The carbon that is necessary to sustain the growth of cementite can be absorbed from the adjacent austenite and it is then not necessary for the ferrite to be supersaturated. It is argued that during nucleation, the cementite should adopt an orientation which provides good lattice matching with *both*  $\alpha$  and  $\gamma$ . If it happens to be the case that there is only one orientation in space which allows good matching with both the adjacent phases, then the theory indicates that only one crystallographic variant of cementite should precipitate for a given variant of ferrite.

It seems intuitively reasonable that a particle at the transformation interface should attempt to lattice match simultaneously with both the adjacent phases. However, the experimental evidence quoted in support of the model (Honeycombe, 1984a) is inadequate. For example, during the interphase precipitation of  $M_{23}C_6$  in chromium-rich steels, the carbide (which has a face-centred cubic lattice) adopts a cube-cube orientation with the austenite, and a Kurdjumov-Sachs orientation with the ferrite. However,  $M_{23}C_6$  in austenite always precipitates in a cube-cube orientation with austenite, even in the absence of any ferrite. Suppose that the carbide precipitates in austenite, and that the austenite then transforms to ferrite, then it follows that the ferrite is likely to adopt a rational Kurdjumov-Sachs type orientation with the austenite, and *consequently* with the  $M_{23}C_6$ , the final three-phase crystallography having nothing to do with simultaneous lattice matching between all three phases.

During interphase precipitation, the  $M_{23}C_6$  could be completely oblivious of the ferrite, even though it may be in contact with the phase, but the good three-phase crystallography would nevertheless follow simply because the  $M_{23}C_6$  has a cube-cube orientation with the

austenite. To test unambiguously, the theory requires a system where the particles which form at the interphase interface are able to adopt many different variants of an orientation relation with the austenite. It is suggested that interphase precipitation of  $\text{Mo}_2\text{C}$  is an example suitable for further work.

Given a Bagaryatskii orientation relationship between lower bainitic ferrite and its internal cementite particles, and a Kurdjumov-Sachs orientation relationship between the ferrite and austenite, it can be shown (Bhadeshia, 1980a) that the three phase crystallography expected on the basis of the lattice matching arguments is:

$$\begin{aligned} [1\ 0\ 0]_\theta &\parallel [0\ \bar{1}\ 1]_\alpha \parallel [1\ 1\ 1]_\gamma \\ [0\ 1\ 0]_\theta &\parallel [1\ \bar{1}\ \bar{1}]_\alpha \parallel [\bar{1}\ 0\ 1]_\gamma \end{aligned}$$

The experimental data for lower bainite are inconsistent with these orientation relations, the cementite failing to lattice match with the austenite. This conclusion remains if the  $\alpha/\gamma$  orientation relationship is of the Nishiyama-Wasserman type.

There is another way of verifying this conclusion. Aaronson et al. (1978) have modelled the growth of cementite which nucleates at the  $\alpha/\gamma$  interface. In this model, the penetration of the cementite into the adjacent ferrite or austenite is determined by the rate at which either of these phases transforms into cementite. The growth of the cementite is treated in terms of a one-dimensional diffusion-controlled growth process. With the Zener approximation of a linear concentration gradient in the parent phase, the penetrations of cementite in ferrite ( $G_\alpha$ ) and in austenite ( $G_\gamma$ ) are given by:

$$G_\alpha \simeq \frac{1}{2} \left( \frac{D_\alpha}{t} \right)^{\frac{1}{2}} \frac{(\bar{c}^\alpha - c^{\alpha\theta})}{[2(c^{\theta\alpha} - c^{\alpha\theta})(c^{\theta\alpha} - \bar{c})]^{\frac{1}{2}}} \quad (3.5)$$

$$G_\gamma \simeq \frac{1}{2} \left( \frac{D_\gamma}{t} \right)^{\frac{1}{2}} \frac{(\bar{c}^\gamma - c^{\gamma\theta})}{[2(c^{\theta\gamma} - c^{\gamma\theta})(c^{\theta\gamma} - \bar{c})]^{\frac{1}{2}}} \quad (3.6)$$

where  $D_\alpha$  is the diffusivity of carbon in ferrite,  $\bar{c}$  is the average carbon concentration in the parent phase ( $\alpha$  or  $\gamma$ ),  $c^{\theta\theta}$  represents the concentration of carbon in the austenite which is in equilibrium with cementite and  $t$  represents the time after the nucleation event. If it is assumed that  $c^{\theta\alpha}$  and  $c^{\theta\gamma}$  are much greater than  $\bar{c}$ ,  $c^{\alpha\theta}$  or  $c^{\gamma\theta}$ , the ratio of growth rates is given by:

$$\frac{G_\alpha}{G_\gamma} = \frac{D_\alpha^{\frac{1}{2}}(\bar{c}^\alpha - c^{\alpha\theta})}{D_\gamma^{\frac{1}{2}}(\bar{c}^\gamma - c^{\gamma\theta})} \quad (3.7)$$

Note that the left hand side of this equation could be replaced by the corresponding ratio of particle dimensions in the two parent phases. A further assumption was made that the carbon concentrations of the austenite and ferrite before the onset of cementite formation are given by  $c^{\gamma\alpha}$  and  $c^{\alpha\gamma}$  respectively. This in turn implies a number of further assumptions which are not consistent with experimental data: that carbide formation does not begin until the formation of all bainitic ferrite is complete, that there is no supersaturation of carbon in the bainitic ferrite and that the bainite transformation does not obey the incomplete-reaction phenomenon.

On the basis of these assumptions, the cementite in bainite essentially grows by drawing on the richer reservoir of carbon in the austenite, and should therefore penetrate to a far greater extent into the austenite than into the ferrite. Contrary to this conclusion, direct observations prove that in the rare cases where a cementite particle in lower bainite happens

to be in contact with the transformation interface, the cementite is confined to the ferrite (Bhadeshia, 1980).

Aaronson et al. (1978) also concluded that since the model predicts that the interphase growth of cementite occurs into both bainitic ferrite and austenite, the debate about whether the carbides nucleate in  $\alpha$  or  $\gamma$  is irrelevant. This is not justified because it assumes that the carbides nucleate at the interphase interface, whereas it is more likely that the carbides which precipitate within the lower bainitic ferrite nucleate and grow from the supersaturated bainitic ferrite.

### 3.4.5 Relief of Strain Energy

The occurrence of a single crystallographic variant of carbide in lower bainite clearly cannot be explained in terms of the interphase precipitation model or the lattice-invariant shear arguments. It is likely that the variant which forms is one that is best suited towards the relief of elastic strains associated with the austenite to lower bainite transformation (Bhadeshia, 1980; Chang et al., 2004). The observation that carbide precipitation modifies the surface relief of lower bainite supports this conclusion, particularly since freshly formed plates, apparently without carbide precipitation, exhibit perfect invariant-plane strain relief (Clark and Wayman, 1970).

If this explanation is accepted, then it begs the question as to why multiple variants of carbides occur during the tempering of martensite. However, an examination of a large number of published micrographs shows that even in tempered martensite, there is usually one dominant variant and in many cases, just one variant of carbide present. Examples can be found in standard textbooks such as that by Honeycombe (1981, Fig. 83), or in research articles (Speich, 1987; Liu and Luo, 2006).

Further discussion of the multiple carbide variants and the role of stress in variant selection can be found in Chapter 8.

### 3.4.6 Epsilon-Carbide

The orientation relationship between  $\varepsilon$ -carbide in tempered martensite was deduced by Jack (1950, 1951) as:

$$(1\ 0\ 1)_\alpha \parallel (1\ 0\ \bar{1}\ 1)_\varepsilon$$

$$(2\ \bar{1}\ 1)_\alpha \parallel (1\ 0\ \bar{1}\ 0)_\varepsilon$$

$$(0\ 1\ 1)_\alpha \parallel (0\ 0\ 0\ 1)_\varepsilon$$

$$(\bar{1}\ \bar{1}\ 1)_\alpha \parallel (1\ \bar{2}\ 1\ 0)_\varepsilon$$

which also implies that:

$$(1\ 0\ 1)_\alpha \simeq 1.37^\circ \text{ from } (1\ 0\ \bar{1}\ 1)_\varepsilon$$

$$[1\ 0\ 0]_\alpha \simeq 5^\circ \text{ from } [1\ 1\ \bar{2}\ 0]_\varepsilon$$

The very same orientation relationship is also found for  $\varepsilon$ -carbide in lower bainite (Huang and Thomas, 1977). The carbide is in the form of plates which are approximately 6-20 nm thick and 70-400 nm long and possess a ragged interface with the matrix. Single-surface trace analysis suggests that on average the particles grow along  $\langle 1\ 0\ 0 \rangle_\alpha$  directions on  $\{0\ 0\ 1\}_\alpha$  habit planes (Lai, 1975).

It has been suggested by Huang and Thomas that  $\varepsilon$ -carbide precipitates at the austenite/bainite interface, because its orientation with the ferrite can be generated by assuming a Kurdjumov-Sachs  $\alpha/\gamma$  orientation, and an  $\varepsilon/\gamma$  relationship in which

$$\begin{aligned} (111)_\gamma &\parallel (0001)_\varepsilon \\ (1\bar{1}0)_\gamma &\parallel (1\bar{2}10)_\varepsilon \end{aligned} \quad (3.8)$$

However, the three phase crystallography is not unique and hence does not explain the observed single variant of carbide in lower bainite.

During the prolonged ageing of bainite, Sandvik (1982a) found that small regions of austenite retained within bainite sheaves transform into  $\varepsilon$  carbide, with the three-phase crystallography described by Huang and Thomas. The observed  $\varepsilon$ -carbide habit plane,  $(101)_\alpha \parallel (0001)_\varepsilon$  is different from that claimed by Lai.

The orientation relationship expected between  $\varepsilon$ -carbide and austenite has until recently been a matter of speculation. The carbide has now been found to precipitate directly in austenite in high-carbon cast iron with the orientation relationship stated in equation 3.8 (Gutierrez et al., 1995). The precipitates are in the form of fine, coherent particles homogeneously distributed throughout the austenite and form in at least three variants of the orientation relationship (Fig. 3.10). When the austenite transforms to martensite, only two of these variants adopt the Jack orientation relationship with the martensite.

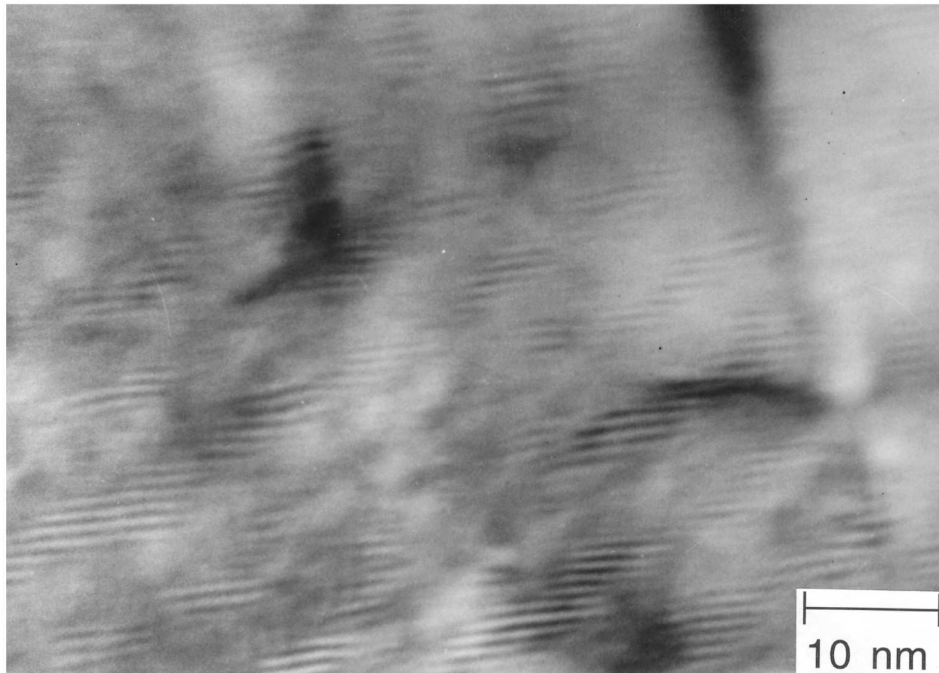


**Figure 3.10** The homogeneous precipitation of  $\varepsilon$ -carbide in austenite (Gutierrez et al., 1995).

### 3.4.7 Eta- and Chi-Carbides

$\eta$ -carbide is a transition  $\text{Fe}_2\text{C}$  carbide in the orthorhombic crystal system. It is usually associated with the tempering of martensite (Hirotzu and Nagakura, 1972; Nagakura et al., 1983) where the martensite/carbide orientation relationship is found to be as follows:

$$\begin{aligned} (1\ 1\ 0)_\eta &\parallel \{0\ 1\ 0\}_\alpha \\ [0\ 0\ 1]_\eta &\parallel \langle 1\ 0\ 0 \rangle_\alpha \end{aligned}$$

The carbide has been observed in lower bainite in grey cast iron, where electron diffraction confirms that (Franetovic et al., 1987a,b):

$$[0\ 0\ 1]_\eta \parallel \langle 1\ 0\ 0 \rangle_\alpha \parallel \langle 0\ \bar{1}\ 1 \rangle_\gamma$$

This information is consistent with the  $\eta$ -carbide/martensite orientation relationship stated earlier and lends further support to the hypothesis that the carbides within lower bainitic ferrite precipitate in a manner analogous to the tempering of martensite.

$\chi$ -Carbide is another transition carbide which is metastable with respect to cementite. It is found during the tempering of martensite, where high-resolution electron microscopy has demonstrated that what at first sight appears to be faulted cementite in fact consists of interpenetrating layers of cementite and  $\chi$ , described as *microsyntactic intergrowth* (Nagakura et al., 1981; Nakamura et al., 1985). The  $\{2\ 0\ 0\}_\chi$  planes are found to be parallel to the  $\{0\ 0\ 1\}_\theta$  planes of different spacing (0.57 and 0.67 nm respectively). Thus, the faults in the cementite really correspond to regions of  $\chi$ , each a few interplanar spacings thick, and this intimate mixture of cementite and  $\chi$  consequently has a nonstoichiometric overall composition expressed by  $\text{Fe}_{2n+1}\text{C}_n$ , where  $n \geq 3$ . Hägg carbide ( $\text{Fe}_5\text{C}_2$ ) and intergrowth with cementite has also been demonstrated (Ghosh et al., 1999; Ghosh and Olson, 2002).

Similar observations have been reported by Ohmori (1986), but for cementite in both tempered martensite and lower bainite, in a Fe-0.7C wt% steel (Fig. 3.11). In both cases, high-resolution electron microscopy (HREM) revealed that the cementite particles contained regions of  $\chi$ -carbide, lending yet more support to the analogy between tempered martensite and lower bainite. This is consistent with Ohmori's observation that cementite in bainitic ferrite increases in size during transformation, as if growing from carbon supersaturated ferrite.

Ohmori (1986) has also claimed that the mechanism of precipitation in the lower bainite was different from that in tempered martensite, on the grounds that the cementite in the lower bainite contained a smaller amount of  $\chi$ -carbide. A difficulty with this conclusion is that the amount of material examined in an HREM experiment is so small that it is unlikely to be representative. The heat-treatments utilised in producing lower bainite and martensite are also different making valid comparisons difficult.

Direct observations on martensite tempering, by Nakamura et al. (1985), indicate that the mechanism by which the mixed  $\chi$ /cementite particles are replaced by cementite can be complicated and site dependent. One of the cementite layers in the mixed particle tends to grow into the surrounding matrix, at the expense of the mixed particle which dissolves. This dissolution is found to occur more rapidly for mixed particles which happen to be located at grain boundaries, presumably because such boundaries provide easy diffusion paths.

It is interesting that the mechanism involves the dissolution of both the cementite and  $\chi$  in the mixed particles. This might be expected if it is assumed that the original particle forms by displacive transformation; the accompanying strain energy could then provide

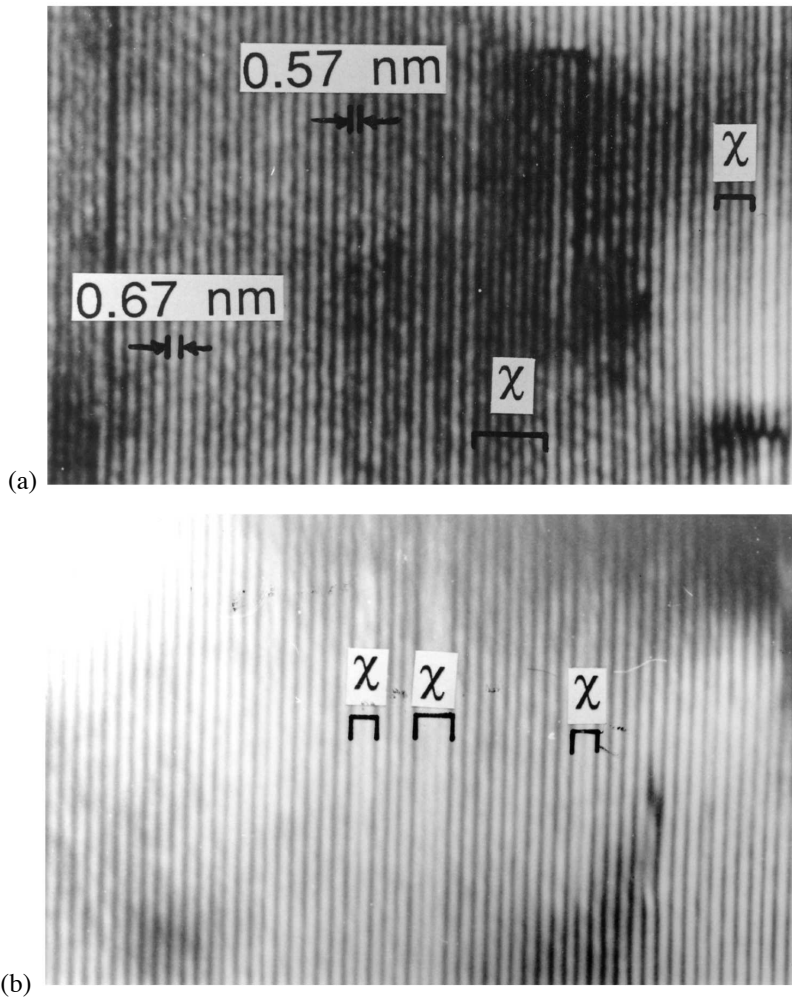


**Figure 3.11** Lattice resolution transmission electron micrographs showing the intergrowth of layers of cementite and  $\chi$ -carbide (Ohmori, 1986). (a) Carbide particle which precipitated in lower bainitic ferrite; (b) carbide particle formed during the tempering of martensite.

the driving force for its replacement by more globular cementite particles forming by reconstructive growth. Also, the boundaries between the  $\chi$  and cementite layers are coherent and would not be expected to be very mobile, in which case, the cementite layers would be kinetically hindered from growing into the adjacent  $\chi$  layers.

### 3.5 Chemical Composition of Bainitic Carbides

It has long been established, using magnetic, chemical and X-ray methods on extracted carbides, that the cementite associated with upper bainite has a substitutional solute content which is close to, or slightly higher than that of the steel as a whole. This is not expected from considerations of chemical equilibrium [see for example, (Hultgren, 1947, 1953)].

Tsivinsky et al. (1955) reported that chromium and tungsten partitioned from austenite into cementite during the growth of pearlite, but not during that of bainite. Chance and Ridley (1981) found that for upper bainite in a Fe-0.81C-1.41Cr wt% alloy, the partition coefficient  $k_{Cr}$ , defined as (wt% Cr in  $\theta$ )/(wt% Cr in  $\alpha$ ) could not be distinguished from unity (Fig. 3.12). Chance and Ridley suggested that partitioning occurs during the pearlite reaction but at the same temperature does not occur with bainite because there is a fast diffusion path along the incoherent interface for pearlite.

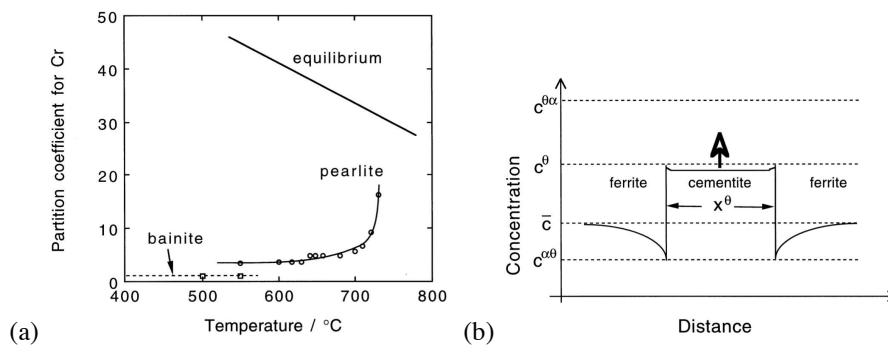


**Figure 3.12** (a) The partition coefficient for chromium in cementite, when the cementite is a part of bainite or pearlite, together with equilibrium data (Chance and Ridley, 1981). The partition coefficient is the ratio of the concentration in cementite to that in the ferrite. (b) The concentration profile that develops during the enrichment of a cementite particle.

These and other results provide compelling evidence that the carbides which form during the bainite reaction or indeed during the tempering of martensite grow by a displacive mechanism. Such a mechanism must naturally involve the diffusion of carbon, but not of substitutional solutes or iron atoms. It is particularly interesting that the precipitation of cementite from martensite or lower bainite can occur under conditions where the diffusion rates of iron and substitutional atoms are incredibly small compared with the rate of precipitation (Figure 2.13). The long-range diffusion of carbon atoms is of course necessary, but because of its interstitial character, substantial diffusion of carbon remains possible even at temperatures as low as  $-60^{\circ}\text{C}$ . The Fe/X ratio thus remains constant everywhere and, subject to that constraint, the carbon achieves equality of chemical potential; the cementite is then said to grow by *paraequilibrium* transformation.

High-resolution evidence supporting carbide growth by paraequilibrium displacive transformation has been published by Sandvik (1982b), Nakamura and Nagakura (1986) and

Taylor et al. (1989a,b). In recent work it has been confirmed that the initial composition of the cementite precipitated during the tempering of martensite is not affected by the heterogeneous nucleation site, whether that is at plate boundaries or within the plates themselves (Thomson and Miller, 1995; Ghosh et al., 1999).

In a remarkable experiment, Babu et al. (1993) have shown using the atom-probe technique that the cementite obtained by tempering martensite is forced to inherit the silicon concentration of the martensite. They did not find any redistribution of substitutional solutes even on the finest conceivable scale; the atom-probe technique has single atom resolution for both chemical and spatial analysis (Fig. 3.13). The results rule out the possibility of local equilibrium at the interface and conclusively establish the paraequilibrium mode of cementite precipitation. The fact that silicon is trapped by cementite is important given that its equilibrium solubility in cementite is virtually zero. It follows from this that the trapped species such as Si must partition with prolonged heat treatment and this is precisely what is observed experimentally (Babu et al., 1993). These conclusions are supported by atom-probe experiments on lower bainite in bearing steels, where both  $\varepsilon$  and  $\theta$  precipitation occurs at 260 °C without the partitioning of substitutional solutes (Song et al., 2013).<sup>4</sup>

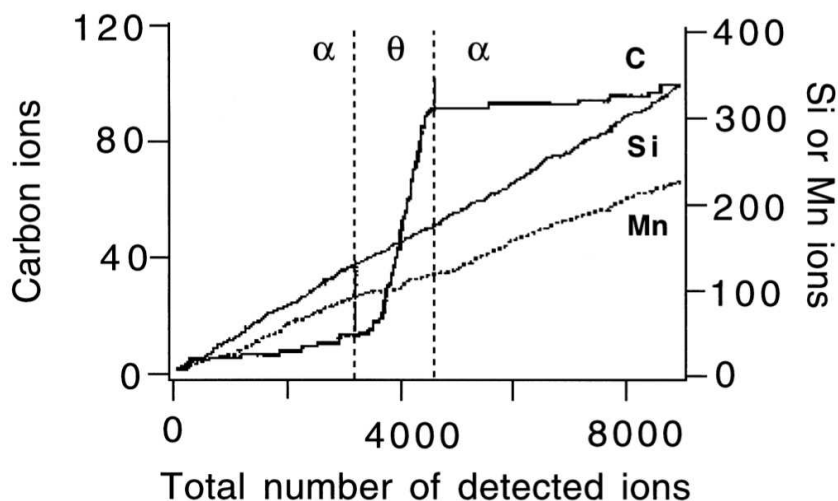


**Figure 3.13** The results of an atomic resolution chemical analysis experiment across a pair of ferrite/cementite ( $\alpha/\theta$ ) interfaces. Any changes in composition are represented by a change in the slope. It is evident that there is no partitioning of silicon or manganese when cementite precipitates from martensite. The alloy used has the chemical composition Fe-1.84C-3.84Si-2.95Mn at%, and was tempered at 350 °C for 30 min (Babu et al., 1993).

To summarise, substitutional solute atoms are trapped in the cementite when the latter precipitates in bainite or martensite. That is, the cementite forms by a paraequilibrium transformation mechanism. In silicon-containing steels the free energy change associated with the paraequilibrium precipitation of cementite must be much smaller than when the

<sup>4</sup>These authors also reported that cementite generated at 500 °C grows by the negligible-partitioning local equilibrium mechanism (section 2.3.1), but the measured data have not been shown to be consistent with NP-LE mechanism.

cementite is free of silicon. It is probable that this is what leads to suppression of cementite in high-silicon bainitic or martensitic steels.

The discussion here has focussed on cementite which is the carbide that has been investigated the most. However, the conclusions about the mechanism of transformation are likely to apply to the other iron-based carbides which form at low temperatures. The iron/substitutional atom ratio in  $\epsilon$ -carbide is known to be identical to that of the martensite from which it precipitates (Barnard et al., 1981b).

Naturally, if the carbides that form initially by a paraequilibrium mechanism are subsequently tempered then equilibrium will encourage solutes to partition between the ferrite and carbide. This effect is most pronounced for silicon given that its solubility in either cementite or  $\epsilon$ -carbide is negligible. Atom-probe data to this effect are illustrated in Fig. 3.14, showing the tendency for silicon to migrate from the carbide into the adjacent ferrite during tempering. Other solutes also redistribute, for example manganese and chromium partition from the ferrite into the cementite (Caballero et al., 2008c).

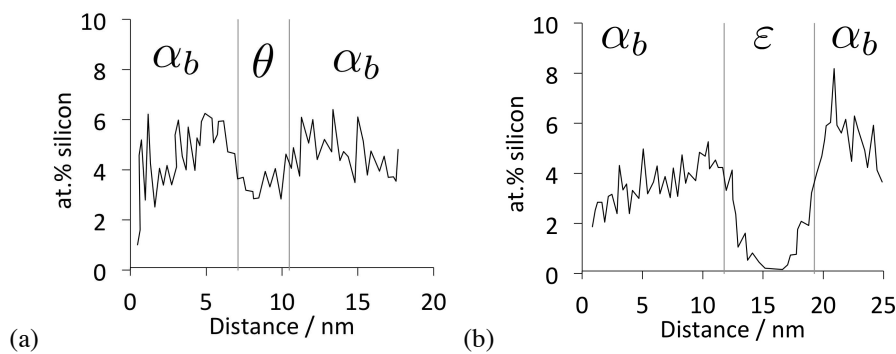


**Figure 3.14** Atom-probe analyses of Fe-0.98C-1.46Si-1.89Mn-0.26Mo-1.26Cr-0.09V wt%, transformed into bainite at 200 °C, and then tempered at (a) 400 °C, 30 min, (b) 450 °C, 30 min. Adapted from Caballero et al. (2008c).

The response of carbides to a stress applied during the precipitation process can reveal further information about their mechanism of formation; this will be discussed in Chapter 8.

### 3.6 Summary

The growth of upper bainite leads to the partitioning of carbon into the residual austenite. If the transformation conditions render the austenite thermodynamically unstable with respect to carbide precipitation, then it eventually decomposes by the formation of cementite and more ferrite. In some alloys, cementite formation is preceded by that of transition iron-carbides such as  $\kappa$  or  $\chi$ . In lower bainite, some of the carbon precipitates from supersaturated ferrite and a portion is partitioned into the remaining austenite. The quantity of carbides that precipitate from the austenite is therefore smaller when compared with upper bainite. Every carbide precipitation reaction that is found in tempered martensite has also been observed in lower bainite with precisely identical crystallographic and morphological characteristics. The very presence of transition carbides is indicative of a carbon-supersaturated bainitic ferrite.

One difference with tempered martensite can be that the carbide particles in any given lower bainitic plate tend to precipitate in a single crystallographic orientation whereas the tempering of martensite usually leads to many crystallographic variants. This is because the self-stress of a lower bainite plate favours precipitation of a particular carbide variant, and this effect is prominent in bainite where the driving force for carbide precipitation is smaller than that associated with the tempering of martensite.

The carbide precipitation reactions for both upper and lower bainite are secondary events which occur after the growth of bainitic ferrite. In some alloys, especially those containing large concentrations of silicon or aluminium, the carbide precipitation reaction can be so sluggish that for practical purposes, the bainite consists of a mixture of only bainitic ferrite and carbon-enriched residual austenite.

The mobility of atoms over the range of temperatures within which bainite grows is extraordinarily small. This and other observations suggest that the carbides grow by a displacive mechanism in which only the interstitial elements diffuse. This is consistent with the absence of any change in substitutional solute content when bainitic carbides precipitate, and with the crystallography of carbide precipitation.

## CHAPTER 4

---

# TEMPERING OF BAINITE

---

### 4.1 Introduction

Tempering is a term historically associated with the heat treatment of martensite in steels. It describes how the microstructure and mechanical properties change as the metastable sample is held isothermally at a temperature where austenite cannot form. The changes during the tempering of martensite can be categorised into stages. During the first stage, excess carbon in solid solution segregates to defects or forms clusters within the solid solution. It then precipitates, either as cementite in low-carbon steels, or as transition iron-carbides in high-carbon alloys. The carbon concentration that remains in solid solution may be quite large if the precipitate is a transition carbide. Further annealing leads to stage 2, in which almost all of the excess carbon is precipitated, and the carbides convert into more stable cementite. Any retained austenite may decompose during this stage. Continued tempering then leads to the spheroidisation of carbides, extensive recovery of the dislocation structure, and finally to the recrystallisation of the ferrite plates into equiaxed grains.

The description presented above is idealised. Many of the reactions ascribed to stage 1 can occur *during* the formation of the martensite when the martensite-start temperature is high, a phenomenon known as *autotempering*. Bainite forms at even higher temperatures so autotempering becomes an unavoidable part of the transformation. The redistribution of carbon from supersaturated ferrite into the residual austenite, and the precipitation of carbides during the bainite reaction, occur rapidly and are genuine autotempering effects (Fig. 4.1). The purpose of this Chapter is to deal primarily with the tempering effects

which occur when a bainitic microstructure is reheated; the *in situ* tempering phenomena are described elsewhere in the text.

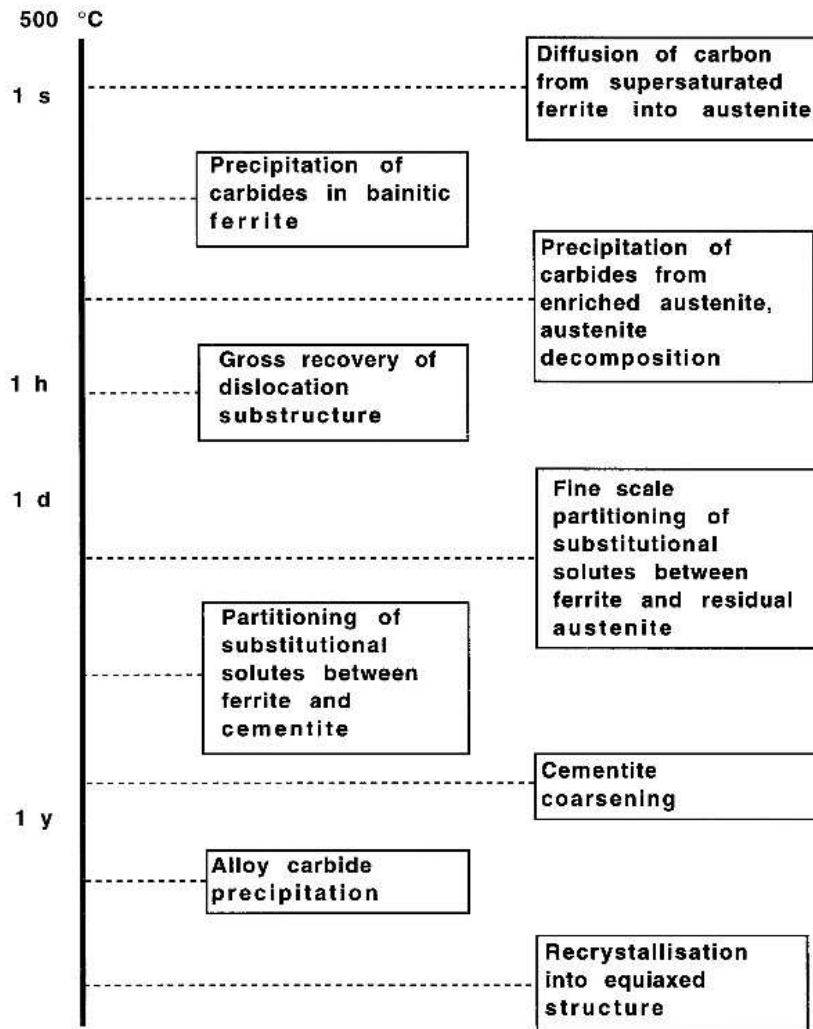


**Figure 4.1** The time scales associated with a variety of tempering phenomena for bainite.

The rate of change of the microstructure and properties during tempering is expected to scale with the degree to which the virgin sample deviates from equilibrium. Bearing this in mind, there are a number of essential differences between the tempering behaviour of bainite and that of martensite.

Bainitic ferrite contains less carbon in solid solution since much of it is precipitated as cementite particles which are coarse when compared with tempered martensitic microstructures. Secondary hardening reactions in alloy steels with a bainitic microstructure are slower than with martensite, because the coarser cementite particles take longer to dis-

solve (Woodhead and Quarrell, 1965). Secondary hardening involves the replacement of metastable cementite with substitutional-solute rich alloy carbides.

When compared with martensite, bainite grows at relatively high temperatures where the microstructure undergoes recovery during transformation. The extent of this recovery is larger than would be associated with autotempered martensite. Consequently, when low-carbon steel bainitic microstructures are annealed at temperatures as high as 700°C (1 h), there is only a slight increase in recovery, and little change in the morphology of the ferrite platelets or the number density of the carbide particles (Irvine et al., 1957b; Bush and Kelly, 1971).

Rapid softening occurs only when the plates of ferrite change into equiaxed ferrite. Whether this change is due simply to grain growth or to recrystallisation has not been investigated. In the former case it is the excess surface energy which constitutes the driving force, whereas during recrystallisation, it is the stored energy due to defects such as dislocations or due to elastic strains in the lattice which provides the major component of the driving force for the reaction. During the change to a more equiaxed microstructure, the cementite spheroidises and coarsens considerably. Continued tempering then causes much smaller changes in hardness with time.

In marked contrast with martensitic steels, small variations in the carbon concentration (0.06-0.14 wt%) have little effect on the bainite tempering curve (Fig. 4.2). Carbon has a potent solid solution strengthening effect. Thus, the strength of martensite drops sharply as the carbon precipitates during tempering. For bainitic microstructures, the carbon is not in solid solution but is precipitated as coarse carbides which contribute little to strength (Irvine et al., 1957a,b). It is expected therefore that the tempering response of bainite is insensitive to the average carbon concentration. Given these differences, it is not surprising that nanoindentation data exhibit much more scatter with martensite than bainite (He et al., 2014) since small variations in the carbon concentration in the martensite will lead to large changes in hardness.

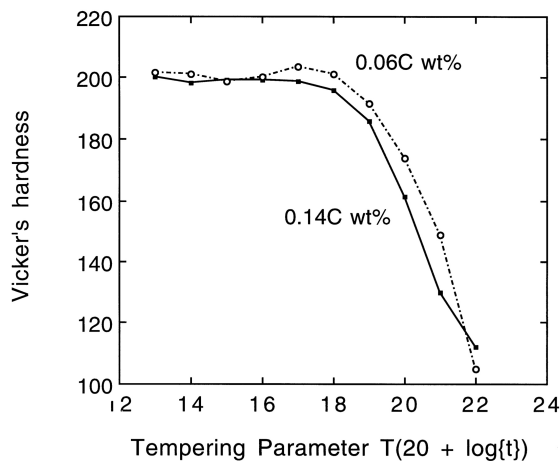


**Figure 4.2** Change in hardness for two bainitic steels containing different carbon concentrations, as a function of a time-temperature tempering parameter (Irvine et al., 1957a). The tempering parameter is defined with the absolute temperature  $T$  and the time  $t$  in hours.

## 4.2 Tempering Kinetics

There are now significant quantitative methods, including commercially available software, for calculating the kinetics of tempering reactions for the purposes of designing alloys or heat-treatments (Robson and Bhadeshia, 1997b,a; Kozeschnik and Buchmayr, 1999; Olson, 2013). Fig. 4.2 illustrates an empirical method of expressing tempering data using a time-temperature parameter, useful because it permits interpolation between experimental data and a method of estimating the effect of anisothermal heat treatments that are common in industrial practice.

The method has its origins in some pioneering work by Hollomon and Jaffe (1945), who proposed that the effectiveness of an isothermal heat treatment should be related to the product:

$$t \exp\{-Q/RT\} \quad (4.1)$$

where  $Q$  is an effective activation energy and the other terms have their usual meanings. The product can be regarded as the integral of the curve of  $\exp\{-Q/RT\}$  versus time. To estimate the period required to achieve the same metallurgical effect at another temperature simply involves the assumption that the product  $t \exp\{-Q/RT\}$ , once evaluated, is constant irrespective of temperature. The product is often called the *kinetic strength* of the heat treatment and provides a rough method for combining the influence of time and temperature. The concept is difficult to justify, especially in circumstances where the driving force varies with temperature or where the mechanism of the metallurgical process alters with temperature. The parameter and many related parameters have nevertheless been useful in cases where rigorous solutions do not exist. Examples include the representation of creep data, weld microstructure calculations (Alberry and Jones, 1977, 1979; Alberry et al., 1983; Ashby and Easterling, 1982; Ashby, 1987), and the rationalisation of martensite tempering data (Hollomon and Jaffe, 1945). Irvine and Pickering have demonstrated its utility in representing the hardness of tempered bainite.

## 4.3 Tempering of Steels Containing Austenite

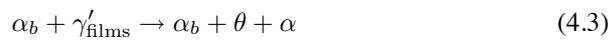
The decomposition of retained austenite during the heat treatment of martensite in quenched steels occurs during the second stage of the tempering process. Appreciable quantities of retained austenite are usually only present in quenched steels which have carbon concentrations in excess of about 0.4 wt%. The conventional wisdom is that the austenite decomposes to bainite but it has been demonstrated that the decomposition occurs instead by a reconstructive mechanism (Kennon and Burgess, 1978). On the other hand, there is clear metallographic evidence that in very high carbon steel (Fe-1.9C-1.5Mn-1.6Si wt%), partially transformed to martensite by cryogenic treatment, the large fraction of untransformed austenite can be induced to form bainite by tempering at 400°C (Barbe et al., 2006). Bainite did not form on tempering at 170°C, but the tempering time was too short (28 h) to permit bainite to form at such a low temperature (Caballero and Bhadeshia, 2004).

In many bainitic steels, the alloy composition is chosen to avoid the retention of austenite. However, large quantities of carbon-enriched austenite ( $\gamma'$ ) can be retained in silicon-rich bainitic steels, in two forms: as thin films between the ferrite plates and as blocks between different sheaves of bainite. Both are enriched in carbon but the films more so because of their isolation between plates of ferrite. The tempering sequence of such  $\alpha_b + \gamma'$  mixtures can be summarised as follows and the experimental evidence for these reactions follows in the subsequent sections:

- Blocky austenite that is large enough to facilitate the development of the cooperative growth of ferrite and cementite, i.e. pearlite, assuming that the temperature is high enough to permit reconstructive diffusion, but low enough to be within the Hultgren extrapolation region so that the austenite is supersaturated with respect to both ferrite and cementite, decomposes as follows:

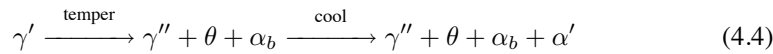


- Under the same circumstances, thin films of austenite tend to decompose into discrete particles of cementite or other carbides, and ferrite in the same orientation as the adjacent bainitic ferrite. The  $\theta$  and  $\alpha$  may not precipitate at the same time:



Because the film austenite is relatively rich in carbon, it is the first to precipitate cementite during tempering. Its volume fraction therefore decreases more rapidly than the blocky austenite, Fig. 4.3. Therefore, although the films of austenite are more stable to deformation-induced martensitic transformation than the coarser regions of austenite (Bhadeshia and Edmonds, 1983b), they are less stable to tempering heat-treatments (Saha Podder and Bhadeshia, 2010; Saha Podder et al., 2011).

When the steel is at a stage where the austenite has not been completely eliminated during tempering, the precipitation of cementite and the resultant depletion of carbon makes the austenite less stable to martensitic transformation if the material is cooled to ambient temperature:



where the amount of austenite is reduced at each stage of the process;  $\gamma''$  refers to austenite that has a composition different from that of  $\gamma'$ . A corollary is that the retained austenite measured at ambient temperature is less than that at the tempering temperature.

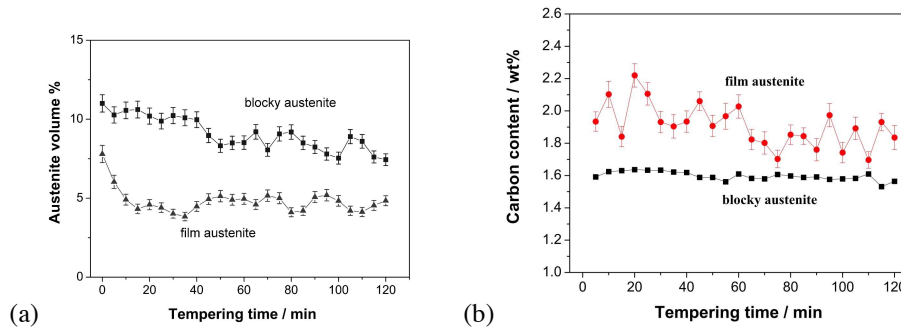


**Figure 4.3** Synchrotron X-ray analysis of Fe-0.39C-4.09Ni-2.05Si wt%, transformed isothermally to a mixture of bainitic ferrite and retained austenite, cooled to ambient temperature and then subjected to isothermal tempering. (a) Change in the amounts of blocky and film-type austenite during tempering at 400 °C; (b) carbon content of retained austenite as a function of tempering time. After Saha Podder et al. (2011).

It is possible to design bainitic steel in which the austenite survives without decomposition during heating to temperatures of 600°C by adding a larger than normal concentration of silicon and aluminium. An example of such an alloy is Fe-1C-2Mn-4Si-0.2Mo-

1.4Al wt%, for which the evolution of retained austenite as a function of temperature during heating at  $5^{\circ}\text{C min}^{-1}$  is shown in Fig. 4.4 (Hulme-Smith et al., 2013b).

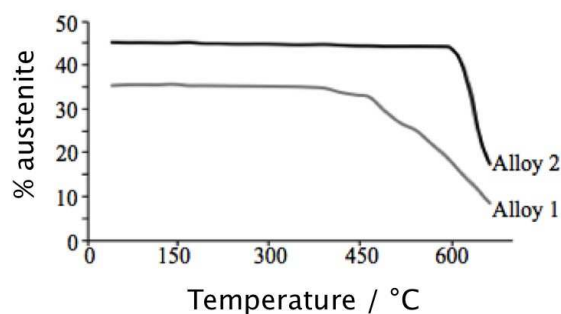


**Figure 4.4** Synchrotron X-ray data showing the amount of retained austenite as a function of temperature during heating. Alloy 1 contains 1.84Si whereas Alloy 2 has 3.89Si-1.43Al (wt%). The detailed compositions are in (Hulme-Smith et al., 2013b).

### 4.3.1 Redistribution of Substitutional Solutes

There is no partitioning of substitutional solutes during the bainite reaction, in spite of the requirements of equilibrium (Chapter 2); it is worth emphasising that the lack of partitioning is complete, in the sense that there is no segregation or desegregation at the  $\alpha_b/\gamma$  interface. However, given the opportunity, the solutes should tend to redistribute in a manner which leads to a reduction in the overall free energy. It is found that when a mixture of bainitic ferrite and austenite is tempered at low temperatures, the solutes partition before the austenite begins to decompose. The partitioning is on a fine scale and can only be detected using atomic resolution techniques. Fig. 4.5 illustrates one such experiment, in which a mixture of bainitic ferrite and austenite was annealed at  $328^{\circ}\text{C}$  for 11 days. There is clear evidence for the diffusion of manganese into the austenite at the interface, with a corresponding depletion zone in the adjacent ferrite. Another case showing partitioning when the bainite is deliberately tempered is illustrated in Fig. 4.6.

Table 4.1 summarises atom-probe data that show that although there is no partitioning at all of substitutional solutes in freshly formed bainite (Chapter 2), tempering does lead to slow changes over limited length scales.

**Table 4.1** Atom-probe data for substitutional solutes following the tempering of mixtures of bainitic ferrite and carbon-enriched retained austenite.

Alloy (wt%)	Heat treatment	Result	Reference
Fe-0.43C-2.24Si-2.82Mn	$T_{\gamma} \rightarrow 328^{\circ}\text{C}$ , 11 days	3 nm region in $\gamma$ at $\gamma/\alpha_b$ interface enriched in Mn	Stark et al. (1990)
Fe-0.98C-1.46Si-1.89Mn-0.26Mo-1.26Cr-0.09V	$T_{\gamma} \rightarrow 200^{\circ}\text{C}$ , 6 days, tempered $400^{\circ}\text{C}$ for 1 h	No movement of substitutional solutes.	Caballero et al. (2008b)
Fe-0.98C-1.46Si-1.89Mn-0.26Mo-1.26Cr-0.09V	$T_{\gamma} \rightarrow 200^{\circ}\text{C}$ , 6 days, tempered $450^{\circ}\text{C}$ for 30 min	Slight enrichment over a distance of 1 nm, of Cr, in vicinity of $\gamma/\alpha_b$ interface. Some $\gamma$ decomposed.	Caballero et al. (2008b)
Fe-0.98C-1.46Si-1.89Mn-0.26Mo-1.26Cr-0.09V	$T_{\gamma} \rightarrow 200^{\circ}\text{C}$ , 6 days, tempered $500^{\circ}\text{C}$ for 30 min	Enrichment of Mn and depletion of Cr and Si in $\theta$ at $\alpha_b/\theta$ interface over a distance less than 20 nm nanometres.	Caballero et al. (2008b)

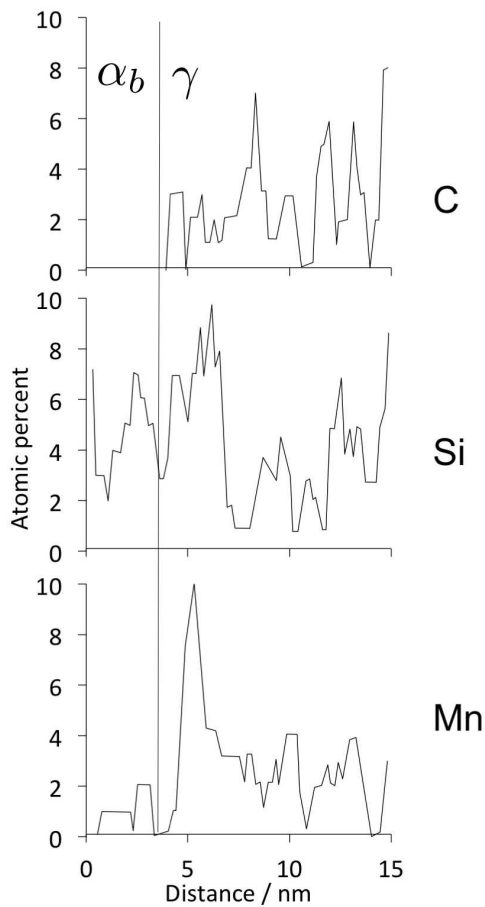


**Figure 4.5** A field ion microscope/atom-probe experiment on an alloy Fe-0.43C-2.24Si-2.82Mn wt%, heat treated at 328 °C for 11 days. This produces a mixture of bainitic ferrite and austenite with the reaction stopping after the first few minutes at temperature, the subsequent holding annealing the microstructure. The position of the  $\alpha_b/\gamma$  is identified to be where significant levels of carbon begin to be detected. (Stark et al., 1990).

#### 4.3.2 Decomposition of Austenite

When the carbon concentration in all the regions of untransformed austenite is larger than or equal to that given by the  $T'_0$  curve, tempering can only induce further transformation by a mechanism involving the diffusion of carbon. The austenite may decompose into a mixture of ferrite and carbides if its carbon concentration exceeds that given by the extrapolated  $\gamma/(\gamma + \text{carbide})$  phase boundary (Fig. 3.1b). The larger regions of austenite form colonies of pearlite with a fine interlamellar spacing, whereas the films of austenite decompose into discrete particles of cementite in a matrix of ferrite (Fig. 4.7). The films are too thin to permit the onset of the cooperative growth needed to establish a pearlite colony. The  $T_c$  (Fig. 3.1b) condition for carbide formation may not be satisfied when tempering at high temperatures, in which case the austenite can transform to ferrite, although not by a bainitic mechanism. Tempering at temperatures which are below  $B_S$  but above the original isothermal transformation temperature can lead to the further transformation of austenite into bainite (Kaputkin et al., 2003).

Tempering need not involve a separate heat-treatment. Microstructural changes can occur when austenite is transformed isothermally to bainite, and then held at the transformation temperature for longer than is necessary to complete the bainite reaction. For

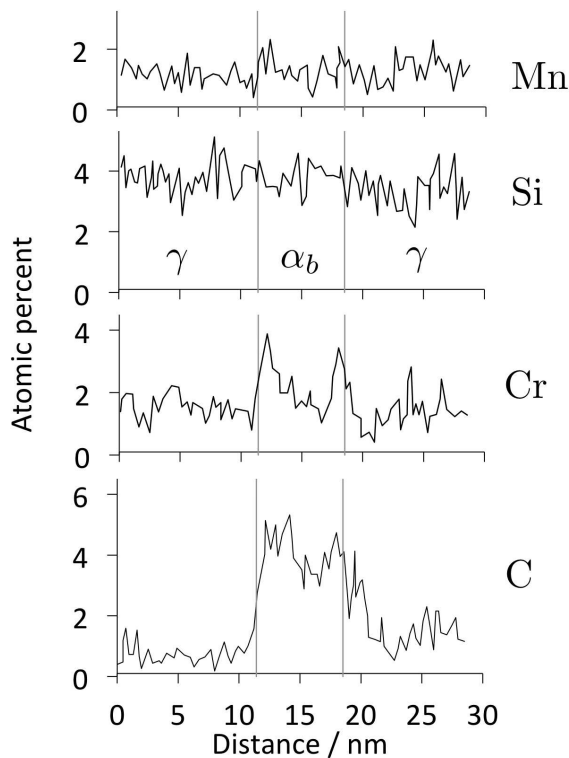


**Figure 4.6** Fe-0.98C-1.46Si-1.89Mn-0.26Mo-1.26Cr-0.09V wt%, transformed and then tempered at 450 °C for 30 min to show the short range diffusion of some of the solutes. The data are collected using an atom-probe. After Caballero et al. (2008c).

example, any residual austenite may decompose slowly as the microstructure attempts to approach equilibrium. There is less bainite and more residual austenite at higher transformation temperatures; this combined with the greater atomic mobility at high temperatures leads to the formation of pearlite colonies following the bainite reaction. Bhadeshia and Edmonds (1979b) reported a case where transformation at a temperature close to  $B_S$  led to the formation of upper bainite within a matter of minutes, to be followed some 30 h later by pearlite; there are numerous similar observations (Jung et al., 1997, e.g.). Fig. 4.8 illustrates, in another alloy, two different reconstructive reactions occurring after the bainite stopped following 30 min at temperature. Continued holding at the isothermal transformation temperature for 43 days led to the decomposition of residual austenite at an incredibly slow rate into two different products (Bhadeshia, 1981a, 1982b). The first of these is alloy pearlite which nucleates at the austenite grain boundaries and develops as a separate transformation. In the other, the original bainite/austenite interfaces move to produce epitaxial growth by a reconstructive mechanism (Fig. 4.8). The interfaces degenerate into a series of irregular perturbations. The ferrite in the perturbations has the same crystallographic orientation as the original bainite – it is in fact contiguous with the bainitic ferrite. It grows with the same substitutional solute content as the parent austenite but does not cause an IPS shape change. It is incredible that the perturbations took 43 days to grow to a length comparable to the thickness of the original bainite plates, which completed transformation in a matter of seconds. Reconstructive growth is bound to be much slower than displacive transformation at low homologous temperatures.

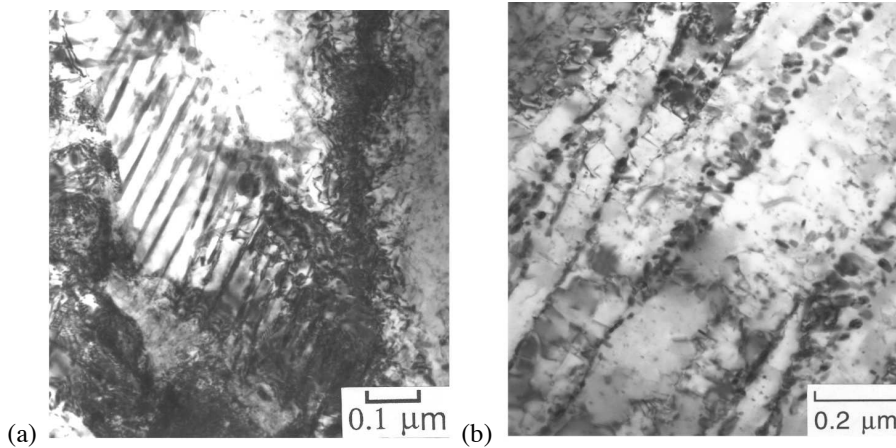


**Figure 4.7** The effect of tempering a mixture of bainitic ferrite and retained austenite, in a Fe-3Mn-2Si-0.4C wt% alloy, at 500 °C for 60 min. The austenite is supersaturated with respect to the precipitation of carbides. (a) The larger blocks of austenite tend to decompose into pearlite. (b) Arrays of discrete carbide particles form between the sub-units of bainitic ferrite when the films of austenite decompose. The microstructure prior to tempering consisted of just bainitic ferrite and residual carbon-enriched austenite.

Similar observations of the epitaxial growth of ferrite and pearlite after the formation of bainite in Fe-Ni-C alloys have been reported by (Ohmori et al., 2001).

### 4.3.3 Tempering of Nanostructured Bainite

Nanostructured bainite consists of an exceptionally fine mixture of bainitic ferrite plates embedded in an equally fine matrix of carbon-enriched retained austenite (Chapter 14). The steels appropriate for the generation of such structures has a high carbon concentration, typically 0.8-1 wt%, and this gives the structure an especially large resistance to tempering. Fig. 4.9a shows that there is at first an increase in hardness, and that the hardness is maintained until the tempering temperature exceeds some 500 °C. This is surprising at first sight because the austenite is expected to decompose into a mixture of ferrite and carbides at lower tempering temperatures.

Suppose the normalised hardness is defined as  $(H - H_{\min}) / (H_{\max} - H_{\min})$ , where  $H$ ,  $H_{\min}$  and  $H_{\max}$  are the hardness, fully softened hardness and hardness before tempering. Fig. 4.9b then permits the comparison of the relative stabilities of the nanostructured bainite and quenched and tempered high-silicon steels. The nanostructured bainite has a far greater resistance to tempering than the tempered martensite, and compares well against the secondary hardening steel.

The decomposition of the austenite leads to the observed initial increase in hardness due to the precipitation of fine cementite; similar results have been reported by Chen et al. (2014). The rich carbon concentration of the austenite ( $\approx 1.2$  wt%) leads to the deposition of a large number density of cementite precipitates precisely at the bainitic ferrite plate boundaries, thus preventing the onset of coarsening or recrystallisation. Fig. 4.10 illustrates the intensity and position of the carbides. Tempering at 730 °C for 7 days does result in a loss of hardness and general coarsening, but the scale of the microstructure remains fine due to the pinning effect of the particles (Fig. 4.10d), and Fig. 4.11 shows that although

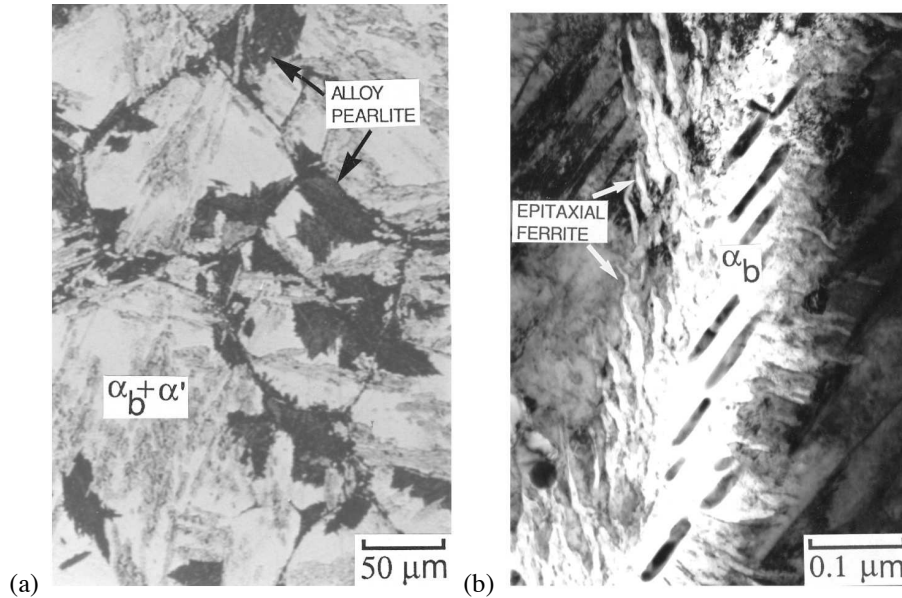


**Figure 4.8** The decomposition of residual austenite once the bainite reaction has stopped. (a) Pearlite colonies; (b) ferrite growing epitaxially from bainite plates. In both cases, the transformation mechanism is reconstructive and does not lead to surface relief.

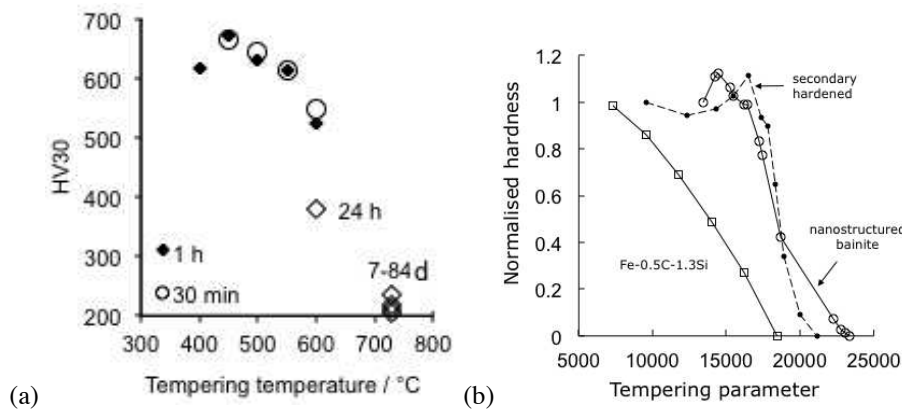


**Figure 4.9** Fe-0.98C-1.46Si-1.89Mn-1.26Cr-0.26Mo-0.09V wt%. (a) Vickers hardness as function of tempering temperature and time; the horizontal line represents virgin microstructure; (b) comparison of temper resistance of nanostructured bainite with that of Fe-0.5C-1.3Si wt% quenched and tempered martensitic steel, and a silicon-rich secondary hardening steel, Fe-0.34C-1.07Si-5.08Cr-1.43Mo-0.92V wt%. The tempering parameter is  $T(20 + \log t)$  where  $T$  is the absolute temperature and  $t$  the tempering time in hours.

there is some precipitation from supersaturated  $\alpha_b$ , the majority comes from the decomposition of the high-carbon retained austenite. Raising the tempering temperature above 730 °C does not help due to the onset of austenite formation (Hasan et al., 2012).

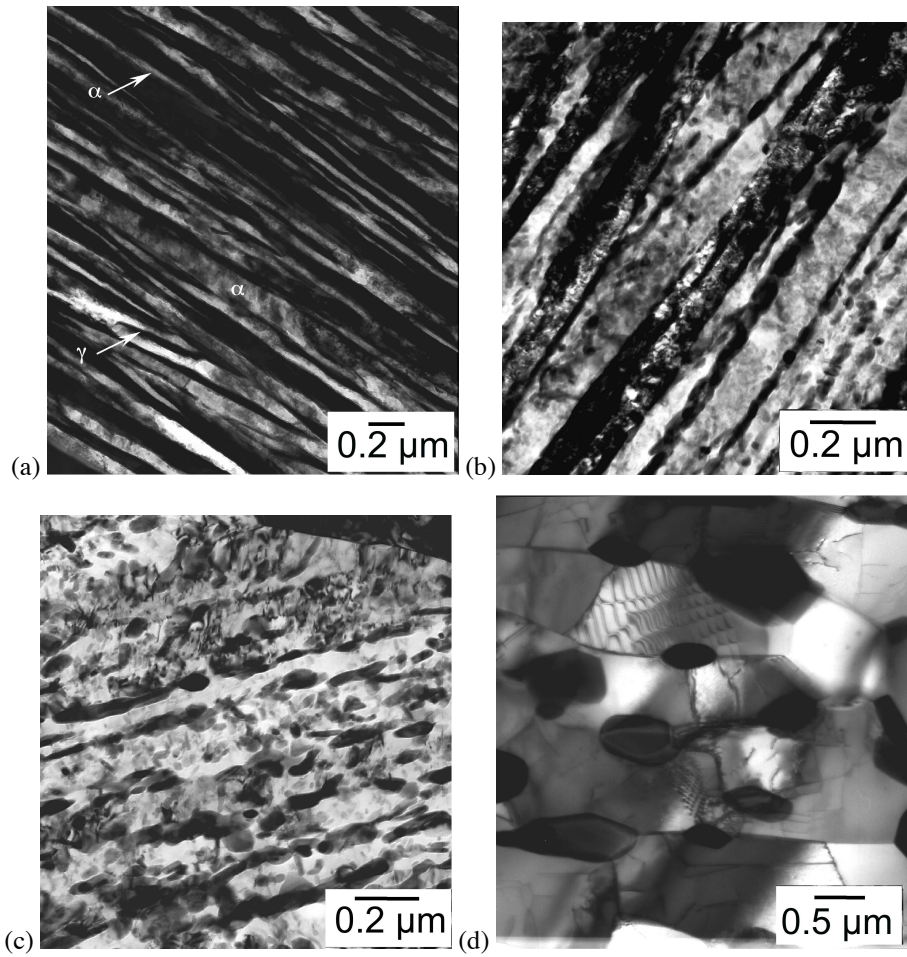


**Figure 4.10** Fe-0.98C-1.46Si-1.89Mn-1.26Cr-0.26Mo-0.09V wt% following transformation to nanostructured bainite and tempering. (a) Untempered. (b) 550 °C, 30 min. (c) 600 °C, 1 h. (d) 730 °C, 7 days, (Garcia-Mateo et al., 2004).

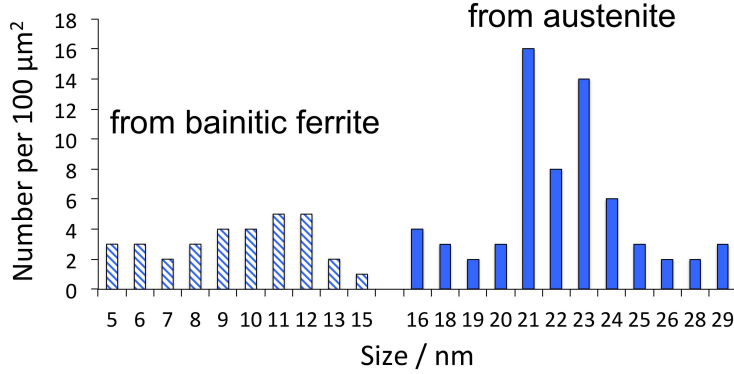


**Figure 4.11** Size distribution of the carbides that precipitate on tempering nanostructured bainite at 475 °C for 60 min. Data from Chen et al. (2014).

#### 4.4 Coarsening of Cementite

Coarsening leads to a minimisation of the energy that is stored in a sample in the form of interfaces. The rate equation for a coarsening process controlled by the diffusion of solute through the matrix is given by (Greenwood, 1956; Lifshitz and Slyozov, 1961; Wagner, 1961):

$$\bar{r}^3 - \bar{r}_o^3 = (8\sigma^{\theta\alpha} x^{\alpha\theta} D_{\text{eff}} V_m^\theta t) / 9RT \quad (4.5)$$

where  $V_m^\theta$  is the molar volume of cementite,  $x^{\alpha\theta}$  is the concentration of carbon in ferrite which is in equilibrium with cementite,  $\bar{r}_3$  is the mean particle radius at time  $t$  and  $\bar{r}_o^3$  is the mean particle radius at time zero, the moment when coarsening is defined to begin.  $\sigma^{\theta\alpha}$  is the cementite-ferrite interface energy per unit area [ $\simeq 690 \text{ J m}^{-2}$ , Li et al. (1966)] and  $D_{\text{eff}}$  is an effective diffusion coefficient for carbon in ferrite. Since there is little change in precipitate volume fraction during coarsening, the diffusion of carbon is coupled to that of iron in such a way that the total volume remains constant.  $D_{\text{eff}}$  is then given by (Li et al., 1966):

$$D_{\text{eff}} = \frac{n_{Fe} D_{Fe}^\alpha D_C^\alpha \Omega_{Fe} [\Omega_{Fe} + (n_C/n_{Fe}) \Omega_C]}{(n_{Fe} D_{Fe}^\alpha \Omega_{Fe}^2) + (n_C D_C^\alpha \Omega_C^2)} \quad (4.6)$$

where  $n_{Fe}$  and  $n_C$  are the numbers of iron or carbon atoms per unit volume of ferrite respectively,  $D_{Fe}^\alpha$  and  $D_C^\alpha$  are the respective diffusivities of iron and carbon in ferrite,  $\Omega_{Fe}$  is the volume per atom of ferrite and  $\Omega_C$  is the volume of a molecule of  $\text{Fe}_3\text{C}$  less  $3\Omega_{Fe}$ . It has been shown that equation 4.5 describes to a fair accuracy, the coarsening kinetics of cementite during the tempering of both upper and lower bainite in a Fe-0.67C-0.73Mn-0.27Si wt% commercial steel (Deep and Williams, 1975). The agreement with theory is best for the higher tempering temperatures, with an underestimation of the coarsening rate at lower temperatures. This discrepancy has been attributed to grain boundary diffusion contributing more to the net flux at low temperatures.

In fact, the microstructures of both tempered martensite and bainite contain two kinds of cementite particles, those located at the lath boundaries and a finer distribution within the laths. In upper bainite the cementite is located only at the lath boundaries. Fig. 4.12 shows experimental data on the coarsening of cementite during the tempering of a medium carbon

steel. The upper bound of each shaded region represents the lath-boundary cementite, the lower bound the intra-lath cementite. The bainitic microstructure is coarse to begin with because of the tempering inherent in the formation of bainite. With martensite the tempering induces the precipitation of cementite, with considerable intra-lath cementite and a larger overall number density of particles. Therefore, the coarsening rate is much larger for martensite; the bainitic microstructure shows greater stability to tempering. A consequence is that the matrix microstructure remains fine over a longer time period for bainite than for martensite.

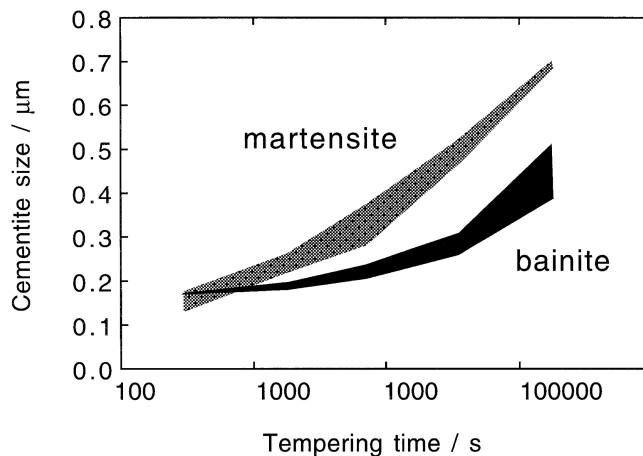


**Figure 4.12** Changes in the size of cementite particles as a function of the tempering time at 700 °C, with different starting microstructures. The upper bound of each shaded region represents the mean size of particles located at lath boundaries. The lower bound corresponds to particles within the laths. The data are for a Fe-0.45C-0.22Si-0.62Mn wt% steel; the bainite was produced by isothermal transformation at 380 °C. After Nam (1999).

A model that deals with the coarsening of cementite under conditions where both grain boundary and lattice diffusion are important has been presented by Venugopalan and Kirkaldy (1977). It takes account of the simultaneous coarsening of carbide particles and ferrite grains, allows for the multicomponent nature of alloy steels and works remarkably well in predicting the mean particle size, ferrite grain size and strength of tempered martensite; it has yet to be applied to bainite.

Elementary coarsening theory suggests that the time-independent particle size distribution, normalised relative to the mean particle radius, should be skewed towards large particles, with a sharp cut off at a normalised radius of 1.5. However, measured distributions for cementite in bainite do not fit this behaviour, the distributions instead being skewed towards smaller particle sizes. Deep and Williams point out that this behaviour is also found for cementite in tempered martensite.

#### 4.5 Secondary Hardening and the Precipitation of Alloy Carbides

Secondary hardening is usually identified with the tempering of martensite in steels containing strong carbide forming elements like Cr, V, Mo and Nb. The formation of these

alloy carbides necessitates the long-range diffusion of substitutional atoms and their precipitation is consequently sluggish. Carbides like cementite therefore have a kinetic advantage even though they may be metastable. Tempering at first causes a decrease in hardness as cementite precipitates at the expense of carbon in solid solution, but the hardness begins to increase again as the alloy carbides form. Hence the term *secondary hardening*. Coarsening eventually causes a decrease in hardness at long tempering times so that the net hardness versus time curve shows a secondary hardening peak.

There is no reason to suspect that the secondary hardening of bainite should be particularly different from that of martensite. Early work did not reveal any pronounced peaks in the tempering curves for bainite, perhaps because of the low molybdenum concentration in the steels used (Irvine et al., 1957b). The peaks were subsequently found during the tempering of a vanadium containing bainitic steel but not for Cr or Mo containing bainitic steels, Fig. 4.13. An unexplained observation was that for the Mo containing steels, the carbide formed on tempering bainite is initially cementite, which then transforms to  $(\text{Fe, Mo})_{23}\text{C}_6$ , whereas on tempering martensite in the same steels the ultimate carbides are found to be  $\text{Mo}_2\text{C}$ .

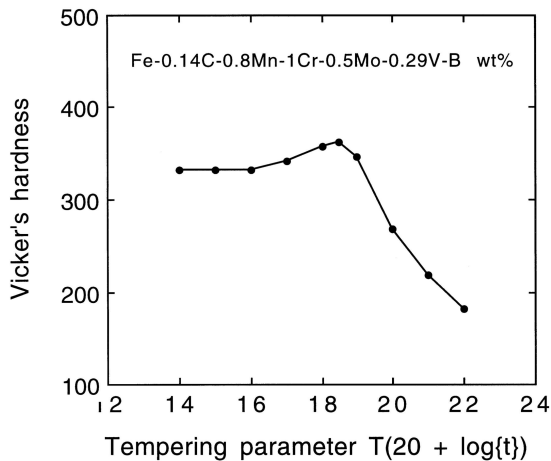


**Figure 4.13** Secondary hardening peak in a vanadium containing bainitic steel. The tempering parameter is defined with the absolute temperature  $T$  and the time  $t$  in hours. After Irvine et al. (1957a).

Later work revealed clear evidence of secondary hardening in low carbon bainitic steels containing up to 2.95 wt% Mo, 2.12 wt% Cr and also in vanadium containing bainitic steels (Baker and Nutting, 1959; Irvine et al., 1957a). Whether or not *peaks* are observed in the tempering curves, the data are all consistent with secondary hardening because the tempering resistance is improved relative to plain carbon steels.

It would be interesting to see whether it is possible to design a steel in which the bainite secondary hardens as it forms. The  $B_S$  temperature would have to be around  $650^\circ\text{C}$  and the alloy would have to be engineered to avoid interference from other transformation products. In a microalloyed steel, minute particles of  $\text{Nb}(\text{C},\text{N})$  have indeed been found to form during bainitic transformation at about  $600^\circ\text{C}$  (Park et al., 2007).

#### 4.6 Changes in the Composition of Cementite

The cementite that precipitates from austenite during the course of the bainite reaction has the same substitutional to iron atom ratio as the austenite, i.e. there is no partitioning of the

substitutional solutes. Its composition is therefore far from equilibrium. Tempering helps the cementite to approach its equilibrium composition by the diffusion of solutes from the ferrite into the cementite.

Most of the chemical data on cementite composition changes during tempering have been obtained using either direct chemical analysis of extracted carbides, or energy dispersive X-ray analysis techniques associated with transmission electron microscopy. These techniques are not well suited for the analysis of carbon or nitrogen concentrations. These two elements can mix to form carbo-nitrides. Thus, atom-probe field ion microscopy has shown that  $M_2C$  carbides found in tempered bainite have an average composition  $[Cr_{0.41}Mo_{0.59}]_2[C_{0.96}N_{0.04}]$  (Josefsson et al., 1987; Josefsson and Andrén, 1989). In the discussion that follows, we shall neglect to consider the carbon and nitrogen, for which there are few data.

Some of the first results on the tempering of bainite were obtained by Baker and Nutting (1959) for a commercial steel with a chemical composition Fe-0.15C-2.12Cr-0.94Mo wt%. The cementite was found to become richer in Cr, Mo and Mn, the degree of enrichment being highest for Cr, with its concentration eventually reaching some 20 wt% (Fig. 4.14).

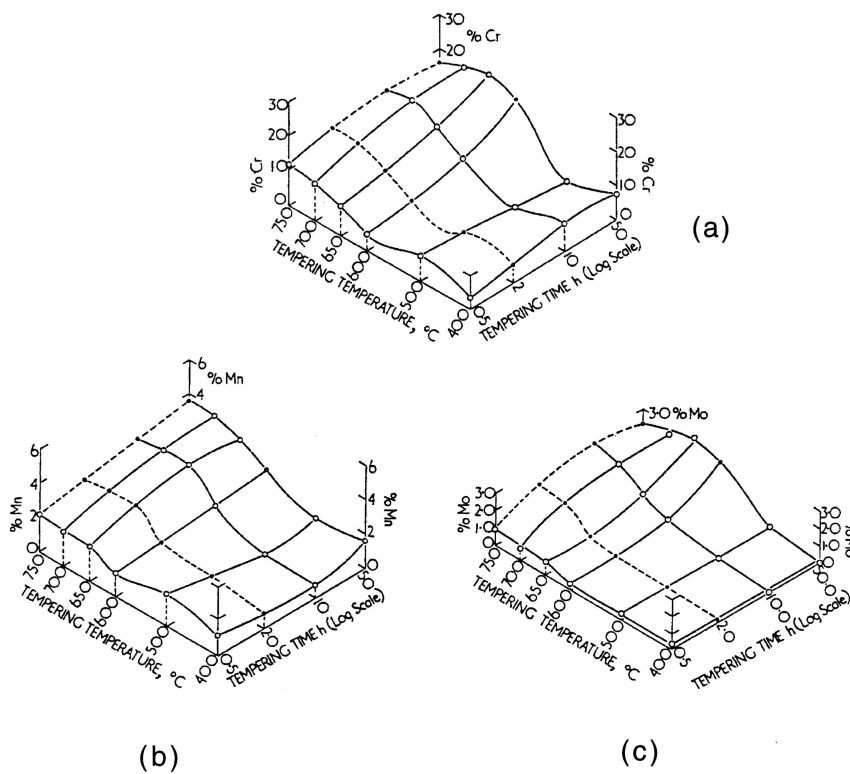


**Figure 4.14** The concentrations of Cr, Mn, and Mo in extracted carbides, as a function of the tempering time and temperature, for a steel with initial microstructure which is bainitic (Baker and Nutting, 1959).

The enrichment of cementite decreases as alloy carbide formation begins, until the cementite eventually starts to dissolve (Fig. 4.15). This is expected since a dissolving particle

of cementite will contain a chromium depleted zone near the moving ferrite/austenite interface.

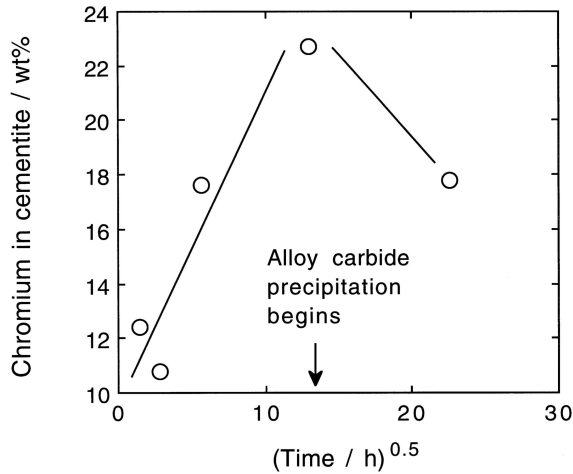


**Figure 4.15** Mean chromium concentration in cementite found in a tempered bainitic microstructure aged at 565°C, in a “ $2\frac{1}{4}$ Cr1Mo” power plant steel (Thomson and Bhadeshia, 1994a,b).

#### 4.6.1 Remanent Life Prediction

The study of changes in the chemical composition of carbides during the tempering of bainite is of commercial importance. Where creep resistant bainitic steels are in service at elevated temperatures over long time periods (30 years), it is important for safety reasons to know accurately, the time-temperature history of the steel at any stage during service. The thermal history of the steel can be related to the amount of creep life remaining in that steel before the accumulated damage becomes intolerable. This remaining creep life is in the power generation industry called the *remanent life* (Bhadeshia et al., 1998).

The accurate estimation of remanent life permits the safe use of existing power plant beyond its original design life. The method can also help anticipate plant closures or it can facilitate the timely replacement of components. Power plant temperatures fluctuate and are difficult to record over long periods of time and for the large number of components involved (Fig. 4.16). Life assessment therefore has to be made on a conservative basis, which leads to expense due to premature closure of plant which has not exhausted its safe life. Any method which gives an accurate measure of the thermal history experienced by the steel during service can lead to savings by enabling more accurate assessments of the remaining creep life. At first sight, the obvious thing to do would be to monitor the temperature everywhere using strategically located thermocouples, but this is impractical over the large time span involved and in the harsh environment of the power station.

The microstructure of the steel, and especially the chemical composition of the cementite, changes during service. These changes can be exploited to assess the effective thermal history experienced by the steel since its implementation. The microstructure is in this context a recorder of time and temperature; for example, the cementite particles in the steel can be monitored by removing a few using extraction replicas. Their compositions can then be measured using a microanalysis technique to determine the extent of enrichment and hence an estimate of the effective service temperature. The interpretation and extrapolation of such data relies on the existence of theory capable of relating the cemen-

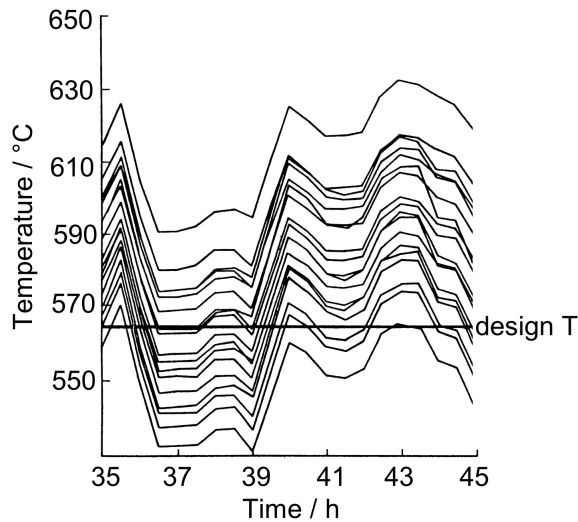


**Figure 4.16** Illustration of the variation in the temperature at different locations on a particular component ("reheater drum") of a 500 MW power station (Cane and Townsend, 1984).

tite composition to heat treatment. Such theory is discussed in a later section, after an introduction to the published work.

The use of cementite composition for thermal history assessment was first applied to the cementite in pearlite, where it was found empirically that the Cr and Mn concentrations varied with  $t^{\frac{1}{3}}$ , where  $t$  is the time at tempering temperature (Carruthers and Collins, 1981). We shall see later that a  $t^{\frac{1}{2}}$  relationship can be justified theoretically.

Afrouz *et al.* (1983) reported similar results on a bainitic steel. The alloy was normalised to give a microstructure of allotriomorphic ferrite and 20% bainite, was then tempered in an unspecified way, and held at 565°C for 70,000 h at a stress of  $\approx 17$  MPa. This service-exposed material was then examined after further tempering at 550°C for a range of time periods. As expected, the chromium and manganese concentrations of the cementite ( $M_3C$ ) increased with time, the manganese possibly showing signs of saturation during the later stages of ageing, and the data for molybdenum exhibiting considerable scatter (Fig. 4.17).

Afrouz *et al.* also austenitised the service-exposed material so that after oil-quenching, a fresh fully bainitic microstructure was obtained; it is likely that both upper and lower bainite were present. This was then tempered at 693°C for an hour to give coarse  $M_3C$  particles at the lath boundaries and within the bainite, and subsequently held at 550°C for a variety of time periods. The change in  $M_3C$  composition was monitored during the latter tempering treatment (Fig. 4.17). The starting composition of the carbide is naturally leaner than that of the service-exposed material and the rate of enrichment was found to be higher for the reheat-treated samples (Fig. 4.17).

#### 4.6.2 Theory for Carbide Enrichment

The process by which carbide particles enrich during tempering has been analysed theoretically (Bhadeshia, 1989). The method is similar to the one employed in determining the time required to decarburise supersaturated plates of ferrite, as discussed in detail in

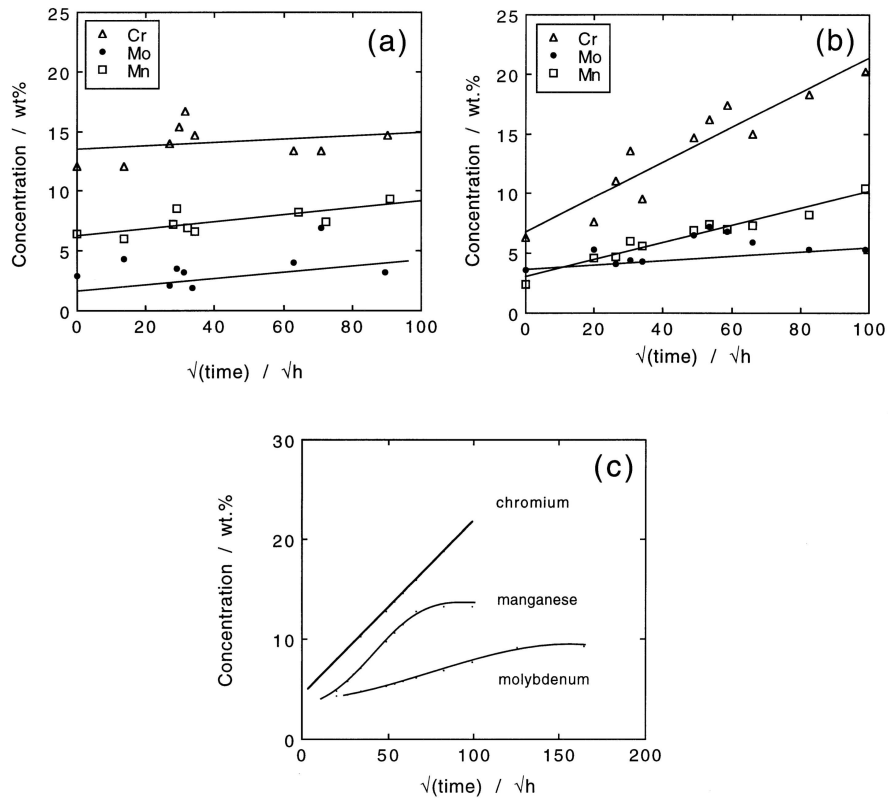


**Figure 4.17** Measured changes in the chemical composition of cementite particles as a function of the square root of time, during ageing at 550 °C. The steel composition is Fe-0.1C-0.24Si-0.48Mn-0.84Cr-0.48Mo wt%. The data have been replotted against  $t^{\frac{1}{2}}$  instead of  $t^{\frac{1}{3}}$  used in the original work. (a) Tempered at 550 °C following service at 565 °C for 70000 h. (b) Heat treated to give a fully bainitic microstructure, stress-relieved at 693 °C for one hour and then tempered at 550 °C for the periods illustrated. Data from Afrouz et al. (1983). (c) Finite difference calculations showing that the enrichment process will inevitably show deviations from the parabolic law at long ageing times (Bhadeshia, 1989).

Chapter 6. The rate of cementite composition change is indicated by:

$$t_c^{\frac{1}{2}} \approx \frac{z_\theta (\bar{x}_i - x_i) \pi^{\frac{1}{2}}}{4D^{\frac{1}{2}} (x_i^{\alpha\theta} - \bar{x}_i)} \quad (4.7)$$

where  $t_c$  is the time required for the carbide to reach a concentration  $x_i$  (the subscript represents a substitutional solute), and  $z_\theta$  is the thickness of the cementite plate (Fig. 4.18a).  $D$  is the diffusion coefficient for the solute in the matrix (assumed to be identical to the corresponding diffusivity in the particle) and  $x_i^{\alpha\theta}$  is the concentration of the substitutional solute in the ferrite which is in equilibrium with the cementite. An important outcome is that the carbide composition should depend on its size (Fig. 4.18b).

The time dependence of concentration is found to be  $t^{\frac{1}{2}}$  rather than the  $t^{\frac{1}{3}}$  which has been assumed in the past. The analysis neglects the overlap of the diffusion fields of different particles, an effect which is inevitable during long term heat treatment. It also neglects diffusion within the carbide, an assumption which needs to be justified given that high-resolution microanalysis reveals gradients within the carbide during the early stages of tempering (Kaneko et al., 2003). Both of these difficulties can be tackled using finite difference methods, which show that the time exponent must vary with time, since the boundary conditions for the diffusion process change with the onset of soft impingement (Fig. 4.17c).

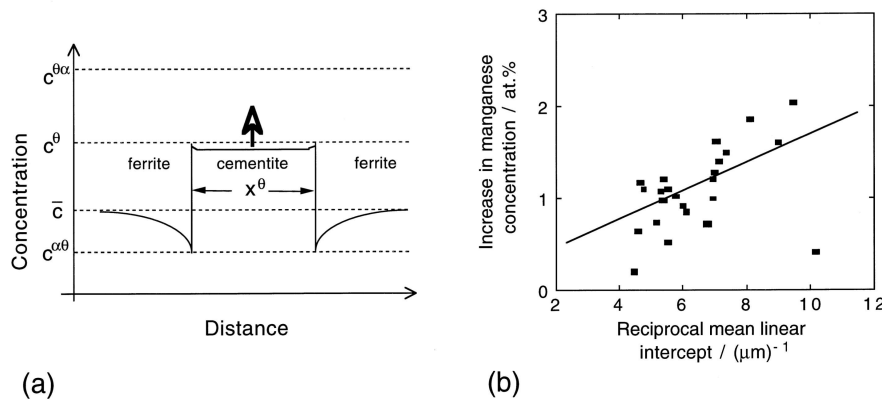


**Figure 4.18** (a) Solute concentration profile that develops during enrichment of cementite.  $c^{\theta\alpha}$  is the concentration in cementite which is in equilibrium with ferrite. (b) Size dependence of the cementite chemical composition for particles extracted from a bainitic microstructure aged for 4 weeks at 565 °C (Wilson, 1991). Detailed analysis shows that the scatter in the data is a consequence of the microanalysis technique. The increase in Mn content is relative to the concentration at the point where the microstructure was first produced.

### 4.6.3 Effect of Carbon on Carbide Enrichment

There are two effects that depend on the carbon concentration of the steel. The ternary Fe-Cr-C phase diagram on the  $M_3C/\alpha$  field shows that an increase in the carbon concentration is accompanied by a decrease in the equilibrium concentration of chromium in the carbide. Thus, the carbide enrichment rate is expected to decrease. A further effect is that

the volume fraction of cementite increases, in general leading to an increase in particle thickness. The thickness increase retards the rate of enrichment (equation 4.7). If the carbide particles are closer to each other then soft-impingement occurs at an earlier stage, giving a slower enrichment at the later stages of annealing.

Local variations in carbon concentration may have a similar effect to changes in average concentration. Such variations can be present through solidification induced segregation, or because of microstructural variations caused by differences in cooling rates in thick sections. It is well known that the microstructure near the component surface can be fully bainitic with the core containing a large amount of allotriomorphic ferrite in addition to bainite. In the latter case the bainite which grows after the allotriomorphic ferrite, transforms from high carbon austenite. The associated carbides are then found to enrich at a slower rate (Fig. 4.19). This discussion emphasises the role of carbon.

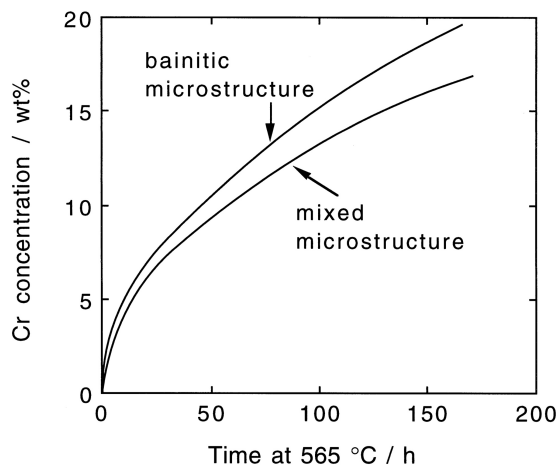


**Figure 4.19**  $2\frac{1}{4}\text{Cr}1\text{Mo}$  steel, cementite enrichment in a fully bainitic microstructure and one which is a mixture of allotriomorphic ferrite and bainite (Thomson and Bhadeshia, 1994a,b).

#### 4.7 Low-Temperature Tempering of Mixed Microstructures

The production of carbide-free bainitic steels now pervades significant sectors of the steel industry, with applications ranging from automotive alloys to large and strong bolts. Because of the incomplete reaction phenomenon, such steels often contain quantities of martensite which inherits the composition of the high-carbon residual austenite left after the bainite reaction stops. This martensite will tend to be brittle. If it cannot be avoided in the microstructure then tempering the steel in the vicinity of  $300^\circ\text{C}$  helps to reduce the carbon in solid solution in the martensite, and consequently to improve the toughness. Thus, Goa et al. (2007) tempered their bainitic steels in this way to obtain remarkable Charpy V-notch toughness values in the range 128-135 J for steels in which the ultimate tensile strength was about 1500 MPa.

#### 4.8 Sequence of Alloy Carbide Precipitation

Cementite is not the equilibrium carbide in many bainitic alloy steels, but it is nevertheless kinetically favoured because its growth mechanism does not require the long-range diffu-

sion of substitutional solutes. The equilibrium combination of phases naturally depends on the steel composition. Alloy carbides become vital in steels where the resistance to creep deformation is of paramount importance; they obviously play a role in secondary hardened steels for use at ambient temperatures but such alloys tend to be martensitic rather than bainitic. Fig. 4.20 shows the equilibrium phases to be found in creep-resistant steels.  $M_{23}C_6$ ,  $M_2X$  and small fractions of carbonitrides are the equilibrium precipitates in the first two alloys which are generally used in the bainitic or partly bainitic microstructures. The other higher alloy steels are martensitic and are susceptible to the formation of Laves phases (intermetallic compounds). It is interesting that cementite is not an equilibrium phase in any of the alloys illustrated.

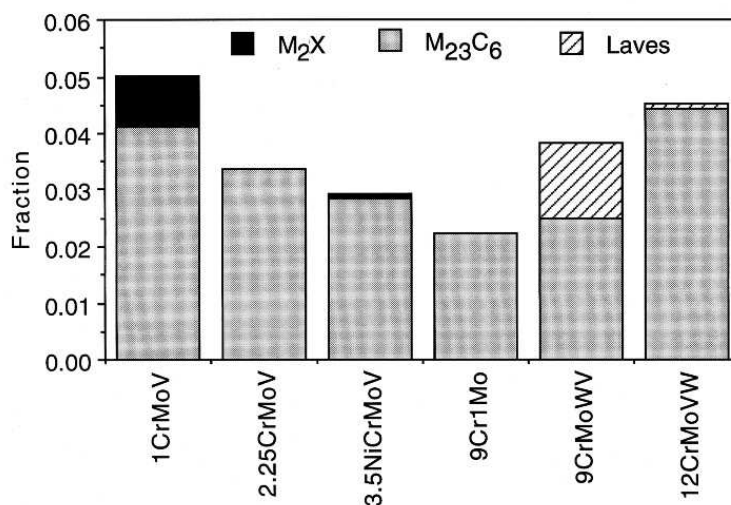


**Figure 4.20** Equilibrium fractions of carbides at 565 °C (838 K) in some common power plant steels, the first two of which frequently are bainitic. The remaining alloys are essentially martensitic. The detailed chemical compositions are given in Table 12.5. Small fractions of vanadium and niobium carbonitrides are present in some steels but are not shown. Thus, the modified 9Cr1Mo contains 0.0009 NbN and 0.003 VN, the 9CrMoWV steel contains 0.0008 NbN and 0.0032 VN.

The approach to equilibrium can be slow, especially when the tempering temperature is less than 600 °C. The change from cementite to the equilibrium carbide may occur via a number of other transition carbides. Baker and Nutting (1959) showed that during the tempering of bainite Fe-2.12Cr-0.94Mo-0.15C wt%, the first alloy carbide to form is  $M_2C$ ,<sup>1</sup> needles of which precipitate independently of the cementite (Fig. 4.21). Later work has shown that the  $M_2C$  contains substantial amounts of other elements; it is better represented as  $M_2C$  (Woodhead and Quarrell, 1965; Murphy and Branch, 1971). This applies to virtually all the alloy carbides in multicomponent steels.

$M_7C_3$  starts to form soon after the precipitation of  $M_2C$ , perhaps at the interface between the Cr-enriched cementite and ferrite.  $M_2C$  then begins to dissolve, giving way to  $M_{23}C_6$ . Both  $M_{23}C_6$  and  $M_7C_3$  are at high temperatures, completely or partly replaced by the equilibrium carbide  $M_6C$ .

<sup>1</sup>'M' refers to a mixture of metal atoms

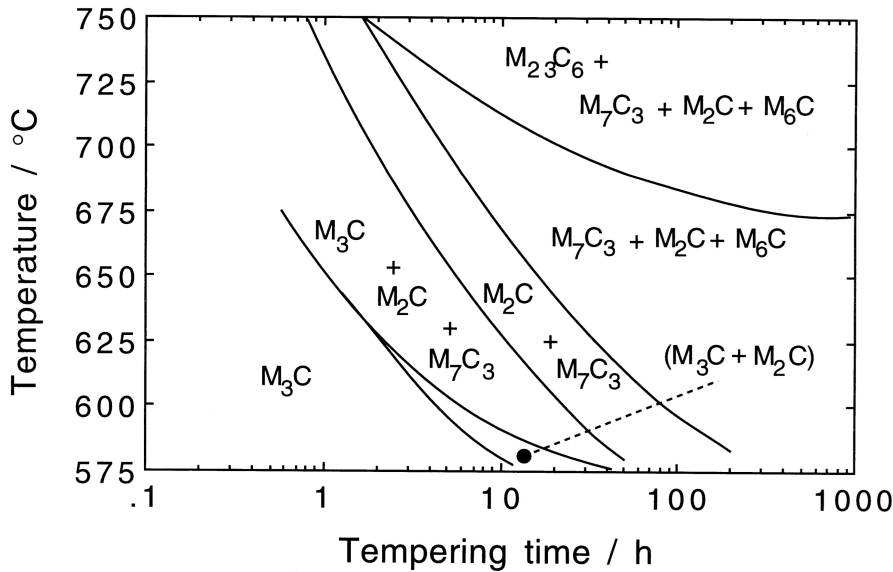
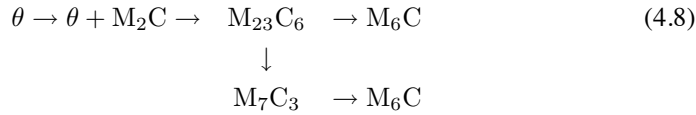


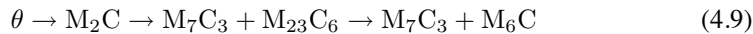
**Figure 4.21** An updated version of the classic Baker-Nutting carbide stability diagram for a  $2\frac{1}{4}$ Cr1Mo steel. After Nutting (1998).

With the exception of  $M_2C$ , new transition carbides seem to precipitate in association with preexisting carbides. The sequence of changes in Fe-2.12Cr-0.94Mo-0.15C wt% can be summarised as follows:

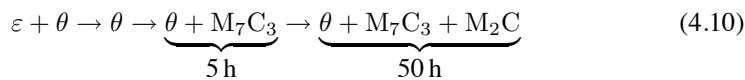


Extremely long tempering experiments (some 200,000 h in the temperature range 520-560°C) confirm that  $M_6C$  is the most stable precipitate. The equilibrium fraction of  $M_6C$  increases at the expense of  $M_{23}C_6$  as the carbon concentration is reduced.

A different sequence has been reported by Pilling and Ridley (1982) for lower carbon Fe-Cr-Mo-C alloys containing lower carbon concentrations (0.018-0.09 wt%) which illustrates the sensitivity of the microstructure to the precise chemical composition:



Yu (1989) has shown that an increase in the silicon concentration to about 0.6 wt% stabilises  $M_6C$  (which is absent in silicon-free  $2\frac{1}{4}$ Cr1Mo steels) since silicon has a relatively high solubility in that carbide. It was also found to accelerate the precipitation of  $M_2C$ ; Tsai and Yang (2003) demonstrated the same effect in modified  $2\frac{1}{4}$ Cr1Mo (Table 12.5) which contains a negligible silicon concentration:



These data are for tempering at 700°C; a comparison with ordinary  $2\frac{1}{4}\text{Cr1Mo}$  (Fig. 4.21) shows that the precipitation of  $\text{M}_2\text{C}$  has been greatly delayed in the modified alloy. Indeed, the  $\text{M}_2\text{C}$  only forms after  $\text{M}_7\text{C}_3$ , whereas the latter forms after  $\text{M}_2\text{C}$  in the ordinary alloy.

An increase in the manganese concentration from 0 to 0.8 wt% was found to accelerate  $\text{M}_7\text{C}_3$  precipitation (Yu, 1989). Enhanced chromium concentrations are known to accelerate the formation of  $\text{M}_{23}\text{C}_6$  and this influences the sensitivity of the microstructure to severe hydrogen attack (Ritchie et al., 1984; Spencer et al., 1989).

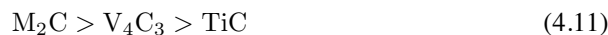
Some of these detailed kinetic effects of the average composition of the steel on the precipitation processes can now be predicted theoretically (Robson and Bhadeshia, 1997b,a). The compositions of three steels used for illustration are given in Table 4.2. These three alloys, whilst of quite different chemical compositions, show similar precipitation *sequences* but on vastly different time scales. For example, at 600°C the time taken before  $\text{M}_{23}\text{C}_6$  is observed is 1 h in the 10CrMoV steel, 10 h in the 3Cr1.5Mo alloy and in excess of 1000 h in the  $2\frac{1}{4}\text{Cr1Mo}$  steel.

**Table 4.2** Concentration (in wt%) of the major alloying elements in the steels used to demonstrate the model.

	C	N	Mn	Cr	Mo	Ni	V	Nb
$2\frac{1}{4}\text{Cr1Mo}$	0.15	-	0.50	2.12	0.9	0.17	-	-
3Cr1.5Mo	0.1	-	1.0	3.0	1.5	0.1	0.1	-
10CrMoV	0.11	0.056	0.50	10.22	1.42	0.55	0.20	0.50

A plot showing the predicted variation of volume fraction of each precipitate as a function of time at 600°C is shown in Fig. 4.22. Consistent with experiments, the precipitation kinetics of  $\text{M}_{23}\text{C}_6$  are predicted to be much slower in the  $2\frac{1}{4}\text{Cr1Mo}$  steel compared to the 10CrMoV and 3Cr1.5Mo alloys. One contributing factor is that in the  $2\frac{1}{4}\text{Cr1Mo}$  steel a relatively large volume fraction of  $\text{M}_2\text{X}$  and  $\text{M}_7\text{C}_3$  forms prior to  $\text{M}_{23}\text{C}_6$ . These carbides deplete the matrix and therefore suppress  $\text{M}_{23}\text{C}_6$  precipitation. The volume fraction of  $\text{M}_2\text{X}$  which forms in the 10CrMoV steel is relatively small, and there remains a considerable excess of solute in the matrix, allowing  $\text{M}_{23}\text{C}_6$  to precipitate rapidly. Similarly, in the 3Cr1.5Mo steel the volume fractions of  $\text{M}_2\text{X}$  and  $\text{M}_7\text{C}_3$  are insufficient to suppress  $\text{M}_{23}\text{C}_6$  precipitation to the same extent as in the  $2\frac{1}{4}\text{Cr1Mo}$  steel.

Phase equilibrium is, of course, a function of temperature as well as the chemical composition. Precipitation sequences may therefore change with the temperature. In a Fe-1Cr-1Mo-0.75V-(B, Ti) wt% bainitic steel Collins (1989) showed that tempering led to the formation of TiC and  $\text{V}_4\text{C}_3$ , both of which also contained molybdenum. The  $\text{V}_4\text{C}_3$  nucleates on TiC particles which form first. The TiC then converts *in situ* into molybdenum-rich  $\text{M}_2\text{C}$  precipitates. At 600°C the stability of the carbides is in the following sequence



whereas at higher temperatures the  $\text{V}_4\text{C}_3$  is more stable than  $\text{M}_2\text{C}$ . The dependence on temperature is important because creep tests are often accelerated by raising the test temperature but the carbide structure at the higher temperature may be different, making the accelerated test unrepresentative.

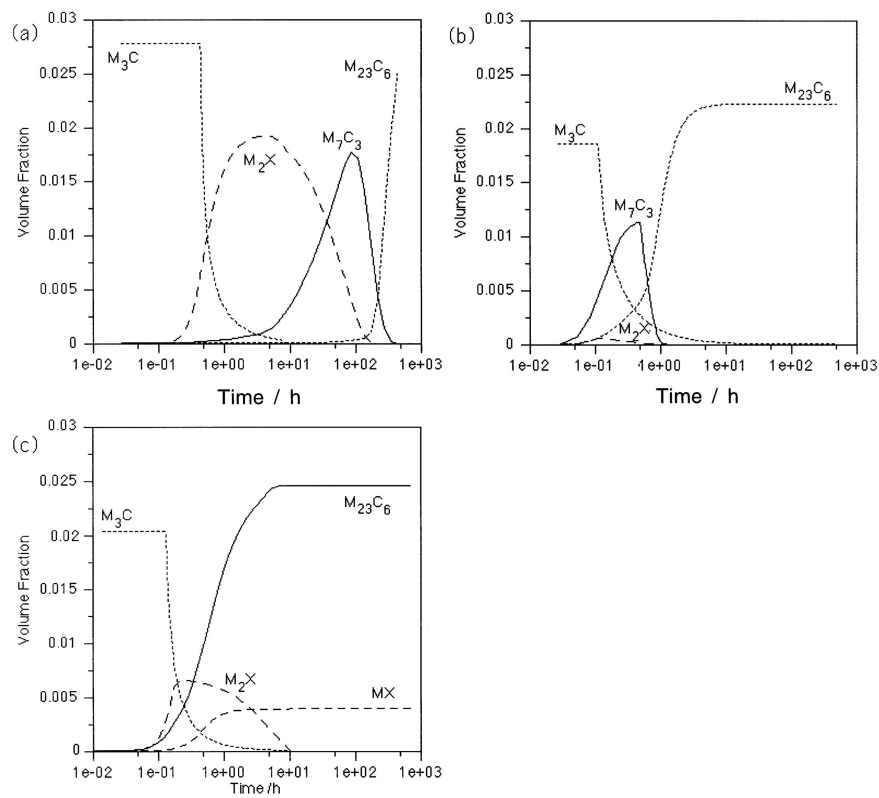


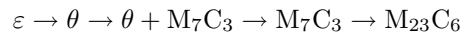
**Figure 4.22** The predicted evolution of precipitate volume fractions at 600 °C for three power plant materials (a) 2 1/4Cr1Mo (b) 3Cr1.5Mo and (c) 10CrMoV. After Robson and Bhadeshia (1997b,a)

#### 4.8.1 Effect of Starting Microstructure on Tempering Reactions

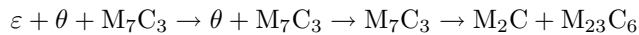
There are no major differences in the alloy carbide precipitation reactions when the microstructure is changed from martensite to bainite (Baker and Nutting, 1959). If allotriomorphic ferrite is present in the microstructure then it may already contain alloy carbides which precipitate during the diffusional growth of the ferrite itself. In the  $2\frac{1}{4}\text{Cr1Mo}$  steel  $\text{M}_2\text{C}$  precipitates present within the allotriomorphic ferrite dissolve during tempering to be replaced by  $\text{M}_{23}\text{C}_6$  and  $\text{M}_6\text{C}$  particles (Baker and Nutting, 1959; Parameswaran et al., 2002). By contrast, alloy carbides do not form during the growth of any of the displacive transformation products, including bainite and martensite.

The distribution and type of precipitates are also influenced by the microstructure (Lee et al., 1989). Thus, in a  $1\text{Cr}\frac{1}{2}\text{Mo}$  steel,  $\text{M}_2\text{C}$  forms the main precipitate within tempered bainite plates whereas mixtures of cementite,  $\text{M}_2\text{C}$ ,  $\text{M}_7\text{C}_3$  and  $\text{M}_{23}\text{C}_6$  are found at the bainite plate boundaries. The boundaries are not only more effective heterogeneous nucleation sites but the cementite particles located there are sources of carbon for the precipitation of alloy carbides. Differences of this kind have also been observed during the tempering of a variety of microstructures in  $2\frac{1}{4}\text{Cr1Mo}$  steel tempered at  $700^\circ\text{C}$  (Tsai and Yang, 2003):

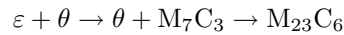
*At bainite lath boundaries:*



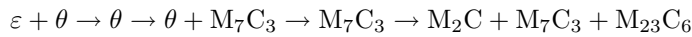
*Inside bainite laths:*



*At martensite lath boundaries:*



*Inside martensite laths:*



There are important two observations to be made from these results. Firstly,  $\text{M}_2\text{C}$  precipitates dominate within the laths, showing no preference for the lath boundaries. This is because  $\text{M}_2\text{C}$  is rich in molybdenum, which is present in low concentrations in all the other carbides. Much of the molybdenum therefore comes from solution in the matrix, making it advantageous to form a uniform dispersion. Secondly, the formation of alloy carbides in bainite is more rapid than in martensite. This might be expected from the higher transformation temperature, the microstructure in effect being partly tempered during transformation.

Any differences in the number density or distribution of nucleation sites will cause changes in the kinetics of precipitation reactions. The equilibrium carbide  $\text{M}_6\text{C}$  forms more rapidly in bainite than in pearlite or allotriomorphic ferrite (Lee et al., 1989).

#### 4.9 Changes in the Composition of Alloy Carbides

Alloy carbides cannot form without the long-range diffusion of substitutional solutes. Given this *necessary* diffusion, it is not surprising that their compositions are at all times

close to equilibrium. Small changes can be induced by one or more of the following phenomena:

- (i) The equilibrium chemical composition of particles with curved interfaces is dependent on the radius of curvature via the Gibbs-Thompson effect.
- (ii) The phase rule allows greater degrees of freedom in steels containing one or more substitutional solutes. Thus, the tie-line controlling the equilibrium composition of the carbide may shift during the precipitation reaction, either as the solute content of the matrix is depleted or as other phases precipitate (Fujita and Bhadeshia, 1999).
- (iii) Carbides adjust to a new equilibrium when the tempering temperature is changed (Strang et al., 1999). It is common in industrial practice to use multiple tempering heat-treatments.

#### 4.10 Precipitate-free Zones

In steels, precipitates nucleate most readily at the prior austenite grain boundaries and their growth depletes solute leading to the formation of a precipitate free-zone parallel to the grain surfaces. Intragranular precipitates are more difficult to nucleate and hence are finer than the grain boundary precipitates at any stage of tempering.

Prolonged tempering leads to a coarsening reaction in which the grain boundary precipitates grow larger whereas those within the grains dissolve. As a consequence, the precipitate-free zone becomes larger during tempering. Fig. 4.23 illustrates how the thickness apparently increases with increasing vigour with the time in service (Mitchell and Ball, 2001); the observed trend is surprising since the rate of thickening ought to decrease with prolonged annealing. This is because the distance over which matter must be transported to the grain boundary precipitates becomes greater as the size of the precipitate-free zone increases; elementary diffusion theory therefore indicates that the thickness should vary with  $t^{\frac{1}{2}}$ .

The importance of the precipitate-free zones in controlling the creep properties of tempered martensitic steels has been emphasised in recent work by Kimura et al. (1997). It is often observed in isothermal plots of creep rupture stress versus time that the stress abruptly decreases after many thousands of hours in service. This undesirable behaviour has been attributed to the onset of localised recrystallisation of the martensitic microstructure in the precipitate-free regions at the austenite grain boundaries.

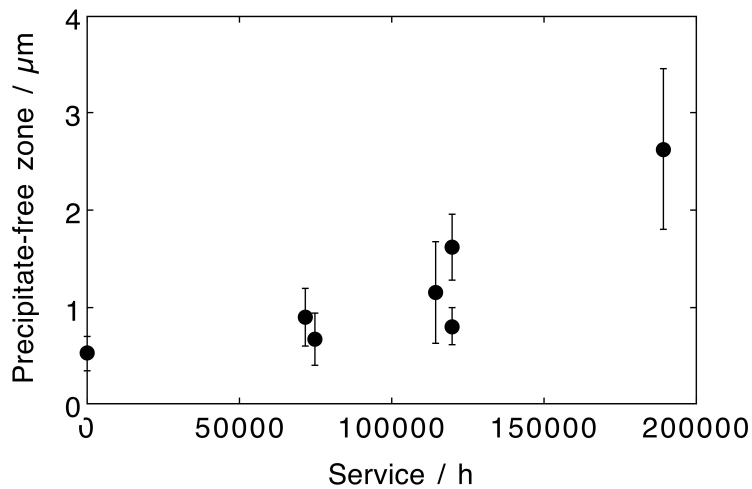


**Figure 4.23** Width of  $\text{M}_2\text{C}$  denuded zone in a  $2\frac{1}{4}\text{Cr1Mo}$  steel as a function of service at a temperature in the range  $520\text{--}560^\circ\text{C}$ . After (Mitchell and Ball, 2001).

#### 4.11 Precipitation Hardening with Copper

The interaction between a particle and a dislocation can be defined as ‘hard’ or ‘soft’ depending on whether the dislocation can cut through the particle. A hard interaction is one in which the dislocation bends around the particle through an angle  $\theta = \pi/2$  (Fig. 4.24) and leaves behind an Orowan loop as it frees itself from the particle. With soft interactions the degree of bending before the dislocation cuts through the precipitate is much less than  $\pi/2$ ; there is no debris left behind as the dislocation breaks away from the particle.

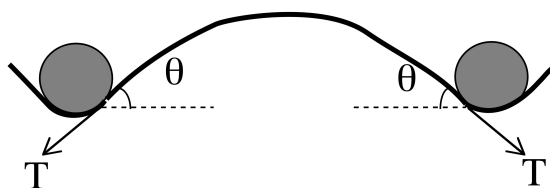


**Figure 4.24** A dislocation bowing between two particles.  $T$  is the dislocation line-tension and  $\theta$  is the angle through which the dislocation bows.

Unlike carbides or oxides, copper is regarded as a soft precipitate in iron; it strengthens the iron by about  $40\text{ MPa}$  per wt% but does not cause a decrease in toughness. Coarser particles of copper are less coherent with the matrix; the critical value of  $\theta$  at which the dislocation cuts through copper precipitates therefore depends on their size, becoming  $\pi/2$  when the particles are about  $80\text{ nm}$  diameter (Nakashima et al., 2002).

Copper-bearing low-carbon steels with a mixed microstructure of ferrite and pearlite are used in heavy engineering applications which demand a combination of strength, toughness and weldability. The same low carbon steels can be transformed to carbide-free bainite, with thin films of retained austenite between the bainite plates (Thompson et al., 1988). Fine particles of copper can be induced to precipitate in the bainitic ferrite and to contribute to the overall strength.

The precipitation of copper occurs from supersaturated bainite either as a consequence of autotempering or when the steel is deliberately tempered (Fourlaris et al., 1996). Thus, no precipitation could be detected following the transformation of some experimental Cu-rich steels in the range 200-400 °C, either in the bainitic ferrite or in its associated cementite. Subsequent tempering at 550 °C resulted in fine copper precipitates in both the ferrite and cementite phases (Fig. 4.25). Copper, which is a substitutional solute, is not in this respect different from any secondary hardening element in steels.

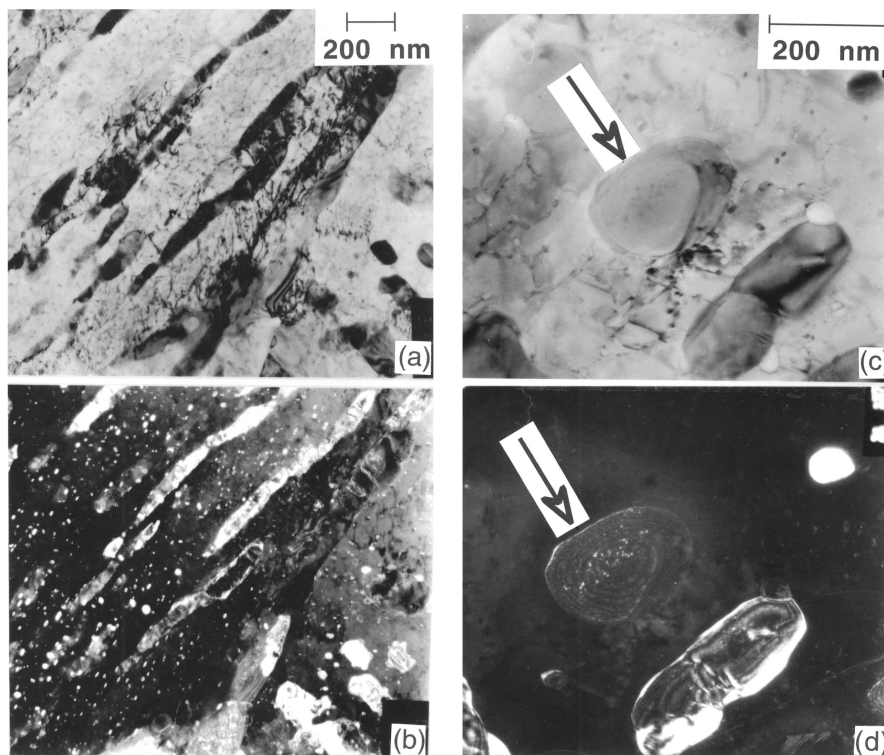


**Figure 4.25** Copper precipitation in bainite obtained by isothermal transformation at 350 °C for 65 minutes, followed by tempering at 550 °C for many hours (Fourlaris et al., 1996). (a,b) Bright field transmission electron micrograph and corresponding dark field image showing copper precipitation in tempered bainitic ferrite. (c,d) Bright field and corresponding dark field image of copper precipitates in the cementite associated with bainite.

The question arises as to whether copper precipitation can be induced in the bainite during continuous cooling to ambient temperature. This would require a very high bainite transformation temperature, higher than 550 °C where substitutional atoms can be mobile. Hase et al. (1999) studied an alloy with the composition Fe-0.009C-0.26Si-1.99Mn-

2Cu wt% with the microstructure generated during continuous cooling transformation. Fig. 4.26 shows that copper precipitation does not occur in the cooling rate range which leads to the formation of bainitic ferrite, but only at slower cooling rates associated with other transformation products which form at higher temperatures.

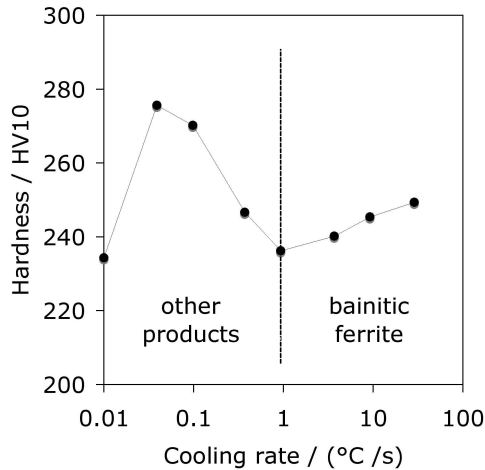


**Figure 4.26** Effect of cooling rate on the hardness of Fe-0.009C-0.26Si-1.99Mn-2Cu wt%, after Hase et al. (1999).

A potential difficulty in quenched and tempered copper precipitation strengthened steels is their tendency to crack during stress-relief heat treatments following welding (Wilson and Gladman, 1988). Although the steels are immune to cold cracking, the copper particles are taken into solution in the heat-affected zone during welding. The stress-relief heat treatment then causes precipitation which hinders the annealing of residual stresses.

#### 4.12 Summary

There are important differences in the tempering behaviour of bainite and martensite because the former autotempers during transformation. Much of the carbon precipitates or partitions from the ferrite during the bainite reaction. Since  $B_S > M_S$ , the extent of autotempering is greatest for bainite, which consequently is less sensitive to additional tempering heat-treatments. The decrease in strength on tempering bainite is smaller because, unlike martensite, there is in general little carbon left in solid solution. Major changes in strength occur only when the microstructure coarsens or with the onset of recrystallisation where equiaxed grains of ferrite replace the bainite plates. Minor changes in strength are due to cementite particle coarsening and a general recovery of the dislocation substructure. Bainitic steels containing strong carbide forming elements show secondary hardening similar to martensitic steels. In most cases, new carbides nucleate on existing metastable carbides, with the exception of  $M_2C$  which forms in isolation on dislocations.

In the context of thermal stability, films of austenite are less stable than larger blocks. Because the films contain relatively more carbon, they precipitate cementite more readily during tempering. This precipitation can be retarded, and hence the thermal stability of the austenite improved, by enhancing the silicon concentration of the steel.



## CHAPTER 5

---

# THERMODYNAMICS

---

### 5.1 Deviations from Equilibrium

Equilibrium is said to exist in a system when it reaches a state in which no further change is perceptible, no matter how long one waits (Pippard, 1981). This could happen if the system sinks into a very deep free energy minimum. Whether this represents the lowest free energy state, it is impossible to say, and a question more of philosophy than of practical consequence. It is more appropriate to refer to the state of metastable equilibrium, which represents a local minimum in free energy but does not exclude the existence of other deeper minima. The laws governing metastable equilibria are exactly identical to those dealing with equilibrium so this procedure has no obvious difficulties.

A bainitic microstructure is far from equilibrium. The free energy change accompanying the formation of bainite in an Fe-0.1C wt% alloy at 540°C is  $-580 \text{ J mol}^{-1}$ , whereas that for the formation of an equilibrium mixture of allotriomorphic ferrite and austenite at the same temperature is  $-1050 \text{ J mol}^{-1}$ . Consequently, the excess energy of bainite is some  $470 \text{ J mol}^{-1}$  relative to allotriomorphic ferrite, equivalent to about 0.04 in units of  $RT_M$ , where  $R$  is the gas constant and  $T_M$  the absolute melting-temperature. This is about an order of magnitude larger than the stored energy of a severely deformed pure metal. It is small, however, when compared against highly metastable materials such as rapidly-quenched liquids which solidify as supersaturated solutions, or multilayered structures containing a large density of interfaces (Table 5.1). Thus, bainitic steels can be welded whereas all the other materials listed with higher stored energies would not survive the welding process.

**Table 5.1** Excess energies of metastable materials; adapted from Turnbull (1981).

Example	Excess energy $RT_M$
Highly supersaturated solution	1
Amorphous solid	0.5
Artificial multilayers	0.1
Bainite	0.04
Cold-deformed metal	0.003

The concepts of equilibrium, metastable equilibrium and indeed, constrained equilibrium, remain useful in spite of the large excess energies. For bainite, we shall apply them in the interpretation of the mechanism of transformation and obtain results which are of very great importance in the design of modern steels.

## 5.2 Chemical Potential

Pure iron can exist in many allotropic forms including ferrite ( $\alpha$ ) and austenite ( $\gamma$ ). These two phases can be said to be in equilibrium when their molar Gibbs free energies are identical;

$$G_m^\alpha = G_m^\gamma \quad (5.1)$$

There is then no net tendency for atoms to transfer from one allotrope to the other, because the free energy of the iron atom in  $\alpha$  is precisely equal to that in  $\gamma$ .

Similarly, for an iron-carbon solid solution, equilibrium is when there is no net tendency for either iron or carbon atoms to transfer between ferrite and austenite, even though the two phases may differ in composition. That is, the free energy of a carbon (or iron) atom must be identical in ferrite and in austenite at equilibrium. It is no longer the case that the ferrite and austenite have identical free energies at equilibrium.

It therefore becomes useful when considering the thermodynamics of solid solutions to partition the free energy of a phase into parts which are attributed to the individual components. This leads to the concept of a chemical potential. The molar Gibbs free energy of a binary solution can be written as a weighted average of its components  $A$  and  $B$ :

$$G_m = x_A \mu_A + x_B \mu_B \quad (5.2)$$

where  $\mu_i$  is the chemical potential of element  $i$  in a solution where its concentration is  $x_i$ . This equation is represented graphically in Fig. 5.1, from which it can be seen that the chemical potential  $\mu_A$  of  $A$  can be interpreted simply to represent the average free energy of a mole of  $A$  atoms *in a solution* of composition  $x_A$ .

Equilibrium is said to exist between homogeneous phases when the chemical potential  $\mu_i$  of each component  $i$  is the same in all the phases present:

$$\mu_i^\gamma = \mu_i^\alpha \quad \text{for all } i. \quad (5.3)$$

This is illustrated in Fig. 5.2, which shows that the equilibrium compositions  $x^{\alpha\gamma}$  and  $x^{\gamma\alpha}$  of ferrite and austenite respectively, can be determined by constructing a tangent which is

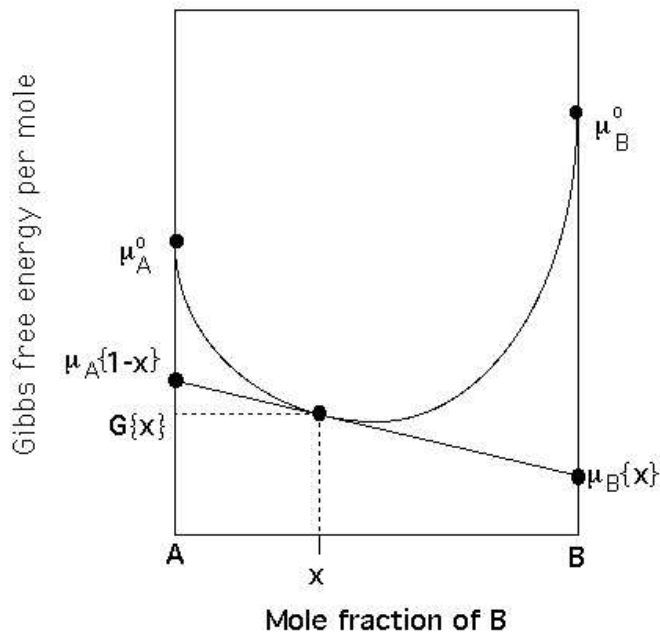


**Figure 5.1** The chemical potentials  $\mu_A$  and  $\mu_B$  for components  $A$  and  $B$  respectively, in a solution containing a mole fraction  $x$  of  $B$  and  $1 - x$  of  $A$ . The potentials are given by the intercepts on the vertical axes of the tangent drawn at  $x$  to the curve representing the solution free energy.  $\mu_A^0$  and  $\mu_B^0$  are the molar Gibbs free energies of pure  $A$  and  $B$  respectively.

common to both the free energy curves. The intercept of the tangent with the vertical axes gives the chemical potentials, which are identical for each species whatever the phase, by virtue of the fact that the tangent is common.

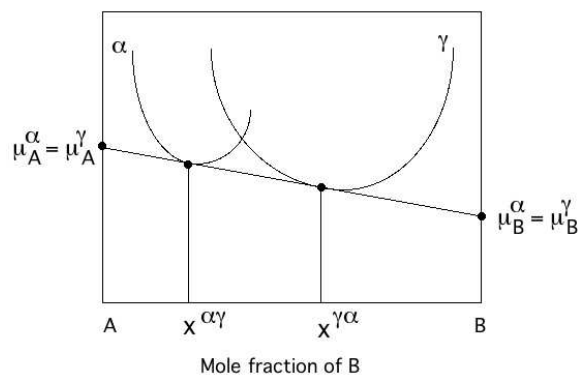


**Figure 5.2** The common tangent construction which defines the equilibrium chemical compositions of the  $\alpha$  and  $\gamma$ .

The concept of equilibrium in terms of phases that are *homogeneous* is rather restrictive. Instead, it is useful to consider equilibrium to exist locally. For example, it is a reasonable approximation that during diffusion-controlled growth, the compositions of the phases in contact at the interface are such as to allow equilibrium to exist locally even though there may be concentration gradients in the matrix ahead of the interface. As long as the phases are not too inhomogeneous, as with some artificial multilayered structures or during spinodal decomposition, classical equilibrium thermodynamics can be applied locally without raising any fundamental difficulties.

A form of constrained equilibrium which arises in substitutionally alloyed steels is *paraequilibrium*, in which the ratio of iron to substitutional solute atoms remains the same everywhere, but subject to that constraint, the carbon atoms achieve a uniform chemical potential at all locations. Either the substitutional solute atoms or the iron atoms are then trapped by the advancing transformation interface. An atom is said to be trapped when its chemical potential increases on transfer across the interface.

Transformation can occur without any composition change at a temperature below  $T_0$ , where the parent and product phases of identical composition have equal free energy (Fig. 1.5).

The concepts of local equilibrium, paraequilibrium and transformation without any change in composition are easy to visualise and formulate. However, between the states of local and paraequilibrium, there can in principle exist an infinite number of alternatives in which the substitutional solutes partly partition between the phases. There may similarly be a gradation between paraequilibrium and composition-invariant transformation in which the extent to which carbon is partitioned may vary. Such intermediate states would have to be stabilised by some other rate-controlling factor such as interface kinetics. They would otherwise tend towards equilibrium, because any perturbation which leads to a reduction in free energy would grow. We shall see in Chapter 6 that the stabilisation of such nonequilibrium states is in certain circumstances possible for solid-state transformations in steels.

### 5.3 Stored Energy due to Transformation

Much of the stored energy of bainite comes from the distortions due to the shape deformation accompanying transformation. For a plate in the form of an oblate ellipsoid of semi-axes  $R$ ,  $R$  and  $y$ , with  $R \gg y$ , the strain energy per mole is given by (Christian, 1958):

$$G_s = \frac{\mu V_m}{1 - \nu} \left[ \frac{2}{9} (1 + \nu) \Delta^2 + \frac{\pi y}{4R} \zeta^2 + \frac{(1 - \nu) \pi y}{3R} \Delta \zeta \right] + \frac{1}{2} \mu V_m \frac{(2 - \nu) \pi y}{4(1 - \nu) R} s^2 \quad (5.4)$$

where  $\mu$  and  $\nu$  are the shear modulus and Poisson's ratio respectively of the surrounding matrix,  $V_m$  is the molar volume of the matrix,  $\Delta$  is the uniform dilatation accompanying transformation,  $\zeta$  is the additional uniaxial dilatation normal to the habit plane and  $s$  is the shear component of the shape change (Fig. 5.3).

The uniform dilatation  $\Delta$  term has been used to interpret the crystallography of bainite but its existence has not been confirmed by measurements and so it is neglected in further discussions. The energy due to the shear and  $\zeta$  strains comes to about  $400 \text{ J mol}^{-1}$  for bainite (Bhadeshia, 1981c). This is less than the corresponding term for martensite, which is about  $600 \text{ J mol}^{-1}$  because bainite plates usually have a smaller aspect ratio ( $y/R$ ).

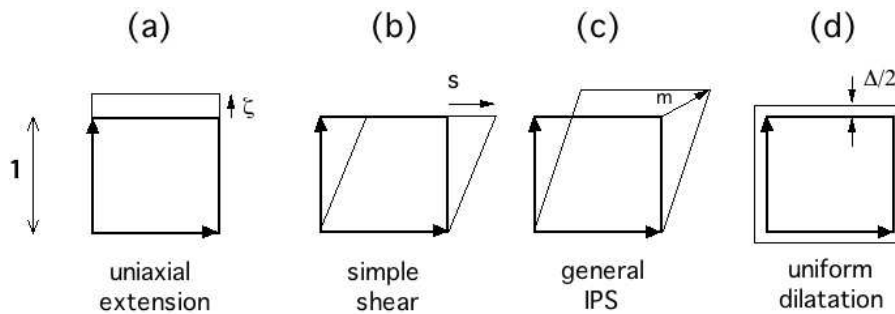


**Figure 5.3** The strains used in equation 5.4. (a) Uniaxial dilatation normal to the habit plane; (b) shear parallel to the habit plane; (c) a combination of shear and uniaxial dilatation which defines the invariant-plane strain (IPS) which is the shape deformation associated with bainite; (d) uniform dilatation.

The shear and dilatational components of the shape change are similar for martensite and bainite.

The stored energy of  $400 \text{ J mol}^{-1}$  applies strictly to an isolated plate of bainite which is elastically accommodated in the surrounding austenite. However, bainite grows as clusters of plates and it may be more appropriate to consider the sheaf as a whole, in which case the stored energy may be reduced by averaging the shear over the thickness of the sheaf in which the bainite plates are separated by intervening films of austenite or other phases.

The strain energy can be reduced by plastic relaxation. This is particularly relevant for bainite because the yield strength of austenite is reduced at high temperatures. The plastic deformation causes an increase in dislocation density, but since the deformation is driven by the shape change, the strain energy calculated on the basis of an elastically accommodated shape change should be an upper limit (Christian, 1979).<sup>1</sup> A material containing dislocations is expected to be more compliant to the application of an elastic stress because the dislocations can bow in response to the stress (Mott, 1952). Ghosh and Olson (2002) have shown that there is a reduction of about 5% in the shear modulus of dislocated-martensite when compared against appropriate single-crystal data. Such a reduction must help reduce the strain energy, which scales with the modulus. There may also be a reduction in the stored energy per unit volume as transformation proceeds because of the tendency of adjacent sheaves to grow in mutually accommodating formations (Hehemann, 1970).

In martensitic reactions, transformation twinning can contribute about  $100 \text{ J mol}^{-1}$  of stored energy; this is not applicable to bainite where the lattice-invariant shear is slip.

<sup>1</sup>Bouaziz et al. (2003) have used the dissipation due to plastic deformation to explain the incomplete reaction phenomenon. However, the plastic work is incorrectly expressed per mole of austenite when the comparison is made against the free energy change accompanying transformation.

## 5.4 Thermodynamics of Growth

### 5.4.1 Substitutional Solutes during Growth

The atom-probe experiments described in Chapter 2 have established that there is no re-distribution of substitutional solutes during the bainite transformation. These experiments cover the finest conceivable scale for chemical analysis. They rule out any mechanism that requires the diffusion of substitutional solutes. This includes the local equilibrium modes of growth.

By contrast, all experimental data show that pearlite grows with the diffusion of substitutional solute atoms (Ridley, 1984; Al-Salman and Ridley, 1984). Chromium, molybdenum, silicon and cobalt have been shown to partition at the reaction front. The extent of partitioning is smaller for manganese and nickel, especially at large undercoolings, but there is localised diffusion (Hillert, 1981; Ridley, 1984). These observations are expected because pearlite is the classic example of a reconstructive transformation.

Solute in iron affect the relative stabilities of austenite and ferrite. This thermodynamic effect is identical for all transformations. We have seen, however, that substitutional solutes do not diffuse at all during displacive transformations whereas they are required to do so during reconstructive transformation. It is for this reason that the observed effect of solutes on the rate of transformation is larger for reconstructive than for displacive transformations (Fig. 5.4).

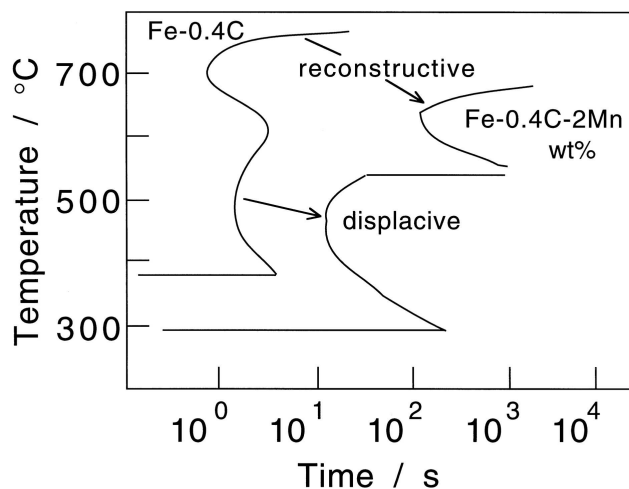


**Figure 5.4** Time-temperature-transformation diagrams showing the larger retarding effect that manganese has on a reconstructive transformation compared with its influence on a displacive transformation.

### 5.4.2 Interstitial Solutes during Growth

It is simple to establish that martensitic transformation is diffusionless by measuring the phase compositions before and after transformation. Bainite forms at somewhat higher

temperatures where the carbon can escape out of the plate within a fraction of a second. Its original composition cannot therefore be measured directly.

There are three possibilities. The carbon may partition during growth so that the ferrite may never contain any excess carbon. The growth may, on the other hand, be diffusionless with carbon being trapped by the advancing interface. Finally, there is an intermediate case in which some carbon may diffuse with the remainder being trapped to leave the ferrite partially supersaturated.

Diffusionless growth requires that transformation occurs at a temperature below  $T_0$ , when the free energy of bainite becomes less than that of austenite of the same composition. Growth without diffusion can only occur if the carbon concentration of the austenite lies to the left of the  $T_0$  curve (Fig. 1.5).

Suppose that the plate of bainite forms without diffusion, but that any excess carbon is soon afterwards rejected into the residual austenite. The next plate of bainite then has to grow from carbon-enriched austenite (Fig. 5.5a). This process must cease when the austenite carbon concentration reaches the  $T_0$  curve. The reaction is said to be incomplete, since the austenite has not achieved its equilibrium composition given by the  $Ae_3$  phase boundary. If, on the other hand, the ferrite grows with an equilibrium carbon concentration then the transformation should cease when the austenite carbon concentration reaches the  $Ae_3$  curve.

It is found experimentally that the transformation to bainite does indeed stop at the  $T_0$  boundary (Fig. 5.5b). The balance of the evidence is that the growth of bainite below the  $B_S$  temperature involves the successive nucleation and martensitic growth of sub-units, followed in upper bainite by the diffusion of carbon into the surrounding austenite. The possibility that a small fraction of the carbon is nevertheless partitioned during growth cannot entirely be ruled out, but there is little doubt that the bainite is at first substantially supersaturated with carbon.

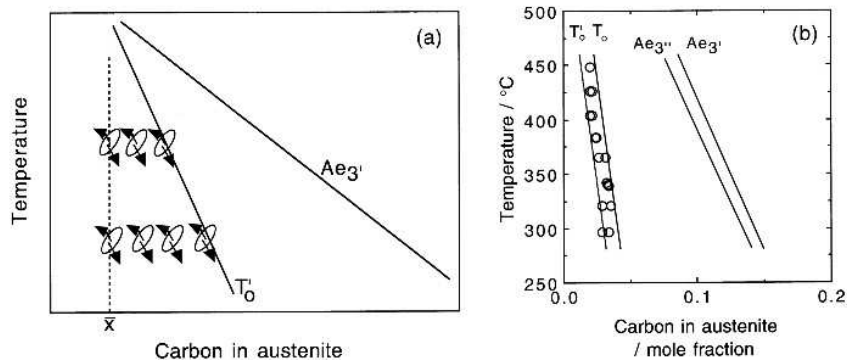


**Figure 5.5** (a) The incomplete-reaction phenomenon. A plate of bainite grows without diffusion, then partitions some of its excess carbon into the residual austenite. The next plate thus grows from carbon-enriched austenite. This process can only continue until  $x_\gamma = x'_{T_0}$ . For paraequilibrium growth, the transformation should proceed until the carbon concentration reaches the  $Ae_3''$  curve. (b) Experimental data on the incomplete reaction phenomenon for Fe-0.43C-3Mn-2.12Si alloy (Bhadeshia and Edmonds, 1979a).

The chemical potentials are not uniform in the steel when the bainite reaction stops. The reaction remains incomplete in that the fraction of bainite is less than that expected from

a consideration of equilibrium between austenite and ferrite. The carbon concentration of the austenite at the point where the bainite reaction stops is far less than given by the  $Ae_{3'}$  phase boundary.<sup>2</sup> This “incomplete reaction phenomenon” explains why the degree of transformation to bainite is zero at the  $B_S$  temperature and increases with undercooling below  $B_S$  in steels where other reactions do not overlap with the formation of bainitic ferrite. The  $T'_0$  curve has a negative slope on a temperature/carbon concentration plot, permitting the austenite to accommodate ever more carbon at lower temperatures.

The experimental evidence for the incomplete reaction phenomenon comes in many forms. The carbon concentration of the residual austenite at the point where the reaction stops has been measured using X-ray techniques, lattice imaging using high resolution transmission electron microscopy, field ion microscopy/atom probe methods (Bhadeshia and Waugh, 1982b), electron energy loss spectroscopy (Scott and Drillet, 2007), quantitative metallography and dilatometry. Real time neutron transmission experiments have also demonstrated the effect (Meggers et al., 1994). It is always found that the concentration is far below that required by equilibrium or paraequilibrium, and is on the whole consistent with that given by the  $T'_0$  curve of the phase diagram. The experimental evidence has been reviewed by Christian and Edmonds (1984). In dilatometric experiments, the length change due to transformation is zero above the  $B_S$  temperature, even though that temperature may be well within the  $\gamma + \alpha$  phase field. The maximum length change then increases with undercooling below the  $B_S$  temperature. Numerous examples of the type illustrated in Fig. 5.6 can be found in the published literature.

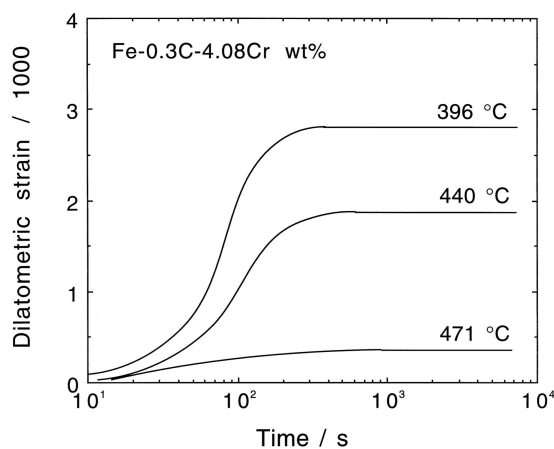


**Figure 5.6** Dilatometric length change data illustrating the incomplete reaction phenomenon for a Fe-0.3C-4.08Cr wt% alloy (Bhadeshia, 1981a).

Dilatometry can also be used to indirectly determine the carbon concentration of the residual austenite by measuring its martensite-start temperature. This measurement is independent of the presence of cementite and hence can be carried out in steels which do not contain cementite inhibitors. Recent results of this type are illustrated in Fig. 5.7 and confirm the incomplete reaction phenomenon.

<sup>2</sup> $Ae_{3'}$  refers to the paraequilibrium  $(\alpha + \gamma)/\gamma$  phase boundary.  $Ae_{3''}$  is the corresponding boundary allowing for the stored energy of bainite

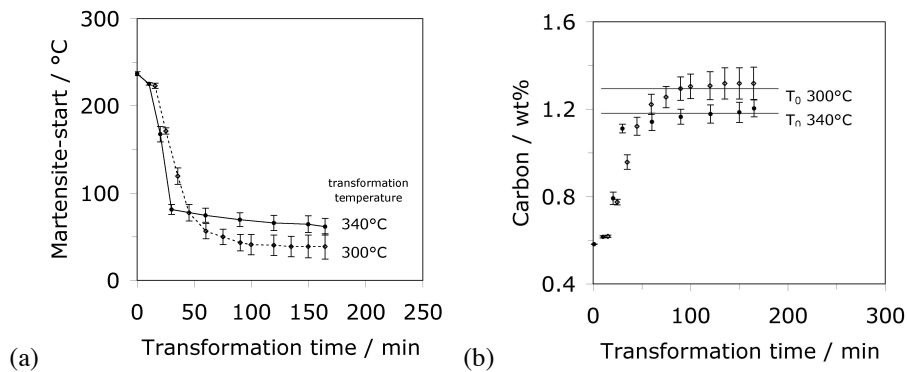


**Figure 5.7** The martensite-start (a) and carbon concentration (b) of residual austenite as a function of isothermal transformation temperature and time. The data are for Fe-0.18C-0.8Mn-1.67Ni-0.56Cr-0.71Mo-0.14Cu wt% steel (Chupatanakul and Nash, 2006).

The failure of the bainite reaction to reach completion reveals the role of carbon during transformation. An important consequence is that the  $T_0$  curve can be used in the design of steels and associated processes.<sup>3</sup> In the context of bainite, the curve gives the limiting carbon concentration  $x_{T_0}'$  of the austenite, a parameter of enormous importance in devising microstructures containing stable austenite. A discussion of the procedure is deferred to Chapters 12 and 13, but Fig. 5.8 illustrates the remarkable predictive ability of the concept for a large variety of steels. In contrast, the  $Ae_{3\gamma}$  phase boundary gives very poor estimates of the austenite composition in the context of bainite.

The incomplete transformation leaves films of austenite between bainite plates. These films improve the properties of steels. It has been found that the thickness of these austenite films can be estimated by assuming that the carbon diffusion field around an existing plate of ferrite prevents the close approach of another parallel plate. This is because the regions of austenite with the highest carbon concentration i.e.  $x_\gamma > x_{T_0}'$  are unable to transform to bainite (Fig. 5.9). This simple theory predicts a dependence of film thickness on the bainite plate thickness since the net quantity of carbon partitioned into the austenite must increase with the thickness of the bainite plate. The correlation can be seen in Fig. 5.9c. Note that a better fit is seen in Fig. 5.9b because those calculations include both the plate thickness and the effects of alloying elements on the  $T_0'$  condition.

Shaposhnikov and Mogutnov (2008) attempted to explain the fact the carbon concentration in austenite after the formation of bainite is much less than  $x_\gamma^{Ae_{3\gamma}'}$  by arguing that  $x_\gamma$  is given by the extrapolated  $(\gamma/\gamma + \theta)$  phase boundary. This is incorrect because the bainite reaction would not stop when this limit is reached because paraequilibrium cementite precipitation does not limit the bainite transformation. Furthermore, the slope of the transformation temperature versus the measured  $x_\gamma$  is negative whereas that of the  $x_\gamma/\gamma + \theta$  phase boundary is positive.

<sup>3</sup>There are now numerous examples of this, a few of which are listed here: Bhadeshia and Edmonds (1983a,b); Thomson et al. (2000); James and Thomson (1999); Kutsov et al. (1999); Matsuda et al. (2002); Jacques et al. (2002); Caballero et al. (2006, 2001a,b); Gomez et al. (2008); Yang and Bhadeshia (2008); Gomez et al. (2009b,a); Caballero et al. (2013a); Sugimoto et al. (2004); Khare et al. (2010); Duong et al. (2014); Das and Haldar (2014); Zhang et al. (2015).

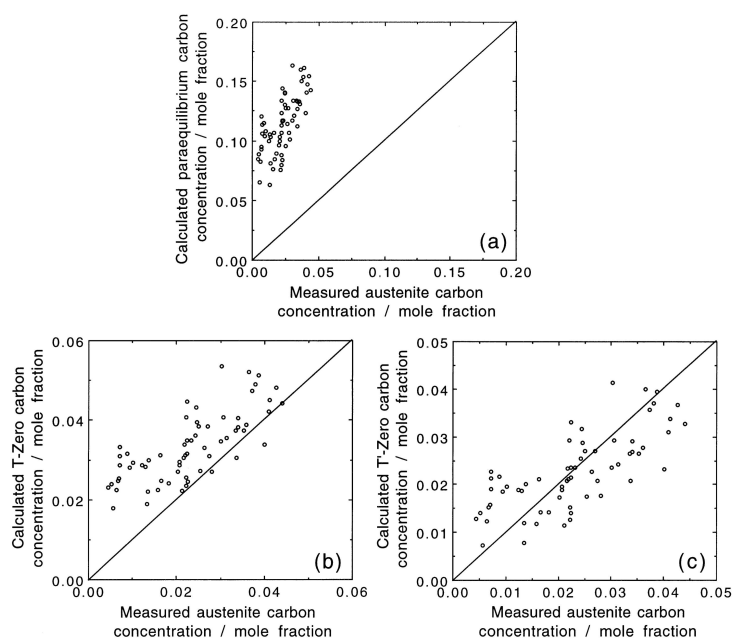


**Figure 5.8** A comparison of the measured carbon concentration of the austenite which remains untransformed when the bainite reaction stops, versus that calculated using the  $A_{e3'}$ ,  $T_0$  and  $T_0'$  criteria. After Chang and Bhadeshia (1995a).

**Alternative Interpretation** In explaining the discrepancies between the measured and calculated diffusion-controlled growth rates of plates of ferrite, Hillert (1960); Hillert and Höglund (2004) proposed that there is a notional thermodynamic barrier to the growth. The barrier is attributed to some of the free energy being dissipated in interfacial processes because the plates involve “coherent” interfaces rather than “incoherent” ones where the growth is proposed to be diffusion-controlled. The method neglects the displacive mechanism by which the plates of ferrite grow, and the necessarily glissile interface associated with the growth, in which case interface processes would be insignificant. The growth data for Widmanstätten ferrite have in fact been analysed satisfactorily using diffusion-controlled growth theory (Bhadeshia et al., 1985) so the discrepancy highlighted (Hillert, 1960) does not in fact exist.

Solute-drag effects (section 6.6.4) are sometimes invoked in order to explain discrepancies in kinetic data. For example, Wu et al. (2003) assigned a binding energy of about  $20\text{--}30\text{ kJ mol}^{-1}$  for molybdenum located at transformation interfaces, but were unable to obtain quantitative closure (Takahashi, 2004). An analysis by Chen et al. (2013) based again on solute within the interface is flawed because it contradicts experimental evidence of the absence of such segregation to the transformation interface and indeed most of the physical characteristics of bainite. Arbitrary potential wells were assumed for the interface.

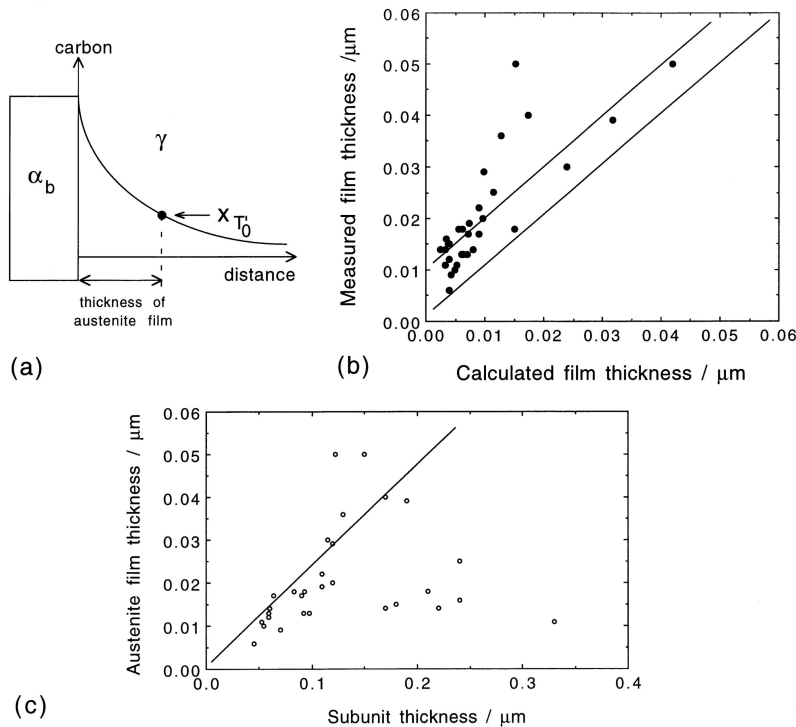


**Figure 5.9** (a) The thickness of the austenite film is determined by the point where the carbon concentration in the residual austenite is  $x_{T_0}$ . (b) Comparison of measured and calculated austenite film thicknesses for a variety of alloys. (c) Austenite film thickness versus that of the adjacent bainite sub-unit (Chang and Bhadeshia, 1995a).

### 5.4.3 Approach to Equilibrium

Although the bainite reaction stops before equilibrium is reached, the remaining austenite can continue to decompose by reconstructive transformation, albeit at a greatly reduced rate. Pearlite often forms sluggishly after bainite. The delay between the cessation of bainite and the start of pearlite varies with the steel composition and transformation temperature. In one example the bainite reaction stopped in a matter of minutes, with pearlite growing from the residual austenite after some 32 h at the transformation temperature of 450°C. In another example, the isothermal reaction to lower bainite at 478 °C was completed within 30 min, but continued heat treatment for 43 days caused the incredibly slow reconstructive transformation to two different products. One of these was alloy-pearlite which nucleated at the austenite grain boundaries and which developed as a separate reaction (Fig. 4.5a). The other involved the irregular, epitaxial and reconstructive growth of ferrite from the existing bainite. The extent of ferrite growth in 43 days was comparable to the thickness of the bainite plates, which took just a few seconds to form (Bhadeshia, 1981a, 1982b).

The two-stage decomposition of austenite is more difficult to establish for plain carbon steels where the reaction rates are large, with the pearlite reaction occurring a few seconds after bainite (Klier and Lyman, 1944). One interesting observation is that in niobium-

containing 0.05 wt% steel, the retardation of allotriomorphic ferrite is sufficient to reveal the incomplete reaction phenomenon for bainite, but considerable overlap occurs between the two reactions in the absence of niobium (Furuhara et al., 2010). This is a consequence of the well-known effect of niobium in retarding the nucleation of allotriomorphic ferrite by segregated niobium at the austenite grain boundaries (section 13.5.4).

## 5.5 Quench and Partitioning

A process in which austenite is transformed partially into martensite, and the temperature is then raised to permit some of the excess carbon to partition into the residual parent phase, is known as the *quench and partitioning* treatment (Speer et al., 2003, 2004, 2015). It has led to a new class of steels that contain retained austenite and tempered martensite, with the former phase stabilised by enrichment with carbon. Although this phenomenon is not strictly connected to bainite, the partitioning process is in principle the same as when supersaturated bainitic ferrite partitions carbon into the austenite shortly after its growth is arrested. There is, however, an important difference; that the fraction of martensite is essentially fixed at the point that partitioning begins since the temperature at which partitioning is induced is greater than that at which martensite forms. In contrast bainite formation continues provided the carbon concentration of the austenite is less than that specified by the  $T_0'$  condition.

It has been known for some time that the retained austenite associated with martensite that grows at high temperatures contains carbon in excess of the average concentration (Rao and Thomas, 1979; Barnard et al., 1981b) although the mechanism involved lacked clarity (Bhadeshia, 1983b).

In their thermodynamic model for the process in which fixed volume fractions of martensite and austenite of average carbon concentration  $\bar{x}$  are in contact, Speer et al. (2003) considered that carbon partitioning is driven by the need to equalise the chemical potential of carbon in the austenite and ferrite. However, given the constraint that the number of iron atoms in the martensite and ferrite is fixed, Fig. 5.10a illustrates the fact that it is possible to have a variety of pairs of tangents touching the  $\alpha$  and  $\gamma$  free energy curves that are consistent with  $\mu_C^\alpha = \mu_C^\gamma$  though  $\mu_{Fe}^\alpha \neq \mu_{Fe}^\gamma$ . To make the selection unique requires the implementation of the following conditions: the first ensuring that the average concentration of carbon lies between that in ferrite and austenite, and the second ensuring mass balance:

$$\bar{x}_C \ni x_C^\alpha \quad \text{and} \quad x_C^\gamma \quad (5.5)$$

$$\bar{N}_C = N_C^\gamma + N_C^\alpha \quad (5.6)$$

where  $N_C$  is the number of carbon atoms in the phase identified by the superscript, and  $\bar{N}_C$  is the total number of carbon atoms. The condition outlined in relation 5.5 is illustrated in Fig. 5.10, and since during quenching and partitioning,  $N_{Fe}^\alpha$  and  $N_{Fe}^\gamma$  are fixed, equation 5.6 leads to:

$$\frac{N_C}{N_{Fe} + N_C} = \frac{N_{Fe}^\alpha}{N_{Fe} + N_C} \left( \frac{N_C^\alpha}{N_{Fe}^\alpha + N_C^\alpha} \right) + \frac{N_{Fe}^\gamma}{N_{Fe} + N_C} \left( \frac{N_C^\gamma}{N_{Fe}^\gamma + N_C^\gamma} \right)$$

$$\text{so that} \quad \bar{x}_C = x_\alpha^\alpha x_C^\alpha + x_\gamma^\gamma x_C^\gamma \quad (5.7)$$

where  $x_\alpha^\alpha$  and  $x_\gamma^\gamma$  represent the mole fractions of the ferrite and austenite respectively. These ideas are relevant to bainite since we now know that considerable excess carbon can be found in solid-solution within the ferrite (Chapter 2).

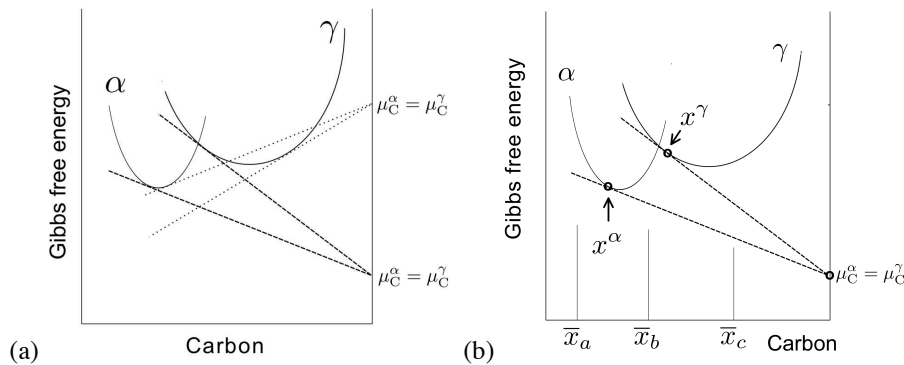


**Figure 5.10** Iron-carbon system. (a) Multiple conditions for which the chemical potential of carbon can be equalised. (b) Illustration of the fact that  $\bar{x} \ni x_C^\alpha$  and  $x_C^\gamma$  so that  $\bar{x}_a$  and  $\bar{x}_c$  would be inconsistent with the selected tangents.

## 5.6 Summary

The thermodynamic description of the bainite reaction is linked to its mechanism of growth and depends on the behaviour of solute atoms during transformation. By far the largest contribution to the stored energy of bainite is due to the invariant-plane strain shape deformation. The contributions from interfacial area are, by comparison, negligible during the growth stage. The dislocation density of bainite has its origins in the plastic accommodation of the shape change. The energy of the dislocations is therefore already accounted for in the estimate of an elastically accommodated shape change.

Substitutional solutes do not partition at all during the bainite reaction. Their primary effect is through their influence on the relative thermodynamic stabilities of the austenite and ferrite phases. The trapping of solutes in the bainite raises its free energy.

The fact that the transformation stops well before equilibrium is achieved is due to a mechanism in which growth is diffusionless, although the carbon atoms are partitioned soon afterwards from supersaturated ferrite. This mechanism has recently become prominent in the design of the so-called quench and partitioning steels, where partially martensitic samples are heat-treated in order to allow carbon to diffuse into the adjacent austenite.



## CHAPTER 6

---

### KINETICS

---

There are three distinct events in the evolution of bainite (Fig. 6.1). A sub-unit nucleates at an austenite grain boundary and lengthens until its growth is arrested by plastic deformation within the austenite. New sub-units then nucleate at its tip, and the sheaf structure develops as this process continues. The average lengthening rate of a sheaf must be smaller than that of a sub-unit because of the delay between successive sub-units. The volume fraction of bainite depends on the totality of sheaves growing from different regions in the sample. Carbide precipitation influences the reaction rate by removing carbon either from the residual austenite or from the supersaturated ferrite.

#### 6.1 Thermodynamics of Nucleation

It was shown in Chapter 5 that the equilibrium compositions  $x^{\alpha\gamma}$  and  $x^{\gamma\alpha}$  of ferrite and austenite respectively, are obtained using the common tangent construction. The same construction can be used to determine the change in free energy  $\Delta G^{\gamma \rightarrow \gamma' + \alpha}$  when austenite of composition  $\bar{x}$  decomposes into the equilibrium mixture of ferrite and carbon-enriched austenite ( $\gamma'$ ), Fig. 6.2a.

The equilibrium fraction of ferrite is given by the lever rule as  $(x^{\gamma\alpha} - \bar{x}) / (x^{\gamma\alpha} - x^{\alpha\gamma})$ . It follows that the free energy change per mole of ferrite is

$$\Delta G_2 = \Delta G^{\gamma \rightarrow \gamma' + \alpha} \times \frac{x^{\gamma\alpha} - x^{\alpha\gamma}}{x^{\gamma\alpha} - \bar{x}}. \quad (6.1)$$

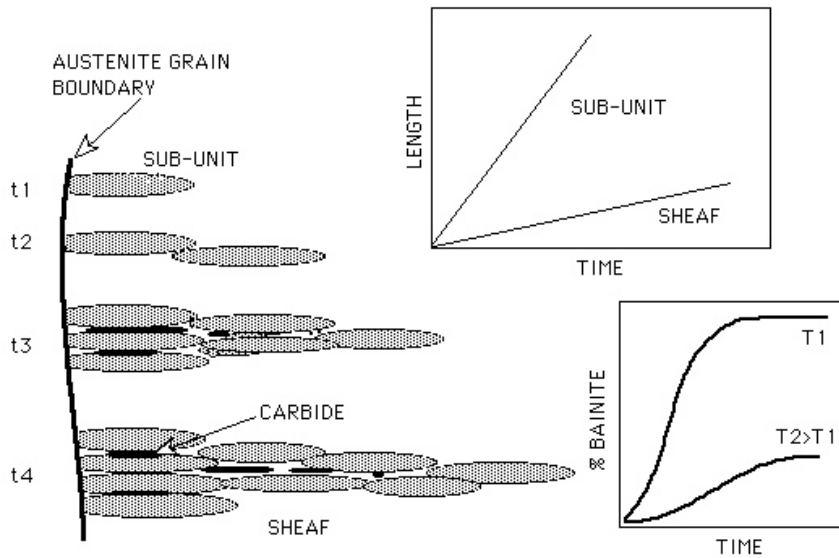


**Figure 6.1** The microstructural features relevant in the kinetic description of a bainitic microstructure. There is the lengthening of sub-units and of sheaves, the latter by the repeated nucleation of sub-units, the precipitation of carbides, and the change in volume fraction as a function of time and temperature.

There is a significant change in the chemical composition of the austenite when it decomposes into the equilibrium mixture of ferrite and austenite. A ferrite nucleus on the other hand has such a small volume that it hardly affects the composition of the remaining austenite. The calculation of the free energy change associated with nucleation must therefore take into account that only a minute quantity of ferrite is formed. Consider the change  $\Delta G_2$  as austenite decomposes to a mixture of ferrite and enriched-austenite of composition  $x^\gamma = x^{\gamma\alpha}$ . As the fraction of ferrite is reduced,  $x^\gamma$  and  $\bar{x}$  move towards each other causing the line  $AB$  to tilt upwards. In the limit that  $x^\gamma = \bar{x}$ ,  $AB$  becomes tangential to the curve at  $\bar{x}$ . The free energy change for the formation of a mole of ferrite nuclei of composition  $x^\alpha$  is then given by  $\Delta G_3$ , Fig. 6.2b.

The greatest reduction in free energy during nucleation is obtained if the composition of the ferrite nucleus is set to a value  $x_m$ , given by a tangent to the ferrite free energy curve which is parallel to the tangent to the austenite free energy curve at  $\bar{x}$ , as shown in Fig. 6.2b. This maximum possible free energy change for nucleation is designated  $\Delta G_m$ .

There is simplification when the transformation occurs without composition change (Fig. 6.2c). The change  $\Delta G^{\gamma \rightarrow \alpha}$  is the vertical distance between the austenite and ferrite free energy curves at the composition of interest.

### 6.1.1 Transformation-Start Temperature

It is a common observation that the Widmanstätten-start ( $W_S$ ) and bainite-start ( $B_S$ ) temperatures are more sensitive to the steel composition than is the  $Ae_3$  temperature. This indicates that the influence of solutes on the nucleation of Widmanstätten ferrite and bainite is more than just thermodynamic (Fig. 6.3a).

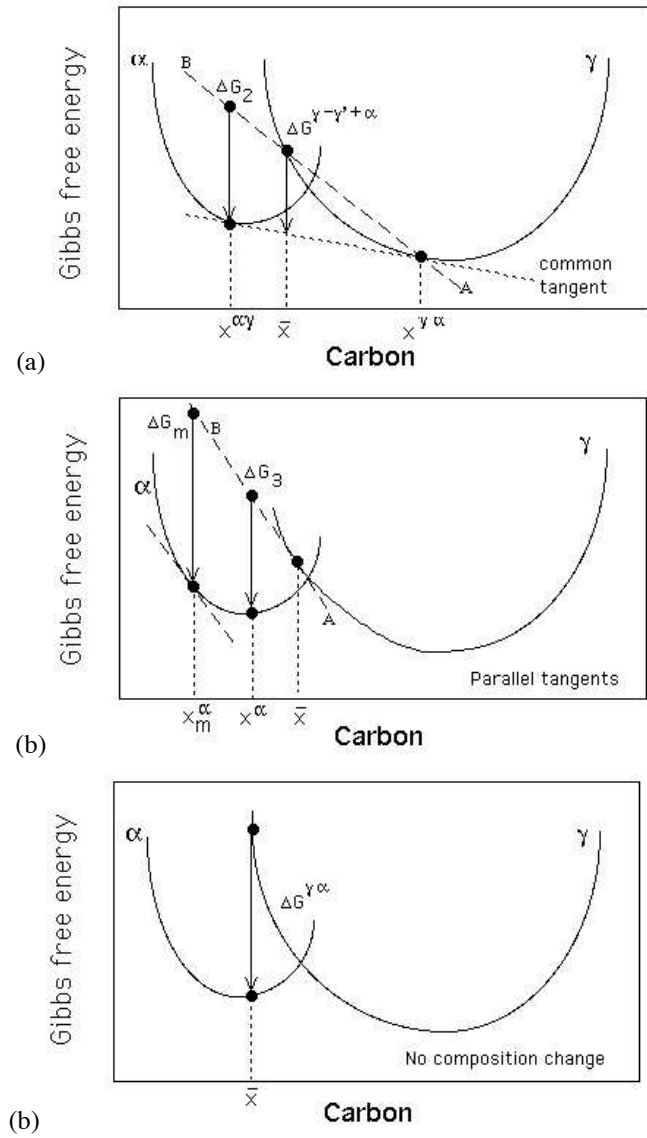


**Figure 6.2** Free energy diagrams illustrating the chemical free energy changes during the nucleation and growth of ferrite from austenite of composition  $\bar{x}$ . The term  $\gamma'$  refers to austenite which is enriched in carbon as a result of the decomposition of austenite of composition  $\bar{x}$  into a mixture of ferrite and austenite.

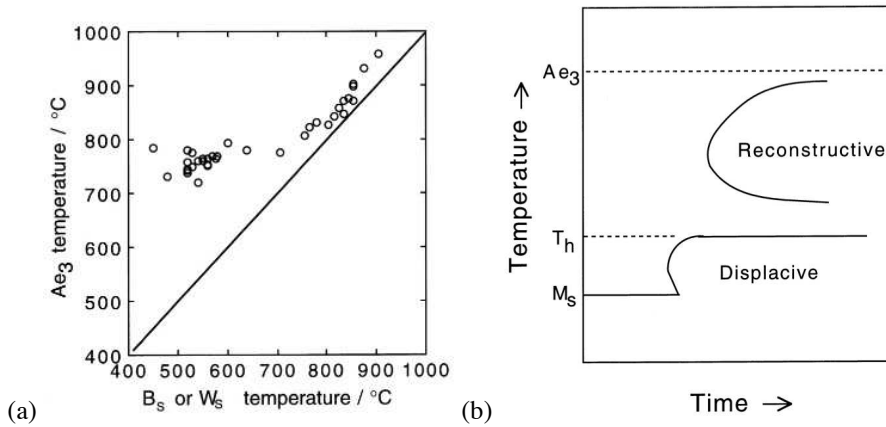


**Figure 6.3** (a) The variation of the Widmanstätten-start and bainite-start temperatures as a function of the  $A_{e3}$  temperature of the steel concerned (Ali and Bhadeshia, 1990). (b) Schematic TTT diagram illustrating the two C-curves and the  $T_h$  temperature.

Some clues to this behaviour come from studies of time-temperature-transformation diagrams, which consist essentially of two C-curves. The lower C-curve has a characteristic flat top at a temperature  $T_h$ , which is the highest temperature at which ferrite can form by displacive transformation (Fig. 6.3b). The transformation product at  $T_h$  may be Widmanstätten ferrite or bainite.

The driving force  $\Delta G_m$  available for nucleation at  $T_h$ , is plotted in Fig. 6.4a, where each point comes from a different steel. The transformation product at  $T_h$  can be Widmanstätten ferrite or bainite, but it is found that there is no need to distinguish between these phases for the purposes of nucleation. The same nucleus can develop into either phase depending on the prevailing thermodynamic conditions. The analysis proves that carbon must partition during the nucleation stage in order always to obtain a reduction in free energy. The situation illustrated in Fig. 6.4b is not viable since diffusionless nucleation would in some cases lead to an increase in the free energy.

The plots in Fig. 6.4 are generated using data from diverse steels. Fig. 6.4a represents the free energy change  $\Delta G_m$  at the temperature  $T_h$  where displacive transformation first occurs. The free energy change can be calculated from readily available thermodynamic data. It follows that Fig. 6.4a can be used to estimate  $T_h$  for any steel. The equation fitted to the data in Fig. 6.4a is (Ali and Bhadeshia, 1990):

$$G_N = C_1(T - 273.18) - C_2 \quad \text{J mol}^{-1} \quad (6.2)$$

where the fitting constants are found to be  $C_1 = 3.637 \pm 0.2 \text{ J mol}^{-1} \text{ K}^{-1}$  and  $C_2 = 2540 \pm 120 \text{ J mol}^{-1}$  for the temperature range 670–920 K.  $G_N$  is to be regarded as a *universal nucleation function*, because it defines the minimum driving force necessary to achieve a perceptible nucleation rate for Widmanstätten ferrite or bainite in any steel. Equations such as 6.2 use thermodynamic databases to calculate the free energies during their derivation. They are, therefore, database dependent so the numerical values will differ appropriately (e.g. Uhm et al., 2005).

There has been a great deal of interest in high-carbon steels with concentrations around 1 wt% since the advent of nanostructured bainite (Chapter 14). Fig. 6.5 shows that such steels do not need special consideration with respect to the nucleation model for ordi-

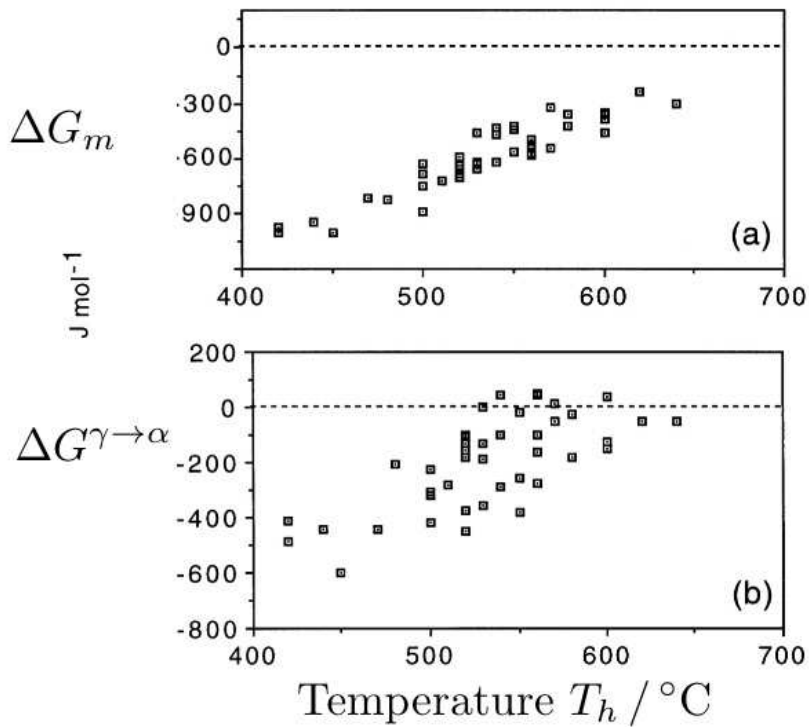


**Figure 6.4** The free energy change necessary in order to obtain a detectable degree of transformation. Each point represents a different steel and there is no distinction made between Widmanstätten ferrite or bainite. (a) Calculated assuming the partitioning of carbon during nucleation. (b) Calculated assuming that there is no change in composition during nucleation. After Bhadeshia (1981c).

nary alloys; austempered ductile irons that also contain a high-carbon concentration in the austenite are consistent with this nucleation model (Laneri et al., 2008).

### 6.1.2 Evolution of the Nucleus

The nucleus is identical for Widmanstätten ferrite and for bainite; it must therefore be growth which distinguishes them. But what determines whether the nucleus evolves into bainite or Widmanstätten ferrite?

The answer is straightforward. If diffusionless growth cannot be sustained at  $T_h$  then the nucleus develops into Widmanstätten ferrite so that  $T_h$  is identified with  $W_S$ . A larger undercooling is necessary before bainite can be stimulated. If, however, the driving force at  $T_h$  is sufficient to account for diffusionless growth, then  $T_h = B_S$  and Widmanstätten ferrite does not form at all.

It follows that Widmanstätten ferrite forms below the  $Ae_3$  temperature when:

$$\begin{aligned} \Delta G^{\gamma \rightarrow \gamma' + \alpha} &< -G_{SW} \\ \Delta G_m &< G_N \end{aligned} \quad (6.3)$$

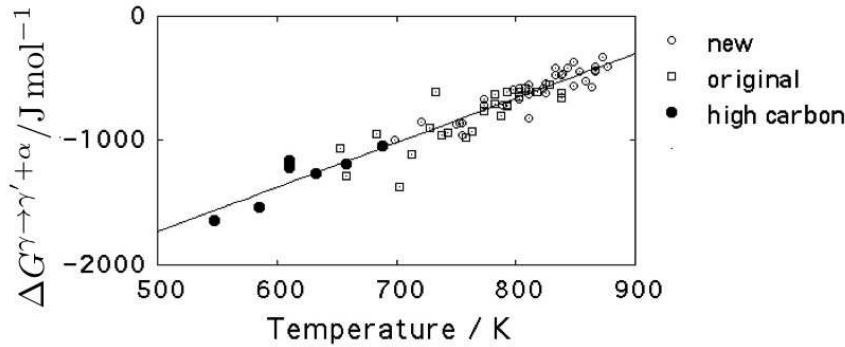


**Figure 6.5** Plot of the free energy change  $\Delta G^{\gamma \rightarrow \gamma' + \alpha}$ , assumed to be an approximation to  $\Delta G_m$ , versus the temperature at which bainite first forms, for a variety of steels (Steven and Haynes, 1956; Chang, 1999; Zhao et al., 2001a; Mateo and Bhadeshia, 2004).

where  $G_{SW}$  is the stored energy of Widmanstätten ferrite (about  $50 \text{ J mol}^{-1}$ ). The first of these conditions ensures that the chemical free energy change exceeds the stored energy of the Widmanstätten, and the second that there is a detectable nucleation rate.

Bainite is expected below the  $T'_0$  temperature when:

$$\begin{aligned} \Delta G^{\gamma \rightarrow \alpha} &< -G_{SB} \\ \Delta G_m &< G_N \end{aligned} \quad (6.4)$$

where  $G_{SB}$  is the stored energy of bainite (about  $400 \text{ J mol}^{-1}$ ). The universal function, when used with these conditions, allows the calculation of the Widmanstätten ferrite-start and bainite-start temperatures from a knowledge of thermodynamics alone.

In this scheme, carbon is partitioned during nucleation, but in the case of bainite, not during growth which is diffusionless. There is no inconsistency in this concept since a greater fraction of the free energy becomes available as the particle surface to volume ratio, and hence the influence of interfacial energy, decreases. The theory explains why both Widmanstätten ferrite and bainite can form during the early stages of isothermal transformation at temperatures close to  $B_S$  (Chang, 1999).

The scheme is illustrated in Fig. 6.6 which incorporates an additional function  $G_N^{\alpha'}$  representing the critical driving force  $\Delta G^{\gamma \rightarrow \alpha} \{M_S\}$  needed to stimulate martensite by an athermal, diffusionless nucleation and growth mechanism. Whereas it is reasonable to set  $G_N^{\alpha'}$  to a constant value for low alloy steels (Bhadeshia, 1981b,d) a function dependent on the strength of the austenite has to be used for steels containing large concentrations of solute (Ghosh and Olson, 1994).

The three common displacive transformations in steels include Widmanstätten ferrite, bainite and martensite. It is intriguing that they are not all found in every steel. Only martensite occurs in Fe-28Ni-0.4C wt%, whereas only bainite and martensite are found in Fe-4Cr-0.3C wt%. This is readily explained: steels *A*, *B* and *C* in Fig. 6.6 contain increasing quantities of austenite stabilising elements, with the driving force for transformation decreasing as the alloy content increases. In steel *A*, all three transformations are expected in turn as the temperature is reduced. For steel *B*, the temperature at which Widmanstätten ferrite nucleation becomes possible also corresponds to that at which bainite can grow. Bainite has a kinetic advantage so Widmanstätten ferrite does not form. Further alloying

increases the stability of the austenite so much that the nucleation of Widmanstätten ferrite and bainite is suppressed to temperatures below  $M_S$  in which case they do not form at all.

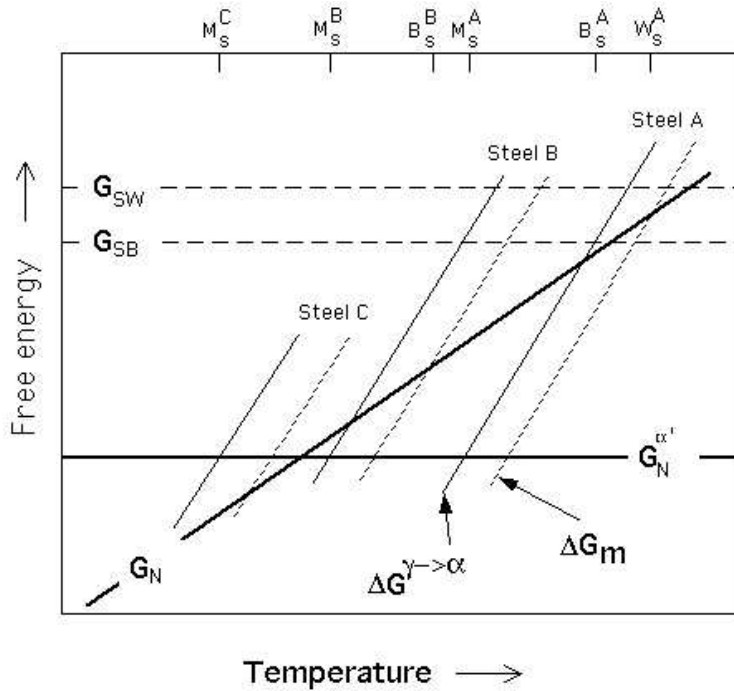


**Figure 6.6** Free energy curves for a low (*A*), medium (*B*) and high (*C*) alloy steel showing the conditions necessary for the nucleation and growth of Widmanstätten ferrite, bainite and martensite.

The nucleation condition for bainite (equation 6.4) becomes redundant for any steel in which Widmanstätten ferrite precedes bainite because they have a common nucleation mechanism.

An interesting prediction emerges from this rationale. For some steels the thermodynamic characteristics are such that the  $\Delta G_m$  curve intersects the  $G_N$  function at two points, Fig. 6.7a (Bhadeshia and Svensson, 1989c). Widmanstätten ferrite then occurs at high temperatures, there is an intermediate temperature range where neither Widmanstätten ferrite nor bainite can nucleate, until bainite formation becomes possible at a lower temperature. The lower C-curve thus splits into two segments, one for Widmanstätten ferrite and a lower temperature segment for bainite (Fig. 6.7b). This prediction from theory has been confirmed experimentally (Ali and Bhadeshia, 1991).

Finally, because  $G_N$  decreases linearly with  $T_h$ , it is expected that the  $W_S$  and  $B_S$  temperatures are depressed to a greater extent by solute additions than the  $Ae_3$  temperature. A larger driving force is needed to achieve a given rate of nucleation when the transformation is depressed to lower temperatures by alloying. A justification for the form of the universal nucleation function  $G_N$  is given in the next section.

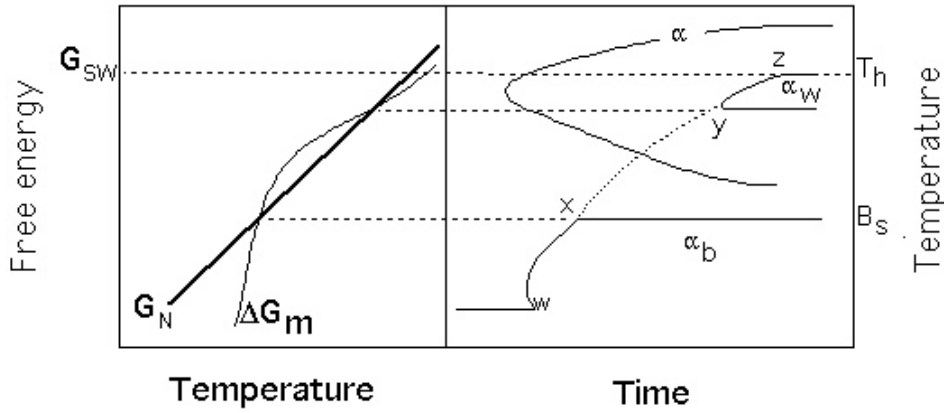


**Figure 6.7** (a) Free energy curves for the nucleation of Widmanstätten ferrite and bainite in a low alloy steel for which the  $\Delta G_m$  and  $G_N$  curves exhibit a double intersection. (b) Calculated TTT diagram for the same steel, showing how Widmanstätten ferrite and bainite form separate C-curves. The Widmanstätten ferrite and bainite C-curves would ordinarily be just one curve, joined by the line  $wxyz$ . After Ali and Bhadeshia (1991).

## 6.2 Possible Mechanisms of Nucleation

Phase fluctuations occur as random events due to the thermal vibration of atoms. An individual fluctuation may or may not be associated with a reduction in free energy, but it can only survive and grow if there is a reduction. There is a cost associated with the creation of a new phase, the interface energy, a penalty which becomes smaller as the particle surface to volume ratio decreases. In a metastable system this leads to a critical size of fluctuation beyond which growth is favoured.

Consider the homogeneous nucleation of  $\alpha$  from  $\gamma$ . For a spherical particle of radius  $r$  with an isotropic interfacial energy  $\sigma_{\alpha\gamma}$ , the change in free energy as a function of radius is:

$$\Delta G = \frac{4}{3}\pi r^3 \Delta G_{\text{chem}} + \frac{4}{3}\pi r^3 \Delta \Delta G_{\text{strain}} + 4\pi r^2 \sigma_{\alpha\gamma} \quad (6.5)$$

where  $\Delta G_{\text{chem}} = G_V^\alpha - G_V^\gamma$ ,  $G_V$  is the Gibbs free energy per unit volume of  $\alpha$  and  $\Delta \Delta G_{\text{strain}}$  is the strain energy per unit volume of  $\alpha$ . The variation in  $\Delta G$  with size is illustrated in Fig. 6.8; the activation barrier and critical size obtained using equation 6.5 are given by:

$$G^* = \frac{16\pi\sigma_{\alpha\gamma}^3}{3(\Delta G_{\text{chem}} + \Delta \Delta G_{\text{strain}})^2} \quad \text{and} \quad r^* = \frac{2\sigma_{\alpha\gamma}}{\Delta G_{\text{chem}} + \Delta \Delta G_{\text{strain}}} \quad (6.6)$$

The important outcome is that in classical nucleation the activation energy varies inversely with the square of the driving force. And the mechanism involves random phase fluctuations. It is questionable whether this applies to cases where thermal activation is in short supply. In particular, an activation barrier must be very small indeed if the transformation is to occur at a proper rate at low temperatures.

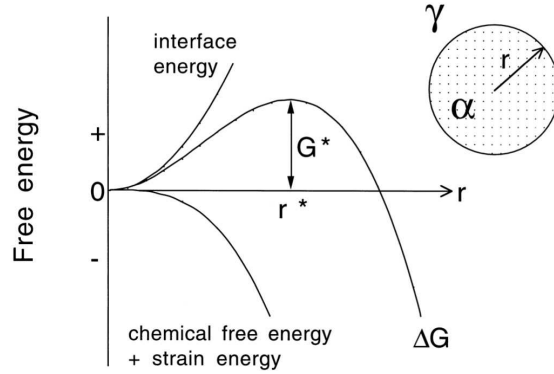


**Figure 6.8** The activation energy barrier  $G^*$  and the critical nucleus size  $r^*$  according to classical nucleation theory based on heterophase fluctuations.

One mechanism in which the barrier becomes sufficiently small involves the spontaneous dissociation of specific dislocation defects which are already present in the parent phase (Christian, 1951; Olson and Cohen, 1976). The dislocations are glissile so the mechanism does not require diffusion. The only barrier is the resistance to the glide of the dislocations. The nucleation event cannot occur until the undercooling is sufficient to support the faulting and strains associated with the dissociation process that leads to the creation of the new crystal structure (Fig. 6.9).

The free energy per unit area of fault plane is:

$$G_F = n_P \rho_A (\Delta G_{\text{chem}} + \Delta G_{\text{strain}}) + 2\sigma_{\alpha\gamma} \{n_P\} \quad (6.7)$$

where  $n_P$  is the number of close-packed planes participating in the faulting process,  $\rho_A$  is the spacing of the close-packed planes on which the faulting is assumed to occur. The fault energy can become negative when the austenite becomes metastable.

For a fault bounded by an array of  $n_P$  dislocations each with a Burgers vector of magnitude  $b$ , the force required to move a unit length of dislocation array is  $n_P \tau_o b$ .  $\tau_o$  is the shear resistance of the lattice to the motion of the dislocations.  $G_F$  provides the opposing stress via the chemical free energy change  $\Delta G_{\text{chem}}$ ; the physical origin of this stress is the fault energy which becomes negative so that the partial dislocations bounding the fault are repelled. The defect becomes unstable, *i.e.* nucleation occurs, when

$$G_F = -n_P \tau_o b \quad (6.8)$$

Take the energy barrier between adjacent equilibrium positions of a dislocation to be  $G_o^*$ . An applied shear stress  $\tau$  has the effect of reducing the height of this barrier (Conrad, 1964; Dorn, 1968):

$$G^* = G_o^* - (\tau - \tau_\mu) v^* \quad (6.9)$$

where  $v^*$  is an activation volume and  $\tau_\mu$  is the temperature independent resistance to dislocation motion (Fig. 6.10). In the context of nucleation, the stress  $\tau$  is not externally applied but comes from the chemical driving force. On combining the last three equations we obtain

$$G^* = G_o^* + \left[ \tau_\mu + \frac{\rho_A}{b} \Delta G_{\text{strain}} + \frac{2\sigma}{n_P b} \right] v^* + \frac{\rho_A v^*}{b} \Delta G_{\text{chem}} \quad (6.10)$$

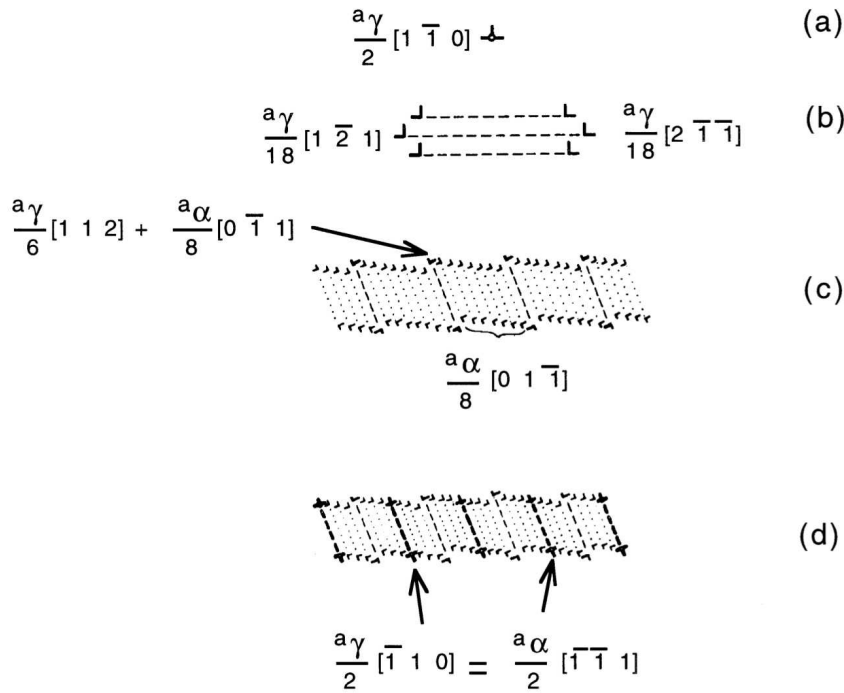


**Figure 6.9** Olson and Cohen model for the nucleation of  $\alpha$  martensite. (a) Perfect screw dislocation in austenite. (b) Three-dimensional dissociation over a set of three close-packed planes. The faulted structure is not yet that of  $\alpha$ . (c) Relaxation of fault to a body-centred cubic structure with the introduction of partial dislocations in the interface. (d) Addition of perfect screw dislocations which cancel the long range strain field of the partials introduced in (c).

It follows that with this model of nucleation the activation energy  $G^*$  will decrease *linearly* as the magnitude of the driving force  $\Delta G_{\text{chem}}$  increases. This direct proportionality contrasts with the inverse square relationship of classical theory.

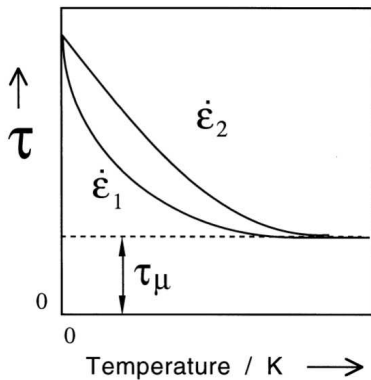


**Figure 6.10** Temperature dependence of the applied stress necessary to move a dislocation at two different strain rates ( $\dot{\epsilon}_2 > \dot{\epsilon}_1$ ).  $\tau_\mu$  is the athermal resistance which never vanishes. After Conrad (1964).

### 6.3 Bainite Nucleation

The linear relationship between  $G_N$  and  $T_h$  (Fig. 6.4) can be used to deduce whether nucleation involves dislocation dissociation or heterophase fluctuations (Bhadeshia, 1981a). The nucleation rate  $I_V$  will have a temperature dependence due to the activation energy:

$$I_V \propto \nu \exp\{-G^*/RT\} \quad (6.11)$$

where  $\nu$  is an attempt frequency. It follows that

$$-G^* \propto \beta T \quad \text{where} \quad \beta = R \ln\{I_V/\nu\} \quad (6.12)$$

We now assume that there is a specific nucleation rate at  $T_h$ , irrespective of the type of steel, in which case  $\beta$  is a constant, negative in value since the attempt frequency should be larger than the actual rate. This gives the interesting result that

$$G_N \propto \beta T \quad (6.13)$$

which is precisely the relationship observed experimentally. This is evidence for nucleation by the dissociation of dislocations with the activation energy proportional to the driving force, as opposed to the inverse square relationship predicted by classical theory. The activation energy  $G^*$  in this model comes from the resistance of the lattice to the motion of dislocations.

Nucleation corresponds to a point where the slow, thermally activated migration of glissile partial dislocations gives way to rapid, breakaway dissociation. This is why it is possible to observe two sets of transformation units, the first consisting of very fine embryo platelets below the size of the operational nucleus, and the second the size corresponding to the rapid growth to the final size. Intermediate sizes are rarely observed because the time period for the second stage is expected to be much smaller than that for the first. Fig. 6.11 shows that in addition to the fully grown sub-units (a few micrometers in length), there is another population of much smaller (submicrometre) particles which represent the embryos at a point in their evolution prior to breakaway dissociation.

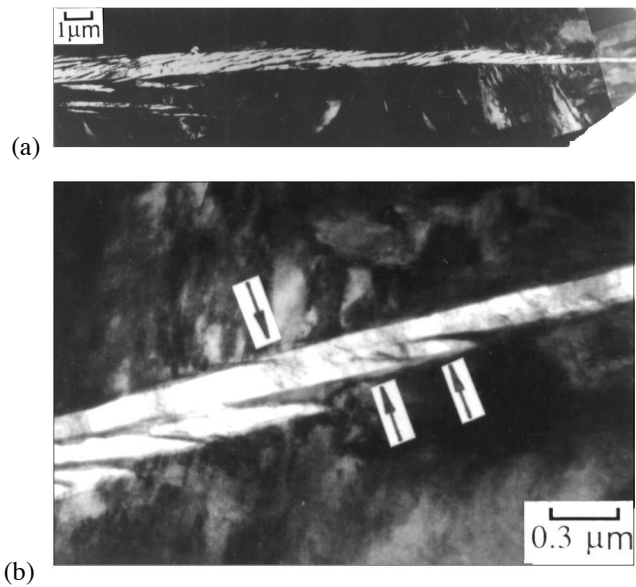


**Figure 6.11** Transmission electron micrograph of a sheaf of bainite in a partially transformed sample. A region near the tip of the sheaf in (a) is enlarged in (b). The arrows in (b) indicate possible sub-operational embryos which are much smaller than the fully grown sub-units seen in (a). After (Olson et al., 1989).

#### 6.4 Empirical Methods for the Bainite-Start Temperature

Steven and Haynes (1956) measured the bainite-start temperature by isothermally transforming a large number of engineering steels with chemical composition in the range (wt%):

Carbon	0.1-0.55	Nickel	0.0-5.0
Silicon	0.1-0.35	Chromium	0.0-3.5
Manganese	0.2-1.7	Molybdenum	0.0-1.0

and expressed their results empirically as:

$$B_S^{\circ}C = 830 - 270w_C - 90w_{Mn} - 37w_{Ni} - 70w_{Cr} - 83w_{Mo} \quad (6.14)$$

where  $w_i$  is the wt% of element  $i$  in solid solution in austenite.

An alternative equation based on 69 steels covers the following range (Lee, 2002):

Carbon	0.1-0.8	Nickel	0.0-4.5
Silicon	0.1-0.7	Chromium	0.0-4.5
Manganese	0.2-1.7	Molybdenum	0.0-2.0

and the resulting equation is given by:

$$B_S^{\circ}C = 745 - 110w_C - 59w_{Mn} - 39w_{Ni} - 68w_{Cr} - 106w_{Mo} + 17w_{Mn}w_{Ni} + 6w_{Cr}^2 + 29w_{Mo}^2 \quad (6.15)$$

and other equations have been surveyed in (Zhao et al., 2001b).

A more general way of applying an empirical relation is to use neural networks, which represent a powerful non-linear regression method (Bhadeshia, 1999b). The method has been applied to the calculation of the  $B_S$  temperature (Garcia-Mateo and Caballero, 2005; García-Mateo et al., 2007). It would be useful to create a neural network model that includes thermodynamic data alongside the chemical composition.

## 6.5 The Nucleation Rate

The linear dependence of the activation energy for nucleation on the driving force can be substituted into a nucleation rate equation to obtain:<sup>1</sup>

$$\begin{aligned} I_V &= C_3 \exp\left\{-\frac{G^*}{RT}\right\} \\ &= C_3 \exp\left\{-\frac{C_4 + C_5 \Delta G_m}{RT}\right\} \end{aligned} \quad (6.16)$$

where  $\Delta G_m$  is the maximum value of  $\Delta G_{\text{chem}}$  (Fig. 6.3c) and  $C_i$  are positive constants. The nucleation rate at  $T_h$  is obtained by setting  $\Delta G_m = G_N$ :

$$I_{T_h} = C_3 \exp\left\{-\frac{C_4 + C_5 G_N}{RT_h}\right\} \quad (6.17)$$

It follows that

$$I_V = I_{T_h} \exp\left\{-\frac{C_4 \Delta T}{RT T_h} - \frac{C_5}{R} \left(\frac{\Delta G_m}{T} - \frac{G_N}{T_h}\right)\right\} \quad (6.18)$$

with  $\Delta T = T_h - T$ . Recall that the  $G_N$  function was justified with martensite nucleation theory assuming that the nucleation rate  $I_{T_h}$  is the same for all steels at  $T_h$ . For two different steels  $A$  and  $B$ ,

$$\frac{I_{T_h^A}}{I_{T_h^B}} = \exp\left\{-\frac{(C_4 - C_2 C_5)(T_h^A - T_h^B)}{RT_h^A T_h^B}\right\} \quad (6.19)$$

Since  $I_{T_h^A} = I_{T_h^B}$  it follows that  $C_4 = C_2 \times C_5$  so that

$$I_V = C_3 \exp\left\{-\frac{C_4}{RT} - \frac{C_4 \Delta G_m}{C_2 RT}\right\} \quad (6.20)$$

In this equation the constant  $C_2$  is known since it comes from the slope of the  $G_N$  function (equation 6.2) so the two unknowns are  $C_3$  and  $C_4$  which are obtained by fitting to experimental data. The pre-exponential factor  $C_3$  is the product of a number density of nucleation sites ( $N_V^0$ ) and an attempt frequency ( $\nu$ ).

Gaude-Fugarolas and Jacques (2006) have adopted a somewhat different approach, still based on the  $G_m$  and  $G_N$  functions (Bhadeshia, 1981c). A function  $f_N$  is defined such that:

$$\begin{aligned} f_N &= \tanh\left\{-\frac{\Delta G_m - G_N}{RT}\right\} && \text{for } \Delta G_m - G_N < 0 \\ f_N &= 0 && \text{for } \Delta G_m - G_N \geq 0 \end{aligned} \quad (6.21)$$

<sup>1</sup>Bhadeshia (1982c); Rees and Bhadeshia (1992); Chester and Bhadeshia (1997)

This is consistent with the nature of the universal nucleation function, which is then used to count the number of successful grain boundary nucleation events in a time interval  $d\tau$  as follows:

$$dI \propto f_N d\tau \quad (6.22)$$

Since the driving force  $\Delta G_m$  varies with the extent of transformation, variation in  $f_N$  has the effect of reducing the nucleation events as the fraction of bainite increases, although the hyperbolic tangent form of the variation has not been justified. Another semi-empirical approach assumes a time dependence,  $I_V \propto \exp\{-t\}$  rather than an explicit dependence on driving force (Katsamas and Haidemenopoulos, 2008).

### 6.5.1 Grain Boundary Nucleation

Equation 6.16 can be adapted for nucleation initiating at the austenite grain boundaries as follows (Matsuda and Bhadeshia, 2004):

$$I_B = C_{3,B} \exp\left\{-\frac{C_{4,B} + C_{5,B} \Delta G_m}{RT}\right\} \quad (6.23)$$

where  $I_B$  is the nucleation rate per unit area of boundary. The constants  $C_i$  are solved by assuming that the initial stages of the transformation are controlled by sub-units nucleating directly on the boundaries so that

$$\frac{V^{\alpha_b}}{V} = V_u S_V I_B t \quad (6.24)$$

where  $V_u$  is the sub-unit volume and  $S_V = 2/\bar{L}$  is the amount of grain boundary surface per unit area that can be related directly to the mean lineal intercept measure of grain size.

## 6.6 Growth Rate

The displacement of an interface requires the atoms of the parent to transfer into and adopt the crystal structure of the product phase. The ease with which this happens determines the interface mobility. There may also be a partitioning of solutes in which case diffusion may limit the movement of the interface. The two processes of diffusion and mobility are in series; the velocity as calculated from the interface mobility must therefore match that due to the diffusion of solute ahead of the interface. Both processes dissipate the available free energy, so motion is always under mixed control. However, a process is said to be diffusion-controlled when most of the free energy is dissipated in the diffusion of solute. Interface-controlled growth occurs when the larger proportion of the free energy is consumed in the transfer of atoms across the interface. The compositions of the phases at the moving interface during diffusion-controlled growth are given approximately by a tie-line of the phase diagram, and other circumstances are illustrated in Fig. 6.12.

### 6.6.1 Theory for the Lengthening of Plates

Particle dimensions during diffusion-controlled growth vary parabolically with time when the extent of the diffusion field increases with particle size. The growth rate thus decreases because the solute has to diffuse over ever increasing distances to reach the far-field concentration. Plates or needles can however grow at a constant rate because solute can be partitioned to their sides.

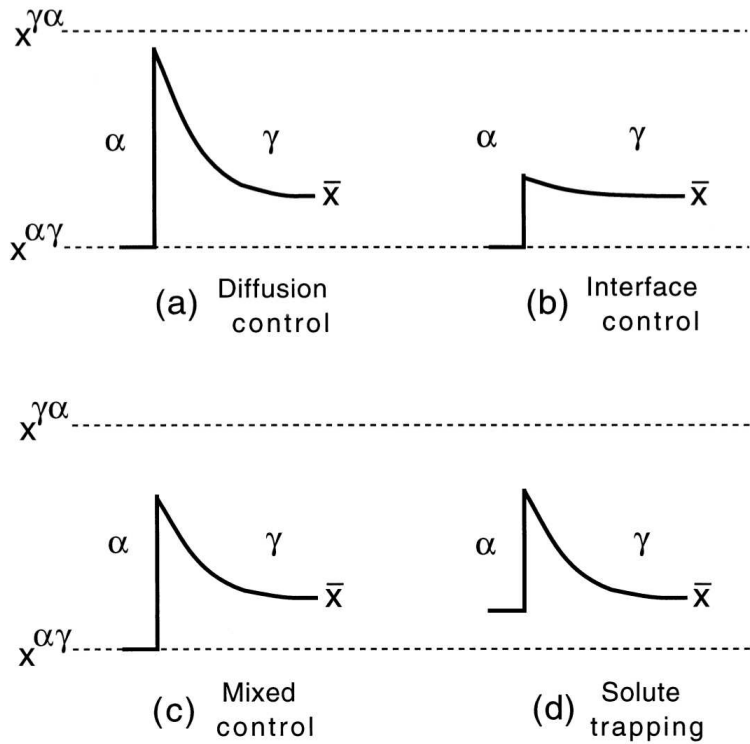


**Figure 6.12** Carbon concentration profiles at a moving  $\alpha/\gamma$  interface. The terms  $x^{\alpha\gamma}$ ,  $x^{\gamma\alpha}$  and  $\bar{x}$  refer to the equilibrium concentrations in the ferrite and austenite respectively, and the average concentration in the alloy as a whole. (a) Diffusion control. (b) Interface control. (c) Mixed control. (d) Solute trapping (discussed later).

The partitioning of interstitial elements during displacive transformation should lead to diffusion-controlled growth because the glissile interface necessary for such transformation has the highest mobility. Iron and any substitutional solute atoms do not diffuse so their role is purely thermodynamic.

The equation for the diffusion-controlled growth of plates whose shape approximates that of a parabolic cylinder (Fig. 6.13) has been solved by Trivedi (1970). The plate lengthening rate  $V_l$  at a temperature  $T$  for steady state growth is obtained by solving:

$$f_1 = \frac{x_r - \bar{x}}{x_r - x^{\alpha\gamma}} \quad (6.25)$$

$$f_1 = (\pi p)^{0.5} \exp\{p\} \operatorname{erfc}\{p^{0.5}\} \left[ 1 + \frac{V_l}{V_c} f_1 S_1\{p\} + \frac{r_c}{r} f_1 S_2\{p\} \right] \quad (6.26)$$

where the Péclet number is

$$p = V_l r / 2\bar{D} \quad (6.27)$$

The weighted-average diffusion coefficient  $\bar{D}$  for carbon in austenite is given by integrating  $D$  (the diffusivity at a specific concentration) over the range  $\bar{x}$  to  $x_r$ , and then dividing the integral by this range.

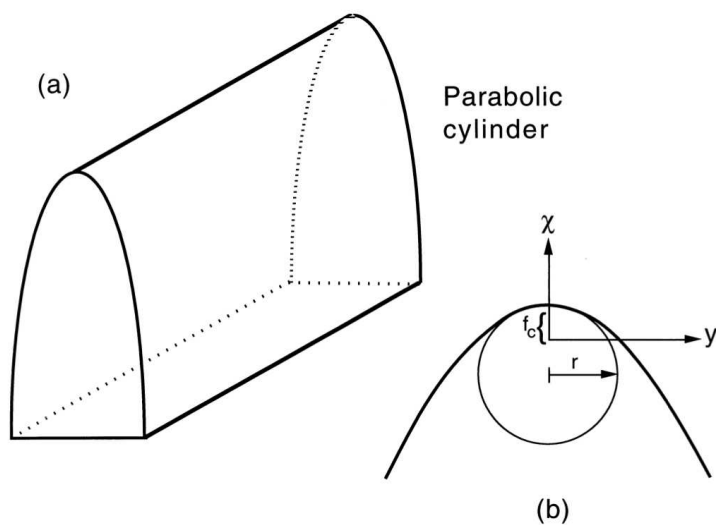


**Figure 6.13** (a) An illustration of the shape of a parabolic cylinder. (b) Definitions of the tip radius  $r$ , the focal distance  $f_c$  and the coordinates.

The function  $S_2\{p\}$  of equation 6.26 depends on the Péclet number (Fig. 6.14); it corrects for variation in composition due to changing curvature along the interface and has been evaluated numerically by Trivedi. The term containing  $S_1$  is prominent when growth is not diffusion-controlled;  $V_c$  is the interface-controlled growth velocity of a flat interface. For diffusion-controlled growth, which is discussed first,  $V_c$  is very large when compared with  $V_l$  and the term containing it can be neglected.

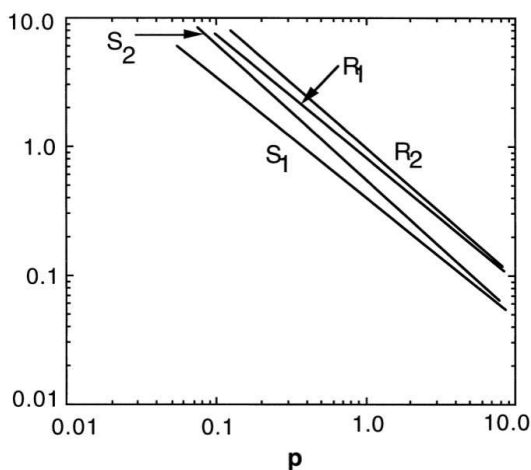


**Figure 6.14** Dependence of Trivedi's functions  $S_1$ ,  $S_2$ ,  $R_1$  and  $R_2$  on the Péclet number  $p$ .

$x_r$  is the carbon concentration in the austenite at the plate tip. It may differ from the equilibrium carbon concentration  $x^{\gamma\alpha}$  because of the Gibbs-Thompson capillarity effect (Christian, 2003a);  $x_r$  decreases as interface curvature increases, and growth ceases at a

critical radius  $r_c$  when  $x_r = \bar{x}$ . For a finite plate tip radius,

$$x_r = x^{\gamma\alpha} [1 + (\Gamma/r)] \quad (6.28)$$

where  $\Gamma$  is the capillarity constant given by Christian (2003a):

$$\Gamma = \frac{\sigma^{\alpha\gamma} V_m}{RT} \frac{(1 - x^{\gamma\alpha})}{(x^{\alpha\gamma} - x^{\gamma\alpha})} \left[ 1 + \frac{d(\ln f_C \{x^{\gamma\alpha}\})}{d(\ln x^{\gamma\alpha})} \right]^{-1} \quad (6.29)$$

where  $\sigma^{\alpha\gamma}$  is the interfacial energy per unit area,  $f_C$  is the activity coefficient of carbon in austenite, and  $V_m$  is the molar volume of ferrite. This assumes that the ferrite composition is unaffected by capillarity, since  $x^{\alpha\gamma}$  is always very small. The critical plate tip radius  $r_c$  can be obtained by setting  $x_r = \bar{x}$ .

Trivedi's solution for diffusion-controlled growth assumes a constant shape, but the solution is not strictly shape-preserving. The concentration  $x_r$  varies over the surface of the parabolic cylinder which should lead to a deviation from the parabolic shape. Trivedi claims that the variation in  $x_r$  has a negligible effect provided the tip radius is greater than  $3r_c$ .

Plate growth theory provides a relation between velocity and tip radius (Fig. 6.15). Additional theory is required to enable the choice of a particular tip radius and hence to fix  $V_l$ . Small tip radii favour fast growth due to the point effect of diffusion, but this is counteracted by the capillarity effect. Zener proposed that the plate should tend to adopt a tip radius which allows  $V_l$  to be maximised but this remains a hypothesis. Work on the dendritic growth of solid from liquid (formally an almost identical problem) has shown that the dendrites do not select the radius corresponding to the maximum velocity. The radius is determined instead by a shape stability criterion (Glicksman et al., 1976; Langer and Muller-Krumbhaar, 1978). If these results can be extrapolated to displacive transformations, and it is doubtful that they can given that the shape is constrained by strain energy minimisation, then calculated velocities would be greatly reduced. This does not fit experimental data where the lengthening rate is slightly higher than the maximum velocity predicted theoretically (Bhadeshia, 1985a).

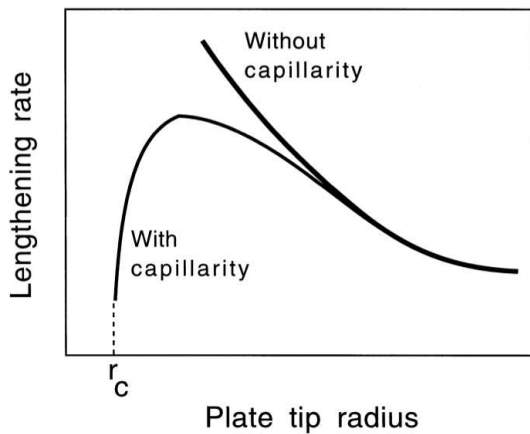


**Figure 6.15** Variation in lengthening rate as a function of the plate tip radius.

The shape of ferrite plates is sometimes more needle-like (lath) than plate-like. Trivedi has obtained a steady-state solution for the diffusion-controlled growth of paraboloids of

revolution, i.e. needles:

$$f_1 = p \exp\{p\} \text{Ei}\{p\} \left[ 1 + \frac{V_l}{V_c} f_1 R_1\{p\} + \frac{r_c}{r} f_1 R_2\{p\} \right] \quad (6.30)$$

where Ei is an exponential integral. The tip radius  $r_c$  is twice as large as that for plates because there are two radii of curvature for a needle tip.

### 6.6.2 Growth Rate of Sheaves of Bainite

After nucleating at austenite grain surfaces, sheaves of bainite propagate by the repeated formation of sub-units, each of which grows to a limited size. New sub-units are favoured near the tips of existing platelets; nucleation in adjacent positions occurs at a much lower rate. Therefore, the overall shape of the sheaf is also that of a plate in three dimensions with growth limited only by austenite grain or twin boundaries.

Most direct observations have used optical microscopy and hence monitor the growth of *sheaves* rather than of the transformation unit which is only about  $0.2 \mu\text{m}$  in thickness. Suppose that a sub-unit reaches its limiting size in a time period  $t_C$ , and that a time interval  $\Delta t$  elapses before the next one is stimulated, then the lengthening rate,  $V_S$ , of a sheaf is given by:

$$V_S = V_l \left( \frac{t_C}{t_C + \Delta t} \right) \quad (6.31)$$

where  $V_l$  is the average lengthening rate of a sub-unit.

Bainite sheaves lengthen at a constant rate although the data show considerable scatter, attributed to stereological effects (Speich and Cohen, 1960; Goodenow et al., 1963; Hawkins and Barford, 1972). Greater concentrations of carbon, nickel or chromium reduce  $V_S$ . The growth of sheaves seems to occur at a constant aspect ratio although thickening continues when lengthening has stopped. This is not surprising since the sheaf can continue to grow by the sub-unit mechanism until the  $T'_0$  condition is achieved.

An assessment of sheaf data shows that the lengthening rate is greater than expected from diffusion-controlled growth, Fig. 6.16. This includes measurements on Fe-Ni-C alloys which are frequently (incorrectly) used to justify the existence of some sort of a solute drag effect. It has been claimed that the sheaf growth-rate is dependent on whether nucleation occurs at grain boundaries or intragranularly, but this is probably incorrect since stereological effects were neglected (Hu et al., 2014c); the analysis also assumed equilibrium rather than paraequilibrium, neglected strain energies, and the interfacial energy necessary for the calculations was not stated.

### 6.6.3 Growth Rate of Sub-Units of Bainite

The growth rate of martensite can be so fast as to be limited only by the speed of sound in the metal. Although bainite grows rapidly, the lengthening rate is much smaller than that for martensite. The interface moves relatively slowly even though it is glissile. This is probably because of the plastic work that is done as the bainite grows. A good analogy is to compare brittle failure in a glass, where cracks propagate rapidly, with cleavage failure in metals which is not as rapid because of the plastic zone which has to move with the crack tip.

The lengthening rate of sub-units has been measured using hot-stage photoemission electron microscopy. Electrons are excited from the surface of the sample using incident

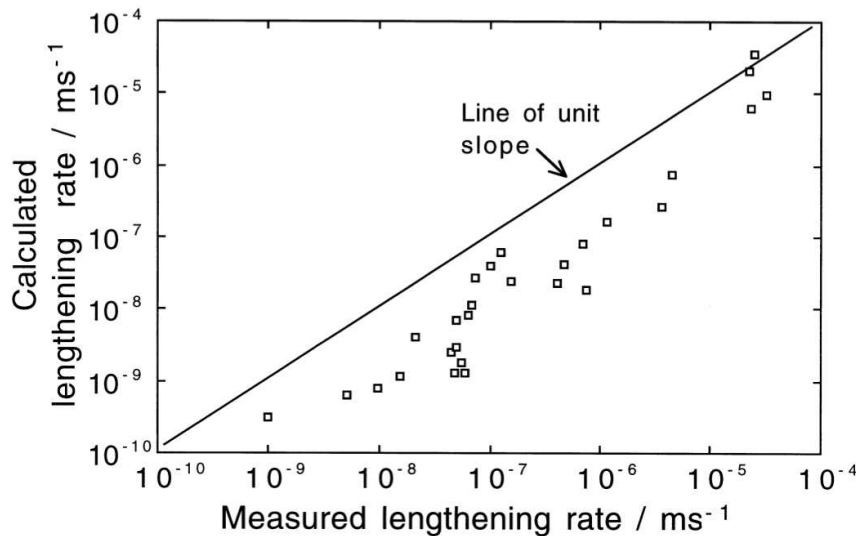


**Figure 6.16** Comparison of published data on the lengthening rate of bainite sheaves against those calculated assuming paraequilibrium carbon-diffusion controlled lengthening (Bhadeshia, 1985a; Ali and Bhadeshia, 1989).

ultraviolet radiation, and it is these photo-emitted electrons which form the image. The technique can resolve individual sub-units of bainite. Fig. 6.17 illustrates a series of micrographs taken at 1 s intervals, showing the growth of bainite sub-units. The measured lengthening rate of the arrowed sub-unit is  $75 \mu\text{m s}^{-1}$ . This is many orders of magnitude larger than that calculated assuming paraequilibrium at the transformation front ( $0.083 \mu\text{m s}^{-1}$ ). Lengthening occurs at a rate much faster than expected from carbon diffusion-controlled growth.<sup>2</sup>

There are interesting observations on the thickening of bainite sub-units. The thickness can increase even after lengthening has halted. An elastically accommodated plate tends to adopt the largest aspect ratio consistent with a balance between the strain energy and the free energy change driving the transformation, Fig. 6.18, in order to achieve thermoelastic equilibrium (Olson and Cohen, 1977).

Bainite plates are not elastically accommodated but it should be possible for the thickness of a plate to increase at constant length if the process is captured at an early stage. Fig. 6.18b shows a large plate of bainite which formed first followed by smaller orthogonal plates. The larger plate is seen to bow between the smaller plates whose tips act as pinning points. The smoothly curved regions of the interface between the pinning points prove that the interface moves continuously rather than by a step mechanism.

The rapid, displacive transformation leads to acoustic emissions that are not evident with solid-state reconstructive transformations (van Bohemen et al., 2002, 2003). Acoustic emission occurs due to elastic waves generated by abrupt changes in the stress field inside

<sup>2</sup>Optical metallography has been used to argue that the bainite transformation is diffusional (Borgenstam et al., 2009), but the evidence is not convincing because it neglects crucial characteristics of bainite, some of which are listed in Table 16.1.

the steel (Wadley and Mehrabian, 1984). As such, they are naturally consistent with displacive transformations. These waves can, with appropriate transducers, be converted into electrical signals. It turns out that the frequency of emissions is significantly greater for bainite than it is for martensite [Fig. 6.19 (van Bohemen et al., 2005)]. To put it another way, the mean lifetime of events is shorter for bainite. The acoustic emissions are interpreted to be a consequence of dislocation sources triggered by the displacive mode of bainitic and martensitic transformation. But the motion of the bainite-austenite interface is relatively jerky, due to the sub-unit mechanism of growth, resulting in a smaller mean free path for interfacial dislocations. Since the original work, there have been a number of reports on acoustic emissions accompanying the rapid formation of bainite or bainite with a midrib of thin-plate martensite (Wozniak, 2008; Wozniak et al., 2011a,b, 2012). The emissions in those cases have been reported to be stronger when associated with martensitic transformation, which may not be surprising given the anelastic effects when the transformation temperature is raised to generate bainite.

In some interesting work, Kuba and van Aken (2013) characterised acoustic emissions due to the rapid melting of indium-rich particles in an aluminium matrix. Such melting is accompanied by a volume change that is comparable to typical phase transformations in steels. It follows that acoustic emissions are not confined to displacive transformations, but as pointed out in that work, the volume change generates these signals only if the relaxation of the product phase occurs in less than  $10^{-5}$  of a second. Such a time scale is inconsistent with solid-state reconstructive transformations in iron, but entirely appropriate for rapidly growing bainite sub-units. In summary, the observation of acoustic emissions accompanying the growth of bainite is additional proof of a displacive mechanism of transformation.

#### 6.6.4 Solute Drag

Solute drag is a process in which free energy is dissipated specifically in the diffusion of solute atoms *within the interface*; it is in this sense distinct from the free energy dissipated in the diffusion of solute within chemical potential gradients in the phases on either side of a moving interface. The atoms of interest are those that in a stationary interface are said to be segregated or desegregated in the structure of the interface. The phenomenon is similar to the drag on dislocations when atoms are attracted to the dislocation cores. Chapter 2 contains a discussion of the atomic resolution experiments which show that there is no excess concentration of solute at or in the bainite/austenite interface. Consequently, there is no reason to expect solute drag effects during the bainite reaction. And indeed, there is no evidence that solute drag effects manifest during the bainite reaction.

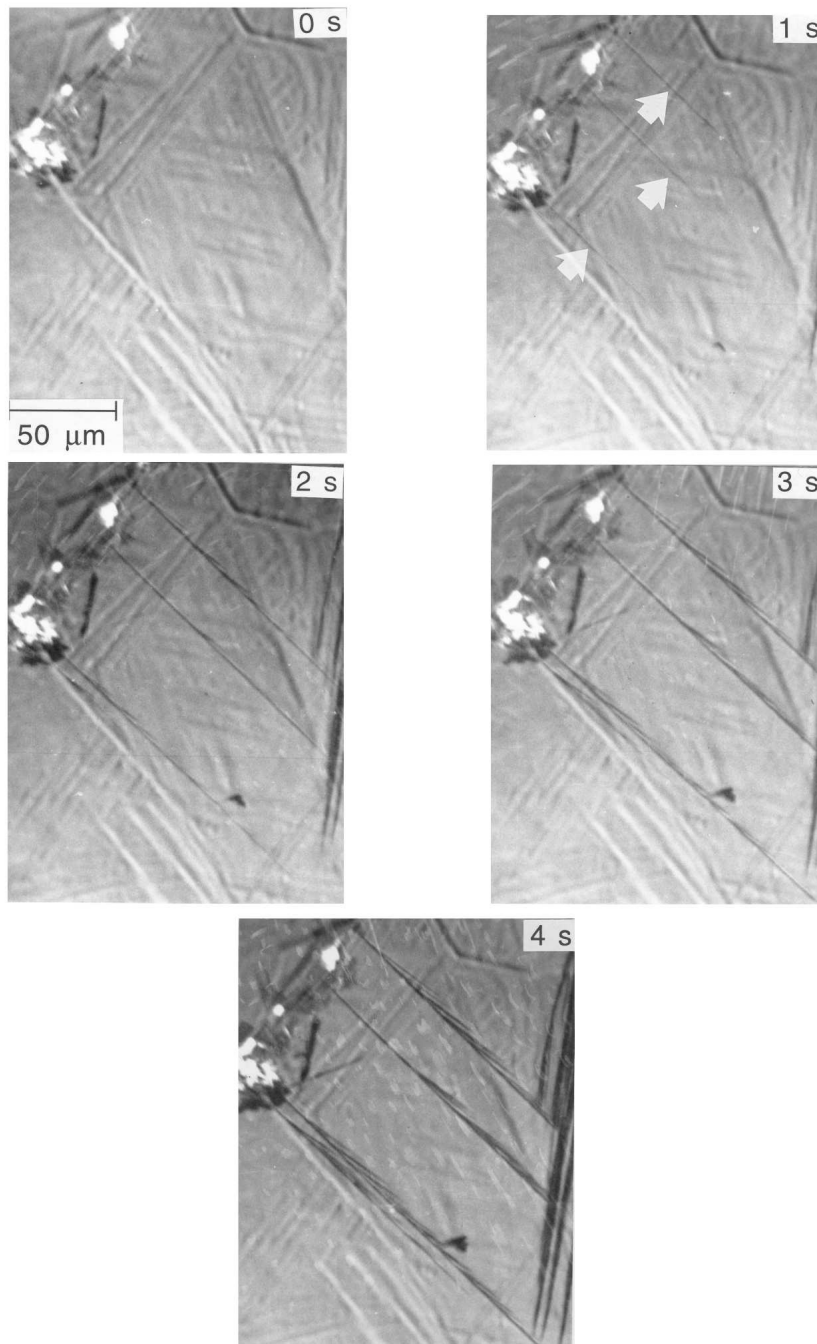


**Figure 6.17** Photoemission electron microscope observations on the growth of individual sub-units in a bainite sheaf (Bhadeshia, 1984). The pictures are taken at 1 s intervals during transformation at 380 °C in a Fe-0.43C-2.02Si-3Mn wt% alloy. The micrograph at 0 s is fully austenitic, the relief being a residue from an earlier experiment.

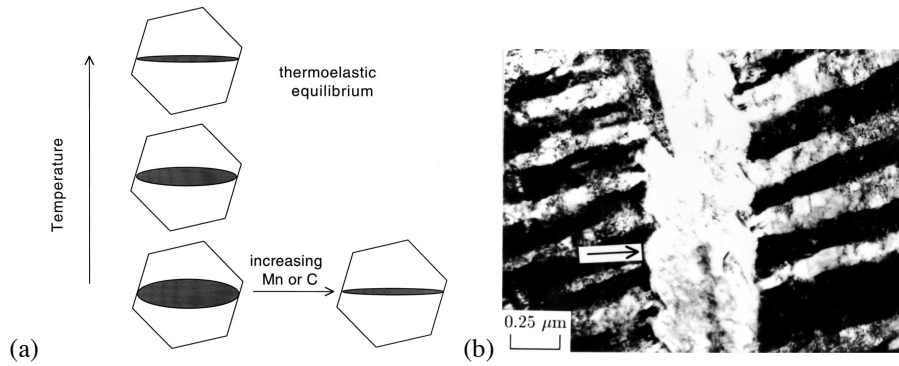


**Figure 6.18** (a) Effect of thermoelastic equilibrium on the aspect ratio of a plate with a fixed length. (b) Bowing of  $\alpha_b/\gamma$  interface at strong pinning points, particularly prominent in regions identified by arrows (Chang and Bhadeshia, 1995b).

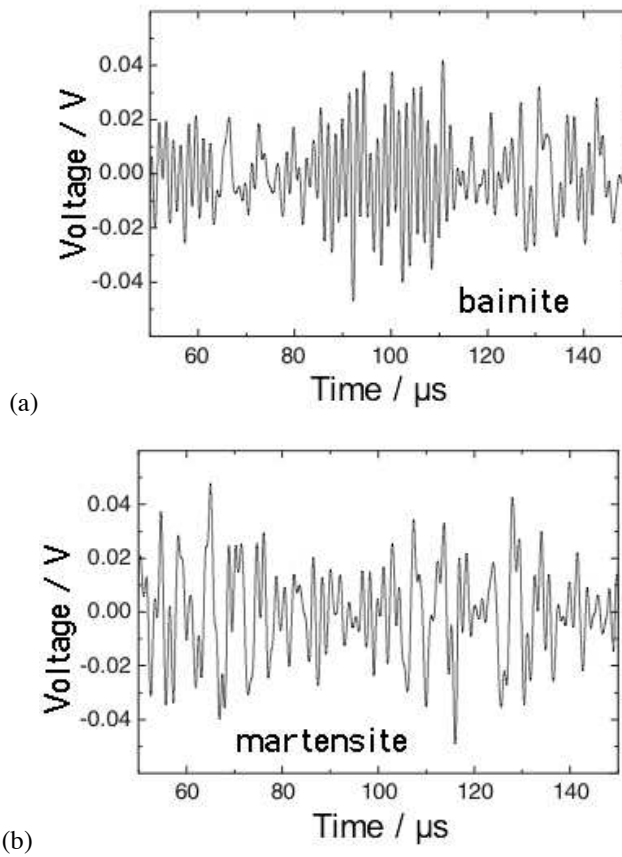


**Figure 6.19** Acoustic emission signal from bainite and from martensite (van Bohemen et al., 2005)

### 6.7 Partitioning of Carbon from Supersaturated Bainitic Ferrite

It is favourable for the carbon that is trapped in bainite to partition into the residual austenite where it has a lower chemical potential. Consider a plate of thickness  $w$  with a one-dimensional flux of carbon along  $z$  which is normal to the  $\alpha/\gamma$  interface, with origin at the interface and  $z$  defined as positive in the austenite (Kinsman and Shyne, 1967). A mass conservation condition gives (Bhadeshia, 1989):

$$\frac{1}{2}w(\bar{x} - x^{\alpha\gamma}) = \int_0^\infty [x_\gamma\{z, t_d\} - \bar{x}] dz \quad (6.32)$$

where  $x^{\alpha\gamma}$  and  $x^{\gamma\alpha}$  are the paraequilibrium carbon concentrations in  $\alpha$  and  $\gamma$  respectively, allowing for stored energy, and  $t_d$  is the time to decarburise the ferrite plate. Since the diffusion rate of carbon in austenite is slower than in ferrite, the rate of decarburisation will be determined by the diffusivity in the austenite. The concentration of carbon in austenite at the interface remains constant for times  $0 < t < t_d$ , after which it steadily decreases as homogenisation occurs. The concentration profile in the austenite is given by:

$$x_\gamma = \bar{x} + (x^{\gamma\alpha} - \bar{x})\operatorname{erfc}\left\{\frac{w}{2(\overline{D}t_d)^{\frac{1}{2}}}\right\} \quad (6.33)$$

which on integration gives:

$$t_d^{\frac{1}{2}} = \frac{w(\bar{x} - x^{\alpha\gamma})\pi^{\frac{1}{2}}}{4\overline{D}^{\frac{1}{2}}(x^{\gamma\alpha} - \bar{x})} \quad (6.34)$$

Some results from this analysis are illustrated in Fig. 6.20.

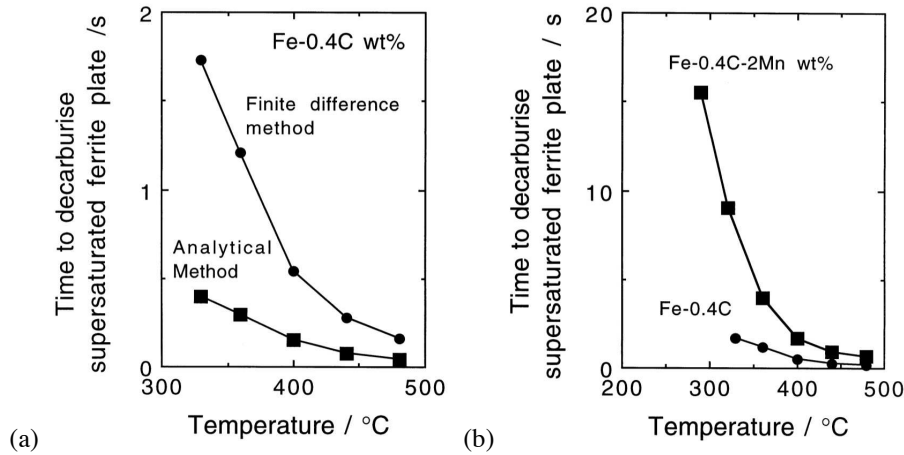


**Figure 6.20** (a) The time to decarburise a plate of thickness  $0.2 \mu\text{m}$ . Calculations using the analytical and finite difference methods are illustrated. (b) The effect of adding an austenite stabilising substitutional solute on the decarburisation time (Mujahid and Bhadeshia, 1992).

Equation 6.34 does not allow for the coupling of fluxes in the austenite and ferrite. It assumes that the diffusivity in the ferrite is so large that any gradients there are eliminated rapidly. A flux balance must in general be satisfied as follows:

$$D_\alpha \frac{\partial x^\alpha}{\partial z} = D_\gamma \frac{\partial x^{\gamma\alpha}}{\partial z} \quad (6.35)$$

where  $D_\alpha$  is the diffusivity of carbon in the ferrite,  $x^\alpha$  is the concentration of carbon in the ferrite at the interface with the gradients evaluated at the interface. Since  $D_\alpha \gg D_\gamma$ ,  $x^\alpha$  will inevitably deviate from  $x^{\alpha\gamma}$  in order to maintain the flux balance. It will only reach the equilibrium value towards the end of the partitioning process. The gradients in the ferrite must also increase with  $x^{\gamma\alpha}$ ; the partitioning process could then become limited by diffusion in the ferrite. As a consequence, the diffusion time as predicted by the finite difference method becomes larger than that estimated by the approximate analytical equation when the transformation temperature is decreased or  $x^{\gamma\alpha}$  increased, as illustrated in Fig. 6.20. Typical concentration profiles that develop during the partitioning process are illustrated in Fig. 6.21.

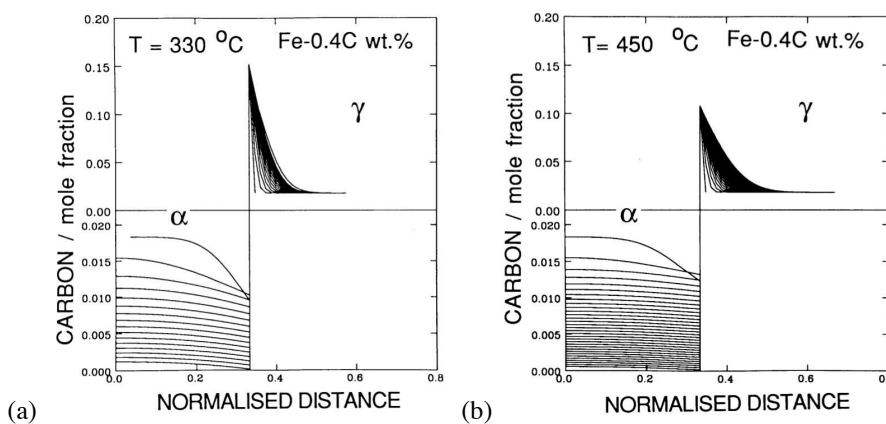


**Figure 6.21** The concentration profiles that develop in ferrite and austenite during the partitioning of carbon from supersaturated bainite (Fe-0.4C wt%, plate thickness  $0.2 \mu\text{m}$ ). (a)  $330^\circ\text{C}$ , the time interval between the concentration contours in each phase being  $0.094 \text{ s}$ . (b)  $450^\circ\text{C}$ , the corresponding time interval is  $0.007 \text{ s}$ . (Mujahid and Bhadeshia, 1992).

The assumption throughout that during the decarburisation process  $x^{\gamma\alpha}$  is fixed at the value given by paraequilibrium between ferrite and austenite is hard to justify since  $x^\alpha \neq x^{\alpha\gamma}$ . Hillert et al. (1993) have avoided this assumption; but the results they obtain are not essentially different from those presented above.

## 6.8 Growth with Partial Supersaturation

There are three scenarios possible in principle:

- (i) a transformation can occur without any composition change as long as there is a reduction in the free energy. The chemical potential is then nonuniform across phase boundaries for all of the atomic species. A net reduction in free energy is still possible because some of the species are trapped in the parent phase and others in the product. Thus, martensitic transformation of steel involves the trapping of carbon in the martensite and iron in the austenite.
- (ii) Equilibrium transformation requires the partitioning of solutes between the phases until the chemical potential for each species is uniform in all locations.

- (iii) In paraequilibrium only carbon has a uniform chemical potential – the substitutional and iron atoms are trapped in the parent or product phases.

These three cases of composition-invariant, equilibrium and paraequilibrium transformation are well-defined. We now deal with the case where the extent of carbon partitioning is between paraequilibrium and composition-invariant transformation:

$$x^{\alpha\gamma} \leq x^\alpha \leq \bar{x} \quad \text{and} \quad \bar{x} \leq x^\gamma \leq x^{\gamma\alpha} \quad (6.36)$$

Some of the carbon is trapped in the product phase but a proportion partitions so that the differences in chemical potential are reduced. The ferrite grows with a *partial supersaturation*, the level of which is fixed by kinetic constraints which we shall now consider.

### 6.8.1 Stability

In Fig. 6.22,  $x_m$  represents the maximum concentration of carbon that can be tolerated in ferrite which precipitates from austenite of composition  $\bar{x}$ . A higher concentration cannot be sustained because there would be an increase in free energy on transformation.

Growth with partial supersaturation, such as the case where the interface compositions are given by  $x^\alpha = x_m$  and  $x^\gamma = \bar{x}$  is expected to be unstable to perturbations since the concentration field must tend to adjust towards lower free energy states. The assembly should then irreversibly cascade towards the equilibrium partitioning of carbon with  $x^\alpha = x^{\alpha\gamma}$ ,  $x^\gamma = x^{\gamma\alpha}$ . Experimental evidence supports this conclusion since the growth rate of Widmanstätten ferrite is found to be consistent with the paraequilibrium partitioning of carbon at all transformation temperatures. These considerations do not necessarily rule out the possibility of carbon trapping because some other physical phenomenon could provide the necessary stabilising influence (Christian and Edmonds, 1984).

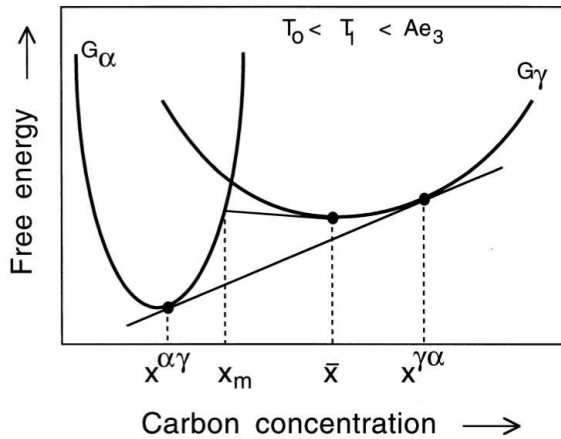


**Figure 6.22** Austenite and ferrite free energy curves illustrating the unstable nature of an assembly in which the ferrite forms with a partial supersaturation of carbon. The line at  $\bar{x}$  is tangent to the  $\gamma$  free energy curve.

There are many processes, including diffusion, which occur in series as the ferrite grows. Each of these dissipates a proportion of the free energy available for transformation. For a given process, the variation in interface velocity with dissipation defines a function which in recent years has been called an *interface response function*. The actual velocity of the interface depends on the simultaneous solution of all the interface response functions, a procedure which fixes the composition of the growing particle.

Fig. 6.23 shows an electrical analogy; the resistors in series are the hurdles to the movement of the interface. They include diffusion in the parent phase, the transfer of atoms across the interface, solute drag, etc. The electrical-potential drop across each resistor corresponds to the free energy dissipated in each process, and the current, which is the same through each resistor, represents the interface velocity. The relationship between the current and potential is different for each resistor, but the actual current is obtained by a simultaneous solution of all such relations.

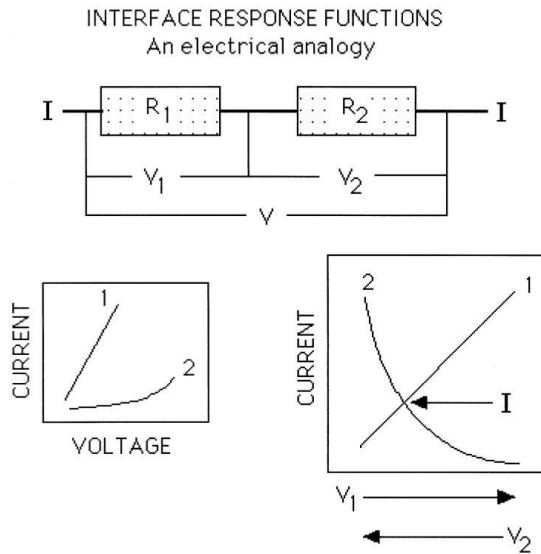


**Figure 6.23** An electrical analogy illustrating the dissipations due to processes which occur in series as the transformation interface moves. The resistors in series are the hurdles to the motion of the interface, the voltage is the driving force and the current the interface velocity. The way in which voltage (driving force) is dissipated as a function of current (velocity) across each resistor is different, since each resistor represents a separate physical process. There is only one interface so all these processes must yield the same velocity, as indicated by the identical current passing through all the resistors.

Following on from this analogy, the available free energy can be partitioned into that dissipated in the diffusion of carbon, a quantity expended in the transfer of atoms across the interface, and in any other process determining the motion of the interface. There are three unknowns: the austenite composition at the interface, the supersaturation and the velocity, so it is necessary to exploit at least three interface response functions. If the tip radius of the plate is considered to be a variable, then the number of unknowns is four; for displacive transformations the radius can be assumed to be fixed by strain energy minimisation. The necessary three interface velocity functions are, therefore, the diffusion field velocity, the velocity determined from interface mobility and a carbon trapping function. Each of these is now discussed in detail.

But to summarise first, the response functions all give different velocities for a given free energy dissipation. The total driving force has to be partitioned into the individual dissipations in such a way that all the response functions give an identical velocity.

### 6.8.2 The Interface Response Functions

**Glissile Interface Mobility** The interfacial mobility is formulated using the theory for thermally activated motion of dislocations (Olson et al., 1989, 1990). This is justified because a glissile interface consists of an array of appropriate dislocations. The interfacial velocity  $V_i$  is then given by:

$$V_i = V_o \exp\left\{-\frac{G^*}{kT}\right\} \quad (6.37)$$

where  $G^*$  is an activation free energy and the pre-exponential factor  $V_o$  can be taken to be  $30 \text{ m s}^{-1}$  based on experimental data from single-interface martensitic transformations (Grujicic et al., 1985). The activation energy  $G^*$  is a function of the net interfacial driving force  $G_{id}$  through the relation (Cocks et al., 1975):

$$G^* = \int_{G_{id}}^{G'_{id}} v^* dG \quad (6.38)$$

where  $G'_{id}$  is the maximum resistance to the glide of interfacial dislocations and  $v^*$  is the activation volume swept by the interface during a thermally activated event. For a wide range of obstacle interactions, the function  $G^*\{G_{id}\}$  can be represented by:

$$G^* = G_o^* \left[1 - \left(\frac{G_{id}}{G'_{id}}\right)^y\right]^z \quad (6.39)$$

where  $G_o^*$  is the activation free energy barrier to dislocation motion in the absence of an interfacial driving force. The constants  $y$  and  $z$  define the shape of the force-distance function and for solid-solution interactions in the Labusch limit (where hardening is due to the average effect of many strain centres), it may be assumed that  $y = 0.5$  and  $z = 1$  (Nabarro, 1982).<sup>3</sup>

Analysis of kinetic data for the interface-controlled nucleation of martensite gives

$$G_o^* = 0.31\mu\Omega \quad (6.40)$$

where  $\mu$  is the shear modulus of the matrix and  $\Omega$  is the volume per atom. Based on the behaviour of Fe-Ni-C alloys (Olson, 1984),  $G'_{id}$  is taken to be:

$$G'_{id} = 1.22 \times 10^{-3}\mu \quad (6.41)$$

**Interface Mobility Based on Absolute Reaction Rate Theory** An empirical model is sometimes used to represent the interface mobility for displacive transformations (Hillert, 1960; Ågren, 1989). It uses chemical rate theory, one of the assumptions of which is that the “reaction” consists of the repetition of unit steps involving the interaction of a small number of atoms. Whereas this may be justified for a process like solidification, the assumptions of chemical rate theory are unlikely to be applicable to displacive transformations in which a large number of atoms move in a disciplined manner.

The interface velocity is given by (Christian, 2003a):

$$V_i = \delta_b f^* \exp\left\{-\frac{G^*}{RT}\right\} \left[1 - \exp\left\{-\frac{G_{id}}{RT}\right\}\right] \quad (6.42)$$

<sup>3</sup>The relationship between the activation energy and driving force is here nonlinear, compared with equation 6.39 of the nucleation theory. The nonlinear function is a better approximation but the linear relation of equation 6.39 suffices for most purposes.

where  $\delta_b$  is the thickness of the interface, and  $f^*$  is an attempt frequency for atomic jumps across the interface. For small  $G_{id}$  the equation simplifies to

$$V_i = MG_{id} \tag{6.43}$$

where  $M$  is a mobility, estimated by Hillert (1975) for reconstructive transformations to be:

$$M = 0.035 \exp\left\{-\frac{17700}{T}\right\} \text{ m}^4 \text{ J}^{-1} \text{ s}^{-1} \tag{6.44}$$

**The Diffusion Field Velocity** The diffusion field velocity depends on the compositions of the phases at the interface. These compositions are illustrated in Fig. 6.24, on a free energy diagram as a function of the amount  $G_{dd}$  of free energy dissipated in the diffusion of solute ahead of the interface. The concentrations  $x^\alpha$  and  $x_I$  are not independent because the choice of either fixes the value of the other uniquely.

The Trivedi solution for plates is probably the best available for diffusion-controlled growth, but there are more convenient approximations. One of these is due to Ivantsov (1947), in which the growth of a parabolic cylinder shaped particle is treated without the inclusion of interface mobility and capillarity effects. The velocity  $V_d$  for steady state growth of ferrite of constant composition  $x^\alpha$  in a steel of composition  $\bar{x}$  is given by:

$$\frac{\bar{x} - x_I}{x^\alpha - x_I} = (\pi p)^{\frac{1}{2}} \exp\{p\} \operatorname{erfc}\{p^{\frac{1}{2}}\} \tag{6.45}$$

where  $x_I$  is the carbon concentration in the austenite at the interface and  $p$  is the Péclet number related to  $V_d$  via equation 6.24.

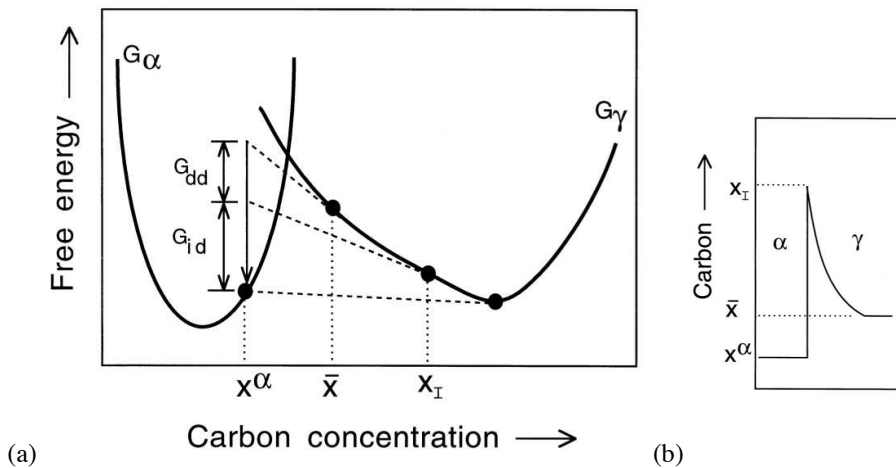


**Figure 6.24** (a) Constant temperature free-energy curves showing the quantities  $G_{dd}$  and  $G_{id}$  for the case where the interface compositions are as illustrated in (b). Note that the net free energy available for interfacial motion *after* allowing for strain energy and interface energy contributions is  $\Delta G$ , which is the sum of the two dissipations  $G_{dd}$  and  $G_{id}$ .

**Solute Trapping Law** Atoms are forced into the product phase during martensitic transformation. The chemical potential of some of these atoms increases as they are engulfed

by the martensite. Similarly, during paraequilibrium transformation some of the immobile substitutional-solutes are forced into the growing crystal. A solute or solvent is said to be trapped when its chemical potential increases on transfer across the interface. The term *solute trapping* is relatively recent (Baker and Cahn, 1969, 1971) but the phenomenon has been known for much longer in the context of transformations in steels.

Fig. 6.25 illustrates a transformation front between the shaded and unshaded crystals, in a binary alloy containing *A* (solvent) and *B* (solute) atoms. The smaller solute atoms prefer to be in the parent phase ( $\gamma$ ). The atoms in the central layer have to move along the vectors indicated in order to transform into the product phase ( $\alpha$ ).  $\lambda$  is a typical diffusion jump distance for the solute atom; the motions required for the atoms in the interfacial layer to adjust to the new crystal structure are rather smaller.

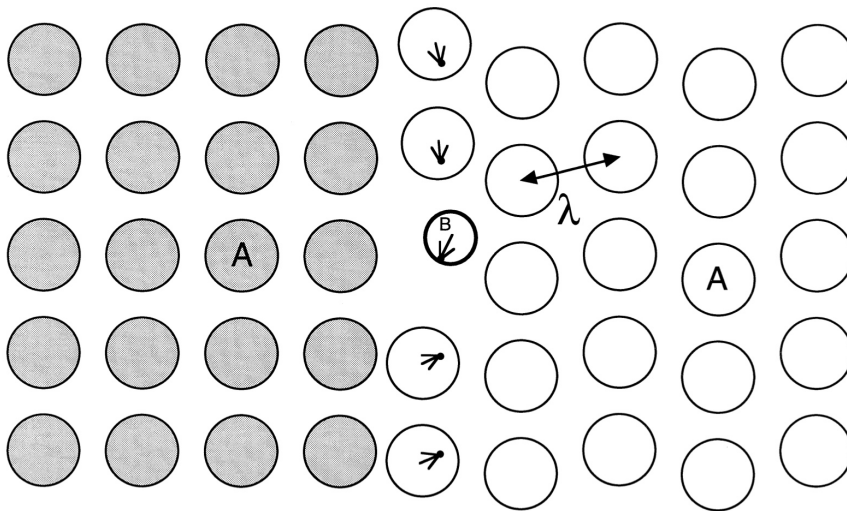


**Figure 6.25** Choreography of solute trapping, adapted from Aziz (1982). The solvent is labelled *A*, solute *B* and the product phase is shaded dark. The transformation front is advancing towards the right.

Solute will be trapped if the interface velocity  $V_k$  is greater than that at which solute atoms can diffuse away. The maximum diffusion velocity is approximately  $D/\lambda$  since  $\lambda$  is the minimum diffusion distance, so that trapping occurs when  $V_k > D/\lambda$ .

The model (Aziz, 1982, 1983) relates interfacial velocity to the partitioning coefficient  $k_p$ , which is the ratio of the concentration in the product phase at the interface to that in the parent phase at the interface:

$$k_p = x^\alpha / x_I \quad (6.46)$$

and  $k_p = k_e$  where  $k_e$  is the equilibrium partition coefficient.

There are two basic mechanisms of interface displacement, one involving propagation by the displacement of steps, and the other by the displacement of all elements of the boundary; this latter mechanism is called “continuous” motion. Aziz has derived slightly different trapping models for these two cases. The step model only permits transformation below the  $T'_0$  temperature of the austenite in the vicinity of the interface. This is in general too restrictive and certainly inapplicable for transformations at temperatures above the  $T'_0$

temperature, of the type being considered here. Goldman and Aziz (1987) have proposed another model for stepped growth, which they call the *aperiodic step model*, in which the steps are assumed to pass at random intervals with transformation restricted to below the  $T'_0$  temperature of the parent phase at the interface. The trapping law turns out to be the same as for the continuous growth model which is suitable for transformation above  $T'_0$ .

The trapping model gives a velocity function of the form

$$V_k = \frac{D\{x_I\}}{\lambda} \frac{k_p - k_e}{1 - k_p} \quad (6.47)$$

where  $\lambda$ , the intersite jump distance, is about 0.25 nm and  $D\{x_I\}$  is the diffusion coefficient of carbon in austenite of composition  $x_I$ . The quantity  $D\{x_I\}/\lambda$  is the diffusion velocity of carbon and trapping becomes prominent when the interface velocity approaches this value. Since the carbon atoms execute jumps across a glissile semi-coherent interface it is appropriate to take the coefficient for volume diffusion of carbon.

We now have the third interface response function, equation 6.47, which varies smoothly with  $x^\alpha$  and  $x_I$ . Note that as  $x^\alpha$  approaches  $\bar{x}$ , the diffusion field velocity diverges (tends towards infinity) and the interfacial dissipation then imposes the condition that  $x_I = \bar{x}$  such that the trapping velocity  $V_k$  also tends towards infinity in the full trapping limit.

### 6.8.3 Data on Transformation with Partial Supersaturation

We now consider results from the two main models for growth involving a partial supersaturation of carbon, that due to Olson *et al.* (1987, 1989, 1990) and, due to Hillert (1960, 1975) and Ågren (1989).

With the three interface response functions, the diffusion field velocity (Ivantsov model, with a plate-tip radius fixed at 1.5 nm), the glissile-interface mobility function and the Aziz solute trapping function, Olson *et al.* solved for the interfacial velocity and phase compositions as a function of transformation temperature. Some of their results are presented in Fig. 6.26, for a Fe-0.4C wt% alloy, illustrating how the supersaturation might vary with the transformation temperature for the both the nucleation and growth stages. With a variety of assumptions about the strain energy of transformation and about the nucleation behaviour, the model has been shown to compare favourably with the measured TTT diagram.

The calculations have been extended to cover a wider range of carbon concentrations. Malecki and Langer (1990) found that for high carbon steels the model is not able to predict the acceleration of the bainite reaction at temperatures just above  $M_S$ , first noted by Howard and Cohen (1948) and discussed in section 6.11.3. Mujahid and Bhadeshia (1993) found that the  $M_S$  temperature is predicted accurately if it is assumed that both nucleation and growth are diffusionless for martensite. The variation in the  $B_S$  temperature as a function of the carbon concentration could also be estimated. However, the absolute values of  $B_S$  could only be brought into agreement with experimental data by allowing the stored energy to be a function of temperature.

The model by Hillert and Ågren is founded on the theory for reconstructive transformations. The interface mobility function used relies on absolute reaction rate theory, which is not appropriate for glissile interfaces. The radius of curvature at the plate tip is treated as a free variable. It is assumed that the curvature adopted is that which gives the highest growth rate. Strain energy due to the mechanism of transformation is neglected. To solve for the three unknowns (austenite and ferrite compositions and the interfacial velocity), a solute drag function due to Hillert and Sundman (1976) is utilised in addition to the interface mobility and diffusion field velocity response functions. It is predicted that there is a

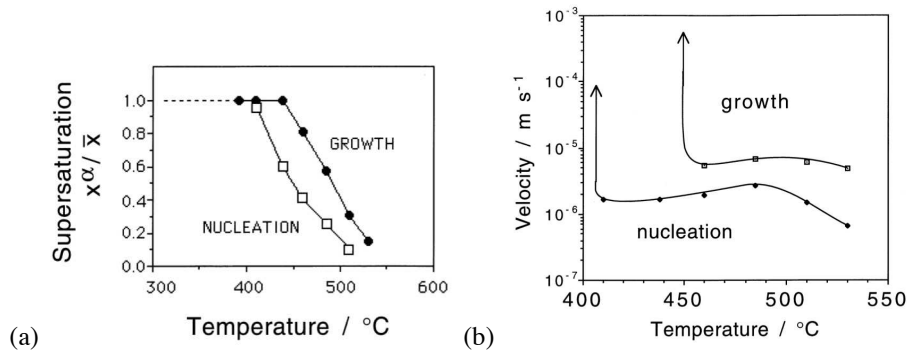


**Figure 6.26** (a) Plot of calculated normalised supersaturation ( $x^\alpha/\bar{x}$ ) of carbon in ferrite versus the isothermal transformation temperature, for a Fe-0.4C wt% alloy, with the data obtained by the simultaneous solution of the interfacial mobility, diffusion field velocity and trapping velocity functions. Martensitic transformation is when both nucleation and growth become diffusionless. (b) The interfacial velocities during the “nucleation” and growth processes.

gradual transition from diffusion-controlled to diffusionless growth as the driving force is increased, although the plate shape is then lost because diffusionless growth occurs with zero interface curvature, i.e. a flat interface!

#### 6.8.4 Summary

Both of the models predict an increase in carbon trapping as the transformation temperature is reduced. They establish the possibility that the transition from bainite to martensite is gradual. However, there remain numerous difficulties in accepting that scenario.

An increasing supersaturation with undercooling is inconsistent with the fact that the bainite reaction stops when the carbon concentration of the residual austenite approaches the  $T_0'$  curve. According to the calculations the carbon concentration of the austenite when transformation stops should be that given by the  $Ae_{3''}$  phase boundary at high temperatures but by the  $T_0'$  curve at low temperatures.

It is assumed that the supersaturation in the ferrite is constant for any given isothermal transformation temperature. On the other hand, there is no reason why the supersaturation should not decrease continuously towards equilibrium as the fraction of transformation increases at a constant temperature. This simply does not happen, e.g. we do not see martensite evolving into Widmanstätten ferrite. In other words, the models are theoretically elegant but do not reflect reality.

### 6.9 Cooperative Growth of Ferrite and Cementite

Ferrite and cementite grow together with a common transformation front during the formation of a pearlite colony. Hultgren (1947) proposed that the essential difference between pearlite and bainite is that in the latter case the cementite and ferrite do not grow cooperatively (Fig. 6.27). The microstructural evolution illustrated is now known to be incorrect, but it is nevertheless often argued that bainite is simply the product of a non-lamellar eutectoid reaction in which the component phases no longer share a common front with the

austenite. This is doubtful for a variety of reasons, one of which is that bainitic ferrite can form without any carbide precipitation at all.

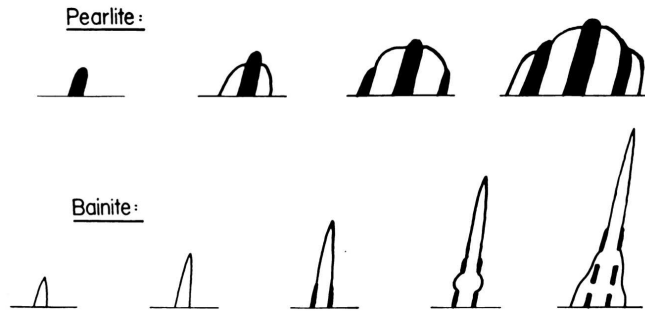


**Figure 6.27** Hultgren's (1947) interpretation of the cooperative and noncooperative growth modes of pearlite and bainite respectively.

There have been attempts to revitalise Hultgren's ideas by adopting a generalised definition of bainite as the product of a non-lamellar, noncooperative mode of eutectoid decomposition. It is further assumed that both pearlite and bainite grow by a reconstructive mechanism in which the transformation front propagates by a ledge mechanism (Lee et al., 1988). It is then claimed that the transition from pearlite to bainite occurs when the cementite and ferrite can no longer grow at the same rate from austenite. The ferrite and cementite cease to grow at the same rate when:

$$\frac{h_{\alpha}}{\lambda_{\alpha}} \neq \frac{h_{\theta}}{\lambda_{\theta}} \quad (6.48)$$

where  $h$  and  $\lambda$  represent the height and interledge spacing respectively. The phases can grow with a common front as long as this ratio is identical for both. The ledges are supposed to move in a direction parallel to the transformation front. They are therefore shared, *i.e.*, they can traverse both ferrite and cementite. Cooperative growth fails when:

$$\frac{h_{\alpha}v_{\alpha}^s}{\lambda_{\alpha}} \neq \frac{h_{\theta}v_{\theta}^s}{\lambda_{\theta}} \quad (6.49)$$

where  $v^s$  is the step velocity. The ledge velocity must change when it moves from the ferrite to the cementite phase to account for the change in the phases which are in local equilibrium, but this is neglected in the analysis.

It is doubtful whether this criterion identifies the essential difference between bainite and pearlite. The character of the transformation interface, whether it is glissile or sessile, is not a part of the analysis.

## 6.10 Overall Transformation Kinetics

### 6.10.1 Isothermal Transformation

A model for a single transformation begins with the calculation of the nucleation and growth rates, but an estimation of the volume fraction requires impingement between particles to be taken into account. This is generally done using the extended volume (Johnson

and Mehl, 1939; Avrami, 1939, 1940, 1941; Kolmogorov, 1937). Referring to Fig. 6.28, suppose that two particles exist at time  $t$ ; a small interval  $\delta t$  later, new regions marked  $a$ ,  $b$ ,  $c$  &  $d$  are formed assuming that they are able to grow unrestricted in extended space whether or not the region into which they grow is already transformed. However, only those components of  $a$ ,  $b$ ,  $c$  &  $d$  which lie in previously untransformed matrix can contribute to a change in the real volume of the product phase ( $\alpha$ ):

$$dV^\alpha = \left(1 - \frac{V^\alpha}{V}\right) dV_e^\alpha \quad (6.50)$$

where it is assumed that the microstructure develops randomly. The subscript  $e$  refers to extended volume,  $V^\alpha$  is the volume of  $\alpha$  and  $V$  is the total volume. Multiplying the change in extended volume by the probability of finding untransformed regions has the effect of excluding regions such as  $b$ , which clearly cannot contribute to the real change in volume of the product. For a random distribution of precipitated particles, this equation can easily be integrated to obtain the real volume fraction,

$$\frac{V^\alpha}{V} = 1 - \exp\left\{-\frac{V_e^\alpha}{V}\right\} \quad (6.51)$$

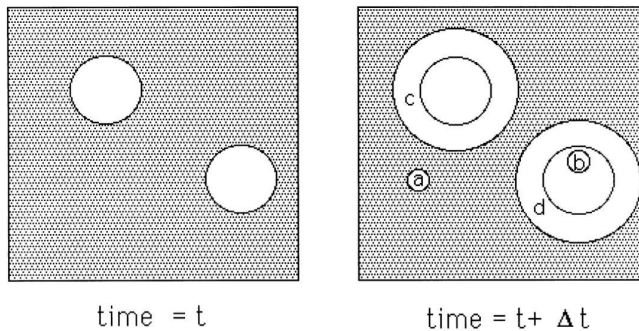


**Figure 6.28** An illustration of the concept of extended volume. Two precipitate particles have nucleated together and grown to a finite size in the time  $t$ . New regions  $c$  and  $d$  are formed as the original particles grow, but  $a$  &  $b$  are new particles, of which  $b$  has formed in a region which is already transformed.

The extended volume  $V_e^\alpha$  is straightforward to calculate using nucleation and growth models and neglecting completely any impingement effects. Consider a simple case where the  $\alpha$  grows isotropically at a constant rate  $G$  and where the nucleation rate per unit volume is  $I_V$ . The volume of a particle nucleated at time  $t = \tau$  is given by

$$v_\tau = \frac{4}{3}\pi G^3(t - \tau)^3 \quad (6.52)$$

The change in extended volume over the interval  $\tau$  and  $\tau + d\tau$  is

$$dV_e^\alpha = \frac{4}{3}\pi G^3(t - \tau)^3 \times I_V \times V \times d\tau \quad (6.53)$$

Substituting into equation 6.51 and writing  $\xi = V^\alpha/V$ , we get

$$\begin{aligned} dV^\alpha &= \left(1 - \frac{V^\alpha}{V}\right) \frac{4}{3} \pi G^3 (t - \tau)^3 I_V V \, d\tau \\ \text{so that} \quad -\ln\{1 - \xi\} &= \frac{4}{3} \pi G^3 I_V \int_0^t (t - \tau)^3 \, d\tau \\ \text{and} \quad \xi &= 1 - \exp\{-\pi G^3 I_V t^4/3\} \end{aligned} \quad (6.54)$$

This equation has been derived for the specific assumptions of random nucleation, a constant nucleation rate and a constant growth rate. There are different possibilities but they often reduce to the general form:

$$\xi = 1 - \exp\{-k_A t^n\} \quad (6.55)$$

where  $k_A$  and  $n$  characterise the reaction as a function of time, temperature and other variables. This equation is frequently used empirically as an economic way of representing experimental data (Radcliffe et al., 1963; Okamoto and Oka, 1985). The temptation to deduce mechanistic information from an empirical application of the Avrami equation should be avoided even when the equation accurately fits the data, since the fitting parameters can be ambiguous. The fact that the equation 6.55 is applied empirically, is sometimes interpreted to be a weakness of the theory, but it can in fact be applied rigorously with explicit nucleation and growth functions as in equation 6.54.

### 6.10.2 Incorrect formulation of incubation time

The time  $\tau$  in equation 6.52 represents the point at which a particle comes into existence and begins to grow. For  $t < \tau$  the particle has zero dimensions. It is therefore, an incubation period for that specific particle. The process is illustrated in Fig. 6.29a, where different particles achieve genesis at different times. The incubation time discussed here should not be confused with an *apparent* incubation time derived from experimental measurements of volume fraction versus time, for example the period  $t_1$  illustrated in Fig. 6.29b, corresponding to the achievement of a specific fraction of transformation. The apparent incubation time will clearly be sensitive to the accuracy of the experimental technique used to monitor the evolution of the volume fraction. The actual incubation time  $\tau$  for individual particles does not appear in the final Avrami equation following integration, for example, equation 6.54. But the equation can be used to derive an apparent incubation time for any particular choice of volume fraction.

There are several reports in the literature that impose apparent incubation periods in the overall transformation kinetics equation [for example, Quidort and Brechet (2002); Luzginova et al. (2008)]. Such equations cannot be used to make predictions because they require a prior knowledge of the incubation periods, and because they are incorrect formulations of the overall transformation kinetics theory (Bhadeshia et al., 2008). They are at best regarded as useful in the quantitative description of known experimental data.

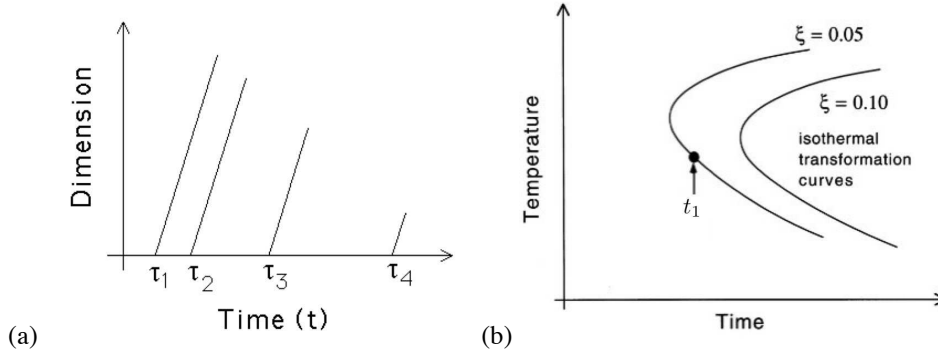


**Figure 6.29** (a) The incubation time  $\tau$  for each particle. In this example, the growth rate is assumed to be constant, but this assumption is not relevant to the definition of  $\tau$ . (b) An apparent incubation time  $t_1$  corresponding to the specified fraction of transformation.

### 6.10.3 Mechanistic Formulation of the Avrami Equation

Reasonable trends can be obtained using an Avrami model founded on the mechanism of the bainite (Singh and Bhadeshia, 1998b).<sup>4</sup> Each nucleus is assumed to transform into one sub-unit of bainite of volume  $u$ . The time required to nucleate is considered to be much greater than that for growth so that the change in extended volume over the interval  $\tau$  and  $\tau + d\tau$  is given by

$$dV_e^\alpha = I_V V u d\tau \quad (6.56)$$

If  $\xi$  is defined as a normalised fraction of bainite, i.e. the fraction of bainite ( $V^\alpha/V$ ) divided by its maximum fraction:

$$\xi = \frac{V^\alpha}{V} / V_V^{\max} \quad \text{where} \quad V_V^{\max} \simeq \frac{x_{T_0'} - \bar{x}}{x_{T_0'} - x^{\alpha\gamma}} \quad (6.57)$$

then the conversion from extended to real volume becomes

$$\begin{aligned} dV^\alpha &= (1 - \xi) dV_e^\alpha \\ &= (1 - \xi) V u I_V d\tau \\ \text{or } V_V^{\max} d\xi &= (1 - \xi) u I_V d\tau \end{aligned} \quad (6.58)$$

For every successful nucleation event, a further number  $p$  of nucleation sites is introduced autocatalytically. It follows that over a period  $\tau$  there will be  $pI_V\tau$  new nucleation sites introduced in addition to those originally present. The total number density  $N_V^T$  of sites at time  $\tau$  therefore becomes

$$N_V^T = N_V^0 + pI_V\tau \quad (6.59)$$

<sup>4</sup>Statements are sometimes made that the Avrami type model requires more fitting constants than others. Thus, Fazeli et al. (2011) claim that the Avrami model required six fitting constants whereas one based on 'nucleation and growth' required just four. This is because they apply the Avrami model empirically, and do not count other fitting factors in the so-called nucleation and growth model, for example their constants  $\alpha$  and  $w_B$ . Similar unjustified claims are made about the superiority of phase field models, as described in Qin and Bhadeshia (2010).

where  $N_V^0$  is the initial number density.<sup>5</sup> The nucleation rate (equation 6.16) therefore becomes time-dependent:

$$I_V = N_V^0 \nu \exp\left\{-\frac{G^*}{RT}\right\} + N_V^0 \nu^2 \tau p \exp\left\{-\frac{2G^*}{RT}\right\} \quad (6.60)$$

On substitution into equation 6.58 we get

$$\frac{V_V^{\max}}{uN_V^0 \nu} \int_0^\xi \frac{d\xi'}{\exp\left\{-\frac{G^*}{RT}\right\}} = \int_0^t \left[1 + p\tau\nu \exp\left\{-\frac{G^*}{RT}\right\}\right] dt' \quad (6.61)$$

which after integration and manipulation gives the time  $t$  to achieve a specified amount of transformation as:

$$t = \frac{-1 + \sqrt{1 - \frac{V_V^{\max}}{uN_V^0} p \ln\{1 - \xi\}}}{p\nu \exp\left\{-\frac{G^*}{RT}\right\}} \quad (6.62)$$

Some example calculations are shown in Fig. 6.30 which illustrates the advantages of formulating the Avrami theory on the basis of transformation mechanism. The maximum fraction decreases as the transformation temperature is raised towards the  $B_S$  temperature, consistent with the incomplete transformation phenomenon. Similarly an increase in the stability of the austenite (change in manganese) retards transformation.

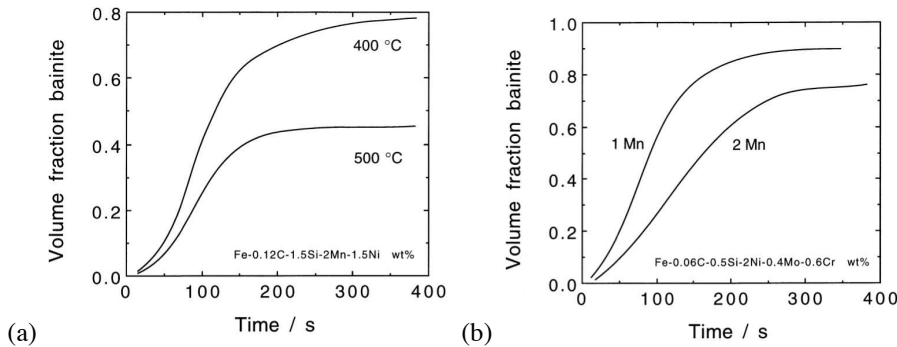


**Figure 6.30** The calculated influence of (a) transformation temperature and (b) manganese concentration on the kinetics of the bainite reaction (Singh and Bhadeshia, 1998b).

The equations above do not deal explicitly with grain boundary nucleation, which requires special theory where two sets of extended space are dealt with (Cahn, 1956), first the coverage of the grain boundary area as transformation proceeds, and the second the overlap of particles as they grow into the volume of the grains (Matsuda and Bhadeshia, 2004). The performance of some of the models described in this chapter has been reviewed (Santofimia et al., 2006). The theory implemented by van Bohemen and Sietsma (2008) includes grain size effects but not the decrease in grain boundary area as transformation proceeds; in effect, the nucleation sites are distributed homogeneously as pre-existing defects, but located presumably at austenite grain boundaries; similar approximations were

<sup>5</sup>Tszeng (2000) has introduced autocatalysis by considering nucleation at the bainite/austenite surface, formulated to allow nucleation on *extended area* rather than real area. This causes the bainite/austenite surface per unit volume to tend to infinity. Similarly,  $w$  in his equations is an extended volume which should not be multiplied by  $I_0$ .

used in (Rees and Bhadeshia, 1992; Chester and Bhadeshia, 1997). Nevertheless, impressive agreement is reported relative to experimental data (van Bohemen and Sietsma, 2008).

#### 6.10.4 Austenite Grain Size Effects

The bainite transformation is much less sensitive to the austenite grain size than is pearlite (Umemoto et al., 1980). Furthermore, elements like boron, which increase the hardenability by segregating to the grain boundaries, have a much smaller effect on bainite than on ferrite. This is because for each bainite plate nucleated at a grain surface, there are a number which are autocatalytically stimulated; the majority of plates in a sheaf do not touch the austenite grain boundaries.

A reduction in the austenite grain size should, nevertheless, lead to an increase in the rate of transformation because of the greater number density of grain boundary nucleation sites (Barford and Owen, 1961). However, Davenport (1941) argued that the grain size has no appreciable effect on the transformation kinetics. In contrast, Graham and Axon (1959) suggested that because the growth of a bainite plate is resisted by the matrix, a smaller grain size should retard growth.

The austenite grain size is best defined by its mean line lineal intercept  $\bar{L}$  because it is related inversely to the grain surface per unit volume  $S_V$  and hence to the number density of nucleation sites  $N_V^0$ :

$$S_V = \frac{2}{\bar{L}} \quad \text{and therefore,} \quad N_V^0 \propto \frac{1}{\bar{L}} \quad (6.63)$$

It follows that the nucleation rate must increase as the austenite grain size decreases. If this is the only effect then there would be an inverse dependence of  $N_V^0$  on  $\bar{L}$ , as is assumed in most models (Chester and Bhadeshia, 1997; van Bohemen and Sietsma, 2008), with the proportionality constant determined experimentally.

The maximum volume  $V_{\max}^S$  of a sheaf which starts from each grain boundary nucleus must be constrained by the grain size, *i.e.*

$$V_{\max}^S \propto \bar{L}^3 \quad (6.64)$$

If this effect is dominant then the overall rate will decrease as the austenite grain size is reduced. Thus, it has been demonstrated experimentally that there is an acceleration of transformation rate as  $\bar{L}$  is reduced when the overall reaction is limited by a slow growth rate, *i.e.* when the sheaf volume remains smaller than the total possible volume of transformation in that grain, and hence is unconstrained by the grain size. Conversely, for rapid growth from a limited number of nucleation sites, a reduction in the austenite grain size reduces the total volume transformed per nucleus and hence retards the overall reaction rate. The two circumstances are illustrated in Fig. 6.31.

When the austenite grain size is not uniform, it is possible to assess the consequences by summing up the contributions from the individual grains, assuming that the volume distribution of grains is known (Gouné et al., 2012).

#### 6.10.5 Anisothermal Transformation Kinetics

A popular method of converting between isothermal and anisothermal transformation data is the *additive reaction rule* of Scheil (1935). A cooling curve is treated as a combination

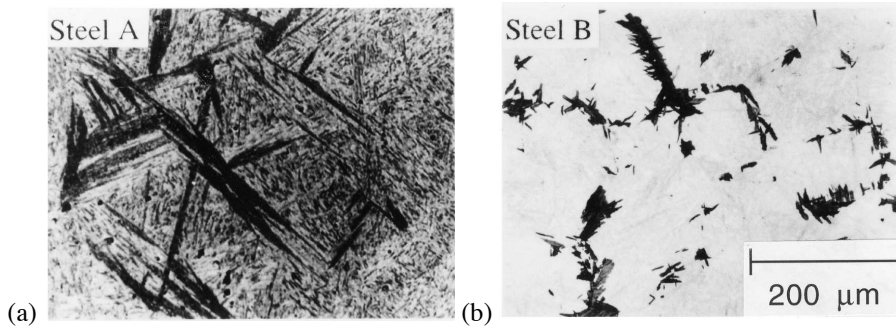


**Figure 6.31** (a) Bainite in a steel where nucleation is sparse and sheaf-growth is rapid. The austenite grains constrain the amount of transformation that each nucleus can cause. Reducing the austenite grain size then causes a net reduction in the overall rate of transformation. (b) Bainite in a steel where the growth rate is small so that the effect of the austenite grain size is simply to promote the nucleation rate. After Matsuzaki and Bhadeshia (1995).

of a sufficiently large number of isothermal reaction steps. Referring to Fig. 6.32, a fraction  $\xi = 0.05$  of transformation is achieved during continuous cooling when

$$\sum_i \frac{\Delta t_i}{t_i} = 1 \tag{6.65}$$

with the summation beginning as soon as the parent phase cools below the equilibrium temperature.

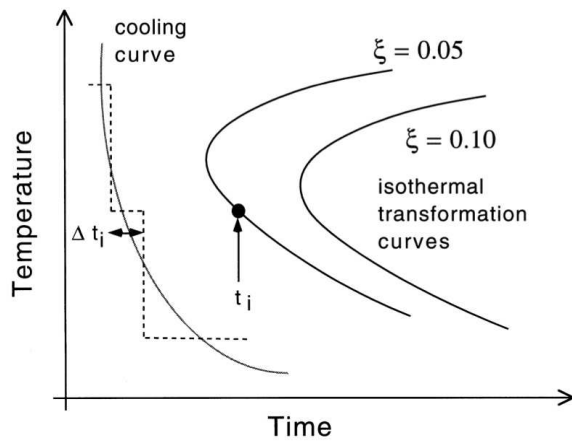


**Figure 6.32** The Scheil method for converting between isothermal and anisothermal transformation data.

The rule can be justified if the reaction rate depends solely on  $\xi$  and  $T$ . Although this is unlikely, there are many examples where the rule has been empirically applied to bainite with success Umemoto et al. (1982). Reactions for which the additivity rule is justified are

called isokinetic, implying that the fraction transformed at any temperature depends only on time and a single function of temperature (Avrami, 1939; Cahn, 1956).

## 6.11 Simultaneous Transformations

A simple modification for two precipitates ( $\alpha$  and  $\beta$ ) is that equation 6.51 becomes a coupled set of two equations,

$$dV^\alpha = \left(1 - \frac{V^\alpha + V^\beta}{V}\right) dV_e^\alpha \quad \text{and} \quad dV^\beta = \left(1 - \frac{V^\alpha + V^\beta}{V}\right) dV_e^\beta \quad (6.66)$$

This can be done for any number of reactions happening together (Robson and Bhadeshia, 1997b; Jones and Bhadeshia, 1997). The resulting set of equations must in general be solved numerically, although a few analytical solutions are possible for special cases which we shall now illustrate (Kasuya et al., 1999).

### 6.11.1 Special Cases

For the simultaneous formation of two phases whose extended volumes are related linearly:

$$V_e^\beta = BV_e^\alpha + C \quad \text{with} \quad B \geq 0 \quad \text{and} \quad C \geq 0 \quad (6.67)$$

then with  $\xi_i = V_i/V$ , it can be shown that

$$\xi^\alpha = \int \exp\left\{-\frac{(1+B)V_e^\alpha + C}{V}\right\} \frac{dV_e^\alpha}{V} \quad \text{and} \quad \xi^\beta = B\xi^\alpha \quad (6.68)$$

If the isotropic growth rate of phase  $\alpha$  is  $G$  and if all particles of  $\alpha$  start growth at time  $t = 0$  from a fixed number of sites  $N_V$  per unit volume then  $V_e^\alpha = N_V \frac{4\pi}{3} G^3 t^3$ . Substitution of the extended volume, equation 6.67 gives

$$\xi^\alpha = \frac{1}{1+B} \exp\left\{-\frac{C}{V}\right\} \left[1 - \exp\left\{-\frac{(1+B)N_V \frac{4\pi}{3} G^3 t^3}{V}\right\}\right] \quad \text{with} \quad \xi^\beta = B\xi^\alpha \quad (6.69)$$

The term  $\exp\{-C/V\}$  is the fraction of parent phase available for transformation at  $t = 0$ ; it arises because  $1 - \exp\{-C/V\}$  of  $\beta$  exists prior to commencement of the simultaneous reaction at  $t = 0$ . Thus,  $\xi^\beta$  is the additional fraction of  $\beta$  that forms during simultaneous reaction. It is emphasised that  $C \geq 0$ . A case for which  $C = 0$  and  $B = 8$  is illustrated in Fig. 6.33.

For the case where the extended volumes are related parabolically (Kasuya et al., 1999):

$$\begin{aligned} \xi^\alpha &= \exp\left\{-\frac{C}{V}\right\} \left[ \sqrt{\frac{\pi}{4A}} \exp\left\{\frac{(1+B)^2}{4A}\right\} \left( \operatorname{erf}\left\{\frac{1+B}{\sqrt{4A}} + \sqrt{AV_e^\alpha}\right\} - \operatorname{erf}\left\{\frac{1+B}{\sqrt{4A}}\right\} \right) \right] \\ \xi^\beta &= \exp\left\{-\frac{C}{V}\right\} \left[ 1 - \exp\left\{-\frac{A(V_e^\alpha)^2 + (1+B)V_e^\alpha}{V}\right\} \right] - \xi^\alpha \end{aligned} \quad (6.70)$$

The volume fractions  $\xi^i$  again refer to the phases that form *simultaneously* and hence there is a scaling factor  $\exp\{-C/V\}$  which is the fraction of parent phase available for coupled transformation to  $\alpha$  and  $\beta$ .

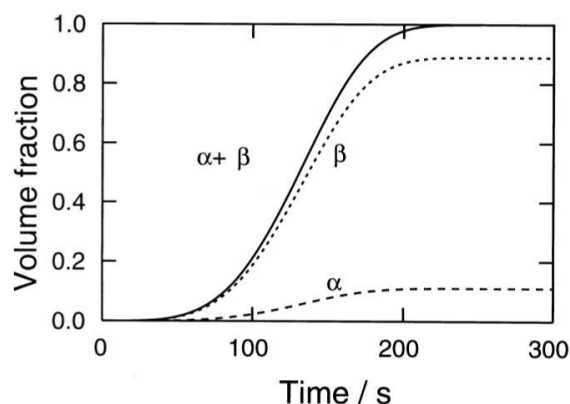


**Figure 6.33** Simultaneous transformation to phases  $\alpha \equiv 1$  and  $\beta \equiv 2$  with  $C = 0$  and  $B = 8$ .

### 6.11.2 Precipitation in Secondary Hardening Steels

Whereas the analytical cases described above are revealing, it is unlikely in practice for the phases to be related in the way described. This is illustrated for secondary hardening bainitic and martensitic steels of the kind used commonly in the construction of power plant. The phases interfere with each other not only by reducing the volume available for transformation, but also by removing solute from the matrix and thereby changing its composition. This change in matrix composition affects the growth and nucleation rates of all the participating phases.

The calculations must allow for the simultaneous precipitation of  $M_2X$ ,  $M_{23}C_6$ ,  $M_7C_3$ ,  $M_6C$  and Laves phase.  $M_3C$  is assumed to nucleate instantaneously with the paraequilibrium composition. Subsequent enrichment of  $M_3C$  as it approaches its equilibrium composition is accounted for. All the phases, except  $M_3C$ , are assumed to form with compositions close to equilibrium. The driving forces and compositions of the precipitating phases are calculated using standard thermodynamic methods.

The interaction between the precipitating phases is accounted for by considering the change in the average solute level in the matrix as each phase forms. This is frequently called the *mean field approximation*. It is necessary because the locations of precipitates are not predetermined in the calculations.

A plot showing the predicted variation of volume fraction of each precipitate as a function of time at  $600^\circ\text{C}$  is shown in Fig. 4.16. It is worth emphasising that there is no prior knowledge of the actual sequence of precipitation, since all phases are assumed to form at the same time, albeit with different precipitation kinetics. The fitting parameters common to all the steels are the site densities and interfacial energy terms for each phase. The illustrated dissolution of metastable precipitates is a natural consequence of changes in the matrix chemical composition as the equilibrium state is approached.

Consistent with experiments, the precipitation kinetics of  $M_{23}C_6$  are predicted to be much slower in the 2.25Cr1Mo steel compared to the 10CrMoV and 3Cr1.5Mo alloys. One contributing factor is that in the 2.25Cr1Mo steel a relatively large volume fraction of  $M_2X$  and  $M_7C_3$  form prior to  $M_{23}C_6$ . These deplete the matrix and therefore suppress  $M_{23}C_6$  precipitation. The volume fraction of  $M_2X$  which forms in the 10CrMoV steel is relatively small, so there remains a considerable excess of solute in the matrix, allowing  $M_{23}C_6$  to precipitate rapidly. Similarly, in the 3Cr1.5Mo steel the volume fractions of

$M_2X$  and  $M_7C_3$  are insufficient to suppress  $M_{23}C_6$  precipitation to the same extent as in the 2.25Cr1Mo steel.

It is even possible in this scheme to treat precipitates nucleated at grain boundaries separately from those nucleated at dislocations, by taking them to be different phases in the sense that the activation energies for nucleation will be different.

### 6.11.3 Time-Temperature-Transformation Diagrams

Transformation curves on TTT diagrams tend to have a C-shape because reaction rates are slow both at high and at low temperatures. The diffusion of atoms becomes difficult at low temperatures whereas the driving force for transformation is reduced as the temperature is raised. The phase diagram thus sets the thermodynamic limits to the decomposition of austenite (Fig. 6.34).

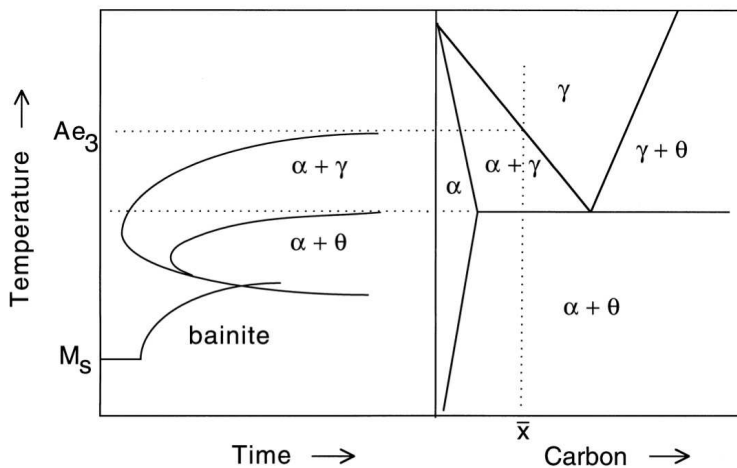


**Figure 6.34** The relationship between a TTT diagram for a hypoeutectoid steel with a concentration  $\bar{x}$  of carbon, and the corresponding Fe-C phase diagram.

Most TTT diagrams can be considered to consist essentially of two C-curves, one for high temperatures representing reconstructive transformations to ferrite or pearlite. The other is for the lower temperatures where substitutional atoms take too long to diffuse, so that reconstructive transformations are replaced by displacive transformations such as Widmanstätten ferrite and bainite. The martensite-start temperature generally features on a TTT diagram as a horizontal line parallel to the time axis (Cohen, 1940).

There are two major effects of alloying additions on transformation kinetics. Solutes which decrease the driving force for the decomposition of austenite retard the rate of transformation and cause both of the C-curves to be displaced to longer times. At the same time they depress the martensite-start temperature (Fig. 6.35). The retardation is always more pronounced for reconstructive reactions where all atoms have to diffuse over distances comparable to the size of the transformation product. This diffusional drag exaggerates the effect of solutes on the upper C-curve relative to the lower C-curve.

For steels where the reaction rate is rapid, it becomes difficult experimentally to distinguish the two C-curves as separate entities. For plain carbon and very low-alloy steels, the

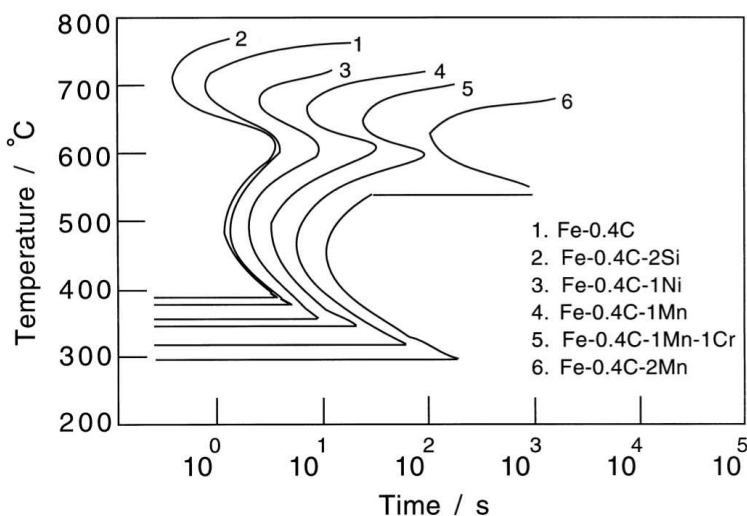


**Figure 6.35** Calculated TTT diagrams showing the C-curves for the initiation of reactions for a variety of steels.

measured diagrams take the form of just a single C-curve over the entire transformation temperature range. This is because the different reactions overlap so much that they cannot easily be distinguished using conventional experimental techniques (Hume-Rothery, 1966). Careful experiments have shown this interpretation to be correct (Brown and Mack, 1973b,a; Kennon and Kaye, 1982). Sometimes the degree of overlap between the different transformation products decreases as the volume fraction of transformation increases (Fig. 6.36). This is because the partitioning of solute into austenite has a larger effect on reconstructive transformations.

As predicted by Zener (1946), when the two curves can be distinguished clearly, the lower C-curve has a flat top. This can be identified with the Widmanstätten-start or bainite-start temperature, whichever is the larger in magnitude (Bhadeshia, 1981c).

There is more detail than implied in the two C-curve description. The upper and lower bainite reactions can be separated on TTT diagrams.<sup>6</sup> There is even an acceleration of the rate of isothermal transformation just above the classical  $M_S$  temperature, due to the formation of isothermal martensite.<sup>7</sup>

Isothermal martensite plates tend to be very thin and are readily distinguished from bainite. Although the overall rate of martensitic transformation appears isothermal, the individual plates are known to grow extremely rapidly. The isothermal appearance of the overall reaction is therefore due to the nucleation process (Smith et al., 1959). The stresses caused by bainitic transformation seem to trigger isothermal martensite; similar recent observations have been attributed to the same effect (Yakubtsov and Purdy, 2011) - the authors refer to the martensite as strain-induced, although their equation for the mechanical

<sup>6</sup>(Schaaber, 1955; White and Owen, 1961; Barford, 1966; Kennon and Burgess, 1978; Bhadeshia and Edmonds, 1979a; Chang, 2004)

<sup>7</sup>(Howard and Cohen, 1948; Schaaber, 1955; Radcliffe and Rollason, 1959; Smith et al., 1959; Brown and Mack, 1973b,a; Babu et al., 1976; Oka and Okamoto, 1986, 1988; Chang et al., 2004)

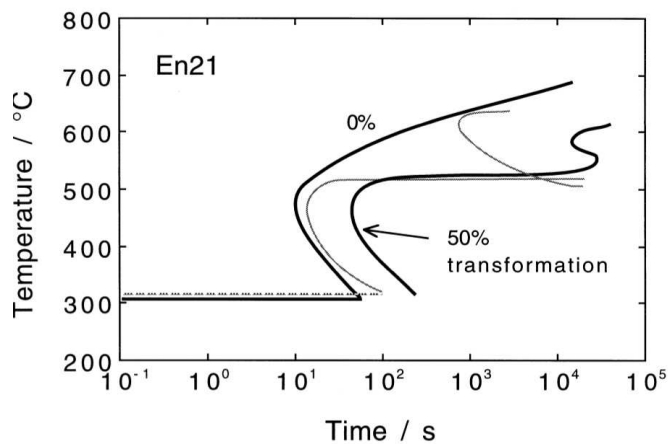


**Figure 6.36** TTT diagram for Steel En21 (Anonymous, 1956). The continuous lines are experimental. The separation of the two constituent C-curves, which is not apparent for the 0% curve is revealed as the extent of reaction increases. The dashed curves are calculated for 0% transformation.

free energy is consistent with a stress-induced transformation (Chapter 8). The rate eventually decreases as the transformation temperature is reduced below the  $M_S$  temperature, giving the appearance of a C-curve with the peak transformation rate located below  $M_S$  (Fig. 6.37).

It is generally considered that cooling to a given temperature below the  $M_S$  temperature produces a fixed amount of athermal martensite. When the sample is then held at that temperature for a prolonged period, it should be possible for the residual austenite to continue transforming into bainite. van Bohemen et al. (2008) have reported observing lower bainitic transformation below the  $M_S$  temperature; they distinguished bainite from autotempered martensite by the number of carbide variants within the plates of ferrite.

#### 6.11.4 Continuous Cooling Transformation Diagrams

Steels are not usually isothermally transformed. It is more convenient to generate the required properties during continuous cooling from the austenitic condition. Continuous cooling transformation (CCT) diagrams are then used to represent the evolution of microstructure (Fig. 6.38).

The rate of transformation in a given steel with a known austenite grain size can be described with just one TTT diagram. However, a different CCT diagrams is required for each cooling function, e.g. whether the cooling rate is constant or Newtonian. It is therefore necessary to plot the actual cooling curves used in the derivation of the CCT diagram (Fig. 6.38). Each cooling curve must begin at the highest temperature where transformation becomes possible (usually the  $A_{e3}$  temperature).

Each CCT diagram requires a specification of the chemical composition of the steel, the austenitisation conditions, the austenite grain size and the cooling condition. The diagrams are therefore specific to particular processes and lack the generality of TTT diagrams.

The CCT diagram is usually partitioned into domains of microstructure; Fig. 6.38 shows the conditions under which bainite and ferrite form. Mixed microstructures are obtained

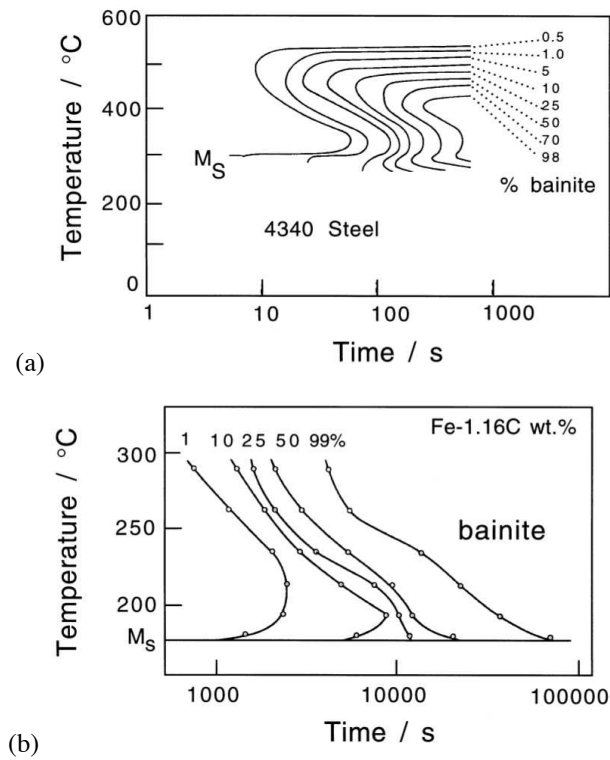


**Figure 6.37** (a) TTT diagram for a Fe-0.39C-0.70Mn-1.7Ni-0.76Cr-0.2Mo-0.28Si-0.22Cu wt% alloy austenitised at 900 °C for 15 minutes. Note the acceleration in the rate of transformation as the  $M_S$  temperature is approached; data from Babu et al. (1976). (b) Similar data for a plain carbon steel (Howard and Cohen, 1948).

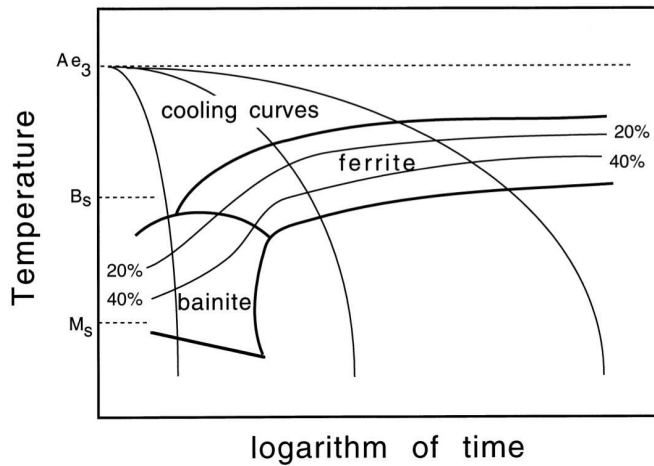


**Figure 6.38** CCT diagram illustrating the cooling curves, constant volume percent contours and transformation temperatures.

when a domain boundary is intersected by a cooling curve. The constant volume fraction contours must be continuous across the domain boundaries to avoid (incorrect) sudden changes in volume fraction as the boundary is crossed, e.g. points *a*, *b* on Fig. 6.39). The contours represent the fraction of austenite which has transformed into one or more phases. It follows that there are constraints on how the zero percent martensite and bainite curves meet, avoiding the double intersection with the cooling curve illustrated in the lower part of Fig. 6.39. Cooling curve *X* which leads to a fully martensitic microstructure, intersects the 0% transformation curve at just one point, without intersecting the region *cd*. Cooling curve *Y*, on the other hand, produces a mixed microstructure with less than 20% of bainite, the remaining austenite transforming to martensite on cooling. The temperature at which martensitic transformation begins (line *abc*) is depressed if bainite forms first and enriches the residual austenite with carbon.

The bainite curve in Fig. 6.39 approaches the  $B_S$  temperature asymptotically along *ef* as the cooling rate decreases consistent with the flat top of the bainite C-curve in the TTT diagram. This is not always the case as shown schematically in Fig. 6.40 (Kunitake, 1971; Schanck, 1969; Lundin et al., 1982). Any transformation which precedes bainite alters the chemical composition of the residual austenite. The main changes occur in the region associated with the vertical line *c* in Fig. 6.40. The temperature at which the bainite first forms is depressed by the changed composition of the austenite. Because the ferrite and bainite domains are separated by a time gap, the continuity of constant volume fraction contours is interrupted. The contours must still be plotted so that their loose ends are connected by a cooling curve as illustrated by *ab* on Fig. 6.40.

Although bainite is depressed to lower temperatures by the prior formation of allotriomorphic ferrite as the cooling rate decreases, the temperature range over which bainite forms is eventually reduced. This is because very slow cooling rates give ample opportunity for transformation to be completed over a smaller temperature range as illustrated by the rising curve *de* on Fig. 6.40.

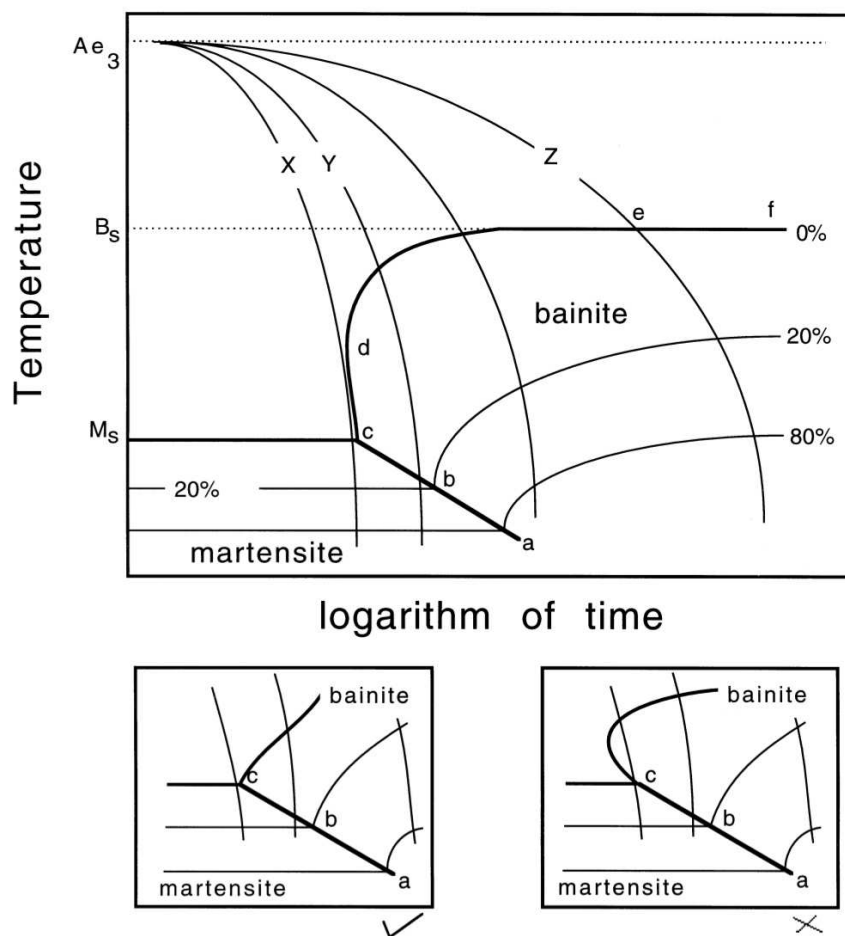


**Figure 6.39** Schematic CCT diagrams illustrating the continuity of constant volume percent contours across microstructure domain boundaries and the correct way in which the zero percent curves of different domains must meet at the point *c*.

All of the features described here can be found in actual TTT and CCT diagrams, for example, the measured diagrams for a “2.25Cr1Mo” steel which is used widely in the bainitic condition for power plant applications (Fig. 6.41).

### 6.11.5 Boron, Sulphur and the Rare Earth Elements

The early commercial development of bainitic steels relied on the effect of boron on the transformation characteristics of low-carbon steels (Chapter 1). Boron retards the heterogeneous nucleation of allotriomorphic ferrite at the austenite grain surfaces, to a greater degree than that of bainite (Fig. 6.42); in some steels there is little or no influence of soluble boron on the rate of the bainite reaction (Mesplont et al., 2002; Khare et al., 2009). This difference in the effect on allotriomorphic ferrite and bainite permits boron-containing steels

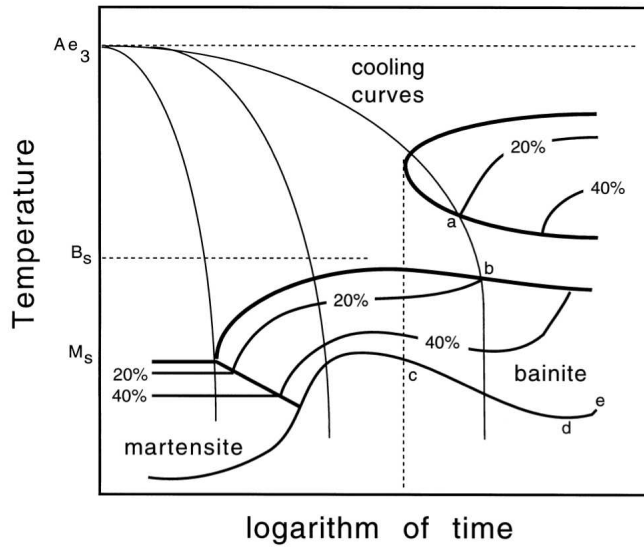


**Figure 6.40** CCT diagram in which the bainite region is strongly influenced by the initial formation of ferrite during continuous cooling transformation.

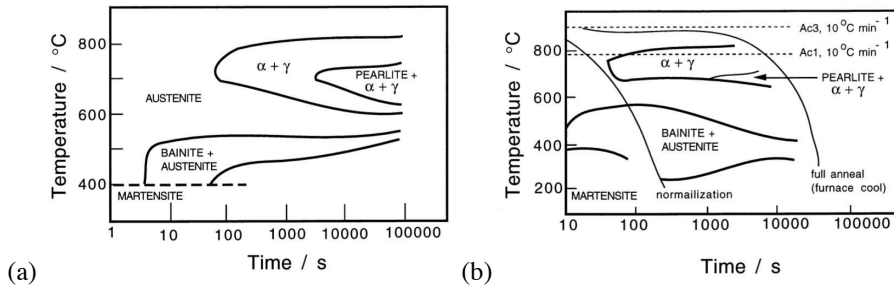


**Figure 6.41** Corresponding TTT and CCT diagrams for a 2.25Cr1Mo steel (Lundin et al., 1982). The CCT diagram shows the terminology used in describing air-cooling from the austenitisation temperature (i.e. normalising) and furnace cooling (i.e. annealing).

to be cooled continuously into fully bainitic microstructures. Elements like manganese are not suitable because they improve the martensite hardenability and hence favour a mixed microstructure of bainite and martensite.

Boron segregates to austenite grain boundaries. In doing so it reduces the grain boundary energy and hence makes the boundaries less effective as heterogeneous nucleation sites. A typical boron addition of  $\approx 0.002$  wt% is sufficient to have a profound effect on transformation kinetics, although the exact amount must clearly depend on the austenite grain size. Too much boron precipitates as borides which stimulate the nucleation of ferrite. The boron is only effective in enhancing hardenability when present in solid solution, not when precipitated as oxides or nitrides (Fig. 6.43). It is for this reason that boron containing steels are usually deoxidised with aluminium. Titanium is added to tie up any nitrogen which may otherwise combine with the boron and render it impotent. It is possible that

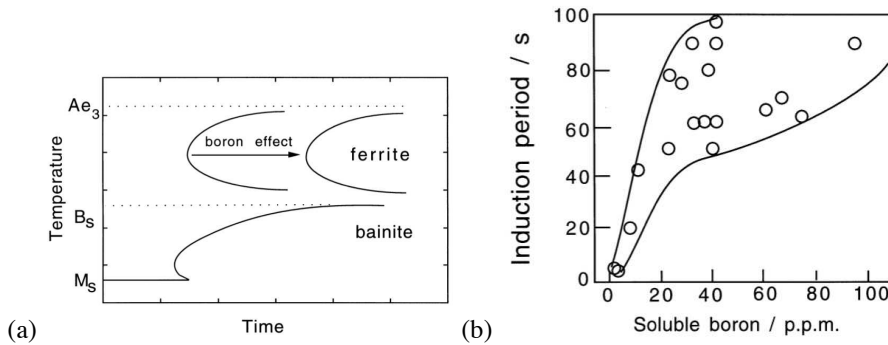


**Figure 6.42** (a) The effect of boron and its analogues (the rare earth elements) on the TTT diagram. There is a pronounced effect on the allotriomorphic ferrite transformation but only a minor retardation of bainitic reaction. (b) Change in the incubation time for the allotriomorphic ferrite reaction as a function of the soluble boron concentration. After Pickering (1978a).

a recent report (Chang et al., 2013) that boron accelerates the initial stages of the nano-structured bainitic transformation (Chapter 14) is due to nucleation being stimulated by its precipitation.

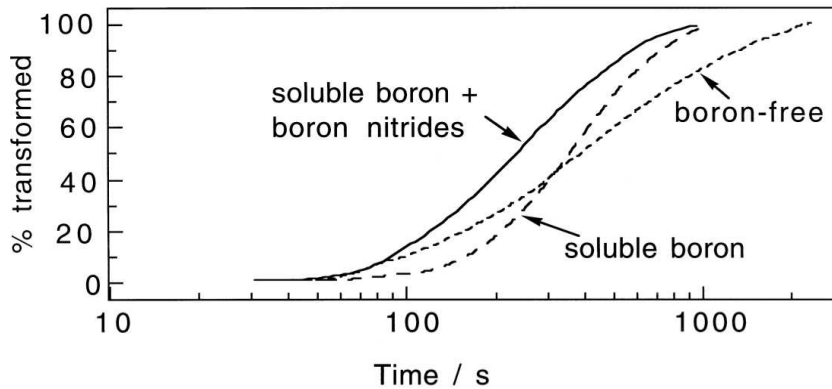


**Figure 6.43** Experimental data due to Ueda et al. (1980) for three steels. The rate of reaction is slow in the sample containing soluble boron and fast in the one containing boron nitride, compared with the boron-free steel.

Carbon also tends to segregate to austenite grain boundaries. In low carbon steels, niobium or titanium form carbides thereby reducing the quantity available for segregation. This leaves the boundaries open to receive boron, so that the effect on hardenability is much greater (Tamehiro et al., 1987b,a; Zhu et al., 2011). Otherwise the boron can be displaced from the grain boundaries by the preferential segregation of carbon. Niobium, titanium and molybdenum, by combining with carbon or clustering with carbon atoms, also suppress the precipitation of  $M_{23}(B, C)_6$ , leaves the boron free to saturate the austenite grain surfaces (Hara et al., 2004).

The efficacy of boron is influenced by the presence of nonmetallic inclusions, especially in steel welds or in inoculated steels where inclusions are added deliberately to induce the

precipitation of desirable forms of bainite. For example, MnS and Al<sub>2</sub>O<sub>3</sub> particles seem to act as heterogeneous nucleation sites for BN and M<sub>23</sub>C<sub>6</sub> during fabrication (Saeki et al., 1986). This reduces the free boron available for segregation to the ferrite nucleation sites (Dionne et al., 1988).

Quite small concentrations of sulphur ( $\approx 0.005$  wt%) can sometimes stimulate the nucleation of bainite (Umemoto et al., 1986b). Iron-rich sulphides precipitate at the austenite grain boundaries and form potent sites for the nucleation of bainite.

Rare-earth elements including cerium, neodymium, lanthanum and yttrium are believed to act in a manner similar to boron (Jingsheng et al., 1988). Attention has been focused on cerium additions of up to 0.134 wt%, where it is found that allotropic ferrite formation is retarded relative to that of bainite. The mechanism is said to involve the segregation of cerium to the austenite grain boundaries. The effect of cerium is dramatically reduced if the phosphorus content exceeds  $\approx 0.02$  wt%, although why this is so has yet to be established. Cerium and lanthanum also form the high melting point oxides Ce<sub>2</sub>O<sub>3</sub> and La<sub>2</sub>O<sub>3</sub>, which may play a role in acting as heterogeneous nucleation sites, although the evidence for this is lacking (Chen and Li, 2007).

An indirect role of elements such as yttrium comes from their ability to getter sulphur, especially in the presence of sulphides which influence the nucleation frequency of ferrite (Abson, 1987).

### 6.11.6 Niobium and hardenability

Niobium has two principal roles; the first is in forming boundary-pinning precipitates during hot deformation, leading ultimately to a refined austenite grain size and hence better mechanical properties (Gladman, 1996; Morrison, 2009; Gray, 1973). Dissolved niobium also retards recrystallisation and recovery during thermomechanical processing and has an important influence on the hardenability of the steel.<sup>8</sup> This latter effect has been known for some time (Rönn, 1963; de Kazinczy et al., 1963); the period required for the initiation of the allotropic ferrite transformation becomes longer in the niobium-containing steel, Fig. 6.44. Niobium has also been reported to retard the kinetics of transformations in a high-alloy (Fe-0.2C-10Cr-0.056Nb wt%) steel where the reactions involve the formation of large amount of chromium carbide in addition to ferrite (Rios and Honeycombe, 1992).

The hardenability is not independent of the austenite grain size, and care has to be exercised to separate the intrinsic effects due to dissolved niobium and the large grain size obtained when the niobium is in solution. Rather like the influence of boron, dissolved niobium does not have a large influence on the bainite reaction (Amin and Pickering, 1981; Rees et al., 1995; Wang et al., 2011); this indicates that the primary role of niobium is in altering the nucleation rate of allotropic ferrite at the austenite grain surfaces. It has been proposed that the bainite-start temperature is slightly depressed by soluble niobium, but the reported experiments do not in fact measure  $B_S$  since they were conducted using continuous cooling transformation (Lee et al., 2005).

**Hardenability Enhancement Mechanisms** It has been suggested that the segregation of niobium and carbon into  $\gamma/\gamma$  boundaries reduces the activity of carbon, causing a reduc-

<sup>8</sup>Rönn (1963); de Kazinczy et al. (1963); Fisher and Geils (1969); Gray (1972, 1973); Tanaka (1981); Eldis and Hagel (1977); Okaguchi et al. (1988); Fossaert et al. (1995); Prasad et al. (2003); Wang et al. (2011); Yan and Bhadeshia (2013). Niobium has also been suggested to increase the hardenability of TRIP-assisted steels (Pereloma et al., 1999), resulting in the increased retention of austenite but the uncertainties in the measurement of phase fractions were not stated, or the full set of fractions was not even reported (Hanzaki et al., 1997).

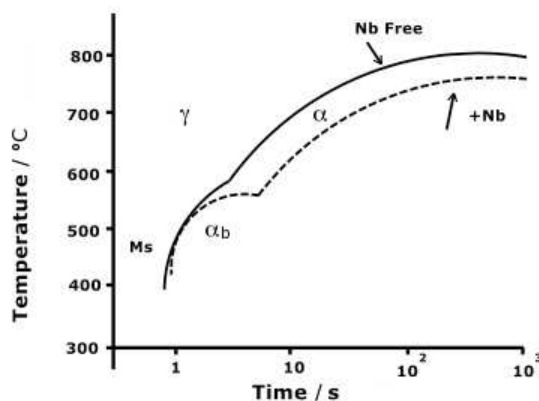


Figure 6.44 TTT diagram adapted from de Kazinczy et al. (1963).

tion of the gradient of carbon in the austenite (Thomas and Michal, 1981). However, this confuses the thermodynamics of the  $\gamma/\gamma$  interface with that in the unperturbed austenite ahead of the  $\alpha/\gamma$  transformation front (Bhadeshia, 1983a).

Like boron, niobium segregation could reduce the  $\gamma/\gamma$  interfacial energy, thus making such boundaries less potent as heterogeneous nucleation sites. There is some evidence to support a reduced nucleation rate (Ouchi et al., 1982; Enomoto et al., 1994). Recent atom-probe studies (Felfer et al., 2012) suggest this kind of segregation but Mn, Si, C and P were also enriched at the boundaries so that the specific role of niobium is uncertain.

The situation becomes more complicated during the thermomechanical processing of austenite because the deformation-induced precipitation of Nb reduces the amount in solid solution. No increase of hardenability was found by continuous cooling of the steel with composition of Fe–0.04C–0.3Si–1.39Mn–0.037Al–0.41Ni–0.025Nb–0.014Ti wt% after 40–60% reduction and holding at 800°C for 5 min (Abe et al., 1988). However, significant lowering of  $Ar_3$  was reported in a steel with composition of Fe–0.09C–0.25Si–1.45Mn–0.011Nb after 69% reduction at 800°C (Abe et al., 1985). It is possible that there was no holding time provided for the precipitation after the deformation and before the continuous cooling in the latter work, but in both cases information was lacking on how much soluble Nb was available for retarding the transformation.

The retardation of the austenite to ferrite transformation has been reported during isothermal heat treatment, i.e. the transformation rate of the steel containing soluble Nb is slower compared to the Nb free steel with similar base composition (Wang et al., 2011; Amin and Pickering, 1981). Consistent with the earlier discussion, this retardation effect was greater for the diffusional transformation to allotriomorphic ferrite than in the displacive transformation to bainite.

Yeo (1963) demonstrated that niobium over the range 0.05–0.8 wt% reduced the  $M_S$  temperature but with the opposite effect when the concentration is less than 0.05 wt%.<sup>9</sup> It can be surmised, therefore, that the hardenability enhancement due to small concentrations of niobium is not by increasing the thermodynamic stability of the austenite. It has been

<sup>9</sup>Hanzaki et al. (1997) quoted this work as a mechanism for hardenability enhancement, but the alloy studied only had 0.035 wt% Nb, below the level where it is observed to reduce  $M_S$ .

speculated that carbide-forming elements such as Mo, Nb and V retard the diffusion of carbon during the transformation from austenite to ferrite (Tamehiro et al., 1987c; Matsuda et al., 1996; Hanzaki et al., 1997) but the effect is insignificantly small (Bhadeshia, 2013a).

Diffusion features in another context when explaining the hardenability change due to niobium additions. Solute drag and ‘solute drag-like effects’ are sometimes said to enhance hardenability (Hanzaki et al., 1997). Solute drag arises when free energy is dissipated when segregated-solute diffuses within a moving interface, and this motion may induce diffusion profiles in the vicinity of the interface, where these latter profiles are not to be confused with the partitioning of solute between phases (Cahn, 1962; Hillert, 1970). There is no theoretical framework for solute drag-like effects, originally proposed to explain discrepancies in the growth rate data for allotriomorphs of ferrite (Bradley and Aaronson, 1981). The logic of the proposed drag-like effect has been critically assessed (Bhadeshia, 1983a). But it is important to note (Deardo et al., 1981) that tracer diffusion data show that the interdiffusion coefficient of niobium in austenite is significantly larger than the self-diffusion coefficient for iron. If this can be extrapolated to an  $\alpha/\gamma$  interface then significant drag effects due to niobium diffusion in the interface are not likely given that iron atoms have to diffuse during diffusional transformations (Bhadeshia, 1985b).

The most plausible mechanism for the role of small concentrations of niobium in retarding the formation of allotriomorphic ferrite seems to be its effect in reducing the  $\gamma/\gamma$  interfacial energy. The change in interfacial energy per unit area, is given approximately by (Yan and Bhadeshia, 2015):

$$\Delta\sigma = \frac{0.006}{0.079} = 0.076 \text{ J m}^{-2} (\text{wt}\% \text{ of soluble niobium})^{-1} \quad (6.71)$$

This can be substituted into a standard model for phase transformations in steels in order to calculate the time-temperature-transformation characteristics as a function not only of the niobium concentration but also the other solutes present in the steel.

## 6.12 Superhardenability

Transformations in a moderately hardenable steel can be retarded by superheating the melt to about 1650 °C during steelmaking, as long as the aluminium concentration is in the range 0.03–0.05 wt% (Brown and James, 1980). This phenomenon is dubbed the *superhardenability effect*; the effect on TTT diagrams is shown in Fig. 6.45.

The effect is most pronounced with high hardenability steels; it is also enhanced by increasing the aluminium concentration to about 0.06 wt% before it saturates (Mostert and van Rooyen, 1982). Superhardenability is not influenced by prolonged holding at the austenitisation temperature, as sometimes happens with hardenability increments due to boron additions. Some of the samples used in the original experiments were cast in air, the others in argon, and tests were carried out for both superheated (1650 °C) and conventional melts (1550 °C), at varying concentrations of aluminium. The superheated melts were held at 1650 °C for a few minutes and then cooled to 1550 °C, where alloying additions were made before casting.

The superheat apparently causes the breakdown of clusters of alloying atoms in the liquid and this influences hardenability (Sachs et al., 1980). This fails to explain why holding a superheated melt at a lower temperature before casting does not reform the clusters and hence eliminate the superhardenability. Furthermore, superheating is not necessary when the melting is carried out under an inert atmosphere.

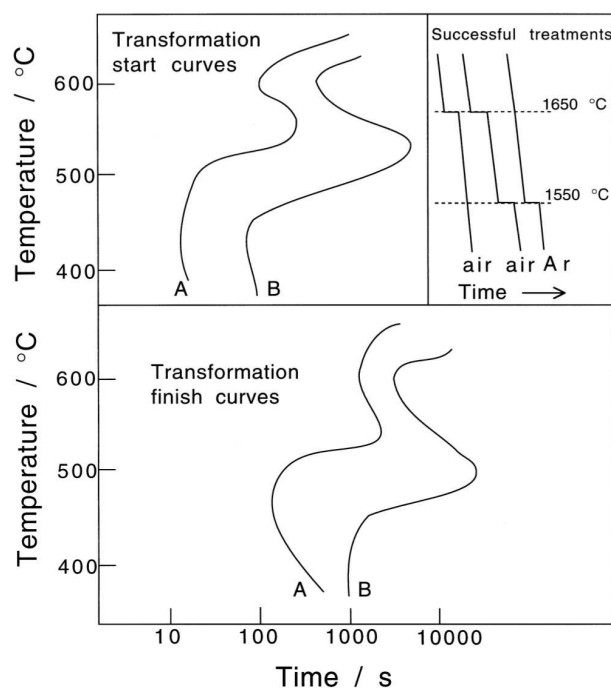


**Figure 6.45** The superhardenability effect. Curves *A* and *B* represent steels which were cast using melt temperatures of 1550 and 1650 °C respectively. The steels have similar compositions but their aluminium concentrations are 0.03 and 0.09 wt% respectively. After Mostert and van Rooyen (1982).

An alternative interpretation is based on nonmetallic inclusions such as manganese oxy-sulphides or titanium oxides in the steel. These can help nucleate ferrite and so reduce hardenability (Chapter 10). Aluminium is a stronger oxidising element than Mn, Si, or Ti. It forms alumina which is ineffective as a heterogeneous nucleation site for ferrite. The preferential formation of alumina would therefore lead to an increase in hardenability. This hypothesis explains several features of the superhardenability effect:

- (i) The need to add aluminium.
- (ii) That superheat is not needed when an inert gas cover is used during steelmaking. This would lead to a reduction in the oxygen concentration and hence the number density of the oxide nucleation sites.
- (iii) Consistent with experimental data, an inclusion effect should not fade during prolonged austenitisation.
- (iv) The additional nucleation sites on inclusions can only contribute significantly in steels which already have a reasonable hardenability, i.e. where any enhancement of nucleation kinetics would have a noticeable outcome.

The potent influence of inclusions is well established in welding metallurgy (Chapter 10). Controlled experiments are now needed, in which the trace element concentrations (Al, Ti, O, N, S, B) are carefully monitored.

### 6.13 Effect of Chemical Segregation

Commercial steels do not have a uniform chemical composition. The thermomechanical processing used in the manufacturing process improves matters but the final product still is heterogeneous. Solute segregation can have a profound effect on the development of microstructure, for example, in the development of bands of transformation products (Fig. 6.46). The segregation structure of solidification is spread out into bands parallel to the rolling plane during deformation. The microstructural bands follow the segregation pattern because it is the local chemical composition that determines the onset of transformation.

The scale of segregation compares with the spacing of the secondary dendrite arms of the solidification microstructure, with a repeat distance of a few tens of micrometres. The peak concentrations are about a factor of two of the mean values. Any coherency strains caused by variations in lattice parameter due to these composition gradients can therefore be neglected. Such strains become important in the theory of spinodal decomposition (or artificial multilayered structures) where the gradients are much larger.

It is the segregation of substitutional solutes which is the real cause of banding. Carbon diffuses rapidly and becomes homogeneous in the austenite; there may be small concentration variations as the carbon attempts to achieve a uniform chemical potential in the presence of substitutional solute gradients (Kirkaldy et al., 1962).

Although carbon is homogeneously distributed in the austenite, the preferential formation of ferrite in the substitutional-solute depleted regions causes a partitioning of carbon into the adjacent substitutionally-enriched regions. The resulting carbon-enriched bands have a profound influence on the development of microstructure, but it is important to realise that the redistribution of carbon is a consequence of solid state transformation and only indirectly due to the solidification process.

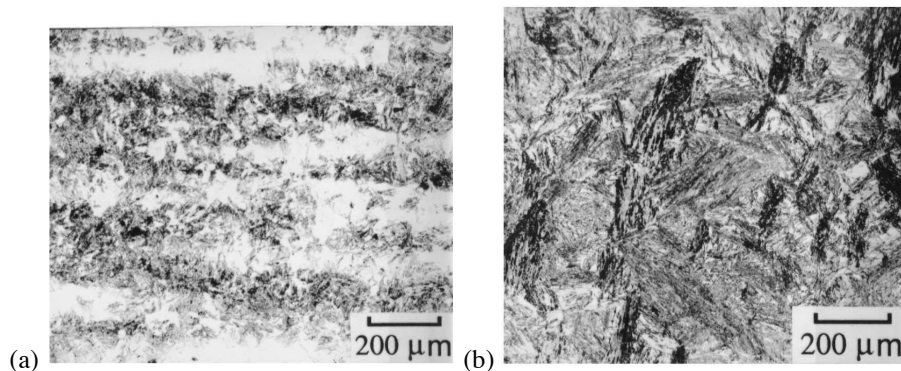


**Figure 6.46** (a) Optical micrograph illustrating the banded microstructure obtained in a heterogeneous steel (300M) after isothermal transformation to bainite; (b) corresponding optical micrograph for the sample which was homogenised prior to isothermal transformation to bainite (Khan and Bhadeshia, 1990).

Davenport (1939) compared the isothermal transformation kinetics of steels containing banding with those which had been homogenised by annealing in the austenitic condition. It is expected that transformation should start first in the solute-depleted regions, and at a temperature which is higher than that for a homogenised steel. The early part of the TTT diagram of segregated steels is expected to reflect the behaviour of the solute-depleted re-

gions. Conversely, the C-curves for the later stages of transformation should reflect slower transformations in the solute-enriched regions. Davenport's experiments did confirm this; the C-curves for the initiation of bainite in the segregated steels were frequently found to be at longer times when compared with homogenised steels.

The observations are summarised in Fig. 6.47. The reaction is faster in the heterogeneous sample at high transformation temperatures, but not as the undercooling below the  $B_S$  temperature increases. The rate is always found to be slower in the heterogeneous samples when considering the later stages of transformation. Experiments by Grange (1971) are consistent with these observations. The fact that the C-curves of the homogeneous and heterogeneous samples cross is difficult to understand if it is argued that transformation should always be easier in the solute-depleted regions.

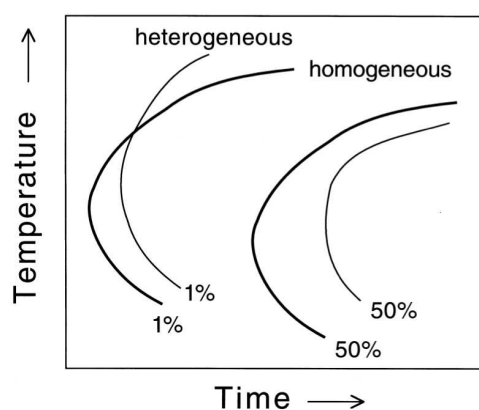


**Figure 6.47** The effect of chemical segregation on the bainite C-curves of TTT diagrams.

The peculiar behaviour illustrated in Fig. 6.47 has been explained quantitatively (Khan and Bhadeshia, 1990). The segregated steel is able to transform in its solute-depleted regions at temperatures above  $B_S$  for the homogeneous alloy. This advantage is maintained at small undercoolings. However, at higher undercoolings the homogeneous steel is able to transform faster because bainite can nucleate uniformly in all regions, whereas it is only able to form in the depleted regions of the heterogeneous alloy.

The carbon partitioned during transformation is localised near the platelets so on a coarser scale it is more uniformly distributed in the homogeneous sample where the bainite grows everywhere. By contrast, most of the partitioned carbon remains in the substitutional solute depleted regions of the segregated sample and retards the development of transformation. The effect is prominent at large undercoolings because the maximum fraction of bainite that can form is greater. Anything which enables the distribution of carbon to become more uniform gives heterogeneous steels a kinetic advantage. For example, slow cooling through the transformation range (Fig. 6.48).

To summarise, when bainite forms during continuous cooling transformation, the reaction may begin at a higher temperature in segregated steels, but both the extent and rate of subsequent transformation should be larger in homogenised alloys.

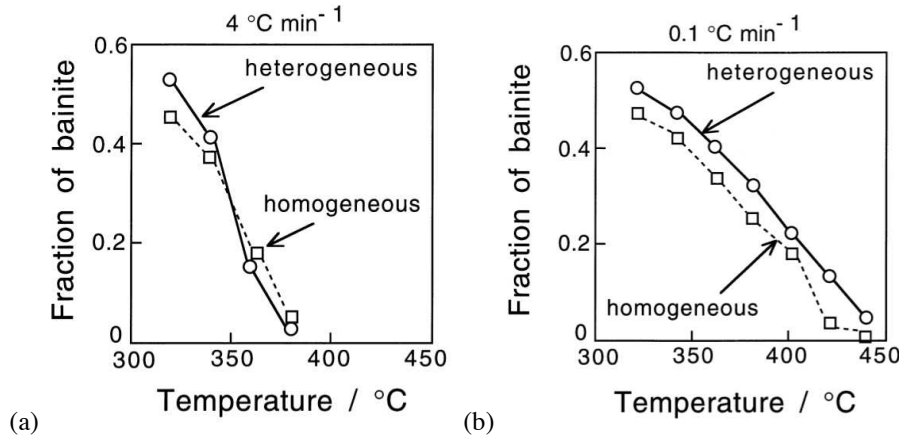


**Figure 6.48** Experiments on homogenised and heterogeneous steel samples in which bainitic transformation was obtained by continuous cooling. (a)  $4\text{ }^{\circ}\text{C min}^{-1}$  (b)  $0.1\text{ }^{\circ}\text{C min}^{-1}$ . The slower cooling conditions permit a more uniform distribution of carbon in the residual austenite, in which case the heterogeneous sample transforms to a greater extent relative to the homogenised sample, at all temperatures.

#### 6.14 Martensitic Transformation in Partially Bainitic Steels

The formation of bainite enriches the residual austenite and introduces strains and defects. This must influence the way in which the residual austenite transforms subsequently to martensite.

The progress of the athermal martensitic transformation is usually described empirically using the Koistinen and Marburger (1959) equation:

$$1 - \xi = \exp\{-C_6(M_S - T_Q)\} \quad (6.72)$$

where  $\xi$  is the volume fraction of martensite,  $T_Q$  is a temperature to which the sample is cooled below  $M_S$  and  $C_6 \simeq 0.011\text{ K}^{-1}$  is a constant obtained originally by fitting to experimental data.

Magee (1970) justified this equation by assuming that the number density of new plates of martensite per unit volume of austenite,  $dN$ , is proportional to the change in the driving force  $\Delta G^{\gamma\alpha}$  on cooling below  $M_S$ :

$$dN = -C_7 d(\Delta G^{\gamma\alpha}) \quad (6.73)$$

where  $C_7$  is a proportionality constant. The change in the volume fraction of martensite is therefore given by:

$$d\xi = \bar{V} dN_V \quad (6.74)$$

where  $dN_V$  is the change in the number of new plates of martensite formed per unit volume of sample, given by  $dN_V = (1 - \xi)dN$ . On combining these equations and substituting  $[d(\Delta G^{\gamma\alpha})/dT]dT$  for  $d(\Delta G^{\gamma\alpha})$  we get:

$$d\xi = -\bar{V}(1 - \xi)C_7 \frac{d(\Delta G^{\gamma\alpha})}{dT} dT \quad (6.75)$$

which on integration between the limits  $M_S$  and  $T_Q$  gives

$$\ln\{1 - \xi\} = \bar{V}C_2 \frac{d(\Delta G^{\gamma\alpha})}{dT} (M_S - T_Q) \quad (6.76)$$

or

$$1 - \xi = \exp\left\{\bar{V}C_2 \frac{d(\Delta G^{\gamma\alpha})}{dT} (M_S - T_Q)\right\}. \quad (6.77)$$

which has a similar form to the equation used by Koistinen and Marburger.

Equation 6.72 takes account only of the chemical composition of the steel via  $\Delta G^{\gamma\alpha}$ , and the transformation temperature  $T_Q$ . However, when dealing with retained austenite that is in a fine state, and perhaps subjected to stresses and strains, it is necessary to modify the theory (Yang and Bhadeshia, 2009; Yang et al., 2012a). Fig. 6.49 shows the sensitivity of  $M_S$  on the austenite grain size. The influence of stress *per se* is expressed via a mechanical driving force (Chapter 8) which supplements the chemical component, and has been estimated on the basis of the shape deformation of martensite as (Olson and Cohen, 1982):

$$\begin{aligned} \Delta G_{\text{mech}} &= -0.86\sigma && \text{for uniaxial tension} \\ \Delta G_{\text{mech}} &= -0.58\sigma && \text{for uniaxial compression} \end{aligned} \quad (6.78)$$

where the driving force is in  $\text{J mol}^{-1}$  and the stress in MPa. Such calculations can in fact be done for arbitrary stress tensors (Kundu et al., 2007), but most experiments are done in a uniaxial mode.

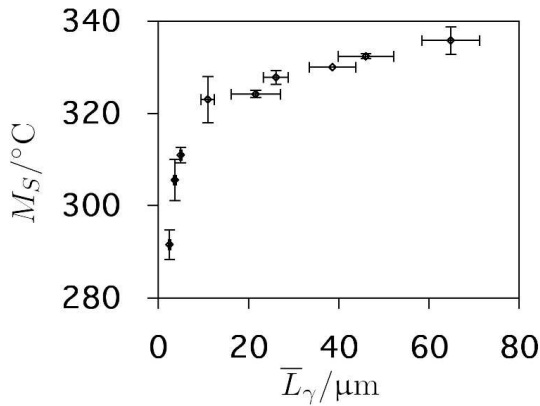


**Figure 6.49** The measured dependence of the martensite-start temperature on the austenite grain size (Yang and Bhadeshia, 2009).

Like bainite, martensite plates do not traverse austenite grain boundaries because a disciplined motion of atoms cannot be sustained across such interfaces. The maximum length of the plate of martensite is therefore equal to the size of the austenite grain in which it grows. The dependence of  $M_S$  on the size of the austenite regions comes from the fact that the aspect ratio of a martensite plate is essentially fixed by strain energy minimisation (equation 5.4), so the volume of austenite that is transformed per plate decreases with the austenite grain size. Given that a certain volume must be achieved in order for a given experimental technique to detect martensite, the  $M_S$  temperature will decrease as the austenite grain size is reduced, as follows (Yang and Bhadeshia, 2009):

$$M_S^o - M_S = \frac{1}{b} \ln \left[ \frac{1}{\bar{L}_\gamma^3} \left\{ \exp\left(-\frac{\ln(1 - \xi)}{m}\right) - 1 \right\} + 1 \right] \quad (6.79)$$

where  $b = 0.2689$ ,  $\bar{L}_\gamma$  in mm, is the mean lineal intercept,  $m = 0.05$  is the aspect ratio of martensite plates, and  $M_S$  is defined when a fraction  $\xi = 0.01$  of martensite is obtained.  $M_S^0$  is the fundamental martensite-start temperature measured for an infinitely large austenite grain size.

One effect of plastic strain prior to transformation is to alter  $\bar{L}_\gamma$  through a change in the shape of the austenite grains. This problem has been solved for a large variety of deformations in which an equiaxed grain is strained (Singh and Bhadeshia, 1998b; Chae et al., 2009), and for uniaxial tension or compression, the result is:

$$\frac{\bar{L}_0}{\bar{L}} = \frac{(1 + 3\sqrt{3})S_{11}^{0.5} + 3(S_{11}^3 + 2)^{0.5}S_{11}^{-1} + (2 + 2S_{11}^3)^{0.5}S_{11}^{-1}}{3(2\sqrt{3} + 1)} \quad (6.80)$$

where  $S_{11} = \exp\{\pm\epsilon\}$  where  $+\epsilon$  and  $-\epsilon$  are the plastic strains in tension and compression respectively, and  $\bar{L}_0$  and  $\bar{L}$  are the lineal intercepts in the undeformed and deformed states respectively.

The second effect of plastic strain is through mechanical stabilisation (Chapter 8), expressed as an additional driving force  $\Delta G_{STA}$  needed in order for the interface to overcome the dislocation density ( $\rho$ ) created by strain prior to transformation (Chatterjee et al., 2006; Maalekian et al., 2007):

$$\Delta G_{STA} = \frac{\mu b}{8\pi(1 - \nu)}(\rho^{0.5} - \rho_0^{0.5}) \quad \text{J m}^{-3}$$

with  $\rho = 2 \times 10^{13} + 2 \times 10^{14}\epsilon \quad \text{m}^{-2}$  (6.81)

where  $\mu$  is the shear modulus of austenite at 80 GPa,  $b = 0.252$  nm is the magnitude of the Burgers vector of the dislocations, and the Poisson's ratio  $\nu = 0.27$ . To summarise, the martensite-start temperature independent of grain size effect is obtained from <sup>10</sup>

$$\Delta G^{\gamma\alpha} + \Delta G_{mech} < \Delta G_{M_S}^{\gamma\alpha} - \Delta G_{STA} \quad (6.82)$$

Calculations for a typical TRIP-assisted steel of composition 0.23C–1.37Si–1.54Mn wt% containing a volume fraction  $V_\gamma = 0.19$  of retained austenite (Ki et al., 2006), assumed to contain 1 wt% of carbon on average, are shown in Fig. 6.50. It is evident that for strains typical of TRIP-assisted steels, there is no substantial effect of plastic strain on the development of martensitic transformation, and stress alone can explain the TRIP phenomenon. Fig. 6.50c,d shows that the small austenite grain size has a substantial effect on the stability of the retained austenite.

### 6.14.1 Autocatalysis

The initial number density  $N_i^0$  of the defects responsible for the nucleation of martensite is not large enough to explain the observed rate of martensitic transformation (Shih et al., 1955; Pati and Cohen, 1951; Olson and Cohen, 1981b). The extra defects necessary to account for the shortfall are obtained by *autocatalysis*. Each plate of martensite creates new embryos in the austenite. Their number density is given by integrating (Lin, 1987):

$$dN = dN_i + d(\xi p) \quad (6.83)$$

<sup>10</sup>The computer program capable of the calculations presented here can be obtained from: <http://www.msm.cam.ac.uk/map/steel/programs/mucg46B.htm>

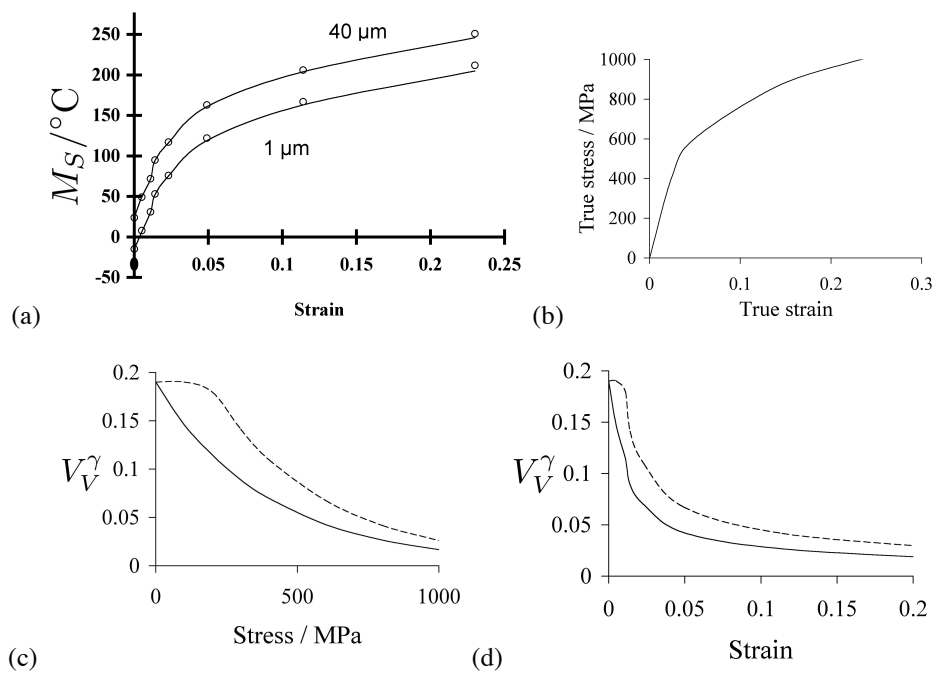


**Figure 6.50** (a) Plot of  $M_S$  as a function of the stress alone (points), or stress combined with strain-effects (curves); (b) the stress-strain curve (Ki et al., 2006) used to relate stress and strain. (c,d)  $V_V^\gamma$  as a function of stress or strain; the continuous and dashed lines represent  $\bar{L}_0$  equal to 40 and 1  $\mu\text{m}$  respectively. After Yang et al. (2012a).

where  $N_i$  is the number density of original nucleation sites which survive at any stage of transformation:

$$N_i = (1 - \xi)N_i^0 p \quad (6.84)$$

where  $p$  is number of autocatalytic sites generated per unit volume of sample, assumed to be related linearly to the volume fraction of martensite and hence to  $\xi$ ,

$$\begin{aligned} p &= C_8 + C_9\xi \\ \text{so that } dN &= (-N_i^0 + C_8 + 2C_9\xi)d\xi \end{aligned} \quad (6.85)$$

Since  $\bar{V}$  is assumed to be constant,

$$d\xi/\bar{V} = (1 - \xi)dN \quad (6.86)$$

so that

$$\int \frac{d\xi}{\bar{V}(1 - \xi)} = \int (-N_i^0 + C_8 + 2C_9\xi)d\xi \quad (6.87)$$

Integration gives

$$p = N_i^0 - \frac{\ln\{1 - \xi\}}{\xi\bar{V}} \quad (6.88)$$

It is found experimentally that:

$$p - N_i^0 = C_{10} + C_{11}(M_S - T_Q) \quad (6.89)$$

On setting  $M_S - T_Q = 0$ , it is found that  $C_{10} = 1/\bar{V}$ . It follows that

$$-\frac{\ln\{1 - \xi\}}{\xi} = 1 + \bar{V}C_6(M_S - T_Q) \equiv 1 + C_{12}(M_S - T_Q) \quad (6.90)$$

This is an alternative kinetic model for the development of martensitic transformation as a function of undercooling below the  $M_S$  temperature. It has been used to rationalise martensite transformation kinetics in fully austenitic samples as well as those which are first partially transformed to bainite.

Although a reasonable fit has been demonstrated (Fig. 6.51), the model tends to overestimate the fraction transformed when the amount of martensite is small.

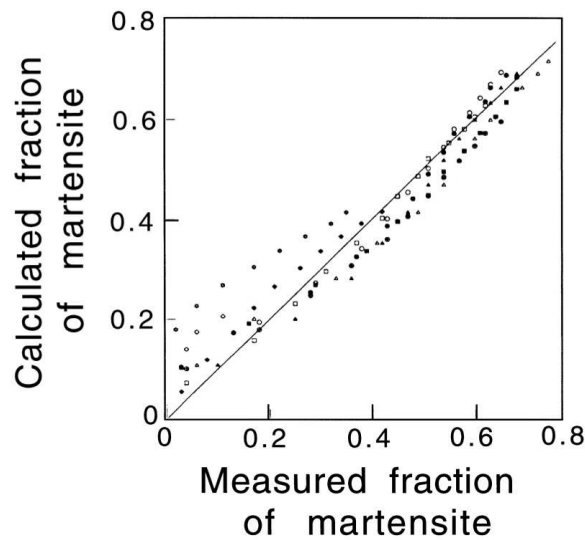


**Figure 6.51** Comparison of experimental results with those calculated by fitting equation 6.90 to the experimental data. After Khan and Bhadeshia (1990).

## 6.15 Phase Field Models

In an ideal scenario, a phase-field model is able to compute quantitative aspects of the evolution of microstructure without explicit intervention, and gives a visual impression of the development of microstructure. The key advantage is that there is no tracking of individual interfaces and that many physical phenomena can be simultaneously modelled within the framework of irreversible thermodynamics. The subject has been widely reviewed<sup>11</sup> but a presentation which is intended to be simple without compromising derivations is available for detailed study (Qin and Bhadeshia, 2011). The intention here is to focus on bainite, with only a cursory introduction to the method.

### 6.15.1 Introduction to Phase Fields

Imagine the growth of a precipitate that is isolated from the matrix by an interface. There are three distinct quantities to consider: the precipitate, matrix and interface. The interface can be described as an evolving surface whose motion is controlled according to the boundary conditions consistent with the mechanism of transformation. The interface in this mathematical description is simply a two-dimensional surface with no width or structure; it is said to be a *sharp interface*.

In the phase-field method, the state of the entire microstructure is represented continuously by a single variable known as the *order parameter*  $\phi$ . For example,  $\phi = 1$ ,  $\phi = 0$  and  $0 < \phi < 1$  represent the precipitate, matrix and interface respectively. The latter is therefore located by the region over which  $\phi$  changes from its precipitate-value to its

<sup>11</sup>(Kobayashi, 1993; Ode et al., 2001; Saito et al., 2002; Chen, 2002; Boettinger et al., 2002; Shen and Wang, 2003; Wang and Khachatryan, 2006)

matrix-value (Fig. 6.52). The range over which it changes is the width of the interface. The set of values of the order parameter over the whole microstructure is the phase field.

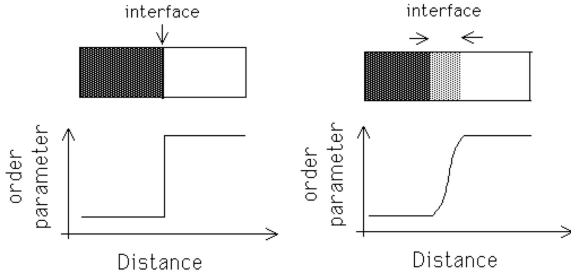


**Figure 6.52** (a) Sharp interface; (b) diffuse interface.

The evolution of the microstructure with time is assumed to be proportional to the variation of the free energy functional with respect to the order parameter:

$$\frac{\partial \phi}{\partial t} = M \frac{\partial g}{\partial \phi} \quad (6.91)$$

where  $M$  is a mobility. The term  $g$  describes how the free energy varies as a function of the order parameter; at constant  $T$  and  $P$ , this takes the typical form:

$$= \int_V \left[ g_0\{\phi, T\} + \epsilon(\nabla\phi)^2 \right] dV \quad (6.92)$$

where  $V$  and  $T$  represent the volume and temperature respectively. The second term in this equation depends only on the gradient of  $\phi$  and hence is non-zero only in the interfacial region; it is a description therefore of the interfacial energy. The first term is the sum of the free energies of the precipitate and matrix, and may also contain a term describing the activation barrier across the interface. For the case of solidification,

$$g_0 = hg^S + (1-h)g^L + Qf \quad (6.93)$$

where  $g^S$  and  $g^L$  refer to the free energies of the solid and liquid phases respectively,  $Q$  is the height of the activation barrier at the interface,

$$h = \phi^2(3 - 2\phi) \quad \text{and} \quad f = \phi^2(1 - \phi)^2 \quad (6.94)$$

Notice that the term  $hg^S + Qf$  vanishes when  $\phi = 0$  (i.e., only liquid is present), and similarly,  $(1-h)g^L + Qf$  vanishes when  $\phi = 1$  (i.e., only solid present). As expected, it is only when both solid and liquid are present that  $Qf$  becomes non-zero. The time-dependence of the phase field then becomes:

$$\frac{\partial \phi}{\partial t} = M[\epsilon \nabla^2 \phi + h'\{g^L - g^S\} - Qf'] \quad (6.95)$$

The parameters  $Q$ ,  $\epsilon$  and  $M$  have to be derived assuming some mechanism of transformation. The advantages and disadvantages of the method have been discussed in detail (Qin and Bhadeshia, 2009) but can be summarised as follows:

**Advantages**

- Particularly suited for the visualisation of microstructural development.
- Straightforward numerical solution of a few equations.
- Number of equations to be solved far less than number of particles in system.
- Flexible method with phenomena such as morphology changes, particle coalescence or splitting and overlap of diffusion-fields. Possible to include routinely, a variety of physical effects such as the composition dependence of mobility, strain gradients, soft-impingement, hard-impingement, anisotropy, etc.

**Disadvantages**

- Very few quantitative comparisons with reality; most applications limited to the observation of shape.
- Large domains computationally challenging.
- Interface width is an adjustable parameter which may be set to physically unrealistic values. Indeed, in most simulations the thickness is set to values beyond those known for the system modelled. This may result in a loss of detail and unphysical interactions between different interfaces.
- The point at which the assumptions of irreversible thermodynamics would fail is not clear.
- The extent to which the Taylor expansions that lead to the popular form of the phase field equation remain valid is not clear.
- The definition of the free energy density variation in the boundary is somewhat arbitrary and assumes the existence of systematic gradients within the interface. In many cases there is no physical justification for the assumed forms. A variety of adjustable parameters can therefore be used to fit an interface velocity to experimental data or other models.

**6.15.2 Phase Field Simulation of Bainite**

The earliest phase field simulation of bainite seems to be by Song et al. (2011) where a bainite sheaf is modelled in two-dimensions, but without the substructure that is evidently present in such sheaves. Growth is modelled as occurring by a paraequilibrium mechanism, i.e., at a rate controlled by carbon diffusion in the austenite ahead of the interface. The width of the bainite plate is set from experimental observations, so that the aspect ratio of the plate changes when it grows. The maximum length of the bainite plate is set to be equal to the measured austenite grain size. Apparently good agreement is obtained with experimental data on the evolution of volume fraction versus time at a constant temperature, but the fit is obtained by adjusting a variety of parameters including the interfacial mobility, plate dimensions, interfacial width, etc. Given that strain energy is neglected, the plate shape is artificially engineered by making the interfacial energy anisotropic.

The model is not physically correct in assuming paraequilibrium, neglecting the consequences of the shape deformation, and the fact that there is no consideration of nucleation

even though the validation presented is of the measured and predicted volume fractions. A further study by Ramazani et al. (2013) makes similar assumptions, with different interfacial mobilities and arbitrary nucleation parameters. These studies both amount to fitting to experimental data using unphysical parameters and therefore are not capable of making predictions.

Strain energy is accounted for in the simulation of bainite by (Arif and Qin, 2013, 2014) using a simplified form of equation 5.4 for an oblate ellipsoid:

$$\frac{G_s}{V_m} = \frac{y}{R} \mu (s_x^2 + s_y^2 + \zeta^2) \quad (6.96)$$

where the coordinates are not well-specified since  $x$  and  $y$  are said to be in the habit plane and therefore  $z$  should be normal to that plane. In equation 5.4,  $s$  refers to the shear parallel to a specific shear direction in the habit plane but Arif and Qin (2014) take it to be the vector sum of some notional shears along  $x$  and  $y$ . The model therefore does not contain information on the orientation of the shear direction in the  $xy$  plane.

Nevertheless, the model includes strain and the shape of the plate is then determined by the largest gradient of the order parameter  $\phi$  rather than by an arbitrary orientation-dependent interfacial energy. The model is faithful to many of the known features of the bainite reaction, for example: autocatalysis, the  $T_0$  condition and that carbon diffuses after growth. The sub-units are allowed to grow to an arbitrary limited size, after which the excess carbon diffuses into the adjacent austenite in a process that is slower than that required for the growth of the sub-unit. To propagate transformation further requires the generation of new sub-units by autocatalysis, which gives the correct sheaf morphology as illustrated in Fig. 6.53. Notice the expected heterogeneous distribution of carbon in the austenite.

At the one extreme, it seems that the method has simply been manipulated to produce images which may or may not be realistic, and to fit to experimental data. At best the method has captured some of the characteristics of bainite, but given the approximations or fitting, no significant new knowledge has emerged from the research.

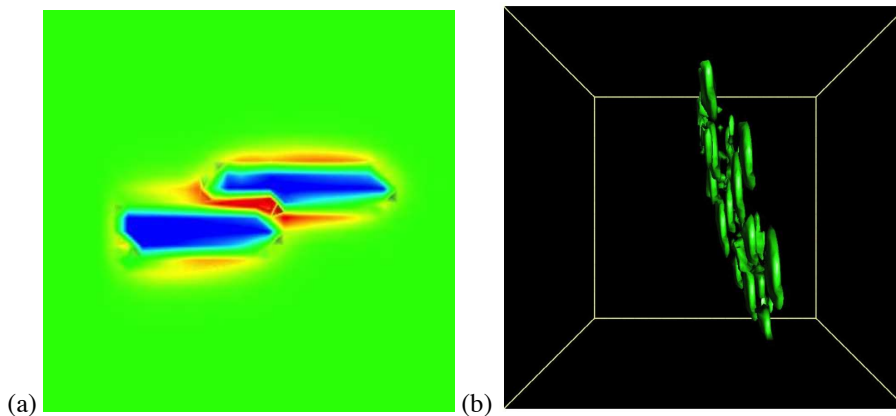


**Figure 6.53** Data from phase field simulation of the growth of bainite. (a) There are two sub-units in this image, which represents the distribution of carbon after each growth event. A blue colour represents low concentration whereas red, a high concentration. (b) Overall morphology of a sheaf. Reproduced with permission from Elsevier, (Arif and Qin, 2013).

## 6.16 Summary

Both the individual platelets and the sheaves of bainite lengthen at rates much faster than permitted by the diffusion of carbon. It must be concluded that they grow with a supersaturation of carbon, the ferrite inheriting the composition of the parent austenite. The excess carbon is soon afterwards partitioned into the residual austenite or precipitates as carbides.

It is possible that not all the carbon is trapped in the ferrite during transformation. However, neither the experimental evidence nor the theory for growth with partial supersaturation is convincing.

Carbon must partition during the nucleation of bainite. The nucleation probably occurs by a displacive mechanism akin to martensite, but with the most potent sites confined to the austenite grain surfaces. Autocatalytic nucleation plays a role but it is not as prominent for bainite as it is for martensite. The activation energy for nucleation varies linearly with the driving force. Nucleation does not therefore rely on heterophase fluctuations, but rather on the dissociation of dislocation clusters. The activation energy is in these circumstances from the resistance to interfacial motion.

The calculation of overall transformation kinetics remains challenging. Whereas some important trends are reproduced, accurate predictions using few parameters are not yet possible. This indicates that important variables remain to be identified. A qualitative result is that bainitic transformation is less sensitive to the austenite grain size when compared with pearlite. This is because sheaf growth occurs by the propagation of sub-units at sites away from the austenite grain surfaces. There is very little work on the phase-field simulation of bainite, with only one study accounting for the thermodynamics and stored energy.

Except at temperatures close to  $B_S$ , homogeneous steels transform more rapidly than those containing chemical segregation. The martensitic decomposition of austenite left untransformed after the growth of bainite can be described adequately by the theory for the martensitic decomposition of fully austenitic samples.

## CHAPTER 7

---

### UPPER AND LOWER BAINITE

---

Although there have been attempts at generalising the definition of bainite, the most appropriate description remains that the microstructure consists of a non-lamellar mixture of ferrite and carbides, which can be classified further into upper and lower bainite. This latter distinction is of value because there are clear differences in the mechanical properties of upper and lower bainite. The two microstructures can be distinguished easily using transmission electron microscopy and hence can be discussed in the context of mechanical properties and the growth mechanism.

Lower bainite is obtained by transformation at relatively low temperatures. Both upper and lower bainite form as aggregates of small plates or laths (sub-units) of ferrite. The essential difference between them is in the nature of the carbide precipitates. Upper bainitic ferrite is free of precipitation, with any carbides growing from the carbon-enriched residual austenite between the plates of ferrite. In addition to this kind of precipitation, there are carbide particles present inside lower bainitic ferrite. We shall see that the precipitates in lower bainitic ferrite can be any of the carbides reported to occur during the tempering of martensite, for example,  $\epsilon$ ,  $\eta$ ,  $\chi$  or cementite.

#### 7.1 Matas and Hehemann Model

The transition between upper and lower bainite is believed to occur over a narrow range of temperatures. It is possible for both forms to occur simultaneously during isothermal transformation near the transition temperature (Pickering, 1967b). Matas and Hehemann

(1961) proposed that the difference between upper and lower bainite comes from a competition between the rate at which carbides can precipitate from ferrite and the speed with which carbon is partitioned from supersaturated ferrite into austenite (Fig. 7.1). Upper bainite forms at higher temperatures, permitting the excess carbon to partition before it can precipitate in the ferrite. In lower bainite, the slower diffusion associated with the reduced transformation temperature provides an opportunity for some of the carbon to precipitate in the supersaturated ferrite.

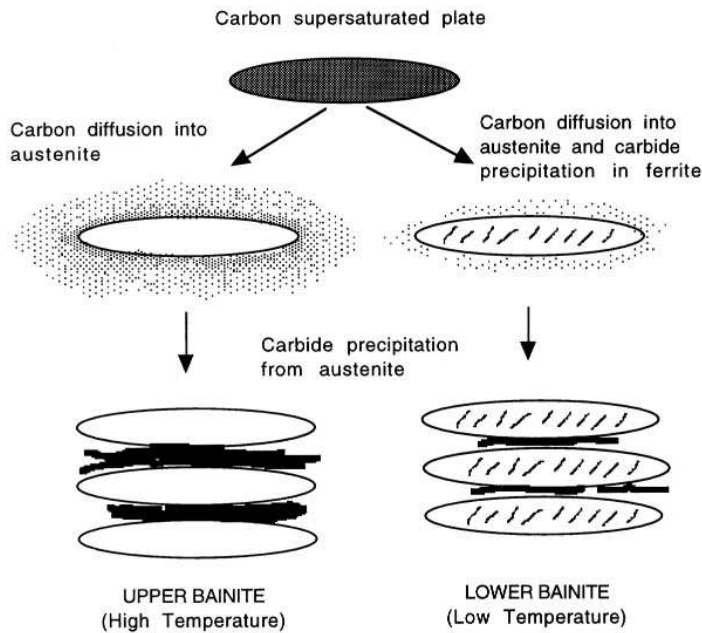


**Figure 7.1** Schematic representation of the transition from upper to lower bainite. After Takahashi and Bhadeshia (1990).

A corollary is that upper bainite should not form when the carbon concentration is large. This is indeed found to be the case in a Fe-7.9Cr-1.1C wt% alloy which has a  $B_S$  temperature of just 300 °C (Srinivasan and Wayman, 1968b), and in a Fe-4.08Cr-0.3C wt% alloy which has a  $B_S$  temperature of 490 °C. It has been shown that in a series of high purity Fe-(0.16-0.81)C wt% alloys, lower bainite is not obtained when the carbon concentration is less than about 0.4 wt% (Ohmori and Honeycombe, 1971) and a found a similar observation has been reported for Fe-Si-C alloys. Only upper bainite formed in a Fe-2Si-1Mn-0.34C wt% steel, whereas both upper and lower bainite could be observed when a higher carbon variant (0.59 wt%) was examined (Tsuzaki et al., 1991b). In high purity, high carbon Fe-0.85-1.8C wt% steels the formation of pearlite gives way directly to that of lower bainite (Oka and Okamoto, 1986).

The model illustrated in Fig. 7.1 has been expressed quantitatively by comparing the time required to decarburise supersaturated ferrite against cementite precipitation kinetics (Takahashi and Bhadeshia, 1990).

## 7.2 Quantitative Model

### 7.2.1 Time to Decarburise Supersaturated Ferrite

The theory for the partitioning of carbon from a supersaturated plate of ferrite has been presented in Chapter 6. The diffusion coefficient of carbon in ferrite is greater than that in austenite. This, together with the assumption that there is local paraequilibrium at the  $\alpha/\gamma$  interface, gives the time  $t_d$  required to decarburise a plate of a specified thickness (equation 6.34). Some results for plain carbon steels are presented in Fig. 7.2. In each case,  $t_d$  is found to go through a minimum as a function of the transformation temperature. This is because the diffusion coefficient of carbon decreases with temperature (leading to an increase in  $t_d$ ), while at the same time, the amount of carbon that the austenite can tolerate increases at lower temperatures.

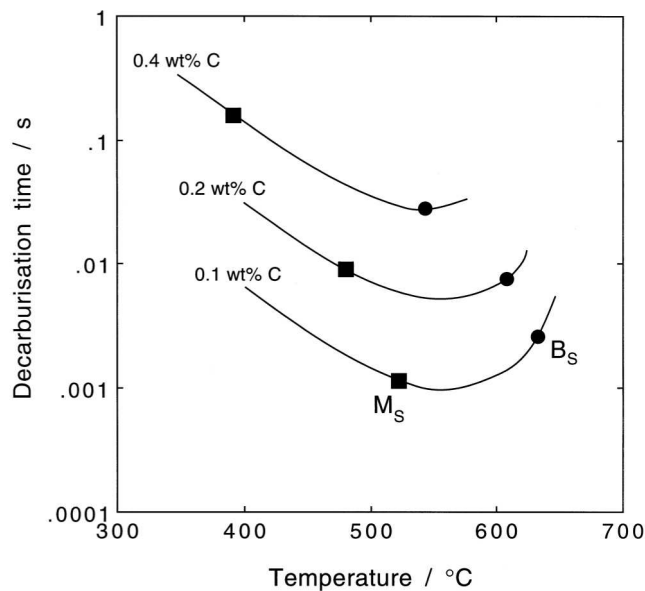


**Figure 7.2** Calculated time for the decarburisation of supersaturated ferrite plates (of thickness 0.2  $\mu\text{m}$ ) in plain carbon steels with 0.1, 0.2 and 0.4 wt% carbon respectively. The calculated martensite-start and bainite-start temperatures are also indicated.

### 7.2.2 Kinetics of Cementite Precipitation

The rate of cementite precipitation from supersaturated ferrite can be calculated as a function of time, temperature and chemical composition; the most difficult kinetic information needed to do this is the number density of nucleation sites, the interfacial energy that determines the activation energy for nucleation and the shape of the nucleus, so there is some inevitable fitting involved. However, for plain carbon steels, and in some cases for alloy steels, martensite tempering data can be adapted to derive reasonable functions for the purpose of predicting the transition from upper to lower bainite (Takahashi and Bhadeshia, 1990, 1991; Lawrynowicz, 2004).

The first change that happens during the tempering of supersaturated martensite is that the excess carbon precipitates in the form of carbides. Prolonged annealing leads to recovery, recrystallisation and coarsening. To derive a function representing precipitation alone, it is necessary therefore to focus on the early stages of tempering.

Speich (1969) reported that the change in hardness of martensite in plain carbon steels after an hour of tempering at temperatures above 320 °C, includes significant contributions from recovery, recrystallisation and coarsening of cementite particles (Fig. 7.3). The data representing hardness changes during tempering below 320 °C can be used to derive a function which expresses the change in the volume fraction of cementite precipitation as a function of time and temperature. An Avrami equation can then be used empirically to represent the tempering reaction:

$$\xi\{t\} = 1 - \exp\{-k_A t^n\} \quad (7.1)$$

where  $\xi\{t\}$  is the volume fraction of cementite normalised by its equilibrium volume fraction at the reaction temperature,  $t$  is the time, and  $k_A$  and  $n$  are rate constants determined from the experimental data. Since it is assumed that  $\xi\{t\}$  is related at any time to the appropriately normalised hardness of the martensite,  $H\{t\}$ , it follows that:

$$\xi\{t\} = (H_0 - H\{t\}) / (H_0 - H_F) \quad (7.2)$$

$H_0$  is the hardness of the as-quenched virgin martensite,  $H_F$  is its hardness when all the carbon has precipitated but before any significant recovery, recrystallisation or coarsening has occurred. The assumption here is that the amount of carbon precipitated is related linearly to the change in hardness during the early stages of tempering.

Using the values of hardness for plain carbon martensite tempered for 1 h at 320 °C, reported by Speich,  $H_F$  can be expressed empirically as a function of the initial hardness and average carbon concentration  $\bar{x}$  (mole fraction), as follows:

$$H_F = H_0 [1 - 1.731 \bar{x}^{0.34}] \quad (7.3)$$

This equation is valid for plain carbon steels containing less than 0.4 wt% carbon, the value of  $H_F$  becoming constant thereafter. The hardness  $H_0$  of plain carbon martensite (< 0.4 wt% carbon) before tempering can be deduced from the data reported by Speich:

$$H_0 = 1267(\text{weight \% carbon})^{0.9} + 240 \quad (7.4)$$

where the hardness of martensite in pure iron is 240 HV (Leslie, 1982). This equation gives the hardness of virgin martensite in plain carbon steels as a function of dissolved carbon. There is evidence that the effect of carbon tends eventually to saturate, so  $H_0$  should be set not exceed about 800 HV irrespective of the carbon concentration (Bhadeshia and Edmonds, 1983a,b). Having established all the data necessary to estimate the amount of cementite precipitated, it remains to evaluate the terms  $k_A$  and  $n$  of the Avrami equation in order to calculate the time  $t_\theta$  for the formation of a specified fraction of cementite as a function of time, temperature and carbon concentration. This can easily be done by fitting the Avrami equation to experimental data on the tempering of martensite.

There are more elaborate theories available for the change in the strength of low-carbon martensite due to the precipitation of cementite, making it possible to estimate  $H_0 - H_F$  independently of the empirical approach described above. The change can be expressed in terms of the decrease in solid solution strengthening as carbon is incorporated into cementite, and a lesser increase in strength as the cementite particles precipitation harden

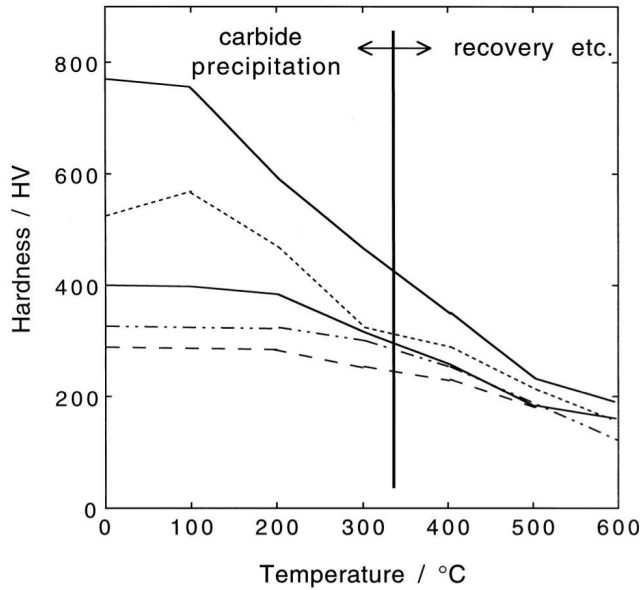


**Figure 7.3** Hardness curves for iron-carbon martensitic samples which were tempered for 1 h at the temperatures indicated; the five curves represent steels with different carbon concentrations - data due to Speich (1969). The data to the left of the vertical line reflect changes due to the precipitation of carbides rather than recovery or coarsening processes.

the martensite. Thus, the yield strength of martensite,  $\sigma_y$ , is expressed as a combination of the intrinsic yield strength, the effect of the dislocation cell structure, and precipitation hardening by cementite (Daigne et al., 1982):

$$\sigma_y = \sigma_0 + k_\varepsilon \varepsilon_1^{-1} + k_p \Delta^{-1} \quad (7.5)$$

where  $\sigma_0$  is the intrinsic strength of martensite (including solid solution strengthening due to carbon),  $\varepsilon_1$  is the average transverse thickness of the cell structure, and  $\Delta$  is the average distance between a particle and its two or three nearest neighbours. The data needed to evaluate the equation are well-founded. A comparison of the calculated strength and measured strength after tempering should give a good idea of the extent of cementite precipitation. When this is done, the relation between hardness and the amount of the precipitation (thus the decrease in solute carbon) is found not to be linear as was assumed in the empirical approach, but the predicted changes in hardness are found to be remarkably consistent with those measured by Speich for the early stages of tempering. This justifies the assumption that much of the hardness change can be attributed to the precipitation of carbon rather than due to other annealing effects such as tempering.

### 7.2.3 Quantitative Estimation of the Transition Temperature

Following the gist of the Matas and Hehemann proposal, a comparison of the time  $t_d$  required to decarburise a plate of ferrite, with the time interval  $t_\theta$  necessary to obtain a detectable amount of cementite precipitation in the ferrite should give a good indication of

whether upper or lower bainite is expected during isothermal transformation. If  $t_d < t_\theta$  then it may be assumed that upper bainite is obtained, and vice versa (Fig. 7.4). A weakness of this theoretical model is that decarburisation and precipitation should really be coupled. A disposable parameter in the model as it stands is the “detectable amount” of cementite precipitation, which has to be fixed by comparison with experimental data.

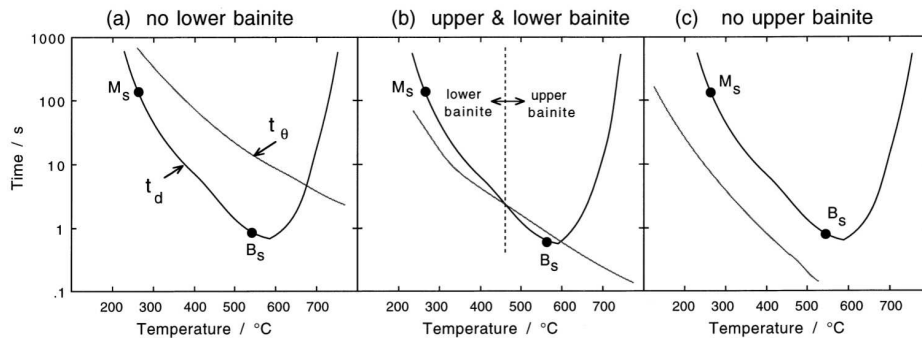


**Figure 7.4** Illustration of how differences in the relative variation of the decarburisation time  $t_d$  and the precipitation time  $t_\theta$  can lead to: (a) a steel which is incapable of transforming to lower bainite; (b) a steel which should, under appropriate conditions, be able to transform to upper or lower bainite; (c) a steel in which bainitic transformation always leads to the formation of lower bainite.

Some calculated data on the plain carbon steels are presented in Fig. 7.5. They indicate that lower bainite should not be observed in plain carbon steels with carbon concentrations less than 0.32 wt%. Furthermore, only lower bainite (i.e. no upper bainite) is expected in steels with carbon concentrations exceeding 0.4 wt%. Steels containing between 0.32 and 0.4 wt% of carbon should exhibit both both upper and lower bainite, depending on the reaction temperatures. Finally, at low temperatures where  $t_\theta$  and  $t_d$  both become large, the times required for precipitation or redistribution of carbon exceed that to complete transformation, consistent with the fact that untempered martensite can be obtained at temperatures near  $M_S$ , with the degree of autotempering of the martensite decreasing as  $M_S$  is reduced.

## 7.2.4 Comparison of Theory and Experimental Data

The general behaviour indicated by the calculations for plain carbon steels, is found to be that observed experimentally. Some interesting work by Oka and Okamoto (1986) proves that there is no upper bainite in plain carbon steels with more than 0.8 wt% of carbon; the only bainite observed in their experiments was classical lower bainite at all temperatures above the  $M_S$  temperature (Fig. 7.6a).

Ohmori and Honeycombe (1971), in a study of plain carbon steels, showed that during isothermal transformation above  $M_S$ , only upper bainite could be obtained in samples containing less than 0.4C wt% (Fig. 7.6b). This is consistent with theory, although their observation that upper bainite can be obtained in steels with a carbon concentration up to about 0.85C wt% is not consistent with the theory, nor with the data reported by Oka and Okamoto (1986).

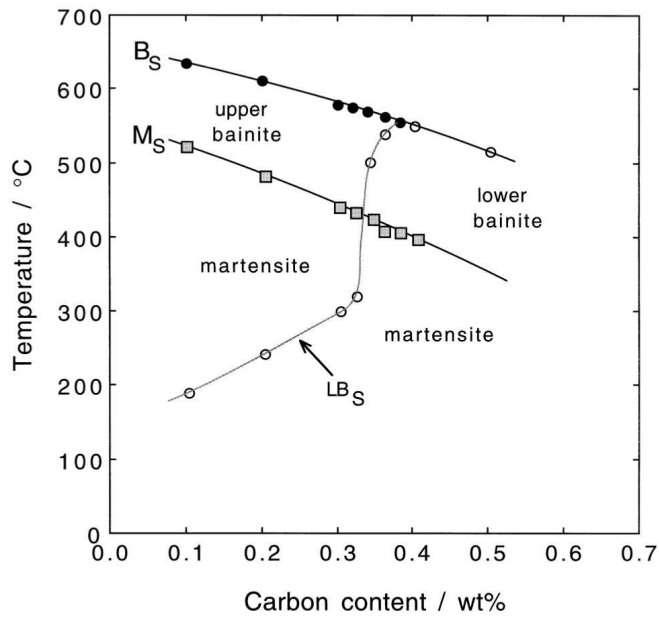


**Figure 7.5** Calculated lower bainite transformation start temperatures for plain carbon steels, as a function of transformation temperature. The calculated martensite-start and bainite-start temperatures are also presented. After Takahashi and Bhadeshia (1990).

Further comparisons against the theory can be found in Takahashi and Bhadeshia (1991); Lawrynowicz (2004). An approximate analysis has been published for Fe-0.38C-0.29Si-0.63Mn-0.93Crwt% steel in which the kinetics of cementite precipitation are assumed to be those for plain carbon steels (Lawrynowicz, 2014).

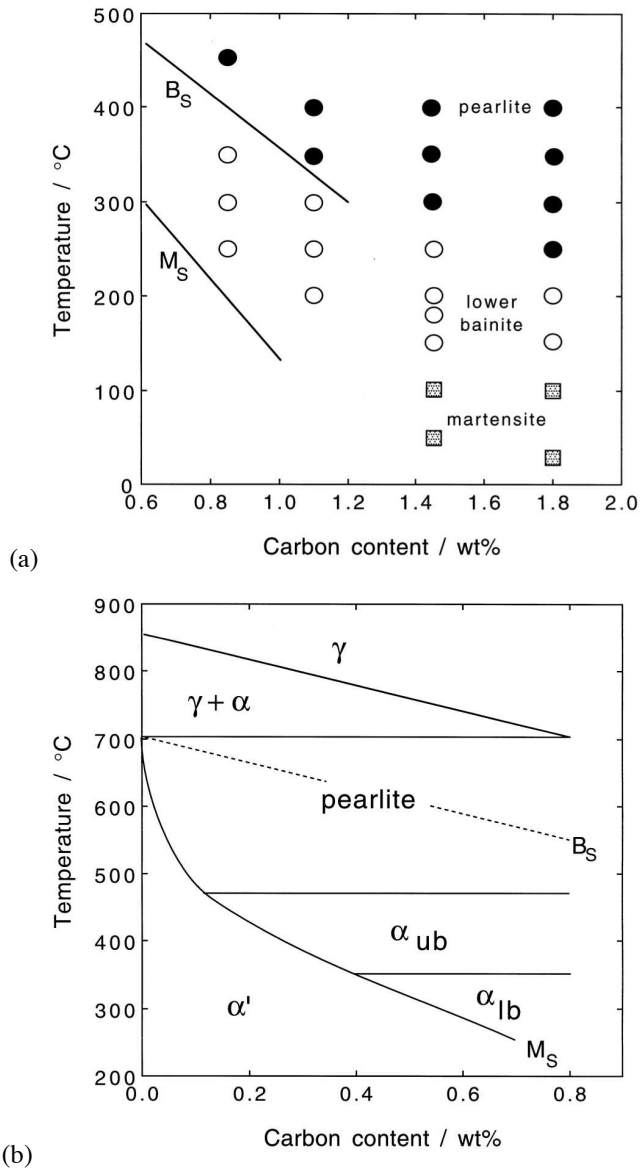


**Figure 7.6** (a) Experimental data (Oka and Okamoto, 1986) illustrating the temperatures at which fine nodules of pearlite, classical lower bainite and martensite were obtained by isothermal transformation of plain carbon steels. The lines represent calculated bainite-start and martensite-start temperatures (Takahashi and Bhadeshia, 1991). (b) The effect of carbon concentration on the temperature range where each microstructure is formed (Ohmori and Honeycombe, 1971).

### 7.3 Mixed Microstructures by Isothermal Transformation

According to the analysis presented above, only lower bainite is expected in plain carbon steels with more than 0.32 wt% of bulk carbon content. However, the calculations are for ferrite plates whose carbon concentration is at first identical to that of the bulk alloy. As transformation proceeds, the austenite becomes enriched in carbon. The bainite which grows from this enriched austenite will inherit a higher than bulk concentration of carbon. This leads to the possibility of upper bainite being followed by lower bainite during isothermal transformation. Mixed microstructures should therefore be obtained in plain carbon steels containing less than 0.32 wt% carbon, especially if the rate of carbide precipitation from the austenite is slow enough to allow the austenite to become enriched.

The maximum carbon concentration that can be tolerated in residual austenite before the bainite reaction stops is given by the  $T'_0$  curve. Therefore if the carbon concentration in residual austenite at the  $T'_0$  curve (i.e.  $x_{T'_0}$ ) is greater than 0.32 wt%, lower bainite can form during the later stages of transformation.

However, the formation of cementite from the residual austenite also becomes possible if  $x_{T'_0} > x^{\gamma\theta}$ , where  $x^{\gamma\theta}$  is a point on the  $\gamma/(\gamma+\theta)$  phase boundary, since the austenite will then be supersaturated with respect to the cementite. The fact that a curve showing the carbon concentration in austenite which is in equilibrium with cementite in plain carbon steels crosses the  $T'_0$  curve at 0.4 wt% of carbon concentration (560 °C), leads to the identification of three regimes for bainite on the Fe-C phase diagram (Fig. 7.7). In steels with more than 0.4 wt% of the initial bulk carbon content (region B), lower bainite is to be expected from the earliest stages of transformation. For steels whose composition lies in region A, lower bainite is expected to be absent during isothermal transformation at all temperatures above  $M_S$ , and this behaviour is valid for any stage of transformation since the austenite cannot be supersaturated with cementite as far as regime A is concerned. The behaviour in the region marked 'C' should be more complex. The residual austenite for these steels may at some stage of transformation contain enough carbon to precipitate cementite. If the kinetics of cementite precipitation from austenite are rapid, then lower bainite may not be obtained in steels with an average carbon concentration less than 0.32 wt%, but otherwise, a mixed microstructure of upper and lower bainite might arise.

Two of the trends described above have been verified by Chang (1999) who not only found that lower bainite-start temperature  $L_S$  could be depressed by retarding the precipitation of cementite, but also showed that a mixture of upper and lower bainite can be obtained by transformation at temperatures just above  $L_S$ .

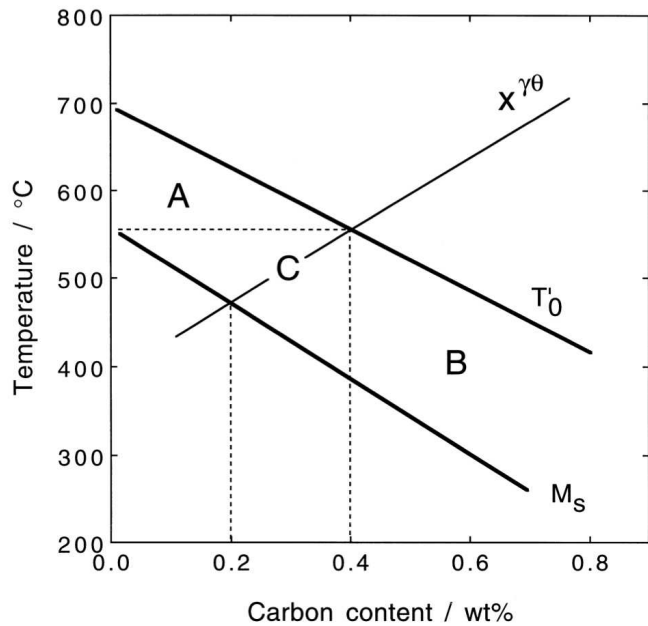


**Figure 7.7** Identification of regimes A, B and C, in which the progress of isothermal transformation can lead to changes in the nature of the transformation product. The line marked  $x^{\gamma\theta}$  is the calculated  $\gamma/(\gamma + \theta)$  phase boundary.

#### 7.4 Other Consequences of the Transition

The growth of bainite plates stops when the glissile interface is clogged by plastic accommodation induced defects. For a given defect density, lower-bainite plates should be longer than those of upper bainite, since the driving force for transformation increases with the undercooling. At lower transformation temperatures the matrix is able to support higher strains without plastic deformation so that the defect density *in the matrix* is expected to be smaller. Step quenching experiments in which an alloy is first partially transformed to lower bainite and then heated rapidly into the upper bainite transformation range are consistent with this since the growth of lower bainite ceases on reaching the higher temperature (Goodenow et al., 1965). This also happens when specimens partially transformed to lower bainite experience an increase in temperature within the lower bainite transformation range (White and Owen, 1961).

#### 7.5 Comparison with Tempering of Martensite

We have seen that the transition from upper to lower bainite can be predicted on the basis of a simple model which compares the rates of decarburisation and precipitation. Lower bainite is in effect generated by a process of autotempering. It follows that there should be a strong comparison with the microstructure of tempered martensite.

When high-carbon martensite is tempered, the first precipitate is usually a transition phase such as  $\epsilon$ -carbide which eventually is replaced by the more stable cementite. Sim-

ilarly, when lower bainite forms in high carbon steels, it contains  $\varepsilon$ -carbide which subsequently transforms into cementite during prolonged holding at the isothermal transformation temperature (Matas and Hehemann, 1961).

The chances of obtaining  $\varepsilon$ -carbide (instead of cementite) in lower bainite increase as the transformation temperature is reduced for the same steel [see Table II, Matas and Hehemann (1961)]. As the transformation temperature is reduced, the time required to decarburise a supersaturated plate of bainite increases. A high carbon concentration can persist in the ferritic matrix for a time period long enough to allow the formation of  $\varepsilon$ -carbide, which does not form if the carbon concentration is less than about 0.25 wt% (Roberts et al., 1957). This explains why a medium carbon Fe-0.43C-3Mn-2Si wt% steel transforms to lower bainite containing cementite particles, although when quenched to martensite, gives  $\varepsilon$ -carbide on tempering (Bhadeshia and Edmonds, 1979a, 1983a). Some of the carbon in the former case is lost to the austenite by diffusion, thus preventing the formation of  $\varepsilon$ -carbide.

## 7.6 Summary

A comparison between the times required to decarburise supersaturated ferrite plates with that required to precipitate cementite within the plates is a reasonable way to interpret the transition from upper to lower bainite. If the decarburisation process dominates, upper bainite is predicted whereas relatively rapid carbide precipitation within the ferrite leads to the microstructure of lower bainite.

A number of predictions from this theory are in agreement with experimental data. Thus, lower bainite cannot form in plain carbon steels containing less than about 0.3 wt% carbon. Similarly, upper bainite is predicted and found to be absent in plain carbon steels containing more than 0.4 wt% carbon.



## CHAPTER 8

---

# STRESS AND STRAIN EFFECTS

---

A displacive transformation can justifiably be regarded as a mode of deformation of the parent phase, with the additional characteristic that the crystallographic structure of that phase is altered in the deformed region (Table 8.1). For this reason, the permanent strain is called *transformation plasticity*. A phase transformation can be triggered by cooling below a certain transformation-start temperature, by the application of a stress in appropriate circumstances or by a combination of these factors. In the latter case, where the chemical driving force and stress act in concert, transformation plasticity can be obtained at stresses that are much smaller than the yield strength of the stable parent phase.

**Table 8.1** Characteristics of different modes of deformation

	Slip deformation	Mechanical twinning	Displacive transformation	Reconstructive transformation
Permanent deformation?	Yes	Yes	Yes	Yes
Invariant-plane strain with large shear?	Yes	Yes	Yes	No
Crystallographic orientation altered?	No	Yes	Yes	Yes
Lattice change?	No	No	Yes	Yes
Density change?	No	No	Yes	Yes

Just as a combination of a plane and a direction constitutes a deformation system for slip or twinning, the habit plane and displacement vector of an invariant-plane strain describe

the deformation system for transformation plasticity. There will in general be 24 of these systems per austenite grain and they may operate simultaneously with varying contributions. Unlike ordinary slip, the different variants of transformation cannot intersect except in special circumstances where inter-variant transformations are possible. The ordinary notion of work hardening does not therefore apply. Work hardening nevertheless manifests itself via an increase in the stability of the austenite as it becomes more finely divided.

Given the large number of transformation variants available per grain, the Taylor criterion leads to the conclusion that transformation plasticity can cause or accommodate any externally imposed, arbitrary shape change assuming that there is sufficient austenite available to cope with the imposed strain. It follows that polycrystalline samples can remain intact at grain boundaries when transformation plasticity is the sole mode of deformation. Furthermore, the transformation plasticity can cause anisotropic changes in shape even in polycrystalline samples transformed without applied stress, if the parent phase is crystallographically textured.

### 8.1 Mechanical Driving Force

Given that displacive transformations in steels cause large strains, it is natural to expect an interaction between any applied stress and the progress of the transformation, in a manner that is related uniquely to the transformation mechanism. The total driving force can be partitioned into a *mechanical* and the more usual *chemical* components (Patel and Cohen, 1953; Delaey and Warlimont, 1975; Christian, 1982). The physical reasoning behind this idea is that the movement of a glissile interface is a combined deformation and transformation process. The work done by the external stress may be added to the chemical free energy change in order to obtain the total free energy difference. The mechanical driving force is assumed to be given by the work done ( $\Delta G_{\text{mech}}$ ) by the external stress system in producing the macroscopic shape deformation:

$$\Delta G_{\text{mech}} = \sigma_N \zeta + \tau s \quad (8.1)$$

where  $\sigma_N$  is the normal stress on the habit plane and  $\tau$  is the component of the shear stress on the habit plane which is parallel to the direction along which the shear displacements of the shape deformation occur (Fig. 8.1).<sup>1</sup> The strains  $\zeta$  and  $s$  have previously been defined as the dilatational and shear components of the shape deformation. Given a free choice of some 12 to 24 crystallographic variants of the transformation product in a grain of austenite, the work done by the shear stress is always expected to be positive for uniaxial loading, whereas that due to the dilatational component depends on the sign of  $\sigma_N$ . For steels, this latter component is small; the observed stress effects reflect the dominant role of the shear component. The exception is when  $\tau$  is small or zero, as would be the case when the applied stress is a hydrostatic pressure. A more general case is where a system of stresses is applied, represented by a  $3 \times 3$  stress tensor  $\sigma_{lm}$  which when multiplied by the unit normal to the martensite habit plane gives the traction  $\mathbf{t}$  describing the state of stress on that plane. The traction can then be resolved into  $\sigma_N$  and  $\tau$  in the normal manner (e.g.

<sup>1</sup>In recent work, the mechanical free energy has been calculated for a compression test involving large plastic strains, by taking the product of the von Mises stresses and strains (Hajiakbari et al., 2010). This is incorrect because much of the work of plastic deformation is dissipated in irreversible processes. The result is grossly exaggerated values of  $\Delta G_{\text{mech}}$ . Furthermore, the strain that is relevant is that due to transformation.

Bhadeshia et al., 2014):

$$\begin{aligned}\sigma_N &= |\mathbf{t}| \cos\{\theta\} \\ \tau &= |\mathbf{t}| \cos\{\beta\} \cos\{\phi\}\end{aligned}\quad (8.2)$$

where  $|\mathbf{t}|$  is the magnitude of  $\mathbf{t}$ ,  $\theta$  is the angle between the habit plane normal and  $\mathbf{t}$ ,  $\beta$  the angle between  $\mathbf{t}$  and the direction of the maximum resolved shear stress, and  $\phi$  the angle between the latter and the direction of shear for the martensite plate concerned. Substituting these terms into equation 8.1 gives the mechanical free energy.

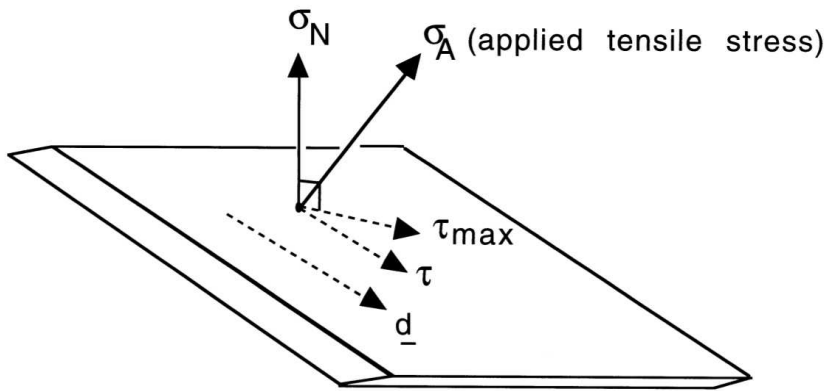


**Figure 8.1** Resolution of the applied stress  $\sigma_A$ . The normal stress  $\sigma_N$ , and the shear stress  $\tau$ , both act on the habit plane. The vector  $\underline{d}$  is the direction along which the shear displacements of the shape deformation lie.  $\tau_{\max}$  is the maximum shear stress on the habit plane, but  $\tau$  is given by resolving  $\tau_{\max}$  along  $\underline{d}$ . Note that  $\underline{d}$  differs slightly from the displacement vector of the invariant-plane strain, which includes a dilatational component in addition to the shear.

It follows from equation 8.1, that since the shear stress remains positive irrespective of whether the sample is pulled in tension or uniaxially compressed, and since the shear component of the shape change is large, a uniaxial stress will always cause an increase in the transformation temperature for displacive transformations in steels. Hydrostatic stress, on the other hand, has no deviatoric components and consequently only interacts with the dilatational component of the shape change. Thus, hydrostatic compression is expected to lead to a decrease in the transformation temperature (Fig. 8.2).

Shear stresses, unlike pressures, cannot strictly be considered as state variables so their use in thermodynamic equations is uncertain (Christian, 1982). This difficulty is unimportant provided irreversible processes such as diffusion or dislocation motion do not act to relieve the shear stresses during the time scale of the experiment. In practice, this means that in the absence of transformation, the state of the system should not be altered if the shear stress is changed and then restored to its original value.

A second complicating factor could arise if the stress influences the very nature of the transformation product, either by stimulating the formation of a metastable phase or by decoupling groups of self-accommodating variants which would form in the absence of stress (Christian, 1982). This would lead to a modification of the chemical driving force term, and as discussed later, there is some evidence to show that there are significant microstructural changes when bainite grows under the influence of an externally applied stress.

Assuming that the interaction of the applied stress is with the macroscopic shape deformation, the stress must favour the growth of those variants for which  $\Delta G_{\text{mech}}$  is maximised. Hence, for a tensile stress, plates which have their habit planes inclined at approximately  $45^\circ$  to the tensile axis will tend to be favoured.<sup>2</sup> This does assume that the applied stress interacts solely with the growth process whereas its interaction with nucleation events could lead to a different criterion for variant selection (Christian, 1982). Indeed, efforts at predicting the martensitic transformation texture from the crystallographic texture of the parent austenite are apparently more successful if it is assumed that variant selection depends on the Bain strain rather than on the macroscopic shape deformation (Ray and Jonas, 1990). The IPS deformation is unlikely to have developed at the nucleation stage, where the particle might be too small to sustain a lattice-invariant deformation. The Bain strain is essential to accomplish the lattice change, so the texture prediction work suggests that variant selection may depend on the interaction of the applied stress with the nucleation process.

Notice that this does not mean that the transformation texture can be predicted by assuming the Bain orientation relationship (Fig. 2.18); the Bain strain simply helps to select the variants. It has been possible in recent work to determine directly the relationship between retained-austenite texture and bainite texture; this work shows that the latter can be more accurately predicted by assuming a Kurdjumov-Sachs type orientation relationship (Fig. 2.17) rather than the Bain orientation (Verlinden et al., 2001).

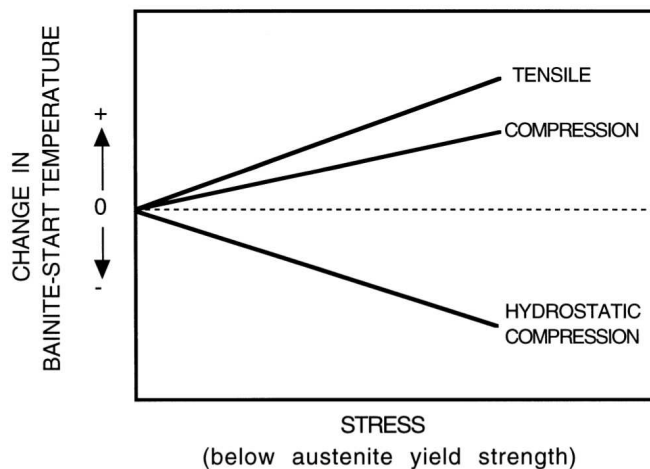


**Figure 8.2** An indication of how the bainite-start temperature should vary as a function of the nature and magnitude of the applied stress.

<sup>2</sup>The angle will not be exactly  $45^\circ$  because the displacement vector of the invariant-plane strain is not quite parallel to the habit plane whenever  $\zeta$  is finite.

## 8.2 The $B_d$ Temperature

The highest temperature at which martensite forms during the cooling of austenite is the  $M_S$  temperature. This can be increased by the application of a suitable stress (Patel and Cohen, 1953). The maximum temperature at which martensite grows under the influence of stress is called the  $M_d$  temperature. There are no similar experiments for bainite but it is possible to piece together evidence to show that the behaviour is similar to that of martensite.

The transformation stresses associated with the growth of lower bainite are known to stimulate upper bainite at temperatures just above  $B_S$ , proving that stress can indeed raise the bainite-start temperature (Goodenow et al., 1969). It should in principle be possible to define a  $B_d$  temperature. Thus, Ya Drozdov et al. (1962) found that no amount of deformation causes the austenite to transform to bainite when the temperature is sufficiently greater than  $B_S$ , i.e.  $T > B_d$ .

The expected stress effects are illustrated in Fig. 8.3, which is based on similar ideas for martensitic transformations. The net driving force available for transformation,  $\Delta G$ , is given by:

$$\Delta G = \Delta G_{\text{chem}} - \Delta G_{\text{mech}}. \quad (8.3)$$

It is assumed that the critical value needed to trigger bainitic transformation at zero stress (i.e.  $\Delta G_{\text{chem}}\{B_S\}$ ) remains constant over the temperature range of interest. The application of a tensile or compressive stress assists the transformation by boosting the overall driving force  $\Delta G$  with the term  $-\Delta G_{\text{mech}}$ , so that the  $B_S$  temperature rises continuously with the magnitude of the applied stress.

Consider a temperature  $B_\sigma$  corresponding to an applied stress  $\sigma$ . When  $\sigma$  becomes greater than the yield strength of the austenite. It is difficult to justify a thermodynamic analysis when the austenite undergoes plastic deformation prior to transformation. The dislocations and other defects generated during plastic deformation will nevertheless influence the progress of transformation. Following the terminology established for martensitic transformations, the region below  $B_\sigma$  is said to represent *stress-assisted* transformation, whereas *strain-induced* transformation describes the regime where the yield stress of the parent phase is exceeded.

The  $B_S$  temperature continues to increase as the stress is raised beyond the yield stress of the austenite. When the  $T'_0$  temperature is reached, the chemical driving force *opposes* transformation so that the mechanical component has to be larger than  $\Delta G_{\text{chem}}\{B_S\}$ . The yield strength of austenite is smaller at high temperatures so a point is reached where the austenite can no longer support a stress large enough to stimulate bainitic transformation; that temperature is  $B_d$  (Fig. 8.3).

Although the picture of the transition between stress and strain-induced transformation (Fig. 8.3) is accurate, there are few studies that properly isolate the two effects. An ideal experiment to study a strain effect would involve the plastic deformation of austenite, the removal of any applied stress, and then phase transformation. This is not how the majority of experiments are conducted; instead, transformation is studied by applying stress and strain simultaneously, typically in a tensile test. It then becomes doubtful as to whether the observed effects of phase transformation are due to plasticity-induced defects or the contribution of the stress to the mechanical component of the driving force,  $\Delta G_{\text{mech}}$ . An analysis of data on TRIP-assisted steels<sup>3</sup> shows that much of the variation

<sup>3</sup>section 13.6.1

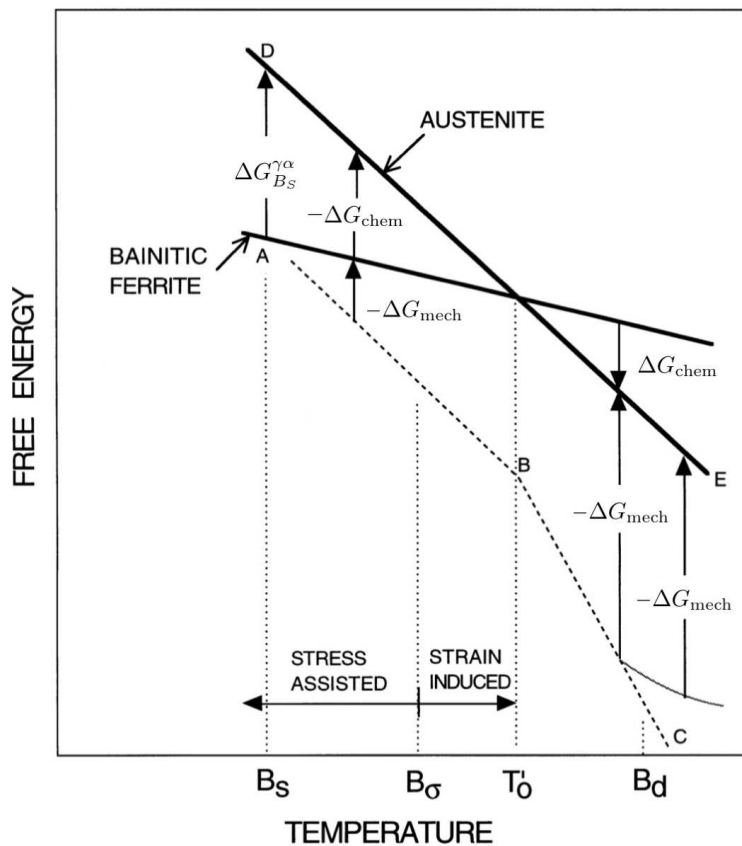


**Figure 8.3** Illustration of the stress-modified  $B_s$ ,  $B_\sigma$  and  $B_d$  temperatures.

in the retained austenite content during deformation can be explained by the interaction of the applied stress with the shape deformation of the martensite, i.e.  $\Delta G_{\text{mech}}$  (Chatterjee and Bhadeshia, 2007); indeed, *in situ* X-ray experiments confirm that austenite decomposition in TRIP-assisted steels can occur at very low plastic strains within the austenite (Jung et al., 2010). One contributing factor to the absence of strain effects is the strength of the carbon-rich austenite, which in the early stages of tensile testing only deforms plastically by martensitic transformation rather than by ordinary slip mechanisms.

### 8.3 General Observations

#### 8.3.1 Externally Applied Stress

There are many independent observations which suggest that stress has an influence on the progress of transformation (Fig. 8.4). The stress need not exceed the yield strength of the austenite in order to influence the kinetics (Maier and Ahrens, 2002), indicating the thermodynamic effect via equation 8.1. A tensile stress during transformation even stimulates bainite beyond that expected from the  $T_0$  condition (Cottrell, 1945).

Small amounts of plastic deformation of austenite during the thermomechanical processing of steels accelerate the rate of the bainite reaction<sup>4</sup>. The rate of reaction increases with the rate of deformation (Ya Drozdov et al., 1962; Mutiu et al., 1977). The increased rate is due to heterogeneous nucleation on deformation induced defects in the austenite (Dubrov, 1969). We shall see in section 8.11 that a large amount of prior deformation can have the opposite effect of stabilising the austenite against transformation.

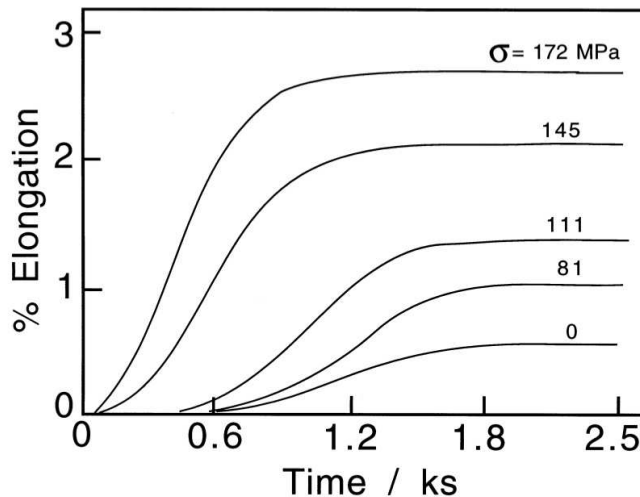


**Figure 8.4** The overall kinetics of bainitic transformation as a function of an externally applied tensile stress. Assuming that the degree of transformation is related to the elongation, the data show an increase in the rate of reaction as a function of the magnitude of the applied stress. After Umemoto et al. (1986a).

### 8.3.2 Internally Generated Stress

The stress influencing transformation need not be applied externally. Internal stresses generated by other transformations also have an effect. Early studies indicated an acceleration in the rate at which upper bainite forms in specimens which are first transformed partially at a lower temperature (Lange and Mathieu, 1938; Jellinghaus, 1952). Martensite is the first phase to form on cooling a steel below the  $M_S$  temperature, but after the initial burst of transformation and a suitable incubation period, the austenite undergoes accelerated decomposition to bainite (Howard and Cohen, 1948). This is because it is deformed by the martensitic transformation. Supporting evidence is found in magnetometric studies, which have revealed that isothermal reaction below the  $M_S$  temperature leads first to the formation of the usual athermal martensite, followed by a small amount of isothermal martensite and an accelerated decomposition to bainite (Ericsson et al., 1976). Similar results have

<sup>4</sup>Cottrell (1945); Jepson and Thompson (1949); Ya Drozdov et al. (1962); Duckworth (1966); Dubrov (1969); Freiwilg et al. (1976); Mutiu et al. (1977); Umemoto et al. (1986a); Tsuzaki et al. (1989); Yang et al. (1995, 1996); Lam and Yang (2000); Liu et al. (2000).

been obtained by Radcliffe and Rollason (1959) and it has been shown that the upper bainite reaction is accelerated in the presence of lower bainite (Fig. 8.5).

A revealing observation is that both the nucleation and growth rates of bainite are accelerated by the proximity of a free surface (Ko, 1953; Hawkins and Barford, 1972). This is because the shape change can be accommodated better at a free surface where the constraint is reduced.

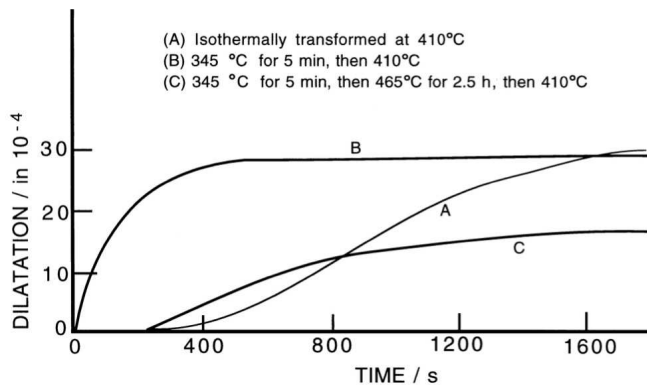


**Figure 8.5** The influence of internal stresses on the rate of transformation at 410°C, in a Fe-0.31C-0.3Si-0.76Mn-3.07Ni-1.22Cr-0.49Mo wt% alloy. Curve A represents isothermal transformation to upper bainite; curve B is for a sample which was first partially transformed to lower bainite and then to upper bainite, showing an acceleration of reaction rate at 410 °C due to the internal stresses generated by the presence of lower bainite; curve C shows how annealing above the  $B_S$  temperature removes the stresses, and their accelerating influence on transformation kinetics (Goodenow et al., 1969).

#### 8.4 Effect on Microstructure

An applied stress will tend to favour the development of crystallographic variants which comply with that stress. This is analogous to the selective operation of a few of the available slip systems in a crystal under stress; it is the systems with the largest Schmid factors which are favoured. Assuming that variant selection is similarly controlled by the interaction of the applied stress with the shape deformation, the stress should cause an alignment of the plates at roughly 45° to the tensile axis. This alignment has been observed in many experiments involving martensitic transformations (Bhadeshia, 1982a). The observations are more difficult for bainite, partly because of the rapid rate of reaction under the influence of stress. The experiments have to be conducted at high temperatures. Further transformation may occur as the sample cools to ambient temperature, confusing the interpretation of the microstructure. Nonetheless, good evidence for microstructural alignment has been reported for bainite platelets, especially when subjected to large stresses during transformation (Bhattacharyya and Kehl, 1955; Umamoto et al., 1986a; Hase et al., 2004; Hozweissig et al., 2012). All of these observations are based on polycrystalline samples, but that does not substantially alter the conclusions. There are so many variants available

per austenite grain that there is a high probability of a plate orientation lying close to the optimum orientation with respect to the stress.

There are more subtle effects of stress on microstructure, even in the absence of any obvious plate alignment, at stress levels as small as 45 MPa. Variant selection leads to the development of a less chaotic microstructure (Jepson and Thompson, 1949; Dubrov, 1969; Bhadeshia et al., 1991). Without stress, each grain of austenite transforms into many different orientations of bainite. Fewer variants develop per austenite grain under the influence of stress, so that the selected orientations can grow unhindered and form thick packets of bainite plates. The sheaves then are longer and their number density per grain smaller when variant selection operates; Fig. 8.6 shows how the structure becomes much more organised during transformation under stress.

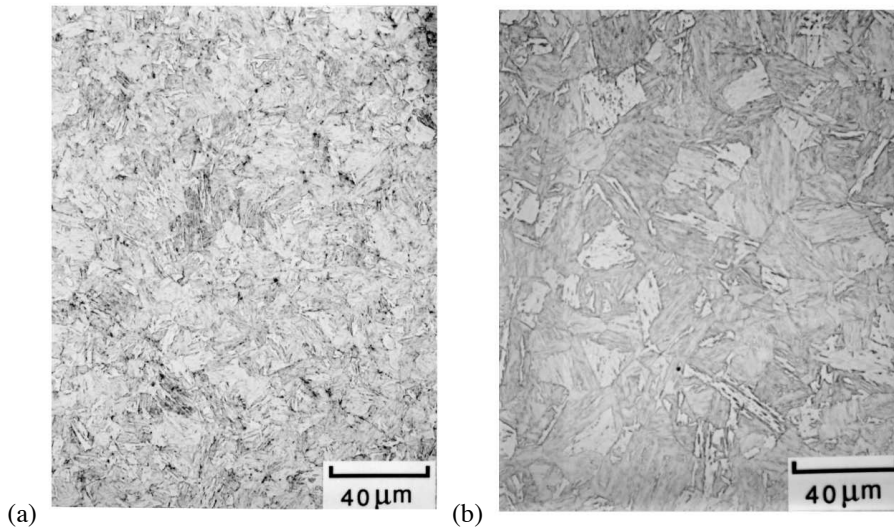


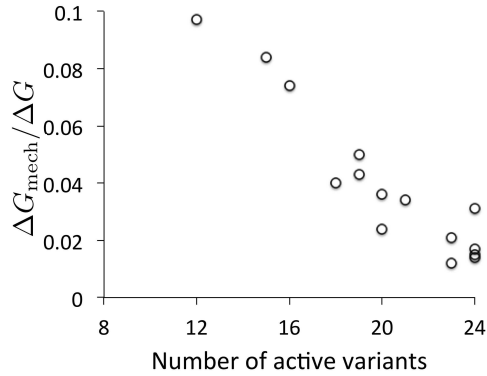
**Figure 8.6** Light micrographs of bainitic microstructures generated in a Fe-0.12C-0.27Si-0.84Mn-0.14Ni-1.48Mo-2.86Cr wt% alloy, by isothermal transformation at 400 °C under the influence of stress. (a) Zero stress; (b) 95 MPa. After Bhadeshia et al. (1991).

#### 8.4.1 Extent of Variant Selection

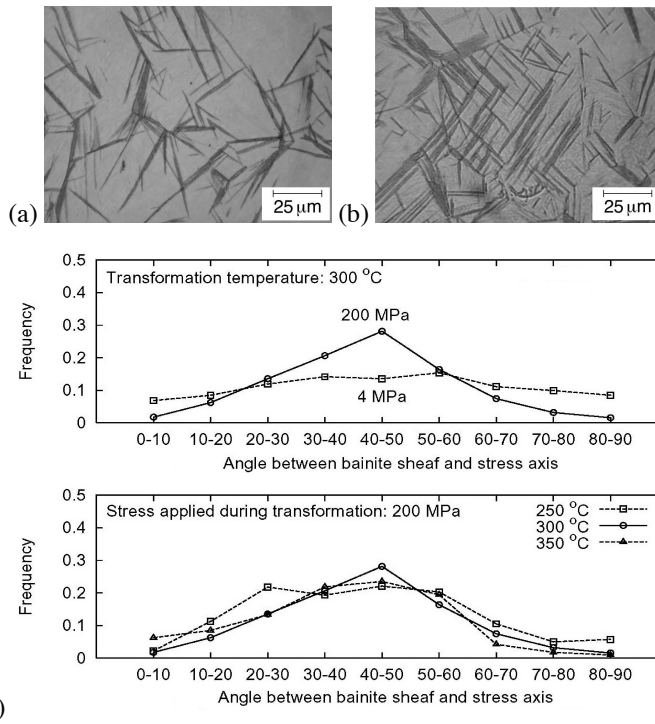
The mechanical free energy is a guide to which crystallographic variant is likely to be favoured. However, if  $\Delta G_{\text{mech}}$  is small in comparison with  $\Delta G_{\text{chem}}$  then the latter will dominate transformation with little or no variant selection. Fig. 8.7 shows in an empirical analysis how the number of active crystallographic variants of bainite scales with the ratio  $\Delta G_{\text{mech}}/(\Delta G_{\text{mech}} + \Delta G_{\text{chem}})$ . This does not indicate the volume fractions of the individual variants, but that kind of information can in principle be calculated using appropriate kinetic theory (Han et al., 2004; Bhadeshia et al., 2014).

Fig. 8.8 shows a particularly strong variant selection effect caused by the ability in the alloy concerned to apply a large stress of 200 MPa whilst still maintaining the stress below the yield strength of the austenite. There is obvious variant selection, and the distribution

of angles of bainite sheaf-traces relative to the tensile-axis peaks at the values expected for the maximum interaction with the applied stress (Hase et al., 2004).<sup>5</sup>



**Figure 8.7** Empirical plot of the ratio of mechanical to total driving force versus the number of active crystallographic variants in an austenite grain. Data from Bhadeshia et al. (1991); Matsuzaki et al. (1994); Kundu et al. (2007); Uslu et al. (2011).



**Figure 8.8** Transformation under the influence of a large compressive stress, still in the elastic regime, applied along the vertical direction of the images. (a) 4 MPa. (b) 200 MPa. (c) Approximate distribution of the angle of bainite sheaf trace relative to the stress axis. After Hase et al. (2004).

<sup>5</sup>Shirzadi et al. (2011) did not find variant selection when pre-deformed austenite transformed into bainite under stress. There are inconsistencies, however. The austenite orientation was recreated assuming a NW whereas there should be 24 variants present. Their interpretation of selection assumes that only favoured variants will be present, whereas in fact there should be dominant variants.

## 8.5 Effect of Hydrostatic Pressure

There is general agreement that the application of hydrostatic pressure causes a retardation of the bainite reaction (Jellinghaus and Friedewold, 1960; Radcliffe et al., 1963; Nilan, 1967). The effect on the time-temperature-transformation diagram is illustrated in Fig. 8.9. The observed retardation is not in itself a feature unique to bainite. All transformations which are accompanied by a reduction in density are expected to be retarded by hydrostatic pressure, which opposes a volume expansion. The effect of hydrostatic pressure is twofold: it reduces the diffusion coefficients by decreasing the available free volume (although the details remain to be established), and it influences the free energy change for transformation. If  $\Delta G_m$  is the molar Gibbs free energy change for a reaction, then since

$$\left(\frac{\partial G}{\partial P}\right)_T = V \quad (8.4)$$

it follows that:

$$\Delta G_m\{P\} - \Delta G_m\{1\} = \int_1^P \Delta V_m dP' \quad (8.5)$$

where  $\Delta V_m$  is the change in molar volume on transformation,  $V$  is the volume and  $P$  is the pressure. The way in which the free energy change for transformation is influenced by the pressure determines how the transformation temperature changes as a function of pressure. An alternative way of expressing this relationship is the Clausius-Clapyeron equation, whence the change in transformation temperature is given by

$$dT^{\gamma\alpha} = T^{\gamma\alpha} \Delta V_m / \Delta H^{\gamma\alpha} \quad (8.6)$$

where  $\Delta H^{\gamma\alpha}$  is the enthalpy change on transformation at the transition temperature  $T^{\gamma\alpha}$ . The equation is approximate in that its derivation depends on the assumption that the enthalpy change does not vary with temperature. With typical values of all the parameters, the variation in transition temperature with pressure should be approximately  $-0.01 \text{ K MPa}^{-1}$  (Denis et al., 1985).

Radcliffe *et al.* also found that the bainite transformation could be suppressed completely by the application of hydrostatic pressure ( $\approx 15 \text{ kbar}$ ) but Nilan, using similar steels, could obtain conventional bainite at the maximum pressures he used (34 kbar). Why these experiments are contradictory is not clear, but Nilan concluded that the transformations at high pressures do not differ substantially from those at ambient pressure.

There is an interesting consequence of hydrostatic pressure in formable bainitic steels containing retained austenite. These so-called TRIP-assisted steels are designed for the automobile industry (Chapter 13); the retained austenite plays a role in the composite microstructure. In particular, its stability to plastic deformation has aroused much interest.

At the same time, the automobile industry has adopted a technique of manufacture, hydroforming, which permits lighter and better engineered components to be made compared with conventional forming techniques. Pyshmintsev et al. (2002) have shown that the hydrostatic pressure inherent in the hydroforming process may be advantageous since the pressure increases the stability of the retained austenite during plastic deformation (Fig. 8.10).

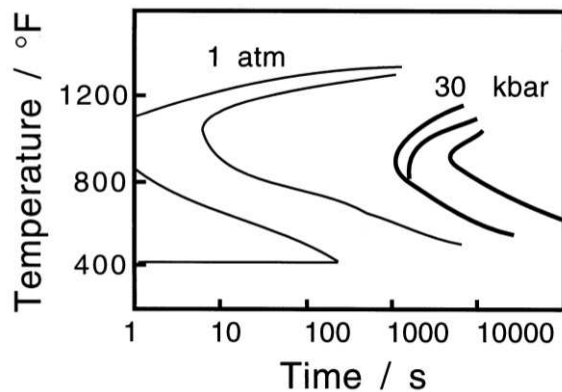


**Figure 8.9** Isothermal transformation diagrams of Fe-0.82C wt% at 1 atmosphere (1 bar and at 30 kbar pressure; after Nilan (1967).

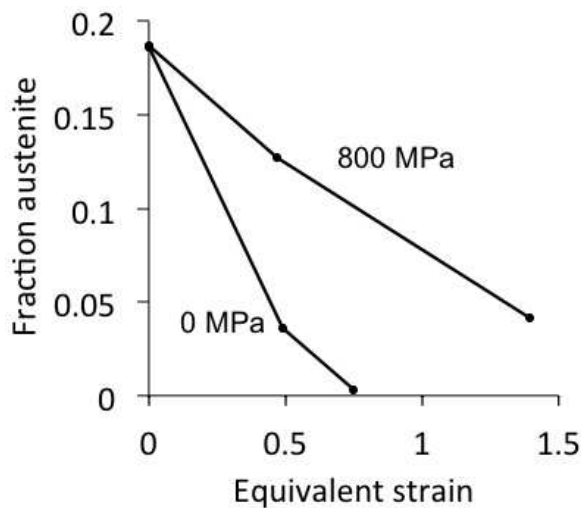


**Figure 8.10** The volume fraction of austenite as a function of tensile strain in samples tested in a hydrostatically pressurised environment, at the pressures indicated on the diagram (Pyshmintsev et al., 2002).

## 8.6 Mechanical Stability of Retained Austenite

In steels where the precipitation of carbides during the bainite reaction is slow, the residual austenite becomes enriched in carbon and a large proportion is retained on cooling to ambient temperature. The austenite, if it decomposes under the influence of stress, can be detrimental to the steel concerned since the resulting high-carbon, untempered martensite is expected to be brittle. There is ample evidence that the austenite retained to ambient temperature after isothermal formation of bainitic ferrite, especially the larger blocky austenite, can decompose to martensite even at relatively small stresses, Fig. 8.11 (Horn and Ritchie, 1978; Kar et al., 1979; Bhadeshia and Edmonds, 1983a,b; George et al., 1985; Tsukatani et al., 1991). Even the stresses induced by ultrasonic immersion can induce the blocks of austenite to transform (Wu et al., 2002). The mechanical stability of retained austenite is therefore important in obtaining good toughness in bainitic steels.

Miihkinen and Edmonds (1987c) have shown that for high silicon steels in which the bainite reaction is allowed to proceed until it stops, the mechanical stability of the retained austenite decreases as the isothermal transformation temperature is increased. The me-

chanical stability was defined as the ratio of retained austenite content after 2% plastic deformation in a tensile test to the original content. Given that the bainite reaction in such steels ceases when the carbon concentration of the residual austenite  $x_\gamma$  approaches  $x_{T_0}$ , and that  $x_{T_0}$  increases with decreasing temperature, the austenite on the basis of its composition is theoretically expected to be more stable as the bainite formation temperature is reduced (Bhadeshia and Edmonds, 1983a). Furthermore, if the  $T_0$  curve can be shifted to higher carbon concentrations by modifying the substitutional solute content then the stability of the austenite is expected to increase, and this has also been confirmed experimentally.

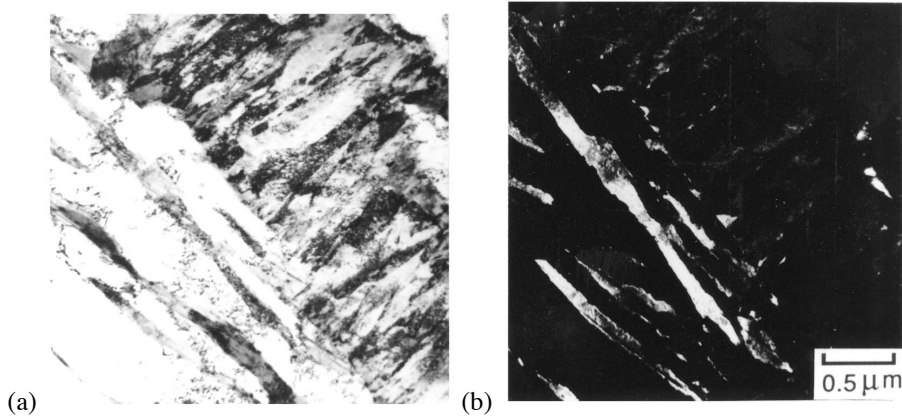


**Figure 8.11** Electron micrographs illustrating the effect of applied stress (850 MPa) on a sample which initially had a microstructure of bainitic ferrite and retained austenite (Bhadeshia and Edmonds, 1983a). The larger regions of austenite transform into martensite but the films are preserved. (a) Bright field image showing a large region of stress-induced martensite; (b) corresponding austenite dark field image. The sample was tempered prior to the application of stress in order to distinguish the martensite which forms during cooling from the bainite transformation temperature, from that which is induced by stress.

It is often necessary to express the volume fraction of retained austenite as a function of plastic strain during deformation. Neglecting for the moment that such tests usually include the simultaneous application of stress and strain, i.e. any martensite that is induced should not strictly be defined as being strain-induced, it may be reasonable to assume that the change in the fraction of martensite ( $dV_V^{\alpha'}$ ) obtained for a given increment of plastic strain ( $d\epsilon$ ) should be proportional to the fraction of remaining austenite:

$$\frac{dV_V^{\alpha'}}{d\epsilon} = k_\gamma V_V^\gamma \quad (8.7)$$

where  $k_\gamma$  is a proportionality constant and  $V_V^\gamma$  is the fraction of austenite remaining untransformed. If the fraction of austenite at zero strain is  $V_V^{\gamma_0}$ , then  $V_V^{\alpha'} = V_V^{\gamma_0} - V_V^\gamma$ , and integration of equation 8.7 gives

$$\ln\{V_V^{\gamma_0}\} - \ln\{V_V^\gamma\} = k_\gamma \epsilon \quad (8.8)$$

This relationship was first derived by Sugimoto et al. (1992a) by fitting to experimental data and is discussed further in section 13.6.1, in the context of TRIP-assisted steels.<sup>6</sup> Equation 8.8 has the constant  $k_\gamma$  that does not generalise to different austenite compositions. To cope with this, Sherif et al. (2004) expressed it differently by including  $\Delta G_{\text{chem}}$  calculated at the deformation temperature:

$$\ln\{V_V^{\gamma_0}\} - \ln\{V_V^\gamma\} = k'_\gamma \Delta G_{\text{chem}} \epsilon \quad (8.9)$$

where  $k'_\gamma = 0.002017 \text{ mol J}^{-1}$  independent of the composition of the austenite. In their critical assessment of the variety of models that exist for the deformation-induced transformation of austenite, Mukherjee et al. (2010) assessed equation 8.9 to generalise well over all the data they assessed. The theory of martensite can also be used to obtain a more systematic model (Olson and Cohen, 1975; Papaefthymiou et al., 2004), taking account of both stress and strain effects. The influence of stress in this model is via the change in the number density of the nucleation site distribution:

$$N_V^{\text{stress}} = N_V^{\circ} \exp\left\{\frac{2C_{15}\sigma_{\alpha\gamma}}{\Delta G d}\right\} \quad (8.10)$$

where  $\Delta G$  has the chemical, mechanical and strain energy terms together with the work of friction as the interface moves;  $d$  is the spacing of the close-packed planes in austenite;  $\sigma_{\alpha\gamma}$  is the interfacial energy per unit area and  $C_i$  are constants.  $N_V^{\circ}$  is the initial distribution of nuclei present in the austenite, which is modified by plastic strain so that:

$$N_V^{\text{strain}} = N_V^{\circ} \exp\left(\frac{2C_{16}\sigma_{\alpha\gamma}}{\Delta G' d}\right) \quad (8.11)$$

where  $\Delta G'$  contains a modified mechanical free energy term. The volume fraction of martensite is then given by:

$$\frac{V^{\alpha'}}{V} = 1 - \exp\left\{V_\tau (N_V^{\text{stress}} + N_V^{\text{strain}})\right\} \quad (8.12)$$

where  $V_\tau$  is the volume per particle; the model clearly requires a number of parameters that are not usually easy to access.

## 8.7 Transformation under Constraint: Residual Stresses

Residual stresses are mostly introduced unintentionally during fabrication (Withers and Bhadeshia, 2001a,b). They are of particular importance in welded structures where they have a detrimental effect. Jones and Alberry (1977) conducted an elegant series of experiments to illustrate the interaction between transformations and residual stress. Using bainitic, martensitic and stable austenitic steels, they demonstrated that transformation plasticity during the cooling of a uniaxially constrained sample from the austenite phase field acts to relieve the build up of thermal stress as the sample cools. By contrast, the

<sup>6</sup>An alternative form,  $\ln\{V_V^{\gamma_0}/(V_V^{\gamma_0} - V_V^\gamma)\} = k_\gamma \epsilon^m$  is also used (Lee et al., 2004). However, this equation does not seem to be well behaved for the case where all of the austenite transforms, or where the strain is zero. Shi et al. (2006) use:  $1 - V_V^\gamma/V_V^{\gamma_0} = 1 - \exp\{-A\epsilon\}$  where  $A$  is an empirical fitting constant.

non-transforming austenitic steel exhibited a continuous increase in residual stress with decreasing temperature, consistent with the degree of thermal contraction. On the other hand, when the steels were transformed to bainite or martensite, the transformation strain compensated for any thermal contraction strains that arose during cooling. Significant residual stresses were therefore found to build up only after transformation was completed, and the specimens approached ambient temperature (Fig. 8.12).

The experiments contain other revealing features. The thermal expansion coefficient of austenite ( $1.8 \times 10^{-6} \text{ K}^{-1}$ ) is much larger than that of ferrite ( $1.18 \times 10^{-6} \text{ K}^{-1}$ ), and yet, the slope of the line prior to transformation is smaller when compared with that after transformation is completed (Fig. 8.12). This is because the austenite yields to accommodate the thermal contraction; this is possible because the yield strength of the austenite is reduced at elevated temperatures.

Ferrite is strong at low temperatures so the slope of the stress/temperature curve (after transformation is complete) is steeper and consistent with the magnitude of thermal contraction strains.

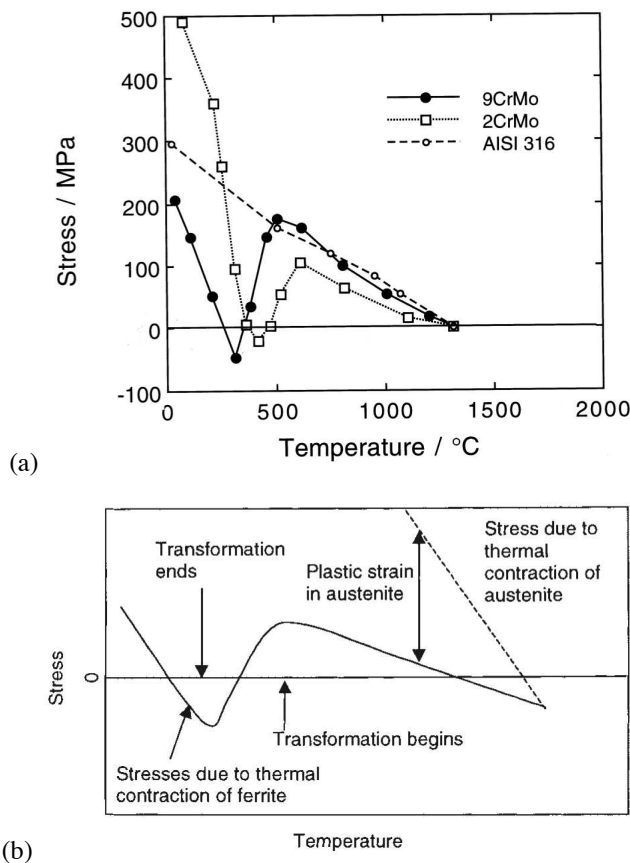


**Figure 8.12** (a) Plot of residual stress versus temperature for a martensitic (9CrMo), bainitic (2CrMo) and austenitic steel (AISI 316). After Jones and Alberry (1977). (b) Interpretation of the Alberry and Jones experiments. The thermal expansion coefficient of austenite is much larger than that of ferrite.

The interpretation of experimental data of the kind illustrated in Fig. 8.12 is difficult in the region of the stress/temperature curve where transformation occurs. The popular view that the volume change due to transformation is the major component of transformation plasticity is probably incorrect for displacive transformations such as bainite or martensite. The shape change due to transformation has a shear component which is much larger than the dilatational term. Admittedly, this shear component should on average cancel out in a fine grained polycrystalline sample containing plates in many orientations. However, the very nature of the stress effect is to favour the formation of selected variants, in which case, the shear component rapidly begins to dominate the transformation plasticity. This is illustrated in Fig. 8.13

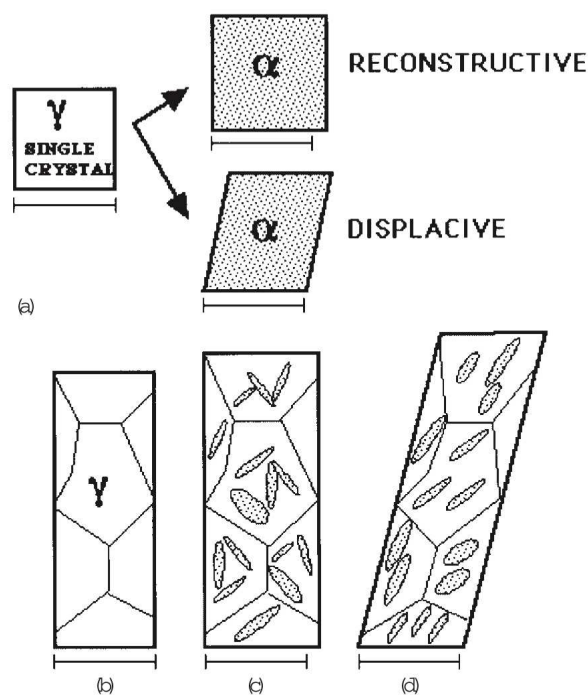


**Figure 8.13** The shape changes accompanying unconstrained transformations. Note that the horizontal scale bars are all of the same length. (a) The two kinds of changes in shape that occur when a single crystal of austenite transforms to a single crystal of ferrite, as a function of the mechanism of transformation. (b) A polycrystalline sample of austenite. (c) A polycrystalline sample of austenite which has partially transformed by a displacive transformation mechanism into a random set of plates of ferrite. (d) A polycrystalline sample of austenite which has partially transformed by a displacive transformation mechanism into an organised set of plates of ferrite.

The residual stress at ambient temperature is larger when the austenite finishes transformation at a high temperature. This is because thermal contraction strains can no longer be compensated by transformation plasticity once the austenite has decomposed. Low transformation temperatures help minimise residual stresses. High strength welding alloys used for making submarine hulls therefore have transformation temperatures which are less than about 250 °C.

Fig. 8.14 illustrates one kind of distortion found in welds, measured in terms of the angle  $\theta$  through which the unconstrained plates rotate as they cool. Table 8.2 shows how the distortion depends on the temperature at which the majority of the transformation is completed, for two manual metal arc welds deposited with a  $60^\circ$  V-joint preparation in a multipass fabrication involving about 11 layers with two beads per layer to complete the joint. The distortion is clearly larger for the case where the transformation is exhausted at the higher temperature.

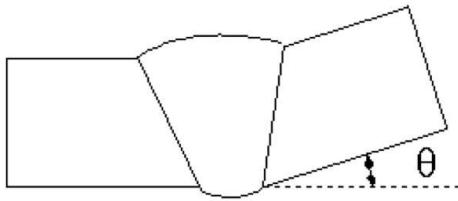


**Figure 8.14** Distortion caused by welding two plates which were originally flat.

**Table 8.2** The chemical compositions (wt%), calculated transformation temperature range ( $\Delta T$ ) and measured distortion  $\theta$  for two manual metal arc, multipass weld deposits. (Unpublished work, Bhadeshia and Svensson, 1994).

C / wt%	Si	Mn	Ni	Mo	Cr	$\Delta T / ^\circ\text{C}$	$\theta^\circ$
0.06	0.5	0.9	-	-	-	802-400	14.5
0.06	0.3	1.6	1.7	0.4	0.35	422-350	8

Transformation plasticity of the kind emphasised by Jones and Alberry has recently been used to reduce residual stresses in weldments.<sup>7</sup> The procedure simply involves using welding-alloys which have a low martensite-start temperature. Welded joints produced using these alloys are found to exhibit improved fatigue life and show a greater resistance to cold cracking due to hydrogen embrittlement (Zenitani et al., 2002).

Large components with complicated shapes can be made using the electric arc spraying of molten steel droplets on to a cold substrate (spray-casting). However, the associated quenching of sprayed material can lead to unacceptable distortions in the final product. Rayment et al. (2004) have used the bainite transformation to counter the development of residual stresses responsible for the distortion, leading to a novel process for the manufacture of tools and dies for the automobile industries.

## 8.8 Anisotropic Strain due to Transformation Plasticity

During their attempts to study the isothermal transformation of austenite using dilatometry, Davenport and Bain (1930) had noticed already that “the volume change (due to

<sup>7</sup>(Ohta et al., 1999a,b, 2003; Ramjaun et al., 2014b,a; Ooi et al., 2014; Ohta et al., 1999a; Eckerlid et al., 2003; Lixing et al., 2004; Darcis et al., 2008; Karlsson and Mráz, 2011; Miki and Masayuki, 2013)

transformation) is not necessarily uniformly reflected in linear change in all dimensions". They even found that the thickness of flat disc specimens actually decreased as the volume increased! These results were stated without interpretation but it is now clear that in polycrystalline samples which are crystallographically textured, anisotropic transformation plasticity can be detected even in the absence of an applied stress (Bhadeshia et al., 1991; Mahnken et al., 2011). When an unstressed polycrystalline sample of austenite is transformed, the shear components of the individual shape deformations of the large number of variants which form along any dimension should tend to cancel out on a macroscopic scale. Similarly, the dilatational component of the IPS shape deformation should average leaving an isotropic volume expansion. When the microstructure within the sample is not random, then the possibility of the individual shape deformations cancelling out over large distances is correspondingly reduced. A non-random microstructure can arise when certain crystallographic variants are favoured when transformation occurs under the influence of an external stress. Alternatively, there may be crystallographic texture and residual stresses within the austenite which cause the biased microstructure; transformation will then lead to a large anisotropy in the strains even in the absence of an applied stress. Anisotropic strains associated with the formation of bainite under the influence of stress are shown in Fig. 8.15; similar data have been reported for martensite (Tsuchida and Tomota, 2000).

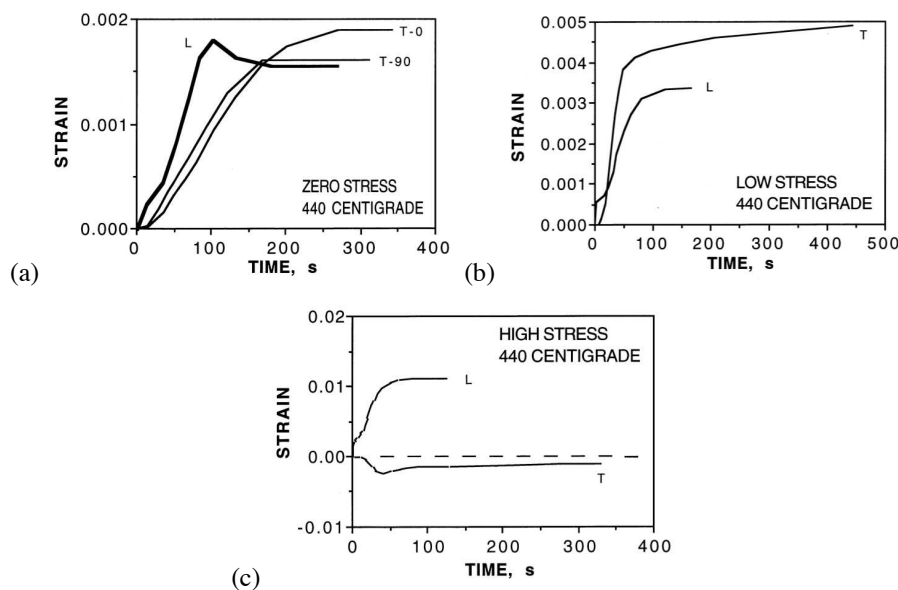


**Figure 8.15** Dilatometric curves showing the dimensional changes during transformation to bainite in a cylindrical sample. T-0 and T-90 refer to the strains monitored along orthogonal transverse directions, and L to the strain along the longitudinal direction. (a) Transformation in the absence of an applied stress; (b) transformation under the influence of a tensile stress of about 45 MPa; (c) 90 MPa. (Bhadeshia et al., 1991).

It has been argued that stress will not lead to the development of texture due to variant selection when the polycrystalline austenite itself has a random distribution of orientations (Wynne et al., 2007). However, the conclusion was reached on the basis of the observed weak transformation textures, and it is true that the latter strengthen as the starting austenite

is textured (e.g. Bhadeshia et al., 2014). A generic view that random austenite will not lead to texture in the transformed state is not correct given variant selection from the 24 possibilities available for each austenite grain.

### 8.8.1 Interactions between Variants

The conventional approach to variant selection is essentially based on the Patel and Cohen work. This relies essentially on a calculation of the mechanical component of the free energy change due to the interaction of the applied stress with the shape deformation of the martensite or bainite plate. It turns out, however, that although this may be true at low volume fractions of transformation and in circumstances where the shape deformation is elastically accommodated, the selection criteria become complex in the event that the material is elastic-plastic (Fischer et al., 1996; Reisner et al., 1999).

Fisher and co-workers have used elastic-plastic mechanics to estimate *interactions* between pairs of crystallographic variants, i.e. when one crystallographic variant is followed by another. It is worth emphasising that the interaction energy is due to the stress fluctuation introduced by the formation of the second variant; it is not the total increment in strain energy and plastic work, which would be there even if there was no interaction between different variants. Thus, the interaction energy between identical variants is zero in the first approximation.

The calculations consist of two terms, the strain energy increment as the second variant forms and the plastic dissipation. The existence of such interactions does not require an externally applied stress. However, interesting results are obtained when variant interactions are calculated in the presence of an applied stress. Given a particular variant, and after applying an external stress, it is found that the second variant is often not the one which should have the highest mechanical driving force relative to the applied stress. This is because the second variant is also influenced by the presence of the first; this intervariant interaction can overwhelm the  $\Delta G_{\text{mech}}$  term. The reason for this behaviour is that during the early stages of transformation, the applied stress dominates selection because the microstresses due to transformation are relatively small. The internally generated stresses begin to dominate the applied stress at larger fractions of transformation.<sup>8</sup>

Whilst it was not possible to generalise about how variant selection should proceed in these circumstances, it was nevertheless concluded that  $\Delta G_{\text{mech}}$  dominated the selection of the second variant of the pair when the applied stress was about 70% of the yield strength of the weaker phase, and  $V_V^\alpha$  remained small.

These results might explain why the transformation plasticity observed when polycrystalline samples decompose to bainite is much smaller than expected theoretically (Bhadeshia, 2002).

## 8.9 Influence of Plastic Strain

Many experiments that claim strain-induced transformation in fact involve the application of both stress and strain, for example during tensile testing of steel containing austenite. This makes the interpretation of data uncertain (Chatterjee and Bhadeshia, 2007). Bokros and Parker (1963) studied single-crystals of austenite that had been deformed prior

<sup>8</sup>But in the absence of an externally applied stress, the method can be used to estimate packet crystallography due to interactions between bainite sheaves (Lubin et al., 2011).

to stress-free martensitic transformation. Plates of martensite that grew across slip bands were found to be favoured because their growth avoided much of the intense dislocation debris on the slip planes. On the other hand, variant selection is not found when polycrystalline austenite is deformed and then induced to undergo stress-free bainitic transformation (Shirzadi et al., 2009). This discrepancy is explained by the fact that plastic deformation in a polycrystalline austenite necessitates the operation of at least five independent slip systems, which should lead to a more homogeneous distribution of dislocations. However, the data relate to plastic strains in the range 0.1-0.33, whereas much larger deformations that pancake the austenite have been demonstrated to lead to a dramatic reduction in the number of variants per grain (Godet et al., 2003).

### 8.10 Stress-Affected Carbide Precipitation

The idea that cementite at low temperatures precipitates by a displacive mechanism with only the partitioning of carbon is not unnatural - this mechanism has been demonstrated for the precipitation of vanadium hydride (Bowles et al., 1977). The evidence for cementite has been discussed in Chapter 3. Although the shape deformation associated with precipitation has yet to be measured, it is believed to be an invariant-plane strain with a shear of 0.211 parallel to the habit plane and a dilatational strain of 0.157 normal to the habit plane (Taylor et al., 1989a).

The effect of the shape change can be revealed by the precipitation microstructure when it is generated under the influence of an externally applied stress (Matsuzaki et al., 1992; Stewart et al., 1994). When martensite is tempered in a stress-free condition, the carbides precipitate in several crystallographic variants in any given plate, in the so-called Widmanstätten pattern. When the tempering is carried out under a uniaxial stress, the variant which presumably complies best with the external stress begins to dominate the microstructure. Eventually, when the stress is large enough, it is only a dominant crystallographic variant is found in any plate of martensite (Fig. 8.16).

The response of the carbide microstructure to the applied stress is precisely that expected from the interaction with the transformation strain. In experiments reported in the literature, the mechanical driving force is similar in magnitude to the chemical driving force for the precipitation of cementite. Thus,  $\Delta G_{\text{mech}} \approx 730 \text{ J mol}^{-1}$  for a stress of 500 MPa, and  $1380 \text{ J mol}^{-1}$  for 950 MPa. This compares with  $\Delta G_{\text{chem}} \approx 1300 \text{ J mol}^{-1}$  at the tempering temperature.

Fig. 8.17 shows that the chemical driving force is sensitive to the carbon concentration of the martensite and to the tempering temperature. It follows that the effect of stress on the development of the carbide microstructure (and the tendency to precipitate a single variant) will be most prominent at low carbon concentrations or at high tempering temperatures. We note that the stress need not be applied externally; it is equally valid to consider the influence of internal stresses due to transformation from austenite.

Lower bainite forms at higher temperatures than martensite so  $\Delta G_{\text{chem}}$  for carbide precipitation is smaller; any partitioning of carbon into austenite reduces  $\Delta G_{\text{chem}}$  further. Therefore, lower bainite plates are more likely to contain only a single carbide variant than martensite, as observed experimentally.

The nitriding of steel creates a particular pattern of residual stress; this stress in turn has been found to lead to the preferential alignment of cementite precipitates because they precipitate under the influence of the stress (Barrallier et al., 2005).

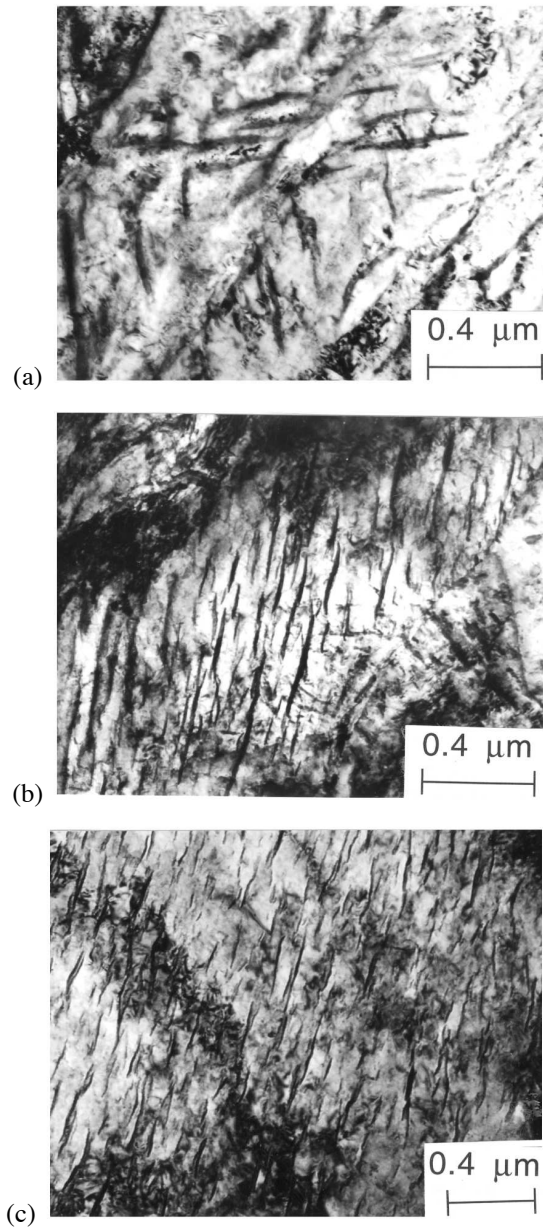


**Figure 8.16** The microstructure of martensite which is tempered under the influence of a uniaxial stress. The number of cementite variants in any given martensite plate decreases at the stress is increased. (a) Zero stress; (b) 500 MPa; (c) 950 MPa. The stress is in all cases below the macroscopic yield strength of the sample at the tempering temperature. After Stewart et al. (1994).

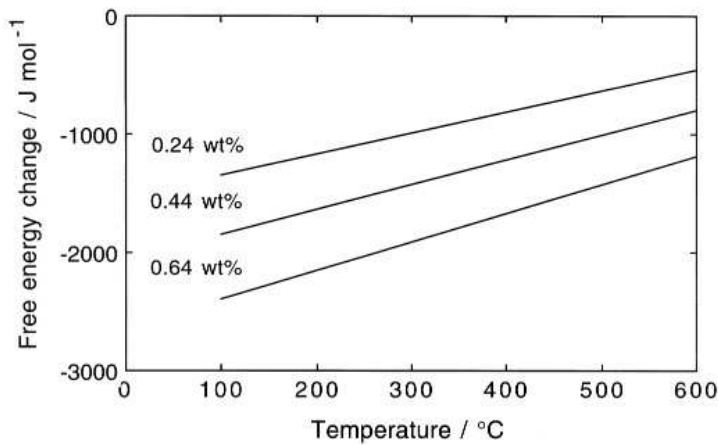


**Figure 8.17** Free energy change accompanying the precipitation of cementite from supersaturated ferrite, as a function of the carbon concentration and temperature (Stewart et al., 1994).

## 8.11 Plastic Deformation and Mechanical Stabilisation

Displacive transformations involve the coordinated movement of atoms; such coordination cannot be sustained against strong defects such as grain boundaries. Thus, martensite plates, which form by a displacive mechanism, cannot cross austenite grain boundaries. Smaller defects such as isolated dislocations hinder the progress of such transformations, but can often be incorporated into the martensite lattice. However, severe deformation of austenite prior to its transformation hinders the growth of martensite, causing a reduction in the fraction of transformation in spite of an increased number density of nucleation sites. This applies to all martensitic transformations, irrespective of material; apart from steels, the phenomenon is, for example, known to occur for martensitic transformations in lithium (Maier et al., 1997), in brass (Spieffeld, 1999) and during mechanical twinning (Christian and Mahajan, 1995).

This retardation of transformation by plastic deformation is called *mechanical stabilisation* and can be explained in terms of the structure of the transformation interface. Displacive transformations occur by the advance of glissile interfaces which can be rendered sessile when they encounter dislocation debris. Thus, whereas an appropriate stress can stimulate displacive transformation in the same way that it enables normal deformation, mechanical stabilisation actually retards the decomposition of the austenite (Bhadeshia, 1999a).

### 8.11.1 Theoretical Basis

The theory for predicting the onset of mechanical stabilisation relies on balancing the force driving the motion of the interface against the resistance of the dislocation debris created by the deformation of the austenite (Chatterjee et al., 2006; Maalekian et al., 2007).

Deformation at low homologous temperatures is produced by the translation of dislocations. For a density  $\rho_d$  of dislocations, each with a Burgers vector of magnitude  $b$ , the

plastic strain is given by

$$\epsilon = \rho_d b L \quad (8.13)$$

where  $L$  is the average distance moved by the dislocations (Honeycombe, 1984b). For a given dislocation density, the spacing between the dislocations is given by  $l = \rho_d^{-\frac{1}{2}}$ . The mean shear stress  $\tau$  needed to force dislocations past each other is, in these circumstances (Honeycombe, 1984b):

$$\tau = \frac{\mu b}{8\pi(1-\nu)l} = \frac{\mu b \rho_d^{\frac{1}{2}}}{8\pi(1-\nu)} \quad (8.14)$$

where  $\mu$  is the shear modulus and  $\nu$  the Poisson's ratio. On combining with equation 8.13 and noting that the force per unit length is  $\tau b$ ,

$$\tau b = \frac{\mu b^{\frac{3}{2}}}{8\pi(1-\nu)} \sqrt{\frac{\epsilon}{L}} \quad (8.15)$$

The mean free distance  $L$  must decrease as the plastic strain increases:

$$L = \frac{\delta D}{\delta + D\epsilon} \quad (8.16)$$

where  $D$  is the original grain size of austenite prior to straining and  $\delta$  is a coefficient about equal to 1  $\mu\text{m}$  (Barlat et al., 2002).

Apart from dislocation strengthening, solid-solution hardening will also contribute a resistance  $\tau_S$  to interface motion (Olson and Cohen, 1976; Ghosh and Olson, 2001). Solid solution hardening coefficients for a variety of solutes in austenite have been reported for tensile strength in Irvine et al. (1969). This adds to the resistance due to any dislocation debris.

The stress  $\tau_T$  driving the motion of the interface originates from the chemical free energy change  $\Delta G$  of transformation (Olson and Cohen, 1976):

$$\tau_T = \phi \Delta G \quad (8.17)$$

where  $\phi$  is a constant assumed to be equal to unity and  $\Delta G = G_\gamma - G_\alpha$ , i.e. the magnitude of the driving force.  $\Delta G$  is a function of temperature and the composition of the steel. The stored energy of martensite is about 600  $\text{J mol}^{-1}$  (Christian, 1979) and that for bainite is about 400  $\text{J mol}^{-1}$  (Bhadeshia, 1981c), quantities that reduce the available driving force. When multiplied by the magnitude of the Burger's vector,  $b$ , this gives the magnitude of force per unit length available for the austenite-martensite interface to move.

Mechanical stabilisation occurs when the stress driving the interface equals that opposing its motion:

$$\begin{aligned} \tau_T &= \tau + \tau_S \\ b\Delta G &= \frac{1}{8\pi(1-\nu)} G b^{\frac{3}{2}} \sqrt{\frac{\epsilon}{L}} + \tau_S b \end{aligned} \quad (8.18)$$

This equation can be used to calculate the critical strain for mechanical stabilisation, in the context of all displacive phase transformations including martensite, bainite and Widmanstätten ferrite. One application is to show quantitatively that the growth of a sub-unit of bainite is stifled by the plastic accommodation of the shape deformation. The resulting shear strain is sufficient to generate local mechanical stabilisation (Chatterjee et al., 2006) and the theory further predicts, as is observed experimentally, that the platelets of bainite should become more slender as the transformation temperature is reduced because the chemical driving force increases with undercooling.

### 8.11.2 Experimental Evidence

The early work on mechanical stabilisation effects focussed on martensitic transformations, but there are now many experiments reported for bainite. Some early experimental data based on hot-rolling experiments can be interpreted to show that bainitic transformation is retarded in deformed austenite, as illustrated in Fig. 8.18. When studying the transformation of partially recrystallised austenite, Mesplont and de Cooman (2003) found that bainite grows preferentially in the recrystallised austenite and is strongly retarded in the deformed grains. This has consequences on the transformation texture since the recrystallised austenite has a different texture to that which is in a deformed state.

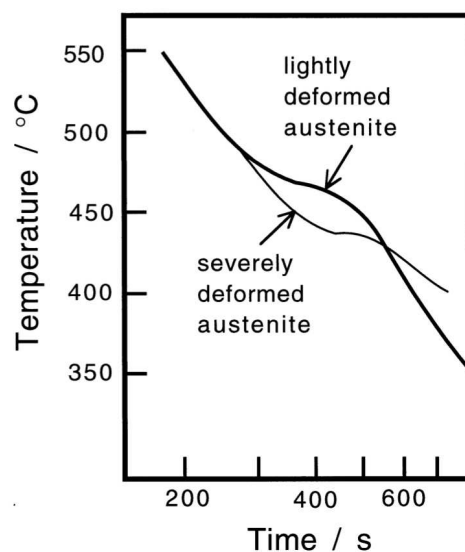


**Figure 8.18** Plots of temperature versus time, for samples undergoing bainitic transformation during cooling. The deviations from linearity indicate the onset of transformation. The reaction is retarded in the austenite deformed to a greater degree before transformation, indicative of mechanical stabilisation. Data from Davenport (1977).

Direct evidence comes from the work of Tsuzaki et al. (1989) who found that although deformed austenite transformed faster, the net volume fraction of bainite decreased when compared with undeformed austenite, Fig. 8.19. Deformed austenite transformed into a smaller maximum quantity of bainite when compared with undeformed samples, even though they initially decomposed at a higher rate. This effect did not occur at higher temperatures, presumably because the amount of bainite that can form is then reduced. Stabilisation therefore only manifests itself when the “easy” regions of austenite are exhausted, i.e. those regions left unaffected by the imposed deformation which is inevitably inhomogeneous. The nonuniformity of stabilisation is reflected in the microstructure. The bainite tends to align along specific directions within individual austenite grains (Fig. 8.20). The dislocation arrays introduced during the plastic deformation of austenite interact with the displacive transformation mechanism to favour some variants of bainite over others (Girault et al., 2001).

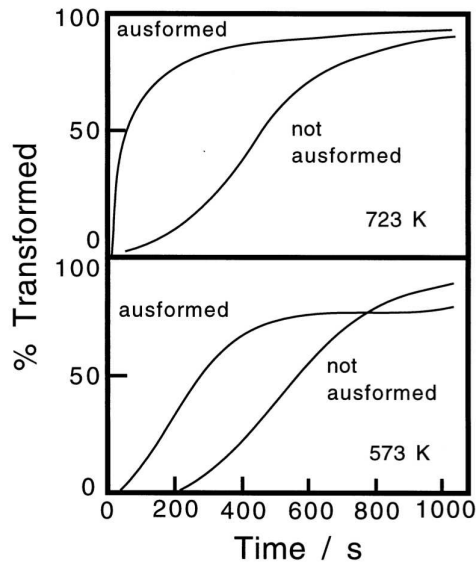


**Figure 8.19** The effect of ausforming on the kinetics of the bainite reaction in a Fe-0.59C-2.01Si-1.02Mn wt% alloy.

As is often the case with martensite in ausformed alloys, bainite plates follow a path whose curvature is determined by the spread of crystallographic orientation in the parent austenite prior to transformation (Fig. 8.20). Indeed, any crystallographic misorientations present in the austenite are precisely inherited by the individual platelets of bainite as a consequence of the displacive transformation mechanism (Godet et al., 2004), as listed in Table 8.3. Note that the spread in the bainitic ferrite is less than in the austenite because it occupies only a small region of the entire austenite grain. Internal stresses may also induce variant selection (Lambers et al., 2011), but would not lead to changes in orientation or in the curvature of plates.

**Table 8.3** The spread in orientation as a function of the extent of plastic strain  $\epsilon$  applied to the austenite prior to transformation into bainite. After Godet et al. (2004).

	$\epsilon = 0$	$\epsilon = 0.2$	$\epsilon = 0.8$
Austenite	2.5°	3.2°	5.0°
Bainitic ferrite	1.2°	1.6°	2.5°

It has been demonstrated using metallography that the bainite transformation can be mechanically stabilised in a manner identical to martensitic transformations (Fig. 8.21). The growth of bainite is retarded by the deformation debris in the austenite. Heterogeneous nucleation becomes more frequent as defects are introduced into the austenite, but their growth by a displacive mechanism is stifled as the interface encounters forests of dislocations. Heavily deformed austenite therefore transforms to a smaller quantity of bainite than undeformed austenite, and any bainite that forms is more refined. Synchrotron experiments that provide a rich source of information including relaxation, volume fraction, stress and strain data as the transformation progresses, confirm that the untransformed austenite un-

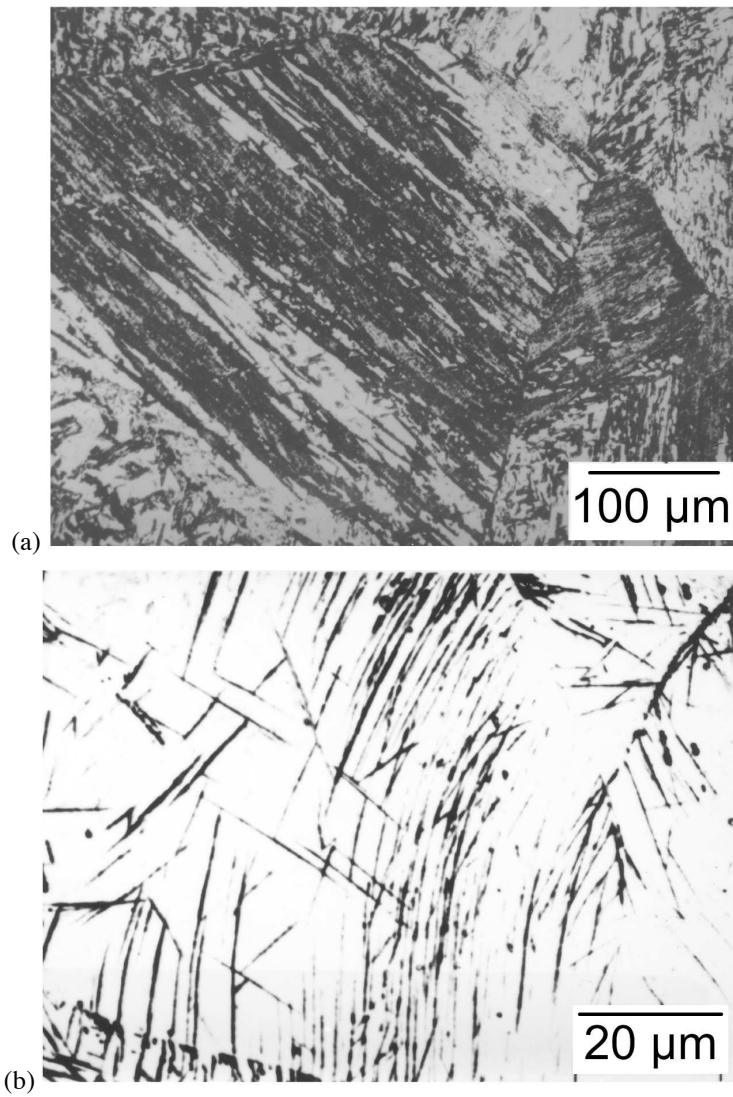


**Figure 8.20** Optical micrographs illustrating the microstructure of an ausformed bainitic steel. (a) Alignment of sheaves of bainite in individual austenite grains. (b) Curved bainite sheaves reflecting the deformation-induced misorientations within the austenite grains. (Tsuzaki et al., 1989).

dergoes plastic relaxation, that in turn causes a retardation of the bainite transformation (Dutta et al., 2013). The broadening of X-ray diffraction peaks of austenite, in the absence of external load, is direct evidence of an increase in its defect density.

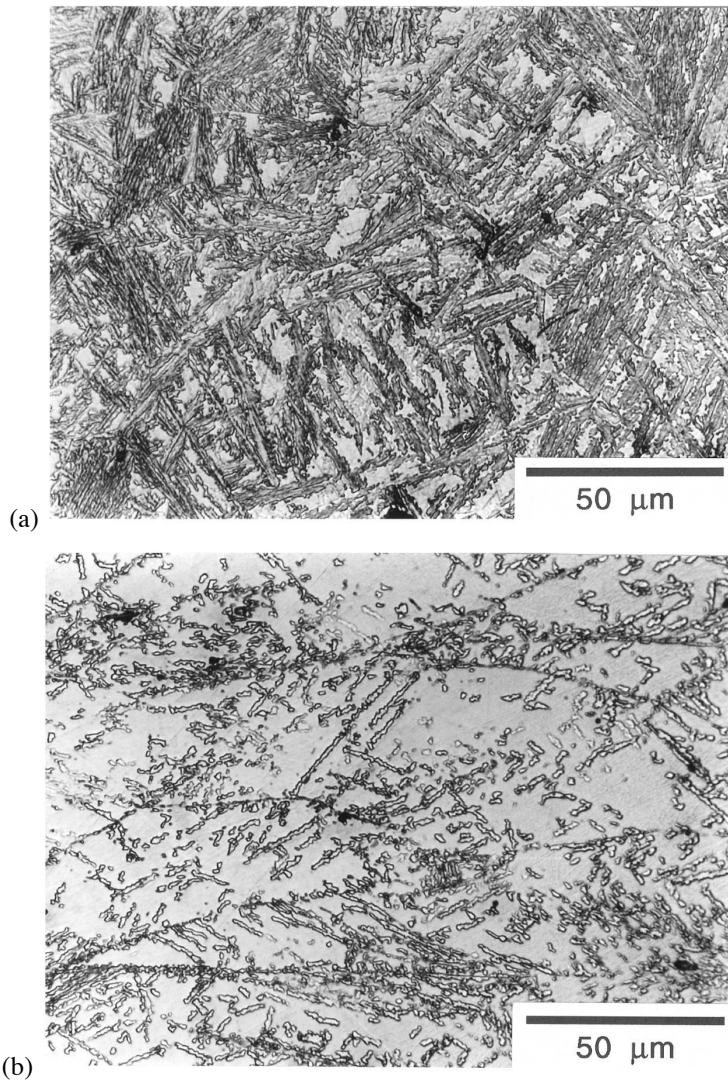


**Figure 8.21** Optical micrographs showing the large effect of mechanical stabilisation in refining the microstructure and in reducing the amount of bainite. (a) Transformation from undeformed austenite. (b) Transformation from plastically deformed austenite (Shipway and Bhadeshia, 1995).

Mechanical stabilisation is evident in quantitative experiments (Singh and Bhadeshia, 1996; Lam and Yang, 2000). There are two intriguing features illustrated in Fig. 8.22, first that transformation from deformed austenite leads to a smaller terminal fraction of bainite. Secondly, although the transformation rate is at first accelerated by deformation, it is eventually retarded relative to the undeformed sample. If this initial acceleration is explained by increasing the number density of nuclei then it is not possible to reach a smaller

terminal fraction given that each nucleus transforms a fixed volume of austenite. On the other hand, if it is assumed that the smaller limiting fraction is due to the reduction in volume transformed per nucleus then it is not possible to explain the initial acceleration. There are other complications described elsewhere, all of which can only be resolved by arguing that the austenite is inhomogeneously deformed (Singh and Bhadeshia, 1998b). The lightly deformed regions transform more rapidly relative to undeformed austenite because of the increase in the defect density. The nucleation rate is larger in the heavily deformed regions but the overall rate of transformation is reduced because each nucleus then transforms to a smaller volume due to mechanical stabilisation of the interface.

There can be complicated effects during the development of mixed microstructures from deformed austenite. Thus, deformation accelerates allotriomorphic ferrite, thereby removing grain boundary nucleation sites and hence promoting acicular ferrite over bainite in subsequent transformation (Wang et al., 2007). Of course, the same deformation limits the amount of acicular ferrite that can form. There is limited evidence that the bainitic and martensitic transformations are both partially suppressed in TRIP-assisted steels when the austenite is in a plastically deformed condition (Zrnik et al., 2007). Pancaked austenite occurs routinely in certain parts of hot press-formed components, where the forming is in the austenitic state.

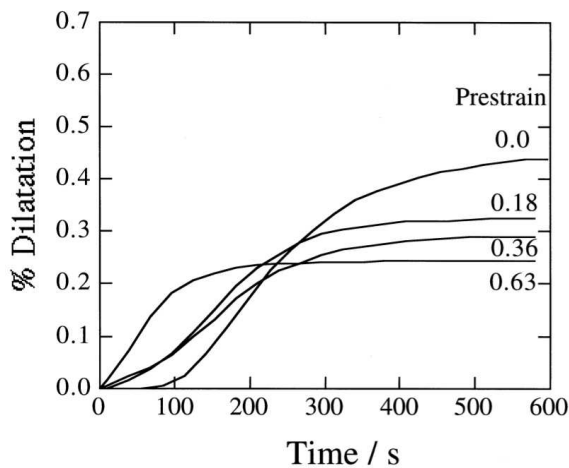


**Figure 8.22** Change in radial dilatation during isothermal transformation to bainite as a function of time and prestrain (the strain in the austenite prior to transformation); values of the prestrain are indicated next to individual curves. After (Singh and Bhadeshia, 1996).

Mechanical stabilisation has now been found for all of the plate-shaped ferritic phases that occur in steels. This includes Widmanstätten ferrite (Shipway and Bhadeshia, 1997; Larn and Yang, 1999, 2000), bainite and martensite,<sup>9</sup> all of which are displacive shear transformations. Mechanical stabilisation has been shown to occur in materials as diverse as lithium (Pichl and Krystian, 1999) and brass (Hornbogen, 1999). By contrast, reconstructive transformations are without exception accelerated if the parent phase is deformed prior to transformation (e.g. Bae et al., 2004). This is because of the increase in the number density of nucleation sites, and because the defects introduced by deformation are destroyed as the new phase grows, rather as in recrystallisation. The elimination of the defects

<sup>9</sup>Machlin and Cohen (1951); Fiedler et al. (1955); Leslie and Miller (1964); Strife et al. (1977); Tsuzaki et al. (1991a); Raghavan (1992); Tsai et al. (2002); Das et al. (2011); van Bohemen and Sietsma (2014); Mangal et al. (2014).

contributes to the driving force for reconstructive transformation. In displacive transformations the defects are *inherited* by the growing phase and hence do not supplement the driving force. With these general observations it is possible to define a disarmingly simple criterion to distinguish these two mechanisms of transformation:

There is no mechanism by which plastic deformation can retard reconstructive transformation. Likewise, only displacive transformations can be mechanically stabilised.

### 8.11.3 Transformation from Recovered Austenite

Austenite that is plastically deformed at high temperatures will, in the absence of recrystallisation, tend to recover if kept at that high temperature. The dislocation structure then organises into cells, the cell-interiors becoming relatively dislocation-free. Yang et al. (2001a) demonstrated that bainite plates are arrested at the cell-boundaries, leading to a refinement in the microstructure. Bimodal distributions of plate lengths are obtained when the austenite microstructure is only partly recovered, the plates being longer in regions where the cell structure is less developed.

In microalloyed steels, the recovery of the dislocation structure may be modified due to strain-induced precipitation. The precipitates may in turn influence the nucleation of bainite.

### 8.11.4 Technological Implications of Mechanical Stabilisation

There are now many structural steels which have a bainitic microstructure but are manufactured using the same thermomechanical processing routes that have been applied so successfully to the ferrite-pearlite steels (Chapter 13). However, this has been done without the realisation that the bainite transformation can be retarded by such processing. The consequences of this for structural steels have simply not been explored but some evidence is available for special steels. Tsuji et al. (1999a) found that the effect of forcing the bainite to grow in severely deformed austenite is to increase the quantity of untransformed austenite. This is precisely what is expected from mechanical stabilisation. Furthermore, it was found that the hardness of ferrite and pearlite does not change much whereas that of bainite increases significantly as it acquires all the crystallographic errors present in the deformed austenite.

In microalloyed steels it is common to find strain-induced niobium carbo-nitride precipitation at dislocations in the deformed austenite. Both the dislocation forest and the precipitates then hinder the progress of the bainite reaction (Yakubstov and Boyd, 2001).

A study of microstructure in a hot-rolled steel indicated that bainite and martensite form in regions where the parent austenite has partially recrystallised but allotriomorphic ferrite in the deformed austenite, Fig. 8.23. This might be expected if the deformed austenite is mechanically stabilised.

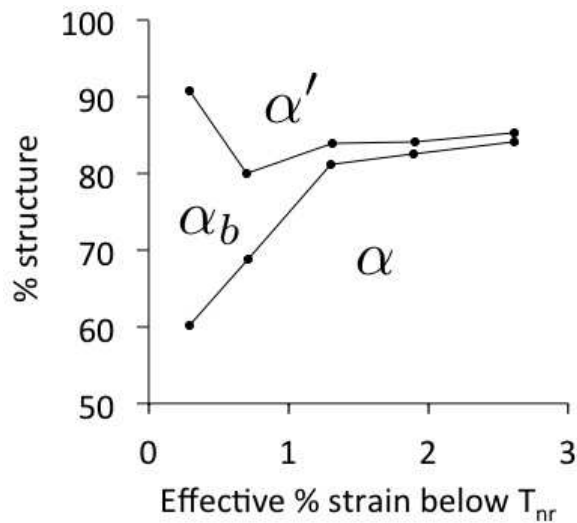


**Figure 8.23** Diminishing quantity of bainite as the amount of deformation in the austenite, prior to transformation, is increased.  $T_{nr}$  is the temperature below which austenite does not recrystallise during hot deformation. After Waterschoot et al. (2002)

## 8.12 Summary

There is little doubt that the bainite reaction is influenced by externally applied stress, and by stresses generated internally due to transformation or heat treatment. This interaction with stress appears to be related to the displacive mechanism of transformation and its invariant-plane strain shape deformation with its large shear component. Stress-assisted transformation can lead to anisotropic dimensional changes whose magnitudes and senses are impossible to explain on the assumption of a reconstructive transformation mechanism. Transformation plasticity is readily detected during the growth of bainite under the influence of stress, the magnitude of the observed effect being excess of that expected from volume change criteria alone.

There is evidence that the response of bainite to stress is similar to that of martensite. The bainite-start temperature is raised by the application of a tensile stress, lowered by hydrostatic compression, and there exists a  $B_d$  temperature beyond which the reaction will not occur whatever the magnitude of the stress. The microstructure of bainite responds to the applied stress, with clear evidence that the growth of certain crystallographic variants is favoured over others. The number of different sheaves per austenite grain decreases, causing the formation of large packets of parallel sheaves; this microstructure may be detrimental to toughness. Further work remains to be done in order to establish the criteria determining variant selection during stress-influenced transformation. Bainite also shows characteristics similar to those associated with the mechanical stabilisation of martensite, when the austenite is deformed prior to the growth of bainite.

Transformation to bainite accelerates under the influence of stress; whether this is predominantly due to enhanced nucleation or growth remains to be resolved. The extent to which the rate of reaction is accelerated increases with the rate of application of stress. On the other hand, heavy plastic-deformation of austenite prior to transformation causes mechanical stabilisation, a phenomenon associated uniquely with displacive transformations. Stabilisation occurs when the glissile  $\alpha_b/\gamma$  interface is unable to overcome the barriers posed by defects present in the austenite prior to transformation.

The primary effect on microstructure during transformation under stress is that of variant selection, which at low stresses reduces the number of sheaves per austenite grain. Variant selection does not lead to an obviously aligned microstructure until larger stresses are applied, in which case the sheaves form on habit planes that are most parallel to the planes of maximum shear stress. Although deviations from the random microstructures that form in the absence of applied stress are often not easily detectable, they reveal themselves unambiguously in the form of anisotropic dimensional changes during transformation.

The response of bainitic transformation to stress is therefore essentially similar to that of martensite, although there are some exceptions because of the higher transformation temperatures. Irreversible processes such as plastic deformation by lattice dislocations or the partitioning of carbon are routine with bainite. This rules out the possibility of reversing the motion of the interface by reversing the stress, making phenomena like shape memory effects or rubber elasticity extremely unlikely with bainite.

The precipitation of cementite also reacts to applied stress with the number of crystallographic variants decreasing as the intensity of the stress increases. This explains the observation of single variants of precipitation in lower bainitic ferrite plates. The number of carbide orientations per plate of ferrite increases when the chemical component of the driving force dominates over any mechanical interactions. So lower bainite, like tempered martensite, does not necessarily have just one variant of precipitated carbide.



## CHAPTER 9

---

### FROM BAINITE TO AUSTENITE

---

Many commercial processes cause the steel to revert into the austenitic condition. The transformation of low-temperature ferrite into high-temperature austenite differs from the case where the latter transforms during cooling. Transformation during cooling follows C-curve kinetics in which the overall transformation rate goes through a maximum as a function of the undercooling below the equilibrium temperature. This is because diffusion coefficients decrease but the driving force increases as the temperature is reduced. By contrast both the diffusivity and driving force for austenite formation increase as a ferritic microstructure is superheated. The rate of transformation increases indefinitely as the temperature is raised, Fig. 9.1.

This kinetic behaviour has interesting consequences. It is commonly observed that reconstructive transformations can be suppressed by cooling rapidly to a low temperature where the lack of atomic mobility prevents further transformation. Austenite can therefore be retained by rapid cooling to ambient temperature, even though it may not be thermodynamically stable. It should be impossible to similarly retain ferrite to high temperatures in the  $\gamma$ -phase field during a heating experiment, since atoms become more mobile at higher temperatures.

Austenite is not always retained when quenched from an elevated temperature. It may transform by a mechanism that does not require diffusion (martensitic). When the  $\alpha \rightarrow \gamma$  transformation occurs during heating, the temperatures involved are usually high enough to permit the rapid reconstructive transformation. It is therefore rare for austenite to grow by a martensitic mechanism.

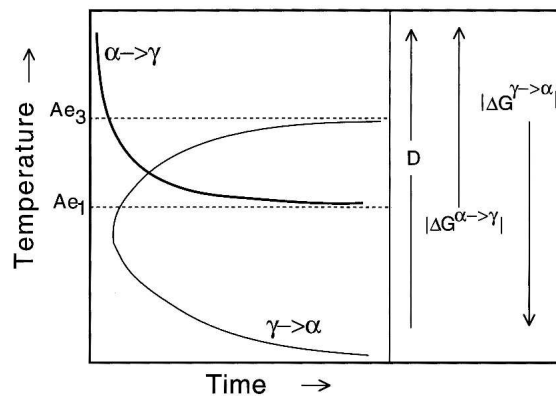


**Figure 9.1** The TTT curves for the  $\gamma \rightarrow \alpha$  reaction, and for the reverse  $\alpha \rightarrow \gamma$  transformation.

In compendiums of time-temperature-transformation diagrams, the kinetics of austenite decomposition are presented as a function of the chemical composition and the austenite grain size. The number of variables to be considered when presenting similar data for transformation to austenite is much larger: the initial microstructure can vary widely. The sophistication with which it is necessary to specify the starting microstructure remains to be determined, but factors such as particle size, the distribution and composition of individual phases, homogeneity of the microstructure, the presence of nonmetallic inclusions, etc. should all be important.

There are two particular examples where a detailed knowledge of austenitisation could be exploited to considerable advantage. During fusion welding, an optimum microstructure is required immediately after deposition from the liquid state. The luxury of homogenisation or other thermomechanical treatments is simply not available or practical. The welding process dissipates heat into the surrounding metal, with regions in the immediate proximity of the fusion surface being heated to temperatures high enough to cause austenitisation. Another example where austenitisation theory could be usefully applied is in the development of new wrought steels (Fe-Ni-Ti), where attempts are being made to utilise microstructures which have been partially austenitised.

There clearly is work to be done on all aspects of the formation of austenite, but the discussion in this chapter is confined to the austenitisation of bainitic microstructures.

### 9.1 Heating a Mixture of Austenite and Upper Bainitic Ferrite

When an iron-carbon alloy is heated to a temperature within the  $\alpha + \gamma$  phase field until equilibrium is established, a small rise or fall in temperature leads to the growth or dissolution respectively, of the austenite until the volume fractions once again satisfy the lever rule (Tsuzaki et al., 1988). The transformation of austenite into allotriomorphic ferrite is in this sense reversible, and exhibits little or no hysteresis. A much larger hysteresis occurs for the martensite to austenite transformation because the martensite tempers during heating and because its growth involves dissipation in the form of irreversible plastic deformation. A substantial hysteresis effect is found experimentally when a mixture of bainitic ferrite and austenite is heated (Fig. 9.2).

If carbides precipitate during the bainite reaction then the final microstructure is unlikely to contain retained austenite. This is especially the case when the average concentration of carbon in the steel is large (Caballero et al., 2005). Carbides may also precipitate when an initial mixture of retained austenite and bainite is heated (Luzginova et al., 2007). The sample must then be heated into the  $\alpha + \gamma$  phase field before austenite can nucleate first and then grow. Of course, if austenite exists in the starting microstructure, and if it remains stable during heating, then it can begin growth as soon as the free energy change becomes negative. For bainite, this may nevertheless require a substantial superheat because the transformation remains incomplete, i.e. it stops when  $x_\gamma \approx x_{T'_0}$  rather than when  $x_\gamma = x_{Ae_3}$ . The temperature therefore has to be raised until the carbon concentration of the residual austenite becomes equal to that given by the  $Ae_3$  phase boundary before the austenite can grow, leading to the hysteresis illustrated in Fig. 9.2.

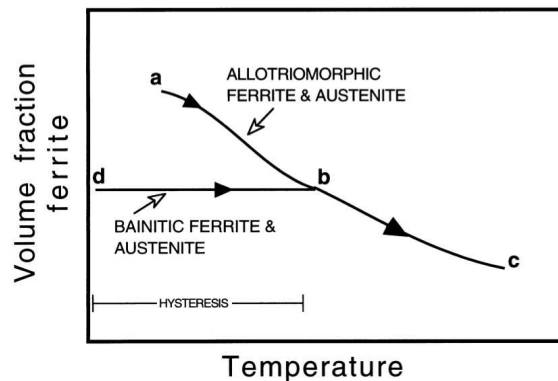


**Figure 9.2** The growth of austenite when mixtures of ferrite and austenite are heated. An equilibrium mixture of allotriomorphic ferrite and austenite begins to transform when the temperature is raised, whereas a large superheat is needed when a mixture of bainitic ferrite and austenite is heated.

These concepts can be revealed in steels which transform to bainite without the precipitation of carbides (Yang and Bhadeshia, 1989b). We have argued above that when a mixture of bainitic ferrite and carbon-enriched austenite is heated sufficiently rapidly to a high enough temperature, the existing austenite can grow without there being a need for nucleation (Fig. 9.3).<sup>1</sup>

Experiments like these have shown that the austenite in low-alloy steels grows by a reconstructive process at all but the fastest of heating rates. A large difference is found between the  $B_S$  and  $A_S$  (austenite-start) temperatures. The austenite only begins to grow when the  $Ae_3$  temperature of the *residual austenite* is reached. Its fraction then increases

<sup>1</sup>This does not preclude new nuclei of austenite; thus, Kessler and Pitsch (1965) found that new regions of austenite nucleated when a mixture of martensite and retained austenite was heated. Whether new nuclei form in microstructures which already contain retained austenite must depend on the superheat since nucleation is most difficult at low driving forces. This, and the general trend illustrated in Fig. 9.2, are confirmed in more recent work by Hara et al. (2009). It is found that the films of austenite when present grow and coalesce to form austenite grains in the original orientation, though new grains may also nucleate at the prior austenite grain boundaries. The films, however, have the advantage in that they do not need to nucleate, so in general they dominate the final austenite grain structure.

from that at the  $A_S$  temperature, to complete transformation at the austenite-finish ( $A_F$ ) temperature, which is the  $A_{e3}$  temperature of the alloy as a whole.

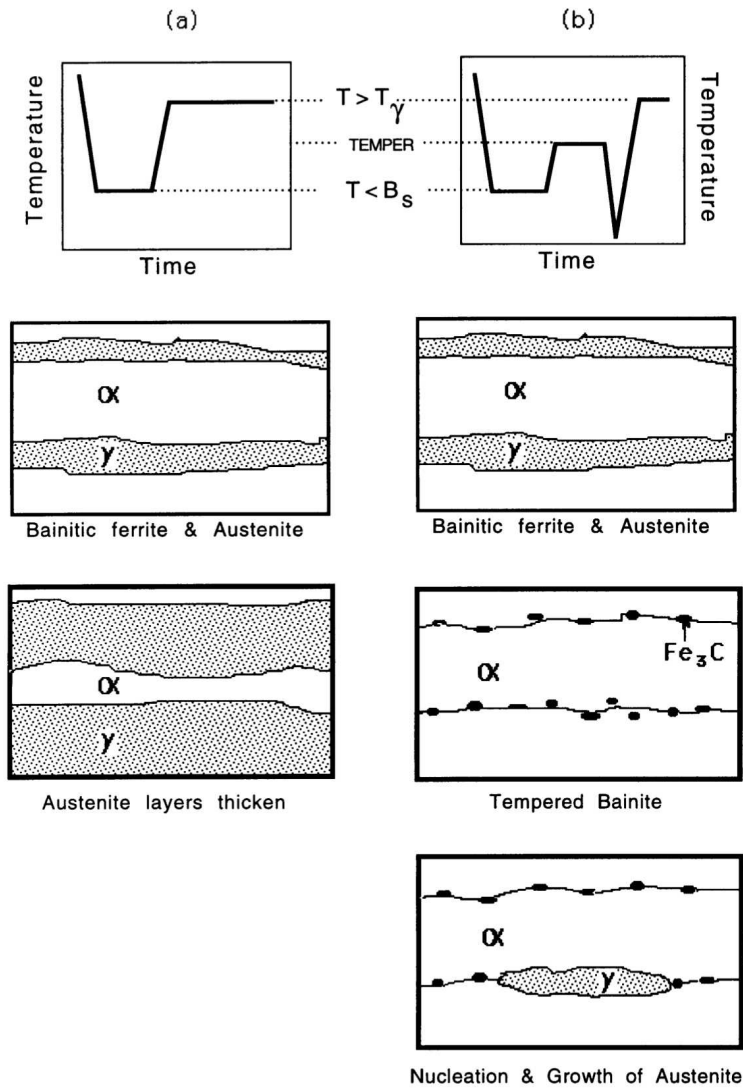


**Figure 9.3** (a) A mixture of bainitic ferrite and austenite is generated by isothermal transformation at a temperature below  $B_S$ ; this microstructure is then reheated to an elevated temperature to permit the austenite to grow. (b) A tempering heat treatment eliminates austenite. It is then necessary to nucleate austenite before it can grow.  $T_\gamma$  is the isothermal austenitisation temperature.

The observed austenitisation behaviour can be understood as follows (Yang and Bhadeshia, 1987a, 1988). When carbide precipitation is avoided, bainite ceases to form when  $x_\gamma = x_{T_0}^\gamma$  (Fig. 9.4). We shall designate this value of  $x_\gamma$  as the initial value  $x_\gamma^I$  obtained by transformation at the temperature  $T_i$ , i.e.

$$x_\gamma^I = x_{T_0}^\gamma \{T_i\} \tag{9.1}$$

as indicated by the point a in Fig. 9.4. Furthermore, we note that:

$$x_{\gamma}^I \ll x_{Ae_3}\{T_i\} \quad (9.2)$$

where  $x_{Ae_3}\{T_i\}$  is marked as point b in Fig. 9.4. Bainite does not form if  $x_{\gamma} > x_{T_0}$  but at that point,  $x_{\gamma}$  is far less than the equilibrium or paraequilibrium concentration. Another way of stating this is to say that the fraction of austenite at  $T_i$  is greater than expected from equilibrium, so there is no tendency for the austenite to grow. This remains the case until the temperature is high enough to satisfy the equation:

$$x_{\gamma}^I = x_{Ae_3}\{A_S\} \quad (9.3)$$

The austenite only begins to grow at  $A_S$  corresponding to the point c in Fig. 9.4. The required superheat  $A_S - T_i$  is a direct effect of the incomplete reaction phenomenon.

The theory predicts that when  $T_{\gamma} > A_S$ , the  $\alpha_b \rightarrow \gamma$  transformation should stop when

$$x_{\gamma} = x_{Ae_3}\{T_{\gamma}\}. \quad (9.4)$$

Neglecting differences in the densities of austenite and ferrite, and assuming that  $x_{\alpha} = 0$ , the equilibrium volume fraction of austenite at  $T_{\gamma}$  is then given by:

$$V_{\gamma}^{\gamma}\{T_{\gamma}\} = \bar{x}/x_{Ae_3}\{T_{\gamma}\}. \quad (9.5)$$

The alloy becomes fully austenitic when  $x_{Ae_3}\{T_{\gamma}\} = \bar{x}$  (point d, Fig. 9.4). The corresponding temperature is designated  $A_F$  so for all  $T_{\gamma} > A_F$ , the alloy transforms completely to austenite.

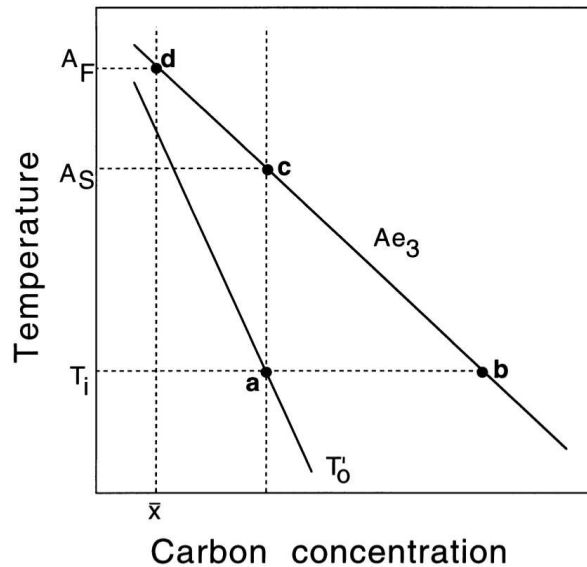


**Figure 9.4** Schematic phase diagram illustrating the theory for austenite growth when the initial microstructure is a mixture of bainitic ferrite and carbon-enriched residual austenite.

### 9.1.1 One-Dimensional Growth from a Mixture of Austenite and Bainitic Ferrite

As discussed earlier, austenite need not nucleate when a mixture of ferrite and austenite is heated. Transformation can occur by the thickening of the austenite films between the bainite plates. This effectively is one-dimensional growth, which we shall assume is diffusion-controlled. The redistribution of carbon must occur inside the austenite during its growth, assuming that its solubility in ferrite can be neglected. Microanalysis has shown that substitutional solutes may partition during austenite formation (Yang and Bhadeshia, 1987a, 1988, 1989b). The extent of partitioning decreases as the transformation temperature  $T_\gamma$ , and hence the driving force, increases. It could be assumed that local equilibrium exists at the interface for low  $T_\gamma$ , with a tendency towards zero bulk partitioning, (i.e. negligible-partitioning local equilibrium or paraequilibrium) as  $T_\gamma \gg Ae_3$ . This makes a full analysis difficult because there are many possibilities between the states of local equilibrium and paraequilibrium.

If local equilibrium is achieved at the interface, the carbon diffusion-controlled growth rate may give an estimate of the factors influencing the kinetics of transformation. This is the basis of the model presented below, which assumes that substitutional solute gradients do not affect the carbon (Kirkaldy, 1958). There is a further assumption that the tie-line of the equilibrium phase diagram, which determines the interface compositions, passes through the average composition of the alloy, which is unlikely in concentrated alloys. Any effects of soft impingement are also neglected.

One-dimensional diffusion-controlled growth leads to a parabolic thickening of films of austenite. The increase in the half-thickness  $q$  of the film is given by:

$$dq = \frac{1}{2}\alpha_1 t^{-\frac{1}{2}} dt \quad (9.6)$$

where  $\alpha_1$  is the one-dimensional parabolic thickening rate constant. The geometry assumed for the thickening of austenite layers is based on the shape of the bainite or acicular ferrite plates which bound the layers. If  $c$  is the largest dimension of such a plate, idealised as a rectangular parallelepiped with sides of length  $a$ ,  $b$  and  $c$ , with  $c = b \gg a$ , then when both of the sides of a ferrite plate are penetrated by the growing austenite, the total area of the  $\gamma/\alpha$  interface which advances into the plate of ferrite is  $2c^2$ . This reduces the thickness of the plate by  $\Delta a/2$  from either side. If the minimum detectable change in volume fraction is  $\Delta V_V$ , then it follows that:

$$\Delta V_V = 2N_V c^2 \int_0^{\Delta a/2} dq \quad (9.7)$$

where  $N_V$  is the initial number of particles of austenite per unit volume, and  $\Delta a_m$  is the minimum detectable increase in thickness. It follows that

$$\Delta V_V = 2N_V c^2 \int_0^\tau \frac{1}{2}\alpha_1 t^{-\frac{1}{2}} dt \quad (9.8)$$

where  $\tau$  is the time taken to achieve the minimum detectable degree of transformation. After integration, equation 9.8 becomes:

$$\Delta V_V = 2\alpha_1 N_V c^2 \tau^{\frac{1}{2}} \quad \text{or} \quad \tau = \left( \frac{\Delta V_V}{2\alpha_1 N_V c^2} \right)^2 \quad (9.9)$$

$$\text{Since } 2N_V c^2 = S_V = 2/\bar{L}_3 \quad \text{it follows that} \quad \tau = \left( \frac{\Delta V_V}{\alpha_1 S_V} \right)^2 \quad (9.10)$$

where  $S_V$  is surface area of  $\gamma/\alpha$  boundary per unit volume, and  $1/\bar{L}_3$  is the mean number of intercepts of  $\gamma/\alpha$  boundary per unit length of test line (DeHoff and Rhines, 1968). It is clear from equation 9.10, that  $\tau$  is dependent not only on  $\alpha_1$  but also on the surface area of  $\gamma/\alpha$  interface per unit volume  $S_V$  for a specific amount of austenitisation.

For the same initial microstructure and a fixed degree of transformation,  $\tau$  should decrease rapidly with increasing  $T_\gamma$ . The microstructure affects  $\tau$  via  $S_V$ . This explains experimental observations of the different rates at which mixtures of  $(\alpha_b + \gamma)$  and  $(\alpha_a + \gamma)$  austenitise, Fig. 9.5a.<sup>2</sup> The distribution of plates in an acicular ferrite microstructure is such that  $S_V$  is smaller than in bainite, making the transformation to austenite relatively slow. It has also been verified experimentally that  $\tau$  is proportional to  $\alpha_1^{-2}$  (Fig. 9.5c).

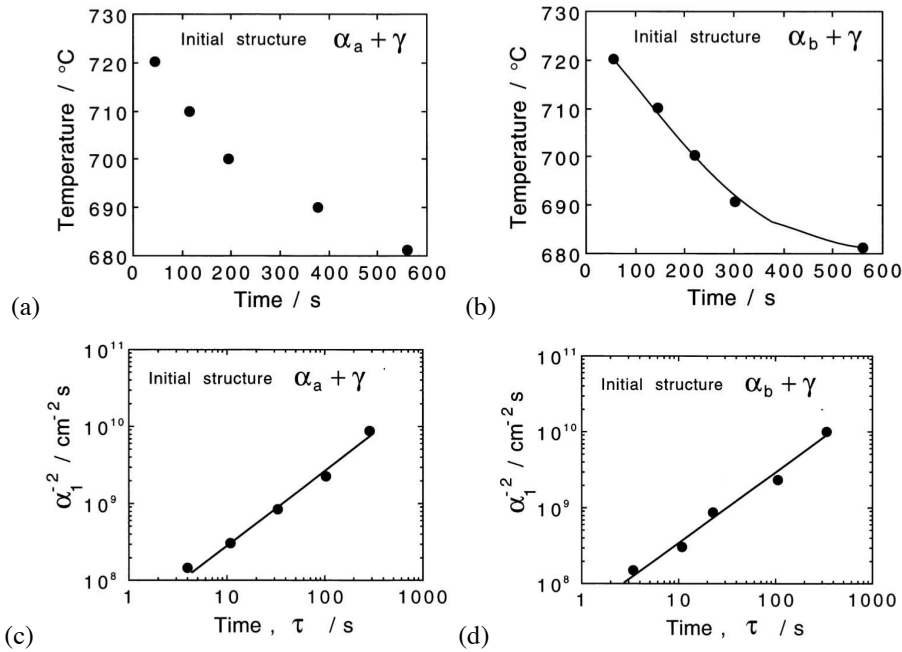


**Figure 9.5** (a,b) TTT diagrams for the growth of austenite from equivalent mixtures of acicular ferrite/austenite, and bainitic ferrite/austenite. (c,d) Linear relationship between the time  $\tau$  taken for a constant volume fraction of austenite growth, versus  $\alpha_1^{-2}$ , where  $\alpha_1$  is the one-dimensional parabolic thickening rate constant for austenite growth (Yang and Bhadeshia, 1989b).

### 9.1.2 Estimation of the Parabolic Thickening Rate Constant

The parabolic rate constant  $\alpha_1$  can be calculated using existing theory for the  $\gamma \rightarrow \alpha$  transformation (Zener, 1949; Dubé, 1947; Bhadeshia, 1985b). Fig. 9.6 shows the carbon concentration profiles in  $\alpha$  and  $\gamma$  before and during austenite growth. The austenite must

<sup>2</sup> $\alpha_a$  stands for acicular ferrite, Chapter 10. The spatial arrangement of plates is different in acicular ferrite when compared against bainite.

become more dilute in carbon as it grows, the rate of interface motion being determined by the diffusion of carbon in the austenite behind the interface. In Fig. 9.6,  $x_\gamma^I$  is the initial carbon concentration in the austenite, given by  $x_\gamma^I = x_{T_0}$ . The carbon concentration of  $\gamma$  at the  $\gamma/\alpha$  interface during austenitisation is  $x^{\gamma\alpha}$  and that of austenite far away from the interface is assumed to remain constant at  $x_\gamma^I$ , as is  $x^{\alpha\gamma}$ . The coordinate  $z$  is normal to the  $\gamma/\alpha$  interface.

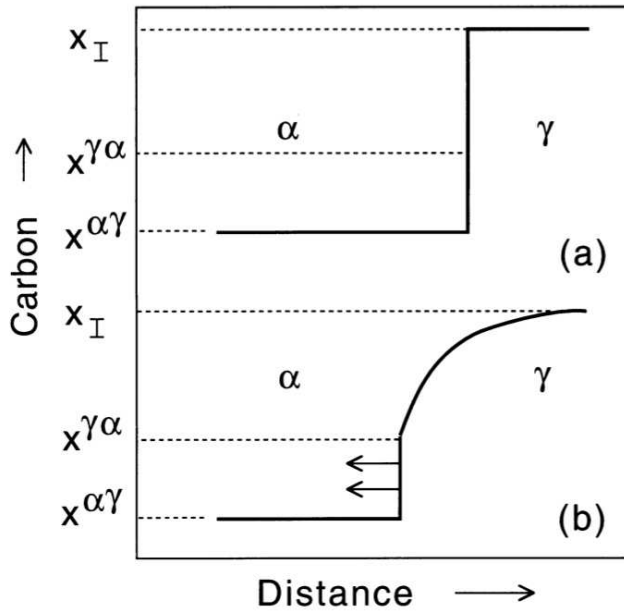


**Figure 9.6** The distribution of carbon, (a) before austenitisation from a mixture of bainitic ferrite and austenite, and (b) during the growth of austenite.

The flux of carbon in the austenite, towards the  $\gamma/\alpha$  interface, at the position of the interface is from Fick's first law given by:

$$J = -D\{x^{\gamma\alpha}\} \left. \frac{\partial x}{\partial z} \right|_{z=Z} \tag{9.11}$$

The rate at which the carbon concentration of austenite is diluted is:

$$R_d = V_d(x_\gamma^I - x^{\alpha\gamma}) \tag{9.12}$$

where  $V_d$  is the velocity of interface (the diffusion-field velocity). Given that

$$Z = \alpha_1 t^{\frac{1}{2}}, \tag{9.13}$$

it follows that:

$$V_d = \frac{dZ}{dt} = \frac{1}{2}\alpha_1 t^{-\frac{1}{2}} \tag{9.14}$$

Consequently, the rate at which the carbon concentration of austenite is diluted is given by:

$$R_d = \frac{1}{2}\alpha_1 t^{-\frac{1}{2}}(x_\gamma^I - x^{\alpha\gamma}). \tag{9.15}$$

Making the approximation that the concentration dependence of the diffusion coefficient of carbon can be represented by its weighted average diffusivity  $\bar{D}$ , conservation of mass at the interface requires that:

$$\frac{1}{2}\alpha_1 t^{-\frac{1}{2}}(x_\gamma^I - x^{\alpha\gamma}) = -\bar{D}\left(\frac{\partial x}{\partial Z}\right)\Big|_{z=Z} \quad (9.16)$$

This equation expresses the condition that as the austenite becomes dilute as its size increases, the change in concentration at the interface is compensated by a diffusion flux of carbon towards the  $\gamma/\alpha$  interface. The differential equation for the matrix is:

$$\frac{\partial x}{\partial t} = \frac{\partial(\bar{D}\partial x/\partial Z)}{\partial Z} \quad (9.17)$$

subject to the boundary conditions  $x = x^{\gamma\alpha}$  at  $z = Z\{t\}$ , and  $x = x_\gamma^I$  at  $t = 0$ . Its solution leads to the following relationship from which  $\alpha_1$  can be determined (Zener, 1949; Dubé, 1947; Atkinson, 1967):

$$f_1 = \frac{x_\gamma^I - x^{\gamma\alpha}}{x_\gamma^I - x^{\alpha\gamma}} = H_1\{\bar{D}\} \quad (9.18)$$

where

$$H_1\{\bar{D}\} = \left(\frac{\pi}{4\bar{D}}\right)^{\frac{1}{2}} \alpha_1 \operatorname{erfc}\left\{\frac{\alpha_1}{2\bar{D}^{\frac{1}{2}}}\right\} \exp\left\{\frac{\alpha_1^2}{4\bar{D}}\right\} \quad (9.19)$$

## 9.2 Anisothermal Transformation

Heat treatments are rarely isothermal in commercial practice. A continuous heating curve can be expressed as a series of small isothermal steps  $i$ , each occurring at a successively higher temperature, with a time interval  $t_i$  associated with each step, section 6.10.5. With Scheil's rule, a specified increment of transformation is achieved during continuous heating when the sum of all the ratios of time steps to incubation periods equals unity:

$$\sum_{i=1}^n \frac{t_i}{\tau_i} = 1 \quad (9.20)$$

where  $\tau_i$  is the time required to reach the specified fraction of transformation at the temperature  $T_i$ . This additivity rule assumes that the reaction is *isokinetic*, meaning that the fraction transformed is dependent only on the time and on a single function of temperature. This is unlikely to be true except in special cases where, for example, nucleation is stifled by site saturation.

## 9.3 Heating a Mixture of Cementite and Bainitic Ferrite

Austenite grows with an equiaxed shape when the initial microstructure is pearlite, but in the form of layers between plates of ferrite when the initial microstructure is bainitic or martensitic (Nehrenberg, 1950), although there are contradictory observations (Law and Edmonds, 1980). What is clear, is that when the austenite forms as layers between the ferrite plates, the steel exhibits a *memory effect*. In this, the original austenite grain structure is regenerated when the transformation to austenite is completed, with respect to both

shape and crystallography (Sadovskii, 1956; Kimmins and Gooch, 1983). Naturally, the austenite grain structure cannot be refined by repeated thermal cycling of the sample into the austenite phase field, when the memory effect operates.

The memory arises because the films grow and coalesce to regenerate the original austenite grain orientations (Kimmins and Gooch, 1983). The memory effect vanishes if the initial microstructure is first annealed to eliminate any retained austenite. Allotriomorphs of austenite are nucleated when these annealed samples are heated into the austenite phase field (Wada and Eldis, 1982).

Retained austenite can decompose during slow heating to the austenitisation temperature, thus destroying the memory effect. Very rapid heating can also eliminate the memory by inducing the nucleation of new austenite grains (Kimmins and Gooch, 1983). The memory is enhanced if the steel contains impurities such as arsenic, phosphorus or tin, which segregate to the prior austenite grain boundaries (Kimmins and Gooch, 1983). The segregation reduces the grain boundary energy, making them less likely as heterogeneous nucleation sites.

An interesting application of austenite formation beginning with bainite has been reported for the thin-slab casting process (Imagumbai, 2006). In contrast to normal processing, the cast ingot is relatively thin, so that the amount of rolling reduction required to reach the final dimensions is small. This has the advantage of reduced processing costs but the disadvantage that the rolling reduction is insufficient to refine the austenite grain structure. By selecting an appropriate steel, a bainitic microstructure can be obtained when the thin slab is quenched from the first hot-rolling operation which follows the casting of a 50 mm slab. The cementite particles in the bainite are spaced a few micrometres apart. The slab is then reheated into the austenite phase field for a period which is not long enough to dissolve the cementite particles. The latter therefore prevent the austenite grains that form from coarsening. As a result, a fine austenite grain structure is obtained which on hot-rolling and accelerated cooling gives an outstanding combination of toughness and strength. The processing sequence is illustrated in Fig. 9.7 and the composition of a typical steel is shown in Table 9.1.

**Table 9.1** Composition of thin-slab cast steel. Concentrations in wt% except Ti, Al, Ca and N which are in parts per million by weight (Imagumbai, 2006).

C	Mn	Nb	Mo	V	Ni	Cu	Si	Ti	Al	Ca	N
0.054	1.58	0.05	0.2	0.05	0.15	0.31	0.19	160	250	18	42

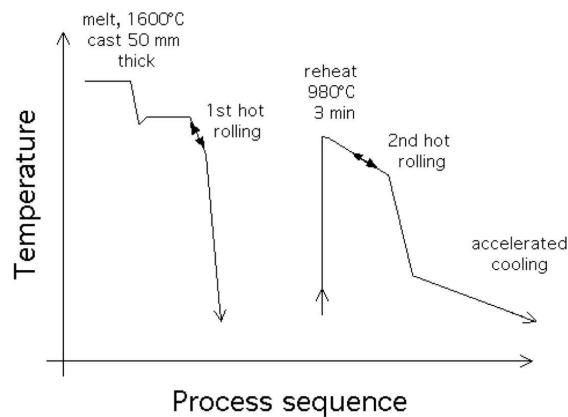


**Figure 9.7** The processing of thin-slab cast steel produced by the partial reaustenitisation of a bainitic microstructure - adapted from Imagumbai (2006).

#### 9.4 Irradiation-Induced Rapid Heating

Surface layers of a steel containing ferrite and pearlite, when irradiated with high-energy electrons, transform into austenite. The effective heating and cooling rates are large because the irradiation effect is confined to a thin surface layer. As a consequence, the carbon concentration in the austenite which grows from pearlite is found to be much larger than in the remainder of the austenite because the rapid thermal cycle does not permit homogenisation over the scale of the microstructure. During cooling, martensite forms in the high carbon regions and bainite in the regions which were originally ferrite (Choi et al., 1999). Rapid inductive heating also leads to an inhomogeneous distribution of carbon in the austenite, so that cooling produces mixed microstructures of ferrite and bainite (Weidig et al., 1999).

#### 9.5 Summary

Microstructures containing a mixture of bainitic ferrite and austenite, when heated, do not require the nucleation of new austenite. Nevertheless, they have to be superheated over a large temperature range before the austenite begins to grow. This is because the bainite reaction stops before equilibrium is achieved so that the fraction of austenite in the initial microstructure is greater than required by equilibrium.

The nucleation of austenite is necessary when the original microstructure does not contain retained austenite. In this case, nucleation generally occurs preferentially at the prior austenite grain boundaries rather than between the ferrite plates. When a microstructure containing retained austenite is heated rapidly, the austenite grows and regenerates the original austenite grain structure, giving the so-called memory effect. This memory can only be destroyed by eliminating the retained austenite either by slow heating or by suitably tempering the initial microstructure (Fig. 9.8).

For any reasonable heating rate, the austenite grows by a reconstructive mechanism with the diffusion of substitutional solutes. The extent of solute partitioning decreases with the

superheat above the equilibrium transformation temperature, but cannot as yet be predicted theoretically.

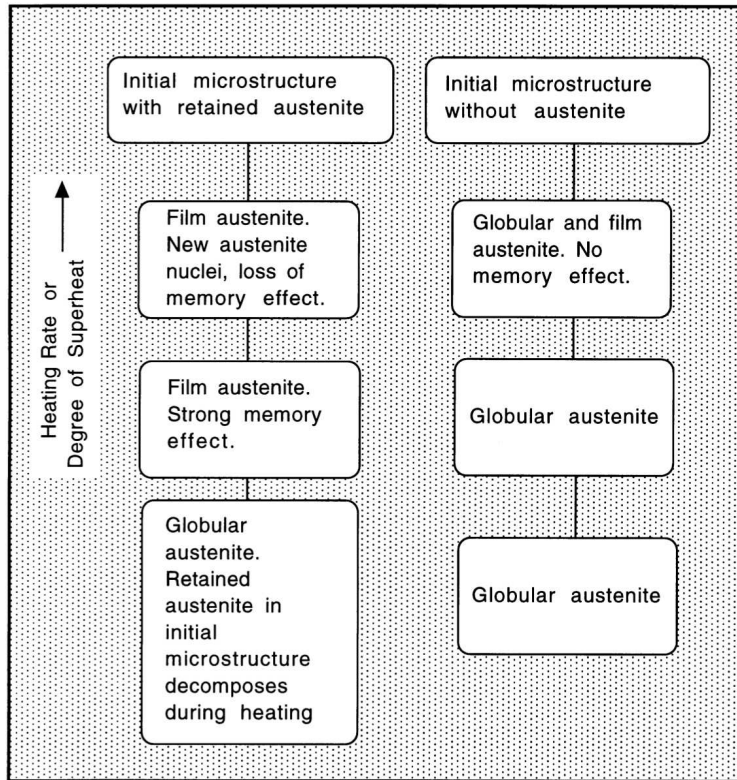


**Figure 9.8** The effects of heating rate and starting microstructure on the morphology of austenite and on the tendency for a memory effect.

## CHAPTER 10

---

# ACICULAR FERRITE

---

### 10.1 General Characteristics and Morphology

Highly organised microstructures can often be found in steels, for example, ferrite plates frequently grow in the form of packets containing parallel plates which are in the same crystallographic orientation. This can be harmful to mechanical properties because cleavage cracks can propagate readily across the packets.

Some of the most useful developments in wrought and welded steel technology have involved *acicular ferrite* (Grong and Matlock, 1986; Abson and Pargeter, 1986). Far from being organised, this microstructure is better described as chaotic. The plates of acicular ferrite nucleate heterogeneously on small nonmetallic inclusions and radiate in many different directions from these point nucleation sites (Fig. 10.1). Crystallographic data show highly misoriented plates nucleated on the same inclusion (Gourgues et al., 2000). Propagating cracks are then deflected on each encounter with a differently oriented acicular ferrite plate. This gives superior mechanical properties, especially toughness.

Acicular ferrite is therefore widely recognised to be a desirable microstructure. This chapter deals with the mechanism by which it forms and with the role of inclusions in stimulating its formation.

The term *acicular* means shaped and pointed like a needle but this is misleading because the true shape is that of a lenticular plate or lath. Measurements on random sections of the plates indicate they are typically about 10 $\mu\text{m}$  long and approximately 1 $\mu\text{m}$  wide, with an aspect ratio smaller than 0.1. Recent serial sectioning experiments which have a depth resolution of about 0.5  $\mu\text{m}$  have confirmed that the shape is between that of a lath

and a plate, with the length, width and thickness normally less than about 36, 6, and 3  $\mu\text{m}$  respectively (Wu et al., 2004; Enomoto et al., 2005; Wu, 2006).

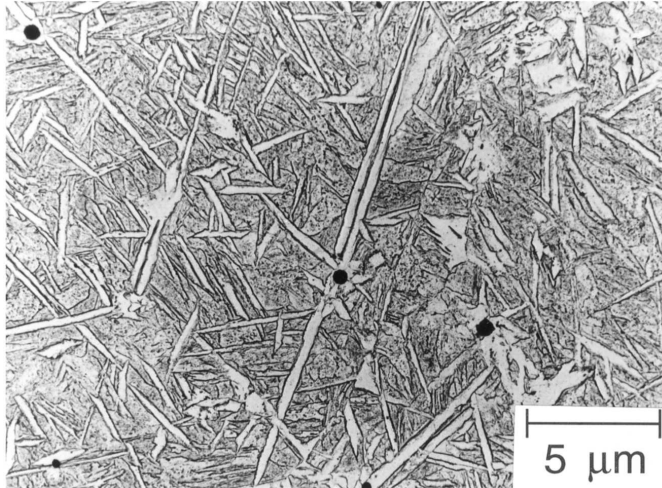


**Figure 10.1** Replica transmission electron micrograph of acicular ferrite plates in a steel weld deposit. After Barritte (1982).

An arc-weld deposit typically contains some  $10^{18} \text{ m}^{-3}$  inclusions of a size greater than 0.05  $\mu\text{m}$ , with a mean size of about 0.4  $\mu\text{m}$ , distributed throughout the microstructure. Inclusions form as oxygen in the liquid weld metal reacts with strong deoxidising elements such as silicon, aluminium and titanium. Slag-forming compounds which form a part of the system designed to protect weld metal from the environment, may also become trapped in the solid at the advancing  $\delta$ -ferrite/liquid interface. Inclusions promote intragranular nucleation of acicular ferrite plates and hence improve toughness without compromising strength. But they also are responsible for the nucleation of voids during ductile fracture, or the nucleation of cleavage cracks during brittle fracture. Achieving a balance between these conflicting factors is the essence of good design. The inclusion microstructure is particularly important in this respect (Fig. 10.2). For example, nonmetallic particles in certain submerged arc weld deposits consist of titanium nitride cores, encapsulated in a glassy phase containing manganese, silicon and aluminium oxides, with a thin layer of manganese sulphide and titanium oxide partly covering the surface of the inclusions (Barbaro et al., 1988). The development of this complex microstructure has been modelled using nucleation and growth theory (Babu et al., 1995).

Inclusions can be oxides or other compounds but the important point is that they may stimulate acicular ferrite (Ito and Nakanishi, 1976). The nucleation of a single plate on an inclusion can in turn stimulate others to nucleate autocatalytically, so that a one-to-one correspondence between the number of active inclusions and the number of acicular ferrite plates is not expected (Ricks and Howell, 1982).

The shape change accompanying the growth of acicular ferrite has been characterised qualitatively as an invariant-plane strain (Fig. 10.3). Like bainite, the shape deformation causes plastic deformation in the adjacent austenite. The resulting dislocations are inherited by the acicular ferrite as it grows, giving a dislocation density which is typically  $10^{14} \text{ m}^{-2}$ , and which contribute some 145 MPa to its strength. The stored energy of acic-

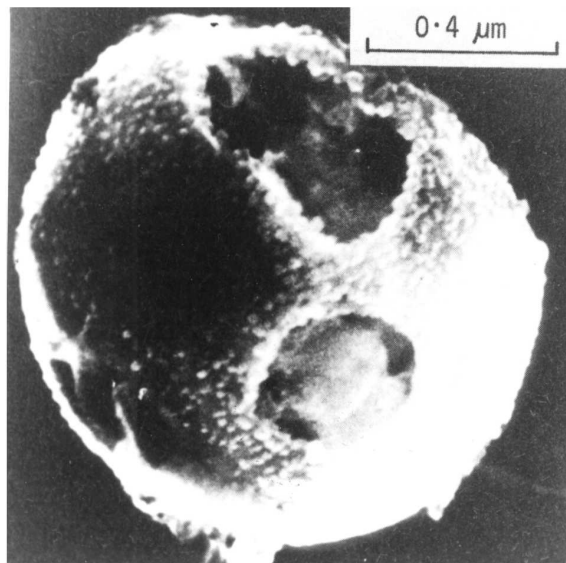


**Figure 10.2** Scanning transmission electron micrograph of a nonmetallic inclusion in a steel weld metal. The inclusion surface is very irregular, and it features many phases. After Barritte (1982).

ular ferrite is similar to that of bainite at about  $400 \text{ J mol}^{-1}$  (Strangwood and Bhadeshia, 1987; Yang and Bhadeshia, 1987b). Consistent with the observed shape change, microanalysis experiments prove that there is no long-range partitioning of substitutional solutes during the formation of acicular ferrite (Strangwood and Bhadeshia, 1987); indeed, atomic resolution experiments have confirmed this the redistribution of such solutes is entirely absent (Chandrasekharaiah et al., 1994).

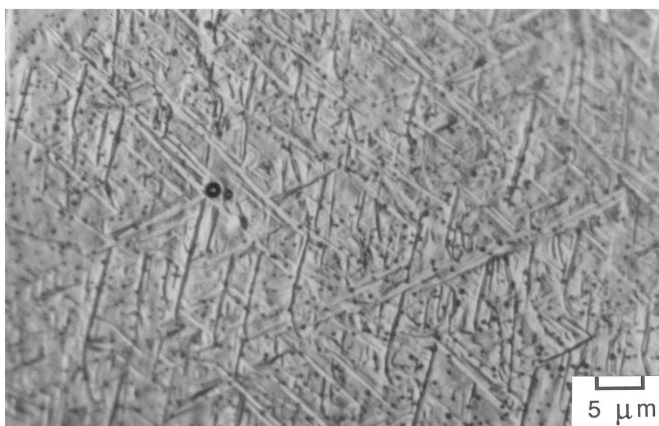


**Figure 10.3** Nomarski interference contrast micrograph illustrating the displacements associated with the formation of acicular ferrite (Strangwood and Bhadeshia, 1987).

Acicular ferrite clearly grows by a displacive mechanism so there are other consequences on the development of microstructure. Thus, plates of acicular ferrite are confined to the grains in which they grow because the coordinated movement of atoms associated with the displacive transformation mechanism cannot be sustained across grain boundaries. The  $\alpha_a/\gamma$  orientation relationship is *always* found to be one in which a close-packed plane of the austenite is nearly parallel to the most densely packed plane of  $\alpha_a$ . Corresponding close-packed directions within these planes are found to be within a few degrees of each other (Strangwood and Bhadeshia, 1987). The fact that acicular ferrite *always* has an orientation with austenite which is within the Bain region has been confirmed recently using orientation imaging microscopy (Miyamoto et al., 2003). It is found that when idiomorphic ferrite nucleates intragranularly on vanadium carbonitride particles, it optimises its fit with the particles and does not therefore have a reproducible orientation relationship with the parent austenite. This is consistent with its reconstructive transformation mechanism. On the other hand, the same study revealed that intragranularly nucleated acicular ferrite always has a near Kurdjumov-Sachs orientation with the austenite, as required by the displacive transformation mechanism.

As with bainite, the size of the acicular ferrite plates increases with transformation temperature; Horii et al. (1988) reported that the apparent plate thickness and length changed from about 1 to 2  $\mu\text{m}$  as the weld cooling rate was reduced.

## 10.2 Mechanism of Growth

The acicular ferrite transformation exhibits the incomplete-reaction phenomenon, an important characteristic of bainite. The extent of reaction decreases towards zero as the transformation temperature is increased towards  $B_S$  (Yang and Bhadeshia, 1987b; Strangwood and Bhadeshia, 1987). Isothermal transformation stops when the carbon concentration of the residual austenite exceeds the  $T'_0$  curve (Fig. 10.4). This implies that acicular ferrite grows supersaturated with carbon, but the excess carbon is shortly afterwards rejected into the remaining austenite.

Acicular ferrite is intragranularly nucleated bainite so it should be possible to switch between these two morphologies by controlling the nucleation site. A bainitic microstructure can be replaced by one containing acicular ferrite by increasing the oxygen, and hence the inclusion content (Ito et al., 1982). After all, the appearance of the acicular ferrite microstructure is only different from that of bainite because it nucleates intragranularly in steels containing a greater number density of inclusions than austenite grain surface nucleation sites (Yang and Bhadeshia, 1987b). Acicular ferrite does not grow in sheaves because their development is stifled by impingement between plates nucleated independently at adjacent sites. Indeed, both microstructures can be obtained under identical isothermal transformation conditions in the same inclusion-containing steel. Bainite forms when the austenite grain size is small because nucleation then predominates at the grain boundaries. Subsequent growth then swamps the interiors of the austenite grains, preventing the development of acicular ferrite. When the austenite grain size is large, the number density of inclusions becomes large relative to boundary nucleation sites promoting the formation of acicular ferrite at the expense of bainite (Fig. 10.5).

This basic theory explains many observations on welds where the heat due to welding produces a gradient of austenite grain size in the heat affected zone (HAZ), with the largest grains adjacent to the fusion surface. When steels containing appropriate inclusions are welded, the ratio of acicular ferrite to bainite is the highest in the HAZ nearest the fusion

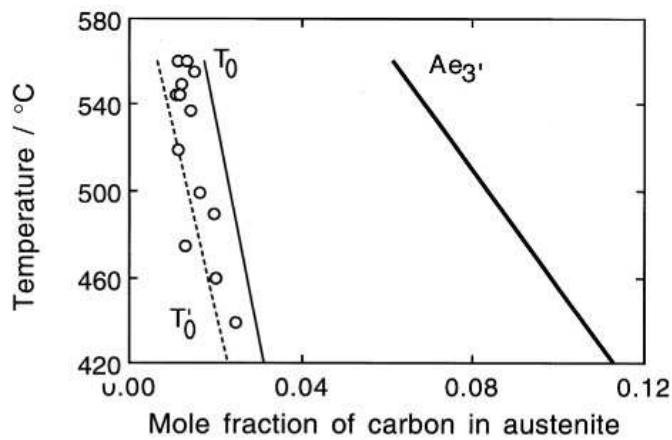


**Figure 10.4** Data from experiments in which the austenite is transformed isothermally to acicular ferrite, showing that the reaction stops when the carbon concentration of the austenite reaches the  $T_0'$  curve (Strangwood and Bhadeshia, 1987).

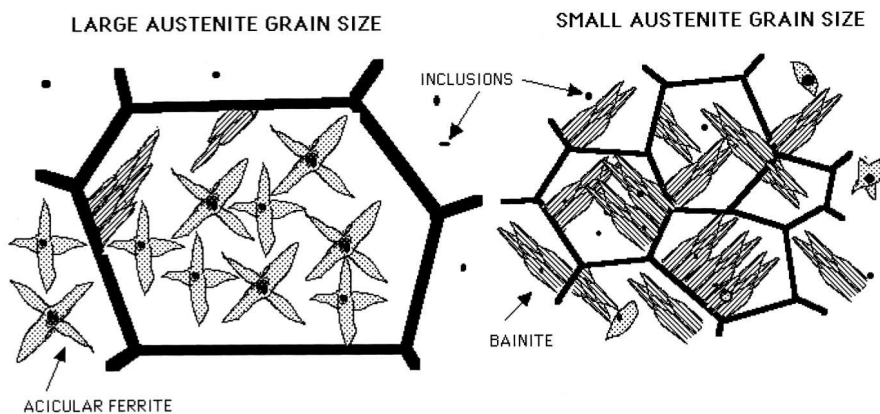


**Figure 10.5** The effect of austenite grain size on the development of microstructure in an inclusion-containing steel. A small grain sized sample has a relatively large number density of grain boundary nucleation sites so bainite dominates the microstructure, whereas a relatively large number density of intragranular nucleation sites leads to a microstructure consisting predominantly of acicular ferrite.

boundary where the austenite grain size is at a maximum (Fig. 10.6a). The acicular ferrite content is always small in the absence of inclusions, Fig. 10.6b (Imagumbai et al., 1985, e.g.).

In another supporting experiment, Harrison and Farrar (1981) removed the inclusions by vacuum remelting a weld; when cooled, the steel transformed into bainite instead of the original acicular ferrite microstructure.

We have emphasised that the transformation mechanism for acicular ferrite is identical to that for bainite. However, all phases can nucleate on inclusions, including Widmanstätten ferrite (Dubé, 1947; Ali and Bhadeshia, 1991). Thewlis et al. (1997) have

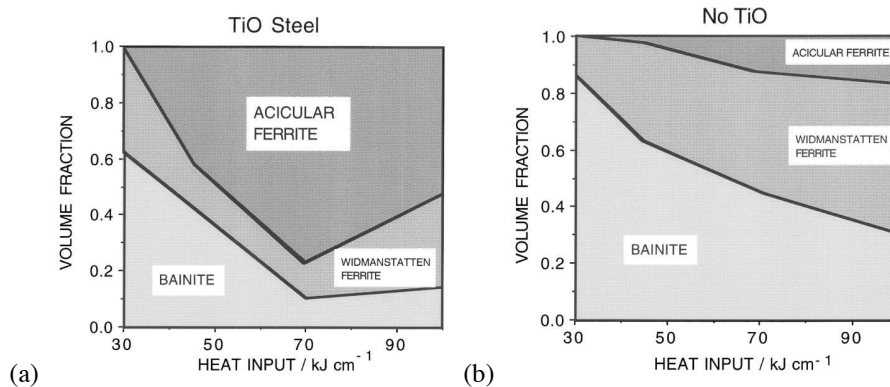


**Figure 10.6** Changes in the microstructure of the heat affected zone of welds, as a function of the heat input during welding. (a) Steel containing titanium oxide particles. (b) Ordinary steel without inclusion inoculation. After Chijiwa et al. (1988).

argued that in some welds the so-called acicular ferrite may predominantly be intragranularly nucleated Widmanstätten ferrite rather than bainite. They reached this conclusion by noting that the estimated bainite-start ( $B_S$ ) temperature was lower than that at which coarse plates nucleated on very large inclusions (3–9  $\mu\text{m}$  diameter). Although there is uncertainty in their calculated  $B_S$  values, the conclusion that a mixed microstructure of intragranularly nucleated Widmanstätten ferrite and intragranularly nucleated bainite (i.e. acicular ferrite) was obtained seems justified. Intragranularly nucleated Widmanstätten ferrite can be distinguished readily from bainite by the scale of the optical microstructure.

Widmanstätten ferrite plates are always much coarser than bainite because what appears as a single plate using optical microscopy is in fact a pair of self accommodating plates. The shape deformation consists of two adjacent invariant-plane strains which mutually accommodate and hence reduce the strain energy, thus allowing the plates to be coarse (Bhadeshia, 1981c).

Acicular ferrite is sometimes considered to be intragranularly nucleated Widmanstätten ferrite on the basis of the observation of “steps” at the transformation interface, which are taken to imply a ledge growth mechanism (Ricks et al., 1982b). The step mechanism of interfacial motion does not necessarily indicate the mechanism of transformation. The observations are in any case weak; perturbations of various kinds can always be seen on transformation interfaces between ferrite and austenite. Such perturbations do not necessarily imply a step mechanism of growth. Evidence that the residual austenite is enriched in carbon is sometimes quoted in support of the contention that  $\alpha_a$  is Widmanstätten ferrite but as pointed out above, the enrichment can occur during or after the transformation event.

The weight of the evidence is that the acicular ferrite recognised in most weld microstructures is intragranularly nucleated bainite. And that the term acicular ferrite should be reserved for this fine microstructure. If coarse Widmanstätten ferrite forms on inclusions then it can be called “intragranularly nucleated Widmanstätten ferrite”. The names given to phases are important because they imply a mechanism of transformation which can be used in theoretical models. It is particularly important to avoid naming mixtures of microstructures.

### 10.3 Mechanism of Nucleation

A popular treatment of acicular ferrite nucleation based on classical heterophase fluctuation theory is due to Ricks et al. (1982a,b). It relies on the occurrence of chance fluctuations in crystal structure. The activation energy ( $G^*$ ) for a fluctuation which is large enough to stimulate critical nucleus depends on the inverse square of the chemical driving force  $G^* \propto \Delta G^{-2}$  (Chapter 6). With this theory it is possible to explain why larger spherical nonmetallic inclusions are more effective for heterogeneous nucleation. An embryo which forms in contact with the surface will have a smaller curvature and a corresponding smaller surface to volume ratio when the inclusion is large. A flat austenite grain surface is therefore expected to be a more potent heterogeneous nucleation site than a spherical inclusion. Furthermore, the energy of the interface between the ferrite and the inclusion is likely to be larger relative to the case when ferrite nucleates on austenite grain surfaces. It follows that the activation energy for nucleation on an inclusion, relative to that for nucleation on an austenite grain surface, should vary as illustrated in Fig. 10.7.

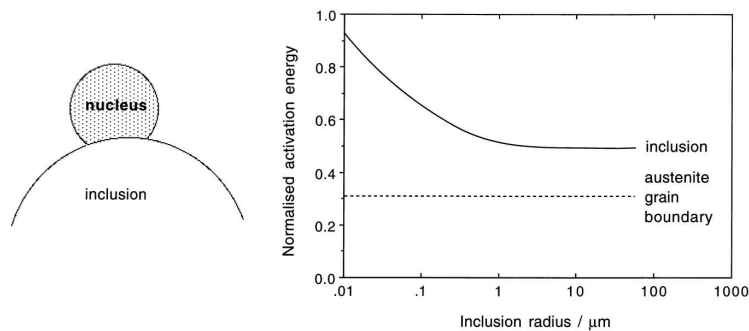


**Figure 10.7** The formation of a truncated spherical nucleus on a spherical inclusion. The activation energy for nucleation has been normalised with respect to that for homogeneous nucleation. The calculations assume that the interfacial energy between austenite and ferrite is the same as that for an austenite grain boundary; that the inclusion/ferrite and inclusion/austenite interface energies are identical and that these are both greater than an austenite grain boundary energy. After Ricks et al. (1982a,b).

An alternative interpretation uses the bainite nucleation theory discussed in Chapter 6. Nucleation is said to occur when an appropriate array of dislocations is able to dissociate rapidly. The activation energy is that for the migration of the embryo/austenite interface; it decreases linearly as the driving force increases. The driving force must be calculated to allow for the diffusion of carbon although the overall mechanism of nucleation remains displacive since the dislocation array considered is glissile.

It follows that the driving force available for nucleation at the highest temperature at which transformation occurs ( $T_h$ ) should be proportional to  $T_h$  (Chapter 6). This is found to be the case as illustrated in Fig. 10.8, which is comparable to Figure 6.4a. The line is identified with the universal nucleation function  $G_N$  that can be used to estimate the acicular ferrite start-temperature for any alloy.

The experiments shown in Fig. 10.8 included both bainite and acicular ferrite, the change in microstructure being achieved by controlling the austenite grain size. It is evi-

dent that both bainite and acicular ferrite can be represented by the same line, emphasising the conclusion that acicular ferrite is simply intragranularly nucleated bainite.

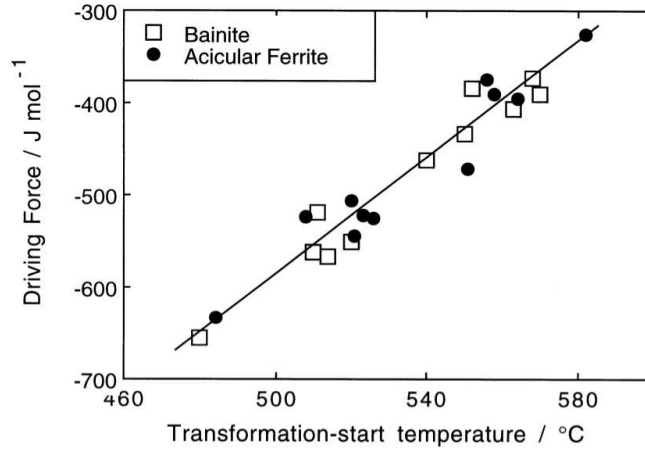


**Figure 10.8** Plot of the driving force available for the nucleation of bainite or acicular ferrite at the temperature  $T_h$ , versus  $T_h$  for a series of welding alloys. Note that each pair of bainite and acicular ferrite points represents a different alloy. After Rees and Bhadeshia (1994).

The displacive mechanism of nucleation relies on the existence of arrays of dislocations. It is conceivable that such arrays are generated in the proximity of nonmetallic inclusions due to stresses caused by differential thermal expansion. Such stresses are more difficult to accommodate for larger inclusions, making large inclusions more potent nucleation sites. Arrays of dislocations are readily found at grain boundaries, accounting for the observation that austenite grain surfaces are most effective as nucleation sites.

#### 10.4 Nucleation and The Role of Inclusions

Non-metallic inclusions in steels have complex multiphase microstructures which make controlled experiments designed to reveal nucleation phenomena rather difficult. A popular idea is that the most potent nucleants have a good *lattice match* with ferrite. There may then exist reproducible orientation relationships between inclusions and the ferrite plates that they nucleate (Mills et al., 1987). The lattice matching is expressed as a mean percentage planar misfit  $\kappa$  (Bramfitt, 1970). Suppose that the inclusion is faceted on  $(h k l)_I$  and that the ferrite deposits epitaxially with  $(h k l)_\alpha \parallel (h k l)_I$ , with a pair of corresponding rational directions  $[u v w]_I$  and  $[u v w]_\alpha$  inclined at an angle  $\phi$  to each other. The interatomic spacings  $d$  along three such directions within the plane of epitaxy are examined to obtain:

$$\kappa = \frac{100}{3} \sum_{j=1}^3 \frac{|d_j^I \cos \phi - d_j^\alpha|}{d_j^\alpha} \quad (10.1)$$

Data calculated in this manner, for a variety of inclusion phases, are presented in Table 10.1. A description of the relationship between two crystals with cubic lattices requires five degrees of freedom, three of which are needed to specify the relative orientation

relationship, and a further two in order to identify the plane of contact between the two crystals. Mills et al. (1987) considered nine different kinds of epitaxy, confined to planes of low crystallographic indices:  $\{0\ 0\ 1\}$ ,  $\{0\ 1\ 1\}$  &  $\{1\ 1\ 1\}$ . The orientation relationships considered are listed in Table 10.1: the Bain orientation implies  $\{1\ 0\ 0\}_\alpha \parallel \{1\ 0\ 0\}_I$  and  $\langle 1\ 0\ 0 \rangle_\alpha \parallel \langle 0\ 1\ 1 \rangle_I$ . The cube orientation occurs when the cell edges of the two crystals are parallel.

**Table 10.1** Misfit values between different substrates and ferrite. The data are from a more detailed set published by Mills et al. (1987) for cases where the misfit is found to be less than 5%. The inclusions all have a cubic-F lattice; the ferrite is body-centred cubic (cubic-I). The data for MnS are from van der Eijk et al. (2002) with the misfit values calculated for 727°C and for the experimentally observed orientation relationship. The data for MgO are from Tsutsumi et al. (2005).

Inclusion	Orientation	Plane of Epitaxy	Misfit %
TiO	Bain	$\{1\ 0\ 0\}_\alpha$	3.0
TiO	$\{1\ 1\ 1\}_{\text{TiO}} \parallel \{1\ 1\ 0\}_\alpha$ $\{1\ \bar{1}\ 0\}_{\text{TiO}} \parallel \{1\ \bar{1}\ 1\}_\alpha$	$\{1\ 1\ 0\}_\alpha$	13.0
TiN	Bain	$\{1\ 0\ 0\}_\alpha$	4.6
$\gamma$ -alumina	Bain	$\{1\ 0\ 0\}_\alpha$	3.2
MgO	Bain	$\{1\ 0\ 0\}_\alpha$	3.8
MgO	$\{1\ 1\ 1\}_{\text{MgO}} \parallel \{1\ 1\ 0\}_\alpha$ $\{1\ \bar{1}\ 0\}_{\text{MgO}} \parallel \{1\ \bar{1}\ 1\}_\alpha$	$\{1\ 1\ 0\}_\alpha$	13.8
Galaxite	Bain	$\{1\ 0\ 0\}_\alpha$	1.8
CuS	Cube	$\{1\ 1\ 1\}_\alpha$	2.8
$\alpha$ -MnS	$\{4\ \bar{2}\ 0\}_{\text{MnS}} \parallel \{1\ \bar{1}\ 0\}_\alpha$ $\langle 1\ \bar{1}\ 0 \rangle_{\text{MnS}} \parallel \langle 0\ 0\ 2 \rangle_\alpha$	$\{1\ 1\ 0\}_\alpha$	5.48
$\beta$ -MnS	$\{4\ \bar{2}\ 0\}_{\text{MnS}} \parallel \{1\ \bar{1}\ 0\}_\alpha$ $\langle 1\ \bar{1}\ 0 \rangle_{\text{MnS}} \parallel \langle 0\ 0\ 2 \rangle_\alpha$	$\{1\ 1\ 0\}_\alpha$	2.25

A comparison with experiments requires not only the right orientation relationship, but the inclusion must also be faceted on the appropriate plane of epitaxy. Experiments, however, demonstrate that the ferrite/inclusion orientation relationship tends to be random (Dowling et al., 1986). The inclusions, which form in liquid steel, are randomly orientated but there is a fixed  $\alpha_a/\gamma$  orientation so it follows that the inclusion/ferrite orientation relation must be random (Fig. 10.9). A contrary view is due to Kluken et al. (1991), who claim that the  $\delta$ -ferrite grains sometimes nucleate on inclusions in the melt. The acicular ferrite should then bear an orientation relationship with the inclusions since it will be related to the  $\delta$ -ferrite via the austenite. Textural measurements have been cited in support of this hypothesis.

Other ways in which inclusions may assist nucleation include stimulation by thermal strains and chemical heterogeneities in the vicinity of the inclusion/matrix interface; alternatively, they may simply be inert sites for heterogeneous nucleation. Pressure bonded ceramic-steel composites have been studied to reveal the potency of pure ceramic phases in stimulating the nucleation of bainite, Table 10.2 (Strangwood and Bhadeshia, 1988; Gregg and Bhadeshia, 1994a,b; Lee et al., 2013). A rather simple model emerges from these ex-

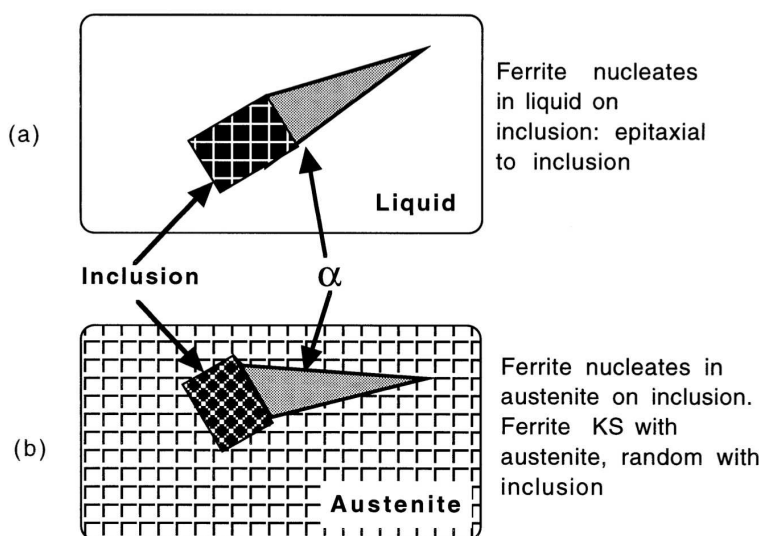


**Figure 10.9** Illustration of the orientation relationship that might develop between acicular ferrite and an inclusion. (a) When ferrite nucleates on an inclusion, with both phases surrounded by liquid; it is possible for the ferrite to adopt a favoured relationship to the inclusion since it is not limited by the liquid. (b) The inclusion, which grows from liquid, is randomly orientated to the austenite. The acicular ferrite, which has fixed orientation relationship with the austenite, must therefore be randomly orientated to the inclusion.

periments, that those ceramics which chemically interact with the adjacent steel are most effective in nucleating bainite. A significant exception is  $\text{TiO}$ , which remains inert and yet enhances bainite formation.

**Table 10.2** List of ceramics found to be chemically active in experiments designed to test for ferrite nucleation at ceramic/steel bonds.

Chemically Active	Chemically Inactive
$\text{TiO}_2$	$\text{TiO}$ , $\text{Ti}_2\text{O}_3$ , $\text{TiC}$ , $\text{TiB}_2$ , $\text{TiN}$
$\text{Al}_2\text{Si}_2\text{O}_7$	$\text{Al}_2\text{O}_3$
$\text{MnO}_2$	$\text{MnO}$
$\text{SiC}$ , $\text{Si}$	$\text{Si}_3\text{N}_4$ , $\text{SiO}_2$
$\text{CoO}$ , $\text{V}_2\text{O}_5$	$\text{ZrO}_2$ , $\text{FeS}$ , $\text{Y}_2\text{O}_3$

There is clear evidence from the bond experiments that some minerals act as sources of oxygen which cause the steel in their vicinity to decarburise, which in turn stimulates the nucleation of bainite. One such mineral is  $\text{TiO}_2$ ; structural and behavioural analogues of  $\text{TiO}_2$  ( $\text{SnO}_2$ ,  $\text{MnO}_2$  and  $\text{PbO}_2$ ) are found to stimulate bainite in the same manner.  $\text{TiO}_2$  and related minerals tend to form oxygen vacancy defects at elevated temperatures, thus releasing oxygen, which can penetrate the adjacent steel. On this hypothesis, all oxygen

producing minerals would be expected to react with the steel, and enhance bainite formation, while non-oxygen producing minerals would not. This contrast in nucleation potential due to differences in the ability to release oxygen is illustrated by examining the nucleation potency of the perovskite structural group of ceramics. *Normal* perovskites ( $ABO_3$  type) are structurally similar to *defect* perovskites ( $BO_3$  type) but the ability of defect perovskites to produce oxygen is much greater. Therefore,  $WO_3$ , which is a defect perovskite is effective in nucleating bainite whereas the normal perovskite  $CaTiO_3$  is found to be ineffective. Indeed, any oxygen source, for example  $KNO_3$ , is found to be effective in stimulating the nucleation of bainite.

Neither  $Ti_2O_3$  nor  $TiO$  is an oxygen source but nevertheless both stimulate bainite.  $Ti_2O_3$  does this by absorbing manganese and hence causing a dramatic depletion in the manganese concentration in the adjacent steel (Gregg and Bhadeshia, 1994a,b; Shim et al., 2001). Since manganese stabilises austenite, its depletion stimulates bainite formation. Shim et al. (2000) confirmed this by demonstrating that  $Ti_2O_3$  is ineffective as a nucleation site when introduced in manganese-free steel. In yet a different mechanism, steel deoxidised with a combination of Mn, Ti and Si, contained Mn-Ti oxides in which the particles were surrounded by manganese depletion zones, and were found to stimulate the intragranular nucleation of ferrite. The depletion was argued to be caused by the growth of the  $MnTi_2O_4$  phase rather than the absorption of manganese by a predominantly titanium-rich oxide (Zhuo et al., 2007).

By contrast,  $TiO$  remains chemically inert; it can assist nucleation by lattice matching. It has a better fit with ferrite than  $TiN$  or  $MgO$ , neither of which are as effective as  $TiO$  in stimulating nucleation. It is not surprising therefore, that the orientation relationship between  $TiO$  and the matrix is important in determining its efficacy as a nucleant for ferrite. When thin, vapour deposited amorphous layers of  $TiO$  on steel are heat treated, they crystallise into a variety of crystallographic textures. Ferrite forms readily when the texture is such that  $\{1\ 0\ 0\}_{TiO}$  planes are parallel to the steel surface, with a much reduced effect when the texture is similarly dominated by  $\{1\ 1\ 1\}_{TiO}$  (Tsutsumi et al., 2005). The misfit data in Table 10.1 show that this is expected on the basis of coherency with the ferrite, the latter texture resulting in poor matching. Tsutsumi et al. (2005) also argue that  $TiO$  is capable of absorbing manganese; this is because the introduction of additional manganese between the  $TiO$  and steel made the oxide less effective in its role of stimulating ferrite. However, the experiment is ambiguous since the introduced manganese could also enhance locally the hardenability of the austenite.

The nucleation mechanisms are summarised in Table 10.3.

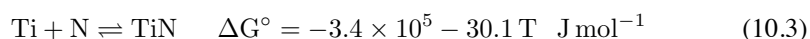
**Table 10.3** Mineral classification according bainite or ferrite nucleation potency.

Effective: oxygen sources	Effective: other mechanisms	Ineffective
$TiO_2$ , $SnO_2$	$Ti_2O_3$	$TiN$ , $CaTiO_3$
$MnO_2$ , $PbO_2$	$TiO$	$SrTiO_3$ , $\alpha-Al_2O_3$
$WO_3$ , $MoO_3$	$MgO$	$\gamma-Al_2O_3$ , $MnAl_2O_4$
$KNO_3$		$NbC$

### 10.4.1 Aluminium and Titanium Oxides

There is evidence that titanium oxides ( $\text{TiO}$ ,  $\text{Ti}_2\text{O}_3$ ,  $\text{TiO}_2$ ) are potent acicular ferrite nucleating agents whereas  $\text{Al}_2\text{O}_3$  is not. Aluminium is a stronger oxidising agent than titanium so it is expected that alumina forms first, followed by titania, which can form as a coating on the alumina particles. Titanium oxide formation requires that there is excess oxygen left after the aluminium has combined with oxygen (Horii et al., 1986, 1988). The aluminium concentration should therefore be kept to a minimum, otherwise titanium oxides do not form even if the steel contains a titanium addition (Ringer et al., 1990).

Titanium nitride is an effective nucleant but is less thermodynamically stable at high temperatures when compared with  $\text{Ti}_2\text{O}_3$ .



where  $\Delta G^\circ$  is the standard free energy of formation (Kubachewski and Evans, 1950). Nevertheless, titanium nitride is often the first to precipitate from the liquid phase.

Notwithstanding this anomaly, considerable progress can be made by assuming that the dissolved elements in a sequence consistent with their oxidising potential. For welds, this usually means that aluminium has the first call on the available oxygen, followed by titanium (Horii et al., 1988). Oxygen can be depleted from the melt by an excess of aluminium, preventing the formation of desirable titanium oxides. A minimisation of the aluminium content has the additional advantage that the total oxygen (and hence the inclusion content) can be reduced whilst keeping the same titanium oxide content. Nitrogen must be controlled to prevent the formation of titanium nitride, perhaps by adding boron as a nitrogen gettering agent. Trace elements like calcium, cerium and other rare earth elements, at the concentrations used for inclusion shape control in wrought alloys, do not influence the development of the acicular ferrite microstructure (Horii et al., 1986, 1988), although recent work has highlighted the possibility of cerium sulphides as potent nucleation sites (Thewlis, 2006). These elements might enter the weld metal via the fused base metal, particularly during high heat input welding where dilution is exaggerated (Fig. 10.10).

Small concentrations of dissolved aluminium seem to promote Widmanstätten ferrite; the mechanism of this effect is not understood (Abson, 1987; Grong et al., 1988; Thewlis, 1989a,b). It may be that the presence of soluble aluminium correlates with a large overall aluminium concentration, in which case the aluminium oxide becomes  $\gamma$ -alumina instead of galaxite. The former is not an effective nucleant for acicular ferrite, thus allowing grain boundary nucleated Widmanstätten ferrite to grow unhindered.

The mean size of nonmetallic inclusions in welds changes only a little with the aluminium concentration (Thewlis, 1989a; Evans, 1990). Although inclusions are essential for improved weld microstructure, they can also nucleate fracture. A compromise level of inclusions is required, but it seems likely that most weld deposits contain more oxygen than is necessary. For example, concentrations less than 120 p.p.m. are adequate in producing an acicular ferrite microstructure in suitably alloyed wrought steels (Prokic-Cvetkovic et al., 2006).

The character of inclusions alters with increasing aluminium concentration. The oxide particles being predominantly  $\text{MnOSiO}_2$  at low Al concentrations, to be replaced by galaxite which is a mixed spinel ( $\text{Al}_2\text{O}_3\text{MnO}$ ) and finally by  $\gamma\text{-Al}_2\text{O}_3$  at higher aluminium concentrations (Thewlis, 1990). Galaxite has a good lattice match with ferrite and so is the desired oxide form (Table 10.1).

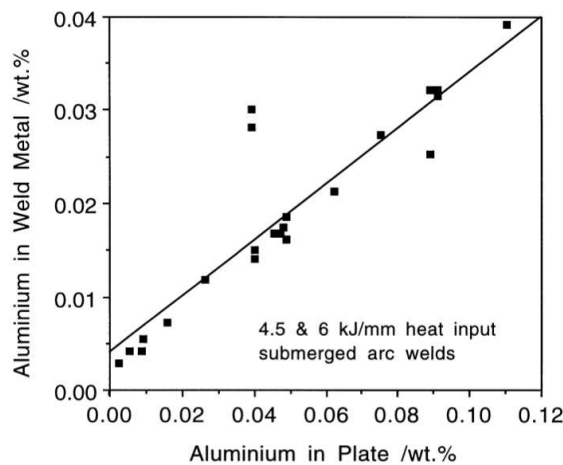
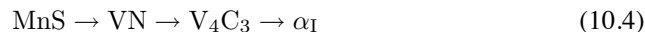


**Figure 10.10** A plot of the aluminium concentration in the weld metal versus that in the steel, illustrating the incorporation of trace elements from the base plate into the weld fusion zone during high heat input welding (Horii et al., 1988).

#### 10.4.2 Sulphur

Manganese sulphide (MnS) particles sometimes act as heterogeneous nucleation sites for acicular ferrite. Using a steel containing 0.07 wt% of sulphur and 0.1 wt% vanadium, Ochi and McEvily (1988) produced a fine dispersion of MnS particles on which they obtained the successive precipitation of vanadium nitride, vanadium carbide and finally, idiomorphic ferrite:



Indeed, the nitride has been shown to lead directly to the nucleation of ferrite via the lattice-matching mechanism (Ishikawa et al., 1994). These results are consistent with other observations that MnS and  $\text{Al}_2\text{O}_3$  are most effective in stimulating intragranular ferrite when they act as substrates for vanadium nitrides or carbides (Shim et al., 2001).<sup>1</sup>

Manganese sulphide which grows on titanium oxide can in turn stimulates the nucleation of acicular ferrite (Yamamoto et al., 1987). Indeed, the acicular ferrite fraction decreased when the sulphur concentration was reduced to less than 0.001 wt%. There are contradictory results; Abson (1987) has concluded that the presence of MnS at the surface of oxide particles inhibits the nucleation of ferrite, and furthermore, that the addition of elements which getter sulphur makes the inclusions more effective. Chijiwa et al. (1988) found an increase in the acicular ferrite fraction as the sulphur concentration was reduced from 0.005 to 0.001 wt%. Ringer et al. (1990) showed that  $\text{Ti}_2\text{O}_3$  particles without any surrounding MnS films can nevertheless be effective in stimulating the intragranular nucleation of ferrite.

<sup>1</sup>Similar results have been reported for the intragranular nucleation of pearlite on vanadium carbide found on MnS (Guo et al., 2002). Since they failed to find a specific orientation between the carbide and austenite, it was concluded that nucleation is stimulated by carbon depletion in the austenite adjacent to the carbide. He et al. (2002) have speculated that it is iron and vanadium clusters which are the nucleation sites, but as pointed out by Babu (2004), their steel may well have contained fine vanadium carbides or carbonitrides.

It is difficult to reconcile these results, but direct observations have clarified the role of manganese sulphide on a titanium oxide  $(\text{Ti, Mn})_x\text{O}$  substrate, Fig. 10.11 (van der Eijk et al., 2002). Manganese sulphide occurs in two crystalline forms;  $\alpha$ -MnS is cubic with the NaCl crystal structure and is stable below  $727^\circ\text{C}$ ; on heating above this temperature it transforms into  $\beta$ -MnS which also is cubic with a ZnS crystal structure and a slightly larger lattice parameter. Table 10.1 shows that the Bramfitt misfit between  $\beta$ -MnS and ferrite is much smaller than with  $\alpha$ -MnS. It is argued that ferrite actually nucleates on the  $\beta$  form, assisted by local manganese depletion in the austenite next to the inclusion (the absolute values of the Mn concentration illustrated in Fig. 10.11 are not reliable since they are all above the average concentration of the steel used). The possibility that TiN particles on the surface of the MnS contribute to the nucleation events cannot be ruled out, although systematic orientation relationships were not found between the nitride and ferrite.

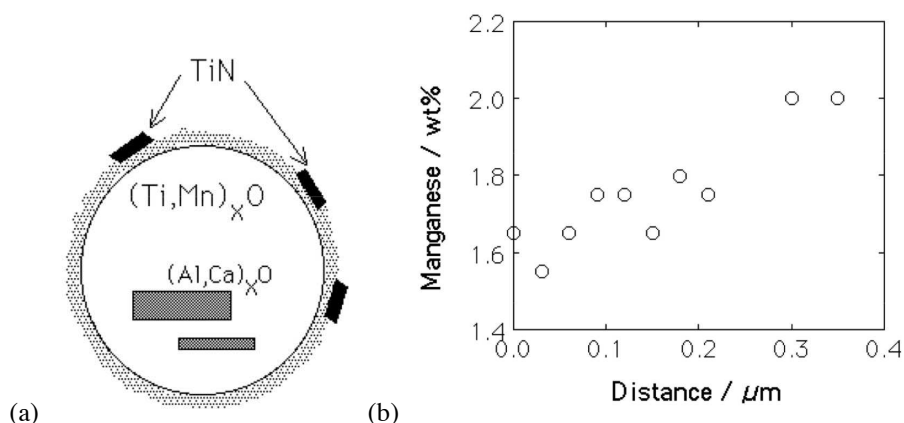


**Figure 10.11** (a) A representation of the measured structure of an inclusion in a steel. (b) Variation in the manganese concentration as a function of distance from the inclusion-matrix interface.

MnS is common in commercial steels as precipitates in the solute-enriched interdendritic regions of the solidification microstructure. The high manganese concentrations in these regions retard ferrite formation. With this in mind, Ueshima (1989) introduced uniform distributions of MnS particles by inducing them to nucleate on oxides. High purity melts, each containing 0.004 wt% of sulphur, were deoxidised using one of Al, Ti, Zr, La, Ce, Hf or Y. Of these, aluminium and titanium led to the most uniform dispersions which were insensitive to the killing time within the range 30-600 s (Fig. 10.12).<sup>2</sup> All of the deoxidising elements studied were able to promote MnS nucleation (Fig. 10.12), but  $\text{Ti}_2\text{O}_3$  and zirconia were particularly effective, with aluminium being the least potent in this respect. The MnS precipitated in the solid-state over a temperature range estimated to be  $1050$ - $1400^\circ\text{C}$ .

Ueshima et al. estimated, using diffusion theory, that a manganese-depleted zone formed in front of the growing MnS particles enhances the formation of ferrite. Mabuchi et al. (1996) proved the existence of these zones during the precipitation of MnS from austenite,

<sup>2</sup>During *killing*, the oxygen concentration in the molten steel is reduced by the addition of metallic elements which have a strong affinity for oxygen. The resulting oxides usually float off into the slag, although fine particles are retained. The killing time is the interval between the point at which the deoxidising element is added and the solidification of the steel.

but found that the local variations in composition are rapidly homogenised once precipitation is completed. The MnS is therefore only active in stimulating ferrite nucleation shortly after precipitation. MnS particles are therefore active as heterogeneous nucleation sites on the first occasion that they precipitate; their potency is reduced if the sample is reheated into the austenite phase field. This has significant implications for the large number of experiments based on reheated weld metals and may explain why the early results are contradictory.

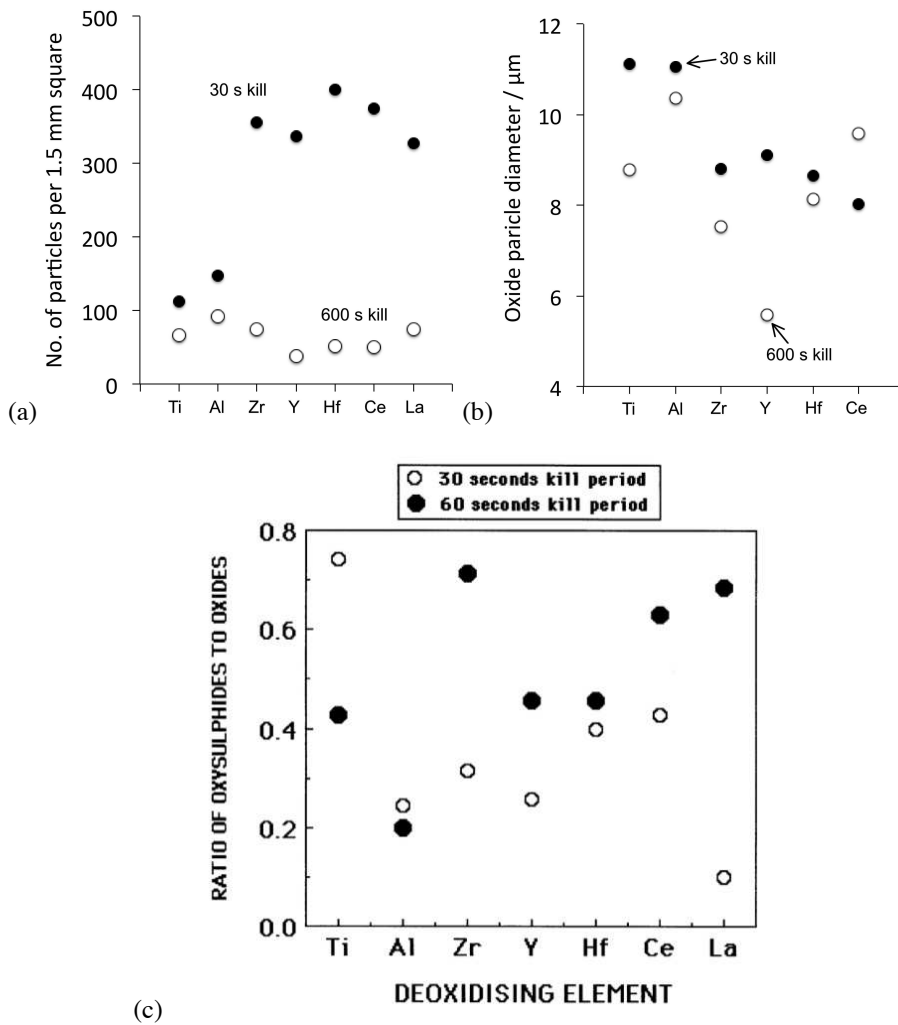


**Figure 10.12** The effects of a variety of deoxidising elements on the nature of oxide and oxysulphide precipitation in steel (Ueshima, 1989). (a) Number density of oxide particles; (b) size of oxide particles; (c) propensity of the oxide to stimulate the solid-state nucleation of sulphide.

Finally, there is evidence that the sulphide coatings found on oxides and silicates in steel weld metal undergoes changes when the metal is reheated into the austenite phase field (Miao and Knott, 2004). A short heat treatment thickens the original coating whereas a prolonged treatment causes the growth of sulphide patches.

### 10.4.3 Phosphorus

Phosphorus is another impurity element which is rarely deliberately added to steels because of its well known tendency to embrittle grain boundaries. Its concentration is usually kept below 50 p.p.m., but in welds the average concentration can exceed 100 p.p.m. Solidification induced segregation can locally raise the concentration to 500 p.p.m. This may alter the kinetics of transformation and hence influence the development of acicular ferrite microstructure in weld deposits (Kluken and Grong, 1989b; Kluken et al., 1990).

The thermodynamic effect of phosphorus is to raise the  $A_{e3}$  temperature by about  $460^\circ\text{C}$  per wt%, over the concentration range of interest (Bastien, 1957), although the consequences of such a big effect are not as large as might be expected (Kirkaldy et al., 1962).

During weld solidification, the phosphorus segregates between the  $\delta$ -ferrite dendrites and cells. When solidification is complete, the  $\delta$ -ferrite transforms to austenite which nucleates heterogeneously at the  $\delta/\delta$  grain boundaries. Kluken and Grong suggest that the austenite grain boundaries coincide with the phosphorus rich regions so this stimulates the formation of acicular ferrite; when they do not do so, ferrite plates grow from the grain boundaries and consume most of the austenite before the intragranular acicular ferrite has a chance to develop.

This hypothesis is then used to explain why the acicular ferrite content of welds decreases suddenly as the ratio of the precipitated aluminium to oxygen concentrations reaches a value of 1.13 (Fig. 10.13a). Beyond that limiting value, the nonmetallic inclusions become pure  $\gamma$ -alumina (Fig. 10.13b), and these apparently stimulate austenite directly from the melt. The resulting austenite grain boundaries are no longer coincident with the phosphorus rich regions, thus leading to Widmanstätten ferrite formation.

These ideas are inconsistent with the fact that phosphorus increases the driving force for the transformation of austenite. A second difficulty is that in a weld, the temperature isotherms change position during cooling, so that the fastest growth direction of the austenite does not coincide with that of the  $\delta$ -ferrite (Dadian, 1987).

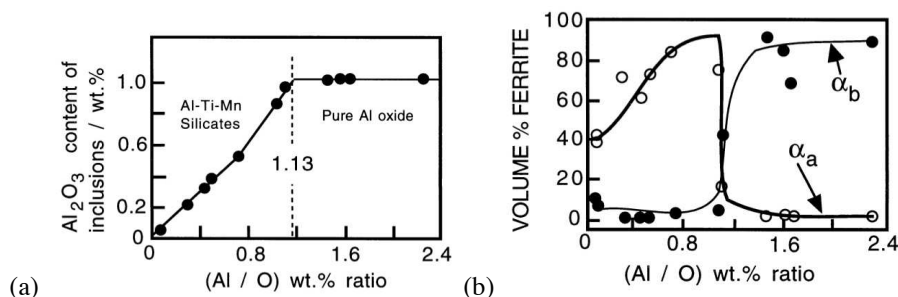


**Figure 10.13** (a) Variation in the volume fraction of acicular ferrite as a function of the precipitated-Al to oxygen ratio; (b) variation in the inclusion chemistry with the same ratio.

### 10.4.4 Nitrogen, Titanium and Boron

Nitrogen is not often a deliberate alloying addition to steels and weld deposits. It is detrimental to the toughness even at concentrations as low as 20-120 p.p.m. The mechanism of embrittlement is strain age-hardening and solid-solution hardening effects, both of which

increase the yield strength and hence the ability of the material to absorb energy by plastic deformation during fracture (Lancaster, 1986; Smaill et al., 1976; Judson and McKeown, 1982; Oldland, 1985).

Some studies suggest that nitrogen has no detectable influence on the acicular ferrite content of welds (Mori et al., 1981), whereas others (Okabe et al., 1983; Ito and Nakanishi, 1975) claim significant changes due to nitrogen. At the small concentrations of nitrogen in ferritic steels, it is unlikely that nitrogen has any significant thermodynamic effect on the  $\gamma \rightarrow \alpha$  transformation. Its influence must be kinetic, perhaps via some interaction with the inclusion phases.

In practice, the effect of nitrogen in weld metals has to be considered alongside that of titanium and boron, both of which form nitrides. It appears that nitrogen, in the absence of boron, has no detectable effect on the development of microstructure (Horii et al., 1986, 1988; Lau et al., 1987, 1988). Boron is added to render austenite grain boundary nucleation sites impotent and hence to promote acicular ferrite. By contrast, nucleation at the interface between  $\text{Ti}_2\text{O}_3$  and austenite is not retarded by boron; its diffusion into the oxide, which contains cation vacancies, leaves behind a boron-depleted zone (Yamamoto et al., 1996). This is not the case with  $\text{Mn}_2\text{TiO}_4$  and  $\text{TiO}$ , where it seems that the boron segregates to the inclusion-matrix interface and hence renders these oxides ineffective as heterogeneous nucleation sites (Hatano, 2005).

Titanium has the function of protecting the boron from oxidation during transfer across the welding arc. It also prevents boron from combining with nitrogen to form boron nitride. Boron must be in solid solution if it is to segregate to and reduce the energy of the austenite grain surfaces, making them less effective nucleation sites.

For a given oxygen and boron concentration, the aluminium and titanium concentrations have to be large enough to get all the available oxygen. Furthermore, there has to be enough titanium left over to combine with any nitrogen to permit boron to remain in solid solution. A method for making rational decisions during the design of titanium and boron containing deposits is illustrated in Fig. 10.14.

The assumptions involved are illustrated by the work of Kluken and Grong (1989a), whose ideas are reproduced below in an explicit formalism. The total volume fraction  $V_V^I$  of inclusions is approximately (Franklin, 1969):

$$V_V^I \simeq 0.05w_{\text{O}} + 0.054(w_{\text{S}} - w_{\text{S}}^{\text{sol}}) \quad (10.5)$$

where  $w_i$  is the concentration of element  $i$  in units of weight percent and  $w_{\text{S}}^{\text{sol}}$  the soluble sulphur concentration, usually assumed to be about 0.003 wt%. The mass fraction of inclusions is:

$$m_I = V_V^I \frac{\rho_I}{\rho_S} \quad (10.6)$$

where  $\rho_S$  and  $\rho_I$  are the steel and inclusion densities, about 7.8 and 4.2 g cm<sup>-3</sup> respectively. It follows that the concentration of Al in the inclusions is given by:

$$w_{\text{Al}}^I = (w_{\text{Al}}^T - w_{\text{Al}}^{\text{sol}})/m_I \quad (10.7)$$

where  $w_{\text{Al}}^T$  and  $w_{\text{Al}}^{\text{sol}}$  represent the total and soluble aluminium concentrations respectively. It is reasonably assumed here that none of the aluminium is combined as nitride.

It may be assumed that the titanium reacts first with oxygen, and that any residual titanium can then proceed to combine with nitrogen. In the absence of active oxygen, the titanium nitride can be estimated by calculating the nitrogen in solution using a solubility

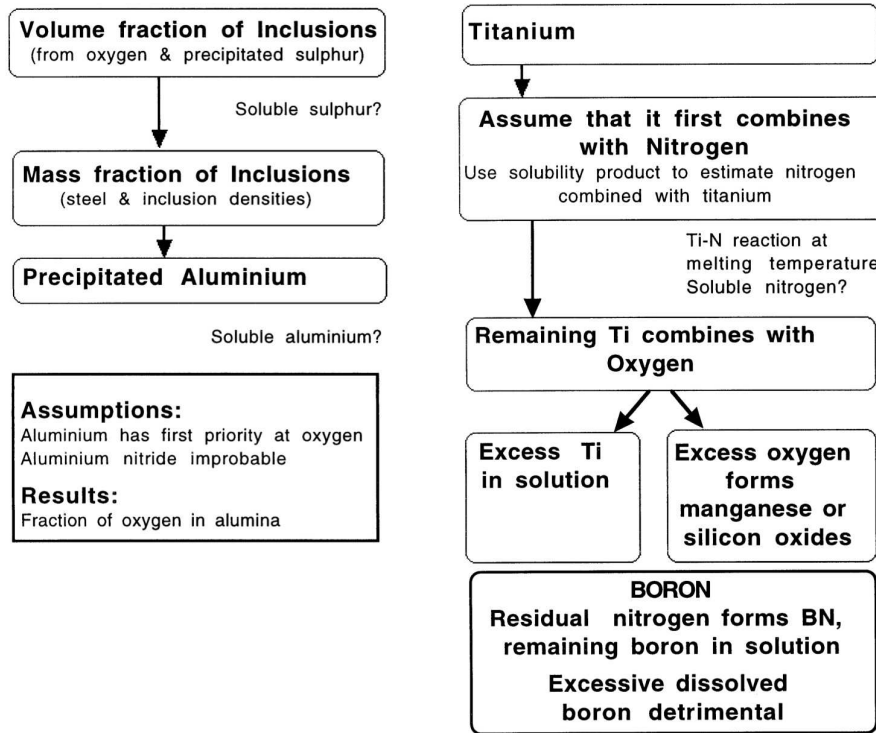


**Figure 10.14** Procedure for the estimation of inclusion microstructure. The assumptions and difficulties associated with the method are placed outside of the main boxes.

product (Matsuda and Okumura, 1978):

$$\log\{[w_{Ti}^{sol}][w_N^{sol}]\} = \frac{8000}{T} + 0.32 \quad (10.8)$$

assuming that the concentration of dissolved titanium is known. The calculation is valid at about the melting temperature of the steel. The quantity of titanium nitride in the inclusion ( $w_{Ti-N}^{I-N}$ ), is then given by:

$$w_{Ti}^{I-N} = A_{Ti}(w_N^T - w_N^{sol})/(m_I A_N) \quad (10.9)$$

where  $A_i$  represents the atomic weight of element  $i$ . It follows that the titanium in the inclusions, tied up as oxide ( $w_{Ti}^{I-O}$ ) is given by

$$w_{Ti}^{I-O} = (w_{Ti}^T - w_{Ti}^{I-N} m_I - w_{Ti}^{sol})/m_I. \quad (10.10)$$

This differs from equation 13a of Klukun and Grong, which does not account for the titanium nitride. The sulphur content of the inclusion is similarly given by:

$$w_S^I = (w_S^T - w_S^{sol})/m_I. \quad (10.11)$$

Assuming that the sulphur is incorporated in the inclusion as manganese sulphide, the concentration of Mn in the inclusion as MnS is given by

$$w_{Mn}^{I-S} = A_{Mn} w_S^I / A_S. \quad (10.12)$$

The next step involving the calculation of the SiO<sub>2</sub> and MnO contents of the inclusion requires some assumption about the relative proportions of these two phases.

$$\begin{aligned}
 \text{If } \theta &= \text{wt\% SiO}_2/\text{wt\% MnO} \\
 \text{and } \beta &= \frac{(\frac{A_{Mn}}{A_O} + 1)\theta}{(\frac{A_{Si}}{2A_O} + 1) + (\frac{A_{Mn}}{A_O} + 1)\theta} \\
 \text{then } w_{Si}^I &= \beta A_{Si}(w_O^T - m_I w_O^{I-Al} - m_I w_O^{I-Ti})/(2m_I A_O) \quad (10.13)
 \end{aligned}$$

where  $w_O^{I-Al}$  and  $w_O^{I-Ti}$  are the concentrations of oxygen in the inclusion, tied up as alumina and titania respectively. It follows that:

$$w_{Mn}^{I-O} = (1 - \beta)A_{Mn}(w_O^T - m_I w_O^{I-Al} - m_I w_O^{I-Ti})/(m_I A_O) \quad (10.14)$$

These estimates require a knowledge of the dissolved Al, Ti and S concentrations and assume that the oxidation state of the titanium is known. Titanium compounds such as TiN, TiC and TiO have similar lattice parameters and crystal structures and are difficult to distinguish using diffraction. Common microanalytical techniques can readily identify titanium but not the light elements. Even when oxygen can be detected, the stoichiometry is difficult to determine since absorption and other corrections are not known for complex shapes. Lau et al. assumed that the Ti is in the form of TiO<sub>2</sub> whereas Klukun and Grong took it to be combined as Ti<sub>2</sub>O<sub>3</sub>. Abson (1987) on the other hand, assumes that in weld deposits, the titanium oxide is TiO. The weakness, however, is the method of partitioning oxygen between the different metallic elements. It can for example, be demonstrated that manganese and silicon oxides are found in systems where oxygen is expected to combine completely with Al and Ti. Moreover, the silicon concentration has been known to influence the ability of titanium to combine with oxygen (Lee and Pan, 1992).

The real picture is evidently complex, but the sequence of reactions should at least determine the microstructure of the inclusions, with the first compounds to precipitate being located at the inclusion core, Fig. 10.15. It is the least reactive elements which should end up at the inclusion surface. Indeed, nonmetallic particles in some submerged arc weld deposits have been identified with titanium nitride cores, surrounded by a glassy phase containing manganese, silicon and aluminium oxides, with a thin layer of manganese sulphide partly covering the inclusion surface (Barbaro et al., 1988). Similarly, in a weld free from aluminium or titanium, the inclusion core was found to be MnO-SiO<sub>2</sub> whereas the addition of only 40 p.p.m. of aluminium introduced alumina in the core (Es-Souni and Beaven, 1990). On the other hand, both these investigations reported the presence of unspecified titanium compounds over a part of the inclusion surface. It is possible that this reflects an incomplete coverage of the titanium compound core by subsequent phases.

#### 10.4.5 Boron and Hydrogen

Experiments using secondary ion mass spectroscopy have revealed a tendency for boron to form a BH<sup>+</sup> complex with hydrogen when both are in solution in steel (Pokhodnya and Shvachko, 1997). A consequence of this is that the mobility of both the boron and hydrogen is reduced. Furthermore, more of the hydrogen gets trapped resulting in a strong correlation between the boron and hydrogen concentrations, as shown in Fig. 10.16.

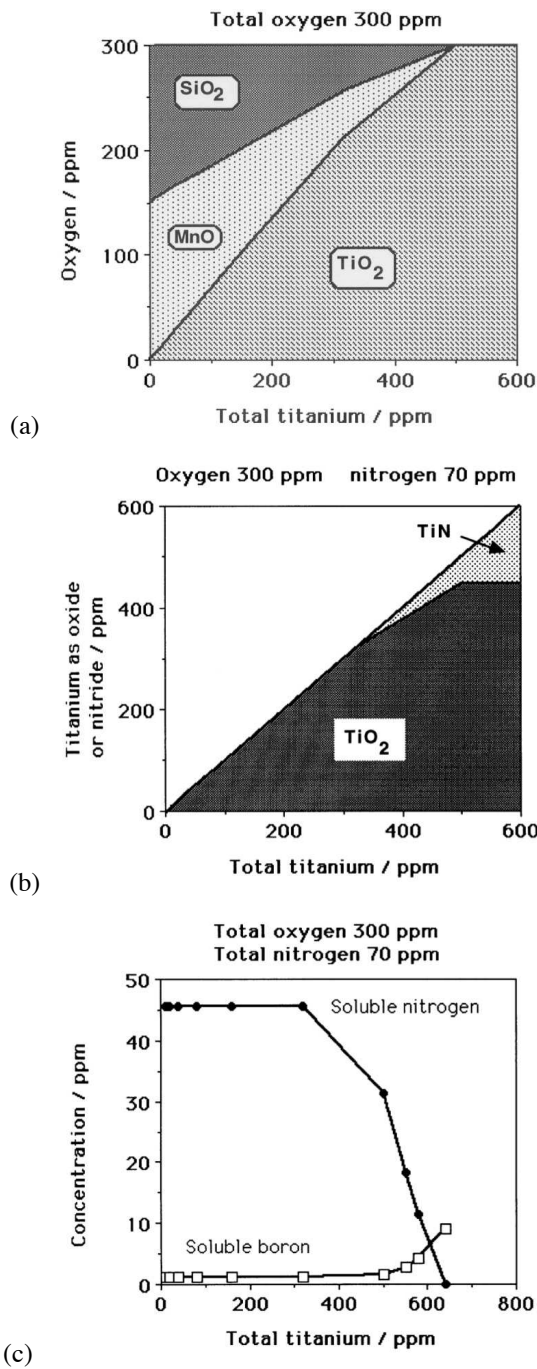


**Figure 10.15** Calculations showing how the components of inclusions in welds change as the chemical composition is altered. Manganese and silicon oxides are progressively replaced by titanium oxide. When the oxygen has reacted completely with titanium, the latter begins to combine with nitrogen and helps to liberate boron.

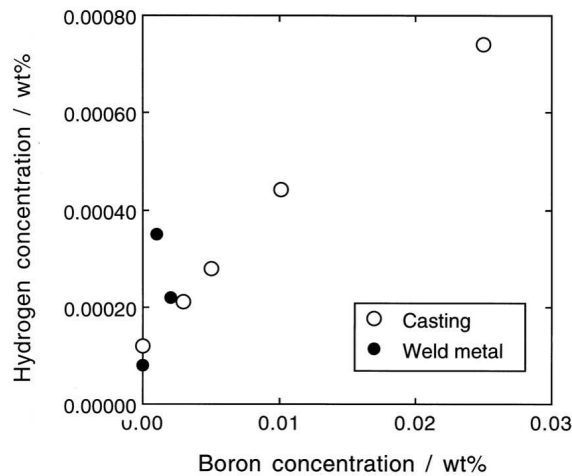


**Figure 10.16** The correlation between the residual hydrogen concentration and the total boron concentration in a series of castings and weld deposits - after Pokhodnya and Shvachko (1997).

#### 10.4.6 Stereological Effects

There is no doubt that plates of acicular ferrite nucleate on inclusions, although once the process begins, other plates can be stimulated autocatalytically. A one-to-one correspondence between the plates of acicular ferrite and inclusions is therefore not expected. It is difficult to establish the presence of an inclusion in a plate using metallography. By analogy with the procedure used by Chart et al. (1975) for aluminium alloys, if the volume of a typical plate of acicular ferrite is taken to be  $10^{-16}\text{m}^3$ , and that of a spherical inclusion  $4 \times 10^{-20}\text{m}^3$ , then of all the grains examined, only 7.4% can be expected to display the nucleating particle. When a particle is detected, its intercept on the plane of section will in general be smaller than its diameter. The estimate by Chart et al. is strictly valid when the grains of the major phase are spherical, which acicular ferrite plates are not. If the acicular ferrite is approximated as a square plate of side  $10\mu\text{m}$  and thickness  $t = 1\mu\text{m}$ , containing an inclusion of radius  $r = 0.2\mu\text{m}$ , the ratio of the mean linear intercepts of the two phases is given by  $4r/6t$  (Mack, 1956). If every plate contains an inclusion, some 13% will show the nucleating particle in a plane section which is large enough.

The estimate assumes that each plate contains just one inclusion, and more importantly, that each observed inclusion is responsible for nucleating the plate in which it is found, i.e. it has not been incorporated accidentally into the plate as a consequence of growth. It is not safe to assume that the observation of a particle in the plate implies that it was responsible for originating the plate when the total fraction of acicular ferrite is large.

An alternative way of establishing the role of autocatalysis is by examining the orientation relationships between adjacent plates in clusters of acicular ferrite plates. The clusters have been found to contain similarly oriented plates with a probability which is larger than random, implying autocatalysis (Yang and Bhadeshia, 1989a).

### 10.5 Effect of Inclusions on the Austenite Grain Size in Welds

A microstructure with large austenite grains has a better chance of transforming to acicular ferrite because the number density of grain boundary nucleation sites is reduced. It is sometimes assumed that the austenite grain size is determined by Zener pinning by inclusions. This analogy is however, not justified since the austenite grains form by the *transformation* of  $\delta$ -ferrite grains which evolve during solidification, whereas Zener pinning deals with the hindrance of grain boundaries during grain growth. The driving force for grain growth typically amounts to just a few Joules per mole, whereas that for transformation from  $\delta$ -ferrite to austenite increases indefinitely with undercooling below the equilibrium transformation temperature. Pinning of  $\delta/\gamma$  interfaces cannot then be effective. A mechanism in which inclusions pin the columnar austenite grain boundaries is also inconsistent with the *shape* of these grains, since the motion of the  $\delta/\gamma$  interfaces along the steepest temperature gradients is clearly not restricted; if pinning were effective, the austenite grains that evolve should be isotropic.

### 10.6 Influence of Other Transformation Products

In weld deposits, acicular ferrite is one of the last transformation products to form after the growth of allotriomorphic and Widmanstätten ferrite. As a consequence, it is bound to be influenced by prior transformation products. Indeed, its volume fraction during continuous cooling transformation of such welds can in many cases be estimated simply by calculating the volume fractions of allotriomorphic and Widmanstätten ferrite, and assuming that the remainder of the austenite transforms to acicular ferrite (Bhadeshia et al., 1985). For the same reason, it is found that in wrought alloys with mixed microstructures, the amount of acicular ferrite decreases with the austenite grain size, as grain boundary nucleated phases such as allotriomorphic ferrite become more dominant (Barbaro et al., 1988). The dependence of the volume fraction of acicular ferrite on the austenite grain size becomes less pronounced as the cooling rate (from the austenite phase field) is increased, since at slow cooling rates, much of the austenite is consumed during the higher temperature formation of allotriomorphic ferrite.

This dependence of the acicular ferrite content on the austenite grain size, in a mixed microstructure of acicular ferrite and allotriomorphic ferrite, can for isothermal reaction be expressed precisely using the relationship:

$$\ln\{1 - i\} \propto S_V \quad (10.15)$$

where  $i$  is the volume fraction of allotriomorphic ferrite divided its equilibrium volume fraction at the temperature concerned and  $S_V$  is the amount of austenite grain surface per unit volume of sample. If a number of reasonable assumptions are made (Bhadeshia et al., 1987) the proportionality can be applied to continuous cooling transformation in low-carbon, low-alloy steels, in which case,  $(1 - i)$  is equal approximately to the volume fraction of acicular ferrite, thus relating the latter to the austenite grain size.

An interesting observation reported by Dallum and Olson (1989) is that in samples containing mixtures of allotriomorphic ferrite, Widmanstätten ferrite and acicular ferrite, a relatively small austenite grain size leads to a coarser acicular ferrite microstructure. They attributed this to an reduction in the  $\alpha_a$  nucleation rate, caused by some unspecified interaction with the prior transformation products ( $\alpha$  and  $\alpha_w$ ). An alternative explanation could be that with a smaller austenite grain size, the volume fractions of  $\alpha$  and  $\alpha_w$  that

form are correspondingly larger, thereby causing a higher degree of carbon enrichment in the residual austenite and hence a significant reduction in the acicular ferrite nucleation rate. A reduction in the nucleation frequency would then permit the fewer plates to grow to larger dimensions before hard impingement with other plates in the vicinity.

Effects like these are of considerable importance in the development of mixed microstructures, but the coarsening of acicular ferrite without any change in shape *per se* is unlikely to lead to any drastic changes in the strength of weld deposits (Bhadeshia and Svensson, 1989a,b). This is because the mean slip distance in a plate does not change much as the plate becomes larger. Of course, it remains to be demonstrated whether toughness is sensitive to small variations in the size and distribution of acicular ferrite.

### 10.6.1 Some Specific Effects of Allotriomorphic Ferrite

We now proceed to consider a particular role of allotriomorphic ferrite formation in influencing the development of acicular ferrite in mixed microstructures. The effect is especially prominent in chromium and molybdenum containing steels. At relatively high concentrations of chromium ( $> 1.5$  wt%) or molybdenum ( $> 0.5$  wt%), the columnar austenite grains of steel weld deposits transform into bainite instead of acicular ferrite. The bainite is in the form of classical sheaves emanating from the austenite grain surfaces, often with layers of austenite left untransformed between the individual platelets of bainitic ferrite. This is in spite of the presence of nonmetallic inclusions, which usually serve to intragranularly nucleate the plates of acicular ferrite. The effect is probably a consequence of the fact that as the amount of allotriomorphic ferrite decreases with increasing solute concentrations, the austenite grain boundaries are freed to nucleate bainite (Fig. 10.17). The observations of Sneider and Kerr (1984) could be interpreted to support this conclusion. In welds containing a variety of chromium concentrations, with microstructures which are predominantly acicular ferrite, the amount of bainite increased directly as the volume fraction of allotriomorphic ferrite decreased. In addition, bainite was not found when the allotriomorphic ferrite volume fraction was greater than 0.08, presumably because in their welds, that quantity was sufficient to completely cover the austenite grain surfaces, and to prevent the grain boundary nucleation of bainite at a lower transformation temperature.

It may not be necessary to entirely cover the austenite grain surfaces with allotriomorphic ferrite, because the ferrite will tend to form at the most potent nucleation sites, thereby disabling the most active areas of the grain surfaces.

Some interesting quantitative data have also been reported by Evans (1986); he found that as the chromium or molybdenum concentration of low-carbon weld deposits is increased, the amount of allotriomorphic ferrite decreases. The volume fraction of acicular ferrite goes through a maximum as a function of concentration. The volume fraction of the remainder of the microstructure, which is described as "ferrite with aligned second phase" therefore increases with concentration, Fig. 10.18. This is the terminology used in the welding industry to describe a microstructure in which parallel plates of ferrite are separated by regions of residual phase such as retained austenite. It really refers to packets of parallel plates of Widmanstätten ferrite or to sheaves of bainitic ferrite. There is some evidence (Bhadeshia et al., 1986) that in typical welds deposits of the type studied by Evans, the fraction of Widmanstätten ferrite decreases to small values (0.04-0.1) as the chromium or molybdenum concentration increases, so that most of the increase in the volume fraction of the "ferrite with aligned second phase" can be ascribed to an increase in the volume fraction of bainite (Fig. 10.18). The fact that bainite is obtained when the austenite grain boundaries are free from other transformation products is also consistent with the obser-

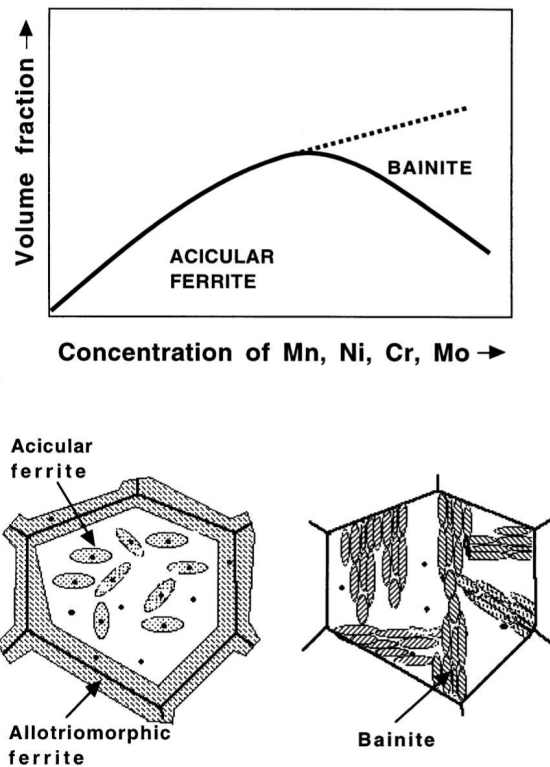


**Figure 10.17** Schematic illustration of the mechanism by which the presence of allotriomorphic ferrite at the austenite grain surfaces induces a transition from a bainitic to acicular ferrite microstructure.

vation that Fe-2.25Cr-1Mo wt% weld deposits used in the power generation industry are well known to have an almost fully bainitic microstructure (variously referred to as conventional bainite or granular bainite) in the as-deposited condition, with classical sheaves in which the platelets of bainitic ferrite are partially separated by films of retained austenite or martensite (Klueh, 1974b; Wada and Eldis, 1982; Kar and Todd, 1982; Lundin et al., 1986; Vitek et al., 1986; McGrath et al., 1989). The large alloy concentration in this steel prevents the growth of allotriomorphic ferrite under normal heat-treatment conditions.

It appears therefore, that at relatively large concentrations of chromium and/or molybdenum, acicular ferrite is in increasing proportions, replaced by classical bainite, until eventually, the microstructure becomes almost entirely bainitic. This effect cannot be attributed to any drastic changes in the austenite grain structure, nor to the inclusion content of the weld deposits (Babu and Bhadeshia, 1990). It turns out in fact, that the Cr and Mo alloys have highlighted a more general condition associated with welds containing high concentrations of alloying additions. Several cases have been reported in the literature, where a similar transition from an acicular ferrite microstructure to one containing a greater amount of bainite is found to occur as the concentration of elements other than Cr or Mo is increased so that the amount of allotriomorphic ferrite is reduced. Horii et al. (1988)

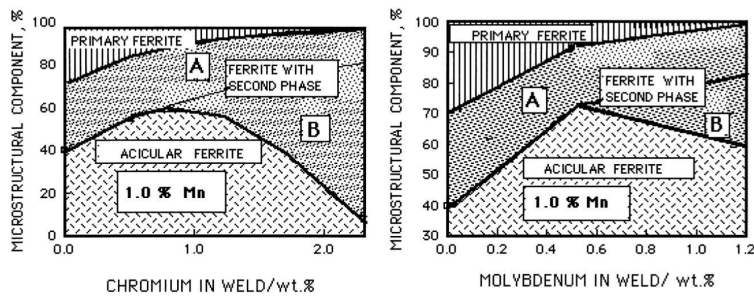


**Figure 10.18** Changes in the as-deposited microstructure of steel welds as a function of chromium or molybdenum concentration (after Evans). Notice that in each case, the fraction of acicular ferrite goes through a maximum as the Cr or Mo concentration increases. The region labelled “ferrite with aligned second phase” by Evans has been subdivided schematically into regions A and B, to represent the Widmanstätten ferrite and bainite microstructures respectively. The maximum occurs because at large alloy concentrations, acicular ferrite is progressively replaced by austenite grain boundary nucleated bainite.

found that in a series of low-alloy steel welds, when the manganese or nickel concentrations exceeded about 1.5 and 2.9 wt% respectively, the weld microstructure was found to exhibit significant quantities of bainite. Interestingly, in the case of the nickel containing steels, the toughness nevertheless improved since nickel in solid solution has a beneficial intrinsic effect on the toughness of iron. It apparently increases the stacking fault energy of body-centred cubic iron; since the dislocations in such iron are three-dimensionally dissociated, the change in stacking fault energy reduces the stress required for plastic flow at low temperatures, relative to that necessary for cleavage fracture – see Leslie (1982).

To summarise, many experiments have indirectly revealed that the cause for the transition from a predominantly acicular ferrite microstructure to one containing substantial amounts of bainite, may be related to the reduction in the coverage of austenite grain boundaries by layers of allotriomorphic ferrite, as the solute concentration exceeds a certain value (Babu and Bhadeshia, 1990). Below that concentration, the steel hardenability is low enough to ensure that the austenite grain surfaces are completely covered by uniform layers of allotriomorphic ferrite, thereby rendering them useless for bainite nucleation, and consequently allowing the development of acicular ferrite by intragranular transformation. As the concentration of austenite stabilising elements is increased, some of the austenite grain surface is left bare and becomes available for the nucleation of bainite sheaves as soon as the temperature falls within the bainite transformation range.

These ideas have been verified directly in experiments on Cr containing steels, which demonstrated that the microstructure can be changed from bainite to acicular ferrite simply by introducing thin layers of allotriomorphic ferrite at the austenite grain surfaces (Fig. 10.19). It appears that the allotriomorphic ferrite/austenite boundaries, even when the  $\alpha/\gamma$  orientation is appropriate, cannot develop into bainite because the adjacent austenite is enriched in carbon, to an extent which drastically reduces its bainite start temperature. A transformation-free zone is therefore found ahead of the allotriomorphic ferrite/austenite interfaces.

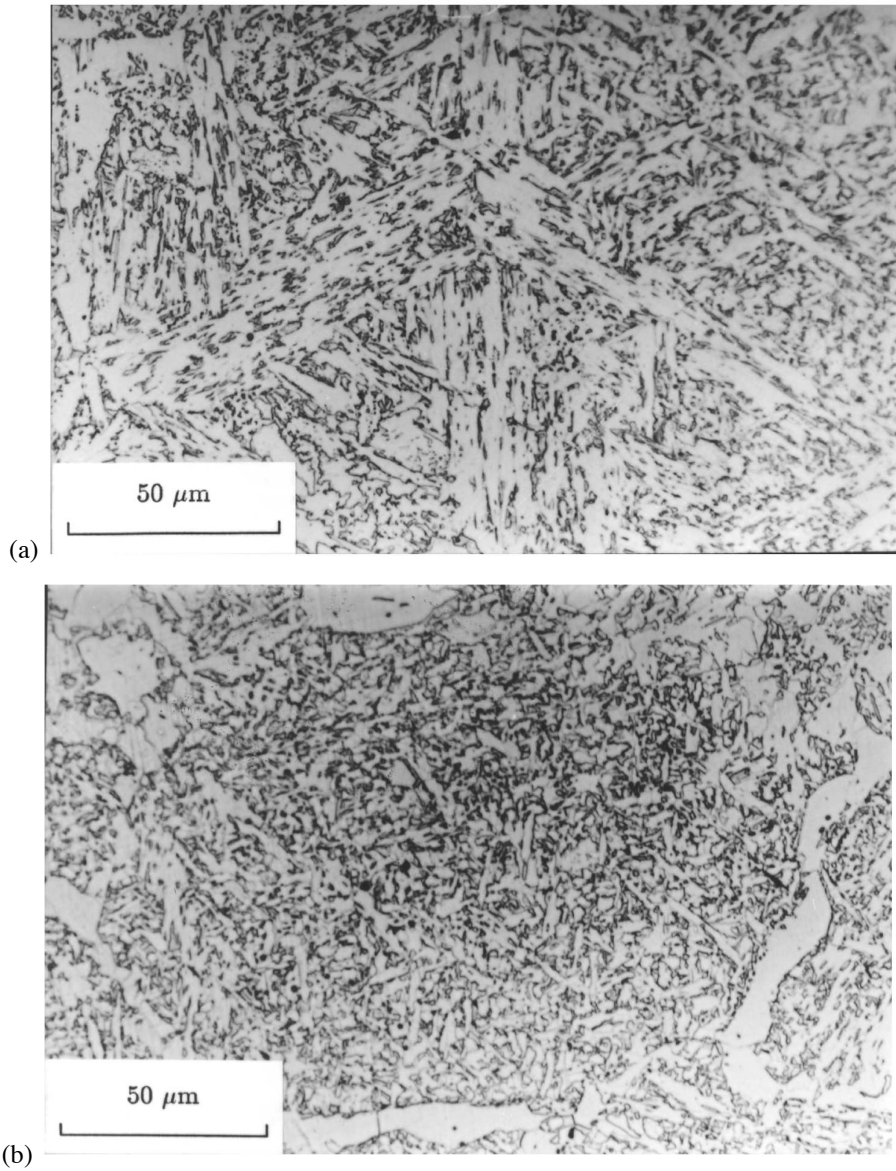


**Figure 10.19** The change from a bainitic microstructure (a) to one which is predominantly acicular ferrite (b), induced by the introduction of a thin layer of allotriomorphic ferrite at the austenite grain surfaces. Both the acicular ferrite and bainite were otherwise obtained by isothermal transformation under identical conditions. After Babu and Bhadeshia (1990).

## 10.7 Lower Acicular Ferrite

We have seen that acicular ferrite and bainite seem to have similar transformation mechanisms. The microstructures might differ in detail because bainite sheaves grow as a series of parallel platelets emanating from austenite grain *surfaces*, whereas acicular ferrite platelets nucleate intragranularly at *point* sites so that parallel formations of plates cannot develop. Some of the similarities between bainite and acicular ferrite are:

- They both exhibit the invariant-plane strain shape deformations with large shear components, during growth. Consequently, the growth of a plate of acicular ferrite or bainite is confined to a single austenite grain (i.e. blocked by a  $\gamma$ -grain boundary); the coordinated movement of atoms implied by the shape change cannot in general be sustained across a border between grains in different crystallographic orientations. A further implication is that plates of acicular ferrite, like bainite, *always* have an orientation relationship with the parent phase, which is within the Bain region. This is not necessarily the case when the transformation occurs by a reconstructive mechanism; it is found that when pearlite nucleates intragranularly on inclusions, the ferrite does not exhibit a specific orientation with the surrounding austenite (Guo et al., 2001).
- There is no substitutional solute partitioning during the growth of either bainite or acicular ferrite (Strangwood and Bhadeshia, 1987; Chandrasekharaiah et al., 1994).
- Both reactions stop when the austenite carbon concentration reaches a value where it becomes thermodynamically impossible to achieve diffusionless growth (Yang and Bhadeshia, 1987b; Strangwood and Bhadeshia, 1987). Any redistribution of carbon from the supersaturated ferrite plates occurs after growth. Growth is thus diffusionless, but is followed immediately afterwards by the rejection of carbon into the residual austenite.
- Acicular ferrite only forms below the bainite-start temperature.
- There is a large and predictable hysteresis in the temperature at which austenite formation begins from a mixed microstructure of acicular ferrite and austenite, or bainite and austenite (Yang and Bhadeshia, 1987a).
- The removal of inclusions from a weld deposit, without changing any other feature, causes a change in the microstructure from acicular ferrite to bainite (Harrison and Farrar, 1981).
- An increase in the number density of austenite grain surface nucleation sites (relative to intragranular sites) causes a transition from acicular ferrite to bainite (Yang and Bhadeshia, 1987a).
- The elimination of austenite grain surfaces by decoration with inert allotriomorphic ferrite leads to a transition from a bainitic to an acicular ferritic microstructure (Babu and Bhadeshia, 1990).

These and other similarities emphasise the point that bainite and acicular ferrite have the same growth mechanisms. There is one anomaly. Like conventional lower bainite in wrought steels, there ought to exist a *lower* acicular ferrite microstructure, in which the intragranularly nucleated plates of  $\alpha_a$  contain plates of cementite inclined at an angle of about  $60^\circ$  to the habit plane (Bhadeshia and Christian, 1990). The transition from upper

to lower bainite occurs when the partitioning of carbon from supersaturated bainitic ferrite into austenite becomes slow compared with the precipitation of carbides in the ferrite, Fig. 7.1 (Hehemann, 1970; Takahashi and Bhadeshia, 1990). Consequently, if the carbon concentration of a steel weld is increased sufficiently (Fig. 7.2), then for similar welding conditions, the microstructure should undergo a transition from acicular ferrite to lower acicular ferrite. An experiment designed to test this, using an exceptionally high carbon weld, has detected lower acicular ferrite (Sugden and Bhadeshia, 1989), supporting the conclusion that acicular ferrite is simply intragranularly nucleated bainite (Fig. 10.20). Lower acicular ferrite is only found when the weld carbon concentration is large enough to permit the precipitation of carbides from the acicular ferrite, before much of the carbon can partition into the residual austenite. This means that in reality, lower acicular ferrite is unlikely to be of technological significance in welds which necessarily have low carbon equivalents. On the other hand, lower acicular ferrite has been detected in a laser welded high-carbon steel (Hall, 1990), and in a medium carbon wrought steel (Díz-Fuentes and Gutiérrez, 2004).

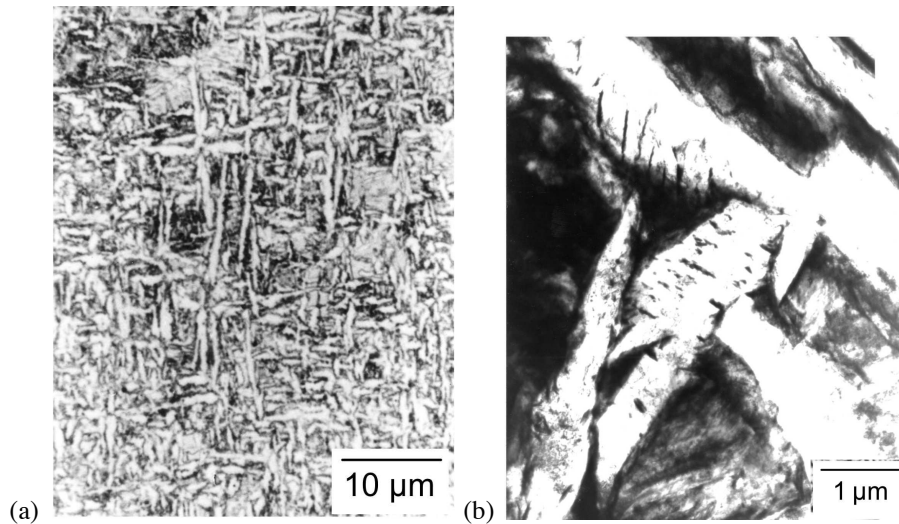


**Figure 10.20** (a) Light micrograph of lower acicular ferrite in an experimental high-carbon steel weld deposit (Sugden and Bhadeshia, 1989b). (b) Corresponding transmission electron micrograph illustrating the carbide particles in the acicular ferrite, in the single crystallographic variant typical of lower bainite in conventional microstructures.

### 10.8 Stress-Affected Acicular Ferrite

Welded fabrications are prone to the development of residual stresses whose magnitudes may approach the yield stress. This may affect the development of the acicular ferrite microstructure during the cooling of the weld to ambient temperature. Dallum and Olson (1989) have shown that stress has little influence on the overall volume fraction of acicular ferrite. Nevertheless, an externally applied stress accelerates transformation and alters the morphology of acicular ferrite as shown in Fig. 10.21. This is not surprising given the displacive character of the transformation.

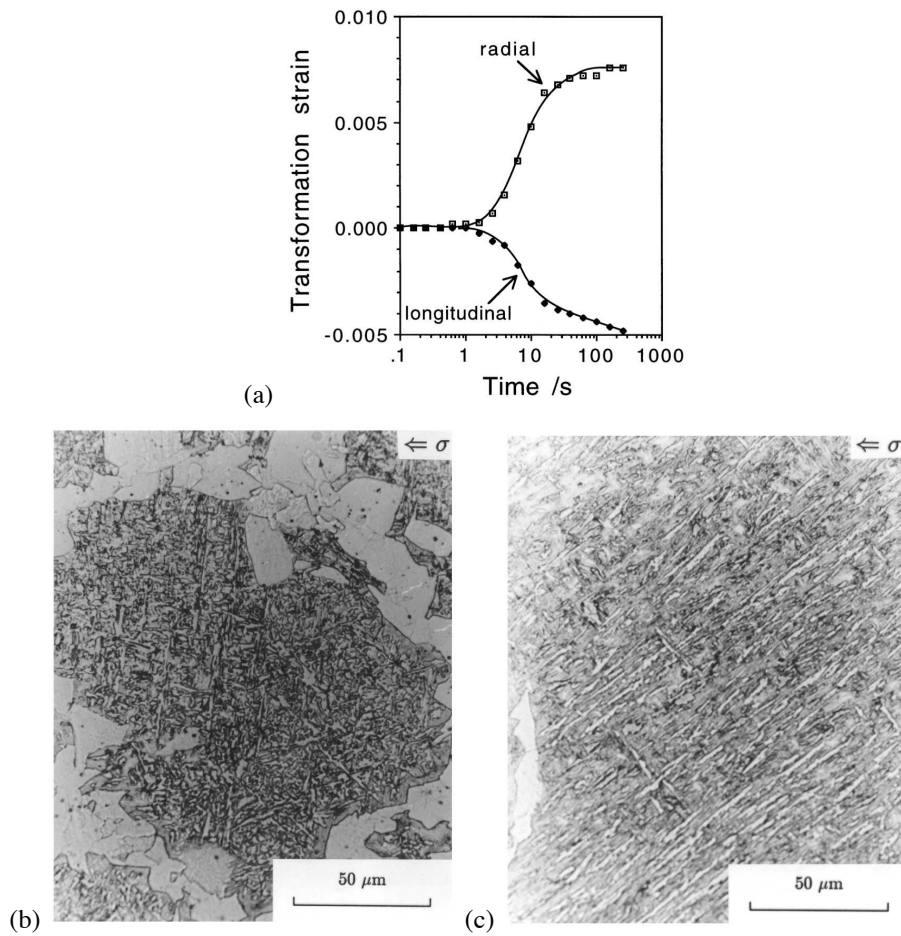


**Figure 10.21** (a) Dilatometric data monitored along orthogonal directions, showing the displacive character of the acicular ferrite reaction, and the acceleration of transformation by the applied stress. (b) The microstructure obtained in the absence of stress. (c) The aligned microstructure generated by the formation only of those acicular ferrite variants which are favoured by the applied stress. The transformation conditions for (b) and (c) are otherwise identical. After Babu and Bhadeshia (1992).

### 10.9 Effect of Strain on the Acicular Ferrite Transformation

The distinguishing feature of acicular ferrite is that it must nucleate intragranularly on inclusions. The amount of acicular ferrite is reduced if the number density of grain boundary nucleation sites is increased relative to the number density of inclusions.

The effect of deforming austenite prior to its transformation is to increase the nucleation potency and number density of the austenite grain boundaries. When the austenite recrystallises during deformation, it usually does so to a finer grain structure. These effects are not helpful in promoting acicular ferrite. This is why the thermomechanical processing of austenite prior to its transformation discourages the formation of acicular ferrite (Shim et al., 2000). It has, however, been shown that in some circumstances the increase in number density of grain boundary nucleation sites caused by thermomechanical processing can be compensated by increasing the hardenability of the steel using molybdenum as a solute (Capdevila et al., 2006).

Transformation from plastically deformed austenite also retards the formation of acicular ferrite by mechanically stabilising the austenite (Chapter 8). This is because the growth of acicular ferrite occurs by a displacive mechanism and the progress of the glissile transformation interface is hindered by the deformation debris present in the austenite (Lee et al., 2003).

### 10.10 Inoculated Acicular Ferrite Steels

We have seen that acicular ferrite in weld deposits is intragranularly nucleated bainite. An acicular ferrite microstructure appears different from that of bainite because its plates nucleate from point sites, the nonmetallic inclusions present in the steel. Adjacent plates of acicular ferrite tend to radiate in many directions from each nucleation site. A propagating crack is therefore frequently deflected as it encounters plates in different crystallographic orientations, leading to an improvement in the toughness.

Bainite and acicular ferrite can be obtained under identical isothermal transformation conditions in the same inclusion-rich steel. Bainite dominates when the austenite grain size is small, i.e. the number density of grain boundary nucleation sites is large relative to the number density of inclusions. Conversely, acicular ferrite is not easily obtained in clean steels.

#### 10.10.1 Structural Steel

It is more than fifteen years now since the invention of steels with deliberate additions of oxide particles to induce the formation of acicular ferrite and hence to achieve better toughness (Nishioka and Tamehiro, 1988).<sup>3</sup> More than 100,000 tonnes of these inoculated steels have been marketed for applications in the offshore oil and gas industries, and for constructions in hostile, deep and cold environments. The steels are now available from more than one manufacturer.

<sup>3</sup>Prior to the advent of the oxide-inoculated wrought steels, high-strength low-alloy steels were sometimes called "acicular ferrite HSLA" steels (Krishnadev and Ghosh, 1979). However, their microstructure consisted of parallel, heavily dislocated laths in identical crystallographic orientation. It is modern practice to restrict the term acicular ferrite to more chaotic microstructures.

Steels destined for the Arctic regions must have adequate toughness at temperatures as low as  $-80^{\circ}\text{C}$ . In some cases, the steels have to be amenable to high heat-input welding ( $4\text{kJ mm}^{-1}$ ) typical in ship construction. It follows that the designed microstructure must be left unchanged by any heat originating from the welding process. Regions of the heat-affected zone which become austenitic must transform back into an appropriate microstructure which is tough.

Inoculated steels have many advantages in this context. The coarse austenite grain structures found in the heat-affected zone adjacent to the fusion boundary favour the development of acicular ferrite plates on the titanium oxides and nitrides.

A typical composition of an inoculated structural steel is Fe-0.08C-0.2Si-1.4Mn-0.012Ti-0.002Al-0.002N wt%. Small concentrations of boron may be added to discourage grain boundary allotriomorphic ferrite and to fix free nitrogen which reduces toughness via a strain hardening mechanism.

The oxide particles effective in stimulating nucleation are about  $2\mu\text{m}$  in size. They are introduced during steel making by controlling the deoxidation practice. Each particle is generally a mixture of many compounds [MnS,  $\text{Al}_2\text{O}_3$ , (Mn,Si)O, etc.] but the key phase responsible for the nucleation of ferrite is  $\text{Ti}_2\text{O}_3$ , although the published experimental evidence is rather limited (Homma et al., 1987; Nishioka and Tamehiro, 1988; Byun et al., 2001).

Aluminium has a strong affinity for oxygen; its concentration must be kept below about 30 p.p.m. to allow titanium to combine with oxygen. The fraction of the total oxide content which is due to titanium decreases as the aluminium concentration increases (Fig. 10.22).

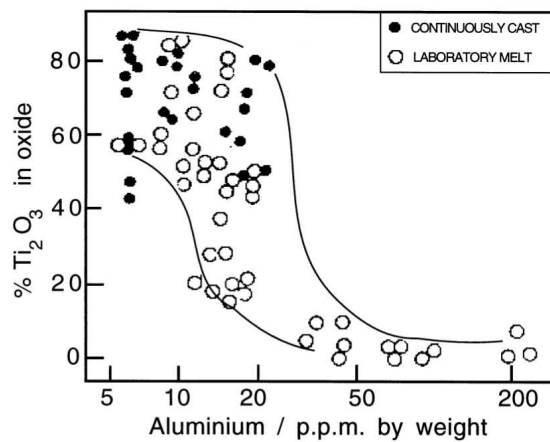


**Figure 10.22** The effect of aluminium concentration on the proportion of  $\text{Ti}_2\text{O}_3$  in the total oxide content of the steel (Chijiwa et al., 1988).

Aluminium dissolved in austenite promotes Widmanstätten ferrite at the expense of acicular ferrite, the fraction of which decreases sharply at concentrations greater than about 70 p.p.m. (Fig. 10.23a). The mechanism of this effect is unknown and the concentration of dissolved aluminium is difficult to control in practice. There is little correlation between the total aluminium concentration and that in solution (Thewlis, 1989a,b).

The effect of inclusions in promoting acicular ferrite saturates at about 120 p.p.m. of oxygen (Fig. 10.23b). The oxide content of the steel should be kept to the minimum con-

sistent with the development of acicular ferrite, because any excess contributes towards the initiation of fracture. Furthermore, a large oxide content causes a reduction in the austenite grain size (Lee et al., 2002), which in turn reduces the ratio of intragranular to grain surface nucleation sites; the consequence is a smaller fraction of acicular ferrite. This is why inoculated steel contains the same amount of oxygen as a fully killed steel; it is the nature of the oxide that is more important than the total concentration of oxygen (Imagumbai et al., 1985).

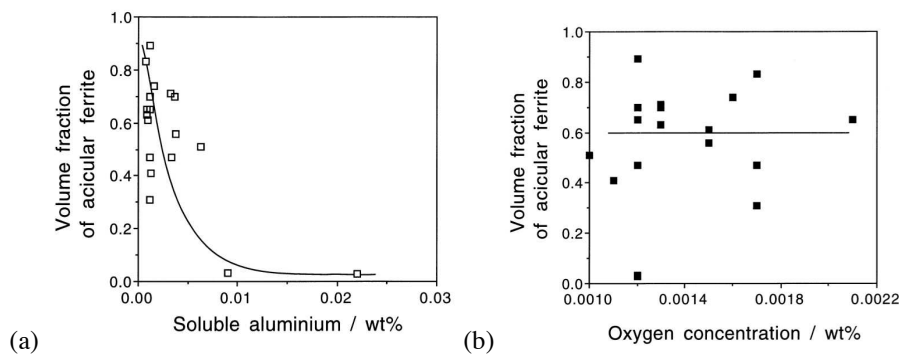


**Figure 10.23** (a) The volume fraction of acicular ferrite as a function of the soluble aluminium concentration; (b) the volume fraction of acicular ferrite as a function of the total oxygen concentration. Data from (Imagumbai et al., 1985).

The nitrogen concentration of inoculated steels must be controlled to avoid the formation of TiN which is not as effective as the oxide in stimulating intragranular nucleation. TiN is also not as stable as the oxide and tends to dissolve in the region of the heat-affected zone adjacent to the fusion boundary of a weld.

The design of inoculated steels includes a consideration of hardenability since phases such as allotriomorphic ferrite and Widmanstätten ferrite must be avoided. This ensures that there is sufficient untransformed austenite available for conversion into acicular ferrite. The hardenability can be enhanced by the careful use of microalloying elements such as Nb, Mo and B, thereby minimising the carbon equivalent of the steel. The silicon concentration should be kept below about 0.2 wt% to avoid large oxide particles.

Recent work has highlighted the potential of cerium sulphide additions to experimental ingots as a means for stimulating the formation of acicular ferrite (Thewlis, 2006). The phases  $Ce_2O_2S$ , CeS and  $Ce_3S_4$  appear in the steel following additions to the melt. The work was stimulated by the fact that latter two phases both have cubic crystal structures with lattice parameters which are multiples of that of ferrite, and hence may stimulate epitaxial nucleation. The details of the crystallography have not yet been resolved, but the method has been shown to work in experimental alloys.

### 10.10.2 Acicular Ferrite Forging Steels

Forging steels contain a high carbon concentration and hence are not welded. Titanium nitride can therefore be used to produce an acicular ferrite microstructure instead of the more usual mixture of ferrite and pearlite (Linaza et al., 1993). The heat-treatment temperatures are never high enough to take the nitride into solution.

The steels listed in Table 10.4 under normal conditions have the microstructure illustrated in Fig. 10.24a, consisting mainly of pearlite and a small quantity of allotriomorphic ferrite. The same steel, when cooled rapidly, transforms to acicular ferrite rather than bainite (Fig. 10.24b,c) because the titanium nitride particles present in the austenite provide abundant sites for intragranular nucleation. The toughness improves but the change is not large at comparable yield strength (Table 10.4). This is because some of the TiN particles can be coarse, greater than  $2\mu\text{m}$ . They are also brittle and hence act to initiate cracks (Rodríguez-Ibabe, 1998).

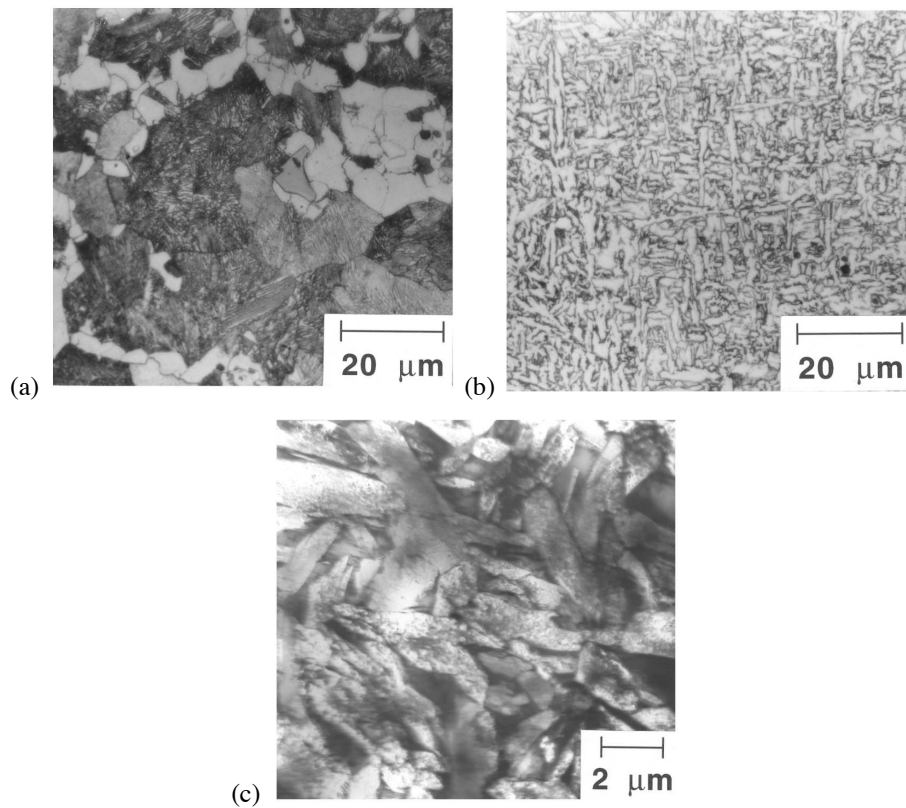


**Figure 10.24** The microstructures of a Ti-V forging steel. (a) Optical micrograph showing a mixture of ferrite and pearlite. (b) Optical micrograph showing the acicular ferrite microstructure. (c) Transmission electron micrograph showing the acicular ferrite microstructure.

### 10.10.3 Steelmaking Technology for Inoculated Alloys

The details of the manufacturing practice for inoculated steels are frequently not published but the aim is to incorporate titanium oxide ( $\text{Ti}_2\text{O}_3$ ) rather than TiN which is less stable at high temperatures.<sup>4</sup> The steelmaking involves deoxidation with titanium, whilst avoiding other strong deoxidisers such as Al, Ca or the rare earth elements. The oxygen concentra-

<sup>4</sup>The process may be as simple as the addition of titanium oxide briquettes into molten steel (Kaltzakorta et al., 2014).

**Table 10.4** Chemical compositions (wt%) and representative mechanical properties of some titanium alloyed forging steels (Linaza et al., 1993).

Alloy	C	Mn	Si	V	Al	Ti	N
Ti-V	0.37	1.45	0.6	0.11	0.024	0.015	0.0162
Ti	0.35	1.56	0.33	-	0.027	0.028	0.0089
Alloy	Microstructure		Yield Strength / MPa		$K_{IC}$ / MPa m <sup>1/2</sup>		
Ti-V	Acicular ferrite		560-666		133-155		
Ti-V	Ferrite & Pearlite		590-650		134-139		
Ti	Acicular ferrite		519		169-176		
Ti	Ferrite & Pearlite		440		162-169		

tion in the molten steel should be between 60 and 120 p.p.m., depending on application. High toughness levels demand a small inclusion (and hence oxygen) content. The steel must otherwise be clean with a minimal concentration of sulphur.

The active inclusions form in the melt or during the solidification stage (Pan and Lee, 1994). The titanium oxide might be added as powder into the melt, or during the casting stage. However, the oxide then tends to cluster, making the distribution of particles uneven. Alternatively, elemental titanium or ferro-titanium may be added to the melt or casting (Nishioka and Tamehiro, 1988; Chijiwa et al., 1988). The titanium then combines with any dissolved oxygen. With this second method, the steel must not be aluminium killed because alumina then forms in preference to titanium oxides, as illustrated in Fig. 10.20. Aluminium-free molten steel is therefore titanium-killed in order to produce an inoculated alloy (Lee and Pan, 1991b,a, 1992, 1993).

It is clear that when particles are added to the molten steel, they may cluster, coalesce or coarsen and react in an undesirable manner. An alternative approach involves the design of special master alloys containing the nucleating particles, added at a late stage in the steel-making process (Grong et al., 2006). This is common practice in the aluminium industry in order to refine the cast microstructure.

A few kilograms of steels containing inoculants can be produced using the electroslag refining process, in which electrodes made from steel are short-circuited into an electrically conducting slag to cause melting. Bandyopadhyay et al. (2006b,a) welded small, sealed tubes containing inoculant powders to the sides of the larger base-steel electrodes. They were in this way able to introduce titanium and niobium particles into a bainitic steel, with a halving in the size of the austenite grains, an increase in tensile properties without any loss of toughness.

An attempt has also been made to add silicon carbide to steel by enclosing the former in steel and melting the composite (Talas, 2006). The silicon carbide essentially decomposes and is absorbed by the steel – the final carbon concentrations reported seem extraordinarily high (4-7 wt%) and may be inconsistent with the observed microstructures.

Finally, it is worth pointing out that although in the context of deliberately added inclusions, the approach has been largely qualitative, efforts are underway to create models based on thermodynamic and kinetic theory to engineer the type and distribution of non-metallic particles in steels (Babu et al., 1995, 1999; Costa e Silva, 2006). If successful then these will be extremely useful in large scale production technologies.

### 10.11 Summary

It is ironic that bainite, when it was first discovered, was called *acicular ferrite* by Davenport and Bain (1930). The terms acicular ferrite and bainite were often used interchangeably for many years after 1930 - see for example, Bailey (1954). There is good evidence that the microstructure which we now call acicular ferrite, consists simply of intragranularly nucleated bainite. Conventional bainite grows in the form of sheaves of parallel plates which nucleate at austenite grain *surfaces*. By contrast, acicular ferrite plates emanate *point* nucleation sites and hence grow in many different directions; the development of a sheaf microstructure is prevented by impingement between plates which have nucleated from adjacent inclusions.

The transformation has otherwise been verified to show all the characteristics of the bainite reaction: the incomplete reaction phenomenon, the absence of substitutional solute partitioning during transformation, an invariant-plane strain shape deformation accompanying growth, a large dislocation density, a reproducible orientation relationship within the Bain region, the lower acicular ferrite, etc. It is of course possible that Widmanstätten ferrite can be nucleated intragranularly on inclusions but that microstructure will necessarily be much coarser than the acicular ferrite discussed here (Ali and Bhadeshia, 1991; Koseki and Thewlis, 2005).

Any factor that increases the number density or potency of intragranular nucleation sites at the expense of austenite grain boundary sites favours a transition from a bainitic to an acicular ferrite microstructure. The transition can in practice be obtained by increasing the austenite grain size, by decorating the grain boundaries with thin, inactive layers of allotriomorphic ferrite, by increasing the inclusion content or by rendering the boundaries impotent with elements like boron. It is well understood that these microstructural factors can only be useful if enough austenite is left untransformed for the development of acicular ferrite – the grain boundary nucleated phases must therefore be kept to a minimum.



## CHAPTER 11

---

### OTHER MORPHOLOGIES OF BAINITE

---

Upper and lower bainite are established terms describing microstructures that can easily be distinguished using routine microscopy and whose mechanisms of formation are well understood. There are, however, a number of other descriptions of steel microstructures that include the word “bainite”. These additional descriptions can be useful in communicating the form of the microstructure. But this must be done with care, avoiding the natural tendency to imagine a particular mechanism of transformation, simply because someone has chosen to coin the terminology.

#### 11.1 Granular Bainite

Of all the unusual descriptions of bainitic microstructures, granular bainite is probably the most useful and frequently used nomenclature. During the early 1950s, continuously cooled low-carbon steels revealed microstructures that consisted of “coarse plates and those with an almost entirely granular aspect”, together with islands of retained austenite and martensite, Fig. 11.1 (Habraken, 1956, 1957; Habraken and Economopoulos, 1967). The structure was designated *granular bainite* and the terminology became popular because many industrial heat treatments involve continuous cooling rather than isothermal transformation. The energy generation industry in particular uses enormous quantities of bainitic microstructures generated by allowing large steel components to cool naturally, Chapter 12. Granular bainite is supposed to occur only in steels that have been cooled continuously; it cannot be produced by isothermal transformation.

The coarse ferrite plates referred to earlier, do not really exist. They are in fact, sheaves of bainitic ferrite with very thin regions of austenite between the sub-units because of the low carbon concentration of the steels involved (Leontyev and Kovalevskaya, 1974; Josefsson and Andrén, 1989). Hence, on an optical scale, they give the appearance of coarse plates (Fig. 11.1a). Many of the original conclusions were reached from microstructural observations which were not of sufficient resolution to establish the fine structure within the sheaves of bainite. Indeed, evidence of this interpretation of so-called coarse plates appeared in the literature as early as 1967 when thin foil TEM observations were made by Habraken and Economopolus, revealing the fine bainitic ferrite platelets within the sheaves. The crystallography of granular bainite is similar to that of ordinary bainite; Fig. 11.2 shows a region identified as granular bainite in a TRIP-assisted steel, revealing the fine crystallographic structure within a region that optically might appear homogeneous (Pereloma et al., 2014).

A characteristic (though not unique) feature of granular bainite is the lack of carbides in the microstructure. The carbon that is partitioned from the bainitic ferrite stabilises the residual austenite, so that the final microstructure contains both retained austenite and some high-carbon martensite. Consistent with observations on conventional bainite, there is no redistribution of substitutional solutes during the formation of granular bainite (Tenuta Azevedo and Galvao da Silva, 1978).

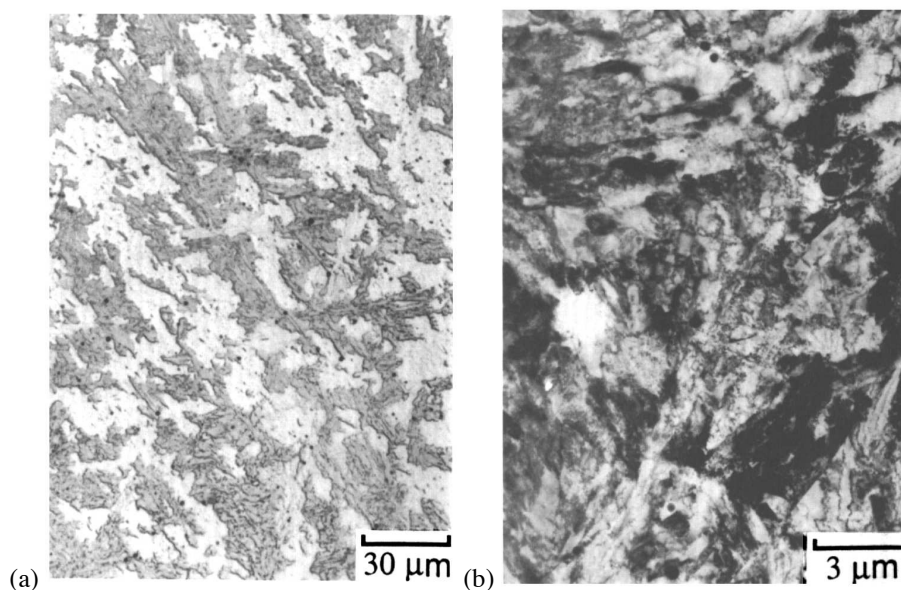


**Figure 11.1** Granular bainite in a Fe-0.15C-2.25Cr-0.5Mo wt% steel. (a) Light micrograph. (b) Corresponding transmission electron micrograph. After Josefsson and Andrén (1989).

The extent of transformation to granular bainite is found to depend on the undercooling below the bainite-start temperature (Habraken and Economopoulos, 1967). This is a reflection of the fact that the microstructure, like conventional bainite, exhibits an incomplete reaction phenomenon.

The evidence therefore indicates that granular bainite is not different from ordinary bainite in its mechanism of transformation. The peculiar morphology is a consequence of two factors: continuous cooling transformation and a low carbon concentration. The former

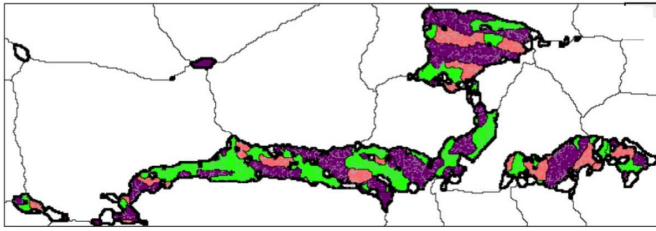


**Figure 11.2** A region of granular bainite in which the crystallography is identified by three colours corresponding to each of the Bain groups. Reproduced with permission of Elsevier, from Pereloma et al. (2014).

permits extensive transformation to bainite during gradual cooling to ambient temperature. The low carbon concentration ensures that any films of austenite or regions of carbide that might exist between sub-units of bainite are minimal, making the identification of individual platelets within the sheaves rather difficult using light microscopy.

Finally, it is interesting that in an attempt to deduce a mechanism for the formation of granular bainite, Habraken in his discussion to Goodenow et al. (1965) proposed that the austenite prior to transformation divides into regions which are rich in carbon, and those which are relatively depleted. These depleted regions are then supposed to transform into granular bainite. The idea is the same as that of Klier and Lyman (1944) and has been shown to be thermodynamically impossible in steels (Aaronson et al., 1966a).

## 11.2 Inverse Bainite

Ferrite is the dominant phase in conventional bainite; carbide precipitation when it occurs is a secondary event. In the so-called “inverse bainite” which is found in hypereutectoid steels, it is the cementite which is the first phase to form (Hillert, 1957). A central plate-like spine of cementite grows directly from austenite (Hehemann, 1970) and then becomes surrounded by a layer of ferrite (Fig. 11.3). The term “inverse” reflects the fact that unlike conventional bainite, cementite is the first phase to precipitate from austenite.

The mechanism of the transformation is virtually unknown; there is no evidence that the growth of the ferrite occurs by a coordinated movement of atoms, and no crystallographic or chemical composition data. Judging from the shape alone, the ferrite probably forms by a reconstructive transformation mechanism. It is premature to classify the transformation as bainite.

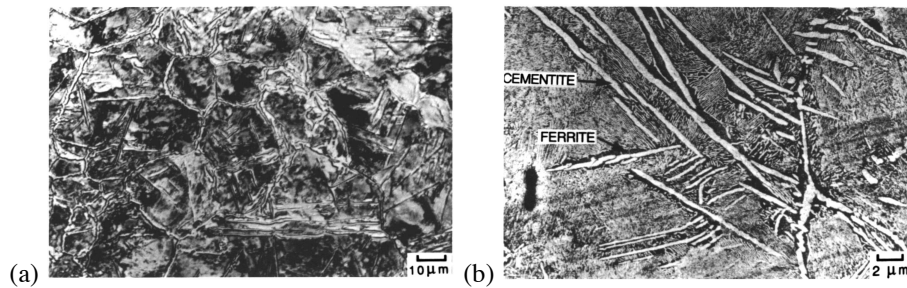


**Figure 11.3** Inverse bainite in a hypereutectoid steel. (a) Light micrograph. (b) Transmission electron micrograph. Micrographs courtesy of M. Farooque and D. V. Edmonds.

### 11.3 Columnar Bainite

“Columnar bainite” is a description of a non-lamellar aggregate of cementite and ferrite, the overall shape of which is like an irregular and slightly elongated colony (Fig. 11.4). The distribution of cementite particles within the colony is rather peculiar, the majority of needle shaped particles being aligned to the longer dimension of the colony. This region is surrounded by a layer of a different microstructure, in which the coarse cementite particles meet the austenite/ferrite interface edge on (Nilan, 1967). The structure is normally observed in hypereutectoid steels (Greninger and Troiano, 1940; Jellinghaus, 1957; Speich and Cohen, 1960) but has been found in lower carbon steels transformed at high pressures (Nilan, 1967). It may be relevant to point out that the eutectoid composition is shifted to lower carbon concentrations by hydrostatic pressure.

The microstructure can be obtained at transformation temperatures comparable with those associated with conventional bainite, but there is no invariant-plane strain surface relief accompanying the growth of “columnar bainite”. It is probable that columnar bainite is more akin to pearlite than bainite, but further investigations are needed to make any sensible decisions about the mechanism of growth.

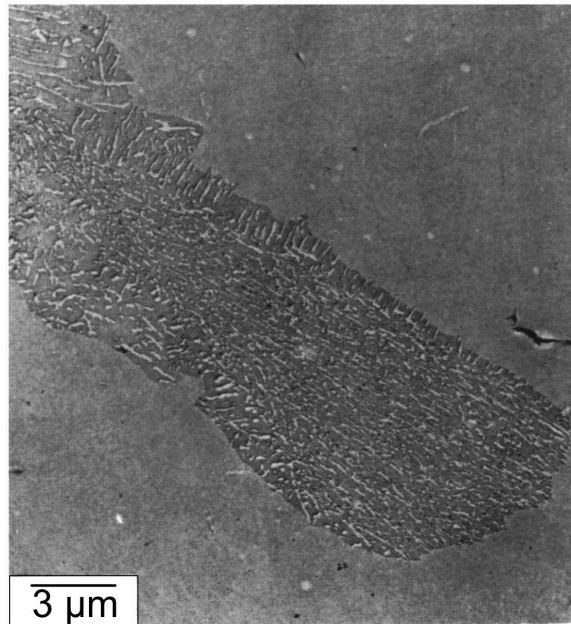


**Figure 11.4** Electron micrograph, obtained using a replica technique, showing a colony of “columnar bainite” in an Fe-0.82C wt% steel following isothermal transformation at 288 °C and at a pressure of 30 kbar (after Nilan, 1967).

#### 11.4 Alloy Pearlite

In steels containing strong carbide forming elements, it is possible to obtain pearlite in which the carbide phase is an alloy carbide (such as  $M_7C_3$  or  $M_2C$ ) instead of cementite. The alloy pearlite can form at temperatures above  $B_S$ , or somewhat below that temperature but only after holding at the transformation temperature for very long time periods (usually many days). On the scale of light microscopy, the pearlite etches as dark nodules (Fig. 11.5), but the colonies tend to have crystallographic facets rather than the nicely rounded colonies of normal pearlite. This is probably a reflection of the orientation dependence of the interfacial energy of the alloy carbide.

Because of this faceting, transmission electron microscopy observations can be misleading. The crystallographically faceted nodules of pearlite at a high resolution give the appearance of parallel ferrite plates with intervening carbides, a microstructure on that scale similar to upper bainite. The terminology “pearlitic bainite” given to this transformation product is misleading. There is gross partitioning of substitutional solutes during the transformation, there is no surface relief effect, the carbide and ferrite phases grow cooperatively, and there is no reason to associate this microstructure with bainite. Hackenberg and Shiflet (2003) incorrectly refer to this microstructure as bainite without any qualifying adjectives, even though the transformation involves the simultaneous diffusional transformation to ferrite and molybdenum carbide.

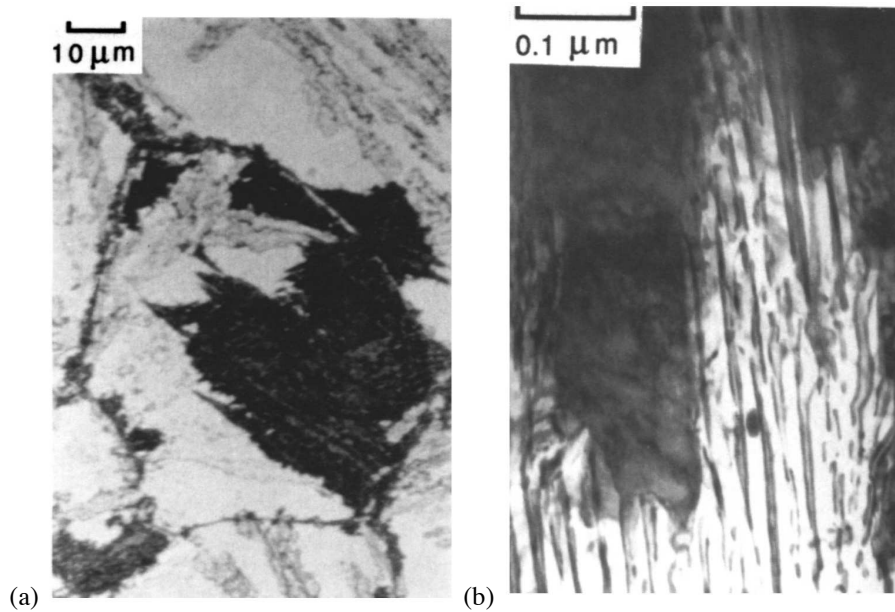


**Figure 11.5** Microstructure of the so-called “pearlitic bainite”, which is really just a pearlite with alloy carbide (in this case  $M_7C_3$ ) instead of cementite. (a) Light micrograph. (b) Transmission electron micrograph.

### 11.5 Grain Boundary Lower Bainite

Bainite nucleation in most steels occurs heterogeneously at the austenite grain boundaries. The nucleation rate of lower bainite can be large at temperatures close to  $M_S$ ; the austenite grain surfaces then become covered by lower bainite sub-units (Fig. 11.6). The rate at which carbon partitions from supersaturated ferrite is slow when transformation is at such low temperatures. Therefore, the sub-units are able to form in arrays without any intervening austenite (Bhadeshia and Edmonds, 1979a). These layers of sub-units have the overall form of allotriomorphs, but there is no doubt that they form individually.

The microstructure has caused some concern in the context of 300M, which is an ultrahigh-strength steel used in the quenched and tempered condition (Padmanabhan and Wood, 1984). The alloy has a very high hardenability - 10 cm diameter sections can be made martensitic by air cooling from the austenitisation temperature. However, optical microscopy revealed the surprising presence of allotriomorphs, which on detailed examination turned out to be the grain boundary lower bainite described above.

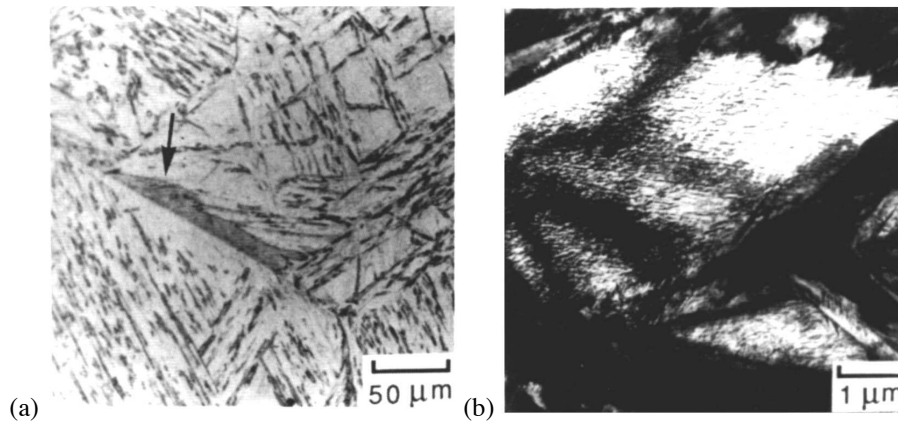


**Figure 11.6** The microstructure of grain boundary lower bainite. (a) Light micrograph. (b) Transmission electron micrograph.

### 11.6 Coalesced Bainite

There is increasing evidence of a tendency to form unusually coarse plates of bainite at large driving forces and relatively low transformation temperatures (Bhadeshia et al., 2006). It seems that separately nucleated platelets which are in the same crystallographic orientation coalesce during prolonged growth. This leads to a markedly bimodal distribution of plate thicknesses, with the fine plates about  $0.2\ \mu\text{m}$  thick and the larger plates many micrometres thick. The latter are detrimental to the toughness of strong steels.

A few coarse plates can be observed on an optical scale, whereas the remaining microstructure consists of much finer plates which can only be resolved using transmission and high-resolution scanning electron microscopy. Some of the observations are based on wrought steels whereas others are from weld metals. Fig. 11.7 shows vividly a higher resolution image with a bimodal size-distribution of bainite.

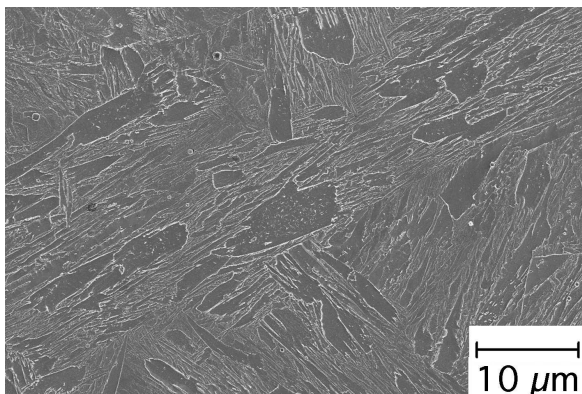


**Figure 11.7** FEG-SEM image showing bimodal distribution of plate sizes in a weld metal (Keehan, 2005; Keehan et al., 2006a,b,c)

A later investigation revealed a similar phenomenon in a wide variety of steels with compositions listed in Table 11.1, with clear evidence that the coarse plates formed by the coalescence of finer platelets (Chang and Bhadeshia, 1996). Fig. 11.8 shows a sheaf of

bainite initiating as many identically oriented platelets at an austenite grain boundary, with each platelet separated by a retained austenite film. The platelets later merge into a single coarse crystal, ending at the point marked 'A'. The films of austenite disappear along the length of the sheaf, resulting in a homogeneous plate. This is what is meant by *coalesced bainite*.

The question then arises as to what happens to the excess carbon in the bainitic ferrite given that the austenite which originally separated the sub-units is eliminated in the coalescence process. The excess carbon can either precipitate within the ferrite as cementite – as has been reported for the coarse plates in both steels (Bhadeshia and Edmonds, 1979a; Padmanabhan and Wood, 1984) and weld metals (Keehan, 2005). The extent of precipitation naturally depends on the carbon concentration of the steel (Keehan et al., 2006c). The excess carbon can also partition into the residual austenite, but because of the thickness of the coarse bainite, only the regions close to the  $\alpha/\gamma$  interface are able to contribute to the partitioning. The central regions of the coarse plate can relieve their excess carbon by the precipitation of cementite, leaving a precipitate-free zone at the peripheries of the plate. This is precisely what is seen in high-resolution micrographs of coalesced bainite in weld metals, Fig. 11.9.

Notice also that in Fig 11.8, the film of austenite around the coalesced part of the plate is much thicker than those separating the individual sub-units at the end opposite to 'A'. This is because a thicker plate is a larger source of carbon available to partition into the adjacent austenite (Chang and Bhadeshia, 1995a).

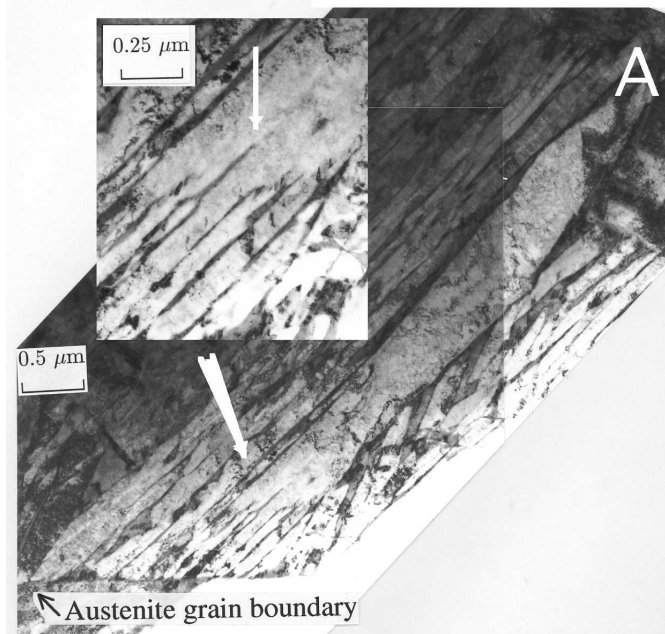


**Figure 11.8** Formation of coalesced bainite, beginning at the austenite grain boundary. The inset shows at a higher magnification, the disappearance of the austenite film as coalescence proceeds as the plates grow, until at the tip marked 'A', the plate is a single, thick unit. Transmission electron micrographs. (Chang and Bhadeshia, 1996).

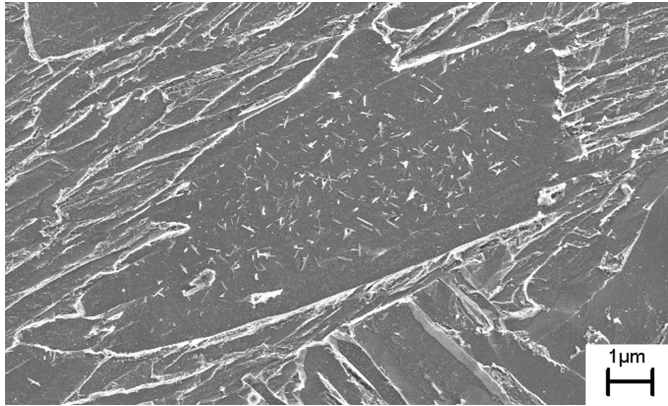


**Figure 11.9** Precipitate-free zone in a coarse plate of coalesced bainite in steel weld metal (Keehan, 2005; Keehan et al., 2006a).

### 11.6.1 Mechanism

Coalesced bainite evidently occurs when adjacent small platelets of bainite (“sub-units”) merge to form a single, larger plate. Some conditions have been proposed to be necessary for its occurrence:

- (i) Since adjacent sub-units of bainite have an almost identical crystallographic orientation, they can in principle merge seamlessly. However, a thicker plate is associated with a greater strain energy due to the shape deformation accompanying the formation of bainite. There must therefore be an adequate driving force to sustain the greater strain energy associated with the coarser plate. This is consistent with the observation that the coarse plates form at large driving forces. An analysis using a theory for elastically accommodated plates (Christian, 2003b) has shown reasonable consistency between the driving force and expected strain energy (Chang and Bhadeshia, 1996).
- (ii) As seen in Fig. 11.8, the coalescence process requires a certain length to establish itself. This is because the adjacent platelets are at first separately nucleated at the austenite grain boundaries. The nucleation process is not coordinated between the different platelets so there is an opportunity to reject excess carbon to form the intervening films of austenite. However, the platelets then can grow at a faster rate (Olson et al., 1990) and advance into fresh austenite, leading to coalescence before the carbon has an opportunity to partition. A requirement for coalescence is therefore that the lengthening of sub-units must be allowed to proceed without hindrance. This implies that coalescence is only possible at the early stages in the transformation of austenite, when growth cannot be hindered by impingement with other regions of bainite. A large austenite grain size must assist the process of coalescence.
- (iii) Mazzaferro et al. (2011) studied microstructural changes accompanying friction stir spot-welds and discovered that the formation of coalesced bainite is enhanced when the transformation occurs in deformed austenite, because there is then a greater probability of inducing similarly oriented bainite plates through variant selection.

- (iv) Anything that stimulates platelets to align should favour the formation of coalesced bainite. Transformation under the influence of a tensile stress dramatically promotes the formation of the coalesced bainite by increasing the probability of growing parallel platelets in close proximity (Fig. 11.10).
- (v) The stabilisation of austenite films that exist between the sub-units, for example by heat treatment, prevents their subsequent coalescence (Pak et al., 2012b).<sup>1</sup>

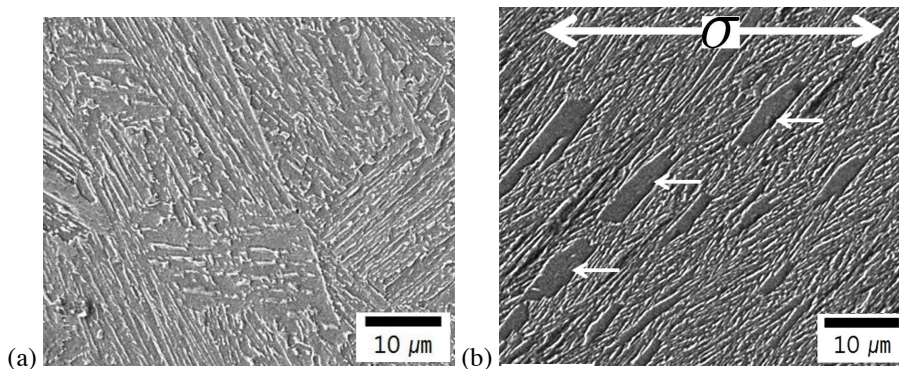


**Figure 11.10** The promotion of coalesced bainite by applying a stress. (a) Stress-free transformation. (b) Transformation under the influence of a tensile stress  $\sigma$  along the orientation indicated. The short arrows show the coalesced bainite. Reproduced with permission, Pak et al. (2012c).

The crystallography of coalescence has been studied for a similar coalescence process occurring between similarly oriented laths of martensite (Pak et al., 2012a). The large plates that form by the coalescence of individual platelets retain vestiges of their origins. There are low-misorientation boundaries left within the coalesced plate, that can be observed using transmission electron microscopy. The original platelets are not in fact in exactly the same orientation because of plastic accommodation effects. Pak et al. (2012a) demonstrated that the rotation of the austenite lattice due to the plastic accommodation of the shape strain explains the accumulation of misorientation between the martensite plates.

It is likely that the mobility of carbon plays a role in making coalescence feasible. A retardation of the partitioning of carbon into the residual austenite should make it easier for plates to coalesce. This may partly explain why coalesced bainite tends to occur at low transformation temperatures; all observations to date have been for temperatures less than approximately 400 °C.

There is a further observation applicable to continuous cooling transformations, in which reactions preceding bainite are suppressed by alloying. A greater quantity of coalesced bainite is then obtained at a slow cooling rate whereas rapid cooling gives more martensite.

<sup>1</sup>Su et al. (2006) also observed the formation of large plates of bainite during transformation under the influence of stress. However, they attributed this to the operation of favoured slip systems in austenite, that permit the better accommodation of transformation strains.

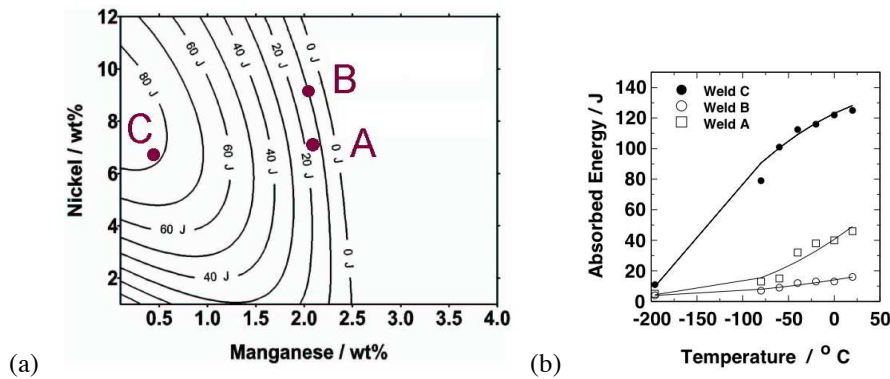


**Figure 11.11** (a) Contours showing the combined effect of manganese and nickel on the calculated toughness for  $-60^{\circ}\text{C}$ , of weld metal produced using arc welding with a heat input of  $1\text{ kJ mm}^{-1}$ , with a base composition (wt%) 0.034 C, 0.25 Si, 0.008 S, 0.01 P, 0.5 Cr, 0.62 Mo, 0.011 V, 0.04 Cu, 0.038 O, 0.008 Ti, 0.025 N, and an interpass temperature of  $250^{\circ}\text{C}$ . (b) Full results for welds A, B, and C.

### 11.6.2 Coalesced Bainite in Weld Metals

Experiments have now confirmed that coarse, coalesced bainite appears in weld metals alloyed such that the bainite forms at temperatures close to the martensite-start temperature (Keehan et al., 2006a,b,c; Svensson, 2007). It leads to a dramatic deterioration in toughness, which can be avoided by careful modifications of composition, for example, by reducing the manganese concentration when both nickel and manganese concentrations are high.

The onset of coalescence has been able to provide a physical explanation of the dependence of the toughness of weld metals on the nickel and manganese concentrations.

Muruganath and co-workers (Muruganath et al., 2002; Keehan et al., 2002) compiled a neural network model which revealed that in strong welds, a large concentration of nickel reduces the toughness when the manganese concentration is also large. In contrast, there is a remarkable improvement in the Charpy properties when nickel is increased whilst keeping the manganese content small. This is illustrated in Fig. 11.11, where the contour plot shows the impact energy at  $-60^{\circ}\text{C}$  for welds A (7Ni-2Mn), B (9Ni-2Mn) and C (7Ni-0.5Mn); the details are described elsewhere (Muruganath et al., 2002; Keehan et al., 2002). Experiments confirmed these empirical predictions but the mechanism of the interaction between Mn and Ni came later through the efforts of Keehan and co-workers. The welds with the relatively poor toughness always contained the coarse coalesced bainite, whereas the low-Mn high-Ni welds with much better toughness did not.

**Table 11.1** Chemical compositions in wt%, of steels and weld metals in which coalesced bainite has been observed.

C	Si	Mn	Ni	Cr	Mo	V	Others	Reference
0.43	2.02	3.0						Bhadeshia and Edmonds (1979a)
0.42	1.64	0.79	1.84	0.79	0.36	0.08		Padmanabhan and Wood (1984)
0.095	1.63	1.99		1.97				Chang and Bhadeshia (1996)
0.1	1.77	2.12	2.0					"
0.27	1.98	2.18		1.9				"
0.27	2.01	2.16	2.07					"
0.26	1.85	2.10						"
0.26	1.93	2.04		1.02				"
0.46	2.10	2.15						"
0.44	2.13	2.14		0.5				"
0.032	0.25	2.02	7.23	0.47	0.63			Keehan et al. (2006a)
0.031	0.27	2.11	9.23	0.48	0.64			"
0.08	0.23	0.56	10.51	1.13	0.29			Keehan et al. (2005)
0.061	0.22	1.21	8.6	0.46	0.41			"
0.030	0.4	0.61	6.11	0.16	0.38	0.018		Keehan et al. (2006c)
0.061	0.34	0.56	6.84	0.15	0.35	0.014		"
0.011	0.38	0.53	7.04	0.14	0.40	0.016		"
0.03	0.23	2.05	7.10	0.43	0.63			Pak et al. (2008)
0.28	1.50	2.04		1.50	0.24		1.48 Co	Caballero et al. (2009a, 2010a)
0.19	1.65	1.64						Mazzaferro et al. (2011)
0.17	0.22	1.32	0.79	0.27	0.53			Pous-Romero and Bhadeshia (2014)

### 11.7 Spiky Pearlite

The discussion here is not about bainite, but a structure that can be confused with bainite on cursory examination. A conventional pearlite colony forms when cementite and ferrite grow together at a common interface with the parent austenite. The carbon that is partitioned into austenite due to ferrite growth is absorbed by the cementite. A colony of pearlite therefore adopts a spherical morphology and planar sections reveal alternating lamellae of ferrite and cementite, but in fact, there are only two crystals in each colony because the cementite and ferrite are connected in three dimensions (Hillert, 1962). However, at large undercoolings the extent of cooperation between the ferrite and cementite decreases and the shape of the colony changes to a form that can be mistaken for bainite if the classification of microstructure is based on a cursory examination of morphology. Fig. 11.12 illustrates the morphologies concerned in a sample that contains both morphologies, the conventional colonies and the spiky form. The cementite within the spiky pearlite is discontinuous while the ferrite is connected throughout. The proof that the structure is not bainite is in Fig. 11.13 that shows the absence of surface relief with the spiky and conventional pearlite, the only displacements due to the light-etching bainite.

The concentration  $x^{\gamma\alpha}$  of carbon in the austenite at the  $\alpha/\gamma$  interface changes at a greater rate than  $x^{\gamma\theta}$  as a function of undercooling below the eutectoid temperature. This is simply a consequence of the slopes of the  $\gamma/\gamma + \alpha$  and  $\gamma/\gamma + \theta$  phase boundaries. This means that the growth rates of ferrite forming on its own, would increase at a greater rate than cementite forming by itself from austenite. The probability therefore, of the breakdown of cooperative growth must increase with the undercooling.

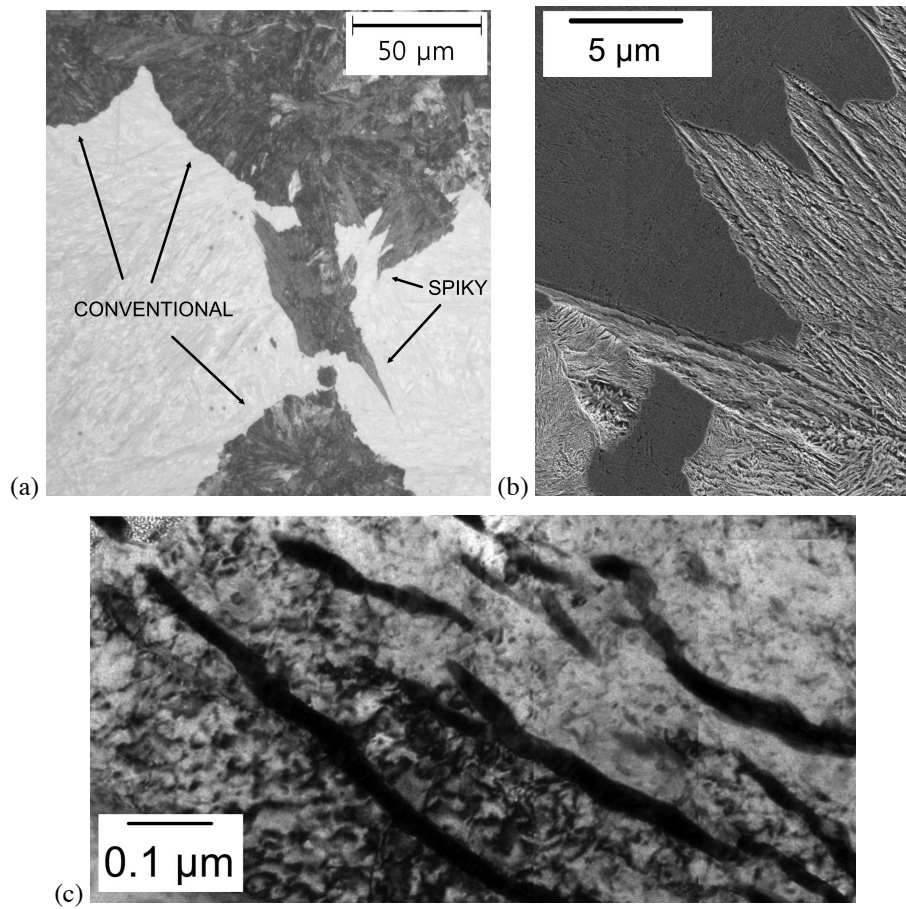


**Figure 11.12** Pearlite in Fe-0.8C-1Mn wt%, transformed at 550 °C, quenched after partial transformation (Seo et al., 2015). (a) Optical micrograph, (b) scanning electron micrograph, (c) transmission electron micrograph.

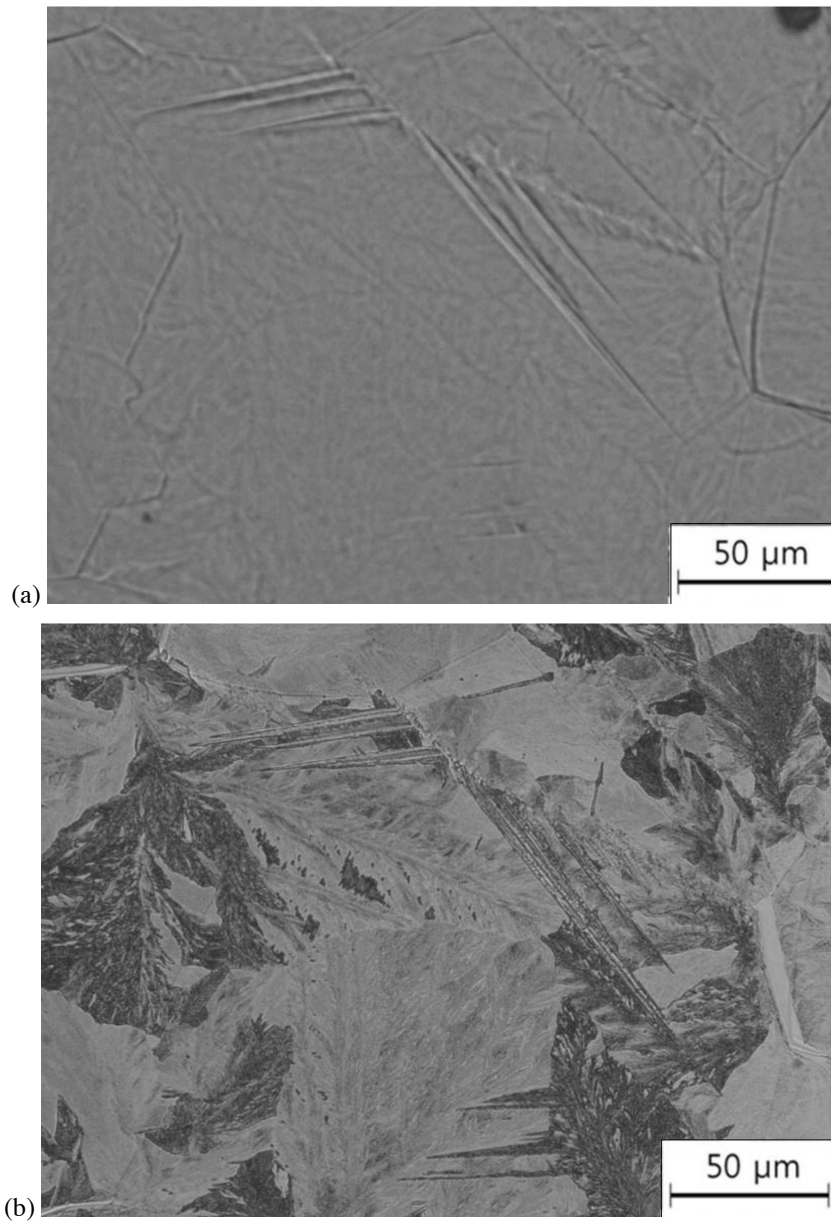


**Figure 11.13** Pearlite in Fe-0.8C-1Mn wt%, transformed at 550 °C, quenched after partial transformation (Seo et al., 2015). The dark-etching spiky form of pearlite where the ferrite and cementite do not grow at a common transformation front does not exhibit any surface upheavals. Nor does any of the pearlite. It is only the few plates of lighter-etching bainite that show the surface relief. (a) Unetched sample, (b) after light etching.

## 11.8 Summary

Granular bainite is basically ordinary bainite generated by continuous cooling transformation of low-carbon steels. The mechanism of inverse bainite is unclear, but it involves the formation of cementite as the primary phase. It is not clear whether the ferrite, when it eventually forms and engulfs the cementite, forms by a reconstructive or displacive mechanism.

Whilst there is some doubt about the mechanism of inverse bainite, the terms columnar- and pearlitic-bainite are undoubtedly misnomers and are best avoided. Columnar bainite is simply an aggregate of cementite and ferrite which grows by a reconstructive transformation mechanism. Pearlitic bainite is simply a crystallographically faceted alloy pearlite.

At high supersaturations, arrays of lower bainite sub-units can rapidly decorate the austenite grain surfaces, giving the appearance of allotriomorphs. This “grain boundary lower bainite” is much harder than allotriomorphic ferrite, and hence is easily distinguished.

That the interpretation of structure can be misleading if the focus is simply on observations using optical microscopy is illustrated by the spiky pearlite. There is no surface relief produced even though the structure at low resolutions looks like bainite. The occurrence of spiky pearlite, associated with the breakdown of cooperative growth, is probably a consequence of the disproportionate increase in the growth rate of ferrite relative to that of cementite..

## CHAPTER 12

---

# MECHANICAL PROPERTIES

---

### 12.1 General Introduction

Many years elapsed after the work of Davenport and Bain before the commercial exploitation of bainitic steels. There were difficulties in obtaining fully bainitic microstructures in sizeable samples of steel. It has long been recognised that the influence of bainite on the mechanical behaviour of a steel is difficult to understand because of the inability to attain fully bainitic microstructures at all transformation temperatures, a consequence of the incomplete reaction phenomenon (Hehemann et al., 1957). Isothermal transformation to bainite was considered impractical on a commercial scale, continuous cooling being the preferred heat treatment. Furthermore, continuous cooling at a rate greater than  $\approx 50 \text{ }^\circ\text{C s}^{-1}$  during transformation was also believed impractical. In these circumstances, lean steels gave mixed microstructures of allotriomorphic ferrite and bainite, whereas richly alloyed steels transformed only partly to bainite, the remaining microstructure consisting of martensite and retained austenite. It was not until low-alloy, low-carbon steels, containing small amounts of boron and molybdenum to suppress proeutectoid ferrite were developed that the potential for commercial exploitation became realistic (Irvine and Pickering, 1957).

Boron is effective in retarding proeutectoid ferrite formation but has a negligible effect on the bainite reaction, allowing bainitic microstructures to be obtained over a wider range of cooling rates. The segregation of boron to the austenite grain boundaries leads to a reduction in their energy, thereby making them less favourable as sites for the heterogeneous nucleation of ferrite. The reason why the effect is more pronounced for allotriomorphic

ferrite than for bainite has not been investigated, but it may be associated with the fact that for bainite, which grows in the form of sheaves of small platelets, the vast majority of platelets nucleate autocatalytically after the initial formation of some platelets at the austenite grain boundaries (Chapter 6). Boron thus increases the bainite hardenability. The level of other alloying additions can, in the presence of boron, be kept low enough to avoid the formation of martensite. Steels of typical composition Fe-0.0033B-0.52Mn-0.54Mo-0.11Si-0.10C wt% were found to yield fully bainitic microstructures with very little martensite during normalising (i.e. air cooling from the austenitising temperature), and permitted the characterisation of the mechanical properties of bainite in isolation.

Many investigations of the mechanical properties fail to recognise that the microstructures studied were not fully bainitic. In the discussion that follows, attention is restricted to cases where the microstructure has been characterised thoroughly, and where it plays a significant role in determining the mechanical properties.

## 12.2 The Strength of Bainite

The strength of bainite can in principle be factorised into components consisting of the intrinsic strength of pure annealed iron ( $\sigma_{Fe}$ ), substitutional solid solution strengthening contributions ( $\sigma_{SS}$ ), strengthening due to carbon in solid solution ( $\sigma_C$ ), and a variety of microstructural components including dislocation strengthening, particle effects and grain size effects. Thus,

$$\sigma = \sigma_{Fe} + \sum_i \sigma_{SS}^i + \sigma_C + k_\epsilon(\bar{L}_3)^{-1} + k_P\Delta^{-1} + C_{10}\rho_d^{0.5} \quad (12.1)$$

where  $\rho_d$  is the dislocation density and  $\Delta$  the average distance between a cementite particle and its two or three nearest neighbours. From measurements done on martensite,  $k_\epsilon$  is approximately 115 MPa m; assuming that the cementite particles are spherical and of a uniform size,  $k_P$  is given approximately by  $0.52 V_\theta$  MPa m, where  $V_\theta$  is the volume fraction of cementite (Daigne et al., 1982). Dislocation theory for body-centred cubic metals gives  $C_{10} = 0.38\mu b \approx 7.34$  Pa m (Keh and Weissmann, 1963). The carbon and substitutional solutes are listed separately because their solid solution strengthening contributions vary differently with concentration. For carbon, the strengthening varies with the square root of concentration (Speich and Warlimont, 1968; Christian, 1971), whereas for the substitutional solutes there is a direct relationship (Leslie, 1982). Equation 12.1 illustrates the form of the relationships, it is in practice difficult to decipher the microstructural contributions because parameters such as grain size and particle spacing cannot be varied independently. Fig. 12.1 illustrates the magnitudes of the terms involved, together with some typical data for a fully bainitic microstructure.

Equation 12.1 assumes that the different contributions can be added linearly; others indicate non-linear summations,  $\sigma^{C_{13}} = \sum \sigma_i^{C_{13}}$ , where  $C_{13}$  is essentially a fitting constant (Kendig and Miracle, 2002; Schänzer and Nembach, 1992). The correct method for the simple summation procedures is obviously not clear, but it can be demonstrated that linear addition sometimes leads to grossly exaggerated strength values (Hasan et al., 2014). It is possible that the problems arise because the components of strength are not independent.

### 12.2.1 Hardness

The hardness of bainite increases linearly with carbon concentration, by approximately 190 HV per wt% (Irvine and Pickering, 1965). This contrasts with a change of about

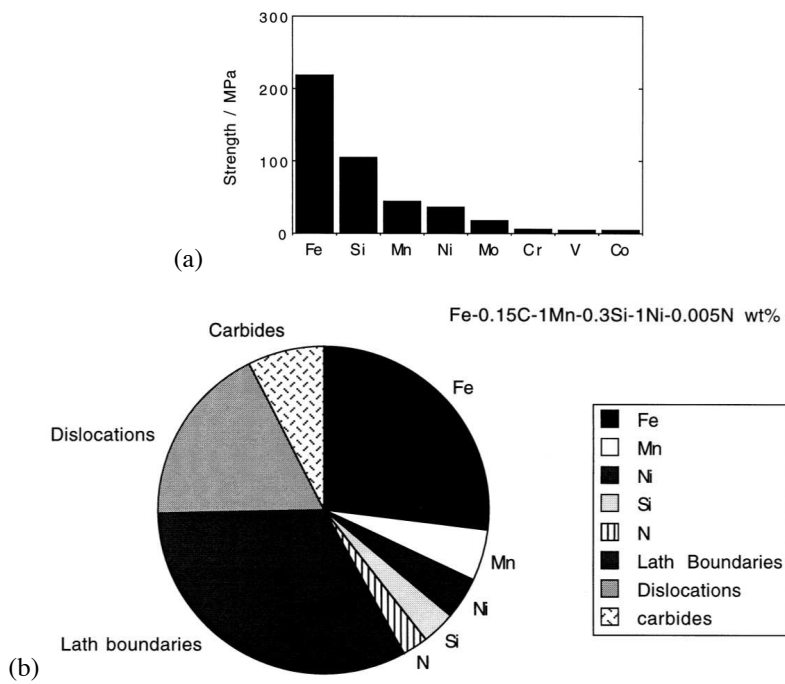


**Figure 12.1** The tensile yield strength of bainite at 25 °C and a strain rate of 0.0025 s<sup>-1</sup>. (a) Typical solid solution strengthening contributions per wt% of solute in ferrite; the intrinsic strength of pure iron is also included - data from Leslie (1982). (b) Estimated contributions to the strength of a fully bainitic sample.

950 HV per wt% in the case of carbon-supersaturated martensite. The austenitising temperature does not influence the hardness unless it is not high enough to dissolve all the carbides (Irvine and Pickering, 1965). For mixed microstructures, the hardness depends on the transformation temperature and composition. This is because the stability of the residual austenite to martensitic transformation changes with its carbon concentration, the limiting value of which depends on the transformation temperature via the  $T_0'$  curve of the phase diagram.

Reconstructive transformations become incredibly slow below  $B_S$  in high-alloy steels. Hence, any austenite left untransformed during the bainite reaction either decomposes into untempered high-carbon martensite or is retained to ambient temperature. In low-alloy steels the residual austenite may transform into some form of degenerate pearlite. These secondary transformations have for a long time been known to influence the hardness of the microstructure. Lyman and Troiano (1946) found that for a series of Fe-Cr-C alloys the hardness for the 0.08 wt% C alloy was insensitive to the isothermal transformation temperature, Fig. 12.2. The low carbon concentration ensures that the microstructure is almost fully bainitic for all of the temperatures studied. This contrasts with higher carbon alloys, where the hardness first decreases as the transformation temperature is reduced; this is because the fraction of bainite increases at the expense of residual phases like martensite and degenerate pearlite.<sup>1</sup>

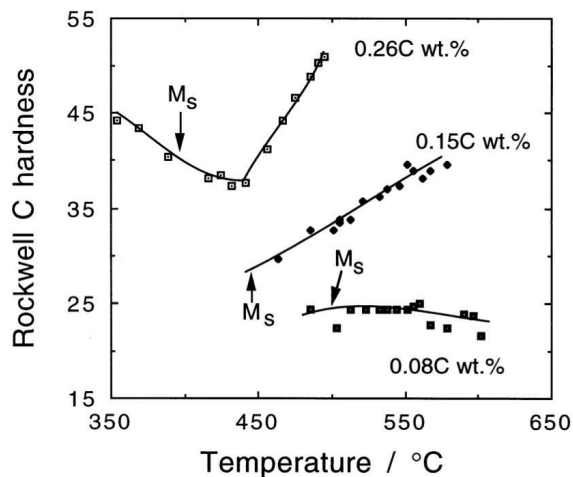


**Figure 12.2** Variation in hardness as a function of the isothermal transformation temperature. After Lyman and Troiano (1946).

The *microhardness* of bainite, in a mixed microstructure of bainite and pearlite obtained by isothermal transformation, is found to be less than that of the pearlite, Fig. 12.3. This remains the case even when the pearlite and bainite have been generated at the same temperature. This behaviour is easy to explain once it is realised that the pearlite grows from *carbon-enriched* austenite and hence contains a much larger fraction of cementite than the bainite. For the same reason, and because martensite contains carbon in solid solution, the martensite in a mixture with bainite must always be harder. With the advent of rapid

<sup>1</sup>This happens even though the dislocation density of bainitic ferrite increases as the transformation temperature decreases (Smith, 1984). The reduction in the quantity of hard phases (martensite, pearlite) compensates for the increase in dislocation density.

and automated microhardness measuring instruments, this knowledge has been exploited to map the distribution of phases in mixed microstructures (Naderi et al., 2008).

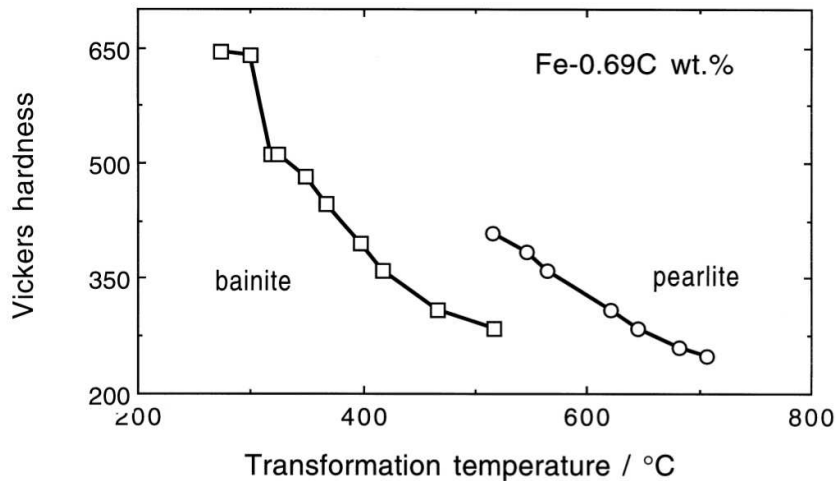


**Figure 12.3** Microhardness data from plain carbon steels transformed isothermally to a mixture of bainite and pearlite - after Ohmori and Honeycombe (1971).

The hardness of bainite is insensitive to the austenite grain size, even though the latter influences the bainite sheaf thickness (Kamada et al., 1976). This is expected since the bainite sub-unit size is hardly influenced by the austenite grain size (Chapter 2). Since the sub-units are much smaller they exert an overriding influence on strength. For the same reason, the hardness of fully bainitic microstructures is not sensitive to the austenitising temperature (Irvine and Pickering, 1965; Kamada et al., 1976).

### 12.2.2 Tensile Strength

Although there is evidence that bainitic ferrite retains an excess concentration of carbon even after annealing (Chapter 2), there must exist a proportion of dislocations that are mobile. Sharp yield points are not observed during tensile tests. The main effect of carbon on strength is through carbide precipitation. Cementite is the most common carbide; it precipitates in a coarse form without substantial coherency strains. Matrix dislocations have to bypass the cementite particles because they are unable to cut through them. It follows that the effect of carbon on the strength of bainite is rather small, approximately 400 MPa per wt% of carbon (Irvine et al., 1957b).

Plates of bainitic ferrite are typically 10  $\mu\text{m}$  in length and about 0.2  $\mu\text{m}$  in thickness. This gives a small mean free path for dislocation glide because the probability of the slip parallel to the plate is small. The effective grain size of the plate is then about twice the plate thickness. It is not surprising that the main microstructural contribution to the strength of bainite is from its fine grain size (Irvine et al., 1957b).

There have been many attempts at an analysis of the grain size contribution to the strength of bainite, most of them being based on the Hall-Petch relationship. This predicts a linear relationship between the strength and the reciprocal of the square root of the grain size. Although most data on bainite can be fitted to the Hall-Petch relation with

$\sigma_y \propto (\bar{L})^{-1/2}$  (Siriwardene, 1955; Pickering, 1967b), the results are difficult to interpret because the platelet size cannot be altered without influencing other variables such as the dislocation density and the number density of carbide particles.

The Hall-Petch relationship relies on a description of macroscopic yielding in which a dislocation pile-up generates a large enough stress concentration to stimulate a dislocation source in an adjacent grain, thereby transmitting deformation across grains. If the grain size is large, then the number of dislocations that can participate in the pile-up increases. The larger stress field of the pile-up makes it easier to stimulate distant sources, thereby leading to a reduction in the yield strength.

This is an unlikely description of events when the grain size is fine. The slip plane dimensions become too small to allow the existence of pile-ups. Yielding is then determined by the stress necessary to expand a dislocation loop across a slip plane (Langford and Cohen, 1969, 1970, 1975). The yield stress in these circumstances varies as the inverse of the grain size,  $\sigma_y \propto (\bar{L})^{-1}$ . The strength of heavily cold-deformed iron and of martensitic samples has been interpreted using such a relationship (Langford and Cohen, 1969, 1970, 1975; Naylor, 1979; Daigne et al., 1982). The changeover from the Hall-Petch to the Langford-Cohen relation should occur when the slip plane dimensions become  $\approx 1 \mu\text{m}$ . An analysis using electron back-scatter diffraction and orientation imaging confirms the inverse dependence of the yield strength on plate size; the steel used had such a low carbon concentration that fully bainitic microstructures were apparently obtained, and even small misorientations between laths contributed to the overall strength (Zhu et al., 2010).

An attempt has been made to separate the effect of bainite grain size and particle strengthening using multiple regression analysis (Gladman, 1972). The results indicate that carbides do not contribute much to the strength of bainite. This probably is a reasonable conclusion, but it has been pointed out that the analysis includes empirical constants which are difficult to justify (Honeycombe and Pickering, 1972).

### 12.2.3 Effect of Austenite Grain Size

We have seen already that the hardness of bainite is insensitive to the austenite grain structure. There have, nevertheless, been many investigations on the role of the austenite grain size and the bainite packet (sheaf) size on the strength. Both of these features are much coarser than the lath size which is probably the parameter with the greatest influence on flow stress. Published plots showing a Hall-Petch dependence of strength on austenite grain size or bainite packet size are probably fortuitous. Experiments have demonstrated that for martensite, the strength does not depend on the austenite grain size in low carbon steels (Brownrigg, 1973). Whether this applies to bainite depends on the effectiveness of the low-misorientation boundaries that exist between neighbouring platelets within a sheaf, in hindering dislocation motion. If there are films of austenite, or carbides separating the platelets within a sheaf, then they should be much more formidable barriers than implied by the small crystallographic misorientations between the sub-units. Since this is the case for most bainitic steels, it is unlikely that the austenite grain size or the packet size have any significant effect on strength.

### 12.2.4 Effect of Tempering on Strength

The hardness and tensile strength of fully bainitic microstructures decrease during tempering, the rate of change being larger for lower bainite, which has a higher starting hardness. As might be expected, it is the highest strength steels which undergo the largest changes

in strength during tempering (Bush and Kelly, 1971). After all, low-strength steels are not much stronger than the strength of the fully tempered microstructure.

The strength at any stage of tempering correlates well with the interparticle spacing, irrespective of the thermal history of the bainite (Deep and Williams, 1975). However, the grain size, particle size and distribution and dislocation density are not independent parameters. For example, studies using low carbon bainitic steels have established that the combined strengthening effects of dislocation density and the ultrafine bainitic ferrite grain size are substantial (McEvily and Magee, 1968). The yield strength is reduced when the microstructure contains retained austenite; apart from being a soft phase, austenite can undergo martensitic transformation under the influence small applied stresses. Tempering at temperatures as high as 540 °C does not lead to the expected reduction in yield strength, because the general softening of the microstructure is compensated by the removal of the soft austenite which decomposes into a harder mixture of ferrite and carbides (Kalish et al., 1965).

There are interesting empirical relationships between strength and transformation characteristics, particularly for low carbon, low alloy, fully bainitic steels. Irvine et al. (1957b) found a negative linear correlation between tensile strength and the “temperature of maximum rate of transformation”, indicating that the alloying element effect on strength can be rationalised simply on the basis of transformation kinetics (Fig. 12.4). For similar steels, the tensile strength is also found to correlate with the  $B_S$  temperature (Coldren et al., 1969). These results may be explained qualitatively: the bainite obtained at lower transformation temperatures should have a finer plate size and a larger dislocation density.

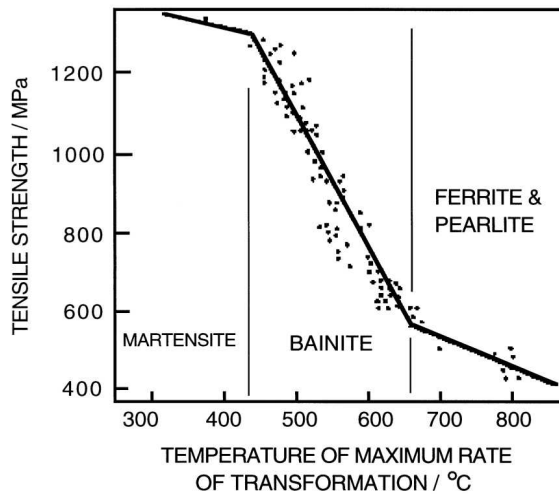


**Figure 12.4** Variation in the tensile strength of structural steels as a function of the temperature at which the rate of transformation is greatest during continuous cooling heat treatment (Irvine et al., 1957b).

### 12.2.5 The Strength Differential Effect

Plastic deformation in metals becomes easier when the sense of the deformation is suddenly reversed. Thus, when the loading is changed from compression to tension (or vice versa), the deformation occurs more easily than would have been the case had it continued in the compressive mode. This is called the *Bauschinger effect*. A simple explanation is

that deformation creates reversible features such as dislocation pile-ups, which relax and hence aid flow in the reverse direction when the sense of the load is changed. The effect therefore becomes less prominent as the total plastic strain increases, since the general build up in defect density makes it difficult for relaxation to occur.

Careful experiments on steels containing either martensite, bainite or Widmanstätten ferrite show that they have a higher yield stress in compression than in tension. This *strength differential effect* (Rauch and Leslie, 1972) persists even at large plastic strains, is independent of the starting sense of the deformation, and is not influenced by cyclic prestraining. It is believed to be associated with microstructures containing a large density of dislocations. It is not, for example, found in annealed ferrite or in ferrite-pearlite mixtures (Leslie, 1982). It has been shown to be inconsistent with an internally induced Bauschinger effect. Since the elastic modulus is similar in both tension and compression, the results cannot be explained in terms of the opening of microcracks during tension but not in compression (Rauch and Leslie, 1972).

There is no complete explanation for the phenomenon (Kennon, 1974), but it may be related to the presence of a nonlinear elastic interaction between dislocations and interstitial carbon atoms, the interaction being asymmetric in tension and compression (Hirth and Cohen, 1970). But it is not clear why the effect should be confined to microstructures with large dislocation densities.

### 12.2.6 Temperature Dependence of Strength

With the exception of creep-resistant alloys, most bainitic steels are used at ambient temperature. However, austempered ductile cast irons, which have a microstructure which is a mixture of graphite, bainitic ferrite, martensite and retained austenite, have found applications in automobile engines where the operating temperature might reach 400–600 K. The strength of the iron hardly changes with temperature up to about 550 K; deformation is resisted by strain ageing due to interstitial carbon atoms in the bainitic ferrite (Shieh et al., 1993, 1995). Serrated stress-strain curves are observed during deformation at higher temperatures, consistent with the classical Portevin-Le Chatelier effect. Thus, the solute atoms are sufficiently mobile to migrate to moving dislocations, which then have to break away, the process repeating during the test. The serrations disappear at even higher temperatures where the carbon can diffuse fast enough to migrate with the dislocation.

### 12.3 Ratio of Proof Stress to Ultimate Tensile Strength

If a material does not exhibit a sharp yield point then it is necessary to define a proof stress corresponding to a specified amount of plastic strain (usually 0.2%). The strain rate of the test should also be defined but this is usually neglected because for steels there is only a 10% increase in the flow stress with an order of magnitude change in strain rate (Knott, 1981). Sharp yield points are not observed in stress-strain curves of bainite so it is usual to specify yielding in terms of a proof stress. The proof-stress to UTS ratio increases as dislocation motion becomes more difficult at lower temperatures, typically from about  $0.67 \rightarrow 0.80$  over the range  $300 \rightarrow 70$  K (Krishnadev and Ghosh, 1979).

It is desirable in high-strength steels to have a proof-stress to UTS ratio,  $r_1$ , which is less than about 0.8. This helps to ensure that there is substantial plastic deformation prior to ductile fracture. A small value of  $r_1$  in many cases correlates with good fatigue resistance. The disadvantage is that the value of the stress that can be used in design is

reduced. Unfortunately, many bainitic steels have  $r_1$  values much smaller than 0.8 even though the UTS may be large (Irvine and Pickering, 1965). The internal strains caused by the displacive transformation and the resultant mobile dislocations ensure a low proof stress. Tempering of bainite at 400 °C has only a minor effect on the microstructure but its recovery raises  $r_1$ .

The gradual yielding behaviour sometimes persists after stress-relief heat-treatments. The microstructure of bainite is heterogeneous, with fine carbide particles which concentrate stress and hence lead to gradual yielding. There is also a variety of obstacles to dislocation motion (solute atoms, precipitates of different sizes, boundaries), each with a different ability to obstruct plastic deformation. Many of the obstacles are not uniformly distributed so there will exist obstacle-free areas into which dislocations can penetrate at low stresses, thus giving rise to a gradual deviation from elastic deformation (Kettunen and Kocks, 1972; Kettunen and Lepistö, 1976).<sup>2</sup>

Another scale of heterogeneity can arise when a large fraction of a phase harder or softer than bainite is included in the microstructure (Hehemann et al., 1957). Plastic deformation at first focuses in the softer phase whose yield strength is effectively reduced (Tomota et al., 1976). The hard phase only begins to deform when the softer phase has strain hardened sufficiently to transfer load. Small values of  $r_1$  for so-called bainitic steels can frequently be explained by the presence of martensite, or retained austenite in the predominantly bainitic microstructure (Coldren et al., 1969). In particular, bainitic steels with austenite yield gradually and hence fail to meet some established industrial specifications which are based on steels with sharp yield points. The specifications need to be modernised to allow for gradual yielding, given that the microstructure strain hardens rapidly, meeting any ultimate strength requirements with ease. It is not surprising in the light of this discussion, that low values of  $r_1$  correlate with large amounts of retained austenite in the microstructure, Fig. 12.5.

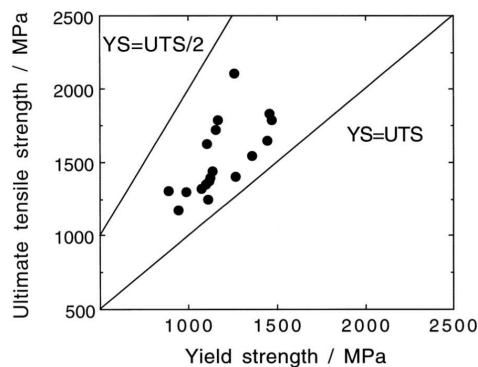


**Figure 12.5** The relationship between the ultimate tensile strength (UTS) and yield strength (YS) in steels with a mixed microstructure of bainitic ferrite, carbon-enriched retained austenite and some martensite (Sandvik and Nevalainen, 1981).

<sup>2</sup>The deformation behaviour of a microstructure as complex as that of bainite is qualitatively consistent with the statistical theory of slip (Kocks, 1966). In this, a crystal is assumed to contain a random distribution of obstacles of differing strength. Dislocations have a finite probability of overcoming obstacles even when the applied stress  $\sigma$  is below the macroscopic yield stress  $\sigma_y$ . The mean free slip area  $A_s$  for dislocation glide varies with  $\sigma/\sigma_y$  and when dislocations can sweep right across the specimen,  $\sigma = \sigma_y$ .

Retained austenite can in part be transformed into martensite by refrigeration in liquid nitrogen or by tempering the steel to form ferrite and carbides.<sup>3</sup> The reduction in austenite content can boost the yield strength without much of a change in the UTS because the retained austenite is in any case reduced by deformation-induced martensitic transformation in the early stages of testing (Kalish et al., 1965). Severe tempering that completely eliminates the austenite does lead to a reduction in strength and a noticeably lower work hardening rate, as illustrated in Fig. 12.6.

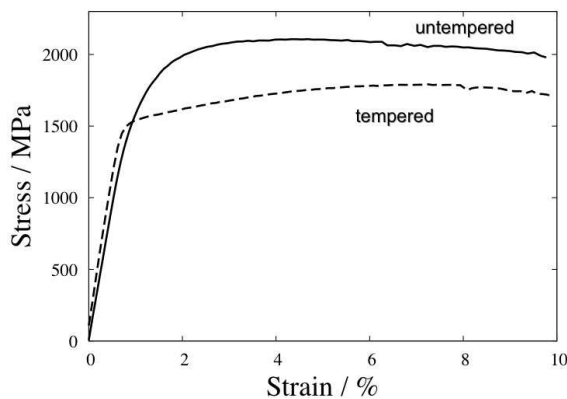


**Figure 12.6** Tensile test data from untempered nanostructured bainite containing 21% retained austenite and after tempering at 500 °C for 24 h to eliminate the austenite. After Hasan et al. (2014).

Gradual yielding is advantageous in forming operations where it helps to avoid “stretcher strains”. These represent Lüders fronts between yielded and unyielded metal. Dual-phase steels are designed to take advantage of the gradual yielding associated with mechanically heterogeneous microstructures. They consist of mixtures of soft proeutectoid ferrite and a hard phase which may be bainite, martensite or indeed, a mixture of three phases.

However, it has been found that intercritically annealed steels containing allotriomorphic ferrite and bainite produced by isothermal transformation can cause discontinuous yielding behaviour because the ferrite strain-ages at the temperature where bainite forms (Krauss and Matlock, 1988). The ageing occurs because of the difference in the solubility of interstitials, between the intercritical annealing temperature and the bainite transformation temperature. It may therefore be possible to avoid quench ageing by generating the required microstructure using continuous cooling heat treatment, thus allowing the interstitials to equilibrate during cooling.

Choi et al. have also shown that discontinuous yielding can be avoided if the hard phase is a mixture of bainite and martensite. This is because the latter forms during cooling from the isothermal transformation temperature and generates fresh interstitial-free dislocations allowing the gradual yielding behaviour to be recovered; similar dislocations are generated if retained austenite in the microstructure undergoes strain-induced transformation into martensite (Rao and Rashid, 1983).

Bainitic dual phase steels are weaker than those containing martensite and they have a larger  $r_1$  ratio; however, they have the advantage of better ductility, formability and fatigue strength (Sudo et al., 1982; Sudo and Iwai, 1983; Kumar et al., 2008). It follows that  $r_1$  is not always a reliable indicator of fatigue performance. There are contradictory results

<sup>3</sup>The liquid nitrogen treatment is less effective when the retained austenite is rich in carbon, as in TRIP-assisted steels, whereas the tempering can cause dramatic changes in the austenite content (Shi et al., 2008)

when the comparison is against normal TRIP-assisted steels that exhibit a greater capacity to work harden (Cai et al., 2011).

The required magnitude of the proof-stress/UTS ratio must be assessed for each application. For pipe-line alloys which are low-carbon bainitic steels, used for the conveyance of oil or gas under pressure, the fabricated pipe is hydrotested prior to service. This involves pressurisation to 125% of the planned operating pressure. If the value of  $r_1$  is too low, there is a possibility of gross plastic deformation with failure during hydrotesting. It is common therefore to specify a minimum value of  $r_1$  which is in the range 0.85-0.90 (Jones and Johnson, 1983). On the other hand, steel columns used in the construction of buildings in earthquake areas are required to absorb energy without failure; a low  $r_1$  value is then an advantage. One difficulty is that the pipe-coating treatment exposes the steel to temperatures of the order of 220 °C for sufficient time to permit interstitial elements to migrate to dislocations and pin them, leading to an increase in  $r_1$  (Duan et al., 2008), an increase that may be unacceptable in the case of strong pipe steels.

## 12.4 Ductility

It was noticed as early as 1957 by Irvine and Pickering, that low-carbon bainitic or martensitic steels always show superior tensile ductility when compared with their high-carbon counterparts, even when the comparison is made at identical strength. Their subsequent work (1965) confirmed that ductility can be improved by reducing the carbon concentration of a fully bainitic microstructure while maintaining its strength using substitutional solid solution strengthening.

Ductile fracture in good quality commercial steels which do not contain many nonmetallic inclusions propagates via the nucleation, growth and coalescence of voids. Macroscopic fracture occurs when the voids link on a large enough scale. If the number density of voids is large, then their mean separation is reduced and coalescence occurs rapidly, giving very little plastic deformation before fracture, i.e. a small overall ductility (Fig. 12.7). The number of carbide particles per unit volume increases with the carbon concentration of bainitic steels (Pickering, 1958). It is these carbides which are responsible for void nucleation in clean steels, so it follows that ductility must decrease with increasing carbon concentration even if the strength remains constant or decreases (Bhadeshia and Edmonds, 1983a,b).<sup>4</sup> The morphology of any cementite has an influence on the development of fracture - long, thin carbides are more susceptible to cracking under applied stress (Stokes et al., 2005).

In steels which do not transform completely to bainite, ductile void formation initiates at the hard regions of untempered martensite which result from transformation of carbon-enriched residual austenite (McCutcheon et al., 1976). Presumably, the brittle failure of martensite provides the nuclei for void growth. This is why the elongation of fully bainitic low-carbon steels is always better than that of tempered martensite of the same strength whereas the situation reverses when the comparison is made at high carbon concentrations (Irvine and Pickering, 1965). It is more difficult to obtain fully bainitic microstructures free from untempered martensite when the carbon concentration is large.

<sup>4</sup>The term *clean* implies the absence of nonmetallic inclusions of a size larger than cementite particles. High-carbon steels, where the cementite particle size may be expected to be large, can be air-melted, and yet be classified as clean. For low-carbon bainitic steels, significant differences in toughness are obtained for the air-melted and vacuum-refined conditions (McEvily and Magee, 1968), so that only the latter can be considered clean.

The linking of voids is associated with internal necking between adjacent voids. Since the necking instability depends on the rate of work hardening, the ductility should decrease if the work hardening rate is small. Experimental results do not bear this out. Deep and Williams (1975) have shown that tempered upper bainite strain hardens more rapidly than tempered lower bainite. And yet, the two microstructures have identical ductilities even when the interparticle spacing and mean carbide size are kept constant. Thus, the effect of work hardening, and indeed of the yield stress, on the ductile failure of bainitic steels is not yet understood.

Ductility trends as indicated by elongation data are inconsistent with reduction of area measurements. Martensitic steels almost always have larger reductions of area in tensile tests against comparable bainitic steels.

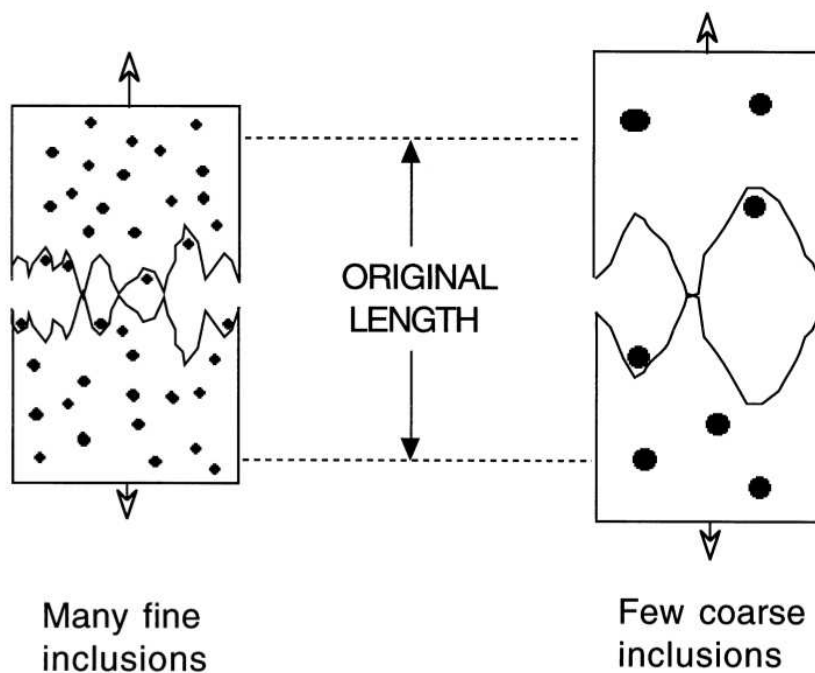


**Figure 12.7** An illustration of how a large density of void nucleating particles can result in fracture with a low overall ductility, even though the material fails by gross plastic deformation on a microscopic scale.

#### 12.4.1 Ductility: The Role of Retained Austenite

Retained austenite itself is a ductile phase but the fact that it can transform into martensite during deformation can alter the mechanical behaviour of the microstructure as a whole. Fully austenitic TRIP (transformation-induced plasticity) steels achieve a high work-hardening rate through the generation of martensite during deformation (Zackay et al., 1967), thus delaying the onset of necking during tensile testing. The martensite contributes to hardening by its very presence as a hard phase. However, there is a tendency

at low strains for favourably oriented martensite plates to form; this compliance of the transformation with the applied stress results in a softening effect (Olson and Azrin, 1978).

There are, naturally, complications when the austenite is present in a mixed microstructure. Both the total elongation, and its uniform component, reach a maximum as a function of the fraction of retained austenite, when the latter is varied by altering the degree of isothermal transformation to bainitic ferrite (Sandvik and Nevalainen, 1981). The difference between the uniform and total elongation decreases as an optimum volume of retained austenite is reached. Further increases in retained austenite content are associated with tensile failure before necking so the difference between uniform and total elongation vanishes.

The best elongation is observed when the retained austenite is present mainly in the form of films between the sub-units of bainite, rather than as blocks between sheaves (Sandvik and Nevalainen, 1981). The optimum austenite content increases as the transformation temperature decreases; this is because a finer microstructure incorporates more of the austenite in film form. For the same reason, elongation becomes less sensitive to retained austenite content as the transformation temperature is reduced. Retained austenite clearly can enhance ductility by transforming and hence reinforcing regions where stress concentrations develop. However, the toughness can be reduced because the untempered martensite produced can crack and hence initiate failure (Jacques et al., 2001a).

It must be emphasised that all these results have yet to be interpreted quantitatively. Changes in retained austenite content cannot easily be made without altering other factors such as the tensile strength and the distribution of the austenite. For example, Miihkinen and Edmonds (1987c) demonstrated a monotonic increase in the uniform and total ductility with retained austenite content.

## 12.5 Impact Toughness

The concept of toughness as a measure of the energy absorbed during fracture is well-developed. It is often measured using notched-bar impact tests of which the most common is the Charpy test. A square section notched bar is fractured under specified conditions and the energy absorbed during fracture is taken as a measure of toughness. The notch is blunt; it concentrates stress thereby increasing plastic constraint so that brittle fracture becomes more likely. The tests are conducted over a range of temperatures, and a plot of the impact toughness versus temperature is called an impact transition curve, which has a sigmoidal shape (Fig. 12.8). The flat region of the curve at high temperatures is the *upper shelf* which represents ductile failure. The corresponding flat region at lower temperatures is called the *lower shelf* and represents cleavage failure. In between these is the transition region with mixed cleavage and ductile fracture; experimental data in this region generally exhibit the largest scatter. The impact transition temperature ( $T_t$ ) is usually defined that at which the fracture surface shows 50% cleavage fracture.

The idealised representation of the mechanism of failure by cleavage in the lower shelf region is not strictly correct. There is frequently a fraction of ductile failure, the extent of which determines the energy absorbed in the lower shelf region of the impact curve (Haušild et al., 2002).

The Charpy test is empirical in that the data cannot be used directly in engineering design. It does not provide the most searching mechanical conditions. The sample has a notch, but this is less potent than the atomically sharp crack. Although the test involves impact loading, there is a requirement to start a brittle crack from rest at the tip of the notch, suggesting that the test is optimistic in its comparison against a propagating brittle

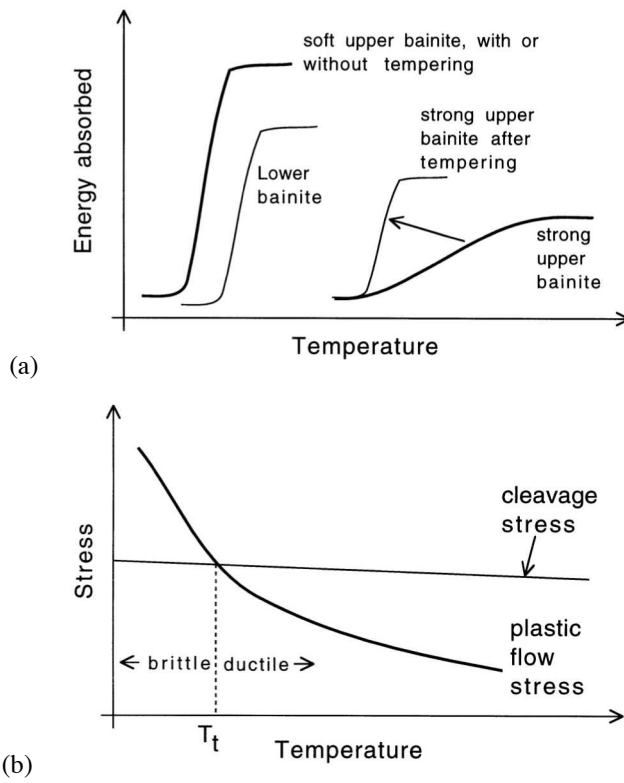


**Figure 12.8** Schematic illustration of impact transition curves (a) and of the cause of the ductile/brittle transition temperature (b) in body-centred cubic metals where the plastic flow stress is much more sensitive to temperature than the cleavage stress.

crack (Cottrell, 1995). Most materials can be assumed to contain sub-critical cracks so that the initiation of a crack seems seldom to be an issue.

The Charpy test is nevertheless a vital quality control measure which is specified widely in international standards and in the ranking of samples in research and development exercises. It is the most common first assessment of toughness and in this sense has a proven record of reliability. The test is usually carried out at a variety of temperatures in order to characterise the ductile-brittle transition intrinsic to body-centred cubic metals with their large Peierls barriers to dislocation motion. In such metals, the cleavage stress is insensitive to temperature, the stress required for plastic flow rises rapidly as the temperature decreases (Fig. 12.8). The increase in plastic flow stress is partly a consequence of the large Peierls barrier but also because of the ubiquitous presence of traces of interstitial elements which interact strongly with dislocation motion.

The curves representing the cleavage and flow stress cross at the transition temperature on a plot of stress versus temperature. Below  $T_t$ , cleavage is easier than plastic flow and vice versa. Any effect that raises the plastic yield stress (such as constraint caused by a notch) without influencing the nucleation or growth of cleavage cracks inevitably leads to an increase in  $T_t$ . Cleavage fracture is fast, occurs with little warning, absorbs minimal energy and is undesirable; a low transition temperature is therefore an important aim in safe design.

It is worth pointing out that the Charpy properties of impure, processed steels are rarely isotropic. Plastic deformation at high temperatures tends to elongate sulphides, giving higher toughness values when the Charpy specimens are machined parallel to the principal deformation direction (Tsunekage et al., 2001). Crystallographic textures induced by deformation may also give rise to the anisotropy of mechanical properties (Joo et al., 2012, 2013)

### 12.5.1 Fully Bainitic Structures

Irvine and Pickering (1963) conducted a major study of the Charpy impact properties of normalised low-carbon bainitic steels (typical composition Fe-0.003B-0.5Mn-0.5Mo-0.1C wt%). Their results are important and simple to interpret because the samples studied were free from proeutectoid ferrite and almost free of martensite.<sup>5</sup>

The impact properties of soft upper bainite were found not to be sensitive to tempering at temperatures as high as 925 K for 1 h, as long as the ferrite retained its plate shape. After all, the upper bainite was obtained by transformation at high temperatures where tempering occurs during transformation, so that imposed tempering has only minor further effects on the microstructure.

When strong upper bainite is obtained by transformation at lower temperatures,  $T_t$  increases but the upper shelf energy decreases. The ductile-brittle transition becomes less well-defined, the region of the impact curve between the upper and lower shelves extends over a larger temperature range (Fig. 12.8). This temperature range becomes narrower, and  $T_t$  and  $\sigma_y$  decrease, on tempering. The larger sensitivity to tempering is consistent with the lower degree of autotempering expected in bainite generated by transformation at low temperatures.

<sup>5</sup>It is the combination of low carbon and low substitutional solute concentration, the ease of cementite precipitation in these steels, and the continuous cooling heat treatment which allow the bainite reaction to consume all of the austenite.

Even higher strength can be obtained by transforming to lower bainite, which surprisingly has good toughness, comparable to the low strength upper bainite. This is because carbide particles in lower bainite are much finer than in upper bainite. Cementite is brittle and cracks under the influence of the stresses generated by dislocation pile-ups (Hahn et al., 1959). The crack may then propagate into the ferrite under appropriate conditions of stress and temperature. The cracks from fine cementite particles are smaller and hence more difficult to propagate into ferrite, which is the reason for the higher toughness of lower bainite when compared with upper bainite.

Consider a microcrack nucleus as a through thickness Griffith crack of length  $c$ . The cleavage stress  $\sigma_F$  is given (McMahon Jr. and Cohen, 1965) by:

$$\sigma_F = \left[ \frac{4E\sigma_p}{\pi(1-\nu^2)c} \right]^{\frac{1}{2}} \quad (12.2)$$

where  $E$  is the Young's modulus of ferrite,  $\nu$  is its Poisson's ratio and  $\sigma_p$  is the plastic work of fracture per unit area of crack surface, an effective surface energy. In bainitic steels,  $\sigma_p$  has been reported to be in the range 72-83 J m<sup>-2</sup> (Rancel et al., 2011). If  $c$  is now set equal to the carbide particle thickness  $c_o$ , then the fracture stress is found to vary as  $c_o^{-\frac{1}{2}}$ . The details of this relationship must of course vary with the shape of carbide particles but the general relationship between  $\sigma_F$  and  $c$  remains the same; for example, when considering mixtures of ferrite and spheroidal carbides, the stress  $\sigma_F$  necessary to propagate cleavage fracture through the ferrite has been shown to be given by (Curry and Knott, 1978):

$$\sigma_F = \left[ \frac{\pi E\sigma_p}{(1-\nu^2)c_d} \right]^{\frac{1}{2}} \quad (12.3)$$

where  $c_d$  is the diameter of the penny-shaped crack resulting from the cleavage of the spheroidal carbide particle.

The identification of the crack length  $c$  with the carbide particle thickness  $c_o$  is a vital assumption which can be justified experimentally for mild steels containing a microstructure of equiaxed ferrite and cementite particles. This is a carbide-controlled fracture mechanism, but the alternative possibility is a grain-size controlled fracture mechanism, in which the fracture stress is that required to propagate cleavage across grains. The parameter  $c$  must then be identified with a grain size dimension, and in the case of bainite, with a packet size. Brozzo et al. (1977) have demonstrated that for low-carbon bainitic steels (containing 0.025-0.50 C wt%) the covariant bainite packet size is the microstructural unit controlling cleavage resistance. It is nevertheless possible that the carbide size controls the cleavage fracture of high-carbon bainitic steels.

## 12.6 Fracture Mechanics Approach to Toughness

Most bainitic steels are used in high-strength applications and failure is not usually accompanied by a large amount of plasticity; they are in this sense "brittle" materials. It is therefore a good approximation to use elasticity theory to represent the stresses in the vicinity of a sharp crack, even though cleavage crack propagation in metals always involves a degree of plastic deformation at the crack tip. Making the further assumption of *linear* elasticity, we have the linear-elastic-fracture-mechanics (LEFM) approximation. One definition of a sharp crack is that the inevitable plastic zone at the crack tip is small enough to permit the LEFM approximation.

A fracture mechanics approach is more reliable than impact testing because a toughness value is obtained which is a material property, essentially independent of specimen geometry effects. The pre-cracked test samples and conditions such as the strain rate are similar to the conditions experienced during service. The results can be used quantitatively to predict whether a structure is likely to fail catastrophically under the influence of the design stress. There are excellent books and reviews on the subject but a brief introduction is necessary for an adequate discussion of the work on bainite.

Using LEFM, it is possible to show that when a uniaxial tensile stress  $\sigma$  is applied, the stress  $\sigma_r$  at a distance  $r$  ahead of a sharp crack tip is given by:

$$\sigma_r = K_I(2\pi r)^{-\frac{1}{2}} \quad (12.4)$$

where  $K_I$  is a stress intensification factor in mode I (tensile) loading.  $K_I$  is a function of the applied stress  $\sigma$  and of the specimen geometry:

$$K_I = \sigma Y\{c/W\} \quad (12.5)$$

where  $Y$  is a compliance function which depends on the crack length  $c$  and on the specimen width  $W$ . For a body of infinite extent, containing a central through-thickness crack of length  $2c$ , normal to  $\sigma$ ,  $Y = (\pi c)^{\frac{1}{2}}$ . For brittle materials,  $K_I$  at fracture takes a unique *critical* value  $K_{IC}$ . The latter is then independent of  $W$  or other dimensional variables; it is a material constant which can be used to design against catastrophic failure in service.

### 12.6.1 Microstructural Interpretation of fracture toughness

In considering the role of microstructure in fracture, it is necessary to distinguish between “large” and “small” particles. With small particles, the phenomenon controlling fracture is the propagation of particle sized microcracks into the surrounding ferrite matrix. For larger particles the cracking of the particle represents the critical event, after which the crack propagates into the matrix and across grain boundaries (Burdekin, 1990). For the most part, high-strength steels such as bainitic or martensitic alloys should, if manufactured properly, lie in the small particle regime where we shall focus attention.

It is sometimes possible to relate  $K_{IC}$  values to microstructural and micromechanistic parameters. It can be argued that the critical value of stress intensity which leads to failure must be associated with corresponding critical values of stress  $\sigma_C$  and distance  $r_C$  (Knott and Cottrell, 1963; Knott, 1966; Ritchie et al., 1973; Knott, 1981):

$$K_{IC} = \sigma_C(2\pi r_C)^{\frac{1}{2}} \quad (12.6)$$

where  $\sigma_C$  is usually identified with  $\sigma_F$  (eq. 12.2), the local stress required to propagate a microcrack nucleus.  $\sigma_F$  varies with carbide thickness, or more generally, with the size of the microcrack nuclei resulting from the fracture of a brittle phase in the steel; it is relatively independent of temperature.

The interpretation of the distance  $r_C$  is less straightforward. The sample used in a fracture toughness test contains a machined notch, but to make the specimen representative of failure during service, it is fatigue loaded to form a sharp crack which grows slowly from the root of the notch. Fatigue loading is stopped as soon as a uniform crack front is established. The specimen is then ready for toughness testing. The fatigue crack tip is sharp, but not as sharp as the tip of a cleavage crack. It does not therefore propagate when the specimen is tensile loaded for the  $K_{IC}$  test. Instead, the stress field extending

from the fatigue crack tip causes brittle particles within a distance  $r_C$  of the tip to fracture. The resulting microcrack nuclei are atomically sharp and propagate into the matrix if the stress  $\sigma_C$  is exceeded. The cleavage cracks then link up with the original fatigue crack and failure occurs rapidly across the specimen section.

It is emphasised that both  $r_C$  and  $\sigma_C$  are for most materials, statistically averaged quantities, since all microstructural features exhibit variations in size, shape and distribution. If the carbide particle size and spatial distribution is bimodal, due perhaps to the presence of a mixture of microstructures, then the  $K_{IC}$  values obtained are likely to show much scatter. The stress field extending from the crack tip effectively samples a finite volume and it is the microstructure of that volume which determines toughness. Bowen and Knott (1986) found that  $K_{IC}$  values determined for mixed microstructures of upper and lower bainite (the former containing coarser cementite) exhibited a large degree of scatter when compared with a microstructure of just upper bainite or just martensite.

The microstructural interpretation of  $K_{IC}$  evidently requires a knowledge of a local tensile stress and a microstructural distance. This approach has been successful in explaining the toughness of mild steels with a microstructure of ferrite and grain boundary cementite (McMahon Jr. and Cohen, 1965; Smith, 1966; Knott, 1981) and to a limited extent of steel weld-deposits which have complex microstructures containing nonmetallic inclusions which initiate failure (Tweed and Knott, 1983; McRobie and Knott, 1985). In some of these cases, the critical microstructural features controlling cleavage fracture resistance have been identified directly, giving faith in the  $r_C$  concept.

Difficulties arise when attempts are made to use this approach for clean bainitic or martensitic structures. The carbides particles are so fine as to make a direct identification of  $r_C$  impossible. The fracture stress  $\sigma_F$  can nevertheless be measured and if it is shown to be constant, then  $\sigma_F$  itself can be used as a measure of "toughness" (Bowen and Knott, 1986), although it is not clear how possible variations in  $r_C$  can be accounted for. A constant  $\sigma_F$  indicates that the critical step in the fracture process is the propagation of a microscopic crack.

Bowen et al. used this approach, together with  $K_{IC}$  studies to explain the toughness of tempered martensite and bainite in a low-alloy steel. In all cases,  $K_{IC}$  values were found to increase with the test temperature over the range 77-300 K. For the same temperature range, the proof stress decreased with increasing temperature. For a given proof stress, the toughness of bainite was always lower than that of tempered martensite (Fig. 12.9). The fracture stress  $\sigma_F$  was in all cases found to be independent of test temperature, but bainite had a lower  $\sigma_F$  than martensite. The results were explained in terms of measured cementite particle size distributions, Fig. 12.9. They showed that it is not the mean carbide particle size which determines toughness, but the coarsest particles to be found in the microstructure. A plot of  $\sigma_F$  versus the reciprocal square root of the coarsest carbide thickness gave a straight line as predicted by the modified Griffith equation (equation 12.2); deviations from this equation occurred at small particle sizes. On this basis, for a given proof stress, the toughness is expected, and found, to increase in the order upper bainite, lower bainite and tempered martensite. Trends like this are also important in the design of welding processes and materials, and there are many qualitative results which confirm that the toughness increases in that order for microstructures in the heat affected zones of steel welds (Inagaki and Hiroyuki, 1984; Harrison and Farrar, 1989).

The reason why the modified Griffith equation fails at small particle sizes is not clear but it means that  $\sigma_F$  becomes relatively insensitive to carbide thickness when the latter is less than about 450 nm.

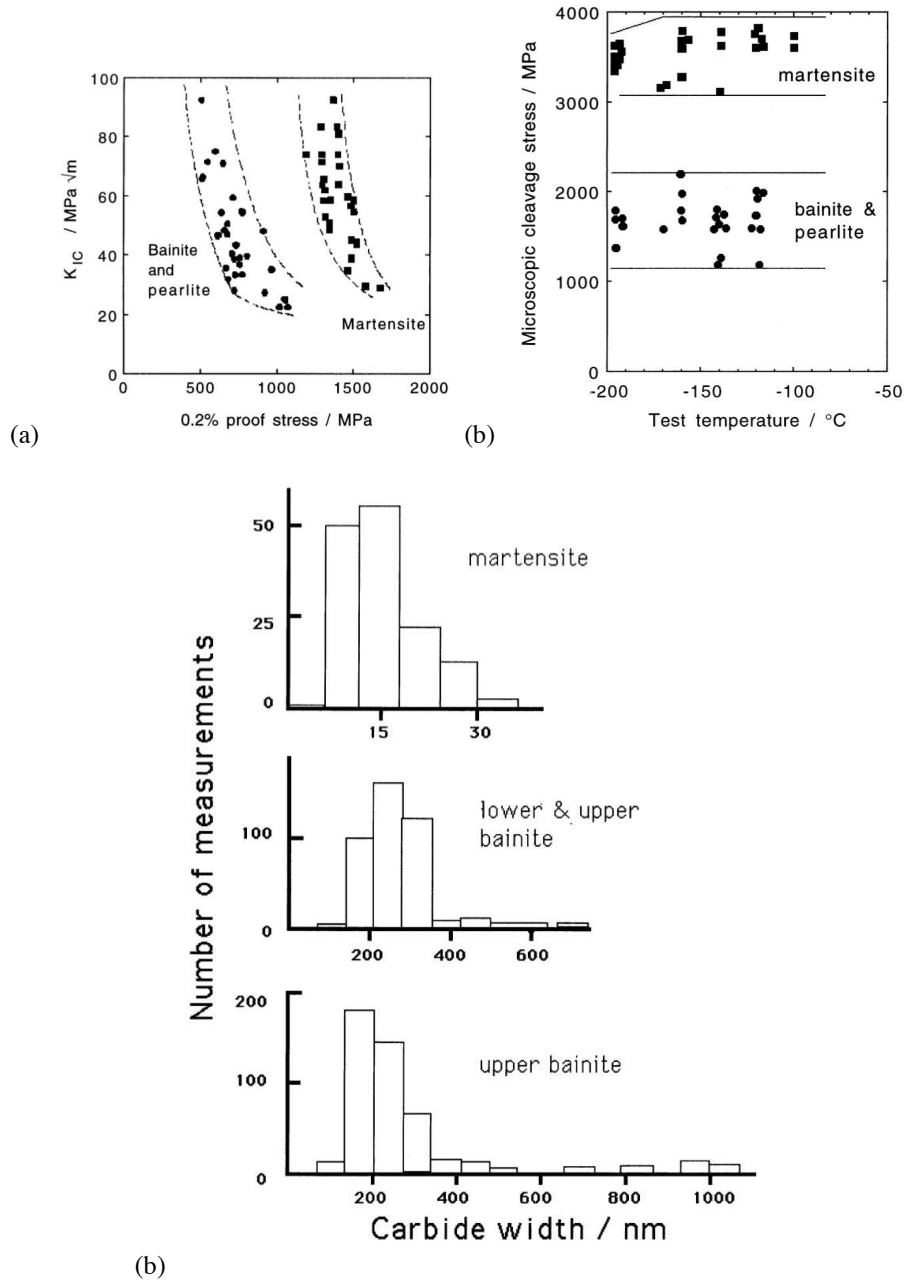


**Figure 12.9** (a)  $K_{IC}$  values plotted against corresponding values of the 0.2% proof stress. (b)  $\sigma_F$  values plotted against test temperature. (c) Carbide size distributions obtained from martensitic and bainitic microstructures – after Bowen and Knott (1986).

It must not be assumed that these results spell doom for bainitic microstructures; they need not always have poor toughness relative to tempered martensite. The size of bainitic carbides can be controlled using suitable alloying additions. Indeed, the carbides can be eliminated completely by adding sufficient Si or Al to the steel. The results are valid only for clean steels in which the fracture mechanism is carbide-nucleated and growth-controlled. That the coarseness of carbides controls the toughness of bainite in clean steels is emphasised by the observation that lower bainite with its finer carbides and higher strength nevertheless has a better toughness than the softer upper bainite. All other things being equal, toughness is expected to improve as the strength is reduced, making plastic deformation easy.

The micromechanistic model for the toughness of bainite contains the terms  $\sigma_C$  and  $r_C$ , the former defining the stress to propagate a microcrack in a cementite particle, and the latter the distance over which the stress is large enough to cause carbide cracking. The distance  $r_C$  is expected to be small in comparison with the width of a bainite sheaf, so the toughness of bainite or martensite should not be dependent on the austenite grain size or the bainite packet size. This prediction has been demonstrated to be the case for tempered martensite (Bowen and Knott, 1986) but contradictory results exist for bainite. Naylor and Krahe (1974) using notched-bar impact tests have shown that a refinement in the bainite packet size leads to an improvement in toughness. The impact transition temperature of bainitic steels is also found to decrease as the austenite grain size decreases (Fig. 12.10), although this might be because the packet size becomes finer at small austenite grain sizes. The austenite grain size in Irvine and Pickering's experiments was varied by controlling the temperature at which hot-rolling finished, or by reheating into the austenite phase field, before the steel was continuously cooled to bainite.

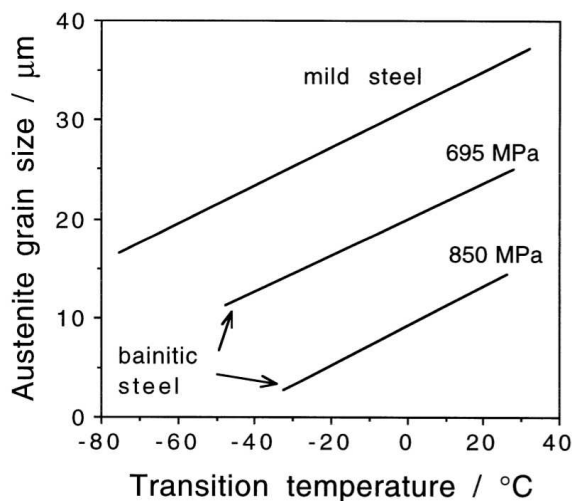


**Figure 12.10** Variation in the impact transition temperature as a function of the austenite grain size - after Irvine and Pickering (1963).

The fracture stress  $\sigma_F$  and the critical distance  $r_C$  do not vary much with temperature, although  $K_{IC}$  for bainite is found experimentally to increase as the test temperature rises. This apparent contradiction arises because of the LEFM approximation. In practice, the effect of temperature is to reduce the yield strength. The size of the plastic zone at the crack tip increases so that more work is done as the crack propagates, leading to an increase in  $K_{IC}$  (Ritchie et al., 1973).

Finally, it is worth noting that the austenite grain size cannot always be varied independently. Some carbides may not dissolve if the required grain size is achieved using a low austenitising temperature; these carbides can be detrimental to toughness (Tom, 1973). As the solubility of the carbides increases with austenitising temperature, so does the average carbon concentration in the austenite; more of the austenite is therefore retained to ambient temperature after partial transformation to martensite or bainite (Mendiratta et al., 1972; Kar et al., 1979). Variations in austenite grain size also influence hardenability; a fine grain structure can be detrimental if it causes the formation of transformation products such as allotriomorphic ferrite during cooling of a high strength steel (Parker and Zackay, 1975).

### 12.6.2 Cleavage Path and Crystallography

Groups of closely oriented grains fracture at a common cleavage front. Cracks are therefore able to propagate undeviated across packets of bainite plates (Pickering, 1967b).<sup>6</sup> Similar results have been reported for weld deposits, where cleavage has been shown to propagate undeflected across packets of bainite, reinitiating only at packet boundaries (Chandel et al., 1985). The size of cleavage facets associated with brittle fracture correlates well with the width of the packets (Naylor and Krahe, 1974), although there are results which indicate that the undeflected crack path is some 1.5 times larger than the width of bainite packets (Ohmori et al., 1974; Brozzo et al., 1977). This larger size occurs when adjacent packets, although in different orientation, nevertheless have their cleavage planes fairly parallel. The cleavage crack path can lie on  $\{1\ 1\ 0\}$ ,  $\{1\ 0\ 0\}$ ,  $\{1\ 1\ 2\}$  or  $\{1\ 2\ 3\}$  ferrite planes (Naylor and Krahe, 1975; Nohava et al., 2003). It has been demonstrated using orientation imaging microscopy that it is only when there is a large change in misorientation that cleavage cracks are deflected (Gourgues et al., 2000; Nohava et al., 2003; Lambert-Perlade et al., 2004b). In other words, it is the “crystallographic” packet size that determines toughness. Furthermore, the smaller the crystallographic grain size, the less is the effect of the presence of local brittle zones because cracks initiated in such zones will tend to be arrested at the large misorientation boundaries; these boundaries are even more effective at stopping the propagation of cracks at higher temperatures within the domain of toughness testing (Lambert-Perlade et al., 2004a).

It is worth emphasising that even similarly oriented bainite plates may be separated by carbides or austenite films. The appropriate grain size for strength calculations is therefore that of the individual platelets; dislocations cannot penetrate the intervening phases between the ferrite plates. Cleavage cracks are not however deflected by brittle cementite so the toughness will depend more on the crystallographic packet size.

The correlations between the cleavage facet size and packet size are for low-carbon, low-alloy steels where the fraction of bainitic ferrite that forms is large and that of cementite, martensite or retained austenite, small. The platelets of ferrite within a packet of bainite therefore touch each other at low misorientation boundaries over large areas, thus giving the crystallographic continuity essential for undeviated cleavage crack propagation. In richly-alloyed steels, the intervening layers of retained austenite may hinder the crack as it passes through a packet, but the exact mechanism is not yet understood.

<sup>6</sup>The terms *packet* and *sheaf* are used interchangeably. The former is conventional terminology in mechanical property studies.

### 12.6.3 Cleavage Crack Initiation

Non-metallic inclusions or small islands of hard martensite crack due to externally applied or internally generated stresses. The resulting stress concentration at the particle-matrix interface induces the crack to move into the surrounding matrix, thereby initiating cleavage fracture. Crack growth can be arrested if the bainite packets are sufficiently fine (Echeverria and Rodriguez-Ibabe, 2003; Lambert-Perlade et al., 2004b).

## 12.7 Temper Embrittlement

There are three kinds of embrittlement phenomena associated with quenched and tempered steels, each of which leads either to a minimum in the toughness as a function of tempering temperature, or to a reduction in the rate at which the toughness improves as the tempering temperature is increased:

### 12.7.1 650°C Reversible Temper Embrittlement

Tempering at temperatures around 650°C promotes the segregation of impurity elements such as phosphorus to the prior austenite grain boundaries, leading to intergranular failure along these boundaries. The reversibility arises because the impurity atmospheres at the grain boundaries can be evaporated by increasing the tempering temperature. Quenching from the higher temperature avoids the re-segregation of impurities during cooling, thus eliminating embrittlement.

In fact, one of the tests for the susceptibility of bainitic microstructures to impurity-controlled embrittlement involves a comparison of the toughness of samples which are water quenched from a high tempering temperature (680°C) with those cooled slowly to promote impurity segregation (Bodnar et al., 1989).

Studies of creep resistant bainitic steels show that phosphorus and tin, and to a lesser extent manganese and silicon, are all embrittling elements (Bodnar et al., 1989). Manganese is known to reduce intergranular fracture strength (Grabke et al., 1987). Silicon, on the other hand, enhances the segregation of phosphorus to the austenite grain boundaries (Smith et al., 1980), and can itself cosegregate with nickel to the grain surfaces (Olefjord, 1978). There are also smaller effects due to arsenic, antimony and sulphur. The tendency for embrittlement correlates strongly with an empirical “*J*” factor:

$$J = w_{Mn} + w_{Si} + 10^4 \times w_{(P+Sn)} \quad (12.7)$$

where the concentrations of elements are in weight percent Fig. 12.11.

To summarise, the impurity-controlled temper embrittlement occurs in bainite as it does in martensite; after all, neither of these transformation products traverse austenite grain surfaces and hence leave them open for impurity segregation. By comparison, reconstructive transformation products such as allotriomorphic ferrite, can grow across and consume the austenite grain surfaces, thereby removing them entirely from the final microstructure.

Finally, it is worth noting that although the science of the embrittlement is well understood, for reasons of cost, commercial steels always contain more impurities than is desirable. Steps must therefore be taken to mitigate the impurity effects. Molybdenum undoubtedly helps mitigate the embrittling effect of phosphorus and it is argued that there is an optimum concentration that is effective in doing so (Fig 12.12). It is used routinely in commercial steels for the specific purpose of eliminating grain boundary embrittlement

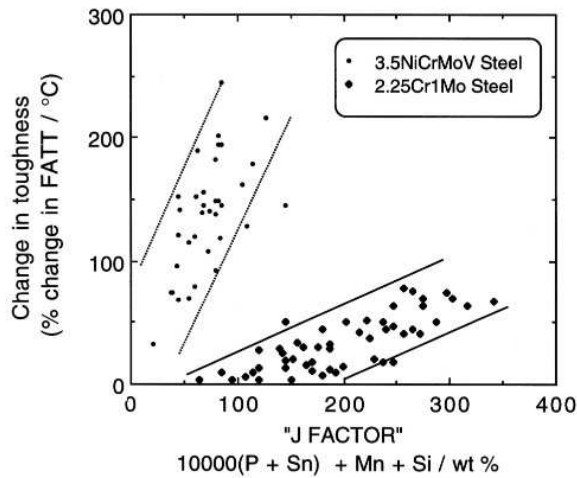


**Figure 12.11** Correlation between the tendency to embrittle and an empirical “*J*” factor which is a function of chemical composition (Watanabe and Murakami, 1981; Bodnar et al., 1989).

(Rose et al., 2014). Dissolved molybdenum is said to inhibit the segregation of phosphorus (scavenging), and that which segregates to boundaries acts by an unknown mechanism to improve the strength of the boundary in the presence of phosphorus (Dumoulin et al., 1980; Islam et al., 2005). Large concentrations of molybdenum become ineffective in steels due to the ready formation of molybdenum-rich carbides. The optimum concentration of Mo in the steel described in Fig. 12.12 is about 0.7 wt%, but this obviously must vary with the overall composition of the steel since the tendency to form carbides depends on the detailed constituents of the alloy (Guillou et al., 1981).

But the story is confused. Surprisingly, molybdenum in Fe-Mo-P alloys is found not to influence the grain boundary concentration of phosphorus (Grabke et al., 1987) and other experiments on steels also do not confirm a scavenging effect of molybdenum (Krauss and McMahan, Jr., 1992). It is suggested that in Fe-Mo-C-P alloys, the formation of molybdenum carbides results in phosphorus localisation in the vicinity of the particles, but this cannot be the full explanation because convincing accumulated experience suggests that molybdenum in solid solution dramatically reduces the tendency for failure at the austenite grain surfaces (Briant and Banerji, 1978; McMahan Jr. et al., 1977; Yu and McMahan Jr., 1980; Guillou et al., 1981). The efficacy of molybdenum additions to counter temper embrittlement is not therefore understood, nor that of vanadium in a similar vein. The subject has recently been reviewed (Bhadeshia and Suh, 2015).

### 12.7.2 300→350 °C Temper Embrittlement

Fracture is again intergranular with respect to the prior austenite grain boundaries which become decorated with coarse cementite particles during tempering. At the same time, the grain boundaries are weakened by impurity segregation. The cementite particles crack under the influence of an applied stress and in this process concentrate stress at the weakened boundaries. These factors combine to cause embrittlement.

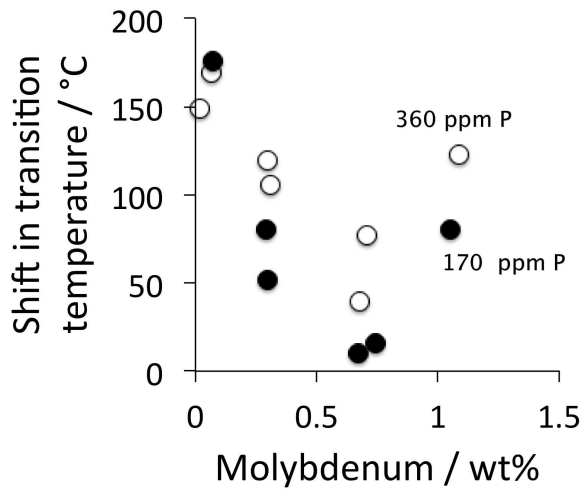


**Figure 12.12** The effect of molybdenum in a 2.25Cr steel containing phosphorus, on the change in the ductile-brittle transition temperature. After (Dumoulin et al., 1980).

### 12.7.3 300→350 °C Tempered-Martensite Embrittlement

This effect is common in clean steels, with fracture occurring transgranularly relative to the prior austenite grain boundaries. It is attributed to the formation of cementite particles at the martensite lath boundaries and within the laths. During tempering, the particles coarsen and become large enough to crack, thus providing crack nuclei which may then propagate into the matrix. As a consequence, untempered low-carbon martensitic steels sometimes have a better toughness than when they are tempered, even though the untempered steel is stronger (Fig. 12.13). The cementite behaves like a brittle inclusion.

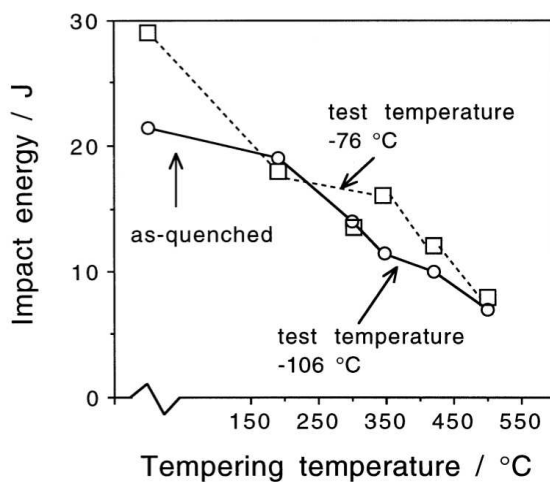


**Figure 12.13** Plot of toughness versus tempering temperature for a high-purity martensitic steel, illustrating that the toughness is reduced even though the strength decreases on tempering (Bhadeshia and Edmonds, 1979c).

Both of the impurity-controlled embrittlement phenomena can be minimised by adding about 0.2-0.5 wt% molybdenum to the steel. One theory suggests that Mo associates with phosphorus atoms in the lattice thereby reducing mobility and hence the extent to which

they segregate to boundaries. Larger concentrations of molybdenum are not useful because precipitation occurs.

In many bainitic microstructures, tempering even at temperatures as high as 550 °C has only a small effect on cementite size and morphology. Consequently, the low-temperature embrittlement phenomena are not found in conventional bainitic microstructures (Ohmori et al., 1974).

When bainite in carbon-containing iron alloys is free from carbides, its microstructure consists of bainitic ferrite, martensite and carbon-enriched retained austenite. In such microstructures, there is a special “embrittlement” effect associated with the decomposition of the austenite during tempering. The effect is specific to clean steels and is associated with a large reduction in the work of fracture even though the failure mode is microscopically ductile. Ductile failure occurs by the nucleation and linkage of microvoids. In the absence of carbide particles, the number of voids nucleated is small, so that the total plastic strain before the voids link is large since they are widely spaced (Fig. 12.7). When the austenite decomposes, the resulting carbides increase the number density of void nucleation sites; the smaller spacing between the voids then reduces the plastic strain to failure, even though the bainite weakens on tempering. The effect is obvious from an examination of fracture surfaces: those from untempered bainite exhibit larger dimples, indicative of widely spaced void nucleation sites (Fig. 12.14). Similar reductions in the ductility and toughness have been correlated versus the decomposition of austenite to carbides in high-silicon bainitic cast irons (Dubensky and Rundman, 1985; Gagne, 1985; Shieh et al., 1993, 1995). Other work has indicated that even the presence of carbides within the lower bainitic ferrite can impair toughness (Miihkinen and Edmonds, 1987a).

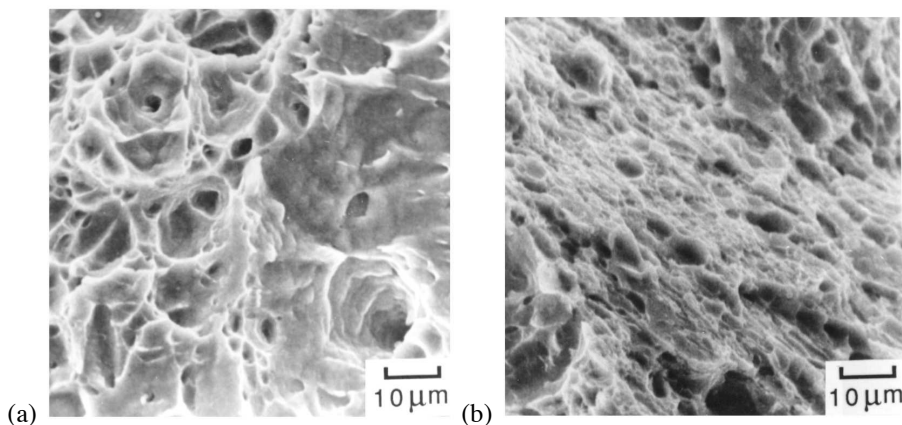


**Figure 12.14** Scanning electron micrographs of the fracture surfaces of untempered (a) and tempered (b) samples, showing the much reduced dimple size in the latter sample which contains numerous carbide particles help nucleate voids.

## 12.8 Fatigue Resistance of Bainitic Steels

Fatigue damage is an important life-limiting factor for metals subjected to cyclic stress the magnitude of which is less than  $\sigma_y$ . The damage is induced by plastic deformation

at stress concentrations; the plastic flow is not fully reversible and hence leads to damage accumulation in each cycle.

There are few studies of fatigue phenomena in bainitic steels because they have not had many structural applications when compared with martensitic alloys. Notable exceptions are the creep-resistant alloys used in the power generation industry, where high cycle fatigue is an issue for rotating parts and thermal fatigue resistance becomes important for plant designed to operate intermittently. Fatigue crack propagation in hydrogen containing environments (chemical or coal conversion plant and pressure vessels) can be life limiting so there are more studies in this area for bainitic alloys. Sub-surface fatigue caused by rolling-contact stresses can similarly limit the life of rails and bearings in the transportation industries.

### 12.8.1 Fatigue of Smooth Samples

Fatigue tests on smooth samples give information on the sensitivity of the specimen to fatigue crack initiation. Such tests are mostly relevant for materials which are clean, i.e. they are free from defects which might propagate under the influence of the applied alternating stress. The results from tests on smooth samples are expressed in the form of an  $S - N$  curve, which is a plot of  $\ln\{\sigma_a\}$  versus  $\ln\{N\}$ , where  $\sigma_a$  is the alternating stress amplitude and  $N$  the number of cycles to failure (Fig. 12.15).

Materials which strain-age show a *fatigue limit* which is a value of the alternating stress amplitude below which fatigue failure does not occur. The fatigue limit is the stress below which fatigue cracking never develops, and is usually ascribed to dynamic strain-ageing in which the mobile dislocations are pinned by interstitials. Another view is that the limit should be identified with the need for plasticity to spread across grain boundaries for the successful propagation of cracks (Oates and Wilson, 1964; Mintz and Wilson, 1965; Petch, 1990). Fatigue cracks are said not to develop when plasticity is confined to the surface regions of the samples. This alternative interpretation is supported by the fact that a fatigue limit can be found even when the test temperature is so low that interstitials can hardly be mobile enough to enable dynamic strain ageing. At the same time the role of interstitials is recognised as an additional factor since the fatigue limit actually rises as the temperature is raised to a point where ageing becomes possible (Petch, 1990).

Notice that even smooth samples will have non-uniformities at the surface. These develop into cracks which are small in comparison with the microstructure but they do not grow when the stress amplitude is below the fatigue limit. The cracks are halted by strong microstructural barriers. Chapetti et al. (1998) have defined the nature of the non-propagating crack and of the microstructural feature which acts as a strong barrier, which must be overcome by raising the stress amplitude beyond the fatigue limit, Table 12.1.

Mild steels with a microstructure of equiaxed proeutectoid ferrite exhibit a fatigue limit. For other materials, an *endurance limit* is defined as the value of the stress amplitude corresponding to a fatigue life of say  $N = 10^8$ . It is worth noting that fatigue stresses are in practice less than half the ultimate tensile strength of the steel, so that the plastic strain per cycle can be small.

Fatigue tests on smooth samples can be carried out with the stress amplitude maintained constant for all cycles, or with the plastic strain amplitude fixed for each cycle (Fig. 12.16). The test chosen depends on the nature of the application, but the two kinds of experiments can reveal different information on the relationship between microstructure and fatigue properties. Clearly, when the strain per cycle is a fixed quantity, the alternating stress amplitude needed to maintain the strain increases with the number of cycles as the material

**Table 12.1** Microstructural observations from smooth specimen fatigue crack growth tests done at stress amplitudes close to the fatigue limit. The non-propagating crack is present at stresses below the fatigue limit but is stopped from advancing by a strong microstructural barrier. After Chapetti et al. (1998).

Microstructure	HV	Non-propagating crack	Strong barrier
Ferrite-Pearlite ( $\alpha + P$ )	127	Across $\alpha$ grain	$\alpha/\alpha$ or $\alpha/P$ grain boundary
Ferrite-Bainite ( $\alpha + \alpha_b$ )	181	Across $\alpha$ grain	$\alpha/\alpha_b$ boundary
Bainite-Martensite ( $\alpha_b + \alpha'$ )	288	Across packets of laths	Austenite grain boundary

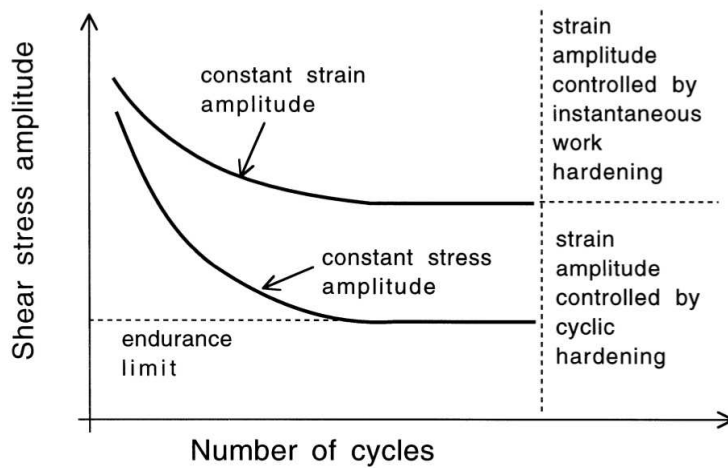


**Figure 12.15** Schematic  $S$ - $N$  curves for fatigue.

fatigue hardens during the test. The hardening eventually reaches a saturation level after many cycles and the stress  $\sigma_a$  does not then vary with  $N$  (Fig. 12.16). During each half cycle  $\sigma_a$  has to be raised to the instantaneous flow stress  $\sigma_{iy}$  which can be determined experimentally by interrupting the test at any stage. As the test proceeds,  $\sigma_{iy}$  can be expected to increase as instantaneous work hardening occurs. If  $\sigma_s$  is the value of  $\sigma_{iy}$  at saturation, the ratio  $r_2 = \sigma_a/\sigma_s$  is always expected to be close to unity because the applied stress  $\sigma_a$  has to rise to the value of  $\sigma_{iy}$  (Kettunen and Kocks, 1967).

For a test in which the alternating stress amplitude is kept constant, the plastic strain per cycle decreases as the material *cyclically hardens*, until this strain eventually reaches an approximately constant value. In cyclic hardening,  $\sigma_a$  is constant but  $\sigma_{iy}$  rises, whereas in fatigue hardening  $\sigma_a \approx \sigma_{iy}$  (Kettunen and Kocks, 1967). During the test,  $\sigma_{iy}$  increases due to cyclic hardening as the mean free slip area for dislocations ( $A_s$ ) decreases.  $\sigma_{iy}$  eventually reaches the saturation value  $\sigma_s$  and at that stage,  $A_s$  remains approximately constant as the fatigue cycles progress.

The area  $A_s$  at saturation may be larger than the mean slip area per obstacle in which case the to and fro movement of dislocations causes an accumulation of damage which eventually may lead to fatigue failure. However, if  $A_s$  is of the order of the mean free slip area per obstacle, because  $\sigma_a$  is low, then the dislocations bow between obstacles, a

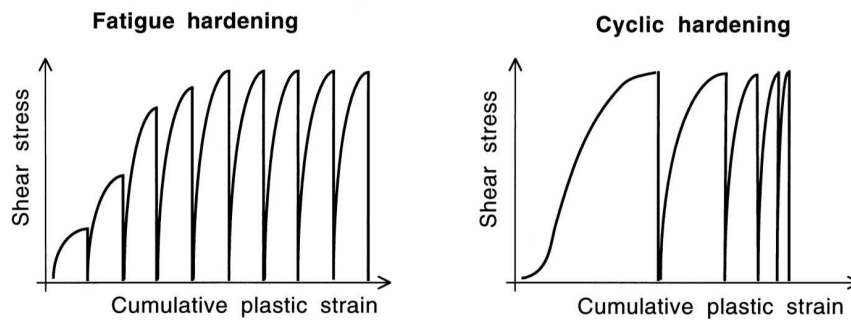


**Figure 12.16** Schematic illustration of constant plastic strain and constant stress fatigue tests - after Kettunen and Kocks (1967).

process which leads to energy dissipation but not to damage accumulation. The applied stress  $\sigma_a$  at which this happens is the endurance limit and fatigue failure does not then occur for many millions of cycles. For cyclic stressing, the ratio  $r_2$  varies with  $\sigma_a$ , but its value corresponding to the endurance limit (i.e.  $r_e$ ) is predicted to be  $\approx 0.65$ - $0.75$  for single crystal specimens (Cocks, 1967). For polycrystalline specimens of lower bainite,  $r_e \approx 0.51$ - $0.55$ , depending on the way in which the saturation flow stress  $\sigma_s$  is defined. Bainite yields gradually so a saturation *proof* stress has to be substituted for  $\sigma_s$ . Kettunen and Lepistö (1976) found that the saturation proof stress defined at a strain of 0.02 gives the best agreement with theory. The stress was measured by testing specimens which had first been fatigue cycled to about 20% of their fatigue life to be sure that the specimens are in a state of saturation. It is a good approximation for lower bainite to take  $r_2 = (\sigma_a/\sigma_y)$  where  $\sigma_y$  is the proof stress obtained from an ordinary uniaxial tensile test, even though the microstructure is then not in the saturated condition.

Cyclic hardening correlates with the rate of work hardening in monotonic tensile tests. The rate decreases both during fatigue tests and during monotonic tensile testing. The endurance limit can be identified with the onset of a critical (low) value of the rate of work hardening, associated with the approach to saturation in the context discussed above. Since the ultimate tensile strength is also determined by the point at which a reduced rate of hardening cannot keep up with increasing stress due to reduction of area, the endurance limit should correlate well with the UTS, and this is experimentally found to be the case (Kettunen and Kocks, 1967, 1972). This correlation should remain valid as long as the failure mode is ductile.

### 12.8.2 Fatigue Crack Growth Rate

For many engineering applications, the steels used can be assumed to contain subcritical cracks, in which case the initiation of cracks is not a controlling feature of fatigue life. The lifetime of the component then depends on the rate at which these cracks can grow slowly to a critical size leading to catastrophic failure. If the plastic zone at the crack tip is small when compared with the characteristic dimensions of the specimen, then most of the material surrounding the tip behaves elastically. Linear elastic fracture mechanics can be used to estimate the stress intensity range  $\Delta K = K_{\text{maximum}} - K_{\text{minimum}}$  at the crack tip

due to the alternating stress. The stress intensity range can be related to the crack growth rate  $da/dN$ , which is the average distance advanced by the crack front per cycle.

Experiments indicate that there is a minimum threshold value of  $\Delta K$  below which subcritical cracks do not propagate (Fig. 12.17). For many applications, the majority of fatigue life is spent at near threshold levels of stress intensity since the crack growth rates there can be incredibly small, the average advance of the crack front sometimes being less than an interatomic spacing per cycle. Beyond the threshold regime, the crack growth rate increases with  $\Delta K$ , until the “Paris Law” regime is reached (Fig. 12.17); here the relationship between the stress intensity range and the crack growth rate is empirically found to be of the form:

$$\frac{da}{dN} = C_4 \Delta K^m \quad (12.8)$$

where  $C_4$  is a constant and  $m$  is called the Paris constant.

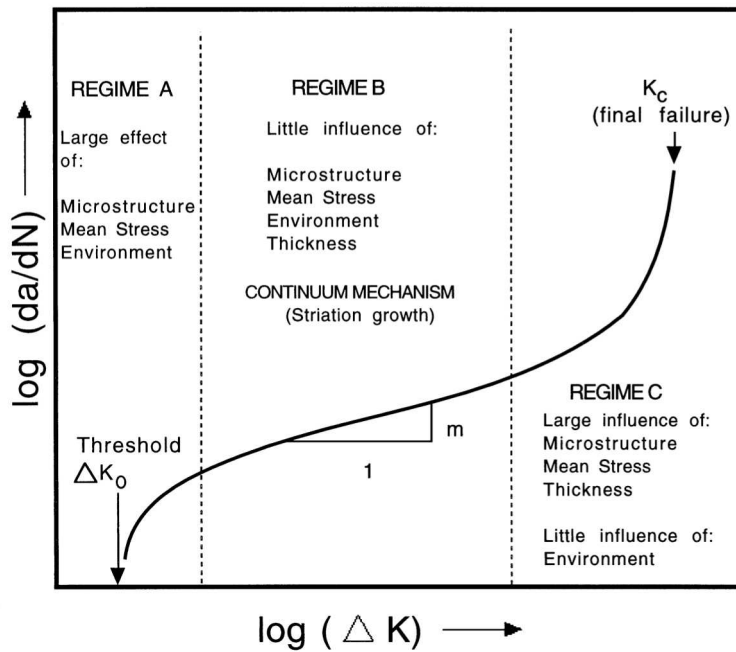


**Figure 12.17** Schematic illustration of the variation in fatigue crack growth rate as a function of the stress intensity range. After Ritchie (1979).

The crack growth rates in regime *A* where the stress intensity range is near the threshold value are found to be most sensitive to microstructure, mean stress and environment (Ritchie, 1979). The threshold region is of practical significance because many cracked components spend a good proportion of their fatigue life in that region. The threshold value of  $\Delta K$  (i.e.  $\Delta K_0$ ) correlates directly with the *cyclic* yield strength (Fig. 12.18) which is in general less than the yield strength as measured in a uniaxial tensile test (Ritchie, 1979).

The sensitivity of  $\Delta K_0$  to strength decreases as the mean stress amplitude increases.<sup>7</sup> This correlation is expected because the plastic zone at the fatigue crack tip is subject to alternating stresses; cyclic deformation of this kind must be different from monotonic strain hardening. Cyclic softening in quenched and tempered martensitic steels is usually attributed to rearrangements of the dislocation substructure and to a reduction in the dislocation density with alternating load. The softening occurs also because some of the plastic strain is reversible, a phenomenon analogous to the Bauschinger effect.

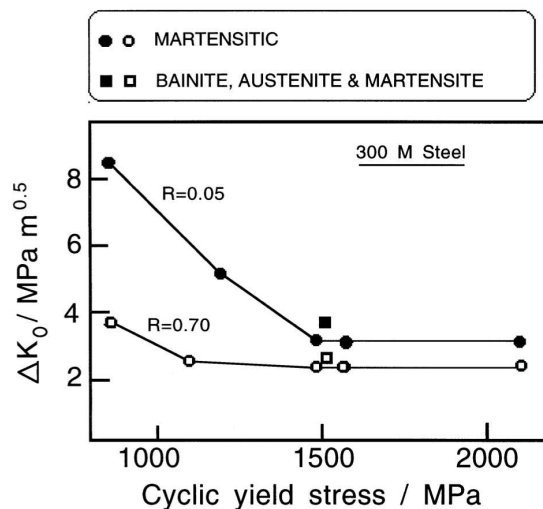


**Figure 12.18** Correlation of the threshold stress intensity range for fatigue crack propagation versus the cyclic yield stress for fully martensitic, and mixed microstructures at two values of  $R$ , which is the ratio of the minimum to maximum stress intensity (Ritchie, 1977b).

With some microstructures, the cyclic yield strength is found to be larger than the ordinary yield strength. In lightly tempered martensitic steels, the cyclic hardening is believed to occur due to dynamic strain ageing (Thielen et al., 1976). For a high strength steel transformed isothermally to a mixed microstructure of bainite, martensite and retained austenite, Ritchie (1977b) found that the deformation-induced transformation of retained austenite to martensite reduced the reversibility of plastic strain during cyclic deformation, causing the cyclic yield strength to exceed the ordinary yield strength and consequently leading to a reduction in  $\Delta K_0$  (Fig. 12.19). Later work on metastable austenitic stainless steel has confirmed that fatigue induced martensitic transformation is accompanied by drastic cyclic hardening (Bayerlein et al., 1992).

Cyclic softening therefore improves the near threshold fatigue crack growth resistance as long as the overall tensile strength is not reduced by a modification of the microstructure. Consistent with this, it is found that in a Fe-0.5Cr-0.5Mo-0.25V wt% steel, coarse grained precipitation hardened ferritic microstructures show significantly lower fatigue

<sup>7</sup>This behaviour contrasts with the fatigue or endurance limit for steels, which increases with strength since it becomes more difficult to initiate cracks in smooth samples as the strength increases. The threshold value of  $\Delta K$  on the other hand, depends on the ability of existing long cracks to grow, an ability which is enhanced by an increase in strength.

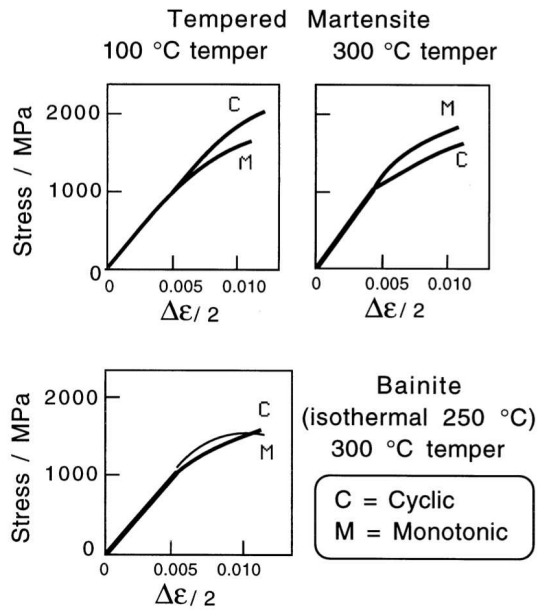


**Figure 12.19** Data illustrating the differences between the cyclic and monotonic yield behaviours for tempered martensite and bainite in 300M steel (Ritchie, 1977b).

crack growth rates near  $\Delta K_0$ , than higher strength bainitic or martensitic microstructures in the same alloy (Benson and Edmonds, 1978). In all cases, the crack path was found to be predominantly transgranular, with the bainite or martensite lath boundaries bearing no obvious relationship with the fracture surface.

A major reason why the threshold region is microstructure sensitive is that at higher stress intensities, the plastic zone size at the crack tip can be many times greater than the grain size or other microstructural feature. Benson and Edmonds showed that in the threshold region, the maximum plastic zone size was about 3-5 times the ferrite grain size, and comparable with the austenite grain size in the case of the bainitic and martensitic microstructures (i.e. a few times larger than the lath or packet size).

In the Paris Law regime (regime B, Fig. 12.18), the material behaves essentially as a continuum with little demonstrable influence of microstructure or mean stress. For ductile materials, the crack advances by a striation mechanism although other modes of fracture might occur at the same time in embrittled materials, giving values of  $m$  which are much larger than the  $m = 2$  value expected theoretically. As the crack continues to grow at increasing  $\Delta K$ , the maximum stress intensity begins to approach the critical value  $K_{IC}$  characteristic of final failure. The growth rate then becomes microstructurally sensitive, the dependency on microstructure reflecting its relationship with toughness. Thus, the austenite associated with bainitic microstructures can be beneficial to fatigue in Regime C (Fig. 12.18). The fracture modes in this regime replicate those found in static fracture, e.g. cleavage or intergranular failure.

### 12.8.3 Two-Parameter Approach to Growth Rate

It has long been known that the fatigue crack growth rate depends not only on the amplitude of the stress cycle but also on the mean stress. In the language of fracture mechanics, growth rate must depend both on  $\Delta K$  and for example,  $K_{\text{maximum}}$  (Vasudevan et al., 1994; Sadananda and Sreenivasan, 2001). Nevertheless, a large number of fatigue experiments focus only on the variation of  $da/dN$  with  $\Delta K$ , and sometimes look at the  $R$ -ratio ( $K_{\text{minimum}}/K_{\text{maximum}}$ ), thus implicitly considering two parameters.

In fact, even the threshold value of the stress intensity range ( $\Delta K_0$ ) is not constant, but decreases dramatically to some minimum value  $\Delta K_0^*$  as  $K_{\text{maximum}}$  is increased. This is because for  $\Delta K < \Delta K_0^*$ , it becomes impossible to reverse plastic flow during a load cycle, so that the accumulation of fatigue damage ceases.

Similarly, when  $K_{\text{maximum}}$  is reduced to a critical value  $K_{\text{maximum}}^*$ , it becomes impossible to sustain the “bond-breaking” processes at the crack tip which are responsible for the creation of new crack surface.

So to summarise, Sadananda and co-workers emphasise that the fracture mechanics approach to fatigue should consider  $da/dN$  to be a function of both  $\Delta K$  and  $K_{\text{maximum}}$ . The Paris law does not do so and hence should only have physical meaning when  $\Delta K = K_{\text{maximum}}$ , i.e.  $R = 1$ . It is argued that the frequent interpretation of the fact that  $\Delta K_0$  varies with  $R$  in terms of crack-closure effects may not be justified. Instead, the relationship is simply a reflection of the fact that one of the variables,  $K_{\text{maximum}}$ , is neglected.

One difficulty with both the crack-closure and the two-parameter approaches is the lack of a theory relating crack propagation with the variables.

### 12.8.4 Arresting Fatigue Cracks

An interesting development in combating fatigue is the so-called fatigue crack arresting steel (Sakano et al., 2005; Katsumoto et al., 2005). The essential feature responsible for the improved performance is the dual phase microstructure in which islands of bainite are dispersed in an otherwise ferritic matrix. This leads to the deflection or arrest of cracks at the island boundaries (Fig. 12.20). In comparisons against structural steels of similar strength (banded ferrite and pearlite or fully bainitic), the fatigue crack growth is found to be about 1.3 times higher in atmospheric tests, and welded samples outperform conventional steels by a factor of about 2. The improvement is maintained when the tests are done in synthetic seawater. The new steel has already been implemented in ships and vessels (Katsumoto et al., 2005). Typical compositions and properties are listed in Table 12.2.

**Table 12.2** Compositions (wt%) and strength of fatigue crack arresting steels (Katsumoto et al., 2005).

C	Si	Mn	Yield Strength / MPa	UTS / MPa
0.06	0.44	1.55	476	579
0.04	0.42	1.45	481	626

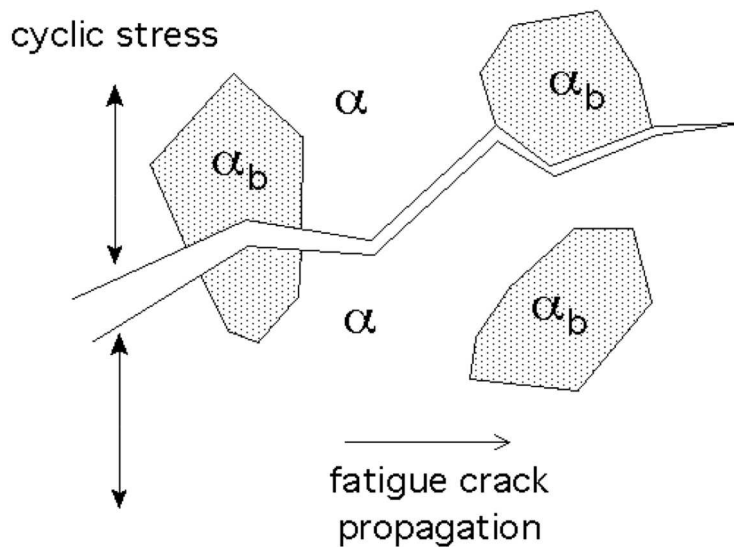


**Figure 12.20** The dual-phase microstructure of bainite ( $\alpha_b$ ) and ferrite ( $\alpha$ ) causes the fatigue crack to adopt a more tortuous path.

### 12.8.5 Fatigue in Laser Hardened Samples

Surface layers of steel components can be heat-treated with minimal distortion using lasers. The action of the laser is to swiftly heat a thin surface layer which then cools rapidly by the transfer of heat into the underlying material, a process known as “self-quenching”. A motivation for surface treatments of this kind is to improve the resistance to fatigue. The microstructure of the surface layer can be martensitic or bainitic depending on the composition and shape of the steel, together with the parameters controlling the laser treatment. The general principles discussed above apply, that the fatigue crack growth rate is insensitive to the microstructure in the Paris law regime, but varies with the microstructure when the stress intensity range is close to the threshold value.

In the threshold regime, Tsay and Lin (1998) have shown that for equivalent hardness, a lower bainitic microstructure has better resistance to cleavage crack propagation than one containing tempered martensite. This is because the latter is more sensitive to grain boundary embrittlement leading to intergranular failure during fatigue at  $\Delta K$  values as low as  $25 \text{ MPa m}^{1/2}$ . Since the tempering temperature was only  $300^\circ\text{C}$ , the weakness of the prior austenite grain boundaries must be associated with coarse cementite particles as discussed in section 12.7. The tendency to form such particles at the prior austenite grain boundaries is reduced for a lower bainitic microstructure since the cementite precipitates during the course of transformation.

It is interesting to note that Tsay and Lin induced the formation of lower bainite during laser treatment by preheating the steel to a temperature of  $300^\circ\text{C}$ , a method used widely in the welding industry.

### 12.8.6 Fatigue and Retained Austenite

Fatigue cracks propagate as damage is accumulated during the cyclic straining of the material at the crack tip. It is natural to expect metastable austenite in the vicinity of the crack tip to transform into martensite, leading effectively to an increase in the strain hardening rate. A high strain hardening rate leads to more rapid crack propagation (Cottrell, 1965), because the ability of the material to accommodate plastic strain then becomes exhausted more readily. The formation of hard martensite in a ductile matrix also decreases the strain preceding fracture.

It might therefore be concluded that the presence of austenite is not beneficial to the fatigue properties. However, this neglects the work that has to be done by the applied stress to induce martensitic transformation (Chanani et al., 1972). Stable austenite might also improve the fatigue properties by increasing the ductility of the microstructure.

Fig. 12.21 shows fatigue crack propagation data from two samples of carbide-free bainitic microstructures in which the strength was altered by varying the isothermal transformation temperature. It is seen that the threshold stress intensity increases and the crack propagation rate decreases, as the fraction of retained austenite increases. This is in spite of the fact that the yield strength of the sample with less austenite is in fact greater.<sup>8</sup>

In other work on carbide-free bainite, even better results have been obtained using a vacuum-melted Fe-0.22C-1.8Si-2.3Mn wt% steel, containing an unspecified amount of chromium (Wei et al., 2004). After tempering the microstructure in the range 295-370 °C for 2 h, it was possible to obtain a threshold stress intensity  $\Delta K_0 \approx 13 \text{ MPa m}^{1/2}$  during fatigue crack growth tests. In the cyclic testing of smooth samples, failure did not occur in 10 million cycles with a stress amplitude of 700 MPa. The yield and ultimate tensile strengths of the samples were about 1340 and 1540 MPa respectively. The tempering heat treatment presumably improved the properties of the small amount of high-carbon martensite present in the initial microstructure.

### 12.8.7 Fatigue and Cementite

Long, thin particles of cementite in the microstructure are particularly susceptible to fracture. High fractions of cementite promote coalescence dominated fatigue failure whereas lower fractions are associated with crack propagation dominated fatigue (Stokes et al., 2005).

### 12.8.8 Corrosion Fatigue

There are few corrosion fatigue data available for bainitic microstructures, but it is known that environmental effects can accelerate fatigue cracks via a conjoint action of stress and corrosion. Many of the effects are attributable to hydrogen embrittlement and much work has been done to establish a correlation between microstructure and the susceptibility to hydrogen. There is, however, a clear correlation between the fatigue crack growth rate in hydrogen-charged specimens and those which have not been similarly charged (Fig. 12.22).

<sup>8</sup>It is sometimes considered that the crack growth increment per cycle should be inversely proportional to the cyclic yield strength. This is because the crack tip opening displacement will be smaller when the yield strength is large. This is opposite to the behaviour illustrated in Fig. 12.21, providing evidence for the beneficial effect of retained austenite

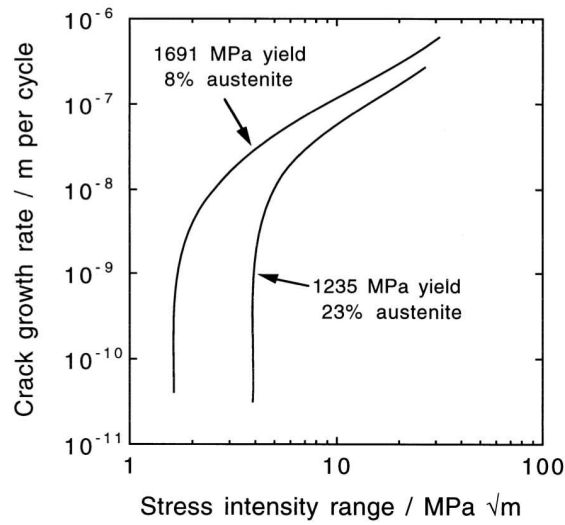


**Figure 12.21** The fatigue crack propagation rate as a function of the stress-intensity range. The chemical composition of the steel is Fe-0.6C-2.3Si-1.5Mn-0.6Cr wt%. The microstructures each consist of a mixture of retained austenite, bainitic ferrite and high-carbon martensite. The high and low yield strength samples are obtained by isothermal transformation at 300 and 370 °C respectively (Wenyan et al., 1997).

Microstructures that are susceptible to rapid crack growth rate also have the fatigue fastest when charged with hydrogen.

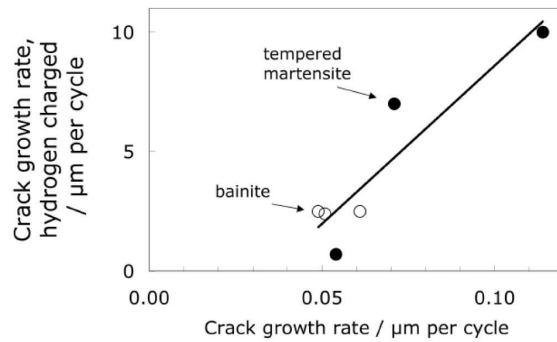


**Figure 12.22** Fatigue crack growth rates in hydrogen-charged and uncharged specimens of bainitic and tempered martensitic samples of Fe-0.3C-1Cr-0.15Mo-0.41Mn wt% steel. Data from Tau et al. (1996).

In Fig. 12.22, the crack growth rates for a given microstructure ( $\alpha'$  or  $\alpha_b$ ) increase with strength. However, for similar strength and toughness (Table 12.3), the bainitic microstructure in general shows a greater resistance to fatigue. The reason for this is not clear, but may have something to do with the trapping of hydrogen (Xu et al., 2011).

**Table 12.3** The strength and toughness of the martensitic and bainitic microstructures for the data plotted in Fig. 12.22. The number after  $\alpha'$  is the tempering temperature and that after the  $\alpha_b$  is the transformation temperature.

	$\sigma_y / \text{MPa}$	$K_{IC} / \text{MPa m}^{1/2}$
$\alpha'$ , tempered at 350 °C	1218	90
$\alpha'$ , tempered at 450 °C	1015	125
$\alpha'$ , tempered at 600 °C	676	118
$\alpha_b$ , transformed at 330 °C	1192	124
$\alpha_b$ , transformed at 330 °C	1005	117
$\alpha_b$ , transformed at 330 °C	647	80

The fresh fracture surfaces created as the crack propagates during fatigue are vulnerable to environmental attack, as long as there is sufficient time available for the hydrogen to diffuse into the region ahead of the crack front. Consequently, corrosion fatigue is less detrimental at high frequencies of cyclic loading.

Corrosion during fatigue also leads to a reduction in the threshold stress intensity, below which normal fatigue crack growth does not occur, to a value designated  $K_{crit}$ . The reduction may be so drastic as to make  $K_{crit}$  of little use as a design parameter, since the section sizes necessary to reduce the design stresses to a level at which crack propagation does not occur may be unrealistically large. In such circumstances, the components are assigned service lives calculated using known corrosion fatigue data.

Although it is intuitively reasonable that corrosion should, by chemical degradation enhance the crack growth rate, there are complications which sometimes lead to an overall reduction in the rate of crack propagation (Dauskardt and Ritchie, 1986). When the stress intensity range and mean stress is low, any corrosion products that form can isolate the crack tip from its environment. Thus, fatigue crack growth in a moist environment occurs at a lower rate than in dry hydrogen (Ritchie et al., 1980; Suresh et al., 1981). Specimens which have been damaged by hydrogen bubble formation prior to fatigue testing can fail more rapidly relative to those in which the bubbles form in the vicinity of the crack front during testing. The expansion associated with bubble formation then induces crack tip closure (Fig. 12.23). All other factors being equal, low strength steels are better at resisting crack growth because plasticity leads to crack tip closure.

### 12.8.9 Gigacycle Fatigue Tests

Ordinary push-pull fatigue tests use loading frequencies in the range 400–1000 Hz (Berger et al., 2008) but by using piezoelectric devices it is possible to test at ultrasonic frequencies of 20–100 kHz (Puškár, 1993; Furuya et al., 2002; Bathias, 2010, 2012). The hour-glass shaped sample is designed so that the point half way along its length is a displacement node where the stress is maximum (Bathias, 2006; Chen et al., 2008). Conventional tests to achieve  $10^{11}$  cycles would take more than a decade to complete, whereas with a 100 kHz ultrasonic machine, the test is completed in less than 300 h. It is nevertheless important to bear in mind that there are anelastic dissipations that can accumulate to raise the temperature of the sample during the test. Indeed, the generation of heat during testing is exacerbated when testing strong steels containing bainite and martensite (Yu et al., 2010). The results may also be compromised if the fatigue processes depend on low rates of

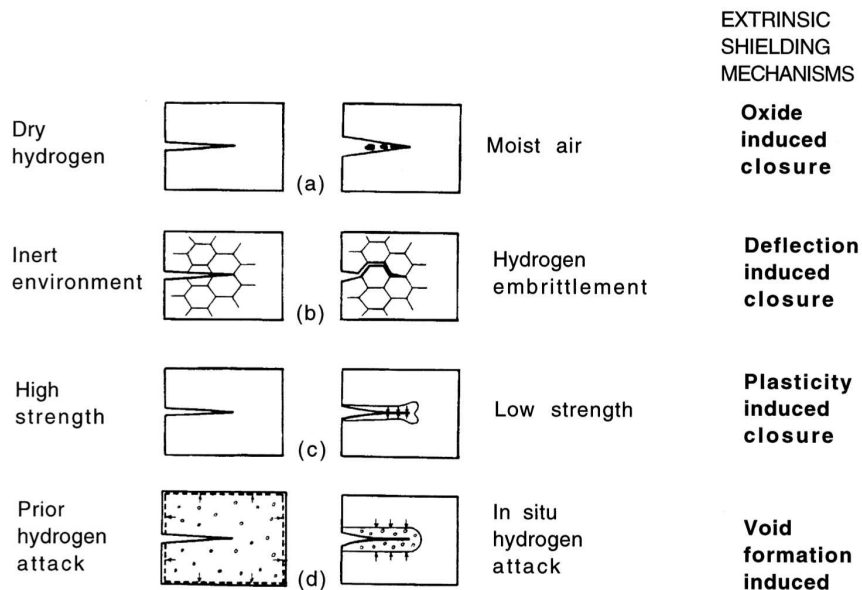


**Figure 12.23** An illustration of the micromechanisms of crack tip shielding, as discussed in the text (Dauskardt and Ritchie, 1986)

loading, for example, those involving the diffusion of hydrogen or particular mechanisms of dislocation relaxation. The results may not therefore correlate with tests done at low loading-frequencies (Fig. 59, Bhadeshia (2012)). The ultrasonic tests tend to underestimate the fatigue properties determined conventionally, even when both kinds of tests use hour-glass samples with small highly-stressed volumes.

Fig. 12.24 shows data where the ratio of minimum to maximum stress is  $-1$ , for a classical bearing steel in two microstructural states. There is no significant difference between the bainitic and martensitic states when data from many different sources are merged, at conventional or ultrasonic test frequencies. On the other hand, data by Mayer et al. (2009) indicate that bainitic bearing steels outperform martensitic microstructures in ultrasonic fatigue tests due to their greater ductility. It is difficult therefore to reach generic conclusions about the performance of the different microstructures in ultrasonic fatigue tests.

### 12.8.10 Rolling Contact Fatigue

In circumstances where a rolling element passes over a substrate, momentary stresses are induced that are a maximum below the contact surface. The nature of the stress can be described approximately as a combination of compression and torsion in phase with respect to their maximum values (Fujita et al., 2000; Burkart et al., 2012). Repeated pulses of stress lead to the accumulation of fatigue damage in the form of microscopic cracks initiating below the contact surface. These cracks then grow, leading eventually to failure by spalling. The phenomenon is of particular importance in the context of bearings and railway lines. Cracks can also initiate at the contact surface if the relative motion includes both sliding and rolling, or when surface damage is exacerbated by a failure of lubrication or debris. Not

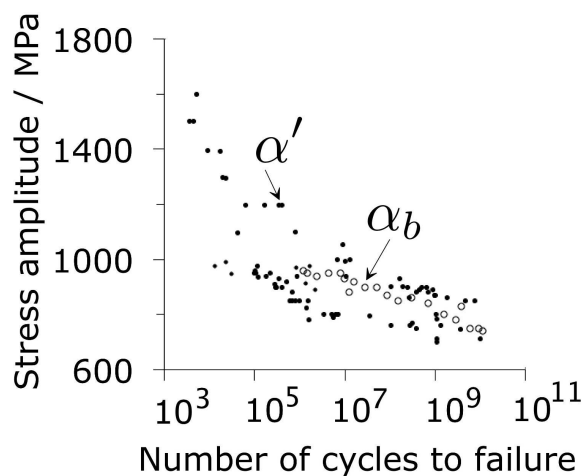


**Figure 12.24** Comparison of tension-compression data for a 1C-1.5Cr bearing-steel heat treated to bainitic and martensitic states, tested at ultrasonic frequencies. Data from Sakai et al. (2002); Baudry et al. (2004); Bathias (2010); Almaraz (2008).

surprisingly, the damage processes are accelerated in the presence of diffusible hydrogen. A great deal of detail is available in a recent review (Bhadeshia, 2012); the purpose here is to emphasise the role of microstructure.

The toughness of the steel influences the rolling contact fatigue life, especially in circumstances where environmental effects that lead to the ingress of hydrogen play a role (Armstrong et al., 1978; Hollox et al., 1981). In the classical 1C-1.5Cr bearing-steel<sup>9</sup> that is used for the vast majority of bearings currently manufactured (Bhadeshia, 2012), a lower bainitic microstructure can be produced by isothermal transformation to hardness levels comparable to those achieved with tempered martensite. It has been argued that the greater toughness of lower bainite, when compared with the twinned martensite, leads to better performance in fatigue (Hollox et al., 1981; von Bergen and Hollox, 1981; Akbasoglu and Edmonds, 1990). The relatively poor toughness of the martensite has been reported to lead to dramatic ultimate fracture whereas the lower bainitic rings failed by slow wear (Hollox et al., 1981). The heat treatment used to generate bainite in 52100 steel usually involves transformation for a few hours at about 250 °C, and hence is more expensive than quenching and tempering, which explains why the latter is the preferred method for well-lubricated bearings. Nevertheless, better combinations of hardness and toughness have been reported with mixed microstructures of bainite and martensite, with the production of the bainitic component completed in just 30 min (Chakraborty et al., 2008).

There are many kinds of damage mechanisms that operate during rolling contact fatigue of the kind encountered in rolling bearings (Bhadeshia, 2012; Evans, 2012; Solano-Alvarez and Bhadeshia, 2014). The most pernicious of these involve crack initiation at loosely-bonded inclusions, embrittled prior austenite grain boundaries or microscopic cracks induced during heat treatment or processing. The faces of these sub-critical cracks then beat against each other as the rolling element passes over the location, leading to a process akin to mechanical alloying. Thus, an intensely deformed local state is created and proeutectoid cementite particles in the vicinity are forced into solution. The locally deformed region thus develops a nanostructure that etches lightly relative to the background because

<sup>9</sup>This typically contains 1 wt% of carbon and is used in the martensitic condition with light tempering to ensure a high hardness of 60 Rockwell C. The alloy is variously known as 52100, 100Cr6, SUJ2, etc.

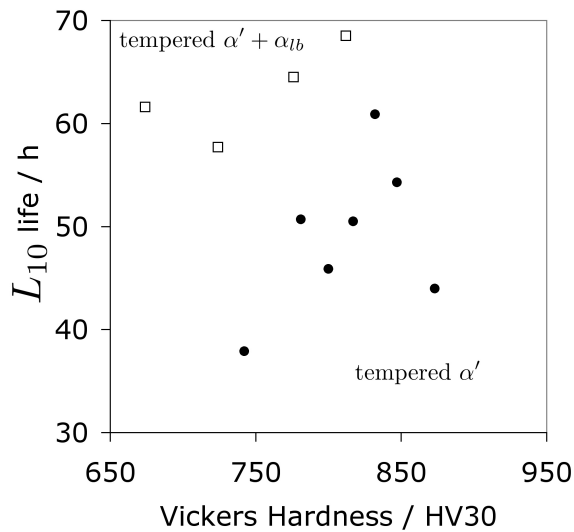


**Figure 12.25** Rolling contact fatigue, accelerated washer-tests conducted at 4.14 GPa, on a 1C-1.5Cr type steel in the quenched and tempered martensitic condition, and on mixtures of lower bainite and martensite tempered at 100 °C.  $L_{10}$  refers to the life where 10% of the samples will have failed. Data from von Bergen and Hollox (1981).

the concentration of defects is so large that the region reacts uniformly to chemical attack, hence the name “white matter”. Furthermore, its hardness is much higher than the surroundings due to the defect density and particularly, the absorption of carbon into solid solution. In fact, cracks are not uniformly surrounded by white matter, presumably because the orientation of the crack-face is not appropriate relative to the contact stress for mechanical alloying.

The rolling contact fatigue life of back-up rolls used in steel mills, that fail from surface initiated cracks, is found to scale with the microstructural parameter  $\sigma_y \sqrt{w}$ , where  $w$  is the bainite sub-unit thickness. The latter controls the effective grain size and hence determines the deflection of cracks across large misorientation boundaries, whereas the yield strength related to the ease of plasticity (Green et al., 2007). These results lend further support to the role of toughness in influencing fatigue life.

Many bainitic microstructures contain retained austenite. The mechanically induced transformation of austenite during rolling contact fatigue can be beneficial in hardening regions where the stresses or strains are localised. Such transformation may also give rise to beneficial residual stresses (Bhadeshia, 2012). For large contact pressures in excess of 5 GPa, it is reported that a greater retained austenite content is beneficial to the life of 1C-1.5Cr steel (Stickels, 1984). The life was found to scale with the retained austenite content, although the prior austenite grain size and the carbon concentration of the martensite were not kept constant in those experiments.

## 12.9 Stress Corrosion Resistance and Hydrogen

Cleavage fracture occurs when a critical stress is exceeded over a region ahead of the crack tip, such as to stimulate the growth of an existing microscopic crack. This critical stress can be reduced by environmental effects. Cleavage fracture then occurs at a critical stress intensity  $K_{ISCC}$  which is about a third of  $K_{IC}$ . This means that stress corrosion can severely limit the effective use of high strength steels. The effect of corrosion manifests primarily via hydrogen embrittlement, the hydrogen being generated by cathodic reaction

at the crack surface. It then diffuses to regions of highest dilatation ahead of the crack tip, leading to a reduction which can be interpreted in terms of a variety of mechanisms, for example, a reduction in the cohesive strength in the region where hydrogen is concentrated (Pfeil, 1926; Troiano, 1960; Oriani and Josephic, 1974), or one where plasticity becomes very localised due to the change in the mobility of dislocations, and a plethora of other possibilities. What is certain is that either diffusible hydrogen is required (Johnson, 1875) so that it can concentrate at a stress concentration or that the hydrogen has to be generated at the crack tip as in stress-corrosion events. And the extent of the embrittlement, although dependent on microstructure, has the greatest sensitivity to strength (Nanninga et al., 2010).

It is difficult to comment on the relationship of  $K_{ISCC}$  with microstructure. Retained austenite has a greater solubility for hydrogen; there are many other hydrogen-traps including dislocations, interfaces, voids, etc. Experiments in which steels (Table 12.4) are heat-treated to produce either carbide-free upper bainite and retained austenite show no significant correlation in the hydrogen concentration following electrolytic charging (Fig. 12.26), even though the original authors (Hojo et al., 2004a) reached the opposite conclusion. Further data confirm that the absorbed hydrogen does not necessarily correlate with retained austenite content (Hojo et al., 2004b). It is probable that the fraction of the retained austenite must exceed the percolation threshold before it influences the ingress of hydrogen into the steel (Fielding et al., 2014).

**Table 12.4** Steels used in hydrogen-charging experiments by Hojo et al. (2004a). The chemical compositions are in wt%.

Microstructure	C	Si	Mn
Bainitic ferrite and retained austenite	0.4	1.49	1.50
Tempered martensite	0.4	0.17	1.42

Whereas solubility data clearly indicate that austenite can dissolve more hydrogen, it is probable that much of the hydrogen in martensitic or bainitic samples is located at defects, of which there are plenty in these microstructures.

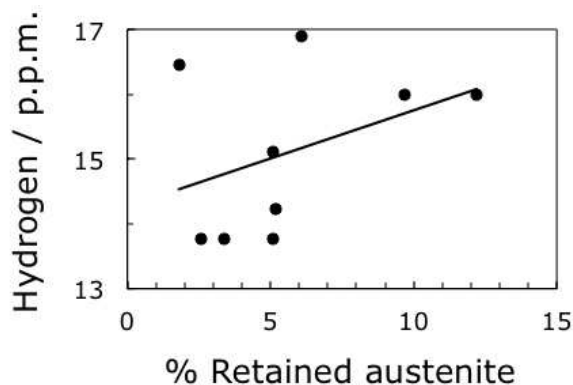


**Figure 12.26** Hydrogen following electrolytic charging of mixtures of retained austenite and bainite as a function of the yield strength. The austenite does not seem to have a major effect on the hydrogen concentration. Data from (Hojo et al., 2004a).

It nevertheless appears that the presence of retained austenite reduces the stress corrosion crack growth rates, by hindering the diffusion of hydrogen to the sites of triaxial

tension ahead of the advancing crack front (Parker, 1977; Ritchie et al., 1978). The diffusivity of hydrogen through austenite can be many orders of magnitude smaller than that in ferrite (Shively et al., 1966). The permeation of hydrogen in high strength steels has been studied using electrochemical techniques (Tsubakino and Harada, 1997). The diffusivity derived from permeation curves is found to be smaller, and the activation energy larger, for steels containing retained austenite. The effect can be dramatic if the austenite has three-dimensional connectivity, because easy diffusion paths through ferrite are then eliminated (Fielding et al., 2014); this is discussed in detail in section 14.15.

Comparative experiments at constant yield strength, on tempered martensite and on a mixed microstructure of lower bainite, martensite and retained austenite, revealed that the sample containing the greater quantity of austenite exhibited better stress corrosion resistance in a NaCl solution (Ritchie et al., 1978). While both samples failed at the prior austenite grain surfaces, the proportion of ductile tearing was greater in the bainitic samples. This was attributed to the ability of retained austenite to act as sinks for impurities thereby reducing segregation to boundaries (Marschall et al., 1962). Embrittled boundaries are more susceptible to stress corrosion (Ritchie, 1977a).

These investigations emphasise the role of retained austenite in improving the resistance to stress corrosion, but the conditions under which the austenite is beneficial are limited (Solana et al., 1987; Kerr et al., 1987). The austenite has to continuously surround the plates of ferrite in order to hinder the diffusion of hydrogen. There are other effects which are more important than that of austenite. Any microstructural modifications which lead to a high density of hydrogen traps (e.g. interfaces between cementite and ferrite) lead to large improvements in stress corrosion resistance.

Kerr et al. and Solana et al. were able to establish some general principles relating microstructure and stress corrosion resistance (SCR). The sensitivity to microstructure was largest at yield strengths less than about 1000 MPa, and when failure occurred by a transgranular mechanism. Furthermore, the largest improvements obtained did not correlate with the presence of retained austenite. Twinned martensite was deleterious to SCR, presumably because twinned martensite is associated with high carbon concentrations and poor toughness; the twins themselves are innocuous. Mixtures of ferrite and martensite were found to be better, correlating with extensive crack branching due to the high density of interphase interfaces. The presence of lower bainite also led to improved SCR, but the effect could not be separated from any due to the associated drop in yield strength. All other factors being equal, reductions in yield strength correlated strongly with improved SCR (Fig. 12.27). Alloy specific effects were also observed and attributed to differences in the density of hydrogen traps. Indeed, any feature of the microstructure which enables the hydrogen to be dispersed, or which promotes crack branching, improves SCR.

One feature not emphasised above is the homogeneity of the microstructure, which now appears to be a critical factor in determining the resistance to sulphide-induced stress-corrosion cracking. Systems which carry fluids contaminated with aqueous hydrogen sulphide ( $H_2S$ ) are susceptible because the wet sulphide reacts with the steel to generate atomic hydrogen which in turn embrittles the steel. Most commercial steels are banded, i.e. the chemical segregation associated with solidification is spread into bands by rolling or other fabrication processes (section 13.5.3). From a microstructural point of view, the bands are either ferrite or pearlite. The pearlite regions have a high average carbon content and are harder, making them more sensitive to hydrogen. Rapid cooling from austenite avoids this difficulty and has been shown to give a more uniform hardness distribution, with a considerably improved stress-corrosion response (Tamehiro et al., 1985a; Carneiro et al., 2003).

There is work using secondary-ion mass spectroscopy on an acicular ferrite microstructure, which suggests that dissolved boron atoms form stable complexes with hydrogen, thereby reducing its mobility (Pokhodnya and Shvachko, 1997).

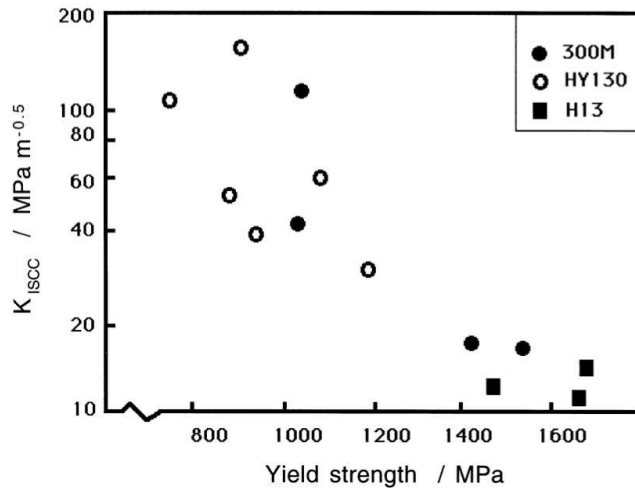


**Figure 12.27** The correlation of stress corrosion cracking resistance versus the yield strength for a variety of steels (Solana et al., 1987).

### 12.10 Delayed Fracture

When hydrogen-containing steels are left under a stress which is below the ordinary tensile yield strength, they tend to fracture by a brittle mechanism, some time after the load is applied (Mazanec and Sejnoha, 1965). The phenomenon is known as *delayed fracture*.

Fig. 12.28a shows the susceptibility of carbide-free mixtures of retained austenite and bainitic ferrite, and of tempered martensite, to delayed fracture. The data are due to Hojo et al. (2004a) for the steels listed in Table 12.4; they are plotted as a function of the yield strength as measured in a tensile test. The delayed fracture strength is measured by hydrogen-charging four-point bend specimens which are then kept loaded for an hour. The stress at which fracture occurs within an hour is that plotted in Fig. 12.28a.

A microstructural effect cannot be deduced from Fig. 12.28a, since the variation in the delayed fracture strength seems to depend largely on the yield strength. At a constant yield strength both microstructures show identical delayed fracture strength. However, more recent work shows that lower bainite with the same yield strength as tempered martensite is more resistant to hydrogen (Tartaglia et al., 2008); the reasons for this are not clear but judging from the fractographs presented, the tempered martensite exhibited a greater tendency for intragranular failure with respect to the prior austenite grain surfaces. Hojo et al. reached a contradictory conclusion but they did so by plotting the data against tensile strength rather than the strength at yield. It is the yield strength that is dependent on the defect density and delayed fracture involves little or no plasticity.

The same interpretation applies when the fraction reduction in tensile elongation due to hydrogen is plotted as a function of the yield strength. It has to be concluded that there is

no specific role of retained austenite in mitigating delayed fracture or changes in ductility due to hydrogen. This would be consistent with the discussion in the previous section where it seems that the hydrogen may largely be trapped at the defects that determine the yield strength.

It has been suggested that a small concentration of niobium (0.02 wt%) increases the static fracture strength of carbide-free bainite, but it is not clear why the effect is reversed on increasing the niobium concentration (Sugimoto et al., 2005). In this case the steels all had almost identical yield strengths.

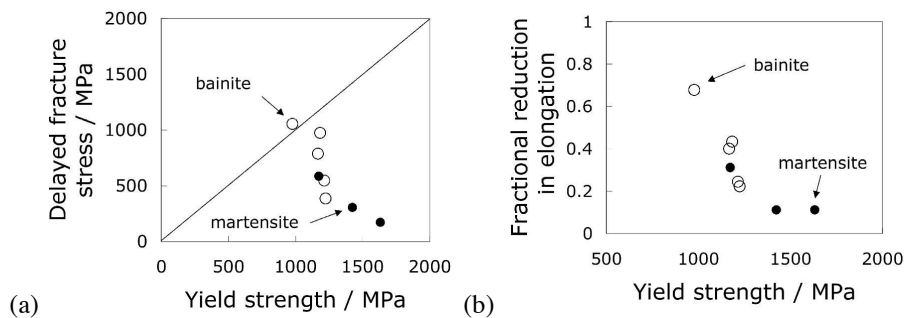


**Figure 12.28** (a) The stress at which hydrogen-charged samples of carbide-free mixtures of retained austenite and bainite, or tempered martensite in the same steel fracture after time under load, compared with the yield strength. The line is the locus of points where there is no reduction in strength due to hydrogen charging. (b) Reduction in elongation when hydrogen charged specimens are tensile tested. Data due to Hojo et al. (2004a).

### 12.11 The Creep Resistance of Bainitic Steels

Creep-resisting steels used in power plant or in the petrochemical industries are based on low-carbon, low-alloy steels containing chromium, molybdenum, tungsten or vanadium as the significant alloying additions. Low-chromium steels, such as the classical  $2\frac{1}{4}\text{Cr1Mo}$  or  $1\text{Cr1MoV}$  alloys have formed the backbone of the power generation and petrochemical industries for at least five decades, for operating temperatures of  $565^\circ\text{C}$  or less. The  $2\frac{1}{4}\text{Cr1Mo}$  is essentially bainitic, whereas the  $9\text{Cr1Mo}$  type alloys developed much later, for higher temperatures and greater corrosion/oxidation resistance, are martensitic. The major applications are in the fabrication of pressure vessels, boiler steam pipes, steam generating and handling equipment, high pressure tubes with thick walls, turbine rotors, superheater tubes, coal to methane conversion plants, petrochemical reactors for the treatment of heavy oils and tar sands bitumen, etc. In addition to creep, they have to be resistant to oxidation and hot-corrosion, sometimes in environments containing hydrogen and sulphur. The pressure vessels in large coal liquefaction and gasification plant may be required to contain mixtures of hydrogen and hydrogen sulphide at pressures up to 20 MPa at  $550^\circ\text{C}$ . The steels have to be weldable and cheap.

Given the demands for service at high temperatures and over 30-50 years, the microstructures must be resistant to other phenomena, such as graphitisation. Protection against graphitisation is one of the reasons why the aluminium concentration is limited to less than 0.015 wt%, and why chromium and molybdenum are used together as alloying additions, because molybdenum on its own promotes the tendency to graphitisation

(Hrivnak, 1987). Ambient temperature properties are relevant because the fabricated components must be safe during periods where elevated temperature operation is interrupted. Fatigue resistance is important to bear in mind but the tolerance to cyclic stresses can frequently be managed by proper engineering design.

The steels might typically be used within the temperature range 480-565 °C, the service stresses being of the order of 15-40 MPa ( $\sigma/E \approx 1-3 \times 10^{-4}$ ). The maximum tolerable creep strain rate is about  $3 \times 10^{-11} \text{ s}^{-1}$ . In power plant, the stresses normally originate from a combination of internal steam pressure and the dead weight of the components in large assemblies. The most important property requirement is creep resistance. A greater creep strength can be exploited to reduce the component wall thickness; the resulting reduction in weight allows the support structures to be reduced in scale. It is often the case that the hoop stresses generated by the pressurised steam can be comparable to those due to the weight of the steam pipes, providing the incentive for weight reduction. Higher alloy steels can be used without additional expense, if they have a higher creep strength. Welding also becomes simpler and cheaper for smaller section sizes. Thermal stresses induced by temperature differences between the inner and outer surfaces of any component are smaller with section size, thereby mitigating any thermal fatigue problems associated with the irregular use of the power plant, due for example to variations in electricity demand. Such flexibility can make a substantial difference to the economic performance of electricity-generating plant.

Typical chemical compositions of bainitic steels used for their creep resistance are given in the upper half of Table 12.5; those listed in the lower half are corresponding martensitic steels presented for comparison. The newer steels tend to contain less manganese in order to reduce their susceptibility to temper embrittlement and banding due to chemical segregation. The hardenability is maintained at reduced manganese concentrations by the overall increase in the concentration of other elements, for example chromium.

The actual chemical composition can in practice vary significantly from the typical value. The specified composition range is generally not tight from a metallurgical point of view (Table 12.5). Indeed, the American Society for Testing Materials has at least twelve standards for the  $2\frac{1}{4}\text{Cr}1\text{Mo}$  steel for different applications (Lundin et al., 1986). It is unfortunate that many publications refer only to the nominal designation, and sometimes do not even mention the carbon concentration of the steel concerned. It is now recognised that very small and apparently innocuous variations in chemical composition can explain large variations in the mechanical properties of creep-resistant steels (Kimura et al., 1997).

An interesting reason for keeping the carbon concentration as low as possible, is that it is often necessary to join these steels to stainless steels. There is then a carbon chemical potential gradient which exists at the junction, causing it to migrate during service at high temperatures (Fig. 12.29). The migration occurs from the low-alloy to the high-alloy steel, causing a decarburised layer to develop in the former and an intense region of carbide precipitation in the latter. The overall integrity of the joint is therefore jeopardised. Naturally, a reduced carbon concentration also leads to inferior creep properties given that the steels rely on alloy carbides for their resistance to creep so that a compromise is necessary (Klueh, 1974a,b).

The standard alloys sometimes contain trace additions of boron and titanium, added presumably to enhance the bainitic hardenability in the manner discussed in Chapter 6. Unintentional trace impurities such as tin and antimony are also known to have disproportionate effects on creep strength for reasons which are not well understood (Collins, 1989). The alloys are usually fabricated by welding, and the filler material used can be chemically

**Table 12.5** Compositions (wt% ) of creep-resistant steels with typical specification ranges. The upper and lower sections of the table represent bainitic and martensitic steels respectively. The sulphur concentration is usually within the range 0.005-0.02 wt%, and that of phosphorus within the range 0.005-0.025 wt%.

Designation	C	Si	Mn	Ni	Mo	Cr	V	Others
0.25CrMoV	0.15	0.25	0.50	0.05	0.50	0.30	0.25	-
range	< 0.18	0.10-0.60	0.40-0.65	-	0.45-0.65	0.25-0.35	0.20-0.30	-
1CrMoV	0.25	0.25	0.75	0.70	1.00	1.10	0.35	-
range	0.24-0.31	0.17-0.27	0.74-0.81	0.60-0.76	0.65-1.08	0.98-1.15	-	-
2.25Cr1Mo	0.15	0.25	0.50	0.10	1.00	2.30	0.00	-
range	< 0.16	< 0.5	0.3-0.6	-	0.9-1.1	2.0-2.5	-	-
Mod. 2.25Cr1Mo	0.1	0.05	0.5	0.16	1.00	2.30	0.25	Ti=0.03 B=0.0024
3.0Cr1.5Mo	0.1	0.2	1.0	0.1	1.5	3.0	0.1	-
range	< 0.16	< 0.5	0.30-0.60	-	0.45-0.65	4.0-6.0	-	-
3.5NiCrMoV	0.24	0.01	0.20	3.50	0.45	1.70	0.10	-
range	< 0.29	< 0.11	0.20-0.60	3.25-4.00	0.25-0.60	1.25-2.00	0.05-0.15	-
9Cr1Mo	0.10	0.60	0.40	-	1.00	9.00	-	-
range	<0.15	0.25-1.00	0.30-0.60	-	0.90-1.10	8.00-10.00	-	-
Mod. 9Cr1Mo	0.1	0.35	0.40	0.05	0.95	8.75	0.22	Nb=0.08 N=0.05
range	0.08-0.12	0.20-0.50	0.30-0.60	<0.2	0.85-1.05	8.00-9.50	0.18-0.25	Nb 0.06-0.10 N 0.03-0.07 Al <0.04
9Cr $\frac{1}{2}$ MoWV	0.11	0.04	0.45	0.05	0.50	9.00	0.20	W=1.84 Nb=0.07 N=0.05
range	0.06-0.13	< 0.50	0.30-0.60	< 0.40	0.30-0.60	8.00-9.50	0.15-0.25	Nb 0.03-0.10 N 0.03-0.09 Al <0.04
12CrMoV	0.20	0.25	0.50	0.50	1.00	11.25	0.30	-
range	0.17-0.23	<0.5	<1.00	0.30-0.80	0.80-1.20	10.00-12.50	0.25-0.35	-
12CrMoVW	0.20	0.25	0.50	0.50	1.00	11.25	0.30	W=0.35
range	0.17-0.23	<0.5	<1.00	0.30-0.80	0.80-1.20	10.00-12.50	0.25-0.35	W<0.70
12CrMoVNb	0.15	0.20	0.80	0.75	0.55	11.50	0.28	Nb 0.30 N 0.06

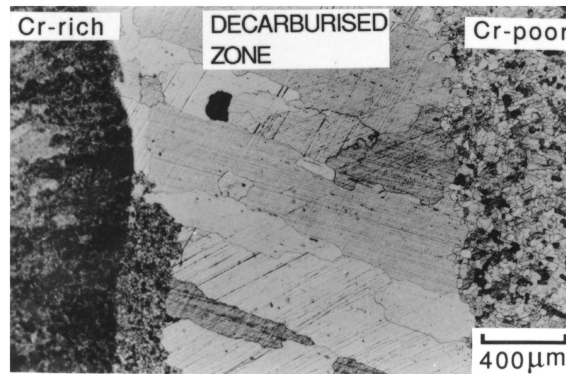


**Figure 12.29** Optical micrograph of a junction between mild steel and a  $2\frac{1}{4}\text{Cr1Mo}$  alloy, showing the development of a decarburised zone in the mild steel side of the joint after tempering (Race, 1992).

different from the parent plate; the CrMoV steels are usually welded with  $2\frac{1}{4}\text{Cr1Mo}$  fillers in order to ensure good creep properties in the weld metal.

### 12.11.1 Heat Treatment

For power plant applications, the steels are usually air cooled (“normalised”) after austenitisation. The component thickness may vary from 12-120 mm; the thickness determines the heat treatment time in order to allow the component to achieve uniform temperature. On the other hand, heat flow analysis shows that the specified periods are excessive and could in principle be reduced (Greenwell, 1990). The temperature to which the steels are heated for austenitisation is usually about  $100^\circ\text{C}$  above the  $A_{e3}$  temperature, or  $50^\circ\text{C}$  above the  $A_{c3}$  temperature when the heating rate is about  $1^\circ\text{C}$  per minute. Lower temperatures lead to correspondingly smaller austenite grain sizes, which can be beneficial to mechanical properties. The creep mechanism in service is not controlled by grain boundary diffusion or sliding, but rather by the motion of dislocations past precipitates.

Given that it is impossible to achieve uniform cooling in large components, it is reasonable to expect variations in the microstructure and mechanical properties as a function of position. For a typical range of chemical compositions encountered within the  $2\frac{1}{4}\text{Cr1Mo}$  designation, the normalised microstructures consist of mixtures of allotriomorphic ferrite and bainite, with the fraction of bainite in the range 0.34-0.94 (Murphy and Branch, 1971). The effect on the mechanical properties due to these variations is pronounced during the early stages of service, but the differences in creep strength vanish over the long term, even when comparisons are done against mixtures of ferrite and pearlite (Kimura et al., 2003).

After normalisation, the steels are given a stress-relief treatment by tempering at  $660\text{-}700^\circ\text{C}$  for some 2-14 h, depending on application and component size. This not only produces the required microstructure containing relatively stable carbides, but also mitigates residual stresses arising from welding operations. These heat treatments are so severe that the precipitates are in an overaged condition (Pilling and Ridley, 1982).

### 12.11.2 $2\frac{1}{4}$ Cr1Mo Type Steels

This is a popular steel which has been used reliably for many decades. Its creep resistance, like that of many low-alloy steels used in the power generation industry, comes from fine and stable dispersions of alloy carbides together with contributions from solid solution strengthening. The latter is especially important in the long term when the carbide dispersions have become ineffective due to coarsening. Molybdenum is particularly effective as a solid solution strengthening element (Lundin et al., 1982, 1986). The alloy design should be such as to avoid tying up all of the molybdenum in the form of carbides. The carbon concentration should therefore be controlled carefully to achieve the best compromise between the need for carbides and solution strengthening. Typical values of the creep rupture strength of  $2\frac{1}{4}$ Cr1Mo steel are illustrated in Fig. 12.30.

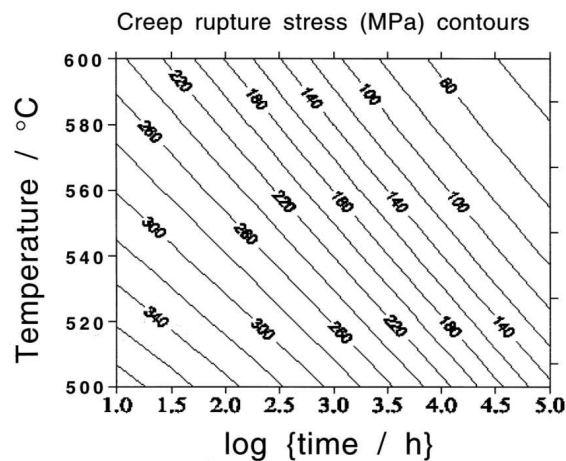


**Figure 12.30** Creep rupture strength of  $2\frac{1}{4}$ Cr1Mo steel as a function of temperature and time.

Investigations have shown that the ferrite/bainite microstructure in  $2\frac{1}{4}$ Cr1Mo steel is stronger in creep than martensite because  $M_2C$ , which is replaced eventually by more stable carbides during service, persists for shorter times in a martensitic microstructure (Baker and Nutting, 1959; Murphy and Branch, 1971).  $M_2C$  is more stable in ferrite than bainite or martensite. These observations have yet to be explained. On the other hand, the effect of initial microstructure becomes less important over long periods of service at elevated temperatures. This is because the tempering that occurs during service brings all microstructures towards a near equilibrium state. Fig. 12.31 shows that the creep rupture strength at low stress is almost identical for the martensitic, bainitic and ferrite+pearlite initial microstructures (Kimura et al., 2003). Although the long-term creep strength is virtually identical for all cases, the greater initial strength of the bainite and martensite leads to a smaller accumulated creep-strain at any instant during service.

### 12.11.3 1CrMoV Type Steels

These steels have been used in the manufacture of rotors for steam turbine power generating plant. 1CrMoV steels are austenitised at temperatures within the range 950-1000°C for 1-14 h and air cooled or furnace cooled to give a fully bainitic or a mixed microstructure.

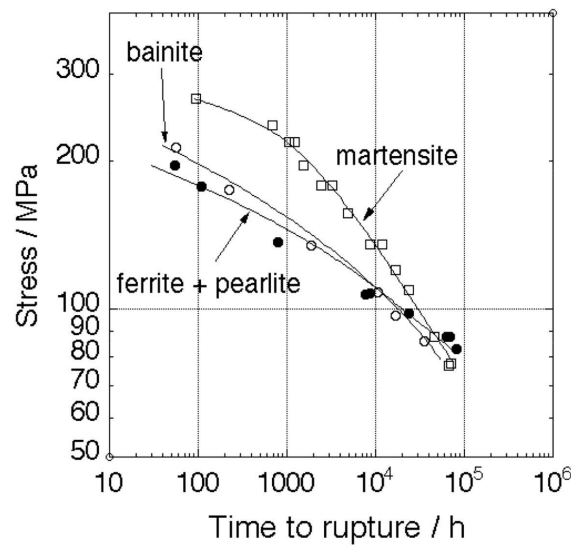


**Figure 12.31** Creep rupture stress as a function of rupture time at 500°C, for a variety of initial microstructures in 2 $\frac{1}{4}$ Cr1Mo steel (Kimura et al., 2003).

ture of ferrite and bainite (Myers et al., 1968; Murphy and Branch, 1969; Strang et al., 1994). Tempering is in the range 690–710 °C for time periods up to 20 h. The resulting microstructure is a fine dispersion of  $V_4C_3$  particles (about  $\approx 12$  nm size) in a matrix of ferrite.<sup>10</sup> Other carbides such as  $M_3C$  and  $M_{23}C_6$  may also form when the carbon concentration is in excess of that required to react with the vanadium. These other carbides are coarse and precipitate mainly at the prior austenite or ferrite grain boundaries.

The alloy is martensitic in the quenched condition; tempering at 690 °C for 20 h converts the martensite into ferrite containing  $V_4C_3$  but for some unknown reason the carbide particles are much coarser with a typical size of 50 nm (Buchi et al., 1965; Myers et al., 1968). The creep strength of 1CrMoV steels in the tempered bainite condition is higher than in a tempered martensitic state, but this may not be due to the finer carbides in the tempered bainite. The observed activation free energy for creep is inconsistent with a process controlled by the climb of dislocations; the spacing between particles is too close to allow dislocation bowing (Myers et al., 1968). It is suggested that it is the interaction of dissolved vanadium with dislocations which controls creep deformation. The finer carbides in the tempered bainite leave a larger concentration of dissolved vanadium since the solubility of solute increases with interface curvature via the Gibbs-Thompson capillarity effect. The greater concentration of soluble vanadium is claimed to be responsible for the better creep strength of tempered bainite. The interaction of vanadium atoms with dislocations must be important, but so must the dispersions of particles since it is unlikely that Fe-V solid solutions would have good creep properties in their own right.

The uniformity of the  $V_4C_3$  dispersion depends on the form of  $M_3C$  present (Buchi et al., 1965). If the vanadium and carbon concentrations are stoichiometrically balanced,

<sup>10</sup>The  $V_4C_3$  precipitates contain some iron, manganese molybdenum and chromium in solid solution, although vanadium is by far the major carbide forming constituent (Senior, 1998).

then  $M_3C$  is eliminated during tempering and the  $V_4C_3$  dispersion is uniform. Otherwise, the regions around  $M_3C$  particles are found to be free from  $V_4C_3$ . Since the  $M_3C$  particles are mostly located at prior austenite or ferrite grain boundaries,  $V_4C_3$ -free zones form at the boundaries. This results in poor creep properties (Buchi et al., 1965; Murphy and Branch, 1969).

#### 12.11.4 $\frac{1}{4}$ CrMoV Type Steels

$\frac{1}{4}$ CrMoV steels have a low hardenability so they are used with microstructures of allotriomorphic ferrite and a small fraction of pearlite. Fine  $V_4C_3$  dispersions form on tempering. These steels have a higher creep ductility than the 1CrMoV alloys at a slightly lower creep strength. The lower creep ductility of 1CrMoV steels is because creep cavitation occurs at both the ferrite/ferrite and ferrite/bainite boundaries, whereas the  $\frac{1}{4}$ CrMoV cavitates mainly at the ferrite/pearlite boundaries which are not as susceptible to cavitation (Murphy and Branch, 1969). It is also argued that a larger fraction of ferrite permits a greater relaxation of stresses, thereby inhibiting cavity nucleation and growth (Jones and Pilkington, 1978).

#### 12.11.5 Enhanced Cr-Mo Bainitic Steels

Many attempts have been made to improve on the properties of the low-alloy creep resistant steels, especially in the context of pressure vessels in hydrogen environments. A higher concentration of alloy carbide forming elements can reduce the stability of cementite, which is prone to hydrogen problems (Ritchie et al., 1984; George et al., 1985). Those alloys containing unstable carbides such as cementite and  $Mo_2C$  react with ingressed hydrogen, leading to decarburisation, cavitation and to the formation of methane bubbles at interfaces. Damage by hydrogen is thought to occur in three stages (Vagarali and Odette, 1981; Shewmon, 1976). The first stage, during which the microstructure and macroscopic mechanical properties are largely unaffected, involves the nucleation and growth of bubbles. This is followed by rapid attack as methane bubbles grow and coalesce into fissures at the grain boundaries, leading to swelling and a deterioration of mechanical properties. The final stage is extensive decarburisation with the dissolution of carbides as the system attempts to maintain an equilibrium carbon concentration in the ferrite.

Thick steel plates (300-400 mm) are required in applications such as coal conversion plant. Conventional steels do not have adequate hardenability so attention has been focussed on improving the popular bainitic  $2\frac{1}{4}$ Cr1Mo steel, with the aim of extending the temperature range over which the alloy can be utilised, whilst maintaining the bainitic microstructure. Modifications include microalloying to improve elevated temperature strength, larger concentrations of chromium for improved resistance to hydrogen embrittlement, carbide stabilising additions such as vanadium and niobium, and nickel, boron and carbon additions for improved bainitic hardenability (Wada and Eldis, 1982; Ishiguro et al., 1982, 1984; Kozasu et al., 1984; Parker et al., 1984; Klueh and Swindeman, 1986).

Ishiguro et al. (1982) developed an alloy which differs from  $2\frac{1}{4}$ Cr1Mo steel in that it has a very low silicon concentration in order to reduce the tendency for grain boundary embrittlement, a lower carbon concentration (0.1 wt%) and 0.25V-0.02Ti-0.002B wt%. It is designated the "Modified  $2\frac{1}{4}$ Cr1Mo" steel, with improved creep strength, impact toughness and resistance to temper embrittlement. The titanium combines with nitrogen, so that the boron can remain in solution and increase hardenability; boron otherwise forms a nitride which is less stable than that of titanium. The creep strength is improved because

of vanadium carbides which make the bainitic microstructure more resistant to tempering (Klueh and Swindeman, 1986). The alloy has applications in coal conversion plants, chemical processing and petrochemical refineries. The microstructure of the alloy is as for the  $2\frac{1}{4}\text{Cr1Mo}$  steel, i.e. bainitic, and this remains the case in the heat affected zones following welding, except at high heat inputs when allotriomorphic ferrite also forms (Tsai and Yang, 2003).

An alloy which has received a lot of attention has the chemical composition Fe-3Cr-1.5Mo-0.1V-1Mn-0.1C wt% developed by Wada and Cox (1982, 1984). After austenitisation at about 1000 °C for two hours and air cooling, it has a microstructure which is essentially a mixture of bainitic ferrite and austenite/martensite, of the kind normally associated with the  $2\frac{1}{4}\text{Cr1Mo}$  steel discussed earlier. The extra alloying elements add to solution hardening, an important factor determining the long-term creep strength.

An advantage of the higher chromium concentration is that cementite is replaced more rapidly by carbides such as  $\text{M}_7\text{C}_3$ ,  $\text{M}_{23}\text{C}_6$  and  $\text{M}_6\text{C}$ , thus rendering the microstructure less susceptible to severe hydrogen attack. Bainite in  $2\frac{1}{4}\text{Cr1Mo}$  steel is far more sensitive to a high pressure hydrogen embrittlement than a tempered martensitic microstructure (Chung et al., 1982). This is because the carbon-enriched retained austenite associated with bainite decomposes into intense clusters of cementite particles which react with hydrogen. The cementite in tempered martensite is more uniformly distributed. At higher chromium concentrations, for example in the 3.5Cr1Mo bainitic steels, the cementite is quickly replaced by  $\text{M}_{23}\text{C}_6$  making the alloy less sensitive to hydrogen exposure (George et al., 1985).

Manganese and silicon contribute to austenite grain boundary embrittlement (Bodnar et al., 1989). A bainitic steel in which the concentration of these elements is minimised is the 3.5Ni3CrMoV alloy which is insensitive to hydrogen and temper embrittlement effects when compared with the  $2\frac{1}{4}\text{Cr1Mo}$  steel (Ritchie et al., 1984). The larger concentration of chromium and vanadium leads to the dissolution of cementite during tempering at 700 °C, thereby improving the resistance to hydrogen effects. Hydrogen sometimes reacts with carbon dissolved in ferrite producing gases such as methane, which precipitate as bubbles under conditions of severe hydrogen attack. This is another reason why 3.5Ni3CrMoV steel performs better because the concentration of carbon in the ferrite which is in equilibrium with alloy carbides is reduced.

The nickel in 3.5Ni3CrMoV steel improves toughness; it also increases the hardenability, allowing sections as thick as 0.4 m to transform into fully bainitic microstructures. The reduction in the  $A_{e3}$  temperature due to nickel permits the use of lower austenitisation temperatures; the resulting refinement of the austenite grain size is beneficial to toughness. Many other steels with lower nickel concentrations have been investigated and found to possess better properties over the conventional  $2\frac{1}{4}\text{Cr1Mo}$  alloy (Spencer et al., 1989).

### 12.11.6 Tungsten Strengthened Steels

The heat associated with the welding of steels introduces a heat-affected zone (HAZ) in the solid metal adjacent to the weld; the heating and cooling cycle within this zone may induce undesirable microstructures such as untempered martensite. Post-weld heat treatments are then used to render any martensite in the HAZ harmless. However, this is not practical for large constructions, which also cannot be heated prior to welding in order to avoid the formation of brittle martensite.

A bainitic steel, known commercially as HCM2S, has been developed to address these difficulties (Komai et al., 1999), Table 12.6. It is a modification of the  $2\frac{1}{4}\text{Cr1Mo}$  alloy with the molybdenum substituted with tungsten; combined with a reduction in the carbon

concentration, this leads to a bainitic microstructure without martensite, allowing welding without pre- or post-weld heat treatment. The maximum hardness obtained for typical cooling rates is reduced to about 300 HV which is some 50 HV below that of  $2\frac{1}{4}$ Cr1Mo steel (Fig. 12.32). The insensitivity of the hardness to the cooling rate is claimed to be desirable in the design of joints.

**Table 12.6** The chemical composition (wt%) of a tungsten-strengthened creep resistant steel known commercially as HCM2S. The concentration of aluminium refers to that dissolved in the ferrite.

C	Si	Mn	P	S	Cr	Mo	W	V	Nb	N	Al	other	
0.05	0.2	0.5	0.015	0.001	2.2	0.1	1.6	0.25	0.05	0.008	0.008	B=0.004	Komai et al. (1999)
0.11	0.20	0.35			3.00	0.75	1.5	0.25					Sikka et al. (2004)
0.11	0.20	0.35			3.00	0.75	1.5	0.25				Ta=0.1	Sikka et al. (2004)

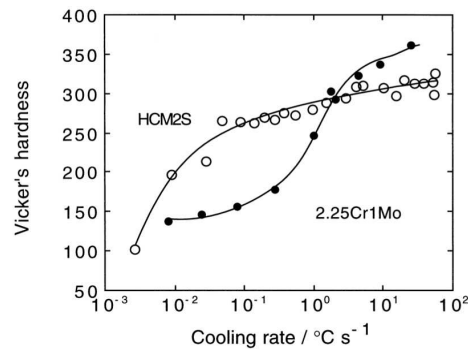


**Figure 12.32** A comparison between the hardness of a tungsten strengthened creep resistant steel and the classical  $2\frac{1}{4}$ Cr1Mo alloy. The cooling rate is an average value in the range 800-300 °C s<sup>-1</sup>. Data from (Komai et al., 1999).

The microstructure of the steel after normalising is bainite and in the tempered condition consists of tempered bainitic ferrite with cementite,  $M_{23}C_6$ ,  $M_7C_3$  and vanadium or niobium carbonitrides. The addition of boron has the effect of stabilising  $M_{23}C_6$  and  $M_{23}(C, B)_6$  on grain boundaries, thereby retarding dynamic recrystallisation during creep (Miyata et al., 1999). All this makes the alloy creep resistant, so much so that tolerable stress at 600 °C is about twice that of  $2\frac{1}{4}$ Cr1Mo, and almost matches the more expensive and difficult-to-weld 9Cr1Mo martensitic steels (Fig. 12.33b).

The tungsten-strengthened bainitic steel has now performed satisfactorily in service for more than three years. Monitoring tests have shown that the alloy performs better than other steels such as  $2\frac{1}{4}$ Cr1Mo (Masuyama et al., 1998). Other tungsten enriched steels with a higher chromium concentration and in one case, a tantalum addition to boost creep strength have been investigated in depth (Sikka et al., 2004) and show excellent combinations of properties provided that the oxidation resistance typical of the 9Cr1Mo alloys is not required (Fig. 12.33b).

It has been suggested that a reduction in the manganese concentration can lead to further improvements in the creep strength (Miyata et al., 1999). It is argued that  $M_6C$  precipita-

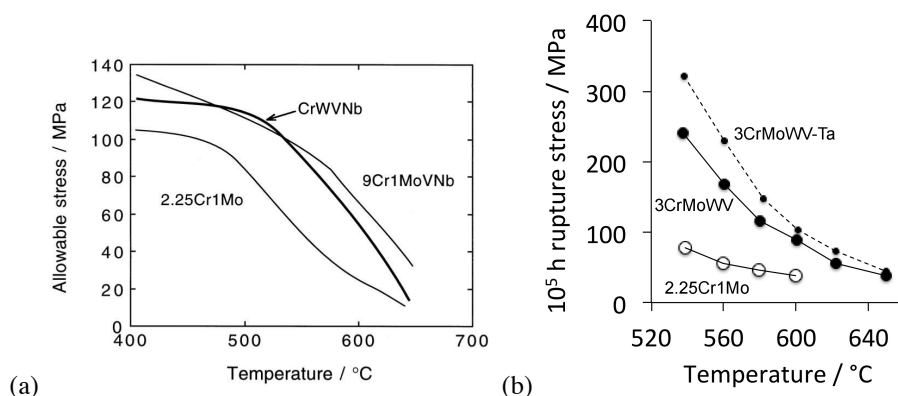


**Figure 12.33** (a) Comparison of the allowable stress, as a function of temperature, for the tungsten-strengthened steel,  $2\frac{1}{4}\text{Cr1Mo}$  and a 9Cr1Mo martensitic steel. After Komai et al. (1999). (b) Comparison against recent tungsten-containing steels. Adapted from Abe (2004).

tion is slower at low manganese concentrations, thus allowing more tungsten to remain in solution to harden the ferrite. Phase diagram calculations indicate that  $M_6C$  is stabilised in such alloys by manganese. A reduction in manganese from 0.5 to 0.01 wt% led to an increase in the creep rupture strength by almost 50 MPa over a wide range of temperatures.

The interpretation of the manganese effect relies on the removal of tungsten from solid solution. However, measurements show that during creep testing at 550 °C less than 0.2 wt% W and at 600 °C less than 0.5 wt% W are removed by precipitation (Miyata et al., 1999; Komai and Masuyama, 2002). It remains to be demonstrated that these small changes can account for the differences in creep strength between high and low manganese variants.

A comparative study of HCM2S with a Mo-containing, W-free alloy ( $2\frac{1}{4}\text{Cr-1Mo-V-Nb}$ ) of otherwise similar composition, except without tungsten and with 1.05 wt% Mo, showed that tungsten retards the evolution of the bainitic microstructure during elevated temperature service (Miyata and Sawaragi, 2001). This is because tungsten has a smaller diffusivity in ferrite than molybdenum. It has also been demonstrated that the MC carbides retain coherency in the W-containing steel in circumstances where they are incoherent in the Mo-containing alloy. Both elements partition into MC and hence influence its crystallographic misfit with the ferrite; it is claimed that a lower misfit exists in the tungsten-containing steel. It is therefore understandable that the W alloy better resists creep deformation (Fig. 12.34).

The new alloy may have a greater susceptibility than  $2\frac{1}{4}\text{Cr1Mo}$  to stress-relief cracking when welded and subsequently heat treated or used in service at elevated temperatures (Nawrocki et al., 2000, 2001). This is because unlike  $2\frac{1}{4}\text{Cr1Mo}$ , its strength does not decrease much on tempering. The precipitation of vanadium carbides strengthens the microstructure. The coarse austenite grains that form in the heat-affected zones of welds then fail by intergranular cracking because the strong material inside the prior austenite grains resists stress relaxation, thereby focussing deformation at the grain boundaries.

### 12.11.7 Regenerative Heat Treatments

Cavitation and other irreversible creep damage occurs at the late stages in the life of creep-resistant steels. During that period, any loss in properties is due largely to microstruc-

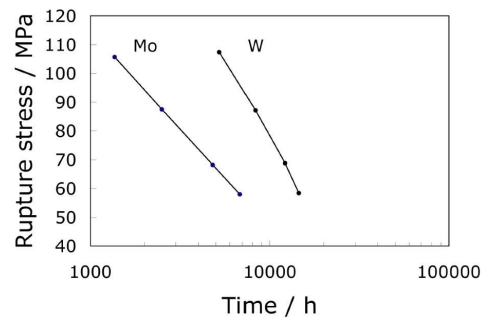


**Figure 12.34** Creep rupture stress data for 923 K. The W-containing alloy is HCM2S whereas the Mo-containing alloy has a similar composition but with tungsten substituted with about 1 wt% of Mo. Data from Miyata and Sawaragi (2001).

tural changes such as carbide coarsening, changes in the configuration of dislocations, and the general approach of the microstructure towards equilibrium. These microstructural changes can in principle be reversed by heating the component back into the austenite phase field and then allowing it to transform into the original microstructure. However, such a heat treatment involves high temperatures which may not be feasible with large components.

A possible alternative is to regenerate just the carbides, by annealing the steel at a temperature ( $\approx 700^\circ\text{C}$ ) above the service temperature, but below that at which austenite can form (Senior, 1998). Some of the carbides would then dissolve to re-precipitate in a fine form during ageing at a lower temperature, thereby regenerating a semblance of the original microstructure.

### 12.11.8 Comparison with Martensitic Creep-Resistant Steels

Modern ferritic creep-resistant steels start with a microstructure which is martensitic. On the other hand, the best established steels of this kind rely on allotriomorphic ferrite or bainite as the starting microstructure. It is therefore pertinent to ask why modern heat-resistant steels are based on martensite.

The probable answer to this has little to do with microstructure. Indeed, when compared under identical conditions, the 9Cr1Mo steel is not better in creep than  $2\frac{1}{4}\text{Cr1Mo}$  (Fig. 12.35); it is only when these alloys are modified with elements such as niobium, vanadium, cobalt and tungsten that they begin to outperform the lower alloy steels.

The 9Cr1Mo alloys were developed for higher temperatures and greater corrosion/oxidation resistance. A greater chromium concentration is needed to obtain the oxidation and corrosion resistance necessary for higher service temperatures. The chromium must then be balanced by other solutes to avoid an excessive fraction of  $\delta$ -ferrite. The net solute content then becomes so large that the steels cannot transform to bainite and hence the martensitic microstructure. This is illustrated by the time-temperature-transformation diagrams for 2.3, 4.3 and 9.3 wt% chromium steels shown in Fig. 12.36.

It could be argued that a martensitic microstructure, which has a large number density of defects, encourages the precipitation of more numerous and finer carbide particles which are better at resisting creep. Fig. 12.37 shows a comparison between bainite and marten-

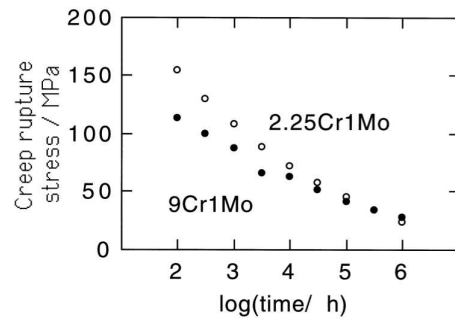


**Figure 12.35** A comparison of the calculated creep rupture strengths of  $2\frac{1}{4}$ Cr1Mo and 9Cr1Mo steels given identical heat treatments (Bhadeshia, 2001b).

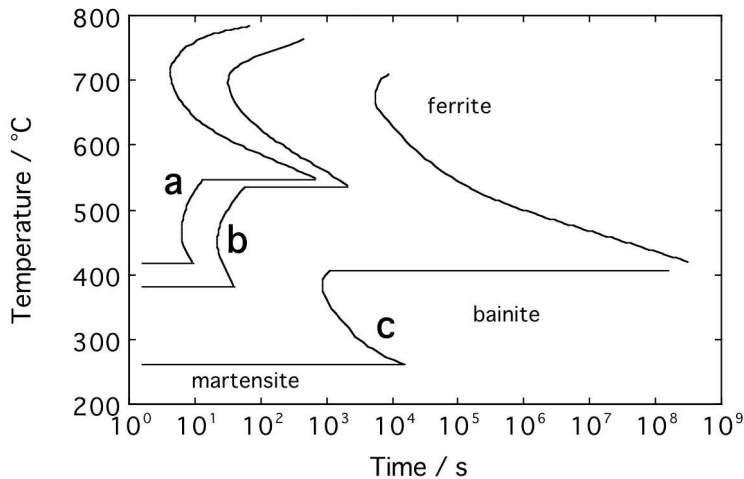


**Figure 12.36** Calculated time-temperature-transformation diagrams for steels **a** (0.15C-0.25Si-0.5Mn-1Mo-2.3Cr wt%), **b** (4.3Cr) and **c** (9.3Cr). The transformation curves refer to zero percent reaction. In each case the upper curve represents diffusional transformation whereas the lower curve represents bainite (Bhadeshia, 2001b).

site in the same steel; whereas the kinetics of precipitation are not identical in the two cases, the differences are very small over the temperature range of interest (500-650 °C). A martensitic microstructure is not therefore necessary in heat-resistant steels; bainite is adequate.

To summarise, the modern trend towards martensitic creep-resistant steels is associated with more with the need to improve the environmental resistance of the alloys rather than microstructural considerations. Indeed, there are well known disadvantages to high hardenability martensitic steels when it comes to weldability.

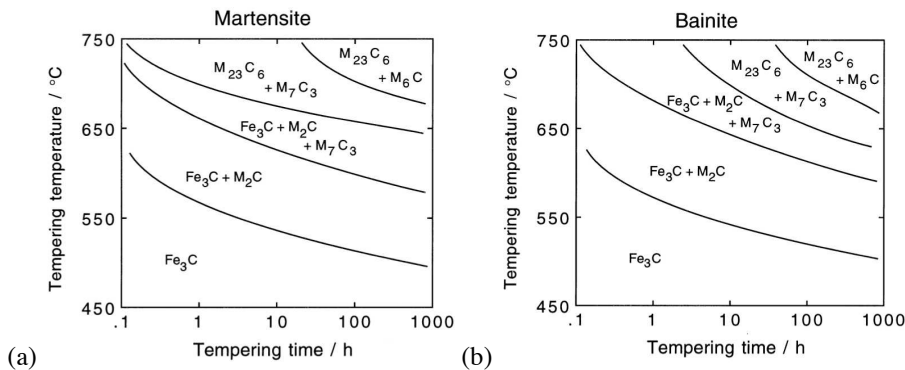


**Figure 12.37** Measured isothermal transformation diagrams for carbide precipitation reactions in  $2\frac{1}{4}$ Cr1Mo steel. (a) Martensitic starting microstructure; (b) bainitic starting microstructure. Adapted from Baker and Nutting (1959).

### 12.11.9 Transition Metal Joints

It is sometimes necessary in steam turbine assemblies to join the low-alloy ferritic steels to austenitic steels which are more suited for corrosive environments. The joints are usually between tubular elements although thicker joints are occasionally needed. The welds between these dissimilar steels are made using a filler material which is either an austenitic stainless steel, or a nickel-base alloy such as “Inconel”. The filler material/ferritic steel interface is quite abrupt when the nickel-base filler is used, even though a true metallurgical bond is achieved.

The ferritic steel is usually the  $2\frac{1}{4}$ Cr1Mo alloy. The chances of a dissimilar metal joint failing during service are large when compared with other welds between like metals. Nath (1982) has suggested that this is because of the complex stresses arising from the different creep properties of the filler, the HAZ and the ferritic base plate. The stresses are such as to intensify creep damage in the vicinity of the weld/base-plate junction.

The microstructure of  $2\frac{1}{4}$ Cr1Mo is essentially bainite, but after welding, that of the heat-affected zone can contain allotriomorphic ferrite. On the other hand, the coarser austenite grain structure in the HAZ adjacent to the fusion boundary has a higher hardenability and hence transforms into bainite. The allotriomorphic ferrite containing region is weak in creep, and is located sandwiched between two stronger regions, the original plate microstructure far away from the weld and the bainite at the fusion boundary. Furthermore, the austenitic (or Inconel) filler material is relatively rigid. This focusses the strain in the ferrite, causing the transition joints to fail prematurely. The joints are sometimes heat treated at  $700^\circ\text{C}$  for 30 minutes after welding for stress relief, but this does lead to a homogenisation of mechanical properties.

Nath (1984) attempted to overcome these problems by reheating the entire welded joint into the austenite phase field at  $950^\circ\text{C}$  for 1 h, followed by air cooling, with the aim of regenerating a fully bainitic microstructure throughout the parent material, including the heat-affected zone. The treatment was successful in improving the creep properties, but the overall performance was still less than that of the unwelded steel. The austenitising heat treatment caused the migration of carbon, which in the case of the ferritic/austenitic joint caused a decarburised zone on the ferrite side of the dissimilar metal interface and a carbon-enriched zone in the austenite on the other side. The carbon migration is driven by

the chemical potential gradient resulting from the different chemical compositions of the ferritic and austenitic steels.

## 12.12 Reduced-Activation Steels

The formation of voids during irradiation with neutrons causes the swelling of metals. Irradiation damage involves the creation of both interstitials and vacancies in equal concentrations, but the former anneal out more rapidly than the latter. The resulting excess concentration of vacancies is relieved by condensation into voids.

Ferrite has a much higher resistance to void swelling than austenite, although nickel base alloys rank alongside the ferritic steels (Little et al., 1991). Point defects introduced by irradiation condense at *neutral* or *biased* sinks. The latter are typically dislocations with large Burgers vectors, attracting more interstitials than vacancies. It follows that a large density of neutral sinks enhances the swelling resistance.

It is believed that in ferritic steels, irradiation induces the formation of two kinds of dislocations, one of which is strongly biased whereas the other is neutral. This provides sinks for both interstitials and vacancies, resulting in a smaller excess of void-forming vacancies. There are differences in the void swelling resistance of creep resistant ferritic steels because of variations in their microstructures. For a given vacancy concentration, a larger number density of vacancy traps leads to a smaller tendency for swelling. Lath boundaries or oxide particles are good vacancy traps.

It is for their swelling resistance that ferritic steels have been considered for structural applications in the construction of the first wall and blanket structures of fusion reactors. But in addition, there is a search for specific alloys whose radioactivity decays most rapidly once they are removed from the radioactive environment. These are the so-called *reduced activation* alloys which have minimal concentrations of Mo, Ni, Nb, Cu and nitrogen, all of which have long-lived radioactive isotopes (Abe et al., 1990; Klueh et al., 1995; Klueh, 2004). For example, molybdenum and niobium in steel can be induced by neutron bombardment to transmute into radioactive species such that the decay time to reach a safe level of radioactivity (25 micro Sieverts per hour) is of the order of  $10^5$  h.

Some of these undesirable elements are key constituents of creep-resistant steels, but they can be eliminated by using tungsten instead of molybdenum and by substituting vanadium and tantalum for niobium. Some examples of steels which have been studied specifically for their reduced activation are listed in Table 12.7.

Early studies revealed that of the first group of steels listed in Table 12.7, the 9Cr-2WVTa alloy in its martensitic condition has a high strength, good toughness and is able to retain its impact properties after irradiation (Fig. 12.38). On the other hand, the low-chromium bainitic steels have the advantage that they do not require a post-weld heat treatment which can be difficult to implement in complex fabricated structures.

Although the high Cr steels show only modest shifts in the ductile-brittle transition temperature following irradiation (Fig. 12.38), difficulties arise when the displacement damage is accompanied by the production of helium by the transmutation of traces of nickel. The helium is insoluble in the matrix and precipitates as small bubbles which embrittle the material. Suppose that the bubble has a radius  $r$ , then for an ideal gas the pressure inside the bubble is  $P = 2\sigma/r$  where  $\sigma$  is the interface energy per unit area. A small bubble can therefore hold a lot more gas under high-pressure than a large bubble. Typically, a 100 Å bubble holds gas at a pressure of  $10^3$  atmospheres whereas the pressure is only 1 atmosphere in a bubble which is  $10^5$  Å in size. Swelling can obviously be minimised by in-

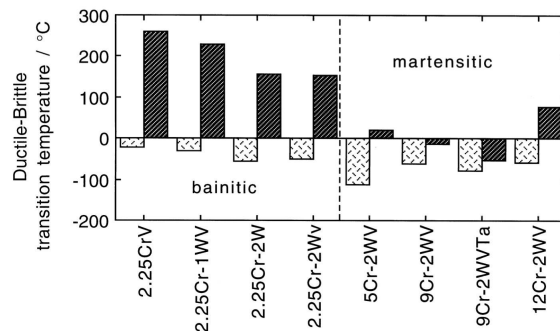


**Figure 12.38** The ductile-brittle transition temperature for normalised and tempered 3 mm diameter bar samples (light bars) and for samples which have been irradiated to about 14 dpa (dark bars). The 12Cr steel contains some  $\delta$ -ferrite in addition to martensite. Some of the bainitic steels may also contain allotriomorphic ferrite. After Klueh and Alexander (1999).

creasing the number density of bubble nucleation sites (Thompson, 1969, p. 356). Carbide particles are bubble nucleation sites but the high chromium steels form coarse  $M_{23}C_6$  particles in contrast to the larger numbers of fine MC or  $M_2C$  particles in the lower chromium alloys, making the latter more suitable for fusion reactor applications. On the other hand, the microstructures of the bainitic steels are much more sensitive to the cooling rate from the austenitic condition. Care has to be taken to ensure that the required fine distribution of carbides is obtained in practice.

Some of the steels listed in Table 12.7 are designed with low chromium concentrations to enhance the impact toughness in the irradiated condition. Klueh and co-workers found that the hardenability could be improved with a slight increase in the chromium concentration supported by additions of B and Ta; this resulted in a refined bainitic microstructure with improved toughness and tempering resistance. Indeed, the 2.6Cr-2WVTaB alloy is found to have mechanical properties comparable to those of the best 9Cr steels. The focus therefore has been on a 3Cr-3WVTa bainitic steel (Chen et al., 2004). It appears that the precipitation of fine tantalum carbides (TaC) during austenitisation refines the austenite grain size. In the absence of Ta, the prior austenite grain boundaries become decorated with relatively coarse  $M_3C$  or  $M_{23}C_6$  particles. The tantalum-containing variant therefore shows a higher strength and toughness than the variant without tantalum.

A fine distribution of carbides promotes toughness whether or not the steel is irradiated. The iron carbides which form in the early stages of tempering can be refined by increasing the silicon or aluminium concentration. It is these carbides which set the scene for the subsequent formation of alloy carbides, so there should be a consequential refinement of the entire carbide microstructure. This idea would be worth exploring in the context of reduced-activation steels.

**Table 12.7** Chemical compositions (wt%) of reduced activation steels (Kluh et al., 1995). All of these steels are bainitic with the exception of the 9Cr and 12Cr steels which are martensitic. The chemical compositions of the first group of steels are nominal.

Steel	C	Si	Mn	Cr	V	W	Ta	B
2 $\frac{1}{4}$ Cr-V	0.1			2.25	0.25			
2 $\frac{1}{4}$ Cr-1WV	0.1			2.25	0.25	1		
2 $\frac{1}{4}$ Cr-2W	0.1			2.25		2		
2 $\frac{1}{4}$ Cr-2WV	0.1			2.25	0.25	2		
5Cr-2WV	0.1			5	0.25	2		
9Cr-2WV	0.1			9	0.25	2		
9Cr-2WVTa	0.1			9	0.25	2	0.07	
12Cr-2WV	0.1			12	0.25	2		
2 $\frac{1}{4}$ Cr-2WVTa	0.1	0.12	0.40	2.41	0.24	2.03	0.05	
2 $\frac{1}{4}$ Cr-2WVB	0.090	0.12	0.38	2.37	0.24	2.04		0.005
2 $\frac{1}{4}$ Cr-2WVTaB	0.093	0.12	0.38	2.36	0.24	2.04	0.05	0.005
2.6Cr-2WVTa	0.11	0.11	0.39	2.59	0.25	2.02	0.05	
2.6Cr-2WVTaB	0.11	0.11	0.39	2.60	0.25	2.07	0.05	0.004
3Cr-3WV	0.097	0.14	0.50	2.96	0.25			
3Cr-3WVTa	0.097	0.14	0.50	2.94	0.25	0.10		
2 $\frac{1}{4}$ Cr-2W	0.11	0.15	0.39	2.48		1.99		
2 $\frac{1}{4}$ Cr-2WV	0.11	0.20	0.42	2.41	0.24	1.98		
9Cr-2WVTa	0.10	0.23	0.43	8.72	0.23	2.09	0.07	

### 12.13 Steels with Mixed Microstructures

Mixed microstructures consisting of bainite and martensite are usually a consequence of inadequate heat treatment or the use of steels with insufficient martensitic-hardenableity.

Early research suggested that bainite in an otherwise martensitic microstructure leads to a deterioration in ductility, toughness and strength (Bailey, 1954; Hehemann et al., 1957). The impairment of properties becomes less severe as the bainite forms at lower transformation temperatures, and is related to the difference in strength between martensite and bainite. As this difference decreases, so does the deterioration in properties (Hehemann et al., 1957).

Tempering homogenises the strength so bainite in a tempered martensite microstructure has less of an effect on the overall properties (Troiano and Klinger, 1952; Hehemann et al., 1957). For the same reason, a mixture of martensite and lower bainite has better properties than one consisting of upper bainite and martensite. The strength of lower bainite more closely matches that of martensite.

There are, however, circumstances in which mixed microstructures are beneficial. Edwards (1969) observed that after tempering, mixtures of lower bainite and martensite were tougher than either martensite or bainite. Mixed microstructures of bainite and tempered-martensite are similarly found to be stronger and tougher than the corresponding homogeneous phases, Fig. 12.39.<sup>11</sup> The toughness improves because the phase that first forms ( $\alpha_b$  or  $\alpha'$ ) geometrically partitions the austenite, thereby refining the size of the microstructure that is subsequently generated (Mutiu et al., 1977). It is argued that this is also why the wear resistance is greater in mixed microstructures of bainite and martensite (Zhou et al., 2001).

It is particularly interesting that the strength of a tempered mixture of lower bainite and martensite can exceed that of the martensite alone, and yet can be tougher (Fig. 12.40). We now proceed to quantitatively explain this behaviour.

The normal way to calculate the strength of a multiphase alloy is to use a rule of mixtures, i.e. to calculate a mean strength from that of each component phase weighted by its volume fraction. However, this is not adequate for the present purposes because of constraint effects. It is well established in fracture mechanics that the yield strength is increased by plastic constraint. This is why a weak brazing alloy can be used to effectively bond much stronger samples, as long as the thickness of the braze material is small enough to be constrained throughout by the surrounding stronger matrix. Indeed, the strength of the joint increases as the thickness of the braze layer decreases.

Dispersions of bainite plates form in austenite which subsequently transforms to much stronger martensite. This is similar to the brazing analogy. The deformation of the bainitic ferrite can therefore be expected to be constrained by the harder martensite. This can be modelled using experimental data available from brazed joints in high strength steels. The brazing alloys used in making the joints were non-ferrous materials which are ordinarily rather weak. The data, in a normalised form, are summarised in Fig. 12.41. The vertical axis is the joint strength normalised with respect to that of the unconstrained braze material; the horizontal axis is the braze thickness normalised relative to a thickness value where the restraint effect vanishes.

<sup>11</sup>(Tomita and Okabayshi, 1983b,a, 1985a,b; Tomita, 1987, 1988, 1991, 2000; Mirak and Nili-Ahmadabadi, 2004; Marcu et al., 2005)

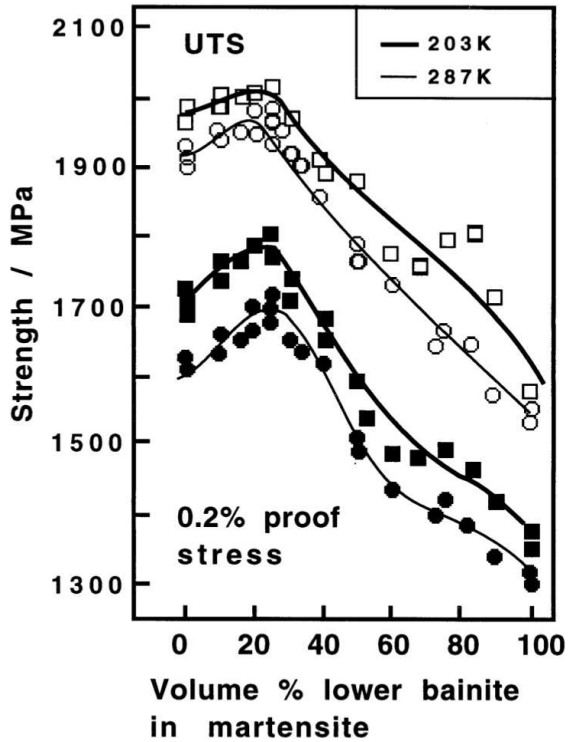


**Figure 12.39** Variation in the 0.2% proof stress as a function of the volume fraction of lower bainite in a mixed, tempered microstructure of lower bainite and martensite. The different curves represent data collected at the temperatures indicated on the diagram.

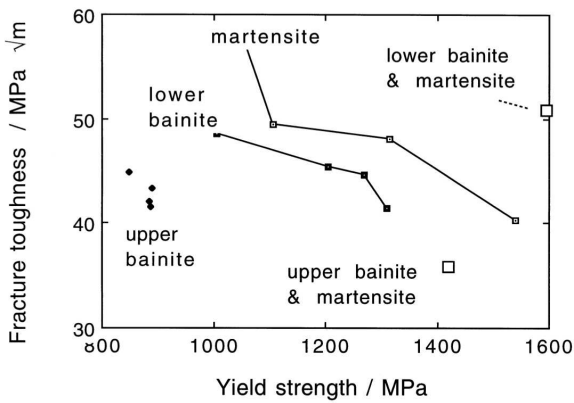


**Figure 12.40** Plot of toughness versus strength for a variety of microstructures in an ultra-high strength steel - data from Tomita (1988).

To analyse the properties of a mixed microstructure, it can be assumed that the normalised bainite thickness is equivalent to the volume fraction of bainite. Using this assumption, and the form of the normalised strength versus normalised thickness plot (Fig. 12.41), the strength of constrained bainite may be represented by the equation:

$$\sigma \approx \sigma_0 [0.65 \exp\{-3.3V_V^{\alpha_b}\} + 0.98] \leq \sigma_M \quad (12.9)$$

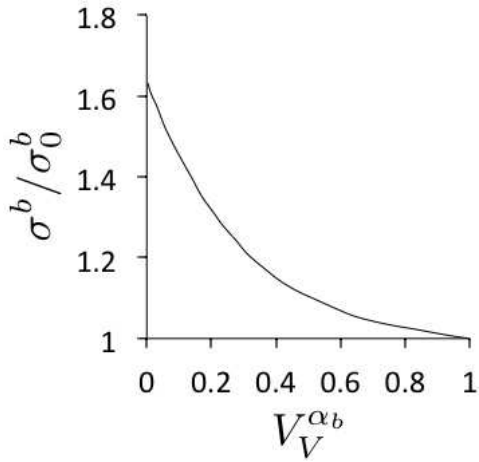


**Figure 12.41** Plot of the normalised strength of a brazed joint versus the normalised thickness of the brazing material, the latter being identified with the fraction of bainite in a martensitic matrix. After Young and Bhadeshia (1994).

where  $\sigma$  and  $\sigma_0$  represent the strengths of constrained and unconstrained bainite respectively,  $\sigma_M$  is the strength of the martensite and  $V_V^{\alpha_b}$  is the volume fraction of the bainite. The strength of bainite is always less than or equal to that of martensite.

When the volume fraction  $V_V^{\alpha_b}$  of bainite is small, its strength nearly matches that of martensite (Fig. 12.42), always remaining above that of bainite on its own. The strength of martensite continues to increase with the fraction of bainite, as the carbon concentration of the residual austenite from which it grows, increases.

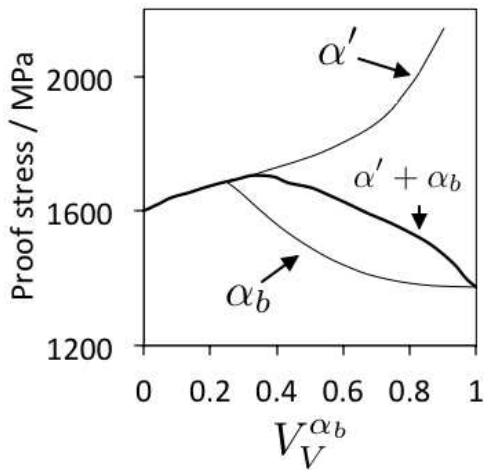


**Figure 12.42** The strength contributions of bainite and martensite in the mixed microstructure.

Fig. 12.43 shows how the strength of the mixed microstructure is predicted. Line (a) on Fig. 12.43 shows that a rule of mixtures cannot account properly for the variations observed. The agreement between calculation and experiment improves (curve b) as allowance is made for the change in the strength of martensite as carbon partitions into the austenite, due to the formation of bainite. The consistency between experiment and theory becomes excellent as constraint effects are also included in the calculations (curve c).

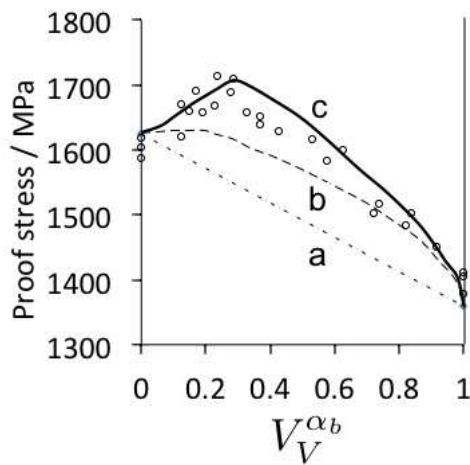


**Figure 12.43** Comparison of calculations against experimental data due to Tomita and Okabayshi (1985a).

It is clear that a simple rule of mixtures, in which the strength is expressed as a weighted average of that of the component phases, does not properly represent the composite properties. A recent study seems to contradict this conclusion; Petit-Grostabussiat et al. (2004) claim that the simple rule is able to satisfactorily represent the behaviour of mixtures of martensite and bainite. This is in spite of the fact that they did not take carbon partitioning or constraint into account. However, the fraction of bainite studied was within the range 0.25–0.7; Fig. 12.40 shows that this range is not sufficient to reveal the non-linear behaviour. Furthermore, Petit-Grostabussiat et al. (2004) did not attempt a prediction of strength; as a result, the behaviours characterised by curve a and curve c are also not revealed.

## 12.14 Summary

The anisotropic, thin-plate shape of bainite ensures that the mean free path for slip is comparable to the plate thickness rather than to the plate length. This means that the major microstructural contribution to strength is via the fine sub-unit size, rather than the sheaf or austenite grain size which are of minor importance as far as the strength is concerned. The sub-unit size is so small, that the Hall-Petch relation does not apply; yield is instead controlled by the stress required to expand dislocation loops. This gives an inverse linear relationship between the yield strength and the sub-unit size.

Bainitic steels usually exhibit continuous yielding behaviour, with proof stress to UTS ratios which can be much smaller than 0.8. This gradual yielding is a consequence of mobile dislocations, the presence of heterogeneities in the microstructure and residual stresses due to transformation. The ratio can be increased by annealing at low temperatures, although there is not much of a change if the bainite transformation temperature is comparable to the annealing temperature.

There is no doubt that higher carbon concentrations lead to a deterioration of ductility, primarily because of the void nucleating tendency of cementite particles. The presence of large regions of untempered martensite in the microstructure can reduce ductility, whereas retained austenite can in some circumstances enhance it.

The impact toughness of upper bainite deteriorates as its strength increases, but that of lower bainite which has much finer carbides is superior at the same strength level. An interpretation in terms of fracture toughness theory has demonstrated that it is the coarsest carbides in the microstructure which control toughness. Consistent with theory, the fracture strength correlates directly with the reciprocal of the square root of the coarsest carbide size. The scatter in toughness data increases as the microstructure becomes more heterogeneous; mixed microstructures of bainite and martensite show greater scatter than fully bainitic samples. During fracture, the cleavage facet dimensions are found to be comparable to those of bainite packets. A refinement of the austenite grain size also reduces the packet size, and consequently leads to an improvement in toughness. All of the impurity controlled temper embrittlement phenomena normally associated with martensite, are found in bainitic steels.

The endurance limit during the fatigue testing of smooth samples correlates well with the UTS of bainitic steels. The threshold stress intensity range for fatigue crack growth is reduced by the presence of retained austenite, because its transformation to martensite prevents the reversal of plastic strain during cyclic deformation. Stable austenite on the whole leads to an improvement in fatigue properties via the ductility it confers to the microstructure. This may in the future become an important consideration in the design of strong bearing-steels that have to endure rolling contact fatigue.

Retained austenite can lead to an improvement in the stress corrosion cracking resistance, by hindering the diffusion of hydrogen. However, comparable benefits can be achieved by any method which increases the number density of hydrogen traps in the microstructure.

Creep resistant alloys containing strong carbide forming elements represent one of the most successful industrial applications of bainitic microstructures. They achieve their creep strength via solid solution strengthening and with the help of fine dispersions of alloy carbides. The most modern of these steels is such that it can be welded without the need for post-weld heat treatments.

Finally, there are now numerous data to suggest that mixed microstructures of bainite and martensite can offer higher strength and toughness than fully martensitic alloys. The mechanism behind this remains to be established.



## CHAPTER 13

---

### MODERN BAINITIC STEELS

---

Steels with yield strengths in excess of 1000 MPa are important in certain applications, but the biggest commercial markets are for lower strength varieties, where the total alloy content rarely exceeds 2 wt%. The alloy design therefore has to be careful with a proper balance of hardenability in the context of large scale steel production technologies. Lean steels tend to transform into mixtures of allotriomorphic ferrite and bainite, whereas any attempt to improve hardenability usually leads to partly martensitic microstructures. The solution therefore lies in low-alloy, low-carbon steels, containing small amounts of boron and molybdenum to suppress allotriomorphic ferrite formation, principles established originally by Irvine and Pickering. Boron increases the bainitic hardenability. Other solute additions can, in the presence of boron, be kept at sufficiently low concentrations to avoid the formation of martensite. Steels like these (Alloy 1, Table 13.1), when normalised, are found to transform almost completely into bainite with only small fractions of martensite or other residual phases.

The other alloys listed in Table 13.1 are examples of some of the latest commercial bainitic steels. A striking feature of the list is that they don't look particularly different in chemical composition. This impression is misleading because each steel has distinct mechanical properties. Trace element concentrations are vital in determining the details of the microstructure as are the thermomechanical processing routes used in their manufacture.

Any alloy development or "advanced material" needs to be considered in the context of what already exists. For this reason, we first discuss the incredibly successful ferrite-pearlite microalloyed steels which set the standard by which any new alloy system must be assessed.

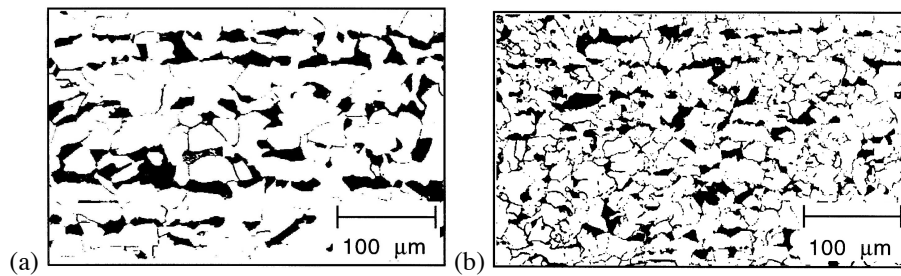


**Figure 13.1** Optical micrographs of banded ferrite-pearlite microstructures in (a) standard, (b) niobium microalloyed structural steel.

### 13.1 Alternatives to the Ferrite-Pearlite Microstructure

The most popular microstructure in the context of structural steels has undoubtedly been a mixture of ferrite and pearlite. There are hundreds of millions of tonnes of this manufactured annually. Typical chemical compositions are given in Table 13.2 together with an indication of the usual mechanical properties. Fig. 13.1 shows that the main effect of microalloying and the associated thermomechanical processing is to refine the microstructure. The niobium carbonitrides that form also strengthen the ferrite by interphase precipitation or by strain-induced precipitation (Pickering, 1978a,b; Honeycombe and Bhadeshia, 1995; Gladman, 1997).

Some of the major applications of structural steels include: oil and gas pipelines ( $\sigma_y = 350$ -485 MPa), drilling rigs and production platforms (345-415 MPa), ships (315-450 MPa), pressure vessels and tubing, earth-moving equipment (345-550 MPa), heavy goods vehicles and automobile components, high-rise buildings (415-530 MPa), bridges (345-485 MPa), transmission towers, fuel and other storage tanks and reinforcement bars for concrete (Pickering, 1992; Bodnar et al., 1997). A few of the attributes that are consistent with these applications include the low cost, ability to produce a variety of forms, weldability, fabricability, reliability under extreme conditions (such as fire and earthquakes and other *forces majeures*).

It seems unlikely in this context that the dominant position of the ferrite-pearlite steels will ever be challenged by alternative steel microstructures, let alone other materials! Nevertheless, we shall describe rivals based on bainite because such steels can be produced using a similar production route and without any additional heat treatments.

**Table 13.1** Typical compositions of advanced bainitic steels (wt%), which are fairly similar in composition with respect to the major solutes, but with different carbon and trace element concentrations and fabrication procedures.

No.	C	Si	Mn	Ni	Mo	Cr	Nb	Ti	B	Al	N	Others	Steel Type
1	0.100	0.25	0.50	-	0.55	-	-	-	0.0030	-	-	-	Early bainitic
2	0.039	0.20	1.55	0.20	-	-	0.042	0.015	0.0013	0.024	0.0030	-	Rapidly cooled bainitic
3	0.081	0.25	1.86	0.20	0.09	-	0.045	0.016	-	0.025	0.0028	-	Rapidly cooled bainitic
4	0.110	0.34	1.51	-	-	-	0.029	-	-	-	-	-	Rapidly cooled bainitic
5	0.100	0.25	< 1.00	-	-	-	-	-	-	-	-	-	Bainitic dual phase
6	0.040	-	0.40	-	-	-	-	-	-	0.05	-	-	Triple phase
7	0.150	0.35	1.40	-	-	-	0.022	0.011	-	0.035	-	-	Bainitic dual phase steel for buildings
8	0.120	1.50	1.50	-	-	-	-	-	-	0.045	0.0035	-	TRIP-assisted
9	0.160	0.38	1.30	-	-	-	-	-	-	0.030	0.0065	-	Low-Si TRIP-assisted
10	0.110	0.06	1.55	-	-	-	-	-	-	1.50	0.0017	-	Al TRIP-assisted
11	0.020	0.20	2.00	0.30	0.30	-	0.050	0.020	0.0010	-	0.0025	-	ULCB
12	0.028	0.25	1.75	0.20	-	0.30	0.100	0.015	-	0.030	0.0035	Cu 0.3, Ca 0.004	ULCB
13	0.080	0.20	1.40	-	-	-	-	0.012	-	0.002	0.0020	O 0.0017	Acicular ferrite, TiO <sub>x</sub>
14	0.080	0.20	1.40	-	-	-	-	0.008	0.0015	0.038	0.0028	-	Acicular ferrite, TiB
15	0.080	0.20	1.40	-	-	-	-	0.019	-	0.018	0.0050	-	Acicular ferrite, TiN
16	0.15	0.80	1.40	-	0.20	-	-	-	-	-	-	V 0.15	Forging (high strength)
17	0.09	0.25	1.00	0.50	1.00	-	0.10	0.02	0.002	0.04	0.006	-	Forging (100% bainitic)
18	0.09	0.40	1.40	-	-	-	0.07	-	-	0.04	0.010	V 0.06	Forging (Nb+V)
19	0.09	0.25	1.40	-	-	-	0.07	0.02	0.002	0.04	0.006	-	Forging (Nb+B)
20	0.18	0.97	2.50	0.02	0.1	0.20	-	0.03	0.0018	0.0095	0.0069	-	Forging (Si-rich)
21	0.12	-	1.60	-	-	-	0.08	-	0.004	-	-	-	Cold-heading
22	0.05	1.23	7.70	1.90	0.45	-	-	0.026	0.002	0.08	0.006	-	Experimental bainitic

**Table 13.2** Typical ferrite-pearlite structural steels.

Type	Composition / wt%				Stress / MPa			Elongation	$C_V$ (-20 °C)
	C	Si	Mn	Nb	$\sigma_y^l$	$\sigma_y^u$	UTS	%	J
Standard	0.11	0.21	1.24		285	320	480	36	55-90
Microalloyed	0.11	0.30	1.40	0.034	395	430	525	32	100-190

Type	Ferrite %	Pearlite %	Ferrite grain size	Pearlite interlamellar spacing
Standard	76	24	15 $\mu\text{m}$	0.22 $\mu\text{m}$
Microalloyed	78	22	9 $\mu\text{m}$	0.22 $\mu\text{m}$

### 13.2 Strength

Strength is a basic engineering specification; steels can be made stronger by transforming the austenite at ever decreasing temperatures (Fig. 12.4) or by increasing hardenability. There are many other strengthening mechanisms available. Unfortunately, toughness does not necessarily increase with strength. The weldability may also deteriorate because the excessive use of alloying elements can cause the formation of untempered hard-phases in the austenitised regions of the heat affected zone or there may be excessive softening in the tempered regions of the HAZ.

The tendency to soften depends on how far the original microstructure deviates from equilibrium (Table 13.3). Large deviations lead naturally to greater rates of softening because the driving force for tempering is the energy stored within the material; the heat simply provides the thermal activation needed to bump the structure to lower energies. Higher strength steels are therefore more likely to be difficult to weld.

**Table 13.3** The stored energy as a function of microstructure, relative to the equilibrium state defined as a mixture of ferrite, cementite and graphite (Bhadeshia, 1998). The phases in cases 1 and 2 involve a partitioning of all elements so as to minimise free energy. In cases 3-5 the iron and substitutional solutes are configurationally frozen (for martensite even the interstitial elements are frozen). Case 6 refers to an iron-based mechanically alloyed oxide-dispersion strengthened (ODS) sample which has the highest reported stored energy prior to recrystallisation (Bhadeshia, 1997b).

Phase Mixture at 300 K in Fe-0.2C-1.5Mn wt%	Stored Energy J mol <sup>-1</sup>
1. Ferrite, graphite & cementite	0
2. Ferrite & cementite	70
3. Paraequilibrium ferrite & paraequilibrium cementite	385
4. Bainite and paraequilibrium cementite	785
5. Martensite	1214
6. Mechanically alloyed ODS metal	55

### 13.3 Bainitic Steels

It is evident that ferrite-pearlite steels are outstanding on any performance criterion which includes cost and reliability. They will certainly not be threatened by the alternative microstructures to be discussed here. On the other hand, the novel microstructures offer a better set of properties for high performance applications where their additional cost is not an issue.

The steels developed by Irvine and Pickering exhibited quite reasonable combinations of toughness and strength, but in time proved to fall short of the best quenched and tempered martensitic steels. Nevertheless, the physical metallurgy principles established during their development have been applied in the metallurgical design of a new generation of bainitic steels, in which the emphasis is on reductions in carbon and other alloying element concentrations, and on processing designed to refine the microstructure. We now proceed to describe developments in these high-technology steels and cast irons based on bainitic microstructures. Many of the lower alloy content steels are thermomechanically processed prior to their transformation so it is appropriate to begin with a description of the key industrial processes in the context of bainite. The range of bainitic alloys currently in use is summarised in Fig. 13.2; the inoculated acicular ferrite steels have already been dealt with in Chapter 10.

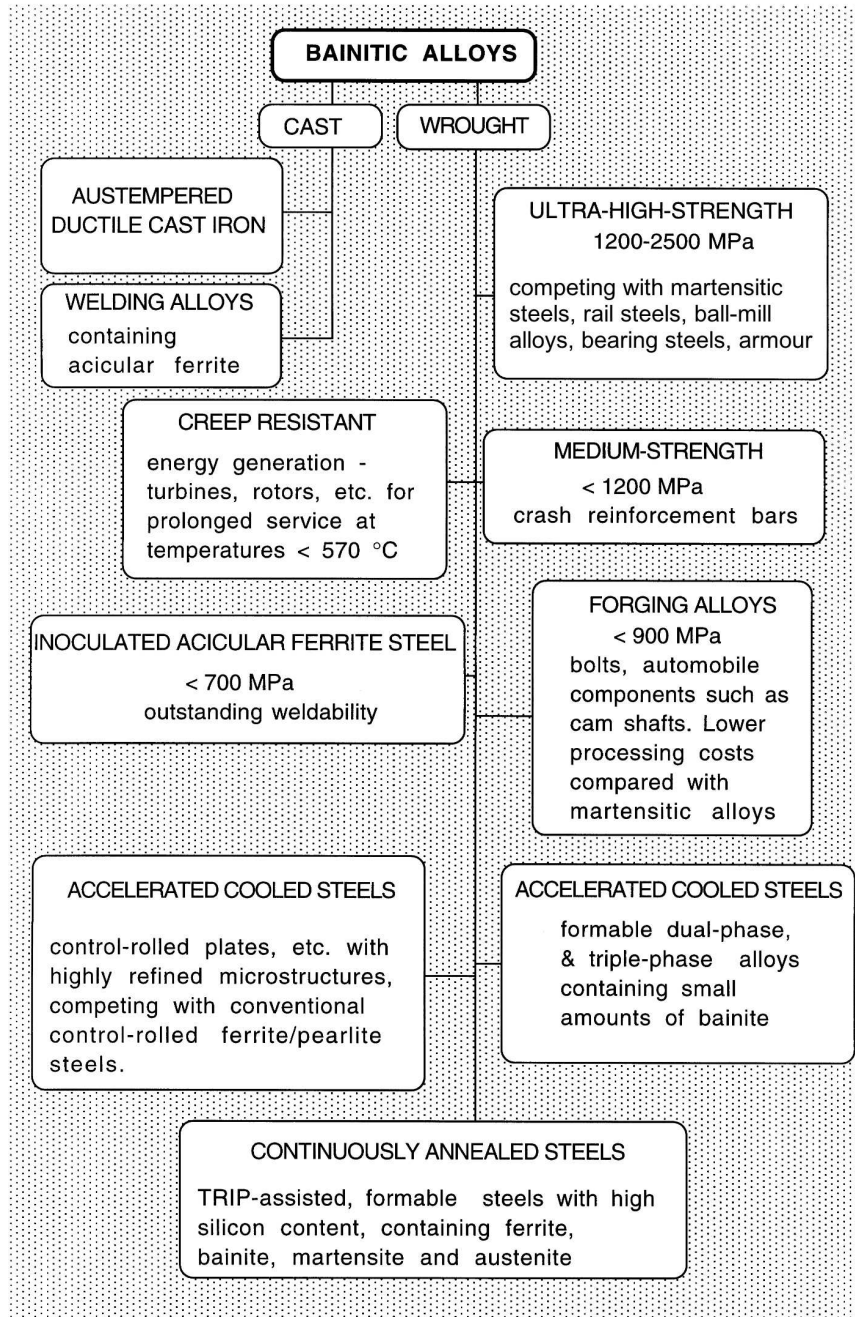


**Figure 13.2** The range of bainitic steels currently available on a commercial basis. TRIP stands for transformation-induced plasticity.

### 13.4 Controlled-Rolling of Bainitic Steels

The strengthening of iron via a reduction in grain size is an attractive option because a small grain size leads also to an improvement in toughness. This simple fact has led to the development of impressive thermomechanical processing technology capable of refining the austenite grain structure prior to its transformation to ferrite (Fig. 13.3). A fine austenite grain size leads to a correspondingly refined ferrite grain structure. The *controlled-rolling* process involves a sophisticated rolling deformation of austenite. The subject has been reviewed by Speich et al. (1984), where the complex procedures and the variety of rolling and alloying practices are discussed in detail. The essence of the process is the reduction of ingots by hot-rolling in the austenite phase field, such that the austenite is induced to recrystallise many times before the finish-rolling temperature is reached. This gives a fine recrystallised austenite grain structure. The growth of these grains during the hot-rolling process is hindered by the use of microalloying additions such as niobium or titanium. These elements are added in small concentrations ( $\approx 0.01\text{--}0.03\text{ wt}\%$ ) to form stable carbides or carbonitrides which impede austenite grain growth. As will be seen later, it can be an advantage if the austenite grains are pancaked (flattened) because such grains transform into finer ferrite. A typical chemical composition of a steel suitable for controlled-rolling into a ferritic microstructure is Fe-0.08C-0.3Si-1Mn-0.03Nb-0.004Nwt%.

Controlled-rolling has been used successfully for over 50 years to produce steels with a ferrite and pearlite microstructure; it has since been adapted for bainitic alloys (Nakasugi et al., 1980, 1981). There are two ways in which a bainitic microstructure can be obtained: the first involves an increase in the cooling rate in order to allow the austenite to supercool into the bainite transformation range. There are many variants of this, including one in which the austenite is given time to 'relax' prior to the onset of bainite. This stimulates dislocation cell formation and the precipitation of microalloying elements on the substructure, thereby leading to a refinement of the effective austenite grain size and hence of the bainite that forms subsequently (Wang and Liu, 2002; Shang et al., 2004; Yang and Putatunda, 2004).

The second is to modify the steel hardenability without substantially changing the processing conditions. Alloying elements such as manganese are boosted in order to retard the formation of allotriomorphic ferrite relative to bainite. Unlike conventional steels for controlled-rolling, TiN particles (of size  $\approx 0.02\ \mu\text{m}$ ) are induced to precipitate during solidification and subsequent cooling to ambient temperature. The precipitation of fine TiN is stimulated by increasing the cooling rate of the molten steel during continuous casting. Slabs of the material are then reheated to a low austenitisation temperature of  $1150\ ^\circ\text{C}$ , the TiN particles inhibiting austenite grain growth. The grain size is reduced during repeated recrystallisation due to controlled-rolling. By inhibiting grain growth, the particles also help to produce a uniform grain structure than is obtained in conventional processes. Finish rolling is carried out at a temperature where recrystallisation does not occur within the time scale of the rolling sequence; the austenite grains are therefore pancaked and have a deformed microstructure just before they start to transform into bainite.<sup>1</sup>

The details of the steelmaking process are important in determining the final properties of control-rolled steels. The higher quality steels are dephosphorised, desulphurised and vacuum degassed prior to casting. Typical concentrations of phosphorus and sulphur after

<sup>1</sup>An interesting variant of this allows the austenite to relax for about 200 s, permitting polygonisation of the dislocation structure. The resulting cell boundaries refine the bainitic microstructure by hindering the lengthening of plates (Wang et al., 2006).

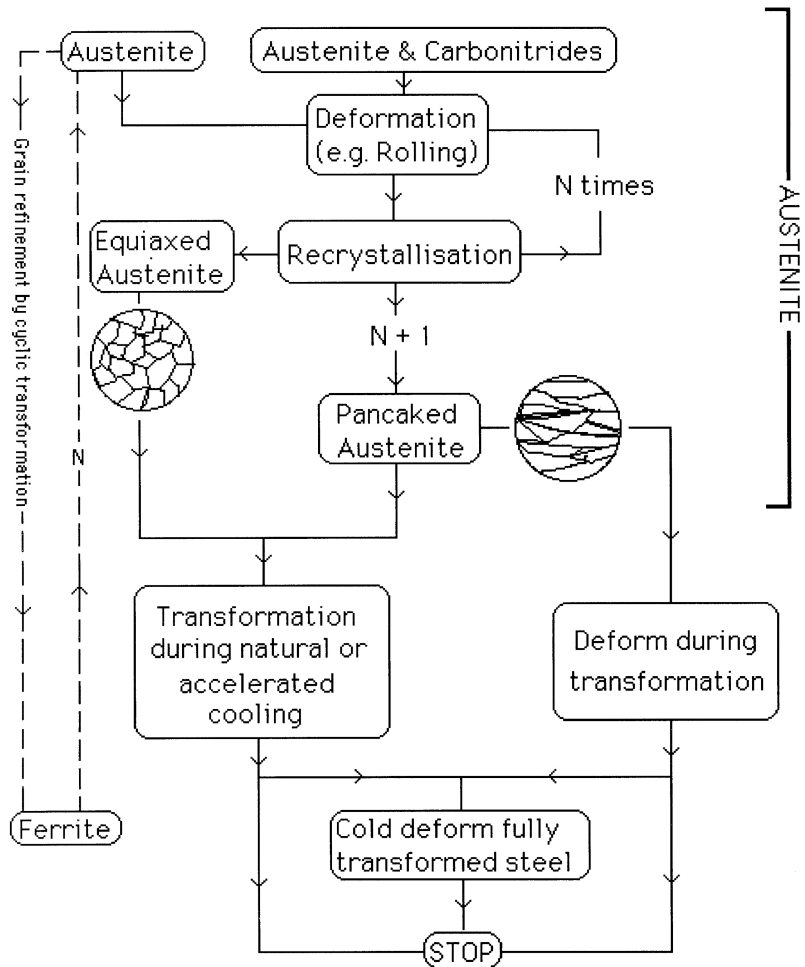


**Figure 13.3** Flow chart illustrating some of the thermomechanical processing routes available for the manufacture of steels.

these treatments are 0.015 and 0.0015 wt% respectively. In circumstances where formability and uniform ductility are important, the steel is usually treated with calcium which has the effect of fixing sulphur and of modifying the shape of the sulphide inclusions.

### 13.4.1 Crystallographic Texture

Polycrystalline materials do not in general contain grains which are randomly oriented. The crystals tend to align along particular orientations determined by the thermomechanical history of the material. This alignment is called *crystallographic texture* and its most important manifestation is in the development of anisotropic mechanical properties. The anisotropy may be exploited, as in deep-drawing steels where the texture is optimised to reduce plastic strain in the thickness direction. It can, on the other hand, be detrimental if the cleavage planes show a tendency to align because the fracture path becomes continuous across many grains. The problem is particularly acute in pipe steels where the orientation dependence of toughness is established for hot-rolled steels in general (Fegredo, 1975; Ray et al., 1995). Microstructural anisotropy due to chemical segregation with banding or elongated grain structure, and associated crystallographic texture are known to be important (Baczynski et al., 1999; Garcia et al., 2007; Joo et al., 2013, 2014).

In wrought steels, it is deformation, recrystallisation or phase transformation which can cause crystallographic texture. All of these processes occur during controlled-rolling. There are excellent reviews on the subject (Tanaka, 1981; Ray and Jonas, 1990), but the purpose here is to highlight the differences of crystallographic texture which arise between conventional and bainitic control-rolled steels.

A convenient (though incomplete) way of representing the texture in rolled sheet is by stating the set  $\{h k l\}\langle u v w \rangle$ , where  $\{h k l\}$  are the Miller indices of the planes which lie roughly parallel to the rolling plane, and  $\langle u v w \rangle$  the Miller indices of the direction in  $\{h k l\}$ , which tends to be parallel to the rolling direction. The texture can sometimes be deconvoluted into components:

$$\text{texture} = \sum_i \lambda_i \{h k l\}_i \langle u v w \rangle_i \quad (13.1)$$

where  $\lambda$  represents the weighting given to a particular type of texture. The major components of the deformation texture of austenite are  $\{1 1 0\}\langle 1 \bar{1} 2 \rangle$  and  $\{1 1 2\}\langle 1 1 \bar{1} \rangle$ , the so-called *brass* and *copper* textures respectively.

Because ferrite has an orientation relationship with the austenite, the brass texture gives rise to a  $\{3 3 2\}\langle 1 1 \bar{3} \rangle$  ferrite texture, and the copper texture to a  $\{1 1 3\}\langle 1 \bar{1} 0 \rangle$  ferrite component (Fig. 13.4). It is found experimentally that the  $\{3 3 2\}\langle 1 1 \bar{3} \rangle$  ferrite texture is beneficial to the deep-drawing qualities of steels and for strength and toughness. Control-rolling should therefore aim to maximise the brass texture component of austenite.

The texture of steel obtained from recrystallised austenite is made up predominantly of  $\{1 0 0\}\langle 0 1 1 \rangle$  ferrite, originating from the  $\{1 0 0\}\langle 0 0 1 \rangle$  *cube* recrystallisation texture of the parent austenite. This variety of ferrite textures can in principle be detrimental to the through-thickness mechanical properties of rolled steels, since the  $\{1 0 0\}$  ferrite cleavage planes tend to align with the rolling plane. The fraction of  $\{1 0 0\}$  normals within  $10^\circ$  of the plate normal tends to increase as the finish rolling temperature decreases, but there does not appear to be any systematic correlation with measures of toughness (Davies et al., 1977). It is possible that the texture is not uniform on a local scale. In fact, the cleavage process itself is not well defined for fine microstructures such as bainite, where the mode of brittle fracture is more accurately described as *quasi-cleavage*. In this, the cleavage

planes are frequently disrupted by fibrous fracture at finely spaced plate boundaries. The complete story is therefore likely to be more complex given that inclusions such as MnS also tend to align parallel to the rolling plane. Whatever the detailed explanation, both the texture and inclusions make it easier for the steel to delaminate parallel to the rolling plane. The texture enhances the toughness along the length and width directions at the expense of the through-thickness properties. It is important therefore to ensure that the austenite is in a deformed, rather than in its recrystallised state just before it begins to transform to allotriomorphic ferrite.

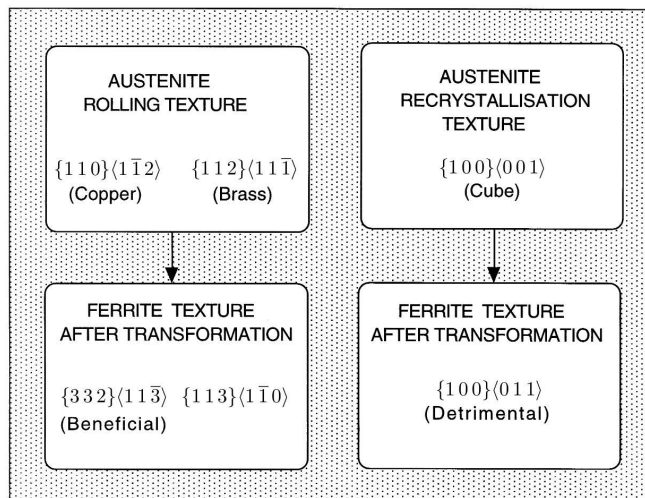


**Figure 13.4** Summary of crystallographic texture phenomena in wrought steels, adapted from Ray and Jonas (1990).

It has been possible to directly measure the texture between retained austenite and bainite (Verlinden et al., 2001). The transformation texture obtained when recrystallised austenite (with a weak texture) transforms into bainite is essentially random. The texture is much stronger when bainite grows in deformed austenite, partly because of variant selection in which each austenite grain transforms into a limited number of crystallographic variants of bainite.

The transformation textures associated with martensitic or bainitic microstructures (or acicular ferrite) are more pronounced when compared with the case where the deformed austenite transforms into allotriomorphic ferrite (Fig. 13.5). It is however, difficult to gauge the significance of the observations as far as delamination is concerned. Although the texture increases in intensity when the deformed-austenite transforms by a displacive mechanism, all of the components are strengthened. Any deleterious influence of the  $\{100\}\langle 011 \rangle$  ferrite component may therefore be masked by stronger components, and there do not seem to be any mechanical property data to indicate that bainitic steels which have been control-rolled have a greater propensity for delamination. Indeed, results to the contrary have been reported by Tamehiro et al. (1985a), who demonstrated that the delamination tendency is greater for conventional control-rolled steels, when compared with the more modern accelerated-cooled ferrite-bainite steels.

The observed differences in the strength of transformation textures are due to the displacive growth mechanisms of martensite, bainite and acicular ferrite; the experimental data have been critically assessed by Ray and Jonas (1990). It appears to be a general result that during controlled-rolling, when the transformation mechanism is reconstructive, all possible variants of the austenite/ferrite orientation relationship occur during transformation. There is therefore no *variant selection* during reconstructive transformations. On the other hand, attempts at predicting the product texture during displacive transformation, without assuming variant selection, have been unsuccessful in explaining experimental observations. The stresses and strains due to deformation favour the formation of particular variants in individual grains.

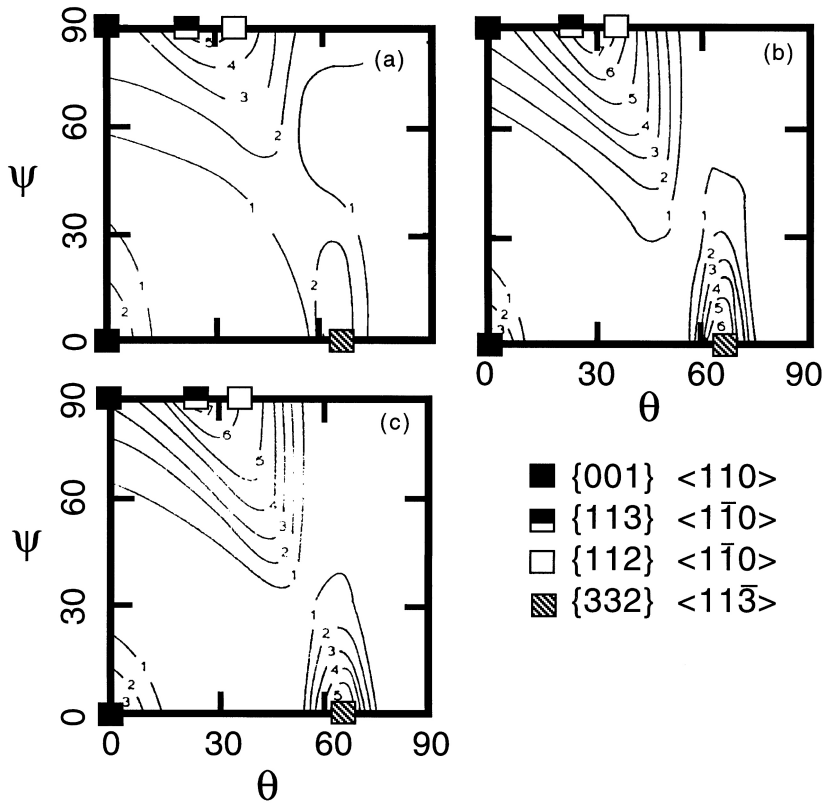


**Figure 13.5** Sections along  $\phi = 45^\circ$  of the crystal orientation distribution functions showing transformation textures of control-rolled steels with a variety of microstructures (Yutori and Ogawa, 1979). For steels the most important features of the orientation distribution function are in the section of Euler space at  $\phi = 45^\circ$  because it contains orientations of the form  $\{1\ 0\ 0\}\langle uvw\rangle$  and the fibre textures  $\{h\ k\ l\}\langle 1\ 1\ 0\rangle$  and  $\{1\ 1\ 1\}\langle uvw\rangle$ . (a) Allotriomorphic ferrite/pearlite; (b) acicular ferrite; (c) martensite. The points represent the exact textures indicated on the diagrams.

### 13.5 Rapidly Cooled Control-Rolled Steels

It was suggested in the previous section that bainitic microstructures can be generated in control-rolled steel either by increasing the hardenability or by changing the cooling rate during processing. The latter is the preferred route because the weldability deteriorates as the hardenability increases. The technology of rapid cooling during controlled-rolling is not trivial given the speed of production, the kinetics of transformation, the need to avoid distortion and nonuniform cooling. Progress has nevertheless been made and the rapidly cooled steels described here are commercially available. It is worth noting that rapidly cooled steels are often referred to as *accelerated cooled steels*.

Accelerated cooling plate mills are not essentially different from conventional rolling mills (Bodnar et al., 1997). The distance from the finishing mill to the point where the plate can be removed from the mill can vary from 12-116 m. The cooling unit uses up to about 45 m of this distance with a variety of water and air systems to achieve a controlled cooling rate which can be as high as  $100\text{ }^{\circ}\text{C s}^{-1}$  for a plate which is 10 mm thick.

#### 13.5.1 Pipeline and Plate Steels

There is a demand for a reduction in the wall-thickness and an increase in the diameter of pipelines for gas transmission. Thinner walls permit faster and less troublesome girth-welding operations. Thinner sections can be achieved by increasing the strength of the steels used, as long as toughness and weldability are not sacrificed in the process. When thickness considerations are not paramount, an increase in strength has the further advantage that the gas can be transmitted more efficiently under increased pressure ( $\approx 10\text{ MPa}$ ).

It is found that if, after thermomechanical processing, the steel is cooled at a rate which is high enough to reduce the amount of allotriomorphic ferrite, but low enough to avoid martensite, then a fine-grained microstructure which is a mixture of allotriomorphic ferrite and bainite is obtained. Such a microstructure has the required higher yield strength and toughness. The cooling rates involved are larger ( $10\text{-}40\text{ }^{\circ}\text{C s}^{-1}$  over the temperature range  $800\text{-}500\text{ }^{\circ}\text{C}$ ) than those appropriate for normal controlled-rolling (Fig. 13.6). The accelerated cooling is achieved using water spray curtains directed on either side of the hot plate such that distortion is avoided; the plates can be as thick as 15 mm. The rapid cooling of thicker plate requires different technology with careful control of water pouring and to cope with the slow rate at which the plate moves through the mill.

It has been demonstrated that the microstructure of these rapidly cooled steels consists of a mixture of ferrite and bainite (Graf et al., 1985). The bainite consists of sheaves of platelets of submicron thickness with a large dislocation density of  $1.7 \times 10^{14}\text{ m}^{-2}$ , compared with  $0.4 \times 10^{14}\text{ m}^{-2}$  in allotriomorphic ferrite. In fact, the dislocation density of the allotriomorphic ferrite in rapidly cooled steels is known to be about four times larger than in other steels containing ferrite, possibly because of plastic deformation caused by the formation of bainite (DeArdo, 1988). The volume fraction of bainite can vary from about  $0.2 \rightarrow 1.0$  depending on the steel composition and cooling conditions. Typical compositions for accelerated-cooled alloys are given as Alloys 2-4 in Table 13.1. Of these, Alloy 2 is the leanest and can be expected to contain the smallest amount of bainite.

The production of the steels is not a continuous process of casting and controlled-rolling followed directly by accelerated cooling. Instead, cast ingots are first allowed to cool to ambient temperature and then reheated for the thermomechanical treatment. This ensures that the coarse austenite grain structure which evolves during ingot cooling is disrupted by transformation to ferrite. The processing involves the reheating of thick ingots to  $1150\text{ }^{\circ}\text{C}$ ,

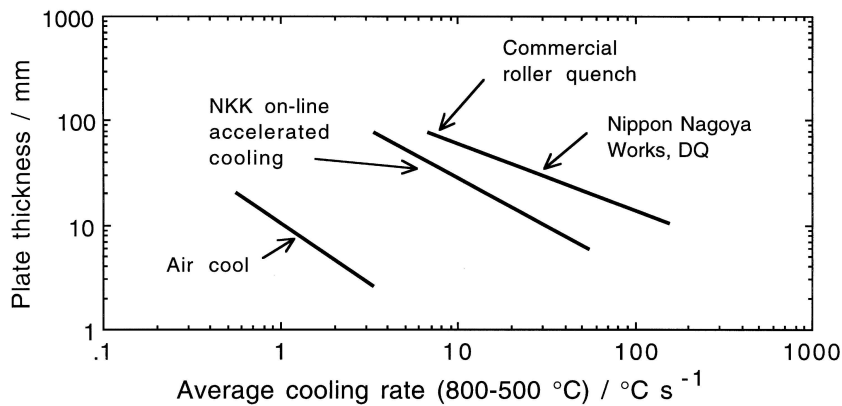


**Figure 13.6** An illustration of the average cooling rates associated with the manufacture of steels for structural applications (Gross et al., 1995).

followed by rolling during cooling of the ingot to  $740^{\circ}\text{C}$ , with the total reduction in thickness being more than 600%, followed by accelerated cooling at  $20^{\circ}\text{C s}^{-1}$  to around  $450^{\circ}\text{C}$  before allowing natural cooling. This treatment alters the normal microstructure, which is a mixture of ferrite and pearlite, to one which consists of ferrite and bainite, resulting in a better combination of mechanical properties. The tensile strength achieved is typically 700 MPa which is about 50–70 MPa higher than that of conventional control-rolled steels; the Charpy impact toughness can be an impressive 160–200 J at  $-20^{\circ}\text{C}$ . The extra strength is attributed to the fine size of bainite plates, although it has been demonstrated that the strength of the allotriomorphic ferrite also increases with the accelerated cooling (Morikawa and Hasegawa, 1985), probably because of the dislocation density increase described above. The steels show gradual yielding, although the relevance of this to pipeline applications is not clear (Collins et al., 1985).

### 13.5.2 Process Parameters

There are many processing variables which influence the properties of steel (Graf et al., 1985; Tamahiro et al., 1985b; Collins et al., 1985). For example, a high ingot-reheating-temperature allows more of the niobium carbonitrides to dissolve in the austenite; the niobium may subsequently precipitate during the  $\gamma \rightarrow \alpha$  reaction to give fine dispersions of interphase precipitates within the ferrite, thereby increasing its strength.

The temperature at which the rolling operation finishes is critical because it should leave the austenite grains in an unrecrystallised, pancake shape. This not only helps refine the microstructure but also helps avoid the undesirable recrystallisation texture of austenite. If the finish rolling temperature is too low then transformation happens during deformation; the deformed ferrite then is stronger but less tough. The finish rolling temperature ( $T_R$ ) also influences the variation in mechanical properties through the thickness of heavy gauge plates (Fig. 13.7). The surfaces, where the cooling rates are greatest, are harder compared with the central regions of the plates. The differences diminish as  $T_R$  is reduced because rolling deformation becomes focused at the plate surfaces, which then transform more rapidly, counteracting the effect of the higher surface cooling rates (Tanaka, 1988).

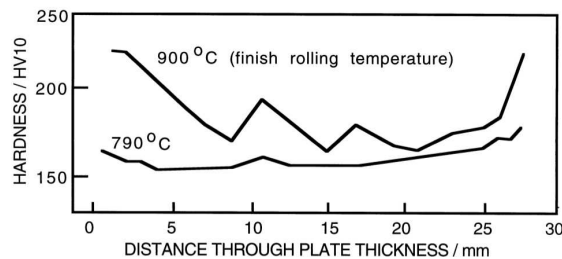


**Figure 13.7** The effect of the temperature at which rolling is completed, on the variation in hardness of a Fe-0.16C-0.63Mn wt% accelerated cooled steel (Tamukai et al., 1981).

Some of the steels processed using accelerated cooling have a high hardenability which introduces martensite into the microstructure with an accompanying reduction in toughness and increase in plate distortion. To avoid this, the cooling is arrested by cutting off the water sprays at temperatures between  $600 \rightarrow 450^\circ\text{C}$ . This has the effect of permitting more bainite to form thus reducing the amount of martensite that can form.

Another related problem occurs in alloys with high hardenability, for example, those containing more than about 1.4 wt% manganese. Thermomechanical processing actually reduces the yield strength even though the tensile strength increases, Fig. 13.8a (Shiga et al., 1983; Amano et al., 1988). This is because martensite replaces bainite as the dominant hard phase so yielding becomes a gradual process, giving the reduction in the proof strength. Although this has clear advantages for applications involving forming operations, the lowering of yield strength is a disadvantage for pipeline and heavy plate fabrications where the design thickness is calculated using yield criteria.

Assuming that the difficulty can be avoided by limiting martensite formation, a two-stage accelerated cooling process has been developed to promote bainite over martensite, while at the same time retaining the high cooling rate required to refine the allotriomorphic ferrite that forms first (Fig. 13.8b). After thermomechanical processing in the austenitic condition, the steel is cooled rapidly ( $25^\circ\text{C s}^{-1}$ ) through the ferrite temperature range in order to obtain the fine ferrite grain size, but the cooling rate is then reduced to about  $3^\circ\text{C s}^{-1}$  over the temperature range where bainite forms, thereby reducing martensite. The temperature  $T_F$  at which the forced cooling is stopped to allow the steel to air cool in the second stage of the process is important. The mechanical properties are less sensitive to  $T_F$  for the two-stage process presumably because much of the bainitic transformation is completed at a relatively high temperature during the second stage (Fig. 13.8). The process succeeds in raising the yield stress of the steel when compared with the conventional accelerated cooling procedure.

A general problem with accelerated cooled steels is that the toughness and microstructure are not maintained in the heat-affected zones due to welding (Nishioka and Tamehiro, 1988). The steels are nevertheless about 50 MPa stronger than conventional control-rolled plates. When this additional strength is not required the carbon-equivalent of the steel can be reduced to improve weldability (Fig. 13.9). Accelerated cooling is not appropriate for heavy gauge plates (20-30 mm thick) because it is not possible to ensure uniform cooling; the central regions of thick plates transform into a ferrite and pearlite microstructure rather than the desired bainite (Collins et al., 1985).

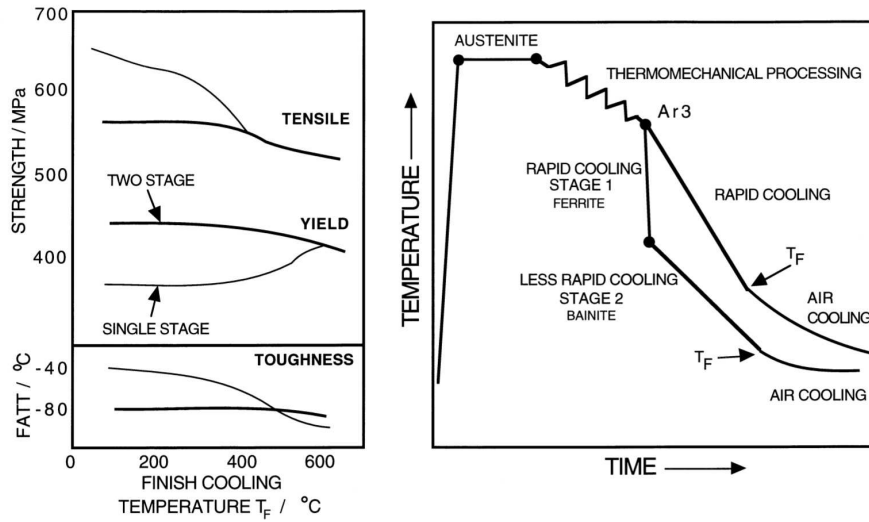


**Figure 13.8** (a) The relationship between the tensile and yield strength, and toughness of accelerated cooled steels as a function of the temperature at which the forced cooled is stopped, for the single and double stage processes. (b) Schematic illustration of the thermomechanical cycles associated with the two-stage accelerated cooling process (Amano et al., 1988).

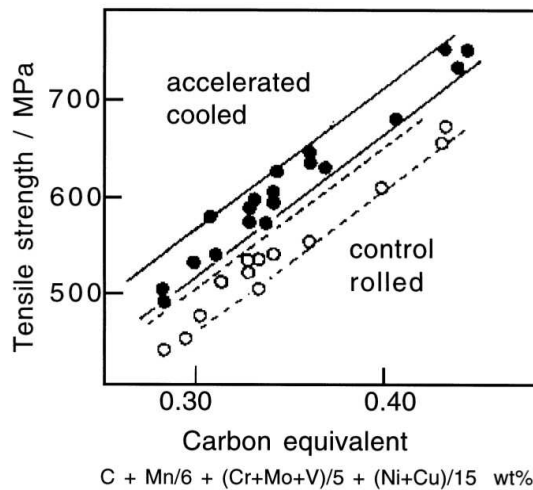


**Figure 13.9** Relationship between the carbon equivalent and tensile strength for conventionally produced control-rolled steels and accelerated cooled steels; the latter have a mixed microstructure of ferrite and bainite (Tamehiro et al., 1985b).

In control-rolled steels, thick plates which are cooled slowly after rolling develop a coarse ferrite grain structure at the surfaces. This is a consequence of the recrystallisation of ferrite grains deformed by rolling in the  $\alpha + \gamma$  phase field, due to heterogeneous deformation. Accelerated cooling avoids this difficulty because it inhibits recrystallisation, particularly at the surface (Tamehiro et al., 1985b).

### 13.5.3 Chemical Segregation

Control-rolled steels are cast continuously so they contain pronounced chemical segregation along the mid-thickness of the plate. For example, the manganese concentration at the centre can reach twice the average value. Ferrite naturally forms first in the manganese-depleted regions; the carbon partitioned as the ferrite grows ends up in the manganese-rich regions of austenite. This exaggerates the hardenability of the manganese-rich regions which transform into bands of hard microstructure.

These bands are susceptible to hydrogen cracking. Hydrogen can be infused into the steel through corrosion reactions or other phenomena. An advantage of the accelerated cooled steels is that they are more microstructurally homogeneous (Fig. 13.10); this is because the ferrite and bainite form at a larger undercooling during accelerated cooling, so transformation occurs everywhere, even in the manganese-rich regions. The gross banding characteristic of ferrite-pearlite microstructures is therefore minimised or avoided altogether (Graf et al., 1985; Tamehiro et al., 1985b). The resulting lower hardness in the segregated zone makes the steel less susceptible to hydrogen-induced cracking. Cracking ceases to be a problem because the hardness in all regions becomes less than about 250 HV (Tamehiro et al., 1985b).

The general conclusion is that microstructures which are homogeneous, and which contain less carbon, are less susceptible to both hydrogen-induced cracking and sulphide stress-corrosion cracking. In low-carbon pipeline steels, a bainitic microstructure is found to be more resistant to these problems than one containing allotriomorphic ferrite (Zhao et al., 2002b).

### 13.5.4 High-temperature processed pipe steel

Some rolling mills do not have the capacity to the large loads associated with the hot deformation of austenite at low temperatures. As a result, a class of pipe steel has been developed for thermomechanical processing at temperatures in excess of 1200 °C for large diameter pipes destined for high-pressure gas transmission systems (Gray et al., 1969; Hulka and Gray, 2001; Stalheim, 2005; Qiao et al., 2009). The development is commercially very successful with many thousands of kilometres of pipe installed. It relies on the application of very low carbon steel (< 0.05 wt%) that has concentrations of niobium as large as 0.1 wt% because the niobium in this case serves two purposes. The first is the traditional role of microalloying additions, to control to the austenite grain structure, and the second, to increase the hardenability of the steel to an extent that fine bainitic structures are obtained over a large range of cooling conditions. The steel is referred to by its American Petroleum Institute designation 'X80'.<sup>2</sup> The properties obtained are quite remarkable,

<sup>2</sup>The two digits after 'X' specify the minimum yield strength requirement of the steel in ksi (Smyth et al., 1990); X80 therefore has a minimum yield strength of 80 ksi (555 MPa). In practice, the ultimate tensile strength of X80 is usually in the range 700-750 MPa (Shiga et al., 1983) and will be dependent on the test orientation (Tamehiro et al., 1987c).

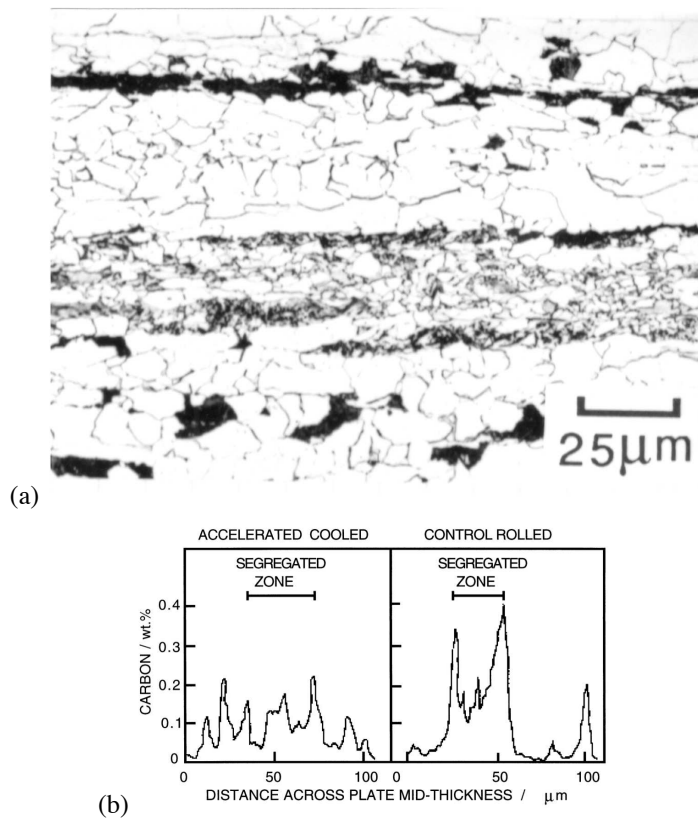


**Figure 13.10** (a) A light micrograph illustrating the effect of chemical segregation along the mid-thickness of heavy gauge plate. (b) Distribution of carbon concentration in the segregated zone for conventional control-rolled and rapidly cooled steel plates (Tamehiro et al., 1985c)

with impressive combinations of strength, toughness and weldability. Not all steels in the X80 category are processed at high temperatures, in which case they may contain greater carbon concentrations and lower niobium levels. A collection of reported compositions of X80 steels is presented in Table 13.4, and the HTP versions contain niobium concentrations close to 0.1 wt%. Stress-strain curves for X80 are illustrated in Fig. 13.11 in the context of other kinds of steels.

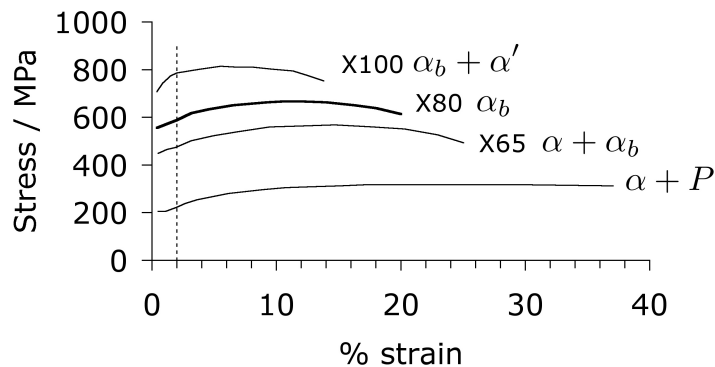


**Figure 13.11** Generic stress-strain curves of thermomechanically processed line-pipe steels, placed in context of ordinary mild steel. The dashed line identifies the yield strength of the pipe following manufacture. A simplified representation of microstructural constituents is indicated beside each curve. Adapted from (Takeuchi et al., 2003).

**Microstructure of HTP-X80** The microstructure of the HTP-X80 steel has been difficult to interpret given its fine scale and low-carbon concentration. The literature therefore tends to be cursory in its descriptions, with terms such as acicular ferrite, bainite and granular structures used. The structure is in fact bainite that forms over the temperature range 500–600 °C, depending on the cooling rate (Yan and Bhadeshia, 2013). The bainite occurs as thin plates separated by thin films of austenite, which later decompose into small cementite particles (Fig. 13.12a). The transformation temperature range over which the bainite is observed, corresponds rather well to the temperatures encountered during cooling conditions typical of line pipe steel as seen in the next section.

**CCT diagrams for X80** Fig. 13.13 shows CCT diagrams from X80 steel with composition typical of HTP-X80 (Table 13.4, rows 11, 12). The essential microstructure is bainitic over the relevant cooling rates but the reactions are substantially accelerated when using a lower austenitisation temperature and transformation from deformed austenite. The use of a higher austenitisation temperature which would lead not only to a larger austenite grain size but also a greater amount of niobium in solid solution in the austenite, has substantially depressed the onset of phase transformation at all of the cooling rates reported (Zeng et al., 2010). In contrast, cooling from just 810 °C and starting from a 40% deformed austenite makes all the reactions faster (Zuo et al., 2010).

**Table 13.4** Typical reported compositions (wt%) of X80 linepipe steels, illustrating the variability within the specified range.

	C	Mn	Si	P	S	Al	Nb	Ti	N	Mo	Cr	Ni	V	Others	Ref.
1	0.070	1.53	0.19	0.018	0.003	0.020	0.045	0.012	0.0045	0.20	-	-	-	Ca 0.0007	Williams et al. (1996)
2	0.075	1.59	0.31	0.018	0.001	0.026	0.057	0.013	0.0060	0.22	-	-	-	Ca 0.0011	Williams et al. (1996)
3	0.072	1.805	0.25	0.0078	0.001	0.031	0.035	0.012	0.004	0.29	0.02	0.26	0.003	Cu 0.009	Moeinifar et al. (2010)
4	0.052	1.60	0.11				0.096	0.014	0.006			0.14	-	Mo+Cr 0.46	Goodall et al. (2012)
5	0.065	1.55	0.29	0.018	0.003		0.076	0.02							Cizek (2001)
6	0.04	1.74	0.37	0.008	0.004		0.075	0.013	0.005	0.31	0.02	0.32		Cu 0.26	Pereloma et al. (1996)
7	0.07	1.35	0.14	0.009	0.003	0.044	0.086	0.047	0.007						Charleux et al. (2001)
8	0.06	1.65					0.034	0.012	0.005	0.24					Maalekian et al. (2012)
9	0.041	1.67	0.196	0.010	0.0006	0.042	0.095	0.011			0.031	0.246		Cu 0.258	Liang et al. (2009)
														B 0.003	
10	0.05	1.78	0.17				0.08	0.03		0.40	0.05	0.05		Cu 0.03	Zeng et al. (2010)
11	0.05	1.85	0.20	< 0.008	< 0.001	0.04	0.09	0.015	0.005		0.02	0.245	0.025	Cu 0.04	Zuo et al. (2010)
12	0.04	1.53	0.27				0.09	-	0.008	0.14			-		Sun et al. (1993)
13	0.08	1.89	0.42	0.012	0.0015	0.038	0.044	0.017	0.0041	< 0.05	< 0.05	0.18	-	Cu 0.19	Graf et al. (1985)
14	0.07	0.9	0.25	0.007	0.0015	0.023	0.04	0.015	0.004	-	-	0.2	0.04	Cu 0.2	Zhao et al. (2002a)
15	0.03	1.7			0.004		0.09	0.02		0.25					Collins et al. (1995)
16	0.035	1.71	-	0.012	0.003	0.028	0.095	0.021	0.009	0.32	0.03	0.02	-	Cu 0.28	Gray (2009)
17	0.04	1.58	0.13	0.013	0.004	0.03	0.098	0.01	0.004	0.02	0.24	0.15	-	Cu 0.03	Gray (2009)
18	0.03	1.75	-	-	0.0008	-	0.099	-	-	-			-	Cu	Hulka (2005)
19	0.06	1.27	0.17	0.005	0.0004	-	0.045		-	0.2	0.55			Cu, Ca	Kushida et al. (1997)
20	0.03	1.75	0.25				0.1	0.014	0.0035				-	Cu+Cr+Ni 0.75	Hulka and Gray (2001)
21	0.05	1.65	0.35				0.11	0.022	0.0094				-	Cu+Cr+Ni 0.3	Hulka and Gray (2001)
22	0.05	1.85					0.09				0.3	0.2	0.03	Cu 0.3	Hulka and Gray (2001)
23	0.05	1.75					0.08	0.01		0.3		0.3		Cu 0.3	Hulka and Gray (2001)
24	0.11	1.58	0.22	0.019	0.003	-	0.05	-	-	-	-	0.18	0.08	-	Iino et al. (1982)

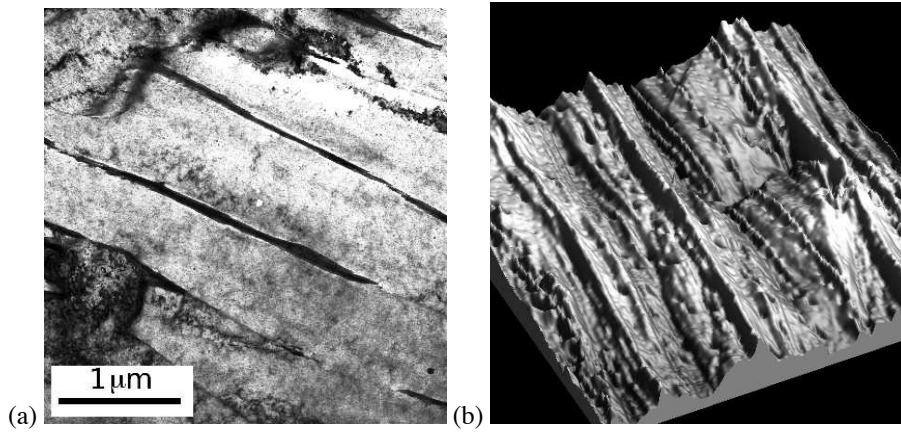


**Figure 13.12** (a) Transmission electron microscopy of bainite in HTP-X80 steel. (b) Surface relief, as determined using atomic force microscopy of bainite in HTP-X80. After Yan and Bhadeshia (2013).

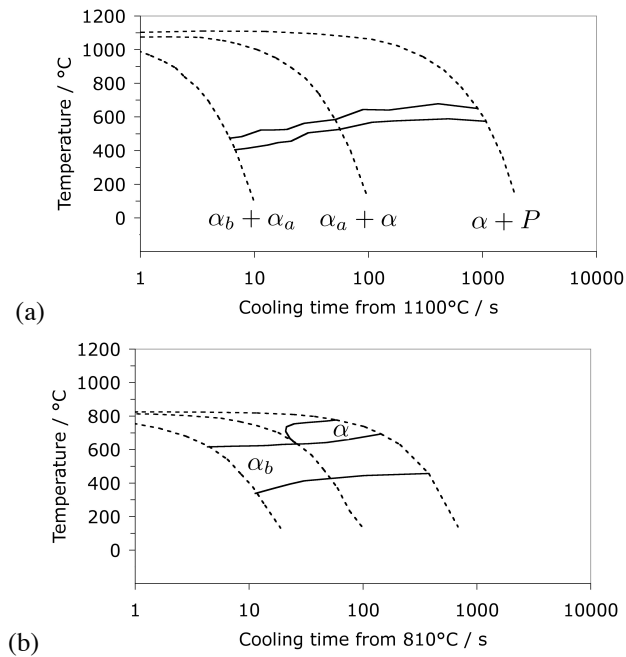


**Figure 13.13** Continuous cooling transformation diagrams, adapted from (Zuo et al., 2010; Zeng et al., 2010). (a) Kinetics associated with a high austenitisation temperature for the alloy listed in row 11 of Table 13.4. (b) Kinetics associated with a low austenitisation temperature with the austenite deformed 40% prior to transformation, for the alloy listed in row 12 of Table 13.4.

### 13.6 Steels with High Formability

The oil crisis of the seventies led to the development of the *dual-phase* steels in an effort to reduce the weight of cars and make them fuel efficient. Conventional automobile steels consist either of mixtures of ferrite and small amounts of pearlite, or wholly of ferrite, with a tensile strength of  $\approx 420$  MPa and sufficient formability. In the context of automobile manufacture, formability includes the effects of operations like deep drawing, bending and the ability to stretch around features such as holes.<sup>3</sup>

Ordinary steels are troublesome in forming operations because they exhibit discontinuous yielding behaviour, which causes the formation of unsightly stretcher strains on the finished products. Dual-phase steels are similar in composition to conventional alloys, but are heat treated to generate a mixed microstructure of ferrite and martensite. Their mechanical properties are characterised by continuous yielding, a small proof to tensile strength ratio and a large uniform elongation (Fig. 13.14). The free dislocations in martensite, the dislocations in the ferrite due to the strain induced by martensitic transformation, Fig. 13.15, and the large difference in hardness between the phases all contribute to yielding behaviour (Furnémont et al., 2004). Although the 0.2% proof stress can be small, the dual phase steels strain harden rapidly so the ultimate tensile strength can be quite large at 500–650 MPa, without loss of formability. More details on dual phase steels can be found in a review by Owen (1980). A typical dual-phase steel would have a chemical composition Fe-0.09C-0.6Si-1.0Mn wt% and would be heat treated to give a mixed microstructure containing about 20% martensite and 80% ferrite. The high silicon concentration is known to enhance formability; alloying elements such as chromium are sometimes added in small concentrations ( $\approx 0.5$  wt%) for hardenability and solid solution strengthening. The carbon concentration is normally less than 0.2 wt% to avoid brittle spot-welds.

One method of heat treatment involves the annealing of strip at a temperature phase  $\alpha + \gamma$  field, followed by cooling at a rate which ensures that the austenite transforms into martensite. However, it is less expensive to integrate the heat treatment into the steel production process, by adjusting the conditions to allow the required microstructure to develop immediately after the hot-rolling and coiling process.

There are difficulties associated with the ferrite–martensite dual-phase steels. They do not have sufficient stretch flangeability and can suffer from localised necking in the heat-affected zones of flash butt welds. The final coiling temperature has to be below  $M_S$  with a sufficiently large cooling rate; this is technically difficult to attain at high mill-speeds. Also, the liberal use of alloying elements is costly and the silicon forms hard and adherent oxides making it difficult to implement surface cleaning prior to hot rolling.

Attempts have therefore been made to create dual-phase steels in which the hard phase is bainite instead of martensite (Esaka et al., 1985). These new dual phase steels are simple in composition (Alloy 5, Table 13.1). They are hot rolled in the austenite phase field to give a fine austenite grain size, cooled rapidly into the bainite transformation region (typically 400 °C) and coiled in that temperature range to promote bainite. The ferrite forms during the cooling operation, and the cooling rate ( $40 \rightarrow 100$  °C s<sup>-1</sup>) determines

<sup>3</sup>A common test involves the measurement of a *hole expansion limit* which is the ratio of the hole radius before and after expansion. The test can be carried out using a cone or a flat punch. Hole expandability increases with the difference between the total elongation and uniform elongation, and depends on the cleanliness of the steel. Since localised necking and subsequent fracture limit the ability of the hole to expand, it is the freedom of the steel from inclusions which often determines acceptability. Microstructures without cementite are, for the same reason, favoured. High strength fully bainitic or martensitic steels which have more homogeneous microstructures, show better hole expandability than, for example, dual-phase steels.

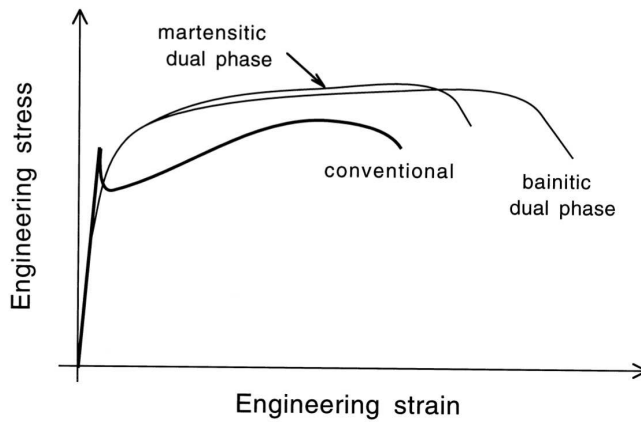


**Figure 13.14** Schematic stress-strain curves comparing the deformation behaviour of conventional high-strength low-alloy automobile steel and that of dual-phase steels. The bainitic dual-phase steel fares better because of its greater retained austenite content.

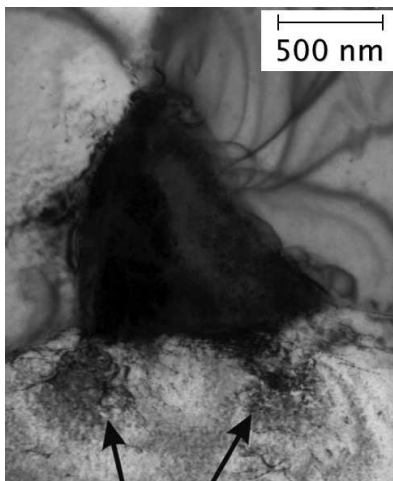


**Figure 13.15** Dislocations induced in ferrite due to martensitic transformation in an island of prior austenite. Reproduced with permission of Maney, from (Furnémont et al., 2004).

the fraction of bainite, which may vary from 0.2-1.0 depending on the cooling conditions and composition. A coiling temperature below  $M_S$  can induce martensite as well, giving a triple-phase steel.

The new steels have better weldability because the bainite which forms in the heat-affected zone is softer than martensite. The martensite does not form in the HAZ because of the lower carbon equivalent of the new steels.

Conventional dual-phase steels have been used in automobile manufacture but not for body panels where their formability is inadequate. Bainitic dual-phase steels are in this context superior, but because the difference between the hardness of ferrite and bainite is relatively small, they sometimes exhibit discontinuous yielding. A compromise solution would be a triple-phase steel containing some martensite in addition to bainite and ferrite, to promote gradual yielding. Sudo et al. (1981, 1982) have demonstrated that triple-phase

steels (Alloy 6, Table 13.1) do have the best combination of mechanical properties for press forming applications.<sup>4</sup> Notice that their triple-phase steel is leaner in alloy content than the dual-phase alloys; the development of the required microstructure therefore depends on more difficult heat treatment practice.

Bainitic dual-phase steels have been developed for the building industry, specifically to exploit their low yield to tensile strength ratio (Terada et al., 1990). High-rise buildings require heavy gauge, strong and weldable steels. It is also necessary for earthquake resistant design, to ensure that the steel has enough ductility after yielding to sustain localised deformation without collapse. Studies of the consequences of earthquakes suggest that steel may be the only cost-efficient construction material which imparts reliability to constructed structures. During an earthquake, the beams and columns of the building framework, which support axial loads, experience bending moments. The maximum bending moment that the beam can support before plastic collapse is reduced when the yield ratio is large. Conventional steels for these applications are quenched to a mixed microstructure of bainite and martensite, which is then tempered; any attempt to increase the yield strength unfortunately also increases the yield ratio. For reasons already discussed, this is not the case for dual-phase steels where the heterogeneity of the microstructure lowers the yield strength but increases the tensile strength. The bainitic dual-phase steel developed for building purposes (Alloy 7, Table 13.1) has a yield ratio of about 0.7 compared with the quenched and tempered martensitic steel for which the ratio is 0.9 (Terada et al., 1990). The steel is produced by controlled rolling, and the temperature where the forced cooling cycle commences determines the exact mix of phases and the precise mechanical properties. Typical properties of plates ranging in thickness from 12-80 mm, are 460 MPa yield strength, 600 MPa tensile strength, 35% elongation and > 200 J of Charpy impact energy at ambient temperature. These properties are not degraded by welding.

### 13.6.1 TRIP-Assisted Steels

TRIP stands for transformation-induced plasticity (Chapter 8); martensitic transformation induced by local stress has the effect of relieving stress concentrations, increasing the work hardening rate, and promoting homogeneous deformation, with consequent improvements in the strength, ductility and toughness of steels. TRIP-assisted steels of the type discussed here are also known as 'continuously annealed steels', because the required microstructure can be generated using a complex heat treatment within a matter of seconds during the processing of steel strip. Their microstructure consists of allotriomorphic ferrite as the major phase mixed with a total of 30-40% of bainite, martensite and carbon-enriched retained austenite. The chemical composition is typically Fe-0.12C-1.5Si-1.5Mn wt% (Alloy 8, Table 13.1); the silicon prevents cementite precipitation so the carbon rejected by bainite enriches the austenite which is retained. Alloy 10 in Table 13.1 is an example of a TRIP-assisted which uses aluminium instead of silicon to suppress cementite (cf. section 3.3.2). There is no difficulty in producing the required microstructure but aluminium in solution does not contribute much to the strength of ferrite. This leaves the aluminium-containing steels somewhat weaker than those which exploit silicon (Girault et al., 2001;

<sup>4</sup>That the introduction of a small amount of martensite into the microstructure of predominantly ferrite-bainite mixtures leads to continuous yielding behaviour has been confirmed (Saha Podder et al., 2007). If the material is subsequently bake-hardened following forming operations, then discontinuous yielding is likely to occur. This may be an advantage if the forming operation is completed since there is an accompanying increase in strength of about 25-60 MPa (Wang et al., 2004b; Timokhina et al., 2010b).

Jacques et al., 2001c); the strength of the Al-containing TRIP steels can be increased whilst maintaining formability by boosting the average carbon concentration and optimising the heat treatment (de Meyer et al., 1999). Aluminium does of course increase the free energy change due to the  $\gamma \rightarrow \alpha$  transformation, in other words, it reduces the hardenability of the steel (Aaronson and Domian, 1966; Mertens et al., 2003; Garcia-Mateo et al., 2003a). This means that a larger quantity of allotriomorphic ferrite, and bainite in subsequent transformation of the residual austenite, may be obtained during intercritical annealing of the TRIP-assisted steels (Suh et al., 2007a,b).

The alloys are used to improve the safety of automobiles without adding to their weight. The strong steel which connects the front bumper to the frame was in the past made of high-strength low-alloy steels with a UTS of about 400 MPa. These have now been replaced by the TRIP-assisted steels with an ultimate tensile strength of 600 MPa with consequent reductions in weight. Side-impact bars with similar microstructures are used with the UTS in the range 900-1500 MPa.

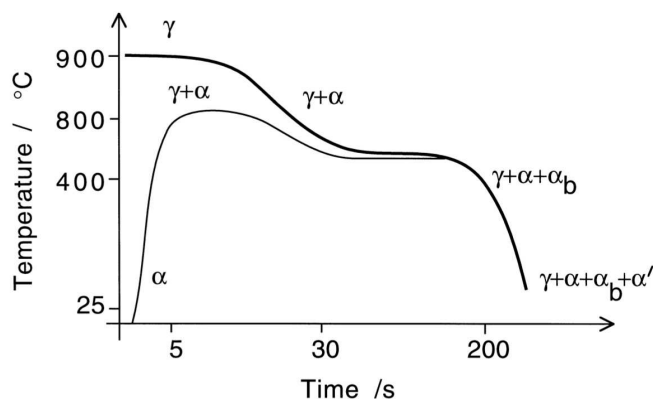


**Figure 13.16** Schematic illustration of the two kinds of heat treatment used to generate the microstructures of TRIP-assisted steels. Some typical times and temperatures are indicated on the graph axes. The lighter curve represents an intercritical annealing heat treatment whereas the bold curve involves transformation from a fully austenitic sample. The terms  $\gamma$ ,  $\alpha$ ,  $\alpha_b$  and  $\alpha'$  represent austenite, allotriomorphic ferrite, bainite and martensite respectively.

There are two kinds of TRIP-assisted steels. In the first case a cold-rolled strip is heated rapidly from ambient temperature to form some austenite (Fig. 13.16). This stage is known as an “intercritical anneal”.<sup>5</sup> The intercritical annealing not only leads to the formation of austenite but also recrystallises the residual ferrite. The strip is then cooled at a controlled rate which may lead to the transformation of the austenite first into allotriomorphic ferrite which during cooling grows epitaxially on the existing ferrite (Zaefferer et al., 2004), and subsequently into bainitic ferrite.<sup>6</sup> This latter reaction causes the austenite to become enriched in carbon, some of which may decompose to martensite on cooling, although a

<sup>5</sup>The  $A_{e1}$  and  $A_{e3}$  temperatures on the iron-carbon phase diagram are often identified as the “critical temperatures”. The term “intercritical annealing” refers to heat treatment in the temperature range  $A_{e1} \rightarrow A_{e3}$  when the alloy is in the  $\alpha + \gamma$  phase field.

<sup>6</sup>Such epitaxial growth of bainite is possible provided the allotriomorphic ferrite is appropriately oriented with respect to the austenite (Babu and Bhadeshia, 1991).

fraction ( $\approx 0.05 - 0.15$ ) may be retained (Fig. 13.17). The stability of the austenite does depend on the microstructure and its state of deformation prior to intercritical annealing (Hashimoto et al., 2002; Huang et al., 2004), with an initial martensitic state giving the best properties because the austenite that is left in the final state is more refined and constrained. If the initial microstructure is a mixture of ferrite and pearlite then the elongation recorded in the final processed state is found to be significantly smaller. A similar observation applies to the so-called quench and partitioning steels (section 5.5), where an initial martensitic structure leads to more mechanically-stable austenite following the relevant heat treatment, due to a refinement of the overall microstructure (Zhang et al., 2014).

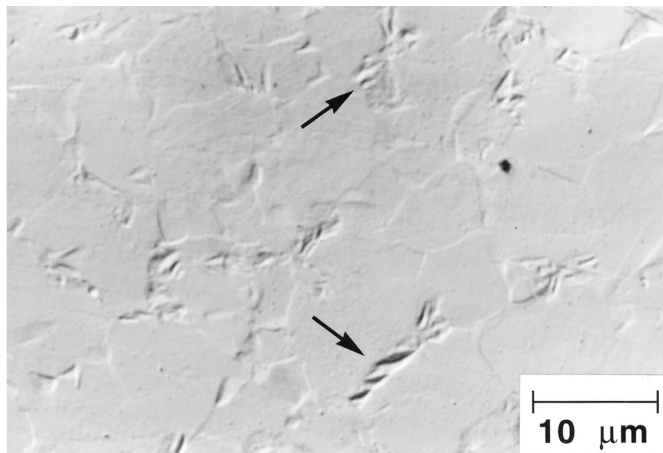


**Figure 13.17** A Nomarski interference micrograph of a TRIP-assisted steel. The sample was metallographically polished, protected against oxidation and then subjected to an intercritical anneal and subsequent partial transformation of the austenite into bainite. The latter phase is here identified by the displacements due to its growth mechanism. Micrograph courtesy of Professor P. Jacques.

The details of the microstructure and mechanical properties can be altered by changing the cooling rate or varying the rate as a function of the temperature. For example, it is common practice to allow more time in the bainite transformation range than at the higher temperatures where allotriomorphic ferrite grows. Fig. 13.18 shows the effect of holding in the bainite transformation temperature range on the final microstructure. An inadequate amount of bainite leaves the austenite susceptible to martensitic transformation. Similarly, because the carbon concentration in the austenite is limited by the  $T_0$  curve (Chapter 1) transformation to bainite at too high a temperature renders the austenite unstable (Matsuda et al., 2002; Nakagaito et al., 2003).

The second kind of heat treatment starts from a hot-rolled strip which is fully austenitic (Fig. 13.16) and forms both allotriomorphic ferrite and bainite during the cooling part of the thermal cycle. This has the advantage that the microstructure can be produced directly from the hot strip which has been rolled to its final dimensions. The process is cheap since the strip does not have to be heated to the intercritical annealing temperature. However, hot-rolling mills are restricted by rolling loads to strips thicker than about 3 mm, although there are modern mills which can cope with 1.4 mm thickness. Cold-rolled strips can, on the other hand, be made routinely into thinner gauges. Hot-rolled strips are preferred for automobile applications where cost is a prime factor in the choice of materials.

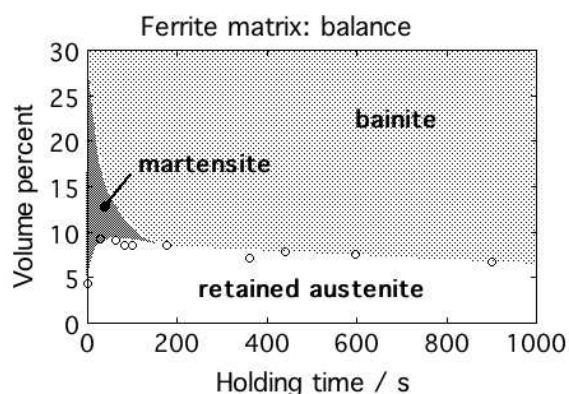


**Figure 13.18** Evolution of room temperature microstructure as a function of the time during isothermal transformation to bainite. Data from Girault et al. (2001).

Virtually all such TRIP-assisted steels are based on the simple Fe-Si-Mn-C system with a narrow composition range. In spite of this, it is possible to obtain a great variety of combinations of the yield strength, ultimate tensile strength and uniform elongation by making subtle changes to the heat treatment (Fig. 13.19).

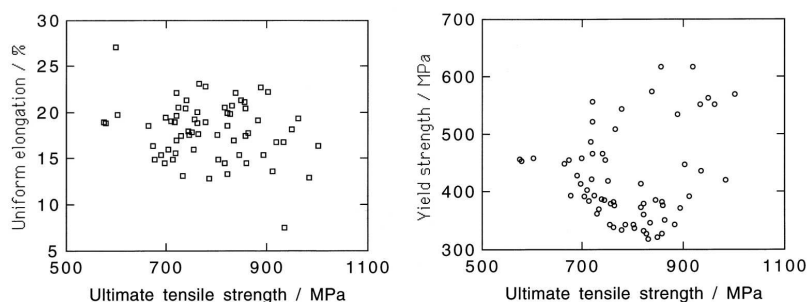


**Figure 13.19** The remarkable range of mechanical properties that can be obtained from TRIP-assisted steels containing allotriomorphic ferrite, bainite, martensite and retained austenite. The steels all are within the composition range 0.15-0.25C, 0.9-2.0Si and 1.4-1.8Mn wt% with a range of processing conditions.

A common parameter used to assess formability in the context of TRIP-assisted steels is the product of the tensile strength and uniform elongation. The parameter is related to retained austenite, but the formability depends on many more variables including the stability of the austenite, the mechanical inhomogeneity of the microstructure, inclusions, carbide particles and the texture of the steel as a whole. When the elongation is modelled by assuming both transformation plasticity and damage via void formation at martensite/austenite interfaces, the role of the damage in determining elongation is found to be small (Fig. 13.20). This may indicate that void formation within the mixture of bainitic ferrite and retained austenite is not the mechanism determining uniform elongation in TRIP-assisted steels. The model is relevant strictly to fully austenitic steels, although it was

originally applied to one containing allotriomorphic ferrite as well, which is the weakest phase in the microstructure.

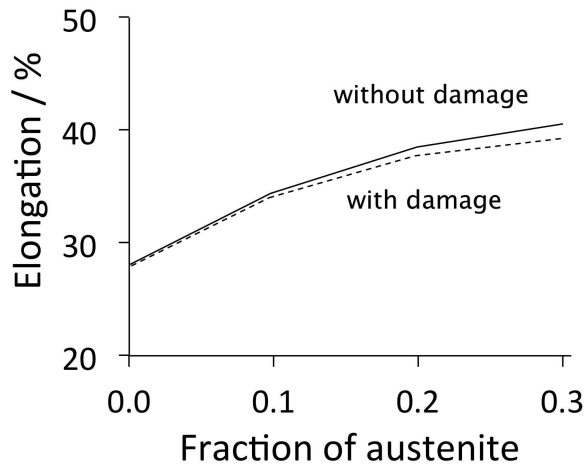


**Figure 13.20** Calculated uniform elongation for two cases, one without accounting for void accumulation, and the other estimating plastic instability via the accumulation of void damage. Adapted from Han et al. (2009).

Although there is no satisfying quantitative interpretation of these general observations, the role of the retained austenite in influencing the work hardening behaviour, and hence the balance between strength and ductility, is reasonably well understood. The formation of hard martensite during deformation must contribute to work hardening, but the amount of martensite is rather small in the overall microstructure. Jacques et al. (2001b) have shown that a significant contribution to work hardening is from dislocations induced into the ferrite by the strains associated with the formation of martensite. These dislocations strengthen the ferrite. The effect also confers a low planar anisotropy during deep-drawing because the transformation-induced work hardening compensates for crystallographic anisotropy in the material (Girault, 1999; Wasilkowska et al., 2004).

The transformation of high-carbon retained austenite into brittle-martensite can be a problem during subsequent deformation, because the martensite cracks causing damage accumulation which culminates in general failure (Furnémont et al., 2000). Low-carbon retained austenite which transforms into low-carbon martensite helps minimise damage. It is, however, difficult to design an alloy which has enough retained austenite to allow the steel to resist plastic instability, but which at the same time has a low carbon concentration.

Coarse regions of martensite in these mixed  $\alpha' + \alpha_b$  microstructures are well-known to embrittle (section 13.9). The tendency for embrittlement is increased when the brittle phases percolate the microstructure (Jacques et al., 2000). The worst case scenario is that the austenite transforms too readily into hard martensite ahead of a crack tip (Fig. 13.21), which may lead to a reduction in toughness; an appropriate stress concentration can accelerate the decomposition of the retained austenite, although hydrostatic stress retards its transformation. This latter effect can be exploited in hydroforming operations (Pyshmintsev et al., 2002). The mechanism by which hydrostatic pressure stabilises austenite is discussed in Chapter 8.

To summarise, the austenite should have sufficient stability to ensure that it transforms at the late stages of deformation when significant damage accumulates in the steel. It is at this point that the TRIP effect can be most beneficial (Tomota et al., 2004). There is good evidence to show that formability is improved when the stability of the austenite is increased whilst maintaining the initial volume fraction constant (Lee et al., 2004). One

way of improving the stability is to add copper, which stabilises austenite by reducing  $|\Delta G^{\gamma\alpha}|$ , the free energy difference between austenite and ferrite.

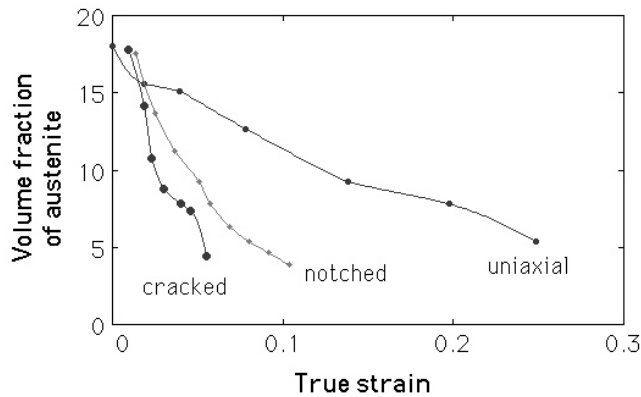


**Figure 13.21** The retained austenite content in a bainitic TRIP steel as a function of the strain and stress triaxiality (Jacques et al., 2000).

Forming operations do not of course involve just uniaxial deformation. Fig. 13.22 compares the stability of austenite to plastic deformation during experiments on TRIP-assisted steel, for both uniaxial and biaxial tension (Streicher et al., 2002). There is some anisotropy in the uniaxial tests because of a degree of banding present in the microstructure. It is surprising, however, that there is not much of a difference in the decomposition of the austenite between the biaxial and uniaxial tests, but in fact they both involve shear of the same magnitude although on different systems.

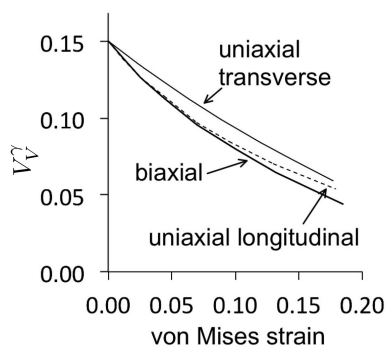


**Figure 13.22** Comparison of the mechanical stability of retained austenite in a typical TRIP-assisted steel during tensile deformation. After Streicher et al. (2002).

**Role of Transformation-Induced Plasticity** TRIP-assisted steels typically exhibit uniform tensile strains of about 15–30%; quite large variations in the uniform elongation are frequently attributed to *transformation strain* as retained austenite is induced to decompose into martensite (Berrahmoune et al., 2004, e.g.). However, it is easily demonstrated that transformation strains can contribute at most 2% to the observed elongation given the small fraction of austenite present in TRIP steels (Bhadeshia, 2002).

Consider the transformation of austenite into martensite. There will be a shape deformation which is characterised as an invariant-plane strain on the habit plane of the martensite. The deformation is a combination of a large shear ( $s \approx 0.26$ ) parallel to the invariant plane and a dilatation ( $\zeta \approx 0.03$ ) normal to the plane (Fig. 13.23).

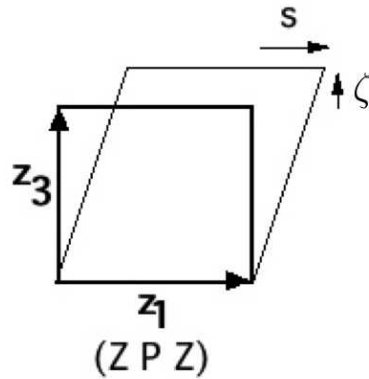


**Figure 13.23** An invariant-plane strain with a shear  $s$  and dilatation  $\zeta$ . The coordinates  $\mathbf{z}_i$  represent an orthonormal set in which  $\mathbf{z}_3$  is normal to the invariant plane and  $\mathbf{z}_1$  is parallel to the shear direction.  $(Z P Z)$  is the deformation matrix describing the strain.

The deformation can be written in matrix form using the basis symbol  $Z$ , as follows (Bowles and Mackenzie, 1954; Mackenzie and Bowles, 1954a; Bhadeshia, 2001c):

$$(Z P Z) = \begin{pmatrix} 1 & 0 & s \\ 0 & 1 & 0 \\ 0 & 0 & 1 + \zeta \end{pmatrix} \quad (13.2)$$

The effect of the invariant-plane strain on a vector  $\mathbf{u}$  is to change it to another vector  $\mathbf{v}$  which is in general distorted and rotated relative to  $\mathbf{u}$ .

Consider a tensile test on a sample which is fully austenitic and polycrystalline. An applied stress can stimulate martensitic transformation, but there are 24 possible crystallographic variants of martensite that can form. A tensile stress has a maximum interaction with the shape deformation when the tensile axis  $\mathbf{u}$ , habit plane normal  $\mathbf{z}_3$  and shear direction  $\mathbf{z}_1$  lie in the same plane and when the axis is at an angle  $\theta$  to the plate normal such that  $\tan\{2\theta\} = s/\zeta$  (Patel and Cohen, 1953). With  $s = 0.26$  and  $\zeta = 0.03$ ,  $\theta = 42^\circ$ ; it follows that the tensile axis, represented as a unit vector with respect to the basis  $Z$ , is given by

$$\begin{aligned} [Z; \mathbf{u}] &= [\sin \theta \ 0 \ \cos \theta] \\ [Z; \mathbf{v}] &= (Z P Z)[Z; \mathbf{u}] = [(\sin \theta + s \cos \theta) \ 0 \ (1 + \zeta) \cos \theta] \end{aligned} \quad (13.3)$$

In a tensile test the effect of constraint due to the grips is to cause the sample to rotate making  $\mathbf{v} \parallel \mathbf{u}$  so that the net strain along the tensile axis is given by

$$1 - |\mathbf{v}|/|\mathbf{u}| = 0.15.$$

This means that when an austenitic tensile test specimen transforms completely into martensite, the maximum tensile elongation due to phase transformation is about 15%. However, the TRIP-assisted steels discussed here typically contain 5-15% retained austenite. Therefore the contribution to elongation from transformation plasticity is the calculated level for a fully austenitic sample multiplied by the volume fraction of austenite (Christian, 1982), i.e. in the range 0.75-2.25%. This assumes the formation of the most favoured variant and complete transformation into that variant. If the variants form at random then the total strain must be even smaller; the shear strains cancel completely in the limit of random transformation.

It is likely that the role of transformation plasticity has been exaggerated in explaining the good mechanical properties of these steels. There are now numerous studies which support this conclusion (Bhadeshia, 2002) that transformation strains *per se* contribute little to the overall uniform elongation.<sup>7</sup> The good uniform elongation properties of TRIP-assisted steels are instead due to the composite deformation behaviour of the major phases with the retained austenite playing a minor role.

The hard phase (martensite or bainite) in dual-phase steels has a large strain hardening exponent, high strength and low ductility. By contrast, the soft phase (ferrite) has a low strain hardening exponent ( $n$ ), low strength ( $\sigma_Y$ ) and high ductility ( $\epsilon_U$ ). When the composite microstructure is stressed, the plastic strain is at first focussed in the more ductile soft phase, which work hardens. Eventually, the harder phase also deforms plastically. This composite deformation behaviour leads to intermediate combinations of  $n$ ,  $\sigma_Y$ ,  $\epsilon_U$  (Bhadeshia and Edmonds, 1980a; Perlade et al., 2003). The dual-phase microstructure thus exploits the high strength and  $n$  values of the hard phase, and the high ductility of the soft phase. The fact that the plastic strain is at first focussed in the soft phase is advantageous since the hard phase can reserve its ductility until the later stages of overall deformation.

Superimposed on the composite deformation is the transformation in which austenite is replaced by much harder martensite, resulting in a better distribution of strains and hence avoiding necking. The transformation also leads to a redistribution of stresses. In uniaxial tension, X-ray diffraction indicates that the austenite has the same internal stress as the ferrite (Sugimoto et al., 1995) prior to its transformation, but that the formation of martensite can relieve some of the stress in the austenite (Sugimoto et al., 1995).

Fig. 13.24 is based on neutron diffraction experiments; the elastic stress within the austenite and ferrite is almost identical. Jacques (2003a) concludes that the unexpectedly large yield strength of the austenite is due to its small grain size and high carbon-content. Another factor which may strengthen austenite must be the elastic constraint of the surrounding matrix. It is evident from Fig. 13.24 that the elastic strain (and hence the stress) in the ferrite stops increasing when the austenite yields. With measurements like these, Jacques was able to show that the yield strength of the austenite increases by some 775 MPa per wt% of carbon in solid solution. It is not clear why this is more than twice the coefficient observed in austenitic stainless steels (Marshall, 1984). In similar work, Tomota and co-workers (2004) have shown that some of the retained austenite can remain stable and elastic even when subjected to a tensile stress of 1 GPa; this supports the fact that the

<sup>7</sup>(Perlade et al., 2003; Timokhina et al., 2004; Onyuna et al., 2004; Tomota et al., 2004; Airod et al., 2004; Petrov et al., 2007)

constrained, carbon-enriched retained austenite in typical TRIP steels is harder than the ferrite.<sup>8</sup>

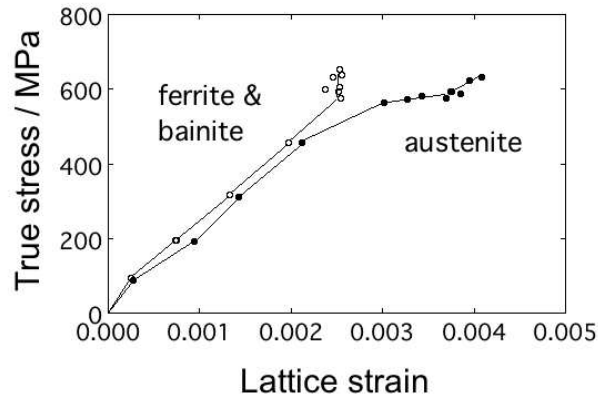


**Figure 13.24** The lattice strain, measured using the  $\{2\ 1\ 1\}_{\alpha}$  and  $\{3\ 1\ 1\}_{\gamma}$  reflections, as a function of the macroscopically applied stress. Data from Jacques (2003a).

It is now known that the good uniform elongation associated with TRIP-assisted steels is due to the composite deformation behaviour of the major phases, with the contribution of the small fraction of austenite playing a minor role in terms of transformation plasticity, but a major contribution with respect to work hardening due to martensitic transformation. This is consistent with the work by Jacques et al. (2001b) who argue that although low-silicon steels contain only a small amount of retained austenite, the composite effect gives uniform elongation which is superior compared with many commercial steels currently used in the manufacture of automobiles.

In order to exploit fully the ability of martensitic transformation to contribute to plasticity, the plates of martensite should not form in random orientations. Variant selection occurs under the influence of the applied stress permitting the shear component of the shape deformation to be exploited (Bhadeshia, 2004). It follows that the stress-induced martensite will develop a crystallographic texture since those variants which comply with the applied stress are favoured. Such a texture has indeed been observed experimentally in the retained austenite of TRIP-assisted steels (Petrov et al., 2007).

**Mechanical Stability of Retained Austenite** It is known that in steels which are fully austenitic at ambient temperature ( $T_a$ ), the greatest elongation is obtained when martensite forms during plastic deformation, i.e. when it is induced beyond the ordinary elastic limit of the material (Tamura and Wayman, 1992). Martensite may form when  $T_a \leq M_{\sigma}$ , the limiting temperature for stress-induced transformation, but in this case the austenite is only subjected to elastic strain, so that the only contribution to plastic strain is from the shape deformation of any martensite that forms. On the other hand, with strain-induced transformation which occurs when  $M_{\sigma} \leq T \leq M_d$  (Chapter 8), the martensite helps to achieve the maximum elongation by increasing the work hardening rate and delaying the

<sup>8</sup>Neutron diffraction experiments by Furnémont (2003) showed that the yield strengths of ferrite, bainite, austenite and martensite are about 500, 650, 900 and 2000 MPa respectively (Jacques, 2004). The dependence of austenite strength on carbon concentration has similarly been measured (Jacques et al., 2006).

onset of necking. Therefore, in fully austenitic TRIP steels, the highest uniform elongation is obtained when  $M_\sigma$  is just below the deformation temperature (Fig. 13.25).

For TRIP-assisted steels, the  $M_\sigma$  temperature is typically just below  $T_a$  at around  $10^\circ\text{C}$  (Cooman et al., 2004), which is according to the discussion above, optimum for maximising the elongation. The way in which  $M_\sigma$  was determined is illustrated in Fig. 13.26, where a single tensile specimen is deformed in a stepwise manner at a variety of temperatures, until the smooth yielding behaviour changes into a clear yield drop. The drop is identified with the load relaxation when martensitic transformation is stress-induced.<sup>9</sup>

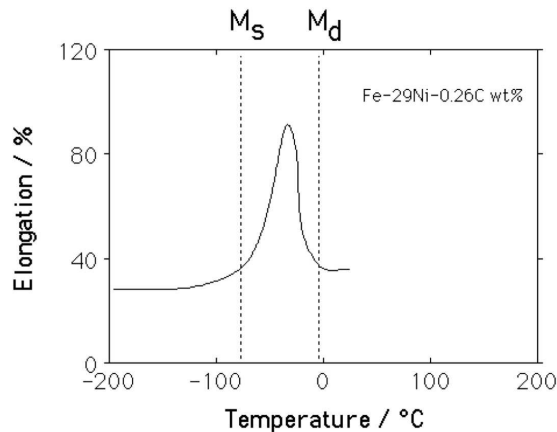


**Figure 13.25** Tensile elongation as a function of test temperature; data from Tamura et al. (1970).

It has been assumed on this basis that in TRIP-assisted steels, which generally contain less than 20% retained austenite, the maximum elongation should occur during deformation at a temperature between  $M_S$  and  $M_d$  (Sugimoto et al., 1992a,b). The  $M_\sigma$  temperature can be determined experimentally using tensile tests. Stable austenite exhibits a smooth transition from elastic to plastic deformation, whereas the onset of stress-induced martensite introduces a yield point in the stress-strain plot (Haidemenopoulos et al., 1989). Experiments like these show that the  $M_\sigma$  temperature of the retained austenite in typical TRIP-assisted steels is about  $10 \pm 5^\circ\text{C}$  (Barbé et al., 2002). Assuming that the results from fully austenitic TRIP-steels can be extrapolated to the alloys containing a fraction of austenite, the measured  $M_\sigma$  temperatures are consistent with maximum elongation.

On the other hand, extrapolating the transformation behaviour of fully austenitic steels is unlikely to represent the stability of small amounts of austenite in a mixed microstructure even if the comparison is done at identical chemical composition (Leslie and Miller, 1964; Rao and Rashid, 1983). This is illustrated in Fig. 13.27, which compares martensitic transformation from a fully austenitic steel against one in which the austenite is present as films or small blocks within a bainitic microstructure (Bhadeshia and Edmonds, 1983a). The instability is expressed as the fraction of austenite that transforms into martensite (i.e.  $V_V^{\alpha'}/V_V^\gamma$ ). It is clear that finely divided austenite dispersed in bainite is much more stable, because of mechanical constraint as well as the strengthening resulting from fine grain size. A similar conclusion has been reached for TRIP-assisted steels by Jacques et al. (2001d)

<sup>9</sup>Further discussion on the mechanical stability of retained austenite in TRIP-assisted steels is in section 6.14.

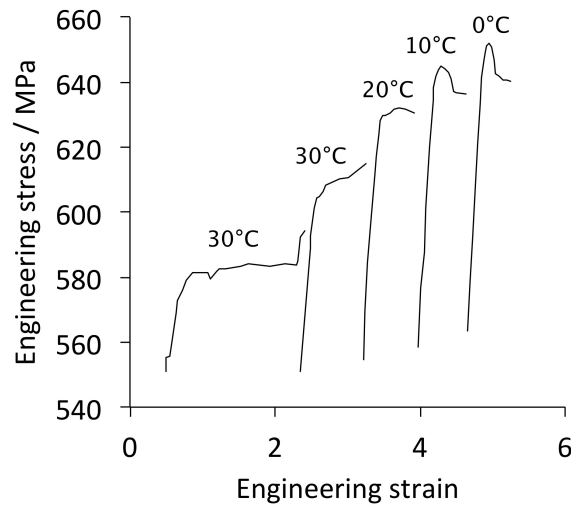


**Figure 13.26** Determination of  $M_{\sigma}$  using a single tensile specimen that is subjected to incremental plastic deformation as the sample temperature is reduced. The appearance of a yield point identifies the onset of stress-induced martensite. After Cooman et al. (2004).

who in addition find that solid-solution strengthening of austenite enhances its mechanical stability; the latter effect was first observed in the context of martensitic transformation (Davies and Magee, 1972).<sup>10</sup>

**Transformation of Fine Austenite Particles** The sheaf microstructure of bainite develops because individual plates are arrested in their growth by the debris created during the plastic accommodation of the shape change (Chapter 2). The typical size at which this arrest occurs is when the sub-unit reaches a length of about 10  $\mu\text{m}$ . However, much of the austenite present in TRIP-assisted steels is in the form of islands or films which are less than a few micrometers in size. It follows that it is not possible for a sheaf structure to develop (Fig. 13.28).

It is also peculiar that the high-carbon martensite which forms during the stress- or strain-induced transformation of the retained austenite is not cracked. It is well known that the martensite plates which form in large austenite grains tend to crack as they grow, frequently leading to acoustic emissions.

**Strain-Induced Transformation** As pointed out in section 8.6, if it is assumed that the change in the fraction of martensite ( $dV_V^{\alpha'}$ ) obtained for a given increment of plastic strain ( $d\epsilon$ ) should be proportional to the fraction of remaining austenite:

$$\frac{dV_V^{\alpha'}}{d\epsilon} = k_{\gamma} V_V^{\gamma} \quad (13.4)$$

where  $k_{\gamma}$  is a proportionality constant and  $V_V^{\gamma}$  is the fraction of austenite remaining untransformed. If the fraction of austenite at zero strain is  $V_V^{\gamma_0}$ , then  $V_V^{\alpha'} = V_V^{\gamma_0} - V_V^{\gamma}$ , so

<sup>10</sup>In another context, the transformation of blocks of austenite can lead to dimensional instabilities which are undesirable in the manufacture of components such as bearings (Luzginova et al., 2007; Bhadeshia, 2012).

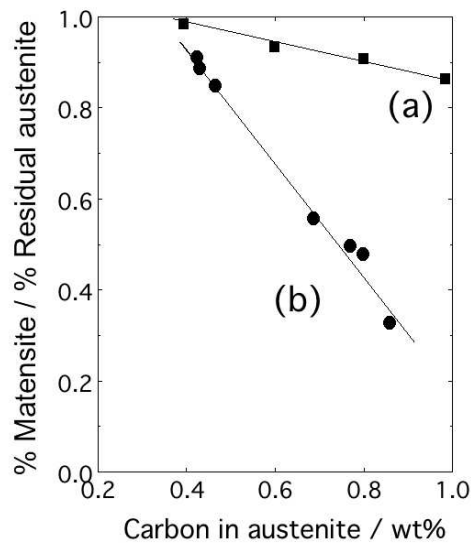


**Figure 13.27** Stability of austenite to martensitic transformation. (a) Initially fully austenitic specimen. (b) Transformation from austenite present in a bainitic microstructure (Bhadeshia and Edmonds, 1983a)

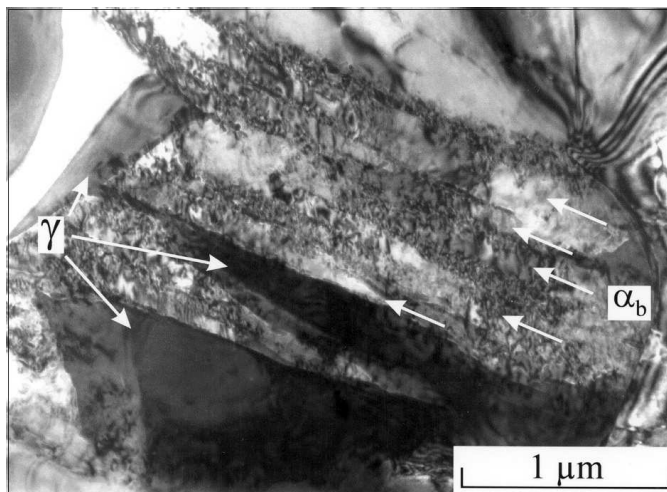


**Figure 13.28** Transmission electron micrograph of bainite morphology in a fine particle of austenite, courtesy of Jacques (2003a).

that

$$\ln\{V_V^{\gamma_0}\} - \ln\{V_V^{\gamma}\} = k_{\gamma}\epsilon \tag{13.5}$$

This relationship between the amount of retained austenite that decomposes to martensite as a function of plastic strain was first derived by Sugimoto et al. (1992a) by fitting to experimental data. A small value of  $k_{\gamma}$  corresponds to austenite which is more resistant to

strain-induced transformation (Fig. 13.29). It follows the  $k_\gamma$  should decrease as the tensile test temperature is increases, since austenite becomes more stable at high temperatures. However, at some point martensitic transformation becomes impossible as  $M_d$  is exceeded; strain-induced bainite is triggered making  $k_\gamma$  increase again. Hence the minimum in the curve of  $k_\gamma$  (Fig. 13.29).

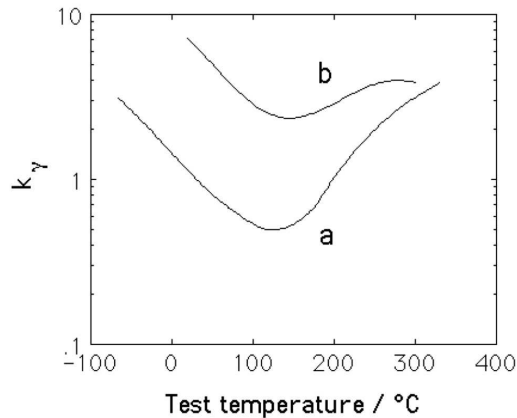


**Figure 13.29** The mechanical stability of retained austenite as a function of the tensile test temperature. The austenite in steel (a) has  $M_S = -61^\circ\text{C}$  whereas that in (b) has  $M_S = -7^\circ\text{C}$ . Data due to Sugimoto et al. (1992a).

In circumstances where the austenite is stable, it undergoes plastic deformation via slip, faulting and mechanical twinning (Bhadeshia and Edmonds, 1979a; Miihkinen and Edmonds, 1987c; Sugimoto et al., 1992a). Mechanical twinning is an unusual deformation mode for austenitic steels containing small concentrations of solutes. However, the retained austenite is constrained by the surrounding bainite and has a large carbon concentration; this may enhance the tendency for mechanical twinning.

**Low or Zero-Silicon TRIP-Assisted Steels** The relatively large silicon concentration causes the formation of hard, adherent oxides making it difficult to implement surface cleaning prior to hot-rolling, resulting in a poor surface finish. The stronger adhesion comes from that fact that the silicon reacts to form Fayalite ( $\text{Fe}_2\text{SiO}_4$ ), which is more coherent with the steel substrate than FeO (Kizu et al., 2001; Song et al., 2012). The steels are therefore confined to applications where the components are hidden from view. Low-silicon TRIP steels do exist (Alloy 9 Table 13.1). Fig. 13.30 compares the microstructures of a pair of steels containing low and high silicon concentrations; the former also has a lower average carbon concentration although the carbon concentrations of the retained austenite (which are limited by the  $T_0$  criterion) are identical (Jacques et al., 2001c).

The important observation from Fig. 13.30 is that in low-silicon steel, the retained austenite decomposes to cementite and ferrite with prolonged heat treatment in the bainite transformation range; this is not the case with the high-silicon steel where cementite is prevented from forming. It is necessary therefore to exercise greater care in the heat treatment of low-silicon TRIP-assisted steels in order to optimise the retained austenite content.

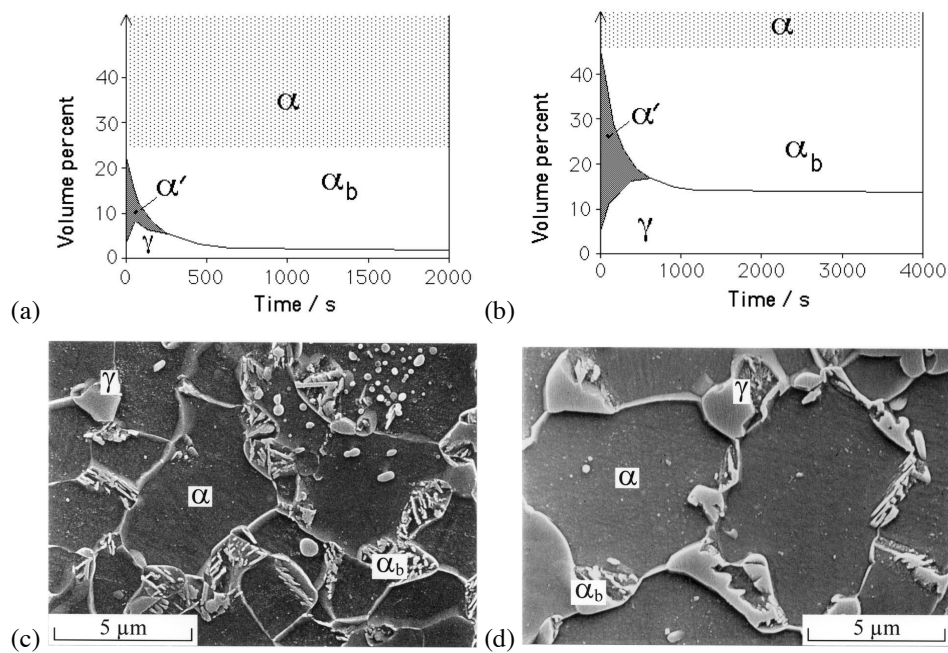


**Figure 13.30** Evolution of room-temperature microstructure as a function of time during isothermal transformation to bainite. (a) Low-silicon steel Fe-0.16C-0.38Si-1.3Mn wt%, transformed at 370 °C following intercritical annealing at 730 °C for 5 min. (b) High-silicon steel Fe-0.29C-1.41Si-1.42Mn wt%, transformed at 360 °C after intercritical annealing at 760 °C for 6 min. (c) Scanning electron micrograph of low-silicon alloy isothermally transformed to bainite for 1800 s. Much of the austenite has decomposed to bainitic ferrite and cementite. (d) Corresponding micrograph for high-silicon steel transformed to bainite for 900 s with plenty of austenite evident. Micrographs courtesy of Professor Pascal Jacques.

Jacques *et al.* argue that although the amount of austenite retained in low-silicon steels is small, the combination of transformation-induced plasticity and the composite effect common in dual-phase steels give mechanical properties which are far superior to many commercial steels (Fig. 13.31).

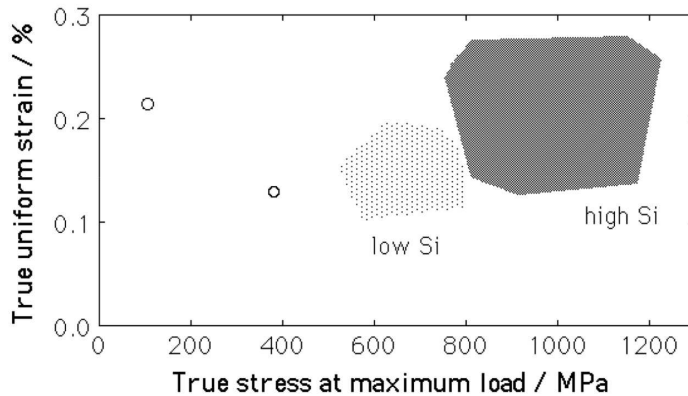


**Figure 13.31** The distribution of mechanical properties achieved in TRIP-assisted steels; the points represent commercial automobile steels (Jacques *et al.*, 2001c).

**Phosphorus in TRIP-Assisted Steels** There is a consensus that phosphorus can help increase the retained austenite content in TRIP-assisted steels that have a microstructure of allotriomorphic ferrite, bainitic ferrite and retained austenite (Chen *et al.*, 1989). Some chemical compositions are listed in Table 13.5. Concentrations up to 0.2 wt% do not seem to lead to a significant deterioration in the uniform ductility, for alloys where the yield strength is less than 600 MPa, and the ultimate tensile strength 600-950 MPa (Chen *et al.*, 1989), although the total elongation has been shown to deteriorate (Jing *et al.*, 2007). There are two reasons for the apparent tolerance of TRIP-assisted steels to large phosphorus concentrations:

- the microstructure is dominated by allotriomorphic ferrite, which forms by a diffusional mechanism and hence can grow across the austenite grain boundaries. Therefore, unlike displacive transformations such as martensite and bainite where the transformation products are confined to individual grains, there are no prior austenite grain boundaries left for phosphorus to segregate to. This makes the microstructure much less sensitive to classical impurity enhanced embrittlement.

This is consistent with the fact that the presence of allotriomorphic ferrite in steel weld metals reduces the propensity to intergranular fracture at the prior austenite grain boundaries (Ichikawa *et al.*, 1996; Bhadeshia, 1997a).

A similar phenomenon is observed during the infiltration of prior austenite grain boundaries by liquid zinc. In a study of the heat-affected zone of steel welds, where the susceptibility to liquid zinc embrittlement is reduced as the allotriomorphic ferrite content increases (Iezawa *et al.*, 1993). The absence of allotriomorphs at the prior austenite grain boundaries made them more sensitive to zinc infiltration, because the prior boundaries have a high-energy structure which is susceptible to wetting and impurity segregation.

- Secondly, the yield strength of the materials is quite low, so that plastic flow may prevent the onset of cleavage. Added to this, the fraction of preserved prior austenite or austenite/austenite grain boundaries in TRIP-assisted steels is small.

Phosphorus is said to retard the formation of cementite and stabilised retained austenite in TRIP-assisted steels (Traint et al., 2002; Zaefferer et al., 2004; Li et al., 2007a). There is no clear theoretical basis for such an effect; it is argued that phosphorus reduces the activity of carbon in cementite (Li et al., 2007b). But this in itself is not a complete interpretation since equilibria between phases should be considered. Furthermore, studies on carburised steel (Hyde et al., 1994) suggest contradictory observations, that phosphorus stimulates the formation of cementite at the austenite grain boundaries, thereby leading to a reduction in the stability of any retained austenite. This is also consistent with the Fe-C-P phase diagram that shows the emergence of cementite as an equilibrium phase when the phosphorus concentration is increased at a constant temperature (Raghavan, 1988), and with phase diagram calculations that show cementite increasing as the phosphorus concentration is raised while maintaining the temperature constant (Wang and van der Zwaag, 2001a, Fig. 6a).

There is a danger that phosphorus concentrations in excess of about 0.2 wt% in TRIP-assisted steels may lead to Fe<sub>3</sub>P precipitation in either the austenite or ferrite phases (Wang and van der Zwaag, 2001b). The consequences of such precipitation do not seem to have been established experimentally. It has been suggested in the context of automotive steels, that the crack path can preferentially pass through bainitic-ferrite interfaces containing segregated phosphorus, although the evidence provided was minimal (Kumar et al., 2013).

**Table 13.5** Phosphorus-containing TRIP-assisted steels. The composition in the case of Zaefferer et al. (2004) seems to be nominal.

C	Mn	Si	Al	P	other	Reference
0.18	1.33	0.45		0.006		Chen et al. (1989)
0.12	1.58	0.53		0.068		Chen et al. (1989)
0.14	1.57	0.53		0.204		Chen et al. (1989)
0.2	1.4	0.5	0.7	0.04		Zaefferer et al. (2004)
0.15	1.60	0.30		0.07		Li et al. (2007b)
0.13	1.38		1.55	0.055	Cu 0.46	Jing et al. (2007)
0.13	1.45		1.66	0.100	Cu 0.48	Jing et al. (2007)
0.22	1.50	0.44	1.34	0.073		Bouquerelet et al. (2008)
0.19	1.50	0.25	0.44	0.015		Jimenez-Melero et al. (2009)
0.22	1.54	0.27	1.75	0.018		Jimenez-Melero et al. (2009)
0.18	1.50	0.26	0.44	0.102		Jimenez-Melero et al. (2009)
0.18	1.83	0.48		0.076		Hou et al. (2011)

**Galvanising of TRIP-Assisted Steels** There are two basic methods of galvanising, by dipping the steel in liquid zinc or by electrolytically depositing the zinc. The typical concentrations of silicon and manganese in TRIP-assisted steels lead to a stable Mn<sub>2</sub>SiO<sub>4</sub> oxide film on the surface during the heat treatment necessary to produce the desired microstructure. This makes it difficult for the zinc to wet the steel surface, making it necessary to electrolytically galvanise such alloys (Mahieu et al., 2002a).

The problem can be alleviated by increasing the humidity in the annealing furnace. The oxide coverage of the surface is then reduced, giving better wetting by zinc (Maki et al.,

2003). The higher humidity causes the internal oxidation of Mn and Si below the steel surface, thus reducing their availability to form  $\text{Mn}_2\text{SiO}_4$  at the surface.

An alternative approach is to eliminate the silicon and add aluminium to retain the cementite-free microstructure. Silicon-free TRIP-assisted steels<sup>11</sup> have been shown to have similar mechanical properties to conventional alloys of this kind. It enhances the hydrogen-induced static-fracture resistance of TRIP-assisted steel, possibly because of its thermodynamic effect in increasing  $x_{T_0}$  (Hojo et al., 2009), or because as first principles calculations indicate, it binds more strongly than silicon to hydrogen (Li et al., 2013). Aluminium causes a localised dilation in austenite, allowing it to better accommodate hydrogen; this effectively forms a trap for hydrogen that reduces its mobility (Song et al., 2014). Aluminium oxidises easily to form alumina by internal oxidation near the surface, again limiting the amount that can form  $\text{FeAl}_2\text{O}_4$  at the free surface when the humidity in the annealing furnace is low. Such a steel can easily be hot-dip galvanised. At high humidity, MnO begins to cover the surface leading to a deterioration in the ability of the liquid zinc to wet the surface (Maki et al., 2003). The aluminium-containing steels are therefore better suited to continuous galvanising lines.

It is clear that silicon and manganese must diffuse to the surface to form oxides. Some of the diffusion flux is via grain boundaries. When phosphorus is present, its segregation to the grain boundaries reduces the boundary diffusion-flux, thereby reducing the extent to which oxides form (Isobe et al., 1998). Such steels are more amenable to wetting by molten zinc. In contrast, the same effect makes it more difficult to form iron-zinc compounds during the galvannealing process (Hisamatsu, 1989).

Apart from obvious effects on corrosion resistance, surface quality and formability, coatings on TRIP-assisted steels are also known to influence the dynamic mechanical properties. It seems that the strength of the coated steel is significantly lower than that of the uncoated variety in high strain-rate experiments. The reasons for this are not entirely clear but may have something to do with mechanical incompatibilities between the coating and substrate (Wei et al., 2007).

**Transformations During Intercritical Annealing** The effect of intercritical annealing is to transform some of the initial microstructure into austenite. The part which does not transform is severely tempered, causing the ferrite to recrystallise; indeed, in cold-rolled steels which are intercritically annealed, the entire microstructure may recrystallise before the  $\alpha \rightarrow \gamma$  transformation (Petrov et al., 2001). The quantity of austenite determines its chemical composition and stability (Fig. 13.32a-c). Austenite nucleates at cementite particles; it has a high carbon concentration to begin with but this becomes diluted as the austenite grows, raising its  $M_S$  temperature and hence reducing the fraction that is retained on cooling to ambient temperature. The size of the austenite grains also influences their stability; larger grains transform more readily to martensite. Intercritical annealing can also lead to the redistribution of the substitutional solutes (Fig. 13.32d), the degree of partitioning depending on the annealing temperature and time.

The heat treatment influences also the crystallographic texture of both the austenite and the recrystallised ferrite (Samajdar et al., 1998). Newly formed austenite grains which nucleate at cementite particles do not show preferred orientation. The texture changes during annealing but the mechanism is not understood.

<sup>11</sup>Fe-0.12C-1.54Mn-0.91Al and Fe-0.18C-1.56Mn-1.73Al wt% (Mahieu et al., 2002a). Further discussion of aluminium-rich TRIP-assisted steels is in section 13.6.2.

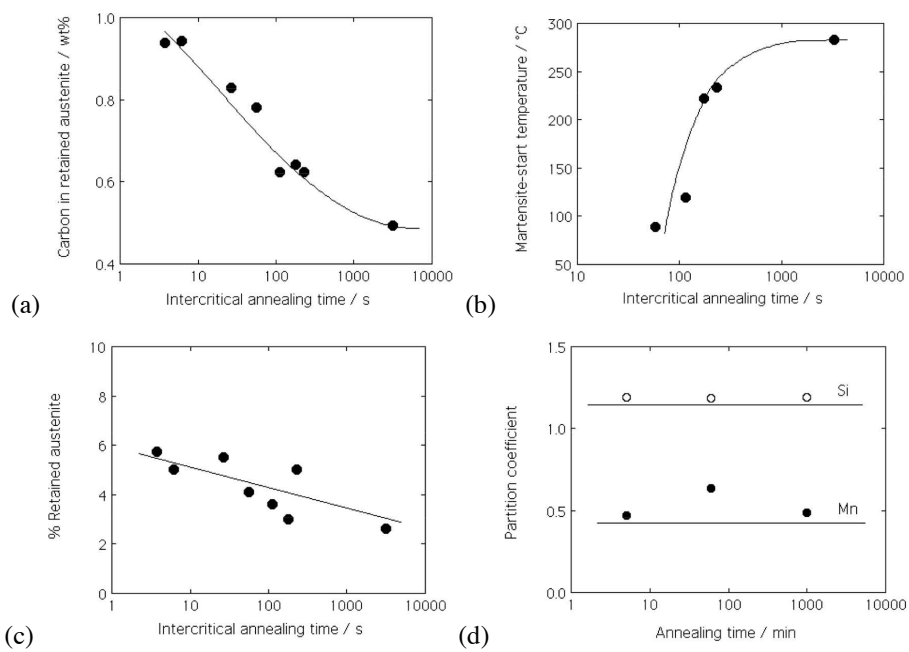


**Figure 13.32** (a-c) Some effects of intercritical annealing on a Fe-0.11C-1.5Si-1.53Mn wt% steel at 750 °C. Data from Samajdar et al. (1998). (d) Ratio of concentration of element in ferrite to that in austenite as a function of the intercritical annealing time, for a steel of approximate composition Fe-0.2C-1.5Si-1.5Mn wt% annealed at 800 °C. The horizontal lines represent values calculated assuming equilibrium partitioning. Data from Minote et al. (1996).

**Thermomechanical Processing** Thermomechanical processing of TRIP steels does not accrue the same benefits as in ferrite-pearlite steels. This is partly because the bainite reaction is suppressed when the austenite is severely deformed, due to the onset of mechanical stabilisation, Fig. 13.33 [Chapter 8; (Basuki and Aernoudt, 1999; Luo et al., 2003)]. The effect is exaggerated by the fact that the allotriomorphic ferrite transformation is accelerated. The larger volume fraction of allotriomorphic ferrite leaves less austenite available for the bainite transformation. It also causes a greater enrichment of the residual austenite with carbon, thereby reducing the amount of bainite that can be obtained (Ryu et al., 2002).<sup>12</sup>

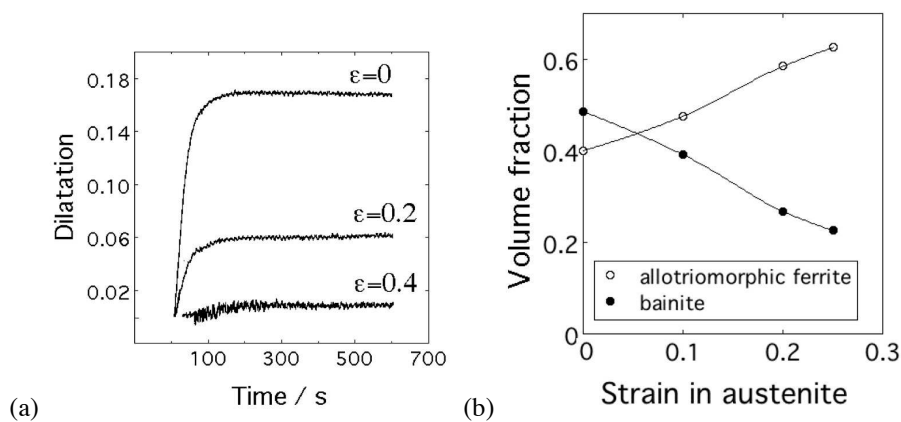


**Figure 13.33** (a) Showing the mechanical stabilisation of the bainite reaction in a TRIP steel as a function of the plastic strain  $\epsilon$  in the austenite. The dilatation is a measure of the amount of bainite that forms and the time is at the temperature where bainite forms (Luo et al., 2003). (b) Showing how the amount of allotriomorphic ferrite is increased when the austenite is plastically strained, leading to a reduction in the fraction of bainite (Basuki and Aernoudt, 1999).

A further effect is to reduce the number of crystallographic variants of bainite that form in each austenite grain. Certain variants are favoured by the residual stresses and dislocation arrays left in the deformed austenite grain structure which then transforms to bainite. This effect has been vividly demonstrated in TRIP steels using orientation imaging microscopy (Girault et al., 2001b; Godet et al., 2004). The bainitic microstructure that forms from deformed austenite is found to be much more organised and limited in crystallographic variants than that from undeformed austenite. This must have consequences on the mechanical properties, but they have yet to be investigated.

Deformation introduces misorientations in the austenite, which are inherited by individual plates of bainite. Godet *et al.* have shown that in a bainite plate which is about  $10\ \mu\text{m}$  in length, the misorientation between the two ends can be as large as  $8^\circ$  when the bainite grows from austenite which has been plastically deformed to a strain of 0.8. The defects responsible for this misorientation must lead to a strengthening of the plates.

<sup>12</sup>Hot-torsion experiments on TRIP-assisted steels where the austenite is left in a plastically deformed state prior to transformation into allotriomorphic ferrite and then bainite, surprisingly indicated no effect on the volume fractions of these products, although quantitative data were not reported (Timokhina et al., 2003).

The effect of transformation from plastically deformed austenite, on the overall development of microstructure, is summarised in Fig. 13.34<sup>13</sup>.

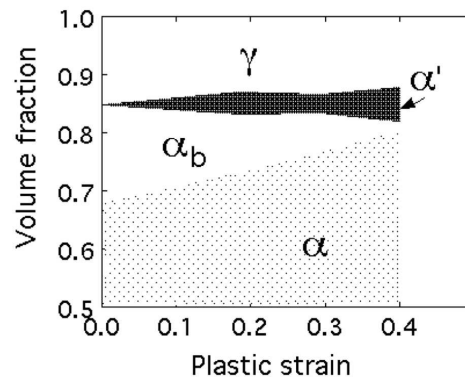


**Figure 13.34** The influence of strain on the development of microstructure in TRIP-assisted steels. Data from Papaefthymiou et al. (2004).

**Effect of Heat Treatment on Final Microstructure** The allotriomorphic ferrite in TRIP-assisted steels can be generated by intercritical annealing or by transformation from a fully austenitic state. Sugimoto et al. (1993) have shown that the distribution of phases in the final mixed microstructure of ferrite, bainite and retained austenite is affected by the choice of heat treatment (Fig. 13.35). Intercritical annealing generally leads to a more uniform dispersion of the hard phase, and smaller regions of allotriomorphic ferrite. As seen from Fig. 13.35b, the ferrite regions are much coarser. This is because during intercritical annealing the number density of austenite regions nucleated is large and the austenite grains do not coarsen at the relatively low heat treatment temperature.

The coarser distribution of phases Fig. 13.35b has been shown to be greatly reduced ductility during tensile deformation Sugimoto et al. (1993). This is expected in a coarse microstructure where the distribution of plastic strain must necessarily be less uniform, thereby increasing the tendency for necking.

A more uniform and refined microstructure also suppresses void formation during biaxial tension of the kind typical in forming operations. The extension possible in a biaxial stretch forming operation is then greater for a uniform microstructure even when the latter has a smaller uniaxial tensile elongation compared with a less uniform microstructure Sugimoto et al. (2002a).

The intercritically annealed microstructure can be refined further by inducing a greater number density of austenite nucleation sites, by heating from a martensitic initial microstructure (Kashima et al., 2003), Fig. 13.35c. Other methods, such as the use of cold-rolling prior to intercritical annealing also lead to refinement of the ultimate microstructure and improved stretch formability (Kashima and Sugimoto, 2004).

<sup>13</sup>Li and Wu (2006) obtained a good combination of mechanical properties in thermomechanically processed TRIP-assisted steels, but the data should ideally be compared against corresponding alloys without similar processing in order to reach a conclusion about the efficacy of the processing route.

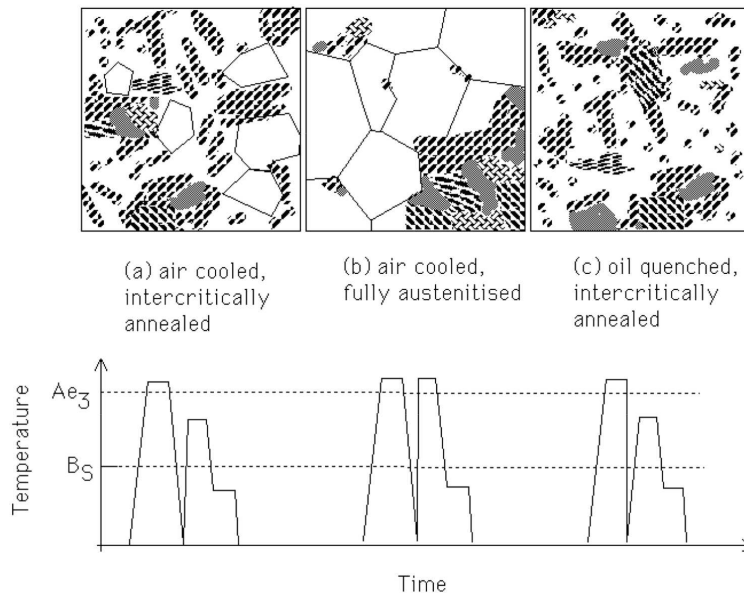


**Figure 13.35** Schematic microstructures of the same steel, with different heat treatments.

**Microalloyed TRIP-Assisted Steels** Attempts have been made to improve the properties of these alloys by microalloying with niobium. Niobium in solid solution seems to increase the quantity of austenite that is retained in TRIP-assisted steels (Zarei-Hanzaki et al., 1995). This observation should not be attributed to an increase in hardenability since niobium actually raises the  $Ae_3$  temperature and hence is a “ferrite stabiliser” (Kirkaldy et al., 1978). There are also contradictory results reported that niobium leads to a decrease in  $V_V^{\gamma}$  (Tang et al., 2007). In the context of grain boundary nucleated transformations, dissolved niobium is able to segregate the austenite grain boundaries thereby retarding the transformation of austenite (Fossaert et al., 1995). However, it is difficult to see how this leads to a different quantity of *retained* austenite in the TRIP-assisted steels.

When the steels are produced from a fully austenitic condition, the primary influence of niobium is as expected, that the austenite grain size is refined by Zener pinning. This in turn accelerates allotriomorphic ferrite formation, causing an increase in the carbon concentration and a decrease in the fraction of the austenite available to form bainite at a lower temperature (Hashimoto et al., 2004). The role of microalloying elements is different when the process begins with intercritical annealing. With sufficiently large niobium concentrations ( $\approx 0.06$  wt%) some precipitation can be induced within the ferrite that forms by the recrystallisation of the microstructure prior to intercritical annealing, leading again to an enhancement of strength (Wang et al., 2014a).

Fine niobium carbides and complex NbMoC precipitates can boost the strength of the allotriomorphic ferrite. Indeed, it has been observed that large number densities ( $10^{22}$ - $10^{23} \text{ m}^{-3}$ ) of minute niobium and molybdenum rich clusters form during cooling to or during the isothermal hold (450-500 °C) used to produce the bainite (Pereloma et al., 2007). The clusters are rich in carbon but depleted in the substitutional solutes compared with NbC or Mo<sub>2</sub>C and they do not seem to possess a crystal structure different from that of

the matrix (Pereloma et al., 2006), Fig. 13.36. In work on isothermally transformed TRIP steel containing just bainitic ferrite, retained austenite and martensite, fine NbC precipitates were found within the bainitic ferrite when the isothermal transformation temperature was highest, at 475 °C. However, these carbides made a negligible contribution to the strength of the steel (Sugimoto et al., 2005).

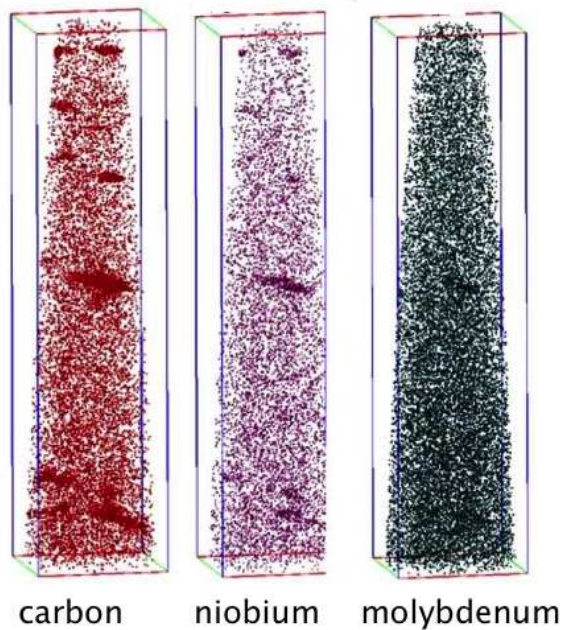


**Figure 13.36** Atom mapping of clusters and particles in ferrite in a Nb-Mo alloyed TRIP-assisted steel. Reproduced with permission of Elsevier, adapted from (Pereloma et al., 2006).

Deliberate additions of nitrogen to TRIP-assisted steels lead to the precipitation of fine aluminium nitrides in austenite. The nitrides restrict the growth of ferrite grains during subsequent intercritical annealing. Thus, the introduction of a mass fraction of AlN of just  $4 \times 10^{-4}$  reduces the ferrite grain size by a factor of two, from about 4 to 2  $\mu\text{m}$ , with a consequent increase in the strength and elongation (Baik et al., 2006).

**Other Composite TRIP-Assisted Steels** As described in section 13.6 the dominant factor controlling the ductility of the so-called TRIP-assisted steels is not retained austenite *per se* but rather the composite deformation effect. The hard phase on its own has a high strength but a low work hardening coefficient which decreases rapidly as deformation progresses, giving a low strain to failure. Sugimoto and coworkers have identified that hardness due to a high dislocation density is detrimental to ductility whereas a lath-like microstructure is beneficial in this context. This observation was confirmed by making a TRIP-assisted steel in which the major phase was not allotriomorphic ferrite but annealed martensite; the hard phase on the other hand was the usual mixture of bainitic ferrite and retained austenite. The annealed martensite retained its lath microstructure but represented the soft part of the composite. The resulting steel exhibited a substantial increase in ductility, at almost identical strength, as illustrated in Fig. 13.37. Similar improvements have been reported when stretch-flangeability and bendability are considered (Sugimoto et al., 2003).

To summarise, the overall behaviour of these composite steels can be enhanced by improving the strain hardening characteristics of the soft phase; most previous research has focussed only on the hard phase and its retained austenite.

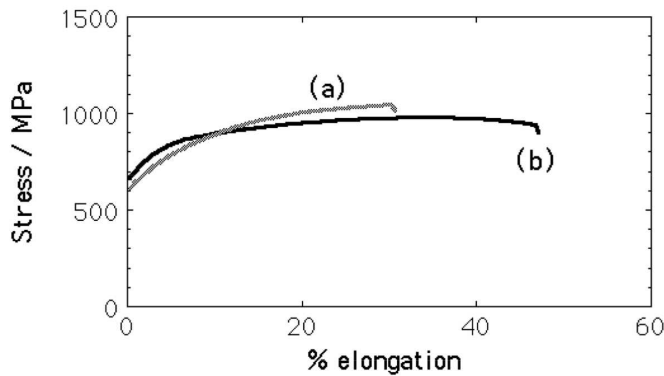
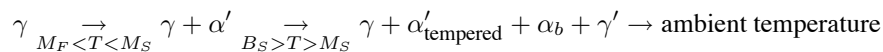


**Figure 13.37** Stress versus strain curves of TRIP-assisted steels. Curve (a) is for a classical microstructure with soft allotriomorphic-ferrite and a harder mixture of bainitic ferrite and retained austenite. Curve (b) is when the allotriomorphic ferrite is replaced with annealed martensite. After Sugimoto et al. (2002b).

It is difficult to achieve good formability at strength levels in excess of 900 MPa when the microstructure is that of ordinary TRIP-assisted steels, i.e. consisting of a mixture of allotriomorphic ferrite, bainite and austenite. The problem can be avoided by eliminating the allotriomorphic ferrite to obtain only bainitic ferrite and retained austenite. This not only increases the strength but by making the microstructure more uniform, gives good stretch-flangeability as measured in hole expansion tests (Sugimoto et al., 2000). Further improvements are achieved by ensuring that most of the austenite is in the form of films rather than blocks which easily transform into martensite (Sugimoto et al., 2002c; Bhadeshia and Edmonds, 1983a,b). The combination of strength and formability achieved in fully bainitic TRIP steels is useful in making components such as the arms of automobile suspension systems.

‘Quench and partitioning steels’ are generally produced by cooling the steel to a temperature below  $M_S$  such that a fraction of martensite is obtained, and then heating to allow some of the excess carbon in the martensite to partition into the residual austenite [section 5.5 (Speer et al., 2015)]. However, more complex variants of the process have been developed as follows (Gao et al., 2013):



The ultimate tensile strength has been reported to be 1655 MPa with a total elongation of 19%, the combination of properties attributed to the mixed microstructure. However, the heat treatment may be too sophisticated for mass production. The chemical composition of the alloy was Fe-0.4C-2Mn-1.8Si-0.5Crwt%, and may therefore have difficulties in applications where resistance spot-welding is required.

**Strain-rate sensitivity** TRIP-assisted steels may be used in circumstances where energy absorption is required at large strain rates of the kind associated with accidental crashes.

The tensile behaviour obtained conventionally has been compared against that measured at much higher strain rates using the split Hopkinson bar test (Verleysen et al., 2005; van Slycken et al., 2006, 2007). Typical data are illustrated in Fig. 13.38a. Aside from an expected increase in the yield strength, the engineering stress-strain curves are similar in the initial stages of deformation to a strain of about 0.15, but plastic instability occurs first in the conventional test. As a result, a greater ultimate tensile strength and total elongation is measured in the test conducted at high strain rate. It appears therefore that the combination of strength and elongation is enhanced when the steel is tested at large strain rates. There is, however, a difficulty that the conventional test is done on large samples with a gauge length of 80 mm, whereas the Hopkinson-bar samples have a gauge length of only 5 mm with all other dimensions smaller than in the conventional test. It is possible that the results are not therefore comparable, because the measured elongation increases at smaller gauge lengths (Hanlon et al., 2015). Indeed, when comparable samples are used, the difference in elongation is not significant, Fig. 13.38b. While the general conclusion regarding sample size effects remains true, there is also a geometry dependence because Sun et al. (2012) report a greater ductility at high strain rates using identical tests in all experiments. In spite of the confusion of data, it probably can be concluded safely that the ductility of TRIP-assisted steels is not compromised at large strain rates.

It is found empirically that the anisotropy of yield is reduced in TRIP-assisted steels when they are tested at high strain rates (Huh et al., 2013).

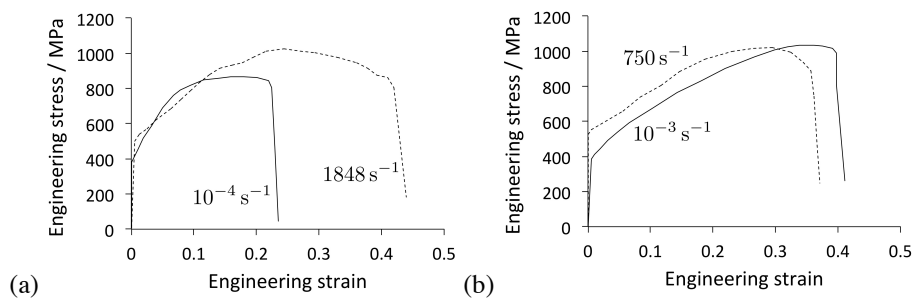


**Figure 13.38** Strain-rate dependence of the tensile properties of TRIP-assisted steels. (a) Data selected from van Slycken et al. (2006) for an Fe-0.21C-1.78Mn-1.53Si wt% steels. (b) Data for specimens of comparable size from Curtze et al. (2009) for an Fe-0.2C-0.4[Si,Cr,Mo]-2.9[Al,Mn] wt% steel.

**Fatigue Strength** TRIP-assisted steels may be used in making suspension parts for cars, in which case their performance in fatigue becomes important. Many of these parts are fabricated by deformation and hence are strained before they enter service. It is found that prestrain increases the high-cycle fatigue limit in tests carried out on smooth samples (Fig. 13.39).

### 13.6.2 $\delta$ -TRIP Steels

Conventional TRIP-assisted steels can suffer from the formation of an adherent surface scale which makes the steel unsuitable for applications where the cosmetic appearance is important (Fukagawa et al., 1994; Okada et al., 1995; Taniguchi et al., 2001). Silicon-rich surface oxide can also make it difficult for zinc to wet the surface of the steel during hot-dip

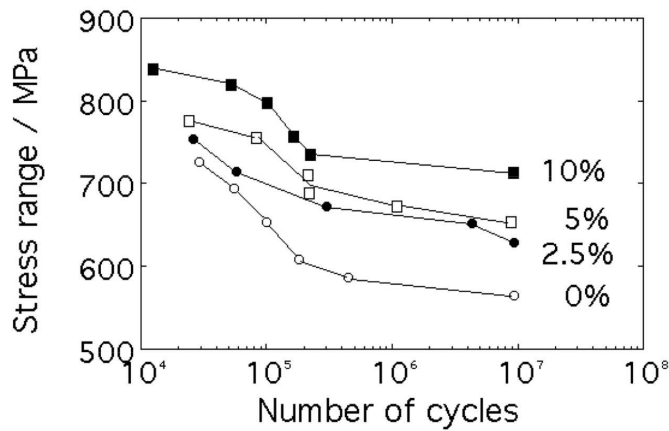


**Figure 13.39** S-N curves for a TRIP-assisted steel with a microstructure of allotriomorphic ferrite, bainite and retained austenite. The high-cycle fatigue tests were conducted on samples which were plastically deformed at the levels indicated, prior to high-cycle fatigue testing. Data from Song et al. (2003).

galvanising (Mahieu et al., 2002a). In an effort to avoid these problems, a computer model was created to discover circumstances in which identical properties can be obtained whilst keeping the silicon to less than 0.5 wt%, while maintaining typical intercritical annealing and isothermal transformation characteristics, with the microstructure retaining sufficient austenite to enhance formability (Chatterjee et al., 2007).

The outcome of the calculations was an entirely unexpected alloy system, Fe-0.4C-2Mn-0.5Si-2Al-0.5Cu wt%. This level of carbon and carbon equivalent is not normal in automotive-body steels because the weldability of the steel might be compromised. However, the calculated phase diagram (Fig. 13.40) indicates that because of the large aluminium concentration, the steel cannot become fully austenitic in the solid state. This also means that it cannot ever become fully martensitic, for example when it undergoes the thermal cycle associated with spot welding.

The as-cast and normalised structure therefore consists of a mixture of  $\delta$ -ferrite dendrites and interdendritic pearlite, Fig. 13.41a. The  $\delta$ -ferrite therefore substitutes for the  $\approx 70\%$  allotriomorphic ferrite found in conventional TRIP-assisted steels. Following intercritical annealing and the partial isothermal transformation of the resulting austenite into bainite, a mixture of phases including about 14% of retained austenite was obtained, Fig. 13.41b, which on tensile testing revealed an excellent combination of strength and ductility, as illustrated in Fig. 13.41c. Furthermore, the role of this austenite in controlling the elongation is revealed by the tensile test conducted at 100 °C in order to increase the thermodynamic stability of the austenite. In this test, the elongation recorded was dramatically reduce because the austenite did not contribute to the TRIP effect.

Such steels in practice are not used in the cast condition but after hot rolling and cold rolling into sheet about 1.5 mm in thickness. The microstructures achieved after the processing into sheet form and then heat treatment are illustrated in Fig. 13.42, which shows that the final microstructure retains  $\delta$ -ferrite but also allotriomorphic ferrite, bainitic ferrite and retained austenite. There has been considerable development work on these alloys,

and a summary of the extraordinary properties obtained are summarised in Fig. 13.43. A comprehensive review on  $\delta$ -TRIP steels has been published (Yi, 2014).

The presence of aluminium reduces the density of the steel; with adaptations in later work, a density reduction of 4% was achieved, and greater reductions are achievable with a balancing of solutes to ensure that some austenite remains. A further advantage is that the  $\delta$ -ferrite persists at all temperatures in the solid-state, so that spot-welding cannot result in a fully martensitic structure in any region of the joint. As a consequence, good welding properties are achieved in spite of the large carbon concentration (Jung et al., 2012). It is no exaggeration to say that this new alloy system, designated  $\delta$ -TRIP steel, emerged from computational modelling alone, which at the outset had the aim of solving a particular surface-engineering issue related to red oxide.

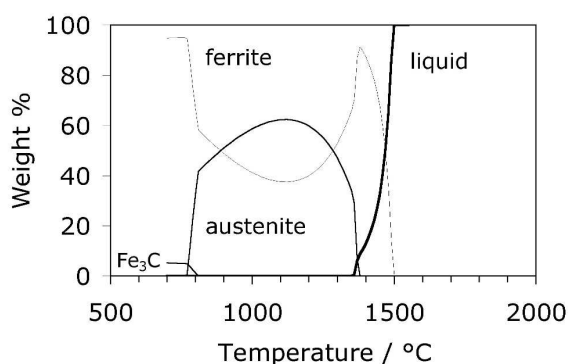


**Figure 13.40** Calculated phase diagram. The detailed chemical composition is Fe-0.36C-1.96Mn-0.73Si-2.22Al wt% (Chatterjee et al., 2007).

### 13.6.3 Weldability of TRIP-assisted steels

A primary requirement for automotive steels is that they should be easy to join using techniques such as resistance spot-welding, laser welding and arc welding, whether this is to themselves or to automotive steels of different chemical compositions. The problem with TRIP-assisted steels is that the welding process produces much greater hardening than is experienced with dual-phase steels of comparable mechanical properties, Fig. 13.44. And the difference in hardening behaviour becomes larger as the strength of the two varieties is increased. The hardness can reach 500 HV within the fusion zone of the welds in TRIP-assisted steels with softening in the adjacent intercritically heated zone of the unmelted plate (Zhao et al., 2009). During deformation, this can lead to a focussing of strain in the softened region, which will limit the elongation prior to fracture.

In the case of the data illustrated in Fig. 13.44, the greater hardness in welded TRIP-assisted steels is a consequence in this case of its larger manganese content. In contrast, dual-phase steels over a wide range of strength maintain a hardness of about 400 HV in the weld nugget (Tumuluru, 2006).

As the solute concentration of the TRIP-assisted steel is increased in order to create stronger varieties, the weld nugget hardness can reach 600 HV, with 450-500 HV in the heat-affected zones. When such welds are subjected to peel or tension tests, the interface between the sheets being joined acts as a notch that focusses stress on the hard weld-nugget, leading to

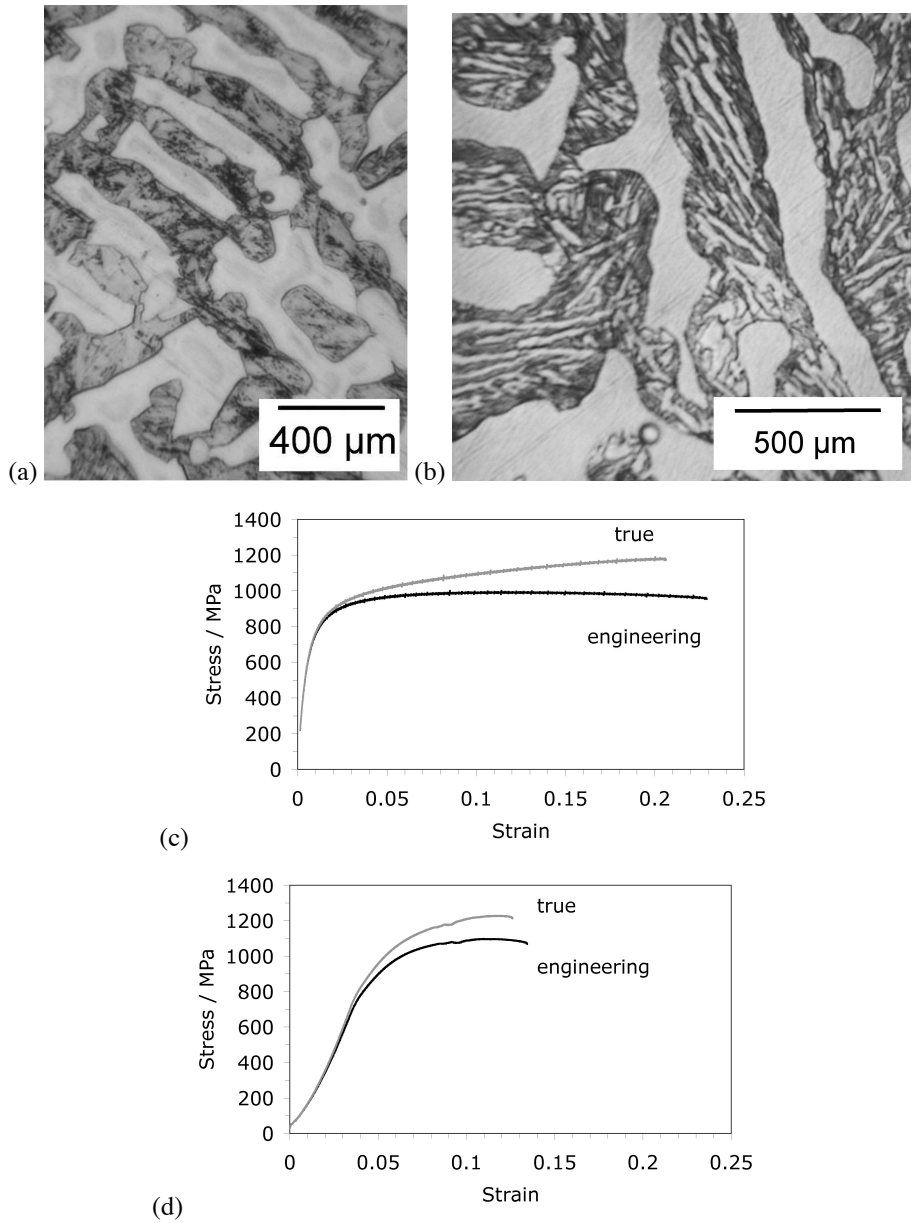


**Figure 13.41** (a) Dendritic structure of  $\delta$ -TRIP steel prior to processing. (b) Following intercritical annealing and partial transformation to bainite. (c) Tensile test at room temperature. The retained austenite content decreased from 14% before the test to 7% after fracture. (d) Tensile test at 100 °C. There was a negligible decrease in the retained austenite content even after fracture. After Chatterjee et al. (2007).

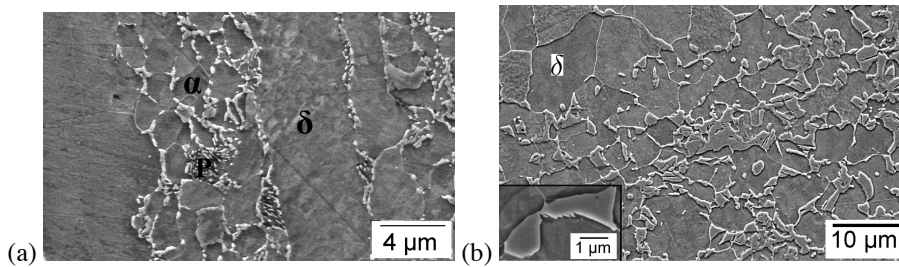


**Figure 13.42**  $\delta$ -TRIP steel. (a) Mixture of allotriomorphic ferrite, pearlite and  $\delta$ -ferrite in hot-rolled steel. (b) As (a) after intercritical annealing at 850 °C followed by isothermal transformation at 400 °C for 600 s. After Yi et al. (2011).

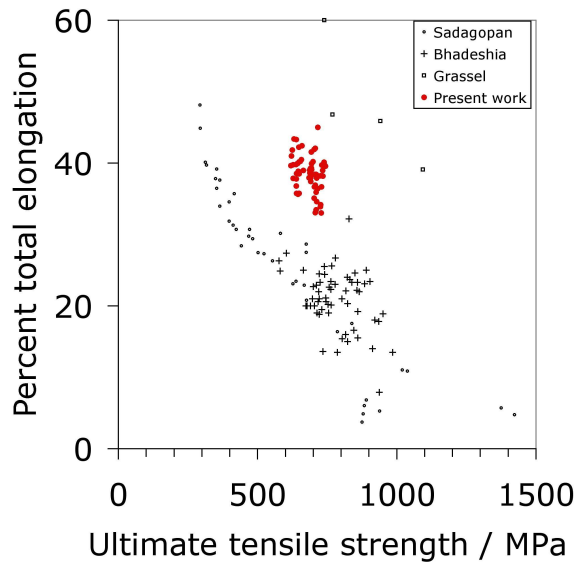


**Figure 13.43** Summary of the mechanical properties obtained for  $\delta$ -TRIP steel (demarcated data) in the context of published data (Yi et al., 2011).

brittle fracture (Haldar, 2014). The failure modes of the welds are also potentially compromised by the large differences in the hardness across the weld and heat-affected zones.

Fig. 13.45 shows some data for an aluminium-rich  $\delta$ -TRIP steel, in its resistance spot-welded condition. The microstructure in the nugget consists of retained  $\delta$ -ferrite and martensite, so that the hardness is always relatively low. The ductility ratio is defined as the strength of the spot weld when tested in cross tension divided by that in shear. Table 13.6 lists some values for dual-phase steels, conventional TRIP-assisted alloys and the  $\delta$ -TRIP steel. In spite of the apparently favourable hardness profile, the ductility ratio does not seem to match that available in dual-phase steels for reasons that are not entirely clear.

### 13.6.4 Dieless-Drawn Bainitic Steels

Wires or rods are conventionally made by drawing, in which a reduction in cross-sectional area is achieved by passing the stock through a die (Fig. 13.46). The drawing reduction

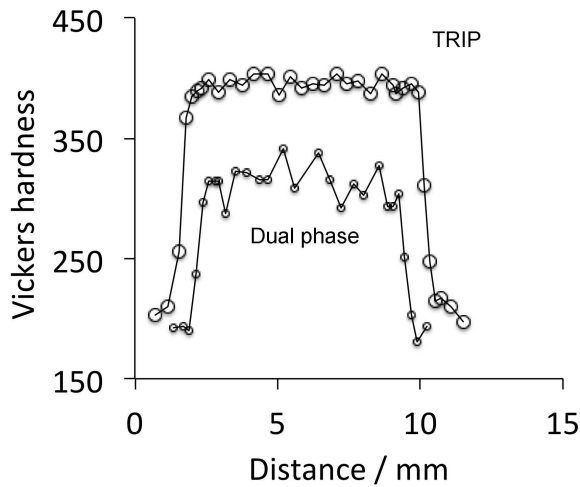


**Figure 13.44** Distribution of hardness across a resistance spot weld in a dual-phase steel (DP590 Fe-0.088C-1Mn-0.31Si- wt%) and TRIP-assisted steel (TRIP590 Fe-0.083C-1.52Mn-1.08Si wt%). Data from Rathbun et al. (2003).

**Table 13.6** Comparison of the mechanical properties of resistance spot-welds in automotive steels (Jung et al., 2012).

Steel	Shear strength / kN	Cross-tension strength / kN	Ductility ratio
Dual phase (590 MPa)	12.2	6.9	0.57
Dual phase (780 MPa)	15.9	9.4	0.59
Conventional TRIP-assisted (780 MPa)	15.7	5.3	0.34
$\delta$ -TRIP (620 MPa)	10.1	4.0	0.39

is determined by the ability of the thinner, work hardened section which leaves the die, to sustain the drawing force without further deformation.

An alternative process achieves the reduction in section using inductive heating. The region of the rod which passes through the hot zone softens and is extended by the drawing force. It stops deforming on leaving the hot zone. The process avoids all the difficulties associated with die erosion and requires a smaller drawing force (Fig. 13.46) because there are no stresses due to die-constraint. Dieless drawing can be applied to a greater variety of shapes, for example, square rods or tubes. The thermomechanical processing combined with accelerated cooling can be used to selectively develop microstructures, including dual-phase mixtures of ferrite and bainite (Weidig et al., 1999). The technology has yet to see major applications but the absence of discontinuous yielding in the dual phase microstructure is an advantage when drawn tubes subsequently have to be formed into complex shapes. Weidig *et al.* have managed to produce predominantly bainitic microstructures using dieless drawing and accelerated cooling in a low-hardenability steel of chemical composition Fe-0.1C-0.14Si-0.7Mn wt%.

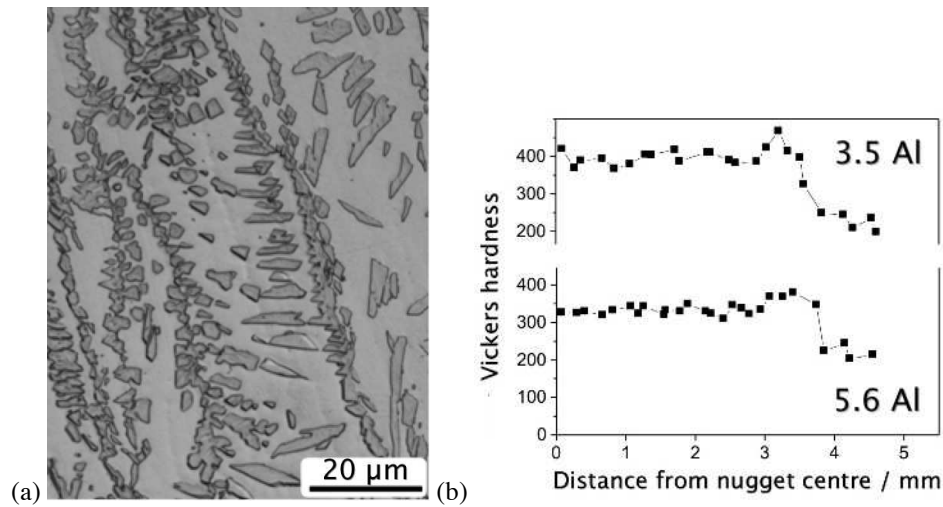


**Figure 13.45** (a) A volume fraction of approximately 0.48  $\delta$ -ferrite in the weld nugget of a high-aluminium  $\delta$ -TRIP steel. (b) Hardness profile across that weld nugget for the 3.5 and 5.6 wt% aluminium  $\delta$ -TRIP steels, both containing 0.3 wt% carbon. After Jung et al. (2012).

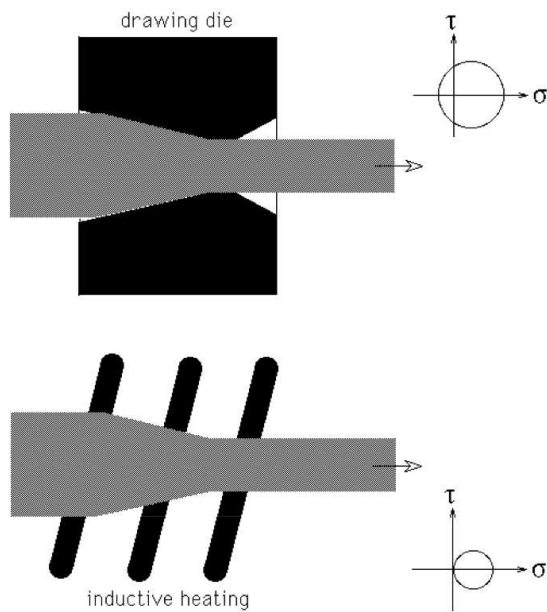


**Figure 13.46** A comparison of conventional drawing with dieless drawing. The Mohr's circle representations of stress are also presented;  $\sigma$  and  $\tau$  represent the normal and shear stresses respectively (Weidig et al., 1999).

### 13.7 Ultra-Low-Carbon Bainitic Steels

Ever since Irvine et al. (1957a), it has been apparent that good mechanical properties can be achieved in bainitic steels by reducing their carbon concentrations. Lower concentrations not only reduce the coarse cementite but also regions of untempered martensite which originate from the incomplete transformation of austenite to bainite. For this latter reason,

large concentrations of substitutional solutes are also detrimental if they limit the extent of transformation to bainite. And yet, the steel must have sufficient hardenability to avoid phases which occur before bainite during continuous cooling transformation.

Irvine and Pickering compromised by choosing a low concentration of carbon at about 0.1 wt% but ensuring hardenability using boron and molybdenum. They were therefore able to produce fully bainitic steels by continuous cooling transformation. Carbon is a potent strengthener of ferrite but for the same reason, it can lead to embrittlement following welding. A low carbon concentration can therefore provide major economies in fabrication, often allowing welding to be carried out without preheat.

The *ultra-low carbon bainitic* (ULCB) bainitic steels use this philosophy (Alloys 11 and 12, Table 13.1). The carbon concentration is limited to the range 0.01-0.03 wt%; the high manganese concentration is necessary to avoid transformation products other than bainite (Nakasugi et al., 1980, 1983; Hulka et al., 1988). A typical continuous cooling transformation diagram is illustrated in Fig. 13.47a, which shows that bainite can be obtained over a very wide range of cooling rates. This makes it possible to manufacture thick plates with uniform microstructure. Because of the low carbon concentration, the hardness is insensitive to cooling rate and depth within the plate (Fig. 13.47b).

The steels are microalloyed so some of the carbon precipitates in austenite as niobium carbide, so that the actual concentration in the austenite prior to its transformation is even smaller than the average value. The resulting reduction in the fraction of martensite improves toughness without undue loss of strength (Fig. 13.47c). The carbon concentration should not be reduced to less than 0.01 wt% since niobium carbide precipitation then decreases, with an accompanying loss of toughness. The niobium carbide and TiN prevent austenite grain growth during controlled-rolling operations and suppress  $\text{Fe}_{23}(\text{C}, \text{B})_6$  and BN precipitation, thereby leaving the boron free to make its contribution to hardenability (Tamehiro et al., 1987b,a). In fact,  $\text{Fe}_{23}\text{CB}_6$  particles should be avoided since they stimulate the nucleation of allotriomorphic ferrite.

Because there is insufficient carbon to combine with niobium in ULCB steels, a substantial proportion of the niobium remains dissolved in austenite. Since the equilibrium between niobium and carbon is temperature dependent, the finish rolling temperature  $T_R$  has a large influence on the state of the niobium (Fig. 13.48a). Less niobium remains in solution as  $T_R$  is reduced due to the greater propensity for strain-induced precipitation during deformation of the austenite at low temperatures.

Changes in the dissolved niobium concentration influence the evolution of microstructure in ULCB steels (Fig. 13.48b). The effect is unlikely to be purely thermodynamic given the small concentrations involved. Soluble niobium strongly retards allotriomorphic ferrite, permitting more bainite to be obtained in the final microstructure. The effect is not obvious in rapidly cooled because the ferrite is suppressed irrespective of the niobium concentration (Fig. 13.48b).

There is a synergistic effect between vanadium and niobium. Vanadium competes for carbon leaving more niobium in solution and thereby promoting a bainitic microstructure (Leber et al., 1987). In low carbon steels that are coiled following hot-rolling, the low-cooling rate following coiling can reduce the strength of the bainite; vanadium can be used to retard the recovery of the microstructure by forming microscopic precipitates that pin the dislocations (Siwecki et al., 2010). The same concept has been used to achieve stable strength levels that are not sensitive to the coiling temperature of steel (?); the stability was achieved by adding just 0.08 wt% of vanadium to Fe-0.04C-1.55Mn-1Cr-0.3Mo wt%, bainitic steel.

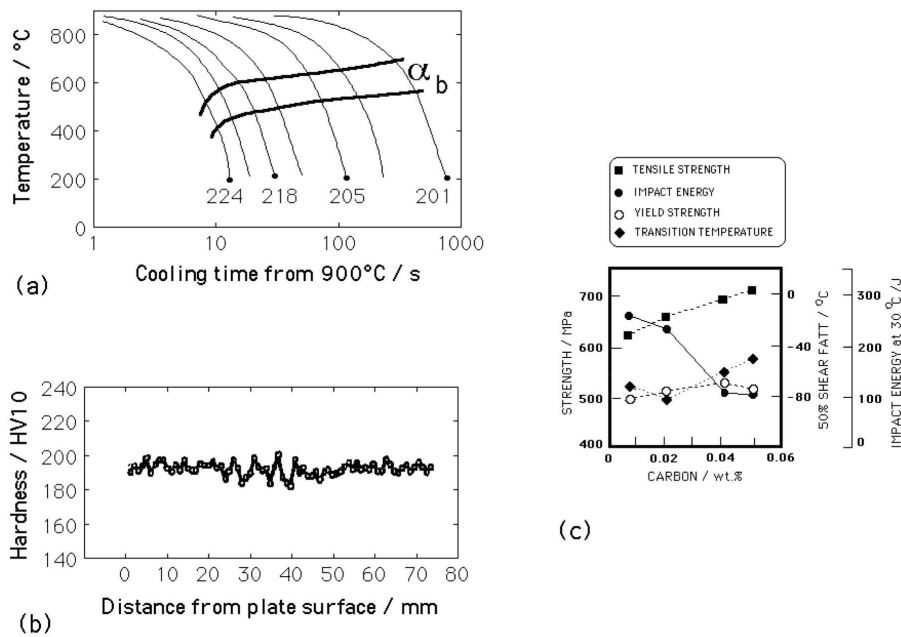


**Figure 13.47** (a) A continuous cooling transformation diagram for an ULCB steel (Fumimaru et al., 2000). The numbers represent hardness values. (b) Hardness as a function of depth in a 75 mm thick plate. (c) Mechanical properties as a function of carbon concentration in thermomechanically processed ultra-low-carbon bainitic steels (Hulka et al., 1988). The fracture assessed impact transition temperature (FATT), an indicator of the ductile-brittle transition temperature, begins to increase as the carbon concentration falls below about 0.02 wt%.

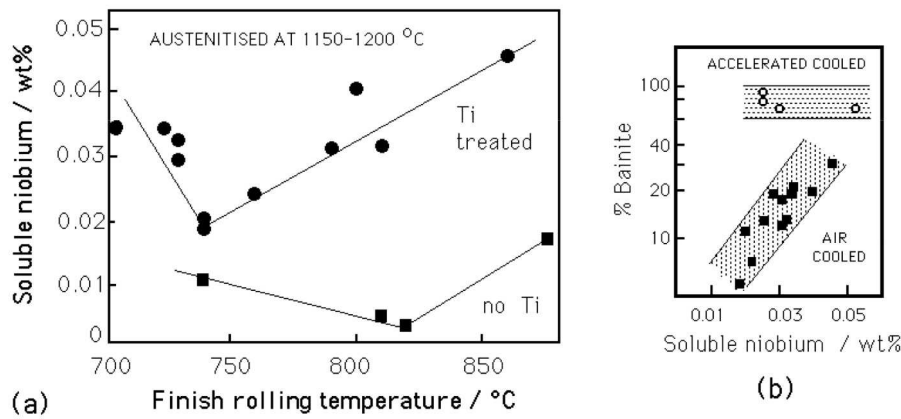


**Figure 13.48** Soluble niobium in ULCB steel (Hulka et al., 1988). (a) Variation in the soluble niobium concentration as a function of the finish rolling temperature; (b) variation in microstructure as a function of the finish rolling temperature.

ULCB steels can have outstanding toughness, strength and weldability combinations when appropriately processed, so they find use in the construction of pipelines in Arctic or submarine environments. They are useful as heavy plates (100 mm thick) and compete against the quenched and tempered varieties such as HY-80 (Gorni and Mei, 2005). The highest strength values are obtained using low finishing temperatures and accelerated cooling. The strength can be increased further by retarding cooling below 550 °C to allow NbC precipitation in the ferrite. This can be achieved by coiling or stacking the hot-steel product.

An alternative strategy for strong low-carbon steels (Alloy 22, Table 13.1) is to boost the manganese concentration, in this case to greater than 7 wt%, in order to avoid reconstructive transformations during continuous cooling (Bhowmik et al., 2012).

### 13.8 Bainitic Forging Steels

Forging is a method of working metal into the required shape by hot or cold plastic deformation. Large objects can be shaped using open forging-dies, whereas the mass production of precise components is done using closed dies which are filled with solid metal using forge pressure. Forging is attractive as a manufacturing process because it reduces the machining costs and can enhance properties along directions consistent with the application. Typical components which are forged range from small scale items such as crankshafts, connecting rods, piston shafts, bolts, axles and fasteners to components which might weigh many tonnes, such as the rotor shafts in steam turbine generators.

Fe-C-Mn-Si mild steels have served the forging industry reliably for many decades. They have been available in two strength ranges, 350-450 MPa ferrite/pearlite alloys, and high strength (> 600 MPa) quench and tempered martensitic steels.<sup>14</sup> With the martensitic steels, the forged components have to be austenitised, quenched, tempered, manipulated to remove distortion due to heat treatment, and finally, stress-relieved (Fig. 13.49a). For large components, the steel has to be heavily alloyed to obtain martensite at all positions.

There have therefore been attempts to reduce costs by reducing the concentrations of alloying elements and by simplifying the heat treatments. Modern forging steels are microalloyed to produce either fine ferrite/pearlite microstructures, or are alloyed to give bainitic or predominantly bainitic microstructures. Unlike martensite, these microstructures can be produced by transformation during cooling from the forging temperature, with savings in heat treatment, handling and fabrication costs (Fig. 13.49b). Strengths as high as 500-700 MPa are readily achieved without compromising toughness and with improved fatigue performance, machinability and weldability. The martensitic steels are still the toughest when it comes to medium carbon steels with a strength of 1200 MPa.

There are special considerations necessary when using directly transformed microalloyed steels; rapid induction heating is often used to heat the stock to forging temperature. The time at the austenitisation temperature has to be long enough to permit microalloying elements such as niobium to dissolve (Wright et al., 1987). The way in which the finished components are stacked after the final forging operation can determine their cooling rates.

The new alloys open up the possibility of *controlled forging*, which by analogy with controlled rolling, aims to refine the austenite grain structure prior to transformation. The final stages of forging are carried out at a temperature where the austenite does not recrystallise or alternatively, it recrystallises to a fine grain size. The disadvantage is that

<sup>14</sup>An excellent review on the subject has been published by Jones et al. (1985).

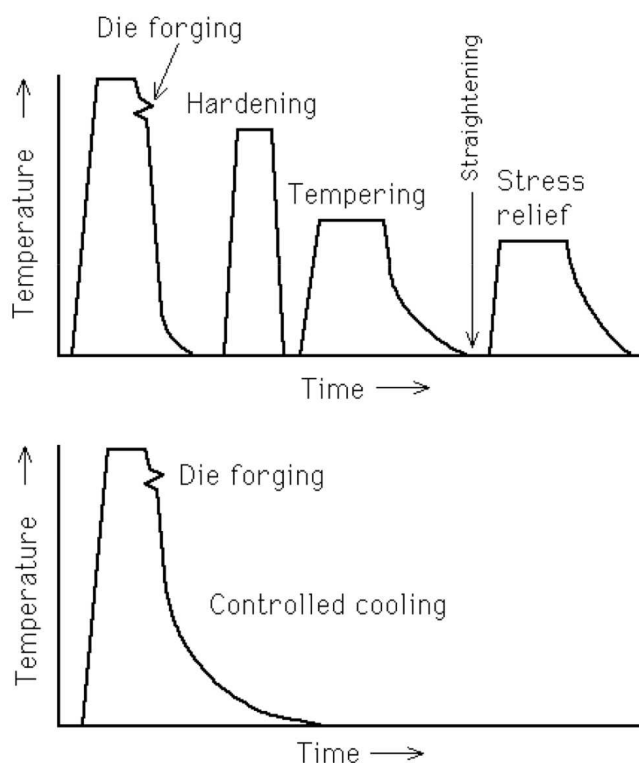


**Figure 13.49** An illustration of the heat treatment procedures for forging steels (Wright et al., 1987). (a) Conventional quenched and tempered martensitic steels; (b) microalloyed forging steels.

reductions in forging temperature cause an increase in the forging force necessitating more powerful production equipment. The increased stress also causes more rapid die wear.

Some of the new forging steels contain carbide forming elements such as Nb, V, Mo (Alloys 16-20, Table 13.1). Tempering causes fine carbide precipitation which strengthens the final product. The response to tempering is related to the amount and type of bainite in the mixed microstructures of  $\alpha$ ,  $\alpha_b$  and pearlite (Leber et al., 1988). The high dislocation density of bainite provides nucleation sites for the carbides, leading to rapid hardening. Predominantly bainitic microstructures are therefore preferred over those containing large fractions of allotriomorphic ferrite. Where niobium and boron additions are used to develop low carbon bainitic microstructures with high work-hardening rates (Alloy 21, Table 13.1), cold deformation can be used to increase the strength of the final product. A good example is the series of steels developed for the production of high-strength bolts by cold heading operations (Heritier et al., 1984).

Strong, bainitic forging steels containing high silicon and molybdenum concentrations have been developed for automobile applications, with a typical composition: Fe-1.4Mn-0.8Si-0.15V-0.2Mo wt% with 0.1-0.40 wt% C (Heitmann and Babu, 1987; Grassl et al., 1989). Such steels are intended to replace quenched and tempered martensitic alloys. The compositions are chosen to avoid the formation of carbides during bainitic transformation, carbides which can be detrimental to toughness. The toughness turns out to be better than that of ferrite-pearlite microstructures at comparable strength levels. However,

at higher carbon concentrations the bainitic steels compare unfavourably with martensitic steels which have superior toughness (Fig. 13.50). Although this might deter the use of bainitic forging steels, their toughness is still more than adequate for many applications, where their cost advantage may be usefully exploited. In this context, titanium microalloying has also been attempted in an effort to refine the structure but the consequent formation of coarse (Ti,V)(C,N) results in reduced fracture toughness Balart et al. (2002). A variant of the carbide-free bainitic forging steel (Alloy 20, Table 13.1), exhibits a higher cyclic yield strength and cyclic hardening than the standard quenched and tempered martensitic steel used in the automotive industry. This has been attributed to the retained austenite and its transformation into martensite on loading (Wirths et al., 2014), but comprehensive fatigue data are not yet available.

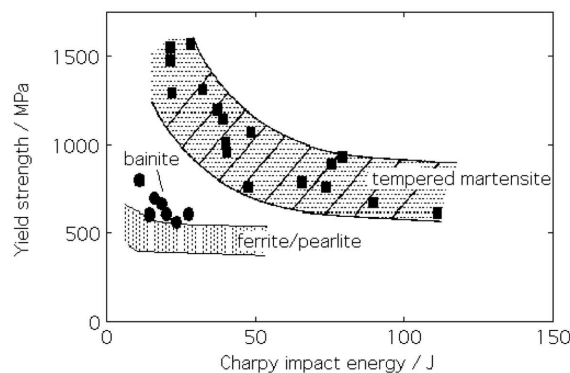


**Figure 13.50** A comparison of the properties of ferrite/pearlite, bainitic and martensitic forging steels (Grassl et al., 1989).

### 13.9 High Strength Bainitic Steels without Carbides

We have seen in Chapters 2,3 that an interesting microstructure results when a silicon or aluminium-alloyed steel is transformed into upper bainite. The carbon that is partitioned into the residual austenite does not precipitate as cementite, but remains there to make the austenite stable at ambient temperature. The microstructure obtained consists of fine plates of bainitic ferrite separated by carbon-enriched regions of austenite (Fig. 13.51).

The potential advantages of this mixed microstructure can be listed as follows:

- (i) Cementite is responsible for initiating fracture in high-strength steels. Its absence is expected to make the microstructure more resistant to cleavage failure and void formation.
- (ii) The bainitic ferrite is almost free of carbon, which intensely strengthens ferrite and hence embrittles it.
- (iii) The microstructure derives its strength from the fine grain size of the ferrite plates, which are less than  $1\ \mu\text{m}$  in thickness. It is the thickness of these plates which determines the mean free slip distance, so that the effective grain size is less than a micrometre. This cannot be achieved by any other commercially viable process. Grain

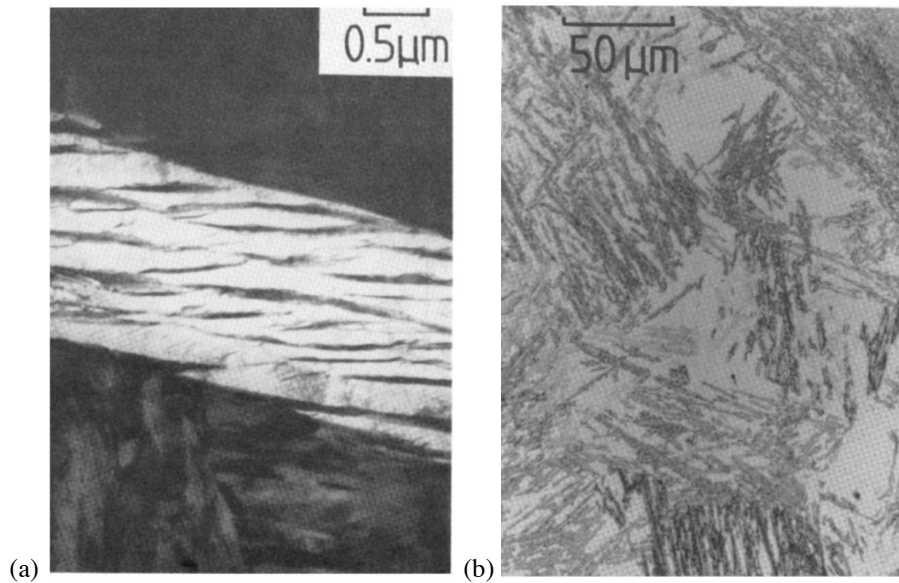


**Figure 13.51** (a) Transmission electron micrograph of bainitic ferrite plates separated by films of stable austenite. (b) Optical micrograph showing the large blocks of austenite left untransformed.

refinement is the only method available for simultaneously improving the strength and toughness of steels.

- (iv) The ductile films of austenite which are intimately dispersed between the plates of ferrite have a crack blunting effect. They further add to toughness by increasing the work of fracture as the austenite is induced to transform to martensite under the influence of the stress field of a propagating crack.
- (v) The diffusion of hydrogen in austenite is slower than in ferrite. The presence of austenite can therefore improve the stress corrosion resistance of the microstructure.
- (vi) Steels with the bainitic ferrite and austenite microstructure can be obtained without the use of expensive alloying. All that is required is that the silicon concentration should be large enough to suppress cementite.

In spite of these appealing features, the microstructure does not always give the expected good combination of strength and toughness. This is because the relatively large *blocky* regions of austenite between the sheaves of bainite (Fig. 13.51b) readily transform into high-carbon martensite under the influence of stress. These untempered, hard and coarse martensite regions severely embrittle the steel (Bhadeshia and Edmonds, 1983a,b; Liu et al., 2006).

If it is assumed that a fraction  $\phi$  of a sheaf consists of films of austenite, then the ratio of the fractions of film and blocky austenite (prior to any martensitic transformation) is given by:

$$\frac{V_V^{\gamma-F}}{V_V^{\gamma-B}} \approx \frac{\phi V_V^{\alpha_b}}{V_V^{\gamma} - \phi V_V^{\alpha_b}} \quad (13.6)$$

where  $V_V^{\gamma-F}$  and  $V_V^{\gamma-B}$  are the volume fractions of film and blocky type retained austenite respectively, and  $V_V^\alpha$  and  $V_V^\gamma$  the total volume fractions of bainitic ferrite and residual austenite respectively. It is found experimentally that both strength and toughness are optimised by achieving a ratio greater than 0.9 (Bhadeshia and Edmonds, 1983a,b; Chen and Li, 2007). Any large blocks of austenite can be consumed by promoting the formation of bainite without precipitating carbides. The maximum fraction of bainite that can be obtained at any temperature is, from the lever rule,

$$V_V^\alpha \approx \frac{x_{T_0} - \bar{x}}{x_{T_0}} \quad (13.7)$$

It follows that there are three ways of eliminating blocky austenite:

- (i) By reducing the isothermal transformation temperature to increase  $x_{T_0}$ . The lower limit is set by either the lower bainite or martensite-start temperature.
- (ii) By reducing the overall carbon concentration of the steel, so that the austenite reaches its limiting composition at a later stage of reaction.
- (iii) By moving the  $T_0$  curves of the phase diagram to larger carbon concentrations. This is achieved by adjusting the concentration and type of substitutional solute (Fig. 13.52a).
- (iv) By using a two-step heat treatment in which isothermal transformation at a high temperature corresponding to faster kinetics, is followed by transformation at a lower temperature where the blocks of austenite are refined by further transformation (Wang et al., 2014b). The austenite stability can then be engineered so that it transforms gently over a large range of strain during deformation, an advantage in preventing early plastic instabilities. The two-step process can be counterproductive in low-carbon steel because the net quantity of retained austenite can be reduced to an inadequate level (Duong et al., 2014).

The effect on toughness in reducing the amount of blocky austenite may be seen in Fig. 13.52b, which shows the large changes in the impact transition temperatures as the ratio of film to blocky austenite is increased in the manner just described. Note that for a duplex  $\alpha + \gamma$  microstructure, the strength actually increases as the fraction of bainitic ferrite increases, so that the better toughness is obtained without sacrificing strength. This concept must be interpreted with caution because it does not account for the size of the austenite blocks; those regions smaller than a typical non-metallic inclusion size are not necessarily detrimental. The factors that need to be considered are (Bhadeshia, 2014b):

1. the proportions of martensite and austenite in the constituent;
2. the chemical compositions of the martensite and austenite. This is necessary in order to estimate the hardness (see for example, Bhadeshia and Edmonds (1983b)). The block is formed from the residue of austenite that is left untransformed following the growth of phases such as ferrite, Widmanstätten ferrite and bainite. All of these leave the austenite richer in carbon provided the average concentration of carbon in the steel is greater than its solubility in ferrite. If the volume fraction of the block is large then its carbon concentration will be low; assuming that brittle behaviour is associated with high carbon, the phase may be less harmful at sufficiently large fractions.

3. The shape of the block. When confined between plates of ferrite, the retained austenite within it is more stable than when it is present as blocks between differently oriented plates (Bhadeshia and Edmonds, 1983a,b). Films of retained austenite are not considered to be damaging to toughness.
4. The mechanical properties of the blocky region relative to its surroundings. If any martensite that forms is not hard, then it is not necessarily harmful.

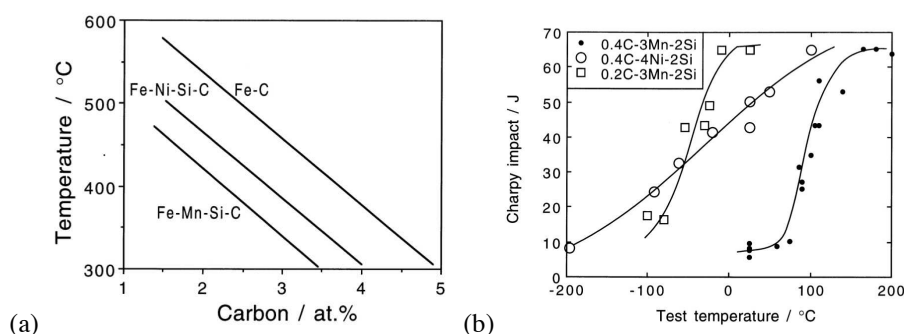


**Figure 13.52** (a)  $T_0$  curves for the alloy-steels listed in the inset of (b), and a corresponding curve for a plain carbon steel. (b) Impact transition curves showing improved toughness without loss of strength, obtained by reducing the amount of blocky austenite in a mixed microstructure of bainitic ferrite and austenite. The Fe-0.43C-2Si-3Mn wt% alloy has  $V_V^{\gamma-F} / V_V^{\gamma-B} = 0.5$ . The reduced carbon Fe-Mn-Si-C steel and the Fe-Ni-Si-C steel both have  $V_V^{\gamma-F} / V_V^{\gamma-B} > 1.5$ . After Bhadeshia and Edmonds (1983a,b).

Typical compositions of high-strength steels which show good toughness are given in Table 13.7; Fig. 13.53 shows how the mechanical properties compare with quenched and tempered steels. It is evident that in some cases, the properties match those obtained from much more expensive maraging steels. Similar toughness optimisation principles have been demonstrated for low-strength silicon-rich bainitic steels (Song et al., 1999).

**Table 13.7** Chemical compositions (wt%) of experimental high-strength steels with microstructures consisting of mixtures of bainitic ferrite and retained austenite. After Caballero et al. (2001a,b).

C	Si	Mn	Ni	Cr	Mo	V	YS / MPa	UTS / MPa	$K_{IC} / \text{MPa m}^{1/2}$
0.3	1.5	2.0	-	1.3	0.25	0.1	1170	1800	
0.3	1.5	-	3.5	1.5	0.25	0.1	1150	1730	125
0.3	1.5	-	3.5	1.5	0.25	-	1100	1625	128

There is a widespread notion in the literature that good toughness is expected in steels containing nickel in solid solution. To show that the results presented in Table 13.8 come from the optimisation procedure in which blocky austenite is eliminated, rather than from the addition of nickel, Caballero et al. (2006) designed a series of seven alloys in which the composition was varied widely while the calculated  $T_0$  curve, the maximum achievable

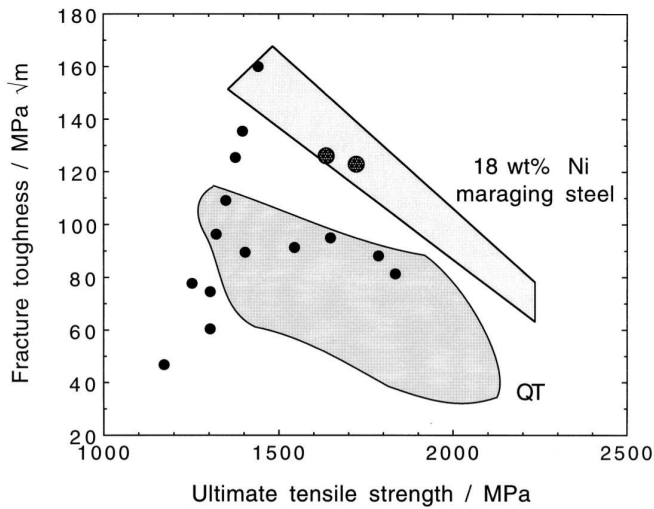


**Figure 13.53** Comparison of the mechanical properties of mixed microstructures of bainitic ferrite and austenite, versus those of quenched and tempered (QT) low-alloy martensitic alloys and maraging steels. The two large points refer to the latest bainitic steels, which match the maraging steel but are thirty times cheaper (about £900 per tonne compared with some £30,000 per tonne for maraging steels). Data from Miihkinen and Edmonds (1987a) and Caballero et al. (2001a,b).

**Table 13.8** Chemical compositions (wt%) of experimental steels used to verify the design procedure for mixtures of bainitic ferrite and retained austenite. After Caballero et al. (2006).

C	Si	Mn	Ni	Cr	Mo	Co	Al
0.3	1.5	2.23			0.25		
0.3	1.5	2.00		0.46	0.25		
0.3	1.5	1.50		1.46	0.25		
0.3	1.5	1.50	1.50	0.17	0.25		
0.3	1.5	2.00		1.16	0.25	1.00	
0.3	1.5	2.00		1.51	0.25	1.50	
0.3	1.5	2.00	1.76	1.51	0.25	1.50	1.00

bainitic ferrite fraction, and TTT diagram were maintained essentially constant. The alloys are listed in Table 13.8.

The properties of these carbide-free bainitic steels do not change much when tempered at temperatures close to the transformation temperature at which the original bainite formed. However, annealing at elevated temperatures or for prolonged periods at low temperatures can lead to the decomposition of the austenite into ferrite and carbides, with a simultaneous drop in strength and toughness, especially the upper shelf energy (Fig. 13.54). The latter effect can be attributed directly to the void nucleating propensity of carbide particles in the tempered microstructure, as illustrated by the much smaller void size evident

in the fracture surface of the tempered sample (Fig. 12.13). A similar deterioration in toughness on tempering a mixture of  $\alpha_b + \gamma$  has been reported by da Cruz et al. (2013).

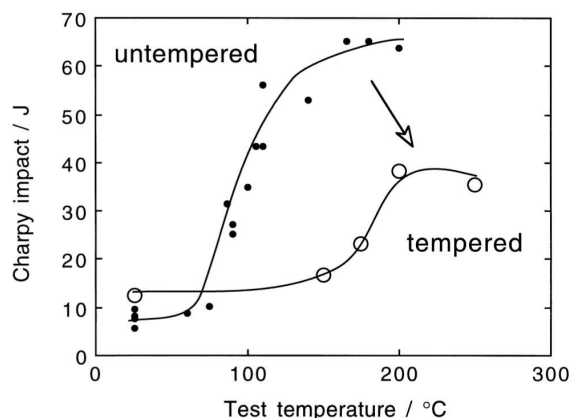


**Figure 13.54** Charpy impact toughness data for Fe-0.43C-2Mn-3Si wt% alloy transformed to a mixture of bainitic ferrite and carbon-enriched retained austenite. The data for the untempered microstructure are from Fig. 13.51. The other data were obtained after tempering the microstructure at 500 °C for 1 h to induce the decomposition of the austenite into a mixture of ferrite and carbides.

The basic concepts described in this section have also been exploited in the manufacture of cast steels (Mandal *et al.*, 2004). One complication is that casting defects such as porosity and unmodified inclusions have to be carefully controlled. Furthermore, the hardenability has to be engineered such that both thin- and thick-walled sections of the casting achieve the required properties and uniform microstructures. The chemical compositions of the cast alloys are otherwise similar to those of wrought steels.

### 13.10 Thermomechanically Processed High-Strength Steels

The alloys described here are not terribly useful in practice, but the phenomena they reveal are interesting and add to the understanding of bainite.

#### 13.10.1 Ausformed Bainitic Steels

Ausforming is the deformation of austenite at temperatures well below  $A_{e3}$ , followed by transformation to martensite or bainite. Its main effect is to increase the strength with a small loss in ductility. The deformation reduces the effective size of the austenite grains leading in turn to a more refined bainite (Kalish *et al.*, 1965; Duckworth, 1966; Edwards and Kennon, 1974, 1978; Umemoto and Tamura, 1986). The microstructure can become biased by the deformation which might favour particular crystallographic variants to form over others (Umemoto and Tamura, 1986).

The bainite that grows from deformed austenite has a greater density of dislocations (Irani, 1967; Edwards and Kennon, 1978). This is because it inherits the dislocations present in the parent austenite. The bainite sheaves adopt a smaller aspect ratio in ausformed samples (Tsunami *et al.*, 1989). Although there is an overall refinement of the

microstructure, each grain of deformed austenite transforms into fewer variants of bainite. Indeed, an entire austenite grain can transform into a single packet of bainite, which may not be desirable from a toughness point of view (Tsuji et al., 1999a). On the other hand, the refinement of cementite particles in ausformed bainite improves the toughness. As a rough estimate, each one percent increment of plastic deformation leads to a 5 MPa increase in strength.

**Table 13.9** Chemical compositions (wt%) of bainitic steels that have been studied with respect to the ausforming process. The steels are not in some cases custom made for ausforming operations.

C	Si	Mn	Ni	Mo	Cr	V	Cu	W	
0.39	1.00	0.25	-	1.39	5.25	0.54	-	-	Kalish et al. (1965)
0.48	0.25	0.86	0.18	0.04	0.98	-	0.09	-	Duckworth (1966)
0.85	-	1.39	-	-	0.59	-	-	0.53	Edwards and Kennon (1978)
0.59	2.01	1.02	-	-	-	-	-	-	Tsuzaki et al. (1989)

Not all steels are suitable for ausforming because the austenite must remain stable during deformation at a low temperature. The steel must exhibit a deep bay in the region of the TTT diagram between the two C-curves representing the reconstructive and displacive reactions (Table 13.9). Some of the alloying elements used to achieve the required hardenability in ausforming steels are also strong carbide formers. It is suspected that there is a precipitation of fine carbides in the austenite during its deformation; this must contribute further to the strength of ausformed samples (Duckworth et al., 1964; Thomas et al., 1965). When strong carbide forming elements are absent, electrical resistivity measurements have shown that deformation does not affect the concentration of dissolved carbon in the austenite (Hoffman and Cohen, 1973).

The plastic deformation of austenite at low temperatures is rarely homogeneous. Slip tends to concentrate into narrow bands (Schmatz and Zackay, 1959; Evans and O'Neill, 1959; Freiwillich et al., 1976). The austenite in the bands then transforms into a peculiar narrow band of ferrite, whose transformation mechanism is not known, although the bands do act as nucleation sites for bainitic ferrite (Jepson and Thompson, 1949; Freiwillich et al., 1976; Edwards and Kennon, 1978). Transmission electron microscopy has shown the bands to consist of single crystals of ferrite, or parallel laths of ferrite whose long axes lie in the plane of the band, together with some retained austenite. The bands also contain carbides which assist the nucleation of ferrite by locally reducing the carbon concentration. It is likely that the microstructure of the band is simply some highly refined form of bainite (Edwards and Kennon, 1978).

The tempering behaviour of ausformed bainite is somewhat different from that of ordinary bainite. The dislocations in the ausformed bainite rearrange into cells, whereas those in the lower dislocation density ordinary bainite remain dispersed (Edwards and Kennon, 1978).

Ausformed steels are not commercially successful because of the expense of the thermomechanical treatment and because of the limited variety of shapes that can be produced. With the exception of some low-carbon bainitic steels, ausformable alloys are costly because of the alloying elements they contain; a typical ausforming steel which is transformed to bainite might contain 5Cr-2Mo-0.5V-0.3Mn-1.0Si wt%. In general, ausformed martensitic steels exhibit better combinations of toughness and strength when compared

with ausformed bainitic steels (Kalish et al., 1965). This is because of the coarser carbides in bainitic steels; it is not therefore surprising that ausformed low-carbon bainitic steels are tougher than martensite in the same alloy (Durbin and Krahe, 1973).

There have been developments in ausformed bainitic steels. Silicon-rich steels respond well to thermomechanical processing because of the absence of cementite (Tsuzaki et al., 1989). A particularly promising application is in the manufacture of wire-springs given that the shape of this product is ideal for thermomechanical processing. Ausformed lower bainite wires have a hardness of 650 HV which is higher than the same spring in its tempered martensitic condition (Tsuji et al., 1999b). Recent work has emphasised the role of retained austenite as a means to enhance toughness (Suzuki et al., 2010), but it would be necessary in the context of spring applications to assess whether this compromises the stress-relaxation behaviour of the steel.

### 13.10.2 Strain Tempered Bainitic Steels

Strain tempering involves the deformation of martensitic or bainitic microstructures, followed by an ordinary isothermal tempering heat treatment. The steel compositions are similar to those of ausformed steel. The process leads to large increases in strength, with some loss in ductility and toughness. The strengthening that is obtained increases with the level of prior deformation, but is not just a reflection of the effects of deformation on the microstructure. The tempering causes an increase in strength as fine carbides precipitate on deformation-defects (Kalish et al., 1965). The effect is greater for bainite than for martensite, because the retained austenite in the former microstructure undergoes stress-induced transformation to harder martensite. Strain tempering is more effective as a method for increasing the yield strength than ausforming, but does reduce ductility.

### 13.10.3 Creep Tempering of Bainite

Both recovery and recrystallisation processes are accelerated when bainite is tempered during creep deformation (Ridal and Quarrell, 1962; Murphy and Branch, 1971). The unstressed regions of creep test samples retain a higher hardness than those in the gauge length. In molybdenum-containing bainitic steels, the transition from  $\text{Mo}_2\text{C} \rightarrow \text{M}_6\text{C}$  is accelerated by creep testing, the change being most noticeable at low temperatures or high strain rates, i.e. when reaction kinetics for the  $\text{Mo}_2\text{C} \rightarrow \text{M}_{23}\text{C}_6$  transition are slow.

It may be that the precipitation rate is increased by the greater number density of nucleation sites in a deformed sample, and by defect-assisted diffusion. However, there are complications in that the  $\text{Mo}_2\text{C} \rightarrow \text{M}_{23}\text{C}_6$  reaction has been reported to be retarded when the microstructure is tempered martensite (Ridal and Quarrell).

Hätterstrand and Andrén (2001) compared the carbide microstructures in crept tempered-martensitic steel with samples of the same steel which had been tempered without creep deformation. The effect of creep strain was to accelerate the coarsening of  $\text{M}_{23}\text{C}_6$  carbides whereas VN precipitates were not similarly affected. This is because the former are located on boundaries whereas the latter precipitate intragranularly and hence cannot take advantage of defect-assisted diffusion. The number density of Laves phase particles, which form during the later stages of tempering, was found to be higher in the strained samples; the defects associated with deformation stimulated the nucleation of Laves phase.

**Orientation changes during creep tempering** Cold-deformation experiments show that once a dislocation cell structure is established, further strain leads to a decrease in the cell

size and a corresponding increase in the crystallographic misorientation between adjacent cells (Langford and Cohen, 1975). The dislocations move and their density and distribution also change during the course of creep deformation. These changes are more complex than those associated with straight annealing, since there is in fact a coarsening of the microstructure. There is certainly an increase in the misorientation between adjacent cells in bainite as shown in Fig. 13.55a but the bainite lath width actually increases with the creep strain (Fig. 13.55b).

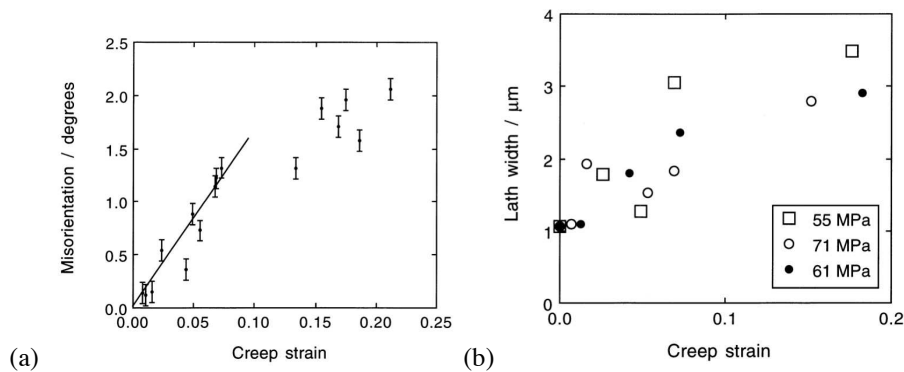


**Figure 13.55** (a) Crystallographic misorientation between adjacent laths of bainite in  $2\frac{1}{4}\text{Cr1Mo}$  steel as a function of the secondary-creep strain. The samples were tested at a variety of stresses and temperatures. (b) Corresponding variations in lath size (Lonsdale and Flewitt, 1978).

The measurements are for a  $2\frac{1}{4}\text{Cr1Mo}$  steel with a bainitic microstructure. The cell structure is found to be much coarser in the same steel when the microstructure is a mixture of ferrite and pearlite, with smaller misorientations between cells. Minute misorientations develop between dislocation cells within individual ferrite grains over a scale of about  $10\ \mu\text{m}$ . This contrasts with the orientation differences between adjacent laths of bainite, which are over distances less than  $1\ \mu\text{m}$ . A different kind of measurement has been reported by Fukuoka et al. (2002), where misorientations are followed not as a function of microstructure, but as a function of position within a large ferrite grain. However, the results are essentially identical to those reported by Lonsdale and Flewitt (1978).

### 13.11 Flash Processing

Some steels can be induced into a bainitic microstructure in tens of milliseconds, using *flash processing* (Cola Jr., 2007). In the original work, a strip shaped sample of steel of typical composition  $0.2\text{C}-0.3\text{Si}-0.7\text{Mn}-0.5\text{Cr}-0.5\text{Ni}-0.2\text{Mo}-0.2\text{Cu}$  wt% was passed through an oxygen-propane fired system that applies heat directly to the steel strip as it passes through the equipment. The rapidly heated  $1.5\ \text{mm}$  thick strip was then directly water quenched. The process naturally is associated with a high productivity, resulting in steel with a yield strength in the range  $786\text{--}1269\ \text{MPa}$  and elongation in the range  $37\%$ , depending largely on the chemical composition.

The original concept has now been generalised to a variety of steels, and the process has been engineered into a more sophisticated form (Tung et al., 2013); a schematic diagram is shown in Fig. 13.56a. Processing times are now of the order of just  $10\ \text{s}$  and product dimensions up to  $6.35 \times 609 \times 3657\ \text{mm}$ . As the steel passes through an induction coil it

is heated at a rate of about  $400\text{ }^{\circ}\text{C s}^{-1}$  to between  $1000\text{--}1100\text{ }^{\circ}\text{C}$ , and shortly afterwards quenched into water; short duration tempering is also available to improve ductility. The ultimate tensile strength and ductility combinations achieved are shown in Fig. 13.56b, bearing in mind that some of the alloy microstructures obtained are mixtures of bainite and martensite, the actual proportions depending on the chemical composition and process control.

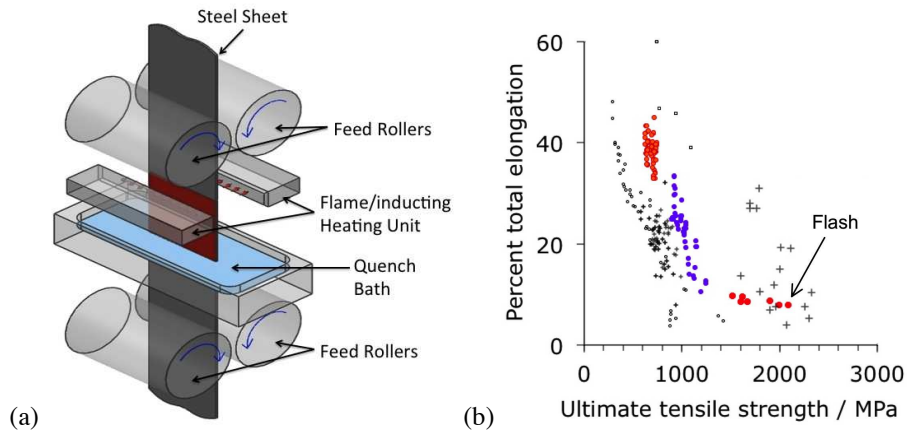


**Figure 13.56** (a) Schematic illustration of the modern variant of flash processing equipment, courtesy of Gary Cola. (b) A comparison of the properties achieved in flash processed steel, against standard automotive steels and nanostructured bainite. Data from Sadagopan et al. (2003); Bhadeshia (2010b); Grässel et al. (2000); Yi et al. (2011); Tung et al. (2013).

The microstructure evolves rapidly during the quench, inconsistent at first sight from the kinetics of transformation expected from the alloy composition. There are two reasons for this (Lolla et al., 2011). The austenite that forms during rapid heating consumes the ferrite first, and cementite particles only partly dissolve, and even when they dissolve, the resulting carbon remains localised in the vicinity of the original cementite. This is a consequence of the short duration of the heat treatment. It leaves much of the austenite depleted in carbon, and hence transforms rapidly on quenching.

Flash processed steel has huge potential, for example in the automotive industry and in the manufacture of armour. In the standard tests used to assess vehicle door side-impact, where a  $320\text{ kg}$  mass is thrown against the test piece at  $5\text{ m s}^{-1}$ , flash processed tubing demonstrated a 20% increase in the bending energy absorbed relative to an industry standard boron-steel (Tung et al., 2013). In resisting armour piercing bullets, it outperformed more costly aluminium, magnesium and titanium alloys. Like all high-strength steels (section 14.17), welding can be problematic because of the inevitable formation of a soft region in the heat-affected zone (Hanold et al., 2013).

### 13.12 Bainite in Rail Steels

Modern railway systems are subjected to intense use, with fast trains and increasing axle loads. Rails have to be more wear resistant and achieve higher standards of straightness and flatness in order to avoid the surface and internal defects which may lead eventually to failure. The shape of the manufactured rail depends to a large extent on the uniformity of

thermomechanical processing; the most advanced mills are computer controlled with continuous feedback from the product during manufacture (Fitzgerald, 1991). In this section we consider advances in the steels used for making rails, particularly the bainitic steels.

### 13.12.1 Track Materials

Although a variety of loadings can adversely affect the life of rails, wear and plastic deformation can lead to unacceptable changes in the rail head profile, changes controlled primarily by a system of rolling contact stresses encountered during service. This system is dependent upon the relative motions of wheel and rail within a small contact zone of about one square centimetre. The motions lead to lateral and longitudinal surface tractions and a spin moment. The rate of rail degradation depends also on the exact location; rail head erosion is at a maximum in regions where the track curves.

**Table 13.10** Compositions (wt%) of typical bainitic and pearlitic rail and wheel steels

No.	C	Si	Mn	Ni	Mo	Cr	V	Nb	B	Al	Ti	Other
1	0.55	0.25	1.00	-	-	-	-	-	-	-	-	Pearlitic rail steel
2	0.80	0.30	1.00	-	-	-	-	-	-	-	-	Pearlitic rail steel
3	0.70	1.90	1.50	-	-	-	-	-	-	-	-	Pearlitic rail steel
4	0.75	0.70	1.00	-	-	1.0	0.1	-	-	-	-	Special grade pearlitic rail steel
5	0.65	0.25	0.70	-	-	-	-	-	-	-	-	Pearlitic tyre steel
6	0.04	0.20	0.75	2.0	0.25	2.8	-	-	< 0.01	0.03	0.03	Bainitic rail steel
7	0.09	0.20	1.00	-	0.50	-	-	-	0.003	0.03	0.03	Experimental bainitic rail steel
8	0.07	0.30	4.50	-	0.50	-	-	0.1	-	-	-	Experimental bainitic rail steel
9	0.10	0.30	0.60	4.0	0.60	1.7	-	-	<0.01	0.03	0.03	Experimental bainitic rail steel
10	0.30	0.20	2.00	-	0.50	1.0	-	-	0.003	0.03	0.03	Experimental bainitic rail steel
11	0.30	1.00	0.70	-	0.20	2.7	-	0.1	-	-	-	Experimental bainitic rail steel
12	0.52	0.25	0.35	1.5	0.25	1.7	-	0.1	<0.01	-	-	Experimental bainitic rail steel
13	0.26	1.81	2.00	-	≈ 0.5	1.93	-	-	0.003	-	-	Experimental bainitic rail steel
14	1.00	0.25	0.25	-	-	1.50	-	-	-	-	-	Roller bearing alloy
15	0.51	0.35	0.80	-	≤ 0.25	-	-	-	-	-	-	Pearlitic tyre steel
16	0.20	1.43	1.91	0.22	0.30	0.03	0.08	-	-	-	-	Bainitic tyre steel

Ordinary rail steels contain about 0.7 wt% of carbon and are pearlitic (Table 13.10). However, special grade steels have been considered for tracks carrying high axle loads or fast trains. Since the steels may be used in continuous welded track, they must be amenable to welding to other kinds of low-grade rail steels. Conventional welding processes include flash butt welding and the thermite process. The Hadfield cast austenitic manganese steels are excellent for wear resistance but are not weldable to ordinary rail steels.

Wear is a system property more than a material property, but it is nevertheless possible to identify material factors which are important. And it is important in the context of rails to distinguish between rolling and sliding wear. The former induces maximum stresses under the contact surface, that can lead eventually to spalling failure by rolling contact fatigue, whereas the latter causes surface shear. As a consequence, the thickness of the deformed layer is smaller with rolling than with sliding (Sato et al., 1993). With eutectoid steels, the wear rate decreases as the hardness increases (Fig. 13.57), although exceptions have been reported (Kalousek et al., 1985a). Fig. 13.57 shows also that the microstructure influences wear; refining the microstructure prolongs the wear-limited rail life (Kalousek and Beynon, 1975).

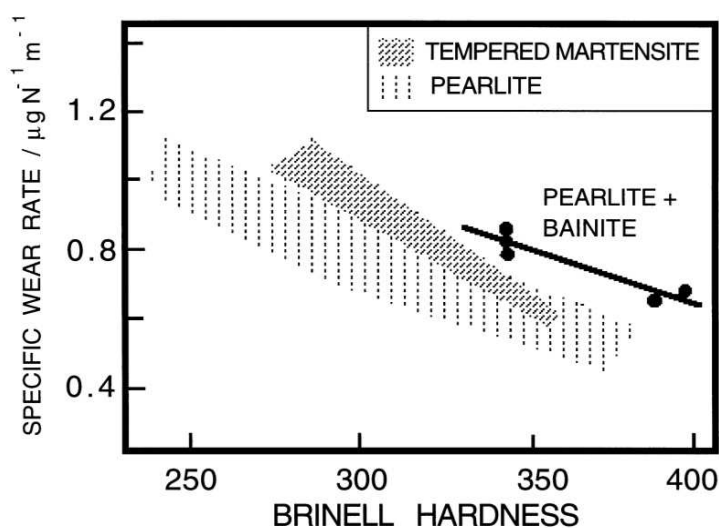


**Figure 13.57** The correlation of hardness with the wear rate for martensitic, bainitic and pearlitic microstructures (Hodgson and Preston, 1988).

The majority of rail steels are of eutectoid composition with a pearlitic microstructure. The pearlite colony size and interlamellar spacing can be refined by transformation at lower temperatures. But a higher level of refinement can be achieved by transforming instead to bainite. We shall consider first the conventional bainitic steels in which the microstructure contains carbides. These are in general found to perform worse than the pearlitic steels. Ghonem et al. (1982) compared the wear and toughness of pearlitic rails with that of an experimental bainitic rail containing chromium and molybdenum. The rail head microstructure consisted of 70% bainite and 30% pearlite but not only was the toughness unacceptable, so was the wear on the gauge face where there is rolling-sliding contact. Heller and Schweitzer (1980) compared the properties and service performance data from bainitic rail steels (alloys 8,11, Table 13.10) with those from a pearlitic rail steel (alloy 4, Table 13.10). The bainitic steels achieved higher tensile and fatigue strengths and performed well in service. There were, however, unspecified problems during welding. Service trials subsequently revealed that the bainitic steels wore faster than conventional pearlitic steel rails, when comparisons were made at the same hardness (Heller and Schweitzer, 1982). Laboratory experiments on a low carbon bainitic steel using rolling/sliding contact has indicated a wear rate some ten times faster than a pearlitic steel of the same hardness (Ichinose et al., 1982). Other results confirm these general trends and show that mixtures of bainite and pearlite are less wear-resistant than fully pearlitic steels, Fig. 13.58 (Kalousek et al., 1985b,a; Mutton, 1985; Makarov et al., 2002).

In contrast, low-carbon bainitic steels (alloy 6, Table 13.10) have been tested successfully for railway crossing applications where impact erosion and fatigue of the crossing nose were the major wear problems with conventional pearlitic rail steels (Callender, 1983; Garnham, 1989). An advantage of low carbon concentrations is that it enables the steels to be welded easily. Tests using pure sliding, cooled, pin-ring tests has demonstrated that low-carbon bainitic steels might have comparable or superior wear resistance to the pearlitic

steels, Fig. 13.58. Even when the pearlitic and bainitic steels have similar wear characteristics, the lower carbon concentration of bainitic steels ensures better ductility, toughness and weldability.

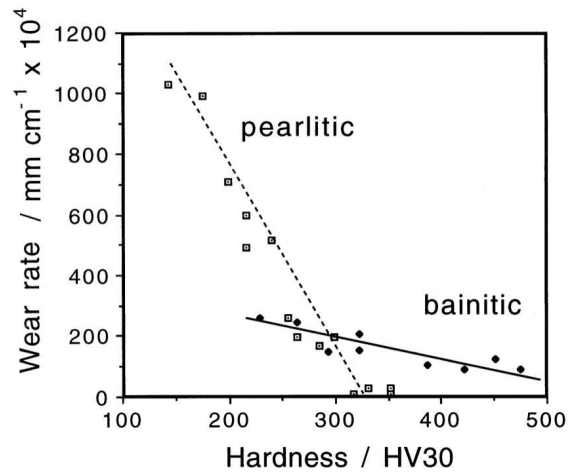


**Figure 13.58** Pin-ring wear rate versus hardness data for pearlitic and bainitic steels (Clayton et al., 1987).

It has been argued that most of the early pessimistic results on bainitic steels could be challenged because they were not systematic investigations and the microstructures had been inadequately characterised (Clayton et al., 1987; Clayton and Danks, 1990). Contradictory results can also be attributed to the different ways in which wear resistance was measured. The pin-ring test is not representative of service conditions where there is rolling-sliding wear. Using tests designed to simulate rolling-sliding wear, Garnham (1989) has demonstrated, using a variety of steels that carbide-free bainite has poor wear resistance relative to pearlite. Although carbide containing bainitic steel performed better, it increased the wear of the mating pearlitic railway wheel steel so that the combined wear rates were generally no better than for pearlite-pearlite combinations. It may be concluded from Garnham's work that bainitic steel is not suitable for railway applications where rolling-sliding wear is the major cause of rail or wheel replacement.

Other work has been more systematic in the assessment of wear resistance (Devanathan and Clayton, 1989). Three steels with carbon concentrations ranging from 0.04 to 0.54 wt% (alloys 8,9 & 12, Table 13.10) were examined in their bainitic condition. The lowest carbon steel, which also had the lowest starting hardness, outperformed pearlitic steels at the same hardness level. This is because the bainitic steel work hardened rapidly and had a greater ductility. The medium carbon steel was similar in its wear performance to pearlite, whereas the higher carbon steel was found to be worse. Microstructural observations (Fig. 13.59) revealed that the high carbon steel was chemically segregated, leading to bands of carbon-rich martensite separated by bainite; cracking initiated at the interfaces between these bands. In contrast, Sharma et al. (2014) found comparable properties between bainitic and pearlitic structures in a 0.7 wt% steel, but the extent of segregation was not reported.

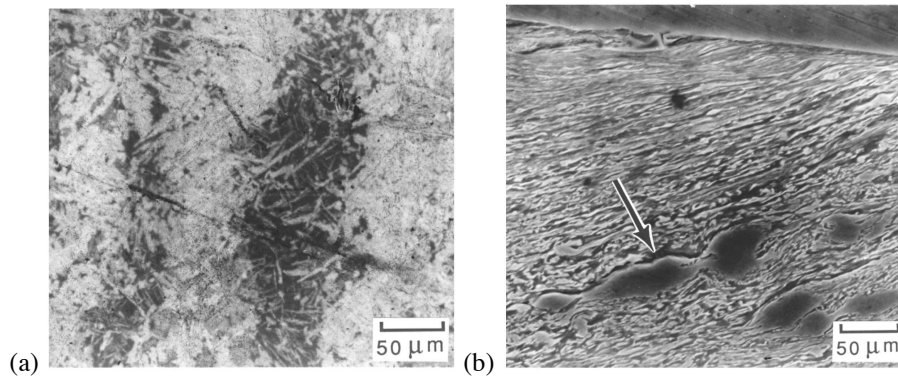


**Figure 13.59** (a) Banding apparent in a high carbon bainitic rail steel (Alloy 12, Table 13.10); (b) cracking at the interface between a pool of martensite and bainite - after Devanathan and Clayton (1989).

### 13.12.2 Silicon-rich Carbide-free Bainitic Rail Steels

We have seen that rail steels are based largely on near eutectoid composition and pearlitic microstructures. It is the carbide phase that is crucial in providing the necessary hardness. A different approach has been based on medium carbon bainitic alloys without any carbides, using precisely the same design philosophy as described for high-strength steels in section 13.9; much of the work is commercially sensitive and the subject of many patents, but there is a brief review article published by Yates (1996) and a paper by Jin and Clayton (1997). The steels contain a large silicon concentration and hence have a microstructure which is a mixture of bainitic ferrite, carbon-enriched retained austenite and some martensite. They have already demonstrated a much improved wear resistance (Fig. 13.60) and rolling-contact fatigue resistance, together with a high toughness even at sub-zero temperatures. A typical composition for the new steel is Fe-0.4C-1.5Si-2.0Mn-0.25Mo wt%, the composition being decided using thermodynamic and kinetic theory as described in section 13.9.

One advantage of the carbide-free bainitic steels is that the hardness throughout the rail section can be maintained at values in excess of 400 HV, which is often achieved in pearlitic steels by a separate head-hardening treatment. The rolling-sliding wear rate for Alloy 13 (carbide-free bainite, Table 13.10) is found to be some ten times smaller than the head-hardened pearlitic steel (Sawley and Kristan, 2003). The carbide-free bainite also has a greater toughness ( $51 \text{ MPa m}^{1/2}$ ) and rolling contact fatigue resistance, and in spite of its greater strength than the pearlite, ends up with similar residual stress distributions following straightening operations.

The origin of the good properties of carbide-free bainite in the context of rail steels lies in the absence of brittle cementite, the ability of the microstructure to undergo large surface-deformations without the creation of excessive debris and the mechanically induced transformation of retained austenite into hard martensite (Chang, 2005).

### 13.12.3 Wheels

Railway wheels conventionally contain a mixture of ferrite and pearlite. A particular problem with wheels is that the alloys must be resistant to microstructural change due to *wheel*

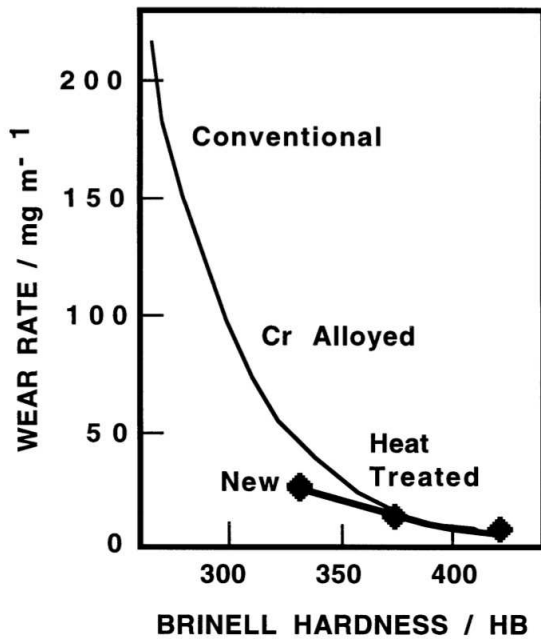


**Figure 13.60** Comparison of the wear rates and hardness levels of conventional rail steels against the new alloys (points) which have a carbide-free microstructure of bainitic ferrite and austenite (Jerath *et al.*, 1991). The points plotted as diamonds are further data on carbide-free bainite by Chang (2005).

*spin burning*. This can lead to the formation of brittle martensite when material at the surface of a pearlitic steel is momentarily heated to a temperature high enough to cause austenite to form. The same material is then cooled rapidly as the heat is dissipated into the underlying bulk of the wheel, causing the austenite to transform into brittle martensite. This effect can be of greater importance than the rolling-sliding wear of the tread (Sawley *et al.*, 1988). Steels containing less carbon and a bainitic microstructure have been shown to outperform the pearlitic steels because their lower hardenability makes martensite formation less likely; if martensite does form, it is not as brittle given the low carbon concentration and high  $M_S$  temperature.

Carbide-free bainitic wheels with composition Fe-0.2C-1.43Si-1.91Mn-0.3Mo wt% have been shown to produce matching properties to higher-carbon wheels that have the ferrite/pearlite structure. The toughness and strength tend to be higher with a Brinell hardness between 235-435 depending on location within the wheel profile (Zhang and Gu, 2007). Tribological properties (10% slip rolling-sliding) are comparable and the material can be produced using the same technologies as for conventional wheels. However, much further work is needed to establish credibility, with long-term, full scale testing to demonstrate worthwhile advantages before claiming success, given the safety-critical nature of rail transport.

#### 13.12.4 Bearing Alloys

Roller bearings represent another fatigue and wear-related application in which bainitic microstructures might have an advantage over the traditional alloys used in the quenched and tempered condition (Akbasoglu and Edmonds, 1990). A comprehensive review on the subject is available elsewhere (Bhadeshia, 2012), but the most common steel used is

the so-called 52100 alloy, with the approximate composition Fe-1C-1.5Cr (Alloy 14, Table 13.10). For roller bearings, the main life-limiting factor is rolling contact fatigue, a parameter which can be sensitive to the environment (oil, water) in which the bearing operates. In conditions of good lubrication, the repeated pulses of shear stress, which are highest under the surface where contact occurs between the rolling element and bearing raceway can lead eventually to spalling. When operating in water-based lubricants, hydrogen evolving from electrochemical reactions can cause embrittlement leading to accelerated fatigue crack growth. In these circumstances, bainitic microstructures fare better than the more hydrogen sensitive martensitic microstructures produced by austenitisation at 850 °C for 20 min, oil quenched and then tempered at 175 °C for 1 h. The tempering temperature can be increased to 250 °C for better toughness, but at the expense of hardness. A lower bainitic microstructure can be produced by isothermal transformation below the  $B_S$  temperature; a typical heat treatment might consist of 250 °C for 40 min.

The 52100 type steels can be made bainitic by isothermal transformation in the temperature range 200–450 °C, with lower bainite dominating the microstructure when the transformation temperature is less than 350 °C (Hollox et al., 1981). Early studies indicated that the carbide in the lower bainite is cementite (Swahn et al., 1976), but atom-probe experiments have demonstrated that  $\epsilon$ -carbide is also present (Song et al., 2013). This is not surprising since lower bainite can be regarded essentially as martensite that tempers during the course of transformation. Tempered martensite in this steel definitely contains  $\epsilon$ -carbide (Borchers and Doffin, 1969; Becker, 1981) and there may well be cementite depending on the tempering conditions. It is likely that there is a greater tendency to form cementite in the bainitic ferrite because there are two demands on the initial excess carbon dissolved in the bainitic ferrite, i.e. partitioning into the residual austenite and precipitation. When the former dominates, the precipitation is predominantly from carbon-enriched austenite (Bhadeshia, 1980). The lower bainitic microstructure observed in 52100 following isothermal transformation at 230 °C is illustrated in Fig. 13.61, (Vetters et al., 2006). Finally, as expected from previous work on the mechanism of carbide precipitation at low temperatures (Chapter 3), both the  $\epsilon$ -carbide and cementite grow under paraequilibrium conditions where the ratio of substitutional solute to iron atoms is maintained constant across the transformation interface.



**Figure 13.61** Lower bainite generated by isothermal transformation of 52100 steel at 230 °C for 10 h (Vetters et al., 2006). Micrograph kindly provided by J. Dong and H.-W. Zoch.

A measured time-temperature-transformation diagram for 52100 steel is illustrated in Fig. 13.63.<sup>15</sup> An alternative diagram, Fig. 13.64, plotted on the same horizontal scale for an almost identical steel which has been austenitised at a lower temperature so that the carbon concentration in the austenite would be reduced; the consequent increase in the driving force for transformation leads to an acceleration of the bainite reaction (Bhadeshia, 1982d). On the other hand, the formation of pearlite is faster when the austenitisation temperature is greater (*cf.* Figs 13.63 & 13.64) because of the larger concentration of carbon dissolved in the austenite. A continuous cooling transformation diagram is shown in Fig. 13.65, illustrating the change in  $M_S$  when martensite is preceded by partial transformation to bainite, due to the enrichment of the residual austenite with partitioned carbon. There are also systematic studies on bearing steels where both isothermal martensite and bainite are shown to form below the  $M_S$  temperature (Wozniak et al., 2011b). Such detail is not reported on the TTT diagrams presented here, but could be of importance given that the heat treatment of bearing steels occurs at particularly low temperatures. Isothermal martensite has been found over the temperature range 130–160 °C in a bearing steel, and bainite at these temperatures is said to evolve from thin plates of twinned martensite (Wozniak et al., 2011b). The subject deserves further study.

The complete transformation to bainite at a temperature just above  $M_S$  (i.e.  $\approx 230^\circ\text{C}$ ) can take some 4 h, which adds to the expense of heat treatment when compared with the quenched and tempered condition.<sup>16</sup> It is possible to accelerate the reaction by first quenching to a temperature about 20 °C below  $M_S$  for less than a minute, and then raising it into the bainite range (Vetters et al., 2006). Step quenching of this kind, but within the bainite transformation range has been known for some time to accelerate the transformation kinetics at the higher temperature.<sup>17</sup> It has been demonstrated experimentally that the two-step treatment of bearing steel can shorten the heat treatment time without sacrificing hardness (Lund et al., 2000; Vetters et al., 2006, 2009; Dong et al., 2010), but it remains to be proven that the process can be adapted to industrial practice. As an example, the complete transformation of 52100 steel at a constant 210 °C takes 33 h, after which the hardness achieved is 60.1 HRC; transforming the majority of the austenite at the same temperature but for 9 h, followed by heating to 250 °C for 1 h, results in a completely bainitic microstructure with a slightly reduced hardness of 59.9 HRC (Lund et al., 2000). A reduced manganese concentration can also accelerate the bainite reaction by reducing the thermodynamic stability of the austenite (Kulakov et al., 1986; Bhadeshia, 1982d).

It is interesting that in a heat treatment where 52100 type steel is first cooled to a temperature below  $M_S$  to rapidly produce up to 30% martensite, and then heated to a higher temperature to transform isothermally to bainite, the evolution of the combined fraction of martensite and bainite follows precisely the same kinetics as those samples transformed directly to bainite Smanio and Sourmail (2011). In other words, the heat treatment time is reduced by the two-step heat treatment by exactly the time taken to form the same fraction of bainite as the martensite formed during cooling below  $M_S$ , Fig. 13.62.

<sup>15</sup>It has to be admitted that a thorough identification of the transformation products, for example whether their formation leads to a shape deformation appropriate for displacive transformation, is lacking. This kind of information is important in phase identification so that the temperature ranges for the formation of pearlite or bainite are not well-defined.

<sup>16</sup>The  $M_S$  temperature depends on the homogeneity of the alloy, the measurement method and interpretation of dilatometric data (Yang and Bhadeshia, 2007). Such considerations do not seem to have been taken into account in published data

<sup>17</sup>(Lange and Mathieu, 1938; Jellinghaus, 1952; Goodenow et al., 1969; Bhadeshia, 2001a)

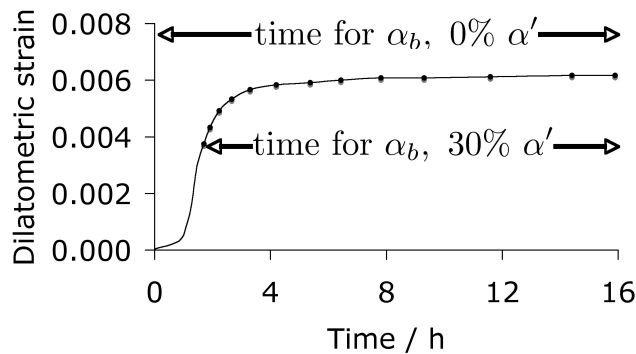


**Figure 13.62** Dilatometer data showing the evolution of  $\alpha_b$  for two cases. The curve is for the case where an initially austenitic sample is transformed isothermally to bainite at 250 °C. The points represent the case where about 30%  $\alpha'$  was induced by cooling below  $M_S$ , followed by heating to 250 °C to form bainite. Adapted from Smanio and Sourmail (2011).

It has been argued that a somewhat softer lower bainitic structure in the 52100 steel outperforms martensite when hydrogen embrittlement is an issue, because of its greater toughness and ductility (Hampshire et al., 1982).<sup>18</sup> This is consistent with independent work on which the time at the austenitisation temperature was controlled to obtain different fractions of undissolved cementite; changing the fraction from 0.09 to 0.01 led to an increase in strength due to the greater carbon concentration in solution within the martensite, causing a deterioration in toughness and fatigue resistance (Park et al., 2007). On a similar rationale, pearlite and upper bainite are avoided since they apparently reduce fatigue life (Hollox et al., 1981).

One advantage of a bainitic microstructure with its constituent carbides is that the reaction in bearing steels such as 52100 is able to progress until almost all of the austenite is consumed. It follows that the retained austenite content is minimal at about 1 vol.% (Mikus et al., 1960) so the transformed steels are dimensionally stable. The heat treatments typical in the production of bainite also help minimise the possibility of quench cracking (Mikus et al., 1960). One disadvantage is that the kinetics of the bainite transformation are more susceptible to the presence of chemical segregation and hence exhibit more pronounced banding than is the case for martensite (Caballero et al., 2009a; Wozniak et al., 2012; Morales-Rivas et al., 2014). This is because of the relatively low driving force associated with the bainite reaction which means that it nucleates first in the solute-depleted regions (Khan and Bhadeshia, 1990).

<sup>18</sup>In contrast, it has been suggested in passing that the “lower hardness and poor wear resistance of bainite compared with that of tempered martensite are considered serious drawbacks” for 52100 type steel (Basu et al., 2007). Evidence supporting this statement was not provided and the alloy is in fact used widely in its bainitic condition.

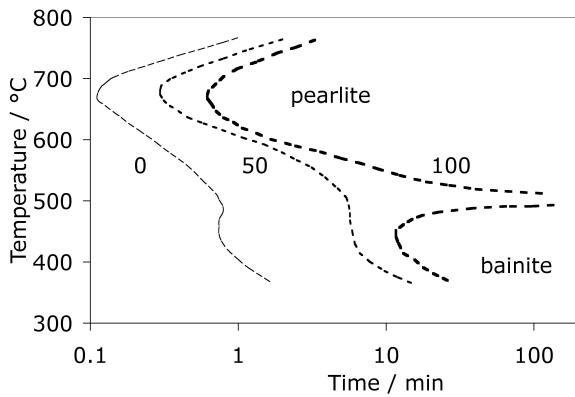


**Figure 13.63** Isothermal transformation diagram for Fe-1.04C-0.32Mn-0.19Si-1.35Cr wt% steel, fully austenitised at 1040 °C for 30 min. The austenite grain size is 40-60 μm. The numbers indicate the percentage of transformation, neglecting proeutectoid cementite precipitated at the austenite grain boundaries when  $T > 450^{\circ}\text{C}$ . Adapted from Stickels (1974).

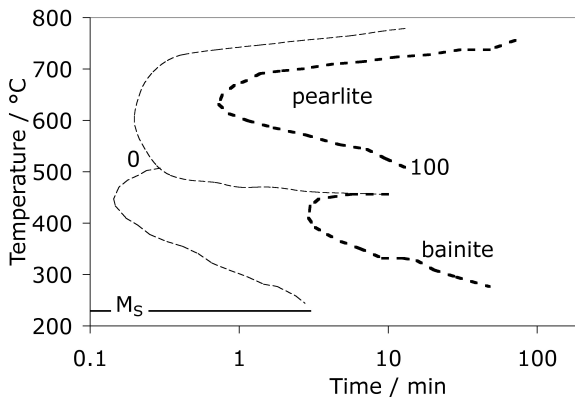


**Figure 13.64** Isothermal transformation diagram for Fe-0.95C-0.44Mn-0.21Si-1.42Cr wt% steel, austenitised in the  $\gamma + \theta$  phase field at 845 °C for 20 min. The numbers indicate the percentage of transformation. Adapted from Veters et al. (2009). It is possible to form a small amount of martensite during isothermal treatment at temperatures below  $M_S$  (Hsu, 1987).

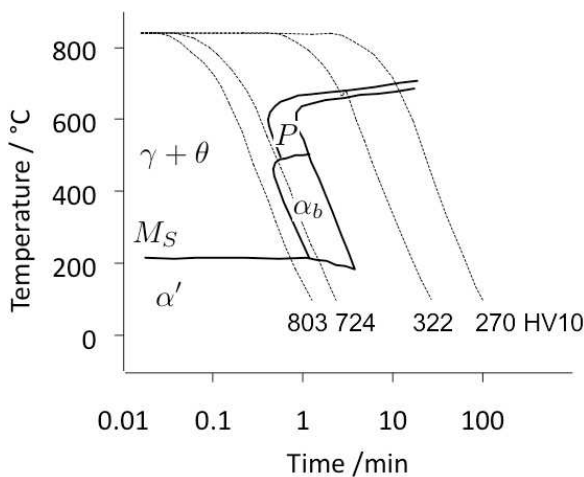


**Figure 13.65** Continuous cooling transformation diagram for an alloy which is nominally 100Cr6: Fe-0.95C-0.36Mn-0.28Si-1.84Cr- wt%. Adapted from Brandis (1972).

### 13.13 Bainitic Cast Irons

Cast irons typically contain 2-4 wt% of carbon with a high silicon concentration and a greater concentration of impurities than steels. The *carbon equivalent* (CE) of a cast iron

helps to distinguish the grey irons which cool into a microstructure containing graphite and the white irons where the carbon is present mainly as cementite. The carbon equivalent is defined as:

$$CE(\text{wt}\%) = w_C + \frac{w_{Si} + w_P}{3} \tag{13.8}$$

A high cooling rate or a low carbon equivalent favour the formation of white cast iron whereas a low cooling rate or a high carbon equivalent promotes grey cast iron.

During solidification, the major proportion of the carbon precipitates in the form of graphite or cementite. When solidification is just complete, the precipitated phase is embedded in a matrix of austenite which has an equilibrium carbon concentration of about 2 wt%. On further cooling, the carbon concentration of the austenite decreases as more cementite or graphite precipitates from solid solution. For conventional cast irons, the austenite then decomposes into pearlite at the eutectoid temperature. However, in grey cast irons, if the cooling rate through the eutectoid temperature is sufficiently slow, then a completely ferritic matrix is obtained with the excess carbon being deposited on the already existing graphite.

White cast irons are hard and brittle; they cannot easily be machined. The phase transformations for hypoeutectic irons (Fig. 13.66) are as follows:

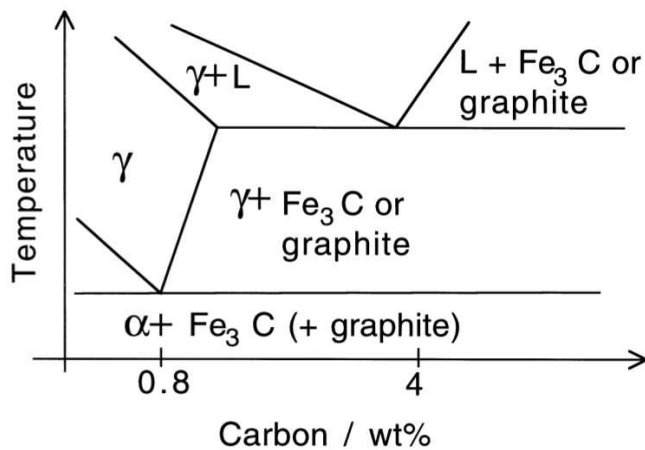
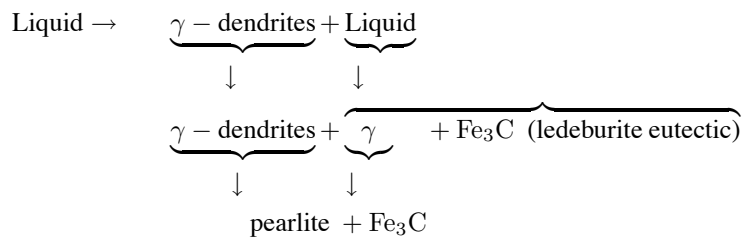


**Figure 13.66** Schematic representation of the iron-carbon phase diagram showing the eutectic and eutectoid reactions.

Grey cast irons are softer with a microstructure of graphite in a transformed-austenite and cementite matrix. The graphite flakes, which are rosettes in three dimensions, have a

low density and hence compensate for the freezing contraction, thus giving good castings free from porosity.

The flakes of graphite have good damping characteristics, good machinability but are stress concentrators, leading to poor toughness.

The addition of minute quantities of magnesium or cerium poisons preferred growth directions and leads to isotropic growth resulting in spheroids of graphite. This spheroidal graphite cast iron has excellent toughness and is used widely, for example in crankshafts.

### 13.13.1 Austempered Ductile Cast Irons

A particular form of cast irons is where the matrix of spheroidal graphite cast iron is not pearlite, but bainite (Fig. 13.67). This results in a major improvement in toughness and strength. The bainite is obtained by isothermal transformation of the austenite at temperatures below that at which pearlite forms.<sup>19</sup>

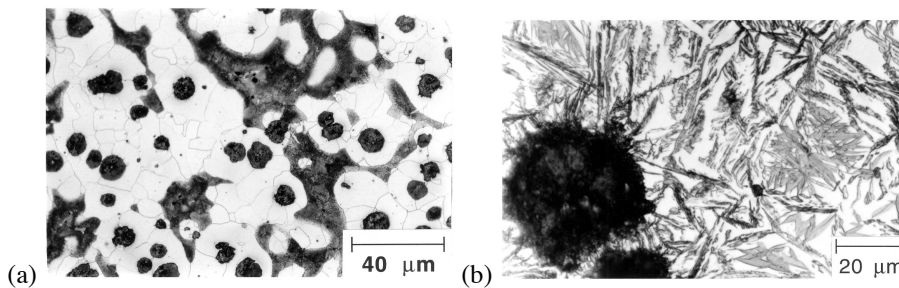


**Figure 13.67** Optical micrographs. (a) The microstructure before austempering. (b) The microstructure after austempering, with graphite in a matrix which is a mixture of bainitic ferrite, retained austenite and some martensite, after Yescas et al. (2001).

The isothermal heat treatment which leads to the formation of bainite is known as *austempering* and the resulting cast iron, which is known as *austempered ductile cast iron*, has much improved ductility and toughness,<sup>20</sup> together with improved abrasion wear resistance. Table 13.11 compares some typical properties.

The alloys have a typical composition Fe-4.0C-2.0Si-0.5Mn-0.06Mg wt%, with a carbon equivalent of about 4.5 (Table 13.12). The nodular iron is prepared by treating the melt with magnesium which alters the flake graphite morphology associated with untreated melts to that of nodular graphite. The solidified iron is then held at 930 °C for 12 hours followed by slow cooling, to give a structure consisting of graphite nodules in a ferritic matrix.

Heat treatment consists of austenitisation at around 950 °C followed by isothermal transformation of the austenite at temperatures where bainite is expected. Because the cast irons have a large silicon concentration (1-2 wt%) or aluminium concentrations (Kiani-Rashid, 2009), carbide precipitation is prevented during the formation of upper bainite so that the microstructure at the isothermal transformation temperature consists of a mixture

<sup>19</sup>The ability to produce bainite without first forming pearlite is sometimes known as *austemperability*, measured by the depth to which pearlite forms during the cooling of a cylindrical bar under specified conditions (Zahiri et al., 2003).

<sup>20</sup>(Dorazil et al., 1982; Blackmore and Harding, 1984; Moore et al., 1985a; Ueda and Takita, 1986; Shea and Ryntz, 1986; Franetovic et al., 1987a,b; Rundman et al., 1988; Shepperson and Allen, 1987; Lu and Zhang, 1989)

**Table 13.11** Comparison of the properties of ADI against ordinary steel and spheroidal graphite cast iron, adapted from Hayrynen et al. (2002).

	“Steel”	Spheroidal graphite iron	ADI
Yield strength / MPa	740	540	830
Ultimate tensile strength / MPa	910	905	1085
Elongation / %	23	11	14
Charpy impact energy, 25 °C / J	325	75	140

**Table 13.12** Typical compositions of austempered ductile cast irons. The cast steels are discussed in section 13.14. ‘RE’ stands for rare earth additions.

Type	Chemical composition / wt%								Reference
	C	Si	Mn	Mo	Cu	S	P	Other	
Typical	3.6	2.0	0.5	-	-	0.02	0.02	Mg=0.06	
Reduced Mn	3.44	2.41	0.15	-	-	0.007	0.0015	Mg=0.064	Putatunda and Gadicherla (1999)
High Al	3.44	1.22	0.10		< 0.005	< 0.005		Mg=0.05, Al=4.88	Kiani-Rashid and Edmonds (2009)
Cast steel	1.0	3.0	2.0			0.012	0.016		Putatunda (2003)
Cast steel	1.0	2.5	1.5		0.5			Cr=1.0	Fu et al. (2007)
Cast steel	0.6-0.8	1.6-3.9	0.3-0.6	0.2-0.4		< 0.04	< 0.04		Li and Chen (2001)
Cast steel	0.76	2.37	0.38	0.29		0.026	0.02		Chen and Li (2006)
Cast steel	0.77	2.36	0.36	0.27		0.011	0.021	RE=0.03	
								Ti=0.023, V=0.039	Chen and Li (2006)
Cast steel	1.07	1.44	0.31	0.01	0.07	0.014	0.014	Al=0.027	Takahashi et al. (1996)
Cast steel	1.09	2.08	0.39	0.01	0.07	0.017	0.018	Al=0.044	Takahashi et al. (1996)
Cast steel	1.02	2.39	0.33	0.01	0.06	0.013	0.018	Al=0.033	Takahashi et al. (1996)

of bainitic ferrite and carbon-enriched residual austenite. Some of the latter phase then decomposes into untempered martensite on cooling to ambient temperature (Moore et al., 1985a; Franetovic et al., 1987a).

An important feature of the heat treatment is that bainite is allowed to form until it reaches a maximum in its volume fraction, but the heat treatment must not go on so long that carbides begin to precipitate from the carbon-enriched austenite. The carbon concentration of the residual austenite at the isothermal transformation temperature can be calculated using the  $T_0'$  boundary (James and Thomson, 1999; Thomson et al., 2000; Kutsov et al., 1999). This is useful because not only can the carbon concentration of the austenite be calculated using the  $T_0$  curve, but so can the maximum fraction of bainitic ferrite since:

$$V_V^{\alpha_b, \max} \approx \frac{\bar{x} - x^\alpha}{x_{T_0} - x^\alpha} \quad (13.9)$$

where  $V_V^{\alpha_b, \max}$  is the maximum fraction of bainitic ferrite,  $\bar{x}$  is the average carbon concentration in the austenite before the formation of bainite,  $x_{T_0}$  is the concentration of carbon given by the  $T_0$  curve of the phase diagram and  $x^\alpha$  is the solubility of carbon in ferrite. The concentration of carbon in the austenite is sometimes approximated as:

$$\begin{aligned} \bar{x}/\text{wt}\% \approx & -0.435 + 3.35 \times 10^{-4}T_\gamma + 1.61 \times 10^{-6}T_\gamma^2 + 0.006w_{\text{Mn}} \\ & -0.11w_{\text{Si}} - 0.07w_{\text{Ni}} + 0.014w_{\text{Cu}} - 0.3w_{\text{Mo}} \end{aligned} \quad (13.10)$$

The interpretation in terms of the  $T_0$  curve explains why the carbon concentration of the austenite is independent of the starting concentration  $\bar{x}$  (Moore et al., 1985b). Cast irons are chemically heterogeneous, a factor that must be taken into account in these calculations.

As emphasised earlier, prolonged heat treatment at the isothermal transformation temperature leads eventually to the diffusional decomposition of the residual austenite into carbides and more ferrite. The period between the achievement of a maximum volume fraction of bainitic ferrite and the onset of carbide precipitation is known as the heat treatment window.

Austempered ductile cast iron behaves in the same manner as silicon-rich steels transformed to bainite, except that the carbon concentration of the austenite depends both on the time and temperature to which the cast iron is heated. This is because the austenite is in contact with graphite and the equilibrium between these phases depends on temperature; the time required to achieve equilibrium also depends on the austenitising temperature. An increase in austenitising time leads to a greater dissolution of the graphite into the austenite, thereby increasing the austenite carbon concentration to a maximum level consistent with the ( $\gamma/\gamma + \text{graphite}$ ) phase boundary (Moore et al., 1987). Consequently, a cast iron isothermally transformed to bainite after holding at the austenitising temperature for a long period gives lower bainite (with  $\eta$  carbides within the bainitic ferrite) whereas the bainite obtained after a short austenitising treatment is upper bainite, free of carbides. This is consistent with the theory for the transition from upper to lower bainite (Chapter 7).

Cast irons need a long time (typically 2 h) at the austenitising temperature to reach equilibrium, when compared with steels (Rouns and Rundman, 1987). This is because the dissolution of graphite produces carbon concentration gradients in the matrix, leading to a heterogeneous microstructure. For reasons which are not clear, the ferrite also seems to take longer to dissolve at the austenitising temperature.

Consistent with the lower carbon level expected in the austenite following a low temperature austenitising treatment, the rate of formation of bainite is found to increase with a decrease in the austenitising temperature (Moore et al., 1985a,b). Of course, the austenite grain size also decreases with the austenitising temperature and may contribute to the

acceleration of transformation, but the effect of carbon is expected to be the main factor responsible for the increased reaction rate.

A further effect of austenitising temperature that is peculiar to the cast irons is the mechanism by which phosphorus embrittles the austenite grain boundaries (Klug et al., 1985). The phosphorus combines with magnesium to form particles (possibly  $Mg_3P_2$ ) at the boundaries. The phase begins to redissolve at the grain boundaries if the austenitisation temperature is too high: for a Fe-3.74C-2.4Si-0.19Mn-0.15Mo-0.02P-0.045Mg wt% alloy, the redissolution becomes important at temperatures exceeding  $\approx 1050^\circ\text{C}$ . The dissolving particles act as a source for free phosphorus which then spreads along the austenite grain. There is then a drop in toughness as fracture occurs preferentially at the embrittled austenite grain boundaries.

As is the case for bainitic steels containing large concentrations of silicon, austempered nodular graphite cast irons have the highest toughness when carbides are absent and when the retained austenite is mechanically stable (Moore et al., 1985a). The time at austenitising temperature therefore is important because it determines the matrix austenite carbon concentration, and hence its stability with respect to both carbide precipitation and martensitic decomposition.

The role of carbide precipitation in causing a reduction in the ductility of bainitic cast irons is not as clear cut as in the wrought alloys. The austempered cast irons contain numerous large graphite particles which should be the main sites for failure initiation. It seems unreasonable to suggest that the much smaller carbides associated with bainite can control failure initiation. It is probable that the reduction in austenite volume fraction and stability caused by carbide precipitation causes the reduced ductility. Fractography could establish this hypothesis.

Common defects in cast irons, such as shrinkage, slag inclusions and films, segregation, and certain eutectic products can negate the benefits achieved by the presence of austenite in the austempered ductile iron (Moore et al., 1987). For example, the brittle interdendritic carbides which form when the molybdenum concentration is greater than 0.5 wt%, makes the iron brittle in spite of the austenite. The problems become more severe for larger castings where cooling rate variations might necessitate larger alloy concentrations at the risk of exaggerating segregation. There is a growing trend towards alloys with reduced concentrations of manganese and molybdenum (Table 13.12) because these have a greater tendency to segregate into the liquid phase when compared with solutes such as Si, Ni, and Cu which partition preferentially into the solid phase (Rundman, 1988; Putatunda and Gadicherla, 1999). In the context of fatigue, it is the clustering of large graphite nodules that initiates cracks (Reed et al., 2004).

It is a well known result for bainitic steels that the retained austenite occurs in two forms. There are the films trapped between the platelets of bainitic ferrite, and the coarser blocky regions of austenite trapped between different bainite sheaves. The blocks tend to transform more easily to untempered high-carbon martensite which causes embrittlement. Their volume fraction therefore needs to be minimised. Similar results have been obtained

for the austempered ductile iron (Moore et al., 1987; Rouns and Rundman, 1987).<sup>21</sup> The ductility decreases as the amount of blocky austenite increases. A smaller fraction of this austenite can be achieved by allowing a longer time  $t_1$  at the austempering temperature assuming that the reaction has not saturated. The difficulty is to ensure that the time  $t_2$ , when the residual austenite begins to decompose to carbides is longer than  $t_1$ . For example, it has been demonstrated that beyond a certain manganese concentration,  $t_2$  is always found to be smaller than  $t_1$  (Moore et al., 1987; Rouns and Rundman, 1987). This limiting manganese concentration is found to depend on the austenitising temperature which determines the carbon concentration in the austenite (Moore et al., 1987). Hence, a higher austenitising temperature should lead to more of the blocky austenite. With lower bainite, the volume fraction of blocky austenite is reduced because some of the carbon is then tied up as carbides in the bainitic ferrite (Moore et al., 1987). However, the higher strength causes a reduction in toughness. Cast irons containing upper bainite generally have a tensile strength in the range 960-1150 MPa with a tensile elongation up to 13%, whereas the corresponding data for lower bainite are 1310-1495 MPa and 5% elongation (Moore et al., 1987).

There are other special effects concerning the bainite transformation in cast irons. In wrought steels, bainite inevitably nucleates at the austenite grain boundaries. In cast irons, the nucleation of bainite is also found to occur at the austenite/graphite interfaces (Moore et al., 1985a). The interface between graphite and iron is weak, and it may in fact be the case that nucleation occurs at the free surface, produced by detachment of the graphite from the matrix. The regions where the nodules of graphite form are in general poorer in alloy concentration, and this might explain their ability to preferentially stimulate the nucleation of bainite (Rouns and Rundman, 1987). Cast irons usually contain chemical segregation which is more pronounced than in steels. Solute concentrations tend to be highest in the interdendritic and intercellular regions, which are the last to solidify (Moore et al., 1985a,b). The problem is made worse by the rather high mean alloy concentration of bainitic cast irons, necessitated by the need for the austenite to have sufficient hardenability to avoid the formation of pearlite, especially for applications where heavy section castings are required (Rundman et al., 1988). The presence of pearlite leads to poor mechanical properties when compared with bainite (Dorazil et al., 1982). The effect of chemical segregation is to give a non-uniform distribution of bainite. Solute-rich regions which are unable to transform to bainite during austempering decompose into untempered, high-carbon martensite on cooling to ambient temperature and cause a marked decrease in ductility (Moore et al., 1985a; Rundman et al., 1988).

A more uniform distribution of bainite can be obtained in spite of the chemical segregation, by holding for a longer time at the isothermal transformation temperature. The regions rich in austenite stabilising elements then have an opportunity to transform. A difficulty is that carbides might form in the regions which transform first to bainite (Moore et al., 1985a,b). Another procedure involves ausforming prior to austempering, the rate of transformation to bainite being higher everywhere, in lightly deformed austenite (Moore

<sup>21</sup>The terminology used to identify the blocky regions is confusing. The regions are designated *untransformed austenite volumes (UAV)*, their volume fraction being measured using point counting on a light microscope. However, the films of austenite within the bainite sheaves are not included in this analysis, even though they are also untransformed. Hence, the volume fractions of austenite reported using X-ray diffraction analysis (which includes both films and blocks) are greater than the values reported for the UAV regions. A further difficulty is that the carbon concentration of the UAV regions is assumed to be unchanged by the formation of bainite (Moore et al., 1986); this is incorrect and must lead to an overestimation of carbon in the remaining microstructure, since some of the microstructural parameters are derived using mass conservation conditions.

et al., 1985a). Ausforming is a specialised treatment involving austenite deformation before transformation and does not seem practicable for cast irons.

There is an effect of segregation which cannot be eliminated by any of the treatments discussed above. The good properties of austempered ductile irons are because of the stable austenite. A short austempering time leads to less carbon enrichment in the residual austenite, which consequently suffers from mechanical instability. Longer times, on the other hand, induce carbide precipitation. There is therefore an optimum austempering time which depends on alloy chemistry. Segregation causes this optimum time period to be different in different regions of the sample, making it impossible to obtain stable austenite throughout the sample (Rundman et al., 1988).

**Elimination of Graphite** Since many of the problems of austempered ductile cast iron arise from chemical segregation associated with the very high carbon concentration, Fu et al. (2007) designed a cast steel with the same composition as the cast iron but without the graphite, i.e. Fe-1C-2.5Si-1.5Mn-1Cr-0.5Cu wt%. The cast steel is then transformed isothermally into a mixture of bainitic ferrite and carbon-enriched retained austenite in a manner similar to the heat treatment used for conventional austempered ductile cast irons. The microstructure thus obtained replicated that of the matrix phase in the cast irons. Using an optimum isothermal transformation temperature of 320 °C, they obtained a microstructure with a tensile strength of 1452 MPa, 3% elongation, a toughness of 65 MPa m<sup>1/2</sup> and an ambient temperature Charpy toughness in excess of 200 J. It is claimed that this combination of properties is better than that associated with ADIs, although it would be interesting to make a comparison of the respective castabilities.

**Two-Stage Heat Treatment** Transformation at a low-temperature followed by slow heating to a temperature below  $B_S$  has been shown to lead to an impressive improvement in the fracture toughness of austempered ductile cast irons, without any loss of strength (Putatunda, 2001). The effect is most pronounced for high initial transformation temperatures (Fig. 13.68). It is possible that the initial heat treatment, which is associated with a larger undercooling, provides for a larger number density of bainite nuclei, thereby making the microstructure more uniform and allowing a more uniform distribution of carbon in the residual austenite.

In another study, Putatunda et al. (2006) have found that a tempering heat treatment at about 500 °C applied to austempered ductile iron causes the austenite to decompose into a mixture of ferrite and carbides. Consistent with observations on steels, this leads to a deterioration in toughness (Bhadeshia and Edmonds, 1983a,b). However, the toughness of the finest microstructure obtained by isothermal transformation at 260 °C was maintained in spite of the decomposition of austenite (Table 13.13). This presumably is because the carbides that form have a small particle size, given that the untempered microstructure is itself fine. The results are nevertheless surprising since they indicate that the retained austenite is not relevant when the microstructure is generated at low transformation temperatures. This conclusion may be limited to cast irons containing graphite, which has a seminal influence on fracture toughness.

### 13.13.2 Abrasive Wear of Bainitic Cast Irons

Cast irons are often used in situations where resistance to abrasive wear is an important requirement. The mechanical properties (high strength and ductility) of austempered cast irons, together with their low cost, make them potential candidates for applications in-

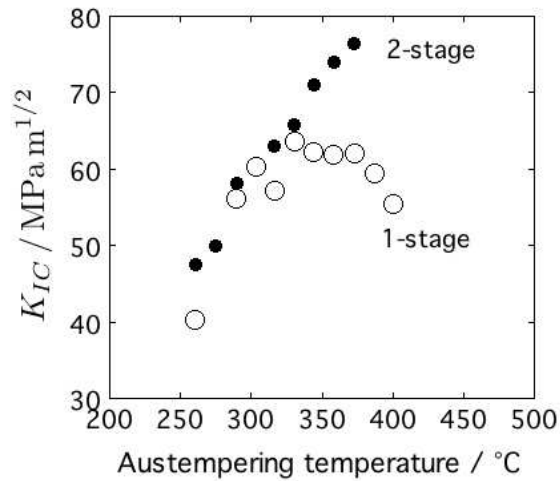


**Figure 13.68** The influence of austempering on the fracture toughness of austempered ductile cast iron. The single-stage heat treatment is conventional, involving the isothermal formation of bainite. In the two-stage heat treatment, the sample is first transformed at a low temperature and then slowly heated through  $30^{\circ}\text{C}$  over 2 h, the temperature never exceeding  $B_S$ .

**Table 13.13** Toughness of austempered ductile iron samples, before and after tempering at  $484^{\circ}\text{C}$  for 2 h. All samples were austenitised at  $927^{\circ}\text{C}$  for 2 h prior to isothermal transformation at the temperature indicated, followed by the tempering heat treatment. Data adapted from Putatunda et al. (2006).

Transformation temperature / $^{\circ}\text{C}$	$K_{IC}/\text{MPa m}^{\frac{1}{2}}$ , untempered	$K_{IC}/\text{MPa m}^{\frac{1}{2}}$ , tempered
260	$45 \pm 1$	$45 \pm 1$
316	$64 \pm 6$	$40 \pm 5$
385	$70 \pm 5$	$29 \pm 5$

volving abrasive wear. Many investigations have now indicated that the austempered ductile cast irons have better abrasive wear resistance when compared with normalised cast irons of the same chemical composition (Lu and Zhang, 1989) or abrasion resistant steels, including the Hadfield manganese steel, of equivalent hardness (Shepperson and Allen, 1987). The improved wear resistance is at least partly a consequence of the stress-induced transformation of austenite into hard, high-carbon martensite (Fig. 13.69), together with the inherent ductility of the microstructure (Shepperson and Allen, 1987). The high work hardening rate usually associated with the transformation induced plasticity may also make a contribution.

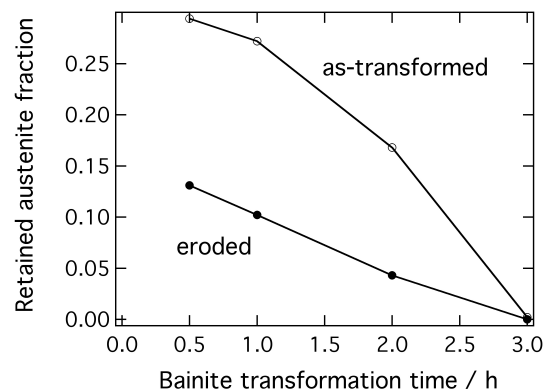


**Figure 13.69** The decomposition of retained austenite during the erosion wear of austempered ductile cast iron using alumina (Hung et al., 2004).

Epsilon-carbide has been demonstrated to precipitate at the same time as the austenite transforms to high-carbon martensite, during abrasion wear experiments on austempered ductile iron (Hung et al., 2002, 2004). The mechanism of precipitation and its consequence on wear is not understood, but it is possible that the carbide is formed when the martensite is locally heated by particle impact.

### 13.13.3 Erosion of Austempered Ductile Cast Iron

The mechanism of erosion due to particle impact depends both on the angle of impact and the mechanical properties of the substrate. Fig. 13.70 shows the wear rate of cast irons with a variety of microstructures, as function of the angle at which silica particles impact the surface (Chang et al., 2005, 2006b).

The mechanism of wear at low angles of incidence is essentially tearing. Softer microstructures are more amenable to tearing; this is why the ferritic matrix has the largest wear rate at the lowest angle.

At high angles of incidence, the silica particles cause the chipping of hard substrates and microscopic extrusions where the particles impact softer microstructures. This is why the wear rate at normal incidence decreases as the test-microstructure changes from martensite, lower bainite, upper bainite and ferrite. Indeed, a heat treatment leading to a microstructure containing more ferrite gives a better erosion resistance at normal incidence (Chang et al., 2006b).

The tearing mechanism of ductile erosion peaks at about 20-30°, whereas erosion is maximised at normal incidence when the substrate is extremely brittle. It is therefore not surprising that the impact angle associated with the peak erosion rate increases with hardness.

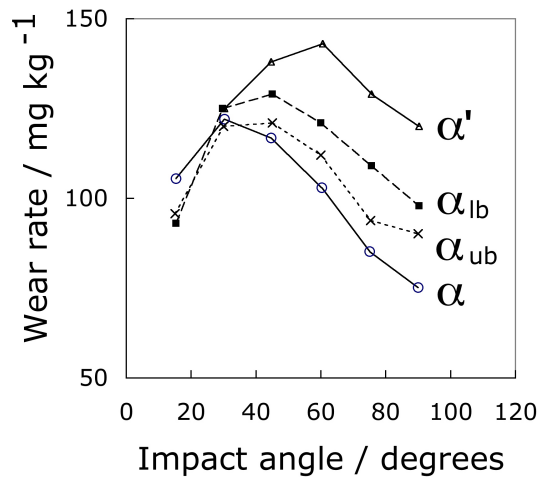


**Figure 13.70** Erosion by silica particles of cast irons with a variety of matrix microstructures (Chang et al., 2005). The hardnesses of  $\alpha$ ,  $\alpha_{ub}$ ,  $\alpha_{lb}$ , and  $\alpha'$  were 112, 298, 420 and 687 HV respectively.

#### 13.13.4 Wear of Mixed Microstructures

Mixtures of allotriomorphic ferrite, bainitic ferrite and retained austenite have been found to outperform fully bainitic or ferrite-pearlite mixtures in abrasive-wear tests (Xua et al., 2004). It is argued that the presence of soft allotriomorphic ferrite reduces exfoliation during abrasion, whereas the hard phase which forms when the austenite decomposes to high carbon martensite contributes to wear resistance. The strain rates involved in abrasive-wear can be very large; this can lead to a substantial increase in the yield strength (for example from 900 to 1200 MPa), and there is additional hardening from the transformation of austenite into martensite (Myszka et al., 2014).

#### 13.14 Bainitic Cast Steels

Cast steel does not contain graphite because the carbon concentration is limited to about 1 wt% while the other solutes have similar concentrations to those found in austempered ductile iron, Table 13.12. The aim is to take advantage of reduced chemical segregation and the absence of graphite to improve properties by generating the same microstructure as in ADI (Fu et al., 2007). The microstructure of the cast steel is similarly generated by isothermal transformation above the martensite-start temperature. The properties obtained following homogenisation at 1000 °C for two hours followed by air cooling, reheating to

900 °C for 2 h and then isothermal transformation for 1 h periods, at the variety of temperatures illustrated in Fig. 13.71.

Putatunda (2003), using an isothermally transformed cast steel of a different chemical composition (Table 13.12), found that the ultimate tensile strength never exceeded 740 MPa with poor elongations, generally less than 1%. However, the steel in its transformed state contained 70-90% of retained austenite with the rest of the structure being carbide-free bainitic ferrite. Such large quantities of retained austenite will reduce the strength and dramatically reduce the toughness since 50-100  $\mu\text{m}$  sized blocks of austenite could be observed in the microstructure. Such blocks are well established to be detrimental to mechanical properties (Bhadeshia and Edmonds, 1983a,b). It is possible that much better properties might be obtained by isothermal transformation for much greater periods than the 6 h used in the original study, in order to permit more of the austenite to decompose into bainitic ferrite, as long as its overall carbon concentration remains below the  $T_0$  limit.

The role of alloying elements is not as well understood when it comes to cast as opposed to wrought carbide-free bainitic steels. Many of the cast steels are adaptations of ADI with reduced carbon concentration in order to eliminate the graphite so it is not clear whether the relatively large silicon concentrations typical of cast iron are needed (Li and Chen, 2001). In cast irons, a key role of the silicon is to encourage graphite formation instead of cementite; since this is not needed in the cast steels, the concentration could easily be reduced to 1.5%, roughly the quantity necessary to prevent the precipitation of cementite from the austenite during the bainite transformation. Chapter 14 deals with wrought steel containing the 1.5wt% Si, containing 1 wt% carbon, concentrations similar to the cast varieties listed in Table 13.12.

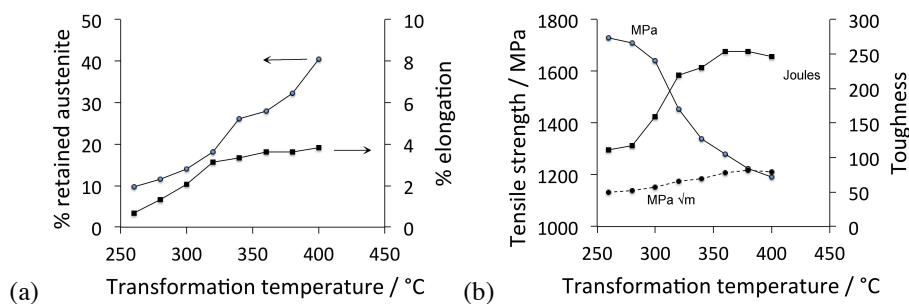


**Figure 13.71** Properties of isothermally transformed cast steel. (a) Retained austenite content and tensile elongation. (b) Strength and toughness, measured at ambient temperature.

In a different approach, the overall carbon concentration was maintained at 1 wt% but the cast steel was allowed to contain about 2.5 volume percent of graphite, thereby reducing the carbon concentration in the austenite. As a consequence, the amount of retained austenite in the structure was reduced, but as seen from Fig. 13.72, the mechanical properties obtained following transformation of the matrix into bainite were not impressive. In general, the elongation of cast steels is really quite poor, Fig. 13.72, which may explain why some publications (Chen and Li, 2006, 2007) do not bother report the ductility of cast carbide-free bainitic steels.

Cast steels of the type described here do not seem to have undergone systematic alloy design and are ripe for a reassessment in the light of what is now known about the mechanism of the bainite transformation, and of quantitative structure-property relationships.

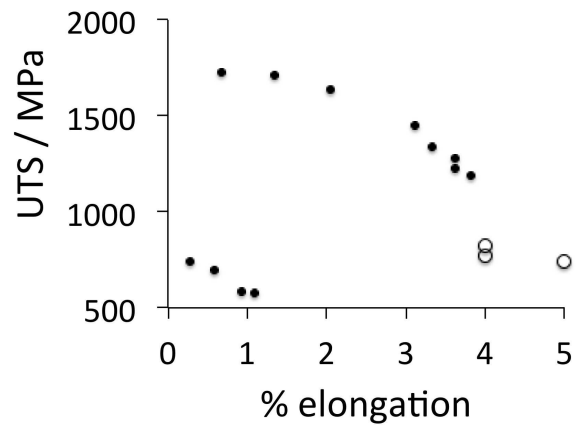


**Figure 13.72** The ultimate tensile strength versus elongation of cast carbide-free bainitic steels. Data from Fu et al. (2007); Putatunda (2003). The open circles represent alloys that are steels but contain some spheroidal graphite (Takahashi et al., 1996).



## CHAPTER 14

---

# NANOSTRUCTURED BAINITE

---

### 14.1 Introduction

One of the biggest successes of the 20th century was the invention of thermomechanical processing that led to the manufacture and application of many billions of tonnes of reliable steel.<sup>1</sup> The key principle in their success is the refined grain size resulting from microalloying; a fine grain size in general enhances both strength and toughness. Steels with a grain size of 10  $\mu\text{m}$  are now routine.

It is not surprising therefore, that when the adjective “nano” became popular in science, vast resources were dissipated in creating nanostructured steels using severe plastic deformation or rapid processing as the mechanisms of refinement. The methods involve such large deviations from normality that they are not commercially viable. The purpose of this chapter is to describe an alternative approach based on bainite, that achieves the required nanostructure but can be produced in large quantities and dimensions at an affordable price, i.e. a first bulk nanostructured metal. Some aspects of the nano-structured bainite are presented in context rather than here: tempering is discussed in Chapter 4, influence of magnetic fields in Chapter 15, stress effects in Chapter 8.

<sup>1</sup>This discovery of the microalloying concept in Sheffield is in my opinion worthy of a Nobel prize given the beauty of the science involved and its tremendous impact on the quality of life.

## 14.2 Nanostructure

It is unfortunate that the term *nanostructure* has become a generic reference to a wide range of grain and precipitate structures, to fancy music devices and even cars. For the present purposes, a nanostructure represents cases where the interfacial area per unit volume,  $S_V$ , is large enough to make the governing length scale  $\bar{L} = 2/S_V$  comparable to the smaller dimensions of carbon nanotubes, i.e. of the order 20–50 nm. There is logic behind this definition, as illustrated by the data in Table 14.1. Thus, a coarse-grained structure containing nanoparticles, or a structure referred to as nanobainite but which has a scale closer to micrometres does not have a large  $S_V$  and hence is not strong. Figure 14.1 shows that the amount of surface per unit volume only becomes sensitive to the grain size when the latter is below about 50 nm.

**Table 14.1** The surface per unit volume for a variety of steel-based structures. Symbols  $t_p$ ,  $r$ ,  $N_V$  refer to the true plate thickness, precipitate radius and number density per unit volume, respectively. The strength values ( $\sigma$ ) quoted are for ambient temperature and are approximate, often estimated from hardness or microhardness. Data from Goa et al. (2007) are excluded because the bainite ‘shear units’ are claimed to be 1.6 nm in thickness, inconsistent with the low strength ( $\sigma_y \approx 1160$ –1250 MPa) of the low-carbon alloys studied.

Structure		Parameters	$S_V / \text{nm}^{-1}$	$\sigma / \text{MPa}$
Nanostructured bainite	Garcia-Mateo et al. (2003b)	$t_p = 20 - 40 \text{ nm}$	$2t_p^{-1} = 0.10 - 0.05$	> 2100
Mechanical milling	Kimura et al. (1999)	$\bar{L} = 20 \text{ nm}$	$2\bar{L}^{-1} = 0.1$	2850
“Nanobainite”	Timokhina et al. (2011a)	$\bar{L} = 200 - 400 \text{ nm}$	$2\bar{L}^{-1} = 0.005 - 0.01$	< 960 MPa
Nanoparticle strengthened	Isheim et al. (2006)	$N_V = 1.1 \times 10^{24} \text{ m}^{-3}$ $r = 1.25 \text{ nm}$	$4\pi r^2 N_V = 0.011$	800
Accumulative roll bonding	Tsuji et al. (1999b)	$\bar{L} = 420 \text{ nm}$	$2\bar{L}^{-1} = 0.005$	870
Severe plastic deformation	Valiev et al. (1996)	$\bar{L} = 100 \text{ nm}$	$2\bar{L}^{-1} = 0.02$	1570
Angular processing	Wang et al. (2004a)	$\bar{L} = 200 \text{ nm}$	$2\bar{L}^{-1} = 0.01$	1150

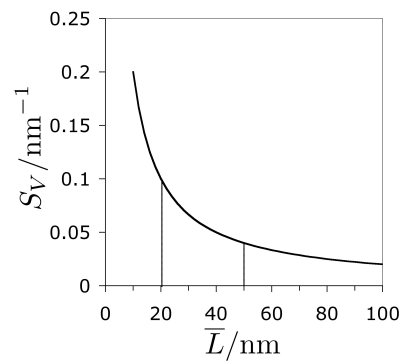


**Figure 14.1** Grain surface per unit volume as a function of the mean linear intercept, a measure of the grain size.

The desire for such materials in the engineering context comes from the expectation of novel mechanical properties, particularly the stress that can be tolerated safely in service. It is difficult to invent such materials because any design must address three basic issues:

- (i) it should ideally be possible to make samples that are large in all dimensions, not simply wires or thin sheets;

- (ii) there are commercially available steels in which the distance between interfaces is of the order of 250-100 nm. The novelty is in approaching a structural scale in polycrystalline metals that is an order of magnitude smaller.
- (iii) The material concerned must be cheap to produce if it is not to be limited to niche applications. A good standard for an affordable material is that its cost must be similar to that of bottled water when considering weight or volume.

These are formidable challenges and the process of design can begin with a consideration of how strength can be achieved. The long-range periodicity that is assumed to typify the crystalline state is in practice punctuated by defects, some of which make a significant contribution to configurational entropy and hence can exist in thermodynamic equilibrium. This kind of entropy scales with the number of entities (atoms) in the crystal and hence it is only possible to approximate perfection in small crystals (Gorsuch, 1959). Such crystals can be strong because in the absence of defects, deformation must occur by the wholesale glide of planes over each other, rather than by the propagation of discontinuities such as dislocations. Micrometre sized crystals of pure iron have achieved strength in excess of 10 GPa (Sears et al., 1954; Brenner, 1956) although in principle the strength can exceed 20 GPa (Clatterbuck et al., 2002). The crystals become weaker as they are made larger, both because of the thermodynamically stabilised defects and also accidents of growth. This is fundamentally why the impressive mechanical properties of carbon *nanotubes* are not maintained, and indeed, should not be expected to be maintained, when the tubes become long (Bhadeshia, 2005b; Ruoff, 2006; Pugno, 2007a,b).

An alternative method for manufacturing sizeable strong materials is to introduce large numbers of defects such as interfaces or dislocations which interfere with the ordinary mechanisms of slip or twinning. The defects can be introduced by deformation. Techniques which involve severe plastic deformation are limited in the shape of the final product and in the quantity that can be produced at reasonable cost. Examples include fine nanostructured-wire with a strength in excess of 5 GPa (Bhadeshia and Harada, 1993); metals subjected to equal-channel angular extrusion in which redundant work is used in order to achieve large plastic strains whilst maintaining the external shape of the object being deformed (Segal, 1999; Horita et al., 2000; Segal, 2002). Accumulative roll-bonding involves the repeated rolling and folding of sheet material in order to accomplish strain increments without thinning the sample entering the rolls; the process is suited for large scale production but does not lead to particularly fine grains, which tend to be closer to micrometres than nanometres in size (Saito et al., 1998).

Thermomechanical processing (Speich et al., 1984) is particularly suited to the large scale production of fine-grained steels by phase transformation from the deformed parent austenite. However, the minimum ferrite grain size achieved in practice is about 1  $\mu\text{m}$ , partly because the speed of production and the thickness of the steel processed leads to recalescence during transformation, thus preventing the achievement of the large undercoolings needed to refine the grain size (Yokota et al., 2004).

There are further difficulties. The ductility decreases sharply as the grain size in a polycrystalline metal is reduced (Howe, 2000, 2009). Secondly, there is often a requirement for rapid heat treatment which becomes impractical for large components.

A recent development seems to avoid all of these problems. A nanostructure has been achieved in large lumps of steel by phase transformation, with the design of the steel based on an understanding of the atomic mechanisms of crystal growth in the solid state (Caballero et al., 2001a,b, 2002; Garcia-Mateo et al., 2003b; Caballero and Bhadeshia, 2004).

### 14.3 Alloy Design

Strong steels can be produced by martensitic transformation but this requires rapid cooling unless use is made of sufficient quantities of costly alloying elements. The bainite reaction has a comparatively greater capacity for control; its structure can be generated by isothermal or continuous cooling transformation.

There are now a handful of aspects of the bainite reaction that can benefit from quantitative treatment (Bhadeshia, 1999a), but the progress on the mechanism of the transformation has now made it possible to design useful steels. Bainite as a phase mixture has been known since the 1930s, but the scale of the structure in ordinary steels is in the micrometre range. The structure can be refined by reducing the transformation temperature, as demonstrated elegantly by Papadimitriou and Fourlaris (1997) who created a bimodal size-distribution of plates by partially transforming the same sample at two different temperatures. It is of interest, therefore, to investigate the lowest temperature at which bainite can form whilst avoiding martensitic transformation.

The highest temperature at which bainite can form in a steel of given composition is the bainite-start temperature; the martensite-start temperature is similarly defined. The details are discussed in Chapter 6, but can be summarised as follows. The chemical free energy change accompanying the diffusionless growth of either bainite or martensite is  $\Delta G^{\gamma \rightarrow \alpha} = G^\alpha - G^\gamma$ . The energy stored inside the steel, for example in the form of elastic strains, must be accounted for; in the case of bainite this amounts to  $G_{SB} \simeq 400 \text{ J mol}^{-1}$ .

The nucleation stage of bainite involves the partitioning of carbon so the chemical free energy change ( $\Delta G_m$ ) more negative; a detectable rate of nucleation is observed when  $\Delta G_m$  becomes less than that given by a function  $G_N$ .  $B_S$  is defined when both the nucleation and growth conditions are satisfied simultaneously (equation 6.4):

$$\underbrace{\Delta G_m < G_N}_{\text{nucleation condition}} \quad \text{and} \quad \underbrace{\Delta G^{\gamma \rightarrow \alpha} < -G_{SB}}_{\text{growth condition}} \quad (14.1)$$

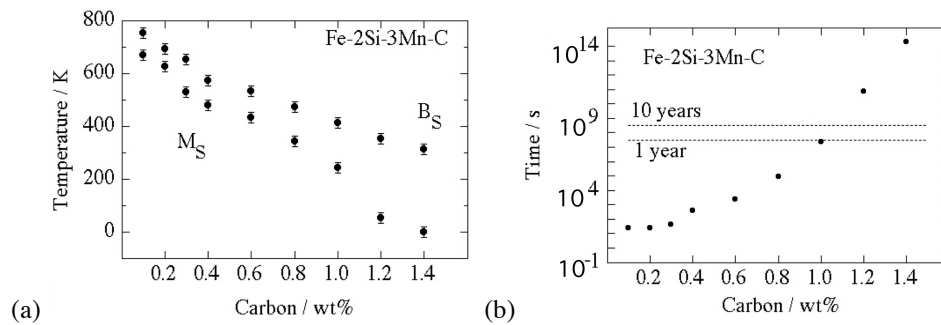


**Figure 14.2** (a) Calculated transformation start temperatures in Fe-2Si-3Mn wt% steel as a function of the carbon concentration. (b) The calculated time required to initiate bainite (Bhadeshia, 1982d).

Martensitic transformation occurs when  $\Delta G^{\gamma \rightarrow \alpha}$  becomes less than a critical value  $\Delta G^{\gamma \rightarrow \alpha} \{M_S\}$  given by the function  $G_N^{\alpha'}$ :

$$\Delta G^{\gamma \rightarrow \alpha} < G_N^{\alpha'} \quad (14.2)$$

Whereas it is reasonable to set  $G_N^{\alpha'}$  to an approximately constant value for low-alloy steels (Kaufman and Cohen, 1958; Imai et al., 1965; Bhadeshia, 1981b,d) a function dependent on the strength of the austenite has to be used for alloys containing large concentrations of solute (Ghosh and Olson, 2001).

Suppose we now use this theory to estimate the lowest temperature at which bainite can form. Such calculations are illustrated in Fig. 14.2a, which shows for an example steel, how the  $B_S$  and  $M_S$  temperatures vary as a function of the carbon concentration. There appears to be no lower limit to the temperature at which bainite can be generated. On the other hand, the rate at which bainite forms slows down dramatically as the transformation temperature is reduced, Fig. 14.2b. It may take hundreds or thousands of years to generate bainite at room temperature. For practical purposes, a transformation time of tens of days is reasonable, corresponding to a carbon concentration of about 1 wt%, in which case bainite can be generated at a temperature as low as 125°C, which is so low that the diffusion distance of an iron atom is an inconceivable  $10^{-17}$  m over the time scale of the experiment!

A steel designed on this basis has been manufactured and characterised (Caballero et al., 2002; Garcia-Mateo et al., 2003c,b); Fig. 14.3a shows the structure obtained following isothermal transformation at 200°C, consisting of platelets of bainitic ferrite with a true thickness in the range 20–40 nm, in an intervening matrix of austenite. This *retained* austenite is important because when it undergoes deformation-induced martensitic transformation, it enhances the work-hardening capacity of the material, thereby avoiding the usual problem of fine-grained metals where ductility diminishes as the grain size is reduced because the material loses the ability to work harden (Howe, 2000). Fig. 14.3b shows that the rate of transformation is sufficiently slow to ensure that very large samples transform uniformly into the nanostructure, commercial examples of which are illustrated in Fig. 14.4. Since the original work, many variations of the alloy have been studied and characterised (listed at the end of this chapter). Some of the elementary properties are discussed next.

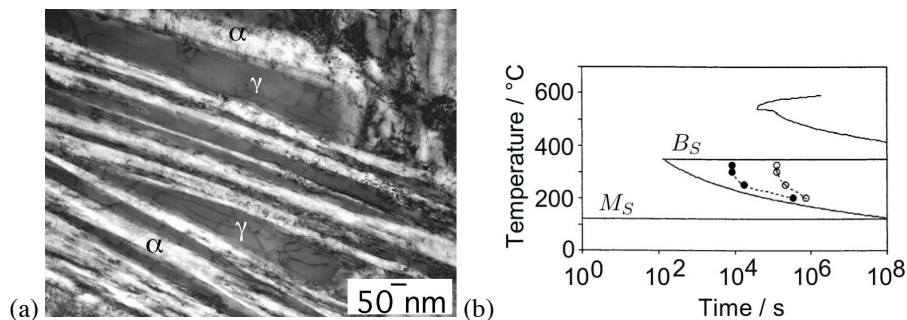


**Figure 14.3** Fe-0.98C-1.46Si-1.89Mn-0.26Mo-1.26Cr-0.09V wt%, transformed at 200°C for 15 days. (a) Structure, after Caballero et al. (2002); Garcia-Mateo et al. (2003c,b). (b) Comparison of calculated and measured transformation kinetics; the filled points and curves represent the detectable start of the reaction, and the open circles the stage where the reaction rate is negligible (Garcia-Mateo et al., 2003b).

The bainite obtained by low-temperature transformation is the hardest ever achieved, with values in excess of 700 HV. Some strength, ductility and toughness data are illustrated in Fig. 14.5. The simple heat treatment involves the austenitisation of a chunk of steel (at say 950°C), followed by a gentle transfer into an oven at the low temperature (say 200°C) to be held there for ten days or so. There is no rapid cooling – residual stresses associated

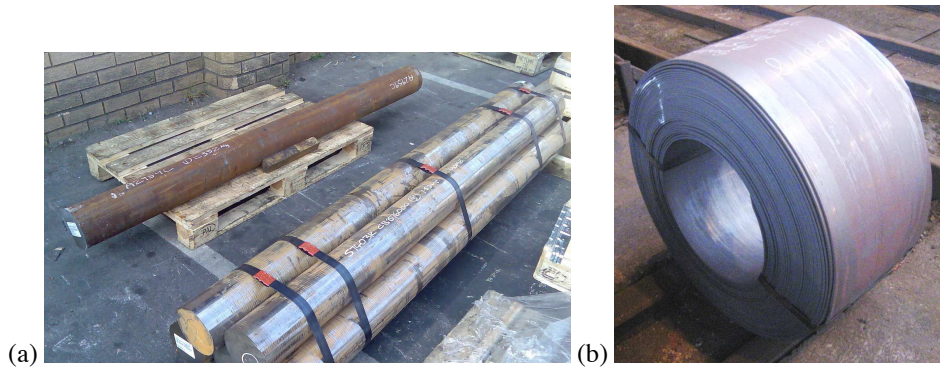


**Figure 14.4** Large-scale manufacture of nanostructured steel: (a) shafts, (b) plates. Photographs courtesy of Rolls Royce plc and Tata Steel, respectively.

with heat treatment are avoided. The size of the sample can be large because the time taken to reach 200°C from the austenitisation temperature is much less than that required to initiate bainite. This is an important commercial advantage.

The influence of tempering on the toughness is illustrated with the data in Table 14.2. The austenite can be assumed to have decomposed into a mixture of ferrite and cementite following tempering at 600 °C. The toughness therefore decreases significantly in spite of the softening associated with the tempering. More detailed discussion of properties will follow after a discussion of the mechanism of transformation.

**Table 14.2** Toughness data. The data marked with asterisks are  $K_Q$  values and hence not strictly valid (Hamdany et al., 2012). The chemical composition is listed in Table 14.6.

Condition	$K_Q$ or $K_{IC}$ / MPa m <sup>0.5</sup>	Hardness / HV10
Untempered sample	31*	645
Tempered 300°C for 6 h	27*	642
Tempered 300°C for 1 month	23*	652
Tempered 400°C for 8 h	23	612
Tempered 450°C for 6 h	20*	626
Tempered 500°C for 6 h	22*	556
Tempered 600°C for 6 h	14*	377

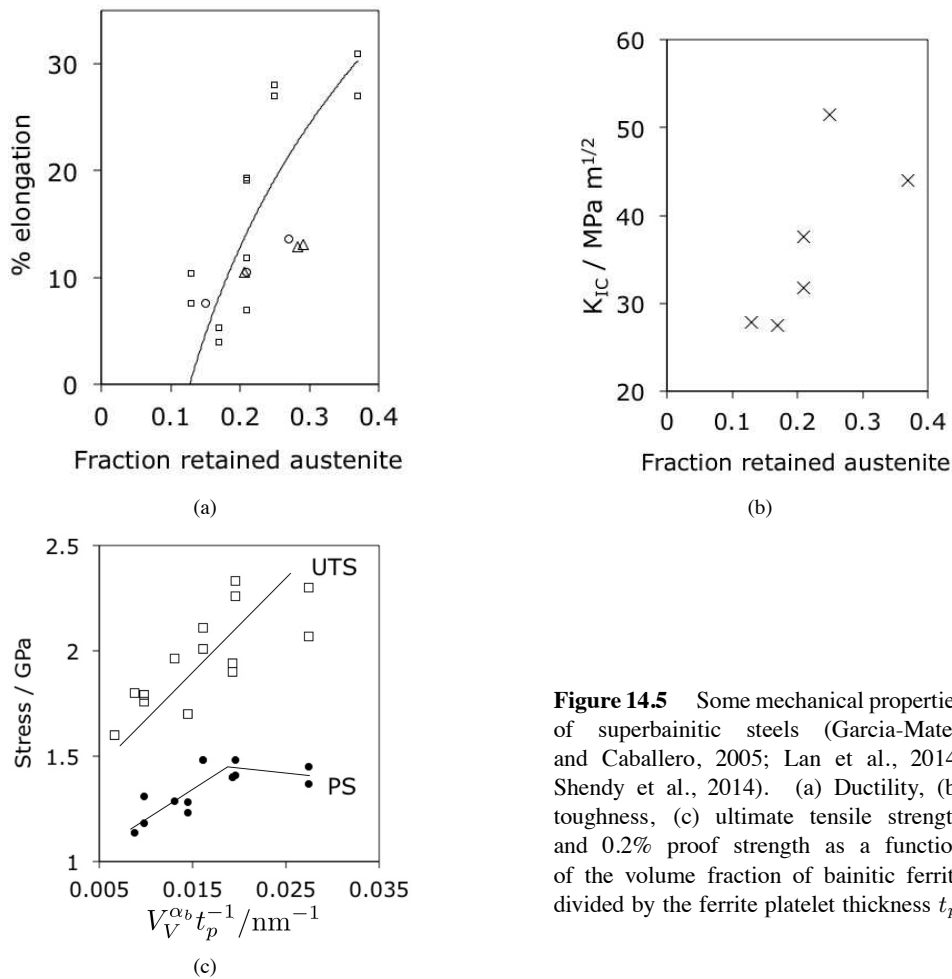


**Figure 14.5** Some mechanical properties of superbainitic steels (Garcia-Mateo and Caballero, 2005; Lan et al., 2014; Shendy et al., 2014). (a) Ductility, (b) toughness, (c) ultimate tensile strength and 0.2% proof strength as a function of the volume fraction of bainitic ferrite divided by the ferrite platelet thickness  $t_p$ .

#### 14.4 Crystallography and Surface Relief

The orientation relationship between the bainitic ferrite and austenite is found to be irrational, with the closely packed planes  $(111)_\gamma$   $0.7 \pm 0.5^\circ$  from  $(101)_\alpha$  and the corresponding close-packed directions  $[\bar{1}01]_\gamma$   $2.5 \pm 1.5^\circ$  from  $[\bar{1}11]_\alpha$  (Zhang and Kelly, 2006).<sup>2</sup> Furthermore, the response of the structure as it evolves, to externally applied stress and plastic strain (Kundu et al., 2007; Shirzadi et al., 2009), is found to be predictable using the crystallographic theory of displacive transformations. The number of crystallographic variants of bainite that form in any given austenite grain increases as the transformation temperature is reduced (Beladi et al., 2009).

<sup>2</sup>Zhang and Kelly (2006) have used terms such as ‘meta upper’ and ‘meta lower’ bainite, but this is unnecessary because the nanostructure they observed is simply a two-phase mixture of bainitic ferrite and carbon-enriched retained austenite.

The displacements caused by the formation of nanostructured bainite have been characterised using atomic force microscopy, Fig. 14.6. The deformation is an invariant-plane strain with an obviously large shear component. The measurements are conducted at the surface so the orientation of the underlying plate is not known. As a consequence, the measured value is an apparent shear  $s_A$ , and the largest value determined is likely to be close to the true shear  $s$ . The latter is therefore estimated to be  $s = 0.46$ , which is much larger than observed for ordinary bainite (section 2.5.2). The large shear is consistent with the slender character of the bainitic ferrite plates that form at low homologous temperatures, and is not unprecedented in the context of solid-state phase transformations in steels Watson and McDougall (1973). It may be that different modes of lattice invariant deformation operate when the transformation occurs in the austenite that is strengthened by the large carbon concentration, and the lower temperature at which transformation was induced.

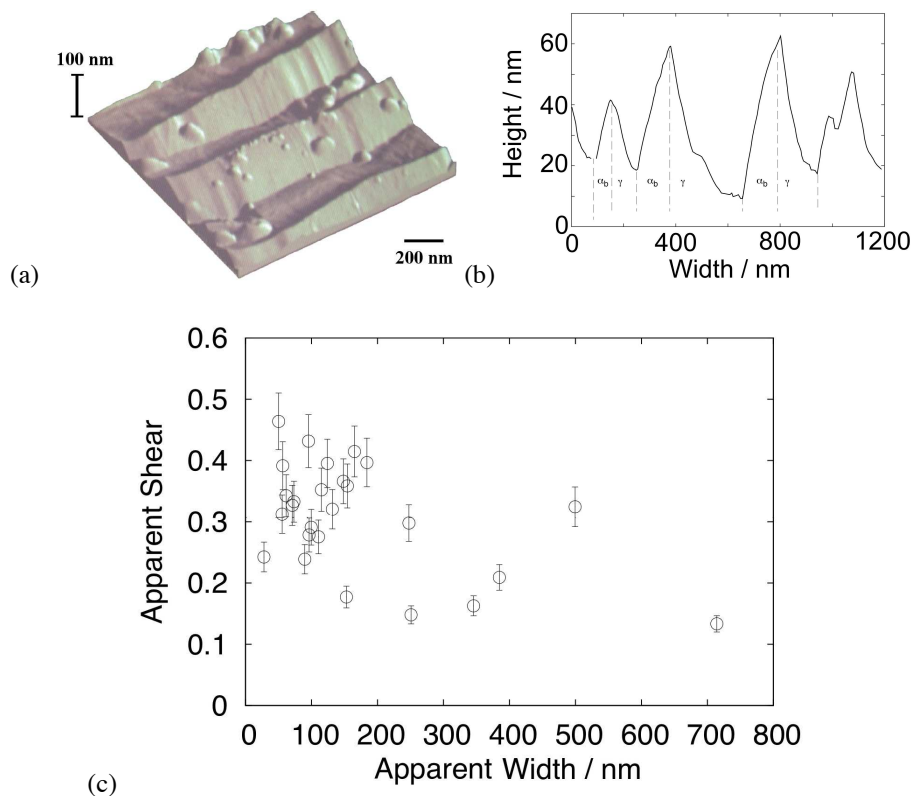


**Figure 14.6** Surface relief due to nanostructured bainite. (a) Atomic force microscope image of relief over an area  $1.4 \mu\text{m} \times 1.4 \mu\text{m}$ . (b) Line scan across surface relief. (c) Summary of measured values of apparent shear  $s_A$ , plotted against width of feature (Peet and Bhadeshia, 2011).

## 14.5 Distribution of Solutes

As expected from a displacive transformation mechanism in which the change in crystal structure is achieved by a deformation, substitutional atoms are configurationally frozen, confirmed using atom-probe analysis (Peet et al., 2004; Caballero et al., 2007), Fig. 14.7.

The carbon concentration in the retained austenite can be as high as 5-7 at%, depending on the transformation conditions (Bruna et al., 2005). Experiments have demonstrated that the carbon concentration in the austenite becomes heterogeneously distributed once it begins to transform into bainitic ferrite because a greater quantity of carbon is trapped in the films of retained austenite enclosed by platelets of bainitic ferrite, than within the larger blocks that persist between different crystallographic variants of bainite (Stone et al., 2008). As a result, two separable peaks are observed associated with each austenite reflection in synchrotron X-ray diffraction experiments as transformation evolves (Fig. 14.8). Similar observations have previously been reported on ordinary bainitic steels, Chapter 3.

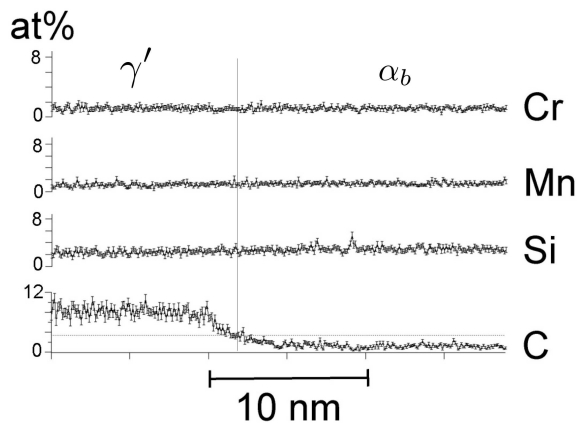


**Figure 14.7** Composition as a function of distance across a  $\gamma'/\alpha_b$  interface. After Peet et al. (2004).

In addition to the heterogeneous composition of the austenite in the partially transformed nanostructure, there are other scales of non-uniformity that are attributable to the partitioning process and the existence of defects.

The dislocations in the nanostructured bainitic ferrite accumulate Cottrell atmospheres of carbon atoms, with the average concentration in a region some 5 nm around the defect reaching about 7.4 at% (Caballero et al., 2007), consistent with saturation (Cocharadt et al., 1955). This is illustrated in Fig. 14.9, showing the extent of the carbon atom atmosphere. Such segregation is of course, expected to occur but its significance is that the carbon that is in the Cottrell atmospheres does not partition into the austenite. Similar segregation to defects occurs in the retained austenite, for example at twin boundaries (Caballero et al., 2007).

Although nanostructured bainite is overwhelmingly a two-phase  $\alpha_b + \gamma'$  mixture, high resolution observations have occasionally revealed minute particles of cementite about 10 nm in size, that grow by a paraequilibrium mechanism, i.e. without the partitioning of substitutional solutes.<sup>3</sup> It is the segregation of carbon to dislocations that causes the direct precipitation of these particles of cementite instead of  $\varepsilon$ -carbide, because the atoms are more stable at dislocations than in that transition carbide (Kalish and Cohen, 1970).

<sup>3</sup>Similar observations of non-stoichiometric, minute particles of cementite or other iron carbides have been reported in atom-probe observations of low-strength bainite in high-silicon steels (Timokhina et al., 2010a). Again, the fraction of carbides is negligible, given the measured large concentration of carbon in the austenite.

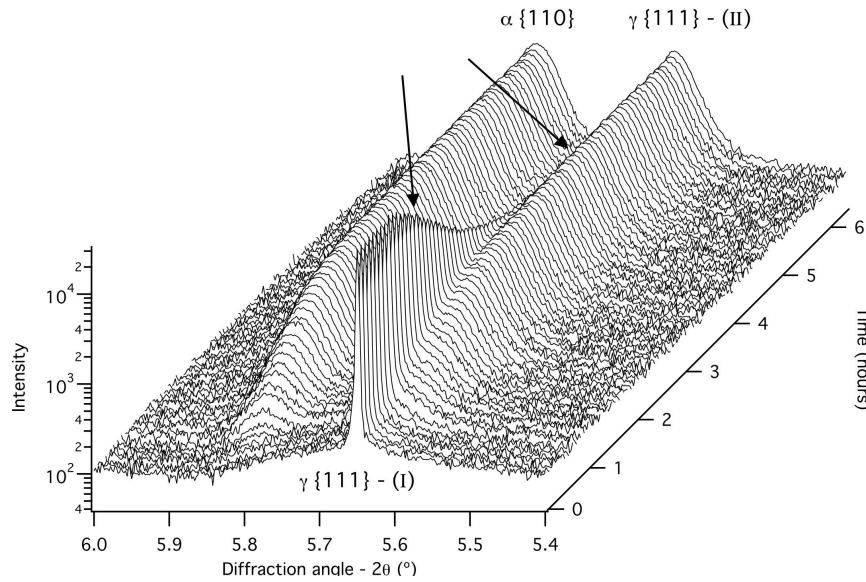


**Figure 14.8** Austenite {111} and ferrite {110} peaks during isothermal heat-treatment at 300°C following austenitisation and transformation into fine bainite. The two arrows show how the initial austenite {111} decreases in intensity whilst at the same time the austenite {111} corresponding to the higher carbon concentration increases in intensity. After Stone et al. (2008).

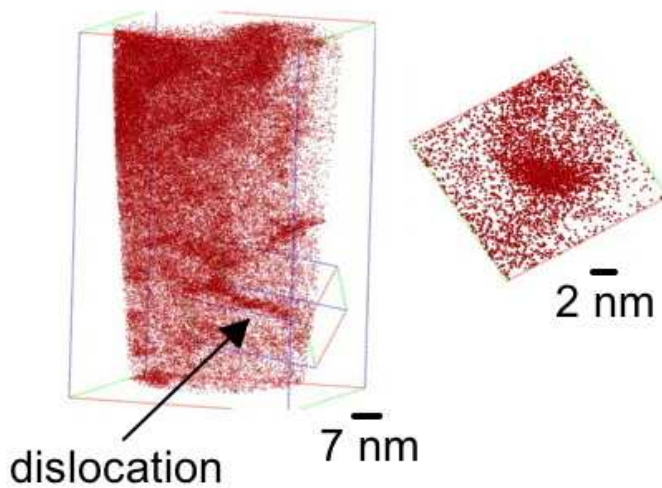


**Figure 14.9** Carbon atom map, showing the 5 at% isoconcentration surface of dislocations in  $\alpha_b$ , together with the map of the cross-section normal to the dislocation line to show the extent of the Cottrell atmosphere. The alloy is Fe-0.98C-1.46Si-1.89Mn-0.26Mo-1.26Cr-0.09V wt%. Reproduced and adapted from Caballero et al. (2007) with permission from Elsevier.

## 14.6 Origin of Elementary Mechanical Properties

Much of the strength and hardness of the structure comes from the incredibly thin dimensions of the bainitic plates. For a true thickness  $t_p$ , the mean linear intercept  $\bar{L} \simeq 2t_p$  (Mack, 1956; Bhadeshia, 1997a); the resulting strengthening is  $\Delta\sigma = 115(\bar{L})^{-1}$  MPa where  $\bar{L}$  is in micrometres. With  $\bar{L} = 35$  nm,  $\Delta\sigma = 1642$  MPa, which decreases to 311 MPa for  $\bar{L} = 185$  nm. Fig. 14.5c illustrates the strength plotted as a function of the volume fraction of bainitic ferrite and  $t_p^{-1}$ . The inverse dependence of hardness on plate thickness is also evident in Fig. 14.10.

The residue of strength after accounting for the plate thickness comes from dislocation forests, the intrinsic strength of the iron lattice and solution strengthening. It has long been known, using atom-probe field-ion microscopy, that bainitic ferrite contains much more carbon than is consistent with equilibrium or paraequilibrium (Chapter 2). Some of this excess carbon is trapped at the dislocations created during the growth of the bainite. The strengthening contributions of the carbon and dislocations cannot therefore be independently calculated, but are small in comparison with that due to plate size. This is why the hardness of the nanostructure is insensitive to tempering, until the onset of plate coarsening at temperatures in excess of 500°C (Garcia-Mateo et al., 2004). A corollary to the effect of excess carbon is that unlike high-temperature bainite (Furnemont et al., 2002), the nanohardness of the thin bainite platelets in the nanostructured steel exceeds that of retained austenite (Lan et al., 2011). The probable explanation for this inversion of hardness is first the fine scale of the plates and second the excess carbon that they contain, when compared against bainite generated at higher temperatures.

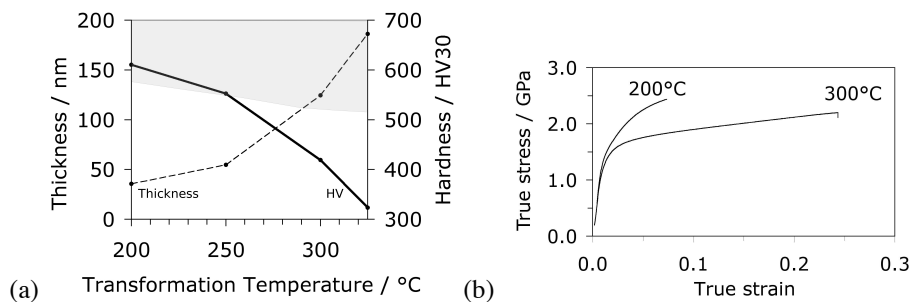


**Figure 14.10** (a) Properties of alloy of composition listed in Fig. 14.3. The axis on the left is the stereologically corrected thickness of the bainitic ferrite plates. The shaded region represents the fraction of austenite as a function of temperature, given by the fraction of the height of the diagram, the rest of the microstructure being bainitic ferrite. (b) Fe-0.79C-1.56Si-1.98Mn-0.24Mo-1.01Cr-1.51Co-1.01Al wt%. True stress-strain curves for bainite generated by transformation at 200°C and 300°C. Data from Garcia-Mateo and Caballero (2005).

Fig. 14.10b shows typical true-stress versus true-strain curves; the gradual yielding is characteristic of composite structures containing a large density of dislocations and the transformation of some austenite during the application of stress. It is intriguing that the elongation increases as the nanostructure is generated at the higher temperature. This is in fact a general observation, perhaps due to the weaker structures obtained after transforming at higher temperatures. However, in this instance, the correlation of ductility with strength is not statistically sensible because there are similar low-carbon, low-strength steels which

do not show the high ductility illustrated in Fig. 14.10b.<sup>4</sup> The explanation seems to lie in the deformation-induced martensitic transformation of the retained austenite during tensile testing. The decomposition of the austenite in this manner has been calculated and measured for a variety of combinations of bainitic ferrite and austenite (Sherif et al., 2004). Fig. 14.11 shows the expected variation in the austenite content  $V_V^\gamma$  with strain for three cases (Bhadeshia, 2008) with the points identifying the failure strain. It is noticeable that fracture occurs when  $V_V^\gamma \simeq 0.1$ . An experimental *in situ* study using neutron diffraction during the tensile test by Sherif (2005) concurs with this conclusion.

It has been suggested that failure occurs when the austenite, which is the toughest of all the phases present, becomes geometrically isolated, i.e. it loses percolation (Bhadeshia, 2008). Garboczi et al. (1995) have modelled the percolation threshold for ellipsoidal objects placed in a matrix. Assuming that the austenite is subdivided by ellipsoidal plates of bainite with an aspect ratio of between about 1/10 and 1/100, the percolation threshold becomes  $p_c \simeq 1.27r$ , i.e.  $0.127 \geq p_c \geq 0.0127$ . This is consistent with the observation that tensile failure occurs when  $V_V^\gamma \simeq 0.1$ . Indeed, this concept has been used in the design of a steel, on the basis of computed TTT diagrams, the  $T_0$  concept and the percolation threshold to obtain the required level of ductility as illustrated in Fig. 14.12.

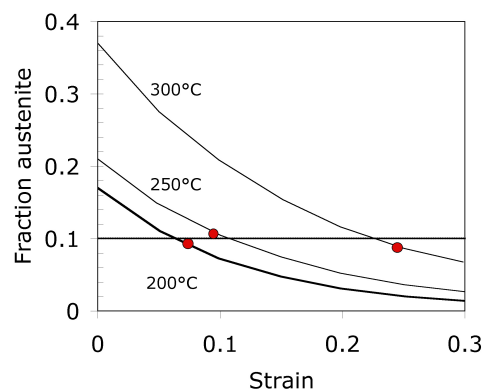


**Figure 14.11** Calculated variation in the fraction of austenite as a function of plastic strain in three nanostructured bainitic samples containing different initial quantities of retained austenite. The isothermal transformation temperatures used to generate the initial structures are annotated. The dots indicate the strain at which the samples break, when the fraction of austenite decreases to a level below the percolation threshold of about 0.1. Data adapted from Garcia-Mateo and Caballero (2005).

Fig. 14.11 indicates that substantial quantities of brittle martensite which forms during deformation can exist in the microstructure before failure occurs. This is because the tendency of the martensite to crack under stress depends on its absolute size, with coarse regions being most susceptible (Chatterjee and Bhadeshia, 2006). It is the fine scale of the retained austenite that permits the deformation-induced martensite to be tolerated without compromising the ductility until the percolation threshold is reached.<sup>5</sup> Fig. 14.5 also il-

<sup>4</sup>(Parker, 1977; Caballero et al., 2001a,b; Putatunda et al., 2009; Wang et al., 2009a,b).

<sup>5</sup>The caveat to this statement is that the toughness may be compromised even when the ductility is enhanced by the fact that the TRIP effect delays plastic instabilities. This is because the fracture toughness at crack initiation can be reduced by the formation of brittle martensite (Jacques et al., 2001a).

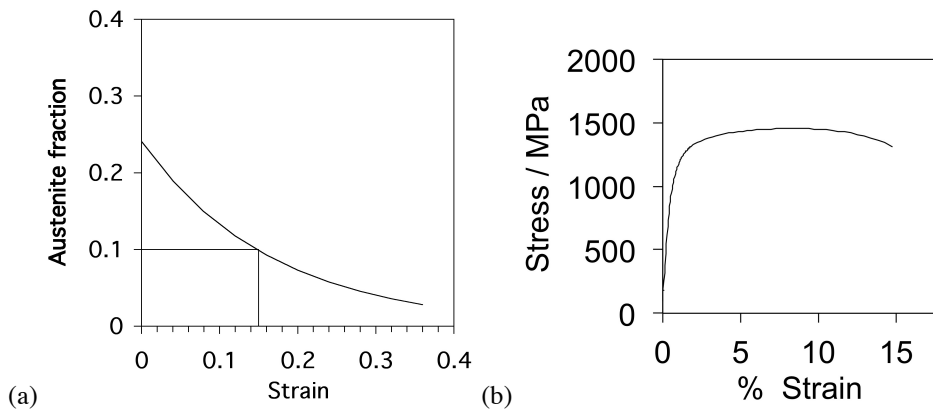


**Figure 14.12** Fe-0.39C-1.47Si-0.54Al-0.24Mo-1.20Mn-0.95Cr-0.91Ni-0.1V-1.04Co-0.99W wt% alloy. (a) Calculated reduction in the retained austenite content as a function of plastic strain. (b) The engineering stress-strain curve for the designed steel, showing a ductility consistent with that defined by the percolation threshold in (a). After Khare et al. (2010).

illustrates that elongation tends towards zero as the volume fraction of austenite tends to 0.1.<sup>6</sup>

Cryogenic cooling has been used to reduce the amount of retained austenite in the nanostructured bainitic steel, on the basis that the refinement of any blocky regions of martensite should lead to an improvement in toughness (Hu et al., 2014b). The resulting change in mechanical properties has yet to be established, but the thermally-induced martensitic regions could have the opposite effect if they act as hard inclusions.

#### 14.6.1 Evolution of Hardness

There are some interesting trends in hardness revealed when isothermal transformation to bainite is interrupted periodically by quenching to ambient temperature. Some martensitic transformation may occur during quenching, especially if the residual austenite is insufficiently stabilised by the extent of transformation. It is not surprising therefore, that there is a monotonic decrease in hardness as progressively more bainite is allowed to form before quenching, Fig. 14.13a. However, the plates of bainite that form on transformation at 200 °C are extremely fine, so the initial softening gives way to substantial hardening (Fig. 14.13b) because much of the strength of nanostructured bainite has its origins in the fine scale of the plates of bainite. The ultimate hardness reaches values comparable to the directly quenched mixture of martensite and retained austenite. This phenomenon has been called *isothermal hardening* (Brown and Baxter, 2004) in analogy with secondary hardening in quenched and tempered martensitic steels.

#### 14.6.2 Compression Tests

The strength in compression is not a particularly important parameter in alloy design because both engineering strength and engineering ductility usually exceed those found in

<sup>6</sup>A discontinuous change in elongation to much lower values as the austenite content decreases below the percolation threshold has been reported for lower strength bainitic steels (Caballero et al., 2008a).

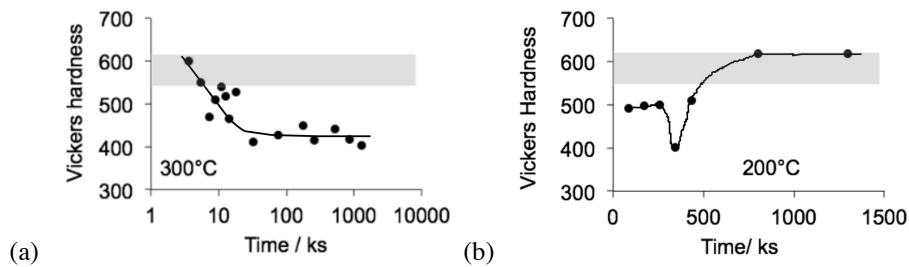


**Figure 14.13** Fe-0.98C-1.46Si-1.89Mn-0.26Mo-1.26Cr-0.09V wt%. Vickers hardness as a function of the isothermal transformation temperature and time. The shaded bands represent the hardness of a mixture of martensite and austenite obtained by water quenching from a fully austenitic state. (a) Transformation at 300 °C. (b) Transformation at 200 °C. After Garcia-Mateo et al. (2003b).

tensile tests. All the results described here are for the purposes of alloy development when sufficient material may not be available for tensile testing. Fig. 14.14 shows a stress-strain curve from the original nanostructured bainite (Caballero et al., 2002). If the initial part of the curve is neglected as the specimen-machine assembly configures itself into intimate contact, the 0.2% proof strength is about 1960 MPa. However, after substantial plastic deformation, the specimen bent so that the deformation became a combination of compression and shear, leading eventually to the cracks illustrated.

Soliman and Palkowski (2007) conducted more controlled compression tests so that much larger ductilities and strengths were achieved in a relatively low carbon nanostructured bainite resulting from isothermal transformation at 210 °C (Table 14.6). The sample yielded at 1.6 GPa, with an ultimate compression strength of 2.85 GPa and a fracture strain of some 45%. The fracture occurred with the onset of bulging that led to circumferential cracks.

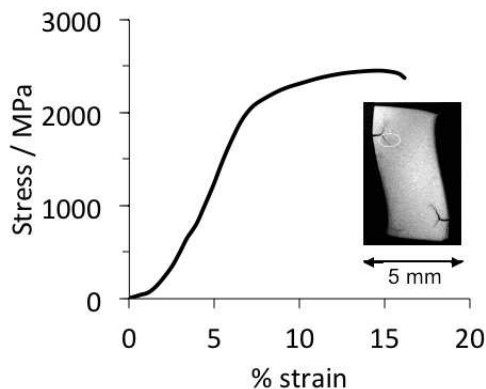


**Figure 14.14** Compression test on the original nanostructured bainite. The inset shows the state of the sample following the arrest of the test (Caballero et al., 2002).

### 14.6.3 Charpy Impact Energy

Although the occurrence of high-carbon, untempered martensite causes failure only when the percolation threshold is reached, its presence must influence the toughness. We have seen already that the fracture toughness as measured using  $K_{IC}$  is reasonably high, but the Charpy impact properties of these nanostructured steels are poor, with only about 5 J

of impact energy absorbed at room temperature. This must be attributed to the fracture of martensite at the high strain rates associated with the impact test. It seems likely that the poor Charpy impact toughness is an intrinsic characteristic of steels containing brittle martensite in structures where softer phases that can accommodate the imposed strain rate are absent. After all, much greater absorbed energies are obtained in the similarly strong Aermet 100 steel where the martensite is toughened by severe tempering (Novotny, 1992).

## 14.7 Impulse Loading

The properties of nanostructured bainite have been measured using impulse loading (Hammond and Proud, 2004).<sup>7</sup> The longitudinal, shear and bulk sound speeds are measured to be 5.85–5.87, 3.18–3.2 and 4.55–4.56  $\text{mm s}^{-1}$ . Fig. 14.15a shows the longitudinal stress developed on impact of a copper flyer plate on to a bainitic steel plate as a function of the flyer plate velocity. The deviation from elastic behaviour occurs at approximately the same longitudinal stress as the pressure-induced, momentary transition to  $\epsilon$ -iron at around 13 GPa, although this is uncertain because an examination of the shear strength versus longitudinal stress indicate the deviation from elasticity to be at 5 GPa. To add to the confusion, other work on carbide-free bainite reports the stress-strain curve to essentially be independent of the strain rate (Fig. 14.15b).

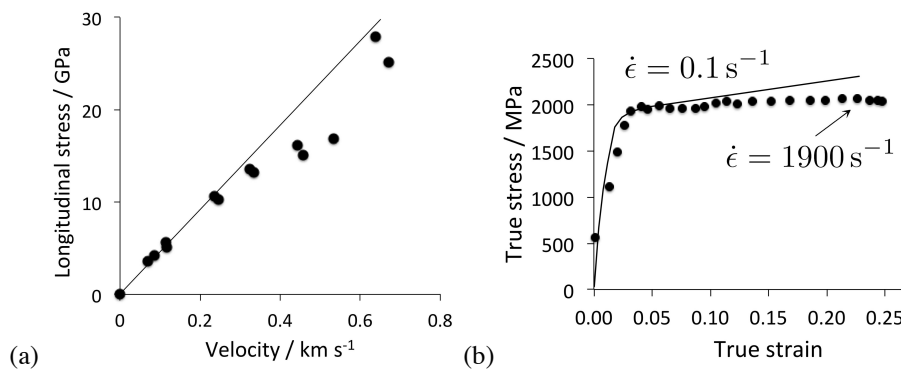


**Figure 14.15** (a) The longitudinal stress developed in the bainite as a function of the velocity of an impacting copper flyer plate. Such a plot is often referred to as a Hugoniot. Adapted from Hammond and Proud (2004). The line indicates elastic response. (b) Strain-rate dependence of stress-strain curve of carbide-free bainite, measured using ordinary tensile testing for the slow rate and Hopkinson split bar for the high rate experiments. Data from Curtze et al. (2008).

In an impact experiment such as that in Hammond and Proud (2004), the planar shock wave is reflected backwards from the free surface of the bainite plate, propagates backwards and interacts with the wave originating from the flyer plate surface. This creates tension inside the material which when it exceeds a *spall strength*, the material fractures roughly parallel to the free surfaces, leading to a detachment known as a spall. The spall strength of nanostructured bainite is about 2 GPa for longitudinal stresses less than those

<sup>7</sup>The paper does not state the chemical composition of the steel studied, but it is in fact the same as in Caballero et al. (2002). The paper does not include any structural information and makes incorrect statements about carbides, phase fractions and X-ray data. It can be assumed that there is  $\alpha_b + \gamma'$  in all the samples studied, with only the lower transformation temperature form being nanostructured.

associated with the transition to  $\epsilon$ -iron (Hammond and Proud, 2004). It would be useful to characterise the structure of the spalls in the vicinity of the fracture using high-resolution techniques.

The nature of adiabatic shear bands that form in carbide-free bainitic steel that has experienced ballistic impact has been studied (Fielding and Bhadeshia, 2014). The material is not nanostructured but is generated by continuous cooling transformation into a mixture of just bainite plates and carbon-enriched retained austenite, and hence may be representative of the behaviour of shear bands in the nanostructured version. Such bands are narrow layers of intensely sheared material in which strain is localised because the heat generated by the rapidity of deformation cannot be dissipated easily by diffusion. The resulting increase in temperature leads to localised softening and hence a focusing of plasticity into bands that are typically  $< 100 \mu\text{m}$  in width (Walley, 2007). The bands reduce the ability of armour to resist projectiles since plugs of material can then detach from the armour. There are observations that austenite can form during the adiabatic heating, leading to 'transformed bands' that are essentially fine martensite, but also others that indicate only intense plasticity: the deformation bands (Wright, 2002).

Fig. 14.16 illustrates the morphology of the shear bands; structural characterisation indicates that the bands resemble warm worked regions that are in an unrecrystallised state and are unlikely to be due to the formation of austenite during adiabatic heating. Transmission microscopy revealed retained austenite within the shear bands; the failure to transform during severe deformation was attributed to mechanical stabilisation. In separate work involving lower velocity projectiles fired at TRIP-assisted steel, the austenite also remained stable in the damaged region, interpreted as the consequence of adiabatic heating that increases its thermodynamic stability (Rodríguez-Martínez et al., 2010).

Shear band formation is clearly a disadvantage in the context of armour and it is possible that the introduction of a large density of fine carbide particles may reduce the tendency to localise plastic deformation by making the structure more resistant to softening at elevated temperatures.

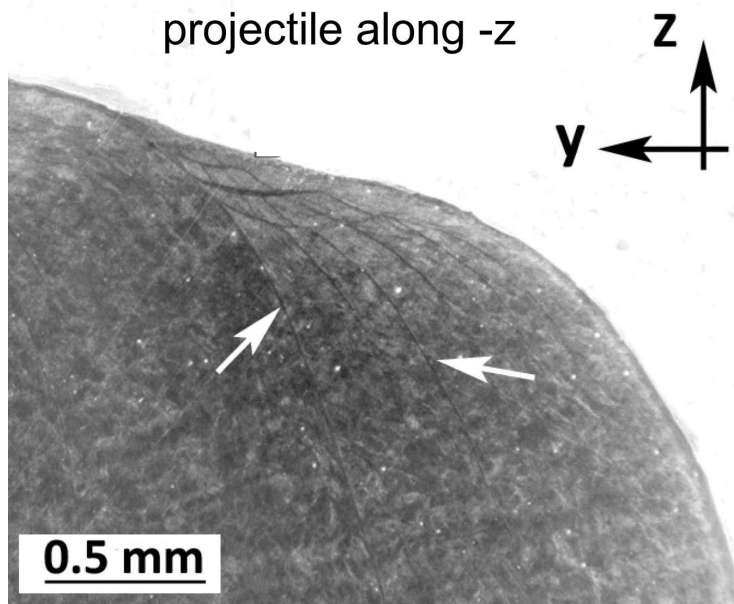


**Figure 14.16** Fine shear bands due to ballistic impact on carbide-free bainitic steel (Fielding and Bhadeshia, 2014).

## 14.8 Fatigue

There is an interest in developing the nanostructured bainitic steels for the manufacture of shafts which have a high surface integrity, but which are subjected during rotation to alternating stresses, making the fatigue performance of the material an important design parameter. The steel in this case must be processed in order to reduce the nonmetallic inclusion content, for example by vacuum arc remelting and vacuum arc refining. The first fatigue tests were in fact done on air melts and gave surprisingly good fatigue properties (Peet et al., 2011). Push-pull fatigue samples 4.5 mm diameter, 12 mm gauge length were used in order to stress a large volume of material. The loading was at 0.25 Hz, with each 4 s cycle consisting of four steps, each of 1 s duration: a hold at the minimum tensile stress, followed by a linear ramp to the maximum stress, hold at that stress and a ramp down to the minimum stress. Failure was mostly initiated at nonmetallic inclusions within the stressed volume, with surface initiation occurring only at the highest of stress amplitudes. Fig. 14.17a shows the S-N curve; a conservative estimate of the endurance limit for which samples survive  $10^7$  cycles was found to be  $\sigma_{\max} = 855$  MPa. This estimate is made by extrapolating from the UTS at 0 cycles to  $10^5$  cycles, but it would not be significantly different if only the data corresponding to the fatigue tests (open circles, Fig. 14.17a) were used.

The fatigue limit in general correlates with the hardness over a range of steels and microstructures, Fig. 14.17b (Garwood et al., 1951; Nishiyama, 1980), up to about 600 HV. This relationship is not unexpected since resistance to plastic deformation, as measured by hardness indentations, determines also the resistance to the plasticity required to initiate and propagate fatigue (Chalant and Suyitno, 1991).

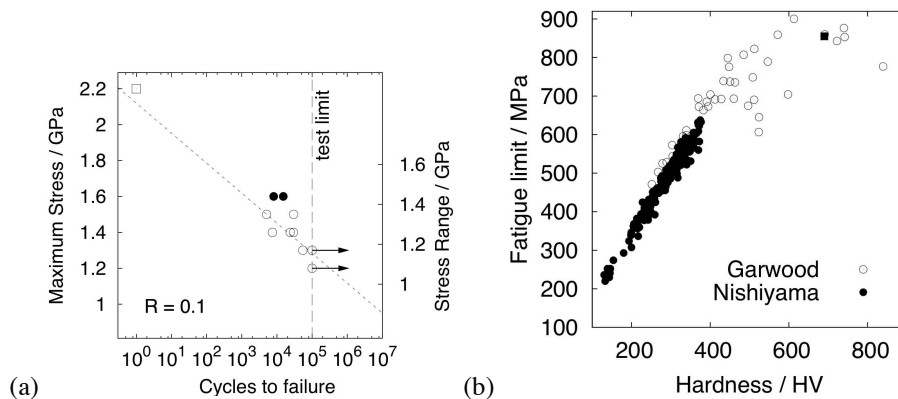


**Figure 14.17** (a) Fatigue life as a function of stress range. The single square is a tensile test result (Garcia-Mateo and Caballero, 2005; Garcia-Mateo et al., 2005), the circles are fatigue data, and the filled circles represent samples which previously survived  $10^5$  cycles at the lower stress but did not fail (arrowed points). (b) Correlation of fatigue life with hardness; the data represented by black dots are for a variety of steels in the normalised, and quenched and tempered conditions (Garwood et al., 1951; Nishiyama, 1980). The square is from Peet et al. (2011).

Rotating-bending tests subject a relatively small volume to the maximum stress when compared with the push-pull variety, and are more sensitive to surface crack initiation. The data illustrated in Fig. 14.18 relate to surface-initiated failure during such testing. The endurance limit correlates directly with the strength of the steel, in this case obtained by transformation at a variety of temperatures. The material transformed at  $200^\circ\text{C}$  corresponds to nanostructured bainite, with an endurance limit of 1005 MPa. The authors drew inferences on the role of retained austenite, but proof was not provided. Clear evidence of the role of structure comes from fractographic studies of nanostructured bainite subjected to high-cycle three-point bending tests, where profuse crack branching was observed on examining the fatigued fracture surfaces.

Rotation-bending tests in combination with notches have been used to deliberately initiate failure at the surface on the grounds that specific components may have stress concentrators at the surface (Sourmail et al., 2013). The volume of material subjected to the maximum stress is then even smaller than that for un-notched rotating-bending tests so that data are not particularly relevant for inclusion nucleated fatigue or where the component is surface-hardened. The branching was said to be associated with stress-induced transformation of retained austenite into high-carbon martensite, Fig. 14.19. That study revealed an exceptionally large fatigue limit for the nanostructured bainite of some 1000 MPa.

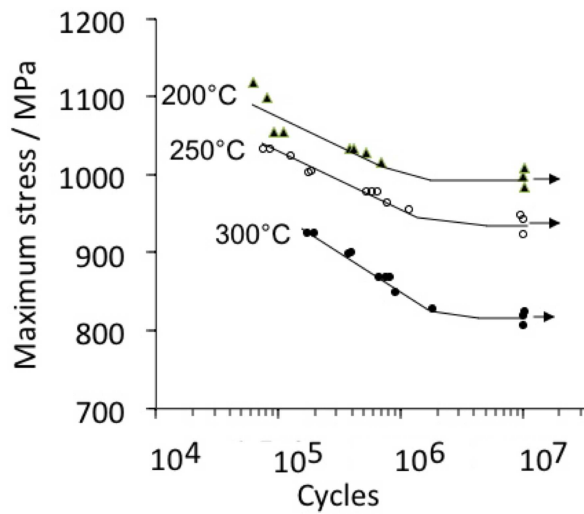


**Figure 14.18** Rotating-bending fatigue tests on nanostructured bainite formed at 200 °C, and coarser bainite due to transformation at higher temperatures. The arrows indicate that the tests completed at about  $10^7$  cycles did not in fact fail. After Shendy et al. (2014).

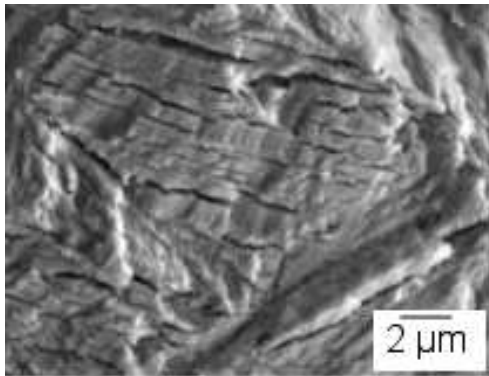


**Figure 14.19** Fractograph showing prominent branching of the main crack. Fe-0.83C-0.81Cr-1.56Si-1.37Mn-0.87W-1.44Al wt%, transformed at 220 °C for 24 h and subjected to bending fatigue with failure occurring at 65,800 cycles for a maximum stress of 1380 MPa. Reproduced with the permission of Elsevier from Yang et al. (2012b).

## 14.9 Acceleration of Transformation

The low-temperature reaction can take between 2-60 days over the range 125-325 °C. When combined with the inherent ability of the steel to resist pearlite formation during cooling, this means that a large steel component can be cooled slowly to  $B_S$ , thus achieving a homogeneous temperature before transformation begins. This encourages the development of uniform properties and should help to avoid the development of residual stresses and hence to minimise distortion.

A transformation that can be completed within minutes or hours would nevertheless be useful when dealing with small components. The difference in free energy between austenite and ferrite ( $\Delta G^{\gamma \rightarrow \alpha} = G^\alpha - G^\gamma$ ) is the driving force for transformation. Both the nucleation and growth rates can be expected to increase as a function of  $|\Delta G^{\gamma \rightarrow \alpha}|$ . The addition of cobalt and aluminium boosts  $|\Delta G^{\gamma \rightarrow \alpha}|$ , causing the rate of transformation

to increase,<sup>8</sup> as illustrated in Fig. 14.20. The kinetics of the transformation can in fact be calculated (Bhadeshia, 1982d) and the level of agreement achieved with experimental data is illustrated in Fig. 14.3b; the agreement is reasonable considering that the temperatures of interest are around 200 °C. Similar calculations (Fig. 14.21) show that the kinetics can be accelerated also by reducing the manganese concentration, as expected from the fact that an increase in its concentration leads to a reduction in the magnitude of  $\Delta G^{\gamma \rightarrow \alpha}$ .

Whereas the solute concentrations influence the displacive transformation kinetics as a consequence of changes in  $\Delta G^{\gamma \rightarrow \alpha}$ , a reduction in the austenite grain size can also accelerate the formation of nanostructured bainite by providing a larger number density of nucleation sites (Garcia-Mateo et al., 2003a). However, there are complications because the potential for site saturation increases, which may lead to an overall reduction in rate (Matsuzaki and Bhadeshia, 1995). Indeed, it has been confirmed that a greater fraction of nanostructured bainite can sometimes be obtained at a larger austenite grain size (Hu et al., 2014a), although in fact, coarse austenite grains are not in general conducive to high toughness in strong steels.

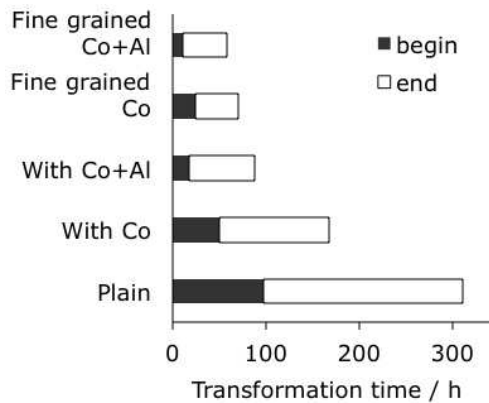


**Figure 14.20** Time of start and stop of nanostructured bainite reaction at 200°C. The plain alloy has the composition Fe-0.98C-1.46Si-1.89Mn-0.26Mo-1.26Cr-0.09V wt%, the others have 1.5 wt% Co or 1.5C-1Al wt% addition (Garcia-Mateo et al., 2003a).

Efforts to accelerate the formation of nanostructured bainite by adjusting the solute content or the austenite grain size will of course increase the rate of the transformations that occur above the  $B_S$  temperature. This may lead to a mixture of transformation products in large components or a non-uniform distribution of phases because the steel becomes sensitive to the cooling rate. An increase in the cooling rate to cope with the reduced bainitic hardenability may lead to residual stresses and distortion in the final component. Phase transformations in steels can also be accelerated by the application of magnetic fields (section 15.9), but the consequences are the same, that unintentional phases are introduced into the microstructure. A 30 Tesla field applied during transformation caused pearlite to replace nanostructured bainite as the predominant nanostructure (Jaramillo et al., 2004, 2005).

An intriguing study by Chang et al. (2013) shows that the addition of boron (0.0024B, 0.0037N, wt%, Table 14.6) significantly accelerates the formation of nanostructured bainite. The authors offered no explanation for the observation, but the effect is clear as shown in Fig. 14.22. And although the initial stages are accelerated, the time taken for the reac-

<sup>8</sup>(Aaronson and Domian, 1966; Kinsman and Aaronson, 1973; Garcia-Mateo et al., 2003a; Soliman and Palkowski, 2007; Curtze et al., 2008; Sidhu, 2013)

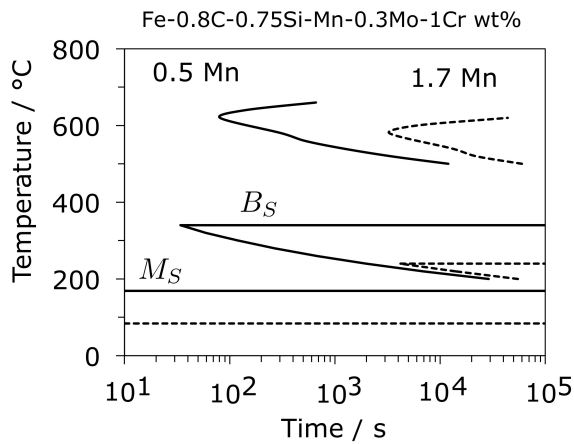


**Figure 14.21** Calculated TTT diagram showing the effect of a reduction in manganese concentration on transformation kinetics in a steel which is otherwise for the production of nanostructured bainite (Secretary of State for Defence et al., 2010).

tions to cease are not different between the two alloys. It is possible that the role of boron in this case is to form boron nitrides at the austenite grain boundaries, with the nitrides stimulating the nucleation of bainite (section 6.11.5). Further growth and development of the transformation would not then be affected.

The idea that the formation of martensite stimulates bainite (section 6.11.3) has been proposed for nanostructured bainite (Gong et al., 2015) but martensite in high-carbon steel is brittle and can crack spontaneously on formation so the method is unlikely to be conducive to good mechanical properties.

#### 14.9.1 Compromise Between Strength and Speed

An interesting assessment of published data on carbide-free bainite has shown that much of the variation in transformation temperatures can be attributed to the changes in the carbon concentration of the steels concerned (Khare et al., 2010). The transformation time increases dramatically as the carbon suppresses the temperature at which bainite can form. Fig. 14.23 represents a neural network analysis of the data, with the upper and lower curves representing the range of uncertainties. Such trends can be used in the design of bainitic steels, where for example, continuous production may require the microstructure to be generated in ten minutes, whereas batch heat treatment can tolerate much greater times.

#### 14.9.2 Cyclic Heat Treatment

There have been suggestions that the rate of transformation can be accelerated by cycling the supercooled austenite within the range  $M_S$  to  $B_S$  (Sista et al., 2007). Single step-changes in the temperature during the course of the reaction have previously been investigated (Goodenow et al., 1969), which indicated that the stresses generated by phase transformation at low temperatures can stimulate that at higher temperatures. However, detailed experiments have failed to confirm the acceleration potential of cyclic transformation when an appropriate comparison is made against the limiting isothermal transformation behaviours (Hasan et al., 2010). The original work does not seem to take account of the excursions of temperature associated with cyclic transformation. Fig. 14.24 shows

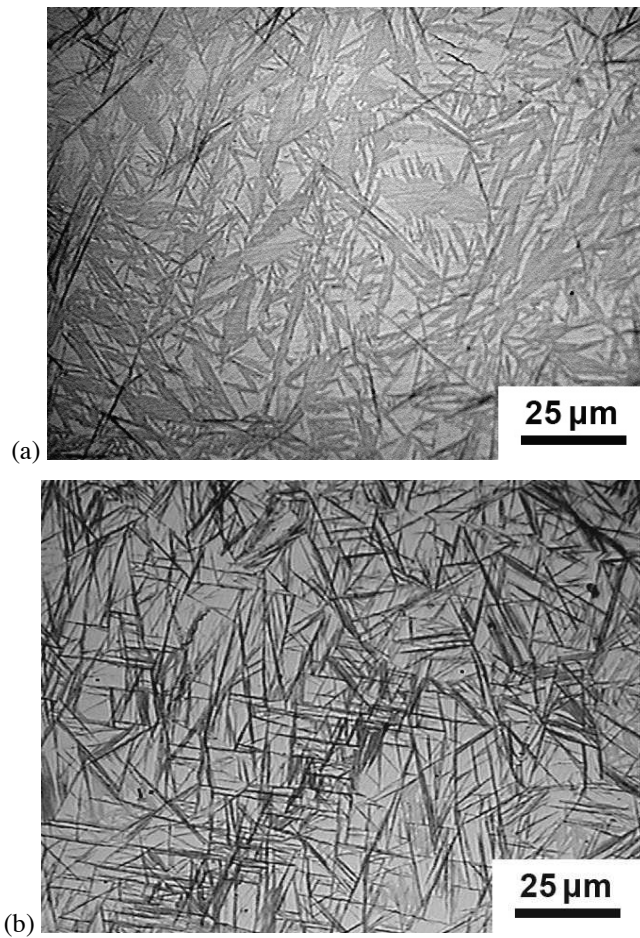


**Figure 14.22** Showing the progress of the bainite reaction following 16 h of transformation at 200 °C, in (a) boron-free steel, showing very few of the dark-etching bainite sheaves, with the remainder being coarse martensite plates and austenite. (b) Boron-containing steel showing a greater extent of transformation to bainite. Micrographs courtesy of Dr Hung-Wei Yen.

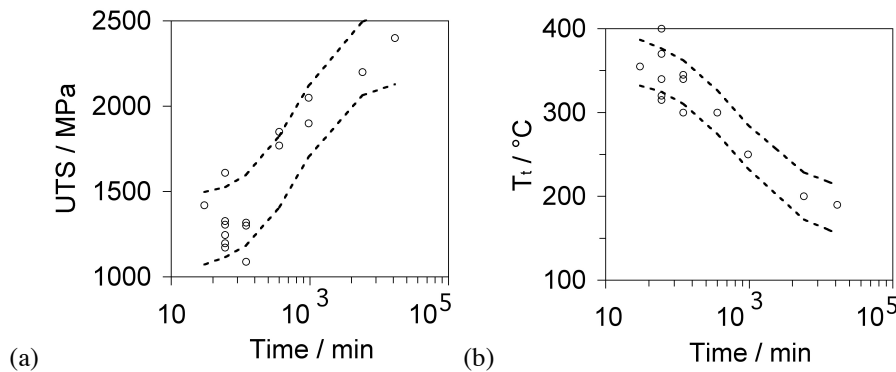


**Figure 14.23** Published experimental data (points) as a function of transformation time (Khare et al., 2010). The curves represent  $\pm 1\sigma$  confidence limits obtained by subjecting the data to a neural network analysis. (a) Ultimate tensile strength as a function of isothermal transformation time. (b) Transformation temperature as a function of isothermal transformation time.

that the ‘curve’ associated with the cyclic transformation falls between the high- and low-temperature isothermal transformation data.

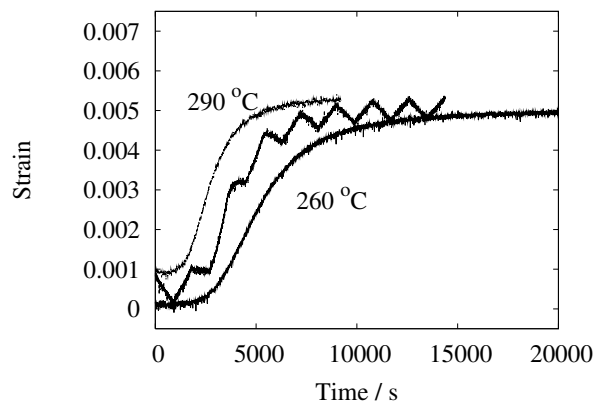


**Figure 14.24** Dilatometric data representing the formation of bainitic ferrite in Fe-0.78C-1.6Si-2.02Mn-0.25Mo-1.01Cr-3.87Co-1.37Al wt% steel. In each case the upper and lower curves represent isothermal transformation at the highest and lowest temperatures respectively, and the zig-zag curves the cyclic treatment: 30 minutes cycle from 290  $\rightarrow$  260  $\rightarrow$  290 °C (Hasan et al., 2010)

## 14.10 Case-Hardening and Cladding

Untempered high-carbon martensitic steels can achieve a maximum hardness of about 800 HV but large concentrations of dissolved carbon tend to make the martensite brittle. One solution is to use a low-carbon steel but to diffuse a larger concentration into the surface which is then transformed into hard martensite in a process known as case-hardening.

This typically gives a wear-resistant layer with a hardness of about 750 HV (Epshtein and Paisov, 1965), but the surface itself remains relatively brittle. Hardness approaching this level can now be achieved by the nanostructured bainite which has the additional advantage of greater toughness.

Case-carburised steel isothermally transformed at 230°C has been shown to lead to extremely fine and hard bainite (620 HV) in the surface layer, with the transformation inducing a compressive stress of about 200 MPa into the surface (Zhang et al., 2008; Wasiluk et al., 2014).<sup>9</sup> Fig. 14.25 shows the variation in carbon concentration and hardness as a function of depth, following isothermal transformation. The hardness obtained following isothermal transformation to bainite at 200 °C is smaller than 230 °C, probably because less transformation is achieved at the lower temperature, leaving more retained austenite in the structure.

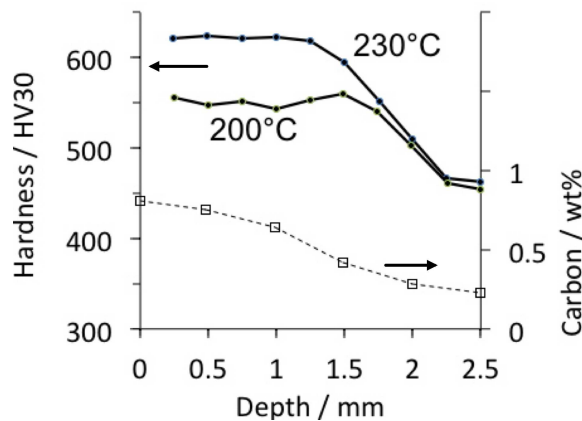


**Figure 14.25** Fe-0.19C-0.57Si-1.77Mn-1.37Cr-0.42Ni-0.33Mo-1.35Al wt% alloy, carburised and then subjected to austenitisation at 950 °C for 20 min, isothermal transformation for 48 h at the temperatures indicated. After Zhang et al. (2008).

Powder produced with the chemical composition of typical nanostructured bainite in wrought steel (Table 14.6) has been used to laser clad the surface of a low-carbon steel (Guo et al., 2014). The cladding was found to be free from cracks or voids, and transformed into the required fine structure by placing the cladding into furnaces immediately after deposition. This is possible because of the relatively slow rate at which the bainite forms. The hardness distribution as a function of the depth below the surface of the clad is illustrated in Fig. 14.26.

There are two distinguishing features of this laser cladding. The chemical segregation due to solidification results in interdendritic regions being enriched in chromium and manganese; these regions do not transform into bainite for the particular experimental conditions used and become martensitic on cooling to ambient temperature. Secondly, the transformation to bainite is faster than expected; this has been attributed to the fine austenite grain size, but it is likely that the bainite forms in regions of the solidification structure that are depleted in solutes such as Cr and Mn.

<sup>9</sup>Similar results have been claimed for bainitic cases produced at higher temperatures; it seems that the distortion associated with the production of the bainitic case is smaller than with the martensitic variety because of the less dramatic quench to the isothermal transformation temperature (Heuer et al., 2009).

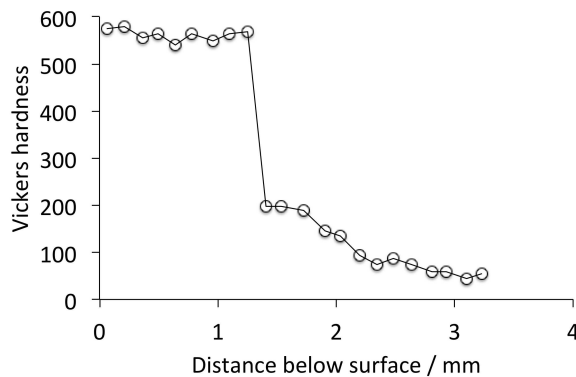


**Figure 14.26** Hardness as a function of depth below the clad surface. Data from Guo et al. (2014).

### 14.11 Powder Metallurgical Nanostructured Bainite

It is unlikely that steel produced using powder metallurgy for the purpose of transformation into nanostructured bainite would have useful mechanical properties in tension. The consolidation of powder using sintering will inevitably leave residual porosity, and the powder route for manufacturing usually leaves the consolidated material with a much larger concentration of oxygen present in the form of oxides. For example, sintering in a  $N_2-H_2$  atmosphere at  $1150^\circ C$  left about 10% porosity in the consolidated steel; subsequent heat treatment to generate nanostructured bainite resulted in ductilities that are just measurable, with the material being unable to support stresses above  $\approx 750$  MPa (Vuorinen et al., 2014). Other difficulties noted included the volatilisation of manganese into the pores and the preferential oxidation of silicon.

Mechanically alloyed powder that is subsequently spark-plasma sintered fares better in that near full-density is achieved, although the material still has a large oxygen concentration of about 0.23 wt% (Lonardelli et al., 2012a). The oxygen is in the form of oxide particles that pin the austenite grain boundaries to such an extent that the  $M_S$  temperature is suppressed for a medium carbon steel (alloy 43, Table 14.6), allowing nanostructured bainite to be generated by transformation at a temperature as low as  $240^\circ C$ , at a rate that is relatively rapid and with tensile ductility reaching about 6% for an ultimate tensile strength of about 1800 MPa. Increasing the carbon concentration (alloy 44, Table 14.6) simply reduces the elongation (Lonardelli et al., 2012b).

### 14.12 Spheroidisation of Nanostructured Bainite

Strong steels sometimes need to be formed into shapes prior to the hardening heat-treatment. As an example, bearing components have a hardness of about 650 HV but the manufacturing process requires the steel to be in a softened condition with a hardness less than 235 HV in order to implement forming and machining operations (Lyons and Hudson, 1967; Bhadeshia, 2012). The discussion in section 4.3.3 indicates that it is very difficult to reduce the hardness of nanostructured bainite to the required levels for fabrication by tempering at all temperatures below that at which austenite formation begins.

There is an alternative process used routinely in the manufacture of bearing steels (Bhadeshia, 2012), that can be adapted for the alloys typically used in producing the nanostructure. The method involves heating to a temperature where a mixture of austenite and

cementite co-exist. It is possible then to cool the steel in such a way that the normal pearlite reaction, in which  $\alpha + \theta$  grow together at a common transformation front, is suppressed. Instead, a divorced eutectoid occurs in which the proeutectoid cementite particles absorb the carbon partitioned by ferrite at the advancing  $\gamma/\alpha$  interface.<sup>10</sup> The cementite particles coarsen in the process of absorbing the partitioned carbon, as illustrated in Fig. 14.27a. The conditions necessary to achieve a divorced eutectoid are shown in Fig. 14.27b, with respect to the spacing between the proeutectoid cementite particles and the undercooling below the eutectoid temperature of the steel.

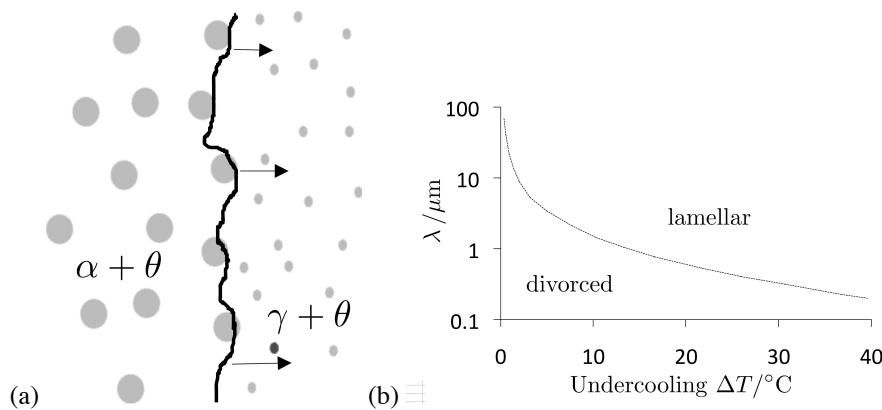
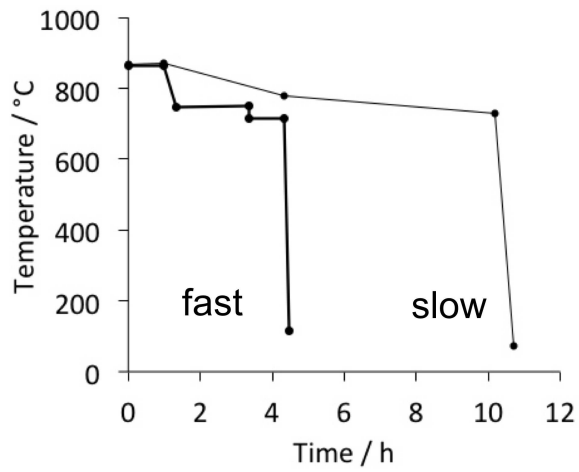


**Figure 14.27** (a) The mechanism of the divorced eutectoid transformation of a mixture of austenite and fine cementite (Verhoeven and Gibson, 1998). (b) Conditions appropriate for the formation of divorced pearlite in a plain-carbon eutectoid steel. The spacing between the proeutectoid cementite particles is  $\lambda$  and  $\Delta T$  is the undercooling below the eutectoid temperature.

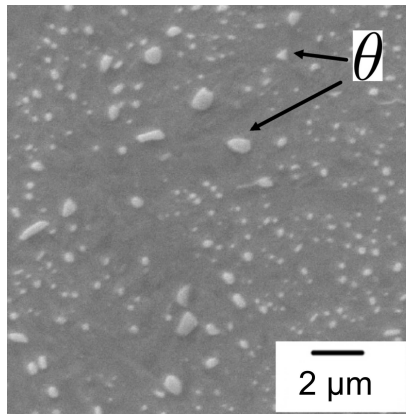
There are two kinds of heat treatments used to initiate spheroidisation based on the divorced eutectoid, Fig. 14.28, for the spheroidisation of ordinary bearing steels such as the classical 52100 alloy (Heron, 1969; Hewitt, 1982; Verhoeven, 2000). In the ‘fast’ treatment the temperature range over which the divorced eutectoid reaction occurs in the 52100 steel was in the range 722–690 °C and slow cooling over that range as in the ‘slow’ version is no longer found to be necessary.

Fig. 14.29 shows the progress of the ‘slow’ divorced eutectoid in an alloy ultimately designed for the production of nanostructured bainite (Luo et al., 2014). The hardness achieved was 255 HV using a heat treatment that takes approximately 10 h, whereas tempering at 708 °C for 42 days achieved a similar hardness (Hasan et al., 2012). The ‘fast’ spheroidisation reaction, not illustrated here, led to a final hardness of 292 HV. It follows that the preferred method for achieving a softened state in steels designed for the production of nanostructured bainite is via the divorced eutectoid, requiring austenitisation in the  $\gamma + \theta$  phase field. Once the fabrication procedures are completed, and if the proeutectoid cementite particles are considered undesirable, then the alloy can be fully austenitised to generate the required hard, nanostructured bainite.

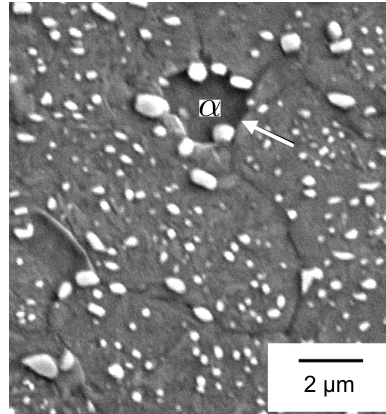
<sup>10</sup>(Honda and Saito, 1920; Whiteley, 1922; Uzlov et al., 1980; Oyama et al., 1984; Verhoeven and Gibson, 1998; Verhoeven, 2000; Basabe et al., 2011; Pandit and Bhadeshia, 2012; Yin and Bhadeshia, 2013).



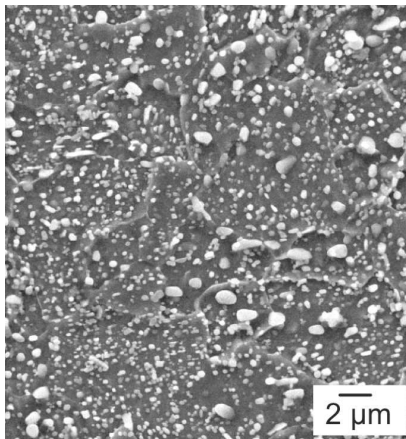
**Figure 14.28** Spheroidisation treatments, each beginning with austenitisation in the  $\gamma + \theta$  phase field. The 'slow' version then involves cooling to  $750^{\circ}\text{C}$  at  $25^{\circ}\text{C h}^{-1}$ , from there cooling to  $690^{\circ}\text{C}$  at  $10^{\circ}\text{C h}^{-1}$  and air cooling from  $680^{\circ}\text{C}$  (Heron, 1969; Hewitt, 1982). The 'fast' version (Verhoeven, 2000), involves cooling to  $722^{\circ}\text{C}$  at  $500^{\circ}\text{C h}^{-1}$ , holding for 2 h, cooling to  $690^{\circ}\text{C}$  and holding for 1 h, followed by air cooling.



(a)



(b)



(c)

**Figure 14.29** Microstructures at stages of the slow spheroidisation treatment. (a) Quenched from the austenitisation temperature to illustrate the proeutectoid cementite particles. (b) Quenched from  $750^{\circ}\text{C}$  to show the divorced eutectoid transformation front (arrow). (c) Final spheroidised structure with a hardness of just 255 HV. After Luo et al. (2014).

### 14.13 Wear of Nanostructured Bainite

There are many mechanisms of wear, the process is dependent on two, three or more body-contact, on the environment and other factors, so tribological studies of nanostructured bainite are in their infancy. It is likely however, that potential applications will drive this subject into studies that are both fundamental in nature and that generate design data. It is often difficult to compare data from different tests so the main discussion in this section relates to the role of the structure in the wear process.<sup>11</sup>

#### 14.13.1 Dry Sliding-Friction

The dry sliding-friction wear resistance of a mixture of nanostructured bainite and martensite in an alloy of composition Fe-0.89C-1.43Si-0.47Cr-0.19Mn wt%, transformed at 200 °C for 8 h, has been studied by Wang et al. (2008). The process involved sliding of the steel plate with a hardness of  $\approx 60$  HRC against a quenched and tempered cylinder-end made from bearing steel with a hardness of 64 HRC, in conditions of 34% humidity. The austenite in the vicinity of the friction surface decomposed under the influence of shear strains, resulting in the formation of an even finer structure with grains of ferrite only a few nanometres in size. It was suggested that these events play a role in determining the wear resistance, which is comparable to that of quenched and tempered martensitic structures. The same conclusions have been reached for a different alloy transformed into a predominantly bainitic nanostructure (Yang et al., 2012c).

Rolling-sliding tests involving cylindrical discs rotating against each other confirm that the nanostructured bainite exhibits lower specific wear rates than for example, the standard 52100 bearing steel with the same hardness (Leiro et al., 2013; Bakshi et al., 2014; Kosuri, 2010). Table 14.3 is a compilation of typical values of the wear rate. The mechanism of wear is not always clear in tests that involve both rolling and sliding. Sliding involves shear at the contact surfaces, whereas rolling contact induces the largest stresses under the contact surface, Fig. 14.30a,b. Experimental measurement of the hardness as a function of depth below the contact surface shows a maximum at a depth of about 50  $\mu\text{m}$ , Fig. 14.30c, consistent with damage initiating below the contact surface, i.e. rolling contact fatigue. The sub-surface hardening probably occurs by a combination of plasticity and the stress-induced transformation of high-carbon retained austenite into martensite. Wear data are summarised in Fig. 14.30d.

Rolling contact fatigue seems to be the main mechanism of wear in the dry rolling-sliding tests conducted thus far on nanostructured bainite. Retained austenite clearly has a role in resistance to this kind of wear (Wang et al., 2008), possibly through its roles in transformation-induced toughness and the hardness of the resulting martensite. This augers well for the development of case-hardening technology based on the nanostructured bainite. Experiments on a carburised surfaces heat treated into the nanostructured bainitic state have shown that their rolling-contact fatigue resistance is superior to that of tempered martensite (Zhang et al., 2011a,c,b). Indeed, the delamination is reduced with the bainitic case, Fig. 14.31.

<sup>11</sup>The focus here is specifically on the carbide-free nanostructured bainite; many studies have been conducted on carbide-free bainite in the context of rail steels, and are described in section 13.12.

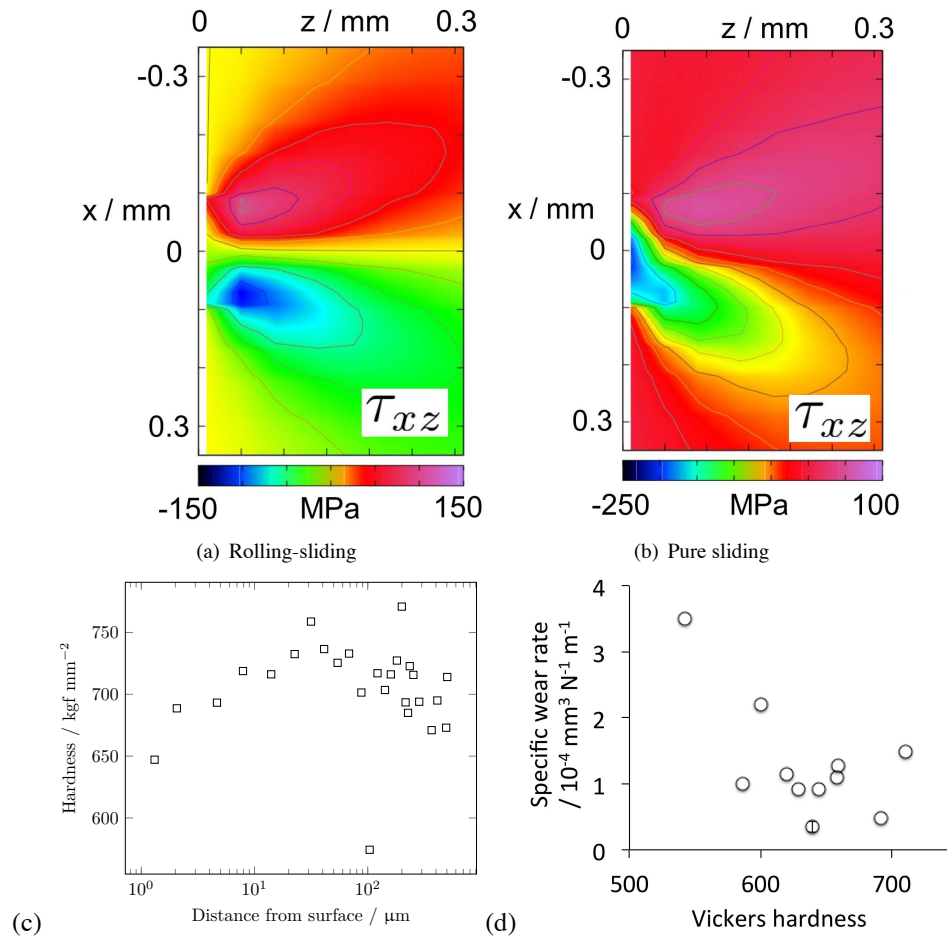


**Figure 14.30** Calculated shear stress  $\tau_{xz}$ , where  $x$  is along the rolling direction and  $z$  is normal to the contact surface. The stress is generated during the counter-rotation of discs in dry rolling-sliding tests, with 5% relative slip. (a) Rolling-sliding with 5% relative slip. (b) Perfect sliding. (c) Hardness as a function of depth below the contact surface, following the wear testing. (d) Compilation of wear data on steels that have been verified to have structures that are mixtures only of bainitic ferrite and retained austenite. After Bakshi et al. (2014).

**Table 14.3** Dry sliding wear data on the hardest, fine mixtures of bainitic ferrite and austenite reported, focussing on the lowest transformation temperatures used to generate the bainite. The Vickers hardness is listed where available, and the chemical compositions are given in wt%. With the exception of tests reported in Wang et al. (2008); Zhang et al. (2011c); Yang et al. (2012c), all the experiments involved rolling-sliding (5%) of counter-rotating discs. In the former case the tests were an adaptation of pin-on-disc experiments. The term  $\dot{W}$  represents the specific wear rate in units  $\text{mm}^3 \text{N}^{-1} \text{m}^{-1}$ . The first row represents a steel that is carburised before wear testing.

C	Si	Mn	Cr	Mo	Misc.	Hardness	Outcome	Ref.
0.19	0.57	1.77	1.37	0.33	0.42Ni, 1.35Al	625	comparable wear to martensite of similar hardness	Zhang et al. (2011c)
0.89	1.43	0.19	0.47			697	comparable wear to martensite of unspecified hardness	Wang et al. (2008)
0.83	1.56	1.37	0.81		1.44Al, 0.87W	685	greater wear resistance than harder tempered-martensite	Yang et al. (2012c)
0.61	1.72	0.75	0.35	0.04	0.12Ni	627	$\dot{W} = 1.0 \text{ to } 1.6 \times 10^{-4}$	Leiro et al. (2011)
0.99	1.50	0.76	0.46			660	$\dot{W} = 1.1 \times 10^{-4}$	Leiro et al. (2013)
0.98	2.90	0.77	0.45			630	$\dot{W} = 0.9 \times 10^{-4}$	Leiro et al. (2013)
0.90	1.65	0.79	0.48			693	$\dot{W} = 0.4 \times 10^{-4}$	Leiro et al. (2013)
0.68	1.60	1.25	1.50			589	$\dot{W} = 1.0 \times 10^{-4}$	Leiro et al. (2013)
0.99	2.47	0.74	0.97	0.03		650	$\dot{W} = 8.6 \times 10^{-6}$	Sourmail et al. (2013)
0.67	1.67	1.31	1.73	0.15	0.12V		$\dot{W} = 1.2 \times 10^{-5}$	Sourmail et al. (2013)
0.83	1.90	2.28	1.44	0.24	0.11V	640	$\dot{W} = 3.5 \times 10^{-5}$	Bakshi et al. (2014)

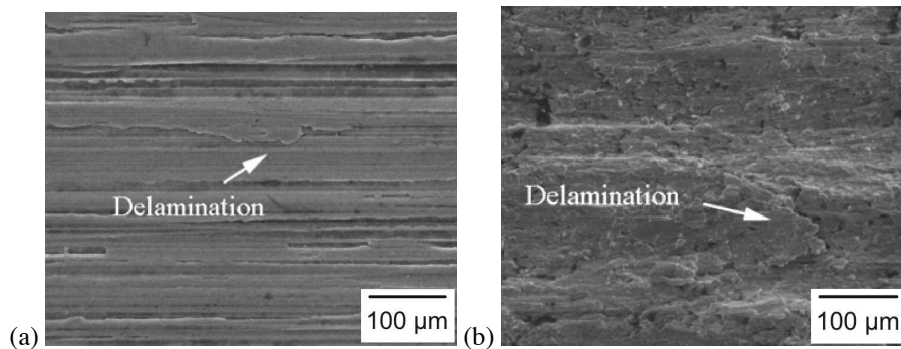


**Figure 14.31** Images of worn surfaces. (a) Nanostructured bainite case. (b) Martensitic case. Reproduced with permission from Elsevier from Zhang et al. (2011c).

### 14.13.2 Three body Abrasion

Three-body abrasive wear tests have been reported on nanostructured bainite (622 HV), pearlite (378 HV) and martensite (739 HV), with all structures generated in the same steel. The process involved abrasion by silicon carbide particles introduced between a rotating rubber wheel and the steel (Bakshi et al., 2013). Surprisingly, there were only small difference in the abrasive wear rate between the three kinds of samples, in spite of the large differences in initial hardness. This is because different mechanisms of abrasion operated in each case. With the soft pearlite, the abrasive particles were found to slide and were sometimes halted in their tracks, leading to extensive pitting. Fragmentation occurred with the untempered martensite, with very little material left adhering to the steel surface. Like pearlite, there was significant plastic deformation at the active surface of the bainite, with good adhesion of the damaged material.

Only the nanostructured bainite exhibited surface hardening to values in excess of 800 HV, whereas both pearlite and martensite softened significantly. This occurred because the surface was re-austenitised and transformed into martensite, causing the hardness to increase.

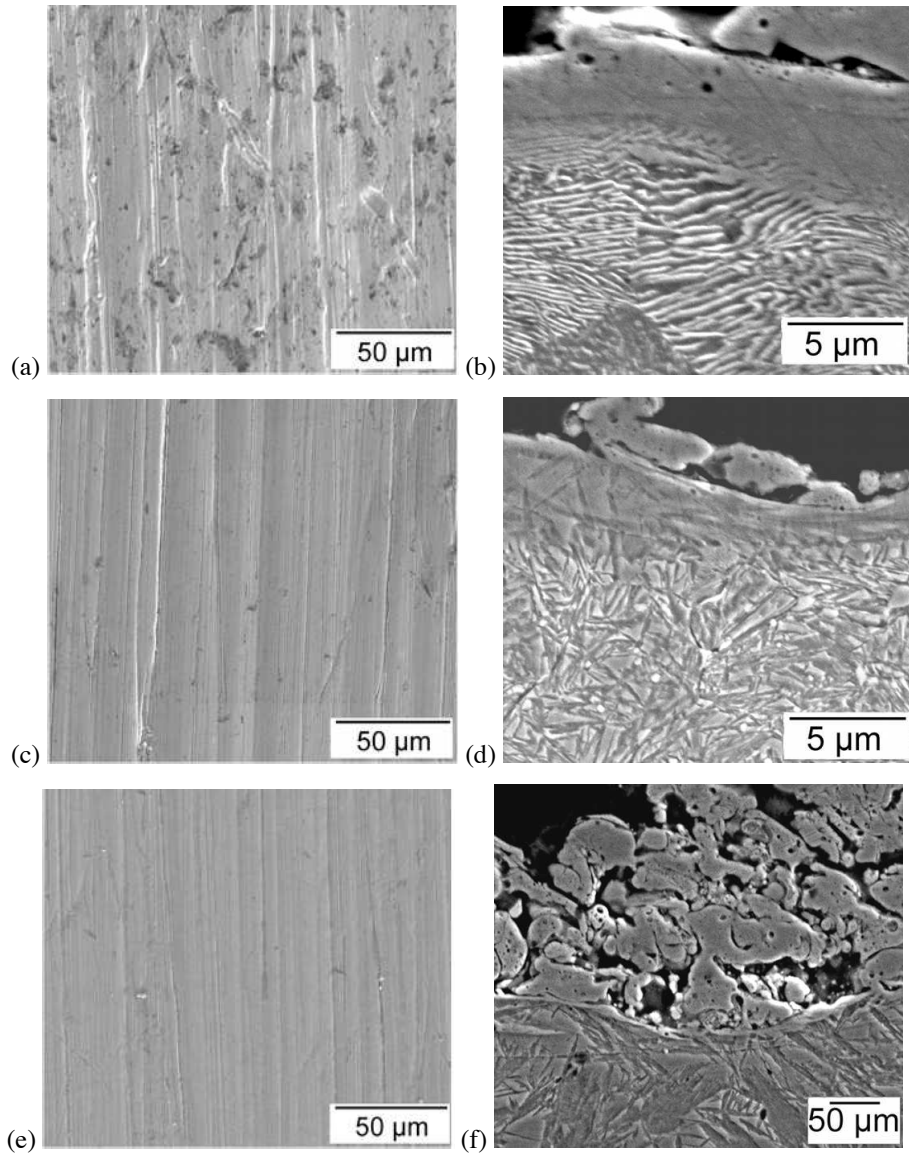


**Figure 14.32** Abraded surfaces and their cross-sections. (a) Soft pearlite, showing significant pitting due to the arrest of abrasive particles during the test. (b) Soft pearlite, showing extensive deformation of pearlite and a continuous white-etching layer. (c) Bainite. (d) Bainite: continuous layer showing evidence of phase transformation following austenitisation. (e) Martensite. (f) Martensite: considerable chip formation. After Bakshi et al. (2013).

### 14.14 Aspects of Corrosion

There are limited studies on the environmental susceptibility of nanostructured bainite. There is an interesting comparison between the high-carbon nanostructured bainite (designated 'HC') and a variant with only 0.33C wt% (LC) with both alloys transformed at 200 °C (Ren et al., 2008). Wedge opening loading specimens were used to study fracture in the presence of specific environments. In this, a load is applied using a constant displacement across the notch, and the resulting crack propagates until the reduction in stress intensity due to the increase in crack length is sufficient to arrest the crack, at which point a threshold value of the stress intensity is obtained. The crack growth rate can also be measured to the point where the crack arrests. The results show that the nanostructured bainite has a poor environmental resistance, with high crack growth rates in all the circumstances listed. This is relevant for all applications where the strong nanostructured bainite is considered for structural applications.

**Table 14.4** Mechanical properties of nanostructured bainite (HC), detailed composition in Table 14.6, and its lower carbon variant LC. All the stress intensities have identical units, MPa m<sup>1/2</sup> and crack growth rates  $da/dt$  are in mm h<sup>-1</sup>. The test in air corresponds to a relative humidity of 25-30%, and 92% for humid air. The 'solution' consists of 0.5 mol L<sup>-1</sup> H<sub>2</sub>SO<sub>4</sub> + 0.25 g L<sup>-1</sup> of As<sub>2</sub>O<sub>3</sub>. Data from Ren et al. (2008).

Alloy	Hardness	$\sigma_y$ MPa	$\sigma_{UTS}$ MPa	% elongation	Charpy energy J	$K_{IC}$ MPa m <sup>1/2</sup>			
HC	623±3 HV	1818	2110	7	13±0.4	34			
LC	501±6 HV	1310	1603	12	51±1.3	94			
	$K_{IE}$ air	$\frac{da}{dt}$	$K_{IE}$ humid air	$\frac{da}{dt}$	$K_{IE}$ water	$\frac{da}{dt}$	$K_{IE}$ solution	$\frac{da}{dt}$	
HC	16.2	2.5	12.2	8.3	9.8	14.5	-	-	
LC					31.5	0.08	23.8	0.42	

It appears that in mixtures of bainitic ferrite and carbon-enriched retained austenite, the latter phase dissolves preferentially in 3.5 wt% NaCl aqueous solution. Therefore, the same steel when transformed at 350 °C has a greater corrosion rate than following transformation into the nanostructured bainite at 200 °C, because the amount of retained austenite is smaller in the latter case. The nanostructured bainite exhibited significantly superior general corrosion resistance to the chloride solution than martensite in the same steel (Hodgson et al., 2011; Kazum et al., 2014).

### 14.15 Hydrogen Migration Through Nanostructure

The diffusion of hydrogen in austenite is much slower than in ferrite so if the latter phase can be totally enclosed inside austenite, then the mobility of hydrogen through the structure should be greatly reduced. Nanostructured bainite forms the ideal test material for this concept given that the amount of retained austenite which is present as thin films is above the percolation threshold. Fig. 14.33 shows first that the diffusivity of hydro-

gen increases sharply as the retained austenite content falls below the threshold value of  $V_V^\gamma \approx 0.1$  in nanostructured bainite (Fielding et al., 2014). Secondly, the duplex steel contains the largest amount of austenite but its morphology is such that there is a continuous path through the ferrite, thus leading to a greater diffusivity than the nanostructured bainite with austenite fraction greater than the percolation threshold.

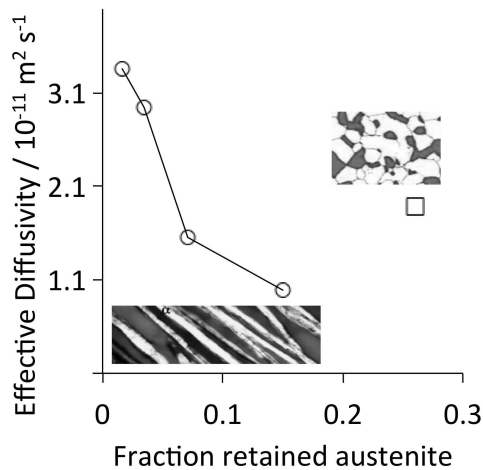


**Figure 14.33** The diffusion coefficient for hydrogen through nanostructured bainite (circles) and a different duplex steel where the austenite does not percolate (square). The amount of austenite in the nanostructured bainite was controlled by tempering heat treatments. After Fielding et al. (2014).

#### 14.16 Low-Carbon Nanostructured Bainite

Structural steels often need to be joined by welding, which involves the local application of a heat source. The diffusion of this heat into the adjacent material causes metallurgical changes which can lead to the formation of brittle martensite when the carbon concentration of the steel is high enough, as is the case with the nanostructured bainitic steels described here. Readily weldable steels generally have carbon concentrations less than 0.2 wt%.

The principal reason for the fine scale of the bainitic structure is the low transformation temperature made possible by the addition of about 1 wt% of carbon. It is feasible that  $B_S$  can also be suppressed by using large concentrations of substitutional solutes in order to minimise the concentration of carbon.

Calculations done using the scheme outlined in section 6.1.2 indicate that carbon is much more effective in maintaining a difference between the  $M_S$  and  $B_S$  temperatures than are substitutional solutes which reduce  $|\Delta G^{\gamma\alpha}|$  simultaneously for martensite and bainite, Fig. 14.34. Substitutional solutes do not partition during any stage in the formation of martensite or bainite; both transformations are therefore identically affected by the way in which the substitutional solute alters the thermodynamic driving force. It is the partitioning of carbon at the nucleation stage which is one of the distinguishing features of bainite when compared with martensite (Table 14.5). This carbon partitioning allows bainite to form at a higher temperature than martensite. This advantage is diminished as the overall carbon concentration is reduced, as illustrated in Figure 14.34.

Unfortunately, theory indicates that the level of substitutional solute required would prevent completely the formation of bainite because the difference between the bainite- and

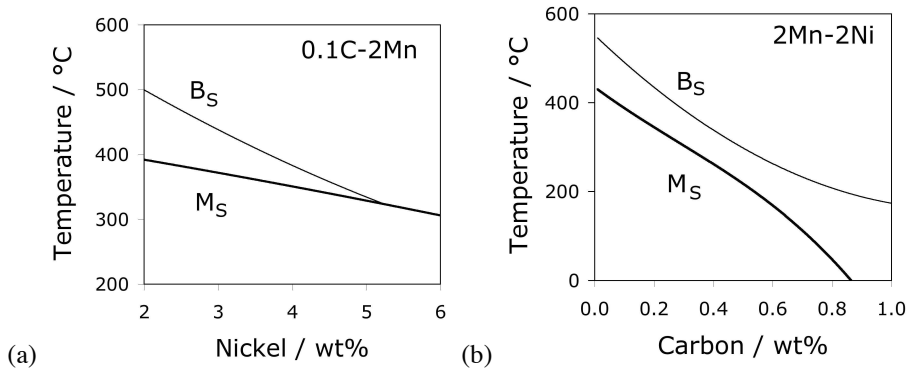


**Figure 14.34** Calculated bainite- and martensite-start temperatures: (a) Fe-0.1C-2Mn wt%, with a variation in nickel concentration; (b) Fe-2Ni-2Mn with a variation in the carbon concentration. After Bhadeshia (2005a).

martensite-start temperatures then vanishes (Bhadeshia, 2005a). Furthermore, the suppression of  $B_S$  well below the  $T'_0$  temperature because the nucleation of bainite becomes more difficult, means that there is a considerable excess of free energy available for the growth phase. As a consequence, the fine platelets of bainite that are initiated, tend to coalesce during the growth stage, negating the advantage of transforming at low temperatures, Fig. 14.35 (Yang and Bhadeshia, 2008). The transformation rates are very slow, for example, some 12 weeks of heat treatment were necessary to produce the structure illustrated in Fig. 14.35. The prospects therefore do not look promising for the design of a low-carbon nanostructured bainite.

**Table 14.5** Subset of Table 16.1, illustrating the essential differences in the mechanisms of displacive transformations in the context of the calculations involved in generating Fig. 14.34.

Martensite $\alpha'$	Bainite $\alpha_b$	Widmanstätten ferrite $\alpha_W$
Diffusionless nucleation	Paraequilibrium nucleation	Paraequilibrium nucleation
Diffusionless growth	Diffusionless growth	Paraequilibrium growth

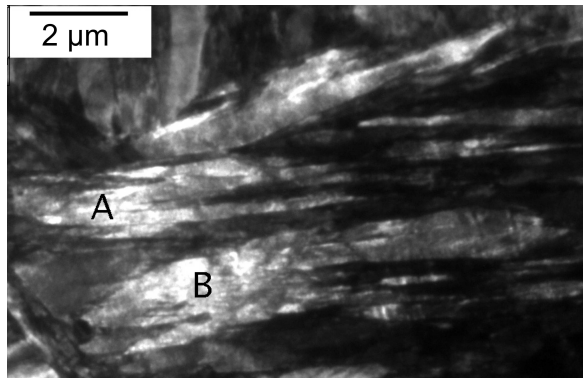


**Figure 14.35** Fe-0.20C-2.5Mn-6.8Ni wt%, transformed isothermally at 280°C (just above  $M_S$ ) for 12 weeks. Transmission electron micrograph. The annotations 'A' and 'B' mark regions where coalescence has occurred – the participating platelets are towards the right of each coalesced region. After Yang and Bhadeshia (2008).

### 14.17 Welding

Nanostructured bainite has been commercialised but only for applications that do not require welding. This is because the class of steels that leads to the desired structure contains too much carbon, a carbon-equivalent in excess of 1, which far exceeds the norms of acceptability for welding.

Indeed, autogenous laser welding of a typical high-carbon bainitic steel (Fe-0.8C-1Si-1.5Mn-1.8Al wt%) has been shown to lead to dramatic cracking within the martensitic weld nugget which has a hardness of 800 HV (Hong et al., 2010). However, it has been shown by experiment that by trailing an induction heating coil behind the moving laser beam, it is possible to avoid such cracks. The induction coil heats up the nugget at some  $100\text{ °C s}^{-1}$  to a temperature of 800 °C, followed by cooling at  $40\text{ °C s}^{-1}$ . This procedure reduces the hardness to just 350 HV and eliminates cracking. The hardness variations from the centre of the weld are illustrated in Fig. 14.36a.

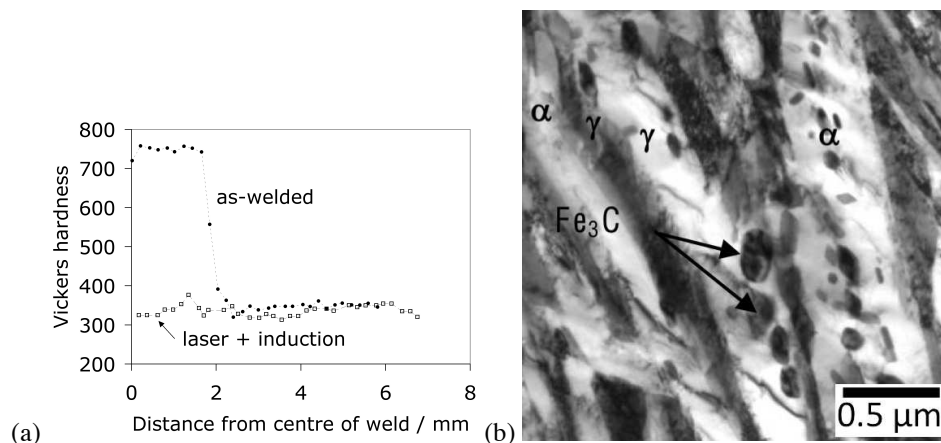


**Figure 14.36** (a) Hardness profiles for both the as laser-welded and the combined laser and induction heated samples. (b) Bright-field transmission electron micrograph showing the structure resulting from simulation of welding heat-affected zone using both laser and induction heating. Data from Hong et al. (2010), micrograph courtesy of S. G. Hong.

A recent review (Fang et al., 2012) of the welding of strong bainite concludes that there are three issues to consider: (a) brittle martensite formation in both the fusion zone and the heat-affected zone in its close proximity, (b) the formation of cementite in the heat-affected zone further away from the weld, and (c) cold cracking in the weld itself. These issues have not yet been investigated in detail, and there are no studies in the open literature which relate the changes in structure to engineering properties. This could in principle be a fertile field of study if an application is found for strong bainite which requires joining.

Cold-cracking and the formation of martensite can be avoided by keeping the plate temperature of 300 °C (above  $M_S$ ) during welding, and as the joint cools towards  $B_S$ , to transfer it into an oven at 250 °C for a prolonged period, where any re-austenitised regions can transform back into nanostructured bainite (Fang et al., 2013). The region of the heat-affected zone that is tempered then becomes the focus for failure in cross-weld tests but the overall properties obtained are reasonable. It is unlikely, however, that the method is practical for large structures or complex shapes.

#### 14.18 Summary

Considerable progress has been made in revealing the mechanism by which nanostructured bainite and its mechanical properties evolve, and in the application of this knowledge towards better design. The steel with this structure can be strong, hard, ductile and reasonably tough. However, because of its high carbon concentration, it is unlikely to be readily weldable. Furthermore, the deformation-induced formation of brittle martensite may make it impossible to achieve a large impact toughness. Applications of the concept have to bear these factors in mind. The exciting outcome is that, for the first time, it is possible to obtain a bulk steel containing an extraordinarily high density of ferrite/austenite interfaces, at a cost which is ordinary, and which can be made in large quantities. Samples of the alloy can be simultaneously large in all three dimensions.

It is quite likely, given the level of worldwide activity in this field (Table 14.6), that the approach used for the design of the nanostructured bainite will lead to another class of steels with a wider range of properties and a greater potential for applications than has been achieved thus far. It is encouraging that different procedures of design are being adopted, for example, the work by Kundu et al. (2009), where artificial neural networks have been used to design and manufacture the fine bainite by transforming at the significantly higher temperature of 300 °C in a matter of hours rather than days, without using expensive alloying elements.

Table 14.6: Composition (wt%) of nanostructured bainitic alloys.

Alloy	C	Si	Mn	Mo	Cr	V	Al	Co	P	S	Other	Reference
1	0.79	1.59	1.94	0.3	1.33	0.11						Caballero et al. (2002); Peet and Bhadeshia (2011); Mateo and Bhadeshia (2004)
2	0.75	1.63	1.95	0.28	1.48	0.1	0.01		0.003	0.003		Peet et al. (2004); Jaramillo et al. (2004); Garcia-Mateo et al. (2012a)
3	0.98	1.46	1.89	0.26	1.26	0.09			< 0.002			Garcia-Mateo et al. (2003c, 2004, 2003b); Caballero et al. (2007, 2008c, 2011a); Mateo and Bhadeshia (2004)
4	0.96	1.41	1.93	0.26	1.22	0.10						Chen et al. (2014)
5	0.61	1.66	1.50	0.34	1.39							Kundu et al. (2009)
6	0.56	1.43	0.58		0.47							da Cruz et al. (2012)
7	0.89	1.43	0.19		0.47				0.010	0.006		Wang et al. (2008)
8	0.80	1.60	1.99	0.25	1.29	0.1			< 0.005	< 0.01		Brown and Baxter (2004)
9	0.88	1.63	2.15	0.25	1.25	0.14						Sidhu et al. (2013)
10	0.82	2.45	2.10	0.27	1.50	0.10						Sidhu et al. (2013)
11	0.88	1.51	2.00	0.28	1.78	0.20						Ren et al. (2008)
12	0.8	1.9	0.1	0.25	1.9		0.7					Huang et al. (2013)
13	0.61	1.72	0.75	0.04	0.35						0.21Ni	Leiro et al. (2011)
14	0.98	2.90	0.77		0.45				0.016	0.014	0.21Cu, 0.16Ni	Garcia-Mateo et al. (2012b)
15	0.97	1.43	1.59		0.26	0.09			0.002	0.001	0.04Ni	Hamdany et al. (2012)
16	0.79	1.51	1.98	0.24	0.98	1.58	1.06					Gong et al. (2010)

... continued from previous page

Alloy	C	Si	Mn	Mo	Cr	V	Al	Co	P	S	Other	Reference
17	0.82	1.63	2.20	0.35			1.62					Koczurkiewicz (2012)
18	0.95	0.91	1.30	0.99	2.30						0.17Ti	Hu et al. (2013, 2014a,b)
19	0.80	1.59	2.01	0.24	1.0			1.51	0.002	0.002		Garcia-Mateo et al. (2003a, 2005); Peet et al. (2011)
20	0.73	1.39	3.76	0.25	1.06			1.01				Mateo and Bhadeshia (2004)
21	0.85	1.49	3.40	0.25	1.01			0.93			0.2Cu	Mateo and Bhadeshia (2004)
22	1.15	2.15		0.25	0.58		0.89	1.58	0.008	0.022		Amel-Farzad et al. (2013)
23	0.78	1.60	2.20	0.24	1.01		1.37	3.87				Jaramillo et al. (2004); Hasan et al. (2012); Hasan (2012); Hu et al. (2013)
24	0.79	1.50	1.98	0.24	0.98		1.06	1.58				Beladi et al. (2008); Timokhina et al. (2011b); Hodgson et al. (2011)
25	0.57	1.52	2.02	0.24	1.21		0.65	1.59	0.042	0.014		Soliman and Palkowski (2007)
26	0.76	1.96	1.4	0.24	1.24		0.7	0.14				Shendy et al. (2014)
27	0.78	1.74	2.15	0.24	0.89		1.02	1.48				Sidhu et al. (2013)
28	0.79	1.56	1.98	0.24	1.01		1.01	1.51	0.002	0.002		Garcia-Mateo et al. (2003a); Hase et al. (2006); Zhang and Kelly (2006)
29	0.82	1.55	2.01	0.25	1.01	0.1	1.03	1.51	< 0.005	< 0.01		Brown and Baxter (2004)
30	0.80	1.84	2.18	0.30	1.04		0.85	1.31				Yoozbashi and Yazdani (2010)
31	0.69	1.92	1.38	0.24	1.39		0.75	0.14				Yoozbashi and Yazdani (2010)

... continued from previous page

Alloy	C	Si	Mn	Mo	Cr	V	Al	Co	P	S	Other	Reference
32	0.71	1.61	2.03	0.27	1.04		0.97	0.5				Li and Jin (2010)
33	0.85	1.75	2.15	0.24	1.39	0.1		1.42				Luo et al. (2014)
34	0.94	1.78	2.20	0.24	1.42	0.1		1.45				Luo et al. (2014)
35	0.83	2.0	2.38	Cr+Mo $\leq$ 1.5		0.1			0.028	0.015		Lan et al. (2011)
36	0.83	1.56	1.37		0.81		1.44		0.012	0.005	0.87W	Yang et al. (2012c)
37	0.80	1.67	3.52	0.24	1.01			1.44			0.2Cu, 0.99W	Mateo and Bhadeshia (2004)
38	0.83	1.90	2.28	0.24	1.44	0.11		1.55	0.011	0.008	0.023Nb	Bakshi et al. (2013)
39	0.80	2.47		1.40					0.10		1.86Ni	Vuorinen et al. (2014)
40	0.80	2.47	2.0	1.36					0.10		1.81Ni	Vuorinen et al. (2014)
41	0.80	1.20		1.44					0.10		1.92Ni	Vuorinen et al. (2014)
42	0.80	0.50		1.45					0.20		1.94Ni	Vuorinen et al. (2014)
43	0.48	1.92		0.24	1.47						2.62Ni	Lonardelli et al. (2012a)
44	0.73	1.82		0.23	1.47						4.12Ni	Lonardelli et al. (2012b)
45	0.80	1.51	1.93	0.28	1.08		1.06	1.59	0.008	0.01	powder	Guo et al. (2014)
46	0.99	2.06	1.02	0.29	1.33	0.10			0.014	0.0049	0.0005B, 0.0037N	Chang et al. (2013)
47	0.99	2.06	1.02	0.28	1.32	0.10			0.014	0.0049	0.0024B, 0.0037N	Chang et al. (2013)

## CHAPTER 15

---

### OTHER ASPECTS

---

#### 15.1 Bainite in Iron and its Substitutional Alloys

Bainite can be distinguished in high-purity iron or iron-alloys which have an interstitial content that is less than 0.01 wt%. Kinetic experiments are difficult to conduct for such alloys because the rate of reaction can be very large. The classification of microstructure therefore has to be based on limited evidence. The question arises as to whether there is any essential difference between martensite and bainite in interstitial-free alloys.

Many experiments have been conducted by monitoring the temperature during rapid cooling. The evolution of latent heat due to transformation can cause inflexions in the cooling curves, which in turn indicate the onset of transformation. Continuous cooling experiments on a Fe-14.43Ni-0.01C wt% alloy revealed two plateaux in a plot of the thermal arrest temperature versus the cooling rate (Wilson et al., 1982). The plateau at the higher temperature was identified with bainite, the other with martensite but the microstructural evidence cited to support this interpretation was simply that the lath width was larger for the higher temperature arrest.

There does not seem to be satisfactory evidence to suggest that there is any difference in the mechanism of transformation between bainite and martensite in interstitial-free alloys. On the basis of the theory discussed in Section 6.1.2, the difference between bainite and martensite should vanish as the carbon concentration is reduced to zero.

## 15.2 The Weldability of Bainitic Steels

The region which is adjacent to the fusion zone of a weld is influenced by heat diffusion from the fusion zone. This region is the *heat-affected zone* (HAZ). Its boundaries need not be precisely defined because the definition depends on purpose. The heat dissipated into the HAZ can be detected as the temperature at any point rises to a maximum and then drops gently towards the far-field temperature. The severity of the heating or cooling cycles, and the peak temperature, depends on the location within the HAZ (Grong, 1997). For steels with a high hardenability, regions of the HAZ that have been austenitised by the heat pulse may during cooling, transform into untempered martensite or to some other hard microstructure. These hard regions are susceptible to cold-cracking due to hydrogen embrittlement and other impurity effects.

This is the main reason why hardenable steels, such as nanostructured bainitic steels, are difficult or impossible to weld (Fig. 15.1). The cooling rate can be reduced during welding to avoid the formation of martensite in the HAZ. This can be done by heating the sample before welding begins. But this *preheating* adds to the cost of manufacture. It has been estimated, for example, that the cost of fabricating an aircraft carrier could be reduced by about £ 3 million if the number of panels requiring preheat can be reduced by 50% (Cullison, 1991).

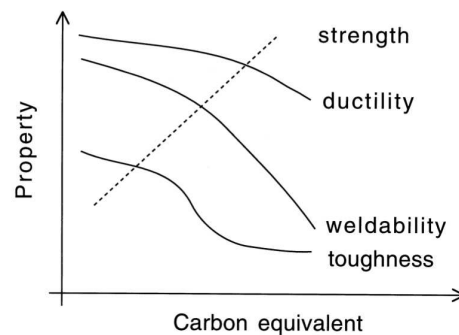


**Figure 15.1** Variation in mechanical properties of the heat-affected zone as a function of the carbon equivalent.

The cold cracking susceptibility correlates empirically with a carbon equivalent (CE), which is a measure of hardenability. There are two popular formulae. The first one is a slightly modified version of the equation originally proposed by Dearden and O'Neill, and adopted by the International Institute for Welding:

$$\text{IIW} > 0.18 \text{ wt\% C} \quad (15.1)$$

$$\text{CE} = w_{\text{C}} + \frac{w_{\text{Mn}} + w_{\text{Si}}}{6} + \frac{w_{\text{Ni}} + w_{\text{Cu}}}{15} + \frac{w_{\text{Cr}} + w_{\text{Mo}} + w_{\text{V}}}{5} \quad \text{wt\%} \quad (15.2)$$

The other equation, due to Ito and Besseyo, has been adopted by the Japanese Welding Engineering Society. It is applied to steels containing less than 0.18 wt% of carbon:

$$\text{Ito - Besseyo} < 0.18 \text{ wt\% C} \quad (15.3)$$

$$CE = w_C + \frac{w_{Si}}{30} + \frac{w_{Mn} + w_{Cu} + w_{Cr}}{20} + \frac{w_{Ni}}{60} + \frac{w_{Mo}}{15} + \frac{w_V}{10} + 5w_B \quad \text{wt\%} \quad (15.4)$$

It is generally accepted that if the carbon equivalent is between 0.35 and 0.55 wt%, then the sample must be preheated prior to welding (the preheat temperature can be as high as 400 °C), and when  $CE > 0.55$ , both pre-heating and post-heating are considered essential to avoid cold-cracking and other difficulties.

The two equations give different values of CE, the Ito and Besseyo method taking a more conservative account of alloying additions. Equation 15.4 is appropriate for modern low-carbon, low-alloy steels such as the ultra-low-carbon bainitic steels [ $C \approx 0.01 \rightarrow 0.03$  wt% (Nakasugi et al., 1980; Lorenz and Duren, 1983)]. For these alloys, the IIW CE gives a pessimistic assessment of weldability whereas the Ito and Besseyo equation works well. It has also been demonstrated (Lorenz and Duren, 1983) that for low-carbon pipeline steels, the IIW CE overestimates the effects of alloying elements like manganese and molybdenum, a more realistic CE being given by:

$$CE = w_C + \frac{w_{Si}}{25} + \frac{w_{Mn} + w_{Cu}}{16} + \frac{w_{Cr}}{20} + \frac{w_{Ni}}{60} + \frac{w_{Mo}}{40} + \frac{w_V}{15} \quad \text{wt\%} \quad (15.5)$$

for weld cooling times of 2-3 s over the temperature range 800-500 °C (these conditions are typical for girth welds in pipelines).

There are good reasons for supposing that the same CE should not apply to medium-carbon and low-carbon steels. There is a disproportionate increase in the growth rates of both allotriomorphic and Widmanstätten ferrite as the carbon concentration drops below  $\approx 0.06$  wt%, when compared with variations in carbon above this value (Bhadeshia, 1985a; Bhadeshia and Svensson, 1993). This is because the average carbon concentration of the alloy approaches the equilibrium solubility of carbon in ferrite. The need to partition carbon into the austenite is thus reduced so that the diffusion-controlled velocity rises sharply.

### 15.3 Electrical Resistance

It follows from the Bloch theorem that anything which disrupts the periodic potential of the lattice causes an increase in the electrical resistance. Thermal vibrations, dislocations, solute atoms and other point defects therefore all contribute to electrical resistance.

The role of dissolved carbon has been modelled by Hoffman and Cohen (1973) using an analogy with the dynamic displacements associated with thermal vibrations. The analogy seems to work well even though the displacements due to carbon are static. Thermal vibrations involve dynamic displacements whose mean square value  $\overline{u_T^2}$  is given by the Debye theory as:

$$\overline{u_T^2} - \overline{u_0^2} = \frac{145}{MT_D} \left( \frac{T}{T_D} \right)^2 \int_0^{T/T_D} \frac{v}{\exp\{v\} - 1} dv \quad (15.6)$$

where  $\overline{u_0^2}$  represents the zero-point quantum vibrations (the units of the displacements are in Å),  $M$  is the atomic weight of iron in grams,  $v$  is a dummy integration variable. Using equation 15.6,  $\overline{u_T^2} - \overline{u_0^2}$  is found to be  $3.25 \times 10^{-5} \text{ nm}^2$  at 295 K at which temperature the measured resistivity  $\rho_T = 9.8 \mu\Omega \text{ cm}$ . The ratio of the resistivity to mean square displacement is to a good approximation found to be constant. If the static displacements due to carbon are known, then this ratio can be used to estimate its contribution to resistivity. The ratio is found to be about  $30.3 \mu\Omega \text{ cm per wt\% C}$ , in excellent agreement with a variety of experimental measurements on martensite.

Bainite is expected to have a lower electrical resistivity than martensite because it has less carbon in solid solution and a lower defect density. On the other hand, its dislocation density is larger than that of pearlite or allotriomorphic ferrite (Chapter 2). Therefore, the electrical resistivity of a specimen fully reacted to bainite is always found to be higher than that of pearlite at the same temperature (Radcliffe and Rollason, 1959). The resistivity decreases in the order austenite, martensite, bainite and pearlite for a given temperature; for a constant microstructure it decreases with temperature (Fig. 15.2).

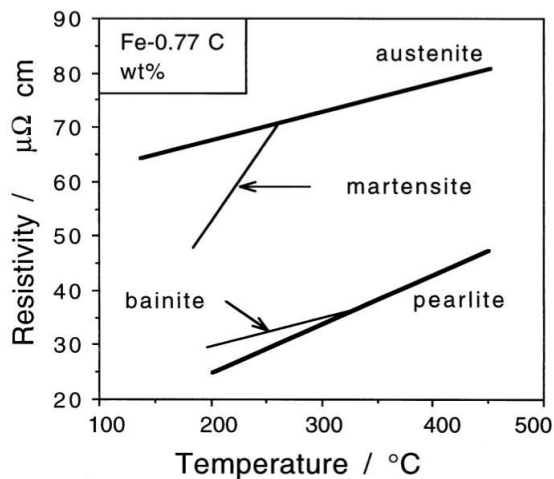


**Figure 15.2** Electrical resistivity of a variety of microstructures in steels (Radcliffe and Rollason, 1959).

Given the differences in resistivity between austenite and bainite, electrical resistance measurements can be used to estimate the fraction of bainite (Simoneau et al., 1978; Yakubtsov and Purdy, 2011):

$$V_V^{\alpha_b} \approx \frac{R^\gamma - R\{t\}}{R^\gamma - R^{\alpha_b}} \quad (15.7)$$

where  $R$  is the resistivity and  $R\{t\}$  the instantaneous resistivity of the sample. If the transformation does not go to completion so that  $R^{\alpha_b}$  cannot be determined, then it is necessary to make independent measurements of the residual austenite, and normalise the equation appropriately. A further assumption is that the resistivity is essentially determined by phase fractions. Carbon in solid solution in austenite is thought to influence resistivity (Simoneau et al., 1978).

#### 15.4 Internal Friction

An elastic material exhibits a stress-strain curve which is precisely reversible. The removal of stress eliminates the strain. The energy stored in the material when under stress is fully recovered. When such a material vibrates in a vacuum it may continue vibrating for an indefinite period of time.

Similar vibrations would decay naturally in an *anelastic* solid, since energy is dissipated by some process occurring within the sample during each vibration. The vibrations are said to be damped. An examination of the damping as a function of temperature and frequency can reveal information about the nature of the dissipative process. *Internal friction*

measurements like these can be used to detect the onset of transformations, since moving interfaces can damp oscillations.

Fig. 15.3 shows typical internal friction spectra from martensite, tempered martensite and bainite in a steel containing 1.23 wt% carbon (Tkalcec and Mari, 2004). The as-quenched structure has much detail as a function of temperature, but the striking comparison is between the tempered martensite and bainite, which exhibit identical internal friction characteristics. This is of course consistent with the fact that bainite can be regarded as martensite that tempers during the course of transformation. The peak at 600 K is identified with the Snoek-Köster relaxation, corresponding to the interaction of carbon atoms with dislocations (Weller, 1983); it is not surprising therefore that it is much stronger when testing untempered martensite.<sup>1</sup>

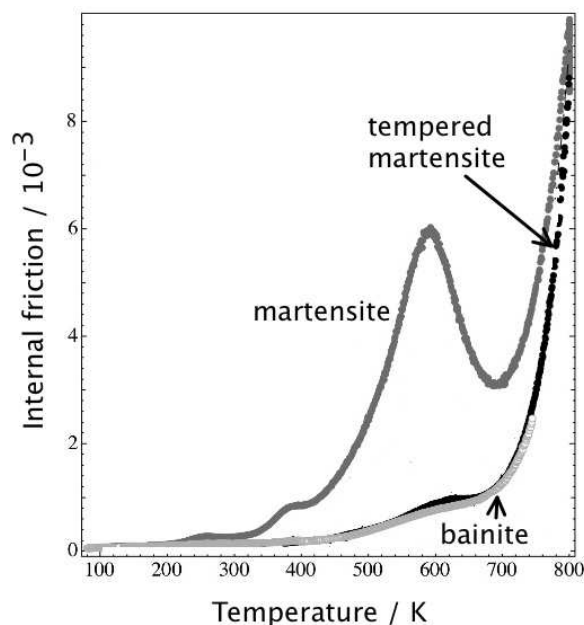


**Figure 15.3** Internal friction data showing almost identical spectra for tempered martensite and bainite. Reproduced with the permission of Elsevier, adapted from Tkalcec and Mari (2004).

## 15.5 Internal Stress

It has long been recognised that the transformation of austenite to martensite causes the development of stresses which are retained in the transformed specimen. These *residual stresses* are usually attributed to the volume change accompanying transformation.

<sup>1</sup>Internal friction measurements conducted during the continuous cooling transformation of a commercial steel to bainite have been interpreted to indicate a *pre-bainitic* microstructural change before the formation of bainite proper (Jihua et al., 1989). The argument is based on an observed rise in damping during continuous cooling at temperatures above  $B_S$ . These experiments are not supported by microstructural evidence nor is the association with bainite proven. The same experiments have demonstrated that the degree of damping decreases monotonically as the transformation progresses, indicating that the concentration of dissipative units (whatever they may be) varies directly with the extent of reaction. The damping at any instant of time increases as the temperature is reduced below  $B_S$ . This is expected because the total amount of bainite that can form increases with undercooling below  $B_S$ .

The volume expansion is not unique to martensite; allotriomorphic ferrite, pearlite, Widmanstätten ferrite, and bainite all cause a decrease in density. There are no data for Widmanstätten ferrite, but the formation of bainite generates residual stresses (Radcliffe and Rollason, 1959; Diesburg et al., 1981). As a general rule, X-ray diffraction peaks from transformations which are displacive (martensite, bainite, Widmanstätten ferrite) are found to be more diffuse than those from reconstructive reactions (allotriomorphic ferrite, pearlite). For example, Radcliffe and Rollason demonstrated a larger lattice strain with martensite and bainite than with pearlite. The diffusion that occurs during reconstructive transformation helps to accommodate the volume change, preventing the development of stresses.

The residual stresses develop mainly because transformation does not usually occur uniformly in all regions of the sample. This can be exploited for case-hardened components, where it is advantageous to have a compressive stress on the surface of the component. The compressive stress prolongs the fatigue life and makes the component more resistant to surface initiated fracture. In steels which are surface carburised and then quenched, the lower carbon core transforms at a higher temperature. The resulting core-volume expansion puts the still austenitic surface regions into tension, though the tensile stress is partly relaxed by plastic deformation. When the surface region eventually transforms to martensite on further cooling, its volume expansion causes stress reversal, so the surface ends up in compression relative to the core (Koistinen, 1958).

Because of the smaller volume expansion that accompanies the transformation to bainite (Goldak et al., 1985), and since plastic relaxation is easier at higher temperatures, a bainitic case is not as effective in introducing a compressive stress at the surface when compared with a martensitic case (Diesburg et al., 1981). Samples containing bainite in the case have lower levels of compressive residual surface stresses. Thus, the performance of case-hardened samples can be improved by adding elements such as molybdenum which encourage martensite to form at the expense of bainite.

## 15.6 Sound Velocity

The speed of sound in metallic materials is given by  $\sqrt{E/\rho}$  where  $E$  is the Young's modulus and  $\rho$  the density. It has been found that in high-strength steels treated to generate a variety of microstructures, the measured sound velocity increases in the order: martensite, bainite, mixtures of pearlite and ferrite, Fig. 15.4 (Gur Hakan and Tuncer, 2005). Density measurements did not correlate with these observations so it was speculated that the differences might be due to modulus variations. Since the velocity of sound in cementite is greater than in ferrite (Scott et al., 2001), an alternative explanation is that it scales with the fraction of cementite.

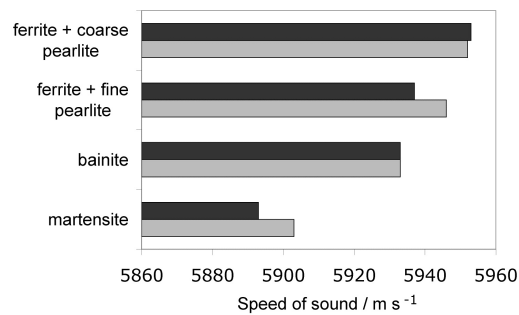


**Figure 15.4** Longitudinal sound velocity in two steels as a function of the microstructure (Gur Hakan and Tuncer, 2005).

### 15.7 Bainite in Iron-Nitrogen Alloys

Both nitrogen and carbon are interstitial solutes in iron and their respective binary phase diagrams with iron show eutectoid reactions in which austenite decomposes into a mixture of ferrite and carbide or ferrite and nitride ( $\text{Fe}_4\text{N}$ ). It is therefore reasonable to expect similar sorts of phase transformations to occur in both alloy systems. It is well established that martensite can form in both Fe-C and Fe-N alloys, but the first report of bainite in an Fe-N alloy was by Bell and Farnell (1969). A Fe-1.8N wt% alloy when transformed isothermally at 350 °C was observed using light microscopy to contain ferrite and  $\text{Fe}_4\text{N}$  with an appearance similar to that of upper bainite in Fe-C alloys. The growth of transformation products was stifled by austenite twin boundaries, consistent with a mechanism in which there is a co-ordinated movement of atoms.

Foet et al. (1988) showed that in a Fe-9N at% alloy, the transformation to bainite is sometimes preceded by the precipitation of  $\text{Fe}_4\text{N}$ , and this seems to have been verified by Jiao et al. (2007). The resulting localised depletion of nitrogen then stimulates the austenite to transform into bainitic ferrite and more  $\text{Fe}_4\text{N}$ , without any change in the lattice parameter of the residual austenite.

Whilst there is evidence for the existence of a bainite reaction in Fe-N alloys, it would be useful to conduct a detailed microstructural characterisation, thermodynamic analysis and crystallographic experiments including the study of surface relief. Nakada et al. (2013) showed that the bainite can form below the  $T'_0$  temperature provided that nitride precipitation occurs first as suggested by Foet et al. (1988); the microstructure consists of fine, dislocated ferrite-plates separated by the  $\text{Fe}_4\text{N}$ , Fig. 15.5.

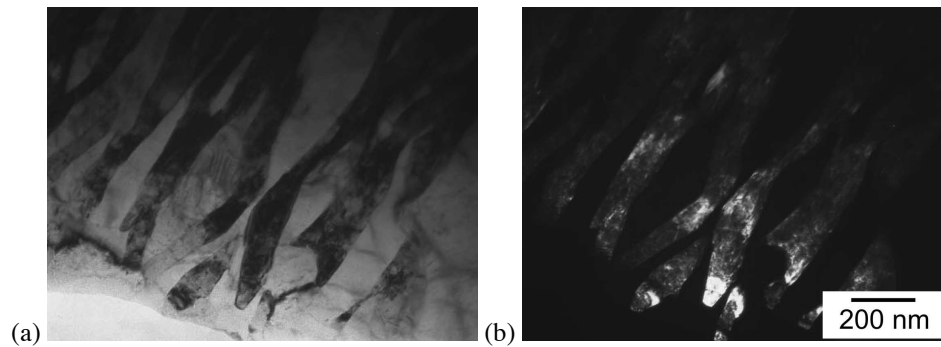


**Figure 15.5** Fe-2.6N wt% alloy transformed isothermally at 570 °C for 1 h, to produce bainite consisting of fine platelets of bainitic ferrite separated by Fe<sub>4</sub>N. (a) Bright field transmission electron micrograph. (b) Corresponding dark-field image of the nitride. Reproduced with permission from Nakada et al. (2013).

### 15.8 Effect of Hydrogen on Bainite Formation

Hydrogen has a bad reputation in the context of steels because when in solution, it undoubtedly embrittles ferrite. However, there are examples in titanium metallurgy where it is introduced temporarily to enable processing, after which it is removed by heat treatment. With this in mind, Yalci and Edmonds (1999) conducted what is probably the first study on the influence of hydrogen on the microstructure and properties of upper bainite.

The studies were conducted on silicon-rich steels to avoid the formation of cementite. The hydrogen was introduced at a pressure of two atmospheres, whilst the alloys were in the austenite phase field. This was followed immediately by isothermal transformation in the bainite temperature range.

The introduction of hydrogen apparently led to a greater amount of upper bainite and the thickness of bainite plates was reduced from  $0.31 \pm 0.06 \mu\text{m}$  to  $0.21 \pm 0.09 \mu\text{m}$  in the hydrogenated alloy. The hardness of the hydrogenated samples was measured to be greater than those that were simply heat treated in helium (Table 15.1). The increase in hardness in the hydrogenated samples is consistent with an increase in the fraction of bainite, since ferrite is at low temperatures harder than austenite.

**Table 15.1** Hardness of Fe-0.2C-3Mn-2.1Si wt% and Fe-0.4C-4.09Ni-1.99Si wt% alloys transformed isothermally at 390 °C after austenitisation at 920 °C for 30 min. The samples were sealed in chambers containing either helium or hydrogen at 2 atmospheres pressure throughout these heat treatments. After Yalci and Edmonds (1999). HV30 refers to the Vickers hardness measured using a 30 kg load.

Alloy	Mn-containing alloy		Ni-containing alloy	
	Helium	Hydrogen	Helium	Hydrogen
HV30	367	409	364	383

## 15.9 Magnetically-Induced Bainite

It has long been known that magnetic fields must influence the transformation from austenite to martensite (Krivoglaz and Sadovskiy, 1964; Kakeshita et al., 1985). The two phases have different magnetic properties so the application of a magnetic field encourages the formation of the ferromagnetic martensite.

Ohtsuka (2006) have shown that the major effect of the field is to raise the transformation temperature and accelerate the rate of transformation (Fig. 15.6). For reasons that are not clear, the field does not lead to any alignment of plates along its orientation so that variant selection of the type observed during stress-affected transformation seems to be absent.

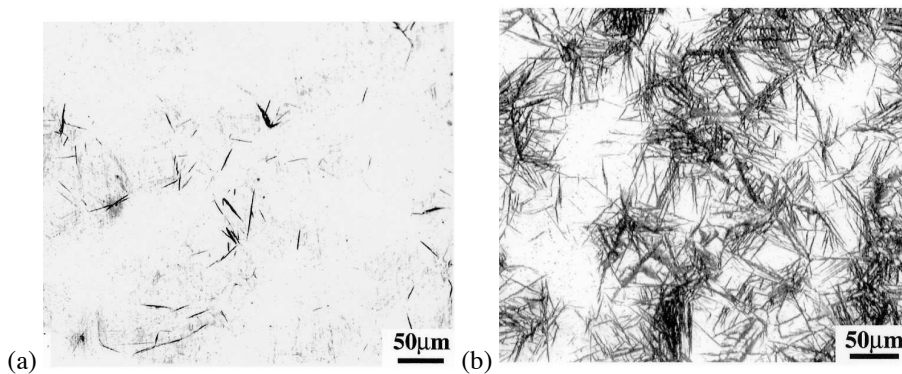


**Figure 15.6** A Fe-0.52C-0.24Si-0.84Mn-1.76Ni-1.27Cr-0.35Mo-0.13V wt% steel austenitised at 1273 K for 600 s and transformed isothermally to bainite at 573 K for 480 s, followed by helium quenching to ambient temperature. (a) Zero magnetic field; (b) sample under the influence of a 10 Tesla magnetic field during transformation. Micrographs courtesy of H. Ohtsuka.

## 15.10 Characterisation of Bainite

The vast set of tools now available to examine structures over a range of length scales and chemical compositions have led to some confusion in the interpretation of data on bainitic steels using simple experiments. The purpose here is not to describe the techniques in depth, nor all the techniques available, but to reinforce the knowledge on certain specific methods of particular use in characterising bainitic microstructures.

### 15.10.1 Optical Microscopy and Hardness

A bainitic plate is typically a quarter of a micrometre in thickness and associated features such as carbides may be even finer. This scale is about half the wavelength of light, making it impossible to resolve the structure using optical microscopy. Nevertheless, when present in mixed microstructures, it is easy to distinguish bainite from untempered martensite. Fig. 15.7 shows two images taken from partially transformed medium-carbon steels, etched using nital. The first one has a small fraction of bainite with untempered martensite in the background. *Sheaves*, not sub-units, of bainite are clearly visible, emanating from

the austenite grain boundaries. They etch darker relative to untempered martensite because they have considerable internal structure as evident in Fig. 2.1. An internal structure provides a lot of interfaces that can be attacked by an etchant.

The second micrograph, Fig. 15.7b has a much greater fraction of bainite, but the light-etching regions are easily distinguished as untempered martensite. Notice also the small traces of bainite within the light-etching regions, which appear like plates, and similarly, the many straight edges of the martensitic regions. Another example of the different etching characteristics of bainite and untempered martensite is Fig. 1.1.

The distinction of bainite from Widmanstätten or allotriomorphic ferrite is easy because they both etch white in mixed microstructures due to the absence of substantive internal structure, Fig. 15.7c and 2.1.

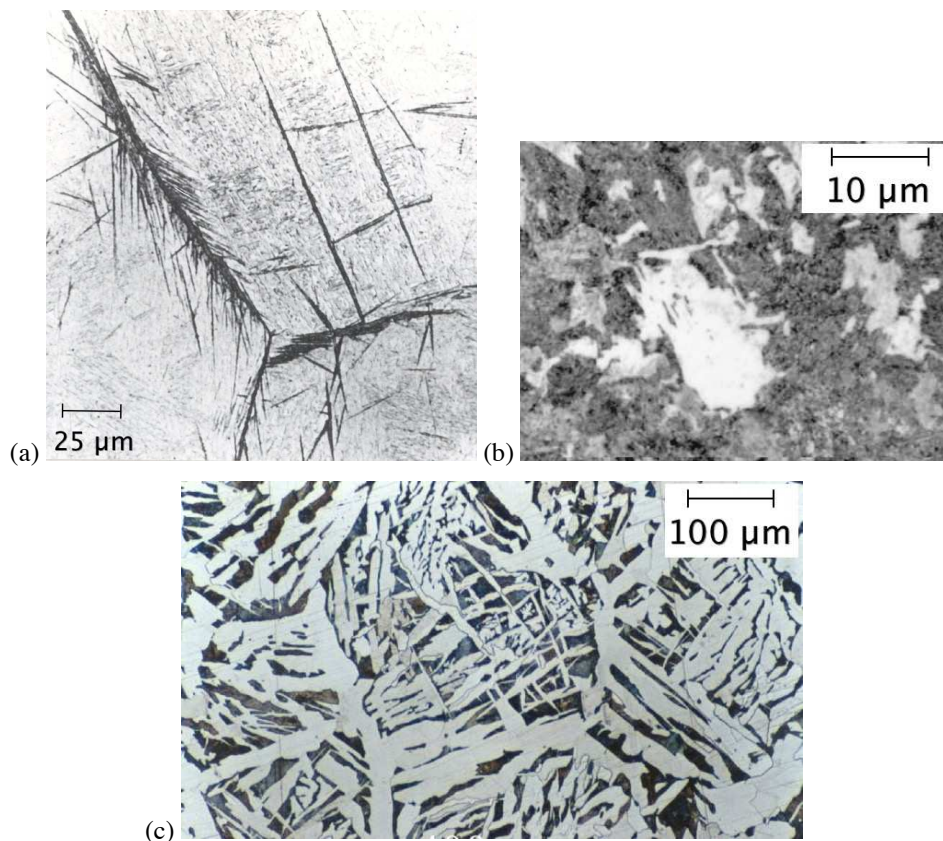


**Figure 15.7** (a,b) Optical micrographs of mixtures of bainite and untempered martensite. (c) Allotriomorphic ferrite, Widmanstätten ferrite and iridescent pearlite.

The internal structure referred to above can either be the retained austenite films between individual sub-units, or carbide particles. Therefore, the difference in etching characteristic between bainite and untempered martensite becomes smaller as the carbon concentration is reduced. In very low carbon steels it therefore becomes impossible to distinguish the phases using optical microscopy. In such circumstances, the hardness of freshly quenched martensite ( $HV_{\alpha'}$ ) and of a fully bainitic sample ( $HV_{\alpha_b}$ ) can be utilised to esti-

mate the relative fractions of the phases:

$$V_V^{\alpha_b} \approx \frac{HV_{\alpha'} - HV}{HV_{\alpha'} - HV_{\alpha_b}}, \quad (15.8)$$

the approximation arising because of the assumption that the hardness of each phase is independent of the volume fraction of bainite. If the hardness data for the pure phases are not available, then the following empirical equations (Blondeau et al., 1975) may be used:

$$\begin{aligned} HV_{\alpha'} &= 127 + 949w_C + 27w_{Si} + 11w_{Mn} + 8w_{Ni} + 16w_{Cr} + 21 \log \dot{T} \\ HV_{\alpha_b} &= -323 + 185w_C + 330w_{Si} + 153w_{Mn} + 65w_{Ni} + 144w_{Cr} + 191w_{Mo} \\ &\quad + (89 + 53w_C - 55w_{Si} - 22w_{Mn} - 10w_{Ni} - 20w_{Cr} - 33w_{Mo}) \times \log \dot{T} \\ HV_{\alpha/P} &= 42 + 223w_C + 30w_{Mn} + 12.6w_{Ni} + 7w_{Cr} + 19w_{Mo} \\ &\quad + (10 - 19w_{Si} + 4w_{Ni} - 8w_{Cr} + 130w_V) \times \log \dot{T} \end{aligned} \quad (15.9)$$

where  $\dot{T}$  is the cooling rate in  $^{\circ}\text{C h}^{-1}$ . The equation applies over the range  $0.1 < w_C < 0.5$ ,  $w_{Si} < 1$ ,  $w_{Mn} < 2$ ,  $w_{Ni} < 4$ ,  $w_{Cr} < 3$ ,  $w_{Mo} < 1$ ,  $w_V < 0.2$ ,  $(w_{Mn} + w_{Ni} + w_{Cr} + w_{Mo}) < 5$ .  $w_i$  represents the wt% of the solute identified in the subscript.

### 15.10.2 Dilatometry

The densities of ferrite and austenite are different, so dilatometry can be used to follow transformations as they occur. This provides extremely powerful information on the evolution of structure. Fig. 15.8a shows a typical isothermal transformation curve where the recorded plastic strain  $\epsilon$ , assumed isotropic, can be used to deduce the fraction of bainite as a function of time. One method of converting  $\epsilon$  into  $V_{\alpha_b}/V$  is by reference to Fig. 15.8b, where the curves marked  $\alpha$  and  $\gamma$  represent the thermal expansion of the ferrite and austenite respectively. The expansivity for  $\alpha$  can be derived by tempering the sample so that there is no austenite, followed by slow heating to a temperature below  $Ae_1$ , and that for  $\gamma$  derived by slow cooling from the austenite phase field to a temperature above  $Ae_3$ , with extrapolation into temperature domains where mixtures of phases exist. This has the assumption that the presence of a small amount of cementite in the tempered sample does not influence the expansivity of the ferrite significantly.

At any particular temperature, the volume fraction of bainite is given by

$$V_V^{\alpha_b} \approx \frac{\epsilon_1}{\epsilon_1 + \epsilon_2} \quad (15.10)$$

where  $\epsilon_1$  is the transformation strain recorded either during continuous cooling or isothermally. Note that both of the experiments illustrated in Fig. 15.8 are necessary in order to interpret the isothermal experiments, because it cannot be assumed that the maximum strain recorded corresponds to 100% of bainite. Furthermore, the maximum strain is a function of temperature since the expansivities of austenite and ferrite are not identical.

The transformation strain can be more accurately converted into the volume fraction of bainite given a knowledge of the lattice parameters of all the phases involved as a function of temperature, composition and phase fractions, but the calculations can be sensitive to errors in such data because, for example, the calculations depend on small differences in the volume per atom of austenite and ferrite (Takahashi and Bhadeshia, 1989; Bhadeshia et al., 1991; Onink et al., 1996; Caballero et al., 2005).

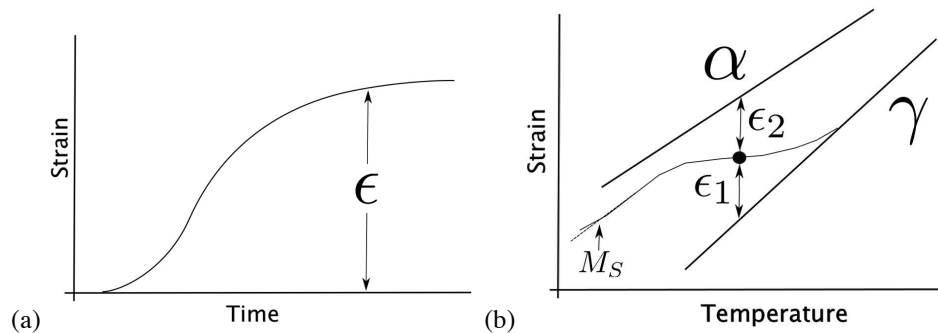


Figure 15.8 Typical dilatometric data.

### 15.10.3 Atomic Force Microscopy

An atomic-force microscope allows the three-dimensional characterisation of surface topography. The specimens can be ordinary metallographic samples and can be studied in the ambient atmosphere.

The technique has been applied to determine the fine microstructure of TRIP steels containing allotriomorphic ferrite, bainitic ferrite, austenite and martensite because their resistance to etching increases in this order (Ros-Yáñez et al., 2001). It follows that the highest peaks on the surface of the etched samples correspond to austenite and martensite, and the lowest ones to allotriomorphic ferrite. The austenite and martensite can be differentiated only by detailed analysis of their surface roughnesses.

Quite remarkable distributions of carbides have been revealed using this technique on electropolished surfaces, because the rate of polishing depends on phase and does not leave the surface perfectly flat (Hayakawa et al., 2002).

### 15.10.4 X-ray Diffraction and Retained Austenite

Diffraction is a convenient way of determining accurately the amount of retained austenite. X-rays typically penetrate about  $10\ \mu\text{m}$ . It is in this sense a surface measurement technique and as such can be affected by the sample preparation method. In particular, deformation of the surface layer can lead to the transformation of the retained austenite. Other techniques such as neutron diffraction and Mössbauer spectroscopy scan greater depths. By comparing these methods against X-ray measurements, Perry et al. (2006) showed that about  $500\ \mu\text{m}$  of the surface needs to be removed by electropolishing or chemical attack in order to avoid influencing the retained austenite content.

A convenient way of measuring the carbon concentration of retained austenite is to determine its lattice parameter, which is expanded by dissolved carbon. The extent of the expansion yields the carbon concentration given a relationship between the concentration and parameter. A number of such relationships have been assessed by Scott and Drillet (2007) by comparison against experiments. This suggests that the variation of the lattice parameter of austenite with the carbon concentration should be  $0.0033\ \text{nm}$  per wt%, with the ambient temperature carbon-free lattice parameter being in the range  $0.3572\text{--}0.3578\ \text{nm}$ ; therefore, the minimum error expected in  $x_\gamma$  is  $\pm 0.24\ \text{wt}\%$ .

### 15.10.5 Electron Backscattered Diffraction

The ability to produce images that include both morphology and crystal orientation of each grain has had a major effect on the understanding of the relationship between structure and properties. The technique is now widespread and has led to a plethora of studies of the crystallography. Some of the important outcomes in the context of bainite can be listed as follows:

1. the role of texture in partly explaining the anisotropic toughness of pipe steels, as reviewed by Joo et al. (2013);
2. the importance of crystallographic grain size as opposed to morphological grain size in determining toughness, reviewed by Gourgues-Lorenzon (2007);
3. the precise measurement of microscopic accommodation strains in austenite surrounding displacive transformation products (Miyamoto et al., 2009);
4. in characterising variant selection when transformation occurs under external influence, assessed by Kundu (2014). In this case there are mixed results since the term 'variant selection' is sometimes applied to the case where there is no external influence or internal drivers, because it is incorrectly assumed that all 24 possible variants must form in any given austenite grain in order for selection to be absent.

An area where considerable care is needed in the interpretation of results is the measurement of orientation relationships. The  $\alpha_b/\gamma$  relationship is irrational and hence there will always be 24 possible variants possible in any given austenite grain. However, the tendency in the majority of papers has been to interpret the orientation in terms of the Nishiyama-Wasserman or Kurdjumov-Sachs relationships which are not appropriate for displacive transformations (Knowles et al., 1982), without realising that the accuracy is compromised by the fact that there is an orientation spread in austenite due to the nature of a displacive transformation which introduces defects within the austenite (Fig. 15.9), and because of the limitations of the technique. With meaningful statistics, the conclusion was reached some time ago that there will be a spread in the orientations measured (Nolze, 2004). The exercise is in any case futile since once the orientation relation has been determined its consequences are rarely discussed since properties are not particularly sensitive to variations within the Bain region.

### 15.10.6 Kernel Average Misorientation

This is a measure of the local grain misorientation around a measurement point, relative to a number of surrounding points, during electron backscatter diffraction, usually conducted in a scanning electron microscope. The diffraction allows the differentiation of austenite and ferrite, but the kernel average helps distinguish allotriomorphic ferrite from bainite. The orientation of the allotriomorphic ferrite does not vary much over the scale of the grains whereas there may be strong gradients once bainite is encountered due to the defects associated with displacive transformation. Fitting is required in order to obtain a threshold value of the kernel average. Fig. 15.10 shows an example where the step size was 100 nm. It is evident that there are resolution problems because the bainite regions appear homogeneous whereas in reality they consist of fine bainitic ferrite plates separated by films of retained austenite. It is understood that electron backscatter diffraction in general underestimates the amount of retained austenite due to resolution issues.

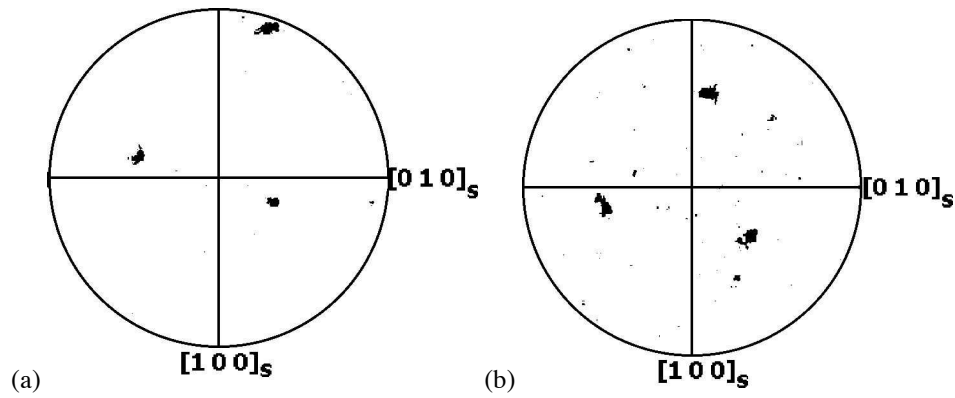


**Figure 15.9** (Pole figures derived using electron backscattered diffraction, from two different austenite grains containing bainite, showing the spread in orientation within the austenite (Kundu et al., 2007).

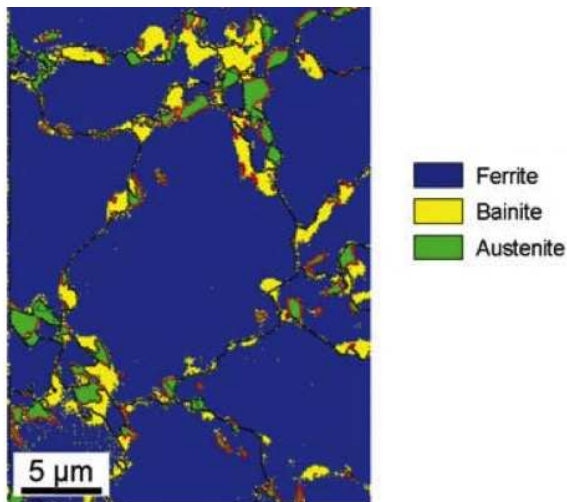


**Figure 15.10** Phase distribution obtained using an optimised kernel average threshold method for a TRIP-assisted steel. The dark lines represent large misorientation grain boundaries, and the red lines are between bainitic ferrite and austenite with the expected orientation relationship. Adapted with permission of John Wiley and Sons, from Zaefferer et al. (2008).

## CHAPTER 16

---

# THE TRANSFORMATIONS IN STEEL

---

Probably the most interesting revelations are made when *all* of the decomposition reactions of austenite are examined together. And the most awkward question seeks to discover the difference between the variety of transformation products. This chapter is intended to be a brief picture of how these transformations fit together, in a way that is consistent with the available experimental and theoretical data (Fig. 16.1).

There is ample evidence that the different forms of ferrite can be categorised into those which grow by displacive transformation and the others which grow by a reconstructive mechanism. Amongst the displacive transformations are Widmanstätten ferrite, bainite, acicular ferrite and martensite, all of which are characterised uniquely by their plate or lath shapes and the striking invariant-plane strain surface relief which accompanies transformation. An important feature of this strain is the large shear component which is the dominant reason for the plate shape of the transformation product. There is no equilibrium at the transformation front; substitutional solutes do not partition between the parent and product phases.

Widmanstätten ferrite grows at high temperatures by a paraequilibrium mechanism in which the plates lengthen at a rate controlled by the diffusion of carbon in austenite. This diffusion does not contradict its displacive character because interstitials can migrate without affecting the IPS shape deformation. The transformation occurs at small driving forces, so that the shape change consists of two adjacent invariant-plane strains which tend to mutually accommodate and hence reduce the strain energy. This also explains the thin-wedge shape of Widmanstätten ferrite because the adjacent plates are different crystallographic variants (Fig. 16.2).

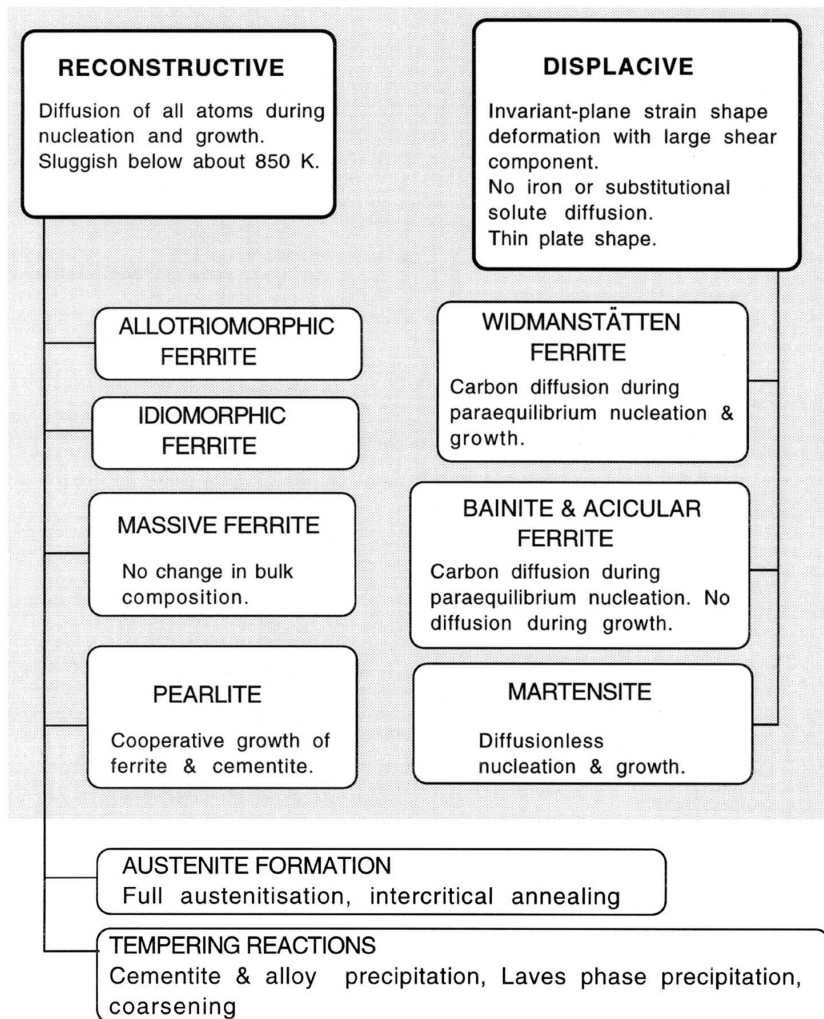


**Figure 16.1** Flowchart summarising the characteristics of transformations in steels.

Carbon must diffuse during the nucleation of both Widmanstätten ferrite and bainite. Nucleation probably occurs by a process akin to the dissociation of arrays of dislocations. This follows from the observation that the activation energy for nucleation is directly proportional to the driving force, rather than the inverse square relationship implied by a heterophase fluctuation model of nucleation. Both Widmanstätten ferrite and bainite develop from the same nucleus; it develops into bainite if diffusionless growth is possible at the temperature where nucleation becomes possible. Otherwise it evolves into Widmanstätten ferrite.

Bainite probably grows without diffusion, but some of the excess carbon is soon after transformation, rejected into the residual austenite. The partitioned carbon may then precipitate as carbides, giving the classical upper bainitic microstructure. At somewhat lower transformation temperatures where the partitioning of carbon is slower, a proportion of the

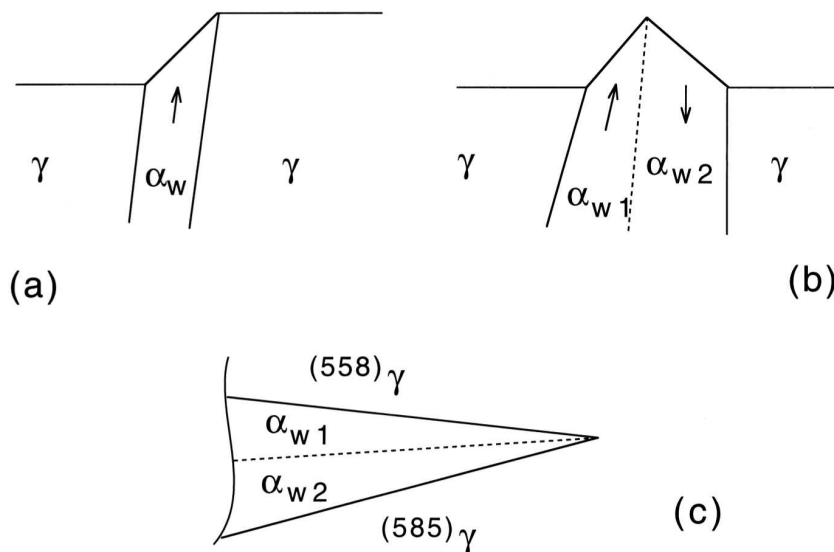


**Figure 16.2** Widmanstätten ferrite. (a) A single invariant-plane strain shape deformation. (b) The combined effect of two mutually accommodating, back-to-back IPS deformations. (c) The morphology of two plates, with different habit plane variants, growing together in a mutually accommodating manner.

excess carbon has the opportunity to precipitate inside the bainitic ferrite. This leads to the lower bainitic microstructure. There is a substantial amount of carbon that stubbornly remains in solid solution within the bainitic ferrite, irrespective of whether it is upper or lower bainite.

Bainite grows at temperatures where the austenite is mechanically weak and unable to elastically accommodate the shape deformation. As a result, the dislocations generated during the plastic deformation of the adjacent austenite, cause a loss of coherency at the  $\alpha_b/\gamma$  interface. The growth of the bainite platelet therefore is arrested before it hits any hard obstacle such as an austenite grain boundary. Continued transformation therefore requires new platelets to form, giving rise to clusters of parallel sub-units with identical crystallographic orientation, habit plane and size. These clusters are known as sheaves of bainite. Acicular ferrite is an alternative, more chaotic morphology of bainite in which the plates are intragranularly nucleated on nonmetallic inclusions and hence grow in many different directions from the nucleation site.

The possibility remains that the transition from Widmanstätten ferrite to bainite involves a gradual increase in carbon supersaturation, rather than a sudden change from paraequilibrium to diffusionless growth.

Martensitic transformation is diffusionless, both during nucleation and during growth.

The reconstructive transformations include allotriomorphic and idiomorphic ferrite, and pearlite in its various forms. It is important to appreciate that all elements, including iron, must diffuse during reconstructive transformation in order to achieve the structural change without the strains characteristic of displacive reactions. None of these transformations are associated with shear strains.

A prominent feature of the eutectoid decomposition reaction which leads to the formation of pearlite is that the ferrite and carbide phases grow with a common transformation front with the austenite. They are said to grow cooperatively.

Fig. 16.1 lists the growth of austenite by a reconstructive mechanism. This is not always the case. However, extraordinarily large heating rates are needed in all practical circumstances to change the growth mode into one which is displacive. The precipitation of alloy carbides undoubtedly occurs by reconstructive transformation with the long-range diffusion of substitutional solutes. However, this is not necessarily the case for the iron carbides, which can grow at temperatures where the diffusion of iron is inconceivable.

### 16.1 Key Characteristics of Transformations in Steels

Table 16.1 lists the key characteristics of phase transformations in steels. It is important during the identification of phases or phase mixtures in steels, to conduct sufficient experiments so that ambiguity is avoided. An example of the application of the method is in the HTP version of pipeline steel, where a plethora of vague microstructural descriptions existed in the literature, prior to investigations based the scheme described here (Chapter 13). The nature of acicular ferrite was similarly established (Chapter 10).

Such identifications can be useful in making predictions about the behaviour of the steel when process or composition modifications are considered.

**Table 16.1** Key transformation characteristics in steels. Martensite  $\alpha'$ , lower bainite  $\alpha_{lb}$ , upper bainite  $\alpha_{ub}$ , acicular ferrite  $\alpha_a$ , Widmanstätten ferrite  $\alpha_w$ , allotriomorphic ferrite  $\alpha$ , idiomorphic ferrite  $\alpha_i$ , pearlite  $P$ , substitutional solutes  $X$ . Consistency of a comment with the transformation concerned is indicated by =, inconsistency by  $\neq$ ; a bullet  $\bullet$  identifies the case where the comment is only sometimes consistent with the transformation. The term *parent*  $\gamma$  implies the  $\gamma$  grain from which the product phase grows. Adapted from Bhadeshia (1992).

Comment	$\alpha'$	$\alpha_{lb}$	$\alpha_{ub}$	$\alpha_a$	$\alpha_w$	$\alpha$	$\alpha_i$	$P$
Nucleation and growth reaction	=	=	=	=	=	=	=	=
Plate shape	=	=	=	=	=	$\neq$	$\neq$	$\neq$
IPS shape change with large shear	=	=	=	=	=	$\neq$	$\neq$	$\neq$
Lattice correspondence during growth	=	=	=	=	$\neq$	$\neq$	$\neq$	$\neq$
Co-operative growth of ferrite and cementite	$\neq$	$\neq$	$\neq$	$\neq$	$\neq$	$\neq$	$\neq$	=
High dislocation density	=	=	=	=	$\bullet$	$\neq$	$\neq$	$\neq$
Necessarily has a glissile interface	=	=	=	=	=	$\neq$	$\neq$	$\neq$
Always has an orientation within the Bain region	=	=	=	=	=	$\neq$	$\neq$	$\neq$
Grows across austenite grain boundaries	$\neq$	$\neq$	$\neq$	$\neq$	$\neq$	=	=	=
High interface mobility at low temperatures	=	=	=	=	=	$\neq$	$\neq$	$\neq$
Acoustic emissions during transformation	=	=	=					
Reconstructive diffusion during growth	$\neq$	$\neq$	$\neq$	$\neq$	$\neq$	=	=	=
Bulk redistribution of X atoms during growth	$\neq$	$\neq$	$\neq$	$\neq$	$\neq$	$\bullet$	$\bullet$	$\bullet$
Displacive transformation mechanism	=	=	=	=	=	$\neq$	$\neq$	$\neq$
Reconstructive transformation mechanism	$\neq$	$\neq$	$\neq$	$\neq$	$\neq$	=	=	=
Diffusionless nucleation	=	$\neq$	$\neq$	$\neq$	$\neq$	$\neq$	$\neq$	$\neq$
Only carbon diffuses during nucleation	$\neq$	=	=	=	=	$\neq$	$\neq$	$\neq$
Reconstructive diffusion during nucleation	$\neq$	$\neq$	$\neq$	$\neq$	$\neq$	=	=	=
Often nucleates intragranularly on defects	=	$\neq$	$\neq$	=	$\neq$	$\neq$	=	$\neq$
Diffusionless growth	=	=	=	=	$\neq$	$\neq$	$\neq$	$\neq$
Local equilibrium at interface during growth	$\neq$	$\neq$	$\neq$	$\neq$	$\neq$	$\bullet$	$\bullet$	$\bullet$
Local paraequilibrium at interface during growth	$\neq$	$\neq$	$\neq$	$\neq$	=	$\bullet$	$\bullet$	$\neq$
Diffusion of carbon during transformation	$\neq$	$\neq$	$\neq$	$\neq$	=	=	=	=
Carbon diffusion-controlled growth	$\neq$	$\neq$	$\neq$	$\neq$	=	$\bullet$	$\bullet$	$\bullet$
Incomplete reaction phenomenon	$\neq$	=	=	=	$\neq$	$\neq$	$\neq$	$\neq$

## 16.2 Notes Related to Table 16.1

Nucleation and growth reactions are of first order in the Ehrenfest classification; in all such reactions, the parent and product phases can coexist, and are separated by well-defined interfaces. Martensitic transformations, although they can be rapid, still involve a nucleation and growth process.

It is significant that all of the ferrite crystals which grow in the form of plates cause an invariant-plane shape deformation which is dominated by shear. The ferrite within pearlite does not have a plate morphology; Hillert showed some time ago that it is wrong to consider pearlite as alternating layers of ferrite and cementite - instead a colony of pearlite is an interpenetrating bicrystal of ferrite and cementite.

Reconstructive diffusion is the flow of matter necessary to avoid the strains characteristic of displacive transformations. A diffusional transformation may phenomenologically be regarded as a combination of a lattice change and a recrystallisation of the product phase, reconstructive diffusion being the flow necessary for the recrystallisation process.

In diffusionless transformations, it is possible to specify (in a localised region at least) how particular vectors, planes and unit cells of one structure (defined by an imaginary labelling of the individual atoms) are derived from *corresponding* vectors, planes and unit cells of the other structure. This is termed a lattice correspondence and it defines a pure lattice deformation which carries the original lattice points, or some fraction of these points into points of the new lattice. When interstitial atoms are present, they may move over large distances during transformation without affecting the lattice correspondence; this is sometimes loosely expressed by stating that there is an atomic correspondence for the solvent and substitutional solute atoms but not for the interstitial atoms. A further relaxation of the condition is to allow the solvent and substitutional solute atoms to be displaced during transformation among the sites specified by the lattice correspondence, but not to create new sites or to destroy any specified sites; in this way the lattice correspondence is preserved but there is no longer an atomic correspondence. Note that in the classification presented above, the single atomic jumps of interstitial atoms needed to destroy Zener ordering (which is produced automatically by the Bain correspondence) are not taken into account.

Even though two crystals may have an identical *bulk* composition, it may not be concluded that their compositions at the transformation interface are identical. There are modes of transformation (e.g. negligible partitioning local equilibrium) where the bulk compositions are predicted to be identical but where the phases differ in the vicinity of the transformation interface. For plain carbon steels, there is no difference between equilibrium and paraequilibrium.

The incomplete reaction phenomenon implies that when a reaction can be studied in isolation, it stops before the phases reach their equilibrium or paraequilibrium compositions when stored energy terms have been accounted for.

An orientation within the Bain region means a reproducible relation which may be irrational but is close to the rational NW or KS relations.

Massive ferrite is not classified as a separate morphology since it can be included within allotriomorphic or idiomorphic ferrite.

## Bibliography

---

- Aaronson, H. I., 1962. The proeutectoid ferrite and the proeutectoid cementite reactions. In: Zackay, V. F., Aaronson, H. I. (Eds.), *Decomposition of Austenite by Diffusional Processes*. Interscience, New York, USA, pp. 387–548.
- Aaronson, H. I., 1969. On the problem of the definitions and the mechanisms of the bainite reaction. In: *The Mechanisms of Phase Transformations in Crystalline Solids*. Institute of Metals, London, U.K., pp. 270–281.
- Aaronson, H. I., Domian, H. A., 1966. Partitioning of alloying elements between austenite and proeutectoid ferrite and bainite. TMS-AIME 236, 781–796.
- Aaronson, H. I., Domian, H. A., Pound, G. M., 1966a. Thermodynamics of the austenite – proeutectoid ferrite transformation I, Fe-C alloys. TMS-AIME 236, 753–767.
- Aaronson, H. I., Domian, H. A., Pound, G. M., 1966b. Thermodynamics of the austenite – proeutectoid ferrite transformation II, Fe-C-X alloys. TMS-AIME 236, 768–780.
- Aaronson, H. I., Laird, C., Kinsman, K. R., 1970. Mechanisms of diffusional growth of precipitate crystals. In: *Phase Transformations*. ASM, Metals Park, Ohio, USA, pp. 313–396.
- Aaronson, H. I., R.Plichta, M., Franti, G. W., Russell, K. C., 1978. Precipitation at interphase boundaries. *Metallurgical Transactions A*, 363–371.
- Aaronson, H. I., Wells, C., 1956. Sympathetic nucleation of ferrite. *Trans. A.I.M.E.* 206, 1216–1223.
- Abe, F., 2004. Bainitic and martensitic creep-resistant steels. *Current Opinion in Solid State and Materials Science* 8, 305–311.
- Abe, F., Araki, H., Noda, T., 1990. Microstructural evolution in bainite martensite and delta-ferrite of low activation Cr-2W ferritic steels. *Materials Science and Technology* 6, 714–723.
- Abe, K., Shimizu, M., Takashima, S., Kaji, H., 1988. Metallurgical meanings of niobium addition in the formation of acicular ferrite in low carbon steel manufactured by accelerated cooling process. In: Tamura, I. (Ed.), *International Conference on Physical Metallurgy of Thermomechanical Processing of Steels and Other Metals*. Vol. 1. Iron and Steel Institute of Japan, Tokyo, Japan, pp. 322–329.
- Abe, T., Tsukada, K., Kozasu, I., 1985. Role of interrupted accelerated cooling and microalloying on weldable HSLA steels. In: Gray, J. M., Ko, T., Zhang, S., Wu, B., Xie, X. (Eds.), *HSLA Steels: Metallurgy and Applications*. ASM International, Metals Park, Ohio, USA, pp. 103–111.
- Abson, D. J., 1987. Nonmetallic inclusions in ferritic steel welds – a review. Tech. Rep. IIW Doc. IX-1486-87, International Institute of Welding, Villepinte, France.

- Abson, D. J., Pargeter, R. J., 1986. Factors influencing the as-deposited strength, microstructure and toughness of manual metal arc welds suitable for C-Mn steel fabrications. *International Materials Reviews* 31, 141–196.
- Adcock, J. N., 1962. The laminar jet system for cooling hot steel strip. *Journal of the Iron and Steel Institute* 200, 909–913.
- Afrouz, A., Collins, M. J., Pilkington, R., 1983. Microstructural examination of 1Cr 0.5Mo steel during creep. *Metals Technology* 10, 461–463.
- Ågren, J., 1989. A simplified treatment of the transition from diffusion controlled to diffusionless growth. *Acta Metallurgica* 37, 181–189.
- Airod, A., Petrov, R., Colas, R., Houbaert, Y., 2004. Analysis of the TRIP effect by means of axisymmetric compressive tests on a Si-Mn bearing steel. *ISIJ International* 44, 179–186.
- Akbasoglu, F. C., Edmonds, D. V., 1990. Rolling contact fatigue and fatigue crack propagation in 1C-1.5Cr bearing steel in bainitic condition. *Metallurgical Transactions A* 21, 889–893.
- Al-Salman, S. A., Ridley, N., 1984. Partitioning of nickel during pearlite growth. *Scripta Metallurgica* 18, 789–791.
- Alberry, P. J., Brunnstrom, R. R. L., Jones, K. E., 1983. Computer model for predicting HAZ structures in mechanised welds. *Metals Technology* 10, 28–38.
- Alberry, P. J., Jones, W. K. C., 1977. Structure and hardness of 0.5CrMoV and 2CrMo simulated HAZ. *Metals Technology* 4, 557–566.
- Alberry, P. J., Jones, W. K. C., 1979. A computer model for the prediction of HAZ microstructure in multipass welds. *Tech. Rep. R/M/R282*, Central Electricity Generating Board, Leatherhead, Surrey, U.K.
- Ali, A., Bhadeshia, H. K. D. H., 1989. Growth rate data on bainite in alloy steels. *Materials Science and Technology* 5, 398–402.
- Ali, A., Bhadeshia, H. K. D. H., 1990. Aspects of the nucleation of Widmanstätten ferrite. *Materials Science and Technology* 6, 781–784.
- Ali, A., Bhadeshia, H. K. D. H., 1991. Microstructure of high strength steel refined with intragranularly nucleated Widmanstätten ferrite. *Materials Science and Technology* 7, 895–903.
- Allen, N. P., Pfeil, L. B., Griffiths, W. T., 1939. The determination of the transformation characteristics of alloy steels. *Tech. Rep. ISI Special Report 2*, Iron and Steel Institute, London, U.K.
- Allten, A. G., 812-829 1954. Discussion to “the effect of silicon on the kinetics of tempering”. *Trans. ASM* 46.
- Allten, A. G., Payson, P., 1953. The effect of silicon on the tempering of martensite. *Trans. ASM* 45, 498–532.
- Almaraz, G. M. D., 2008. Prediction of very high cycle fatigue failure for high strength steels, based on the inclusion geometrical properties. *Mechanics of Materials* 40, 636–640.
- Amano, K., Hatomura, T., Shiga, C., Enami, T., Tanaka, T., 1988. Effect of accelerated cooling condition on ferritic and subsequent second phase transformation from deformed austenite. In: Ruddle, G. E., Crawley, A. F. (Eds.), *Accelerated Cooling of Rolled Steel*. Pergamon Press, Oxford, U. K., pp. 43–56.
- Amel-Farзад, H., Faridi, H. R., Rajabpour, F., Abolhasani, A., Kazemi, S., Khaledzadeh, Y., 2013. Developing very hard nanostructured bainitic steel. *Materials Science & Engineering* 559, 68–73.
- Amin, R. K., Pickering, F. B., 1981. Ferrite formation from thermo-mechanically processed austenite. In: DeArdo, A. J., Ratz, G. A., Wray, P. J. (Eds.), *Thermomechanical processing of microalloyed austenite*. TMS-AIME, Pittsburgh, USA, pp. 377–403.
- Andrews, K. W., 1963. The structure of cementite and its relation to ferrite. *Acta Metallurgica* 11, 939–946.
- Anonymous, 1955. Techniques for electron metallography. *Tech. Rep. STP 155*, American Society for Testing and Materials, Philadelphia, USA.
- Anonymous, 1956. Atlas of isothermal transformation diagrams, Special Report No. 56. The Iron and Steel Institute, London, U.K.
- Antia, D. P., Fletcher, A., Cohen, M., 1944. Structural changes during the tempering of high-carbon steel. *Trans. A. S. M.* 32, 290–331.
- Arif, T. T., Qin, R., 2014. A phase-field model for the formation of martensite and bainite. *Advanced Materials Research* 922, 31–36.
- Arif, T. T., Qin, R. S., 2013. A phase-field model for bainitic transformation. *Computational Materials Science* 77, 230–235.
- Armstrong, E. L., Leonardi, S. J., Murphy, W. R., Wooding, P. S., 1978. Evaluation of water-accelerated bearing fatigue in an oil-lubricated ball bearings. *Lubrication Engineering* 34, 15–21.
- Ashby, M. F., 1987. Technology of the 1990's: advanced materials and predictive design. *Proceedings of the Royal Society A* 322, 393–407.
- Ashby, M. F., Easterling, K. E., 1982. Diagrams for grain growth in welds. *Acta Metallurgica* 30, 1969–1978.
- Atkinson, C., 1967. Concentration dependence of diffusivity in the growth or dissolution of precipitates. *Acta Metallurgica* 15, 1207–1211.
- Austin, A. E., Schwartz, C. M., 1952. Electron- diffraction study of iron carbides in bainite and tempered martensite. *Proc. ASTM* 52, 592–596.

- Austin, A. E., Schwartz, C. M., 1955. Decomposition of austenite and martensite. *Proc. American Society for Testing and Materials* 55, 623–625.
- Avrami, M., 1939. Kinetics of phase change 1. *Journal of Chemical Physics* 7, 1103–1112.
- Avrami, M., 1940. Kinetics of phase change 2. *Journal of Chemical Physics* 8, 212–224.
- Avrami, M., 1941. Kinetics of phase change 3. *Journal of Chemical Physics* 9, 177–184.
- Aziz, M. J., 1982. Model for solute redistribution during rapid solidification. *Journal of Applied Physics* 53, 1150–1168.
- Aziz, M. J., 1983. Dissipation theory treatment of the transition from diffusion-controlled to diffusionless solidification. *Applied Physics Letters* 43, 552–554.
- Azuma, M., Fujita, N., Takahashi, M., Senuma, T., Quidort, D., Lung, T., 2005. Modelling upper and lower bainite transformation in steels. *ISIJ International* 45, 221–228.
- Babu, B. N. P., Bhat, M. S., Parker, E. R., Zackay, V. F., 1976. A rapid magnetometric technique to plot isothermal transformation diagrams. *Metallurgical Transactions A* 7, 17–22.
- Babu, S. S., 2004. The mechanism of acicular ferrite in weld deposits. *Current Opinion in Solid State and Materials Science* 8, 267–278.
- Babu, S. S., Bhadeshia, H. K. D. H., 1990. Transition from bainite to acicular ferrite in reheated Fe-Cr-C weld deposits. *Materials Science and Technology* 6, 1005–1020.
- Babu, S. S., Bhadeshia, H. K. D. H., 1991. Direct study of grain boundary allotriomorphic ferrite crystallography. *Materials Science & Engineering A* 142, 209–220.
- Babu, S. S., Bhadeshia, H. K. D. H., 1992. Stress and the acicular ferrite transformations. *Materials Science and Engineering A* A156, 1–9.
- Babu, S. S., David, S. A., Vitek, J. M., Mundra, K., DebRoy, T., 1995. Development of macro- and microstructures of C-Mn low alloy steel welds – inclusion formation. *Materials Science and Technology* 11, 186–199.
- Babu, S. S., Hono, K., Sakuri, T., 1993. APFIM studies on martensite tempering of Fe-C-Si-Mn steel. *Applied Surface Science* 67, 321–327.
- Babu, S. S., Reidenbach, F., David, S. A., Bollinghaus, T., Hoffmeister, H., 1999. Effect of high energy density welding processes on inclusion and microstructure formation in steel welds. *Science and Technology of Welding and Joining* 4, 63–73.
- Babu, S. S., Specht, E. D., David, S. A., Karapetrova, E., Zschack, P., Peet, M., Bhadeshia, H. K. D. H., 2005. In-situ observations of lattice parameter fluctuations in austenite and transformation to bainite. *Metallurgical & Materials Transactions A* 36A, 3281–3289.
- Babu, S. S., Specht, E. D., David, S. A., Karapetrova, E., Zschack, P., Peet, M., Bhadeshia, H. K. D. H., 2007. Time-resolved X-ray diffraction investigation of austenite and transformation to bainite. In: Suzuki, K., Furuhara, T. (Eds.), *1st International Symposium on Steel Science*. Iron and Steel Institute of Japan, Iron and Steel Institute of Japan, Tokyo, Japan, pp. 1–7.
- Baczynski, G. J., Jonas, J. J., Collins, L. E., 1999. The influence of rolling practice on notch toughness and texture development in high-strength linepipe. *Metallurgical & Materials Transactions A* 30, 3045–3054.
- Bae, Y. H., Lee, J. S., Choi, J. K., Choo, W. Y., Hong, S. H., 2004. Effects of austenite conditioning on austenite/ferrite phase transformation in HSLA steel. *Materials Transactions* 45, 137–142.
- Bagaryatskii, Y. A., 1950. Possible mechanism of martensite decomposition. *Doklady Akademii Nauk, SSSR* 73, 1161–1164.
- Baik, S. C., Park, S. H., Kwon, H., Kim, D. I., Oh, K. H., 2006. Effects of nitrogen on the mechanical properties of cold rolled TRIP-aided steel sheets. *ISIJ International* 46, 599–605.
- Bailey, E. F., 1954. Effect of nonmartensite decomposition products on the properties of quenched and tempered steels. *Trans. A. S. M.* 46, 830–850.
- Bain, E. C., 1921a. The application of X-ray crystal analysis to metallurgy. *Industrial and Engineering Chemistry* 16, 692–698.
- Bain, E. C., 1921b. Studies of crystal structure with X-rays. *Chemical and Metallurgical Engineering* 25, 657–664.
- Bain, E. C., 1924. The nature of martensite. *Trans. AIME* 70, 25–46.
- Bain, E. C., 1939. *Alloying Elements in Steel*. American Society of Materials, Cleveland, Ohio, USA.
- Bain, E. C., 1963. Metal structure and the hardenability of steel, 1920 to 1940: personal recollections. In: Smith, C. S. (Ed.), *Sorby Centennial Symposium on the History of Metallurgy*. Gordon and Breach Publishers, London, U.K., pp. 121–138.
- Baker, J. C., Cahn, J. W., 1969. Solute trapping by rapid solidification. *Acta Metallurgica* 17, 575–578.
- Baker, J. C., Cahn, J. W., 1971. Thermodynamics of solidification. In: *Solidification*. ASM, Metals Park, Ohio, USA, pp. 23–58.
- Baker, R. G., Nutting, J., 1959. The tempering of Cr Mo steel after quenching and normalising. *Journal of the Iron and Steel Institute* 192, 257–268.
- Bakshi, S. D., Leiro, A., Prakash, B., Bhadeshia, H. K. D. H., 2014. Dry rolling/sliding wear of nanostructured bainite. *Wear* 316, 70–78.

- Bakshi, S. D., Shipway, P. H., Bhadeshia, H. K. D. H., 2013. Three-body abrasive wear of fine pearlite, nano-structured bainite and martensite. *Wear* 308, 46–53.
- Balart, M. J., Davis, C. L., Strangwood, M., 2002. Fracture behaviour in medium-carbon Ti-V-N and V-N microalloyed ferritic-pearlitic and bainitic forging steels with enhanced machinability. *Materials Science & Engineering A* 328, 48–57.
- Bandyopadhyay, T. R., Rao, P. K., Prabhu, N., 2006a. Development of ultrahigh strength steel through electroslag remelting with inoculation. *Ironmaking and Steelmaking* 33, 337–343.
- Bandyopadhyay, T. R., Rao, P. K., Prabhu, N., 2006b. Effect of inoculation during electroslag refining on grain size. *Ironmaking and Steelmaking* 33, 331–336.
- Barbaro, F. J., Edwards, R. H., Easterling, K. E., 1988. The composition and morphology of nonmetallic inclusions in HSLA steel weld metals. In: *Proc. 7th Int. Conf. Sustralian X-ray Analysis Association*. University of Western Australia, Australia, pp. 1–15.
- Barbé, L., de Meyer, M., Cooman, B. C. D., 2002. Determination of ms tempeprature of dispersed phase in TRIP-aided steel. In: Cooman, B. C. D. (Ed.), *International Conference on TRIP-aided High Strength Ferrous Alloys*. Verlag Mainz, Aachen, Germany, pp. 65–69.
- Barbe, L., Samek, L., Verbeken, K., Conion, K., Cooman, B. C. D., 2006. Neutron diffraction analysis of martensite ageing in high-carbon FeCMnSi steel. *International Journal of Materials Research* 97, 1123–1129.
- Barford, J., 1966. Kinetic aspects of the bainite reaction. *Journal of the Iron and Steel Institute* 204, 609–614.
- Barford, J., Owen, W. S., 1961. Effect of austenite grain size and temperature on rate of bainite formation. *Journal of the Iron and Steel Institute* 197, 146–157.
- Barlart, F., Glazov, M. V., Brem, J. C., Lege, D. J., 2002. Critical assessment of the micromechanical behaviour of dual phase and TRIP-assisted multiphase steels. *Canadian Metallurgical Quarterly* 18, 919–939.
- Barnard, S. J., Smith, G. D. W., Garratt-Reed, A. J., Sande, J. V., 1981a. Atom probe studies: Role of Si in tempering of martensite, Cr diffusion in bainite. In: H. I. Aaronson, D. E. Laughlin, M. S., Wayman, C. M. (Eds.), *Solid-Solid Phase Transformations*. TMS-AIME, Materials Park, Ohio, USA, pp. 881–885.
- Barnard, S. J., Smith, G. D. W., Sarikaya, M., Thomas, G., 1981b. Carbon atom distribution in a dual phase steel, an atom probe study. *Scripta Metallurgica* 15, 387–392.
- Barrallier, L., Traskine, V., Botchenkov, S., 2005. Morphology of intergranular cementite arrays in nitrided chromium-alloyed steels. *Materials Science & Engineering A* 93, 247–253.
- Barritte, G. S., 1982. The microstructure of weld metals in low alloy steels. Ph.D. thesis, University of Cambridge, Cambridge, U. K.
- Basabe, V. V., Jonas, J. J., Ghosh, C., 2011. Formation of deformation-induced divorced eutectoid pearlite above the Ae1. *Advanced Materials Research* 409, 829–834.
- Bastien, P. G., 1957. The mechanism of formation of banded structures. *Journal of the Iron and Steel Institute* 187, 281–291.
- Basu, A., Chakraborty, J., Shariff, S. M., and S. V. Joshi, G. P., Sundararajan, G., Majumdar, J. D., Manna, I., 2007. Laser surface hardening of austempered (bainitic) ball bearing steel. *Scripta Materialia* 56, 887–890.
- Basuki, A., Aernoudt, E., 1999. Effect of deformation in the intercritical area on the grain refinement of retained austenite of 0.4C TRIP steel. *Scripta Materialia* 40, 1003–1008.
- Bathias, C., 2006. Piezoelectric fatigue testing machines and devices. *International Journal of Fatigue* 28, 1438–1445.
- Bathias, C., 2010. Gigacycle fatigue properties of bearing steels. *Journal of ASTM International* 7, JAI102712.
- Bathias, C., 2012. Gigacycle fatigue of bearing steels. *Materials Science and Technology* 28, 27–33.
- Baudry, G., Marines, I., Bathias, C., Doucet, J. P., Vittori, J. F., Rathery, S., 2004. Very high cycle (gigacycle) fatigue of a wide range of alternative engineering materials used in automotive industry. In: *Third International Conference on Very High Cycle Fatigue*. TMS, pp. 1–8.
- Bayerlein, M., Mughrabi, H., Kesten, M., Meier, B., 1992. Improvement of the strength of a metastable austenitic stainless. *Materials Science & Engineering A* 159, 35–41.
- Becker, P. C., 1981. Microstructural changes around non-metallic inclusions caused by rolling-contact fatigue of ball-bearing steels. *Metals Technology* 8, 234–243.
- Beladi, H., Adachi, Y., Timokhina, I., Hodgson, P. D., 2008. Nano-structured bainitic steels: Microstructure characteristics and mechanical properties. *CAMP-ISIJ* 21, 540.
- Beladi, H., Adachi, Y., Timokhina, I., Hodgson, P. D., 2009. Crystallographic analysis of nanobainitic steels. *Scripta Materialia* 60, 455–458.
- Bell, T., Farnell, B. C., 1969. The isothermal decomposition of nitrogen austenite to bainite. In: *Mechanism of Phase Transformations in Crystalline Solids*. Institute of Materials, London, U.K., pp. 282–287.
- Benson, J. P., Edmonds, D. V., 1978. Effect of microstructure on fatigue in threshold region low alloy steel. *Metal Science* 12, 223–232.
- Berger, C., Pyttel, B., Schwerdt, D., 2008. Beyond HCF – is there a fatigue limit? *Materialwissenschaft und Werkstofftechnik* 39, 769–776.

- Berrahmoune, M. R., Berveiller, S., Inal, K., Moulin, A., Patoor, E., 2004. Analysis of the martensitic transformation at various scales in TRIP steel. *Materials Science & Engineering A* 378, 304–307.
- Beshers, D. N., 1965. An investigation of interstitial sites in the BCC lattice. *Journal of Applied Physics* 36, 290–300.
- Bhadeshia, H. K. D. H., 1978. Theory and significance of retained austenite in steels. Ph.D. thesis, University of Cambridge, Cambridge, U. K.
- Bhadeshia, H. K. D. H., 1980. The lower bainite transformation and the significance of carbide precipitation. *Acta Metallurgica* 28, 1103–1114.
- Bhadeshia, H. K. D. H., 1981a. Bainite: The incomplete-reaction phenomenon and the approach to equilibrium. In: H. I. Aaronson, D. E. Laughlin, M. S., Wayman, C. M. (Eds.), *Solid-Solid Phase Transformations*. TMS-AIME, Materials Park, Ohio, USA, pp. 1041–1048.
- Bhadeshia, H. K. D. H., 1981b. The driving force for martensitic transformation in steels. *Metal Science* 15, 175–177.
- Bhadeshia, H. K. D. H., 1981c. Rationalisation of shear transformations in steels. *Acta Metallurgica* 29, 1117–1130.
- Bhadeshia, H. K. D. H., 1981d. Thermodynamic extrapolation and the martensite-start temperature of substitutionally alloyed steels. *Metal Science* 15, 178–180.
- Bhadeshia, H. K. D. H., 1982a. An aspect of the nucleation of ‘burst’ martensite in steels. *Journal of Material Science* 17, 383–386.
- Bhadeshia, H. K. D. H., 1982b. Bainite: Mobility of the transformation interface. *Journal de Physique: Colloque C4* 43, 449–454.
- Bhadeshia, H. K. D. H., 1982c. Bainite: Overall transformation kinetics. *Journal de Physique Colloque C4* 43, 443–448.
- Bhadeshia, H. K. D. H., 1982d. A thermodynamic analysis of isothermal transformation diagrams. *Metal Science* 16, 159–165.
- Bhadeshia, H. K. D. H., 1983a. Considerations of solute drag in relation to transformations in steels. *Journal of Material Science* 18, 1473–1481.
- Bhadeshia, H. K. D. H., 1983b. On the carbon content of retained-austenite in quenched steels. *Metal Science* 17, 151–152.
- Bhadeshia, H. K. D. H., 1984. Solute-drag, kinetics and the mechanism of the bainite transformation. In: Marder, A. R., Goldstein, J. I. (Eds.), *Phase Transformations in Ferrous Alloys*. TMS-AIME, Ohio, USA, pp. 335–340.
- Bhadeshia, H. K. D. H., 1985a. Critical assessment: Diffusion-controlled growth of ferrite plates in plain carbon steels. *Materials Science and Technology* 1, 497–504.
- Bhadeshia, H. K. D. H., 1985b. Diffusional formation of ferrite in iron and its alloys. *Progress in Materials Science* 29, 321–386.
- Bhadeshia, H. K. D. H., 1989. Theoretical analysis of changes in cementite composition during the tempering of bainite. *Materials Science and Technology* 5, 131–137.
- Bhadeshia, H. K. D. H., 1992. *Bainite in Steels*, 1st edition. Institute of Materials, London, U.K.
- Bhadeshia, H. K. D. H., 1997a. Models for the elementary mechanical properties of steel welds. In: Cerjak, H., Bhadeshia, H. K. D. H. (Eds.), *Mathematical Modelling of Weld Phenomena 3*. Vol. 3. Institute of Materials, London, pp. 235–255.
- Bhadeshia, H. K. D. H., 1997b. Recrystallisation of practical mechanically alloyed iron base and nickel base superalloys. *Materials Science and Engineering A* 223, 64–77.
- Bhadeshia, H. K. D. H., 1998. Alternatives to the ferrite-pearlite microstructures. *Materials Science Forum* 284–286, 39–50.
- Bhadeshia, H. K. D. H., 1999a. The bainite transformation: Unresolved issues. *Materials Science & Engineering A* 273–275, 58–66.
- Bhadeshia, H. K. D. H., 1999b. Some phase transformations in steels. *Materials Science and Technology* 15, 22–29.
- Bhadeshia, H. K. D. H., 2001a. *Bainite in Steels*, 2nd edition. Institute of Materials, London, U.K.
- Bhadeshia, H. K. D. H., 2001b. Design of ferritic creep-resistant steels. *ISIJ International* 41, 621–640.
- Bhadeshia, H. K. D. H., 2001c. *Geometry of Crystals*. 2nd edition, Institute of Materials.
- Bhadeshia, H. K. D. H., 2002. TRIP-assisted steels? *ISIJ International* 42, 1059–1060.
- Bhadeshia, H. K. D. H., 2003. Advances in the kinetic theory of carbide precipitation. *Materials Science Forum* 426–432, 35–42.
- Bhadeshia, H. K. D. H., 2004. Reliability of weld microstructure and property calculations. *Welding Journal, Research Supplement* 83, 237s–243s.
- Bhadeshia, H. K. D. H., 2005a. Hard bainite. In: Howe, J. M., Laughlin, D. E., Lee, J. K., Dahmen, U., Soffa, W. A. (Eds.), *Solid-Solid Phase Transformations*, TMS-AIME, Warrendale, USA. Vol. 1. TMS-AIME, Warrendale, Pennsylvania, USA, pp. 469–484.

- Bhadeshia, H. K. D. H., 2005b. Large chunks of very strong steel. *Materials Science and Technology* 21, 1293–1302.
- Bhadeshia, H. K. D. H., 2008. Properties of fine-grained steels generated by displacive transformation. *Materials Science and Engineering A* 481–482, 36–39.
- Bhadeshia, H. K. D. H., 2010a. A personal commentary on “transformation of austenite at constant subcritical temperatures”. *Metallurgical and Materials Transactions A* 41, 1351–1390.
- Bhadeshia, H. K. D. H., 2010b. Problems in the calculation of transformation texture in steels. *ISIJ International* 50, 1517–1522.
- Bhadeshia, H. K. D. H., 2012. Steels for bearings. *Progress in Materials Science* 57, 268–435.
- Bhadeshia, H. K. D. H., 2013a. About calculating the characteristics of the martensite-austenite constituent. In: *Welding of High Strength Pipeline Steels*. TMS, Metals Park, Ohio, USA, pp. 99–106.
- Bhadeshia, H. K. D. H., 2013b. Comments on ‘determination of  $M_s$  temperature’ by T. Sourmail and V. Smanio. *Materials Science and Technology* 29, 889.
- Bhadeshia, H. K. D. H., 2014a. Displacements caused by the growth of bainite in steel. *The Banaras Metallurgist* 19, 1–7.
- Bhadeshia, H. K. D. H., 2014b. Local brittle zones and the role of niobium. *Materials Science Forum* 783–786, 2129–2135.
- Bhadeshia, H. K. D. H., 2015. Anomalies in carbon concentration determinations from nanostructured bainite. *Materials Science and Technology* 31, <http://dx.doi.org/10.1179/1743284714Y.0000000655>.
- Bhadeshia, H. K. D. H., Abreu, H., Kundu, S., 2008. Calculation of crystallographic texture due to displacive transformations. *International Journal of Materials Research* 99, 342–346.
- Bhadeshia, H. K. D. H., Chinthia, A., Kundu, S., 2014. Model for multiple stress affected martensitic transformations, microstructural entropy and consequences on scatter in properties. *Materials Science and Technology* 30, 160–165.
- Bhadeshia, H. K. D. H., Christian, J. W., 1990. The bainite transformation in steels. *Metallurgical & Materials Transactions A* 21A, 767–797.
- Bhadeshia, H. K. D. H., David, S. A., Vitek, J. M., Reed, R. W., 1991. Stress induced transformation to bainite in a Fe-Cr-Mo-C pressure vessel steel. *Materials Science and Technology* 7, 686–698.
- Bhadeshia, H. K. D. H., Edmonds, D. V., 1979a. The bainite transformation in a silicon steel. *Metallurgical Transactions A* 10A, 895–907.
- Bhadeshia, H. K. D. H., Edmonds, D. V., 1979b. The bainite transformation in a silicon steel. *Metallurgical Transactions A* 10A, 895–907.
- Bhadeshia, H. K. D. H., Edmonds, D. V., 1979c. Tempered martensite embrittlement: Role of retained austenite and cementite. *Metal Science* 13, 325–334.
- Bhadeshia, H. K. D. H., Edmonds, D. V., 1980a. Analysis of the mechanical properties and microstructure of a high-silicon dual phase steel. *Metal Science* 14, 41–49.
- Bhadeshia, H. K. D. H., Edmonds, D. V., 1980b. The mechanism of bainite formation in steels. *Acta Metallurgica* 28, 1265–1273.
- Bhadeshia, H. K. D. H., Edmonds, D. V., 1983a. Bainite in silicon steels: a new composition-property approach I. *Metal Science* 17, 411–419.
- Bhadeshia, H. K. D. H., Edmonds, D. V., 1983b. Bainite in silicon steels: a new composition-property approach II. *Metal Science* 17, 420–425.
- Bhadeshia, H. K. D. H., Harada, H., 1993. High-strength (5 GPa) steel wire: an atom-probe study. *Applied Surface Science* 67, 326–333.
- Bhadeshia, H. K. D. H., Keehan, E., Karlsson, L., Andrén, H. O., 2006. Coalesced bainite. *Transactions of the Indian Institute of Metals* 59, 689–694.
- Bhadeshia, H. K. D. H., Strang, A., Gooch, D. J., 1998. Ferritic power plant steels: Remanent life assessment and the approach to equilibrium. *International Materials Reviews* 43, 45–69.
- Bhadeshia, H. K. D. H., Suh, D. W., 2015. Is a low-phosphorus content in steel a product requirement? *Ironmaking and Steelmaking* 42, DOI 10.1179/1743281214Y0000000261.
- Bhadeshia, H. K. D. H., Svensson, L.-E., 1989a. Effect of alloying additions on the microstructure & properties of vertical up manual metal arc welds – i. *Joining and Materials* 2, 182–187.
- Bhadeshia, H. K. D. H., Svensson, L.-E., 1989b. Effect of alloying additions on the microstructure & properties of vertical up manual metal arc welds – ii. *Joining and Materials* 2, 236–238.
- Bhadeshia, H. K. D. H., Svensson, L.-E., 1989c. The microstructure of submerged arc weld deposits for high strength steels. *Journal of Materials Science* 24, 3180–3188.
- Bhadeshia, H. K. D. H., Svensson, L.-E., 1993. Modelling the evolution of microstructure in steel weld metals. In: Cerjak, H., Easterling, K. E. (Eds.), *Mathematical Modelling of Weld Phenomena*. Vol. 1. The Institute of Materials, London, pp. 109–182.
- Bhadeshia, H. K. D. H., Svensson, L.-E., Grefott, B., 1985. Model for the development of microstructure in low alloy steel (Fe-Mn-Si-C) weld deposits. *Acta Metallurgica* 33, 1271–1283.

- Bhadeshia, H. K. D. H., Svensson, L.-E., Gretoft, B., 1986. Analysis of the primary microstructure of Cr & Mo containing weld. In: 4th Scandinavian Symposium on Materials Science. Norwegian Institute of Technology, Trondheim, Norway, pp. 153–158.
- Bhadeshia, H. K. D. H., Svensson, L.-E., Gretoft, B., 1987. Prediction of microstructure of the fusion zone of multicomponent steel weld deposits. In: David, S. A. (Ed.), *Advances in Welding Technology and Science*. ASM International, Warrendale, Pennsylvania, USA, pp. 225–229.
- Bhadeshia, H. K. D. H., Waugh, A. R., 1982a. An atom-probe study of bainite. In: Aaronson, H. I., Laughlin, D. E., Sekerka, R. F., Wayman, C. M. (Eds.), *Solid-Solid Phase Transformations*. TMS-AIME, Warrendale, Pennsylvania, USA, pp. 993–998.
- Bhadeshia, H. K. D. H., Waugh, A. R., 1982b. Bainite: An atom probe study of the incomplete reaction phenomenon. *Acta Metallurgica* 30, 775–784.
- Bhat, M. S., 1977. Microstructure and mechanical properties of AISI 4340 steel modified with Al and Si. Ph.D. thesis, Lawrence Berkeley Laboratories, California, USA.
- Bhattacharjee, D., Knott, J. F., Davis, C. L., 2004. Charpy-impact-toughness prediction using an “effective” grain size for thermomechanically controlled rolled microalloyed steels. *Metallurgical & Materials Transactions A* 35, 121–130.
- Bhattacharyya, S., Kehl, G. L., 1955. Isothermal transformation of austenite under externally applied stress. *Trans. A. S. M.* 47, 351–379.
- Bhowmik, N., Ghosh, S. K., Haldar, A., Chattopadhyay, P. P., 2012. Low carbon high manganese bainitic steel. *Materials Science and Technology* 28, 282–287.
- Bilby, B. A., Christian, J. W., 1956. Martensitic transformations. In: *The Mechanism of Phase Transformations in Metals*. The Institute of Metals, London, U.K., pp. 121–172.
- Blackmore, P. A., Harding, R. A., 1984. The effects of metallurgical process variables on the properties of austempered ductile irons. *Journal of Heat Treating* 3, 310–325.
- Blondeau, R., Maynier, P., Dollet, J., Vieillard-Baron, B., 1975. Estimation of hardness, strength and elastic limit of C- and low-alloy steels from their composition and heat treatment. *Memoires Scientifiques Rev. Metallurg.* 72, 759–769.
- Bodnar, R. L., Ohhashi, T., Jaffee, R. I., 1989. Effects of Mn, Si and purity on the design of CrMo bainitic alloy steels. *Metallurgical Transactions A* 20, 1445–1460.
- Bodnar, R. L., Shen, Y., Lin, M., Elwood, D. W., Feher, F. C., Roe, G. J., 1997. Accelerated cooling on Burns Harbor’s 160” plate mill. In: *Materials Solutions ‘97 on Accelerated Cooling/Direct Quenching Steels*. ASM International, Metals Park, Ohio, USA, pp. 3–13.
- Boettinger, W. J., Warren, J. A., Beckermann, C., Karma, A., 2002. Phase-field simulation of solidification. *Annual Review of Materials Research* 32, 163–194.
- Bokros, J. C., Parker, E. R., 1963. The mechanism of the martensite burst transformation in Fe-Ni single crystals. *Acta Metallurgica* 11, 1291–1301.
- Borchers, V. H., Doffin, K., 1969. Kinetik der bildung des karbids Fe<sub>2</sub>C in stahl 100Cr6. *Archiv für das Eisenhüttenwesen* 40, 493–498.
- Borgenstam, A., Hillert, M., Ågren, J., 2009. Metallographic evidence of carbon diffusion in the growth of bainite. *Acta Materialia* 57, 3242–3252.
- Bouaziz, O., Quidort, D., Maugis, P., 2003. Bainite transformation stasis controlled by plastic work in austenite. *Revue de Métallurgie* 100, 103–108.
- Bouquerel, J., Verbeke, K., Krizan, D., Barbe, L., Verleysen, P., Houbaert, Y., 2008. Evaluation of the static stress-strain behaviour of phosphorus alloyed and titanium micro-alloyed TRIP steels. *Steel Research International* 79, 784–792.
- Bowen, P., Knott, J. F., 1986. Size effects on the microscopic fracture stress in martensitic microstructures. *Metallurgical Transactions A* 17, 231–241.
- Bowles, J. S., Kennon, N. F., 1960. Crystallographic aspects of the bainite transformation. *Journal of the Australian Institute of Metals* 5, 106–113.
- Bowles, J. S., Mackenzie, J. K., 1954. The crystallography of martensite transformations, part I. *Acta Metallurgica* 2, 129–137.
- Bowles, J. S., Muddle, B. C., Wayman, C. M., 1977. The crystallography of the precipitation of beta vanadium hydride. *Acta Metallurgica* 25, 513–520.
- Bowles, J. S., Wayman, C. M., 1979. The growth mechanism of AuCu II plates. *Acta Metallurgica* 27, 833–839.
- Bradley, J. R., Aaronson, H. I., 1981. Growth kinetics of grain boundary ferrite allot. in Fe-C-X alloys. *Metallurgical Transactions A* 12, 1729–1741.
- Bradley, J. R., Rigsbee, J. M., Aaronson, H. I., 1977. Growth kinetics of grain boundary ferrite allot. in Fe-C alloys. *Metallurgical Transactions A* 8, 323–333.
- Bramfitt, B. L., 1970. The effect of carbide and nitride additions on the heterogeneous nucleation behaviour of liquid iron. *Metallurgical Transactions* 1, 1987–1995.

- Brandis, H., 1972. Vergleichende untersuchungen an DEW-100 Cr 6 und zwei niedriglegierten wälzlagerstählen amerikanischer entwicklung. Tech. Rep. 227/72, Deutsche Edelstahlwerke Aktiengesellschaft Krefeld Forschungsinstitut, Germany.
- Brenner, S. S., 1956. Tensile strength of whiskers. *Journal of Applied Physics* 27, 1484–1491.
- Briant, C. L., Banerji, S. K., 1978. Intergranular failure in steel: role of grain boundary composition. *International Metals Reviews* 4 (164-199).
- Brown, G. T., James, B. A., 1980. Superhardening in medium-carbon steel. *Metals Technology* 7, 261–268.
- Brown, P. M., Baxter, D. P., 2004. Hyper-strength bainitic steels. In: *Materials Science and Technology 2004*. TMS, Warrendale, Pennsylvania, USA, pp. 433–438.
- Brown, P. W., Mack, D. J., 1973a. Electrical resistivity and microstructural changes accompanying the isothermal decomposition of austenite. *Metallurgical Transactions* 4, 2639–2643.
- Brown, P. W., Mack, D. J., 1973b. Isothermal transformation trends in a eutectoid steel. *Metallurgical Transactions* 4, 2850–2851.
- Brownrigg, A., 1973. Boron in steel – a literature review. *The Journal of the Australasian Institute of Metals* 18, 124–136.
- Brozzo, P., Buzzichelli, G., Mascanzoni, A., Mirabile, M., 1977. Microstructure and cleavage resistance of low-C bainitic steels. *Metal Science* 11, 123–130.
- Bruna, P., Pradell, T., Crespo, D., Garcia-Mateo, C., Bhadeshia, H. K. D. H., 2005. Mössbauer spectroscopy of low temperature bainite. In: Garcia, M., Marco, J. F., Plazaola, F. (Eds.), *Industrial Applications of the Mössbauer Effect*. American Institute of Physics, Maryland, U.S.A., pp. 338–343.
- Buchi, G. J. P., Page, J. H. R., Sidey, M. P., 1965. Creep properties and precipitation characteristics of 1CrMoV steel. *Journal of the Iron and Steel Institute* 203, 291–298.
- Buerger, M. J., 1951. Crystallographic aspects of phase transformation. In: R. Smoluchowski, J. E. Mayer, W. A. W. (Ed.), *Phase Transformations in Solids*. John Wiley and Sons Inc., New York, USA, pp. 183–211.
- Bunshah, R. F., Mehl, R. F., 1953. Rate of propagation of martensite. *Trans. A.I.M.E.* 193, 1251–1258.
- Burdekin, F. M., 1990. Ductile and brittle failure in steel/pressure vessel assessments. In: Charles, J. A., Smith, G. C. (Eds.), *Advances in Physical Metallurgy*. Institute of Metals, London, U.K., pp. 23–46.
- Burkart, K., Bomas, H., Schroeder, R., Zoch, H.-W., 2012. Rolling contact and compression-torsion fatigue of 52100 steel with special regard to carbide distribution. In: *Advances in rolling contact fatigue strength testing and related substitute technologies*. ASTM International, West Conshohocken, PA, USA, pp. 218–236.
- Bush, M. E., Kelly, P. M., 1971. Strengthening mechanisms in bainitic steels. *Acta Metallurgica* 19, 1363–1371.
- Byun, J. S., Shim, H. H., Suh, J. Y., Oh, Y. J., Cho, Y. W., Shim, J. D., Lee, D., 2001. Inoculated acicular ferrite microstructure and mechanical properties. *Materials Science & Engineering A* 319-321, 326–331.
- Caballero, F. G., Allain, S., Cornide, J., Puerta-Velásquez, J. D., García-Mateo, C., Miller, M. K., 2013a. Design of cold rolled and continuous annealed carbide-free bainitic steels for automotive application. *Materials and Design* 49, 667–680.
- Caballero, F. G., Bhadeshia, H. K. D. H., 2004. Very strong bainite. *Current Opinion in Solid State and Materials Science* 8, 251–257.
- Caballero, F. G., Bhadeshia, H. K. D. H., Mawella, K. J. A., Jones, D. G., Brown, P., 2001a. Design of novel high-strength bainitic steels: Part I. *Materials Science and Technology* 17, 512–516.
- Caballero, F. G., Bhadeshia, H. K. D. H., Mawella, K. J. A., Jones, D. G., Brown, P., 2001b. Design of novel high-strength bainitic steels: Part II. *Materials Science and Technology* 17, 517–522.
- Caballero, F. G., Bhadeshia, H. K. D. H., Mawella, K. J. A., Jones, D. G., Brown, P., 2002. Very strong, low-temperature bainite. *Materials Science and Technology* 18, 279–284.
- Caballero, F. G., Chao, J., Cornide, J., Garcia-Mateo, C., Santofimia, M. J., Capdevila, C., 2009a. Toughness deterioration in advanced high strength bainitic steels. *Materials Science & Engineering A* 525, 87–95.
- Caballero, F. G., Chao, J., Cornide, J., Garcia-Mateo, C., Santofimia, M. J., Capdevila, C., 2010a. Toughness of advanced high strength bainitic steels. *Materials Science Forum* 638-642, 118–123.
- Caballero, F. G., Garcia-Mateo, C., de Andrés, C. G., 2005. Dilatometric study of re-austenitisation of high silicon bainitic steels: Decomposition of retained austenite. *Materials Transactions* 46, 581–586.
- Caballero, F. G., García-Mateo, C., Santofimia, M. J., Miller, M. K., de Andrés, C. G., 2009b. New experimental evidence on the incomplete transformation phenomenon in steel. *Acta Materialia* 57, 8–17.
- Caballero, F. G., Mateo, C. G., Chao, J., Santofimia, M. J., Capdevila, C., de Andrés, C. G., 2008a. Effects of morphology and stability of retained austenite on the ductility of TRIP-aided bainitic steels. *ISIJ International* 48, 1256–1262.
- Caballero, F. G., Miller, M., Yen, H. W., Jimenez, J. A., Mateo, C. G., Rivas, L. M., Yang, J. R., 2014. Carbon supersaturation and tetragonal bainitic ferrite in nanocrystalline bainitic steels, TMS2014, 143rd Annual Meeting and Exhibition, San Diego, USA.
- Caballero, F. G., Miller, M. K., Babu, S. S., Garcia-Mateo, C., 2007. Atomic scale observations of bainite transformation in a high carbon high silicon steel. *Acta Materialia* 55, 381–390.

- Caballero, F. G., Miller, M. K., Clarke, A. J., Garcia-Mateo, C., 2010b. Examination of carbon partitioning into austenite during tempering of bainite. *Scripta Materialia* 63, 442–445.
- Caballero, F. G., Miller, M. K., Garcia-Mateo, C., 2008b. The approach to equilibrium during tempering of a bulk nanocrystalline steel: an atom probe investigation. *Journal of Materials Science* 43, 3769–3774.
- Caballero, F. G., Miller, M. K., Garcia-Mateo, C., 2010c. Tracking solute atoms during bainite reaction in a nanocrystalline steel. *Materials Science and Technology* 26, 889–898.
- Caballero, F. G., Miller, M. K., Garcia-Mateo, C., 2011a. Atom probe tomography analysis of precipitation during tempering of a nanostructured bainitic steel. *Metallurgical & Materials Transactions A* 42, 3660–3668.
- Caballero, F. G., Miller, M. K., Garcia-Mateo, C., 2011b. Slow bainite: an opportunity to determine the carbon content of the bainitic ferrite during growth. *Solid State Phenomena* 172–174, 111–116.
- Caballero, F. G., Miller, M. K., Garcia-Mateo, C., Cornide, J., 2013b. New experimental evidence of the diffusionless transformation nature of bainite. *Journal of Alloys and Compounds* 577, S626–S630.
- Caballero, F. G., Miller, M. K., Garcia-Mateo, C., Cornide, J., Santofimia, M. J., 2012. Temperature dependence of carbon supersaturation of ferrite in bainitic steels. *Scripta Materialia* 67, 846–849.
- Caballero, F. G., Miller, M. K., Mateo, C. G., Capdevila, C., Babu, S. S., 2008c. Redistribution of alloying elements during tempering of a nanocrystalline steel. *Acta Materialia* 56, 188–199.
- Caballero, F. G., Santofimia, M. J., Capdevila, C., Garcia-Mateo, C., de Andrés, C. G., 2006. Design of advanced bainitic steels by optimisation of TTT diagrams and  $T_0$  curves. *ISIJ International* 46, 1479–1488.
- Caballero, F. G., Santofimia, M. J., García-Mateo, C., de Andrés, C. G., 2004. Time-temperature-transformation diagram within the bainitic temperature range in a medium carbon steel. *Materials Transactions* 45, 3272–3281.
- Cabus, C., Regle, H., Bacroix, B., 2007. Orientation relationship between austenite and bainite in a multiphased steel. *Materials Characterization* 58, 332–338.
- Cahn, J. W., 1956. The kinetics of grain boundary nucleated reactions. *Acta Metallurgica* 4, 449–459.
- Cahn, J. W., 1962. The impurity drag effect in grain boundary motion. *Acta Metallurgica* 10, 789–798.
- Cai, M. H., Ding, H., Lee, Y. K., Tang, Z. Y., Zhang, J. S., 2011. Effects of Si on microstructural evolution and mechanical properties of hot-rolled ferrite and bainite dual-phase steels. *ISIJ International* 51, 476–481.
- Callender, W. R., 1983. Bainitic transformation and novel bainitic rails steels. Ph.D. thesis, University of Sheffield.
- Cane, B. J., Townsend, R. D., 1984. Prediction of remaining life in low alloy steels. Tech. Rep. PRD/L/2674/N84, Central Electricity Generating Board, Leatherhead, Surrey, U.K.
- Capdevila, C., Ferrer, J. P., García-Mateo, C., Caballero, F. G., Lopez, V., de Andrés, C. G., 2006. Influence of deformation and molybdenum content on acicular ferrite formation in medium carbon steels. *ISIJ International* 46, 1093–1100.
- Carneiro, R. A., Ratnapuli, R. C., de Freitas C. Lins, V., 2003. Influence of chemical composition and microstructure of API linepipe steels on hydrogen induced cracking and sulphide stress corrosion cracking. *Materials Science & Engineering A* 357, 104–110.
- Carruthers, R. B., Collins, M. J., 1981. Use of scanning transmission electron microscopy in estimation of remanent life of pressure parts. In: *Quantitative Microanalysis with High Spatial Resolution*. Metals Society, London, U.K., pp. 108–111.
- Chae, J. Y., Qin, R. S., Bhadeshia, H. K. D. H., 2009. Topology of the deformation of a non-uniform grain structure. *ISIJ International* 49, 115–118.
- Chakraborty, J., Bhattacharjee, D., Manna, I., 2008. Austempering of bearing steel for improved mechanical properties. *Scripta Materialia* 59, 247–250.
- Chalant, G., Suyitno, B. M., 1991. Effects of microstructure on low and high cycle fatigue behaviour of a microalloyed steel. In: Jono, M., Inoue, T. (Eds.), *Proceedings of the 6th International Conference on Mechanical Behaviour of Materials*. Vol. VI. Pergamon Press, Oxford, Elsevier Science, Kyoto, Japan, pp. 511–516.
- Chanani, G. R., Antolovich, S. D., Gerberich, W. W., 1972. Fatigue crack propagation in TRIP steels. *Metallurgical Transactions* 3, 2661–2672.
- Chance, J., Ridley, N., 1981. Chromium partitioning during isothermal transformation of a eutectoid steel. *Metallurgical Transactions A* 12A, 1205–1213.
- Chandel, R. S., Orr, R. F., Gianetto, J. A., McGrath, J. T., Patchett, B. M., Bicknell, A. C., 1985. Microstructure and properties of narrow gap welds in 2.25Cr 1Mo steel. Tech. Rep. ERP/PMRL 85-16(OP-J) 1985, Canadian Metallurgical Society (CANMET), Manitoba, Canada.
- Chandrasekharaiah, M. N., Dubben, G., Kolster, B. H., 1994. Atom probe study of retained austenite in ferritic weld metal. *Welding Journal, Research Supplement* 71, 247s–252s.
- Chang, C. I., Lee, C. J., Huang, J. C., 2004. Relationship between grain size and Zener-Holloman parameter during friction stir processing in AZ31 Mg alloys. *Scripta Materialia* 51, 509–514.
- Chang, H. T., Yen, H. W., Lin, W. T., Huang, C. Y., Yang, J. R., 2013. Heat treatment of superbainitic steels. *International Journal of Heat Treatment and Surface Engineering* 7, 8–15.

- Chang, L. C., 1999. Bainite transformation temperatures in high-silicon steels. *Metallurgical & Materials Transactions A* 30, 909–916.
- Chang, L. C., 2004. Microstructures and reaction kinetics of bainite transformation in Si-rich steels. *Materials Science & Engineering A* 368, 175–182.
- Chang, L. C., 2005. The rolling/sliding wear performance of high silicon carbide-free bainitic steels. *Wear* 258, 730–743.
- Chang, L. C., Bhadeshia, H. K. D. H., 1995a. Austenite films in bainitic microstructures. *Materials Science and Technology*, 874–881.
- Chang, L. C., Bhadeshia, H. K. D. H., 1995b. Metallographic observations of bainite transformation mechanism. *Materials Science and Technology* 11, 106–108.
- Chang, L. C., Bhadeshia, H. K. D. H., 1996. Microstructure of lower bainite formed at large undercoolings below the bainite start temperature. *Materials Science and Technology* 12, 233–236.
- Chang, L. C., Hsui, I. C., Chen, L. H., Lui, T. S., 2005. A study on particle erosion behavior of ductile irons. *Scripta Materialia* 52, 609–613.
- Chang, L. C., Hsui, I. C., Chen, L. H., Lui, T. S., 2006b. Effects of heat treatment on the erosion behavior of austempered ductile irons. *Wear* 260, 783–793.
- Chapetti, M. D., Kitano, T., Tagawa, T., Miyata, T., 1998. Fatigue limit of blunt-notched components. *Fatigue and Fracture in Engineering Materials and Structures* 21, 1525–1536.
- Charleux, M., Poole, W. J., Militzer, M., Deschamps, A., 2001. Precipitation behavior and its effect on strengthening of an HSLA-Nb/Ti steel. *Metallurgical & Materials Transactions A* 32, 1635–1647.
- Chart, T. G., Counsell, J. F., Jones, G. P., Slough, W., Spencer, P. J., 1975. Provision and use of thermodynamic data for the solution of. *International Metals Reviews* 20, 57–82.
- Chatterjee, S., Bhadeshia, H. K. D. H., 2006. TRIP-assisted steels: cracking of high carbon martensite. *Materials Science and Technology* 22, 645–649.
- Chatterjee, S., Bhadeshia, H. K. D. H., 2007. TRIP-assisted steels: Stress or strain-affected martensitic transformation. *Materials Science and Technology* 23, 1101–1104.
- Chatterjee, S., Muruganath, M., Bhadeshia, H. K. D. H., 2007.  $\delta$ -TRIP steel. *Materials Science and Technology* 23, 819–827.
- Chatterjee, S., Wang, H. S., Yang, J. R., Bhadeshia, H. K. D. H., 2006. Mechanical stabilisation of austenite. *Materials Science and Technology* 22, 641–644.
- Chen, C. Y., Chen, C. C., Lin, J. S., 2014. Morphology feature of nanostructure bainitic steel after tempering treatment. *International Journal of Mechanical, Industrial Science and Engineering* 8, 876–879.
- Chen, H., Zhu, K., Zhao, L., van der Zwaag, S., 2013. Analysis of transformation stasis during the isothermal bainitic ferrite formation in Fe-C-Mn and Fe-C-Mn-Si alloys. *Acta Materialia* 61, 5458–5468.
- Chen, H. C., Era, H., Shimizu, M., 1989. Effect of phosphorus on the formation of retained austenite and mechanical-properties in Si-containing low-carbon steel sheet. *Metallurgical & Materials Transactions A* 20, 437–445.
- Chen, L.-Q., 2002. Phase-field models for microstructure evolution. *Annual Reviews in Materials Science* 32, 113–140.
- Chen, X., Li, Y., 2006. Effects of Ti, V, and rare earth on the mechanical properties of austempered high silicon cast steel. *Metallurgical & Materials Transactions A* 37, 3215–3220.
- Chen, X., Li, Y., 2007. Fracture toughness improvement of austempered high silicon steel by titanium, vanadium and rare earth elements modification. *Materials Science & Engineering A* 444, 298–305.
- Chen, Y. J., Wei, B. S., Hsu, W. N., 2008. Ultrasonic fatigue testing of aluminium and magnesium alloys. *Journal of the Chinese Society of Mechanical Engineers* 29, 299–308.
- Chen, Z., Shan, Z.-W., Wu, N. Q., Sikka, V., Hua, M.-J., Mao, S. X., 2004. Fine carbide-strengthened 3Cr-3WV Ta bainitic steel. *Metallurgical & Materials Transactions A* 35, 1281–1288.
- Chester, N., Bhadeshia, H. K. D. H., 1997. Mathematical modelling of bainite transformation kinetics. *Journal de Physique IV (Colloque) C5*, 41–46.
- Chijiwa, R., Tamehiro, H., Hirai, M., Matsuda, H., Mimura, H., 1988. Extra high toughness titanium oxide steel plates for offshore structures and line pipe. In: *Offshore Mechanics and Arctic Engineering*. ASME, New Jersey, USA, pp. 165–172.
- Choi, H. C., Ha, T. K., Shin, H. C., Chang, Y. W., 1999. The formation kinetics of deformation twin and deformation induced  $\epsilon$ -martensite in an austenitic Fe-C-Mn steel. *Scripta Materialia* 40, 1171–1177.
- Christian, J. W., 1951. A theory for the transformation in pure cobalt. *Proceedings of the Royal Society of London A* 206A, 51–64.
- Christian, J. W., 1962. The origin of surface relief effects in phase transformations. In: Zackay, V. F., Aaronson, H. I. (Eds.), *Decomposition of austenite by diffusional processes*. Interscience, New York, USA, pp. 371–386.
- Christian, J. W., 1965a. Military transformations: an introductory survey. In: *Physical properties of martensite and bainite*, Special Report 93. Iron and Steel Institute, London, U.K., pp. 1–19.
- Christian, J. W., 1965b. *Theory of Transformations in Metals and Alloys*. Pergamon Press, Oxford, U. K.

- Christian, J. W., 1971. The strength of martensite. In: Kelly, A., Nicholson, R. (Eds.), *Strengthening Methods in Crystals*. Elsevier, Netherlands, pp. 261–329.
- Christian, J. W., 1975. *Theory of Transformations in Metals and Alloys, Part I*, 2nd Edition. Pergamon Press, Oxford, U. K.
- Christian, J. W., 1979. Thermodynamics and kinetics of martensite. In: Olson, G. B., Cohen, M. (Eds.), *International Conference on Martensitic Transformations ICOMAT '79*. Alpine Press, Massachusetts, USA, pp. 220–234.
- Christian, J. W., 1982. Deformation by moving interfaces. *Metallurgical Transactions A* 13, 509–538.
- Christian, J. W., 1990. Simple geometry and crystallography applied to ferrous bainites. *Metallurgical transactions A* 21, 799–803.
- Christian, J. W., 1992. Tetragonal martensites in ferrous alloys – a critique. *Materials Transactions, JIM* 33, 208–214.
- Christian, J. W., 1994. Crystallographic theories, interface structures and transformation mechanisms. *Metallurgical & Materials Transactions A* 25, 1821–1839.
- Christian, J. W., 1997. Lattice correspondence atomic site correspondence and shape change in diffusional-displacive phase transformations. *Progress in Materials Science* 42, 109–124.
- Christian, J. W., 2003a. *Theory of Transformations in Metals and Alloys, Part I*, 3rd Edition. Pergamon Press, Oxford, U. K.
- Christian, J. W., 2003b. *Theory of Transformations in Metals and Alloys, Part II*, 3rd Edition. Pergamon Press, Oxford, U. K.
- Christian, J. W., Crocker, A. G., 1980. Dislocations in Solids, ed. F. R. N. Nabarro. North Holland, Amsterdam, Holland, Ch. 3, p. 369.
- Christian, J. W., Edmonds, D. V., 1984. The bainite transformation. In: Marder, A. R., Goldstein, J. I. (Eds.), *Phase Transformations in Ferrous Alloys*. TMS-AIME, Warrendale, Pennsylvania, USA, pp. 293–327.
- Christian, J. W., Mahajan, S., 1995. Deformation twinning. *Progress in Materials Science* 39, 1–157.
- Chung, D. W., Todd, J. A., Youngs, J. K., Parker, E. R., 1982. Hydrogen attack of thick section pressure vessel steels. In: Semchyshen, M. (Ed.), *Advanced Materials for Pressure Vessel Service with Hydrogen at High Temperatures and Pressures*. American Society of Mechanical Engineers, New York, USA, pp. 25–52.
- Chupatanakul, S., Nash, P., 2006. Dilatometric measurement of carbon enrichment in austenite during bainite transformation. *Journal of Materials Science* 41, 4965–4969.
- Cizek, P., 2001. Transformation behaviour and microstructure of an API X80 linepipe steel subjected to simulated thermomechanical processing. In: 10th International Metallurgical and Materials Conference METAL 2001. Tanger Ltd., Ostrava, Czech Republic, pp. Paper 94, 1–8.
- Clark, H. M., Wayman, C. M., 1970. Surface relief effects in solid-state phase transformations. In: Zackay, V. F., Aaronson, H. I. (Eds.), *Phase Transformations*. ASM, Metals Park, Ohio, USA, pp. 59–114.
- Clatterbuck, D. M., Chrzan, D. C., Jr., J. W. M., 2002. The inherent tensile strength of iron. *Philosophical Magazine Letters* 82, 141–147.
- Clayton, P., Danks, D., 1990. Effect of interlamellar spacing on the wear resistance of eutectoid steels under rolling-sliding conditions. *Wear* 135, 369–389.
- Clayton, P., Sawley, K. J., Bolton, P. J., Pell, G. M., 1987. Wear behaviour of rail steel. *Wear* 120, 199–220.
- Coates, D. E., 1972. Diffusion controlled precipitate growth in ternary systems I. *Metallurgical Transactions* 3, 1203–1212.
- Coates, D. E., 1973a. Diffusion controlled precipitate growth in ternary systems II. *Metallurgical Transactions* 4, 1077–1086.
- Coates, D. E., 1973b. Diffusional growth limitation and hardenability. *Metallurgical Transactions* 4, 2313–2325.
- Cochardt, A. W., Shoek, G., Wiedersich, H., 1955. Interaction between dislocations and interstitial atoms in body-centered cubic metals. *Acta Metallurgica* 3, 533–537.
- Cocks, U. F., 1967. Statistical treatment of penetrable obstacles. *Canadian Journal of Physics* 45, 737–755.
- Cocks, U. F., Argon, A. S., Ashby, M. F., 1975. Thermodynamics and kinetics of slip. *Progress in Materials Science* 19, 1–219.
- Cohen, M., 1940. Discussion on paper by A. B. Greninger and A. R. Troiano. *Trans. A. S. M.*, 537.
- Cohen, M., 1946. The martensite transformation (discussion to Troiano and Greninger 1946). *Metal Progress* 50, 303–307.
- Cohen, M., Machlin, E. S., Paranjpe, V. G., 1950. *Thermodynamics in Physical Metallurgy*. ASM, Ohio, U. S. A.
- Cola Jr., G. M., 2007. Properties of bainite nucleated by water quenching in 80 ms. In: Furuhashi, T., Tsuzaki, K. (Eds.), *1st International Symposium on Steel Science*. Iron and Steel Institute of Japan, Tokyo, Japan, pp. 187–190.
- Coldren, A. P., Cryderman, R. L., Semchyshen, M., 1969. Strength and impact properties of low carbon structural steels containing Mo. In: *Steel Strengthening Mechanisms*. Climax Molybdenum Co., Ann Arbor, Michigan, USA, p. 17.

- Collins, L. E., Baragar, D. L., Bowker, J. T., Kostic, M. M., Subramanian, S. V., June 1995. Steckel mill process optimization for production of X70 and X80 gas transmission linepipe. In: *Microalloying '95 Conference Proceedings*. Iron and Steel Society Inc., Pittsburgh, USA, pp. 141–147.
- Collins, L. E., Knight, R. F., Ruddle, G. E., Boyd, J. D., 1985. Laboratory development of accelerated cooling of microalloyed plate steels. In: Southwick, P. D. (Ed.), *Accelerated Cooling of Steel*. TMS-AIME, Ohio, USA, pp. 261–282.
- Collins, M. J., 1989. Carbide stabilities in a Cr Mo V bolting steel. *Materials Science and Technology*, 323–327.
- Conrad, H., 1964. Thermally activated deformation of metals. *Journal of Metals* 145, 582–588.
- Cooman, B. C. D., Barbé, L., Mahieu, J., Krizan, D., Samek, L., Meyer, M. D., 2004. Mechanical properties of low alloy intercritically annealed cold rolled TRIP sheet steel containing retained austenite. *Canadian Metallurgical Quarterly* 43, 13–24.
- Cornide, J., Miyamoto, G., Caballero, F. G., Furuhashi, T., Miller, M. K., Garcia-Mateo, C., 2011. Distribution of dislocations in nanostructured bainite. *Solid State Phenomena* 172-174, 117–122.
- Costa e Silva, A., 2006. Thermodynamic aspects of inclusion engineering in steels. *Rare Metals* 25, 412–419.
- Cottrell, A. H., 1945. Tensile properties of unstable austenite and its low temperature decomposition products. *Journal of the Iron and Steel Institute* 151, 93P–104P.
- Cottrell, A. H., 1995. Fifty years on the shelf. *International Journal of Pressure Vessels and Piping* 64, 171–174.
- Crosky, A., McDougall, P. G., Bowles, J. S., 1980. The crystallography of the precipitation of alpha rods from beta Cu Zn alloys. *Acta Metallurgica* 28, 1495–1504.
- Cullison, A., 1991. Conference reflects keen interest in microalloyed steels. *Welding Journal* 70, 80–82.
- Curry, D. A., Knott, J. F., 1978. Effects of microstructure on cleavage fracture stress in steel. *Metal Science* 12, 511–514.
- Curtze, S., Kundu, M., Kuokkala, V.-T., Datta, S., Chattopadhyay, P. P., 2008. Dynamic properties of new generation high-strength steels for armoring applications. *Society for Experimental Mechanics – 11th International Congress and Exhibition on Experimental and Applied Mechanics 2008* 4, 2051–2057.
- Curtze, S., Kuokkala, V.-T., Hokka, M., Peura, P., 2009. Deformation behavior of TRIP and DP steels in tension at different temperatures over a wide range of strain rates. *Materials Science & Engineering A* 507, 124–131.
- da Cruz, J. A., Rodrigues, T. F. M., Viana, V. D. C., Santos, D. B., 2012. Bainite formation at low temperatures in high C-Si steel and its mechanical behaviour. *Materials Science Forum* 706-709, 173–180.
- da Cruz, J. A., Vilela, J. J., Gonzalez, B. M., Santos, D. B., 2013. Effect of retained austenite on impact toughness of the multi-phase bainitic-martensitic steel. *Advanced Materials Research* 922, 298–303.
- Dadian, M., 1987. The contribution of welding to the understanding of metallurgical phenomena. In: David, S. A. (Ed.), *Advances in the Science & Technology of Welding*. ASM International, Materials Park, Ohio, USA, pp. 101–117.
- Daigne, J., Guttman, M., Naylor, J. P., 1982. Influence of lath boundaries and carbide distribution on the yield strength of 0.4%C tempered martensitic steels. *Materials Science and Engineering* 56, 1–10.
- Dallum, C. B., Olson, D. L., 1989. Stress and grain size effects on weld metal ferrite formation. *Welding Journal, Research Supplement* 68, 198s–205s.
- Darcis, P. P., Katsumoto, H., Payares-Asprino, M. C., Liu, S., Siewert, T. A., 2008. Cruciform fillet welded joint fatigue strength improvements by weld metal phase transformations. *Fatigue and Fracture of Engineering Materials and Structures* 31, 125–136.
- Das, A., Chakraborti, P. C., Tarafder, S., Bhadeshia, H. K. D. H., 2011. Analysis of deformation induced martensitic transformation in stainless steels. *Materials Science and Technology* 27, 366–370.
- Das, S., Haldar, A., 2014. Continuously cooled ultrafine bainitic steel with excellent strength-elongation combination. *Metallurgical & Materials Transactions A* 45, 1844–1854.
- Dauskardt, R. H., Ritchie, R. O., 1986. Fatigue crack propagation behaviour in pressure vessel steels for high pressure hydrogen service. *ASME PVP* 114, 17–18.
- Davenport, A. S., 1941. *TMS-AIME* 145, 301–340.
- Davenport, A. T., February 1974. The crystallography of upper bainite. *Tech. Rep. Project 12051*, Republic Steel Research Center, Ohio, USA.
- Davenport, A. T., 1977. The influence of hot deformation on an as-hot-rolled bainitic steel. In: Ballance, J. B. (Ed.), *The Hot Deformation of Austenite*. TMS-AIME, Warrendale, Pennsylvania, USA, pp. 517–536.
- Davenport, E. S., 1939. Isothermal transformation in steels. *Trans. A. S. M.* 27, 837–886.
- Davenport, E. S., Bain, E. C., 1930. Transformation of austenite at constant subcritical temperatures. *Trans. Am. Inst. Min. Metall. Engng.* 90, 117–154.
- Davenport, E. S., Bain, E. C., Paxton, H. W., 1970. Transformation of austenite at constant subcritical temperatures. *Metallurgical Transactions* 1, 3479–3500.
- Davies, G. J., Kallend, J. S., Morris, P. P., 1977. The influence of hot deformation of austenite on the properties of ferrite through the development and inheritance of texture. In: Ballance, J. B. (Ed.), *The Hot Deformation of Austenite*. TMS-AIME, Warrendale, Pennsylvania, USA, pp. 599–616.

- Davies, R. G., Magee, C. L., 1970a. Austenite ferromagnetism and martensite morphology. *Metallurgical Transactions* 1, 2927–2931.
- Davies, R. G., Magee, C. L., 1970b. Occurrence of the various martensite morphologies. In: *Proc. 2nd Int. Conf. on the Strength of Metals and Alloys*. ASM, Metals Park, Ohio, USA, pp. 817–821.
- Davies, R. G., Magee, C. L., 1971. Influence of austenite and martensite strength on martensite morphology. *Metallurgical Transactions* 2, 1939–1947.
- Davies, R. G., Magee, C. L., 1972. Microcracking in ferrous martensites. *Metallurgical Transactions* 3, 307–313.
- de Kazinczy, F., Axn'as, A., Pachleitner, P., 1963. Some properties of niobium-treated mild steel. *Jernkontorets Annaler* 147, 408–433.
- de Meyer, M., Vanderschueren, D., de Cooman, B. C., 1999. Influence of substitution of Si by Al on the properties of cold-rolled C-Mn-Si TRIP steels. *ISIJ International* 39, 813–822.
- DeArdo, A. J., 1988. Accelerated cooling: A physical metallurgy perspective. In: Ruddle, G. E., Crawley, A. F. (Eds.), *Accelerated cooling or rolled steel*. Pergamon Press, Oxford, U. K., pp. 3–26.
- Deardo, A. J., Gray, J. M., Meyer, L., 1981. Fundamental metallurgy of niobium in steel. In: Stuart, H. (Ed.), *Niobium '81*. TMS-AIME, Warrendale, Pennsylvania, USA, pp. 685–759.
- Deep, G., Williams, W. M., 1975. The isothermic annealing of bainite. *Canadian Metallurgical Quarterly* 14, 85–96.
- DeHoff, R. T., Rhines, F. N., 1968. *Quantitative Microscopy*. McGraw Hill, New York.
- Delaey, L., Warlimont, H., 1975. Crystallography and thermodynamics of SME-martensites. In: Perkins, J. (Ed.), *Shape Memory Effects in Alloys*. Springer, U.S.A., pp. 89–114.
- Delagnes, D., Lamesle, P., Mathon, M., Mebarki, N., Levaillant, C., 2005. Influence of silicon content on the precipitation of secondary carbides and fatigue properties of a 5%Cr tempered martensitic steel. *Materials Science & Engineering A* 394, 435–444.
- Deliry, J., 1965. Nouveau carbure de fer transformation bainitique dans les aciers au carbone silicium. *Memoires Scientifiques Rev. Metallurg.* 62, 527–550.
- Denis, S., Gautier, E., Simon, A., Beck, G., 1985. Stress-phase-transformation interactions – basic principles, modelling and calculation of internal stresses. *Materials Science and Technology* 1, 805–814.
- Devanathan, R., Clayton, P., 1989. Rolling/sliding wear behaviour of three bainitic steels, personal Communication.
- Diesburg, D. E., Kim, C., Fairhurst, W., 1981. Microstructural and residual stress effects on the fracture of case-hardened steels. In: *Heat Treatment '81*. Metals Society, London, U.K., pp. 178–184.
- Dionne, S., Krishnadev, M. R., Collins, L. E., Boyd, J. D., 1988. Influence of processing and cooling rate on the transformation kinetics. In: Ruddle, G. E., Crawley, A. F. (Eds.), *Accelerated Cooling of Rolled Steel*. Pergamon Press, Oxford, U. K., pp. 71–84.
- Diz-Fuentes, M., Gutiérrez, I., 2004. Acicular ferrite in low and medium carbon steels: morphological and crystallographic aspects. In: Lamberights, M. (Ed.), *2nd Int. Conf. on Thermomechanical Processing of Steels*. Verlag Stahleisen GmbH, Dusseldorf, Germany, pp. 123–130.
- Dong, J., Vettters, H., Hoffmann, F., Zoch, H. W., 2010. Microstructure and fatigue strength of the bearing steel 52100 after shortened bainitic treatment. *Journal of ASTM International* 7, JAI 102511.
- Dorazil, E., Barta, B., Munsterova, E., Stransky, L., Huvar, A., 1982. High strength bainitic ductile cast iron. *AFS International Cast Metals Journal* 22, 52–62.
- Dorazil, E., Svejcar, J., 1979. Study of the upper bainite in silicon steel. *Archiv für das Eisenhüttenwesen* 50, 293–298.
- Dorn, J. E., 1968. Low temperature dislocation mechanisms. In: Rosenfield, A. R., Hahn, G. T., Bement, A. L., Jaffee, R. I. (Eds.), *Dislocation dynamics*. McGraw Hill, New York, p. 27.
- Dowling, J. M., Corbett, J. M., Kerr, H. W., 1986. Inclusion phases+ nucleation of acicular ferrite in SMA welds. *Metallurgical Transactions A* 17, 1611–1623.
- Duan, D. M., Zhou, J., Rothwell, B., Horsley, D., Pussegoda, N., 2008. Strain aging effects in high strength line pipe materials. In: *2008 7th International Pipeline Conference*. Vol. 3. ASME, New York, USA, pp. 317–326.
- Dubé, C. A., 1947. The decomposition of austenite in hypoeutectoid steels. Ph.D. thesis, Carnegie Institute of Technology, Pittsburgh, USA.
- Dubé, C. A., Aaronson, H. I., Mehl, R. F., 1958. La formation de la ferrite proeutectoide dans les aciers au carbone. *Revue de Metallurgie* 55, 201–210.
- Dubensky, W. J., Rundman, K. B., 1985. An electron microscopy study of carbide formation in austempered ductile iron. *AFS Transactions* 93, 389–394.
- Dubrov, V. A., 1969. High temperature metallographic analysis of the influence of stress on the bainitic transformation kinetics. *Physics of Metals and Metallography* 28, 126–131.
- Duckworth, W. E., 1966. Thermomechanical treatment of metals. *Journal of Metals* 18, 915–922.
- Duckworth, W. E., Taylor, P. R., Leak, D. A., 1964. Ausforming behaviour of En24, En30B and an experimental 3%Cr-Ni-Si steel. *Journal of the Iron and Steel Institute* 202, 135–142.

- Dumoulin, P., Guttman, M., Foucault, M., Palmier, M., Wayman, C. M., Biscondi, M., 1980. Role of molybdenum in phosphorus-induced temper embrittlement. *Metal Science* 14, 1–15.
- Dunne, D. P., Wayman, C. M., 1971. The crystallography of ferrous martensite. *Metallurgical Transactions* 2, 2327–2341.
- Duong, V. T., Song, Y. Y., Park, K. S., Bhadeshia, H. K. D. H., Suh, D. W., 2014. Austenite in transformation-induced plasticity steel subjected to multiple isothermal heat-treatments. *Metallurgical & Materials Transactions A* 45, 4201–4209.
- Durbin, M., Krahe, P. R., 1973. Controlled rolling and the properties of very low C, high Mn steels containing strong carbide formers. In: *Processing and Properties of low-Carbon Steel*. TMS-AIME, Warrendale, Pennsylvania, USA, pp. 109–131.
- Dutta, R. K., Huizenga, R. M., Amirthalingam, M., Gao, H., King, A., Hermans, M. J. M., Richardson, I. M., 2014. Synchrotron diffraction studies on the transformation strain in a high strength quenched and tempered structural steel. *Materials Science Forum* 777, 231–236.
- Dutta, R. K., Huizenga, R. M., Amirthalingam, M., King, A., Hermans, M. J. M., Richardson, I. M., 2013. Transformation-induced diffraction peak broadening during bainitic and martensitic transformations under small external loads in a quenched and tempered high strength steel. *Metallurgical & Materials Transactions A* 44, 4011–4014.
- Echeverria, A., Rodriguez-Ibabe, J. M., 2003. The role of grain size in brittle particle induced fracture of steels. *Materials Science & Engineering A* 346, 149–158.
- Eckerlid, J., Nilsson, T., Karlsson, L., 2003. Fatigue properties of longitudinal attachments welded using low transformation temperature filler. *Science and Technology of Welding and Joining* 8, 353–359.
- Edwards, D. P., 1969. Toughness of martensite and bainite in a 3%Ni Cr Mo V steel. *Journal of the Iron and Steel Institute* 207, 1494–1502.
- Edwards, R. H., Kennon, N. F., 1974. Kinetics of bainite formation from deformed austenite. *Journal of the Australian Institute of Metals* 19, 45–50.
- Edwards, R. H., Kennon, N. F., 1978. The morphology and mechanical properties of bainite formed from deformed austenite. *Metallurgical Transactions A* 9, 1801–1809.
- Eldis, G. T., Hagel, W. C., 1977. Effects of microalloying on the hardenability of steels. In: Doane, D. V., Krikaldy, J. S. (Eds.), *Hardenability concepts with applications to steels*. TMS-AIME, Warrendale, Pennsylvania, USA, pp. 397–415.
- Enomoto, M., Nojiri, N., Sato, Y., 1994. Effects of vanadium and niobium on the nucleation kinetics of proeutectoid ferrite at austenite grain boundaries in Fe-C and Fe-C-Mn alloys. *Materials Transactions, JIM* 35, 859–867.
- Enomoto, M., Wu, K. M., Inagawa, T., Nanba, S., 2005. Three-dimensional observation of ferrite plate in low carbon steel weld. *ISIJ International* 45, 756–762.
- Entin, R., 1962. The elementary reactions in the austenite – pearlite, bainite transformations. In: y, V. F. Z., Aaronson, H. I. (Eds.), *Decomposition of austenite by diffusional processes*. Interscience, New York, pp. 295–211.
- Epshtein, G. N., Paisov, I. V., 1965. Surface hardening of case hardened steel by rolling. *Metal Science and Heat Treatment* 6, 742–745.
- Ericsson, C. E., Bhat, M. S., Parker, E. R., Zackay, V. F., 1976. Isothermal studies of bainitic and martensitic transformations in some low alloy steels. *Metallurgical Transactions A* 7, 1800–1803.
- Es-Souni, M., Beaven, P. A., 1990. Microanalysis of inclusion/matrix interfaces in weld metals. *Surface and Interface Analysis* 16, 504–509.
- Esaka, K., Matsumura, Y., Koyama, T., Tashiro, M., 1985. Hot rolled plain carbon steel sheets with a good combination of high strength and formability. In: *HSLA Steels: Metallurgy and Applications*. ASM International, Ohio, USA, pp. 248–250.
- Eterashvili, T. V., Utevsky, L. M., Spasskiy, M. N., 1981. martensite crystallography packets laths orientations twin relate in engineering steel. *Physics of Metals and Metallography* 48, 113–121.
- Evans, G. M., 1986. Effect of Mo on the microstructure and properties of C-Mn welds. Tech. Rep. IIA 666 86, International Institute of Welding, Paris, France.
- Evans, G. M., 1990. The effect of aluminium in shielded metal-arc C-Mn steel multi-run deposits. Tech. Rep. II-A-796-90, International Institute of Welding, Paris, France.
- Evans, M.-H., 2012. White structure flaking in wind turbine gearbox bearings: effects of ‘butterflies’ and white etching cracks. *Materials Science and Technology* 28, 3–22.
- Evans, P. R. V., O’Neill, H., 1959. The effect of rolling unstable austenitic 0.76% C steel at 220–300°C. *Journal of the Iron and Steel Institute* 191, 34–44.
- Fang, K., Yang, J., Zhao, D., Song, K., Yan, Z., Fang, H., 2012. Review of nanobainite steel welding. *Advanced Materials Research* 482-484, 2405–2408.
- Fang, K., Yang, J. G., Liu, X. S., Song, K. J., Fang, H. Y., Bhadeshia, H. K. D. H., 2013. Regeneration technique for welding nanostructured bainite. *Materials & Design* 50, 38–43.

- Fazeli, F., Jia, T., Militzer, M., 2011. Critical assessment of bainite models for advanced high strength steels. *Solid State Phenomena* 172-174, 1183–1188.
- Fegredo, D. M., 1975. Effect of rolling at different temperatures on the fracture toughness anisotropy of a C-Mn structural-steel. *Canadian Metallurgical Quarterly* 14, 243–255.
- Felfer, P. J., Killmore, C. R., Williams, J. G., Carpenter, K. R., Ringer, S. P., Cairney, J. M., 2012. A quantitative atom probe study of the Nb excess at prior austenite grain boundaries in a Nb microalloyed strip-cast steel. *Acta Materialia* 60, 5049–5055.
- Fiedler, H. C., Averbach, B. L., Cohen, M., 1955. The effect of deformation on the martensitic transformation. *Transactions of the American Society for Metals* 47, 267–290.
- Fielding, L. C. D., Bhadeshia, H. K. D. H., 2014. Shear band structure in ballistically tested bainitic steels. *Materials Science and Technology* 30, 812–817.
- Fielding, L. C. D., Song, E. J., Han, D. K., Bhadeshia, H. K. D. H., Suh, D. W., 2014. Hydrogen diffusion and the percolation of austenite in nanostructured bainitic steel. *Proceedings of the Royal Society of London A* 470, 20140108.
- Fischer, F. D., Sun, Q.-P., Tanaka, K., 1996. Transformation-induced plasticity (TRIP). *Applied Mechanics Reviews* 49, 317–364.
- Fisher, G. L., Geils, R. H., 1969. The effect of columbium on the alpha-gamma transformation in a low alloy Ni-Cu steel. *Trans. Metall. Soc. AIME* 245, 2405–2412.
- Fisher, J. C., Hollomon, J. H., Turnbull, D., 1949. Kinetics of the austenite to martensite transformation. *Metals Transactions* 185, 691–700.
- Fisher, R. M., 1958. Precipitation of carbides in unalloyed and low alloy steels. In: 4th International Conference on Electron Microscopy. Springer Verlag, Berlin, Germany, pp. 579–588.
- Fitzgerald, F., 1991. Steel – technical achievements and challenges. *Metals and Materials* June, 378–387.
- Foet, J., Rochegude, P., Hendry, A., 1988. Low temperature ageing of Fe-N austenite. *Acta Metallurgica* 36, 501–505.
- Fondekar, M. K., Rao, A. M., Mallik, A. K., 1970. Strain tempering of bainite. *Metallurgical Transactions* 1, 885–890.
- Fors, D. H. R., Wahnström, G., 2008. Nature of boron solution and diffusion in  $\alpha$ -iron. *Physical Review B* 77, 132102.
- Forster, F., Scheil, E., 1936. Akustische untersuchung der bildung von martensitnadeln. *Zeitschrift für Metallkunde* 28, 245–247.
- Forster, F., Scheil, E., 1937. Messung der bildungszeit der martensitnadeln. *Naturwissenschaften* 25, 439–440.
- Fossaert, C., Rees, G., Maurickx, T., Bhadeshia, H. K. D. H., 1995. The effect of niobium on the hardenability of microalloyed austenite. *Metallurgical and Materials Transactions A* 26A, 21–30.
- Fourlaris, G., Baker, A. J., Papadimitriou, G. D., 1996. Effect of copper additions on the isothermal bainitic transformation in hypereutectoid copper and copper-nickel steels. *Acta Materialia* 44, 4791–4805.
- Franetovic, V., Sachdev, A., Ryntz, E. F., 1987a. A TEM study of austempered lower bainitic nodular cast iron. *Metallography* 20, 15–36.
- Franetovic, V., Shea, M. M., Ryntz, E. F., 1987b. TEM study of austempered nodular iron: influence of Si content austenitising time and austempering temperature. *Materials Science & Engineering* 96, 231–245.
- Franklin, A. G., 1969. Comparison between a quantitative microscope and chemical methods. *Journal of the Iron and Steel Institute* 207, 181–186.
- Freiwilgig, R., Kudraman, J., Chraska, P., 1976. Bainite transformation in deformed austenite. *Metallurgical Transactions A* 7, 1091–1097.
- Fridberg, J., Torndahl, L.-E., Hillert, M., 1969. Diffusion in iron. *Jernkontorets Annaler* 153, 263–276.
- Fu, H., Miao, Y., Chan, X., Qiao, B., 2007. Effect of austempering on the structures and performances of cast high carbon Si-Mn steel. *Steel Research International* 78, 358–363.
- Fujita, N., Bhadeshia, H. K. D. H., 1999. Precipitation reactions in 10CrMoV steel: Comparison with theory. In: Strang, A., McLean, M. (Eds.), *Modelling of Microstructural Evolution in Creep Resistant Materials*. Institute of Materials, London, pp. 105–114.
- Fujita, S., Matsuoka, S., Murakami, T., 2000. Effect of hydrogen on fatigue behaviour of bearing steel under cyclic torsion with compressive mean stress. In: *Mechanics of Materials*. Japan Society of Mechanical Engineers, Tokyo, Japan, pp. 241–243.
- Fukagawa, T., Okada, H., Maehara, Y., 1994. Mechanism of red scale defect formation in Si-added hot-rolled steel sheets. *ISIJ International* 34, 906–911.
- Fukuoka, C., Morishima, K., Yoshizawa, H., Mino, K., 2002. Misorientation development in grains of tensile strained and crept 2.25Cr1Mo steel. *Scripta Materialia* 46, 61–66.
- Fullman, R. L., 1953. Measurement of approximately cylindrical particles in opaque samples. *Trans. A.I.M.M.E.* 197, 1267–1268.
- Fumimaru, K., Toshiyuki, H., Keniti, A., 2000. Extremely-low carbon bainitic steels for new structural steel products. *Revue de Métallurgie* 97, 1235–1244.

- Furnémont, Q., 2003. The micromechanics of TRIP-assisted multiphase steels. Ph.D. thesis, Université Catholique de Louvain, Belgium.
- Furnémont, Q., Jacques, P., Pardoën, T., Delannay, F., 2000. Influence of the mechanical stability of retained austenite on the damaging micromechanisms in TRIP-assisted multiphase steels. In: Miannay, D., Costa, P., Francois, D., Pineau, A. (Eds.), *Advances in Mechanical Behaviour, Plasticity and Damage*. Elsevier, Netherlands, pp. 859–864.
- Furnémont, Q., Kempf, M., Jacques, P. J., Göken, M., Delannay, F., 2002. On the measurement of the nanohardness of the constitutive phases of TRIP-assisted multiphase steels. *Materials Science and Engineering A* 328A, 26–32.
- Furnémont, Q., Lacroix, G., Godet, S., Conlon, K. T., Jacques, P. J., 2004. Critical assessment of the micromechanical behaviour of dual phase and TRIP-assisted multiphase steels. *Canadian Metallurgical Quarterly* 43, 35–42.
- Furuhara, T., Kawata, H., Morito, S., Maki, T., 2006. Crystallography of upper bainite in Fe-Ni-C alloys. *Materials Science & Engineering A* 431, 228–236.
- Furuhara, T., Kawata, H., Morito, S., Miyamoto, G., Maki, T., 2008. Variant selection in grain boundary nucleation of upper bainite. *Metallurgical & Materials Transactions A* 39, 1003–1013.
- Furuhara, T., Miyajima, N., Moritani, T., Maki, T., 2003. Interphase boundary structures of lath martensite and bainite in steel. *Journal de Physique IV* 112, 319–322.
- Furuhara, T., Yamaguchi, T., Miyamoto, G., Maki, T., 2010. Incomplete transformation of upper bainite in Nb bearing low carbon steels. *Materials Science and Technology* 26, 392–397.
- Furuya, Y., Masuoka, S., Abe, T., Yamaguchi, K., 2002. Gigacycle fatigue properties for high-strength low-alloy steel at 100 Hz, 600 Hz, and 20 kHz. *Scripta Materialia* 46, 157–162.
- Gagne, M., 1985. The influence of Mn and Si on structure and properties of austempered ductile iron. *AFS Transactions* 93, 801–812.
- Gao, G., Zhang, H., Tan, Z., Liu, W., Bai, B., 2013. A carbide-free bainite/martensite/austenite triplex steel with enhanced mechanical properties treated by a novel quenching-partitioning-tempering process. *Materials Science & Engineering A* 559, 165–169.
- Garboczi, E. J., Snyder, K. A., Douglas, J. F., Thorpe, M. F., 1995. Geometrical percolation threshold of overlapping ellipsoids. *Physical Review E* 52, 819–828.
- Garcia, O. L., Petrov, R., Bae, J. H., Kestens, L., Kang, K. B., 2007. Microstructure-texture related toughness anisotropy of API-X80 pipeline steel. *Advanced Materials Research* 15-17, 840–845.
- García-Mateo, C., Caballero, F. G., 2005. Role of retained austenite on tensile properties of steels with bainitic microstructures. *Materials Transactions* 46, 1839–1846.
- García-Mateo, C., Caballero, F. G., Bhadeshia, H. K. D. H., 2003a. Acceleration of low-temperature bainite. *ISIJ International* 43, 1821–1825.
- García-Mateo, C., Caballero, F. G., Bhadeshia, H. K. D. H., 2003b. Development of hard bainite. *ISIJ International* 43, 1238–1243.
- García-Mateo, C., Caballero, F. G., Bhadeshia, H. K. D. H., 2003c. Low-temperature bainite. *Journal de Physique Colloque* 112, 285–288.
- García-Mateo, C., Caballero, F. G., Bhadeshia, H. K. D. H., 2005. Mechanical properties of low-temperature bainite. *Materials Science Forum* 500-501, 495–502.
- García-Mateo, C., Caballero, F. G., Miller, M. K., Jimenez, J. A., 2012a. On measurement of carbon content in retained austenite in a nanostructured bainitic steel. *Journal of Materials Science* 47, 1004–1010.
- García-Mateo, C., Caballero, F. G., Sourmail, T., Kuntz, M., Cornide, J., Smanio, V., Elvira, E., 2012b. Tensile behaviour of a nanocrystalline bainitic steel containing 3 wt% silicon. *Materials Science & Engineering A* 549, 185–192.
- García-Mateo, C., Capdevila, C., Caballero, F. G., de Andrés, C. G., 2007. Artificial neural network modeling for the prediction of critical transformation temperatures in steels. *Journal of Materials Science* 42, 5391–5397.
- García-Mateo, C., Peet, M., Caballero, F. G., Bhadeshia, H. K. D. H., 2004. Tempering of a hard mixture of bainitic ferrite and austenite. *Materials Science and Technology* 20, 814–818.
- Garnham, J., 1989. Rail steels, personal Communication.
- Garwood, M. F., Zurburg, H. H., Erickson, M. A., 1951. Correlation of Laboratory Tests and Service Performance: Interpretation of tests and correlation with service. *ASM*, Ch. 1, pp. 1–77.
- Garwood, R. D., 1954-1955. *Journal of the Institute of Metals* 83, 64–68.
- Gaude-Fugarolas, D., Jacques, P. J., 2006. A new physical model for the kinetics of the bainite transformation. *ISIJ International* 46, 712–717.
- George, T., Parker, E. R., Ritchie, R. O., 1985. Susceptibility to hydrogen attack of a thick section 3Cr1Mo1Ni pressure vessel steel – role of cooling rate. *Materials Science and Technology* 1, 198–208.
- Ghoniem, H., Kalousek, J., Stone, D., 1982. Fracture and wear characteristics of Cr-Mo bainitic steel, speciality steels and hard materials. In: *Speciality Steels and Hard Materials*. Pergamon Press, Oxford, Pretoria, South Africa, pp. 259–265.

- Ghosh, G., Campbell, C. E., Olson, G. B., 1999. Analytical electron microscopy study of paraequilibrium cementite precipitation in ultra-high strength steel. *Metallurgical & Materials Transactions A* 30, 501–512.
- Ghosh, G., Olson, G. B., 1994. Kinetics of FCC→BCC heterogeneous martensitic nucleation. *Acta Metallurgica and Materialia* 42, 3361–3370.
- Ghosh, G., Olson, G. B., 2001. Computational thermodynamics and kinetics of martensitic transformation. *Journal of Phase Equilibria* 22, 199–207.
- Ghosh, G., Olson, G. B., 2002. Precipitation of paraequilibrium cementite: experiments, thermodynamic and kinetic modelling. *Acta Materialia* 50, 2099–2119.
- Girault, E., 1999. Bainitic transformation in TRIP-assisted steels and its influence on mechanical properties. Ph.D. thesis, Katholieke Universiteit Leuven, Belgium.
- Girault, E., Godet, S., Jacques, P., Bocher, P., Verlinden, B., van Humbeeck, J., 2001b. Effect of hot-rolling on the formation of isothermal bainite in a 0.4C-1.5Si-1.4Mn steel. *Journal de Physique IV (Proceedings)* 11, 217–222.
- Girault, E., Mertens, A., Jacques, P., Houbaert, Y., Verlinden, B., van Humbeeck, J., 2001. Comparison of the effects of silicon and aluminium on the tensile behaviour of multiphase TRIP-assisted steels. *Scripta Materialia* 49, 139–152.
- Gladman, T., 1972. Letter, personal Communication to Honeycombe and Pickering (1972).
- Gladman, T., 1996. *The Physical Metallurgy of Microalloyed Steels*. IOM Communications, London.
- Gladman, T., 1997. *Physical Metallurgy of Microalloyed Steels*. Institute of Materials, London, U.K.
- Glicksman, M. E., Schaefer, R. J., Ayres, J. D., 1976. Dendritic growth – a test of theory. *Metallurgical Transactions A* 7, 1747–1759.
- Goa, K., Wang, L. D., Zhu, M., Chen, J. D., Shi, Y. J., Kang, M. K., 2007. Refinement of grain and enhancement of impact toughness for low-alloying ultra-high strength bainite steels. *Acta Metallurgica Sinica* 43, 315–320.
- Godet, S., Glez, J. C., He, Y., Jonas, J. J., Jacques, P. J., 2004. Grain-scale characterization of transformation texture. *Journal of Applied Crystallography* 37, 417–425.
- Godet, S., Kim, B. K., Jacques, P. J., Szpunar, J., Jonas, J. J., Delannay, F., 2003. Microtextural study of variant selection by EBSD in a bainitic steel containing retained austenite. *Journal de Physique IV* 112, 309–312.
- Goldak, J., Patel, B., Bibby, M., Moore, J., 1985. Computational weld mechanics, personal Communication.
- Goldman, L. M., Aziz, M. J., 1987. Aperiodic stepwise growth model for the velocity and orientation dependence of solute trapping. *Journal of Materials Research* 2, 524–527.
- Gomez, G., Pérez, T., Bhadeshia, H. K. D. H., 2008. Strong bainitic steels by continuous cooling transformation. In: Pérez, T. (Ed.), *New Developments on Metallurgy and Applications of High Strength Steels*. Tenaris, Buenos Aires, Argentina, pp. 571–582.
- Gomez, G., Pérez, T., Bhadeshia, H. K. D. H., 2009a. Air-cooled bainitic steels for strong, seamless pipes, part 2: Properties and microstructure of rolled material. *Materials Science and Technology* 25, 1508–1512.
- Gomez, M., Garcia, C. I., Haezebrouck, D., DeArdo, A. J., 2009b. Design of composition in (Al/Si)-alloyed TRIP steels. *ISIJ International* 49, 302–311.
- Gong, W., Tomota, Y., Harjo, S., Su, Y. H., Aizawa, K., 2015. Effect of prior martensite on bainite transformation in nanobainite steel. *Acta Materialia* 85, 243–249.
- Gong, W., Tomota, Y., Koo, M. S., Adachi, Y., 2010. Effect of ausforming on nanobainite steel. *Scripta Materialia* 63, 819–822.
- Goodall, G. R., Gianetto, J., Bowker, J., Brochu, M., 2012. Thermal simulation of HAZ regions in modern high strength steel. *Canadian Metallurgical Quarterly* 51, 58–66.
- Goodenow, R. H., Barkalow, R. H., Hehemann, R. F., 1965. Bainite transformations in hypoeutectoid steels. In: *Physical properties of martensite and bainite*, Special Report 93. Iron and Steel Institute, London, U.K., pp. 135–141.
- Goodenow, R. H., Barkalow, R. H., Hehemann, R. F., 1969. Bainite transformations in hypoeutectoid steels. In: *Physical properties of martensite and bainite*, Special Report 93. Iron and Steel Institute, London, pp. 135–141.
- Goodenow, R. H., Matas, S. J., Hehemann, R. F., 1963. Growth kinetics and the mechanism of the bainite transformation. *TMS-AIME* 227, 651–658.
- Gordine, J., Codd, I., 1969. The influence of Si up to 1.5 wt% on the tempering of a spring steel. *Journal of the Iron and Steel Institute* 207, 461–467.
- Gorni, A. A., Mei, P. R., 2005. Development of alternative as-rolled alloys to replace quenched and tempered steels with tensile strength in the range of 600–800 MPa. *Journal of Materials Processing Technology* 162–163, 298–303.
- Gorsuch, P. D., 1959. On the crystal perfection of iron whiskers. *Journal of Applied Physics* 30, 837–842.
- Gouné, M., Bouaziz, O., Allain, S., Zhu, K., Takahashi, M., 2012. Kinetics of bainite transformation in heterogeneous microstructures. *Materials Letters* 67, 187–189.
- Gourgues, A. F., Flower, H. M., Lindley, T. C., 2000. Electron backscattering diffraction study of acicular ferrite, bainite, and martensite steel microstructures. *Materials Science and Technology* 16, 26–40.

- Gourgues-Lorenzon, A. F., 2007. Application of electron backscatter diffraction to the study of phase transformations. *International Materials Reviews* 52, 65–128.
- Grabke, H. J., Hennesen, K., Moller, R., Wei, W., 1987. Effects of manganese on the grain boundary segregation, bulk and grain boundary diffusivity of P in ferrite. *Scripta Metallurgica* 21, 1329–1334.
- Graf, M. K., Hillenbrand, H. G., Peters, P. A., 1985. Accelerated cooling of plate for high-strength large-diameter pipe. In: Southwick, P. D. (Ed.), *Accelerated Cooling of Steel*, TMS AIME. pp. 165–180.
- Graham, L. W., Axon, H. J., 1959. *Journal of the Iron and Steel Institute* 191, 361–365.
- Grange, R. A., 1971. Effect of microstructural banding on steel. *Metallurgical Transactions* 2, 417–426.
- Grässel, O., Kruger, L., Frommeyer, G., Meyer, L. W., 2000. High strength Fe-Mn-(Al, Si) TRIP/TWIP steels development-properties-application. *International Journal of Plasticity* 16, 1391–1409.
- Grassl, K., Thompson, S. W., Krauss, G., 1989. New options for steel selection for automotive applications. Tech. Rep. 890508, Society of Automotive Engineers, Warrendale, Pennsylvania, USA.
- Gray, J. M., 1972. Metallurgy of high-strength low-alloy pipeline steels: present and future possibilities. Tech. Rep. 7201, Molycorp.
- Gray, J. M., 1973. Effect of niobium (columbium) on transformation and precipitation processes in high strength low alloy steels. In: *Heat Treatment '73*. Metals Society, London, U.K., pp. 19–28.
- Gray, J. M., April 2009. A guide for understanding and specifying chemical composition of high strength linepipe steels. Tech. rep., Microalloyed steel.
- Gray, J. M., Wilkening, W. W., Russell, L. G., 1969. Transformation characteristics of very-low-carbon steels. Tech. rep., U. S. Steel, USA.
- Green, M. R., Rainforth, W. M., Frolish, M. F., Beynon, J. H., 2007. The effect of microstructure and composition on the rolling contact fatigue behaviour of cast bainitic steels. *Wear* 263, 756–765.
- Greenwell, B. S., 1990. Letter, personal Communication.
- Greenwood, G. W., 1956. The growth of dispersed precipitates in solutions. *Acta Metallurgica* 4, 243–248.
- Gregg, M., Bhadeshia, H. K. D. H., 1994a. Bainite nucleation from mineral surfaces. *Acta Metallurgica et Materialia* 43, 3321–3330.
- Gregg, M., Bhadeshia, H. K. D. H., 1994b. Titanium-rich mineral phases and the nucleation of bainite. *Metallurgical & Materials Transactions A* 25, 1603–1610.
- Greninger, A. B., Troiano, A. R., 1940. Kinetics of the austenite to martensite transformation in steel. *Trans. ASM* 28, 537.
- Grong, O., 1997. *Metallurgical Modelling of Welding*, 2nd Edition. Maney, London.
- Grong, O., Klukun, A. O., Bjornbakk, B., 1988. Effect of N on weld metal toughness in self-shielded flux cored arc welding. *Joining and Materials* 1, 164–169.
- Grong, O., Kolbeinsen, L., van der Eijk, C., Tranell, G., 2006. Microstructure control of steels through dispersoid metallurgy using novel grain refining alloys. *ISIJ International* 46, 824–831.
- Grong, O., Matlock, D. K., 1986. Microstructural development in steel weld metals. *International Metals Reviews* 31, 27–48.
- Gross, J. H., Stout, R. D., Czyryca, E. J., 1995. Thermomechanical processing of HY130 steel. *Welding Journal, Research Supplement* 74, 53–62.
- Grujicic, M., Olson, G. B., Owen, W. S., 1985. Mobility of martensitic interfaces. *Metallurgical & Materials Transactions A* 16, 1713–1722.
- Guillou, R., Guttman, M., Dumoulin, P., 1981. Role of molybdenum in phosphorus-induced temper embrittlement of 12%Cr martensitic stainless steel. *Metal Science* 15, 63–72.
- Guo, W., Dong, H., Lu, M., Zhao, X., 2002. The coupled effects of thickness and delamination on cracking resistance of X70 pipeline steel. *International Journal of Pressure Vessels and Piping* 79, 403–412.
- Guo, Y., Li, Z., Yao, C., Zhang, K., Lu, F., Feng, K., Huang, J., Wang, M., Wu, Y., 2014. Microstructure evolution of Fe-based nanostructured bainite coating by laser cladding. *Materials and Design* 63, 100–108.
- Guo, Z., Furuhashi, T., Maki, T., 2001. The influence of (MnS+VC) complex precipitate on the crystallography of intergranular pearlite transformation in Fe-Mn-C hypereutectoid alloys. *Scripta Materialia* 45, 525–532.
- Gur Hakan, C., Tuncer, B. O., 2005. Characterization of microstructural phases of steels by sound velocity measurement. *Materials Characterization* 55, 160–166.
- Gutierrez, I., Aranzabal, J., Castro, F., Urcola, J. J., 1995. Homogeneous formation of epsilon carbides within austenite during isothermal transfm. of a ductile iron at 410°C. *Metallurgical & Materials Transactions A* 26, 1045–1060.
- Habraken, L. J., 1956. Bainitic transformation of steels. *Revue de Métallurgie* 53, 930–944.
- Habraken, L. J., 1957. *Comptes Rendus* 19, 126–135.
- Habraken, L. J., Economopoulos, M., 1967. Bainitic microstructures in low-C alloy steels and their mechanical properties. In: *Transformation and Hardenability in Steels*. Climax Molybdenum Co., Ann Arbor, Michigan, USA, pp. 69–107.
- Hackenberg, R. E., Shiflet, G. J., 2003. A microanalysis study of the bainite reaction at the bay in Fe-C-Mo. *Acta Materialia* 51, 2131–2147.

- Haezebrouck, D. M., 1987. Nucleation and growth of a single martensitic particle. Ph.D. thesis, Massachusetts Institute of Technology, Boston, USA.
- Hägg, G., 1934. Pulverphotogramme eines neuen eisencarbides. *Zeitschrift für Kristallographie* 89, 92–94.
- Hahn, G. T., Averbach, B. L., Owen, W. S., Cohen, M., 1959. *Fracture*. MIT Press, Cambridge, MA, USA.
- Haidemenopoulos, G. N., Grujicic, M., Olson, G. B., Cohen, M., 1989. Transformation microyielding of retained austenite. *Acta Metallurgica* 37, 1677–1682.
- Hajiakbari, F., Ahmadabadi, M. N., Poorganji, B., Furuhashi, T., 2010. Microstructure evolution through heavy compression aided by thermodynamic calculations. *Journal of Materials Science* 45, 4689–4695.
- Haldar, A., August 2014. Personal communication, letter.
- Hall, B., 1990. The microstructure and properties of laser welds in steels. Ph.D. thesis, University of Cambridge, Cambridge, U. K.
- Hamdany, A. A., Fattal, D. A., Jabbar, T. A., Bhadeshia, H. K. D. H., 2012. Estimation of the fracture toughness of tempered nanostructured bainite. *Materials Science and Technology* 28, 685–689.
- Hammond, R. I., Proud, W. G., 2004. Does the pressure-induced alpha-epsilon transition occur for all low-alloys steels? *Proceedings of the Royal Society of London A* 460, 2959–2974.
- Hampshire, J. M., Nash, J. V., Hollox, G. E., 1982. Materials evaluation by flat washer testing. In: Hoo, J. J. C. (Ed.), *Rolling contact fatigue testing of bearing steels*. American Society for Testing of Materials, Pennsylvania, USA, pp. 46–66.
- Han, H. N., Lee, C. G., Oh, C.-S., Lee, T.-O., Kim, S.-J., 2004. A model for deformation behaviour and mechanically induced martensitic transformation of metastable austenitic steel. *Acta Materialia* 52, 5203–5214.
- Han, H. N., Oh, C. S., Kim, G., Kwon, O., 2009. Design method for TRIP-aided multiphase steel based on a microstructure-based modelling for transformation-induced plasticity and mechanically induced martensitic transformation. *Materials Science and Engineering A* 499, 462–468.
- Hanlona, D. N., van Bohemen, S. M. C., Celotto, S., 2015. Critical assessment 10: Tensile elongation of strong automotive steels as function of testpiece geometry. *Materials Science and Technology* 31, 385–388.
- Hannemann, H., Hofmann, W., Wiester, H., 1932. *Arch. Eisenhüttenwesen* 6, 199.
- Hanold, B., Babu, S. S., Cola, G., Ream, S., Nagy, B., Victor, B., 2013. Investigation of HAZ softening in laser welding of AHS/high hardness steels. In: Babu, S., Bhadeshia, H. K. D. H., Cross, C. E., David, S. A., DebRoy, T., DuPont, J. N., Koseki, T., Liu, S. (Eds.), *Trends in Welding Research*. ASM International, Ohio, U. S. A., pp. 15–20.
- Hanzaki, A. Z., Hodgson, P. D., Yue, S., 1997. Retained austenite characteristics in thermomechanically processed Si-Mn transformation-induced plasticity steels. *Metallurgical and Materials Transactions A* 28, 2405–2414.
- Hara, T., Asahi, H., Uemori, R., Tamehiro, H., 2004. Role of combined addition of niobium and boron and of molybdenum and boron on hardenability in low carbon steels. *ISIJ International* 44, 1431–1440.
- Hara, T., Maruyama, N., Shinohara, Y., Asahi, H., Shigesato, G., Sugiyama, M., Koseki, T., 2009. Abnormal ferrite to austenite transformation behavior of steels with a martensite and bainite microstructure at a slow reheating rate. *ISIJ International* 49, 1792–1800.
- Harrison, P. L., Farrar, R. A., 1981. Influence of oxygen-rich inclusions on the  $\gamma \rightarrow \alpha$  transformation. *Journal of Materials Science* 16, 2218–2226.
- Harrison, P. L., Farrar, R. A., 1989. Application of continuous cooling transformation diagrams for the welding of steels. *International Materials Reviews* 34, 35–51.
- Hasan, H. S., 2012. Effect of transformation temperature on microstructure and mechanical properties of bainite. *Engineering and Technology Journal* 30, 2165–2174.
- Hasan, H. S., Peet, M., Bhadeshia, H. K. D. H., Wood, S., Watson, E., 2010. Temperature cycling and the rate of the bainite transformation. *Materials Science and Technology* 26, 453–456.
- Hasan, H. S., Peet, M. J., Avettand-Fénoël, M.-N., Bhadeshia, H. K. D. H., 2014. Effect of tempering upon the tensile properties of a nanostructured bainitic steel. *Materials Science & Engineering A* 615, 340–347.
- Hasan, H. S., Peet, M. J., Bhadeshia, H. K. D. H., 2012. Severe tempering of bainite generated at low transformation temperatures. *International Journal of Materials Research* 103, 1319–1324.
- Hase, K., Garcia-Mateo, C., Bhadeshia, H. K. D. H., 2006. Bimodal size-distribution of bainite plates. *Materials Science and Engineering A* A438-440, 145–148.
- Hase, K., Hoshino, T., Amano, K., 1999. Extremely low carbon bainitic high-strength steel bar produced without heat treatment having excellent matchability and toughness. In: Midea, S. J., Pfaffmann, G. D. (Eds.), *Heat Treating*. ASM International, Metals Park, Ohio, USA, pp. 479–485.
- Hase, K., Mateo, C. G., Bhadeshia, H. K. D. H., 2004. Bainite formation influenced by large stress. *Materials Science and Technology* 20, 1499–1505.
- Hashimoto, S., Ikeda, S., Sugimoto, K., Miyake, S., 2004. Effects of Nb and Mo addition to 0.2C-1.5Si-1.5Mn wt% steel on mechanical properties of hot rolled TRIP-aided steel sheets. *ISIJ International* 44, 1590–1598.
- Hashimoto, S., Kashima, T., Ikeda, S., Sugimoto, K., 2002. Effect of morphology of retained austenite on strength and ductility of TRIP-aided steel sheets. *Tetsu-to-Hagane* 88, 42–47.

- Hatano, H., 2005. Effects of Nb and Mo on microstructure and toughness of simulated HAZ in 590 MPa class low carbon bainitic steels. *Tetsu-to-Hagané* 91, 875–881.
- Hätterstrand, M., Andrén, H., 2001. Influence of strain on precipitation reactions during creep of an advanced 9% chromium steel. *Acta Materialia* 49, 2123–2128.
- Haušild, P., Nedbal, I., Berdín, C., Prioul, C., 2002. Influence of ductile tearing on fracture energy in the ductile-brittle transition temperature range. *Materials Science & Engineering A* 335, 164–174.
- Hawkins, M. J., Barford, J., 1972. Experimental kinetics of bainite formation. *Journal of the Iron and Steel Institute* 210, 97–105.
- Hayakawa, M., Matsuoka, S., Tsuzaki, K., 2002. Microstructural analyses of grain boundary carbides of tempered martensite in medium carbon steel by atomic force microscopy. *Materials Transactions* 43, 1758–1766.
- Hayrynen, K. L., Brandenberg, K. R., Keough, J. R., 2002. Applications of austempered ductile cast irons. *Trans. American Foundrymen Society* 2, 929–938.
- He, B. B., Zhu, K., Huang, M. X., 2014. On the nanoindentation behaviour of complex ferritic phases. *Philosophical Magazine Letters*, <http://dx.doi.org/10.1080/09500839.2014.921348>.
- He, J., Lin, L.-B., Lu, T.-C., Wang, P., 2002. Effects of electron- and/or  $\gamma$ -irradiation upon the optical behavior of transparent  $\text{MgAl}_2\text{O}_4$  ceramics: Different color centers induced by electron-beam and  $\gamma$ -ray. *Nuclear Instruments and Methods in Physics Research B* 191, 596–599.
- Heckel, R. W., Paxton, H. W., 1961. On the morphology of proeutectoid cementite. *Trans. A. S. M.* 53, 539–554.
- Hehemann, R. F., 1970. The bainite transformation. In: Aaronson, H. I., Zackay, V. F. (Eds.), *Phase Transformations*. American Society of Materials, Materials Park, Ohio, USA, pp. 397–432.
- Hehemann, R. F., Luhan, V. J., Troiano, A. R., 1957. The influence of bainite on mechanical properties. *Trans. A. S. M.* 49, 409–426.
- Heitmann, W. F., Babu, P. B., 1987. Influence of bainite in the microstructure on tensile and toughness properties of microalloyed steel bars and forgings. In: Krauss, G., Banerji, S. K. (Eds.), *Microalloying Forging Steels*. TMS-AIME, Warrendale, Pennsylvania, USA, pp. 55–72.
- Heller, W., Schweitzer, R., 1980. High-strength pearlitic steel does well in comparative tests against bainitic steels.
- Heller, W., Schweitzer, R., 1982. Hardness, microstructure and wear behaviour of rail steels. In: *2nd Int. Conf. Heavy Haul Railways*, Colorado Springs, USA, pp. 282–286.
- Heritier, B., Maitrepierre, P., Rofes-Vernis, Syckaert, A., 1984. HSLA steels in wire rod and bar applications. In: Korchynsky, M. (Ed.), *HSLA Steels – Technology and Applications*. ASM International, Metals Park, Ohio, USA, pp. 981–990.
- Heron, L. E., 1969. Spheroidise annealing of steel tube for bearings. *Metallurgia* 80, 53–58.
- Heuer, V., Löser, K., Ruppel, J., 2009. Dry bainitizing – a new process for bainitic microstructures. *Journal of Heat Treatment and Materials* 64, 28–33.
- Hewitt, W., 1982. The spheroidise annealing of high carbon steel and its effect on subsequent heat treatment. *Heat Treatment of Metals* 3, 56–62.
- Hillert, M., 1953. *Paraequilibrium*. Tech. rep., Swedish Institute for Metals Research, Stockholm, Sweden.
- Hillert, M., 1957. Role of interfacial energy during solid-state phase transformations. *Jernkontorets Annaler* 141, 757–789.
- Hillert, M., 1960. The growth of ferrite, bainite and martensite. Tech. rep., Swedish Institute for Metals Research, Stockholm, Sweden.
- Hillert, M., 1962. The formation of pearlite. In: Zackay, V. F., Aaronson, H. I. (Eds.), *Decomposition of austenite by diffusional processes*. Interscience, New York, USA, pp. 197–237.
- Hillert, M., 1970. The role of interfaces in phase transformations. In: *Mechanism of Phase Transformations in Crystalline Solids*. Monograph and Report Series No. 33. Institute of Metals, London, U.K., pp. 231–247.
- Hillert, M., 1975. Diffusion and interface control of reactions in alloys. *Metallurgical Transactions A* 6, 5–19.
- Hillert, M., 1981. An analysis of the effect of alloying elements on the pearlite reaction. In: H. I. Aaronson, D. E. Laughlin, M. S., Wayman, C. M. (Eds.), *Solid-Solid Phase Transformations*. TMS-AIME, Materials Park, Ohio, USA, pp. 789–806.
- Hillert, M., 2011. Discussion of “a personal commentary on transformation of austenite at constant subcritical temperatures”. *Metallurgical & Materials Transactions A* 42, 541–542.
- Hillert, M., Höglund, L., 2004. Comments on kinetics model of isothermal pearlite formation in a 0.4C-1.6Mn steel. *Scripta Materialia* 50, 171–173.
- Hillert, M., Höglund, L., Ågren, J., 1993. Escape of carbon from ferrite plates in austenite. *Acta Metallurgica and Materialia* 41, 1951–1957.
- Hillert, M., Sundman, B., 1976. A treatment of the solute drag on moving grain boundaries and phase interfaces in binary alloys. *Acta Metallurgica* 24, 731–743.
- Hirotsu, Y., Nagakura, S., 1972. Crystal structure and morphology of the carbide precipitated from martensitic high-C steel during the 1st stage of tempering. *Acta Materialia* 20, 645–655.

- Hirth, J. P., Cohen, M., 1970. On the strength-differential phenomenon in hardened steel. *Metallurgical Transactions A* 1, 3–8.
- Hisamatsu, Y., 1989. Science and technology of zinc and zinc alloy coated steel sheet. In: *International Conference on Zinc and Zinc Alloy Coated Steel Sheet – GALVATECH'89*. Iron and Steel Institute of Japan, Tokyo, Japan, pp. 3–12.
- Hobbs, R. M., Lorimer, G. W., Ridley, N., 1972. Effect of silicon on the microstructure of quenched and tempered medium carbon steels. *Journal of the Iron and Steel Institute* 210, 757–764.
- Hodgson, P., Timokhina, I., Xiong, X., Adachi, Y., Beladi, H., 2011. Understanding of the bainite transformation in a nano-structured bainitic steel. *Solid State Phenomena* 172-174, 123–128.
- Hodgson, W. H., Preston, R. R., 1988. Rails for the 1990s. *Bulletin of the Canadian Institute of Mining and Metallurgy* 81, 95–101.
- Hofer, L. J. E., Cohn, E. M., Peebles, W. C., 1949. The modifications of the carbide,  $Fe_2C$ ; their properties and identification. *Journal of the American Chemical Society* 71, 189–185.
- Hoffman, D. W., Cohen, M., 1973. Static displacements and the electrical resistivity of interstitial alloys. *Acta Metallurgica* 21, 1215–1223.
- Hojo, T., Song, S. M., Sugimoto, K., Mukai, Y., Ikeda, S., 2004a. Hydrogen embrittlement of ultra high strength low alloy TRIP-aided steel. In: *2nd Int. Conf. on Advanced Structural Steels*. Chinese Society for Metals, Beijing, China, pp. 638–641.
- Hojo, T., Song, S. M., Sugimoto, K., Nagasaka, A., Ikeda, S., Akamizu, H., Mayuzumi, M., 2004b. Hydrogen embrittlement of ultra high strength low alloy TRIP-aided steels. *Tetsu-to-Hagané* 90, 65–69.
- Hojo, T., Sugimoto, K., Mukai, Y., Ikeda, S., 2009. Effects of aluminium on delayed fracture properties of ultra high strength low alloy TRIP-aided steels. *ISIJ International* 48, 824–829.
- Hollomon, J. H., Jaffe, L. D., 1945. Time temperature relations in tempering steel. *Trans. Met. Soc. AIME* 162, 223–249.
- Hollox, G. E., Hobbs, R. A., Hampshire, J. M., 1981. Lower bainite bearings for adverse environments. *Wear* 68, 229–240.
- Homma, H., Ohkita, S., Matsuda, S., Yamamoto, K., 1987. Improvement of HAZ toughness in HSLA steel by introducing finely dispersed Ti-oxide. *Welding Journal, Research Supplement* 66, 301s–309s.
- Honda, E., Nishiyama, Z., 1932. On the nature of the tetragonal and cubic martensites. *Science Reports of Tohoku Imperial University* 21, 299–331.
- Honda, K., Saito, S., 1920. On the formation of spheroidal cementite. *Journal of the Iron and Steel Institute* 102, 261–267.
- Honeycombe, R. W. K., 1981. *Steels*, 2nd Edition. Edward Arnold, London, U.K.
- Honeycombe, R. W. K., 1984a. Carbide precipitation in ferrite. In: *Marder, A. R., Goldstein, J. I. (Eds.), Phase Transformations in Ferrous Alloys*. TMS-AIME, Warrendale, Pennsylvania, USA, pp. 259–280.
- Honeycombe, R. W. K., 1984b. *The Plastic Deformation of Metals*. Edward Arnold, London, U.K.
- Honeycombe, R. W. K., Bhadeshia, H. K. D. H., 1995. *Steels: Microstructure and Properties*, 2nd edition. Butterworths-Hiemann, London.
- Honeycombe, R. W. K., Pickering, F. B., 1972. Ferrite and bainite in alloy steels. *Metallurgical Transactions* 3, 1099–1112.
- Hong, S. G., Cho, M. H., Lee, J. S., 2010. Effect of post weld rapid heat treatment on microstructural evolution in high-carbon bainitic steel welds. In: *63rd Annual Assembly and International Conference of the International Institute of Welding*. Vol. AWST-10/99. International Institute of Welding, France, pp. 47–51.
- Horii, Y., Ohkita, S., Wakabayashi, M., Namura, M., 1986. Toughness of large-heat input weld metal for low temperature steels. *Tech. Rep. May*, Nippon Steel Corporation, Tokyo, Japan.
- Horii, Y., Ohkita, S., Wakabayashi, M., Namura, M., 1988. Study on the toughness of large-heat input weld metal for low temperature service TMCP steel. *Tech. Rep. 37*, Nippon Steel Corporation, Tokyo, Japan.
- Horita, Z., Furukawa, M., Nemoto, M., Langdon, T. G., 2000. Development of fine grained structures using severe plastic deformation. *Materials Science and Technology* 16, 1239–1245.
- Horn, R. M., Ritchie, R. O., 1978. Mechanisms of tempered martensite embrittlement in low alloy steels. *Metallurgical Transactions A* 9, 1039–1053.
- Hornbogen, E., 1999. A comparative study of ausforming of shape memory alloys with A2 and B2 structures. *Materials Science & Engineering A* 273-275, 630–633.
- Hou, X. Y., Xu, Y. B., Zhao, Y. F., Wu, D., 2011. Microstructure and mechanical properties of hot rolled low silicon TRIP steel containing phosphorus and vanadium. *Journal of Iron and Steel Research, International* 18, 40–45.
- Howard, R. T., Cohen, M., 1948. Austenite transformation above and within the martensite range. *Trans. A.I.M.E.* 176, 364–400.
- Howe, A. A., 2000. Ultrafine grained steels: industrial prospects. *Materials Science and Technology* 16, 1264–1266.

- Howe, A. A., 2009. Industry perspective on ultrafine grained steels. *Materials Science and Technology* 25, 815–819.
- Hozweissig, M. J., Canadinc, D., Maier, H. J., 2012. In-situ characterization of transformation plasticity during an isothermal austenite-to-bainite phase transformation. *Materials Characterisation* 65, 100–108.
- Hrivnak, I., 1987. Guide to the welding and weldability of CrMo and CrMoV heat resisting steels. Tech. Rep. X G-319/c-87, International Institute of Welding, Paris, France.
- Hsu, T. Y., 1987. Heat treating process for stabilization of retained austenite in a 1C-1.5Cr ball bearing steel. *Industrial Heating* 54, 22–23.
- Hu, F., Hodgson, P. D., Wu, K. M., 2014a. Acceleration of the super bainite transformation through a coarse austenite grain size. *Materials Letters* 122, 240–243.
- Hu, F., Hodgson, P. D., Wu, K. M., Shirzadi, A. A., 2014b. Refinement of retained austenite in super-bainitic steel by a deep cryogenic treatment. *ISIJ International* 54, 222–226.
- Hu, F., Wu, K., 2011. Isothermal transformation of low temperature super bainite. *Advanced Materials Research* 146-147, 1843–1848.
- Hu, F., Wu, K. M., Zheng, H., 2013. Influence of Co and Al on bainitic transformation in super bainitic steels. *Steel Research International* 84, 1060–1065.
- Hu, Z. W., Xu, G., Hu, H. J., Wang, L., Xue, Z. L., 2014c. In situ measured growth rates of bainite plates in an Fe-C-Mn-Si superbainitic steel. *International Journal of Minerals, Metallurgy and Materials* 21, 371–378.
- Huang, D. H., Thomas, G., 1977. Metallography of bainitic transformation in silicon containing steels. *Metallurgical Transactions A* 8, 1661–1674.
- Huang, H., Sherif, M. Y., Rivera, P. E. J., 2013. Combinatorial optimization of carbide-free bainitic nanostructures. *Acta Materialia* 61, 1639–1647.
- Huang, J., Poole, W. J., Miltzer, M., 2004. Austenite formation during intercritical annealing. *Metallurgical & Materials Transactions A* 35, 3363–3374.
- Huh, J., Huh, H., Lee, C. S., 2013. Effect of strain rate on plastic anisotropy of advanced high strength steel sheets. *International Journal of Plasticity* 44, 23–46.
- Hulka, K., November 2005. The role of niobium in low carbon bainitic HSLA steel. In: *Proceedings of the 1st international conference on super-high strength steels*. Rome, Italy, pp. 1–12.
- Hulka, K., Gray, J. M., 2001. High-temperature processing of line-pipe steels. In: *Niobium 2001*. TMS-AIME, Warrendale, Pennsylvania, USA, pp. 587–612.
- Hulka, K., Heisterkamp, F., Hachtel, L., 1988. Correlation of processing, microstructure and mechanical properties in 0.03-0.1 wt% Nb steel. In: *DeArdo, A. J. (Ed.), Processing, Microstructure and Properties of HSLA Steels*. TMS-AIME, Warrendale, Pennsylvania, USA, pp. 153–167.
- Hull, D., 1954. The characteristics of the martensite transformation. *Bulletin of the Institute of Metals* 2, 134–139.
- Hulme-Smith, C. N., Lonardelli, I., Dippel, A. C., Bhadeshia, H. K. D. H., 2013a. Experimental evidence for non-cubic bainitic ferrite. *Scripta Materialia* 69, 409–412.
- Hulme-Smith, C. N., Lonardelli, I., Peet, M. J., Dippel, A. C., Bhadeshia, H. K. D. H., 2013b. Enhanced thermal stability in nanostructured bainitic steel. *Scripta Materialia* 69, 191–194.
- Hulme-Smith, C. N., Peet, M. J., Lonardelli, I., Dippel, A. C., Bhadeshia, H. K. D. H., 2015. Further evidence of tetragonality in bainitic ferrite. *Materials Science and Technology* 31, 254–256.
- Hultgren, A., 1920. *A Metallographic Study on Tungsten Steels*. John Wiley & Sons, Inc., New York, USA.
- Hultgren, A., 1947. Isothermal transformation of austenite. *Transactions of the American Society for Metals* 39, 915–1005.
- Hultgren, A., 1951. Isotherm omvandling av austenit. *Jernkontorets Annaler* 135, 403–494.
- Hultgren, A., 1953. Isothermal transformation of austenite and partitioning of alloying elements in low alloy steels. Tech. Rep. Series 4, Swedish Academy of Sciences, Stockholm, Sweden.
- Hume-Rothery, W., 1966. *The Structures of Alloys of Iron*. Pergamon Press, Oxford, U. K.
- Hung, F. Y., Chen, L. H., Lui, T. S., 2002. A study on the particle erosion of upper bainitic austempered ductile iron. *Wear* 252, 985–991.
- Hung, F. Y., Chen, L. H., Lui, T. S., 2004. Phase transformation of an austempered ductile iron during an erosion process. *Materials Transactions* 45, 2981–2986.
- Hyde, R. S., Krauss, G., Matlock, D. K., 1994. Phosphorus and carbon segregation: Effects on fatigue and fracture of gas-carburized modified 4320 steel. *Metallurgical and Materials Transactions A* 25, 1229–1240.
- Ichikawa, K., Horii, Y., Motomatsu, R., Yamaguchi, M., Yurioka, N., 1996. Mechanical properties of weld metal of fire resistant steel by large heat input submerged arc welding. *Quarterly Journal of Japan Welding Society* 14, 27–32.
- Ichinose, H., Takehara, J., Ueda, M., 1982. High strength rails produced by two-stage flame heating and slack-quenching. In: *2nd Int. Conf. on Heavy Haul Railways*, Colorado Springs, USA. pp. 178–182.
- Iezawa, T., Inoue, T., Hirano, O., Okazawa, T., Koseki, T., 1993. Effect of boron on liquid Zn embrittlement in HAZ of STKT590 steel tube for power transmission tower. *Tetsu-to-Hagane* 79, 96–102.

- Iino, M., Nomura, N., Takezawa, H., Takeda, T., 1-5 November 1982. Engineering solutions to the H<sub>2</sub>S problem in linepipes. In: Interrante, C. G., Pressouyre, G. M. (Eds.), *Current solutions to hydrogen problems in steels*. American Society for Metals, Washington, D. C., USA, pp. 159–167.
- Imagumbai, M., 2006. Ultrafine grained HSLA steel made from bainitic heterogeneity. In: 3rd Int. Conf. on Advanced Structural Steels. Korean Institute of Metals and Materials, Seoul, Republic of Korea, pp. 156–161.
- Imagumbai, M., Chijiwa, R., Aikawa, N., Nagumo, M., Homma, H., Matsuda, S., Mimura, H., 1985. Advanced steels for low-temperature service. In: Gray, J. M. (Ed.), *HSLA Steels: Metallurgy and Applications*. ASM International, Materials Park, Ohio, USA, pp. 557–566.
- Imai, Y., Izumiyama, M., Tsuchiya, M., 1965. Thermodynamic study on the transformation of austenite into martensite in Fe-N and Fe-C systems. *Scientific Reports: Research Institute of Tohoku University A17*, 173–192.
- Inagaki, M., Hiroyuki, M., 1984. Quality and reliability in welding. Tech. rep., Welding Institute of the Chinese Mechanical Engineering Society, Hangzhou, China.
- Irani, J. J., 1967. The application of thermomechanical treatments to steels. Tech. Rep. MG/A/60/67, British Iron and Steel Research Association, Sheffield, U. K.
- Irvine, K. J., Gladman, T., Pickering, F. B., 1969. The strength of austenitic stainless steels. *Journal of the Iron and Steel Institute* 207, 1017–1028.
- Irvine, K. J., Pickering, F. B., 1957. Low carbon bainitic steels. *Journal of the Iron and Steel Institute* 187, 292–309.
- Irvine, K. J., Pickering, F. B., 1958. High carbon bainitic steels. *Journal of the Iron and Steel Institute* 188, 101–112.
- Irvine, K. J., Pickering, F. B., 1963. The impact properties of low carbon bainitic steels. *Journal of the Iron and Steel Institute* 201, 518–531.
- Irvine, K. J., Pickering, F. B., 1965. High carbon bainitic steels. In: *Physical properties of martensite and bainite*, Special Report 93. Iron and Steel Institute, London, pp. 110–125.
- Irvine, K. J., Pickering, F. B., Heselwood, W. C., 1957a. The physical metallurgy of low-carbon, low-alloy steels containing boron. *Journal of the Iron and Steel Institute* 186, 54–67.
- Irvine, K. J., Pickering, F. B., Heselwood, W. C., Atkins, M., 1957b. The physical metallurgy of low-C low-alloy steels containing boron. *Journal of the Iron and Steel Institute* 186, 54–67.
- Isheim, D., Gagliano, M. S., Fine, M. E., Seidman, D. N., 2006. Interfacial segregation at Cu-rich precipitates in a high-strength low-carbon steel studied on a sub-nanometer scale. *Acta Materialia* 54, 841–849.
- Ishiguro, T., Murakami, Y., Mima, S., Watanabe, J., 1982. A 2.25Cr1Mo pressure vessel steel with improved creep rupture strength. Tech. Rep. STP 755, American Society for Testing and Materials, New York, USA.
- Ishiguro, T., Ohnishi, K., Murakami, Y., Mima, S., Watanabe, J., 1984. Development of a 3Cr-1Mo-0.25V-Ti-B pressure vessel steel for the enhanced design stress. In: Swift, R. A. (Ed.), *Research on Chrome-Moly Steels*. American Society of Mechanical Engineers, New Mexico, USA, pp. 43–51.
- Ishikawa, F., Takahashi, T., Ochi, T., 1994. Intragranular ferrite nucleation in medium carbon steels. *Metallurgical & Materials Transactions A* 25, 929–936.
- Islam, M. A., Knott, J. F., Bowen, P., 2005. Kinetics of phosphorus segregation and its effect on low temperature fracture behaviour in 2.25Cr-1Mo pressure vessel steel. *Materials Science and Technology* 21, 76–84.
- Isobe, M., Kato, C., Mochizuki, K., 1998. Effect of additional annealing on hot-dip galvanizability of Si and Mn added IF steel. In: 39th Mechanical Working and Steel Processing Conference. Vol. 35. Iron and Steel Society of AIME, Colorado, USA, pp. 121–125.
- Ito, Y., Nakanishi, M., 1975. Study on Charpy impact properties of weld metal with submerged arc welding. Tech. Rep. XII-113-75, International Institute of Welding, Paris, France.
- Ito, Y., Nakanishi, M., 1976. Study on Charpy impact properties of weld metal with SAW. *The Sumitomo Search* 15, 42–62.
- Ito, Y., Nakanishi, M., Komizo, Y., 1982. Effects of oxygen on low carbon steel weld metal. *Metal Construction* 14, 472–478.
- Ivantsov, G. P., 1947. Temperature field around spherical, cylindrical and acircular crystal growing in a supercooled melt. *Doklady Akademii Nauk, SSSR* 58, 567–569.
- Jack, K. H., 1950. Results of further X-ray structural investigations of the iron-carbon and iron-nitrogen systems and of related interstitial alloys. *Acta Crystallographica* 3, 392–394.
- Jack, K. H., 1951. Structural transformations in the tempering of high-carbon martensitic steels. *Journal of the Iron and Steel Institute* 169, 26–36.
- Jacques, P., 2003a. Transformation-induced plasticity in steels. In: *Thermodynamics, Microstructures and Plasticity*. Kluwer Academic Publishers, London, U.K., pp. 241–150.
- Jacques, P., Furnémont, Q., Pardoën, T., Delannay, F., 2000. The role and significance of martensite on the mechanical properties of TRIP-assisted multiphase steels. In: Miannay, D., Costa, P., Francois, D., Pineau, A. (Eds.), *Advances in Mechanical Behaviour, Plasticity and Damage*. Elsevier, Netherlands, pp. 823–828.

- Jacques, P., Furnemont, Q., Pardoën, T., Delannay, F., 2001a. Role of martensitic transformation on damage and cracking resistance in TRIP-assisted multiphase steels. *Acta Materialia* 49, 139–152.
- Jacques, P., Harlet, P., Delannay, F., 2002. Critical assessment of the phase transformations occurring during the heat-treatment of TRIP-assisted multiphase steels. In: de Cooman, B. C. (Ed.), *International Conference on TRIP-Aided High Strength Ferrous Alloys*. Wissenschaftsverlag Mainz GmbH, Aachen, Germany, pp. 129–134.
- Jacques, P. J., 2003b. Experimental investigation of the influence of the austenite grain size on the mechanism and kinetics of the bainite transformation in steels. *Journal de Physique IV* 112, 297–300.
- Jacques, P. J., 2004. Transformation-induced plasticity for high strength formable steels. *Current Opinion in Solid State and Materials Science* 8, 259–265.
- Jacques, P. J., Furnemont, Q., Godet, S., Pardoën, T., Conion, K. T., Delannay, F., 2006. Micromechanical characterisation of TRIP-assisted multiphase steels by in situ neutron diffraction. *Philosophical Magazine A* 86 (2371-2392).
- Jacques, P. J., Furnemont, Q., Mertens, A., Delannay, F., 2001b. On the sources of work hardening in multiphase steels by transformation-aided plasticity. *Philosophical Magazine A* 81, 1789–1812.
- Jacques, P. J., Girault, E., Martens, A., Verlinden, B., van Humbeeck, J., Delannay, F., 2001c. The development of cold rolled TRIP-assisted multiphase steels. Al-alloyed TRIP-assisted multiphase steels. *ISIJ International* 41, 1068–1074.
- Jacques, P. J., Ladrière, J., Delannay, F., 2001d. Interactions between phases and mechanical stability of retained austenite in TRIP steels. *Metallurgical & Materials Transactions A* 32A, 2759–2768.
- James, J. S., Thomson, R. C., 1999. Microstructural modelling of austempered ductile iron. In: Koiwa, M., Otsuka, K., Miyazaki, T. (Eds.), *Solid→Solid Phase Transformations '99*. Japan Institute of Metals, Tokyo, Japan, pp. 1473–1476.
- Jang, J. H., Bhadeshia, H. K. D. H., Suh, D. W., 2012. Solubility of carbon in tetragonal ferrite in equilibrium with austenite. *Scripta Materialia* 68, 195–198.
- Jang, J. H., Kim, I. G., Bhadeshia, H. K. D. H., 2009. Substitutional solution of silicon in cementite: a first-principles study. *Computational Materials Science* 44, 1319–1326.
- Jang, J. H., Kim, I. G., Bhadeshia, H. K. D. H., 2010. First-principles calculations and the thermodynamics of cementite. *Materials Science Forum* 638-642, 3319–3324.
- Jaramillo, R. A., Babu, S. S., Ludtka, G. M., Kisner, R. A., Wilgen, J. B., Mackiewicz-Ludtka, G., Nicholson, D. M., Kelly, S. M., Murugananth, M., Bhadeshia, H. K. D. H., 2004. Effect of 30 Tesla magnetic field on transformations in a novel bainitic steel. *Scripta Materialia* 52, 461–466.
- Jaramillo, R. A., Babu, S. S., Miller, M. K., Ludtka, G. M., Mackiewicz-Ludtka, G., Kisner, R. A., Wilgen, J. B., Bhadeshia, H. K. D. H., 2005. Austenite decomposition in Fe-C-Si-Mn steel under 30 Tesla magnetic field. In: Howe, J. M., Laughlin, D. E., Lee, J. K., Dahmen, U., Soffa, W. A. (Eds.), *Solid-Solid Phase Transformations*, TMS-AIME, Warrendale, USA. TMS-AIME, Warrendale, Pennsylvania, USA, pp. 873–878.
- Jellinghaus, W., 1952. Anregung der zwischenstufen-umwandlung des stahles durch kleine mengen von  $\alpha$ -eisen. *Archiv für das Eisenhüttenwesen* 23, 459–470.
- Jellinghaus, W., 1957. *Arch. Eisenhüttenwesen* 28, 469–481.
- Jellinghaus, W., Friedewold, H., 1960. *Archiv für das Eisenhüttenwesen* 31, 309–317.
- Jepson, M. D., Thompson, F. C., 1949. Acceleration of the rate of isothermal transformation of austenite. *Journal of the Iron and Steel Institute* 162, 49–56.
- Jiao, D., Luo, C. P., Liu, J., 2007. Isothermal transformation of high-nitrogen austenite. *Scripta Materialia* 56, 613–616.
- Jihua, Z., Shuchuan, C., Hsu, T. Y., 1989. An investigation of internal friction within the incubation period of the bainitic transformation. *Acta Metallurgica* 37, 241–246.
- Jimenez-Melero, E., van Dijk, N. H., Zhao, L., Sietsma, J., Offerman, S. E., Wright, J. P., van der Zwaag, S., 2009. The effect of aluminium and phosphorus on the stability of individual austenite grains in trip steels. *Acta Materialia* 57, 533–543.
- Jin, N., Clayton, P., 1997. Effect of microstructure on rolling/sliding wear of low carbon bainitic steels. *Wear* 202, 202–207.
- Jing, C., Suh, D. W., Oh, C. S., Wang, Z., Kim, S. J., 2007. Effects of phosphorous addition on mechanical properties and retained austenite stability of 0.15C-1.5Mn-1.5Al TRIP-aided cold rolled steels. *Metals and Materials International* 13, 13–19.
- Jingsheng, Y., Zongsen, Y., Chengjian, W., 1988. Rare earths and the mechanical properties of steel. *Journal of Metals* 40, 26–31.
- Johnson, W. A., Mehl, R. F., 1939. Reaction kinetics in processes of nucleation and growth. *TMS-AIMME* 135, 416–458.
- Johnson, W. H., 1875. On some remarkable changes produced in iron and steel by the action of hydrogen and acids. *Proceedings of the Royal Society of London* 23, 168–179.

- Jones, B. L., DeArdo, A. J., Garcia, C. I., Hulka, K., Luthy, H., 1985. Microalloyed forging steels – a worldwide assessment. In: Gray, J. M., Ko, T., Shouhua, Z., Baorong, W., Xishan, X. (Eds.), *HSLA Steels: Metallurgy and Applications*. ASM International, Metals Park, Ohio, USA, pp. 875–864.
- Jones, B. L., Johnson, D. L., 1983. The metallurgical design of major pipelines. In: *Steels for line pipe and pipeline fittings*. Maney, London, U.K., pp. 14–21.
- Jones, C. L., Pilkington, R., 1978. Influence of microstructure on creep crack growth in Cr Mo V steel. *Metallurgical Transactions A* 9, 865–871.
- Jones, S., Bhadeshia, H. K. D. H., 1997. Competitive formation of inter- and intragranularly nucleated ferrite. *Metallurgical & Materials Transactions A* 28A, 2005–2103.
- Jones, W. K. C., Alberry, P. J., 1977. A model for stress accumulation in steels during welding. In: *Residual stresses in welded construction and their effects*. TWI, Abington, U.K., pp. 15–26.
- Joo, J. S., Suh, D. W., Bhadeshia, H. K. D. H., 2013. Mechanical anisotropy in steels for pipelines. *ISIJ International* 53, 1305–1314.
- Joo, M. S., Suh, D. W., Bae, J. H., Bhadeshia, H. K. D. H., 2012. Role of delamination and crystallography on anisotropy of Charpy toughness in API-X80 steel. *Materials Science & Engineering A* 546, 314–322.
- Joo, M. S., Suh, D.-W., Bae, J.-H., Bhadeshia, H. K. D. H., 2014. Toughness anisotropy in X70 and X80 linepipe steels. *Materials Science and Technology* 30, 439–440.
- Josefsson, B., Andrén, H.-O., 1988. Microstructure of granular bainite. *Journal de Physique Colloque* 49, C6–293 – C6–298.
- Josefsson, B., Andrén, H. O., 1989. Microstructure and thermodynamic behaviour of a Cr-Mo submerged arc weld metal in the as-welded state. In: David, S. A., Vitek, J. M. (Eds.), *Recent Trends in Welding Science and Technology (TWR'89)*. ASM International, Metals Park, Ohio, USA, pp. 243–247.
- Josefsson, B., Kvist, A., Andrén, H. O., 1987. Atom probe microanalysis of weld metal in a submerged arc welded Cr-Mo steel. *Journal de Physique: Colloque C6* 48, 435–440.
- Judson, P., McKeown, D., 1982. Advances in the control of weld metal toughness. In: Coton, H. C. (Ed.), 2nd Int. Conf. Offshore Welded Structures. TWI, Abington, U.K., p. paper 3.
- Jung, G. S., Lee, K. Y., Lee, J. B., Bhadeshia, H. K. D. H., Suh, D.-W., 2012. Spot weldability of TRIP assisted steels with high carbon and aluminium contents. *Science and Technology of Welding and Joining* 17, 92–98.
- Jung, J. H., Kim, H. S., de Cooman, B. C., 2010. Yielding behavior of Nb micro-alloyed C-Mn-Si TRIP steel studied by in-situ synchrotron X-ray diffraction. *ISIJ International* 50, 620–629.
- Jung, Y. C., Ohmori, Y., Nakai, K., Ohtsubo, H., 1997. Bainite transformation in a silicon steel. *ISIJ International* 37, 789–796.
- Kajiwara, S., 2003. HREM study on the ledge structures, transient lattices and dislocation structures at the austenite-martensite and austenite-bainite interfaces in Fe-based alloys. *Journal de Physique IV* 112, 61–83.
- Kajiwara, S., Ogawa, K., Kikuchi, T., Okamoto, H., Oka, M., 1999. High resolution electron microscopy studies of the austenite-martensite and austenite-bainite interfaces in Fe-based alloys. In: M. Koiwa, K. Otsuka, T. M. (Ed.), *Solid-Solid Phase Transformations '99 (JIMIC-3)*. Japan Institute of Metals, Tokyo, Japan, pp. 969–972.
- Kakeshita, T., Shimizu, K., Kijima, S., Yu, Z., Date, M., 1985. Magnetic field induced martensitic transformations in Fe Ni C invar and non invar alloys. *Trans. JIM* 26, 630–637.
- Kalish, D., Cohen, M., 1970. Structural changes and strengthening in the strain tempering of martensite. *Materials Science and Engineering* 6, 156–166.
- Kalish, D., Kulin, S. A., Cohen, M., 1965. Bainitic structures and thermomechanical treatments applied to steel. *Journal of Metals* 17, 157–164.
- Kalousek, J., Beynon, G., 1975. Rail metallurgy. Tech. Rep. S497-75, Canadian Pacific Technical Reports.
- Kalousek, J., Fegredo, D. M., Laufer, E. E., 1985a. The wear resistance and worn metallography of pearlite, bainite, and tempered martensite rail steel microstructure of high hardness. *Wear*, 199–222.
- Kalousek, J., Fegredo, D. M., Laufer, E. E., 1985b. Wear resistance and worn metallography of pearlite, bainite and tempered martensite rail steel microstructures. *Wear* 105, 199–222.
- Kaltzakarta, I., Callejo, L. M., Idoyaga, Z., 2014. TiO<sub>2</sub> nanoparticle addition into molten steel: From lab scale to industrial scale. *Materials Science Forum* 783-786, 813–817.
- Kamada, A., Koshizuka, N., Funakoshi, T., 1976. Effect of austenite grain size and C content on microstructure and toughness of tempered martensite and bainite. *Trans. ISIJ* 16, 407–416.
- Kaneko, K., Fujita, K., Sadakata, A., Tomokiyo, Y., Matsumura, S., 2003. Nanostructural and nanoelemental analysis of metastable M<sub>3</sub>C -type carbides with alloy-rich layer in heat resistant 2Cr-martensitic steel. *Scripta Materialia* 48, 761–765.
- Kang, M., Zhu, M., Zhang, M., 2005. Mechanism of bainite nucleation in steel, iron and copper alloys. *Journal of Materials Science and Technology* 21, 437–444.
- Kang, M. K., Sun, J. L., Yang, Q. M., 1990. High temperature TEM in situ study of lower bainite carbide precipitation. *Metallurgical Transactions A* 21, 853–858.
- Kang, Y., Bhadeshia, H. K. D. H., 2006. Roughness of bainite. *Materials Science and Technology* 22, 645–652.

- Kaputkin, D. E., Kaputkina, L. M., Prokoshkin, S. D., 2003. Transformation of retained austenite during tempering of high carbon steel. *Journal de Physique IV* 112, 275–278.
- Kar, R. J., Horn, R. M., Zackay, V. F., 1979. The effect of heat treatment on microstructure and mechanical properties in 52100 steel. *Metallurgical Transactions A* 10, 1711–1717.
- Kar, R. J., Todd, J. A., 1982. Discussion on transformation characteristics. *ASTM STP* 755, 361–362.
- Karlsson, L., Mráz, L., 2011. Increasing fatigue life with low transformation temperature (LTT) welding consumables. *Zváranie svarování* 1-2, 8–15.
- Kashima, T., Sugimoto, K., 2004. Development of TRIP-aided cold rolled steel sheets with the excellent stretch formability. *Tetsu-to-Hagané* 90, 49–55.
- Kashima, T., Tsukasa, Y., Sugimoto, K., Hashimoto, S., 2003. Effect of initial microstructures before annealing on ductility of TRIP aided steel sheets. *Tetsu-to-Hagané* 89, 609–615.
- Kasuya, T., Ichikawa, K., Fuji, M., Bhadeshia, H. K. D. H., 1999. Real and extended volumes in simultaneous transformations. *Materials Science and Technology* 15, 471–473.
- Katsamas, A. I., Haidemenopoulos, G. N., 2008. A semi-empirical model for the evolution of retained austenite via bainitic transformation in multiphase TRIP steels. *Steel Research International* 79, 875–884.
- Katsumoto, H., Konda, N., Arimochi, K., Hirota, K., Isoda, A., Kitada, H., Sakano, M., Yajima, H., 2005. Development of structural steel with high resistance to fatigue crack initiation and growth. In: *24th Int. Conf. on Offshore Mechanics and Arctic Engineering*. ASME, New York, USA, pp. 1–9.
- Kaufman, L., Cohen, M., 1958. Thermodynamics and kinetics of martensitic transformation. *Progress in Metal Physics* 7, 165–246.
- Kawata, H., Sakamoto, K., Moritani, T., Morito, S., Furuhashi, T., Maki, T., 2006. Crystallography of ausformed upper bainite structure in Fe-9Ni-C alloys. *Materials Science & Engineering A* 438-440, 140–144.
- Kazum, O., Kannan, M. B., Beladi, H., Timokhina, I., Hodgson, P., Khoddam, S., 2014. Aqueous corrosion performance of nanostructured bainitic steel. *Materials and Design* 54, 67–71.
- Keehan, E., 2005. Effect of microstructure on mechanical properties of high-strength steel weld metals. Ph.D. thesis, Chalmers University, Sweden, <http://www.msm.cam.ac.uk/phase-trans/2005/keehan.html>.
- Keehan, E., Andrén, H.-O., Karlsson, L., Muruganath, M., Bhadeshia, H. K. D. H., 2002. Microstructural and mechanical effects of nickel and manganese on high strength steel weld metals. In: David, S. A., DebRoy, T. (Eds.), *Trends in Welding Research*. ASM International, Materials Park, Ohio, USA, pp. 695–700.
- Keehan, E., Karlsson, L., Andrén, H.-O., 2006a. Influence of C, Mn and Ni on strong steel weld metals: Part 1, effect of nickel. *Science and Technology of Welding and Joining* 11, 1–8.
- Keehan, E., Karlsson, L., Andrén, H. O., Bhadeshia, H. K. D. H., 2005. Understanding mechanical properties of novel high strength steel weld metals through high-resolution microstructural investigations. In: David, S. A., DebRoy, T., Lippold, J. C., Smartt, H. B., Vitek, J. M. (Eds.), *Trends in Welding Research*. ASM International, Materials Park, Ohio, USA, pp. 969–974.
- Keehan, E., Karlsson, L., Andrén, H.-O., Bhadeshia, H. K. D. H., 2006b. Influence of C, Mn and Ni on strong steel weld metals: Part 2, increased impact toughness. *Science and Technology of Welding and Joining* 11, 9–18.
- Keehan, E., Karlsson, L., Andrén, H.-O., Bhadeshia, H. K. D. H., 2006c. Influence of C, Mn and Ni on strong steel weld metals: Part 3, increased strength. *Science and Technology of Welding and Joining* 11, 19–24.
- Keh, A. S., 1963. Imperfections and plastic deformation of cementite in steel. *Acta Metallurgica* 11, 1101–1103.
- Keh, A. S., Weissmann, S., 1963. Deformation substructure in bcc metals. In: G. Thomas, J. W. (Ed.), *Electron Microscopy and the Strength of Crystals*. Interscience, New York, USA, pp. 231–300.
- Kehoe, M., Kelly, P. M., 1970. The role of carbon in the strength of ferrous martensite. *Scripta Metallurgica* 4, 473–476.
- Kelly, P. M., Nutting, J., 1960. The martensite transformation in carbon steels. *Proceedings of the Royal Society of London A* 259, 45–58.
- Kendig, K. L., Miracle, D. B., 2002. Strengthening mechanisms of an Al-Mg-Sc-Zr alloy. *Acta Materialia* 50, 4165–4175.
- Kennon, N. F., 1974. Questions about martensite and bainite. *Journal of the Australian Institute of Metals* 19, 3–18.
- Kennon, N. F., Burgess, P. B., 1978. The second stage of tempering. *Metals Forum* 1, 185–190.
- Kennon, N. F., Kaye, N. A., 1982. Isothermal transformation of austenite to pearlite and bainite. *Metallurgical Transactions A* 13, 975–978.
- Kerr, R., Solana, F., Bernstein, I. M., Thompson, A. W., 1987. Microstructural effects on the stress corrosion cracking behavior of medium and high strength steels. *Metallurgical Transactions A* 18, 1011–1019.
- Kessler, H., Pitsch, W., 1965. Der orientierungszusammenhang bei der ruckumwandlung der martensits in austenit in eisen-nickel-legierungen. *Acta Metallurgica* 13, 871–874.
- Kettunen, P., Lepistö, T., 1976. Cyclic work-hardening and fatigue in a bainitic steel. *Trans. JIM* 17, 63–72.
- Kettunen, P. O., Kocks, U. F., 1967. A possible relation between work hardening and fatigue failure. *Scripta Metallurgica* 1, 13–17.

- Kettunen, P. O., Kocks, U. F., 1972. Fatigue hardening and fatigue life. *Acta Metallurgica* 20, 95–103.
- Khan, S. A., Bhadeshia, H. K. D. H., 1990. The bainite transformation in chemically heterogeneous 300M high-strength steel. *Metallurgical Transactions A* 21A, 859–875.
- Khare, S., Lee, K. Y., Bhadeshia, H. K. D. H., 2009. Relative effects of Mo and B on ferrite and bainite kinetics in strong steels. *International Journal of Materials Research* 100, 1512–1520.
- Khare, S., Lee, K. Y., Bhadeshia, H. K. D. H., 2010. Carbide-free bainite: Compromise between rate of transformation and properties. *Metallurgical & Materials Transactions A* 41A, 922–928.
- Ki, Z., Wu, D., Hu, R., 2006. Austempering of hot rolled Si-Mn TRIP steels. *Journal of Iron and Steel Research International* 13, 41–46.
- Kiani-Rashid, A. R., 2009. The bainite transformation and the carbide precipitation of 4.88% aluminium austempered ductile iron investigated using electron microscopy. *Journal of Alloys and Compounds* 474, 490–498.
- Kiani-Rashid, A. R., Edmonds, D. V., 2009. Microstructural characteristics of Al-alloyed austempered ductile irons. *Journal of Alloys and Compounds* 47, 391–398.
- Kim, Y. M., Shin, S. Y., Lee, H., Wang, B., Lee, S., Kim, N. J., 2007. Effects of molybdenum and vanadium addition on tensile and Charpy impact properties of API X70 linepipe steels. *Metallurgical & Materials Transactions A* 38, 1731–1742.
- Kimmins, S. T., Gooch, D. J., November 1983. Austenite memory effect in 1Cr-1Mo-0.75V(Ti, B) steel. *Metal Science* 17, 519–532.
- Kimura, K., Kushima, H., Abe, F., Yagi, K., 1997. Inherent creep strength and long term creep strength properties of ferritic steels. *Materials Science & Engineering A* 234–236, 1079–1082.
- Kimura, K., Watanabe, T., Hongo, H., Yamazaki, M., Kinugawa, J., Irie, H., 2003. Effects of full annealing heat treatment on long-term creep strength of 2.25Cr-1Mo steel welded joint. *Quarterly Journal of Japan Welding Society* 21, 195–203.
- Kimura, Y., Hidaka, H., Takaki, S., 1999. Work-hardening mechanism during super-heavy plastic deformation in mechanically milled iron powder. *Materials Transactions, JIM* 40, 1149–1157.
- King, A. D., Bell, T., 1975. Crystallography of grain boundary proeutectoid ferrite. *Metallurgical Transactions A* 6, 1419–1429.
- Kinsman, K. R., Aaronson, H. I., 1973. Influence of Al, Co, and Si upon the kinetics of the proeutectoid ferrite reaction. *Metallurgical and Materials Transactions B* 4, 959–967.
- Kinsman, K. R., Shyne, J. G., 1967. Thermal stabilization of austenite in iron-nickel-carbon alloys. *Acta Metallurgica* 15, 1527–1543.
- Kirkaldy, J. S., 1958. Diffusion in multicomponent metallic systems i – phenomenological theory for substitutional solid solution alloys. *Canadian Journal of Physics* 36, 899–925.
- Kirkaldy, J. S., Thomson, B. A., Baganis, E., 1978. Prediction of multicomponent equilibrium and transformation diagrams for low alloy steels. In: Doane, D. V., Kirkaldy, J. S. (Eds.), *Hardening concepts with applications to steels*. TMS-AIME, Materials Park, Ohio, USA, pp. 82–125.
- Kirkaldy, J. S., von Destinon-Forstmann, J., Brigham, R. J., 1962. Simulation of banding in steels. *Canadian Metallurgical Quarterly* 59, 59–81.
- Kizu, T., Nagataki, Y., Inazumi, T., Hosoya, Y., 2001. Effects of chemical composition and oxidation temperature on the adhesion of scale in plain carbon steels. *ISIJ International* 41, 1495–1501.
- Klier, E. P., Lyman, T., 1944. The bainite reaction in hypoeutectoid steels. *Trans. A. S. M.* 158, 395–422.
- Klueh, R. L., 1974a. The effect of carbon on 2.25Cr-1Mo steel, microstructure and tensile properties. *Journal of Nuclear Materials* 54, 41–54.
- Klueh, R. L., 1974b. The effect of carbon on 2.25Cr-1Mo steel. Pt. II creep rupture. *Journal of Nuclear Materials* 54, 55–63.
- Klueh, R. L., 2004. Reduced-activation bainitic and martensitic steels for nuclear fusion applications. *Current Opinion in Solid State and Materials Science* 8, 239–250.
- Klueh, R. L., Alexander, D. J., 1999. Effect of heat treatment and irradiation temperature on impact properties of Cr-W-V ferritic steels. *Journal of Nuclear Materials* 265, 262–272.
- Klueh, R. L., Alexander, D. J., Kenik, E. A., 1995. Development of low-Cr, Cr-W steels for fusion. *Journal of Nuclear Materials* 227, 11–23.
- Klueh, R. L., Swindeman, R. W., 1986. The microstructure and mechanical properties of a modified 2.25Cr1Mo steel. *Metallurgical Transactions A* 17, 1027–1034.
- Klug, R. C., Hintz, M. B., Rundman, K. B., 1985. Embrittlement of austempered nodular irons: grain boundary P enrichment resulting from precipitate decomposition. *Metallurgical Transactions A* 16, 797–805.
- Kluken, A. O., Grong, O., 1989a. Mechanisms of inclusion formation in Al-Ti-Si-Mn deoxidised steel weld metals. *Metallurgical Transactions A* 20, 1335–1349.
- Kluken, A. O., Grong, O., Hjelen, J., 1991. The origin of transformation textures in steel weld metals containing acicular ferrite. *Metallurgical Transactions A* 17, 1611–1623.
- Kluken, A. O., Grong, O., Rorvik, G., 1990. Solidification microstructures and phase transformations in Al-Ti-Si-Mn deoxidised steel weld metals. *Metallurgical Transactions A* 21, 2047–2058.

- Kluken, A. P., Grong, O., 1989b. Structure property relationships in reheated SA steel weld metals. In: S. A. David, J. V. (Ed.), *Recent Trends in Welding Science and Technology (TWR'89)*. ASM International, Materials Park, Ohio, USA, pp. 781–786.
- Knott, J. F., 1966. Effects of hydrostatic tension on the fracture of mild steel. *Journal of the Iron and Steel Institute* 204, 104–111.
- Knott, J. F., 1981. *Fundamentals of Fracture Mechanics*. Butterworths, London, Ch. 9, pp. 234–241.
- Knott, J. F., Cottrell, A. H., 1963. Notch brittleness in mild steel. *Journal of the Iron and Steel Institute* 201, 249–260.
- Knowles, K. M., Smith, D. A., Clark, W. A. T., 1982. On the use of geometric parameters in the theory of interphase boundaries. *Scripta Metallurgica* 16, 413–416.
- Ko, T., 1953. The formation of bainite in an En21 steel. *Journal of the Iron and Steel Institute* 175, 16–18.
- Ko, T., Cottrell, S. A., 1952. The formation of bainite. *Journal of the Iron and Steel Institute* 172, 307–313.
- Kobayashi, R., 1993. Modeling and numerical simulations of dendritic crystal growth. *Physica D* 63, 410–423.
- Kocks, U. F., 1966. A statistical theory of flow stress and work hardening. *Philosophical Magazine* 13, 541–566.
- Koczurkiewicz, B., 2012. The effect of time and temperature variations during isothermal annealing on the mechanical properties of high carbon bainitic steel. *Materials Science Forum* 706-709, 2158–2163.
- Koistinen, D. P., 1958. The distribution of residual stresses in carburized cases and their origin. *Trans. A. S. M.* 50, 227–241.
- Koistinen, D. P., Marburger, R. E., 1959. A general equation prescribing the extent of the austenite-martensite transformation in pure iron-carbon alloys and plain carbon steels. *Acta Metallurgica* 7, 59–60.
- Kolmogorov, A. N., 1937. On statistical theory of metal crystallisation. *Izvestiya Akad. Nauk SSSR (Izvestia Academy of Science, USSR) Ser. Math.* 3, 335–360.
- Komai, N., Masuyama, F., 2002. Microstructural degradation of advanced low alloy steel T23 base metal and weldments during creep. In: *7th Leige Conference on Materials for Advanced Power Engineering*. Schriften des Forschungszentrum Jülich, Jülich, Germany, pp. preprint pages 1–16.
- Komai, N., Masuyama, F., Ishihara, I., Yokoyama, T., Yamadera, Y., Okada, H., Miyata, K., Sawaragi, Y., 1999. Development and application of 2.25Cr-1.6W (HCM2S steel large diameter and thick section pipe. In: *Advanced Heat Resistant Steels for Power Generation*. IOM Communications, London, pp. 1–12.
- Konoval, G., Zwell, L., Gorman, L. A., Leslie, W. C., 1959. X ray diffraction pattern of carbide in low-C Fe-Si alloys. *Nature* 184, 1862–1863.
- Koo, M., Xu, P., Tomota, Y., Suzuki, H., 2009. Bainitic transformation behavior studied by simultaneous neutron diffraction and dilatometric measurement. *Scripta Materialia* 61, 797–800.
- Korenko, M. K., 1973. *Martensitic transformations in high magnetic fields*. Ph.D. thesis, Massachusetts Institute of Technology, Boston, USA.
- Koseki, T., Thewlis, G., 2005. Inclusions assisted microstructure control in C-Mn and low alloy steel welds. *Materials Science and Technology* 21, 867–879.
- Kosuri, G., 2010. *Rolling/sliding wear resistance of steels with different microstructures*. Master's thesis, Lulea University of Technology, Sweden.
- Kozasu, I., Suzuki, H., Yamada, M., Tagawa, H., 1984. Alloy modification in 2-1/4Cr-1Mo and 3Cr-1Mo steels for high temperature and high pressure hydrogen service. In: Swift, R. A. (Ed.), *Research on Chrome-Moly Steels*. American Society of Mechanical Engineers, New York, USA, pp. 53–76.
- Kozeschnik, E., Bhadeshia, H. K. D. H., 2008. Influence of silicon on cementite precipitation in steels. *Materials Science and Technology* 24, 343–347.
- Kozeschnik, E., Buchmayr, B., 1999. MATCALC- a simulation tool for multicomponent thermodynamics, diffusion and phase transformations. In: Cerjak, H. (Ed.), *International Seminar on the Numerical Analysis of Weldability*. Vol. 5. Maney, London, U.K., pp. 349–361.
- Krauss, B. Y. C. G., Matlock, D. K., 1988. Bainite formation and deformation behaviour in an ntercritically annealed Fe-1Mn-0.09C steel. *Scripta Metallurgica* 22, 1575–1580.
- Krauss, G., McMahon, Jr., C. J., 1992. Low toughness and embrittlement phenomena in steels. In: Olson, G. B., Owen, W. S. (Eds.), *Martensite*. ASM International, Ohio, USA, pp. 295–322.
- Kriesement, O., Wever, F., 1956. The bainite reaction in high carbon steels. In: *Mechanism of Phase Transformations in Metals*, Monograph and Rep. Ser. No. 18. Institute of Metals, London, U.K., pp. 253–263.
- Krishnadev, M. R., Ghosh, R., 1979. Low-T mechanical behaviour of and 'acicular ferrite' HSLA steel. *Metallurgical Transactions A* 10, 1941–1944.
- Krivoglaz, M. A., Sadvskiy, V. D., 1964. Effect of strong magnetic fields on phase transformations. *Fiz. Met. Metalloved.* 18, 23–27.
- Kuba, M. M., van Aken, D. C., 2013. Analysis of acoustic emission during the melting of embedded indium particles in an aluminum matrix: A study of plastic strain accommodation during phase transformation. *Metallurgical & Materials Transactions A* 44, 3444–3455.
- Kubachewski, O., Evans, E. L., 1950. *Metallurgical Thermochemistry*. Pergamon Press, Oxford, U. K.

- Kulakov, A. N., Kagan, A. S., Kapyrin, A. A., 1986. Kinetics of austenite transformation and internal stresses in bainitic hardening of bearing steel. *Metal Science and Heat Treatment* 28, 255–257.
- Kumar, A., S. B., S., Ray, K. K., 2013. Fatigue crack growth behaviour of ferrite-bainite dual phase steels. *Materials Science and Technology* 29, 1507–1512.
- Kumar, A., Singh, S. B., Ray, K. K., 2008. Short fatigue crack growth behaviour in ferrite-bainite dual-phase steels. *ISIJ International* 48, 1285–1292.
- Kundu, M., Ganguly, S., Datta, S., Chattopadhyay, P. P., 2009. Simulating time temperature transformation diagrams of steels using artificial neural networks. *Materials and Manufacturing Processes* 24, 169–173.
- Kundu, S., 2007. Transformation strain and crystallographic texture in steels. Ph.D. thesis, <http://www.msm.cam.ac.uk/phase-trans/2000/phd.html#kundu>, University of Cambridge, Cambridge, U. K.
- Kundu, S., 2014. Critical assessment 1: Outstanding issues in crystallographic variant selection in displacive transformations. *Materials Science and Technology* 30, 867–869.
- Kundu, S., Hase, K., Bhadeshia, H. K. D. H., 2007. Crystallographic texture of stress-affected bainite. *Proceedings of the Royal Society A* 463, 2309–2328.
- Kunitake, T., 1971. Reactor steel studies. In: in Lundin et al. (1982), K. O. Q. (Ed.), *Steels Research in Japan*.
- Kurdjumov, G. V., 1933. Studies upon the widmanstätten structure, IV. The Fe-C alloys. *Trans. A.I.M.M.E.* 105, 253–255.
- Kurdjumov, G. V., Sachs, G., 1930. Über den mechanismus der stahlhärtung. *Zietschrift für Physik A Hadrons and Nuclei* 64, 325–343.
- Kushida, T., Okaguchi, S., Hamada, M., Yamamoto, A., Ohnishi, K., Fujino, J., 1997. Study of X80 grade high strength line pipe for sour service. In: *Corrosion '97: National Association of Corrosion Engineers Annual Conference*. - NACE International, Houston, U.S.A., pp. NACE-97024.
- Kutsov, A., Taran, Y., Uzlov, K., Krimmel, A., Evsyukov, M., 1999. Formation of bainite in ductile iron. *Materials Science & Engineering A* 273-275, 480–484.
- Lai, G. Y., 1975. On the precipitation of epsilon-carbide in lower bainite. *Metallurgical Transactions A* 6, 1469–1471.
- Lambers, H. G., Tschumak, S., Maier, H. J., Canadinc, D., 2011. On the bainitic and martensitic phase transformation behavior and the mechanical properties of low alloy 51CrV4 steel. *International Journal of Structural Changes in Solids* 3, 15–27.
- Lambert-Perlade, A., Gourgues, A. F., Besson, J., Sturel, T., Pineau, A., 2004a. Mechanisms and modelling of cleavage fractures in simulated heat-affected zone microstructures in HSLA steel. *Metallurgical & Materials Transactions A* 35, 1039–1053.
- Lambert-Perlade, A., Gourgues, A. F., Pineau, A., 2004b. Austenite to bainite phase transformation in the heat-affected zone of a high strength low alloy steel. *Acta Materialia* 52, 2337–2348.
- Lan, H., Du, L., Zhou, N., Liu, X., 2014. Effect of austempering route on microstructural characterization of nanobainitic steel. *Acta Metall. Sin. (Engl. Lett.)* 27, 19–26.
- Lan, H. F., Liu, X. H., Du, L. X., 2011. Ultra-hard bainitic steels processed through low temperature heat treatment. *Advanced Materials Research* 156-157, 1708–1712.
- Lancaster, J. F., 1986. *Metallurgy of Welding*, 4th Edition. Allen and Unwin, London, U.K.
- Laneri, K., Bruna, P., Crespo, D., 2008. Microstructural characterisation and kinetics modelling of vermicular cast irons. *Materials Science and Technology* 24, 1214–1221.
- Lange, H., Mathieu, K., 1938. On the progress of austenite decomposition in the supercooled state in iron-nickel-carbon alloys. *Mitteilungen Kaiser-Wilhelm-Institut für Eisenforschung* 20, 125–134.
- Langer, E. W., 1968. An investigation of carbide precipitation in iron. *Metal Science Journal* 2, 59.
- Langer, J. S., Muller-Krumbhaar, H., 1978. Theory of dendritic growth i. elements of a stability analysis. *Acta Metallurgica* 26, 1681–1687.
- Langford, G., Cohen, M., 1969. Strain hardening of iron by severe plastic deformaton. *ASM Transactions Quarterly* 62, 623–638.
- Langford, G., Cohen, M., 1970. Calculation of cell size strengthening of wire-drawn iron. *Metallurgical Transactions I*, 1478–1480.
- Langford, G., Cohen, M., 1975. Microstructural analysis by high-voltage electron diffraction of severely drawn iron wires. *Metallurgical Transactions A* 6, 901–910.
- Larn, R. H., Yang, J. R., 1999. Effect of compressive deformation of austenite on the Widmanstätten ferrite transformation in Fe-Mn-Si-C steel. *Materials Science & Engineering A* 264, 139–150.
- Larn, R. H., Yang, J. R., 2000. Effect of compressive deformation of austenite on bainitic ferrite transformation in Fe-Mn-Si-C steels. *Materials Science & Engineering A* 278, 278–291.
- Lau, T. W., Sadowski, M. M., North, T. H., Weatherly, G. C., 1987. Effect of nitrogen on the toughness of HSLA weld deposits. In: Koo, J. Y. (Ed.), *Welding Metallurgy of Structural Steels*. TMS-AIME, Warrendale, Pennsylvania, USA, pp. 349–365.

- Lau, T. W., Sadowski, M. M., North, T. H., Weatherly, G. C., 1988. Effect of nitrogen on properties of submerged arc welds. *Materials Science and Technology* 4, 52–61.
- Laverroux, M., Pineau, A., 1974. Influence of precipitation in austenite on the morphology of martensite in Fe-N-Co-Ta alloys. *Scripta Metallurgica* 8, 351–356.
- Law, N. C., Edmonds, D. V., 1980. The formation of austenite in a low-alloy steel. *Metallurgical Transactions A* 11, 33–46.
- Lawrynowicz, Z., 2002. Carbon partitioning during bainite transformation in low alloy steels. *Materials Science and Technology* 18, 1322–1324.
- Lawrynowicz, Z., 2004. Transition from upper to lower bainite in Fe-C-Cr steel. *Materials Science and Technology* 20, 1447–1454.
- Lawrynowicz, Z., 2012. An investigation of the mechanism of bainite transformation in experimental 0.2C-1V-2Mn steel. *Advances in Materials Science* 12, 19–30.
- Lawrynowicz, Z., 2014. Rationalisation of austenite transformation to upper or lower bainite in steels. *Advances in Materials Science* 14, 14–23.
- Le-Houillier, R., Begin, G., Dubé, A., 1971. A study of the peculiarities of austenite during the bainite transformation. *Metallurgical Transactions* 2, 2645–2653.
- Leber, H., Luthy, H., Form, W., 1987. Combined effect of Nb and V in a forged low carbon steel. In: Krauss, G., Banerji, S. K. (Eds.), *Microalloying Forging Steels*. TMS-AIME, Warrendale, Pennsylvania, USA, pp. 189–206.
- Leber, H. J., Garcia, C. I., Palmiere, E. J., DeArdo, A. J., 1988. Strength of Nb-bearing low-C bainitic forging steels. In: DeArdo, A. J. (Ed.), *Processing, Microstructure and Properties of HSLA Steels*. TMS-AIME, Warrendale, Pennsylvania, USA, pp. 425–473.
- Lee, C. G., Kim, S. J., Lee, T. H., Lee, S., 2004. Effect of volume fraction and stability of retained austenite on the formability of a 0.1C-1.5Si-1.5Mn-0.5Cu TRIP-aided steel. *Materials Science & Engineering A* 371, 16–23.
- Lee, C. G., Kim, S. J., Oh, C. S., Lee, S., 2002. Effects of heat treatments and Si additions on the mechanical properties of 0.1 wt% C TRIP-aided cold-rolled steels. *ISIJ International* 42, 1162–1168.
- Lee, C. H., Bhadeshia, H. K. D. H., Lee, H. C., 2003. Effect of plastic deformation on the formation of acicular ferrite. *Materials Science & Engineering A* 360, 249–257.
- Lee, C. H., Nambu, S., Inoue, J., Koseki, T., 2013. Ferrite formation behavior from non-metallic compounds in steels. In: Babu, S., Bhadeshia, H. K. D. H., Cross, C. E., David, S. A., DebRoy, T., DuPont, J. N., Koseki, T., Liu, S. (Eds.), *Trends in Welding Research*. ASM International, Ohio, U. S. A., pp. 43–47.
- Lee, H. J., Spanos, G., Shiflet, G. J., Aaronson, H. I., 1988. Mechanisms of the bainite (non-lamellar eutectoid) reaction and a fundamental distinction between the bainite and pearlite (lamellar eutectoid) reactions. *Acta Metallurgica* 36, 1129–1140.
- Lee, J. L., Pan, Y. T., 1991a. Effect of killing time on the microstructure and toughness of the heat-affected zone in Ti-killed steels. *Metallurgical & Materials Transactions A* 22, 2818–2822.
- Lee, J. L., Pan, Y. T., 1992. Effect of Si on microstructure and toughness of simulated HAZ in Ti killed steel. *Materials Science and Technology* 8, 236–244.
- Lee, J. L., Pan, Y. T., 1993. Effect of S on microstructure and toughness of simulated HAZ in Ti killed steels. *Tech. Rep. 7*, China Steel, Taipei, Taiwan.
- Lee, J. L., Wang, S. C., Cheng, G. H., 1989. Transformation processes and products for C-Mn steels during continuous cooling. *Materials Science and Technology* 5, 674–681.
- Lee, J. Y., Pan, Y. T., 1991b. Microstructure and toughness of the simulated heat-affected zone in Ti- and Al-killed steels. *Materials Science & Engineering A* 136, 109–119.
- Lee, Y. K., 2002. Empirical formula of isothermal bainite start temperature of steels. *Journal of Material Science Letters* 21, 1253–1255.
- Lee, Y. K., Hong, J. M., Cho, C. S., Lee, J. K., 2005. Continuous cooling transformation temperatures and microstructures of niobium bearing microalloyed steels. *Materials Science Forum* 475–479, 65–68.
- Leiro, A., Kankanala, A., Vuorinen, E., Prakash, B., 2011. Tribological behaviour of carbide-free bainitic steel under dry rolling/sliding conditions. *Wear* 273, 2–8.
- Leiro, A., Vuorinen, E., Sundin, K. G., Prakash, B., Sourmail, T., Smanio, V., Caballero, F. G., Gracia-Mateo, C., Elvira, R., 2013. Wear of nano-structured carbide-free bainitic steels under dry rolling-sliding conditions. *Wear* 298–299, 42–47.
- Leontyev, B. A., Kovalevskaya, G. V., 1974. On the bainitic transformation mechanism of austenite. *Fiz. Met. Metalloved.* 38, 1050–1055.
- Leslie, W. C., 1982. *The Physical Metallurgy of Steels*. McGraw Hill, New York.
- Leslie, W. C., Miller, R. L., 1964. The stabilization of austenite by closely spaced boundaries. *ASM Transactions Quarterly* 57, 972–979.
- Lewis, D., 1929. Transformation of austenite into martensite in an 0.8 percent carbon steel. *Journal of the Iron and Steel Institute* 119, 427.

- Li, H. Y., Jin, X. J., 2010. Determination of dislocation density in nanostructured bainitic steels. *Journal of Shanghai Jiaotong University* 44, 613–615.
- Li, J. C. M., Oriani, R. A., Darken, L. S., 1966. Thermodynamics of stressed solids. *Zeitschrift für Physikalische Chemie Neue Folge* 49, 271–290.
- Li, L., Cooman, B. C. D., Liu, R. D., Vleugels, J., Zhang, M., Shi, W., 2007a. Design of TRIP steel with high welding and galvanizing performance in light of thermodynamics and kinetics. *Journal of Iron and Steel Research* 14, 37–41.
- Li, X., Zhu, D., Wang, X., 2007b. Evaluation on dispersion behavior of the aqueous copper nano-suspensions. *Journal of Colloid and Interface Science* 310, 456–463.
- Li, Y., Chen, C., Zhang, F., 2013. Al and Si influences on hydrogen embrittlement of carbide-free bainitic steel. *Advances in Materials Science and Engineering* 2013, 382060.
- Li, Y., Chen, X., 2001. Microstructure and mechanical properties of austempered high silicon cast steel. *Materials Science & Engineering A* 308, 277–282.
- Li, Z., Wu, D., 2006. Effects of hot deformation and subsequent austempering on the mechanical properties of Si-Mn TRIP steels. *ISIJ International* 46, 121–128.
- Liang, P., Li, X., Du, C., Chen, X., 2009. Stress corrosion cracking of X80 pipeline steel in simulated alkaline soil solution. *Materials and Design* 30, 1712–1717.
- Lifshitz, I. M., Slyozov, V. V., 1961. Kinetics of precipitation from supersaturated solid solutions. *Journal of the Physics and Chemistry of Solids* 19, 35–50.
- Lin, M., 1987. Autocatalytic kinetics of martensitic transformations. Tech. Rep. Research proposal, MIT, Boston, USA.
- Linaza, M. A., Romero, J. L., Rodriguez-Ibabe, J. M., Urcola, J. J., 1993. Improvement of fracture toughness of forging steels microalloyed with titanium by accelerated cooling after hot deformation. *Scripta Metallurgica and Materialia* 29, 1217–1222.
- Little, E. A., Mazey, D. J., Hanks, W., 1991. Effects of ion irradiation on the microstructure of an ODS steel. *Scripta Metallurgica and Materialia* 25, 1115–1118.
- Liu, C., Zhao, Z., Bhole, S. D., 2006. Lathlike upper bainite in a silicon steel. *Materials Science & Engineering A* 434, 289–293.
- Liu, C. C., Yao, K. F., Liu, Z., 2000. Quantitative research on effect of stresses and strains on bainitic transformation kinetics and transformation plasticity. *Materials Science and Technology* 16, 643–647.
- Liu, J., Luo, C. P., 2006. Precipitation behavior of the lower bainitic carbide in a medium-carbon steel containing Si, Mn and Mo. *Materials Science & Engineering A* 438–440, 153–157.
- Lixing, H., Dongpo, W., Wenxian, W., Tainjin, Y., 2004. Ultrasonic peening and low transformation temperature electrodes used for improving the fatigue strength of welded joints. *Welding in the World* 48, 34–39.
- Lolla, T., Cola, G., Narayanan, B., Alexandrov, B., Babu, S. S., 2011. Development of rapid heating and cooling (flash processing) process to produce advanced high strength steel microstructures. *Materials Science and Technology* 27, 863–875.
- Lonardelli, I., Bortolotti, M., van Beek, W., Girardini, L., Zadra, M., Bhadeshia, H. K. D. H., 2012a. Powder metallurgical nanostructured medium-carbon bainitic steel: Kinetics, structure and *in situ* thermal stability studies. *Materials Science and Engineering A* 555, 139–147.
- Lonardelli, I., Girardini, L., Maines, L., Menapace, C., Molinari, A., Bhadeshia, H. K. D. H., 2012b. Nanostructured bainitic steel obtained by powder metallurgy approach: structure, transformation kinetics and mechanical properties. *Powder Metallurgy* 55, 256–259.
- Lonsdale, D., Flewitt, P. E. J., 1978. The role of grain size on the ductile-brittle transition of a 2.25Cr-1Mo steel. *Metallurgical Transactions A* 9, 1619–1623.
- Lord, M., 1998. Design and modelling of ultra-high strength steel weld deposits. Ph.D. thesis, University of Cambridge, U. K.
- Lorenz, K., Duren, C., 1983. Evaluation of large diameter pipe steel weldability by means of the carbon equivalent. In: *Steels for line pipe and pipeline fittings*. Metals Society, London, U.K., pp. 322–332.
- Lu, G. Z., Zhang, H., 1989. Sliding wear characteristics of austempered ductile iron with and without laser hardening. In: Ludema, K. C. (Ed.), *Wear of Materials*. ASME, San Antonio, Texas, USA, pp. 225–231.
- Lubin, S., Gourgues-Lorenzon, A. F., Bacroix, B., Regle, H., 2011. Micromechanical modelling of microtexture formation in low alloy steel bainite. *Solid State Phenomena* 172–174, 1228–1233.
- Lund, T., Larsson, S., Ölund, P., 2000. Method of complete bainite hardening. Tech. Rep. 6149743, United States Patent, Hofors, Sweden.
- Lundin, C. D., Kelley, S. C., Menon, R., Kruse, B. J., 1986. Stress rupture behaviour of postweld heat treated 2.25Cr 1Mo steel weld metal. Tech. Rep. Bulletin 315, Welding Research Council, New York, USA.
- Lundin, C. D., Kruse, B. J., Pendley, M. R., 1982. High temperature properties of 2.25Cr1Mo weld metal. *Welding Research Council Bulletin* 277, 1–27.
- Luo, D., Peet, M. J., Ooi, S. W., Yan, P., Yin, Z., Bhadeshia, H. K. D. H., 2014. Spheroidisation of hypereutectoid state of nanostructured bainitic steel. *Materials Science and Technology* 30, 1282–1286.

- Luo, H., Zhao, L., Kruijver, O., Sietsma, J., van der Zwaag, S., 2003. Effect of intercritical deformation on bainite formation in Al-containing TRIP steel. *ISIJ International* 43, 1219–1227.
- Luzginova, N., Zie, L., Sietsma, J., 2007. Evolution and thermal stability of retained austenite in SAE 52100 bainitic steel. *Materials Science & Engineering A* 448, 104–110.
- Luzginova, N. V., Zhao, L., Sietsma, J., 2008. Bainite formation kinetics in high carbon alloyed steel. *Materials Science and Engineering A* 481–482, 766–769.
- Lyman, T., Troiano, A. R., 1946. Influence of carbon content upon the transformations in 3% chromium steel. *Trans. ASM* 37, 402–448.
- Lyons, J. V., Hudson, M. J., 1967. Machining properties of high-carbon chromium bearing steels. Tech. Rep. Special Report 94, Iron and Steel Institute, London, U.K.
- Maalekian, M., Kozeschnik, E., Chatterjee, S., Bhadeshia, H. K. D. H., 2007. Mechanical stabilisation of eutectoid steel. *Materials Science and Technology* 23, 610–612.
- Maalekian, M., Radis, R., Militzer, M., Moreau, A., Poole, W. J., 2012. In situ measurement and modelling of austenite grain growth in a Ti/Nb microalloyed steel. *Acta Materialia* 60, 1015–1026.
- Mabuchi, H., Uemori, R., Fujioka, M., 1996. Role of Mn depletion in intra-granular ferrite transformation in the heat affected zone of welded joints with large heat input in structural steels. *ISIJ International* 36, 1406–1412.
- Machlin, E. S., Cohen, M., 1951. Burst phenomenon in the martensitic transformation. *Trans. Metall. Soc. AIME* 191, 746–754.
- Mack, C., 1956. On clumps formed when convex laminae or bodies are placed at random in two or three dimensions. *Proceedings of the Cambridge Philosophical Society* 52, 246–250.
- Mackenzie, J. K., Bowles, J. S., 1954a. The crystallography of martensite transformations II. *Acta Metallurgica* 2, 138–147.
- Mackenzie, J. K., Bowles, J. S., 1954b. The crystallography of martensite transformations III FCC to BCT transformations. *Acta Metallurgica* 2, 224–234.
- Magee, C. L., 1970. The nucleation of martensite. In: Aaronson, H. I., Zackay, V. F. (Eds.), *Phase Transformations*. ASM International, Materials Park, Ohio, USA, pp. 115–156.
- Mahieu, J., Maki, J., de Cooman, B. C., Claessens, S., 2002a. Phase transformation and mechanical properties of Si-free CMnAl TRIP-aided steel. *Metallurgical & Materials Transactions A* 33, 2573–2580.
- Mahieu, J., van Dooren, D., Barbe, L., de Cooman, B. C., 2002b. Influence of Al, Si, and P on the kinetics of intercritical annealing of TRIP-aided steels: thermodynamic prediction and experimental verification. In: Cooman, B. C. D. (Ed.), *International Conference on TRIP-aided High Strength Ferrous Alloys*. Verlag Mainz, Aachen, Germany, pp. 159–164.
- Mahnken, R., Schneidt, A., Tschumak, S., Maier, H. K., 2011. On the simulation of austenite to bainite phase transformation. *Computational Materials Science* 50, 1823–1829.
- Maier, C., Blaschko, O., Pichl, W., 1997. Influence of plastic deformation on the martensitic phase transition in lithium. *Physical Review B* 55, 113–116.
- Maier, H. J., Ahrens, U., 2002. Isothermal bainitic transformation in low alloy steels: factors limiting prediction of the resulting material's properties. *Zeitschrift für Metallkunde* 93, 712–718.
- Makarov, A. V., Schastlivtsev, V. M., Gorkunov, E. S., Tabatchikova, T. I., Kogan, L. K., Kolobylin, Y. M., Zadvorkin, S. M., Khlebnikova, Y. V., Yakovleva, I. K., Gavrilova, L. D., Solomein, M. N., 2002. Feasibility of testing hardness and wear resistance of eutectoid high-carbon steels with the structure of thin-plate pearlite by magnetic and electromagnetic methods. Translation in *Russian Journal of Nondestructive Testing* 38, 767–787.
- Maki, J., Mahieu, J., de Cooman, B. C., Classen, S., 2003. Galvanisability of silicon-free CMnAl TRIP steels. *Materials Science and Technology* 19, 125–131.
- Maki, T., 1990. Microstructure and mechanical properties of ferrous martensites. *Materials Science Forum* 56–58, 157–168.
- Maki, T., Shimooka, S., Arimoto, T., Tamura, I., 1973. Morphology of thin plate-like martensite in Fe-Ni-C alloys. *Trans. JIM* 14, 62–67.
- Maki, T., Shimooka, S., Fujiwara, S., Tamura, I., 1975. Formation temperature and growth behaviour of thin plate martensite in Fe-Ni-C alloys. *Trans. JIM* 16, 35–41.
- Maki, T., Tamura, I., 1986. Shape memory effect in ferrous alloys. In: *ICOMAT 86 (International Conference on Martensitic Transformations)*. Japan Institute of Metals, Tokyo, Japan, pp. 963–970.
- Malecki, P., Langer, E. W., 1990. Dissolution of cementite with alloying elements in austenite. *Scandinavian Journal of Metallurgy* 19, 182–186.
- Mangal, A., Biswas, P., Lenka, S., Singh, V., Singh, S. B., Kundu, S., 2014. Dilatometric and microstructural response of variant selection during martensitic transformation. *Materials Science and Technology* 30, 1116–1124.
- Marcu, T., Molinari, A., Straffellini, G., Berg, S., 2005. Microstructure and tensile properties of 3%Cr-0.5%Mo high carbon PM sintered steels. *Powder Metallurgy* 48, 139–143.

- Marschall, C. W., Hehemann, R. F., Troiano, A. R., 1962. The characteristics of 9% Ni low carbon steel. *Trans. A. S. M.* 55, 135–148.
- Masuyama, F., Komai, N., Yokoyama, T., Yamamoto, S., Miyata, K., Igarashi, M., 1998. 3-year experience with 2.25Cr-1.6W (HCM2s) and 12Cr-0.4Mo-2W (HCM12A) steel tubes in power boiler. *JSME International Journal* 41, 1098–1104.
- Matas, S., Hehemann, R. F., 1960. Retained austenite and the tempering of martensite. *Nature* 187, 685–686.
- Matas, S. J., Hehemann, R. F., 1961. The structure of bainite in hypoeutectoid steels. *TMS-AIME* 221, 179–185.
- Mateo, C. G., Bhadeshia, H. K. D. H., 2004. Nucleation theory for high-carbon bainite. *Materials Science and Engineering A* 378A, 289–292.
- Mateo, C. G., Caballero, F. G., 2005. Ultrahigh-strength bainitic steels. *ISIJ International* 45, 1736–1740.
- Matsuda, F., Fukada, Y., Okada, H., Shiga, C., Ikeuchi, K., Horii, Y., Shiwaku, T., Suzuki, S., 1996. Review of mechanical and metallurgical investigations of martensite-austenite constituent in welded joints in Japan. *Welding in the World* 37, 134–154.
- Matsuda, H., Bhadeshia, H. K. D. H., 2004. Kinetics of the bainite transformations. *Proceedings of the Royal Society of London A* A460, 1710–1722.
- Matsuda, H., Kitano, F., Hasegawa, K., Urabe, T., Hosoya, Y., 2002. Metallurgy of continuously annealed high strength TRIP steel sheet. *Steel Research* 73, 211–217.
- Matsuda, S., Okumura, N., 1978. Effect of distribution of TiN particles on the austenite grain size of low carbon low alloy steels. *Trans. ISIJ* 18, 198–205.
- Matsuzaki, A., Bhadeshia, H. K. D. H., 1995. Effect of austenite grain size and bainite morphology on the overall transformation kinetics of the bainite reaction in steels. *Materials Science and Technology* 15, 518–521.
- Matsuzaki, A., Bhadeshia, H. K. D. H., Harada, H., 1992. Tempering of martensite under the influence of externally applied stress. In: G. R. Speich Symposium, 34th Mechanical Working and Steel Processing. TMS-AIME, Warrendale, Pennsylvania, USA, pp. 47–52.
- Matsuzaki, A., Bhadeshia, H. K. D. H., Harada, H., 1994. Stress-affected bainitic transformation in a Fe-C-Si-Mn alloy. *Acta Metallurgica and Materialia* 42, 1081–1090.
- Mayer, H., Haydn, W., Schuller, R., Issler, S., Bacher-Höchst, M., 2009. Very high cycle fatigue properties of bainitic high carbon-chromium steel under variable amplitude conditions. *International Journal of Fatigue* 31, 1300–1308.
- Mazanec, K., Sejnoha, R., 1965. Delayed fractures in martensite. *Trans. Metall. Soc. AIME* 233, 1602–1607.
- Mazzaferro, C. C. P., Ramos, F. D., Mazzaferro, J. A. E., Rosendo, T. S., Tier, M. A. D., Silva, A. M., dos Santos, J. F., Reguly, A., 2011. Microstructure evaluation and mechanical properties of a friction stir spot welded TRIP 800 steel. *Welding International* 25, 630–690.
- McCutcheon, D. B., Trumper, T. W., Embury, J. D., 1976. Controlled rolling of acicular ferrite plate. *Revue de Métallurgie* 73, 143–174.
- McEvily, A. J., Magee, C. L., 1968. Transformation-structure-property characteristics of low-C alloy steels. In: *Low Alloy Steels*. Iron and Steel Institute, London, U.K., pp. 111–117.
- McGrath, J. T., Chandel, R. S., Orr, R. F., Gianetto, J. A., 1989. A review of factors affecting the structural integrity of weldments in heavy wall reactor vessels. *Canadian Metallurgical Quarterly* 28, 75–83.
- McMahon Jr., C. J., Cianelli, A. K., Feng, H. C., 1977. The influence of Mo on P-Induced temper embrittlement in Ni-Cr steel. *Metallurgical Transactions A* 8, 1055–1057.
- McMahon Jr., C. J., Cohen, M., 1965. Initiation of cleavage in polycrystalline iron. *Acta Metallurgica* 13, 591–604.
- McRobie, D. E., Knott, J. F., 1985. Effects of strain and strain aging on fracture toughness of C-Mn weld metal. *Mater. Sci. Technol.* 1 (5), 357–365.
- Meggers, K., Priesmeyer, H. G., Trela, W. J., Bowman, C. D., Dahms, M., 1994. Real time neutron transmission investigation of the austenite to bainite transformation in grey iron. *Nuclear Instruments and Methods in Physics Research B* 88, 423–429.
- Mehl, R. F., 1939. Hardenability of Alloy Steels. ASM, Metals Park, Ohio, USA.
- Mehl, R. F., 1948. Decomposition of austenite by nucleation and growth processes. *Journal Iron and Steel Institute* 159, 113–129.
- Mendiratta, M. G., Sasser, J., Krauss, G., 1972. Effect of dissolved carbon on microcracking in martensite of an Fe-1.39C alloy. *Metallurgical Transactions* 3, 351–353.
- Mertens, A., Jacques, P. J., Zhao, L., Kruijver, S. O., Sietsma, J., Delannay, F., 2003. On the influence of aluminium and silicon contents on the kinetics of bainite transformation of intercritical austenite. *Journal de Physique IV* 112, 304–308.
- Mesplont, C., de Cooman, B. C., 2003. Effect of austenite deformation on crystallographic texture during transformations in microalloyed bainitic steel. *Materials Science and Technology* 19, 875–886.
- Mesplont, C., Vandeputte, S., de Cooman, B. C., 2002. Dilatometric study of the effect of soluble boron on the continuous and isothermal austenite decomposition in 0.15C-1.6Mn steel. *Zeitschrift für Metallkunde* 93, 1108–1118.

- Miao, P., Knott, J. F., 2004. Formation of sulphide 'patches' on inclusions in C – Mn steel weld metal. *Materials Science and Technology* 20, 1440–1446.
- Miikkinen, V. T. T., Edmonds, D. V., 1987a. Fracture toughness of two experimental high strength bainitic low alloy steels containing silicon. *Materials Science and Technology* 3, 441–449.
- Miikkinen, V. T. T., Edmonds, D. V., 1987b. Microstructural examination of two experimental high strength bainitic low alloy steels containing silicon. *Materials Science and Technology* 3, 422–431.
- Miikkinen, V. T. T., Edmonds, D. V., 1987c. Tensile deformation of two experimental high-strength bainitic low alloy steels containing silicon. *Materials Science and Technology* 3, 432–440.
- Miki, C., Masayuki, T., 2013. Fatigue strength improvement of out-of-plane welded joints of steel girder under variable amplitude loading. *Welding in the World* 57, 823–840.
- Mikus, E. B., Hughel, T. J., Gerty, J. M., Knusden, A. C., 1960. The dimensional stability of a precision ball bearing material. *Trans. ASM* 52, 307–320.
- Miller, R. F., Benz, W. G., Unverzagt, W. E., 1940. The creep strength of 17 low alloy steels at 1000 f. *Proceedings of ASTM* 40, 771–781.
- Mills, A. R., Thewlis, G., Whiteman, J. A., 1987. Nature of inclusions in steel weld metals and their influence on the formation of acicular ferrite. *Materials Science and Technology* 3, 1051–1061.
- Minote, T., Torizuka, S., Ogawa, A., Nikura, M., 1996. Modelling of transformation behaviour and compositional partitioning in TRIP steel. *ISIJ International* 36, 201–207.
- Mintz, B., Wilson, D. V., 1965. Strain ageing during the fatigue of carbon steels. *Acta Metallurgica* 13, 947–956.
- Miracle, D. B., 2015. High entropy alloys and their development as structural materials. *Materials Science and Technology* 31, DOI 10.1179/1743284714Y.0000000749.
- Mirak, A. R., Nili-Ahmadabadi, M., 2004. Effect of modified heat treatments on the microstructure and mechanical properties of a low alloy high strength steel. *Materials Science and Technology* 20, 897–902.
- Mitchell, D. R. G., Ball, C. J., 2001. Quantitative X-ray diffraction and analytical electron microscopy study of service-exposed 2.25Cr1Mo steels. *Materials Characterization* 47, 17–26.
- Miyamoto, G., Oh, J. C., Hono, K., Furuhashi, T., Maki, T., 2007. Effect of partitioning of Mn and Si on the growth kinetics of cementite in tempered Fe-0.6 mass% C martensite. *Acta Materialia* 55, 5027–5038.
- Miyamoto, G., Shibata, A., Maki, T., Furuhashi, T., 2009. Precise measurement of strain accommodation in austenite matrix surrounding martensite in ferrous alloys by electron backscatter diffraction analysis. *Acta Materialia* 57, 1120–1131.
- Miyamoto, G., Shinyoshi, T., Yamaguchi, J., Furuhashi, T., Maki, T., Uemori, R., 2003. Crystallography of intragranular ferrite formed on (mns+v(c,n)) complex precipitate in austenite. *Scripta Materialia* 48, 371–377.
- Miyata, K., Igarashi, M., Sawaragi, Y., 1999. Effect of trace elements on creep properties of 0.06C-2.25Cr-1.6W-0.1Mo-0.25V-0.05Nb steel. *ISIJ International* 39, 947–958.
- Miyata, K., Sawaragi, Y., 2001. Effect of Mo and W on the phase stability of precipitates in low Cr heat resistant steels. *ISIJ International* 41, 281–289.
- Moeinifar, S., Kokabi, A. H., Hosseini, H. R. M., June 2010. Influence of peak temperature during simulation and real thermal cycles on microstructure and fracture properties of the reheated zones. *Materials and Design* 31 (6), 2948–2955.
- Moore, D. J., Rouns, T. N., Rundman, K. B., 1985a. The effect of heat treatment, mechanical deformation, and alloying element additions on the rate of bainite formation in austempered ductile irons. *Journal of Heat Treating* 4, 7–24.
- Moore, D. J., Rouns, T. N., Rundman, K. B., 1985b. Structure and mechanical properties of austempered ductile iron. *AFS Transactions* 93, 705–718.
- Moore, D. J., Rouns, T. N., Rundman, K. B., 1986. Effect of manganese on structure and properties of austempered ductile iron: processing window concept. *AFS Transactions* 94, 255–264.
- Moore, D. J., Rouns, T. N., Rundman, K. B., 1987. The relationship between microstructure and tensile properties in austempered ductile irons. *AFS Transactions* 95, 765–774.
- Morales-Rivas, L., Roelofs, H., Hasler, S., Garcia-Mateo, C., Caballero, F. G., 2014. Complex microstructural banding of continuously cooled carbide-free bainitic steels. *Materials Science Forum* 783-786, 980–985.
- Morgan, E. R., Dancy, T. E., Korshynsky, M., 1965. Improved HSLA steels through hot strip mill controlled cooling. *Blast furnace and steel plant* 53, 921–929.
- Mori, N., Homma, H., Okita, S., Wakabayashi, M., 1981. Mechanism of toughness improvement in Ti-B weld metals. *Tech. Rep. IX 1196 81*, International Institute of Welding, Paris, France.
- Morikawa, H., Hasegawa, T., 1985. Microstructures and strengthening factors of accelerated cooled steel. In: Southwick, P. D. (Ed.), *Accelerated Cooling of Steel*. TMS-AIME, Ohio, USA, pp. 83–96.
- Moritani, T., Miyajima, N., Furuhashi, T., Maki, T., 2002. Comparison of interphase boundary structure between bainite and martensite in steel. *Scripta Materialia* 47, 193–199.
- Mormiroli, J. P., Bauer-grosse, E., Gantois, M., 1983. Crystalline defects in  $M_7C_3$  carbides. *Philosophical Magazine A* 48, 311–327.
- Morrison, W. B., 2009. Microalloy steels – the beginning. *Materials Science and Technology* 25, 1066–1073.

- Mostert, R. J., van Rooyen, G. T., 1982. Superhardening effect in Mo-free steel. In: Speciality steels and hard materials. Pergamon Press, Oxford, U. K., pp. 229–238.
- Mott, N. F., 1952. A theory of work-hardening of metal crystals. *Philosophical Magazine* 43, 1151–1178.
- Mujahid, S., Bhadeshia, H. K. D. H., 1992. Partitioning of carbon from supersaturated ferrite plates. *Acta Metallurgica and Materialia*, 389–396.
- Mujahid, S., Bhadeshia, H. K. D. H., 1993. Partitioning of carbon from supersaturated ferrite plates. *Acta Metallurgica and Materialia* 40, 389–396.
- Mukherjee, M., Bhattacharyya, T., Singh, S. B., 2010. Models for austenite to martensite transformation in TRIP-aided steels: A comparative study. *Material and Manufacturing Processes* 25, 206–210.
- Murphy, M. C., Branch, G. D., 1969. The microstructure, creep and creep-rupture properties of Cr-Mo-V steam turbine castings. *Journal of the Iron and Steel Institute* 206, 1347–1364.
- Murphy, M. C., Branch, G. D., 1971. Metallurgical changes in 2.25CrMo steels during creep rupture test. *Journal of the Iron and Steel Institute* 209, 546–561.
- Muruganath, M., Bhadeshia, H. K. D. H., Keehan, E., Andr n, H. O., Karlsson, L., 2002. Strong and tough steel welds. In: Cerjak, H., Bhadeshia, H. K. D. H. (Eds.), *Mathematical Modelling of Weld Phenomena 6*. IOM Communications, London, U.K., pp. 205–230.
- Muti , T. A., Kinderman, A. J., Bernstein, I. M., 1977. The effects of concurrent deformation on the transformation kinetics. In: Ballance, J. B. (Ed.), *The Hot Deformation of Austenite*. TMS-AIME, Warrendale, Pennsylvania, USA, pp. 410–427.
- Mutton, P. J., 1985. The influence of microstructure of the wear behavior of rail and wheel materials. M.App.Sc. thesis, University of Melbourne.
- Myers, J., Willoughby, G., Ham, R. K., 1968. The creep behaviour of a 1% Cr-M-V rotor steel. Tech. Rep. RD/L/R/1514, Central Electricity Generating Board, Leatherhead, Surrey, U.K.
- Myszka, D., Cybula, L., Wiczorek, W., 2014. Influence of heat treatment conditions on microstructure and mechanical properties of austempered ductile iron after dynamic deformation test. *Archives of Metallurgy and Materials* 59, 1171–1179.
- Nabarro, F. R. N., 1982. Stress equivalence in the theory of solution hardening. *Proceedings of the Royal Society of London A* 381, 285–292.
- Naderi, M., Saeed-Akbari, A., Bleck, W., 2008. Quantitative and qualitative investigation of the heterogeneous microstructures using surface hardness mapping and dilatation data. *Materials Letters* 62, 1132–1135.
- Nagakura, S., Hirotsu, Y., M. Kusunoki and, T. S., Nakamura, Y., 1983. Crystallographic study of the tempering of martensitic carbon steel by electron microscopy and diffraction. *Metallurgical Transactions A* 14, 1025–1031.
- Nagakura, S., Suzuki, S., Kusunoki, M., 1981. Structure of the precipitated particles at the third stage of tempering of martensitic iron-carbon steel studied by high resolution electron microscopy. *Transactions of the Japan Institute of Metals* 22, 699–709.
- Nakada, N., Fukuzawa, N., Tsuchiyama, T., Takaki, S., Koyano, T., Iwamoto, T., Omori, Y., 2013. Isothermal transformation in Fe-N hypereutectoid alloy. *ISIJ International* 53, 139–144.
- Nakagaito, T., Shimizu, T., Furukimi, O., Sakata, K., 2003. The effect of microstructure on the formation of retained austenite in TRIP-assisted steel. *Tetsu-to-Hagane* 89, 841–847.
- Nakamura, Y., Mikami, T., Nagakura, S., 1985. *In situ* high temperature electron microscopic study of the formation and growth of cementite particles in the third stage of tempering. *Transactions of the Japan Institute of Metals* 26, 876–885.
- Nakamura, Y., Nagakura, S., 1986. Decomposition of retained austenite during the tempering of martensitic high carbon steel studied by *in situ* electron microscopy. In: *International Conference on Martensitic Transformations ICOMAT '86*. Japan Institute of Metals, Tokyo, Japan, pp. 386–391.
- Nakashima, K., Futamura, Y., Tsuchiyama, T., Takaki, S., 2002. Interaction between dislocation and copper particles in Fe-Cu alloys. *ISIJ International* 42, 1541–1545.
- Nakasugi, H., Matsuda, H., Tamehiro, H., 1980. Development of controlled rolled ultra low carbon bainitic bainite low carbon controlled rolled linepipe steel for large diameter linepipe. In: *Alloys for the 80s*. Climax Molybdenum Co., Michigan, USA, pp. 213–224.
- Nakasugi, H., Matsuda, H., Tamehiro, H., 1981. Ultra-low carbon bainitic steel for line pipes. In: *Steels for line pipe and pipeline fittings*. Metals Society, London, U.K., pp. 90–95.
- Nakasugi, H., Matsuda, H., Tamehiro, H., 1983. Ultra-low carbon bainitic steel for line pipes. In: *Steels for line pipe and pipeline fittings*. Metals Society, London, U.K., pp. 909–95.
- Nam, W. J., 1999. Effect of initial microstructure on the coarsening behaviour of cementite particles. *ISIJ International* 39, 1181–1187.
- Nanninga, N., Grochowksi, J., Heldt, L., Rundman, K., 2010. Role of microstructure, composition and hardness in resisting hydrogen embrittlement of fastener grade steels. *Corrosion Science* 52, 1237–1246.

- Nath, B., 1982. Creep rupture and creep crack growth behaviour of transition joints. In: David, S. A., Slaughter, G. M. (Eds.), *Welding Technology of Energy Applications*. Oak Ridge National Laboratory, Tennessee, USA, pp. 1–25.
- Nawrocki, J. G., Dupont, J. N., Robino, C. V., Marder, A. R., 2000. Stress-relief cracking susceptibility of a new ferritic steel – part 1: single pass heat affected zone simulations. *Welding Journal, Research Supplement* 79, 355s–362s.
- Nawrocki, J. G., Dupont, J. N., Robino, C. V., Marder, A. R., 2001. Stress-relief cracking susceptibility of a new ferritic steel – part 2: multi pass heat affected zone simulations. *Welding Journal, Research Supplement* 80, 18s–24s.
- Naylor, J. P., 1979. Influence of lath morphology on the yield stress and transition temperature of martensitic-bainitic steels. *Metallurgical transactions A* 10, 861–873.
- Naylor, J. P., Krahe, P. R., 1974. The effect of bainite packet size on toughness. *Metallurgical Transactions* 5, 1699–1701.
- Naylor, J. P., Krahe, P. R., 1975. Cleavage planes in lath type bainite and martensite. *Metallurgical Transactions* 6, 594–598.
- Nehrenberg, A. E., 1950. The growth of austenite as related to prior structure. *Journal of Metals* 188, 162–174.
- Nemoto, M., 1974. Growth of bainite in an Fe-Ni-C alloy. In: *High Voltage Electron Microscopy*. Academic Press, New York, USA, pp. 230–234.
- Nilan, T. G., 1967. Morphology and kinetics of austenite decomposition at high pressure. *Trans. Met. Soc. AIME* 239, 898–909.
- Nishioka, K., Tamahiro, H., 1988. High-strength Ti-oxide bearing line pipe steel for low temperature service. In: *Microalloying '88*. ASM International, Ohio, U. S. A., pp. 1–9.
- Nishiyama, S., 1980. Statistical analysis of fatigue test data. *Journal of the Society of Materials Science, Japan* 29, 24–29.
- Nishiyama, Z., 1934. X-ray investigation of the mechanism of the transformation from face centered cubic lattice to body centered cubic. *Science Reports of Tohoku Imperial University* 23, 637–634.
- Nohava, J., Hausild, P., Karlik, M., Bompard, P., 2003. Electron backscattering diffraction analysis of secondary cleavage cracks in a reactor pressure vessel steel. *Materials Characterization* 49, 211–217.
- Nolze, G., 2004. Characterisation of the fcc/bcc orientation relationship by EBSD using pole figures and variants. *Zeitschrift für Metallkunde* 95, 744–755.
- Norström, L. A., 1976. On the yield strength of quenched low carbon lath martensite. *Scandinavian Journal of Metallurgy* 5, 159–165.
- Novotny, P. M., 1992. Fundamentals of aging and tempering in bainitic and martensitic steel products. In: G. R. Speich Symposium, 34th Mechanical Working and Steel Processing. Iron and Steel Society of AIME, Warrendale, Pennsylvania, pp. 215–236.
- Nutting, J., 1998. The structural stability of low alloy steels for power generation applications. In: Viswanathan, R., Nutting, J. (Eds.), *Advanced Heat Resistant Steels for Power Generation*. Institute of Materials, London, U.K., pp. 12–30.
- Oates, G., Wilson, D. V., 1964. The effects of dislocation locking and strain ageing on the fatigue limit of low-carbon steel. *Acta Metallurgica* 12, 21–33.
- Oblak, J. M., Goodenow, R. H., Hehemann, R. F., 1964. Morphology of bainite in hypoeutectoid steels. *TMS-AIME* 230, 258–259.
- Oblak, J. M., Hehemann, R. F., 1967. Structure and growth of Widmanstätten ferrite and bainite. In: *Transformation and Hardenability in Steels*. Climax Molybdenum, Michigan, USA, pp. 15–38.
- Ochi, Y., McEvily, A. J., 1988. An evaluation of the fatigue crack-growth and fracture-toughness characteristics of rail steels. *Engineering Fracture Mechanics* 29, 159–172.
- Ode, M., Kim, S. G., Suzuki, T., 2001. Recent advances in the phase-field model for solidification. *ISIJ International* 4, 1076–1082.
- Ogawa, K., Kajiwara, S., 2006. Basic difference between martensitic and bainitic transformations revealed by high-resolution electron microscopy. *Materials Science & Engineering A* 438–440, 90–94.
- Ohmori, Y., 1971. The crystallography of the lower bainite transformation in a plain carbon steel. *Trans. ISIJ* 11, 95–101.
- Ohmori, Y., 1986. Precipitation of iron carbides in lower bainite and tempered martensite in Fe-C alloys. In: *International Conference on Martensitic Transformations ICOMAT '86*. Japan Institute of Metals, Tokyo, Japan, pp. 5878–594.
- Ohmori, Y., 1989. Crystallographic analysis of lower bainite in Fe-0.7%C alloy. *Materials Transactions, JIM* 30, 487–497.
- Ohmori, Y., 2002. Crystallographic aspects of bainite transformation in steels. *Scripta Materialia* 47, 201–206.
- Ohmori, Y., Honeycombe, R. W. K., 1971. The isothermal transformation of plain carbon steels. Supplement to *Trans. ISIJ* 11, 1160–1164.

- Ohmori, Y., Jung, Y. C., Nakai, K., Shiori, H., 2001. Bainite transformation and diffusional migration of bainite/austenite broad faces in Fe-9Ni-C alloys. *Acta Materialia* 49, 3149–3162.
- Ohmori, Y., Ohtani, H., Kunitake, T., 1971. The bainite in low-C low-alloy high strength steels. *Trans. ISIJ* 11, 250–259.
- Ohmori, Y., Ohtani, H., Kunitake, T., 1974. Tempering of the bainite and the bainite/martensite duplex structure in low carbon low alloy steel. *Metal Science* 8, 357–366.
- Ohta, A., Matsuoka, K., Nguyen, N. T., Maeda, Y., Suzuki, N., 2003. Fatigue strength improvement of lap welded joints of thin steel plate using low transformation temperature welding wire. *Welding Journal, Research Supplement* 82, 77s–83s.
- Ohta, A., Suzuki, N., Maeda, Y., Hiraoka, K., Nakamura, T., 1999a. Superior fatigue crack growth properties in newly developed weld metal. *International Journal of Fatigue* 21, S113–S118.
- Ohta, A., Watanabe, O., Matsuoka, K., Shiga, C., Nishijima, S., Maeda, Y., Suzuki, N., Kubo, T., 1999b. Fatigue strength improvement by using newly developed low transformation temperature welding material. *Welding in the World* 43, 38–42.
- Ohtsuka, H., 2006. Effects of a high magnetic field on bainitic transformation in Fe-based alloys. *Materials Science & Engineering A* 438–440, 136–139.
- Oka, M., Okamoto, H., 1986. Isothermal transformations in hypereutectoid steels. In: *International Conference on Martensitic Transformations ICOMAT '86*. Japan Institute of Metals, Tokyo, Japan, pp. 271–275.
- Oka, M., Okamoto, H., 1988. Swing back in kinetics near  $M_S$  in hypereutectoid steels. *Metallurgical Transactions A* 19, 447–452.
- Okabe, R., Koshizuka, N., Tanaka, M., Katamine, A., San-Nomiya, Y., 1983. *Trans. ISIJ* 23, 390.
- Okada, H., Dukagawa, T., Okamoto, A., Azuma, M., Matsuda, Y., 1995. Prevention of red scale formation during hot rolling of steels. *ISIJ International* 35, 886–891.
- Okaguchi, S., Hashimoto, T., Ohtani, H., 1988. Effect of niobium, vanadium and titanium on transformation behavior of HSLA steel in accelerated cooling. In: *Physical Metallurgy of Thermomechanical Processing of Steels and Other Metals*. Vol. 1. Iron and Steel Institute of Japan, Tokyo, Japan, pp. 330–336.
- Okamoto, H., Oka, M., 1985. Isothermal martensite transformation in a 1.80 wt% C steel. *Metallurgical transactions A* 16, 2257–2262.
- Okamoto, H., Oka, M., 1986. Lower bainite with midrib in hypereutectoid steels. *Metallurgical Transactions A* 17, 1113–1120.
- Oldland, R. B., 1985. Al and N effects on the microstructure and properties of single pass SMA welds. *Australian Welding Research* December, 31–43.
- Olson, G. B., 1984. Personal communication, Northwestern University.
- Olson, G. B., 2013. Genomic materials design: The ferrous frontier. *Acta Materialia* 61, 771–781.
- Olson, G. B., Azrin, M., 1978. Transformation behaviour of TRIP steels. *Metallurgical transactions A* 9, 713–721.
- Olson, G. B., Bhadeshia, H. K. D. H., Cohen, M., 1989. Coupled diffusional-displacive transformations. *Acta Metallurgica* 37, 381–389.
- Olson, G. B., Bhadeshia, H. K. D. H., Cohen, M., 1990. Coupled diffusional/displacive transformations, Part II: Solute trapping. *Metallurgical & Materials Transactions A* 21A, 805–809.
- Olson, G. B., Cohen, M., 1975. Kinetics of strain-induced martensitic transformation. *Metallurgical Transactions A* 6A, 791–795.
- Olson, G. B., Cohen, M., 1976. A general mechanism of martensitic nucleation, Parts I-III. *Metallurgical Transactions A* 7A, 1897–1923.
- Olson, G. B., Cohen, M., 1977. Reply to 'on the equilibrium temperature in thermoelastic martensitic transformations'. *Scripta Metallurgica* 11, 345–347.
- Olson, G. B., Cohen, M., 1979. Interphase boundary dislocations and the concept of coherency. *Acta Metallurgica* 27, 1907–1918.
- Olson, G. B., Cohen, M., 1981a. A perspective on martensitic nucleation. *Annual Reviews in Materials Science* 11, 1–30.
- Olson, G. B., Cohen, M., 1981b. Theory of martensitic nucleation: a current assessment. In: H. I. Aaronson, D. E. Laughlin, M. S. (Ed.), *Proc. Int. Conf. Solid→Solid Phase Transformations*. TMS-AIME, Warrendale, Pennsylvania, USA, pp. 1209–1213.
- Olson, G. B., Cohen, M., 1982. Stress-assisted isothermal martensitic transformation: application to TRIP steels. *Metallurgical Transactions A* 13, 1907–1914.
- Olson, G. B., Owen, W. S., 1976. Stress field of a martensitic particle and the conditions for thermoelastic behaviour. In: *New aspects of martensitic transformations*. Japan Institute of Metals, Tokyo, Japan, pp. 105–110.
- Olson, G. B., Tsuzaki, K., Cohen, M., 1987. Statistical aspects of martensitic nucleation. *Mat. Res. Soc. Symposium Proc.* 57, 129–148.

- Onink, M., Tichelaar, F. D., Brackman, C. M., Mittemeijer, E. J., van der Zwaag, S., 1996. Quantitative analysis of dilatation by decomposition of Fe-C austenites; calculation of volume change upon transformation. *Z. Metallkunde* 87, 1–32.
- Onyuna, M., Oettel, H., Martin, U., Weiss, A., 2004. On the deformation behaviour and martensitic transformation of metastable austenitic steels. *Advanced Engineering Materials* 6, 529–535.
- Ooi, S. W., Gamham, J. E., Ramjaun, T. I., 2014. Low transformation temperature weld filler for tensile residual stress reduction. *Materials and Design* 56, 773–781.
- Oriani, R. A., Josephic, P. H., 1974. Equilibrium aspects of hydrogen-induced cracking of steels. *Acta Metallurgica* 22, 1065–1074.
- Ouchi, C., Sampei, T., Kozasu, I., 1982. The effect of hot rolling condition and chemical composition on the onset temperature of  $\gamma/\alpha$  transformation after hot rolling. *Transactions of the Iron and Steel Institute of Japan* 22, 214–222.
- Owen, W. S., 1954. The effect of silicon on the kinetics of tempering. *Trans. ASM* 46, 812–829.
- Owen, W. S., 1980. Can a simple heat treatment help to save Detroit? *Metals Technology* 7, 1–13.
- Owen, W. S., Wilson, E. A., Bell, T., 1964. The structure and properties of quenched iron alloys. In: Zackay, V. F. (Ed.), *High strength materials*. Wiley, New York, USA, pp. 167–212.
- Oyama, T., Sherby, O. D., Wadsworth, J., Walser, B., 1984. Application of the divorced eutectoid transformation to the development of fine-grained, spheroidized structures in ultrahigh carbon steels. *Scripta Metallurgica* 18, 799–804.
- Padmanabhan, R., Wood, W. E., 1984. Occurrence of blocky martensite in 300M steel. *Materials Science and Engineering* 66, 1–11.
- Pak, J. H., Bhadeshia, H. K. D. H., Karlsson, L., 2012a. Mechanism of misorientation development with coalesced martensite. *Materials Science and Technology* 28, 918–923.
- Pak, J. H., Bhadeshia, H. K. D. H., Karlsson, L., Keehan, E., 2008. Coalesced bainite by isothermal transformation of reheated weld metal. *Science and Technology of Welding and Joining* 13, 593–597.
- Pak, J. H., Suh, D. W., Bhadeshia, H. K. D. H., 2012b. Bainite: Fragmentation of crystallographically homogeneous domains. *International Journal of Materials Research* 103, 476–482.
- Pak, J. H., Suh, D. W., Bhadeshia, H. K. D. H., 2012c. Promoting the coalescence of bainite platelets. *Scripta Materialia* 66, 951–953.
- Pan, Y. T., Lee, J. Y., 1994. Development of  $\text{TiO}_x$ -bearing steels with superior heat-affected zone toughness. *Materials & Design* 15, 331–338.
- Pandit, A. S., Bhadeshia, H. K. D. H., 2012. Divorced pearlite in steels. *Proceedings of the Royal Society A* 468, 2767–2778.
- Papadimitriou, G., Fourlaris, G., 1997. A TEM investigation of the stepped bainite reaction in silicon steels. *J. de Physique IV* 7, C5 131–136.
- Papaefthymiou, S., Bleck, W., Kruijver, S., Sietsma, J., Zhao, L., van der Zwaag, S., 2004. Influence of intercritical deformation on microstructure of TRIP steels containing Al. *Materials Science and Technology* 20, 201–206.
- Parameswaran, P., Vijayalakshmi, M., Raghunathan, V. S., 2002. Influence of prior microstructure on tempering stages in 2.25Cr1Mo steel. *High Temperature Materials and Processes* 21, 251–267.
- Park, J. S., Lee, Y. K., 2007. Nb(C,N) precipitation kinetics in the bainite region of a low-carbon Nb-microalloyed steel. *Scripta Materialia* 57, 109–112.
- Park, K. S., Cho, S. J., Lee, K. Y., Kim, G. S., Lee, C. S., 2007. Effect of volume fraction of undissolved cementite on the high cycle fatigue properties of high carbon steels. *International Journal of Fatigue* 29, 1863–1867.
- Parker, E. R., 1977. Interrelations of compositions, transformation kinetics morphology and mechanical properties of alloy steels. *Metallurgical Transactions A* 8A, 1025–1042.
- Parker, E. R., Ritchie, R. O., Spencer, P. N., Todd, J. A., 1984. An advanced 3Cr-1Mo steel for hydrogen service. In: *Research on Chrome-Moly Steels*. American Society of Mechanical Engineers, New York, USA, pp. 109–116.
- Parker, E. R., Zackay, V. F., 1975. Microstructural features affecting fracture toughness of high strength steels. *Engineering Fracture Mechanics* 7, 371–375.
- Patel, J. R., Cohen, M., 1953. Criterion for the action of applied stress in the martensitic transformation. *Acta Metallurgica* 1, 531–538.
- Pati, S. R., Cohen, M., 1951. Nucleation of isothermal martensitic transformation. *Acta Metallurgica* 34, 189–199.
- Paxton, H. W., Austin, J. B., 1972. Historical account of the contributions of E. C. Bain. *Metallurgical Transactions* 3, 1035–1042.
- Peet, M., Babu, S. S., Miller, M. K., Bhadeshia, H. K. D. H., 2004. Three-dimensional atom probe analysis of carbon distribution in low-temperature bainite. *Scripta Materialia* 50, 1277–1281.
- Peet, M., Bhadeshia, H. K. D. H., 2011. Surface relief due to bainite transformation at 473 K. *Metallurgical & Materials Transactions A* 42, 3344–3348.

- Peet, M. J., Hill, P., Rawson, M., Wood, S., Bhadeshia, H. K. D. H., 2011. Fatigue of extremely fine bainite. *Materials Science and Technology* 27, 119–123.
- Pereloma, E., Beladi, H., Zhang, L., Timokhina, I., 2012. Understanding the behavior of advanced high-strength steels using atom probe tomography. *Metallurgical & Materials Transactions A* 43, 3958–3971.
- Pereloma, E. V., Al-Harbi, F., Gazder, A. A., 2014. The crystallography of carbide-free bainites in thermomechanically processed low Si transformation-induced plasticity steels. *Journal of Alloys and Compounds* 615, 96–110.
- Pereloma, E. V., Bayley, C., Boyd, J. D., 1996. Microstructural evolution during simulated OLAC processing of a low-carbon microalloyed steel. *Materials Science & Engineering A* 210, 16–24.
- Pereloma, E. V., Timokhina, I. B., Hodgson, P. D., 1999. Transformation behaviour in thermomechanically processed C-Mn-Si TRIP steels with and without Nb. *Materials Science & Engineering A* 273–275, 448–452.
- Pereloma, E. V., Timokhina, E. V., Miller, M. K., Hodgson, P. D., 2007. Three-dimensional atom probe analysis of solute distribution in thermomechanically processed TRIP steels. *Acta Materialia* 55, 2587–2598.
- Pereloma, E. V., Timokhina, I. B., Russell, K. F., Miller, M. K., 2006. Characterization of clusters and ultrafine precipitates in Nb-containing C-Mn-Si steels. *Scripta Materialia* 54, 471–476.
- Perlade, A., Furnemont, Q., Mertens, A., Delannay, F., 2003. A physically based model for TRIP-aided carbon steels behaviour. *Materials Science & Engineering A* 356, 145–152.
- Perry, L. K., Ryan, D. H., Gagon, R., 2006. Studying surfaces and thin films using Mössbauer spectroscopy. *Hyperfine Interactions* 170, 131–143.
- Petch, N. J., 1990. Theory of yield point and of strain ageing in steel. In: Charles, J. A., Smith, G. A. (Eds.), *Advances in Physical Metallurgy*. Institute of Metals, London, U.K., pp. 11–22.
- Petit-Grostabussiat, S., Taleb, L., Jullien, J. F., 2004. Experimental results on classical plasticity of steels subjected to structural transformations. *International Journal of Plasticity* 20, 1371–1386.
- Petrov, R., Kestens, L., Houbaert, Y., 2001. Recrystallisation of a cold rolled TRIP-assisted steel during reheating for intercritical annealing. *ISIJ International* 41, 883–890.
- Petrov, R., Kestens, L., Wasilkowska, A., Houbaert, Y., 2007. Microstructure and texture of a lightly deformed TRIP-assisted steel characterized by means of the EBSD technique. *Materials Science & Engineering A* 447, 285–297.
- Pfeil, L. P., 1926. The effect of occluded hydrogen on the tensile strength of iron. *Proceedings of the Royal Society of London* 112, 182–195.
- Pichl, W., Krystian, M., 1999. Martensitic transformation and mechanical deformation of high-purity lithium. *Materials Science & Engineering A* 273–275, 209–212.
- Pickering, F. B., 1958. Mechanism of bainite formation in low-alloy steels containing up to 0.4% carbon. In: 4th International Conference on Electron Microscopy. Springer Verlag, Berlin, pp. 626–637.
- Pickering, F. B., 1967a. The structure and properties of bainite in steels. In: *Transformation and Hardenability in Steels*. Climax Molybdenum, Ann Arbor, Michigan, USA, pp. 109–132.
- Pickering, F. B., 1967b. The structure and properties of bainite in steels. In: *Transformation and hardenability in steels*. Climax Molybdenum Co., Michigan, USA, pp. 109–132.
- Pickering, F. B., 1978a. *Physical Metallurgy and the Design of Steels*. Applied Science Publishers, page 104, Essex, U.K.
- Pickering, F. B., 1978b. *Physical Metallurgy and the Design of Steels*. Applied Science Publishers, Essex, U. K.
- Pickering, F. B., 1979. The development of ultrahigh strength steels – a historical case study. In: *Phase Transformations*. Vol. 2. Institution of Metallurgists, London, pp. VI–7.
- Pickering, F. B., 1992. *Constitution and Properties of Steels*. Vol. 7. VCH Publishers, eds R. W. Cahn, P. Haasen and E. J. Kramer, London, U.K., Ch. High-strength low-alloy steels, pp. 335–399.
- Pilling, J., Ridley, N., 1982. Tempering of 2.25Cr1Mo low carbon steels. *Metallurgical Transactions A* 13, 557–563.
- Pippard, A. B., 1981. *Classical Thermodynamics*. Cambridge University Press, Cambridge, U. K.
- Pitsch, W., 1962. Der orientierungszusammenhang zwischen zementit und austenit. *Acta Metallurgica* 10, 897–900.
- Pokhodnya, I. K., Shvachko, V. I., 1997. Effect of hydrogen on structure of steel welds. *International Journal of Hydrogen Energy* 22, 285–289.
- Pomey, J., 1966. Revenu de la martensite et reaction bainitique inferieure: Cas des aciers au carbone-silicium et des aciers au carbone. *Memoires Scientifiques Rev. Metallurg.* 63, 507–532.
- Portevin, A., Chevenard, M. P., 1937. Les transformations au refroidissement des aciers. *Comptes Rendus Acad. Sci. Paris* 204, 772.
- Portevin, A., Jolivet, H., 1938. Sur un mode de décomposition de l'austénité. *Comptes Rendus* 207, 1412–1414.
- Pous-Romero, H., Bhadeshia, H. K. D. H., 2014. Coalesced martensite in pressure vessel steels. *Journal of Pressure Vessel Technology* 136, 031402.
- Prado, J. M., 1986. Bainitic transformation in steels. *Journal of Materials Science Letters* 5, 1075–1076.

- Prado, J. M., Catalan, J. J., Marsal, M., 1990. Dilatometric study of isothermal phase transformation in Fe-C-Mn. *Journal of Materials Science* 25, 1939–1946.
- Prasad, S. N., Mediratta, S. R., Sarma, D. S., 2003. Influence of austenitisation temperature on the structure and properties of weather resistant steels. *Materials Science & Engineering A* 358, 288–297.
- Prokic-Cvetkovic, R., Milosavljevic, A., Sedmak, A., Popovic, O., 2006. The influence of the oxygen equivalent in a gas-mixture on the structure and toughness of microalloyed steel weldments. *Journal of the Serbian Chemical Society* 71, 313–321.
- Pugno, N. M., 2007a. The role of defects in the design of space elevator cable: from nanotube to megatube. *Acta Materialia* 55, 5269–5279.
- Pugno, N. M., 2007b. Space elevator: out of order? *Nano Today* 2 (44–47).
- Purdy, G. R., Weichert, D. H., Kirkaldy, J. S., 1964. The growth of proeutectoid ferrite in ternary Fe-C-Mn austenites. *Trans. TMS-AIME* 230, 1025–1034.
- Putatunda, S., Singar, A. V., Tackett, R., Lawes, G., 2009. Development of a high strength high toughness ausferritic steel. *Materials Science & Engineering A* 513–514, 329–339.
- Putatunda, S. K., 2001. Fracture toughness of a high carbon and high silicon steel. *Materials Science and Engineering A* 297, 31–43.
- Putatunda, S. K., 2003. Influence of austempering temperature on microstructure and fracture toughness of a high-carbon and high-silicon and high-manganese cast steel. *Materials & Design* 24, 435–443.
- Putatunda, S. K., Gadicherla, P. K., 1999. Influence of austenitizing conditions on ductile iron (ADI) with ferritic as cast structure. *Materials Science & Engineering A* 268, 15–31.
- Putatunda, S. K., Kesani, S., Tackett, R., Lawes, G., 2006. Development of austenite free ADI (austempered ductile cast iron). *Materials Science & Engineering A* 435–436, 112–122.
- Pušár, A., 1993. Ultrasonic fatigue testing equipment and new procedures for complex material evaluation. *Ultrasonics* 31, 61–67.
- Pyshmintsev, I. Y., de Meyer, M., de Cooman, B. C., Savray, R. A., Shveykin, V. P., Vermeulen, M., 2002. Influence of stress state on plasticity of TRIP-aided steel. *Metallurgical & Materials Transactions A* 33A, 1659–1665.
- Qiao, Z. X., Liu, Y. C., Yu, L. M., Gao, Z. M., 2009. Incompleted bainitic transformation characteristics in an isochronally annealed 30CrNi3MoV steel. *Journal of Alloys and Compounds* 474, 334–340.
- Qin, R. S., Bhadeshia, H. K. D. H., 2009. Phase-field model study of the effect of interface anisotropy on the crystal morphological evolution of cubic metals. *Acta Materialia* 57, 2210–2216.
- Qin, R. S., Bhadeshia, H. K. D. H., 2010. Phase field method. *Materials Science and Technology* 26, 803–811.
- Qin, R. S., Bhadeshia, H. K. D. H., 2011. Applications of phase field modelling. *Current Opinion in Solid State and Materials Science* 15, 81–82.
- Quidort, D., Brechet, Y. J. M., 2002. Model of isothermal and non-isothermal transformation kinetics of bainite in 0.5% C steels. *ISIJ International* 42, 1010–1017.
- Race, J. M., 1992. Carbon diffusion across dissimilar steel welds. Ph.D. thesis, University of Cambridge, Cambridge, U. K.
- Radcliffe, S. V., Rollason, E. C., 1959. The kinetics of the formation of bainite in high purity Fe-C alloys. *Journal of the Iron and Steel Institute* 191, 56–65.
- Radcliffe, S. V., Schatz, M., Kulin, S. A., 1963. The effects of high P on the isothermal transformation of austenite in Fe-C alloys. *Journal of the Iron and Steel Institute* 201, 143–153.
- Raghavan, V., 1988. *Phase Diagrams of Ternary Iron Alloys*. Vol. 3. Indian Institute of Metals, Calcutta, India, Ch. -, pp. 33–44.
- Raghavan, V., 1992. Kinetics of martensitic transformations. In: Olson, G. B., Owen, W. S. (Eds.), *Martensite*. ASM International, Ohio, USA, pp. 197–226.
- Raghavan, V., Entwisle, A. R., 1965. Isothermal martensite kinetics in iron alloys. In: *Physical properties of martensite and bainite*, Special Report 93. Iron and Steel Institute, London, U.K., pp. 29–37.
- Ramazani, A., Li, Y., Mukherjee, K., Prael, U., Bleck, W., Abdurakhmanov, M. S., Reisgen, U., 2013. Microstructure evolution simulation in hot rolled DP600 steel during gas metal arc welding. *Computational Materials Science* 68, 107–116.
- Ramjaun, T. I., Stone, H. J., Karlsson, L., Kelleher, J., Moat, R. J., Kornmeier, J. R., Dalaei, K., Bhadeshia, H. K. D. H., 2014a. Effect of inter-pass temperature on residual stresses in multi-pass welds produced using a low transformation temperature filler alloy. *Science and Technology of Welding and Joining* 19, 44–51.
- Ramjaun, T. I., Stone, H. J., Karlsson, L., Kelleher, J., Ooi, S. W., Dalaei, K., Kornmeier, J. R., Bhadeshia, H. K. D. H., 2014b. Effects of dilution and baseplate strength on stress distributions in multipass welds deposited using low transformation temperature filler alloys. *Science and Technology of Welding and Joining* 19, 461–467.
- Rancel, L., Gomez, M., S. F. Medina a, d. I. G., 2011. Measurement of bainite packet size and its influence on cleavage fracture in a medium carbon bainitic steel. *Materials Science & Engineering A* 530, 21–27.

- Rao, B. V. N., Rashid, M. S., 1983. Direct observations of deformation-induced retained austenite transformation in a vanadium-containing dual-phase steel. *Metallography* 16, 19–37.
- Rao, B. V. N., Thomas, G., 1979. Transmission electron microscopy characterization of dislocated lath martensite. In: *International Conference on Martensitic Transformations ICOMAT '79*. MIT Press, Boston, USA, pp. 12–21.
- Rao, B. V. N., Thomas, G., 1980. Structure-property relations and the design of Fe-4Cr-C base structural steels for high strength and toughness. *Metallurgical Transactions A* 11 (441–457).
- Rathbun, R. W., Matlock, D. K., Speer, J. G., 2003. Fatigue behavior of spot welded high-strength sheet steels. *Welding Journal* 82 (207–281).
- Rauch, G. C., Leslie, W. C., 1972. The extent and nature of the strength differential effect in steel. *Metallurgical Transactions* 3, 373–385.
- Ray, A., Paul, S. K., Jha, S., 1995. Effect of inclusions and microstructural characteristics on the mechanical properties and fracture behavior of a high-strength low-alloy steel. *Journal of Materials Engineering and Performance* 4, 679–688.
- Ray, R. K., Jonas, J. J., 1990. Transformation textures in steels. *International Materials Reviews* 35, 1–37.
- Rayment, T., Hoile, S., Grant, P. S., 2004. Phase transformations and control of residual stresses in thick spray-formed steel shells. *Metallurgical and Materials Transactions A* 35, 1113–1122.
- Reed, P. A. S., Thomson, R. C., James, J. S., Putman, D. C., Lee, K. K., Gunn, S. R., 2004. Modelling of microstructural effects in the fatigue of austempered ductile iron. *Materials Science & Engineering A* 346, 273–286.
- Rees, G. I., Bhadeshia, H. K. D. H., 1992. Bainite transformation kinetics, Part I, modified model. *Materials Science and Technology* 8, 985–993.
- Rees, G. I., Bhadeshia, H. K. D. H., 1994. Thermodynamics of acicular ferrite nucleation. *Materials Science and Technology* 10, 353–358.
- Rees, G. I., Perdrix, J., Maurickx, T., Bhadeshia, H. K. D. H., 1995. The effect of niobium in solid solution on the transformation kinetics of bainite. *Materials Science and Engineering A* 194, 179–186.
- Reisdorf, B. G., 1963. The tempering characteristics of some 0.4 pct carbon ultrahigh-strength steels. *TMS-AIME* 227, 1334–1341.
- Reisner, G., Fischer, F. D., Wen, Y. H., Werner, E. A., 1999. Interaction energy between martensitic variants. *Metallurgical & Materials Transactions A* 30, 2583–2590.
- Ren, X. C., Chu, W. Y., Su, Y. J., Qiao, L. J., 2008. Environment fracture susceptibility of high-strength bainitic low alloy steels containing silicon. In: *Evaluation, inspection and monitoring of structural integrity, Fracture Mechanics Symposium*. East China University Science and Technology Press, Shanghai, China, pp. 457–462.
- Ricks, R. A., Barritte, G. S., Howell, P. R., 1982a. The influence of second phase particles on diffusional phase transformations in steels. In: *Aaronson, H. I., Laughlin, D. E., Sekerka, M., Wayman, C. M. (Eds.), Solid→Solid Phase Transformations*. TMS-AIME, Warrendale, Pennsylvania, USA, pp. 463–468.
- Ricks, R. A., Barritte, G. S., Howell, P. R., 1982b. The nature of acicular ferrite in HSLA steel weld metals. *Journal of Material Science* 17, 732–740.
- Ricks, R. A., Howell, P. R., 1982. Bowing mechanism for interphase boundary migration in alloy steels. *Metal Science* 16, 317–322.
- Ridal, K. A., Quarrell, A. G., 1962. Effect of creep deformation upon carbide transformations in ferritic alloy steels. *Journal of the Iron and Steel Institute* 200, 366–373.
- Ridley, N., 1984. The pearlite reaction. In: *Marder, A. R., Goldstein, J. I. (Eds.), Phase Transformations in Ferrous Alloys*. TMS-AIME, Warrendale, Pennsylvania, USA, pp. 201–236.
- Ringer, S. R., Barbaro, F., Krauklis, P., Easterling, K. E., 1990. Coarsening phenomena in the microstructures of Ti microalloyed steels. In: *Microstructure control to achieve properties in modern steels*. Institute of Metals and Materials Australasia, Sydney, Australia, pp. 1–7.
- Rios, P. R., Honeycombe, R. W. K., 1992. Effect of niobium on decomposition of austenite in 0.2C-10Cr steel. *Materials Science and Technology* 8, 1057–1062.
- Ritchie, R. O., 1977a. Influence of impurity segregation on temper embrittlement and on slow fatigue crack growth and threshold behavior in 300M high strength steel. *Metallurgical Transactions A* 8, 1131.
- Ritchie, R. O., 1977b. Influence of microstructure on near-threshold fatigue crack propagation in ultra high strength steel. *Metal Science* 11, 368–381.
- Ritchie, R. O., 1979. Near threshold fatigue-crack propagation in steels. *International Metals Reviews* 4, 205–230.
- Ritchie, R. O., Cedeno, M. H. C., Zackay, V. F., Parker, E. R., 1978. Effect of silicon additions and retained austenite on stress corrosion cracking in ultrahigh strength steel. *Metallurgical Transactions A* 9, 35–40.
- Ritchie, R. O., Knott, J. F., Rice, J. R., 1973. Relationship between critical tensile stress and fracture toughness in mild steel. *Journal of Mechanics and Physics of Solids* 21, 395–410.
- Ritchie, R. O., Parker, E. R., Spencer, P. N., Todd, J. A., 1984. A new series of advanced 3CrMoNi steels for thick section pressure vessels in high temperature and pressure hydrogen service. *Journal of Materials for Energy Systems* 6, 151–162.

- Ritchie, R. O., Suresh, S., Moss, C. M., 1980. Near-threshold fatigue crack growth in 2.25Cr-1Mo pressure vessel steel in air and hydrogen. *Journal of Engineering Materials and Technology* 102, 293–299.
- Roberts, C. S., Averbach, B. L., Cohen, M., 1957. Mechanism and kinetics of the first stage of tempering. *Trans. A. S. M.*, 576–579.
- Robertson, J. M., 1929. The microstructure of rapidly cooled steel. *Journal of the Iron and Steel Institute* 119, 391–419.
- Robson, J. D., Bhadeshia, H. K. D. H., 1997a. Modelling precipitation sequences in power plant steels, Part 2: Application of kinetic theory. *Materials Science and Technology* 28A, 640–644.
- Robson, J. D., Bhadeshia, H. K. D. H., 1997b. Modelling precipitation sequences in power plant steels: Part I, kinetic theory. *Materials Science and Technology* 13, 631–639.
- Rodriguez-Ibabe, J. M., 1998. Role of microstructure in toughness behaviour of microalloyed steels. *Materials Science Forum* 284–286, 51–62.
- Rodríguez-Martínez, J. A., Pesci, R., Rusinek, A., Arias, A., Azera, R., Pedroche, D. A., 2010. Thermo-mechanical behaviour of TRIP 1000 steel sheets subjected to low velocity perforation by conical projectiles at different temperatures. *International Journal of Solids and Structures* 47, 1268–1284.
- Rönn, L., 1963. Niobis inverkan på TTT-diagrammet av ett mjukt stål.
- Ros-Yáñez, T., Houbart, Y., Mertens, A., 2001. Characterisation of TRIP-assisted multiphase steel surface topography by atomic force microscopy. *Materials Characterization* 47, 93–104.
- Rose, A. J., Mohammed, F., Smith, A. W. F., Davies, P. A., Clarke, R. D., 2014. Superbainite: laboratory concept to commercial product. *Materials Science and Technology* 30, 1094–1098.
- Rouns, T. N., Rundman, K. B., 1987. Constitution of austempered ductile iron and kinetics of austempering. *AFS Transactions* 95, 851–874.
- Rudberg, E., 1952. Avbildning i rymden av fria energien för ternära system. *Jernkontorets Annaler* 136, 91–112.
- Rundman, K. B., 1988. Quote, personal Communication.
- Rundman, K. B., Moore, D. J., Hayrynen, K. L., Dubensky, W. J., Rouns, T. N., 1988. Microstructure and mechanical properties of austempered ductile iron. *Journal of Heat Treating* 5, 79–95.
- Ruoff, R. S., 2006. Time, temperature, and load: the flaws of carbon nanotubes. *Proc. National Academy of Sciences of the USA* 103, 6779–6780.
- Russell, K. C., 1971. The role of quenched-in embryos in solid-state nucleation process. *Metallurgical Transactions* 2, 5–12.
- Ryu, H. B., Speer, J. G., Wise, J. P., 2002. Effect of thermomechanical processing on the retained austenite content in a Si-Mn TRIP steel. *Metallurgical & Materials Transactions A* 33, 2811–2816.
- Sachs, K., Ralph, B., Salter, J., 1980. Transformation kinetics of superhardening steel – the mechanism of superhardening. In: *Heat Treatment '79*. Metals Society, London, U.K., pp. 141–146.
- Sadagopan, S., Wong, C., Huang, M., Yan, B., Urban, D., 2003. Formability characterisation of new generation of high strength steels. Tech. Rep. TRP 0012, American Iron and Steel Institute, Pittsburgh, USA.
- Sadananda, K., Sreenivasan, R., 2001. Analysis of fatigue crack growth behavior in niobium-hydrogen alloys using the unified approach to fatigue damage. *International Journal of Fatigue* 23, 357–364.
- Sadovskii, V. D., 1956. The kinetics and structural mechanisms of phase transformations when heating steel. *Probl. Metalloverskie Term Obrab*, 31–52.
- Saeki, M., Kurosawa, F., Matsuo, M., 1986. Micro and state analysis as the basis for microalloying techniques. *Trans. ISIJ* 26, 1017–1035.
- Saha Podder, A., Bhadeshia, H. K. D. H., 2010. Thermal stability of austenite retained in bainitic steels. *Materials Science & Engineering A* 527, 2121–2128.
- Saha Podder, A., Bhattacharjee, D., Ray, R. K., 2007. Effect of martensite on the mechanical behavior of ferrite-bainite dual phase steels. *ISIJ International* 47, 1058–1064.
- Saha Podder, A., Lonardelli, I., Molinari, A., Bhadeshia, H. K. D. H., 2011. Thermal stability of retained austenite in bainitic steel: an *in situ* study. *Proceedings of the Royal Society A* 467, 3141–3156.
- Sahu, P., 2005. Bainite and stress-induced martensite in an AISI type 300 steel: an X-ray diffraction study of the microstructure by the Rietveld method. *Journal of Applied Crystallography* 38, 112–120.
- Saito, Y., Suwa, Y., Ochi, K., Aoki, T., Goto, K., Abe, K., 2002. Kinetics of phase separation in ternary alloys. *Journal of the Physical Society of Japan* 71, 808–812.
- Saito, Y., Tsuji, N., Utsunomiya, H., Sakai, T., Hong, R. G., 1998. Ultra-fine grained bulk aluminum produced by accumulative roll-bonding (ARB) process. *Scripta Materialia* 39, 1221–1227.
- Sakai, T., Sato, Y., Oguma, N., 2002. Characteristic S-N properties of high-carbon-chromium-bearing steel under axial loading in long-life fatigue. *Fatigue & Fracture of Engineering Materials & Structures* 25, 765–773.
- Sakano, M., Nimura, D., Matumoto, K., Isoda, A., Kondo, S., Arimochi, K., Konda, N., 2005. Improving fatigue strength of welded beams by using fatigue crack growth arresting steel. In: *Eurosteel Conference on Steel and Composite Structures*. Unknown, Maastricht, Netherlands, p. paper 425.
- Samajdar, I., Girault, E., Verlinden, B., Aernoudt, E., van Humbeeck, J., 1998. Transformations during intercritical annealing of a TRIP-assisted steel. *ISIJ International* 38, 998–1006.

- Sandvik, B. J. P., 1982a. The bainite reaction in Fe-Si-C alloys: the primary stage. *Metallurgical Transactions* 13A, 777–787.
- Sandvik, B. J. P., 1982b. The bainite reaction in Fe-Si-C alloys: The secondary stage. *Metallurgical & Materials Transactions A* 13A, 789–800.
- Sandvik, B. P. J., Nevalainen, H. P., 1981. Structure-property relationships in commercial low-alloy bainitic-austenitic steel with high strength, ductility, and toughness. *Metals Technology* 8, 213–220.
- Sandvik, B. P. J., Wayman, C. M., 1983. Lath martensite: Crystallographic and substructural features. *Metallurgical transactions A* 14, 809–822.
- Santofimia, M. J., Caballero, F. G., Capdevila, C., García-Mateo, C., de Andrés, C. G., 2006. Evaluation of displacive models for bainite transformation kinetics in steels. *Materials Transactions* 47 (1492–1500).
- Sarikaya, M., Tokushige, H., Thomas, G., 1986. Lath martensite and bainite in low alloy steels. In: *International Conference on Martensitic Transformations ICOMAT '86*. Japan Institute of Metals, Tokyo, Japan, pp. 613–618.
- Sato, M., Anderson, P. M., Rigney, D. A., 1993. Rolling-sliding behaviour of rail steels. *Wear* 162–164, 159–172.
- Sawley, K., Kristan, J., 2003. Development of bainitic rail steels with potential resistance to rolling contact fatigue. *Fatigue & Fracture of Engineering Materials & Structures* 26, 1019–1029.
- Sawley, K. J., Benyon, J. A., Jones, E. G., 1988. Bainitic steels for railway wheels. In: *9th International Wheelset Congress*. Quebec, Canada, pp. paper 2–6.
- Schaaber, O., 1955. Some observations on isothermal austenite transformation near the martensite start temperature. *Journal of Metals* 199, 559–560.
- Schanck, J. L., 1969. Isothermal transformation diagram for chromium-molybdenum alloy steels facilitate their heat treatment. *Industrial Heating* September, 1664.
- Schänzer, S., Nembach, E., 1992. The critical resolved shear stress of  $\gamma'$ -strengthened nickel-based superalloys with  $\gamma'$ -volume fractions between 0.07 and 0.47. *Acta Metallurgica et Materialia* 40, 803–813.
- Scheil, E., 1935. Anlaufzeit der austenitumwandlung. *Archiv für das Eisenhüttenwesen* 12, 565–567.
- Schissler, J. M., Arnould, J., Metauer, G., 1975. Etude de la décomposition de l'austénite post-bainitique d'alliages fer-carbone-silicium à 1%C-4%Si au cours d'un maintien isotherme à 420°C, influence d'une addition de 1% de manganèse. *Memoires Scientifiques Rev. Metallurg.* 72, 779–793.
- Schmatz, D. J., Zackay, V. F., 1959. Mechanical properties of deformed metastable austenitic UHS steel. *Trans. ASM* 51, 476–494.
- Schrader, A., Wever, F., 1952. Zur frage der eignung des elektronenmikroskops für die gefügeuntersuchung von stählen. *Archiv für das Eisenhüttenwesen* 23, 489–495.
- Scott, C. P., Drillet, J., 2007. A study of the carbon distribution in retained austenite. *Scripta Materialia* 56, 489–492.
- Scott, H. P., Williams, Q., Knittle, E., 2001. Stability and equation of state of cementite to 73 GPa: implications for carbon in the earth's core. *Geophysical Research Letters* 28, 1875–1878.
- Sears, G. W., Gatti, A., Fullman, R. L., 1954. Elastic properties of iron whiskers. *Acta Metallurgica* 2, 727–728.
- Secretary of State for Defence, Bhadeshia, H. K. D. H., Mateo, C., Brown, P., 2010. Bainite steel and methods of manufacture thereof. *Tech. Rep. GB2462197*, Intellectual Property Office, London, U.K.
- Segal, V. M., 1999. Equal channel angular extrusion: from macromechanics to structure formation. *Materials Science & Engineering A* 271, 322–333.
- Segal, V. M., 2002. Severe plastic deformation: simple shear versus pure shear. *Materials Science & Engineering A* 338, 331–334.
- Senior, B. A., 1998. The effects of retempering on the microstructure of ferritic steels. *Tech. Rep. TPRD/L/3220/R87*, Central Electricity Generating Board, Leatherhead, Surrey, U.K.
- Seo, S. W., Bhadeshia, H. K. D. H., Suh, D. W., 2015. Pearlite growth rate in Fe-C and Fe-Mn-C steels. *Materials Science and Technology* 31, 487–493.
- Shackleton, D. N., Kelly, P. M., 1965. Morphology of bainite. In: *Physical properties of martensite and bainite*, Special Report 93. Iron and Steel Institute, London, U.K., pp. 126–134.
- Shang, C., Wang, X. M., Yang, S. W., He, X. L., 2004. Refinement of packet size in low carbon bainitic steel by special thermo-mechanical control process. *Journal of the University of Science and Technology, Beijing* 11, 221–224.
- Shaposhnikov, N. G., Mogutnov, B. M., 2008. Paraequilibria in the Fe-Si-C system and their relation to the bainite transformation in steels. *Russian Metallurgy (Metally)* 2008, 174–179.
- Sharma, S., Sangal, S., Mondal, K., 2014. Reciprocating sliding wear behavior of newly developed bainitic steels. *Metallurgical & Materials Transactions A* 45, 5451–5468.
- Shea, M. M., Ryntz, E. F., 1986. Austempering nodular iron for optimum toughness. *Trans. American Foundrymen's Society* 94, 683–688.
- Shen, C., Wang, Y., 2003. Incorporation of  $\gamma$ -surface to phase field model of dislocations: simulating dislocation dissociation in fcc crystals. *Acta Materialia* 52, 683–691.

- Shendy, B. R., Yoozbashi, M. N., Avishan, B., Yazdani, S., 2014. An investigation on rotating bending fatigue behavior of nanostructured low-temperature bainitic steel. *Acta Metallurgica Sinica (English Letters)* 27, 233–238.
- Shepperson, S., Allen, C., 1987. The abrasive wear behaviour of austempered spheroidal cast irons. In: Ludema, K. C. (Ed.), *Wear of Materials*. ASME, San Antonio, Texas, USA, pp. 575–583.
- Sherif, M., Garcia-Mateo, C., Sourmail, T., Bhadeshia, H. K. D. H., 2004. Stability of retained austenite in TRIP-assisted steels. *Materials Science and Technology* 20, 319–322.
- Sherif, M. Y., 2005. Characterisation and development of nanostructured, ultrahigh strength, and ductile bainitic steels. Ph.D. thesis, University of Cambridge.
- Shewmon, P., 1976. Hydrogen attack in carbon steel. *Metallurgical Transactions A* 7, 279–222.
- Shi, W., Li, L., Cooman, B. C. D., Wollants, P., Yang, C. X., 2008. Thermal stability of retained austenite in TRIP steel after different treatments. *Journal of Iron and Steel Research International* 15, 61–64.
- Shi, W., Li, L., Yang, C. X., Fu, R. Y., Wang, L., Wollants, P., 2006. Strain-induced transformation of retained austenite in low-carbon low-silicon TRIP steel containing aluminum and vanadium. *Materials Science and Engineering A* 429, 247–251.
- Shieh, C. S., Din, T. A., Lui, T. S., Chen, L. H., 1993. Effect of nodule size & Si content on tensile deformation of austempered spheroidal graphite cast iron at elevated temperatures. *AFS Transactions* 133, 365–371.
- Shieh, C. S., Lui, T. S., Chen, L. H., 1995. Tensile characteristics of austempered ductile case iron in the temperature regime 300–693 K. *Materials Transactions, JIM* 36, 620–625.
- Shiga, C., Amano, K., Hatomura, T., Saito, Y., Hirose, K., Choji, T., 1983. Ferrite-fine bainite steel line pipe of X70 and X80 grades for low-temperature service. In: *Steels for Line Pipe and Pipeline Fittings*. Metals Society, London, U.K., pp. 127–135.
- Shih, C. H., Averbach, B. L., Cohen, M., 1955. Some characteristics of the isothermal martensitic transformation. *Journal of Metals* 203, 709–710.
- Shim, J. H., Oh, Y. J., Suh, J. Y., Cho, Y. W., Shim, J. D., Byun, J. S., Lee, D. N., 2000. Hot deformation and acicular ferrite microstructure in c-mn steel containing  $Ti_2O_3$  inclusions. *ISIJ International* 40, 819–823.
- Shim, J. H., Oh, Y. J., Suh, J. Y., Cho, Y. W., Shim, J. D., Byun, J. S., Lee, D. N., 2001. Ferrite nucleation potency of non-metallic inclusions in medium carbon steels. *Acta Materialia* 49, 2115–2122.
- Shimizu, K., Ko, T., Nishiyama, Z., 1964. Transmission electron microscope observation of the bainite of carbon steel. *Trans. JIM* 5, 223–228.
- Shipway, P. H., Bhadeshia, H. K. D. H., 1995. Mechanical stabilisation of bainite. *Materials Science and Technology* 11, 1116–1128.
- Shipway, P. H., Bhadeshia, H. K. D. H., 1997. Mechanical stabilisation of Widmanstätten ferrite. *Materials Science & Engineering A* 223, 179–186.
- Shirzadi, A. A., Abreu, H., Cayron, C., Ubhi, S., 2011. Combined effect of stress and strain on crystallographic orientation of bainite. *Ironmaking and Steelmaking* 38, 519–524.
- Shirzadi, A. A., Abreu, H., Pocock, L., Klobcar, D., Withers, P. J., Bhadeshia, H. K. D. H., 2009. Bainite orientation in plastically deformed austenite. *International Journal of Materials Research* 100, 40–45.
- Shively, J. H., Hehemann, R. F., Troiano, A. R., 1966. Hydrogen permeability in a stable austenitic stainless steel. *Corrosion* 22, 253–266.
- Sidhu, G., 2013. Modeling and characterization of high carbon nanobainitic steels. Ph.D. thesis, Ryerson University, Ontario, Canada.
- Sidhu, G., Bhole, S. D., Essadiqi, E., Chen, D. L., 2013. Characterization of isothermally heat-treated high carbon nanobainitic steels. *Journal of Materials Engineering and Performance* 22, 3070–3076.
- Sikka, V. K., Klueh, R. L., Maziasz, P. J., Babu, S., Santella, M., Paules, J. R., Jawad, M. H., Orie, K. E., 2004. High-strength Fe-3Cr-W (Mo) steel for petrochemical applications. In: *Proc. ASME/JSME Conf. on Pressure Vessel and Piping*. Vol. 476. ASME International, New York, USA, pp. 97–106.
- Simoneau, R., Bégin, G., Marquis, A. H., 1978. Progress of NbCN precipitation in HSLA steels as determined by electrical resistivity measurements. *Metal Science* 12, 381–386.
- Singh, S. B., Bhadeshia, H. K. D. H., 1996. Quantitative evidence for mechanical stabilisation of bainite. *Materials Science Forum* 12, 610–612.
- Singh, S. B., Bhadeshia, H. K. D. H., 1998a. Estimation of bainite plate-thickness in low-alloy steels. *Materials Science and Engineering A* 245, 72–79.
- Singh, S. B., Bhadeshia, H. K. D. H., 1998b. Topology of grain deformation. *Materials Science and Technology* 15, 832–834.
- Siriwardene, P. P. G. L., 1955. Metallography of low-carbon alloy steels. Ph.D. thesis, University of Cambridge, Cambridge, U. K.
- Sista, V., Nash, P., Sahay, S. S., 2007. Accelerated bainitic transformation during cyclic austempering. *Journal of Materials Science* 42, 9112–9115.
- Siwecki, T., Eliasson, J., Lagneborg, R., 2010. Vanadium microalloyed bainitic hot strip steels. *ISIJ International* 51, 760–767.

- Smaill, J. S., Keown, S. R., Erasmus, L. A., 1976. Effect of titanium additions on the strain-aging characteristics and mechanical properties of carbon-manganese reinforcing steels. *Metals Technology* 3, 194–201.
- Smanio, V., Sourmail, T., 2011. Effect of partial martensite transformation on bainite reaction kinetics in different 1% C steels. *Solid State Phenomena* 172-174, 821–826.
- Smith, E., 1966. Physical basis of yield and fracture. In: *Proceedings of Conf. on Physical Basis of Yield and Fracture*. Institute of Physics and Physical Society, Oxford, U. K., pp. 36–45.
- Smith, G. M., 1984. The microstructure and yielding behaviour of some Ti steels. Ph.D. thesis, University of Cambridge, Cambridge, U. K.
- Smith, G. V., Mehl, R. F., 1942. Lattice relationships in decomposition of austenite to pearlite bainite and martensite. *Trans. A.I.M.M.E.* 150, 211–226.
- Smith, J. F., Reynolds, J. H., Southworth, H. N., 1980. The role of Mn in the temper embrittlement of a 3.5Ni-Cr-Mo-V steel. *Acta Metallurgica* 28, 1555–1564.
- Smith, M. F., Speich, G. R., Cohen, M., 1959. Anomalous kinetics of the bainitic transformation just above the martensitic range. *Trans. Metall. Soc. AIME* 215, 528–530.
- Smith, R., Bowles, J. S., 1960. The crystallography of the cubic to orthorhombic transformation in the alloy AuCu. *Acta Metallurgica* 8, 405–415.
- Smyth, D., Lessard, R. G., Minden, F., 1990. *ASM Handbook: Irons, Steels, and High-Performance Alloys*. Vol. 1. ASM International, Ch. 25, pp. 327–336.
- Solana, F., Takamata, C., Bernstein, I. M., Thompson, A. W., 1987. Role of retained austenite in stress corrosion cracking of steels. *Metallurgical Transactions A* 18, 1023–1028.
- Solano-Alvarez, W., Bhadeshia, H. K. D. H., Solan 2014. White-etching matter in bearing steel: Part II: distinguishing cause and effect in bearing steel failure. *Metallurgical & Materials Transactions A* 45, 4916–4931.
- Soliman, M., Palkowski, H., 2007. Ultra-fine bainite structure in hypoeutectoid steels. *ISIJ International* 47, 1703–1710.
- Song, E. J., Bhadeshia, H. K. D. H., Suh, D. W., 2014. Interaction of aluminium with hydrogen in twinning-induced plasticity steel. *Scripta Materialia* 87, 9–12.
- Song, E. J., Suh, D. W., Bhadeshia, H. K. D. H., 2012. Oxidation of silicon containing steel. *Ironmaking and Steelmaking* 39, 599–604.
- Song, S. M., Kandaka, S., Sugimoto, K., Kobayashi, M., 1999. Impact properties of low-alloy trip steel sheets. In: Tanimoto, T., Morii, T. (Eds.), *6th International SAMPE Symposium*, Society for the Advancement of Material and Process Engineering, Covina, California, USA, pp. 333–336.
- Song, S. M., Sugimoto, K., Kandaka, S., Gutamura, A., Kobayashi, M., Masuda, S., 2003. Effects of prestraining on high-cycle fatigue strength of high-strength low alloy TRIP-aided steels. *Materials Science Research International* 9, 223–229.
- Song, W., Pahl, U., Bleck, W., Mukherjee, K., 2011. Phase field simulations of bainitic phase transformations in 100Cr6. In: *Materials fabrication, properties, characterisation and modelling*. J. Wiley & Sons, New Jersey, USA, pp. 417–425.
- Song, W., von Appen, J., Coi, P., Dronskowski, R., Raable, D., Bleck, W., 2013. Atomic-scale investigation of  $\epsilon$  and  $\theta$  precipitates in bainite in 100Cr6 bearing steel by atom probe tomography and ab initio calculations. *Acta Materialia* 61, 7582–7590.
- Sourmail, T., Caballero, F. G., Garcia-Mateo, C., Smanio, V., Ziegler, C., Kuntz, M., Elvira, R., Leiro, A., Vuorinen, E., Teeri, T., 2013. Evaluation of potential of high Si high C steel nanostructured bainite for wear and fatigue applications. *Materials Science and Technology* 29, 1166–1173.
- Speer, J., Matlock, D. K., Cooman, B. C. D., Schroth, J. G., 2003. Carbon partitioning into austenite after martensite transformation. *Acta Materialia* 51, 2611–2622.
- Speer, J. G., de Moor, E., Clarke, A. J., 2015. Critical assessment 7: Quenching and partitioning. *Materials Science and Technology* 31, 3–9.
- Speer, J. G., Edmonds, D. V., Rizzo, F. C., Matlock, D. K., 2004. Partitioning of carbon from supersaturated plates of ferrite, with application to steel processing and fundamentals of the bainite transformation. *Current Opinion in Solid State and Materials Science* 8, 219–237.
- Speich, G. R., 1962. Growth kinetics of bainite in 3% Cr steel. In: Zackay, V. F., Aaronson, H. I. (Eds.), *Decomposition of Austenite by Diffusional Processes*. Interscience, New York, USA, pp. 353–386.
- Speich, G. R., 1969. Tempering of low-carbon martensite. *Trans. Met. Soc. AIME* 245, 2553–2564.
- Speich, G. R., 1987. Secondary hardening in ultrahigh-strength steels. In: G. B. Olson, M. Azrin, E. S. W. (Ed.), *Innovations in ultrahigh-strength steel technology*. US Army Materials Technology Laboratory, Massachusetts, USA, pp. 89–112.
- Speich, G. R., Cohen, M., 1960. The growth rate of bainite. *TMS-AIME* 218, 1050–1059.
- Speich, G. R., Cuddy, L. J., Gordon, C. R., DeArdo, A. J., 1984. Formation of ferrite from control-rolled austenite. In: Marder, A. R., Goldstein, J. I. (Eds.), *Phase Transformations in Ferrous Alloys*. TMS-AIME, Warrendale, Pennsylvania, USA, pp. 341–389.

- Speich, G. R., Warlimont, H., 1968. Yield strength and transformation substructure of low carbon martensite. *J. Iron and Steel Institute* 206, 385–392.
- Spencer, P. N., Dauskardt, R. H., Parker, E. R., Ritchie, R. O., 1989. Fracture toughness, fatigue crack propagation and creep rupture behaviour in thick section weldments of 3CrMo pressure vessels. *High Temperature Technology* 7, 17–26.
- Spiefeld, J., 1999. Marforming and martempering of a Cu Zn Al shape memory alloy. *Materials Science & Engineering A* 273-275, 639–643.
- Srinivasan, G. R., Wayman, C. M., 1968a. The crystallography of the bainite transformation. *Acta Metallurgica* 16, 621–636.
- Srinivasan, G. R., Wayman, C. M., 1968b. Isothermal transformation in an Fe-7.9Cr-1.1C alloy. *Trans. Met. Soc. AIME* 242, 78–81.
- Srinivasan, G. R., Wayman, C. M., 1968c. TEM study of the bainite transformation in Fe-Cr-C alloys. *Acta Metallurgica* 16, 609–620.
- Stalheim, D., 2005. The use of high temperature processing (HTP) for high strength oil and gas transmission pipeline applications. In: *Proceedings of the 5th HSLA Steels Conference, Iron and Steel Supplement. Vol. 40.* pp. 699–704.
- Stark, I., Smith, G. D. W., 1987. A FIM/atom probe study of phase transformations in Mo steels. *J. de Physique IV C48*, 447–452.
- Stark, I., Smith, G. D. W., Bhadeshia, H. K. D. H., 1988. The element distribution associated with the incomplete reaction phenomenon in steels: an atom probe study. In: Lorimer, G. E. (Ed.), *Phase Transformations '87.* Institute of Metals, London, U.K., pp. 211–215.
- Stark, I., Smith, G. D. W., Bhadeshia, H. K. D. H., 1990. Distribution of substitutional alloying elements during the bainite transformation. *Metallurgical Transactions A* 21, 837–844.
- Steven, W., Haynes, A. G., 1956. The temperature of formation of martensite and bainite in low alloy steels. *Journal of the Iron and Steel Institute* 183, 349–359.
- Stewart, J. W., Thomson, R. C., Bhadeshia, H. K. D. H., 1994. Cementite precipitation during tempering of martensite under the influence of an externally applied stress. *Journal of Materials Science* 29, 6079–6084.
- Stickels, C. A., 1974. Carbide refining heat treatment for 52100 bearing steels. *Metallurgical Transactions* 5, 865–874.
- Stickels, C. A., 1984. Rolling contact fatigue tests of 52100 bearing steel using a modified NASA ball test rig. *Wear* 199-210.
- Stokes, B., Gao, N., Lee, K. K., Reed, P. A. S., 2005. Effects of carbides on fatigue characteristics of austempered ductile iron. *Metallurgical & Materials Transactions A* 36, 977–988.
- Stone, H. J., Peet, M. J., Bhadeshia, H. K. D. H., Withers, P. J., Babu, S. S., Specht, E. D., 2008. Synchrotron X-ray studies of austenite and bainitic ferrite. *Proceedings of the Royal Society A* 464, 1009–1027.
- Strang, A., Beech, S. M., Gooch, D. J., 1994. Remanent life evaluation of 1crmov steam turbine rotors. In: Coutsouradis, D. (Ed.), *Materials for Advanced Power Engineering.* pp. 549–560.
- Strang, A., Vodarek, V., Bhadeshia, H. K. D. H., 1999. Modelling of microstructural development in creep resistant 12Cr power plant steels. In: Strang, A., McLean, M. (Eds.), *Modelling of Microstructural Evolution in Creep Resistant Materials.* Institute of Materials, London, U.K., pp. 129–150.
- Strangwood, M., Bhadeshia, H. K. D. H., 1987. Mechanism of acicular ferrite formation in alloy steel weld depos. In: David, S. A. (Ed.), *Advances in Welding Technology and Science.* ASM International, Materials Park, Ohio, USA, pp. 209–213.
- Strangwood, M., Bhadeshia, H. K. D. H., 1988. Nucleation of ferrite at ceramic/steel interfaces. In: Lorimer, G. W. (Ed.), *Phase Transformations '87.* Institute of Metals, London, U.K., pp. 471–474.
- Streicher, A. M., Speer, J. G., Matlock, D. K., 2002. Forming response of retained austenite in a C-Si-Mn high strength TRIP sheet steel. *Steel Research* 73, 287–293.
- Streicher-Clarke, A. M., Speer, J. G., Matlock, D. K., de Cooman, B. C., Williamson, D. L., 2005. Analysis of lattice parameter changes following deformation of a 0.19C-1.63Si-1.59Mn transformation- induced plasticity sheet steel. *Metallurgical & Materials Transactions A* 36, 907–918.
- Strife, J. R., Carr, M. J., Ansell, G. S., 1977. Effect of austenite prestrain above the  $M_d$  temperature on the  $M_s$  temperature in Fe-Ni-Cr-C alloys. *Metallurgical Transactions A* 8A, 1471–1484.
- Su, T. J., Aeby-Gautier, E., Denis, S., 2006. Morphology changes in bainite formed under stress. *Scripta Materialia* 54, 2185–2189.
- Sudo, M., Higashi, M., Hori, H., Iwai, T., Kame, S., Shibata, Z., 1981. Effects of microstructures on the mechanical properties of multiphase sheet steels. *Trans. Iron Steel Institute of Japan* 21, 820–827.
- Sudo, M., Iwai, T., 1983. Deformation behaviour and mechanical properties of ferrite-bainite-martensite (triphase) steel. *Trans. ISIJ* 23, 294–302.
- Sudo, M., Tsukatani, I., Shibata, Z., 1982. Effect of microstructure on the plastic anisotropy and mechanical properties of triphase sheet steel. In: *Metallurgy of Continuous Annealed Sheet Steel.* AIME, USA, pp. 310–319.

- Sugden, A. A. B., Bhadeshia, H. K. D. H., 1989. Lower acicular ferrite. *Metallurgical Transactions A* 20, 1811–1818.
- Sugimoto, K., Iida, T., Sakaguchi, J., Kashima, T., 2000. Retained austenite characteristics and tensile properties in a TRIP type bainitic sheet steel. *ISIJ International* 40, 902–908.
- Sugimoto, K., Kikuchi, R., Tsunezawa, M., Hashimoto, S., Kashima, T., Ikeda, S., 2003. Stretch-flangeability and bendability of HSLA TRIP-aided sheet steels with annealed martensitic matrix. *Tetsu-to-Hagané* 89, 1065–1070.
- Sugimoto, K., Kobayashi, M., Hashimoto, S., 1992a. Ductility and strain-induced transformation in a high-strength TRIP aided dual phase steel. *Metallurgical Transactions A* 23A, 3085–3091.
- Sugimoto, K., Kobayashi, M., Matsushima, H., Hashimoto, S., 1995. X-ray residual stress and strain-induced transformation of retained austenite in TRIP-aided dual-phase steels. *Transactions of the Japan Society of Mechanical Engineers* 61, 80–86.
- Sugimoto, K., Kobayashi, M., Nagasaka, A., Hashimoto, S., 2002a. Warm stretch-formability of TRIP aided dual-phase sheet steels. *ISIJ International*, 1407–1414.
- Sugimoto, K., Misu, M., Kobayashi, M., Shirasawa, H., 1993. Effect of second phase morphology on retained austenite morphology and tensile properties in a TRIP aided dual phase steel sheet. *ISIJ International* 33, 775–782.
- Sugimoto, K., Tsunezawa, M., Hojo, T., Ikeda, S., 2004. Ductility of 0.1-0.6C-1.5Si-1.5Mn ultra high-strength TRIP-aided sheet steels with bainitic ferrite matrix. *ISIJ International* 44, 1608–1614.
- Sugimoto, K., Usui, N., Kobayashi, M., Hashimoto, S., 1992b. Effects of volume fraction and stability of retained austenite on ductility of TRIP-aided dual-phase steels. *ISIJ International* 32, 1311–1318.
- Sugimoto, K. I., Kanada, A., Kikuchi, R., Hashimoto, S. I., Kashima, T., Ikeda, S., 2002b. Ductility and formability of newly developed high strength low alloy TRIP-aided sheet steels with annealed martensite matrix. *ISIJ International* 42, 910–915.
- Sugimoto, K. I., Nakano, K., Song, S. M., Kashima, T., 2002c. Retained austenite characteristics and stretch-flangeability of high-strength low-alloy TRIP type bainitic sheet steels. *ISIJ International* 42, 450–455.
- Sugimoto, K. K., Muramatsu, T., Hojo, T., Hashimoto, S., Mukai, Y., 2005. Ultra high strength C Si Mn Nb Mo TRIP-aided sheet steels. In: Fekete, J. R., Pradhan, R. (Eds.), *Materials Science and Technology 2005*. pp. 15–24.
- Suh, D. W., Oh, C. S., Han, H. N., Kim, S. J., 2007a. Dilatometric analysis of austenite decomposition considering the effect of non-isotropic volume change. *Acta Materialia* 55, 2659–2669.
- Suh, D. W., Park, S. J., Oh, C. S., Kim, S. J., 2007b. Influence of partial replacement of Si by Al on the change of phase fraction during heat treatment of TRIP steels. *Scripta Materialia* 57, 1097–1100.
- Sun, W. P., Militzer, M., Bai, D. Q., Jonas, J. J., 1993. Measurement and modelling of the effects of precipitation on recrystallization under multipass deformation conditions. *Acta Metallurgica et Materialia* 41, 3595–3604.
- Sun, X., Soulam, A., Choi, K. S., Guzman, O., Chen, W., 2012. Effects of sample geometry and loading rate on tensile ductility of TRIP800 steel. *Materials Science & Engineering A* 541, 1–7.
- Suresh, S., Zamiski, G. F., Ritchie, R. O., 1981. Oxide-induced crack closure: an explanation for near-threshold corrosion fatigue crack growth behavior. *Metallurgical Transactions A* 12, 1435–1443.
- Suzuki, T., Ono, Y., Miyamoto, G., Furuhashi, T., 2010. Effects of Si and Cr on bainite microstructure of medium carbon steels. *ISIJ International* 50, 1476–1482.
- Svensson, L.-E., 2007. Microstructure and properties of high strength weld metals. *Materials Science Forum* 539-543, 3937–3942.
- Swahn, H., Becker, P. C., Vingsbo, O., 1976. Electron-microscope studies of carbide decay during contact fatigue in ball bearings. *Metal Science* 10, 35–39.
- Swallow, E., Bhadeshia, H. K. D. H., 1996. High resolution observations of displacements caused by bainitic transformation. *Materials Science and Technology* 12, 121–125.
- Takahashi, M., 2004. Recent progress: kinetics of the bainite transformation in steels. *Current Opinion in Solid State and Materials Science* 8, 213–217.
- Takahashi, M., Bhadeshia, H. K. D. H., 1989. Interpretation of dilatometric data for transformations in steels. *Journal of Materials Science Letters* 8, 477–478.
- Takahashi, M., Bhadeshia, H. K. D. H., 1990. Model for transition from upper to lower bainite. *Materials Science and Technology* 6, 592–603.
- Takahashi, M., Bhadeshia, H. K. D. H., 1991. A model for the microstructure of some advanced bainitic steels. *Materials Transactions JIM* 32, 689–696.
- Takahashi, T., Abe, T., Tada, S., 1996. Effect of bainite transformation and retained austenite on mechanical properties of austempered spheroidal graphite cast steel. *Metallurgical & Materials Transactions A* 27, 1589–1598.
- Takaki, S., 2003. Limit of dislocation density and ultra-grain-refining on severe deformation in iron. *Materials Science Forum* 426-432, 215–222.

- Takeuchi, I., Fujino, J., Yamamoto, A., Okaguchi, S., 2003. The prospects for high-grade steel pipes for gas pipelines. *Pipes and Pipelines International* 48, 33–43.
- Talas, S., 2006. Microstructural characterization of SiC added structural steel. *Kovove Materialy* 44, 169–173.
- Tamehiro, H., Habu, R., Yamada, N., Matsuda, H., Nagumo, M., 1985a. Properties of large diameter line pipe steel produced by accelerated cooling after controlled rolling. In: Southwick, P. D. (Ed.), *Accelerated Cooling of Steel*. TMS-AIME, Warrendale, Pennsylvania, USA, pp. 401–414.
- Tamehiro, H., Habu, R., Yamada, N., Matsuda, H., Nagumo, M., 1985b. Properties of large diameter line pipe steel produced by accelerated cooling after controlled rolling. In: Southwick, P. D. (Ed.), *Accelerated Cooling of Steel*. pp. 401–414.
- Tamehiro, H., Murata, M., Habu, R., Nagumo, M., 1987a. Optimum chemical composition and thermomechanical processing condition for niobium-boron steel. *Trans. ISIJ* 27, 130–138.
- Tamehiro, H., Murata, M., Habu, R., Nagumo, M., 1987b. Optimum microalloying of niobium and boron in hsla steel for thermomechanical processing. *Trans. ISIJ* 27, 120–129.
- Tamehiro, H., Nishioka, K., Murata, M., Habu, R., Kawada, Y., 1987c. Properties of high toughness X80 line pipe steels. In: *Int. Symposium on Accelerated Cooling of Rolled Steel*. Canadian Institute of Metals, Winnipeg, Canada, pp. 1–8.
- Tamehiro, H., Takeda, T., Matsuda, S., Yamamoto, K., Okumura, N., 1985c. Effect of accelerated cooling after controlled rolling on hydrogen induced cracking resistance of line pipe steel. *Trans. ISIJ* 25, 982–988.
- Tamukai, S., Onoe, Y., Nakajima, H., Umeno, M., Iwanaga, K., Sasaji, S., 1981. Production of extremely low carbon equivalent HT-50. *Tetsu-to-Hagane* 67, S1334.
- Tamura, I., Maki, T., Hoto, H., Tomota, Y., Okada, M., 1970. Strength and ductility of austenitic iron alloys accompanying strain-induced martensitic transformation. In: *2nd Int. Conf. on Strength of Metals and Alloys*. Vol. 3. ASM, Ohio, U. S. A., pp. 894–899.
- Tamura, I., Wayman, C. M., 1992. Martensitic transformations and mechanical effects. In: *Martensite*. ASM International, Metals Park, Ohio, USA, pp. 228–242.
- Tanaka, T., 1981. Controlled rolling of steel plate and strip. *International Metals Reviews* 4, 185–212.
- Tanaka, T., 1988. Overview of accelerated cooled steel plate. In: Ruddle, G. E., Crawley, A. F. (Eds.), *Accelerated Cooling of Rolled Steel*. Pergamon Press, Oxford, U. K., pp. 187–208.
- Tang, Z., Ding, L. D., Li, L., 2007. Microstructures and mechanical properties of Si-Al-Mn TRIP steel with niobium. *Journal of Materials Science and Technology* 23, 790–794.
- Taniguchi, S., Yamamoto, K., Megumi, D., Shibata, T., 2001. Characteristics of scale/substrate interface area of Si-containing low-carbon steels at high temperatures. *Materials Science & Engineering A* 308, 250–257.
- Taran, Y. N., Uzlov, K. I., Kutsov, A. Y., 1997. Bainite reaction kinetics in austempered ductile iron. *Journal de Physique IV (Colloque)* 7, C5–429–434.
- Tartaglia, J. M., Lazzari, K. A., Hui, G. P., Hayrynen, K. L., 2008. A comparison of mechanical properties and hydrogen embrittlement resistance of austempered vs quenched and tempered 4340 steel. *Metallurgical & Materials Transactions A* 39, 559–576.
- Tau, L., Chan, S. L. I., Shin, C. S., 1996. Hydrogen enhanced fatigue crack propagation of bainitic and tempered martensitic steels. *Corrosion Science* 38, 2049–2060.
- Taylor, K. A., Olson, G. B., Cohen, M., Vander Sande, J., 1989a. Carbide precipitation during stage 1 tempering of FeNiC martensite. *Metallurgical Transactions A* 20, 2717–2736.
- Taylor, K. A., Olson, G. B., Cohen, M., Vander Sande, J., 1989b. Spinodal decomposition during aging of FeNiC martensites. *Metallurgical Transactions A* 20, 2749–2765.
- Tenuta Azevedo, A. L., Galvao da Silva, E., 1978. Mossbauer study of retained austenite in a low C low alloy steel. *Scripta Metallurgica* 12, 113–117.
- Terada, Y., Chijiwa, R., Tamehiro, H., Kikuma, T., Funato, K., 1990. High-strength structural steel plate with low yield ratio and good weldability. In: *First International Conference on New Manufacturing Technology*. Chiba, Japan, pp. 1–6.
- Thewlis, G., 1989a. Pipeline welds – effect of pipe material and consumables composition. *Joining and Materials* 2, 25–31.
- Thewlis, G., 1989b. Pipeline welds – effect of pipe material and consumables composition. *Joining and Materials* 2, 125–129.
- Thewlis, G., 1990. Transformation kinetics of submerged arc weld metal. *Tech. Rep. IXJ 165 90*, 1–11, British Steel Corporation.
- Thewlis, G., 2006. Effect of cerium sulphide particle dispersions on acicular ferrite microstructure development in steels. *Materials Science and Technology* 22, 153–166.
- Thewlis, G., Whiteman, J. A., Senogles, D. J., 1997. Dynamics of austenite to ferrite phase transformation in ferrous weld metals. *Materials Science and Technology* 13, 257–274.
- Thielen, P. N., Fine, M. E., Fournelle, R. A., 1976. Cyclic stress strain relations and strain controlled fatigue of 4140 steel. *Acta Metallurgica* 24, 1–10.

- Thomas, G., Schmatz, D., Gerberich, W., 1965. Structure and strength of some ausformed steels. In: Zackay, V. F. (Ed.), *High Strength Materials*. John Wiley & Sons, Inc., New York, USA, pp. 251–326.
- Thomas, M. H., Michal, G. M., 1981. The influence of niobium and Nb(C,N) precipitation on the formation of proeutectoid ferrite in low alloy steels. In: Aaronson, H. I., Laughlin, D. E., Sekerka, R. F., Wayman, C. M. (Eds.), *Proceedings of an international conference on solid-solid phase transformation*. TMS-AIME, pp. 469–473.
- Thompson, M. W., 1969. *Defects and Radiation Damage in Metals*. Cambridge University Press, Cambridge, U. K.
- Thompson, S. W., Colvin, D. J., Krauss, G., 1988. On the bainitic structure formed in a modified A710 steel. *Scripta Metallurgica* 22, 1069–1074.
- Thomson, R. C., Bhadeshia, H. K. D. H., 1994a. Changes in chemical composition of carbides in 2.25Cr-1Mo power plant steel: part 1. *Materials Science and Technology* 10, 193–204.
- Thomson, R. C., Bhadeshia, H. K. D. H., 1994b. Changes in chemical composition of carbides in 2.25Cr-1Mo power plant steel: part 2. *Materials Science and Technology* 10, 205–208.
- Thomson, R. C., James, J. S., Putman, D. C., 2000. Modelling microstructural evolution and mechanical properties of austempered ductile iron. *Materials Science and Technology* 16, 1412–1419.
- Thomson, R. C., Miller, M. K., 1995. Partitioning of substitutional solute elements during the tempering of martensite in Cr and Mo containing steels. *Applied Surface Science* 87–88, 185–193.
- Timokhina, I., Beladi, H., Xiong, X. Y., Adachi, Y., Hodgson, P., 2011a. Application of advanced experimental techniques for the microstructural characterization of nanobainitic steels. *Solid State Phenomena* 172–174, 1249–1254.
- Timokhina, I. B., Beladi, H., Xiong, X. Y., Adachi, Y., Hodgson, P. D., 2011b. Nanoscale microstructural characterization of a nanobainitic steel. *Acta Materialia* 59, 5511–5522.
- Timokhina, I. B., Beladi, H., Xiong, X. Y., Pereloma, E. V., Hodgson, P. D., 2010a. Nano-scale analysis of nano-bainite formed in advanced high strength steels. *Materials Science Forum* 654–656, 102–105.
- Timokhina, I. B., Hodgson, P. D., Pereloma, E. V., 2003. Effect of deformation on the microstructure and properties of TRIP steel. *Metallurgical & Materials Transactions A* 34, 1599–1609.
- Timokhina, I. B., Hodgson, P. D., Pereloma, E. V., 2004. Effect of microstructure on the stability of retained austenite in TRIP steels. *Metallurgical and Materials Transactions A* 35, 2331–2340.
- Timokhina, I. B., Pereloma, E. V., Ringer, S. P., Zheng, R. K., Hodgson, P. D., 2010b. Characterization of the bake-hardening behavior of transformation induced plasticity and dual-phase steels using advanced analytical techniques. *ISIJ International* 50, 574–582.
- Tkalec, I., Mari, D., 2004. Internal friction in martensitic, ferritic and bainitic steel: cold work effects. *Materials Science & Engineering A* 370, 213–217.
- Tom, T., 1973. Lawrence Berkeley Laboratory Report 1856. Ph.D. thesis, University of California, Berkeley, Berkeley, Germany.
- Tomita, Y., 1987. Improved lower temperature fracture toughness of ultrahigh strength 4340 steel through modified heat treatment. *Metallurgical Transactions A* 18, 1495–1501.
- Tomita, Y., 1988. Effect of microstructure on plane strain fracture toughness of AISI 4340 steel. *Metallurgical Transactions A* 19, 2513–2521.
- Tomita, Y., 1991. Development of fracture toughness of ultrahigh strength low alloy steels for aircraft and aerospace applications. *Materials Science and Technology* 7, 481–489.
- Tomita, Y., 2000. Development of fracture toughness of ultrahigh strength, medium carbon, low alloy steels for aerospace applications. *International Materials Reviews* 45, 27–37.
- Tomita, Y., Okabayshi, K., 1983a. Heat treatment for improvement in lower temperature mechanical properties of 0.4% C Cr Mo ultrahigh strength steel. *Metallurgical Transactions A* 14, 2387–2393.
- Tomita, Y., Okabayshi, K., 1983b. Improvement in lower temperature mechanical properties of 0.40 C-Ni-Cr-Mo ultrahigh strength steel with 2nd phase. *Metallurgical Transactions A* 14, 485–492.
- Tomita, Y., Okabayshi, K., 1985a. Mechanical properties of 0.4C Ni Cr Mo high strength steel having a mixed structure of martensite and bainite. *Metallurgical Transactions A* 16, 73–82.
- Tomita, Y., Okabayshi, K., 1985b. Modified heat treatment for lower temperature improvement of the mechanical properties of two ultrahigh strength low alloy steels. *Metallurgical Transactions A* 16, 83–91.
- Tomota, Y., Kuroki, K., Mori, T., Tamura, I., 1976. Tensile deformation of two ductile phase alloys: flow curves of  $\alpha/\gamma$  Fe-Cr-Ni alloys. *Materials Science and Engineering* 24, 85–94.
- Tomota, Y., Tokuda, H., Adachi, Y., Wakita, M., Minakawa, N., Moriai, A., Morii, Y., 2004. Tensile behavior of TRIP-aided multi-phase steels studied by in situ neutron diffraction. *Acta Materialia* 52, 5737–5745.
- Traint, S., Pichler, A., Hauenberger, K., Stiaszny, P., Werner, E., 2002. Influence of silicon, aluminium, phosphorus and copper on the phase transformations of low alloyed TRIP-steels. *Steel Research* 73, 259–266.
- Trivedi, R., 1970. Role of interfacial free energy and interface kinetics during the growth of precipitate plates and needles. *Metallurgical Transactions* 1, 921–927.

- Troiano, A. R., 1960. Role of H and other interstitials in the mechanical behaviour of metals. *Trans. ASM* 52, 54–80.
- Troiano, A. R., Klinger, L. J., 1952. Limitations of the end-quench hardenability test. *Trans. A. S. M.* 44, 775–801.
- Troiano, A. T., Greninger, A. B., 1946. The martensite transformation. *Metal Progress* 50, 303–307.
- Tsai, M. C., S. Chiou, C., Du, J. S., Yang, J. R., 2002. Phase transformations in AISI 410 stainless steel. *Materials Science & Engineering A* A332, 1–10.
- Tsai, M. C., Yang, J. R., 2003. Microstructural degeneration of simulated heat-affected zone in modified 2.25Cr1Mo steel during high temperature exposure. *Journal of Materials Science* 38, 2373–2391.
- Tsay, L. W., Lin, Z. W., 1998. Effect of laser beam radiation on fatigue crack propagation in AISI 4150 steel. *Fatigue and Fracture in Engineering Materials and Structures* 21, 1549–1558.
- Tsvinsky, S. V., Kogan, L. I., Entin, R. I., 1955. *Problems of Metallography and the Physics of Metals*. State Scientific Press, ed. B. Ya Lyubov, Moscow, Russia, pp. 185–199.
- Tsubakino, H., Harada, H., 1997. Effect of retained austenite on the hydrogen permeation behavior in high strength steels. *Tetsu-to-Hagané* 83, 587–592.
- Tsuchida, N., Tomota, Y., 2000. A micromechanic modeling for transformation induced plasticity in steels. *Materials Science & Engineering A* 285, 345–352.
- Tsujii, N., Ayada, M., Takashima, T., Saito, Y., 1999a. Ausformed bainite in SUP7 spring steel. *Tetsu-to-Hagané* 85, 419–426.
- Tsujii, N., Saito, Y., Utsunomiya, H., Tanigawa, S., 1999b. Ultra-fine grained bulk steel produced by accumulative roll-bonding (ARB) process. *Scripta Materialia* 40, 795–800.
- Tsukatani, I., Hashimoto, S., Inoue, T., 1991. Effects of Si & Mn addition on mech. properties of high strength of rolled sheet steel containing retained austenite. *ISIJ International* 31, 992–1000.
- Tsunekage, N., Kobayashi, K., Tsubakino, H., 2001. Influence of sulphur and vanadium additions on toughness of bainitic steels. *Materials Science and Technology* 17, 847–855.
- Tsutsumi, M., Kato, H., Koseki, T., 2005. Investigation of factors affecting ferrite transformation from steel-oxide interface. In: David, S. A., DebRoy, T., Lippold, J. C., Smartt, H. B., Vitek, J. M. (Eds.), *Trends in Welding Research*. ASM International, Materials Park, Ohio, USA, pp. 987–992.
- Tsuya, K., 1956. On the characteristics of the bainite transformation. *Journal of the Mechanical Laboratory of Japan* 2, 20–27.
- Tsuzaki, K., Fukasaku, S., Tomota, Y., Maki, T., 1991a. Effect of prior deformation of austenite on the gamma-epsilon martensitic transformation in Fe-Mn alloys. *Trans. JIM* 32, 222–228.
- Tsuzaki, K., Nakao, C., Maki, T., 1991b. Formation temperature of bainitic ferrite in Si-containing steels. *Materials Transactions, JIM* 32, 658–666.
- Tsuzaki, K., Ueda, T., Fujiwara, K., Maki, T., 1989. Increase in retained austenite by ausforming in an austempered silicon steel. In: *New Materials and Processes for the Future*. Society for Advancement of Material and Process Engineering, California, USA, pp. 799–804.
- Tsuzaki, K., Yamaguchi, K., Maki, T., Tamura, I., 1988.  $\alpha \rightarrow \gamma$  transformation behaviour during heating from the  $\alpha + \gamma$  region in 0.18% C steel. *Journal of the Japan Institute of Metals* 74, 1430–1437.
- Tszeng, T. C., 2000. Autocatalysis in bainite transformations. *Materials Science & Engineering A* 293, 185–190.
- Tumuluru, M. D., 2006. Resistance spot welding of coated high-strength dual-phase steels. *Welding Journal* 85, 31–37.
- Tung, D. J., Lolla, T., Babu, S. S., Cola Jr., G. M., 2013. Flash processing produces unique combination of properties in steels. *Advanced Materials and Processes* 171, 48–50.
- Turnbull, D., 1981. Metastable structures in metallurgy. *Metallurgical Transactions A* 12, 695–708.
- Tweed, J. H., Knott, J. F., 1983. Effect of reheating on microstructure and toughness of C-Mn weld metal. *Metal Science* 17, 45–54.
- Ueda, S., Ishikawa, M., Ohashi, N., 1980. Enhanced nucleation of polygonal ferrite grain in interior of austenite grain in boron bearing steel. In: Banerji, S. K., Morral, J. E. (Eds.), *Boron in steel*. TMS-AIME, Warrendale, Pennsylvania, USA, pp. 181–198.
- Ueda, Y., Takita, M., 1986. Impact strength and isothermal transformation diagram of ADI. In: *Austempered Ductile Iron: Means to Improved Performance, Productivity and Cost*. ASME, New York, USA, pp. 141–147.
- Ueshima, Y., 1989. Effect of oxide inclusions on MnS precipitation in low-C steel. *Tetsu-to-Hagané* 75, 501–508.
- Uhm, S., Moon, J., Lee, C., Yoon, J., Lee, B., 2005. Bainitic transformation model in low alloy carbon steels considering the effect of reaction constant in JMA equation. *Materials Science Forum* 475–479, 3157–3160.
- Umemoto, M., Bando, S., Tamura, I., 1986a. Morphology and transformation kinetics of bainite in Fe-Ni-C and Fe-Ni-Cr-C alloys. In: *International Conference on Martensitic Transformations ICOMAT '86*. Japan Institute of Metals, Tokyo, Japan, pp. 595–600.
- Umemoto, M., Furuhashi, T., Tamura, I., 1986b. Effects of austenitising temperature on the kinetics of the bainite reaction at constant austenite grain size in Fe-C and Fe-Ni-C. *Acta Metallurgica* 34, 2235–2245.

- Umemoto, M., Horiuchi, K., Tamura, I., 1982. Transformation kinetics of bainite during isothermal holding and continuous cooling. *Trans. Iron Steel Institute of Japan* 22, 854–861.
- Umemoto, M., Komatsubara, N., Tamura, I., 1980. Prediction of hardenability effects from isothermal transformation kinetics. *Journal of Heat Treating* 1, 57–64.
- Umemoto, M., Tamura, I., 1986. Ferrite grain refinement by work-hardening of austenite and accelerated cooling. In: Gray, J. M. T., Ko, T., Shouhuma, Z., Boarong, W., Xishan, X. (Eds.), *HSLA Steels: Metallurgy and Applications*. pp. 373–382.
- Uslu, M. C., Canadine, D., Lambers, H. G., Tschumak, S., Maier, H. J., 2011. Modeling the role of external stresses on the austenite-to-bainite phase transformation in 51CrV4 steel. *Modelling and Simulation in Materials Science and Engineering* 19, 045007.
- Uzlov, I. G., Parusov, V. V., Dolzhenkov, I. I., 1980. Mechanism and kinetics of the transformation of austenite to divorced pearlite. *Metal Science and Heat Treatment* 22, 366–367.
- Vagarali, S. S., Odette, G. R., 1981. A model for the growth of hydrogen attack cavities in carbon steels. *Metallurgical Transactions A* 12, 2071–2082.
- Valiev, R. Z., Ivanisenko, Y. V., Rauch, E. F., Baudelet, B., 1996. Structure and deformation behaviour of Armco iron subjected to severe plastic deformation. *Acta Materialia* 44, 4705–4712.
- van Bohemen, S. M. C., Hermans, M. J. M., den Ouden, G., Richardson, I., 2002. A study of acoustic emission energy generated during bainite and martensite formation. *Journal of Applied Physics D* 35, 1889–1894.
- van Bohemen, S. M. C., Hermans, M. J. M., den Ouden, G., Richardson, I. M., 2003. Acoustic emission monitoring of bainite formation during continuous cooling. *Journal de Physique IV* 112, 301–304.
- van Bohemen, S. M. C., Santofimia, M. J., Sietsma, J., 2008. Experimental evidence for bainite formation below  $M_S$  in Fe-0.66C. *Scripta Materialia* 58, 488–491.
- van Bohemen, S. M. C., Sietsma, J., 2008. Modeling of isothermal bainite formation based on the nucleation kinetics. *International Journal of Materials Research* 99, 739–747.
- van Bohemen, S. M. C., Sietsma, J., 2014. Kinetics of martensite formation in plain carbon steels: critical assessment of possible influence of austenite grain boundaries and autocatalysis. *Materials Science and Technology* 30, 1024–1033.
- van Bohemen, S. M. C., Sietsma, J., Hermans, M. J. M., Richardson, I. M., 2005. Analysis of acoustic emission signals originating from bainite and martensite formation. *Philosophical Magazine* 85, 1791–1804.
- van der Eijk, C., Walmsley, J., Grong, O., 2002. Effects of titanium containing oxide inclusions on steel weldability. In: David, S. A., Vitek, J., Lippold, J., Smartt, H. (Eds.), *Trends in Welding Research*. ASM International, Materials Park, Ohio, USA, pp. 730–735.
- van Slycken, J., Verleysen, P., Degrieck, J., Degrieck, J., de Cooman, B. C., 2007. Dynamic response of aluminium containing TRIP steel and its constituent phases. *Materials Science & Engineering A* 460–461, 516–524.
- van Slycken, J., Verleysen, P., Degrieck, J., Samek, L., de Cooman, B. C., 2006. High-strain-rate behavior of low-alloy multiphase aluminum-and silicon-based transformation-induced plasticity steels. *Metallurgical & Materials Transactions A* 37, 1527–1539.
- Vasudevan, A. K., Sadananda, K., Louat, N., 1994. A review of crack closure, fatigue crack threshold and related phenomena. *Materials Science & Engineering A* 188, 1–22.
- Vasudevan, P., Graham, L. W., Axon, H. J., 1958. The kinetics of bainite formation in a plain carbon steel. *Journal of the Iron and Steel Institute* 190, 386–391.
- Venugopalan, D., Kirkaldy, J. S., October 1977. New relations for predicting the mechanical properties of quenched and tempered low alloy steels. In: Doane, D. V., Kirkaldy, J. S. (Eds.), *Hardenability Concepts with Applications to Steels*. The Metallurgical Society of AIME, Warrendale, PA, pp. 249–268.
- Verhoeven, J. D., 2000. The role of the divorced eutectoid transformation in the spheroidization of 52100 steel. *Metallurgical & Materials Transactions A* 31, 2431–2438.
- Verhoeven, J. D., Gibson, E. D., 1998. The divorced eutectoid transformation in steel. *Metallurgical & Materials Transactions A* 29, 1181–1189.
- Verleysen, P., van Slycken, J., Degrieck, J., de Cooman, B. C., Samek, L., 2005. Impact-dynamic behaviour of Al-TRIP steel. In: Carpinteri, A., Mai, Y. W., Ritchie, R. O. (Eds.), *11th International Congress on Fracture*. Curran Associates Inc., New York, USA, pp. 3666–3671.
- Verlinden, B., Bocher, P., Girault, E., Aernoudt, E., 2001. Austenite texture and bainite/austenite orientation relationships in TRIP steel. *Scripta Materialia* 45, 909–916.
- Vetters, H., Dong, J., Bornas, H., Hoffmann, F., Zoch, H.-W., 2006. Microstructure and fatigue strength of the roller-bearing steel 100Cr6 (SAE 52100) after two-step bainitisation and combined bainitic-martensitic heat treatment. *International Journal of Materials Research* 97, 1432–1440.
- Vetters, H., Dong, J., Zoch, H.-W., 2009. Effect of residual austenite on properties of tool steel following shortened treatments in lower bainitic phase. *International Heat Treatment and Surface Engineering* 3, 131–135.
- Vilella, J. R., Guellich, G. E., Bain, E. C., 1936. On naming the aggregate constituents in steel. *Trans. ASM* 24, 225–252.

- Vitek, J., Packan, N. H., David, S. A., 1986. Microstructural evaluation of Fe-3Cr-1.5Mo-0.1V thick section electron beam welds. In: David, S. A. (Ed.), *Advances in Welding Technology and Science*. ASM International, Warrendale, Pennsylvania, USA, pp. 203–207.
- von Bergen, R. T., Hollox, G. E., 1981. Effect of lower bainite on rolling contact fatigue of bearing steels. In: *Advances in the Physical Metallurgy and Applications of Steels*. The Metals Society, London, U.K., pp. 105–110.
- Vuorinen, E., Vang, J., Carradot, M., Johansson, P., Navara, E., 2014. Powder metallurgically produced carbide free bainite. *Materials Science Forum* Vol. 782 (2014) pp 480–486 782, 480–486.
- Wada, T., Cox, T., 1982. 3Cr-1Mo steel for pressure vessels in hydrogen service. In: Semchyshe, M. (Ed.), *Advanced Materials for Pressure Vessel Service with Hydrogen at High Temperatures and Pressures*. American Society of Mechanical Engineers, New York, USA, pp. 111–121.
- Wada, T., Cox, T. B., 1984. A new 3Cr-1.5Mo steel for pressure vessel applications. In: Swift, R. A. (Ed.), *Research on Chrome-Moly Steels*. American Society of Mechanical Engineers, New York, USA, pp. 77–93.
- Wada, T., Eldis, G. T., 1982. Transformation characteristics of 2.25Cr-1Mo steel. *ASTM STP 755* (343–362).
- Wadley, H. N. G., Mehrabian, R., 1984. Acoustic emission for materials processing: a review. *Materials Science & Engineering* 65, 245–263.
- Wagner, C., 1961. Theorie der alterung von niederschlägen durch umlösen (Ostwald-Reifung). *Zeitschrift für Elektrochemie* 65, 581–591.
- Wakasa, K., Wayman, C. M., 1981. Crystallography and morphology of ferrous lath martensite. *Metallography* 14, 49–60.
- Walley, S. M., 2007. Shear localisation: a historical overview. *Metallurgical & Materials Transactions A* 38A, 2629–2654.
- Wang, B., Xu, X., Liu, X., Wang, G., 2007. Effect of deformation of austenite on continuous cooling transformation microstructures for 22CrSH gear steel. *Journal of Iron and Steel Research, International* 14, 69–73.
- Wang, C., Ding, H., Zhang, J., Wu, H., 2014a. Effect of intercritical annealing time on the microstructures and tensile properties of a high strength TRIP steel. *Acta Metallurgica Sinica (English Letters)*, DOI 10.1007/s40195-014-0061-3.
- Wang, J., van der Zwaag, S., 2001a. Theoretical study of phosphorus containing TRIP steel, part 1: determination of the phosphorus concentration. *Zeitschrift für Metallkunde* 92, 1299–1305.
- Wang, J., van der Zwaag, S., 2001b. Theoretical study of phosphorus containing TRIP steel, part 2: analysis of the potential TRIP effect. *Zeitschrift für Metallkunde* 92, 1306–1311.
- Wang, L., Ding, F., Wang, B., Zhu, M., Zhong, Y., Liang, J., 2009a. Influence of super fine substructure on toughness of low-alloying ultra high strength structure steel. *Acta Metallurgica Sinica* 45, 292–239.
- Wang, L., Parker, S., Rose, A., West, G., Thomson, R., 2011. Effect of niobium on transformations from austenite to ferrite in low carbon steels. In: *Proceedings of the 6th International Conference on High Strength Low Alloy Steels*. pp. 208–212.
- Wang, T. S., Yang, J., Shang, C. J., Li, X. Y., Lv, B., Zhang, M., Zhang, F. C., 2008. Sliding friction surface microstructure and wear resistance of 9SiCr steel with low-temperature austempering treatment. *Surface & Coatings Technology* 202, 4036–4040.
- Wang, W., Liu, S., 2002. Alloying and microstructural management in developing SMAW electrodes for HSLA-100 steel. *Welding Journal, Research Supplement* 81, 132s–145s.
- Wang, X., Shang, C., Yang, S., He, X., Liu, X., 2006. The refinement technology for bainite and its application. *Materials Science & Engineering A* 438–440, 162–165.
- Wang, X. D., Zhong, N., Rong, Y. H., Hsu, T. Y., Wang, L., 2009b. Novel ultrahigh-strength nanolath martensitic steel by quenching-partitioning-tempering process. *Journal of Materials Research* 24, 260–267.
- Wang, X. L., Wu, K. M., Hu, F., Yu, L., Wan, X. L., 2014b. Multi-step isothermal bainitic transformation in medium-carbon steel. *Scripta Materialia* 74, 56–59.
- Wang, Y., Ma, E., Valiev, R. Z., Zhu, Y., 2004a. Tough nanostructured metals at cryogenic temperatures. *Advanced Materials* 16, 328–331.
- Wang, Y. Z., Khachatryan, A. G., 2006. Multi-scale phase field approach to martensitic transformations. *Materials Science & Engineering A* 438–440, 55–63.
- Wang, Z. C., Kim, S. J., Lee, C. G., Lee, T. H., 2004b. Bake-hardening behaviour of cold-rolled CMnSi and SMnSiCu TRIP-aided steel sheets. *Journal of Materials Processing Technology* 151, 141–145.
- Wasilkowska, A., Tsiouridis, P., Werner, E., Pichler, A., Traint, S., 2004. Microstructure and tensile behaviour of cold-rolled TRIP-aided steels. *Journal of Materials Processing Technology* 157–158, 633–636.
- Wasiluk, K., Wasiak, K., Skolek, E., Swiatnicki, W., 2014. Formation of nanobainitic structure in carburized layer of structural steels. In: *Metal 2014*. Tanger Ltd., Ostrava, Czech Republic, pp. 1–7.
- Wassermann, G., 1933. Einflüsse der  $\alpha$ - $\gamma$ -umwandlung eines irreversiblen nickelstahls auf kristallorientierung und zugfestigkeit. *Arch. Eisenhüttenwes.* 6, 347–351.

- Watanabe, J., Murakami, Y., 1981. Prevention of temper embrittlement of CrMo steel vessels by the use of low-silicon forged shells. Tech. rep., American Petroleum Institute preprint no. 28-81, pages 216-224, quoted by Bodnar et al. 1989.
- Waterschoot, T., Kestens, L., de Cooman, B. C., 2002. Hot rolling texture development in CMnCrSi dual phase steels. Metallurgical & Materials Transactions A 33, 1091-1102.
- Watson, J. D., McDougall, P. G., 1973. The crystallography of Widmanstätten ferrite. Acta Metallurgica 21, 961-973.
- Wechsler, M. S., Lieberman, D. S., Read, T. A., 1953. On the theory of the formation of martensite. Trans. AIME Journal of Metals 197, 1503-1515.
- Wei, D. Y., Gu, J. L., Fang, H. S., Bai, B. Z., Yang, Z. G., 2004. Fatigue behavior of 1500 MPa bainite /martensite duplex-phase high strength steel. International Journal of Fatigue 26, 437-442.
- Wei, X. C., Fu, R. Y., Li, L., 2007. Influence of zinc electro-plated coating on dynamic tensile properties of TRIP-aided steels. Surface and Coating Technology 201, 6922-6927.
- Weidig, U., Kaspar, R., Pawelski, O., Rasp, W., 1999. Multiphase microstructure in steel bars produced by dieless drawing. Steel Research 70, 172-177.
- Weller, M., 1983. The Snoek-Köster relaxation in body-centred cubic metals. Journal de Physique Colloques 44(C9), 63-82.
- Wenyan, L., Jingxin, Q., Hesheng, S., 1997. Fatigue crack growth behaviour of a Si-Mn steel with carbide-free lathy bainite. Journal of Material Science 32, 427-430.
- Wever, F., Jellinghaus, W., 1932. Transformation kinetics of austenite – II – dilatometry investigations of austenite decomposition. Mitt. Kaiser-Wilhelm-Inst. Eisenforschung 14, 85.
- Wever, F., Lange, H., 1932. The transformation kinetics of austenite – I – magnetic investigations of the decomposition of austenite. Mitt. Kaiser-Wilhelm-Inst. Eisenforschung 14, 71-83.
- White, J. S., Owen, W. S., 1961. The effect of up-quenching on the kinetics of bainite formation. Journal of the Iron and Steel Institute 197, 241-243.
- White, R. M., 2007. Quantum Theory of Magnetism. Springer, New York, USA.
- Whiteley, J. H., 1922. The formation of globular pearlite. Journal of the Iron and Steel Institute 105, 339-357.
- Wiestner, H. J., 1932. Photographs of the martenite crystallization. Zeitschrift für Metallkunde 24, 276-277.
- Williams, J. G., Killmore, C. R., Barbaro, F. J., Piper, J., Fletcher, 1996. High strength ERW linepipe manufacture in Australia. Materials Forum 20, 13-28.
- Wilson, E. A., Allen, S. P., Butler, J., 1982.  $\gamma \rightarrow \alpha$  transformation in Fe-15Ni. Metal Science 16, 539-542.
- Wilson, E. A., Shatansky, D. V., Ohmori, Y., 2001. A study of transformations in continuously cooled Fe-15Ni alloys. ISIJ International 41, 866-875.
- Wilson, F. G., Gladman, T., 1988. Aluminium nitride in steel. International Materials Reviews 33, 211-283.
- Wilson, P., 1991. Remanent creep life prediction in low-alloy ferritic steel power plant components. Ph.D. thesis, University of Cambridge, Cambridge, U. K.
- Winchell, P. G., Cohen, M., 1962. The strength of martensite. Trans. ASM 55, 347-361.
- Wirths, V., Wagener, R., Bleck, W., Melz, T., 2014. Bainitic forging steels for cyclic loading. Advanced Engineering Materials 922, 813-818.
- Withers, P. J., Bhadeshia, H. K. D. H., 2001a. Residual stress part 1 – measurement techniques. Materials Science and Technology 17, 355-365.
- Withers, P. J., Bhadeshia, H. K. D. H., 2001b. Residual stress part 2 – nature and origins. Materials Science and Technology 17, 366-375.
- Woodhead, J. H., Quarrell, A. G., 1965. Role of carbides in low alloy creep resisting steels. Journal of the Iron and Steel Institute 203, 605-620.
- Wozniak, T. Z., 2008. Acoustic phenomena near  $M_S$  in hypereutectoid steels. Materials Characterisation 59, 708-716.
- Wozniak, T. Z., Jelenkowski, J., Rozniatowski, K., Ranachowski, Z., 2012. Effect of microstructure on rolling contact fatigue of bearings. Materials Science Forum 726, 55-62.
- Wozniak, T. Z., Rozniatowski, K., Ranachowski, Z., 2011a. Acoustic emission in bearing steel during isothermal formation of midrib. Metals and Materials International 17, 365-373.
- Wozniak, T. Z., Rozniatowski, K., Ranachowski, Z., 2011b. Application of acoustic emission to monitor bainitic and martensitic transformation. Kovove Materialy 49, 319-331.
- Wright, P. H., Harrington, T. L., Szilva, W. A., White, T. R., 1987. What the forger should know about microalloy steels. In: Krauss, G., Banerji, S. K. (Eds.), Microalloying Forging Steels. TMS-AIME, Warrendale, Pennsylvania, USA, pp. 541-566.
- Wright, T. W., 2002. The physics and mathematics of adiabatic shear bands. Cambridge University Press, Cambridge, U. K.
- Wu, C. Z., Chen, Y. J., Shih, T. S., 2002. Phase transformations in austempered ductile iron by microjet impact. Materials Characterization 48, 43-54.

- Wu, K. M., 2006. Three-dimensional analysis of acicular ferrite in a low-carbon steel containing titanium. *Scripta Materialia* 54, 569–574.
- Wu, K. M., Enomoto, M., 2002. Three dimensional morphology of degenerate ferrite in Fe-Mo-C. *Scripta Materialia* 46, 569–574.
- Wu, K. M., Inagawa, Y., Enomoto, M., 2004. Three-dimensional morphology of ferrite formed in association with inclusions in low carbon steel. *Materials Characterization* 52, 121–127.
- Wu, K. M., Kagayama, M., Enomoto, M., 2003. Kinetics of ferrite transformation in an Fe-0.28mass%C-3mass%Mo alloy. *Materials Science & Engineering A* 343, 143–150.
- Wynne, B., Hutchinson, B., Ryde, L., 2007. Effect of stress on transformation plasticity and texture in a tool steel. *Scripta Materialia* 57, 473–476.
- Xu, L., Wei, D. Y., Yu, Y., Zhang, H., Bai, B. Z., 2011. Effect of microstructure on corrosion fatigue behavior of 1500 MPa level carbide-free bainite/martensite dual-phase high strength steel. *Journal of Iron and Steel Research, International* 18, 63–67.
- Xua, P., Bai, B., Yin, F., Fang, H., Nagai, K., 2004. Microstructure control and wear resistance of grain boundary allotriomorphic ferrite/granular bainite duplex steel. *Materials Science & Engineering A* 385, 65–67.
- Ya Drozdov, B., Kogan, L. I., Entin, R. I., 1962. Influence of stresses and strains on the kinetics of the intermediate austenite transformation. *Physics of Metals and Metallography* 13, 135–138.
- Yakel, H. L., 1985. Crystal structure of stable and metastable iron-containing carbides. *International Metals Reviews* 30, 17–40.
- Yakubstov, I. A., Boyd, J. D., 2001. Bainite transformation during continuous cooling of low carbon microalloyed steel. *Materials Science and Technology* 17, 296–301.
- Yakubstov, I. A., Purdy, G. R., 2011. Analyses of transformation kinetics of carbide-free bainite above and below the athermal martensite-start temperature. *Metallurgical & Materials Transactions A* 43, 437–446.
- Yalci, H. K., Edmonds, D. V., 1999. The effect of hydrogen on the bainite transformation. *Journal of Materials Science* 34, 711–717.
- Yamamoto, K., Hasegawa, T., Takamura, J., 1996. Effect of boron on intra-granular ferrite formation in Ti-oxide bearing steels. *ISIJ International* 36, 80–86.
- Yamamoto, K., Matsuda, S., Haze, T., Chijiwa, R., Mimura, H., 1987. Newly developed Ti-oxide bearing steel having high HAZ toughness. In: *Residual and Unspecified Elements in Steel*. ASTM International, Pennsylvania, USA, p. STP1042.
- Yan, J. Y., Zhang, W. Z., Borgenstam, A., 2013. Observations of surface relief of proeutectoid widmanstätten cementite plates in a hypereutectoid carbon steel. *Metallurgical & Materials Transactions A* 44, 4143–4149.
- Yan, P., Bhadeshia, H. K. D. H., 2013. Mechanism and kinetics of solid-state transformation in high-temperature processed linepipe steel. *Metallurgical & Materials Transactions A* 44, 5468–5477.
- Yan, P., Bhadeshia, H. K. D. H., 2015. The austenite-ferrite transformation in enhanced-niobium, low-carbon steel. *Materials Science and Technology* 31, <http://dx.doi.org/10.1179/1743284714Y0000000673>.
- Yan, P., Güngör, O. E., Thibaux, P., Bhadeshia, H. K. D. H., 2010. Crystallographic texture of induction-welded and heat-treated pipeline steel. *Advanced Materials Research* 89–91, 651–656.
- Yang, H.-S., Bhadeshia, H. K. D. H., 2007. Uncertainties in the dilatometric determination of the martensite-start temperature. *Materials Science and Technology* 23, 556–560.
- Yang, H.-S., Bhadeshia, H. K. D. H., 2008. Designing low-carbon, low-temperature bainite. *Materials Science and Technology* 24, 335–342.
- Yang, H. S., Bhadeshia, H. K. D. H., 2009. Austenite grain size and the martensite-start temperature. *Scripta Materialia* 60, 493–495.
- Yang, H.-S., Suh, D. W., Bhadeshia, H. K. D. H., 2012a. More complete theory for the calculation of the martensite-start temperature in steels. *ISIJ International* 52, 162–164.
- Yang, J., Putatunda, S. K., 2004. Improvement in strength and toughness of austempered ductile cast iron by a novel two-step austempering process. *Materials & Design* 25, 219–230.
- Yang, J., Wang, T. S., Zhang, B., Zhang, F. C., 2012b. High-cycle bending fatigue behaviour of nanostructured bainitic steel. *Scripta Materialia* 66, 363–366.
- Yang, J., Wang, T. S., Zhang, B., Zhang, F. C., 2012c. Sliding wear resistance and worn surface microstructure of nanostructured bainitic steel. *Wear* 282–283, 81–84.
- Yang, J. R., Bhadeshia, H. K. D. H., 1987a. Reaustenitisation in steel weld deposits. In: Koo, J. Y. (Ed.), *Welding Metallurgy of Structural Steels*. TMS-AIME, Warrendale, Pennsylvania, USA, pp. 549–563.
- Yang, J. R., Bhadeshia, H. K. D. H., 1987b. Thermodynamics of the acicular ferrite transformation in alloy-steel weld deposits. In: David, S. A. (Ed.), *Advances in Welding Technology and Science*. ASM International, Materials Park, Ohio, USA, pp. 187–191.
- Yang, J. R., Bhadeshia, H. K. D. H., 1988. The bainite to austenite transformation. In: Lorimer, G. W. (Ed.), *Phase Transformations '87*. pp. 365–373.
- Yang, J. R., Bhadeshia, H. K. D. H., 1989a. Orientation relationships between adjacent plates of acicular ferrite. *Materials Science and Technology* 5, 93–97.

- Yang, J. R., Bhadeshia, H. K. D. H., 1989b. Reaustenitization experiments on some high-strength steel weld deposits. *Materials Science and Engineering A* 118, 155–170.
- Yang, J. R., Huang, C. Y., Chiou, C. S., 1995. Influence of plastic deformation and cooling rates on the microstructural constituents of an ultra-low carbon bainitic steel. *ISIJ International* 35, 1013–1019.
- Yang, J. R., Huang, C. Y., Hsieh, W. H., Chiou, C. S., 1996. Mechanical stabilization of austenite against bainitic reaction in Fe-Mn-Si-C bainitic steel. *Materials Transactions JIM* 37, 579–585.
- Yang, Y.-S., Son, K.-J., Cho, S.-K., Hong, S.-G., Kim, S.-K., Mo, K.-H., 2001a. Effect of residual stress on fatigue strength of resistance spot weldment. *Science and Technology of Welding and Joining* 6, 397–401.
- Yang, Z. G., Zhang, C., Bai, B. Z., Fang, H. S., 2001b. Observation of bainite surface reliefs in Fe-C alloy by atomic force microscopy. *Materials Letters* 48, 292–298.
- Yates, J. K., 1996. Innovation in rail steel. *Science in Parliament* 53, 2–3.
- Yeo, R. B. G., 1963. Effects of some alloying elements on the transformation of Fe-22.5Ni wt% alloys. *Trans. Metall. Soc. AIME* 227, 884–890.
- Yescas, M., Bhadeshia, H. K. D. H., MacKay, D. J. C., 2001. Retained austenite in austempered ductile cast irons. *Materials Science & Engineering A* 311, 162–173.
- Yi, H. L., 2014. Review on  $\delta$ -transformation-induced plasticity (TRIP) steels with low density: The concept and current progress. *Journal of Materials*, DOI: 10.1007/s11837-014-1089-6.
- Yi, H. L., Lee, K. Y., Bhadeshia, H. K. D. H., 2011. Extraordinary ductility in Al-bearing  $\delta$ -TRIP steel. *Proceedings of the Royal Society A* 467, 234–243.
- Yin, Z. X., Bhadeshia, H. K. D. H., 2013. Divorced eutectoid transformation in high Mn bearing steel. *Advanced Materials Research* 634-638, 1798–1802.
- Yokota, T., Garcia-Mateo, C., Bhadeshia, H. K. D. H., 2004. Formation of nanostructured steel by phase transformation. *Scripta Materialia* 51, 767–770.
- Yoozbashi, M. N., Yazdani, S., 2010. Mechanical properties of nanostructured, low temperature bainitic steel designed using a thermodynamic model. *Materials Science & Engineering A* 527, 3200–3205.
- Young, C. H., Bhadeshia, H. K. D. H., 1994. Strength of mixtures of bainite and martensite. *Materials Science and Technology* 10, 209–214.
- Yu, D., Chen, D., Zheng, J., He, Y., Shen, F., 1989. Phase transformation unit of bainitic ferrite and its surface relief in low and medium carbon alloy steels. *Acta Metallurgica Sinica* 2, 161–167.
- Yu, J., 1989. Carbide stability diagrams in 2.25Cr1Mo steels. *Metallurgical Transactions A* 20, 1561–1564.
- Yu, J., McMahon Jr., C. J., 1980. The effects of composition and carbide precipitation on temper embrittlement of 2.25 Cr-1 Mo steel: Part I. Effects of P and Sn. *Metallurgical & Materials Transactions A* 11, 277–289.
- Yu, Y., Gu, J. L., Xu, L., Shou, F. L., Bai, B. Z., Liu, Y. B., 2010. Very high cycle fatigue behaviors of Mn-Si-Cr series bainite/martensite dual phase steels. *Materials and Design* 31, 3067–3072.
- Yutori, T., Ogawa, R., 1979. Formation of transformation texture in controlled rolled steels. *Tetsu-to-Hagane* 61, 991–1011.
- Zackay, V. F., Parker, E. R., Farh, D., Busch, R., 1967. The enhancement of ductility in high-strength steels. *Trans. ASM* 60, 252–259.
- Zaefferer, S., Ohlert, J., Bleck, W., 2004. A study of microstructure, transformation mechanisms and correlation between microstructure and mechanical properties of a low alloyed TRIP steel. *Acta Materialia* 52, 2765–2778.
- Zaefferer, S., Romano, P., Friedel, F., 2008. EBSD as a tool to identify and quantify bainite and ferrite in low-alloyed Al-TRIP steels. *Journal of Microscopy* 230, 499–508.
- Zahiri, S. H., Davies, C. H. J., Peroloma, E. V., 2003. Simultaneous prediction of austemperability and processing window for austempered ductile iron. *Materials Science and Technology* 19, 1761–1770.
- Zarei-Hanzaki, A., Hodgson, P. D., Yue, S., 1995. Influence of bainite on retained austenite characteristics in Si-Mn TRIP steels. *ISIJ International* 35, 79–85.
- Zener, C., 1946. Kinetics of the decomposition of austenite. *Trans. Am. Inst. Min. Metall. Engng.* 167, 550–595.
- Zener, C., 1949. Theory of growth of spherical precipitates from solid solution. *Journal of Applied Physics* 20, 950–953.
- Zeng, X., Lu, J., Wang, W., 2010. Effect of cooling rate of hot-deformed austenite on structure and property of X80 pipeline steel. *Special Steel* 31, 63–665.
- Zenitani, S., Hayakawa, N., Yamamoto, J., Hiraoka, K., Shiga, C., Morikage, Y., Kubo, T., Yasuda, K., 2002. Prevention of cold cracking in high strength steel welds by applying newly developed low transformation temperature welding consumables. In: David, S. A., DebRoy, T. (Eds.), 6th International Trends in Welding Research Conference. ASM International, Materials Park, Ohio, USA, pp. 569–574.
- Zhang, F. C., Wang, T. S., Zhang, P., Zhang, C. L., Lv, B., Zhang, M., Zhang, Y. Z., 2008. A novel method for the development of a low-temperature bainitic microstructure in the surface layer of low-carbon steel. *Scripta Materialia* 59, 294–296.

- Zhang, J., Ding, H., Misra, R. D. K., Wang, C., 2014. Enhanced stability of retained austenite and consequent work hardening rate through pre-quenching prior to quenching and partitioning in a Q-P microalloyed steel. *Materials Science & Engineering A* 611, 252–256.
- Zhang, M. R., Gu, H. C., 2007. Microstructure and properties of carbide free bainite railway wheels produced by programmed quenching. *Materials Science and Technology* 23, 970–974.
- Zhang, M.-X., Kelly, P. M., 1998. Determination of carbon content in bainitic ferrite and carbon distribution in austenite by using CBKLD. *Materials Characterisation* 40, 159–168.
- Zhang, M.-X., Kelly, P. M., 2006. Crystallography of carbide-free bainite in a hard bainitic steel. *Materials Science and Engineering A* A438-440, 272–275.
- Zhang, P., Zhang, F. C., Yan, Z. G., Wang, T. S., Qian, L. H., 2011a. Rolling contact fatigue property of low-temperature bainite in surface layer of a low carbon steel. *Materials Science Forum* 675-677, 585–588.
- Zhang, P., Zhang, F. C., Yan, Z. G., Wang, T. S., Qian, L. H., 2011b. Rolling contact fatigue property of low-temperature bainite in surface layer of a low carbon steel. *Materials Science Forum* 675-677, 585–588.
- Zhang, P., Zhang, F. C., Yan, Z. G., Wang, T. S., Qian, L. H., 2011c. Wear property of low-temperature bainite in the surface layer of a carburized low carbon steel. *Wear* 271, 697–704.
- Zhang, Z., Wu, X. C., Li, N., Min, Y. A., 2015. Alloy optimisation of bainitic steel for large plastic mould. *Materials Science and Technology* 31, <http://dx.doi.org/10.1179/1743284714Y.0000000744>.
- Zhao, J. Z., Mesplont, C., de Cooman, B. C., 2001a. Kinetics of phase transformations in steels: A new method for analysing dilatometric results. *ISIJ International* 41, 492–497.
- Zhao, L., Wibowo, M. K., Hermans, M. J. M., van Bohemen, S. M. C., Sietsma, J., 2009. Retention of austenite in the welded microstructure of a 0.16C-1.6Mn-1.5Si (wt%) TRIP steel. *Journal of Materials Processing Technology* 209, 5286–5292.
- Zhao, M., Yang, K., Shan, Y., 2002a. The effect of thermo-mechanical process on microstructures and mechanical properties of a commercial pipeline steel. *Materials Science & Engineering A* 335, 14–20.
- Zhao, M.-C., Shan, Y.-Y., Xiao, F. R., Yang, K., Li, Y. H., 2002b. Investigation on the H<sub>2</sub>S-resistant behaviors of acicular ferrite and ultrafine ferrite. *Materials Letters* 57, 141–145.
- Zhao, S. X., Wang, W., Mao, D. L., 2007. On bainite nucleation at carbon depleted zone around edge dislocation. *Key Engineering Materials* 334-335, 121–124.
- Zhao, Z., Liu, C., Liu, Y., Northwood, D. O., 2001b. A new empirical formula for the bainite upper temperature limit of steel. *Journal of Material Science* 36, 5045–5056.
- Zhou, R., Jiang, Y., Lu, D., Zhou, R., Li, Z., 2001. Development and characterization of a wear resistant bainite/martensite ductile iron by combination of alloying and a controlled cooling heat-treatment. *Wear* 250, 529–534.
- Zhu, K., Bouaziz, O., Oberbillig, C., Huang, M., 2010. An approach to define the effective lath size controlling yield strength of bainite. *Materials Science & Engineering A* 527, 6614–6619.
- Zhu, K., Oberbillig, C., Musik, C., Loison, D., Jung, T., 2011. Effect of B and B + Nb on the bainitic transformation in low carbon steels. *Materials Science and Engineering A* 528, 4222–4231.
- Zhuo, X., Wang, Z., Wang, W., Lee, H. G., 2007. Thermodynamic calculations and experiments on inclusions to be nucleation sites for intragranular ferrite in Si-Mn-Ti deoxidized steel. *Journal of the University of Science and Technology Beijing* 14, 14–21.
- Zrník, J., Stejskai, O., Nový, Z., Hornák, P., Fújda, M., 2007. Structure dependence of the TRIP phenomenon in Si-Mn bulk steel. *Materials Science & Engineering A* 462, 253–258.
- Zuo, B., Wang, Y., Mi, Z., Zhao, A., 2010. Research on CCT curve of pipeline steel X80. *Hot Working Technology* 39, 12–14.

## Author index

- Ågren, 126, 149, 157, 160  
 Aaronson, 7, 14, 17, 29, 52, 78, 162, 289  
 Abdurakhmanov, 193  
 Abe F, 112  
 Abe, F, 346, 358  
 Abreu, 216, 226  
 Abson, 179, 251  
 Adachi, 27, 456, 495  
 Adcock, 14  
 Aeby-Gautier, 296  
 Aernoudt, 376, 405, 407  
 Afrouz, 103  
 Ahmadabadi, 209  
 Ahrens, 213  
 Aikawa, 255  
 Aizawa, 475  
 Akamizu, 342  
 Akbasoglu, 340, 438  
 Al-Harbi, 288  
 Alberry, 90  
 Alexander, 358  
 Alexandrov, 432  
 Ali, 134, 255, 285  
 Allain, 167  
 Allen, 444  
 Allen C, 450  
 Allen NP, 6  
 Allen, SP, 495  
 Almaraz, 339  
 Amano, 115, 380  
 Amirthalingam, 57  
 Amrithalingam, 233  
 Andrés, 27, 101, 293  
 Andrés, 280  
 Andrews, 76  
 Araki, 358  
 Aravas, 220  
 Arias, 470  
 Arif, 193  
 Arimochi, 334  
 Armstrong, 340  
 Arnould, 61  
 Asahi, 178  
 Ashby, 90  
 Atkins, 309  
 Austin, 1, 66  
 Averbach, 66, 187  
 Avettand-Fénoël, 304  
 Avishan, 472  
 Avrami, 162  
 Axon, 166  
 Ayada, 235  
 Aziz, 158  
 Azrin, 315  
 Azuma, 22  
 Babu SS, 7, 27, 33, 69, 84, 172, 252, 275, 432, 433, 474  
 Babu, BNP, 173  
 Babu, PB, 422  
 Bacroix, 226  
 Baczynski, 375  
 Bae JH, 317, 375  
 Bae YH, 234  
 Baganis, E, 409  
 Bagaryatskii, 75  
 Bai B, 411, 451  
 Bai BZ, 46, 336  
 Bai DQ, 384  
 Baik SC, 410  
 Bailey, 361  
 Bain, 1–3, 224  
 Baker, 66, 100, 101, 107, 349  
 Baker JC, 158  
 Bakshi, 482  
 Ball, 112  
 Bando, 213, 215  
 Bandyopadhyay, 284  
 Barakalow, 54  
 Barbacki, 69  
 Barbaro, 252, 263, 384  
 Barford, 148, 166, 172  
 Barlat, 423  
 Barnard, 71, 85  
 Barrallier, 226  
 Barritte, 253  
 Barta, 444  
 Bastien, 266  
 Basuki, 407  
 Bathias, 339  
 Baudry, 339  
 Bauer-grosse, 61  
 Baxter, 495  
 Bayerlein, 332  
 Beaven, 269  
 Beech, 350  
 Beladi, 27, 456, 487  
 Bell, 33, 501  
 Benjamin, 307  
 Benson, 333  
 Berdin, 315  
 Berg, 361  
 Bergen, 340  
 Bernstein, 343, 361  
 Beshers, 56  
 Besson, 323  
 Beynon, 433  
 Bhadeshia, 1, 7, 21, 24–28, 33, 40, 45, 57, 69, 79, 91, 94, 102, 126, 160, 186, 187, 190, 196, 215, 224, 228, 260, 293, 296, 313, 368, 409, 416, 457, 461, 474, 479, 482, 490, 495  
 Bhat, 72, 173

- Bhattacharjee, 340, 389  
 Bhattacharyya, 215  
 Bhole, 474  
 Bhowmik, 421  
 Bicknell, 323  
 Bilby, 48  
 Bjornbakk, 262  
 Blackmore, 444  
 Blaschko, 228  
 Bleck, 84, 193, 307, 408  
 Bocher, 376, 407  
 Bodnar, 324, 368, 378  
 Boettinger, 190  
 Bohle, 424  
 Bokros, 226  
 Bomas, 340  
 Bompard, 323  
 Borgenstam, 72, 149  
 Bortollotti, 495  
 Botchenkov, 226  
 Bouaziz, 167, 308  
 Bouguerel, 412  
 Bouquerel, 412  
 Bowen, 322, 325  
 Bowker, 384  
 Bowles, 5, 33, 42, 44, 51, 226  
 Boyd, 179, 235  
 Brackman, 505  
 Bradley, 31  
 Branch, 348, 349  
 Brenner, 457  
 Briant, 325  
 Brochu, 384  
 Brown GT, 181  
 Brown PM, 495  
 Brown PW, 172  
 Brozzo, 318, 323  
 Bruna, 134  
 Buchi, 350  
 Buerger, 5  
 Bunshah, 12  
 Burdekin, 319  
 Burkart, 340  
 Busch, 315  
 Bush, 89, 309  
 Butler, 495  
 Buzzichelli, 318  
 Byun, 261  
 Byun JS, 281
- Caballero, 22, 27, 32, 143, 167, 280, 297, 457, 467,  
 472, 482, 495, 505  
 Cahn JW, 158  
 Cai MH, 313  
 Callejo, 284  
 Campbell, 84  
 Canadinc, 215, 231  
 Cane, 102  
 Cansdinc, 216  
 Capdevila, 143, 167, 280, 297, 467, 505  
 Carneiro, 343
- Carradot, 495  
 Carruthers, 103  
 Cayron, 216  
 Cedeno, 343  
 Celotto, 412  
 Chae, 186  
 Chakrabarti, 428  
 Chakraborty, 340  
 Chan SLI, 337  
 Chan X, 448, 452  
 Chandel, 274, 323  
 Chandrasekharaiah, 253, 277  
 Chang, 21  
 Chang HT, 474  
 Chang LC, 172, 203, 293, 297, 450  
 Chang, LC, 79, 437  
 Chao, 297, 467  
 Chapetti, 328  
 Charleux, 384  
 Chatterjee, 187, 212, 226, 228, 413  
 Chattopadhyay, 421, 469, 495  
 Chen, 190  
 Chen C, 405  
 Chen CC, 495  
 Chen CY, 495  
 Chen DL, 474  
 Chen H, 126  
 Chen HC, 404  
 Chen LH, 310, 327, 450  
 Chen X, 179, 384, 424  
 Chen YJ, 218  
 Chen Z, 359  
 Cheng, 111  
 Chengjian, 179  
 Chester, 143, 167  
 Chijiiwa, 255, 263, 389  
 Chintha, 216  
 Chiou, 213, 234  
 Cho CS, 179  
 Cho MH, 490  
 Cho YW, 261, 281  
 Choi HC, 249  
 Choi JK, 234  
 Choi P, 84  
 Choi, BY, 312  
 Choji, 380  
 Choo, 234  
 Christian, 5, 10, 15, 25, 48, 51, 52, 56, 208, 228,  
 277, 304  
 Chu W, 495  
 Chu WY, 487  
 Chung, 352  
 Cizek, 384  
 Clark, 53, 79  
 Classen, 405  
 Clatterbuck, 457  
 Clayton, 437  
 Coates, 28, 29  
 Codd, 64  
 Cohen, 13, 24, 40, 46, 66, 84, 148, 160, 187, 208,  
 213, 220, 226, 290, 308, 310, 318, 429

- Cohn, 61  
 Cola, 432, 433  
 Coldren, 309  
 Collins, 103, 348, 379  
 Collins LE, 179, 375  
 Colvin, 72  
 Conlon, 387, 397  
 Cooman, 217, 235  
 Corbett, 259  
 Cornide, 27, 297, 495  
 Cottrell, 6, 213, 319  
 Cox, 352  
 Crespo, 134  
 Crosky, 33  
 Cryderman, 309  
 Cuddy, 373  
 Cullison, 496  
 Curtze, 412, 469  
 Cybula, 451  
 Czyryca, 378
- Díaz-Fuentes, 278  
 da Silva, 296  
 Daigne, 23, 304, 308  
 Dallum, 272  
 Darcis, 223  
 Das S, 125  
 Date, 503  
 Datta, 469, 495  
 Dauskardt, 109, 338, 352  
 Davenport, 1  
 Davenport AS, 166  
 Davenport AT, 20, 230  
 Davenport ES, 183, 224  
 David, 7, 215, 224, 252, 274, 505  
 Davies, 20, 376, 443  
 Davis, 423  
 de Cooman, 68, 128, 212, 230, 390, 404, 405, 412  
 de Freitas C. Lins, 343  
 DeArdo, 14, 373, 378, 421, 422  
 DebRoy, 252  
 Deep, 98, 309  
 Degang, 7, 64  
 Degrieck, 412  
 Delaey, 208  
 Delagnes, 72  
 Delannay, 390, 467  
 Delanny, 125, 226, 397  
 Delany, 401  
 Deliry, 61, 66, 68  
 Denis, 296  
 Devanathan, 435  
 Diesburg, 500  
 Din, 310, 327  
 Ding H, 313, 391, 409  
 Dionne, 179  
 Dippel, 57, 92  
 Domian, 29, 289  
 Dong J, 440  
 Dorazil, 444  
 dos Santos, 296
- Dowling, 259  
 Drillet, 70, 506  
 Dronskowski, 84  
 Drozdov, 213  
 Du JS, 234  
 Du C, 384  
 Du L, 409  
 Du LX, 465, 495  
 Duan DM, 313  
 Dube, 14, 255  
 Dubensky, 66, 327, 444  
 Dubrov, 213, 215  
 Duckworth, 213, 429  
 Dunne, 46  
 Duong VT, 125, 425  
 Dupont, 354  
 Durbin, 430  
 Dutta, 57, 233
- Easterling, 252, 263  
 Echeverria, 324  
 Eckerlid, 223  
 Economopolus, 287  
 Edmonds, 26, 48, 66, 128, 172, 218, 247, 263, 289,  
 313, 315, 333, 340, 424, 438, 444  
 Edwards, 252, 361, 429, 430  
 Eijk, 259, 280  
 Eldis, 179, 248, 351  
 Elvira, 482, 495  
 Elwood, 368  
 Embury, 313  
 Enomoto, 20, 252  
 Entin, 7, 83, 213  
 Entwisle, 40  
 Era H, 404  
 Erasmus, 266  
 Ericsson, 213  
 Es-Souni, 269  
 Esaka, 388  
 Essadiqi, 474  
 Eterasivili, 34  
 Evans GM, 262, 273, 275  
 Evans PRV, 429  
 Evsyukov, 32, 125
- Fairhurst, 500  
 Fang H, 451, 490  
 Fang HS, 46, 336  
 Fang K, 490  
 Farh, 315  
 Farnell, 501  
 Farooque, 289  
 Farrar, 255, 277, 320  
 Fattal, 460  
 Fegredo, 375, 433  
 Feher, 368  
 Ferrer, 280  
 Fielding, 470  
 Fine, 332  
 Fischer, 225  
 Fisher GL, 179

- Fisher JC, 56  
 Fisher, RM, 64  
 Fitzgerald, 433  
 Fletcher, 384  
 Flewitt, 432  
 Flower, 251, 323  
 Foct, 501  
 Fondekar, 26, 66  
 Form, 419  
 Fors, 56  
 Forster, 12  
 Fossaert, 179, 409  
 Fournalis, 21, 114  
 Fournelle, 332  
 Franetovic, 67, 444  
 Franti, 78  
 Freiwillich, 213  
 Fridel, 507  
 Frommeyer, 432  
 Fu H, 448, 452  
 Fu RY, 220, 405  
 Fujda, 234  
 Fujioka, 264  
 Fujita, 22, 105  
 Fujita S, 340  
 Fukagawa, 413  
 Fukuoka, 432  
 Fukuzawa, 501  
 Fullman, 23  
 Fumimaru, 419  
 Funakoshi, 307  
 Funato, 389  
 Furnemont, 387, 397, 465, 467  
 Furuhashi, 27, 40, 53, 71, 179, 209, 254, 277, 430, 507  
 Futamura, 113
- Gómez, 39  
 Ga, ZM, 72  
 Gadicheria, 444  
 Gagon, 506  
 Ganguly, 495  
 Gantois, 61  
 Gao, 106  
 Gao G, 411  
 Gao N, 313, 336  
 Garcia, 375, 421, 422  
 Garcia de Andres, 143, 167, 467, 505  
 Garcia-Mateo, 22, 27, 143, 167, 216, 280, 297, 457, 467, 472, 482  
 Garnham, 435  
 Garwood, 15  
 Gavrilova, 435  
 Gazder, 288  
 George, 351, 352  
 Gerberich, 429  
 Ghonem, 433  
 Ghosh, 81, 84, 136, 421, 458  
 Ghosh G, 71  
 Ghosh, R, 280, 310  
 Gianetto, 274, 323, 384
- Girardini, 479, 495  
 Girault, 376, 390, 401, 405  
 Gladman, 179, 368  
 Glez, 25, 231, 407  
 Godet, 25, 33, 226, 231, 387, 397, 407  
 Goldman, 158  
 Gomez, 125  
 Gong, 495  
 Gong W, 475  
 Gooch, 102, 247, 350  
 Goodall, 384  
 Goodenow, 54, 148, 204, 440  
 Gordine, 64, 71  
 Gordon, 373  
 Gorkunov, 435  
 Gorman, 61  
 Gorsuch, 457  
 Gouné, 167  
 Gourgues, 40, 251, 323  
 Gourgues-Lorenzon, 226, 507  
 Grabke, 324, 325  
 Graf, 25, 378  
 Graham, 166  
 Grant, 223  
 Grassel, 432  
 Grassl, 422  
 Gray, 179, 382, 384  
 Green, 341  
 Gregg, 260, 261  
 Gregory, 3  
 Greninger, 5, 290  
 Gretoft, 272  
 Griffith, 318  
 Grochowksi, 342  
 Grong, 251, 259, 262, 266, 283  
 Gross, 378  
 Gu, 336  
 Guillou, 325  
 Guitierrez, 278  
 Gunn, 446  
 Guo Y, 495  
 Guo Z, 277  
 Gur Hakan, 500  
 Gutamura, 412  
 Gutierrez, 39  
 Guttman, 304
- Häag, 61  
 Habraken, 287  
 Habu, 178  
 Hachtel, 419  
 Haezebrouck, 20  
 Haidemenopoulos, 220  
 Hajiakbari, 209  
 Haldar, 125, 416, 421  
 Ham, 350  
 Hamdany, 460, 495  
 Han HN, 216, 393  
 Hanhold, 433  
 Hanks, 358  
 Hanlon, 412

- Hannemann, 12  
 Hara, 178  
 Harada, 226, 343  
 Harada H, 216  
 Harding, 444  
 Harjo, 475  
 Harlet, 125  
 Harrington, 421  
 Harrison, 255, 277, 320  
 Hasan, 97, 304, 495  
 Hase, 40, 115, 216, 495, 507  
 Hasegawa, 125, 267, 379  
 Hashimoto, 218, 391, 401, 408–410  
 Hatano, 267  
 Hatomura, 380  
 Haušlid, 315  
 Hausild, 323  
 Hawkins, 148  
 Hayakawa, 223, 506  
 Haydn, 339  
 Hayrynen, 344, 444, 446  
 Haze, 263  
 He BB, 89  
 He K, 263  
 He X, 235, 373  
 He XL, 373  
 He Y, 25, 231, 407  
 Heckel, 14  
 Hehemann, 18, 54, 64, 66, 68, 196, 204, 277, 303, 343, 361  
 Heisterkamp, 419  
 Heitmann, 422  
 Heldt, 342  
 Heller, 433  
 Hendry, 501  
 Hennesen, 324  
 Heritier, 422  
 Hermans, 57, 233, 416  
 Heselwood, 309  
 Hesheng, 336  
 Hidaka, 456  
 Higashi, 389  
 Hill, 472  
 Hillenbrand, 378  
 Hillert, 12, 28, 126, 149, 157  
 Hintz, 446  
 Hirai, 255  
 Hiraoka, 223  
 Hirose, 380  
 Hirota, 334  
 Hirotsu, 61  
 Hiroyuki, 320  
 Hirth, 310  
 Hisamatsu, 405  
 Hjelen, 259  
 Hobbs, 64  
 Hodgson, 27, 389, 407, 409, 433, 456, 474, 487  
 Hofer, 61  
 Hoffman, 429  
 Hoffmann, 440  
 Høglund, 126  
 Hoile, 223  
 Hojo, 342, 410  
 Hojo T, 405  
 Hokka, 412  
 Holloman, 90  
 Hollox, 340  
 Homma, 255, 266, 281  
 Honda, 56  
 Honeycombe, 54, 79, 179, 196, 228, 308, 368  
 Hong, 234  
 Hong JM, 179  
 Hong SG, 490  
 Hongo, 348, 349  
 Hono K, 71  
 Hori, 389  
 Horii, 254, 262, 275  
 Horita, 457  
 Horiuchi, 168  
 Horn, 315, 323  
 Hornak, 234  
 Hornbogen, 234  
 Horsley, 313  
 Hoshino, 115  
 Hosoya, 125, 401  
 Hosseini, 384  
 Hou TP, 495  
 Houbart, 390  
 Houillier, 70  
 Howard, 12, 160, 213  
 Howe, 457  
 Hozweissig, 215  
 Hsu TY, 499  
 Hsui IC, 450  
 Hu F, 21, 32, 425, 474, 495  
 Hua MJ, 359  
 Huang, 66, 213, 495  
 Huang CY, 474  
 Huang J, 391, 495  
 Huang M, 308, 432  
 Huang MX, 89  
 Huh H, 412  
 Huh J, 412  
 Hui GP, 344  
 Huizenga, 57, 233  
 Hulka, 382, 384, 419, 421  
 Hull, 48  
 Hulme-Smith, 57, 92  
 Hultgren, 10, 29, 83, 162  
 Hume-Rothery, 172  
 Hung FY, 450  
 Huvar, 444  
 Ichikawa, 169  
 Ichinose, 435  
 Idoyaga, 284  
 Igarashi, 353  
 Ikeda, 342, 391, 405, 409, 410  
 Imagumbai, 255  
 Inagaki, 320  
 Inagawa, 252  
 Inazumi, 401

- Inoue, 218, 260  
Irie, 348, 349  
Irvine, 14, 64, 89, 90, 100, 306, 307, 317  
Ishikawa, 178, 263  
Ishugiro, 351  
Islam, 325  
Islam:2005, 325  
Isobe, 405  
Isoda, 334  
Issler, 339  
Ito, 254  
Iung, 178  
Ivantsov, 158  
Iwai, 313, 389  
Iwamoto, 501  
Iwanaga, 379
- Jabbar, 460  
Jack, 61  
Jacques, 25, 39, 125, 226, 231, 387, 390, 397, 401, 407, 465, 467  
Jaffee, 324  
James, 125, 181  
James JS, 446  
Jana, 26  
Jang JH, 71  
Jaramillo, 474, 495  
Jellinghaus, 213, 290, 440  
Jepson, 213, 215  
Jiang Y, 361  
Jiao D, 501  
Jihua, 499  
Jin N, 437  
Jin XI, 27, 495  
Jing C, 404  
Jingsheng, 179  
Jingxin, 336  
Johansson, 495  
Johnson, 162  
Johnson, DL, 313  
Jonas, 226, 231, 375, 384, 407  
Jones, 90  
Jones BL, 313, 421  
Jones CL, 351  
Jones, R, 169  
Joo MS, 317, 375, 507  
Josefsson, 27, 38, 101  
Josephic, 342  
Judson, 266  
Jullien, 364  
Jung G, 416  
Jung JH, 212  
Jung YC, 51, 66
- Kajiwara, 53  
Kakeshita, 503  
Kalish, 429  
Kallend, 376  
Kalousek, 433  
Kaltzakorta, 284  
Kamada, 307  
Kame, 389  
Kandaka, 412, 426  
Kaneko, 105  
Kang KB, 375  
Kang M, 7  
Kang MK, 64  
Kang Y, 24  
Kannan, 487  
Kaputkin, 93  
Kaputkina, 93  
Kar, 274, 323  
Karapetrova, 7  
Karlik, 323  
Karlsson, 223, 293, 296  
Karuklis, 263  
Kashima, 391, 408, 410  
Kaspar, 249  
Kasuya, 169  
Katamine, 266  
Kato, 259, 405  
Katsumoto, 334  
Kaufman, 458  
Kawata, 40  
Kazinczy, 179  
Kazum, 487  
Keehan, 297  
Keehan:2005, 293  
Keh, 304  
Kehl, 215  
Kehoe, 71  
Kelley, 274, 346  
Kelly, 20, 71, 76, 474  
Kelly, PM, 309  
Kendig, 304  
Keniti, 419  
Kennon, 44, 172, 310  
Keown, 266  
Kerr, 259, 343  
Kesten, 332  
Kestens, 317, 375  
Kettunen, 311, 329  
Khan, 183  
Khare, 178  
Khlebnikova, 435  
Khoddam, 487  
Kiani-Rashid, 444  
Kijima, 503  
Kikuchi, 53, 410  
Kikuma, 389  
Killmore, 384  
Kim BK, 226  
Kim C, 500  
Kim DI, 410  
Kim G, 393  
Kim HS, 212  
Kim IG, 71  
Kim SJ, 216, 220, 389, 404  
Kimmins, 247  
Kimura, 112, 346, 348, 349, 456  
Kinderman, 361  
King, 33, 233

- Kinsman, 31  
 Kinugawa, 348, 349  
 Kirkaldy, 28, 183, 244, 266, 409  
 Kisner, 474  
 Kitada, 334  
 Kitano, 125, 328  
 Kizu, 401  
 Klier, 6, 289  
 Klinger, 361  
 Klobčar, 226  
 Klueh, 274, 351, 358  
 Klug, 446  
 Kluken, 259, 262, 266  
 Kmoatsubara, 166  
 Knittle, 500  
 Knott, 266, 310, 319, 320, 325  
 Knowles, 53, 507  
 Ko, 12, 13, 64  
 Kobayashi, 190, 317, 401, 408, 412, 426  
 Kocks, 311, 329  
 Koczurkiewicz, 495  
 Kogan, 83, 213, 435  
 Koistinen, 185  
 Kokabi, 384  
 Kolbeinsen, 283  
 Kolmogorov, 162  
 Kolobylin, 435  
 Komai, 353  
 Komizo, 254  
 Konda, 334  
 Kondo, 334  
 Konoval, 61  
 Koo M, 7  
 Koo MS, 495  
 Korenko, 20  
 Koseki, 259, 260, 285  
 Koshizuka, 266, 307  
 Kosuri, 482  
 Kovalevskaya, 287  
 Koyama, 388  
 Koyano, 501  
 Kozasu, 351  
 Kozeschnik, 72, 90, 187, 228  
 Krahe, 322, 430  
 Krauss, 72, 312, 323, 325, 422  
 Kriesement, 13, 62  
 Krimmel, 32, 125  
 Krishnadev, 179, 280, 310  
 Kristan, 437  
 Krivoglaz, 503  
 Kruger, 432  
 Kruijver, 390, 407, 408  
 Kruse, 274, 346  
 Krystian, 234  
 Kubaschewski, 262  
 Kubo, 223  
 Kulakov, 440  
 Kulin, 164  
 Kumar A, 313, 404  
 Kund, 472  
 Kundu, 507  
 Kundu M, 469, 495  
 Kundu S, 40, 186, 216  
 Kunitake, 175, 323  
 Kuntz, 495  
 Kuokkala, 412, 469  
 Kurdjumov, 7, 33  
 Kuroki, 311  
 Kurosawa, 179  
 Kushida, 384  
 Kushima, 112, 346  
 Kutsov, 32, 70, 125  
 Kwon H, 410  
 Kwon O, 393  
 L, YH, 382  
 Lacroix, 387  
 Lai, 64  
 Lambers, 216, 231  
 Lambert-Perlade, 323  
 Lamesle, 72  
 Lan HF, 465, 495  
 Laneri, 134  
 Lange, 213, 440  
 Langer, 72  
 Langford, 308  
 Larn, 234  
 Lau, 267  
 Laufer, 433  
 Laverroux, 20  
 Law, 247  
 Lawryniewicz, 69, 70, 72, 197, 201  
 Lazzari, 344  
 Leak, 429  
 Leber, 419, 422  
 Lee BS, 134  
 Lee CG, 216, 220, 389  
 Lee CH, 134, 260, 280  
 Lee CS, 412  
 Lee DN, 261, 281  
 Lee HC, 280  
 Lee HG, 261  
 Lee HJ, 162  
 Lee HY, 313  
 Lee JB, 416  
 Lee JK, 179  
 Lee JL, 111, 269  
 Lee JS, 234, 490  
 Lee JY, 283  
 Lee KK, 313, 336, 446  
 Lee KY, 178, 416  
 Lee S, 220  
 Lee SY, 282  
 Lee TH, 220, 389  
 Lee TO, 216  
 Lee YK, 143, 179, 313  
 Leiro, 472, 482  
 Leont'yev, 287  
 Lepistö, 311  
 Leslie, 61, 275, 310  
 Levaillant, 72  
 Lewis, 3

- Li Y, 424  
Li HY, 27, 495  
Li JCM, 98  
Li L, 220, 390, 404, 405, 409  
Li X, 384  
Li XY, 482  
Li Y, 179, 193, 405  
Li Z, 361, 408, 495  
Liang P, 384  
Liebermann, 5, 42  
Lin JS, 495  
Lin M, 187, 368  
Lin WT, 474  
Lin ZW, 335  
Linaza, 282  
Lindley, 251, 323  
Little, 358  
Liu C, 143, 424  
Liu CC, 213  
Liu J, 79, 501  
Liu RD, 404  
Liu S, 373  
Liu TS, 310  
Liu W, 411  
Liu X, 234, 373  
Liu XH, 465, 495  
Liu XS, 490  
Liu Y, 143  
Liu YC, 72  
Liu Z, 213  
Lixing, 223  
Loison, 178  
Lolla, 432  
Lonardelli, 57, 92, 479, 495  
Londardelli, 91  
Lonsdale, 432  
Lopez, 280  
Lord, 71  
Lorimer, 64  
Louat, 334  
Lu D, 361  
Lu F, 495  
Lu GZ, 444, 450  
Lu J, 384  
Lubin, 226  
Ludtka, 474  
Luhan, 303  
Lui TS, 327, 450  
Lundin, 15, 175, 274, 346  
Luo CP, 79, 501  
Luo H, 407  
Luthy, 419, 421  
Lv B, 482  
Lyman, 6, 289, 306
- Ma E, 456  
Maalekian, 187, 228, 384  
Mabuchi, 264  
Mack, 172  
Mackenzie, 5, 42  
Mackiewicz-Ludtka, 474
- Maeda, 223  
Magee, 20, 40, 185, 309  
Mahajan, 228  
Mahieu, 405  
Mahnken, 224  
Maier, 213, 215, 216, 224, 228, 231  
Maines, 479, 495  
Maitrepierre, 422  
Makarov, 435  
Maki, 20, 40, 53, 71, 196, 240, 254, 277, 507  
Maki, J, 405  
Malecki, 160  
Mandal, 428  
Manna, 340  
Mao SX, 359  
Marburger, 185  
Marcu, 361  
Marder, 354  
Mari, 499  
Marschall, 343  
Martens, 401  
Mascanzoni, 318  
Masuda, 412  
Masumura, 388  
Masuyama, 353  
Matas, 64, 66, 68, 196  
Mateo, 32  
Mathieu, 213  
Mathon, 72  
Matlock, 68, 128, 251, 312, 416  
Matsuda, 125, 255, 263, 267, 281, 373  
Matsuda H, 144  
Matsumura, 105  
Matsuo, 179  
Matsuoka, 223, 340, 506  
Matsuzaki, 216, 226  
Matumoto, 334  
Maurickx, 409  
Mayer, 339  
Mayuzumi, 342  
Mazanec, 344  
Mazey, 358  
Mazzaferro, 297  
Mazzaferro, CCP, 296  
Mazzaferro, JAE, 296  
McCutcheon, 313  
McDougall, 33, 46  
McEvily, 309, 313  
McGrath, 274, 323  
McKeown, 266  
McMahan Jr., 325  
McMahon, 318  
Mebarki, 72  
Medina, 39  
Mediratta, 179  
Mehl, 3, 11, 12, 162  
Meier, 332  
Menapace, 479, 495  
Mendiratta, 323  
Menon, 274, 346  
Mertens, 390

- Mesplont, 178, 230  
 Metauer, 61  
 Meyer, 432  
 Meyer, 217  
 Miao, 266, 448  
 Miao Y, 452  
 Miihkinen, 66, 218  
 Mikami, 81  
 Miki, 223  
 Militzer, 384, 391  
 Miller, 15, 27, 84, 410  
 Mills, 259  
 Milosavljevic, 262  
 Mima, 351  
 Mimura, 255, 263  
 Mino, 432  
 Minote, 405  
 Mintz, 328  
 Mirabile, 318  
 Miracle, xvi, 304  
 Mirak, 361  
 Misra, 391  
 Mitchell, 112  
 Mittemeijer, 505  
 Miyajima, 53  
 Miyake, 409  
 Miyamoto, 27, 254, 507  
 Miyamoto G, 71, 430  
 Miyata, 328, 353, 354  
 Mochizuki, 405  
 Moeinifar, 384  
 Mogutnov, 71  
 Molinari, 91, 361, 479, 495  
 Moller, 324  
 Moon JO, 134  
 Moore, 444, 446  
 Mori T, 311  
 Mori, N, 266  
 Morikage, 223  
 Morikawa, 379  
 Morishima, 432  
 Moritani, 40, 53  
 Morito, 40  
 Mormiroli, 61  
 Morris PP, 376  
 Morrison, 179  
 Moss, 338  
 Mostert, 181  
 Muddle, 226  
 Mughrabi, 332  
 Mujahid, 160  
 Mukai Y, 405  
 Mukherjee, 193  
 Mundra, 252  
 Murakami, 325  
 Murakami T, 340  
 Murakami, T, 252  
 Murakami, Y, 351  
 Muramatsu, 410  
 Murata, 178  
 Murphy, 107, 348, 349  
 Muruganath, 293, 474  
 Musik, 178  
 Musterova, 444  
 Mutiu, 361  
 Mutui, 213  
 Myers, 350  
 Myszka, 451  
 Naderi, 307  
 Nagai K, 451  
 Nagakura, 61, 81  
 Nagasaka, 342, 408  
 Nagataki, 401  
 Nagumo, 178, 255  
 Nagy, 433  
 Nakada N, 501  
 Nakagura, 61  
 Nakai, 51  
 Nakajima, 379  
 Nakamura, 81, 84, 223  
 Nakanishi, 254  
 Nakao, 196  
 Nakashima, 113  
 Nakasugi, 373, 419  
 Nam, 99  
 Nambu, 260  
 Namura, 254, 262  
 Nanba, 252  
 Nanninga, 342  
 Naryanan, 432  
 Nath, 358  
 Navara, 495  
 Nawrocki, 354  
 Naylor, 23, 304, 308, 322  
 Nebal, 315  
 Nehrenberg, 247  
 Nembach, 304  
 Nemoto, 26  
 Nevalainen, 26, 38, 311  
 Nguyen, 223  
 Nicholson, 474  
 Nikura, 405  
 Nilan, 290  
 Nili-Ahmadabadi, 361  
 Nimura, 334  
 Nishioka, 280, 380  
 Nishiyama, 33, 56, 64  
 Noda, 358  
 Nohava, 323  
 Nolze, 33, 507  
 Norström, 27  
 North, 267  
 Northwood, 143  
 Novy, 234  
 Nutting, 20, 66, 101, 107, 349  
 O'Neill, 429  
 Oates, 328  
 Oberbillig, 178, 308  
 Oblak, 18, 54, 66  
 Ochi, 263

- Ode, 190  
 Odette, 351  
 Ogawa, 53, 377, 405  
 Oh CS, 216, 393, 404  
 Oh JC, 71  
 Oh KH, 410  
 Oh YJ, 261, 281, 282  
 Ohashi, 178  
 Ohhashi, 324  
 Ohkita, 254, 262  
 Ohmori, 45, 51, 54, 64, 76, 94, 196, 323  
 Ohnishi, 351  
 Ohta, 223  
 Ohtani, 323  
 Ohtsuka, 503  
 Oka, 53, 164, 172, 196  
 Okabayashi, 361  
 Okabe, 266  
 Okada, 413  
 Okaguchi, 179  
 Okamoto, 53, 164, 172, 196, 503  
 Okita, 266, 281  
 Okumura, 267  
 Oldland, 266  
 Olson DL, 272  
 Olson GB, 24, 36, 40, 46, 71, 81, 84, 90, 136, 160, 186, 187, 226, 315, 458  
 Omori, 501  
 Onink, 505  
 Ono Y, 430  
 Onoe, 379  
 Oriano, 342  
 Orr, 274, 323  
 Owen, 10, 36, 64, 166, 204, 387  
  
 Packan, 274  
 Padmanabhan, 297  
 Page, 350  
 Pak JH, 296, 297  
 Palkowski, 474  
 Palmiere, 422  
 Pan, 269, 283  
 Papadimitriou, 21, 458  
 Papaefthymiou, 220, 408  
 Parameswaran, 111  
 Pardoen, 397, 467  
 Pargeter, 251  
 Park, 100  
 Park KS, 125, 425  
 Park SH, 410  
 Parker, 109, 173, 226, 315, 323, 343, 351, 352  
 Patchett, 323  
 Patel, 208  
 Pati, 187  
 Pawelski, 249  
 Paxton, 1  
 Pedroche, 470  
 Peebles, 61  
 Peet, 7, 46, 57, 69, 92, 95, 304, 457, 461, 472, 495  
 Pei Y, 179  
 Pereloma, 27, 179, 288, 384, 389, 407, 410, 443  
  
 Perez, 125  
 Perlade, 40  
 Perry, 506  
 Pesci, 470  
 Petch, 328  
 Peters, 378  
 Petit-Grostabussiat, 364  
 Petrov, 317, 375  
 Peura, 412  
 Pfeil, 342  
 Pichl, 228, 234  
 Pichler, 393  
 Pickering, 21, 26, 64, 90, 100, 196, 306, 307, 317, 368  
 Pilkington, 103, 351  
 Pilling, 108, 348  
 Pineau, 20, 323  
 Pippard, 117  
 Pitsch, 75  
 Plichta, 78  
 Pocock, 226  
 Podder, 91, 389  
 Pokhodnya, 269, 344  
 Pomey, 61, 68  
 Poole, 391  
 Poorganji, 209  
 Popovic, 262  
 Portevin, 5  
 Pound, 289  
 Prabhu, 284  
 Prado, 7  
 Prael, 193  
 Prakash, 482  
 Prasad, 179  
 Preston, 433  
 Prioul, 315  
 Prokic-Cvetkovic, 262  
 Prokoshkin, 93  
 Pugno, 457  
 Purdy, 28, 173  
 Pussegoda, 313  
 Putatunda, 444, 446, 448, 452  
 Putman, 125, 446  
 Pyshmintsev, 217  
  
 Qian LH, 482  
 Qiao B, 448, 452  
 Qiao L, 495  
 Qiao LJ, 487  
 Qiao ZX, 72, 382  
 Qin RS, 186, 190, 193  
 Quarell, 89  
 Quidort, 22  
  
 Raabe, 84  
 Radcliffe, 164, 213, 498  
 Raghavan, 40  
 Raghunathan, 111  
 Ramazani, 193  
 Ramjaun, 223  
 Rancel, 39

- Rao BVN, 312  
 Rao PK, 284  
 Rashid, 312  
 Rasp, 249  
 Rathbun, 416  
 Ratnapuli, 343  
 Rauch, 310  
 Rawson, 472  
 Ray KK, 313, 404, 428  
 Ray RK, 375, 389  
 Rayment, 223  
 Ream, 433  
 Reed, 42, 446  
 Reed PAS, 313, 336  
 Reed RW, 224, 505  
 Reed TA, 5  
 Rees, 143, 167, 179, 409  
 Regle, 226  
 Reguly, 296  
 Reisdorf, 71  
 Reisingen, 193  
 Reisner, 225  
 Ren X, 495  
 Ren XC, 487  
 Reynolds, 324  
 Rice, 319  
 Richardson, 57, 233  
 Ridley, 64, 348  
 Rigsbee, 31  
 Ringer, 263, 389  
 Rios, 179  
 Ritchie, 109, 315, 319, 331, 332, 338, 343, 351  
 Rivera, 495  
 Rizzo, 128  
 Roberts, 68  
 Roberts, CS, 66  
 Roberts:1957, 64  
 Robertson, 3  
 Robino, 354  
 Robson, 90, 109, 169  
 Rochegude, 501  
 Rodriguez-Ibabe, 282, 324  
 Rodriguez-Martinez, 470  
 Roe, 368  
 Rofes-Vernis, 422  
 Rollason, 213, 498  
 Romano, 507  
 Romero, 282, 297  
 Ronn, 179  
 Rorvik, 266  
 Rosendo, 296  
 Rothwell, 313  
 Rouns, 444  
 Rudberg, 29  
 Rundman, 66, 327, 342, 444, 446  
 Ruoff, 457  
 Rusinek, 470  
 Russell, 7, 78, 410  
 Russell LG, 382  
 Ryan, 506  
 Ryntz, 67, 444  
 Ryu HB, 407  
 Sachdev, 67  
 Sachs, 33  
 Sadagopan, 432  
 Sadakata, 105  
 Sadananda, 334  
 Sadvovskii, 247, 503  
 Sadowski, 267  
 Saeed-Akbari, 307  
 Saeki, 179  
 Saito, 190, 235, 380, 456  
 Sakai, 339  
 Sakamoto, 40  
 Sakano, 334  
 Samajdar, 405  
 San-Nomiya, 266  
 Sanchez Morino, 317  
 Sandvik, 26, 34, 35, 38, 45, 54, 66, 311, 315  
 Santofimia, 22, 167, 297, 467  
 Sarikaya, 34  
 Sarma, 179  
 Sasaji, 379  
 Sasser, 323  
 Savray, 217  
 Sawley, 437  
 Schänzer, 304  
 Schaaber, 172  
 Schanck, 175  
 Schastlivtsev, 435  
 Schatz, 164  
 Scheil, 168  
 Schissler, 61  
 Schlesler, 193  
 Schmatz, 429  
 Schneidt, 224  
 Schrader, 70  
 Schroth, 128  
 Schuller, 339  
 Schwartz, 66  
 Schweitzer, 433  
 Scott, 70, 500, 506  
 Sears, 457  
 Sedmak, 262  
 Segal, 457  
 Sejnoha, 344  
 Semchyhsen, 309  
 Senior, 350  
 Senuma, 22  
 Seo SW, 299  
 Shackleton, 76  
 Shan, 359, 382  
 Shang, 235, 373  
 Shang C, 373  
 Shang CJ, 482  
 Shaposhnikov, 71  
 Shatansky, 51  
 Shroeder, 340  
 Shea, 67, 444  
 Shen, 368  
 Shendy, 472

- Shepperson, 444, 450  
 Sherif, 95, 495  
 Shewmon, 351  
 Shi TS, 218  
 Shi W, 220, 390, 404  
 Shibata, 313, 389, 507  
 Shieh, 310, 327  
 Shiflet, 162  
 Shiga, 223, 380  
 Shih, 187  
 Shim HH, 281  
 Shim JD, 261, 281  
 Shim JH, 261, 263  
 Shimizu, 64, 503  
 Shimizu M, 404  
 Shin CS, 337  
 Shinyoshi, 254  
 Shiori, 51  
 Shipway, 234, 482  
 Shirzadi, 216, 226, 495  
 Shively, 343  
 Shuchuan, 499  
 Shvachko, 269, 344  
 Shveykin, 217  
 Sidey, 350  
 Sidhu, 474  
 Sietsma, 57, 167, 390, 407, 408, 416  
 Sikka, 359  
 Simmons, 3  
 Simth, E, 320  
 Singh, 21, 166, 186, 313  
 Singh SB, 404  
 Siriwardene, 308  
 Smaill, 266  
 Smanio, 472, 482, 495  
 Smith DA, 53  
 Smith GDW, 27, 71, 85, 92  
 Smith GM, 25, 306  
 Smith GV, 3, 5, 11, 12  
 Smith JF, 324  
 Smith MF, 172  
 Solana, 343  
 Soliman, 474  
 Solomein, 435  
 Song EJ, 401, 405  
 Song KJ, 490  
 Song SM, 342, 412, 426  
 Song W, 84, 193  
 Song YY, 125, 425  
 Sorby, 1  
 Sourmail, 143, 472, 482, 495  
 Southworth, 324  
 Spanos, 162  
 Spasskiy, 34  
 Specht, 7, 69  
 Speer, 68, 128, 407, 416  
 Speich, 45, 79, 148, 290, 304, 373  
 Spencer, 109, 351, 352  
 Sreenivasan, 334  
 Srinivasan, 26, 35, 45, 64, 196  
 Stalheim, 382  
 Stark, 27, 92  
 Stejskai, 234  
 Stewart, 226  
 Stickels, 64, 341  
 Stokes, 313, 336  
 Stone, 7, 69  
 Stout, 378  
 Straffelini, 361  
 Strang, 102, 350  
 Strangwood, 253, 260, 277, 423  
 Stransky, 444  
 Streicher-Clarke, 68  
 Sturel, 323  
 Su TJ, 296  
 Su Y, 495  
 Su YH, 475  
 Su YJ, 487  
 Sudo, 313, 389  
 Sugimoto, 220, 342, 345, 391, 401, 405, 408–410, 412, 426  
 Suh, 187  
 Suh DW, 125, 186, 296, 299, 317, 325, 401, 404, 405, 413, 416, 425, 507  
 Suh JY, 261, 281  
 Sun, 64, 225  
 Sun WP, 384  
 Sundin, 482  
 Suresh, 338  
 Suzuki, 351  
 Suzuki H, 7  
 Suzuki T, 430  
 Suzuki, N, 223  
 Svensson, 272, 296  
 Swallow, 21, 25, 45, 46  
 Swararagi, 354  
 Swindeman, 351  
 Syckaert, 422  
 Szilva, 421  
 Szpunar, 226  
 Tabatchikova, 435  
 Tagawa, 328, 351  
 Takahashi, 22, 27, 167, 196, 197, 201, 263, 277, 505  
 Takaki, 25, 113, 456, 501  
 Takamatate, 343  
 Takamura, 267  
 Takashima, 235  
 Takehara, 435  
 Takita, 444  
 Talas, 284  
 Taleb, 364  
 Tamehiro, 178, 255, 280, 373, 376, 382, 389  
 Tamukai, 379  
 Tamura, 20, 166, 168, 179, 213, 215, 240, 311  
 Tan Z, 411  
 Tanaka, 179, 225, 266, 375, 379  
 Tang, 409  
 Tanigawa, 456  
 Taniguchi, 413  
 Taran, 32, 70, 125

- Tartaglia, 344  
 Tashiro, 388  
 Tau, 337  
 Taylor, 84, 226, 429  
 Teeri, 472  
 Terada, 389  
 Thewlis, 255, 259, 262, 285  
 Thielen, 332  
 Thomas, 34, 66, 429  
 Thompson AW, 343  
 Thompson FC, 213  
 Thompson MW, 359  
 Thompson SW, 72, 422  
 Thomson, 84, 106, 125, 226, 446  
 Thomson BA, 409  
 Tichelaar, 505  
 Tier, 296  
 Timokhina, 27, 389, 407, 410, 456, 487  
 Tkalcec, 499  
 Todd, 109, 274, 351, 352  
 Tomita, 361  
 Tomokiyo, 105  
 Tomota, 7, 311, 475, 495  
 Tomoto, 224  
 Torizuka, 405  
 Toshiyuki, 419  
 Traint, 393, 404  
 Tranell, 283  
 Traskine, 226  
 Trivedi, 144, 158  
 Troiano, 5, 303, 306, 342, 343, 361  
 Trumper, 313  
 Tsai, 111, 234, 352  
 Tsay, 335  
 Tschumak, 216, 224, 231  
 Tsipouridis, 393  
 Tsivinsky, 83  
 Tsubakino, 317, 343  
 Tsuchida, 224  
 Tsuchiyama, 113, 501  
 Tsuji, 235, 456  
 Tsukatani, 218, 313  
 Tsunekage, 317  
 Tsunetzawa, 410  
 Tsutsumi, 259  
 Tsuya, 45  
 Tsuzaki, 196, 213, 240, 429, 430, 506  
 Tuncer, 500  
 Turnbull, 117  
 Tweed, 320
- Ubhi, 216  
 Ueda, 178, 435, 444  
 Uemori, 178, 254, 264  
 Ueshima, 264  
 Uhm SG, 134  
 Umemoto, 166, 168, 179, 213, 215  
 Umeno, 379  
 Urabe, 125  
 Urban, 432  
 Urcola, 282
- Uslu, 216  
 Utevsky, 34  
 Utsunomiya, 456  
 Uzlov, 32, 70, 125
- Vagarali, 351  
 Valiev, 456  
 van Beek, 495  
 van Bohemen, 167, 173, 412, 416  
 van der Eijk, 283  
 van der Zwaag, 126, 407, 408, 505  
 van Humbeeck, 390, 401, 405  
 van Rooyen, 181  
 van Slycken, 412  
 Vander Sande, 84, 226  
 Vang, 495  
 Vasudevan, 334  
 Venugopalan, 99  
 Verleysen, 412  
 Verlinden, 376, 390, 401, 405  
 Vermeule, 217  
 Veters, 440  
 Victor, 433  
 Viella, 3  
 Vieugels, 404  
 Vilella, 5, 290  
 Vitek, 215, 224, 252, 274, 505  
 von Appen, 84  
 Vuorinen, 472, 482, 495
- Wada, 248, 351, 352  
 Wahnström, 56  
 Wakabayashi, 254, 262, 266  
 Wakasa, 34  
 Walley, 470  
 Walmsley, 259  
 Wan XL, 21, 425  
 Wang, 404  
 Wang B, 234  
 Wang C, 391, 409  
 Wang G, 234  
 Wang L, 220  
 Wang M, 495  
 Wang SC, 111  
 Wang TS, 472, 482  
 Wang W, 261, 373, 384  
 Wang X, 235, 373  
 Wang XL, 21, 425  
 Wang XM, 373  
 Wang Y, 456  
 Wang Z, 261, 404  
 Wang ZC, 389  
 Warlimont, 208, 304  
 Wasilkowska, 393  
 Wasserman, 33  
 Watanabe, 325, 348, 349, 351  
 Watson, 46  
 Waugh, 27  
 Wayman, 18, 26, 34, 45, 46, 51, 64, 79, 196, 226  
 Weatherly, 267  
 Wechsler, 5, 42

- Wei XC, 405  
Wei, DY, 336  
Wei, W, 324  
Weidig, 249  
Weissman, 304  
Wen, 225  
Wenyan, 336  
Werner, 225, 393  
Wessel, 487  
Wever, 5, 12, 62, 70  
White, 2, 172, 204, 421  
Whiteman, 259  
Wibowo, 416  
Wieczorek, 451  
Wiester, 12  
Wilgen, 474  
Wilkening, 382  
Williams, 389  
Williams JG, 384  
Williams Q, 500  
Williams WF, 389  
Williams WM, 309  
Williamson, 68  
Willoughby, 350  
Wilson, 51, 105  
Wilson, DV, 328  
Wilson, EA, 495  
Winchell, 72  
Wise, 407  
Withers, 69, 220, 226  
Wollants, 220, 390  
Wong, 432  
Woodhead, 89, 107  
Wright, 421  
Wu CZ, 218  
Wu D, 408  
Wu H, 409  
Wu K, 32  
Wu KM, 20, 21, 252, 425, 474, 495  
Wu NQ, 359  
Wu Y, 495
- Xiao FR, 382  
Xu P, 7  
Xu X, 234  
Xu Y, 503  
Xua P, 451
- Yagi, 112, 346  
Yajjima, 334  
Yakovleva, 435  
Yakubstov, 235  
Yakubstov, 173  
Yamada, 351  
Yamaguchi, 240, 254  
Yamamoto, 223, 263, 267, 281, 353  
Yamazaki, 348, 349  
Yan, 46  
Yan B, 432  
Yan JY, 72  
Yan P, 382
- Yan Z, 490  
Yan ZG, 482  
Yang JR, 352  
Yang CX, 220, 390  
Yang HS, 125, 186, 489  
Yang J, 472, 482  
Yang JG, 490  
Yang JR, 72, 111, 213, 234, 242, 253, 254, 277, 474  
Yang K, 382  
Yang QM, 64  
Yang S, 235, 373  
Yang SW, 373  
Yang ZG, 46, 336  
Yao, 213  
Yasuda, 223  
Yates, 437  
Yazdani, 472, 495  
Yen HW, 474  
Yi HL, 413, 432  
Yi KW, 282  
Yin F, 451  
Yokoyama, 353  
Yoon J, 134  
Yoozbashi, 472, 495  
Yoshizawa, 432  
Young CH, 361  
Youngs, 352  
Yu J, 66, 108, 325  
Yu L, 21, 425  
Yu LM, 72  
Yu Z, 503  
Yuan Y, 235  
Yue, 409  
Yutori, 377
- Zackay, 173, 315, 323, 343  
Zadra, 495  
Zadvorkin, 435  
Zaefferer, 404, 507  
Zaera, 470  
Zahiri, 443  
Zarei-Hanzaki, 409  
Zener, 9, 13  
Zeng X, 384  
Zenitani, 223  
Zhang B, 472  
Zhang C, 46, 495  
Zhang F, 405  
Zhang FC, 472, 482  
Zhang H, 411, 444, 450  
Zhang J, 391, 409  
Zhang K, 495  
Zhang M, 404, 482  
Zhang MX, 75  
Zhang P, 482  
Zhang WZ, 72  
Zhao D, 490  
Zhao L, 126, 390, 407, 408, 416  
Zhao MC, 382  
Zhao SX, 9

Zhao Z, 143, 424  
Zheng H, 495  
Zheng RK, 389  
Zhou J, 313  
Zhou R, 361  
Zhou RF, 361  
Zhu K, 89, 126, 167, 178, 308  
Zhu Y, 456  
Zhuo, 261  
Ziegler, 472  
Zoch, 340, 440  
Zongsen, 179  
Zrnik, 234  
Zschack, 7  
Zwell, 61

## Subject index

- $\beta$ -iron, 2
- $\chi$ -carbide, 68, 81, 83
- $\eta$ -carbide, 67, 81
- $\kappa$ -carbide, 68
- $\varepsilon$ -carbide, 64, 205
- Interfacial structure
  - atomic steps, 52
- Accelerated cooling
  - two-stage, 380
- Accommodation, 36
  - elastic, 25
  - plastic, 20
- Acicular ferrite
  - $\gamma$  grain size, 254
  - atom probe data, 253
  - depletion zones, 261
  - diffusionless growth, 254
  - dislocation density, 252
  - hardenability effects, 275
  - inclusions, 258
  - inoculated steels, 280
  - intragranular nucleation, 252
  - lower  $\alpha_a$ , 278
  - nucleation mechanism, 256
  - orientation relationship, 254
  - shape, 251
  - shape deformation, 252
  - steelmaking, 283
  - stress-induced, 278
  - thermodynamics, 254
- Acoustic emissions, 149
  - speed of sound, 500
- Additivity rule, 168
- ADI
  - fatigue, 446
  - high aluminium, 444
  - large strain-rates, 451
- Armour, 433, 470
- Atomic force microscopy, 506
- Ausforming, 230
  - bainite block size, 40
- Austempered ductile iron
  - austemperability, 443
  - heat treatment, 445
  - segregation, 447, 448
  - toughness, 448
- Austenitisation, 240
  - $\theta + \alpha$ , 247
  - anisothermal, 247
  - hysteresis, 240
  - kinetics, 244
  - parabolic thickening, 245
  - rapid heating, 249
  - thermodynamics, 242
- Autocatalysis, 40, 165, 187
- Autotempering, 204
- Bain strain, 42
- Bainite
  - crystallographic theory, 44
  - excess carbon, 32
  - nonferrous, 15
- Bainite-start temperature, 141, 142
  - neural network, 143
- Bainitic ferrite
  - bimodal, 21, 24, 235, 293, 425, 458
  - decarburisation, 154
  - tetragonal, 57
- Bake hardening, 389
- Banding, 183
- Bauschinger effect, 309
- Bearing steels, 340
  - rolling contact fatigue, 340
  - white matter, 341
- Boron, 14, 176, 178, 367, 474
- Burst transformation, 40
- Capillarity, 147
- Carbides
  - $\varepsilon$ -carbide, 450
  - Bagaryatskii orientation, 75
  - cementite kinetics, 197
  - coarsening, 98
  - composition change, 103, 111
  - crystal structure, 61
  - Isaichev orientation, 75
  - Pitsch orientation, 75
  - precipitation kinetics, 70, 72
  - shape deformation, 226
  - stress induced, 226
  - thermodynamics, 62
  - three-phase crystallography, 76
- Carbon
  - nonuniform distribution, 68, 193, 448
  - partitioning, 68, 153, 196, 197, 463
  - sampling volume, 68
- Carbon-free alloys, 495
- Cast steel, 452
- CCT diagrams, 173
- Cementite
  - precipitation kinetics, 197
  - silicon solubility, 71
- Characterisation
  - atomic force microscopy, 506
  - dilatometry, 505
  - Electron backscatter diffraction, 507
  - hardness, 505
  - Kernel average misorientation, 507
  - optical microscopy, 505
  - X-ray diffraction, 506
- Chemical potential, 118
- Chemical segregation, 183

- Classification, 14
- Coalesced bainite, 293
- Columnar bainite, 290
- Copper precipitates, 113
- Creep resistant, 15, 345
  - alloy types, 346
  - heat treatment, 348
- Crystallography
  - bainite lath, 54
  - block size, 39, 40
  - grain size, 40
  - lattice-invariant deformation, 53
  - misorientations, 34, 231
  - orientation spread, 231
  - packet size, 40
  - theory of martensite, 42
- Curie temperature, 2
- Discovery, 3
- Dislocation density, 25
  - acicular ferrite, 253
  - quantitative estimation, 27
- Displacive transformation, 51
- Dual phase
  - bainitic, 313, 389
  - buildings, 389
  - yield ratio, 389
- Ductility, 313
  - void formation, 313
  - void linking, 314
- Ductility:retained austenite, 314
- Electrical resistance, 497
- Fatigue
  - bending, 472
  - crack-branching, 472
  - gigacycle tests, 338
  - nanostructured bainite, 472
  - push-pull, 472
  - rolling contact fatigue, 339
  - rotating-bending, 472
- Flash processing, 432
- Forging steels, 423
- Formability, 387
- Galvanising
  - TRIP steels, 405
- Gibbs-Thompson effect, 147
- Granular bainite, 287
  - crystallography, 288
- Growth
  - diffusion controlled, 144
  - diffusion field, 158
  - dissipations, 158
  - elastic waves, 149
  - interface controlled, 144
  - lengthening, 144
  - measured rate, 148
  - needle, 144
  - of sheaf, 148
  - partial supersaturation, 154, 160
  - plates, 144
  - solute trapping, 144
  - stability, 155
  - sub-units, 148
  - thermoelastic equilibrium, 149
  - thickening, 149
- Growth rate, 144
- Habit plane
  - sheaf, 45
- Hardness, 306
  - mapping, 307
  - microhardness, 306
- History, 1
- Hydroforming, 217
- Hydrogen
  - delayed fracture, 344
  - structural refinement, 502
- Hydrogen embrittlement, 342
- Hydrostatic pressure, 217
- Interface
  - relaxation, 53
  - required coherency, 42
  - structure, 53
- Interface mobility
  - glissile, 157
  - reaction rate theory, 157
- Interfacial structure, 51, 52
  - coherency dislocations, 52
- Internal friction, 498, 499
- Interstitial atoms
  - interstices, 56
- Interstitial atoms
  - octahedral interstices, 56
  - partitioning, 51
  - tetrahedral interstices, 56
- Invariant line strain, 42
- Invariant plane strain, 49
- Inverse bainite, 289
- Kinetics
  - austenite grain size, 167
- Lath
  - growth direction, 54
  - size, 21
- Lattice correspondence, 49, 51
- Lattice-invariant deformation, 43
- Ledge mechanism
  - superledges, 52
- Lower bainite, 13, 196
  - transition from upper bainite, 195, 201
- Magnetic field effects, 503
  - nanostructured bainite, 474
- Martensite
  - crystallography, 43
  - isothermal, 173
  - nucleation, 187

- strain-induced, 220
  - tempered, 204
- Massive ferrite, 514
- Mechanical driving force, 208
- Mechanical stabilisation, 228, 407
  - heterogeneous deformation, 234
  - recovered austenite, 235
  - theory, 228
- Mechanisms of transformation, 512
- Microalloyed steels
  - niobium carbo-nitride, 235
- Midrib, 58
- Military transformation, 5
- Nanoindentation, 89, 465, 482
- Nanostructure, 457
  - bainite, 457
  - case hardening, 477
  - corrosion, 487
  - dislocation density, 27
  - fatigue, 472
  - laser cladding, 477
  - magnetic field effects, 474
  - non-uniform carbon distribution, 69
  - powder metallurgy, 477, 479
  - spark plasma sintered, 477, 479
  - surface relief, 461
  - synchrotron experiments, 69
  - tempering, 95
  - welding, 490
  - wire, 457
  - work hardening, 460
- Niobium, 345, 382
  - and boron, 178
  - hardenability, 179
  - interfacial energy, 181
  - mechanism, 179
  - TRIP-assisted steel, 179, 409
- Nitrogen
  - bainite in Fe-N, 501
- NP-LE, 28
- Nucleation, 40
  - activation energy, 141
  - dislocation dissociation, 138
  - displacive transformations, 136
  - evolution, 135
  - mechanism, 138
  - quantitative theory, 141
  - rate, 143
  - two  $W_S$  temperatures, 137
  - universal function, 134
- Orientation relationship, 33
- Orientation relationships
  - Bain region, 514
- Overall transformation kinetics, 162
  - simultaneous reactions, 169
- P-LE, 28
- Paraequilibrium, 28, 29, 120
  - solute trapping, 120
- Partitioning
  - atom probe, 27
- Pearlite, 368
  - cooperative growth, 12
  - non-cooperative growth, 299
  - spiky, 299
- Phase field simulation, 190
- Photoemission electron microscopy, 148
- Pipe steel, 313
- Plastic deformation
  - displacive transformation, 207
  - mechanical twinning, 207
  - slip, 207
- Portevin-Le Chatelier effect, 310
- Proof strength/UTS ratio, 310
- Quench and partitioning, 68, 128, 391
  - triplex microstructure, 411
- Rails
  - carbide-free, 436, 437
  - rolling contact fatigue, 437
  - wear rate, 437
  - wheels, 437
- Rare earth elements, 176
- Reconstructive diffusion, 28, 514
- Reconstructive transformation, 207
- Reduced activation steels, 358
- Residual stress, 220, 499
- Retained austenite
  - ADI, 446
  - blocky, 21, 91, 218, 315, 411, 424
  - film, 91
  - mechanical stability, 218
  - thermal stability, 91, 390
  - X-ray diffraction, 506
- Secondary ferrite, 63
- Secondary hardening
  - kinetics, 170
- Segregation, 382
- Severe plastic deformation, 456
- Shape deformation, 21
- Sheaf, 18
  - fractal dimension, 24
  - morphology, 18
  - phase field simulation, 193
- Snoek-Köster, 499
- Solute drag, 150, 181
- Solute trapping, 158
- Spinodal, 7, 289
- Spring steel, 430
- Stereology, 23
- Stored energy, 120
  - bainite, 136
  - martensite, 136
  - Widmanstätten ferrite, 136
- Strain energy, 48
- Strength
  - $\gamma$  grain size, 308
  - components, 306

- Hall-Petch, 308
- heterogeneous, 311
- Langford-Cohen, 308
- non-linear summation, 304
- solid solution, 306
- strength differential, 309
- tensile, 307
- transformation temperature, 309
- yield to UTS ratio, 313
- Strength:effect of tempering, 308
- Stress-induced
  - externally applied stress, 212
  - internally generated stress, 213
  - variant selection, 216
- Sub-units
  - bimodal, 21
  - habit plane, 54
  - mechanism, 18
  - morphology, 18
  - phase field simulation, 193
  - thickness, 21
- Sulphur, 176
- Superhadenability, 181
- Surface relief, 21, 45
  - acicular ferrite, 252, 253
  - carbides, 79
  - cementite, 72
  - nanostructured bainite, 461
  - Nomraski contrast, 35
  - plastic accommodation, 46
  - reconstructive diffusion, 28
  - shear, 46
  - twin displacement, 35
  - virtual operations, 49
- Tempering, 87
  - austenite decomposition, 93
  - autotempering, 89
  - precipitation sequence, 106
  - remanent life, 102
  - secondary hardening, 89, 99
  - tempering parameters, 90
- Thermomechanical processing
  - finish temperature, 379
- Thermal expansion, 57
- Thermodynamics, 9
  - $B_S$  temperature, 132
  - $W_S$  temperature, 132
  - nucleation, 131
  - stored energy, 458
- Thermomechanical processing, 379
- Thin plate martensite, 59
- Toughness
  - Charpy test, 315
  - cleavage path, 323
  - crystallography, 323
  - ductile-brittle transition, 315
  - microstructural interpretation, 319
- Toughness:fracture mechanics, 318
- Transformation plasticity
  - anisotropic strain, 224
- TRIP, 225
- TRIP-assisted, 389
  - $\delta$ -TRIP, 413, 416
  - $\delta$ -TRIP weld, 416
  - anisotropy, 393
  - fatigue strength, 412
  - fayalite, 405
  - galvannealing, 405
  - hydrogen, 405
  - initial structure, 391
  - microalloying, 408
  - phosphorus, 404
  - strain rate, 469
  - strain-induced, 220
  - strain-rate sensitivity, 411
  - stress-induced, 212
  - thermomechanical processing, 407, 408
  - welding, 416
- TTT diagrams, 134, 171
- Universal nucleation function, 134
- Upper bainite, 13, 196
- Upper to lower bainite transition, 196
- Variant selection, 225
  - active variants, 216
  - coalesced bainite, 296
  - plastic strain, 226
- Wear
  - abrasive, 448
  - cast iron, 450
  - erosion, 450
  - mixed microstructures, 451
  - precipitation, 450
  - rolling-sliding, 482
- Weldability, 496
  - carbon equivalent, 496
- Widmanstätten ferrite, 134, 509
  - shear strain, 46
- X80 pipe steel, 382
- Zener ordering, 514

# BRADSHAW BRAINSTEIN STREETS

THIRD  
EDITION

B0819



Maney

# BAINITE IN STEELS 3rd edn

by H. K. D. H. Bhadeshia

---

This is the third edition of the book, much expanded to include and incorporate important developments in the subject over the last fifteen years. The book represents a comprehensive treatise on all aspects of the bainite transformation, from the choreography of atoms during the phase change to length scales that are typical of engineering applications. The alloy design that emerges from this explains the role of solute additions, and the pernicious effects of impurities such as hydrogen. The picture presented is self-consistent and therefore is able to guide the reader on the exploitation of theory to the design of some of the most exciting steels, including the world's first bulk nanostructured metal.

